

Yong Yuan  
Junzhi Cui  
Herbert A. Mang  
*Editors*

# Computational Structural Engineering

 Springer

# Computational Structural Engineering

*“This page left intentionally blank.”*

Yong Yuan • Junzhi Cui • Herbert A. Mang

Editors

# Computational Structural Engineering

Proceedings of the International Symposium on  
Computational Structural Engineering, held in  
Shanghai, China, June 22–24, 2009

Organisers



Tongji University  
Chinese Academy of Engineering  
Vienna University of Technology

 Springer

*Editors*

Yong Yuan  
Tongji University  
Shanghai  
China

Junzhi Cui  
Academy of Mathematics  
and System Sciences  
Beijing, China

Herbert A. Mang  
Vienna University of Technology  
Austria

ISBN-13: 978-90-481-2821-1      e-ISBN-13: 978-90-481-2822-8  
Springer Dordrecht Heidelberg London New York

Library of Congress Control Number: 2009928775

© 2009 Springer Science+Business Media, B.V.

No part of this work may be reproduced, stored in a retrieval system, or transmitted in any form or by any means, electronic, mechanical, photocopying, microfilming, recording or otherwise, without written permission from the Publisher, with the exception of any material supplied specifically for the purpose of being entered and executed on a computer system, for exclusive use by the purchaser of the work.

Printed on acid-free paper

9 8 7 6 5 4 3 2 1

springer.com

# Table of Contents

Preface	xix
International Advisory Committee	xxi
Scientific Committee	xxiii
Organizing Committee	xxv
Supporting Organizations and Sponsors	xxvii

## Invited Papers

Computational Multi-Scale Methods and Evolving Discontinuities <i>René de Borst</i>	3
Damage Cumulation Analysis of Welded Joints under Low Cycle Loadings <i>Zuyan Shen and Aihui Wu</i>	11
Ageing Degradation of Concrete Dams Based on Damage Mechanics Concepts <i>Somasundaram Valliappan and Calvin Chee</i>	21
Multi-Scale and Multi-Thermo-Mechanical Modeling of Cementitious Composites for Performance Assessment of Reinforced Concrete Infrastructures <i>Koichi Maekawa</i>	37
Statistical Multi-Scale Method of Mechanics Parameter Prediction for Rock Mass with Random Cracks/Joints Distribution <i>J.Z. Cui, Fei Han and Y.J. Shan</i>	49
Computational Simulation Methods for Composites Reinforced by Fibres <i>Vladimír Kompiš, Zuzana Murčínková, Sergey Rjasanow, Richards Grzhibovskis and Qing-Hua Qin</i>	63
Underground Structures under Fire – From Material Modeling of Concrete under Combined Thermal and Mechanical Loading to Structural Safety Assessment <i>Thomas Ring, Matthias Zeiml and Roman Lackner</i>	71

Computational Multiscale Approach to the Mechanical Behavior and Transport Behavior of Wood <i>K. Hofstetter, J. Eitelberger, T.K. Bader, Ch. Hellmich and J. Eberhardsteiner</i>	79
The Finite Cell Method: High Order Simulation of Complex Structures without Meshing <i>Ernst Rank, Alexander Düster, Dominik Schillinger and Zhengxiong Yang</i>	87
Theoretical Model and Method for Self-Excited Aerodynamic Forces of Long-Span Bridges <i>Yaojun Ge and Haifan Xiang</i>	93
<b>Structural Stability</b>	
Imperfection Sensitivity or Insensitivity of Zero-Stiffness Postbuckling ... That Is the Question <i>Xin Jia, Gerhard Hoefinger and Herbert A. Mang</i>	103
A Step towards a Realistic Probabilistic Analysis of Buckling Loads of Bridges <i>Ahmed Manar, Kiyohiro Ikeda, Toshiyuki Kitada and Masahide Matsumura</i>	111
Parametric Resonance of the Free Hanging Marine Risers in Ultra-Deep Water Depths <i>Hezhen Yang and Huajun Li</i>	119
Simulation of Structural Collapse with Coupled Finite Element-Discrete Element Method <i>Xinzheng Lu, Xuchuan Lin and Lieping Ye</i>	127
Tunnel Stability against Uplift Single Fluid Grout <i>Fangqin Yang, Jiaxiang Lin, Yong Yuan and Chunlong Yu</i>	137
Effects of Concentrated Initial Stresses on Global Buckling of Plates <i>A.Y.T. Leung and Jie Fan</i>	145
Application of a Thin-Walled Structure Theory in Dynamic Stability of Steel Radial Gates <i>Zhiguo Niu and Shaowei Hu</i>	153
Research on the Difference between the Linear and Nonlinear Analysis of a Wing Structure <i>Ke Liang and Qin Sun</i>	159

A New Slice Method for Seismic Stability Analysis of Reinforced Retaining Wall <i>Jiangqing Jiang and Guolin Yang</i>	167
Hysteretic Response and Energy Dissipation of Double-Tube Buckling Restrained Braces with Contact Ring <i>Zhanzhong Yin, Xiuli Wang and Xiaodong Li</i>	173
<b>Seismic Engineering</b>	
Numerical Simulation and Analysis for Collapse Responses of RC Frame Structures under Earthquake <i>Fuwen Zhang, Xilin Lu and Chao Yin</i>	183
High-Order Spring-Dashpot-Mass Boundaries for Cylindrical Waves <i>Xiuli Du and Mi Zhao</i>	193
Unified Formulation for Real Time Dynamic Hybrid Testing <i>Xiaoyun Shao and Andrei M. Reinhorn</i>	201
Research on Seismic Response Reduction of Self-Anchored Suspension Bridge <i>Meng Jiang, Wenliang Qiu and Baochu Yu</i>	209
Seismic Response of Shot Span Bridge under Three Different Patterns of Earthquake Excitations <i>Daochuan Zhou, Guorong Chen and Yan Lu</i>	217
Seismic Response Analysis on a Steel-Concrete Hybrid Structure <i>Zeliang Yao and Guoliang Bai</i>	227
Seismic Behavior and Structural Type Effect of Steel Box Tied Arch Bridge <i>Jin Gan, Weiguo Wu and Hongxu Wang</i>	235
The Seismic Behavior Analysis of Steel Column-Tree Web Connection with Bolted-Splicing <i>Yuping Sun and Liping Nie</i>	243
Direct Displacement-Based Seismic Design Method of High-Rise Buildings Considering Higher Mode Effects <i>Xiaoling Cui, Xingwen Liang and Li Xin</i>	253
Rotational Components of Seismic Waves and Its Influence to the Seismic Response of Specially-Shaped Column Structure <i>Xiangshang Chen, Dongqiang Xu and Junhua Zhang</i>	267

Seismic Assessment for a Subway Station Reconstructed within High-Rise Building <i>Zhengkun Lin, Zhiyi Chen and Yong Yuan</i>	273
A Simplified Method for Estimating Target Displacement of Pile-Supported Wharf under Response Spectrum Seismic Loading <i>Pham Ngoc Thach and Shen Yang</i>	281
The Fractal Dimensionality of Seismic Wave <i>Lu Yu and Zujun Zou</i>	291
Chaotic Time Series Analysis of Near-Fault Ground Motions and Structural Seismic Responses <i>Dixiong Yang and Pixin Yang</i>	301
Parameters Observation of Spatial Variation Ground Motion <i>Yanli Shen, Qingshan Yang and Lingyan Xuan</i>	309
Inelastic Response Spectra for Bi-directional Earthquake Motions <i>Feng Wang</i>	319
Seismic Dynamic Reliability Analysis of Gravity Dam <i>Xiaochun Lu and Bin Tian</i>	331
Application of Iterative Computing of Two-Way Coupling Technique in Dynamic Analysis of Sonla Concrete Gravity Dam <i>Trinh Quoc Cong and LiaoJun Zhang</i>	341
Full 3D Numerical Simulation Method and Its Application to Seismic Response Analysis of Water-Conveyance Tunnel <i>Haitao Yu, Yong Yuan, Zhiyi Chen, Guanxi Yu and Yun Gu</i>	349

### **Dynamic Interactions**

Comparison of Different-Ordered Polynomial Acceleration Methods <i>Changqing Li and Menglin Lou</i>	361
An Effective Approach for Vibration Analysis of Beam with Arbitrary Sections <i>Shuang Li, Changhai Zhai, Hongbo Liu and Lili Xie</i>	375
Analyses on Vortex-Induced Vibration with Consideration of Streamwise Degree of Freedom <i>Changjiang He, Zhongdong Duan and Jinping Ou</i>	383

Equivalent Static Loading for Ship-Collision Design of Bridges Based on Numerical Simulations <i>Junjie Wang and Cheng Chen</i>	391
Signature Turbulence Effect on Buffeting Response of a Long-Span Bridge with a Centrally-Slotted Box Deck <i>Ledong Zhu, Chuanliang Zhao, Shuibing Wen and Quanshun Ding</i>	399
Simulation of Flow around Truss Girder with Extended Lattice Boltzmann Equation <i>Tiancheng Liu, Gao Liu, Hongbo Wu, Yaojun Ge and Fengchan Cao</i>	411
Computational Comparison of DES and LES in Channel Flow Simulation <i>Zhigang Wei and Yaojun Ge</i>	417
A Micro-Plane Model for Reinforced Concrete under Static and Dynamic Loadings <i>Junjie Wang, Bifeng Ou, Wei Cheng and Mingxiao Jia</i>	425
Behavior Optimization of Flexible Guardrail Based on Numerical Simulation <i>Peng Zhang, Deyuan Zhou and Yingpan Feng</i>	435
A Stochastic Finite Element Model with Non-Gaussian Properties for Bridge-Vehicle Interaction Problem <i>S.Q. Wu and S.S. Law</i>	445
Numerical Analysis on Dynamic Interaction of Mega-Frame-Raft Foundation-Sand Gravel Soil Structure <i>Bin Jia, Ruheng Wang, Wen Guo and Chuntao Zhang</i>	453
<b>Fluid and Structures</b>	
Structural Static Performance of Cable-Stayed Bridges with Super Long Spans <i>Jinxin Cao, Yaojun Ge and Yongxin Yang</i>	461
Parametric Oscillation of Cables and Aerodynamic Effect <i>Yong Xia, Jing Zhang and Youlin Xu</i>	469
CFD Numerical Simulation of Vortex-Induced Vibration of a Stay Cable under a Wind Profile <i>Wenli Chen and Hui Li</i>	477

Aerodynamic Interference Effect between Large Wind Turbine Blade and Tower <i>Nianxin Ren and Jinping Ou</i>	489
Windborne Debris Damage Prediction Analysis <i>Fangfang Song and Jinping Ou</i>	497
Engineering Characteristics Analysis of Typhoon Wind Field Based on a Mesoscale Model <i>Xing Tang and JinPing Ou</i>	505
Geometrical Nonlinearity Analysis of Wind Turbine Blade Subjected to Extreme Wind Loads <i>Guoqing Yuan and Yu Chen</i>	521
Dynamic Response and Reliability Analysis of Wind-Excited Structures <i>Zhangjun Liu and Jie Li</i>	529
Wind-Induced Self-Excited Vibration of Flexible Structures <i>Tingting Liu, Wenshou Zhang, Qianjin Yue and Jiahao Lin</i>	537
Evaluation of Strength and Local Buckling for Cooling Tower with Gas Flue <i>Shitang Ke, Yaojun Ge and Lin Zhao</i>	545
Numerical Study on Vortex Induced Vibrations of Four Cylinders in an In-Line Square Configuration <i>Feng Xu, Jinping Ou and Yiqing Xiao</i>	553
Dynamic Response Analysis of TLP's Tendon in Current Loads <i>Gongwei Yan, Feng Xu, Hang Zhu and Jinping Ou</i>	569
Flutter Performance and Surrounding Flow Structures of Central-Slotted Box Girders <i>Yongxin Yang, Yaojun Ge and Wei Zhang</i>	577
Dynamic Analysis of Fluid-Structure Interaction on Cantilever Structure <i>Jixing Yang, Fan Lei and Xizhen Xie</i>	587

### **Mechanical Modeling of Wood and Wood Products**

A Computational Approach for the Stress Analysis of Dowel-Type Connections under Natural Humidity Conditions <i>Stefania Fortino and Tomi Toratti</i>	597
--	-----

FE-Based Strength Analysis of Penglai Pavilion <i>Jingsi Huo, Biyong Xiao, Hui Qu and Linan Wang</i>	603
Transient Simulation of Coupled Heat, Moisture and Air Distribution in Wood during Drying <i>Zhenggang Zhu and Michael Kaliske</i>	613
Three-Dimensional Numerical Analysis of Dowel-Type Connections in Timber Engineering <i>Michael Kaliske and Eckart Resch</i>	619
Aseismic Character of Chinese Ancient Buildings by Pushover Analysis <i>Qian Zhou and Weiming Yan</i>	627
Aseismic Effects of Masonry Walls Embedded in Chinese Ancient Wooden Buildings by Wen-chuan Earthquake <i>Qian Zhou and Weiming Yan</i>	635
Numerical Simulation of Semi-Rigid Element in Timber Structure Based on Finite Element Method <i>Yunkang Sui, Yingya Chang and Hongling Ye</i>	643
<b>Structural Dynamics</b>	
Numerical Investigation of Blasting-Induced Damage in Concrete Slabs <i>Yuan Wang, Zheming Zhu, Zhangtao Zhou and Heping Xie</i>	655
Research on Analysis Method for Concrete Column to Resist Vehicle Bomb <i>Jianyun Sun, Guoqiang Li, Chunlin Liu and Suwen Chen</i>	669
Numerical Analysis of Blast Loads inside Buildings <i>Xiaojing Yin, Xianglin Gu, Feng Lin and Xinxin Kuang</i>	681
Numerical Simulation for Response of Reinforced Concrete Slabs under Blast Loads <i>Xinxin Kuang, Xianglin Gu, Feng Lin and Xiaojing Yin</i>	691
Numerical Simulation of Internal Blast Effects on a Subway Station <i>Qiuyun Hu and Yong Yuan</i>	699
Quantitative Study on Frequency Variation with Respect to Structural Temperatures <i>Yong Xia, Zelong Wei and Youlin Xu</i>	707

Experimental Study on Vibration Behavior of Cold-Form Steel Concrete Composite Floor <i>Ziwen Jia and Xuhong Zhou</i>	715
Method of Reverberation Ray Matrix for Dynamic Response of Space Structures Composed of Bar Elements with Damping Effect <i>Guoqiang Cai, Guohua Nie and Huiyuan Zhang</i>	725
A Study of Bending-Bending-Torsional Coupled Vibrations of Axially-Loaded Euler-Bernoulli Beams Including Warping Effects <i>Fang Zhang and Guoyan Wang</i>	733
Damage Analysis of 3D Frame Structure under Impulsive Load <i>Julin Wang and Taisheng Yang</i>	743
Experimental and Numerical Approach to Study Dynamic Behaviour of Pavement under Impact Loading <i>Cherif Asli, Zhiqiang Feng, Gérard Porcher and Jean Jacques Rincent</i>	755
Dynamic Analysis of Vertical Loaded Single Pile in Multilayered Saturated Soils <i>Jun Yu, Haiming Chen, Zhao Yang and Cheng Liu</i>	761
Local Dynamic Response in Deck Slabs of Concrete Box Girder Bridges <i>Jianrong Yang and Jianzhong Li</i>	771
Steady-State Response of a Beam on an Elastic Foundation Subjected to a Moving Structure <i>Zhang Tao and Gangtie Zheng</i>	781
Building Structures Vibration Differential Equations under Random Excitation <i>Bin He</i>	787
<b>Structural Diagnosis, Control and Optimization</b>	
On the Tapping-Scan Method Designed for the Damage Detection of Bridge Structures <i>Xiaowei Dai, Yao Zhang and Zhihai Xiang</i>	797
Structure Damification Diagnose System by Radial Basis Function Neural Network <i>Keqin Yan and Tao Cheng</i>	805

Study on Curvature Modal Shapes of the Damage Reinforced Concrete Beams <i>Gang Xue, Xiaoyan Guo and Zhenhua Dong</i>	815
Direct Index Method of Damage Degree Identification Based on Local Strain Model Shape Area of Damage Structure <i>Peiying Gu, Chang Deng and Fusheng Wu</i>	823
Improved Genetic Algorithm for Structural Damage Detection <i>Jose E. Laier and Jesus D.V. Morales</i>	833
Damage Identification Method for Tunnel Lining Based on Monitoring Stresses Data <i>Qineng Weng</i>	841
A Method of Structure Damage Identification for Shear Buildings <i>Feng Li, Julin Wang and Zeping Zang</i>	851
Application of Artificial Neural Network for Diagnosing Pile Integrity Based on Low Strain Dynamic Testing <i>Canhui Zhang and Jianlin Zhang</i>	857
Parametric Study on Damage Control Design of SMA Dampers in Steel Frames <i>Xiaoqun Luo, Hanbin Ge and Tsutomu Usami</i>	863
Comparison Research of Three Vibration Control Plans on a Super-Tall Building with Connective Structure <i>Wang Dayang, Zhou Yun and Wang Lichang</i>	871
Amplitude Control of Limit Cycle in Coupled Van Der Pol System <i>Han Xiao, Jiashi Tang and Jianmin Wang</i>	879
Structural Form Intelligent Optimization and Its Data Mining Methods <i>Shihai Zhang, Shujun Liu, Jinping Ou and Guangyuan Wang</i>	885
A New Methodology for Designing Minimum-Weight Dual-Material Truss Structures with Curved Support Boundaries <i>Peter Dewhurst, Ning Fang and Sriruk Srithongchai</i>	895
Optimization Design of Deepwater Steel Catenary Risers Using Genetic Algorithm <i>Hezhen Yang, Ruhong Jiang and Huaqun Li</i>	901

Two Methodologies for Stacking Sequence Optimization of Laminated Composite Materials <i>Dianzi Liu, Vassili Toropov, David Barton and Ozz. Querin</i>	909
Minimum Cost Design of a Welded Stiffened Pulsating Vacuum Steam Sterilizer <i>Yunkang Sui, Cairui Yue and Huiping Yu</i>	917
A Framework of Multiobjective Collaborative Optimization <i>Haiyan Huang and Deyu Wang</i>	925
An Optimal Design of Bi-Directional TMD for Three Dimensional Structure <i>Jianlin Zhang, Ke Zeng and Jiesheng Jiang</i>	935
<b>Numerical Methods and Numerical Simulation</b>	
A Thermo-Mechanical Model for Fire Exposed RC Structure <i>Matthias Aschaber, Christian Feist and Günter Hofstetter</i>	945
Numerical Modeling of Retrained RC Columns in Fire <i>Yihai Li, Bo Wu and Martin Schneider</i>	951
Temperature Field of Concrete Beam Based on Simulated Temperature-Time Curves <i>Limin Lu, Yong Yuan, Chunlong Yu and Xian Liu</i>	959
Numerical Tests of Spalling Delamination of Concrete at Elevated Temperatures <i>Yufang Fu, Lianchong Li, Wanheng Li and Jinquan Zhang</i>	965
Highlighting the Effect of Gel-Pore Diffusivity on the Effective Diffusivity of Cement Paste – A Multiscale Investigation <i>Xian Liu, Roman Lackner and Christian Pichler</i>	973
An Efficient Nonlinear Meshfree Analysis of Shear Deformable Beam <i>Dongdong Wang and Yue Sun</i>	983
Variance-Based Methods for Sensitivity Analysis in Civil Engineering <i>Zdeněk Kala and Libor Puklický</i>	991
Coupled Multi-Physical Fields Analysis of Early Age Concrete <i>Yiming Zhang and Yong Yuan</i>	999

Rigid Plasticity Analysis of Defect Beam Suffering Step Loads <i>Nansheng Li, Xingzhou Li and Yu Wang</i>	1007
A Computational Approach to the Integration of Adaptronical Structures in Machine Tools <i>Michael F. Zaeh, Matthias Waibel and Matthias Baur</i>	1017
Adaptive Nearest-Nodes Finite Element Method and Its Applications <i>Yunhua Luo</i>	1029
An Orthogonalization Approach for Basic Deformation Modes and Performance Analysis of Hybrid Stress Elements <i>Canhui Zhang</i>	1037
Nonlinear Numerical Analysis on a New Type of Composite Shell <i>Qibin Zhang, Zhuobin Wei and Changhong Huang</i>	1043
Rectangular Membrane Element with Rotational Degree of Freedom <i>Guiyun Xia, Maohong Yu, Chuanxi Li and Jianren Zhang</i>	1051
Coupling Analysis on Seepage and Stress in Jointed Rock Tunnel with the Distinct Element Method <i>Yanli Wang, Yong Wang and Yifei Dai</i>	1059
3D Finite Element Simulation of Complex Static and Dynamic Fracture in Quasi-Brittle Materials <i>Xiangting Su, Zhenjun Yang and Guohua Liu</i>	1065
A Practical Method to Determine Critical Moments of Bridge Decks Using the Method of Least Squares and Spreadheets <i>Jackson Kong</i>	1073
Monte Carlo Simulation of Complex 2D Cohesive Fracture in Random Heterogeneous Quasi-Brittle Materials <i>Xiangting Su, Zhenjun Yang and Guohua Liu</i>	1081
Short-Term Axial Behavior of Preloaded Concrete Columns Strengthened with Fiber Reinforced Polymer Laminate <i>Dechun Shi and Zheng He</i>	1089
Nonlinear Numerical Simulation on Composite Joint between Concrete-Filled Steel Tubular Column and Steel Beams-Covered Concrete under Low-Cycle Reversed Loading <i>Chiyun Zhao, Hua Li, Menghong Wang and Liyun Li</i>	1099

Performance Evaluation of the High Rise Structural Form Selection Based on Fuzzy Inference Network <i>Shihai Zhang, Shujun Liu, Jinping Ou and Guangyuan Wang</i>	1107
Deflection Analysis of Pretensioned Inverted T-Beam with Circular Web Openings Strengthened with GFRP by Response Surface Method <i>Hock Tian Cheng, Bashar S. Mohammed and Kamal Nasharuddin Mustapha</i>	1119
2-D Numerical Simulation of Crack Growth by Three Kinds of Growth Criteria <i>Weizhou Zhong, Jingrun Luo, Shuncheng Song, Gang Chen and Xicheng Huang</i>	1125
Nonlinear Numerical Simulation on Shearing Performance of RC Beams Strengthened with Steel Wire Mesh-Polymer Mortar <i>Chiyun Zhao, Sihua Deng, Yajing Chen, Shimin Huang and Qiulai Yao</i>	1135
<b>Application and Others</b>	
Flexural Behavior of HS Composite Beams via FEM <i>Huilin Zhao, Shashi Kunnath and Yong Yuan</i>	1145
Study on Design and Mechanics of Bucket Foundation Offshore Platform with Two Pillars <i>Meng Jiang, Lihua Han and Rixiang Zhang</i>	1155
Study on Hysteretic Behavior of Double Angle Connections <i>Aiguo Chen, Ruizeng Shan and Qiang Gu</i>	1163
Research on Limit Span of Self-Anchored Suspension Bridge <i>Wenliang Qiu, Meng Jiang and Zhe Zhang</i>	1173
Study on Percolation Mechanism and Water Curtain Control of Underground Water Seal Oil Cavern <i>Cheng Liu</i>	1181
Finite Element Analysis on the Static Intensity and Dynamic Characteristics of Drilling Rig Derricks <i>Lijun Liu, Fuquan Chen and Yan Yu</i>	1189
Design Standards Comparison of Reinforced Concrete Strengthening Using FRP Composite in Chinese and ACI Codes <i>Asal Salih Oday, Yingmin Li, Mohammad Agha Houssam, Al-Jbori A'ssim, Thabit Saeed Ayad and Lu Wang</i>	1197

Think about Structural Fail State to Solve Geometric Reliability <i>Junbo Tao and Zhangdun Wu</i>	1207
Research on the Optimum Stiffness of Top Outriggers in Frame-Core Structure with Strengthened Story <i>Yuan Su, Chuanyao Chen and Li Li</i>	1217
Numerical Analysis of Mechanical Multi-Contacts on the Interfaces in a PEM Fuel Cell Stack <i>Zhiming Zhang, Christine Renaud and Zhiqiang Feng</i>	1225
Analysis Model for Concrete Infill Slit-Wall <i>Xufeng Mi, Lin Wang and Guobao Zhou</i>	1231
Test Data Processing Method of Fracture Experiments of Dam Concrete for Inverse Analysis <i>Zhifang Zhao, Lijian Yang, Zhigang Zhao and Minmin Zhu</i>	1239
Surface Reconstruction of the “False” Tools to Compensate for the Springback in Sheet Forming Process <i>Yuming Li, Fabien Bogard, Boussad Abbes and Yingqiao Guo</i>	1249
Grey-Correlation Analysis of Factors Influencing Xiamen Xiang’an Subsea Tunnel Surrounding Rock Displacement <i>Haiming Chen, Xiong Chen and Jun Yu</i>	1259
Secondary Development of FLAC <sup>3D</sup> and Application of Naylor K-G Constitutive Model <i>Juan Kong, Juyun Yuan and Xiaoming Pan</i>	1267
Experimental Validation on the Simulation of Steel Frame Joint with Several Frictional Contacts <i>Hongfei Chang and Junwu Xia</i>	1275
Numerical Investigation on Tubular Joints Strengthened by Collar Plate <i>Yongbo Shao, Yongsheng Yue, Yanfei Jin, Tao Li and Jichao Zhang</i>	1283
Research on Structural Health Monitoring of Seaport Wharf <i>Changhong Huang and Zhuobin Wei</i>	1291
Quantity of Flow through a Typical Dam of Anisotropic Permeability <i>R.R. Shakir</i>	1301

*“This page left intentionally blank.”*

# Preface

Following the great progress made in computing technology, both in computer and programming technology, computation has become one of the most powerful tools for researchers and practicing engineers. It has led to tremendous achievements in computer-based structural engineering and there is evidence that current developments will even accelerate in the near future. To acknowledge this trend, Tongji University, Vienna University of Technology, and Chinese Academy of Engineering, co-organized the International Symposium on Computational Structural Engineering 2009 in Shanghai (CSE'09).

CSE'09 aimed at providing a forum for presentation and discussion of state-of-the-art development in scientific computing applied to engineering sciences. Emphasis was given to basic methodologies, scientific development and engineering applications. Therefore, it became a central academic activity of the International Association for Computational Mechanics (IACM), the European Community on Computational Methods in Applied Sciences (ECCOMAS), The Chinese Society of Theoretical and Applied Mechanic, the China Civil Engineering Society, and the Architectural Society of China.

A total of 10 invited papers, and around 140 contributed papers were presented in the proceedings of the symposium. Contributors of papers came from 20 countries around the world and covered a wide spectrum related to the computational structural engineering.

As Chair of the Organizing Committee of CSE'09, I would like to thank all the participants and the authors for their contributions. We would also like to gratefully acknowledge the guidance and cooperation provided by the International Advisory Committee and the Scientific Committee as well as the support provided by the members of the Local Organizing Committee. In particular, we appreciate the financial support provided by the National Natural Science Foundation of China, the Eurasia-Pacific Uninet, and the Ministry of Science and Technology of the People's Republic of China.



Zuyan Shen  
Academician of Chinese Academy of Engineering  
Professor of Tongji University  
Shanghai, China

*“This page left intentionally blank.”*

# International Advisory Committee

**Honorary Chair:** Sun, Jun

**Chair:** Mang, Herbert

**Members:**

Arantes e Oliveira, Eduardo	The Technical University of Lisbon	Portugal
Belytschko, Ted	Northwestern University	USA
Bittnar, Zdenek	Czech Technical University in Prague	Czech Republic
Burczynski, Tadeusz	Silesian University of Technology	Poland
Chen, Houqun	China Institute of Water Resources and Hydro-power Research	China
Cheng, Gengdong	Dalian University of Technology	China
Cheung, Y.K.	The University of Hong Kong	Hong Kong, China
Cui, Junzhi	Chinese Academy of Sciences	China
De Borst, René	Eindhoven University of Technology	The Netherlands
Hughes, Thomas J.R.	The University of Texas at Austin	USA
Kanok-Nukulchai, Worsak	Asian Institute of Technology	Thailand
Ko, Jan-ming	The Hong Kong Polytechnic University	Hong Kong, China
Kompis, Vladimir	Academy of the Armed Forces of General M.R.Štefánik	Slovak Republic
Ladevèze, Pierre	LMT-ENS Cachan	France
Lee, C.F.	The University of Hong Kong	Hong Kong, China
Li, Guoqiang	Tongji University	China
Li, Jiachun	Institute of Mechanics, Chinese Academy of Sciences	China
Maekawa, Koichi	The University of Tokyo	Japan
Mang, Herbert	Vienna University of Technology	Austria
Mota Soares, Carlos	Instituto Superior Técnico – IDMEC	Portugal
Oñate, Eugenio	CIMNE	Spain
Ou, Jinping	Dalian University of Technology	China
Owen, Roger	University of Wales	UK
Papadrakakis, Manolis	National Technical University of Athens	Greece
Qin, Shunquan	China Zhongtie Major Bridge Engineering Group CO., LTD	China
Ramm, Ekkehard	University of Stuttgart	Germany
Reddy, J.N.	Texas A&M University	USA

xxii International Advisory Committee

Reinhorn, A.M.	State University of New York	USA
Schrefler, Bernhard	University of Padua	Italy
Shen, Weiping	Shanghai Jiao Tong University	China
Shen, Zuyan	Tongji University	China
Tang, Chun'an	Northeastern University	China
Tarnai, Tibor	Budapest University of Technology and Economics	Hungary
Usami, Tsutomu	Meijo University	Japan
Valliappan, Somasundaram	The University of New South Wales	Australia
Wiberg, Nils Erik	Chalmers University of Technology	Sweden
Wriggers, Peter	The University of Hannover	Germany
Xiang, Haifan	Tongji University	China
Xie, Heping	Sichuan University	China
Yang, Yongbin	National Taiwan University	Taiwan, China
Yuan, Si	Tsinghua University	China
Yuan, Mingwu	Beijing University	China
Zhang, Chuhan	Tsinghua University	China

# Scientific Committee

**Chair:** Cui, Junzhi

**Members:**

Allix, Olivier	LMT-ENS Cachan	France
Chen, Dailin	China Academy of Building Research	China
Dyke, Shirley	Washington University in St. Louis	USA
Du, Xiuli	Beijing University of Technology	China
Eberhardsteiner, Josef	Vienna University of Technology	Austria
Fang, Qin	PLA University of Science and Technology	China
Fish, Jacob	Rensselaer Polytechnic Institute	USA
Ge, Hanbin	Meijo University	Japan
Ge, Yaojun	Tongji University	China
Hao, Hong	The University of Western Australia	Australia
Hellmich, Christian	Vienna University of Technology	Austria
Hofstetter, Günter	The University of Innsbruck	Austria
Hori, Muneo	The University of Tokyo	Japan
Huang, Zongming	Chongqing University	China
Idelsohn, Sergio	CIMNE	Argentina
Jin, Weiliang	Zhejiang University	China
Jin, Xianlong	Shanghai Jiao Tong University	China
Kunnath, Sashi K.	University of California at Davis	USA
Lackner, Roman	Technical University of Munich	Germany
Li, Hongnan	Dalian University of Technology	China
Li, Hui	Harbin Institute of Technology	China
Li, Jie	Tongji University	China
Li, Yungui	China Academy of Building Research	China
Li, Zhongkui	Tsinghua University	China
Li, Zhongxian	Tianjin University	China
Lou, Menglin	Tongji University	China
Lu, Xilin	Tongji University	China
Lu, Yong	University of Edinburgh	UK
Meschke, Günther	Ruhr-University Bochum	Germany

xxiv Scientific Committee

Mo, Haihong	South China University of Technology	China
Nie, Jianguo	Tsinghua University	China
Rank, Ernst	TU München	Germany
Teng, Jun	Harbin Institute of Technology	China
Wall, Wolfgang	Technical University Munich	Germany
Wang, Zifa	Institute of Engineering Mechanics, China Earth- quake Administration	China
Wu, Zhishen	Ibaraki University	Japan
Xiao, Yan	Hunan University	China
Xu, Youlin	The Hong Kong Polytechnic University	Hong Kong, China
Ye, Liaoyuan	Yunnan University	China
Ye, Zhiming	Shanghai University	China
Yuan, Yong	Tongji University	China
Zhang, Hongwu	Dalian University of Technology	China
Zhang, Yongxing	Chongqing University	China

# Organizing Committee

## **Honorary Chair:**

Shen, Zuyan	Tongji University	China
-------------	-------------------	-------

## **Co-chair:**

Yuan, Yong	Tongji University	China
------------	-------------------	-------

Eberhardsteiner, Josef	Vienna University of Technology	Austria
------------------------	---------------------------------	---------

## **Members:**

Chen, Zhiyi	Tongji University	China
-------------	-------------------	-------

Hu, Qiuyun	Tongji University	China
------------	-------------------	-------

Jia, Xin	Vienna University of Technology	Austria
----------	---------------------------------	---------

Jiang, Shouchao	Tongji University	China
-----------------	-------------------	-------

Liu, Liyu	Tongji University	China
-----------	-------------------	-------

Liu, Xian	Vienna University of Technology	Austria
-----------	---------------------------------	---------

Pöll, Martina	Vienna University of Technology	Austria
---------------	---------------------------------	---------

Xu, Jiancong	Tongji University	China
--------------	-------------------	-------

Yu, Guangxi	Tongji University	China
-------------	-------------------	-------

Zeiml, Matthias	Vienna University of Technology	Austria
-----------------	---------------------------------	---------

Zhou, Ying	Tongji University	China
------------	-------------------	-------

*“This page left intentionally blank.”*

# Supporting Organizations and Sponsors



International Association for Computational Mechanics



European Community on Computational Methods in Applied Sciences



The Chinese Society of Theoretical and Applied Mechanics



CCES Institute of Computer Application in Civil Engineering



Architectural Society of China



National Natural Science Foundation of China



Eurasia-Pacific Uninet



Science and Technology Commission of Shanghai Municipality

## **INVITED PAPERS**

*“This page left intentionally blank.”*

# Computational Multi-Scale Methods and Evolving Discontinuities

René de Borst<sup>1\*</sup>

<sup>1</sup>Department of Mechanical Engineering, Eindhoven University of Technology,  
5600 MB Eindhoven, The Netherlands

**Abstract.** This contribution discusses modern concepts in multi-scale analysis. Emphasis is placed in the discussion on so-called concurrent approaches, in which computations are carried out simultaneously at two or more scales. Since analyses at a lower level typically involve more discontinuities to be considered, attention is also paid to the proper modelling of evolving discontinuities. Another related problem is the treatment of discontinuities for problems that involve the modelling of diffusion phenomena in addition to a stress analysis, since this also requires the application of multi-scale concepts. As a further step the coupling of dissimilar media is considered like continuum to discrete models.

**Keywords:** multi-scale analysis, multi-physics, discontinuities, fracture, finite element method

## 1 Introduction

Multi-scale methods are quickly becoming a new paradigm in many branching of science, including in simulation-based engineering. This also holds true for computational mechanics, where multi-scale approaches are among the most important strategies to further our understanding of the behaviour of engineering and biomedical materials. Indeed, this understanding and the tools that are being developed in multi-scale computational mechanics also greatly assist the engineering of new materials.

In multi-scale analyses a greater resolution is sought at ever smaller scales. In this manner it is possible to incorporate the physics more properly and therefore, to construct models that are more reliable and have a greater range of validity at the engineering scales. When resolving smaller and smaller scales, discontinuities become more and more prominent. Whereas at the macroscopic scales, one is used to think merely of cracks and shear bands, now also discontinuities like grain boundaries, solid-solid boundaries such as in phase transformations, and discrete

---

\* Corresponding author, e-mail: R.d.Borst@tue.nl

dislocation movement come into consideration. Moreover, non-mechanical effects, like magneto-electro-chemical fields, humidity and temperature, can cause non-negligible effects, and have to be considered simultaneously.

We will start by a succinct classification of multi-scale computational methods. Next, we will focus on evolving discontinuities that arise at different scales, and discuss methods that can describe them. Examples include multi-scale analyses where coupling of evolving discontinuities is considered with non-mechanical fields, and discrete-to-continuum coupling strategies.

## 2 Multi-Scale Methods

There is an important difference between upscaling methods and concurrent multi-scale computing. In the former class of methods constitutive models at higher scales are constructed from observations and models at lower, more elementary scales. By a sophisticated interaction between experimental observations at different scales and numerical solutions of constitutive models at increasingly larger scales, physically-based models and their parameters can be derived at the macroscopic scale. We consider methods of computational homogenization to belong to this class, e.g. Kouznetsova *et al.* (2004).

In concurrent multi-scale computing one strives to solve the problem simultaneously at several scales by an a priori decomposition. In an intuitive manner this idea has been used in engineering for decades, if not for centuries. Also in computational science, large-scale problems have been solved, and local data, for instance displacements, forces or velocities, have been used as boundary conditions for the resolution of more detail in a part of the problem. Recent years have witnessed the development of multi-scale methods in computational science, which set out at coupling fine scales and coarse scales in a more systematic manner.

## 3 Evolving Discontinuities

When scaling down, discontinuities arise which need to be modelled in an explicit manner. When the discontinuity has a stationary character, such as at grain boundaries, this is not so difficult, since it is possible to adapt the discretization such that the discontinuity, either in displacements or in displacement gradients, is modelled explicitly. An evolving discontinuity, e.g. a crack, is more difficult to handle. A possibility is to adapt the mesh upon every change in the topology. Another approach is to model discontinuities within the framework of continuum mechanics. A fundamental problem is then that standard continuum models do not furnish a length scale which is indispensable for describing fracture, or, more precisely, they result in a zero length scale. Since the energy dissipated in the failure

process is given per unit area of material that has completely degraded, and since a vanishing internal length scale implies that the area in which failure occurs goes to zero, the energy dissipated in the failure process also tends to zero. Two approaches have been followed to avoid this physically unrealistic situation, namely via discretization or via regularization of the continuum, Figure 1, de Borst (2008).

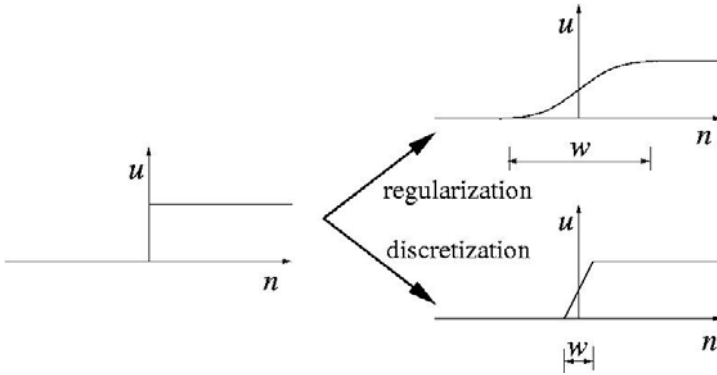


Figure 1. Regularization and discretization as possibilities for modeling discontinuities in a continuous medium.

In view of the fact that discretization provides only a partial remedy to the ill-posedness of the underlying initial value problem, and that difficulties that still persist with regularization strategies – notably, the unresolved issue of additional boundary conditions, the need to use very fine meshes in the zone of the regularized discontinuity, and the need to determine additional material parameters from tests that impose an inhomogeneous deformation field – has been a contributing factor to revisit the research into (more flexible) methods to capture arbitrary, evolving discontinuities in a discrete sense.

At present, four such methods exist: Zero-thickness interface elements, meshless or mesh-free methods, the partition-of-unity method which exploits the partition-of-unity property of finite element shape functions – also known as the extended finite element method, and discontinuous Galerkin methods (de Borst, 2006). Zero-thickness interface elements and the partition-of-unity method have become the most widely used methods in solid mechanics, and therefore, we shall discuss them in some detail. Mesh-free methods were originally thought to behold a great promise for fracture analyses due to the fact that this class of methods does not require meshing, and subsequent remeshing upon crack propagation, but the high costs, and especially the difficulties to properly redefine the support of a node when it is partially cut by a crack, have led to a decreased interest. However, they are of importance, if only because out of the research into this class of methods, the analysis methods that exploit the partition-of-unity property of finite element shape functions have arisen, which are now believed to be the most viable option

or large-scale fracture analyses, see Figure 2 for an example of dynamic crack propagation.

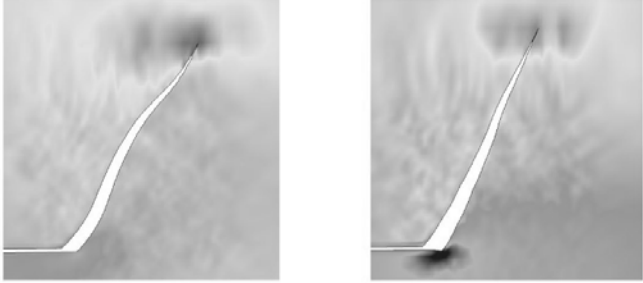


Figure 2. Analysis of dynamic crack propagation by a partition-of-unity based finite element method (Remmers *et al.*, 2008).

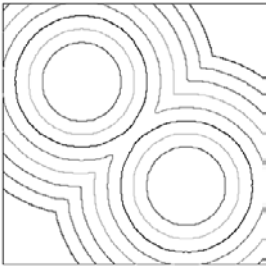


Figure 3. Evolution of level sets that describe the expansion of two circles (numerical solution via finite elements, Valance *et al.*, 2008).

For moving discontinuities such as Lüders bands or Portevin-le Chatelier bands, e.g. Wang *et al.* (1997), at a macroscopic scale, phase propagation fronts or dislocations at a mesoscopic scale, a geometric description of the propagating discontinuity by level sets has recently gained much popularity, in particular for three-dimensional situations. Conventionally, the partial differential equations that arise in level set methods, in particular the Hamilton-Jacobi equation, are solved by finite difference methods. However, such methods are less suited for irregular domains, and it seems awkward to use finite differences for the capturing of a discontinuity, while in a subsequently stress analysis finite elements are used. For this reason, a finite element method has recently been proposed for solving the governing equations of level set methods. The initialization of the level sets, the discretization on a finite domain and the stabilization of the resulting finite ele-

ment method will be discussed. Special attention will be given to the proper treatment of the internal boundary condition, which is achieved by exploiting the partition-of-unity property of finite element shape functions (Valance *et al.*, 2008), Figure 3 for an example.

## 4 Coupling between Length Scales

The partition-of-unity method can be conceived naturally as a variational two-scale method. We will demonstrate this for a two-phase medium, and show how a model for flow inside the discontinuity – the fine scale – can be coupled naturally to the flow and deformation in the surrounding porous medium – the large scale. From the micromechanics of the flow in the cavity, identities can be derived that couple the local momentum and the mass balances to the governing equations for a fluid-saturated porous medium, which are assumed to hold on the macroscopic scale. By exploiting the partition-of-unity property of the finite element shape functions, the position and direction of the fractures become independent from the underlying discretization. The finite element equations are derived for this two-scale approach and integrated over time. The resulting discrete equations are nonlinear due to the cohesive crack model and the nonlinearity of the coupling terms (Réthoré *et al.*, 2007, 2008), see Figure 4 for an example.

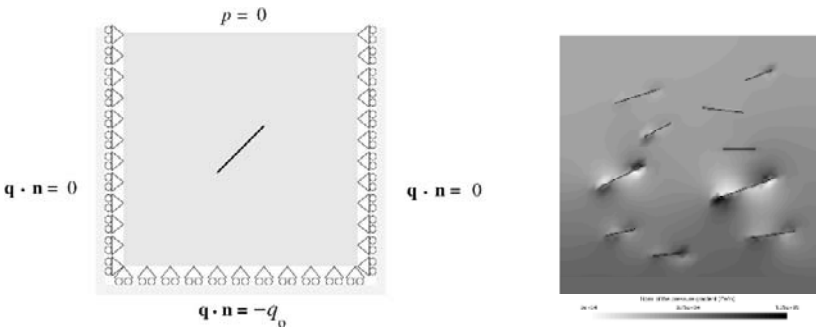


Figure 4. Flow in a fractured porous medium. Left: Geometry and boundary conditions. Right: Gradient of the pressure field in the fluid (Réthoré *et al.*, 2007).

While in the preceding case the equations at the scales that are coupled are similar in the sense that at both scales a continuum approach is taken, this is not so when coupling a molecular dynamics approach to a finite element method which is used for discretization of the continuum model in the remainder of the domain. This holds a fortiori when coupling a molecular dynamics method which describes fracture at the tip of a crack to a finite element method in which the partition-of-unity property is exploited to model the crack in the wake of its tip as a traction-

free discontinuity. In particular the proper energy transfer between both domains in case of dynamic loading is not trivial. Zonal coupling methods between the atomistic and continuum models are favored, since these schemes allow for avoiding spurious wave reflections and a minimization of energy losses due to the a priori partitioning of the energy between both models in the transition zone. The coupling conditions are enforced via Lagrange multipliers (Aubertin *et al.*, 2009). The results for fracture simulations show multiple branching, which is reminiscent of recent results from simulations on dynamic fracture using cohesive-zone models, Figure 5.

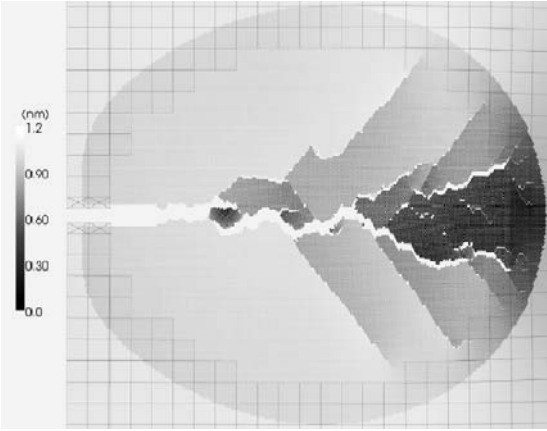


Figure 5. Dynamic fracture by a combined molecular dynamics – finite element simulation (Aubertin *et al.*, 2009).

## 5 Concluding Remarks

Some challenges in computational mechanics have been addressed, in particular the emerging concept of multi-scale analysis, which appears to become a new paradigm in computational science, the importance of accounting for one or several diffusion-like phenomena in addition to a stress analyses for many contemporary problems in mechanics and in materials science, the necessity to track and compute evolving discontinuities, which appear at a variety of scales, and the difficulties of coupling various scales in concurrent multi-scale analyses. Merely some directions have been pointed out, and completeness is not claimed.

## Acknowledgement

Financial support from the DGA and from the region Rhône-Alpes is gratefully acknowledged.

## References

- Aubertin, P., de Borst, R. and Réthoré, J. (2009). Energy conservation of atomistic/continuum coupling. *International Journal of Numerical Methods in Engineering*, doi: 10.1002/nme.2542.
- de Borst, R. (2006). Modern domain-based discretization methods for damage and fracture. *International Journal of Fracture*, 138: 241-262.
- de Borst, R. (2008). Challenges in computational materials science: Multiple scales, multi-physics and evolving discontinuities. *Computational Materials Science*, 43: 1-15.
- Kouznetsova V.G., Geers, M.G.D., and Brekelmans W.A.M. (2004). Multi-scale second-order computational homogenization of multi-phase materials: a nested finite element solution strategy. *Computer Methods in Applied Mechanics and Engineering*, 193: 5525-5550.
- Remmers, J.J.C., de Borst, R. and Needleman, A. (2008). The simulation of dynamic crack propagation using the cohesive segments method. *Journal of the Mechanics and Physics of Solids* 56: 70-92.
- Réthoré, J., de Borst, R. and Abellan, M.-A. (2007). A two-scale approach for fluid flow in fractured porous media. *International Journal of Numerical Methods in Engineering* 71: 780-800.
- Réthoré, J., de Borst, R. and Abellan, M.-A. (2008). A two-scale model for fluid flow in an unsaturated porous medium with cohesive cracks, *Computational Mechanics*, 42: 227-238.
- Valance, S., de Borst, R., Réthoré, J. and Coret, M. (2008). A partition-of-unity based finite element method for level sets. *International Journal of Numerical Methods in Engineering*, 76: 1513-1527.
- Wang, W.M., Sluys, L.J. and de Borst, R. (1997). Viscoplasticity for instabilities due to strain softening and strain-rate softening. *International Journal of Numerical Methods in Engineering*, 40: 3839-3964.

*“This page left intentionally blank.”*

# Damage Cumulation Analysis of Welded Joints under Low Cycle Loadings

Zuyan Shen<sup>1</sup> and Aihui Wu<sup>1,2\*</sup>

<sup>1</sup>College of Civil Engineering, Tongji University, Shanghai 200092, P.R. China

<sup>2</sup>College of Aerospace Engineering and Applied Mechanics, Tongji University, Shanghai 200092, P.R. China

**Abstract** A method for damage cumulation analysis of welded joints under low-cycle loading is presented in this paper. A damage cumulation model for steel weld material is first generated based on results of tensile and strain-controlled low cycle fatigue tests carried out on specimens extracted from a welded T-joint. Finite element sub-program has been generated in the framework of a commercial FE package to predict the hysteretic behavior of welded joints under low cycle loadings considering damage cumulation of both steel and weld materials. Damage cumulation effect may be taken into account in seismic analysis of new welded structures and residual-strength/life prediction for maintenance or repair of existing structures.

**Keywords:** damage accumulation, low cycle fatigue, steel welded joints, hysteretic model, finite element analysis, seismic analysis

## 1 Introduction

Failure of structural components is associated with a damage cumulation process, which leads to a deterioration in the stiffness, strength and energy dissipation capacity of components and structures. Therefore, a more appropriate and reliable design method should be able to take into account this damage cumulation process. Considerable work has been done by Shen and co-researchers (Shen and Dong, 1997; Shen et al, 1998; Shen and Song, 2004; Shen and Wu, 2007) on developing a reliable, systematic and practical analytical method to take into account the damage cumulation effect in seismic analysis of steel structures.

The reliability of a structure depends on that of its weakest part. Welded connections are widely used in steel structures and have, unfortunately, been proven often acting as the weakest part due to the inherent imperfections resulted from the

---

\* Corresponding author, e-mail: a.wu@tongji.edu.cn

welding process. These imperfections make the welded connection more susceptible to damage cumulation and the damage mechanism more complicated than other structural components. Further study is thus necessary for structural safety to establish a more reliable damage cumulation seismic analysis of welded connections.

Wohler ( $S-N$ ) method is often applied in studying the behavior of welded joints under low-cycle fatigue (Ferreira et al., 1998; Ghosh, 2004; Sonsino et al., 2004). The common way of incorporating damage cumulation in analyses of welded joints is to formulate a comprehensive equation, which relates directly the damage variable to the number of cycles, in the framework of thermodynamic based on the damage variable defined and the dissipation potential function assumed (Chen and Zhao, 2005; Cheng et al., 1996; Madi et al., 2004). The constants defined in the  $D-N$  relation were determined from experimental measurements. Such  $S/D-N$  methods have serious disadvantages: the model is applicable only to the components with the material and the loading conditions tested, the experimental procedure is too complicated to apply in practice, and it is not possible to use in a subsequent numerical seismic response analysis unless the damage model is included in the constitutive equation and the hysteretic model. In this study, a damage cumulation model of weld defined at the material level, whose application is limited to weld geometry or loading types, is generated based on simple and standard tests.

## 2 Damage Cumulation Model for Weld Material

Compared to a hysteretic model for a structure component which is reliable only for the type of geometry and loading conditions tested, a hysteretic model at material level with a reliable numerical method has wider applicability as experiments are more expensive, time-consuming, and not always feasible.

Shen and Dong (1997) proposed a non-linear damage cumulation model based on plastic strain for structural steel which takes the complete loading history and energy dissipation as well as the effect of the maximum plastic strain into account. The model was developed based on the cyclic response of the material with the constants determined from regression analysis of a series of experimental results of simple standard tensile and cyclic tests. In this paper, Shen's damage model for steel was first used for weld material and experiments were then carried out for further refinement and determination of specific material parameters for weld material. Figure 1 shows the damage model adopted, where  $\varepsilon_n^p$  and  $\varepsilon_{n+1}^p$  are the plastic strain in the  $n^{\text{th}}$  and  $(n+1)^{\text{th}}$  half cycle, respectively;  $E^{D(n)}$  and  $E^{D(n+1)}$  the Young's modulus at the  $n^{\text{th}}$  and  $(n+1)^{\text{th}}$  half cycle;  $\sigma_s^{D(n)}$  and  $\sigma_s^{D(n+1)}$  the yield strength of the  $n^{\text{th}}$  and  $(n+1)^{\text{th}}$  half cycle;  $k^{(n)}$  and  $k^{(n+1)}$  the hardening coefficient of the  $n^{\text{th}}$  and  $(n+1)^{\text{th}}$  half cycle; and  $\gamma$  and  $\eta$  the constants. More details of the model can be found in the references (Shen and Wu, 2007; Shen and Dong, 1997).

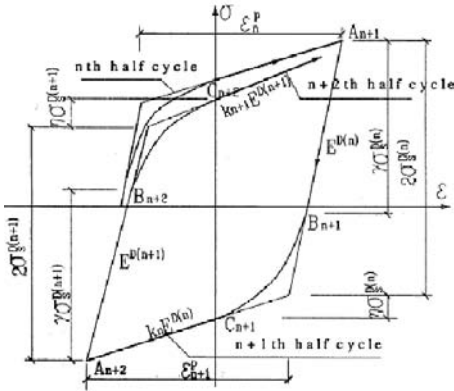


Figure 1. The proposed hysteretic model considering damage cumulation for structural steel

### 3 Experimental Study

Specimens used in this study were extracted from welded T-joints, which is one of the commonly used joint types in engineering practice. Two steel plates of nominal dimensions  $100 \times 1200 \times 30$  mm and  $200 \times 1200 \times 30$  mm were joined by two fillet welds to form a T-joint (Wu, 2007).

#### 3.1 Test Procedure

The steel plates used were GB/T700 Q235 and GB/T1591 Q345 structural steel, with a specified yield strength of not less than 225 MPa for Q235 and 325 MPa for Q345 and a tensile strength of between 375 and 460 MPa for the specific thickness for Q235 and between 470 and 630 MPa for Q345, respectively. Standard tensile and strain controlled low cycle fatigue tests were carried out on both the steel and weld materials.

Fully-reversed tension-compression low-cycle fatigue tests were carried out on both steel and weld materials. Full stress-strain response for each load cycle was recorded digitally by a computer. Hysteretic behavior of the materials was studied from experimental observation and stress-strain curves obtained, based on which, a proper damage cumulation model was proposed and the material parameters defined in the model were determined by carrying out regression analysis on the hysteretic curves obtained from the tests.

For each material type to be studied, six specimens (eight for W235) were manufactured, of which four were tested under constant strain amplitude of 0.0075, 0.0125, 0.0150 and 0.0175 respectively. The other two (four for W235) specimens were subjected to continuously ascending or descending varying strain amplitudes in order to study the effect of loading sequence on the material parameters defined in the damage model.

### 3.2 Results and Discussion

The average values of those obtained from test records of the yield/proof strength  $\sigma_y$ , ultimate tensile strength  $\sigma_u$ , yield strain  $\varepsilon_y$  and ultimate strain  $\varepsilon_u$  are listed in Table 1. Properties of the two fillet welds from the same weldment show slight difference, more in the magnitude of stress than in the strain hardening behavior, due to the influence of welding process.

Table 1. Tensile test results for weld materials

Material	$\sigma_y$ (MPa)	$\sigma_u$ (MPa)	$\varepsilon_y$	$\varepsilon_u^P$
W235L	444.8	575.0	0.0020	0.1228
W345L	365.5	482.1	0.0059	0.1190
W345R	388.8	508.5	0.0039	0.1149

Table 2. Number of half cycles to failure

Specimen	$n$			$n_0$		
	W235	W345L	W345R	W235	W345L	W345R
1	1352	-	257	7	-	1
2	328	612	440	6	4	4
3	194	989	969	4	6	8
4	134	1549	2603	4	3	1
5	260	431	592	9	4	4
6	202	188	1434	2	2	4
7	604	-	-	4	-	-
8	1180	-	-	2	-	-

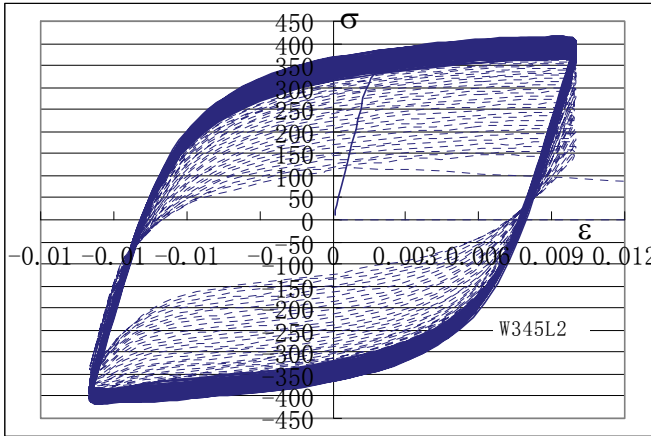


Figure 2. Experimental hysteretic curve for weld specimen W345L2

Deterioration of material properties is an important feature of cyclic loading and a consequence of damage cumulated in the material. The maximum stress reached in each half cycle,  $\sigma_{\max}^n$ , was plotted versus the number of load cycles,  $n$ , for the W235 and W345 weld materials, respectively. It is clearly shown from these curves that the W235 and W345 weld are both cyclic softening materials. The yield stress,  $\sigma_s^{D(n)}$  versus number of half cycles curves show the same trend as that of maximum stress.

Loading sequence is seen to have significant effect on the deteriorate rate of stress by comparing the  $\sigma_{\max}^n - n/N_f$  curves for specimens W235-5 and W235-6 which were subjected to ascending strain amplitude with that of specimens W235-7 and 8 with descending strain loading. The high - low loading sequence increases clearly the deterioration rate of material properties.

The final results of the material constants  $\beta$ ,  $\xi_1$ ,  $\xi_2$ , and  $\xi_3$  for the specimens tested can be obtained from regression analysis of the experimental curves, which show a higher scatter than that presented in (Shen and Dong, 1997) for steel. The more complicated microstructure of weld material than steel is one of the reasons.

### 3.3 Modified Damage Cumulation Model for Weld Material

It is evidence for the weld material tested from the cyclic experiment that upon the first few loadings no damage happens despite the plastic deformation appeared. To accommodate this phenomenon, the damage variable model was modified accordingly by including a damage initiating half-cycle number,  $n_0$ , in the damage variable equation, i.e.

$$D = (1 - \beta) \frac{\varepsilon_m^p}{\varepsilon_u^p} + \sum_{i=n_0}^N \beta \frac{\varepsilon_i^p}{\varepsilon_u^p} \tag{1}$$

The number of half-cycles showing cyclic hardening was determined from the  $\sigma_s^{D(n)} - n$  curve for each weld specimen and is listed in Table 2. The average number of half-cycles for the eight tested weld specimens is 4.

It is seen from the  $\sigma_{max}^n - n$  plot that the deterioration of stress may be divided in three stages ignoring the initial few cycles: I, the micro crack initiation period where the stress decreases rapidly with increase of load cycles; II, the steady crack growing period where the deterioration appears to be relatively stable; and III, the macro crack propagation period where the rate of deterioration becomes fast again until final failure occurs.

Normalize the  $\sigma_s^n$  results with the initial yield stress  $\sigma_s$ , plot with the damage variable  $D$  as shown in Figure 3 for specimen W345L3, assume a linear relation for the first and third stages for simplicity, the relationship between instance yield stress at each half cycle and the damage variable can be expressed in the same form for the three stages:  $\sigma_s^D = (b - kD)\sigma_s$ . Table 3 lists the results of parameter  $k$  and  $b$  for W345L materials obtained from regression analysis. The scatter of model constants is obviously smaller than that of  $\xi_1$ , and  $\xi_2$ .

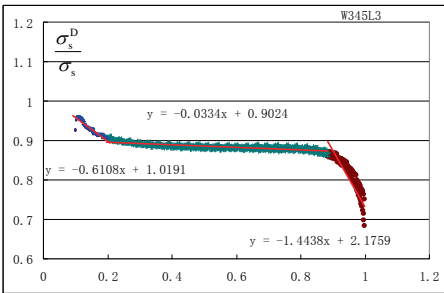


Figure 3.  $\sigma_s^n / \sigma_s - D$  curve for specimen W345L3

Table 3. Yield stress model constants for W345L material

	$k_I$	$D_I$	$k_{II}$	$b_{II}$	$D_{II}$	$k_{III}$	$b_{III}$
W345L-2	0.542	0.244	0.026	0.966	0.93124	1.003	1.876
W345L-3	0.610	0.213	0.033	0.902	0.9064	1.443	2.175
W345L-4	0.593	0.177	0.030	0.812	0.9388	-0.714	0.114
W345L-5	-	-	0.021	1.083	0.939	1.143	2.137
W345L-6	0.398	0.392	0.066	1.122	-	-	-

In summary, the damage cumulation model for weld material under low-cycle fatigue loading can be generated by (Wu, 2007):

$$\begin{cases} \sigma = \sigma_{An} + E^D(\varepsilon - \varepsilon_{An}), & |\sigma_{An} - \sigma_s| \leq \gamma\sigma_s^{D(n-1)} \\ \sigma = a\varepsilon^2 + b\varepsilon + c, & \gamma\sigma_s^{D(n-1)} < |\sigma_{An} - \sigma_s| \leq (2 + \eta)\sigma_s^{D(n-1)} \\ \sigma = \sigma_{Cn} + k^{n-1}E^D(\varepsilon - \varepsilon_{Cn}), & |\sigma_{Cn} - \sigma_s| > (2 + \eta)\sigma_s^{D(n-1)} \end{cases}$$

$$\sigma_s^D = \begin{cases} (1 - k_I D)\sigma_s & 0 < D < 0.2254 \\ (b_{II} - k_{II} D)\sigma_s & 0.2254 < D < 0.9031 \\ (b_{III} - k_{III} D)\sigma_s & 0.9031 < D < 1 \end{cases}$$

$$E^D = \begin{cases} (1 - k_I^E D)\sigma_s & 0 < D < 0.2254 \\ (b_{II}^E - k_{II}^E D)\sigma_s & 0.2254 < D < 0.9031 \\ (b_{III}^E - k_{III}^E D)\sigma_s & 0.9031 < D < 1 \end{cases}$$

$$k_n = k_0 + \xi_3 \sum_{i=1}^n \frac{\varepsilon_i^p}{\varepsilon_u^p}$$

The damage cumulation model proposed in this study is validated by comparing the calculated hysteretic curve with that obtained from tests, as shown in Figure 4 for specimen W345L2. The model shows satisfactory agreement with the test result and the discrepancies seen owing to the averaging of the values from various specimens, in addition to the scatter of the test result itself.

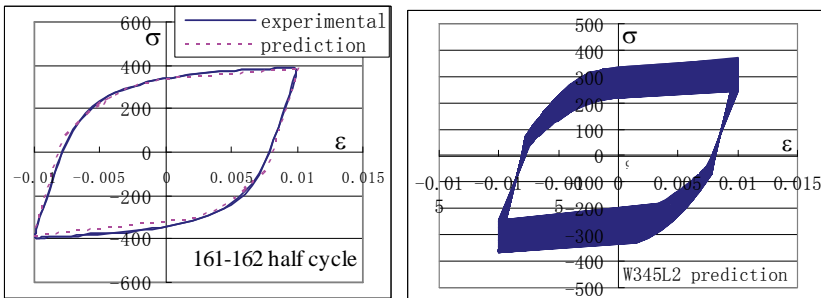


Figure 4. Comparison of hysteretic curves between predicted and experimental results

## 4 FE Simulation Incorporating the Damage Cumulation Model

Shen and co-authors have generated in-house FE programs (TSSDA and D&C model) for steel members considering the damage cumulation effect based on the damage cumulation model developed for steel material. However, the practical application of the programs is limited as they were developed in-house and are thus difficult for the outside design engineers to apply. A sub-program is thus developed within the framework of a widely used FE package ANSYS for calculation of hysteretic behavior of welded joints using the damage cumulation model presented in this paper. Such a model will be greatly helpful for the practical application of damage cumulation in seismic analysis.

The main feature of an FE analysis incorporating damage cumulation is the dynamic variation and the plastic strain history dependent of the material constitutive relation during the cyclic loading process. Material constitutive relation needs to be updated between cycles in the FE analysis using the damage cumulation model developed in this study. All these can be achieved using the APDL function provided by ANSYS. The FE sub-program has been validated by comparing the predicted load-displacement of the testing specimen with experimental measurements, as shown in Figure 5.

By incorporating the damage cumulation models for both weld material generated in this study and structural steel proposed in previous studies, the hysteretic response and the remaining strength/life at any time during the loading history of welded joints of any geometrical type can be predicted using the ANSYS sub-program generated.

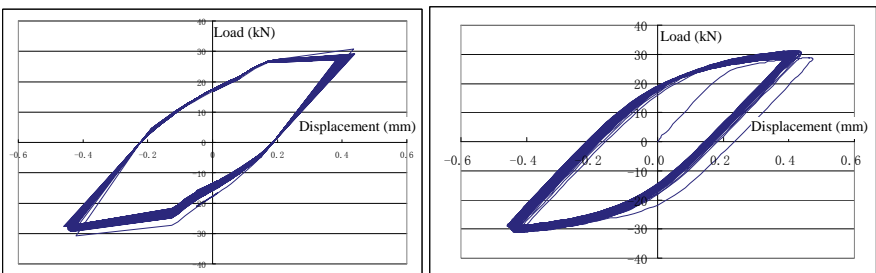


Figure 5. Comparison of load-displacement curve between predicted and experimental measurements

## 5 Conclusions and Future Work

A damage cumulation model for steel weld material is presented in this paper. The model is defined in material level based on tensile and strain-controlled low cycle

fatigue tests; its application is thus not limited to the geometry and boundary conditions tested as for hysteretic model in member level. Finite element sub-program incorporating the proposed damage cumulation model has been generated for predicting the hysteretic behavior of welded joints.

Loading sequence is found from the experimental results to have significant effect on the hysteretic behavior of the weld material. Seismic loading is in no means a constant amplitude cyclic loading, thus more experiments need to be carried out in order to characterize more accurately the behavior of steel and weld materials under random cyclic loadings.

Prediction and experiment of welded T-joints under cyclic loading are currently undertaken to demonstrate further the application of the damage cumulation model generated in this study. A full seismic analysis of a welded structure considering damage cumulation effect will also be performed, the success of which will inevitably provide a valuable alternative to expensive cyclic experiments on structural members and even structures.

## References

- Chen X., Zhao S.M. (2005) Evaluation of fatigue damage at welded tube joint under cyclic pressure using surface hardness measurement. *Engineering Failure Analysis*, 12: 616-622.
- Cheng G.X., Zuo J.Z., Lou Z.W., et al (1996) Continuum damage model of low-cycle fatigue and fatigue damage analysis of welded joint. *Engineering Fracture Mechanics*, 55(1): 155-161.
- Ferreira J., Castiglioni C. A., Calado L., et al. (1998) Low cycle fatigue strength assessment of cruciform welded joints. *Journal of Constructional Steel Research*, 47: 223-244.
- Ghosh A. (2004) Modern approach of design of welded components subjected to fatigue loading. *Journal of Structural Engineering*, 130(5): 812-820.
- Madi Y., Recho N., Matheron P. (2004) Low-cycle fatigue of welded joints: Coupled initiation propagation model. *Nuclear Engineering and Design*, 228: 174-194.
- Shen Z.Y., Dong B. (1997) An experiment-based cumulative damage mechanics model of steel under cyclic loading. *Advances in Structural Engineering*, 1(1): 39-46.
- Shen Z.Y., Dong B., Cao W. (1998) A hysteretic model for plane steel member with damage cumulation effects. *Journal of Constructional Steel Research*, 48(2/3): 79-87.
- Shen Z.Y., Song Z. (2004) FEM analysis of steel members and connections considering damage cumulation effects under cyclic loading. *International Journal of Applied Mechanics and Engineering*, 9(1): 47-62.
- Shen Z.Y., Wu A. (2007) Seismic analysis of steel structures considering damage cumulation. *Frontiers of Architecture and Civil Engineering in China*, 2(1): 1-11.
- Sonsino C.M., Lagoda T., et al (2004) Damage accumulation under variable amplitude loading of welded medium- and high-strength steels. *International Journal of Fatigue*, 26: 487-495.
- Wu A. (2005) Damage cumulation model and analysis of welded joints. Postdoctoral Research Report. Tongji University, Shanghai [in Chinese].

*“This page left intentionally blank.”*

# Ageing Degradation of Concrete Dams Based on Damage Mechanics Concepts

Somasundaram Valliappan<sup>1\*</sup> and Calvin Chee<sup>2</sup>

<sup>1</sup>School of Civil & Environmental Engineering, University of New South Wales, Sydney, NSW 2052, Australia

<sup>2</sup>Infrastructure Division, Hyder consulting Pty. Ltd., Locked Bag 6503, North Sydney, NSW 2060, Australia

**Abstract.** A numerical approach is presented in this paper for the analysis of large concrete dams due to ageing degradation, based on damage mechanics concepts. The proposed method can be used to analyse the seismic responses of aged concrete dams by combining techniques such as degradation evaluation methods, damage mechanics, finite element/boundary element methods. The effect of ageing degradation is taken into account by introducing a degradation factor into formulations of damage mechanics.

**Keywords:** ageing degradation, damage mechanics, concrete dams, finite element method, seismic responses

## 1 Introduction

Infrastructures in Australia, as well as in the world, are ageing. Ageing can lead to changes in engineering properties and may affect the dynamic behaviour, structural resistance/capacity, mode and location of failure. The ageing effects may impact the ability of structural system to withstand various challenges from operation, environment and natural events such as earthquakes.

Many of early dams in Australia were of concrete. Most of them have been in service for over 50 years. The Australian National Committee on Large Dams (ANCOLD) coordinated concerns on dam safety in the late 1960s (Murley, 2002). ANCLOD report addresses the ageing effects including deterioration of concrete and cracking being the main causes of inadequacy of aged concrete dams.

The ageing of dams can be defined as partial or total loss of their capacity to achieve the purpose for which they were constructed, via a slow, progressive and irreversible process that occurs over a long period. Dam ageing is a growing con-

---

\* Corresponding author, e-mail: somaval@bigpond.net.au

cern, as the number of older dams in the world and their average age are increasing. The International Commission on Large Dams (ICOLD) recognized this, and in 1994 published the bulletin 93: Ageing of Dams and Appurtenant Works — Review and Recommendations, in which it was stated that ‘Ageing is a major class of deterioration in dams and appurtenant works and will be of increasing concern as time goes by’. The question of ‘Ageing and rehabilitation of concrete and masonry dams and appurtenant works’, was raised at 21st ICOLD CONGRESS (Montreal, Canada, June 2003). The types and causes of ageing phenomena for concrete and masonry dams, and their rehabilitation techniques were discussed extensively.

Although concrete is inherently durable, some concrete dams may need to be improved because of deficiencies in their design and construction, or as a result of environmental attack (Corns et al., 1988). The ageing process can directly affect the dam by changing the characteristics of the materials of which it is made, leading to a loss in its resistance capacity. Common problems associated with ageing of reinforced concrete include alkali-aggregate reaction (AAR), freezing and thawing, leaching, sulphate attack, cracking due volume changes led by temperature variation, corrosion of concrete and debonding of steel, *etc.* (ICOLD, 1994; Jaberooti and Golabtoonchi, 2003; Zhang, 1991).

Even though most of the structures generally have substantial safety margins when properly designed the available margins for aged or degraded concrete structures are not clearly known. Although ageing effects on safety of old concrete dams are widely realized by engineers, research effort reported on quantified analysis of aged concrete dams is rare. Boros-Meinike and Jankowski (2003) presented an attempt to find a relationship between the vertical displacement recorded at the dam crest and the age of the dam. A model for concrete strength-time function up to fifty years was proposed by Tango and Andriolo (2003). Aiming to verify the applicability of the model and method for concrete dams, simulations of predictions were made and compared with the effective results of quality control data from Brazilian dams. Using 3-D finite element method, Hrabowski *et al.* (2003) analysed the thermal cracking in Zatonie Dam.

The effects of degradation processes on structural integrity and dam safety can sometimes be obvious and in other cases such as AAR, detailed modelling, using special purpose finite element analyses, is necessary to identify the mechanisms and forecast potential effects such as cracking. The seismic safety of existing large concrete dams is an important research topic owing to ageing processes altering their strength and stiffness, as well as revised predictions of their structural resistance due to earthquakes. As pointed out by Sen and Ventatesha (1991), development of models, methods and analysis for dams to take into account ageing characteristics is one of the important research areas on aged concrete dams. Various methods available for this purpose are probabilistic degradation evaluation approach, damage/fracture mechanics methods, non-destructive detection method, *etc.*

Time dependent changes in structural properties are random in nature. Safety evaluation of new and existing structures can be conducted rationally within a probabilistic framework. Probability methods are widely used for condition assessment of existing structures. The mathematical formalism of a probabilistic risk assessment (PRA) provides a means for identifying ageing structural components that may play a significant role in mitigating structural risk. Structural condition assessments supporting a decision regarding continued service can be rendered more sufficient if guided by the logic of a PRA.

Degradation effects can be quantified with fragility curves developed for both undegraded and degraded components. Fragility analysis is a technique for assessing, in probabilistic terms, the capability of a structure to withstand a specified event. Fragility modelling requires a focus on the behavior of the system as a whole and, specifically, on things that can go wrong with the system. The fragility modelling process leads to a median-centred (or likely) estimate of system performance, coupled with an estimate of the variability or uncertainty in performance. Braverman *et al.* (2004) reported the fragility analyses performed for concrete structural members and other passive components of nuclear power plants (NPPs). Structural performance in the presence of uncertainties is depicted by a fragility (or conditional probability of failure). Ellingwood (1998) addressed the issues related to structural ageing in probabilistic risk assessment of NPPs, and proposed a probabilistic framework to assess degradation in certain critical structural component or system capacities due to reinforcement corrosion or concrete deterioration from aggressive environmental influences. Naus *et al.* (1999) summarized the research program addressing ageing of nuclear power plant concrete structures. A reliability-based methodology was developed that can be used to facilitate quantitative assessments of current and future structural reliability and performance of concrete structures in NNPs. The methodology is able to take into account the nature of past and future loads, and randomness in strength and in degradation results from environmental factors. A methodology was presented by Tekie and Ellingwood (2003) for developing fragilities of concrete gravity dams to assess their performance against seismic hazards. Based on the fragility model constructed for concrete gravity dams, fragility and sensitivity analysis can be performed for probabilistic safety assessment, in which the uncertainties in dam-foundation system are represented by statistical data.

An alternative method to evaluate the safety of engineering structures is by using damage/fracture methods. When engineering materials are subjected to unfavourable conditions such as temperature variation, chemical action, mechanical loading, microscopic defects and cracks may develop inside the materials. This 'damage' causes reduction in strength that may lead to failure and shorten the operating life of the structures. This deterioration in mechanical properties of a material is known as a 'damage' process (Valliappan *et al.*, 1990).

Because of the significant influence of damage on engineering material properties, a number of studies have been carried out on modelling and numerical methods for crack growth in concrete and concrete structures under various loading conditions.

For example, Plazzari (1998) studied the uplift pressure effects in cracked concrete gravity dams by performing a parametric study on the influence of uplift pressure on stress intensity factors and crack-propagation angle. A non-linear visco-elastic tension-softening constitutive model for cracked and ageing concrete was developed by Karihaloo and Santhikumar (1995). It combines a micro-mechanical model for tension softening with a Kevin chain rheological model. The ageing phenomenon is included through the concept of consolidation theory and the introduction of an ageing function – the same for all Kevin chain units. A nonlinear joint element model with a coupled shear-tensile behavior for realistic finite element analysis of dam-reservoir system was developed by Ahmadi et al. (2001). Reservoir upstream radiation, and bottom partial absorption of acoustic waves, as well as water compressibility are considered. Lackner and Mang (2001) developed an adaptive finite element calculation scheme for the analysis of concrete structures with special emphasis on a softening in consequence of cracking. Horii and Chen (2003) discussed the problems in cracking modelling, computational algorithm, and damping implementation in conjunction with safety assessment of concrete dam against earthquakes. The return-mapping algorithm in computational plasticity is used for the dynamic analysis of crack growth in concrete using the analogy of the formulation for the crack-embedded element with that of computational plasticity.

The team of Valliappan (Zhang and Valliappan, 1998) has been one of the pioneers in developing numerical methods using damage mechanics for structures, such as concrete dams. Coupled finite element-boundary element method was developed for the dynamic analysis of structures including the effect of damage. Valliappan and Yazdchi (1999a, 1999b) presented the earthquake analysis of concrete gravity dams based on continuum damage mechanics approach and extended this to the analysis of arch dams. Yazdchi et al. (1999) adopted the coupled finite element-boundary element method for dynamic soil-structure interaction analysis and nonlinear seismic behavior of concrete gravity dams.

A unified approach is presented in this paper for the stability analysis of large concrete dams with age-related degradation by combining techniques such as degradation evaluation method, damage mechanics and finite element method. The Koyna dam in India is employed as the example in the numerical analysis to illustrate the proposed method.

## 2 Methodology

To consider the effect of aged-related degradation on the safety assessment of aged concrete dams, ageing degradation is quantified according to various mechanical and environmental operation conditions. A new damage model, which takes into account the effect of ageing degradation, is proposed. A dynamic two-dimensional finite element method coupled with the proposed damage model has

been developed to evaluate damage initiation and propagation for aged concrete dams.

## ***2.1 Quantification of Aging Degradation of Concrete Dams***

Aged-related degradation of concrete is a complicated process. Degradation of concrete can be caused by adverse performance of either its cement-paste matrix or aggregate materials under chemical or physical attack. Physical attack mechanisms for concrete include freeze/thaw cycling, thermal exposure/thermal cycling, and fatigue or vibration. Degradation of mild steel reinforcing concrete can occur as a result of corrosion, elevated temperature, or fatigue effects. Prestressing concrete is susceptible to the same degradation mechanism as mild steel concrete, primarily due to tendon relaxation and concrete creep and shrinkage.

Ageing degradation of concrete and reinforced concrete materials, which accumulates over time by various processes depending on the operating environment and services conditions, will reduce the strength of structures or their components. Generally, the ageing degradation of a structure or a structural component can be expressed by

$$R(t) = R_0 G(t) \quad (1)$$

in which  $R_0$  is the component capacity in the undegraded (original) state, and  $G(t)$  is a time dependent degradation function defining the fraction of initial strength remaining at time  $t$ . The degradation mechanisms are uncertain, experimental data are lacking, and thus the function  $G(t)$  should be treated as stochastic. However, as it has been found that the variability in  $G(t)$  is of minor importance when compared to mean degradation and local process characteristics (Mori and Ellingwood, 1993), it is assumed that  $G(t)$  is deterministic and equal to mean  $E[g(t)] = G(t)$ .

For reinforced concrete structures, most significant resistance deterioration mechanisms have been identified quantitatively (Naus, 1986; Vu and Stewart, 2000). Corrosion of reinforcement is one of the most damaging mechanisms affecting the strength of reinforced or prestressed concrete structures over time, and followed by sulphate attack, freeze-thaw cycling, and reactive aggregate reactions within the concrete. Quantitative degradation models are available for some of the degradation mechanisms (Vesikari, 1988).

In this research, time-dependent ageing degradation function is assumed to be given by (Mori and Nonaka, 2001)

$$G(t) = 1 - a\sqrt{t} \quad (2)$$

in which  $a = 0.03$ , and  $t$  is the age of the dam.

## 2.2 Dynamic Finite Element Analysis of Aged Concrete Dams Using Damage Mechanics

Since the safety margin reserved in the existing critical structures is large, they are considered to be safe even against an earthquake, or other hostile loadings larger than expected in their design. However, the past experience shows that engineering structures are susceptible to ageing degradation under various attacks, which may affect the dynamic properties of the structures. Whether the aged structures can still withstand the challenges from natural events such as earthquakes is a great concern of engineers. Therefore, time-dependent degradation effects should be included when structural safety and reliability are evaluated for aged dam structures.

In the past, many investigators have studied the effect of cracking on the seismic response of concrete structures using the concept of fracture mechanics. The concept of fracture mechanics requires complete details of initiation and propagation of cracks within the structure and the location, dimensions and physical properties of fracture in the rock foundation. Besides, the numerical modelling of such individual fracture requires special techniques such as quarter-point element, re-meshing, *etc* (Valliappan and Ang, 1985; Murti and Valliappan, 1985). Therefore, the application of fracture mechanics is limited to problems where only a few well-defined fractures are encountered. For large-scale problems where extensive microcracking may develop, it may not be suitable, especially in dynamic analysis.

The concept of continuum damage mechanics has been used to study the effect of microcracking on the seismic response of concrete structures (Valliappan et al. 1996). Damage mechanics provides an average measure of material degradation due to microcracking, interfacial debonding, nucleation and coalescence of voids. In the microcracking of brittle materials under tensile stress, damage is regarded as describing the elastic degradation. This material degradation is reflected in the non-linear behaviour of the structures.

### 2.2.1 Finite Element Equations of Motion for Damage Materials

The equation of motion for the seismic analysis of an anisotropic body including damage can be written as:

$$[M]\{\ddot{U}\} + [C^*]\{\dot{U}\} + \{P^*(\{U\})\} = \{F_{st}\} + \{F_{eq}\} \quad (3)$$

where  $[M]$  is the mass matrix of the system and consists of element mass matrices  $[m]^e$

$$[m]^e = \int_{\Omega_e} \rho^{(e)} [N]^T [N] d\Omega \quad (4)$$

$\rho^{(e)}$  and  $[N]$  represent mass density and shape function matrix for an element, respectively.  $[C^*]$  is the damping matrix of the system, whereas  $\{P^*(\{U\})\}$  represents the vector of restoring forces,  $\{F_{st}\}$  is static (preseismic) load vector and  $\{F_{eq}\}$  is the earthquake load vector.  $\{P^*(\{U\})\}$  is a nonlinear function of displacement and stress-strain history depending on the constitutive law. It can be given by

$$\{P^*(\{U\})\} = [K^*] \{U\} \quad (5)$$

where  $[K^*]$  is the system stiffness and is obtained from the assemblage of an element stiffness matrices  $[k]^{(e)}$

$$[k]^e = \int_{\Omega_e} [B]^T [T_\sigma] [\tilde{E}^*]^{(e)} [T_\sigma]^T [B] d\Omega \quad (6)$$

where  $[T_\sigma]$  is the co-ordinate transformation matrix,  $[\tilde{E}^*]$  is the damaged constitutive matrix taking into account the age-related degradation in the orthotropic damage space, and  $[B]$  is the strain-displacement matrix.

The vector of static loads due to self weight of the dam for an element is calculated according to

$$\{f_{st}\}^e = \int_{\Omega_e} \rho^{(e)} [\Psi]^T \begin{Bmatrix} 0 \\ g \end{Bmatrix} d\Omega \quad (7)$$

in which  $g$  is the gravitational acceleration. Assuming that the free-field excitation at the interface of foundation and structure results from a rigid-body motion  $u^G(t)$ , the load vector due to earthquake excitation is given by

$$\{F_{eq}\} = - \begin{bmatrix} m_{ss} & m_{sg} & 0 \\ m_{gs} & m_{gg} & 0 \\ 0 & 0 & 0 \end{bmatrix} \begin{Bmatrix} T_s^G \\ T_g^G \\ 0 \end{Bmatrix} \ddot{u}^G(t) \quad (8)$$

where  $m_{ij}$  are the mass matrices of the structure only, the indices  $s$  and  $g$  mark the degrees of freedom of the structure and those shared by structure and foundation, respectively, while the index  $G$  stands for the rigid-body motion. The matrices  $T_i^G$ ,  $i = s, g$ , contain the geometrical transformation between the structure and the free-field motion  $u^G(t)$ . Also  $\ddot{u}^G(t)$  is the acceleration time history of an earthquake.

### 2.2.2 Damage Evolution

For the complete dynamic analysis of damaged materials, besides the appropriate constitutive law, it is necessary to specify the damage kinetic equation of the form

$$\dot{D} = \dot{D}(\sigma_{ij}(\varepsilon_{ij}), D, \dots) \quad (9)$$

$$\text{or } D = D(\sigma_{ij}(\varepsilon_{ij}), \dots) \quad (10)$$

where  $\sigma_{ij}$  is the state of stress at a particular point,  $D$  is the damage tensor at that point, and  $\dot{D}$  represents the rate of damage. The most common damage kinetic equation that is used widely is based on power function of tensile normal stress and was introduced first by Kachanov (1982),

$$\dot{D} = \begin{cases} A \left( \frac{\sigma}{1-D} \right)^n, & \sigma > \sigma_d \\ 0, & \sigma \leq \sigma_d \end{cases} \quad (11)$$

where  $A > 0$ ,  $n > 1$  are material constants depending on the rate of loading,  $\sigma$  is the uniaxial tensile stress, and  $\sigma_d$  is the stress at damage threshold. For this model, one needs experimental results to obtain parameters  $A$  and  $n$ , but these results are not available for all kind of loading. As proposed by Bazant and Lin (1988) and applied by Ghrib and Tinawi (1995), a second model based on Equation (10) can be used for seismic analysis.

As is well known, concrete and geomaterial eventually exhibit strain softening, leading to a complete loss of strength. In these materials, the secant modulus decreases with increasing strain (Lubliner et al., 1989). A widely used assumption has been adopted to a triangular stress-strain diagram for uniaxial loading. This gives a linear strain softening relationship. But various experimental evidences indicate that it is more realistic to assume a strain softening curve with a steep initial decline followed by an extended tail (Lubliner et al., 1989). Then an exponential strain softening model can be given by

$$\begin{cases} \sigma(\varepsilon) = E\varepsilon & \varepsilon \leq \varepsilon_0 \\ \sigma(\varepsilon) = f_t' \left[ 2e^{-a(\varepsilon-\varepsilon_0)} - e^{-2a(\varepsilon-\varepsilon_0)} \right] & \varepsilon_0 < \varepsilon < \varepsilon_{cr} \\ \sigma(\varepsilon) = 0 & \varepsilon \geq \varepsilon_{cr} \end{cases} \quad (12)$$

in which  $f_t'$  is the tensile strength and  $\varepsilon_0$  is the corresponding strain threshold,  $E$  is the modulus of elasticity and  $a$  is a dimensionless constant, and  $\varepsilon_{cr}$  is the maximum strain. For aged degraded structures,  $E$  and  $f_t'$  in Equation (12) are given by Equation (1) due to ageing degradation. When its corresponding stress is equal to  $0.02 f_t'$ , the maximum strain  $\varepsilon_{cr}$  is calculated by

$$\varepsilon_{cr} = \varepsilon_0 + \frac{4.6}{a} \quad (13)$$

The fracture energy per unit area,  $G_f$ , is defined as

$$G_f = l_{ch} g_t \quad (14)$$

where  $g_t$  is total area under stress-strain curve as (Lubliner et al.,1989)

$$g_t = \int_0^{\infty} \sigma(\varepsilon) d\varepsilon = \frac{3f_t'}{2a} + \frac{f_t'}{2E} \quad (15)$$

$l_{ch}$  is the characteristic length. From the above two equations, the constant  $a$  can be given by

$$a = \frac{3}{\varepsilon_0 \left[ \frac{2EG_f}{l_{ch} f_t'^2} - 1 \right]} \geq 0 \quad (16)$$

Based on the hypothesis of strain energy equivalence, the anisotropic damage parameters can be defined in terms of Young's modulus as (Valliappan et al., 1990)

$$D_i = 1 - \sqrt{\frac{E_i^*}{E_i}} \quad (17)$$

and hence from Equation (12) the proper definition of damage for uniaxial case is

$$D_i = 1 - \sqrt{\left(\frac{\varepsilon_0}{\varepsilon}\right) \left[ 2e^{-a(\varepsilon - \varepsilon_0)} - e^{-2a(\varepsilon - \varepsilon_0)} \right]} \tag{18}$$

### 3 Numerical Example

To validate the proposed method for ageing degradation of concrete dams, Koyna Dam in India, as shown in Figure 1, has been analysed. The idealized geometry of dam is 103.0m high, with a width of 70.0m at the base and 14.8m at the top. While the upstream of the dam is assumed vertical, its downstream has two different slopes. The dam is modelled as a two dimensional plane strain case and is discretized with four noded isoparametric finite elements. A fine mesh is used in the zone near elevation 66.5m, where cracking is anticipated, and in the area closer to the dam base. The dam is assumed to be fixed at its base. The material properties of the dam chosen are as follows: modulus of elasticity  $E=30.0 \times 10^6$  kPa; Poisson’s ratio  $\nu=0.20$ ; density of concrete  $\rho=2600.0$  kg/m<sup>3</sup>; tensile strength  $f_t' = 1.8 \times 10^3$  kPa, and fracture energy of concrete material for unit area  $G_f=180.0$  N/m.

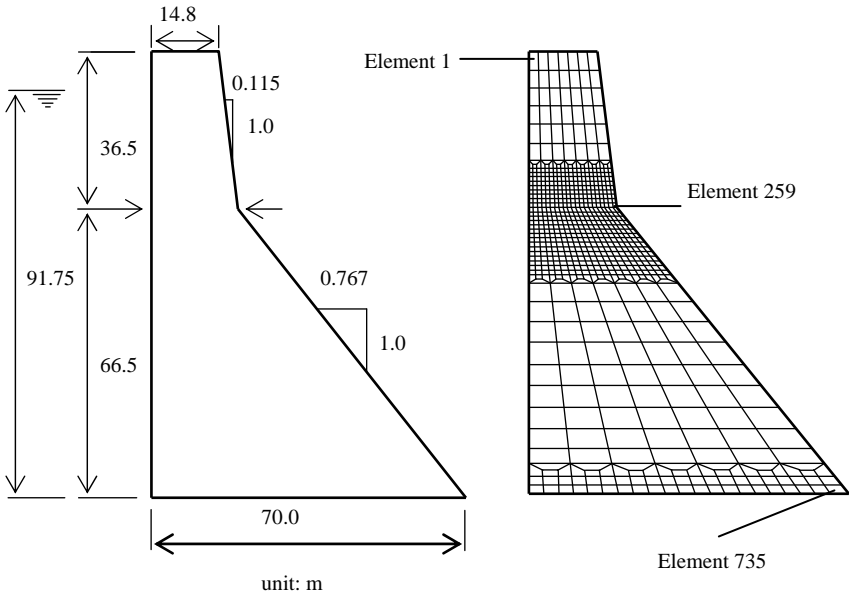


Figure 1. Koyna dam model and FE discretization.

The loading consists of self-weight of the dam, hydrostatic as well as hydrodynamic effects of the reservoir, the transverse and vertical components of earthquake loadings. The hydrodynamic loading is estimated using the added mass technique proposed by Westergaard (1931). Koyna earthquake acceleration record is used as input earthquake, as shown in Figure 2. The peak accelerations are scaled to  $0.4g$  in the transverse direction and  $0.28g$  in vertical direction. The input earthquake loading is assumed at the base of the dam.

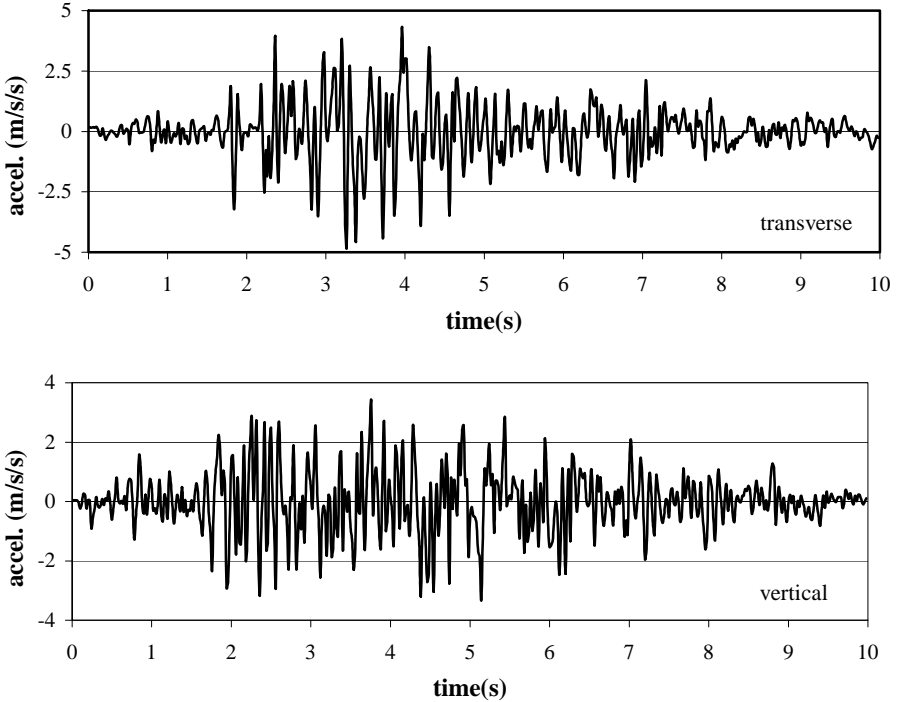


Figure 2. Acceleration time histories of Koyna earthquake.

The dam is analysed in time domain using Newmark Method with time step 0.02 second. The numerical analyses were carried out for two cases: without considering ageing effects, and considering the ageing degradation effects for the dam at 30 years of age. Structural responses and damage parameters were obtained for both cases to check the effect of ageing degradation on seismic behavior of the dam structures.

Figure 3 shows the time histories of displacement in horizontal direction at dam crest. It can be seen clearly that the displacement of the aged dam is larger than the case without considering ageing degradation. This is due to the decrease in the strength of concrete and also due to more severe damage of the aged dam during earthquake.

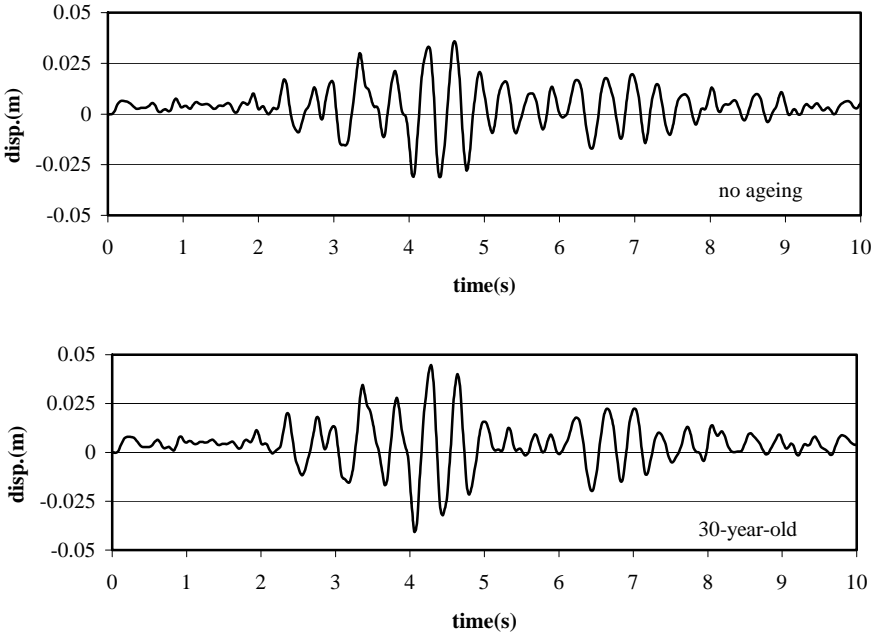


Figure 3. Time histories of horizontal displacement of crest.

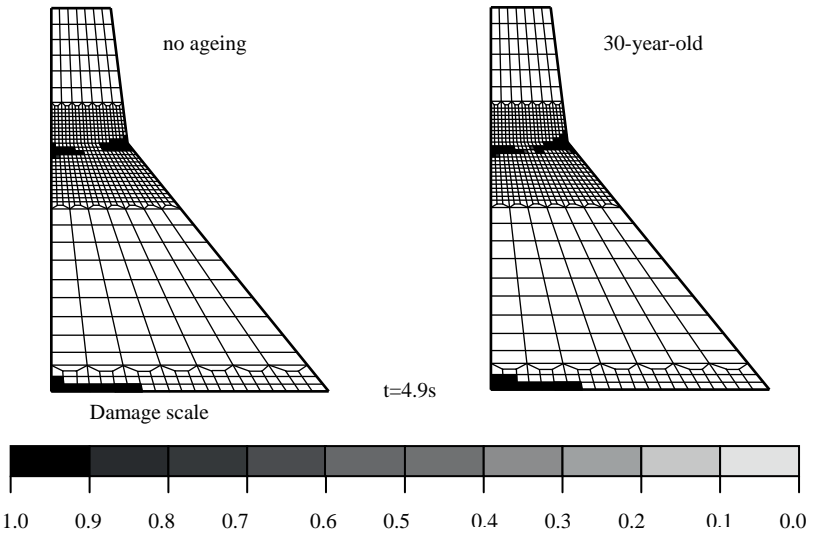


Figure 4. Damage patterns for un-aged and aged dam models.

The damage patterns of the dam (at time = 4.9 second) without and with consideration of ageing degradation effect are shown in Figure 4. Comparing the damage patterns of these two cases, it can be seen that the damage of the aged dam extends deeper into the dam neck. At the same time, the base of the aged dam has also been subjected to more damage than the dam without ageing effects.

## 4 Conclusions

Irrespective of the fact that ageing of dams is a slow process, degradation of concrete can change its physical properties and hence the behaviour of dams after several decades thus reducing their capacity to withstand hostile natural events such as earthquakes.

Using techniques such as finite element method, damage mechanics and ageing degradation evaluation method, a unified approach is presented for dynamic analysis of large concrete gravity dam with ageing degradation effect. The proposed method was validated by the numerical results obtained from the analysis of Koyuna dam. These results show more severe damages occur for aged dam structures when ageing degradation is taken into consideration.

There are many uncertainties associated with aged concrete dams, especially, the time-dependent degradation mechanisms are only known vaguely and imprecisely. To deal with these uncertainties, fuzzy set theory initiated by Zadeh in 1965, is a suitable tool to investigate the effects of uncertainties. Based on the method presented by Valliappan and Pham (1995), fuzzy finite element method can be applied to check the effect of uncertainties to evaluate the safety of aged concrete dams.

## References

- Ahmadi M. T., Izadina M. and Bachmann H. (2001). A discrete crack joint model for nonlinear dynamic analysis of concrete arch dam. *Computers and Structures*, 79(4): 403-420.
- ANCOLD (1992). Status of dam safety in Australia. *ANCOLD Bulletin*, 91: 9-29.
- Bazant Z. P. and Lin F. B. (1988). Non-local smeared cracking model for concrete fracture. *Journal of Structural Engineering, ASCE*, 114(11): 2493-2510.
- Boros-Meinike D. and Jankowski W. (2003). A monitoring-based assessment of the ageing process of selected Polish dams. *Proc. 21<sup>st</sup> ICOLD Congress on Large Dams*, Q 82, R 1, Montreal, Canada.
- Braverman J. I., Miller C. A. C., Hofmayer H., Ellingwood B. R., Naus D. J., and Chang T. Y. (2004). Degradation assessment of structures and passive components at nuclear power plant. *Nuclear Eng. Design*, 228(1-3): 283-304.
- Corns C. F., Jansen R. B. and Lombardi G. (1988). Concrete dam performance and remedial measures. *Advanced Dam Engineering for Design, Construction, and Rehabilitation* (Editor: R.B. Robert), 578-608.

- Ellingwood B. R. (1998). Issues related to structural ageing in probabilistic risk assessment of nuclear power plant. *Reliability Eng. System Safety*, 62(3): 171-183.
- Enright M. P., Frangopol D. M. and Hearn G. (1996). Degradation of reinforced concrete bridges under aggressive conditions. *Materials for the New Millennium*, ASCE (Editor: K. P. Chong), 2: 978-987.
- Ghrib F. and Tinawi R. (1995). An application of damage mechanics for seismic analysis of concrete gravity dams. *Earthquake Engineering and Structural Dynamics*, 24(2): 157-173.
- Horii H. and Chen S. C. (2003). Computational fracture analysis of concrete gravity dams by crack-embedded elements – Toward an engineering evaluation of seismic safety. *Eng. Fracture Mech.*, 70(7-8): 1029-1045.
- Hrabowski W., Urbanski A. and Konwerska-Habowska J. (2003). In situ investigation and numerical analysis of thermal cracking in Zatonie Dam. *Proc. 21<sup>st</sup> ICOLD Congress on Large Dams*, Q 82, R 2, Montreal, Canada.
- ICOLD (1994). Ageing of dams and appurtenant works. Bulletin 93, International Commission on Large Dams.
- Jabarooti M. R. and Golabtoonchi I. (2003). Alkali-aggregate reactivity in south-east of Iran. *Proc. 21<sup>st</sup> ICOLD Congress on Large Dams*, Q 82, R 5, Montreal, Canada.
- Kachanov L. M. (1982). Continuum model of medium with crack. *J. Eng. Mech.*, ASCE, 106(5): 1039-1081.
- Karihaloo B. L. and Santhikumar S. (1995). Application of visco-elastic tension-softening constitutive model to cracked and ageing concrete. *Construction and Building Materials*, 13(1-2): 15-21.
- Lackner R. and Mang H. A. (2001). Adaptivity in computational mechanics of concrete structures. *Int. J. Num. Anal. Methods Geomech.*, 25(7): 711-739.
- Lublinter J., Oliver, J., Oller S. and Onate E. (1989). A plastic damage model for concrete. *Int. J. Solids and Structures*, 25(3): 299-326.
- Mori Y. and Ellingwood B. R. (1993). Reliability-based service-life assessment of ageing concrete structures. *J. Struct. Eng.*, ASCE, 119(5): 1600-1621.
- Mori Y. and Nonaka M. (2001). LRFD for assessment of deteriorating existing structures. *Structural Safety*, 23: 297-313.
- Murley K. (2000). Surveillance and safety of dams. *Dam Technology in Australia 1850-1999* (Editor: B. Cole), 209-225.
- Murti V. and Valliappan S. (1986). The use of quarter point element in dynamic crack analysis. *Eng. Fracture Mech.*, 23: 585-614.
- Naus D. J. (1986). Concrete component ageing and its significance relative to life extension of nuclear power plant. Report No. NUREG/CR-4652. Oak Ridge National Laboratory.
- Naus D. J., Oland C. B., Ellingwood B. R., Hookham C. J. and Graves H. L. (1999). Summary and conclusions of a program addressing ageing of nuclear power plant concrete structures. *Nuclear Eng. Design*, 194: 73-96.
- Plizzari G. A. (1998). On the influence of uplift pressure in concrete gravity dams. *Eng. Fracture Mech.*, 59(3): 253-267.
- Sen S. C. and Venkatesha C. R. (1991). Concrete and masonry dams. *Proc. 1<sup>st</sup> Conf. Research Needs in Dam Safety*, New Delhi, India, Vol. 1, III1-7.
- Tango C. E. S. and Andriolo F. R. (2003). Applying an age function to data from dam jobs – Simulation of concrete strength prediction. *Proc. 21<sup>st</sup> ICOLD Congress on Large Dams*, Q 82, R 81, Montreal, Canada.
- Tekie P. B. and Ellingwood B. R. (2003). Seismic fragility assessment of concrete gravity dams. *Earth Eng. Struct. Dyn.*, 32(14): 2221-2240.
- Valliappan S. and Ang K. K. (1985). Dynamic analysis applied to rock mechanics problems. *5<sup>th</sup> Int. Conf. on Numerical Methods in Geomechanics*, Nagoya: 119-132.
- Valliappan S., Murti V. and Zhang W. (1990). Finite element analysis of anisotropic damage mechanics problems. *Eng. Fracture Mech.*, 35(6): 1061-1071.

- Valliappan S. and Pham T. (1995). Fuzzy logic applied to numerical modelling of engineering problems. *Computational Mechanics Advances*, 2(3): 213-281.
- Valliappan S., Yazdchi M. and Khalili N. (1996). Earthquake analysis of gravity dams based on damage mechanics concept. *Int. J. Num. Analyt. Meth. Geomech.*, 20(10): 725-752.
- Valliappan S. and Yazdchi M. (1999). Seismic response of concrete gravity dams – A continuum damage mechanics approach. *Discretization Meth. Struc. Mech.* (Editors: H. A. Mang and F. G. Rammerstorfer). Kluwer Academic Publishers: 123-130.
- Valliappan S., Yazdchi M and Khalili N. (1999). Seismic analysis of arch dams – A continuum damage mechanics approach. *Int. J. Num. Meth. Eng.*, 45(11): 1695-1724.
- Vesikari E. (1988). Service life of concrete structures with regard to corrosion of reinforcement. Finland: Research Reports, Espoo.
- Vu K. A. T. and Stewart M. G. (2000). Structural reliability of concrete bridge including improved chloride-induced corrosion models. *Structural Safety*, 22(4): 313-333.
- Yazdchi M., Khalili N., and Valliappan S. (1999). Nonlinear seismic behavior of concrete gravity dams using coupled finite element-boundary element technique. *Int. J. Num. Meth. Eng.*, 44(1): 101-130.
- Westergaard H. M. (1931). Water pressures on dams during earthquakes. *Transactions of ASCE*, 98: 418-433.
- Zadeh L. A. (1965). Fuzzy Sets. *Information and Control*, 8(3): 338-353.
- Zhang W. and Valliappan S. (1998). Continuum damage mechanics theory and application, part I-theory. *Int. J. Damage Mech.*, 7: 250-273.
- Zhang Y. and Ma L. (1991). Relation between the ageing of concrete dams and the ambient temperature. *Proc. 17<sup>th</sup> ICOLD Congress on Large Dams*, Q 65, R 15, Vienne, Austria.

*“This page left intentionally blank.”*

# Multi-Scale and Multi-Thermo-Mechanical Modeling of Cementitious Composites for Performance Assessment of Reinforced Concrete Infrastructures

Koichi Maekawa<sup>1\*</sup>

<sup>1</sup>Department of Civil Engineering, University of Tokyo, Japan

**Abstract.** Coupled analysis of mass transport and damage mechanics associated with steel corrosion is presented for structural performance assessment of reinforced concrete. Multi-scale modeling of micro-pore formation and transport phenomena of moisture and ions are mutually linked for predicting the corrosion of reinforcement and volumetric changes. The interaction of crack propagation with corroded gel migration is simulated. Two computer codes for multi-chemo physical simulation (*DuCOM*) and nonlinear dynamic mechanics of structural concrete (*COM3*) were combined and verified by the laboratory scale experiments of damaged reinforced concrete members under static and dynamic loads, and has been applied to safety and serviceability assessment of existing infrastructures.

**Keywords:** multi-scale modeling, life-cycle assessment, coupled analysis

## 1 Introduction

In the scheme of performance-based design with more transparency to society, performance assessment methods occupy a central position from a viewpoint of structural engineering. This rational way of assuring the overall quality of infrastructures may create cost-beneficial design and construction that exactly satisfies several requirements assigned to engineers. Life-cycle performance of structures is being explicitly required and appropriate design methods for both materials and structures are sought in several organizations. Needs to verify remaining functionality of damaged existing facilities is rising for extending service life. To meet these challenges, keenly expected is an explicit prediction and simulation of structural life serviceability and safety under specified loads and ambient conditions.

---

\* Corresponding author, e-mail: koichi\_maekawa@civil.t.u-tokyo.ac.jp

In this paper, the author proposes an integrated platform of solid mechanics and thermo-hydro dynamics of materials and structures with multi-scales of referential control volume on which each chemo-physics is applied. In more detail, the constitutive model is discussed with regard to cracking in RC elements, and overlay of thermo-hydro state variables is presented for multi-scale and multi-chemo mechanical coupling with soil foundation. Recent application of the multi-scale approach to practical problems is introduced and the future development is discussed as an integrated knowledge-base of structures and soil foundation.

## 2 Multi-Directional Crack Mechanics

A scheme of RC modeling used for an integrated platform of both safety and life-cycle assessment is simply illustrated in Figure 1 (Maekawa, et al., 1999, 2003, 2008). Multi-directional cracking and its interaction are taken into account by the active crack approach (Maekawa, et al., 2003) on the smeared compression stress field (Collins and Vecchio, 1982). All microscopic physical states (cracking, yielding, crack shear slip, remaining stiffness of fractured materials) are included in the constitutive modeling. These stress carrying mechanisms are composed of compression/tension parallel and normal to cracking and shear transfer. By the active crack method (Maekawa, et al., 2003), the primary cracking of governing nonlinearity of structural concrete is identified if some cracks intersect non-orthogonally. Here, path-dependent parameters are renewed only along the active crack in each load step of time.

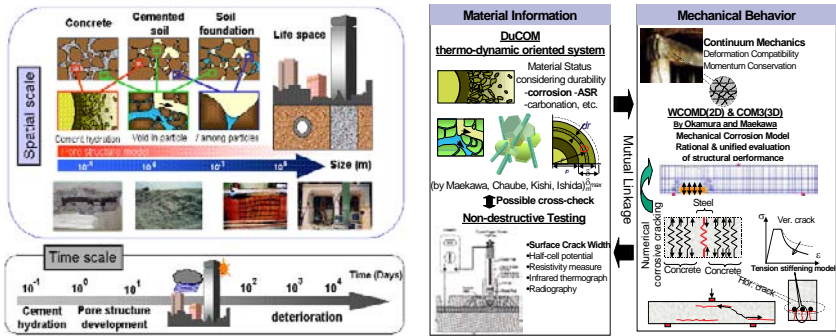


Figure 1. Coupling of thermo-hydro dynamics and damage mechanics for life cycle assessment of structures with soil foundation interaction.

Plastic localization of reinforcement is of importance for rationally simulating largely deformed elements. The spatial averaging of local stress and strain along reinforcement is applied for structural analysis with finite elements as shown in



analysis is authorized as a tool to examine the seismic safety performance in the scheme of designing LNG storage tanks and RC aqua-ducks for nuclear power plant facilities for practice in Japan (JSCE, 1999).

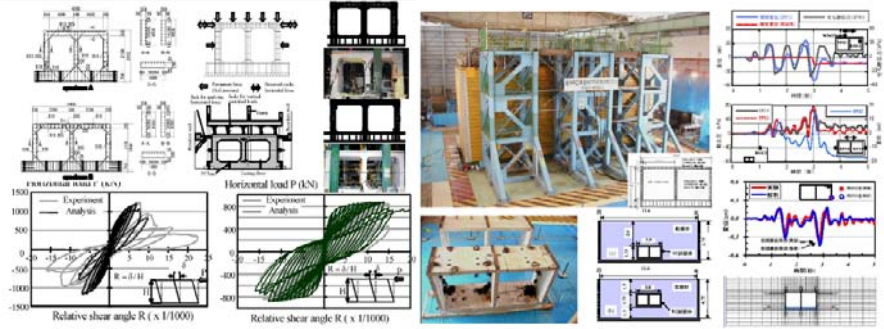


Figure 3. RC underground box-vents subjected to dynamic shear (JSCE, 1999)

### 3 Thermo-Hydro Chemo-Physical Modeling

State variables of thermo-hydro dynamics are further required for life-cycle assessment, especially for durability assessment related to material properties. Volumetric change caused by temperature and long-term moisture equilibrium in micro-pores are associated with cracking and corresponding serviceability, and corrosion of reinforcement has much to do with migration of chemicals through micro-pores. Thus, the coupled system was proposed (Maekawa, et al., 2003, 2008) to simulate the entire thermo-mechanical states of constituent material and structures. For computing the thermo hydro equilibrium, multi-scale analysis platform *DuCOM* (Maekawa, et al., 1999, 2008) was used. Micro-pore geometry and spaces are idealized by statically formulated pore distribution and internal moisture balance is simultaneously solved with mass conservation requirement. The moisture migration and diffusivity are computed based on the micro-pore size distribution and the linked condensed water channel (see Figure 4).

Chloride ion migration and other chemical reactions such as carbonation and calcium leaching are overlaid on this system (Maekawa, et al., 2008). The conductivity and diffusion characteristics for mass transport are calculated based upon computationally formed micro-pore structure. The computation of multi-chemo-physical events is carried out by means of the sequential processing with closed-loop predictor-corrector method. The temperature dependent volume change is considered as an offset strain in constitutive modeling. But, concrete shrinkage associated with microclimate in CSH gel and capillary pores is directly linked with the macroscopic constitutive model (see Figure 5) with regard to micro-pore pressure and disjoining pressure originated from Van der Waals and Coulomb forces.

Micro-corrosion rate is also computed by simulating migration of O<sub>2</sub>-CO<sub>2</sub> gas and chloride ion (Maekawa, et al., 2008), and the effect of corrosion is integrated in the structural analysis (Toongoenthong, et al., 2004). These state variables are incorporated into the constitutive modeling before cracking. In this computation, the thermo-dynamic equilibrium requirements are simultaneously solved such as multi-ion balance, proton electro-balance, adsorption-desorption isotherm. Then, we have approximately 230 simultaneous equations to be solved numerically for chemo-physical and mechanical behaviors of different scales.

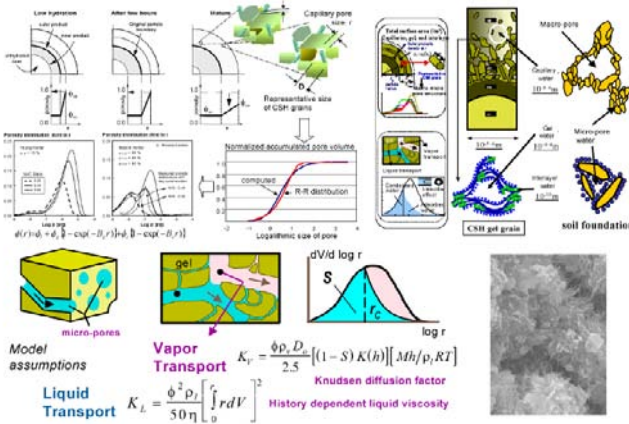


Figure 4. Statistical expression of CSH micro-porosity and the moisture equilibrium.

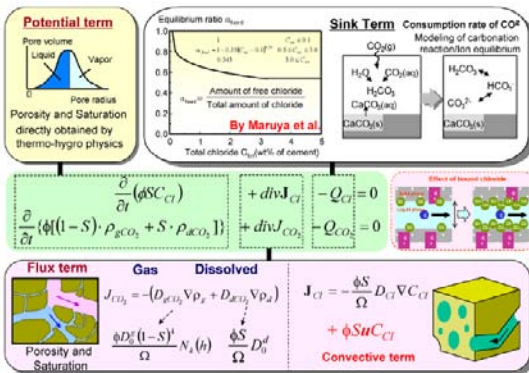
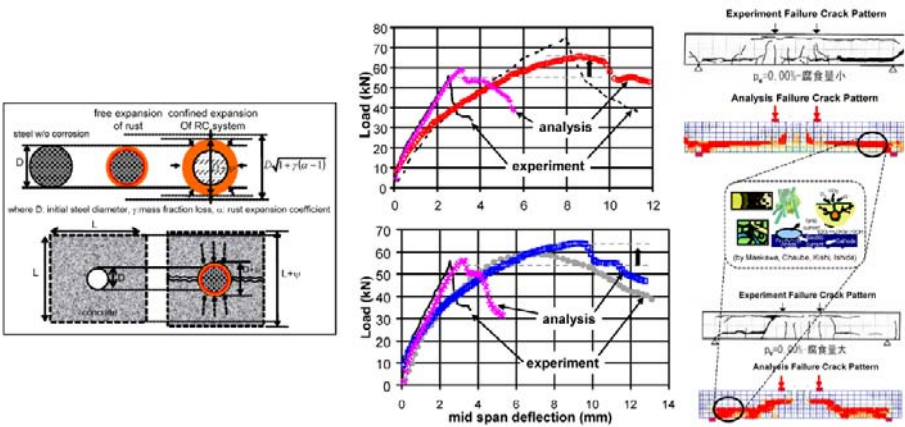


Figure 5. Micro-Modeling of CSH gel and capillary pores and multi-chemo physics.

### 4 Coupling of Damage Mechanics with Chemo-Physical Events

Cracking is also influential in mass transport of gases and dissolved ions. These cracks through which ion substances can easily migrate are mutually linked with thermo-hydro dynamic analysis by the hierarchy type of multi-scale modeling. This simulation can be mainly used for life-cycle assessment of structural concrete and examination of remaining functions of existing infrastructures. Cracking of concrete causes accelerated diffusion of chloride. It may allow deeper penetration of chloride and other substances. In the analysis, diffusivity of substances is regarded as a variable in terms of computed averaged strain of concrete finite elements.

The corroded steel produces volumetric expansion and results in internal self-equilibrated stress, which may lead to additional cracking around reinforcing bars. Figure 6 illustrates the way to amalgamate the damage mechanics and volume expansion of generated corrosion gels. The effect of corrosion gel product formation is considered in the constitutive modeling of reinforcement in the transverse direction. The non-corroded core steel and the corroded clusters with different mechanical properties are treated as a fictitious aging material of varying volumetric stiffness and expansion according to the magnitude of corrosion. This growing steel is embedded in each finite element similar to smeared crack approach as well. If the corrosion is concentrated around the anchorage zone of main reinforcement, its structural capacity gets reduced with the different crack propagation pattern from those of sound ones (Toongoenthong, et al., 2004a, 2004b) as shown in Figure 6 (right).



a) Load-displacement relation. b) Failure crack pattern.  
 Figure 6. Simulated shear capacity and cracking of corrosion beam (Okada et al. 1988).

The diagonal crack which reaches the bending compression zone is initiated by the corrosion crack tip created along the longitudinal main reinforcement. Finally,

the diagonal crack is driven to the beam support. Apparently, the localized corrosion is seen to deteriorate the anchorage performance of longitudinal reinforcement. The acceleration test of corrosion of steel in RC beam by galvanostatic charge also substantiated this simulation result.

When the corrosion cracking develops over the beam, shear safety performance differs from the non-damaged reference case (Sato, et al., 2003). Figure 6 shows load-displacement relations for RC non-damaged reference and corroded specimen, which was submerged into a sodium pond for accelerated corrosion. Here produced was uniformly distributed corrosion along the whole longitudinal steel of 2.1% as the mass loss. Main reinforcing bars were bent up 90 degree inside the anchorage zone. Thus, comparatively satisfactory anchorage capacity is expected. In this case, the stiffness of the beam is much reduced but the capacity is a bit increased in both experiment and analysis. The macroscopic bond loss in the shear span leads to retarded propagation of diagonal shear cracking and may elevate the shear capacity. Computation can capture this property.

Autogenous and drying shrinkage, which is computed by solving the moisture migration under ambient conditions (Mabrouk, et al., 2004), can be directly included in the constitutive modeling of concrete in each finite element as shown in Figure 7 and Figure 8. The coupling of concrete creep in compression, shrinkage and post-cracking time-dependent tension stiffness models yields consistent behavioral simulation with reasonable accuracy for long-term deflection.

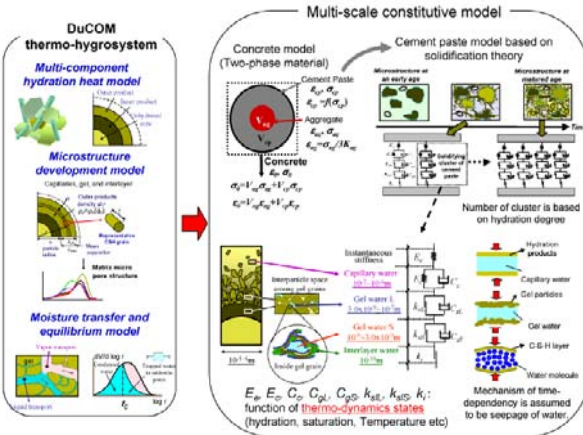


Figure 7. Solidification modeling of hardening cement hydrate and concrete composites (Asamoto, et al. 2006, Maekawa, et al. 2008).

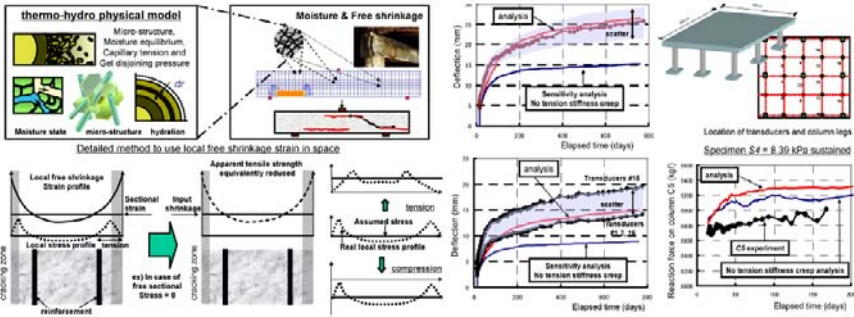


Figure 8. Simulated shear capacity and cracking of corrosion beam under fatigue loads (experiment by Guo and Gilbert, 2002).

Figure 9 shows the application examples for the seismic performance assessment of existing aqua-ducks of nuclear power plants and a 100-years old railway bridge in Tokyo (Sogano, et al., 2001). The point of analysis is the residual seismic performance with corrosive damages and uneven settlement of the soil foundation. Some initial damage remains in the form of cracking, and arch ribs were strengthened by additional RC arch inside layer in the past. The seismic ground motion was applied to the numerically aged structural concrete and the computed response was used for safety and serviceability assessment in practice. The seismic remaining performance was numerically investigated and the sustainable life with light retrofit was judged.

The corrosion damaged RC underground box culverts shows reduced seismic performance as shown in Figure 10. The coupled simulation re-produces the steel corrosion and associated cracking, which may influence on the dynamic responses. But, if damaged structures are surrounded by soil foundation, sensitivity of damage and steel corrosion tends to be less compared to on-ground structures. In this case, the full 3D soil-structure system can be analyzed to assess the overall safety performance under traffic and seismic actions.

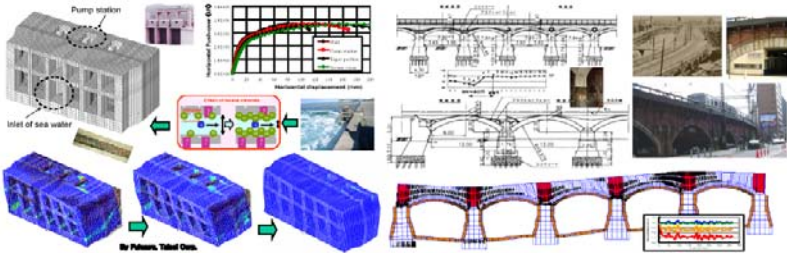


Figure 9. Safety assessment of infrastructures against earthquake –nuclear plant facility and 100 years-old railway bridges (Sogano, et al. 2001).

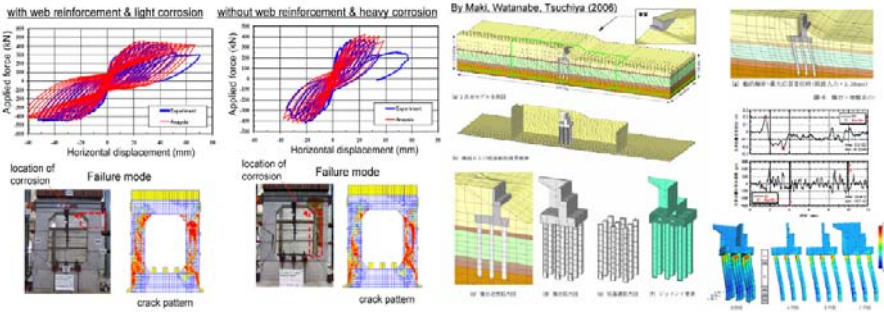


Figure 10. Safety assessment of infrastructures against earthquake –corroded aqua-ducs (Matsuo et al. 2007) and soil-structure interactions (Maki, et al.).

Figure 11 shows the PRC bridge in which plenty of cracks were induced to the viaducts due to excessive shrinkage of concrete and heavy reinforcement. The compliance of the viaduct in each span was reported to be much increased and the fatigue life was questioned. JSCE concrete committee (2005) investigated the detailed damage and corresponding remaining fatigue life by using the coupled chemo-mechanical simulation. For verification of the analysis method, the design live load (1500 kN) was applied on the deck and the incremental deflection was measured as shown in Figure 11. The simulation was reported to be closer to the reality of the damaged PRC bridge.

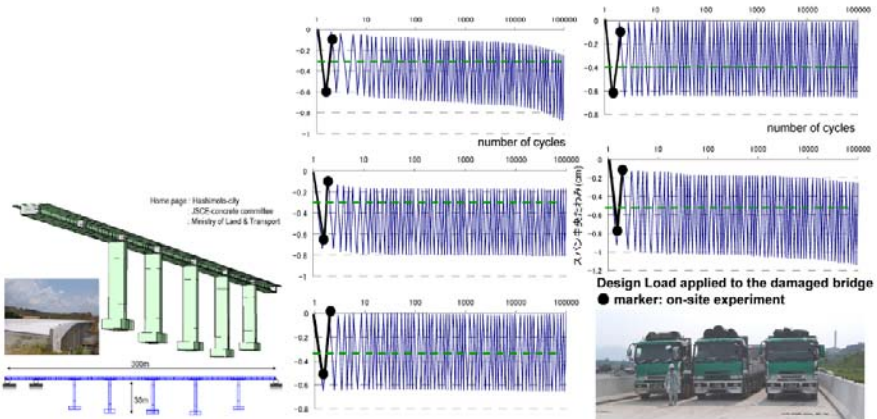


Figure 11. Shrinkage cracking and RC bridge pier: Simulation of remaining fatigue life.

## 6. Conclusions

Chemo-physical and mechanical modeling of concrete with greatly different scales of geometry was presented, and synthesized on a unified computational platform, which may bring about quantitative assessment of structural concrete performances of interaction with soil foundation. The safety assessment method was extended to the life-cycle issue with multi-scaled information on microclimate states of cementitious composites under macroscopic ambient boundary conditions. Currently granted is a great deal of knowledge earned by the past development. At the same time, we face a difficulty to quantitatively extract consequential figures from them. The author expects that the systematic framework on the knowledge-based technology will be extended efficiently and can be steadily taken over by engineers in charge.

## References

- Asamoto S., Ishida, T. and Maekawa K. (2006). Time-dependent constitutive model of solidifying concrete based on thermodynamic state of moisture in fine pores, *Journal of Advanced Concrete Technology*, 4(2): 301-323.
- Collins M. P. and Vecchio F. (1982). The response of reinforced concrete to in-plane shear and normal stresses, *University of Toronto*.
- Guo X. H. and Gilbert R. I. (2001). An experimental study of reinforced concrete flat slabs under sustained service loads, UNICIV Report No.R-407.
- Japan Society of Civil Engineers. (1999). Recommendation for structural performance verification of LNG underground storage tanks, Tokyo: *Concrete Library of JSCE*, No. 98.
- Japan Society of Civil Engineers. (2005). Report on safety and serviceability of ASR damaged RC structures, Tokyo: *Concrete library of JSCE*, No.124.
- Japan Society of Civil Engineers (2005). Intermediate technical report on damage and repair of Tarui highway bridge, special sub-committee.
- Komine H. and Ogata N. (1999). Experimental study of swelling characteristic of sand-bentonite mixture for nuclear waste disposal, *Soils and Foundations*, 39(2): 83-97.
- Li C. Q. (2003). Life-cycle modeling of corrosion-affected concrete structures: Propagation, *Journal of Structural Engineering, ASCE*, 129(6): 753-761.
- Mabrouk R., Ishida T. and Maekawa K. (2004). A unified solidification model of hardening concrete composite for predicting the young age behavior of concrete, *Cement and Concrete Composites*, 26: 453-461.
- Maekawa K., Pimanmas A. and Okamura H. (2003). *Nonlinear Mechanics of Reinforced Concrete*, London: Spon Press.
- Maekawa K., Chaube R. P. and Kishi T. (1999). *Modeling of Concrete Performance*, London: Spon Press.
- Maekawa K., Ishida K. and Kishi T. (2008). *Multi-scale Modeling of Structural Concrete*, London: Taylor and Francis.
- Matsuo T., Miyagawa Y., Akiyama T. and Iwamori A. (2007). Real-scale loading experiment of RC box culverts with corroded reinforcement, *Transaction of JSCE*, 62(5).
- Okada K., Kobayashi K. and Miyagawa T. (1988). Influence of longitudinal cracking due to reinforcement corrosion on characteristics of reinforced concrete members, *ACI Structural Journal*, 85(2): 134-140.

- Sakurai N. (2005). A study on rationalization of the shape steel bridge, *Journal of JSCE*, 794, 794\_67-794\_86.
- Sato H. et al. (1995). Diffusion behavior for Se and Zr in sodium-bentonite, *Scientific Basis for Nuclear Waste Management XVIII*, 353: 269-276.
- Satoh Y. et al. (2003). Shear behavior of RC member with corroded shear and longitudinal reinforcing steels, *Proceedings of the JCI*, 25(1): 821-826.
- Sogano T. et al. (2001). Numerical analysis on uneven settlement and seismic performance of Tokyo brick bridges, *Structural Engineering Design*, No.17, JR-East, 96-109.
- Soraoka H., Adachi M., Honda K., and Tanaka K. (2001). Experimental study on deformation performance of underground box culvert, *Proceedings of the JCI*, 23(3): 1123-1128.
- Toongoenthong K. and Maekawa K. (2004a). Multi-mechanical approach to structural performance assessment of corroded RC members in shear, *Journal of Advanced Concrete Technology*, 3(1): 107-122.
- Toongoenthong K. and Maekawa K. (2004b). Interaction of pre-induced damages along main reinforcement and diagonal shear in RC members, *Journal of Advanced Concrete Technology*, 2(3): 431-443.

*“This page left intentionally blank.”*

# Statistical Multi-Scale Method of Mechanics Parameter Prediction for Rock Mass with Random Cracks/Joints Distribution

J.Z. Cui<sup>1,2\*</sup>, Fei Han<sup>1</sup> and Y.J. Shan<sup>2</sup>

<sup>1</sup> Department of Applied Mathematics, Northwestern Polytechnical University, Xi'an 710129, China

<sup>2</sup> Academy of Mathematics and System Sciences, Chinese Academy of Sciences, Beijing 100190, China

**Abstract.** In this paper a statistical multi-scale method for the mechanics parameter prediction of the rock mass with random distribution of multi-scale cracks/joints is presented. First the micro-structure of the rock mass with random distribution of multi-scale cracks/joints is represented. Then the statistical second-order two-scale method for the mechanics performance predictions of the rock mass structure with random cracks/joints distribution is presented, including the statistical second-order two-scale expression on the vector-valued displacement, strain tensor and stress tensor, and the algorithm procedure of statistical multi-scale computation for the mechanics parameters. Finally some numerical results for mechanical parameters for the rock mass with random distributions of multi-scale joints/cracks by statistical multi-scale method are shown.

**Keywords:** rock mass mechanics, mechanics parameter prediction, statistical multi-scale method, rock mass with random distribution of multi-scale cracks/joints

## 1 Introduction

With the rapid advance of engineering science, especially computing technology, the computational engineering science is developing very fast. A variety of numerical methods for the predicting the physical and mechanical performance of materials was developed in last decade.

According to their micro-structure the composite materials can be divided into two classes: composite materials with periodic configurations (Cui et al. 1997 Cui and Shan 2000) and composite materials with random distribution (Li and Cui 2004). A lot of random composite materials exist in nature and human life, such

---

\* Corresponding author, e-mail: cjz@lsec.cc.ac.cn

as rock mass and concrete (Shan et al. 2002). Due to the difference of their micro-configurations it needs to make use of different numerical methods to evaluate the physical and mechanical performance of them.

For the composite materials with random distribution some works have been done for predicting the physics and mechanical properties of random particulate composites (Li and Cui 2005 Yu et al. 2008). Many approaches can be used to the calculation of macroscopic stiffness parameters, such as the law of mixture, Hashin-Shtrikman upper and lower bounds method, self-consistent approach and Eshelby effective inclusion method etc. However, in regard to the prediction for strength parameters there are few theoretical techniques available, and most of them are based on the greatly simplification of real composite structures. Till now there is still no multi-scale analysis method to predict the physical and mechanical performance of the rock mass structure with random joints or/and cracks distribution.

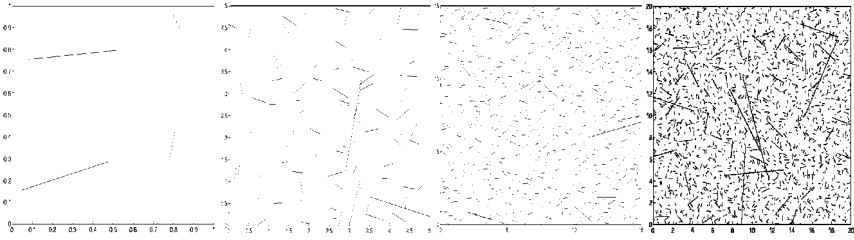
In this paper a new statistical multi-scale method is presented to predict the mechanical performance of rock mass with random joint and/or crack distribution and related structures.

The remainder of this paper is outlined as follows. In section 2 the representation of the rock mass with random distributions of multi-scale joints/cracks briefly described. The section 3 is devoted to the statistical second-order two-scale formulation for the prediction of the materials with random distribution and related structure. In section 4 the algorithm procedure for statistical multi-scale computation of rock mass with random distributions of multi-scale joints/cracks is given. In section 5 some numerical results for mechanical parameters of the rock mass with random distributions of multi-scale joints/cracks are shown.

## 2 Multi-Scale Representation of Rock Mass with Random Joint/Crack Distribution

The materials with random joint/crack distribution, such as rock mass and damaged materials, can be represented as follows: all of the joints inside investigated structure are divided into several groups in their lengths  $l^j$  and  $\varepsilon^j > l^j > \varepsilon^{j+1}$ .

From the survey of engineering geology and the fitting method of statistic data, for each group of joints/cracks the probability distribution of the joints inside structure  $\Omega$  can be described as follows:



a. Joints In  $\varepsilon^4$ -Screen b. Joints In  $\varepsilon^3$ -Screen c. Joints In  $\varepsilon^2$ -Screen d. Joints In  $\varepsilon^1$ -Screen

Figure 1. The Joint Statistical Model of the Four Screen Scales in Rock Mass

1. The long joints, whose length  $l > \alpha L$  and  $L$  is the size of structure  $\Omega$ , are considered determinate, generally, choose  $\alpha \approx 10^{-1}$ .
2. Choose  $\varepsilon^j$  ( $j=1,2,\dots,m$ ) and  $\alpha L > \varepsilon^1 > l^{j-1} > \varepsilon^j > 0$  the statistical model of joints with the length  $l^j$  satisfied  $\varepsilon^j > l^j > \varepsilon^{j+1}$  can be determined in following way:
  - (a) Specify the density of joint distribution and the distribution model of central points of joints, for example, uniform distribution in  $\Omega$ .
  - (b) Specify the distribution model for trace lengths of joint surfaces, for example, normal distribution round the value of some length.
  - (c) Specify the distribution model for inclinations of joint surfaces in  $[0, \pi/2]$ , for example, some normal distribution round some angle. And specify the distribution model for trends of joint surfaces in  $[-\pi/2, \pi/2]$ , for example, some normal distribution round some angle.
3. For most of rock mass structures there is some jointing inside joint surfaces, and it occupies a certain thickness. So the thickness of jointing must be specified, for example, it is supposed to be a function depended on its trace length.
4. The physical or mechanical parameters of intact rock and jointing must be prescribed.

From previous representation in rock mass structure  $\Omega$  one can obtain a sample of every group of joints with lengths  $l^j$  ( $j=1,2,\dots,m$ ) where  $\varepsilon^j > l^j > \varepsilon^{j+1}$ , and then periodically obtain a concrete distributions  $\{a_{ij}^\varepsilon(x, \omega)\}$  and  $\{a_{ijk}^\varepsilon(x, \omega)\}$  on physical and mechanical parameters on  $\Omega$ . As example, a sample distribution for a kind of rock mass is shown in Figure 1.

### 3 Statistical Second-Order Two-Scale Formulation of the Structure with Random Joint/Crack Distribution

#### 3.1 Statistical Two-Scale Formulation for the Composites with Random Distribution

In this section based on the representation previously the structures with random distribution of one scale joints/cracks is investigated, and it has only same  $\varepsilon$ -size statistic screen. Its elasticity problem with mixed boundary conditions can be expressed as follows:

$$\left\{ \begin{array}{l} \frac{\partial}{\partial x_j} \left[ a_{ijhk}^\varepsilon(x, \omega) \frac{1}{2} \left( \frac{\partial u_h^\varepsilon(x, \omega)}{\partial x_k} + \frac{\partial u_k^\varepsilon(x, \omega)}{\partial x_h} \right) \right] = f_i(x) \quad x \in \Omega \\ \sigma_i(x, \omega) = \nu_j^{(1)} a_{jihk}^\varepsilon(x, \omega) \frac{1}{2} \left( \frac{\partial u_h^\varepsilon(x, \omega)}{\partial x_k} + \frac{\partial u_k^\varepsilon(x, \omega)}{\partial x_h} \right) = p_i(x) \quad x \in \Gamma_2 \\ \mathbf{u}^\varepsilon(x, \omega) = \bar{\mathbf{u}}(x) \quad x \in \Gamma_1 \\ (\Gamma_1 \cap \Gamma_2 = \emptyset, \quad \Gamma_1 \cup \Gamma_2 = \partial\Omega) \end{array} \right. \quad (1)$$

where suppose that  $a_{ijhk}^\varepsilon(x, \omega)$  ( $i, j, h, k=1, \dots, n$ ) are the elastic coefficients of the random distribution with  $\varepsilon$ -size periodicity, and the jointing between joint surfaces and matrix are considered isotropic homogenous materials and continuous transition zones, so  $\{a_{ijhk}^\varepsilon(x, \omega)\}$  is highly oscillating, but continuously varying.

Below SSOTS method will be discussed for the problem (1). Let  $\xi = \frac{x}{\varepsilon} - \left[ \frac{x}{\varepsilon} \right] \in Q^s$  denotes the local coordinates on 1-normalized cell of  $\varepsilon$ -cell  $\varepsilon Q^s \subset \Omega$ . Then  $a_{ijhk}^\varepsilon(x, \omega) = a_{ijhk}(\xi, \omega)$  and  $\mathbf{u}^\varepsilon(x, \omega) = \mathbf{u}(x, \xi, \omega)$ . Inspired by the paper or books (Cui & Yang 1996 Oleinik et al. 1992 Jikov et al. 1994), by using constructive way following formulas on SSOTS solution of previous problem were obtained: The displacement solution of problem (1) can be expressed as follows

$$\begin{aligned} \mathbf{u}^\varepsilon(x, \omega) = & \mathbf{u}^0(x) + \varepsilon \mathbf{N}_{\alpha_1}(\xi, \omega) \frac{\partial \mathbf{u}^0(x)}{\partial x_{\alpha_1}} + \varepsilon^2 \mathbf{N}_{\alpha_1 \alpha_2}(\xi, \omega) \frac{\partial^2 \mathbf{u}^0(x)}{\partial x_{\alpha_1} \partial x_{\alpha_2}} \\ & + \varepsilon^3 \mathbf{P}_1(x, \xi, \omega) \quad x \in \Omega, \end{aligned} \quad (2)$$

where  $\mathbf{u}^0(x)$  is the homogenization solution defined on global  $\Omega$ ,  $\mathbf{N}_{\alpha_1}(\xi, \omega)$  and  $\mathbf{N}_{\alpha_1\alpha_2}(\xi, \omega)$  ( $\alpha_1, \alpha_2 = 1, \dots, n$ ) are n-order matrix-valued functions defined on 1-normalized  $Q$ , and they have following forms

$$\mathbf{N}_{\alpha_1}(\xi, \omega) = \begin{pmatrix} N_{\alpha_1 11}(\xi, \omega) & \cdots & N_{\alpha_1 1n}(\xi, \omega) \\ \vdots & \cdots & \vdots \\ N_{\alpha_1 n1}(\xi, \omega) & \cdots & N_{\alpha_1 nm}(\xi, \omega) \end{pmatrix} \quad (3)$$

$$\mathbf{N}_{\alpha_1\alpha_2}(\xi, \omega) = \begin{pmatrix} N_{\alpha_1\alpha_2 11}(\xi, \omega) & \cdots & N_{\alpha_1\alpha_2 1n}(\xi, \omega) \\ \vdots & \cdots & \vdots \\ N_{\alpha_1\alpha_2 n1}(\xi, \omega) & \cdots & N_{\alpha_1\alpha_2 nm}(\xi, \omega) \end{pmatrix} \quad (4)$$

And  $\mathbf{N}_{\alpha_1}(\xi, \omega)$ ,  $\mathbf{N}_{\alpha_1\alpha_2}(\xi, \omega)$  ( $\alpha_1, \alpha_2 = 1, \dots, n$ ) and  $\mathbf{u}^0(x)$  are determined in following ways:

1. For any sample  $\omega^s$ ,  $\mathbf{N}_{\alpha_1 m}(\xi, \omega^s)$  ( $\alpha_1, m = 1, \dots, n$ ) are the solutions of following problems

$$\begin{cases} \frac{\partial}{\partial \xi_j} \left[ a_{ijk}(\xi, \omega^s) \frac{1}{2} \left( \frac{\partial N_{\alpha_1 km}(\xi, \omega^s)}{\partial \xi_k} + \frac{\partial N_{\alpha_1 km}(\xi, \omega^s)}{\partial \xi_h} \right) \right] = - \frac{\partial a_{ija_1 m}(\xi, \omega^s)}{\partial \xi_j} & \xi \in Q^s \\ \mathbf{N}_{\alpha_1 m}(\xi, \omega^s) = 0 & \xi \in \partial Q^s \end{cases} \quad (5)$$

2. From  $\mathbf{N}_{\alpha_1 m}(\xi, \omega^s)$ , the homogenization elasticity parameters  $\{\hat{a}_{ijk}(\omega^s)\}$  corresponding to the sample  $\omega^s$  are calculated in following formula

$$\hat{a}_{ijk}(\omega^s) = \int_{Q^s} \left( a_{ijk}(\xi, \omega^s) + a_{ijpq}(\xi, \omega^s) \frac{1}{2} \left( \frac{\partial N_{hpk}(\xi, \omega^s)}{\partial \xi_q} + \frac{\partial N_{hpk}(\xi, \omega^s)}{\partial \xi_p} \right) \right) d\xi \quad (6)$$

3. One can evaluate the expected homogenized coefficients  $\{\hat{a}_{ijk}\}$  in following formula

$$\widehat{a}_{ijkh} = \frac{\sum_{s=1}^M \widehat{a}_{ijkh}(\omega^s)}{M}, \quad M \rightarrow +\infty \quad (7)$$

4. For any sample  $\omega^s$ ,  $\mathbf{N}_{\alpha_1\alpha_2m}(\xi, \omega^s)$  ( $\alpha_1, \alpha_2, m = 1, \dots, n$ ) are the solutions of following problems

$$\left\{ \begin{array}{l} \frac{\partial}{\partial \xi_j} \left[ a_{ijkh}(\xi, \omega^s) \frac{1}{2} \left( \frac{\partial N_{\alpha_1\alpha_2hm}(\xi, \omega^s)}{\partial \xi_k} + \frac{\partial N_{\alpha_1\alpha_2km}(\xi, \omega^s)}{\partial \xi_h} \right) \right] = \widehat{a}_{i\alpha_2m\alpha_1} \\ -a_{i\alpha_2m\alpha_1}(\xi, \omega^s) - a_{i\alpha_2hk}(\xi, \omega^s) \frac{\partial N_{\alpha_1hm}(\xi, \omega^s)}{\partial \xi_k} \quad \xi \in Q^s \\ -\frac{\partial}{\partial \xi_j} (a_{ijkh}(\xi, \omega^s) N_{\alpha_1hm}(\xi, \omega^s)) \\ \mathbf{N}_{\alpha_1\alpha_2m}(\xi, \omega^s) = 0 \quad \xi \in \partial Q^s \end{array} \right. \quad (8)$$

5.  $\mathbf{u}^0(x)$  is the solution of the homogenization problem with the homogenized parameters  $\{\widehat{a}_{ijkh}\}$  defined on global  $\Omega$

$$\left\{ \begin{array}{l} \frac{\partial}{\partial x_j} \left[ \widehat{a}_{ijkh} \frac{1}{2} \frac{\partial}{\partial x_j} \left( \frac{\partial u_h^0(x)}{\partial x_k} + \frac{\partial u_k^0(x)}{\partial x_h} \right) \right] = f_i(x), \quad x \in \Omega \\ \mathbf{u}^0(x) = \bar{\mathbf{u}}(x), \quad x \in \Gamma_1 \\ \sigma_i(x) = \nu_j \widehat{a}_{ijkh} \frac{1}{2} \left( \frac{\partial u_h^0(x)}{\partial x_k} + \frac{\partial u_k^0(x)}{\partial x_h} \right) = p_i, \quad x \in \Gamma_2 \\ (\Gamma_1 \cap \Gamma_2 = \emptyset, \quad \Gamma_1 \cup \Gamma_2 = \partial\Omega) \end{array} \right. \quad (9)$$

6. The strains can be evaluated approximately in following formulas:

$$\begin{aligned}
\varepsilon_{hk} \left( \frac{x}{\varepsilon}, \omega \right) &= \frac{1}{2} \left( \frac{\partial u_h^0(x)}{\partial x_k} + \frac{\partial u_k^0(x)}{\partial x_h} \right) \\
&+ \sum_{l=1}^2 \varepsilon^l \sum_{\langle a \rangle = l} \frac{1}{2} \left[ N_{ahm} \left( \frac{x}{\varepsilon}, \omega \right) D_{ak}^{l+1} u_m^0(x) + N_{akm} \left( \frac{x}{\varepsilon}, \omega \right) D_{ah}^{l+1} u_m^0(x) \right] \\
&+ \sum_{l=1}^2 \varepsilon^{l-1} \sum_{\langle a \rangle = l} \frac{1}{2} \left[ \frac{\partial N_{ahm}}{\partial \xi_k} + \frac{\partial N_{akm}}{\partial \xi_h} \right] \left( \frac{x}{\varepsilon}, \omega \right) D_a^l u_m^0(x)
\end{aligned} \tag{10}$$

where  $\alpha = (\alpha_1, \alpha_2, \dots, \alpha_l)$ ,  $D_a^l u_m^0(x) = \frac{\partial^l u_m^0(x)}{\partial x_{\alpha_1} \partial x_{\alpha_2} \dots \partial x_{\alpha_l}}$ . And then the stress tensor can be calculated in following formulae

$$\sigma_{ij}(x, \omega) = a_{ijhk} \left( \frac{x}{\varepsilon}, \omega \right) \varepsilon_{hk} \left( \frac{x}{\varepsilon}, \omega \right) \tag{11}$$

### 3.2 Computation of the Strength

As the strain and stress tensor anywhere inside the investigated structure are obtained, the elasticity limit strength for the structure made from rock mass can be evaluated. Until now there is no strength criterion for the structure of rock mass with lots of random joints or/and cracks. In this paper, we employ the strength criterions on homogenous materials and the status of joint or/and crack expansions to define the elasticity limit strength of the structure of rock mass.

It's worthy to note that the employed strength criterion should be different for the different status of intact rock and jointing, such as tension and compression, the maximum principal stress theory should be cited for rock mass. In our computation, only the formulation of maximum stress criterion is shown. The formulas of other strength criterions can be easily found in textbook of solid mechanics or mechanics of rock mass.

The maximum principal stress theory assumes that failure occurs when the maximum principal stress  $\sigma_1$  in the complex stress system equals to that at the yield point in the tensile test, where  $\sigma_1$ ,  $\sigma_2$  and  $\sigma_3$  are the three principal stresses under the three dimensional complex stress states.

For a sample  $\omega^s$ , all of strains and stresses inside any  $\varepsilon$ -cell belonging to the structure can be obtained through the formulas presented previously. Then, the

strength  $S(\omega^s)$  of the structure with random joint or/and crack distribution is obtained as the elasticity limit criterions is reached at some point for the sample  $\omega^s$ . Thus to repeat previous calculation so many times, from Kolmogorov strong law of the large number, it follows that the expected strength  $\hat{S}$  can be evaluated by following formula:

$$\hat{S} = \frac{\sum_{s=1}^M S(\omega^s)}{M} \quad (12)$$

However, the expected strength  $\hat{S}$  can not totally represent the strength properties of the structure of random joint/crack distribution. The yield of some location may lead to the collapse of the whole structure. Therefore, the minimal strength of the structure of random joint/crack distribution is sometime worthier than the expected one for the design of rock mass structures. The minimal strength can be defined as following formula:

$$S_{\min} = \min_{s=1, \dots, M} \{S(\omega^s)\} \quad (13)$$

#### 4 The Procedure of MSA Computation Based on SSOTS

Based on the multi-scale representation of the rock mass with random joint/crack distribution in Section 2 and the SSOTS formulation in Section 3, the algorithm procedure of predicting the mechanical parameters of structure with random joint/crack distribution is following:

1. Generate a distribution model  $P$  of joints or/and cracks based on the statistical characteristics of the random joint or/and crack distribution, and determine the material coefficients  $\left\{a_{ijk} \left(\frac{x}{\varepsilon}, \omega^s\right)\right\}$  on  $\varepsilon Q(\varepsilon)$  as follows:

$$a_{ijk} \left(\frac{x}{\varepsilon}, \omega^s\right) = \begin{cases} a_{ijk}, & x \in \varepsilon \hat{Q}(\varepsilon) \\ a'_{ijk}, & x \in \varepsilon \tilde{Q}(\varepsilon) \end{cases}, \quad \omega^s \in P, \quad (14)$$

where  $\varepsilon\widehat{Q}(\varepsilon)$  is the domain of intact rock and  $\varepsilon\widetilde{Q}(\varepsilon)$  the domain of joints and jointing in  $\varepsilon Q(\varepsilon)$  and  $\{a_{ijk}\}$  and  $\{a'_{ijk}\}$  are the material coefficients of them, respectively.

2. Evaluate FE solution  $\mathbf{N}_{\alpha_1 m}^h(\xi, \omega^s)$  ( $\alpha_1, m = 1, \dots, n$ ) of  $\mathbf{N}_{\alpha_1 m}(\xi, \omega^s)$  by solving problem (5) for  $\omega^s \in P$ . Then the sample homogenization coefficients  $\{\hat{a}_{ijk}^r(\omega^s)\}$  can be calculated through formula (6). And then to evaluate FE solution  $\mathbf{N}_{\alpha_1 \alpha_2 m}^h(\xi, \omega^s)$  of  $\mathbf{N}_{\alpha_1 \alpha_2 m}(\xi, \omega^s)$  ( $\alpha_1, m = 1, \dots, n$ ) for  $\omega^s \in P$  by solving problem (8).
3. For  $\omega^s \in P$ ,  $s = 1, 2, \dots, M$ , step 1 to 2 are repeated  $M$  times. Then  $M$  sample homogenization coefficients  $\{\hat{a}_{ijk}(\omega^s)\}$  are obtained. The expected homogenization coefficients  $\{\widehat{a}_{ijk}\}$  for the rock mass with random joint or/and crack distribution can be evaluated in formulae (7).
4. The homogenization solution  $\mathbf{u}^0(x)$  can be obtained by solving homogenization problem (9) with the homogenization coefficients  $\{\widehat{a}_{ijk}\}$ . For some typical structures/components,  $\mathbf{u}^0(x)$  can be exactly obtained from solid mechanics.
5. For the sample  $\omega^s$ , evaluate the stain fields anywhere inside the investigated structure by  $\mathbf{N}_{\alpha_1 m}^h\left(\frac{x}{\varepsilon}, \omega^s\right)$ ,  $\mathbf{N}_{\alpha_1 \alpha_2 m}^h\left(\frac{x}{\varepsilon}, \omega^s\right)$  ( $\alpha_1, m = 1, \dots, n$ ), and  $\mathbf{u}^0(x)$  through formulas (10) in section 3. The stresses can be calculated through Hooke's Law (11).
6. By using the strength  $S_m$  of intact rock, the strength  $S_p$  of jointing and the criterion of joint or/and crack expansion, the elasticity limit load of the structure for  $\omega^s$  can be determined by using iteration procedure. After that, the strength limit of the structure for  $\omega^s$ , denoted by  $S(\omega^s)$ , is calculated according to the critical load and the homogenization stiffness parameters  $\{\hat{a}_{ijk}(\omega^s)\}$ .
7. For  $\omega^s \in P$ ,  $s = 1, 2, \dots, M$ , step 5 to 6 are repeated. Then  $M$  sample strengths  $S(\omega^s)$  are obtained. The expected strength  $\widehat{S}$  and the minimal

strength  $S_{\min}$  for the structure with random joint/crack distribution can be evaluated in formulae (12) and (13).

If there are so plenty of random joints or/and cracks inside structure and the differences of their sizes are very large. One should divide all of random joints or/and cracks into several classes according to their size. They are divided into 4 classes,  $N=4$ , shown in Figure 1. As  $\{\widehat{a}_{ijhk}^r\}$ ,  $\widehat{S}^r$  and  $S_{\min}^r$  ( $r=4$ ) are obtained, they are used as the elastic coefficients and strength of new intact rock in the next cycle with  $r=N-1$ , i.e. if it's not the first cycle ( $r \neq N$ ), the material coefficient of the intact rock is the homogenized coefficient  $\{\widehat{a}_{ijhk}^{r+1}\}$ , and the elasticity limit strength of the intact rock are the strength  $\widehat{S}^{r+1}$  and  $S_{\min}^r$ , respectively, which are evaluated in former cycle with  $(r+1)$  class.

As the last cycle  $r = 1$  is completed, the expected homogenization coefficients  $\{\widehat{a}_{ijhk}^1\}$  and expected elasticity limit strength  $\widehat{S}^1$  and  $S_{\min}^1$  are obtained. And then  $\widehat{S}^1$  and  $S_{\min}^1$  are defined as the effective elastic coefficients and expected / minimal strength of the investigated structure/component made from the rock mass with random distribution of multi-scale joints or/and cracks.

## 5 Numerical Experiments

To verify the previous algorithm, the homogenized coefficients of the rock mass are evaluated. Three models of random joint distribution in 2-D case are considered in three examples, respectively.

In every example, the joints are divided into four classes  $G_1, G_2, G_3$  and  $G_4$  by the length of joint trace, the length of whose statistic screen is denoted by  $\mathcal{E}^1, \mathcal{E}^2, \mathcal{E}^3$  and  $\mathcal{E}^4$ , respectively, and the length of joints in every class is supposed to be uniform distribution in a certain interval  $[a,b]$ , shown in Table 1, and there are 4 joints in every  $\mathcal{E}^i$ -screen, and the thickness of the jointing in every joint is 1% of its length.

Table 1. The screen size and interval of each class

	Statistics Screen Scale	Intervals of Each Group
$G_1$	$\mathcal{E}^4 = 1\text{m}$	[0.1-0.25]
$G_2$	$\mathcal{E}^3 = 5\text{m}$	[0.5-1.0]
$G_3$	$\mathcal{E}^2 = 15\text{m}$	[2.5-5.0]
$G_4$	$\mathcal{E}^1 = 20\text{m}$	[7.5-10]

And in each example, the material coefficients of intact rock and jointing are supposed to be same, shown in Table 2.

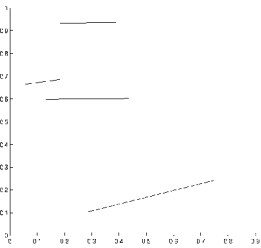
For the first example, the inclination of the joints in each class is supposed to be uniform distribution between  $0^\circ$  and  $360^\circ$ , denoted by UD ( $0^\circ, 360^\circ$ ). For the second example, the inclination of the joints in each class is supposed to be normal distribution with expectation  $0^\circ$  and mean square deviation  $10^\circ$ , denoted by ND ( $0^\circ, 10^\circ$ ). For the last example, the inclination of the joints in each group is supposed to be normal distribution with expectation  $50^\circ$  and mean square deviation  $10^\circ$ , denoted by ND ( $50^\circ, 10^\circ$ ).

Table 2. The material coefficients of intact rock and jointing

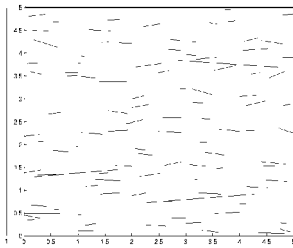
Intact rock	Jointing
$\begin{pmatrix} 3.3333E4 & 8.3333E3 & 0 \\ 8.3333E3 & 3.3333E4 & 0 \\ 0 & 0 & 1.25E4 \end{pmatrix}$	$\begin{pmatrix} 3.3333E2 & 8.3333E1 & 0 \\ 8.3333E1 & 3.3333E2 & 0 \\ 0 & 0 & 1.25E2 \end{pmatrix}$

Table 3. The expected homogenized results of each scale screen for UD ( $0^\circ, 360^\circ$ )

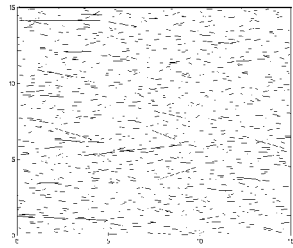
$\mathcal{E}^4 \begin{pmatrix} 3.0086 E4 & 7.064 E3 & 0 \\ 7.064 E3 & 2.9810 E4 & 0 \\ 0 & 0 & 1.1441 E4 \end{pmatrix}$	$\mathcal{E}^3 \begin{pmatrix} 2.7614E4 & 6.272E3 & 0 \\ 6.272E3 & 2.7708E4 & 0 \\ 0 & 0 & 1.0720E4 \end{pmatrix}$
$\mathcal{E}^2 \begin{pmatrix} 2.5695 E4 & 5.528 E3 & 0 \\ 5.528 E3 & 2.4810 E4 & 0 \\ 0 & 0 & 9.833 E3 \end{pmatrix}$	$\mathcal{E}^1 \begin{pmatrix} 2.2026 E4 & 4.623 E3 & 0 \\ 4.623 E3 & 2.1843 E4 & 0 \\ 0 & 0 & 8.666 E3 \end{pmatrix}$



a. Joints in  $\mathcal{E}^4$ -screen



b. Joints in  $\mathcal{E}^3$ -screen



c. Joints in  $\mathcal{E}^2$ -screen

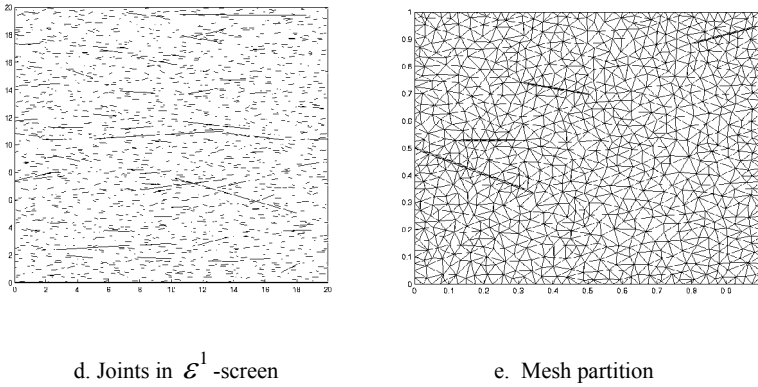


Figure 2. The statistical model of joints for ND ( $0^\circ, 10^\circ$ ) and mesh partition

By virtue of above specified data and the simulation method of the joints, the joints in each screen can be easily generated for one sample. In order to show clearly the distribution of the joints in the rock mass, the joints in  $\mathcal{E}^i$ -screen are generated as well the joints in the screen smaller than  $\mathcal{E}^i$  together. The distribution model of joints for one sample of UD ( $0^\circ, 360^\circ$ ), ND ( $0^\circ, 10^\circ$ ) and ND ( $50^\circ, 10^\circ$ ) is shown in Figure 1, Figure 2 and Figure 3, respectively.

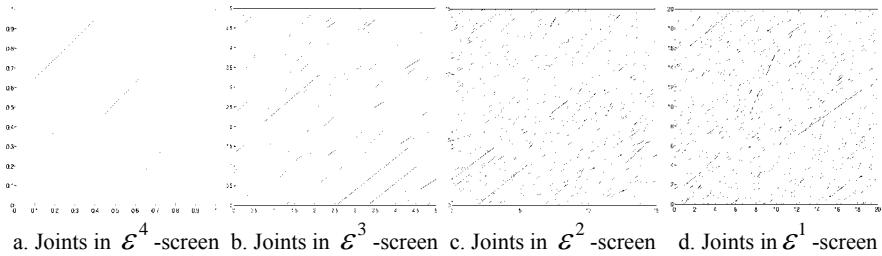


Figure 3. The Joints Statistical Model For ND ( $50^\circ, 10^\circ$ )

Table 4. The expected homogenized results of each scale screen for ND ( $0^\circ, 10^\circ$ )

$\mathcal{E}^4$	$\begin{pmatrix} 3.2589E4 & 6.868E3 & 0 \\ 6.868E3 & 2.7364E4 & 0 \\ 0 & 0 & 1.1186E4 \end{pmatrix}$	$\mathcal{E}^3$	$\begin{pmatrix} 3.1960E4 & 5.815E3 & 0 \\ 5.815E3 & 2.3089E4 & 0 \\ 0 & 0 & 1.0148E4 \end{pmatrix}$
$\mathcal{E}^2$	$\begin{pmatrix} 3.1271E4 & 4.853E3 & 0 \\ 4.853E3 & 1.9136E4 & 0 \\ 0 & 0 & 9.072E3 \end{pmatrix}$	$\mathcal{E}^1$	$\begin{pmatrix} 3.0351E4 & 3.846E3 & 0 \\ 3.846E3 & 2.3089E4 & 0 \\ 0 & 0 & 1.0148E4 \end{pmatrix}$

Table 5. Final result

UD	$\begin{pmatrix} 2.2026E4 & 4.623E3 & 0 \\ 4.623E3 & 2.1843E4 & 0 \\ 0 & 0 & 8.666E3 \end{pmatrix}$
ND(0o,10o)	$\begin{pmatrix} 3.0351E4 & 3.846E3 & 0 \\ 3.846E3 & 1.4995E4 & 0 \\ 0 & 0 & 7.755E3 \end{pmatrix}$
ND(50o,10)	$\begin{pmatrix} 2.1005E4 & 8.194E3 & 2.094E3 \\ 8.194E3 & 2.1873E4 & 2.592E3 \\ 2.094E3 & 2.592E3 & 9.810E3 \end{pmatrix}$

The 50 distribution samples of the joints in each screen for every example are sampled. Every sample with joints is partitioned as shown in Figure 2.e. And the expected homogenized coefficients can be calculated by the procedure given in section 4. The detailed results of UD and ND(0°,10°) are given in Table 3 and Table 4, respectively. The detailed results of ND (50°,10°) are omitted owing to the limitation of space. The final expected homogenized results for UD (50°,10°), ND (0°,10°) and ND (50°,10°) are given in Table 5.

By using SMS method in this paper the elasticity limit strengths of the rock mass with random joints/cracks distribution, including tension and compression, bending and twist, have been calculated, and the numerical results on expected elasticity strength and minimal elasticity strength were obtained. For the space limitation of this paper those on rock mass strength are omitted here.

## 5 Conclusions

In this paper one kind of structures of rock mass with plenty of joints or/and cracks is considered, they are defined as the structures of the materials with random distribution of multi-scale joints or/and cracks. And the micro-structure of rock mass with plenty of multi-scale joints or/and cracks is represented.

A new statistically second-order two-scale methods for the predicting the mechanics performances of them is presented, including the second-order two-scale asymptotic expression on the displacement vector, the formulations of the expected homogenization constitutive parameters, elasticity limit strength, and the algorithm procedures.

For some different random distribution models the expected homogenization constitutive parameters are predicted by SSOTS method. And the numerical experiments show that the micro-behaviors inside the structure with plenty of joints or /and cracks can be captured exactly by SSOTS method. And all of numerical results show that SSOTS method is valid and available.

## References

- Cui J.Z. and Shan Y.J. (2000). The two-scale analysis algorithms for the structure with several configurations of small periodicity, *Computational Techniques for Materials, Composites and Composite Structures*, B.H.V. Topping (Ed.), Civil-Comp Press.
- Cui J.Z., Shih T.M. and Wang Y.L. (1997). The two-scale analysis method for bodies with small periodic configuration, *Structural Engineering and Mechanics*, 7(6): 601-614, Invited Paper in CASC97, Sydney, Australia, Proc. of CASC97.
- Cui J.Z. and Yang H.Y. (1996). A dual coupled method of boundary value problems of PDE with coefficients of small period, *Int. J. Comp. Math.* 14: 159-174.
- Jikov V.V., Kozlov S.M. and Oleinik O.A. (1994). *Homogenization of differential operators and integral functions*, Berlin: Springer.
- Li Y.Y. and Cui J.Z. (2004). Two-scale analysis method for predicting heat transfer performance of composite materials with random grain distribution, *Science in China Ser. A Mathematics*, 47: 101-110.
- Li Y.Y. and Cui J.Z. (2005). The multi-scale computational method for mechanics parameters of composite materials with random grain distribution, *Journal of Composites Science & Technology*, 65: 1447-1458.
- Oleinik O.A., Shamaev A.S. and Yosifian G.A. (1992). *Mathematical problems in elasticity and homogenization*, Amsterdam: North-Holland.
- Shan Y.J., Cui J.Z. and Liang F.G. (2002). Expected slide path method for stability analysis of rock mass based on statistics model of joints and stress field, *Chinese Journal of Rock Mechanics and Engineering*, 21(2): 151-157.
- Yu Y., Cui J.Z. and Han F. (2008). An effective computer generation method for the composites with random distribution of large numbers of heterogeneous grains, *Computational Methods in Engineering and Science*. Proceeding of the EPMESC X, Sanya, China, 2006, pp. 273, to be published on CST.

# Computational Simulation Methods for Composites Reinforced by Fibres

Vladimír Kompiš<sup>1\*</sup>, Zuzana Murčinková<sup>2</sup>, Sergey Rjasanow<sup>3</sup>,  
Richards Grzhibovskis<sup>3</sup> and Qing-Hua Qin<sup>4</sup>

<sup>1</sup>DSSI, j.s.c., Wolkrova 4, 82105 Bratislava, Slovakia

<sup>2</sup>Technical University Košice, Faculty of Manufacturing Technologies, Štúrova 31,  
080 01 Prešov, Slovakia

<sup>3</sup>Department of mathematics and Computer Science, University of Saarland, Germany

<sup>4</sup>Department of Engineering, Australian National University, ACT 0200, Australia

**Abstract.** Trefftz-FEM (T-FEM), Adaptive Cross Approximation BEM (ACA BEM) and Method of Continuous Source Functions (MCSF) are presented for simulation of Composites Reinforced by Short Fibres (CRSF) with the aim to show possibilities of reduction the problem of complicated and important interactions in such composite materials.

**Keywords:** Trefftz-FEM, adaptive cross approximation BEM, method of continuous source functions, composite materials, short fibres

## 1 Introduction

Fibres are the most effective reinforcing material. Outstanding mechanical, thermal and electro-mechanical properties of Carbon Nano-Tubes (CNT), carbon fibres and some other fibres are well known. Composites Reinforced by Short Fibres/tubes (CRSF) are often defined to be materials of future with excellent electro-thermo-mechanical (ETM) properties. Understanding the behaviour of such composite materials is essential for structural design. Computational simulations play an important role in this process. Usually, strength, stiffness, thermal and electrical conduction of fibres are much larger than those of the matrix material. Very large is also the aspect ratio of the short fibres. Because of these properties very large gradients are localized in all ETM fields along the fibres and in the matrix. The fields define the interaction of the fibres with the matrix, with the other fibres, with the boundaries of the domain/structure. Accurate computational simulation of the fields is important for correct assessment of the material behaviour.

---

\* Corresponding author, e-mail: vladimir.kompis@aos.sk

In this paper FEM, BEM and the new developed MCSF are compared for simulation of CRSF. The problems with in-homogeneities can be reduced when the FEM using special (Trefftz-type) functions are used for the formulation. The BEM reduces the original 3D formulation to the problem on the fibre-matrix boundary. Although, the resulting Galerkin system is fully populated, novel techniques can be applied to approximate it by a data-sparse structure. In this study the Adaptive Cross Approximation (ACA) procedure combined with the H-matrix technique is used to achieve this reduction of complexity and storage requirements. Drastic reduction of the problem enables the Fast Multi-pole (FM) BEM (Liu et al., 2005) by which the kernel functions of boundary integrals are substituted by corresponding truncated Taylor series expansion and resulting discrete dipoles and moments are substituted for the continuum in far field interaction. However, the near field interaction is solved by classical BEM formulation. Boundary meshless methods usually need neither the discretization of the domain, nor the boundary. In the special problem like CRSF, 1D distributed source functions by the MCSF enable to reduce drastically the problem comparing to the FMBEM also for the near field interaction. All the three methods are presented in simulation of the CRSF problems.

## 2 Description of the Methods Used in Computation Models

Trefftz- (T-) type formulations were developed with the aim to enable formulation of domain field by boundary parameters using shape functions which satisfy the governing equations in corresponding domain/subdomain. Commercial FEM package PROCISION (A Guide to Procision 3.5, 1999) contains two types of T-elements: polynomial and nonpolynomial, stress concentration elements. The last one element properly reflects asymptotic behaviour of exact solution in the region of stress concentration. The solution is obtained by adaptive procedure by comparing the strain energy in computational steps and it is stopped when the change in the last two steps is smaller than 1%. The T-FE's can be much larger than classical FE's also for complicated shape of the element. The global and local (element) errors are evaluated from the sub-domain (element) boundary conditions. The accuracy of the element is increased by increasing the order of the T-polynomials of the shape function and it can increase up to 12<sup>th</sup> order in the models.

The second approach used in this study is the Boundary Element Method (BEM) for equations of linear elastostatics (Lamè system of equations). More precisely, we implement a Galerkin formulation of BEM with piecewise linear basis functions to interpolate the displacement field and piecewise constant basis functions for the tractions on the boundary. The input data consist of the phase geometry, material parameters, and the conditions at infinity. Hence, an interface problem is formulated, and the solution on the matrix-fibre boundary is found by inverting the Steklov-Poincarè operator. The operator is expressed through the

hyper-singular, the double layer, the adjoint double layer, and the single layer operators and its Galerkin discretization turns out to be symmetric and positive definite matrix. This enables us to use the conjugate gradient iterative method to find the solution. Moreover, we use a hierarchical clustering of boundary elements to partition each of the Galerkin matrices into blocks. The blocks that represent interactions of well separated clusters are replaced by their low rank approximants. The approximants are found by means of the ACA procedure (Rjasanow and Steinbach, 2007; Bebendorf and Grzhibovskis, 2006). The overall complexity and memory requirement of the described Galerkin BEM is, up to a log factor, linear in terms of the number of mesh nodes. The accuracy, however, is of order two for the displacement field and the stress field inside either phase or matrix material. Mathematical properties of the method were extensively explored and its approximation errors were rigorously estimated (Rjasanow and Steinbach, 2007). We underline the mathematically justified second order accuracy of the stress field inside the domains as main advantage of this technique in our study.

The third approach is a boundary meshless method, the MCSF (Kompiš et al., 2008), which uses 1D continuous forces (the fundamental or Kelvin solution well known from the BEM), dipoles and couples along the fibre axis to simulate the fibre-matrix interaction. The interaction is simulated by satisfying continuity of displacements and strains along the fibre-matrix interface in collocation points located on the interface. The continuous distribution of the source functions is approximated by non-uniform rational B-splines (NURBS). Cubic B-splines have been used in the models. The aspect ratio of the fibres is usually very large and the stiffness of the fibres is often much larger than the stiffness of the matrix. Then the axial stiffness of the fibre is also much larger than its bending and tangential stiffness and it is possible to assume that the strain is constant in each cross section of the fibre in the fibre direction. If the fibres are symmetrically distributed around a fibre than fictive forces or dipoles in fibre direction and other dipoles perpendicular to fibre direction continuously distributed along the fibre axis can correctly simulate the interaction of the fibre with the matrix and with other fibres. Moreover, discrete dipoles are added in the fibre ends in order to improve inter-domain continuity in the end parts of the fibre. However, if the fibres are irregularly distributed in the matrix and/or they are curved, then additional couples with their vectors perpendicular to the fibre axis are necessary to obtain resulting cross sectional force acting approximately in the fibre axis and so, to simulate the stiffening effect with good accuracy. The integrals giving resulting action of the source functions in the collocation points are quasi-singular or quasi-hyper-singular and are evaluated numerically or analytically by symbolic manipulation. Heat sources and heat dipoles are used as source functions to simulate the temperature field interactions of fibres with matrix and with other fibres (Kompiš and Murčínková, 2009). Number of collocation points is usually larger than the number of parameters defining the intensities of source functions and the problem is solved in the least square sense. The matrix is full and so restricted for computations of large problems by smaller computers. Technique similar to those used for ACABEM

(Rjasanow and Steinbach, 2007; Bebendorf and Grzhibovskis, 2006) and FMBEM as mentioned above can contribute to further reduction of the models based on the MCSF.

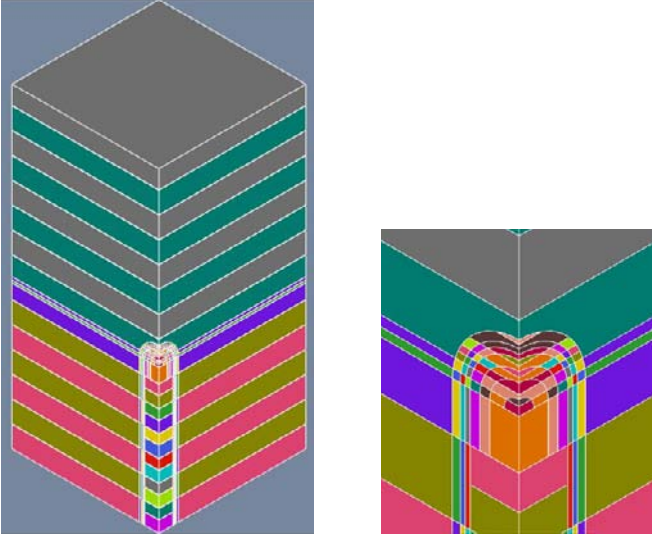


Figure 1 T-FEM mesh and detail on fibre end

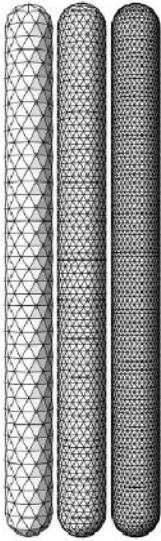


Figure 2 BEM meshes

Table 1. Comparison of results for one fibre with aspect ratio 1:10

R=5, L=100	T-FEM	ACA BEM	MCSF
Number of equations	-	1266	36
Number of elements	88	840	-
Stress ZZ [MPa]	262	265	249

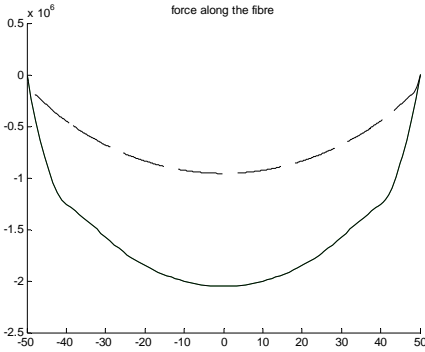


Figure 3 Force distribution along a single fibre in the matrix with aspect ratios 1:10 (solid line) and 1:50 (dash line) by MCSF

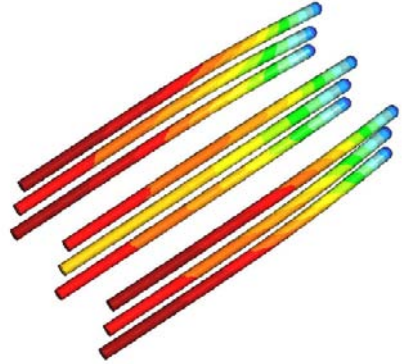


Figure 4 Stress ZZ in the fibre direction for a patch of 3 x 3 x 3 fibres by T-FEM

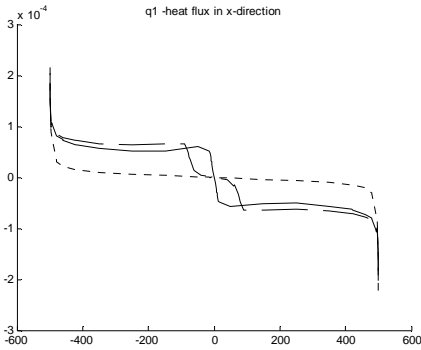


Figure 5 Heat flow through the fibre surface in perpendicular direction along fibre axis of R=1, L=1000

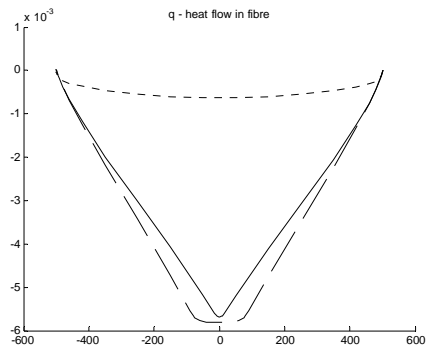


Figure 6 Heat flow through the cross-section along fibre axis of R=1, L=1000

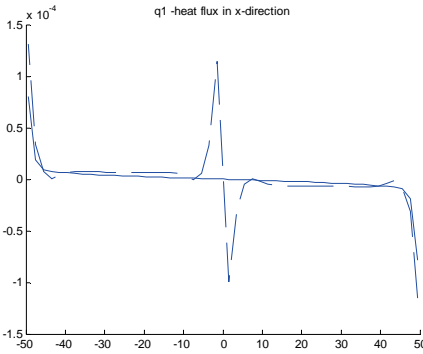


Figure 7 Heat flow through the fibre surface in perpendicular direction along fibre axis of  $R=1, L=100$

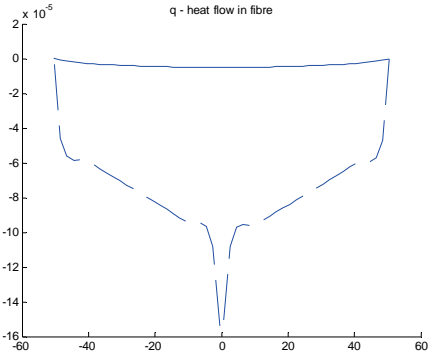


Figure 8 Heat flow through the cross-section along fibre axis of  $R=1, L=100$

### 3 Computational Results and Conclusions

Computations were performed for several problems in order to compare all FEM, BEM and meshless formulations for linear elasticity and stationary heat flow in solids. Only some results are included due to restrictions of the paper. More details and results will be published later. Figures 1 and 2 contain the mesh for Trefftz FEM and for BEM used for one fibre with aspect ratio 1:10. The results obtained by all methods are compared in Table 1. Because of linear problems, all quantities are dimensionless. Material modules of matrix and fibre are  $10^4$  and  $10^6$ , respectively, for one fibre and 1900 and  $1.9 \times 10^6$ , respectively, for patch  $3 \times 3 \times 3$  fibres without overlap. Figure 3 gives force distribution along a single fibre in the matrix with aspect ratios 1:10 and 1:50, respectively. Stresses in the fibre direction for a patch of  $3 \times 3 \times 3$  fibres by T-FEM are presented in Figure 4. Figures 5 to 8 present heat flow in the fibre both in fibre direction (through the fibre/matrix interface in Figures 5 and 7 and resulting flow through the fibre cross-section in Figures 6 and 8). In all cases the fibres with of radius  $R = 1$  and length  $L = 1000$  (Figures 5 and 6) and  $L = 100$  (Figures 7 and 8) are regularly distributed in layers with or without overlap. The fibre axes are spaced by 16 from each other in perpendicular direction and gaps of 16 and 160, respectively in the fibre direction in the examples given in Figures 5 and 6 and by 2 and with gap of 2 in examples shown in Figures 7 and 8. In Figures 5 and 6, dot line represents results of model without and solid line with overlap and gap 16, dash line with overlap and gap 160. In Figures 7 and 8, solid line represents results of model without and dash line with overlap.

The results show that both elasticity and temperature fields have similar behaviour. The fibres, which are much stiffer and have much better conductivity than the matrix, can considerably increase the stiffness and conductivity of the composite material in the fibre direction. There is very strong interaction between all fibres and matrix and neighbour fibres and the topology of the fibres can strongly influence the effect. The stress in fibre direction can exceed the stresses in the matrix and in the fibre-matrix interface by several orders and so the short fibres are the most effective reinforcing material. All three methods imply considerable problem reduction the largest one is achieved by the MCSF.

## References

- A Guide to PROCISION 3.5 (1999). Procision Analysis Inc., Mississauga, Ontario, Canada.
- Bebendorf M., Grzhibovskis R. (2006). Accelerating Galerkin BEM for linear elasticity using adaptive cross approximation, *Math. Meth. Appl. Sci.*, 29, 1721-1747.
- Kompiš V., Murčinková Z. (2009). Heat flow in composites reinforced by short fibres, Proc. of Conference *Computer Methods in Mechanics*, Zielona Gora, May 18-21.
- Kompiš V., Štiavnický M., Kompiš M., Murčinková Z., Qin Q.H. (2008). Method of continuous source functions for modelling of matrix reinforced by finite fibres. In V. Kompiš (ed.) *Composites with Micro- and Nano-Structure, Computational Modeling and Experiments*, Springer Series Computational Methods in Applied Sciences, Springer Science + Business Media B.V.
- Kompiš V., Štiavnický M., Qin Q.H. (2009). Efficient solution for composites reinforced by particles. In G. D. Manolis, D. Polyzos (eds.) *Recent Advances in Boundary Element Methods*, Springer Series Computational Methods in Applied Sciences, Springer Science + Business Media B.V.
- Liu Y. L., Nishimura N., Otani Y., Takahashi T., Chen X. L., Munakata H. (2005). A fast boundary element method for the analysis of fiber-reinforced composites based on a rigid-inclusion model, *ASME Journal of Applied Mechanics*, 72, 115-128.
- Rjasanow S., Steinbach O. (2007). *The Fast Solution of Boundary Integral Equations*, Springer Series in Mathematical and Analytical Technology with Applications to Engineering, Springer-Verlag, Berlin/Heidelberg/NewYork.

*“This page left intentionally blank.”*

# Underground Structures under Fire – From Material Modeling of Concrete Under Combined Thermal and Mechanical Loading to Structural Safety Assessment

Thomas Ring<sup>1\*</sup>, Matthias Zeiml<sup>1</sup>, Roman Lackner<sup>2</sup>

<sup>1</sup> Institute for Mechanics of Materials and Structures, Vienna University of Technology, Karlsplatz 13/202, 1040 Vienna, Austria

<sup>2</sup> Material-Technology Unit, University of Innsbruck, Technikerstraße 13, 6020 Innsbruck, Austria

**Abstract** Tunnel cross-sections are analyzed applying different material models (linear-elastic and linear-elastic/ideal-plastic) and modes to consider fire loading (equivalent temperature loading and nonlinear temperature distribution). The influence of spalling and the effect of combined thermal and mechanical loading (by consideration of Load Induced Thermal Strains – LITS) on the numerical results is investigated.

**Keywords:** fire, underground structures, concrete, equivalent temperature, thermo-mechanical material behavior, tunnel analysis

## 1 Motivation

Tunnel structures have to fulfill requirements as regards their bearing capacity and serviceability before as well as during/after fire accidents. In engineering practice, the determination of the structural safety of tunnels subjected to fire loading is based on the so-called equivalent-temperature concept, assuming linear-elastic material behavior. The equivalent temperature load is calculated by setting equal the respective stress resultants  $N_{equ}$  and  $M_{equ}$  within a clamped beam with the stress resultants resulting from the real (nonlinear) temperature distribution (see Fig. 1 and Kusterle et al. [2004]):

$$T_m = \frac{N_{equ}}{\alpha E_{equ} A} \quad \text{and} \quad \Delta T = \frac{M_{equ}}{\alpha E_{equ} I}. \quad (1)$$

In Eq. (1),  $A$  [m<sup>2</sup>] and  $I$  [m<sup>4</sup>] are the cross-sectional area and the moment of inertia, respectively, whereas  $\alpha$  [K<sup>-1</sup>] is the thermal expansion coefficient of concrete.

---

\* Corresponding author, e-mail: thomas.ring@tuwien.ac.at

$E_{equ}$  [MPa] is the equivalent Young's modulus, given by

$$E_{equ} = \sum_{i=1}^N \frac{E_{c,i}(T_i)A_i}{A}, \quad (2)$$

where  $E_{c,i}(T_i)$  [MPa] and  $A_i$  [m<sup>2</sup>] are Young's modulus and cross-sectional area of the  $i$ -th layer (with  $N$  [-] as the number of layers). In a second step, the parameters  $T_m$  [°C],  $\Delta T$  [°C/m], and  $E_{equ}$  serve as input for the linear-elastic analysis.

In this paper, selected results from a structural safety assessment of different tunnel cross-sections under fire are presented. Hereby, the influence of different material models and modes to consider fire loading (equivalent temperature loading or non-linear temperature distribution) as well as the influence of combined thermal and mechanical loading on the strain behavior of concrete (via the introduction of Load Induced Thermal Strains – LITS) is investigated.

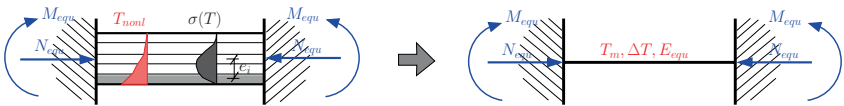


Fig. 1: Model for determination of equivalent temperature loading ( $T_m$  and  $\Delta T$ ) [Kusterle et al. 2004], giving the same stress resultants  $N_{equ}$  and  $M_{equ}$  as the corresponding nonlinear temperature distribution

## 2 Numerical Model

The finite-element analyses are performed using thick (layered) shell elements (see Fig. 2 and Savov et al. [2005]; Zeiml et al. [2008]; Ring [2008]). The layer concept enables for (i) assignment of different temperatures and, hence, of temperature-dependent material parameters to the respective layers and (ii) consideration of spalling by de-activation of the respective near-surface layers. Concrete and steel

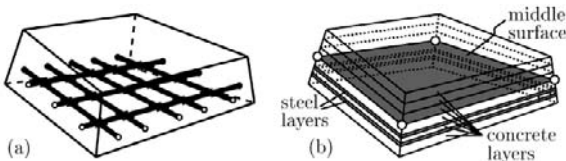


Fig. 2: Illustration of employed layer concept [Savov et al. 2005; Zeiml et al. 2008; Ring 2008]: (a) real cross-section, (b) layered finite element

are considered by separate layers, the reinforcement bars are transformed into a homogeneous steel layer of equivalent thickness. As outlined in [Savov et al. 2005], the steel reinforcement is simulated by a 1D plasticity model formulated in the direction of the reinforcement bars, whereas a plane-stress plasticity model for concrete is used. In case the effect of combined thermal and mechanical loading on the strain behavior of concrete is considered, the empirical relation for LITS proposed in [Thelandersson 1987] is employed. The temperature-dependent material parameters are taken from national/international standards [CEB 1991; ÖNORM EN1992-1-2 2007].

### 3 Application

#### 3.1 Geometric Properties and Loading Conditions

The numerical model described in the previous section is used to analyze different double-track railway tunnel cross-sections (see Fig. 3). Hereby, the mechanical load consists of the self-weight of the tunnel lining, earth load with an overburden of 1.50 and 1.75 m, respectively, and the traffic load resulting from a road crossing above the tunnel. The bottom of the tunnel is covered by a gravel layer as rail bedding which is considered to protect this part of the tunnel structure from fire loading. Therefore,

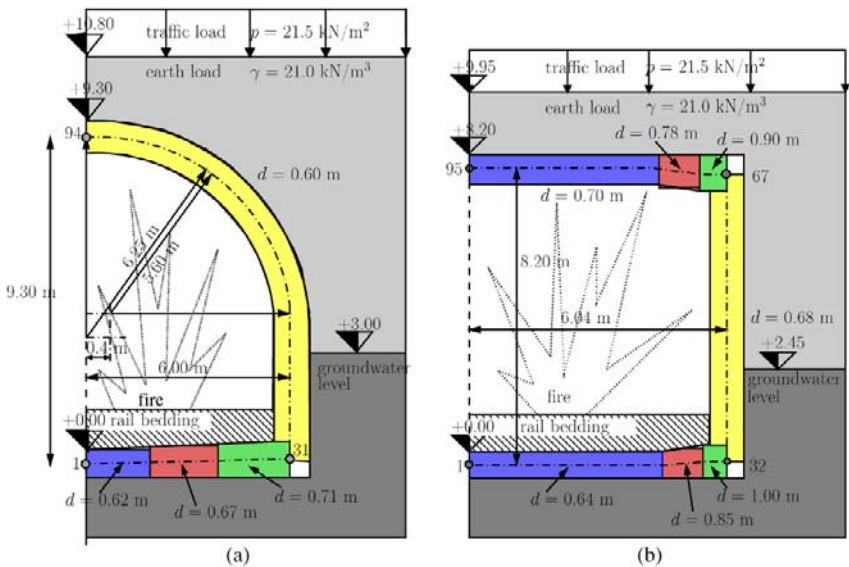


Fig. 3: Investigated concrete tunnels: (a) circular and (b) rectangular tunnel cross-section

temperature loading is applied only at the side wall and the top of the tunnel. The duration of the fire load is set to 180 min with an increase of the surface temperature up to 900°C within the first 20 min and a constant surface temperature of 900°C until the end of the fire load (see Savov et al. [2005] for details). In addition to fire load, different spalling scenarios are considered, with a final spalling depth  $d_s^\infty$  [m] to be reached after 30 min of fire loading (with  $d_s^\infty = 0$  m and  $d_s^\infty = 0.2$  m, see Zeiml et al. [2008] for details). Furthermore, different material models and modes of temperature loading are employed, i.e.,

- Linear-elastic material behavior and equivalent temperature  $\langle E, \text{no LITS} - T_m, \Delta T \rangle$ ,
- Linear-elastic/ideal-plastic material behavior without consideration of LITS and nonlinear temperature  $\langle EP, \text{no LITS} - T_{nonl} \rangle$ , and
- Linear-elastic/ideal-plastic material behavior with consideration of LITS and nonlinear temperature  $\langle EP, \text{with LITS} - T_{nonl} \rangle$ .

### 3.2 Results and Discussion

In the following, representative numerical results are presented, illustrating (i) the influence of different models to describe the material behavior of heated concrete, (ii) the effect of spalling on the compliance of the structure, and (iii) the differences in the structural behavior of the two considered cross-sections.

**3.2.1 Effect of material modeling and temperature loading** In this subsection, numerical results obtained from different material models for concrete and different modes of temperature loading are compared. Fig. 4(a) shows the level of loading  $L$  of the reinforcement, which is defined as the ratio between the actual steel stress  $\sigma_s$  [MPa] and the (temperature-dependent) yield strength  $f_y(T)$  [MPa]. In case of  $L = 0$ , the steel reinforcement is unloaded, whereas  $L = 1$  indicates that the maximum possible loading is reached. The consideration of linear-elastic/ideal-plastic material behavior and nonlinear temperature distribution (EP –  $T_{nonl}$ ) leads to significantly higher steel stresses. In case of  $\langle EP, \text{no LITS} - T_{nonl} \rangle$ ,  $L = 1$  in both (inner and outer) steel layers is reached after 75 min, leading to the development of a plastic hinge at the top corner of the tunnel. This plastic hinge is caused by the restraint introduced by thermal loading. Consideration of LITS as in case of  $\langle EP, \text{with LITS} - T_{nonl} \rangle$ , reduces the stresses resulting from thermal loading, reducing in turn the level of loading of the outer steel layer which reaches a value of 1 only towards the very end of fire loading (see Fig. 4(a)).

The bending-moment distribution presented in Fig. 4(b) indicates a significant increase in bending moment in the fire-exposed regions. The differences between the results obtained from  $\langle E, \text{no LITS} - T_m, \Delta T \rangle$  and  $\langle EP, \text{no LITS} - T_{nonl} \rangle$  are small. In case of  $\langle EP, \text{no LITS} - T_{nonl} \rangle$ , however, a redistribution of bending moment is

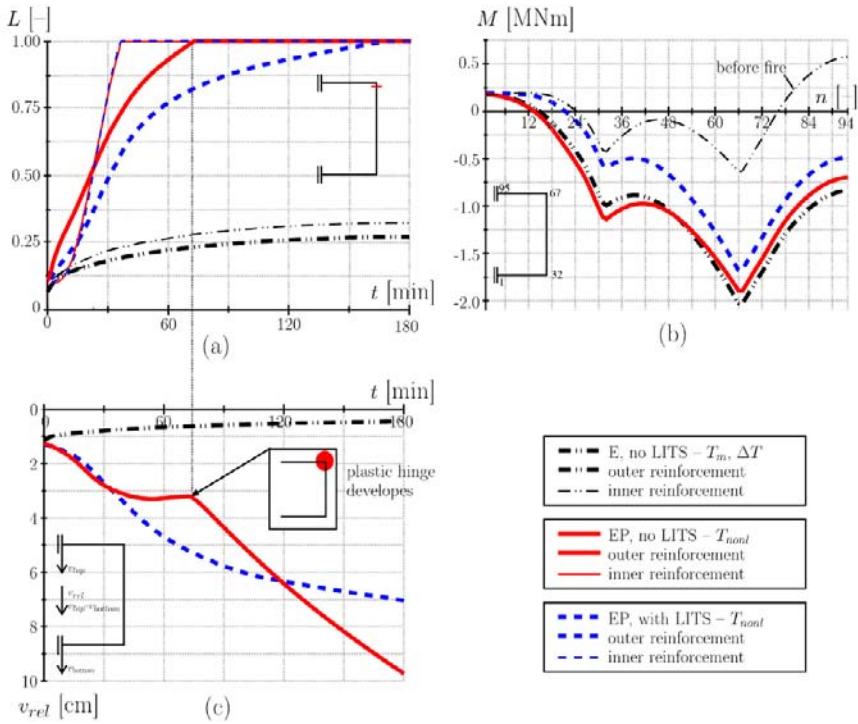


Fig. 4: Structural analysis of rectangular cross-section considering different material models: (a) evolution of level of loading of steel reinforcement at top corner of tunnel; (b) distribution of bending moment before fire (thin line) and after 3 h of fire loading (thick lines); (c) evolution of vertical convergence

observed which is caused by changing stiffnesses after a plastic hinge has developed at the top corner of the tunnel.

The evolution of the vertical convergence of the rectangular tunnel cross-section is presented in Fig. 4(c). In case linear-elastic material behavior and the equivalent temperature distribution  $\langle EP, \text{no LITS} - T_m, \Delta T \rangle$  are considered, thermal loading results in an uplift of the top of the tunnel and therefore a continuous decrease of its convergence. In case of  $\langle EP, \text{no LITS} - T_{nonl} \rangle$ , the convergence increases until the thermal loading starts to lift the tunnel, lateron causing the development of a plastic hinge as indicated in Fig. 4(a). This formation of a plastic hinge is followed by a sharp increase in compliance of the tunnel lining (see Fig. 4(c)). In case  $\langle EP, \text{with LITS} - T_{nonl} \rangle$  is considered, the increased compliance of heated concrete and, thus, the reduced stresses avoid the development of a plastic hinge (except for the very end of fire loading). Hence, the increase of the vertical convergence is smoother.

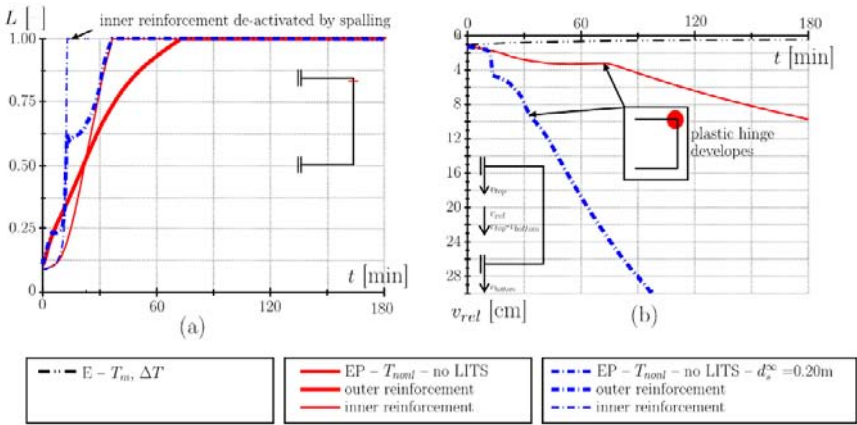


Fig. 5: Structural analysis of rectangular cross-section considering different spalling scenarios: (a) evolution of level of loading of steel reinforcement at top corner of tunnel; (b) evolution of vertical convergence

**3.2.2 Effect of spalling** Spalling has a considerable effect on the structural performance of a tunnel since it can result in loss of the inner reinforcement layer. As shown in Fig. 5(a), the inner reinforcement is lost after 12 min in case spalling is considered (see line for  $d_s^\infty = 0.2$  m). This promotes the formation of a plastic hinge since plasticity in the outer reinforcement is reached earlier. Additionally, the reduction of the cross-section of the lining in consequence of spalling considerably increases the overall compliance of the tunnel, as illustrated in Fig. 5(b).

**3.2.3 Effect of shape of tunnel cross-section** The shape of the cross-section has a significant influence on the structural performance of a tunnel under fire loading. In Figs. 6(a) and (b), the bending-moment distribution is presented for the circular as well as the rectangular tunnel, showing a higher magnitude for the bending moment for the rectangular cross-section. This difference is explained by the geometric shape of the circular cross-section following the force trajectories of the applied loading. Accordingly, the plastic hinge occurred later in time for the circular cross-section compared to the rectangular cross-section. Considering LITS in the analysis leads to a bending-moment reduction during fire loading in comparison to the analysis performed neglecting LITS (see Figs. 6(a) and (b)).

As mentioned before, spalling can lead to loss of the inner steel reinforcement, which is more crucial for the rectangular cross-section (see Fig. 6(c)), leading to the observed large compliance. The circular tunnel cross-section, on the other hand, is less sensitive against spalling. This is illustrated by comparing the lines considering/neglecting spalling for both cross-sections, which shows a larger increase for the rectangular cross-section.

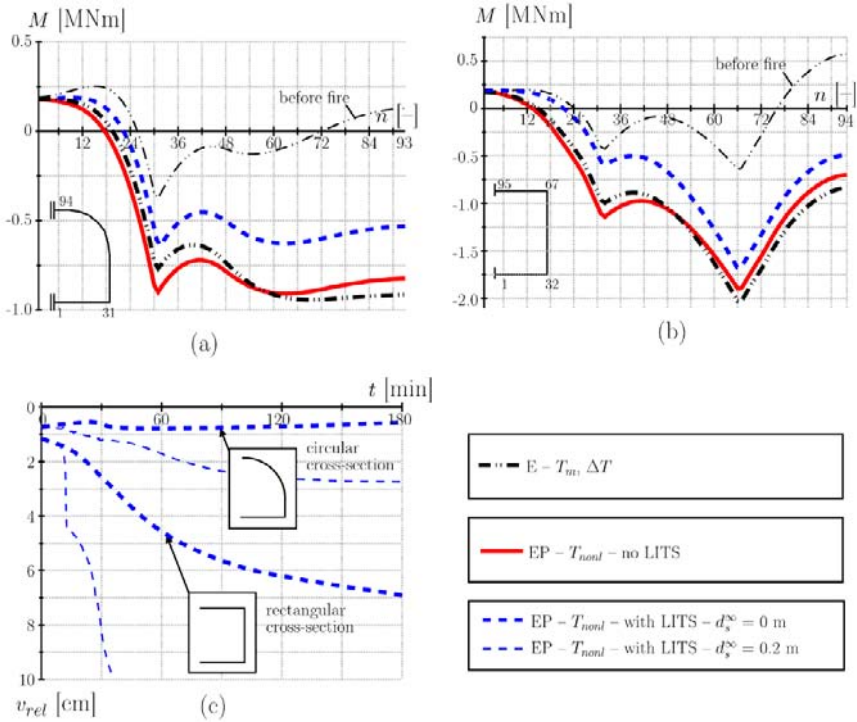


Fig. 6: Structural analysis of different cross-sections: distribution of bending moment before fire (thin line) and after 3 h of fire loading (thick lines) for (a) circular and (b) rectangular cross-section; (c) evolution of vertical convergence

## 4 Conclusions and Outlook

The results of a structural safety assessment of tunnels subjected to fire loading showed a strong dependence on the considered material model and whether or not spalling is taken into account. In contrast to the state-of-the-art engineering analysis mode, characterized by linear-elastic material behavior and the so-called equivalent temperature loading, the application of linear-elastic/ideal-plastic material models and consideration of the real (nonlinear) temperature distribution led to stress and force redistribution within the tunnel cross-section. Additionally, consideration of the effect of combined thermal and mechanical loading on the strain behavior of heated concrete allowed the realistic estimation of the stresses resulting from thermal loading and whether or not plastic regions/hinges occur within the cross-section. Hence, a realistic determination of the structural performance of un-

derground structures subjected to fire loading requires realistic description of the nonlinear material behavior of heated concrete.

The geometric properties of the tunnel cross-section have a significant influence on the sensitivity of the structure to fire loading. The performed analyses showed that the rectangular cross-section is more sensitive to fire loading than the circular cross-section. Consideration of spalling led to an increase of the compliance of the lining, showing a large increase of deformations for the rectangular cross-section.

Ongoing research focuses on the improvement of the employed material model by replacing the empirical LITS-relation and accounting for the influence of combined thermal and mechanical loading on the strain behavior of heated concrete by a micromechanics-based approach.

## References

- CEB (1991). *Fire Design of Concrete Structures, Bulletin d'Information 208*. CEB, Lausanne, Switzerland.
- Kusterle, W., Lindlbauer, W., Hampejs, G., Heel, A., Donauer, P.-F., Zeiml, M., Brunensteiner, W., Dietze, R., Hermann, W., Viechtbauer, H., Schreiner, M., Vierthaler, R., Stadlober, H., Winter, H., Lemmerer, J., and Kammeringer, E. (2004). Brandbeständigkeit von Faser-, Stahl- und Spannbeton [Fire resistance of fiber-reinforced, reinforced, and prestressed concrete]. Technical Report 544, Bundesministerium für Verkehr, Innovation und Technologie, Vienna [in German].
- ÖNORM EN1992-1-2 (2007). *Eurocode 2 – Bemessung und Konstruktion von Stahlbeton- und Spannbetontragwerken – Teil 1-2: Allgemeine Regeln – Tragwerksbemessung für den Brandfall [Eurocode 2 – Design of concrete structures – Part 1-2: General rules – Structural fire design]*. European Committee for Standardization (CEN) [in German].
- Ring, T. (2008). Finite element analysis of concrete structures subjected to fire load considering different element types and material models. Master's Thesis, Vienna University of Technology, Vienna, Austria.
- Savov, K., Lackner, R., and Mang, H. A. (2005). Stability assessment of shallow tunnels subjected to fire load. *Fire Safety Journal*, 40:745–763.
- Thelandersson, S. (1987). Modeling of combined thermal and mechanical action in concrete. *Journal of Engineering Mechanics (ASCE)*, 113(6):893–906.
- Zeiml, M., Lackner, R., Pesavento, F., and Schrefler, B. A. (2008). Thermo-hydro-chemical couplings considered in safety assessment of shallow tunnels subjected to fire load. *Fire Safety Journal*, 43(2):83–95.

# Computational Multiscale Approach to the Mechanical Behavior and Transport Behavior of Wood

K. Hofstetter<sup>1</sup>, J. Eitelberger<sup>1</sup>, T.K. Bader<sup>1</sup>, Ch. Hellmich<sup>1</sup> and J. Eberhardsteiner<sup>1\*</sup>

<sup>1</sup>Vienna University of Technology Institute for Mechanics of Materials and Structures, Karlsplatz 13/202, A-1040 Vienna, Austria

**Abstract.** Moisture considerably affects the macroscopic material behavior of wood. Since moisture takes effect on wood at various length scales, a computational multiscale approach is presented in this paper in order to explain and mathematically describe the macroscopic mechanical and transport behavior of wood. Such an approach allows for appropriate consideration of the underlying physical phenomena and for the suitable representation of the influence of microstructural characteristics of individual wood tissues on the macroscopic behavior. Continuum (poro-)micromechanics is applied as homogenization technique in order to link properties at different length scales. Building the model on universal constituents with tissue-independent properties and on universal building patterns, the only tissue-dependent input parameters are wood species, mass density, moisture content, and temperature. All these parameters are easily accessible, what renders the models powerful and easily applicable tools for practical timber engineering.

**Keywords:** continuum poro-micromechanics, moisture diffusivity, wood

## 1 Introduction

Wood meets in a convincing manner the demands on both a modern, efficient building material and a renewable resource in line with the claim for sustainable development of our society. Its full potential is yet to be exploited, since insufficient understanding of the material behavior and its so far quite poor covering in computational models limit its use for complex engineering structures. The strong influence of moisture on wood in terms of considerable variations of material properties depending on the moisture content and extensive dimensional changes

---

\* Corresponding author, e-mail: ej@mail.tuwien.ac.at

upon changes of the moisture content further complicate its engineering application. Since moisture takes effect on wood at various length scales, a computational multiscale approach is used herein in order to explain and mathematically describe the macroscopic mechanical and transport behavior of wood. Such an approach allows for appropriate consideration of the underlying physical phenomena and for the suitable representation of the influence of microstructural characteristics of individual wood tissues on the macroscopic behavior.

Continuum (poro-)micromechanics is applied as homogenization technique in order to link properties at different length scales. The fundamentals of this method and its application to the prediction of elastic properties, elastic limit states, and transport properties under stationary conditions of wood are discussed.

## 2 Fundamentals of Continuum Micromechanics

Continuum micromechanics (Zaoui 2002) is based on the identification of a so-called ‘Representative Volume Element (RVE)’, which represents the microstructure of a macroscopically or statistically homogeneous material. This microstructure is described in terms of so-called phases, which are related to the inhomogeneities within the RVE. The phases are characterized by their volume fractions, their (average) mechanical properties, and their morphology in terms of inclusion shape and spatial distribution, or connectedness of the phases. The mechanical response of the RVE to homogeneous deformations acting on its boundary is determined in terms of average phase stresses and phase strains on the basis of solutions for matrix-inclusion problems (Eshelby 1957). The relation between these and the mean stress in the RVE yields an estimate for the ‘homogenized’ stiffness of a material (Zaoui 2002)

$$C^{\text{hom,est}} = \sum_r f_r C_r : \left[ I + P_r^0 : (C_r - C^0) \right]^{-1} : \left\{ \sum_s f_s \left[ I + P_s^0 : (C_s - C^0) \right] \right\}^{-1} \quad (1)$$

where  $C_r$  and  $f_r$  denote the elastic stiffness and the volume fraction of phase  $r$ , respectively, and  $I$  is the fourth-order unity tensor. The two sums are taken over all phases of the heterogeneous material in the RVE. The fourth-order tensor  $P_r^0$  accounts for the characteristic shape of phase  $r$  in a matrix with stiffness  $C^0$ . Different choices of the stiffness of the embedding material in the matrix-inclusion problem result in different homogenization schemes, such as the Mori-Tanaka scheme and the self-consistent scheme (Zaoui 2002).

Macroscopic strength properties or elastic limit states are generally resulting from local failure of a single phase, e.g. phase  $n$ . Evaluation of a local failure criterion requires a relation between macroscopic loading and local phase strains in phase  $n$ . Since the detailed stress and strain distributions inside a phase are not known, the effective strain concept was proposed (Suquet 1997). According to this concept the microscale failure criterion is evaluated for some ‘effective strains’

suitably characterizing the (non-uniform) strain field in this phase. In order to appropriately represent (strength-governing) local strain peaks, quadratic strain averages (second-order moments) (Dormieux et al. 2002),  $\bar{\bar{\boldsymbol{\varepsilon}}}_{n,v}$  and  $\bar{\bar{\boldsymbol{\varepsilon}}}_{n,d}$ , are chosen as effective strains herein. They can be estimated through derivatives of the potential energy stored in the RVE with respect to the bulk modulus  $k_n$  and the shear modulus  $\mu_n$  of the considered phase (Dormieux et al. 2002).

In poro-elastic materials, the pore pressure in the pore space can be treated in the framework of continuum poro-micromechanics by considering this pore pressure as eigenstress acting at the microscale (Hellmich et al. 2005). Applying the concepts developed for upscaling of eigenstresses (Zaoui 2002), poro-elastic properties can be upscaled, so that, finally, macroscale poro-elastic properties depending on microstructural characteristics can be derived (Hellmich et al. 2005, Chateau et al. 2002).

Assuming that the macroscopic transport behavior is controlled by Fickian diffusion in material components at smaller length scales, effective transport properties under steady state conditions can be derived pursuing a strategy analogous to that described for elastic properties before: Average phase fluxes and corresponding average phase concentration gradients resulting from a homogeneous concentration gradient acting on the boundary of the RVE are derived from Eshelby-type solutions for matrix-inclusion problems. Thereon, effective diffusivities of the material can be estimated from the relation between the applied homogeneous concentration gradient and the mean resulting flux in the RVE. The latter is evaluated as mean of the average fluxes in each phase over the volume of the RVE. Finally, the estimate for the effective diffusivity reads as (Dormieux et al. 2006)

$$\mathbf{D}_{\text{hom}} = \sum_r f_r \mathbf{D}_r : \left[ \mathbf{1} + \mathbf{P}_r^0 : (\mathbf{D}_r - \mathbf{D}^0) \right]^{-1} : \left\{ \sum_s f_s \left[ \mathbf{1} + \mathbf{P}_s^0 : (\mathbf{D}_s - \mathbf{D}^0) \right]^{-1} \right\}^{-1} \quad (2)$$

where  $\mathbf{D}_r$  and  $f_r$  denote the diffusivity and the volume fraction of phase  $r$ , respectively,  $\mathbf{P}_r^0$  is the second-order Hill tensor of phase  $r$  in a matrix material with diffusivity  $\mathbf{D}^0$ , and  $\mathbf{1}$  is the second-order unity tensor. Again, the two sums are taken over all phases of the heterogeneous material in the RVE.

### 3 Multiscale Model for Wood Elasticity and Elastic Limit States

Wood exhibits a hierarchical architecture and structural features at various length scales. As for mechanical properties, a four-step homogenization scheme is suitable for prediction of the macroscopic behavior (Hofstetter et al. 2005, 2009): The first step concerns the mixture of hemicelluloses and lignin at a length scale of some nanometers in an amorphous material denoted as polymer network. In the moist state, water-filled pores in this matrix are considered in the framework of

poro-elasticity. Wood is not a poro-elastic material in the strict sense, since the pore space is only formed upon moisture uptake. However, assuming undrained conditions (i.e. constant water content in the cell wall also under mechanical loading), poro-elasticity provides a suitable representation of the mechanical behavior of wood in the moist state. In the second homogenization step, inclined fiber-like aggregates of crystalline cellulose and of amorphous cellulose, exhibiting typical diameters of 20-100 nm, are embedded in this polymer network, constituting the cell wall material. The 'homogenized' stiffnesses of the polymer network and of the cell wall material are determined by means of continuum (poro-)micro-mechanics, namely through self-consistent and Mori-Tanaka homogenization steps, respectively, as described in (Zimmermann et al. 1994). At a length scale of about one hundred microns, the material softwood is defined, comprising cylindrical pores (lumens) in the cell wall material of the preceding homogenization step. Its stiffness can be again estimated by means of the Mori-Tanaka scheme. Finally, at a length scale of several millimeters, hardwood comprises additional larger cylindrical pores denoted as vessels, which are embedded in the softwood-type material homogenized before. Estimates for the stiffness of hard-wood are obtained in an analogous procedure as in the third homogenization step.

Macroscopic elastic limit states are derived on the basis of the experimental evidence (Zimmermann et al. 1994) that macroscopic failure is initiated by shear failure of lignin in the wood cell wall. Strain peaks in lignin are approximated by quadratic strain averages over this phase. Applying the concepts of multistep localization, derivation of the macroscopic potential energy with respect to the shear modulus and bulk modulus of this phase provides access to these strain averages.

Based on the universal elastic properties of the nanoscaled constituents (crystalline and amorphous) cellulose, hemicellulose and lignin (see Hofstetter et al. 2005, 2009 for the values), the multiscale model allows for prediction of wood tissue-specific macroscopic elastic properties from tissue-specific chemical composition and microporosity. For the prediction of elastic limit states for arbitrary macroscopic loading, the shear strength of lignin is added to these input data.

Among other experimental results (Hofstetter et al. 2005, 2009), elastic limit states measured under biaxial loading conditions with various ratios of principal stresses  $\sigma I/\sigma II$  on spruce wood samples were used for model validation (Hofstetter et al. 2009). The load is applied either parallel to the longitudinal (L) and radial (R) direction ( $\alpha=0^\circ$ ) or deviating from these directions by a loading angle  $\alpha=30^\circ$  in the LR-plane. The failure surfaces predicted for the mean density of all samples (solid lines in Figure 1) and for their maximum and minimum density, respectively, (dashed lines in Figure 1) enclose most of the experimental strength data (marked by crosses in Figure 1). At predominant tensile loading parallel to the grain (L-direction), a remarkable number of experimental points lies outside the predicted failure surface related to lignin failure. These points refer to situations where lignin failure does not directly cause overall composite material failure because of still intact cellulose fibrils, so that the (predicted) elastic limit falls below the (measured) ultimate strength.

## 4 Multiscale Model for Moisture Diffusivity of Wood

At stationary conditions, the moisture transport behavior of wood can be suitably described by superimposing the moisture flows in the cell walls (bound water) and the cell lumens (water vapor), which are both Fickian in good approximation. Since the diffusive properties of the cell wall vary only slightly between different wood species, they are considered as universal and as starting point of the multi-

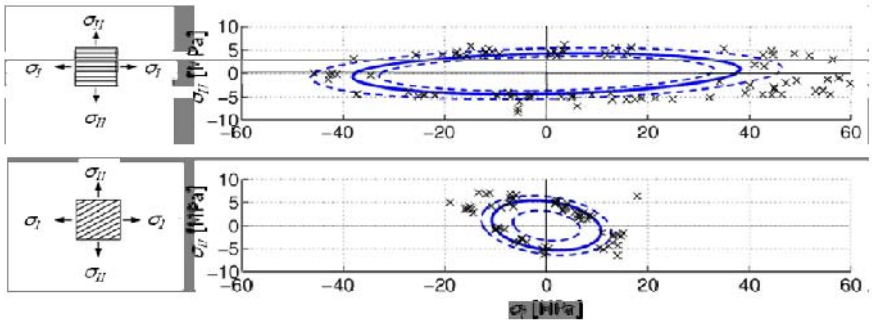


Figure 1. Model-predicted failure surface (lines) and experimental results (crosses) of biaxial tests on spruce wood.

scale model for wood diffusivity. Their dependence on the moisture content and on temperature is considered by phenomenological analytical relations fitted to experimental data (Eitelberger, 2009). Thereon, effective moisture transport properties of softwood and hardwood are derived analogously to homogenization steps three and four of the multiscale model for wood elasticity. In order to resolve the influence of the growth ring structure, an additional homogenization step is introduced here based on the rules of mixture. Parallel arrangement of layers of higher and lower mass density results in predictions for diffusivities in tangential (T) direction, while their arrangement in series provides estimates for the radial (R) direction.

Model validation is again based on comprehensive experimental data from the literature for moisture diffusivities in the three principal material directions, namely longitudinal, radial, and tangential direction, across a variety of different wood species and samples (Eitelberger, 2009). A correlation plot showing experimental results for effective diffusivities on the abscissa and corresponding model predictions on the ordinate is presented in Figure 2. The differentiation between different material directions and between softwood and hardwood samples is made by different markers. Across all samples and material directions, a very good agreement of model predictions and experimental results is found.

## 5 Conclusions

Multiscale models for elastic properties as well as diffusion properties of wood are presented. Their physical basis results in universal applicability of the models across different wood samples and species and in suitable descriptions of the macroscopic material behavior. Building the model on universal constituents with tissue-independent properties and on universal building patterns, the only tissue-dependent input parameters are wood species, mass density, moisture content, and temperature. All these parameters are easily accessible, what renders the models powerful and easily applicable tools for practical timber engineering. Moreover, insight into the microstructural origin of the macroscopic behavior of wood is gained.

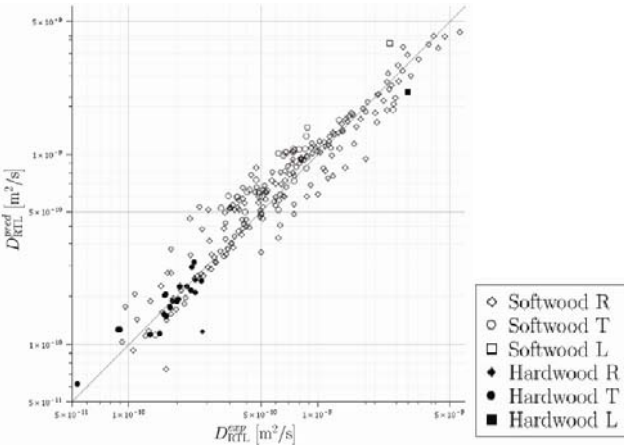


Figure 2. Comparison of measured and model-predicted effective diffusivities

## References

Chateau X. and Dormieux L. (2002). Micromechanics of saturated and unsaturated porous media. *International Journal for Numerical and Analytical Methods in Geomechanics*, 26: 831-844.

Dormieux L., Kondo D., and Ulm F. J. (2006). *Microporomechanics*, Wiley & Sons.

Dormieux L., Molinari A. and Kondo D. (2002). Micromechanical approach to the behavior of poroelastic materials. *Journal of the Mechanics and Physics of Solids*, 50(10): 2203-2231.

Eitelberger J. and Hofstetter K. (2009). Multiscale homogenization model for transport processes in wood below the fiber saturation point, in preparation.

Eshelby J. D. (1957). The determination of the elastic field of an ellipsoidal inclusion and related problems. *Proceedings of the Royal Society of London Series A, Mathematical and Physical Sciences*, 241(1226): 376-396.

- Hofstetter K., Bader Th. K., Hellmich Ch. and Eberhardsteiner J. (2006). Wood strength properties predicted from microstructure and composition, *European Journal of Mechanics*, submitted for publication.
- Hofstetter K., Hellmich Ch., and Eberhardsteiner J. (2005). Development and experimental verification of a continuum micromechanics model for the elasticity of wood. *Europ. J. Mech. A/Solids*, 24: 1030-1053.
- Hellmich C. and Ulm F. J. (2005). Drained and undrained poroelastic properties of healthy and pathological bone: A poro-micromechanical investigation. *Transp. Porous Media*, 58(3): 243-268.
- Suquet P. (1997). *Continuum Micromechanics*. Springer Verlag, New York.
- Zaoui A. (2002). Continuum micromechanics: Survey. *ASCE J. Eng. Mech.*, 128: 808-816.
- Zimmermann T., Sell J., and Eckstein D. (1994). Rasterelektronenmikroskopische untersuchungen an zugbruchflächen von fichtenholz. *Holz als Roh- und Werkstoff*, 52: 223-229 [in German].

*“This page left intentionally blank.”*

# The Finite Cell Method: High Order Simulation of Complex Structures without Meshing

Ernst Rank<sup>1\*</sup>, Alexander Düster<sup>1</sup>, Dominik Schillinger<sup>1</sup> and Zhengxiong Yang<sup>1</sup>

<sup>1</sup>Chair for Computation in Engineering Technische Universität München, Arcisstraße 21, 80290 München, Germany

**Abstract.** A smooth integration of geometric models and numerical simulation has been in the focus of research in computational mechanics for long, as the classical transition from CAD-based geometric models to finite element meshes is, despite all support by sophisticated preprocessors, very often still error prone and time consuming. High order finite element methods bear some advantages for a closer coupling, as much more complex surface types can be represented by p-elements than by the classical low order approach. Significant progress in the direction of model integration has recently been made with the introduction of the ‘iso-geometric analysis’ concept, where the discretization of surfaces and the Ansatz for the shape functions is based on a common concept of a NURBS-description. In this paper we discuss a recently proposed different approach, the *Finite Cell Method*, which combines ideas from fictitious domain methods with high order approximation techniques. The basic idea is an extension of a partial differential equation beyond the physical domain of computation up to the boundaries of an embedding domain, which can easier be meshed. The actual domain is only taken into account using a precise integration technique of ‘cells’ which are cut by the domains’ boundary. If this extension is smooth, the solution can be well approximated by high order polynomials. The method shows exponential rate of convergence for smooth problems and good accuracy even in the presence of singularities.

**Keywords:** finite cell method, embedding domain, fictitious domain, high-order methods, p-extension, meshless methods, solid mechanics

---

\* Corresponding author, e-mail: rank@inf.bauwesen.tu-muenchen.de

# 1 The Finite Cell Method

The Finite Cell Method (Parvizian, 2007; Düster, 2008) is a fictitious domain like extension to the classical finite element method. Let us assume that on a domain  $\Omega$  with the boundary  $\partial\Omega$  a problem of linear elasticity is described in weak form by  $B(u,v)=F(v)$  where the bilinear form is

$$B(u,v) = \int_{\Omega} [Lv]^T C [Lu] d\Omega \tag{1}$$

in which  $L$  is the standard strain-displacement operator and  $C$  is the elasticity matrix. The domain of computation is now embedded in the domain  $\Omega_e$  with the boundary  $\partial\Omega_e$  (Figure 1).

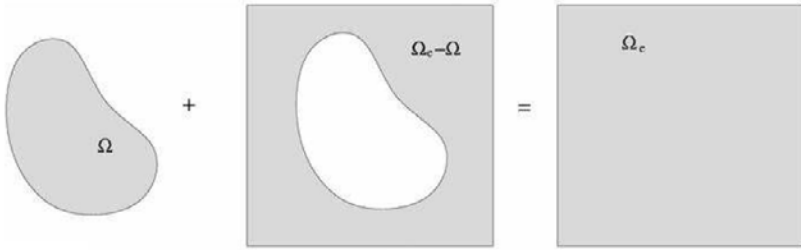


Figure 1. The domain  $\Omega$  is extended to  $\Omega_e$ .

The weak form of the equilibrium equation for the embedding domain  $\Omega_e$  is given by  $B_e(u,v) = F_e(v)$ , where the bilinear form is

$$B_e(u,v) = \int_{\Omega_e} [Lv]^T C_e [Lu] d\Omega \tag{2}$$

in which  $C_e$  is the elasticity matrix of the extended domain, given as

$$C_e = \begin{cases} C & \text{in } \Omega \\ C^{(2)} & \text{in } \Omega_e \setminus \Omega \end{cases}$$

Note that in the case of a “zero extension”, where  $C^{(2)} = 0$ , the bilinear functional (2) turns to

$$\begin{aligned}
B_e(u, v) &= \int_{\Omega} [Lv]^T C [Lu] d\Omega + \int_{\Omega_e \setminus \Omega} [Lv]^T 0 [Lu] d\Omega \\
&= \int_{\Omega_e} [Lv]^T \alpha C [Lu] d\Omega = B(u, v)
\end{aligned} \tag{3}$$

where

$$\alpha = \begin{cases} 1.0 & \text{in } \Omega \\ 0.0 & \text{in } \Omega_e \setminus \Omega \end{cases}$$

The linear functional

$$F_e(v) = \int_{\Omega_e} \alpha v^T f d\Omega + \int_{\Gamma_N} v^T t_N d\Gamma + \int_{\Gamma_1} v^T \bar{t} d\Gamma \tag{4}$$

considers the volume loads  $f$ , prescribed traction  $t_N$  along  $\Gamma_N$  interior to  $\Omega_e$  and prescribed traction  $\bar{t}$  at the boundary of the extended domain.  $\Gamma_1$  in (4) is the Neumann boundary of  $\Omega_e$  and  $\bar{t}$  is set to 0 on  $\Gamma_1$ . Due to the boundary condition, the last term in (4) can be assumed 0. The extended domain is now discretized in a mesh being independent of the original domain. To distinguish from classical elements they will be called finite cells.

The union of all cells forms the extended domain  $\Omega_\varepsilon = \bigcup_{c=1}^m \Omega_c$ , where  $\Omega_c$  is the domain represented by a cell, and the extended domain is divided into  $m$  cells.

At the discretized level, (2) turns to

$$B_e(u, v) = \sum_{c=1}^m \int_{\Omega_c} [Lv]^T \alpha C [Lu] d\Omega \tag{5}$$

The global stiffness matrix  $K$  is the result of proper assembling of  $k^c$ , given as

$$k^c = \int_{-1}^1 \int_{-1}^1 \int_{-1}^1 (LN)^T \alpha C (LN) \|J\| d\xi d\eta d\zeta \tag{6}$$

in which  $\|J\|$  is the determinant of the Jacobian matrix. In contrast to classical fictitious domain methods high order polynomials are used as shape functions  $N$ . Their definition, implementation issues and basic properties of p-extensions can, e.g. be found in (Szabo, 1991, 2004; Düster, 2001).

The approximation of the original problem (1) over the domain has thus been replaced by a problem over an extended domain, yet with discontinuous coefficients. Therefore the integrand in (6) may be discontinuous within cells being cut by the boundary. Different integration variants have been investigated. Low order integration like trapezoidal rule on a refined grid can be used while the integration points are distributed uniformly in the cell. Also Gaussian integration with higher number of integration points on the original cell or on sub-cells is applicable.

## 2 Numerical Examples

In a first two-dimensional example the FCM is investigated for a model problem of porous media. The finite element mesh for the reference solution is shown in Figure 2a, where a plate under extension is perforated with 49 holes. The lower boundary is clamped. Without any preferences, a mesh of  $41 \times 41$  cells (Figure 2b) is defined and shape functions with polynomial order  $p=8$  are used. Sub-cells to perform accurate integration are not necessary since the cells are dense enough. The reference solution is obtained by a fine uniform unstructured mesh of 6106 elements while a  $p$ -extension up to  $p=8$  ensures convergence. Figure 2c gives the stress contours and Figure 2d compares the stress distribution along the diagonal cut-line, which is in very good agreement with the reference solution while the maximum error in von Mises stresses is less than 1%.

In the second example a three-dimensional problem is investigated. Again, we consider a porous domain, now including 27 ellipsoidal holes of varying shape and spacing. The 3D domain is discretized by  $8 \times 8 \times 8$  hexahedral cells of polynomial degree  $p=8$ . In order to accurately account for the geometry of the holes, an adaptive integration scheme is applied to compute the stiffness matrices. The adaptive integration is based on a composed Gaussian quadrature applying sub-cells, which are introduced on cell level for integration purposes only. In a first step the volume of a broken cell is computed by successively increasing the number of sub-cells until the change of the computed volume falls below a prescribed

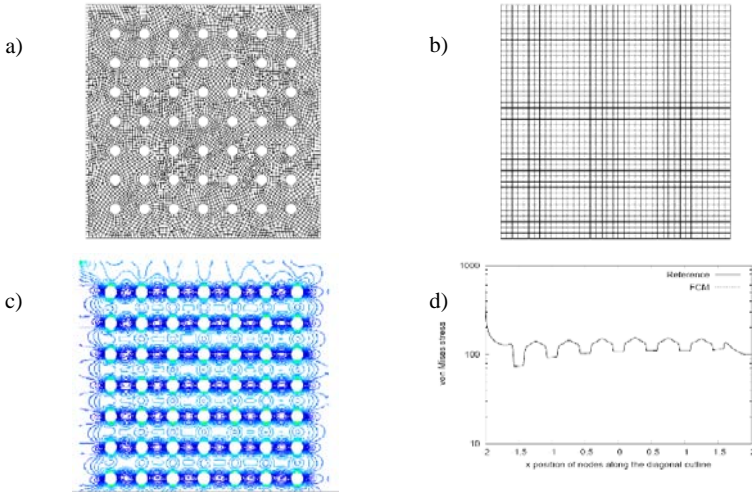


Figure 2. 2D model for a porous domain. a) Regular finite element mesh b) Finite Cell grid c) von Mises stress contours for finite cell computation d) von Mises stress along cutting

threshold. Since the computation of the volume is cheap, this first step can be carried out very efficiently. Once the number of sub-cells is determined, the more expensive computation of the stiffness matrix of the cells is performed, applying a composed Gaussian quadrature on the sub-cells.

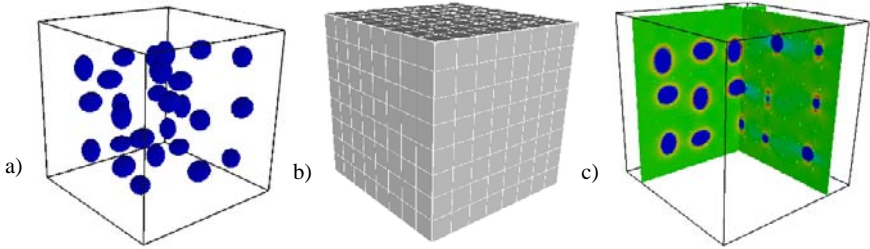


Figure 3. 3D model for a porous domain. a) Domain with 27 holes b) Grid with 512 cells c) von Mises stress contours for finite cell computation with  $p=8$

From Figure 3 it is evident, that the FCM provides the possibility to compute also complex three-dimensional porous domains without the burden to generate complicated meshes resolving the geometrical features of the problem. Future work will concentrate on the question of how to choose the size and the polynomial degree of the cells in order to provide most efficient computations.

## References

- Düster A., Bröker H., and Rank E. (2001). The p-version of the finite element method for three-dimensional curved thin walled structures, *Int. J. Num. Meth. Engrg.* 52: 673-703.
- Düster A., Parvizian J., Yang Z. and Rank E. (2008). The finite cell method for 3D problems of solid mechanics, *Comput. Meth. Appl. Mech. Engrg.* 197: 3768-3782.
- Parvizian J., Düster A. and Rank E. (2007). Finite cell method h- and p-extension for embedded domain problems in solid mechanics, *Comput. Mech.* 41: 121-133.
- Szabo B. and Babuska I. (1991). *Finite Element Analysis*. John Wiley and Sons.
- Szabo B., Düster A. and Rank E. (2004). The p-version of the finite element method. Volume 1, Chapter 5 in: *The Encyclopedia of Computational Mechanics*, John Wiley and Sons, 119-139.

# Theoretical Model and Method for Self-Excited Aerodynamic Forces of Long-Span Bridges

Yaojun Ge<sup>1,2\*</sup> and Haifan Xiang<sup>1,2</sup>

<sup>1</sup>State Key Laboratory of Disaster Reduction in Civil Engineering, Shanghai 200092, China

<sup>2</sup>Department of Bridge Engineering, Tongji University, Shanghai 200092, China

**Abstract.** This paper introduces theoretical model and methods for computationally determining aerodynamic forces of long-span bridges under wind-induced vibration, and emphasis is placed on self-excited aerodynamic force model and numerical identification of model's parameters, flutter derivatives. Through a serious analysis of the thin-plate cross section, the H-shaped section, and the closed box section, the main problems and the key prospects are concluded.

**Keywords:** long-span bridge, aerodynamic action, self-excited force, theoretical model, numerical identification

## 1 Introduction

Soon after the infamous incident of the original Tacoma Narrows Bridge in 1940, there were attempts to explain the wind induced bridge vibration as something similar to what had been known as an airfoil flutter, but much of this study is based on experimental investigations of unsteady aerodynamics from various wind tunnel tests of bridge structures. Withstanding the rapid developments in computer technology and computational wind engineering in recent years, the complexity of the unsteady flow field and of the associated motion-induced aerodynamics cannot impede the use of computational methods and analysis tools. Several numerical models and computational approaches have demonstrated sufficient accuracy for the results to be reliably used in the flutter analysis of cable-supported bridges (Ge and Xiang, 2006).

---

\* Corresponding author, e-mail: yaojunge@tongji.edu.cn

## 2 Theoretical Model of Self-Excited Aerodynamic Forces

For an arbitrary bridge deck section, for example in Figure 1, the motion of the deck can be represented by vertical displacement  $h$ , lateral displacement  $p$ , torsional displacement  $\alpha$  and their first order derivatives ( $\dot{h}, \dot{p}, \dot{\alpha}$ ) and second order derivatives ( $\ddot{h}, \ddot{p}, \ddot{\alpha}$ ) with the respect of time. Based on the assumption that structural vibration is linear, the self-excited aerodynamic force on a bridge deck section is expressed as follows:

$$F_f = F(h, p, \alpha, \dot{h}, \dot{p}, \dot{\alpha}, \ddot{h}, \ddot{p}, \ddot{\alpha}) = A_h h + A_p p + A_\alpha \alpha + A_{\dot{h}} \dot{h} + A_{\dot{p}} \dot{p} + A_{\dot{\alpha}} \dot{\alpha} + A_{\ddot{h}} \ddot{h} + A_{\ddot{p}} \ddot{p} + A_{\ddot{\alpha}} \ddot{\alpha} \quad (1)$$

where  $A_x$ ,  $A_{\dot{x}}$  and  $A_{\ddot{x}}$  ( $x = h, p, \alpha$ ) are the self-excited force parameters related to above nine vibration variables.

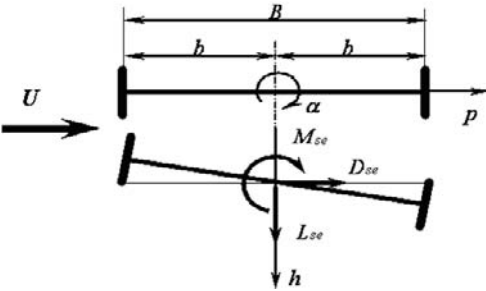


Figure 1. Displacements and self-excited aerodynamic forces.

Bridge flutter analysis is usually based on the assumption that displacements of a structure are tiny and with harmonic vibration pattern, that is,

$$x = x_m \sin \omega_x t, \quad \dot{x} = x_m \omega_x \cos \omega_x t, \quad \ddot{x} = -x_m \omega_x^2 \sin \omega_x t = -\omega_x^2 x \quad (2)$$

where  $x_m$  is the amplitude of displacement; and  $\omega_x$  is the circular frequency of vibration. Obviously, the first, second and third terms can be combined with the seventh, eighth and ninth terms in Equation (1), respectively, as

$$A_x x + A_{\ddot{x}} \ddot{x} = A_x x + A_{\ddot{x}} (-\omega_x^2 x) = (A_x - \omega_x^2 A_{\ddot{x}}) x = B_x x \quad (3)$$

Consequently, the self-excited aerodynamic force of a bridge deck section can be expressed through six state variables and six aerodynamic parameters as follows:

$$F_f = B_h h + B_p p + B_\alpha \alpha + A_{\dot{h}} \dot{h} + A_{\dot{p}} \dot{p} + A_{\dot{\alpha}} \dot{\alpha} \quad (4)$$

Self-excited aerodynamic force of a bridge deck section is commonly consisted of lift component  $L_{se}$ , drag component  $D_{se}$  and pitching moment component  $M_{se}$

shown in Figure 1. Each component of the self-excited force can be expressed in the form of Scanlan's representation with eighteen flutter derivatives as follows:

$$L_{se} = \frac{1}{2} \rho U^2 B \left( KH_1^* \frac{\dot{h}}{U} + KH_2^* \frac{B\dot{\alpha}}{U} + K^2 H_3^* \alpha + K^2 H_4^* \frac{h}{B} + KH_5^* \frac{\dot{p}}{U} + K^2 H_6^* \frac{p}{B} \right) \quad (5)$$

$$D_{se} = \frac{1}{2} \rho U^2 B \left( KP_1^* \frac{\dot{p}}{U} + KP_2^* \frac{B\dot{\alpha}}{U} + K^2 P_3^* \alpha + K^2 P_4^* \frac{p}{B} + KP_5^* \frac{\dot{h}}{U} + K^2 P_6^* \frac{h}{B} \right) \quad (6)$$

$$M_{se} = \frac{1}{2} \rho U^2 B^2 \left( KA_1^* \frac{\dot{h}}{U} + KA_2^* \frac{B\dot{\alpha}}{U} + K^2 A_3^* \alpha + K^2 A_4^* \frac{h}{B} + KA_5^* \frac{\dot{p}}{U} + K^2 A_6^* \frac{p}{B} \right) \quad (7)$$

where  $\rho$  is the air density;  $U$  is the mean wind speed;  $B$  is the bridge deck width;  $K=B\omega/U$  is the reduced frequency; and  $H_i^*$ ,  $P_i^*$  and  $A_i^*$  ( $i=1, 2, \dots, 6$ ) are called as flutter derivatives for a bridge deck section and are functions of the reduced frequency  $K$ .

It should be noted that the self-excited aerodynamic force expressed as Eqs. (5), (6) and (7) is based on two assumptions. Firstly, if the displacement of structural vibration were not assumed to follow harmonic vibration, the self-excited force should be represented with using 27 flutter derivatives instead of 18 ones. Secondly, if the self-excited force were considered having nonlinear relationship with structural vibration displacement, the expressions of the self-excited force would involve the second order even high-order terms of the motional structural variables. Therefore, the Scanlan expressions of self-excited aerodynamic force, with eighteen flutter derivatives, are theoretically perfect with the above-mentioned two assumptions.

### 3 Numerical Identification of Flutter Derivatives

Numerical identification of flutter derivatives for bridge deck sections is a computational method based on computational fluid dynamics (CFD). In general, there are three primary numerical methods to simulate turbulence flow, namely, direct numerical simulation (DNS), Reynolds-averaged Navier Stokes (RANS) and large eddy simulation (LES). In this section, three kinds of numerical identification methods for flutter derivatives are introduced and compared. The first method is a finite-element-based DNS method, called FEM-FLUID, developed in Tongji University (Cao, 1999). The second method is based on random vortex method of DNS, called RVM-FLUID, which was also developed in Tongji University (Zhou,

2002). The commercial software FLUENT based on RANS is used as the last method (Zhai, 2006). In order to make the comparison of these three methods, the numerical identification of flutter derivatives was performed on three typical sections including a thin plate with theoretical values available, an H-shaped section based on Tacoma Narrows Bridge and a closed box section of Great Belt Bridge.

### 3.1 Flutter derivatives of thin plate

The flutter derivatives of a thin plate were firstly derived by Theodorsen known as Theodorsen’s thin airfoil theory based on the thermo-flow theory of in-viscous flow and the conservation law of vortices. The  $k-\omega$  SST turbulence model was adopted in the identification with the FLUENT software, and the FEM and RVM software were performed in smooth flow. Though all three kinds of computation considered the effect of viscous flow, flow separation could be neglected at high Reynolds number and tiny amplitude of vibration. Hence, the computational results should be closed to Theodorsen’s theoretical results.

The computational conditions for a theoretical thin plate are given as follows: the ratio of width  $B$  to thickness  $H$  is 100 ( $B/H=100$ ); Reynolds number is  $10^5$ ; time steps ( $U\Delta t/B$ ) are 1/200 for FLUENT, 1/125 for FEM and 1/40 for RVM, respectively; computational fine grids are decided after the comparison of different cases; and the amplitudes of harmonic vibration are 0.1 m for vertical vibration and  $3^\circ$  for torsional vibration. The numerically identified derivatives ( $A_i^*$  and  $H_i^*$  with  $i=1, 2, 3, 4$ ) from these three methods are shown in Figure 2 together with theoretical results.

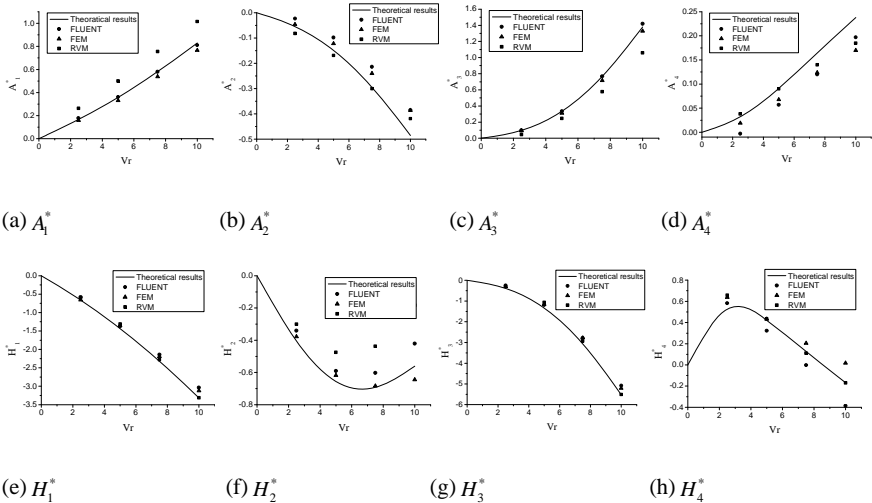


Figure 2. Flutter derivatives of thin plate

### 3.2 Flutter Derivatives of H-Shaped Section

The second application considered is that of the H-shaped section of the original Tacoma narrows bridge shown in Figure 1. The main geometry of this section is given as follows: the width  $B$  is 11.9m; the height  $H$  is 2.38m; and the thickness  $t$  of deck plate and outside board is 0.238m. The effect of Reynolds number on an H-shaped section is very little, and Reynolds number is also  $10^5$ . The computational conditions are set to be the same as the thin plate. Table 1 lists the results of numerically identified derivatives ( $A_i^*$  and  $H_i^*$  with  $i=1, 2, 3, 4$ ) based on three methods together with those from the wind tunnel testing and the numerical computation (Larsen and Walther, 1997). The numerical results are given only at the reduced frequencies being 4 and 6 respectively, since the reduced frequency is about 5 under the flutter failure of the original Tacoma narrows bridge.

Table 1. Flutter derivatives of H-shaped section

Flutter derivat.	FLUENT		FEM		RVM		Testing		Computer	
	$V_r=4$	$V_r=6$	$V_r=4$	$V_r=6$	$V_r=4$	$V_r=6$	$V_r=4$	$V_r=6$	$V_r=4$	$V_r=6$
$A_1^*$	0.348	0.200	0.122	0.016	0.395	0.298			0.285	-0.10
$A_2^*$	0.107	0.255	0.099	0.227	-0.08	0.126	0.098	0.313	0.022	0.194
$A_3^*$	0.135	0.218	0.197	0.225	0.154	0.292			0.399	0.155
$A_4^*$	-0.29	-0.47	-0.22	-0.20	-0.36	-0.56			-0.38	-0.26
$H_1^*$	-0.70	-3.07	-1.58	-3.87	-2.17	-4.31	-2.97	-3.74	-0.88	-3.98
$H_2^*$	1.20	2.46	0.831	1.58	1.02	2.13	0.910	-0.62	0.928	3.25
$H_3^*$	-0.79	-3.81	-0.87	-4.14	0.002	-3.60	0.403	-2.68	-0.35	-3.12
$H_4^*$	-0.20	-1.53	-0.51	-0.22	-1.67	-3.10			-1.00	-1.00

### 3.3 Flutter Derivatives of Closed Box

The thin plate represents a streamlined section while the H-shaped section is definitely a bluff body. It is significant to consider a box section as an intermediate between a thin plate and an H-shaped section. The third application considered is that of a closed box section of Great Belt Bridge. The computational conditions are set to be the same as the first two sections. The numerically identified derivatives ( $A_i^*$  and  $H_i^*$  with  $i=1, 2, 3, 4$ ) are plotted in Figure 3, and compared with those from the experiment and the computation (Walther, 1994).

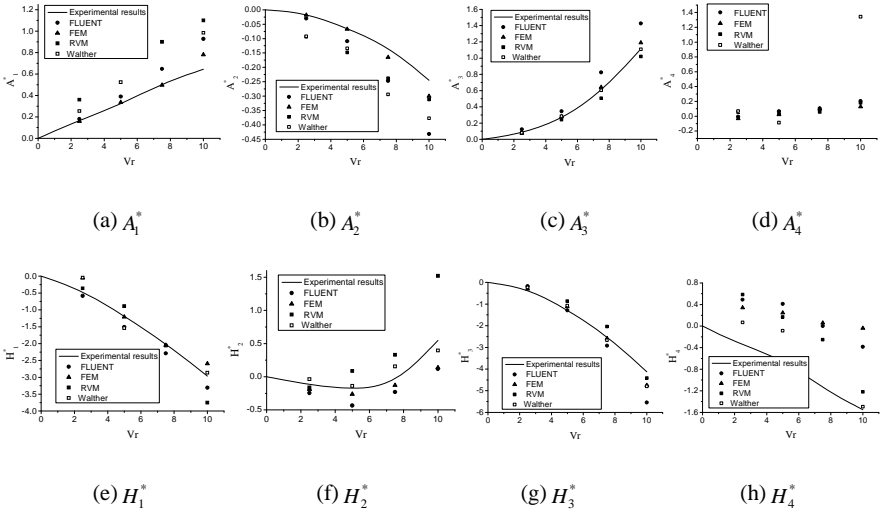


Figure 3. Flutter derivatives of closed box

From the numerical identified flutter derivatives in Figure 2, Table 1 and Figure 3, it can be concluded that the variation of the numerically identified flutter derivatives with reduced frequencies is the same as that of experimentally identified or theoretically calculated ones although FLUENT, FEM and RVM are based on different computational method for turbulence simulation. The relative errors of flutter derivatives identified by these three softwares are  $\pm 24.4\%$  for the thin plate,  $\pm 23.6\%$  for the H-shaped section and  $\pm 25.7\%$  for the closed box, respectively, which shows that these three methods have similar computational accuracy. For the thin plate, comparing with those of theoretical results, the mean absolute errors of numerically identified flutter derivatives are  $\pm 2.95\%$  for FLUENT,  $\pm 1.86\%$  for FEM and  $\pm 3.71\%$  for RVM, respectively. The mean absolute errors comparing with experimental results for the H-shaped section for FLUENT, FEM and RVM are  $\pm 37.3\%$ ,  $\pm 30.4\%$  and  $\pm 34.4\%$ , respectively, and those for the closed box are  $\pm 11.5\%$ ,  $\pm 6.14\%$  and  $\pm 17.1\%$ , respectively. It can be concluded that the FEM method is the most accurate method among these three methods.

### 4. Conclusions

The model of self-excited aerodynamic forces intend to represent non-linearity and arbitrary vibration pattern instead of linear relationship and harmonic structural vibration. The above-mentioned computational software including FLUENT, FEM and RVM as well as some others are not very sensitive to deal with small appendages on bridge decks such as railings, and are still limited in the approx-

imate estimation but not serious application in bridge flutter evaluation. Great efforts should be made towards the replacement of wind tunnel testing.

## Acknowledgements

The work described in this paper is partially supported by the NSFC Grants 50538050 and 90715039 and the MOC Grant 2006-318-494-26.

## References

- Cao F.C. (1999). Numerical simulation of aeroelastic problems in bridges. Doctoral dissertation of Tongji University, China [in Chinese].
- Ge Y.J., Xiang H.F. (2006). Computational models and methods for aerodynamic flutter of long-span bridges. *Proceedings of the 4<sup>th</sup> International Symposium on Computational Wind Engineering*, Yokohama, Japan, July 16-19.
- Larsen A., Walther J.H. (1997). Aeroelastic analysis of bridge girder section based on discrete vortex simulations. *Journal of Wind Engineering and Industrial Aerodynamics*, 97(67-68).
- Walther J.H. (1994). Discrete vortex method for two-dimensional flow past bodies of arbitrary shape undergoing prescribed rotary and translational motion, PhD Thesis of Technical University of Denmark, Denmark.
- Zhai Z.X. (2006). Numerical identification of aerodynamic parameters for bridge sections. Master degree dissertation of Tongji University, Shanghai, China [in Chinese].
- Zhou Z.Y. (2002). Numerical calculation of aeroelastic problems in bridges by discrete vortex method. Post-doctoral research report of Tongji University, China [in Chinese].

*“This page left intentionally blank.”*

# **STRUCTURAL STABILITY**

*“This page left intentionally blank.”*

# Imperfection Sensitivity or Insensitivity of Zero-Stiffness Postbuckling ... That Is the Question

Xin Jia<sup>1\*</sup>, Gerhard Hoefinger<sup>1</sup> and Herbert A. Mang<sup>1</sup>

<sup>1</sup> Institute for Mechanics of Materials and Structures, Vienna University of Technology, Karlsplatz 13/202, 1040 Vienna, Austria

**Abstract.** Zero-stiffness postbuckling of a structure is characterized by a secondary load-displacement path along which the load remains constant. In sensitivity analysis it is usually considered as a borderline case between imperfection sensitivity and imperfection insensitivity. However, it is unclear whether zero-stiffness postbuckling is imperfection sensitive or insensitive. In this paper, Koiter's initial postbuckling analysis is used as a tool for sensitivity analysis. Distinction between two kinds of imperfections is made on the basis of the behavior of the equilibrium path of the imperfect structure. New definitions of imperfection *insensitivity* of the postbuckling behavior are provided according to the classification of the imperfections. A structure with two degrees of freedom with a zero-stiffness postbuckling path is studied, considering four different imperfections. The results from this example show that zero-stiffness postbuckling is a transition case from imperfection sensitivity to imperfection insensitivity for imperfections of the first kind and that it is imperfection *insensitive* for imperfections of the second kind.

**Keywords:** zero-stiffness postbuckling, Koiter's initial postbuckling analysis, classification of imperfections, imperfection insensitivity, constant potential energy

## 1 Introduction

In the course of sensitivity analysis of the initial postbuckling behavior of a structure, a special case may occur that is referred to as *zero-stiffness postbuckling* (Tarnai, 2003). It is characterized by a secondary path with a constant load. In this paper the question will be answered whether zero-stiffness postbuckling is imperfection sensitive or imperfection insensitive.

---

\*Corresponding author, email: xin.jia@tuwien.ac.at

The investigation is restricted to static, conservative systems with a finite number  $N$  of degrees of freedom as conforms to the FEM. The material is assumed to be rigid. Multiple bifurcation will be excluded.

## 2 Theory

### 2.1 Koiter's Initial Postbuckling Analysis

The behavior of a static, conservative system can be deduced from the potential energy function  $V(\mathbf{u}, \lambda) : \mathbf{R}^N \times \mathbf{R} \rightarrow \mathbf{R}$ . The vector  $\mathbf{u} \in \mathbf{R}^N$  contains the displacement coordinates. The parameter  $\lambda \in \mathbf{R}$  is a load multiplier scaling a constant reference load  $\mathbf{P} \in \mathbf{R}^N$ . Therefore,

$$\mathbf{G}(\mathbf{u}, \lambda) := V_{,u} = \mathbf{F}^I(\mathbf{u}) - \lambda \mathbf{P} \quad (1)$$

may be interpreted as an out-of-balance force which vanishes along any equilibrium path in the  $u - \lambda$  - space. Here,  $\mathbf{F}^I(\mathbf{u})$  is the vector of internal forces. The secondary path is parameterized by a scalar  $\eta$ , with  $\eta = 0$  corresponding to the bifurcation point  $(\mathbf{u}_C, \lambda_C)$ . The displacement offset between the primary and the secondary path is defined by the vector  $\mathbf{v}(\eta) \in \mathbf{R}^N$ . Thus,  $\bar{\mathbf{u}}(\eta) = \tilde{\mathbf{u}}(\lambda(\eta)) + \mathbf{v}(\eta)$  describes the displacement along the secondary path, where  $\tilde{\mathbf{u}}(\lambda(\eta))$  denotes the displacement vector along the primary path. Insertion of the series expansions

$$\lambda(\eta) = \lambda_C + \lambda_1 \eta + \lambda_2 \eta^2 + \lambda_3 \eta^3 + O(\eta^4) \quad (2)$$

$$\mathbf{v}(\eta) = \mathbf{v}_1 \eta + \mathbf{v}_2 \eta^2 + \mathbf{v}_3 \eta^3 + O(\eta^4) \quad (3)$$

into the specialization of  $\mathbf{G}$  for the secondary path, i.e.,  $\mathbf{G}(\eta) = \mathbf{G}(\tilde{\mathbf{u}}(\lambda(\eta)) + \mathbf{v}(\eta), \lambda(\eta)) = \mathbf{0}$ , yields the new series expansion

$$\mathbf{G}(\eta) = \mathbf{G}_{0C} + \mathbf{G}_{1C} \eta + \mathbf{G}_{2C} \eta^2 + O(\eta^3) = \mathbf{0} \quad (4)$$

with  $\mathbf{G}_{nC} = \mathbf{G}_{,\eta^n} \Big|_{\eta=0} / n! \forall n \in \mathbf{N}$ . Since (4) must hold for arbitrary values of  $\eta$ ,  $\mathbf{G}_{nC} = \mathbf{0} \forall n \in \mathbf{N}$ . This condition paves the way for successive calculation of the unknowns  $v_1, \lambda_1, v_2, \lambda_2$ , etc.

### 2.2 Classification of Imperfections

For perfect systems undergoing bifurcation buckling, the imperfections are classified in two categories depending on whether or not the imperfect system has a bifurcation point. Godoy (2000) and Ikeda et al. (2007) introduce an imperfection vector  $\mathbf{E}$  which is calculated from the potential energy function referring to the imperfect structure

$$V^* = V^*(\mathbf{u}, \lambda, \varepsilon): \mathbf{R}^N \times \mathbf{R} \times \mathbf{R} \rightarrow \mathbf{R} \tag{5}$$

where  $\varepsilon \in \mathbf{R}$  denotes the imperfection parameter, and  $*$  denotes variables or functions of the imperfect structure. The imperfection vector is defined as

$$\mathbf{E} = \frac{\partial^2 V^*}{\partial \mathbf{u} \partial \varepsilon} \Big|_{\mathbf{u}=\bar{\mathbf{u}}} . \tag{6}$$

$\mathbf{E}$  describes the difference of the out-of-balance force between the perfect and the imperfect structure depending on the imperfection parameter  $\varepsilon$ . The classification of imperfections gives:

- $\mathbf{E}^T \cdot \mathbf{v}_1 = 0$  for imperfections of first kind,  $\varepsilon_I$ , (7)

- $\mathbf{E}^T \cdot \mathbf{v}_1 \neq 0$  for imperfections of second kind,  $\varepsilon_{II}$ . (8)

### 2.3 Definitions of and Criteria for Imperfection Insensitivity

Imperfections of first kind:

- **Definition I:**  $\varepsilon_I \in [-\zeta, \zeta]$ , where  $\zeta$  is an arbitrary small positive value. If all imperfect structures in this interval are still stable at the bifurcation point  $C^*$ ,

then the *initial* postbuckling path of the corresponding perfect structure is *imperfection insensitive* with respect to  $\varepsilon_I$ .

- **Criterion I:** If, in Equation(2),

$$\lambda_{m_{\min}} > 0 \wedge m_{\min} \text{ is even, where } m_{\min} := \min\{m \mid m \in \mathbf{N} \setminus \{0\}, \lambda_m \neq 0\}, \quad (9)$$

then the *initial* postbuckling path is *imperfection insensitive* with respect to  $\varepsilon_I$ .

Imperfections of second kind:

- **Definition II:**  $\varepsilon_{II} \in [-\zeta, 0) \cup (0, \zeta]$ , where  $\zeta$  is an arbitrary small positive value. If no imperfect structure in this interval has a load-displacement path with a snapthrough point  $(\mathbf{u}_{D^*}, \lambda_{D^*})$  with  $\lambda_{D^*} < \lambda_C$ , then the *initial* postbuckling path of the corresponding perfect structure is *imperfection insensitive* to  $\varepsilon_{II}$ .
- **Criterion II:** See **Definition II**.

### 3 Condition for Zero-Stiffness Postbuckling

For zero-stiffness postbuckling, the external load remains constant. Hence, all load coefficients in Equation (2) vanish, i.e.,

$$\lambda = \lambda_C, \quad (10)$$

$$\lambda_i = 0 \quad \forall i \in \mathbf{N} \setminus \{0\}. \quad (11)$$

Considering load coefficients  $\lambda_i = \lambda_i(\boldsymbol{\kappa})$ , where  $\boldsymbol{\kappa} = \{\kappa_1, \kappa_2, \dots\}$  is a set of design parameters,

$$\lambda_i(\boldsymbol{\kappa}) = C_0(\boldsymbol{\kappa}_0) \cdot C_i(\boldsymbol{\kappa}_i) \quad \forall \boldsymbol{\kappa}_i \subseteq \boldsymbol{\kappa} \quad \forall \boldsymbol{\kappa}_0 \subseteq \boldsymbol{\kappa} \quad (12)$$

with

$$C_0(\boldsymbol{\kappa}_0) = 0 \quad (13)$$

is a necessary and sufficient condition for zero-stiffness postbuckling.

## 4 Properties of Zero-Stiffness Postbuckling

### 4.1 Internal Force along a Zero-Stiffness Equilibrium Path

Substituting (10) into (1) and setting the result equal to zero yields

$$\mathbf{F}^I(\bar{\mathbf{u}}) = \lambda_c \cdot \mathbf{P}. \quad (14)$$

Equation (14) shows that the internal force along the zero-stiffness path is a constant.

### 4.2 Potential Energy along a Zero-Stiffness Equilibrium Path

Since the external load does not change along the zero-stiffness equilibrium path, the difference between the work done by the external load on the displacement at an arbitrary point on the secondary path and the one on the displacement at the bifurcation point is obtained as

$$W = (\lambda_c \cdot \mathbf{P}) \cdot \bar{\mathbf{u}} - (\lambda_c \cdot \mathbf{P}) \cdot \mathbf{u}_c, \quad (15)$$

The change of the strain energy is given as

$$\Delta U = U(\bar{\mathbf{u}}) - U(\mathbf{u}_c). \quad (16)$$

By the law of conservation of energy,

$$W = \Delta U. \quad (17)$$

Insertion of (15) and (16) into (17) yields

$$V(\bar{\mathbf{u}}) = U(\bar{\mathbf{u}}) - (\lambda_c \cdot \mathbf{P}) \cdot \bar{\mathbf{u}} = U(\mathbf{u}_c) - (\lambda_c \cdot \mathbf{P}) \cdot \mathbf{u}_c = V(\mathbf{u}_c). \quad (18)$$

Equation (18) indicates that the potential energy along the zero-stiffness equilibrium path is a constant.

### 5 Examples

A planar, static, conservative system with two degrees of freedom (Figure 1) is studied to illustrate the special situation of zero-stiffness postbuckling. It was originally studied in Schranz et al. (2006) and later in Steinboeck et al. (2008).

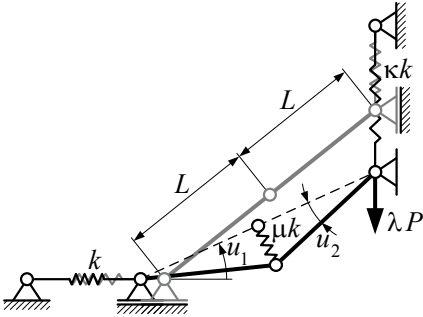


Figure 1. Two-bar system

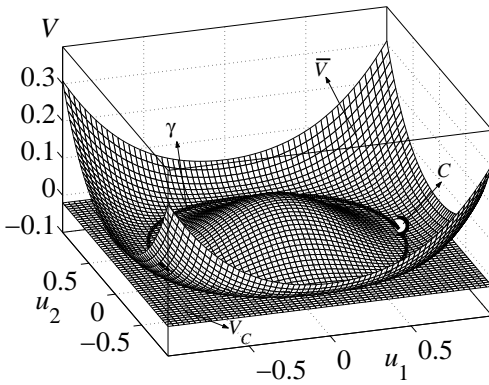
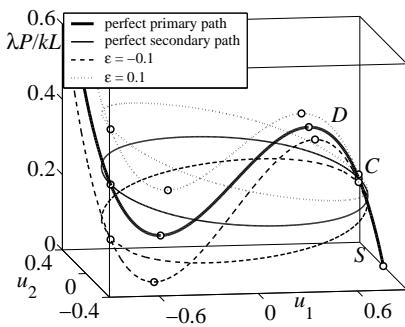


Figure 2. Surface  $\bar{V}(\mathbf{u})$  containing the curve  $\gamma(\eta)$  which represents the zero-stiffness postbuckling mode

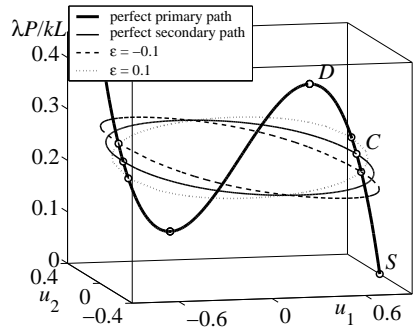
Figure 2 shows the surface  $\bar{V}(\mathbf{u}) = (\mathbf{u}, V(\bar{\mathbf{u}}, \lambda(\bar{\mathbf{u}}))) \forall \mathbf{u} \in \mathbf{R}^2$ . Its intersection with the horizontal plane  $V_c = (\mathbf{u}, V(\mathbf{u}_c)) \forall \mathbf{u} \in \mathbf{R}^2$  is the closed curve  $\gamma(\eta) = (\bar{\mathbf{u}}(\eta), V(\bar{\mathbf{u}}(\eta), \lambda(\bar{\mathbf{u}}(\eta)))) \forall \eta \in \mathbf{R}$  which represents the potential energy along the zero-stiffness path containing the bifurcation point  $C = (\mathbf{u}_c, V(\mathbf{u}_c))$ .

In an infinitesimal neighborhood of  $\gamma(\eta)$ ,  $\bar{V}(\mathbf{u})$  coincides (apart from terms that are of higher order small) with the potential-energy surface  $V(\mathbf{u}, \lambda)$ . In the infinitesimal neighborhood of an arbitrary point on  $\gamma(\eta)$ ,  $V_{,uu} \geq 0$ , where the equals sign holds for  $\gamma(\eta)$ . Consequently, the zero-stiffness postbuckling path is stable. Therefore, zero-stiffness postbuckling can be classified as imperfection insensitive.

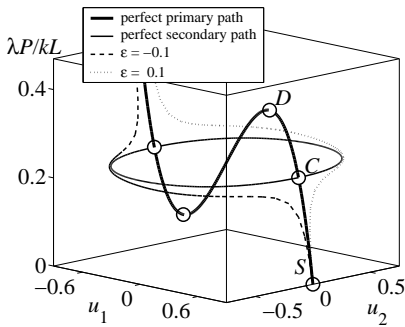
Four different imperfections are considered herein, including an imperfection of the stiffness of the top spring, an imperfection of the stiffness of the lateral spring, a shift of the load and a change of the initial angle between two rods. The first two imperfections belong to the first kind, and the last two to the second kind of imperfections. Figure 3 displays the equilibrium paths of the perfect and the imperfect structure for different imperfections.



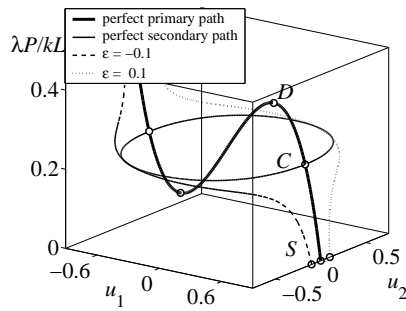
(a) Imperfection of stiffness of top spring



(b) Imperfection of stiffness of lateral spring



(c) Shift of load



(d) Change of initial angle between two rods

Figure 3. Equilibrium paths of perfect and imperfect structures.

## 6 Conclusions

From the theoretical investigation and the results of the examples, it follows that zero-stiffness postbuckling

- represents a case of transition from imperfection sensitivity to insensitivity for imperfections of first kind;
- is characterized by a stable postbuckling equilibrium path with constant potential energy and, hence, is imperfection insensitive to imperfections of second kind.

## References

- Godoy, L.A. (2000). *Theory of elastic stability: Analysis and sensitivity*. Taylor & Francis.
- Ikeda, K. Ohsaki, M. (2007). Generalized sensitivity and probabilistic analysis of buckling loads of structures. *Int. J. Non-linear Mech.* 42: 733-743.
- Koiter W. (1945). On the stability of elastic equilibrium, Translation of 'Over de stabiliteit van het elastisch evenwicht'. In NASA TT F-10833, Polytechnic Institute Delft, H.J. Paris Publisher: Amsterdam, 1967.
- Schranz C., Krenn B., Mang H.A. (2006). Conversion from imperfection-sensitive into imperfection-insensitive elastic structures II: Numerical investigation. *Comput. Methods Appl. Mech. Engrg.* 195: 1458-1479.
- Steinboeck A., Jia X., Hoefinger G., Mang H.A. (2008). Conditions for symmetric, antisymmetric, and zero-stiffness bifurcation in view of imperfection sensitivity and insensitivity. *Comput. Methods Appl. Mech. Engrg.* 197: 3623-3636.
- Tarnai, T. (2003). Zero stiffness elastic structures, *Int. J. Mech. Sci.* 45(3): 425-431.

# A Step towards a Realistic Probabilistic Analysis of Buckling Loads of Bridges

Ahmed Manar<sup>1\*</sup>, Kiyohiro Ikeda<sup>1</sup>, Toshiyuki Kitada<sup>2</sup> and Masahide Matsumura<sup>2</sup>

<sup>1</sup>Dept. of Civil & Environmental Eng., Tohoku University, Sendai 980-8579, Japan

<sup>2</sup>Dept. of Civil Eng., Osaka City University, Sumiyoshi-ku, Osaka 558-8585, Japan

**Abstract.** The probabilistic variation of buckling loads of bridges subjected to live load variations is evaluated. For this purpose, the imperfection sensitivity law is extended to live loads. The formulated relation is validated numerically for multiple imperfection pattern vectors subject to normally distributed live loads. A more realistic case is realized based on measured random traffic loads. Computational cost of stability analysis to investigate the probabilistic variation in buckling loads caused by the real random traffic loads has been reduced by utilizing the imperfection sensitivity law.

**Keywords:** buckling, loads imperfection sensitivity, probabilistic variation

## 1 Introduction

The imperfection sensitivity in buckling problems has been the subject of numerous investigations. The main motivation for such studies is that initial imperfections often cause a significant reduction in buckling strength. Practically, the magnitude or type of imperfections is subject to random variations. In view of this fact, the study of the imperfection sensitivity in buckling problems must be combined with probabilistic analysis. Several methodologies have been utilized to overcome such undetermined probabilistic variation. Such probabilistic variation was investigated numerically by using Monte-Carlo simulations (Edlund and Leopoldson, 1975; Elishakoff, 1978). The probabilistic nature of buckling was studied in (Elishakoff and Arbocz, 1978; Elishakoff, 1983; Arbocz and Hol, 1991) by obtaining the buckling strength numerically or experimentally for a number of random initial imperfections with known probabilistic properties. The imperfection sensitivity law by Koiter (1945) that relates the critical loads to the imperfection magnitude for a given imperfection mode has been extended to deal with the worst imperfection and the probability density function of buckling strength with the

---

\* Corresponding author, e-mail: manar\_ahmed1@yahoo.com

presence of random initial imperfections in loading (Ikeda and Murota, 2002; Ohsaki and Ikeda, 2007; Ikeda and Ohsaki, 2007). In Ikeda's work (Ikeda and Ohsaki, 2007), the Koiter imperfection sensitivity law for a single imperfection parameter was extended to be applicable to a number of imperfection variables defined as a single pattern vector normalized by a single imperfection parameter. Although real data about initial imperfections are preferred in investigating the reliability of buckling, few researches used real measured imperfection values. Arbocz and Ho1 (1991) utilized measured initial imperfections of axially compressed cylindrical shells to evaluate the statistical nature of their critical loads. The imperfection sensitivity probabilistic analysis was directed to describe the probabilistic variation of buckling caused by generated normally distributed imperfections in external loads of truss structures in (Ohsaki and Ikeda, 2007; Ikeda and Ohsaki, 2007).

In the evaluation of the probabilistic buckling strength of realistic structures, the external loads are known to greatly vary and need to be the spot of more researches with realistic external varied loads. This paper is a contribution toward a more realistic analysis in this field, the probabilistic variation of buckling loads of bridges subjected to real random traffic loads variation is evaluated. For this purpose, the imperfection sensitivity law is generalized to be applicable to multiple imperfection pattern vectors.

## 2 Mathematical Formulations

### 2.1 Imperfection Sensitivity Law

In the asymptotic theory for an imperfect system that is introduced in Ikeda's work (Ikeda and Ohsaki, 2007), the imperfection vector  $\tilde{\mathbf{v}}$  is defined as,

$$\tilde{\mathbf{v}} = \varepsilon \mathbf{d}, \quad (1)$$

where  $\mathbf{d}$  is called the imperfection pattern vector which is normalized by a single parameter of initial imperfection  $\varepsilon$ . The imperfection sensitivity law for a simple unstable-symmetric bifurcation point is presented as,

$$\tilde{f}_c = -((- \alpha)^{3/2} \mathbf{a}^T \mathbf{d} \varepsilon)^{2/3} + \beta \mathbf{b}^T \mathbf{d} \varepsilon, \quad (2)$$

where  $\alpha$  and  $\beta$  are constants,  $\mathbf{a}$  and  $\mathbf{b}$  are called the "first-order imperfection influence vector" and the "second-order one", respectively (Ikeda and Ohsaki, 2007).

## 2.2 Generalization of Sensitivity Law

In this paper, we define the general case of imperfections where the imperfection vector  $\tilde{\mathbf{v}}$  is defined as,

$$\tilde{\mathbf{v}} = \sum_{i=1}^n \varepsilon_i \mathbf{d}_i = (\tilde{v}_1, \dots, \tilde{v}_n)^T, \quad (3)$$

where  $\varepsilon_i$  is an imperfection parameter,  $\mathbf{d}_i$  is an imperfection pattern.

The generalized imperfection sensitivity law for a simple unstable-symmetric bifurcation point is presented here as,

$$\tilde{f}_c = (\mathbf{p}^T \tilde{\mathbf{v}})^{2/3} + \mathbf{q}^T \tilde{\mathbf{v}}, \quad \mathbf{p}^T = (p_1, \dots, p_n), \quad \mathbf{q}^T = (q_1, \dots, q_n), \quad (4)$$

where  $\mathbf{p}$  and  $\mathbf{q}$  are called the anti-symmetric imperfection sensitivity coefficient vector and the symmetric one, respectively. In bilateral symmetric structures, each applied imperfection pattern can be decomposed into two patterns; symmetric pattern and anti-symmetric one. Following this, we can calculate the imperfection sensitivity coefficients vectors  $\mathbf{p}$  and  $\mathbf{q}$  separately by numerical analysis.

## 2.3 Probabilistic Variation of Buckling Load

The probability density function of buckling loads can be derived through the generalized sensitivity law equation (4) under the assumption that initial imperfections vector  $\tilde{\mathbf{v}}$  are subject to known probabilistic variations.

Redefine equation (4) with the use of constant variables  $c$ ,  $d$  and  $e$  as,

$$\tilde{f}_c = c^{2/3} + d = e + d, \quad (5)$$

then, mean and variance for parts  $c$  and  $d$  in equation (5) can be calculated using the probabilistic properties of  $\tilde{\mathbf{v}}$ . The probability density function of the buckling load reduction  $\tilde{f}_c$  in equation (5) is given in an integral form as ,

$$\phi_{\tilde{f}_c} = \int_{-\infty}^0 \phi_e(e) \phi_d(\tilde{f}_c - e) de, \quad (-\infty < \tilde{f}_c < \infty), \quad (6)$$

where,  $\phi_e$  and  $\phi_d$  are the probability density functions of  $e$  and  $d$ , respectively.

### 3 Numerical Analysis

The present Koiter-based generatized imperfection sensitivity law is validated in the presence of normally distributed multiple imperfection patterns in live loads, then the law is utilized for probabilistic treatment of buckling load reduction caused by real measured random traffic loads. Two truss models are analyzed. For both of the two models, all members have same linear elastic properties, vertical loads are applied on bottom chords.

The load vector is expressed as

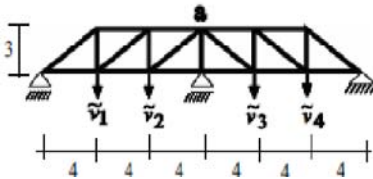
$$\mathbf{F} = f(\mathbf{f}_D + \mathbf{f}_{PL} + \tilde{\mathbf{v}}), \tag{7}$$

where  $f$  is the load parameter,  $\mathbf{f}_D$  is the dead load pattern vector,  $\mathbf{f}_{PL}$  is the perfect live load pattern vector, and  $\tilde{\mathbf{v}}$  is the generalized imperfection vector in live loads,  $\tilde{\mathbf{v}} = (\tilde{v}_1, \tilde{v}_2, \tilde{v}_3, \dots, \tilde{v}_n)^T$ .

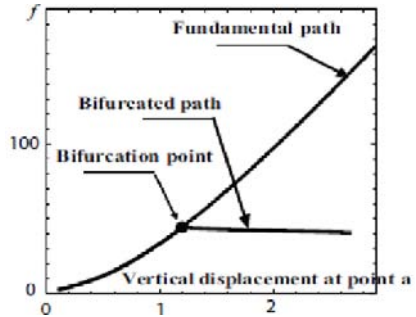
#### 3.1 Normally Distributed Imperfections in Live Loads

The truss shown in Figure 1(a) is considered.

The perfect truss model was analyzed for  $\tilde{\mathbf{v}} = 0$ , a simple unstable-symmetric bifurcation point was detected. Perfect equilibrium paths are shown in Figure 1(b).



(a) Truss model.



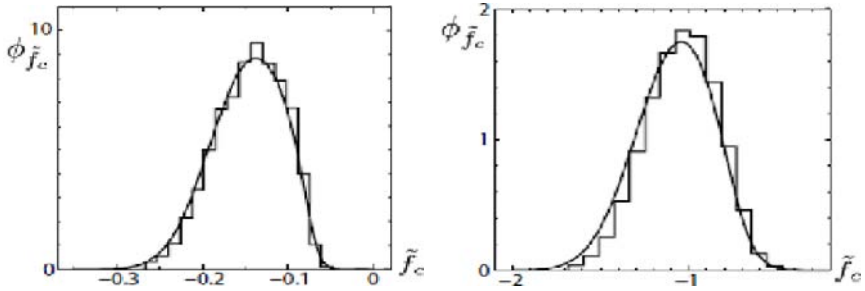
(b) Perfect equilibrium paths of the truss.

Figure 1. Truss model and perfect equilibrium paths of the truss

The truss was analyzed under the effect of normally distributed multiple imperfection patterns in live loads, as shown in Figure 1(a), the average of the imperfection parameter  $\tilde{v}_i$  is taken within range 1% up to 10 % of the perfect live

loads. The probability density function of the buckling load reduction is obtained using equation (6) and plotted with continues lines in Figure 2.

Results are compared with the numerical results of Monte-Carlo simulation that are plotted with broken lines in Figure 2, it shows good agreement specially for small values of imperfection.



(a) Imperfection = 1 % of perfect live loads

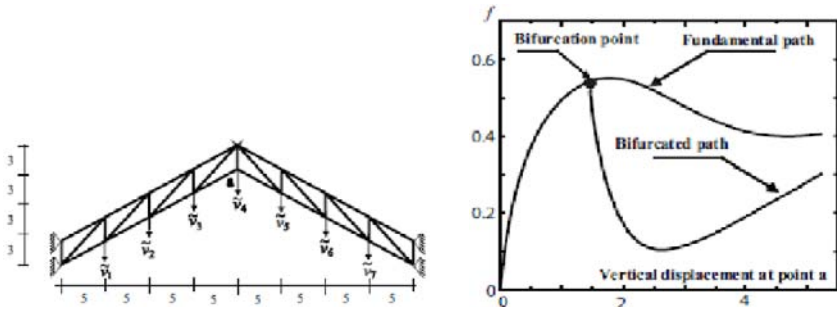
(b) Imperfection = 10 % of perfect live loads

Figure 2. Probabilistic variation of buckling loads for multiple-degree live loads imperfection vector.

### 3.2 Real Measured Live Loads Data

A more realistic case is considered by using a set of real live loads data.

The arch truss shown in Figure 2(a) has the perfect equilibrium paths shown in Figure 3(b), it has a simple unstable-symmetric bifurcation point. The real measured imperfections in live loads is introduced as shown in Figure 3(a).



(a) Truss arch bridge.

(b) Equilibrium paths of the arch truss.

Figure 3. Truss arch bridge and equilibrium paths of the arch truss.

The probability density of the buckling reduction is computed using the present generalised sensitivity law and the results are compared with the Monte-Carlo simulation of the finite element analysis results as it is explained next.

- The measured real live loads data is introduced as imperfections vector  $\tilde{\mathbf{v}}$  in equation (7).

- Finite element analysis is used to compute the reduction in buckling, histogram of buckling reduction results is plotted in Figure 4 with continuous lines.

- Vectors  $\mathbf{p}$  and  $\mathbf{q}$  in equation (4) are plotted by several numerical finite element analysis.

- The measured real live loads data is introduced as imperfections vector  $\tilde{\mathbf{v}}$  in equation (4).

- The reduction in buckling  $\tilde{f}^c$  is computed directly by using equation (4), finally the histogram of the buckling reduction using the second approach, is shown in Figure 4 with dash lines. In the second approach, no use of equation equation (6) and a lot of numerical analysis computational cost is saved.

A good agreement between results of the above two approaches is clear from Figure 4, this agreement demonstrates the superiority of the second approach.

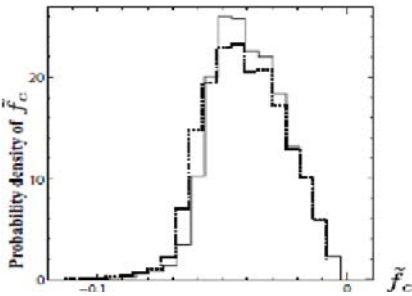


Figure 4. Probabilistic variation of buckling loads for real imperfection patterns in live loads.

## 4 Conclusions

The Koiter-based imperfection sensitivity law is utilized for probabilistic treatment of buckling loads of bridges under random varied traffic loads. Computational cost is saved by utilizing the generatized imperfection sensitivity law. Results that have been obtained with the use of the generatized imperfection sensitivity law are in good agreement with the numerical results.

## References

- Arbocz J, Hol JMAM (1991) Collapse of axially compressed cylindrical shells with random imperfections. *AIAA, JI* 29(12), 2247-2256.
- Edlund BLO, Leopoldson ULC (1975) Computer simulation of the scatter in steel member strength. *Comput. Struct.* Vol. 5(4), 209-224.
- Elishakoff I (1978) Impact buckling of thin bar via Monte Carlo method. *J. Appl. Mech.*, ASME, Vol. 45(3), 586-590.
- Elishakoff I, Arbocz J (1982) Reliability of axially compressed cylindrical shells with random axisymmetric imperfections. *Int. J. Solids Struct.* Vol. 18(7), 543-585.
- Elishakoff I (1983) *Probabilistic Method in the Theory of Structures*. J. Wiley, New York
- Ikeda K, Murota K (2002) *Imperfect Bifurcation in Structures and Materials-Engineering use of Group-theoretic Bifurcation Theory*. Springer, New York NY.
- Ikeda K, Ohsaki M (2007) Generalized sensitivity and probabilistic analysis of buckling loads of structures. *Int. J. Non-Linear Mech.*, Vol. 42(6), 733-743.
- Koiter WT (1945) On the stability of elastic equilibrium. Dissertation, Delft Univ. of Tech., Holland (English Trans.: NASA Tech. Trans. F10:833, 1967).
- Ohsaki M, Ikeda K (2007) *Stability and Optimization of Structures-Generalized Sensitivity Analysis*. Mechanical Engineering Series, Springer, New York NY.

*“This page left intentionally blank.”*

# Parametric Resonance of the Free Hanging Marine Risers in Ultra-Deep Water Depths

Hezhen Yang<sup>1\*</sup> and Huajun Li<sup>2</sup>

<sup>1</sup> State Key Lab of Ocean Engineering, Shanghai Jiao Tong University, Shanghai 200030, P.R China

<sup>2</sup> College of Engineering, Ocean University of China, Qingdao 266100, P.R China

**Abstract.** The study is focused in the parametric instability of the deep-sea risers due to the platform heave motions. As offshore hydrocarbon resources exploration and exploitation moving to much deeper waters, risers play more important roles than before, and face with many technological challenges. The riser resonance can produce disastrous results, such as environment pollution and economical loss. In this work, firstly, the governing motion equation of the marine riser is formulated. Then the stability behavior of the risers with and without nonlinear damping is investigated by employing the Floquet theory. During the numerical solution of the governing equation, the coupling between the modes was considered. Finally, special attention has been paid to the effect of damping for the parametric unstable region changes. The results show that damping can effectively reduce unstable regions. Several useful suggestions are proposed for the design of deep-sea riser structures.

**Keywords:** deep-sea riser, parametric excitation, instability, vibration response

## 1 Introduction

As offshore exploration and production activities progresses into deep and ultra-deep waters, long slender marine structures design becomes a more and more critical issue, both when considering oil field development costs and technological feasibility (Yang and Li, 2003; Huang and Li, 2006). Marine risers are widely used in ocean resource exploitation, extending from a platform at the sea surface to a wellhead connection at the sea floor, such as a fluid-conveyed curved pipe drilling crude oil, natural gas, other undersea economic resources, and then transporting those to the production lines (Bai, 2001).

---

\* Corresponding author, e-mail: yanghz@sjtu.edu.cn

Unquestionably, the risers for ultra-deep water have complex dynamic characteristics (Fu and Yang, 2009). One of the critical issues involving riser design is parametric resonance regarding platform heave motions (McCone, 1993). Parametric resonance can occur and produce disastrous results unless the vibration periods of the external dynamical forces and the structure are well separated. Riser failure results in reduction or cessation of revenue. It may also lead to spillage or pollution and may even endanger lives. Hence, a great deal of attention should be paid to instability assessment of deep-sea risers under parametric excitation.

The instability of deepwater risers is associated with fluctuation of the axial tension in the riser caused by vertical motion of the floating platform. Patel and Seyed (1995) presented an overview of the status of analysis techniques and the development of hydrodynamic analysis techniques for riser design. Many research papers have been published about Vortex-induced vibration. However, relatively few papers deal with parametrically excited deep-sea risers. Thampi and Niedzwecki (1992) presented the influence of parametric excitation on the dynamic behavior of marine risers using Markov methods.

The purpose of this work is to develop an analytical model for the deep-sea risers and to gather a picture of stability regimes of this kind of structure. This paper is structured as follows. Firstly, the governing motion equation of the marine riser is formulated. Then the stability behavior of the risers with and without nonlinear damping is investigated by employing the Floquet theory. During the numerical solution of the governing equation, the coupling between the modes was considered. Finally, special attention has been paid to the effect of damping for the parametric unstable region changes. The work is finalized by conclusion remarks of the parametric analysis in deep-sea riser.

## 2 Formulation

### 2.1 Governing Equation of Motion

The equation of motion can be written in a simplified form as follows:

$$EI \frac{\partial^4 w(z,t)}{\partial z^4} - \frac{\partial}{\partial z} \left[ T(t) \frac{\partial w(z,t)}{\partial z} \right] + (m_r + m_f + m_a) \frac{\partial^2 w(z,t)}{\partial t^2} = f(z,t) \quad (1)$$

The time varying tension force is included in the equation of motion. The oscillating component is assumed to be simple harmonic. The resulting equation of motion yields:

$$EI \frac{\partial^4 w(z,t)}{\partial z^4} - \frac{\partial}{\partial z} \left[ (T(z) + S(z) \cos \Omega t) \frac{\partial w(z,t)}{\partial z} \right] + (m_r + m_f + m_a) \frac{\partial^2 w(z,t)}{\partial t^2} = 0 \quad (2)$$

where  $T(z)$  static component of the tension force (N);  $S(z)$  amplitude of time varying component of the tension force (N);  $\Omega$  frequency of parametric excitation (rad/s)

This infinite set of ordinary differential equations can be approximated by a finite system of  $2N$  first-order coupled equations:

$$\begin{cases} \frac{dy_n}{d\tau} = y_{N+n}, \\ \frac{dy_{N+n}}{d\tau} = -\zeta A_1 y_{N+n} - \Omega_n^2 y_n - \kappa \sin(\bar{\Omega}\tau) \sum_{m=1}^{\infty} B_{mn} y_m \end{cases} \quad n, m = 1, 2, \dots, N, \quad (3)$$

where  $n$  and  $N$  stand for, respectively, the mode number and the total number of modes considered. In matrix notation, Equation (3) can be written as:

$$\dot{\mathbf{y}} = \mathbf{A}(\tau) \mathbf{y} \quad (4)$$

where  $\mathbf{y} = [y_1, y_2, \dots, y_{2N}]^T$ ,  $\mathbf{A}(\tau)$  is a  $2N \times 2N$  matrix, which is periodic in time, i.e.  $\mathbf{A}(\tau) = \mathbf{A}(\tau + 2\pi/\bar{\Omega})$ . Stability of the equilibrium of Equation (4) can be studied employing the Floquet theory, which is briefly outlined in the next subsection.

## 2.2 Implementation of Floquet Method

Floquet theory is fundamental to analysis the response and stability of systems governed by time-varying differential equations. It states that for a system of ordinary differential equations with periodic coefficients, for example Equation (2), over the period  $T = 2\pi/\Omega$  the transient solution has the form:

$$\{x(\psi)\} = [A(\psi)] \{c_k e^{\eta_k \psi}\} \quad (5)$$

where  $[A(\psi)]$  is periodic with period  $T$ ;  $\eta_k$  are complex characteristic numbers;  $c_k$  are constants found from the initial conditions:

$$\{c_k\} = [A(0)]^{-1} \{x(0)\} \tag{6}$$

Then, the stability of the system can be determined from the values  $\eta_k$ . The Floquet transition matrix [Q] of the system is defined by:

$$\{x(T)\} = \begin{bmatrix} x(1) & x(2) & \dots & x(2Z) \end{bmatrix} \begin{Bmatrix} x_1(0) \\ x_2(0) \\ \vdots \\ x_{2Z}(0) \end{Bmatrix} = [Q] \{x(0)\} \tag{7}$$

From Equation (5):

$$\begin{aligned} \{x(0)\} &= [A(0)] \{c_k\} \\ \{x(T)\} &= [A(0)] [\lambda_k] \{c_k\} \end{aligned} \tag{8}$$

where  $[A(0)] = [A(T)]$  and  $\lambda_k = e^{\eta_k T}$ . Substituting Equation (8) into Equation (7), yields:

$$[Q][A(0)] \{c_k\} - [A(0)] [\lambda_k] \{c_k\} = \{0\} \tag{9}$$

Since the coefficients  $c_k$  are arbitrary, one must have:

$$([Q] - \lambda_i [I]) \{a_0\}_i = \{0\} \tag{10}$$

where  $\{a_0\}_i$  is the  $i^{\text{th}}$  column of matrix [A(0)], such that  $\{a_0\}_i \neq \{0\}$ ,  $i=1, \dots, 2Z$ .

$$\text{Then, } |[Q] - \lambda_i [I]| = 0 \tag{11}$$

Thus,  $\lambda_k$ , are the eigenvalues of matrix [Q] and, in general, they are complex numbers. Once  $\lambda_k$  are found, one can determine  $\eta_k$  as:

$$\eta_k = \frac{1}{T} \ln(\lambda_k) = \hat{\sigma}_k + i \hat{\omega}_k \tag{12}$$

where

$$\hat{\sigma}_k = \frac{1}{T} \ln |\lambda_k| = \frac{1}{2T} \ln \left[ (\lambda_k)_R^2 + (\lambda_k)_I^2 \right]$$

$$\hat{\omega}_k = \frac{1}{T} \arctan \left[ (\lambda_k)_I / (\lambda_k)_R \right] \pm j \frac{2\pi}{T}, \quad j \in N$$
(13)

Values of  $\hat{\sigma}_k > 0$  indicate instability.

### 3 Description of Case Study

To illustrate the analysis procedures, parametric resonance studies are performed for a representative deep-sea riser configuration. During the riser installation process, the riser is suspended from the floating units. The corresponding model of the riser is shown in Figure 1. Parameters of the steel riser properties are given in Table 1.

Table 1 Parameters of the steel riser properties

Riser property	value
Young's modulus	2.1E+11Pa
Seawater density	1025kg/m3
Steel density	7850kg/m3
Outside diameter	0.5m
Riser length	3000m
Normal drag coefficient	1.1
Added mass coefficient	1.0
Wall thickness	0.025m
Mass of tension ring	15000kg

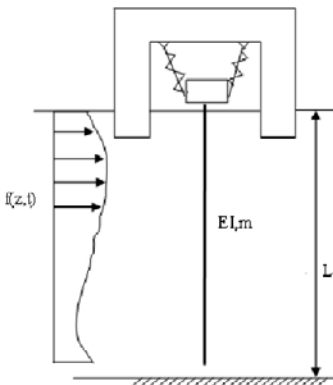


Figure 1. Configuration of deep-sea riser

## 4 Results

To better understand the dynamics of riser systems, parametric vibration and stability of deepwater risers have been investigated. Analysis of the equations of motion is performed using techniques founded in Floquet theory allowing for the determination of both system response and stability properties.

### 4.1 Stability Chart Construction

The parametric stability of a system is best represented by a stability chart. Some representative results are presented in this section. Stability is determined by analyzing the eigenvalues of a fundamental solution set at the end of one period of the parametric excitation. Any eigenvalue with a modulus greater than unity indicates the existence of a region of instability for the given set of system parameters. In these cases, stability plots that show stable and unstable system parameter ranges can be quite useful. By appropriate utilization of these analysis parameters, the designer will be quickly able to evaluate the dynamic behavior of a given system over a range of realistic operating conditions.

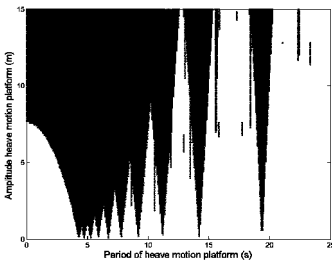


Figure 2. Stability chart for damping  $c=0$

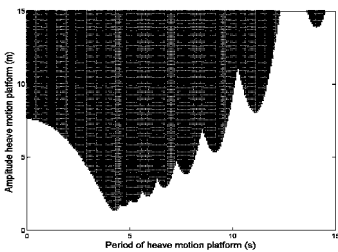


Figure 3. Stability chart of deep-sea riser damping  $c=0.5$ , (shaded areas are unstable)

System parameters are varied and stability determined in order to produce stability maps over the entire operating range. The corresponding grid point on the parameter plane is represented by a dot. The stability charts are plotted, reflecting the unstable regimes, with frequency parameter as the abscissa and amplitude parameters as the ordinate. Figure 2, Figure 3 shows the parametric stability charts for the deepwater riser. The parametric stability charts, for damping  $c=0$ , are shown in Figure 2, while Figure 3 depicts the stability charts, for damping  $c=0.5$ . These charts are expected to serve as invaluable tools in the design of deepwater risers. From observation of the stability charts, it is found that the parametric instability regions shrink, if system damping increased. Figure 3 shows that the addition of damping has a stabilizing effect. On the other way, many narrow instability regions associated with higher modes would appear.

### 4.2 Effects of Damping

The effect of damping is estimated through comparative calculations of the structure's behavior with and without damping effects, as shown in Figure 4. Comparing Figures, while the instability regions are reduced in the lower frequency parameter range, some of the previously stable regions have now become unstable for higher frequency parameter values. There is a significant reduction in the instability regions. For a designed riser system, the best solution is a system where the unstable regions are as small as possible. According to the above analysis, it is possible to minimize the unstable regions by changing the damping properties of the system. There are several physical options for designers to achieve the minimization, such as by adding dampers, by new damped materials etc.

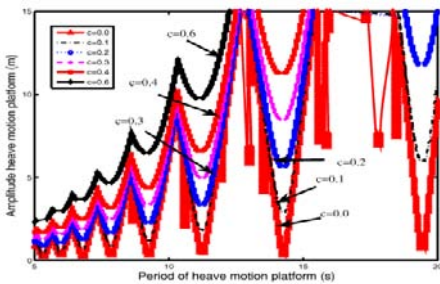


Figure 4. Instability regions for different damped riser system

### 5 Conclusion Remarks

Riser systems play an important role in determining export options, vessel selection, and seabed layout. The present work attempts to present the formulation and

algorithm required for the simulation of the parametric resonances of a deep-sea riser, discriminating it from other dynamic phenomena. A generally valid analytical tool oriented to the design of risers, specific to stability analysis, was derived. The numerical calculations concerned the effect of the system damping for the parametric excitation frequencies, which guide the dynamic system to lie within a region of coupled instability.

The guideline for design of ultra deepwater risers considering parametric instability was proposed. The structure safety may be increased and the cost reduced if an accurate analysis can be performed for the riser design. It is shown that the unstable system could be controlled effectively by the suggested approaches. For a more complete mathematical modeling of the deepwater riser under consideration, the inclusion of these effects should be investigated in a future study.

## Acknowledgments

This work was financially supported by the National Key Natural Science Foundation of China (Grant No. 50739004) and the Research Fund for the Doctoral Program of Higher Education (Grant No. 20070248104).

## References

- Bai Y. (2001). *Pipelines and Risers*. Elsevier Ocean Engineering Book Series, Vol. 3.
- Fu J.J. and Yang H.Z. (2009). Dynamic response analysis of a deepwater steel catenary riser at the touchdown point, *Ocean Engineering* [in Chinese].
- Huang W.P. and Li H.J. (2006). A new type of deepwater riser in offshore oil & gas production: The steel catenary riser, *Periodical of Ocean University of China*, 36(5): 775-780.
- Huang W.P. and Wang A.Q. et al. (2007). Experimental study on VIV of span of subsea pipeline and improved model of lift force. *Gongcheng Lixue/Engineering Mechanics*, 24(12): 153-157.
- McCone A.J. (1993). Technical Challenges in the Design of Flexible Pipes, *Offshore and Arctic Operation*, ASME, 1-3.
- Patel M.H. and Seyed F.B. (1995). Review of flexible riser modeling and analysis techniques. *Engineering Structures*, 17(4): 293-304.
- Thampi S.K. and Niedzwecki J.M. (1992). Parametric and external excitation of marine risers. *Engineering Mechanics*, 118(5): 943-960.
- Yang H.Z. and Li H.J. (2003). Damage localization of offshore platform under ambient excitation. *China Ocean Engineering*, 17(3): 495-504.

# Simulation of Structural Collapse with Coupled Finite Element-Discrete Element Method

Xinzheng Lu<sup>1\*</sup>, Xuchuan Lin<sup>1</sup> and Lieping Ye<sup>1</sup>

<sup>1</sup>Department of Civil Engineering, Tsinghua University, Beijing 100084, P.R. China

**Abstract.** Structural progressive collapse is a great threat to life safety and therefore it is necessary to study its mechanism in detail. Numerical simulation is significant to study the whole process of progressive collapse in structural level. Since collapse is a complicated procedure from continuum into discrete fragments, numerical model should be competent in nonlinear deformation before collapse and breaking and crashing of fragments after collapse. Coupled Finite element-discrete element method on simulating structural progressive collapse is proposed to meet the requirements. Relatively accurate models, such as fiber model and multi-shell shell model, are introduced to construct the finite element model of structure. In the analysis, the failed finite elements will be removed and replaced with granular discrete elements according to the criteria of equivalent total mass and volume so that the impacting and heaping of fragments can be taken into account. The sample with the coupled method shows that this method not only possesses the advantages of finite element method but also simulates the behavior of fragments well.

**Keywords:** finite element, discrete element, coupling calculation, progressive collapse, numerical model

## 1 Introduction

Progressive collapse causes great casualties and property losses, so progressive collapse should be strictly avoided in structural design. Though buildings which meet the present design codes generally possess enough collapse resistant capacity under conventional loads, however, it is important to carry out further detailed research on structural progressive collapse. Since collapse is an ultimate safety state of a structure, with a better understanding of collapse state, a better evaluation of a building's safety margin can be obtained. It is the typical mode of progressive collapse that failure first occurs at weak part of a structure and if there

---

\* Corresponding author, e-mail: luxz@tsinghua.edu.cn

is no sufficient alternative loading path, then failure expands to the whole structure. Therefore, the study on collapse helps to find and enhance the weak part of a structure and can effectively improve its collapse resistant performance.

Since progressive collapse is a structural behaviour and buildings are generally huge, large scale tests are often too difficult to carry out with the limitation of time and cost. Therefore, numerical simulation is a significant method to study progressive collapse. Besides accidental impact and blast, rare strong earthquakes like Wenchuan Earthquake, which was more than nine degree in seismic intensity in a region with seven-degree design intensity, can unavoidably cause massive local failures. How to control the expansion of local failure to ensure the overall stability of structure is an important aspect of structural safety research. To investigate this problem, collapse process especially the expanding process of local damage has to be studied and simulation on the whole process of progressive collapse is necessary.

Collapse is a complex process from continuous body into discrete one, which puts forward high requirements for its numerical model. The model should not only can simulate behaviours before collapse, such as nonlinear deformation and energy dissipation, but also can simulate the rigid-body displacement of fragments and impact among damaged components after collapse begins. Many numerical methods were proposed to simulate this two-stage process and the existing numerical methods can be roughly classified into two categories, finite element method (FEM) and non-continuum mechanics method. Some scholars simulate the collapse process with dynamic finite element software LS-DYNA. Lu & Jiang (2001) simulated the collapse of World Trade Centre and the numerical results are close to the real conditions. Liu et al. (2007) and Shi et al. (2007) constructed 3-D solid-element models to simulate progressive collapse due to impact of blast load. Lu et al. (2007) and Miao et al. (2007) developed fiber model THUFIBER based on commercial finite element software MSC.MARC and the model gave a good simulation on the collapse mechanism of RC frames under different loads. K. Khandelwal and Tawil (2005) introduced multi-scale finite element models into the simulation of progressive collapse of an eight-story steel frame under blast loads. In this multi-scale method, micro scale models are validated by experimental results, macro scale models by micro scale models and structural scale models by macro scale models. This method allows researchers to accurately and economically study the potential for progressive collapse in steel building frames. Isobe and Tsuda (2003) applied a new finite element code using Adaptively Shifted Integration (ASI) technique with a linear Timoshenko beam element to the seismic collapse analysis of RC framed structures. In the beam element, the fracture of a section was simulated by shifting the numerical integration point with simultaneous release of the resultant forces. As to non-continuum mechanics method, Qin et al. (2001) and Sun et al. (2002) proposed a particle-truss model for collapse analysis of the RC bridge and the reinforcement concrete is modelled as particles connected with nonlinear springs. The model had a good simulation of failure behaviour after collapse. Xuan et al. (2003) and Wang

and Lü (2004) put forward a discrete element model for collapse simulation of RC frame with shear-type deformation. In this model, every floor is a rigid body without rotation displacement and the adjacent stories are connected with an axial spring and a shear spring. Zhao (2008) proposed 2-D DEM model for collapse of RC frame and the frame was discretized into rectangular elements. Miao et al. (2005) employed discrete element method (DEM) to simulate the collapse process of a three-dimension masonry structures under earthquakes. The model was made up of block elements connected with springs in both transverse and longitudinal directions and the numerical results are close to those of the shaking table test. Cui et al. (2002) employed 3-D rigid body-spring element method to simulate the collapse process of Malpasset Arch Dam.

Finite element method (FEM) appear good performance in simulating structural behaviour before collapse, but has difficulties in dealing with the behaviours in the process of progressive collapse, such as fracture of components, impact and stack load of fragments. Yet non-continuum mechanics method is much more competent in simulates the behaviour after collapse. If these two kinds of methods can work together and take their own advantages, the simulation will be largely improved. According to this point, Munjiza and Bangash (2004) proposed a combined finite-discrete element model and it produced good numerical results for structures made up of RC column or column type members, though it failed to take account of slabs and non-structural components. In the paper, coupled finite element-discrete element method for progressive collapse of RC buildings was proposed and its technique details are given. The simulation results show that this new method not only keeps the advantages of FEM but also gives a good simulation on impact and stacking of fragments.

## **2 Finite Element Models for Collapse**

Structural components of RC buildings mainly consist of beam, column, wall and floor slab. To obtain a more accurate result, fiber beam element model (Wang et al., 2007) is proposed for beam and column, and multi-layer shell element model (Men and Lu, 2006) for wall and slab, detailed illustration can be found in Lu et al. (2008).

## **3 Discrete Element Model for Collapse**

Discrete element method (DEM) is used to study assemblies of distinct interacting particles or general shaped bodies. One of the common models is constructed with spherical particles which are particularly called as granular discrete element. Granular discrete element method (GDEM) not only possesses the basic motion

features of non-continuum, but also has a simple contact algorithm. The coupled finite element-discrete element method uses granular discrete elements to simulate the fragments in the collapse of structures. On one hand, the size of finite element is very small compared to the structural members and the discrete elements are generated from the further discretization of finite elements, so the effect of the shape of discrete elements on the collapse process is quite small. On the other hand, the main concern on this collapse model is the effects of impact and stack load in the collapse process.

### 3.1 Generation of Granular Discrete Element

Once a four-node quad finite element is deactivated (removed from the model), nine granular discrete elements will be generated instead of this quad element, shown as Figure 1. The generation process keeps the equivalent total mass and volume and the initial motion states of every discrete element, such as coordinates, velocities and accelerations are obtained with linear interpolation based on the four nodes of the deactivated finite element.

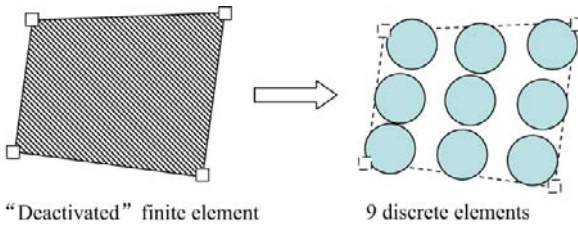


Figure 1 The “deactivated” element is replaced with 9 discrete elements

### 3.2 Motion Law of Granular Discrete Element

The sphere element can be regarded as a particle when moving, the motion equation at the moment  $t_i$  is

$$m\ddot{u}(t_i) + \eta\dot{u}(t_i) = p(t_i) \tag{1}$$

where  $m$  is mass of the discrete element,  $\mathbf{p}$  is vector of external forces at  $t_i$ ,  $\mathbf{u}$  is displacement vector at  $t_i$ ,  $\eta$  is damping coefficient.

Central difference method is applied to compute the motion state. If the time step is constant, that is  $\Delta t_i = \Delta t$ , we get

$$\dot{u}_i = (u_{i+1} - u_{i-1}) / (2\Delta t) \quad (2)$$

$$\ddot{u}_i = (u_{i+1} - 2u_i + u_{i-1}) / \Delta t^2 \quad (3)$$

By substitution of Equation (2) and Equation (3) into Equation (1), we obtain

$$\left(\frac{m}{\Delta t^2} + \frac{c}{2\Delta t}\right)u_{i+1} = p(t_i) + \frac{2m}{\Delta t^2}u_i - \left(\frac{m}{\Delta t^2} - \frac{c}{2\Delta t}\right)u_{i-1} \quad (4)$$

Then displacement, velocity and acceleration of a discrete element at every moment can be calculated through Equation (2), Equation (3) and Equation (4).

### 3.3 Contact Judgment

Contact between two discrete elements happens if the distance between their spherical centers is no larger than the total length of their radiuses. The contact criterion (Wei et al., 2008) for element  $i$  and element  $j$  is

$$(r_i + r_j) \times CNC \geq R_{ij} \quad (5)$$

$$R_{ij} = \sqrt{(x_i - x_j)^2 + (y_i - y_j)^2 + (z_i - z_j)^2} \quad (6)$$

where  $r_i$ ,  $r_j$  are radiuses of element  $i$  and element  $j$  respectively,  $R_{ij}$  is the distance between the spherical centers of element  $i$  and element  $j$ ,  $CNC$  is a coefficient relevant to the medium where elements soak, usually  $CNC \geq 1.0$  and  $CNC = 1.0$  in this paper.

To simulate the impact of fragments to structures, contact between discrete element and finite element needs to be accomplished. The finite element is simplified as 9 spheres with the similar process in Section 3.1 and thus, the contact between discrete element and finite element is transformed into that between two discrete elements.

## 4 Program Implementation and Example

Coupled finite element-discrete element method was implemented through secondary development of commercial finite element software MSC.MARC 2005 and the details are as follows:

(a) Deactivation of finite elements and generation of discrete elements.

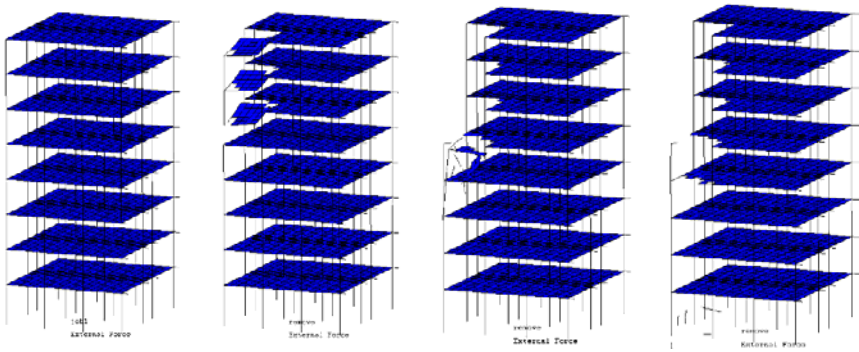
When a finite element is damaged, it will be deactivated (removed) by a user subroutine called UACTIVE. This process is controlled by the deactivating criteria (Lu et al. 2008). Once the deformation of a finite element is too large, the element will be removed and the critical deformation can be determined in terms of maximum strain. The criteria defined in present work is the same as those in Lu et al. (2008) and other criteria can also be defined by UACTIVE.

The deactivated element is transformed into nine discrete elements as mentioned in Section 3.1. The program gives the initial condition of discrete elements and record the motion state, mass and volume in the whole process.

(b) Contact.

During collapse, impact and stack load of fragments have a significant effect on the stories below, so contact should be taken into account. There are three types of contact, contact between finite elements, contact between discrete elements and contact between finite elements and discrete elements. The first type of contact can be directly set in finite element software MSC.MARC and the second and third can be defined by user subroutine UBGITR. UBGITR will be called at the beginning of each iteration.

(c) Effect of impact and stack loads.



(a) t=0.0s

(b) t=1.0s

(c) t=2.0s

(d) t=3.0s

Figure 2 Collapse procedure simulated with finite element method (FEM)

When the discrete elements collide with finite element structure, contact happens and user subroutine FORCDT will exert contact forces to the nodes of relevant finite elements.

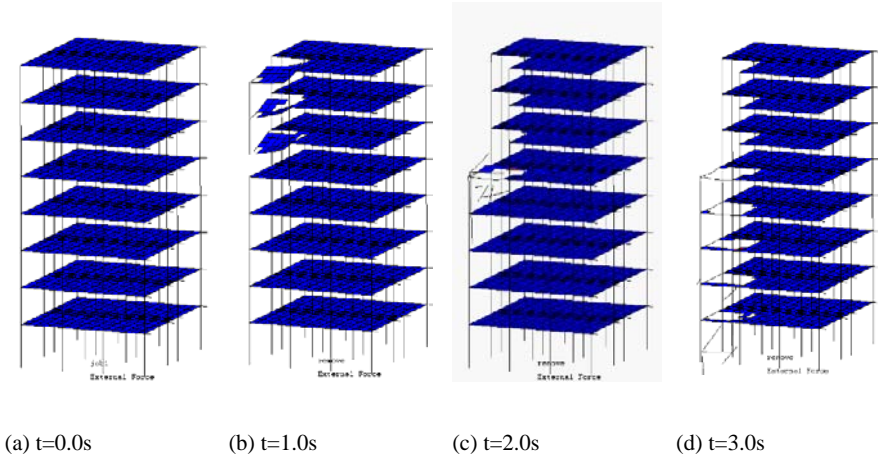


Figure 3 Collapse procedure simulated with coupled Finite element-discrete element method

A numerical example of an eight-story frame is carried out to observe the effect of coupled finite element-discrete element method. Columns and beams are modeled with fiber beam element model and slabs with multi-layer shell element model. Progressive collapse occurred after the corner column of the fifth story was removed. Two methods were applied to simulate collapse, one is FEM and the other is coupled finite element-discrete element method. The results from FEM are listed in Figure 2 and those from coupled finite element-discrete element method (F/DEM) are listed in Figure 3. It is noted that discrete elements can not be seen in Figure 11 because the program hasn't support this function. At the beginning of collapse (before  $t=2.0s$ ), structural response of FEM is similar to that of F/DEM. When  $t=1.0s$ , the slabs above the removed column break from the slabs around and drop off. When  $t=2.0s$ , the fallen slabs crash through the fifth floor. However, these two methods appear distinct results at  $3.0s$ . With FEM, the progressive collapse is stopped after the fourth floor slabs drop. With F/DEM, all the floor slabs below the removed column are smashed. It is shown that the model based on F/DEM shows a better simulation on impact and stack load in the process of progressive collapse than that based on FEM.

## 5 Conclusions

Numerical simulation is an important tool to study progressive collapse. Collapse of structure is a complicated process from continuum into discrete bodies, which put forward requirements for the numerical model. The model should not only simulate the nonlinear behaviors before collapse, but also simulate impact and stack load of fragments during the collapse. Finite element method has advantages in simulating continuum while discrete element method in simulating the non-continuous behaviors after collapse starts. Coupled finite element-discrete element method (F/DEM) is proposed and implemented based on existing finite element software. Keeping the advantages of FEM, the method applies DEM to simulate the fragments in collapse. The numerical results show that this coupled FEM-DEM method has a better simulation on impact and stack load in progressive collapse than FEM.

## Acknowledgements

This research is supported by National Science Foundation of China (No. 50808106 & 90815025).

## References

- Cui Y.ZH. and Zhang CH.H., et al. (2002). Numerical modeling of dam-foundation failure and simulation of arch dam collapse. *Shuili Xuebao*, 6:1-8 [in Chinese].
- Isobe D. and Tsuda M. (2003). Seismic collapse analysis of reinforced concrete framed structures using the finite element method. *Earthquake Engineering and Structural Dynamics*, 32: 2027-2046.
- Khandelwal K. and El-Tawil S. (2005). Multiscale computational simulation of progressive collapse of steel frames. *Proceedings of the ASCE Structures Congress*, May 2005.
- Liu J.B., Liu Y.B. and Yang J.G. (2007). Simulation of earthquake ruins structure for the Earthquake Rescue Training Base of China. *Journal of Disaster Prevention and Mitigation Engineering*, 27(suppl.): 428-432 [in Chinese].
- Lu X.ZH. and Jiang J.J. (2001). Dynamic finite element simulation for the collapse of World Trade Center. *China Civil Engineering Journal*, 34(6): 8-11 [in Chinese].
- Lu X.ZH. and Lin X.CH. (2008). Numerical Simulation for the progressive collapse of concrete building due to earthquake. *The 14th World Conference on Earthquake Engineering*, October 12-17, 2008, Beijing, China.
- Lu X.ZH., Zhang Y.SH. and Jiang J.J. (2007). Simulation for the collapse of reinforced concrete frame by blasting based on fiber model. *Blasting*, 24(2): 1-6 [in Chinese].
- Men J. and Lu X.ZH. (2006). Application of multi-layer model in shell wall computation. *Protective Structure* 28:3, 9-13 [in Chinese].

- Miao J.J. and Gu X.L. (2005). Numerical simulation analysis for the collapse response of masonry structures under earthquakes. *China Civil Engineering Journal*, 38(9), 45-52 [in Chinese].
- Miao ZH.W. and Lu X.ZH. (2007). Simulation for the collapse of RC frame tall buildings under earthquake disaster. *Computational Mechanics*, Proceedings of ISCM 2007, July 30 August 1, Beijing, China.
- Munjiza A., Bangash T. and John N.W.M. (2004). The combined finite-discrete element method for structural failure and collapse. *Engineering Fracture Mechanics*, 469-483.
- Qin D. and Fan L.CH. (2001). Numerical simulation on collapse process of reinforced concrete structures. *Journal of Tongji University*, 29(1): 80-83 [in Chinese].
- Shi Y.CH., Li ZH.X. and He H. (2007). Numerical analysis of progressive collapse of reinforced concrete under blast loading. *Journal of PLA University of Science and Technology*, 18(6): 652-658 [in Chinese].
- Sun L.M., Qin D. and Fan L.CH. (2002). A new model for collapse analysis of reinforced concrete. *China Civil Engineering Journal*, 35(6): 53-58 [in Chinese].
- Wang Q. and Lü X.L. (2004). Application of the DEM to the seismic response analysis of frame structures. *Earthquake Engineering and Engineering Vibration*, 24(5): 73-78 [in Chinese].
- Wang X.L., Lu X.ZH. and Ye L.P. (2007). Numerical Simulation for the Hysteresis Behavior of RC Columns under Cyclic Loads. *Engineering Mechanics*, 24(12):76-81 [in Chinese].
- Wei L.H. and Chen CH.G. (2008). Study on three-dimensional discrete element and parameter adoption. *Journal of Chongqing Jiaotong University (Natural Science)*, 27(4): 618-621, 629.
- Xuan G., Gu X.L. and Lü X.L. (2003). Numerical analysis of collapse process for RC frame structures subjected to strong earthquakes. *Earthquake Engineering and Engineering Vibration*, 23(6): 24-30 [in Chinese].
- Zhao F.L. (2008). Simulation analysis for collapse of reinforced concrete frame structures under earthquake based on the discrete element method. Master thesis of Tongji University, Shanghai [in Chinese].

*“This page left intentionally blank.”*

# Tunnel Stability against Uplift Single Fluid Grout

Fangqin Yang<sup>1\*</sup>, Jiayang Lin<sup>3</sup>, Yong Yuan<sup>2</sup> and Chunlong Yu<sup>1</sup>

<sup>1</sup>Department of Geotechnical Engineering, Tongji University, Shanghai 200092, P.R. China

<sup>2</sup>Key Laboratory of Geotechnical and Underground Engineering of Ministry of Education, Tongji University, Shanghai 200092, P.R. China

<sup>3</sup>Shanghai Tunnel Engineering Co. Ltd, Shanghai 200082, P. R. China

**Abstract.** During shield tunnelling, as segments are cleared off by the shield, annular void occurs between shield tail inner side and lining outer side. The void must be back-filled with grout subsidence to ensure compacted filling, the grout subsidence caused the tunnel uplift. This paper studies the relationship between early strength of grout subsidence and tunnel stability upon shield tunneling. Influence of the rate of tunneling on tunnel stability against uplift is also studied. A longitudinal and transverse calculation model is established to investigate tunnel uplift, which results in grout strength increase. In analysis, safety criteria of structural lining are verified. Finally, relevant construction technological measures are suggested against tunnel uplift for shield tunneling.

**Keywords:** shield tunnelling, tunnel stability, uplift, calculation model

## 1 Introduction

Uplift during shield tunnelling is caused by transversal and longitudinal actions mutually. The uplift magnitude is related to the overburden in addition to tunnel's own weight. During shield tunnelling, annular void occurs around and between shield tail inner side and lining outer side. The void must be back-filled with injected grout to ensure compacted filling and to minimize tunnel uplift or surface subsidence, which is caused by ground settlement around the annulus. In order to ensure full filling of the annulus, good working performances is required for the grout subsidence, such as pumpability, flowability, and early strength. Otherwise, Flow ability grout subsidence which is the fluid substances in early time. Caused greater uplift magnitude and, the lining and bolt would be safe against uplift too.

---

\* Corresponding author, e-mail: fangqin.yang@163.com

Firstly, the following theoretical analysis of uplift during shield tunnelling is advanced in this paper: Influence on compression strength of simultaneous grout injection is studied, then through formula, it can be found that the rate of tunnelling is very important on Tunnel Stability against Uplift. Secondly, Calculation model in tunnel longitudinal and transverse direction are put forward. The above theory is applied with a Project against Uplift of Tunnel during Tunnelling.

## **2 Theoretical Analysis of Uplift during Shield Tunnelling**

### ***2.1 Influences on Compression Strength of Simultaneous Grout Injection***

If compression strength (some day) of a single grout subsidence is greater than the confined compression strength of ground. It is therefore to be believed that some day after segments cleared off by shield tail, uplift acting upon tunnel by the grout has become relatively smaller, i.e. tunnel tends to be more stable.

### ***2.2 Influence of the Rate of Tunnelling on Tunnel Stability against Uplift***

Setting shield tunnelling rate at  $V$ , after time  $T$ , grout reaches strength as that of ground, following grout strength variation. Also uplift  $q$  on tunnel varies ( $q$  is shown in Figure 2). Therefore, at the location  $L = V * T$  from shield tail, uplift on tunnel is a function of time  $F(t)$ . Starting from area of shield tail, the resultant uplift  $Q$  is calculated as:

$$Q = \int_0^L q dl = V^2 \int_0^T F(t) dt \quad (1)$$

From Equation (1), it can be seen that uplift on tunnel is proportional to the square of rate of shield tunnelling. Therefore, it is necessary to stringently control the rate of shield tunnelling to effectively lower uplift on tunnel.

### ***2.3 Analysis on Safety against Uplift during Tunnelling***

Uplift during shield tunnelling is caused by transversal and longitudinal actions mutually.

### 2.3.1 Calculation in Tunnel Longitudinal Direction

A numerical analysis has been conducted for tunnel in longitudinal direction during shield tunnelling. Once elastic foundation beam has been taken for treatment, given the compression modulus of ground mass, then compression module at various ages of grout could be deduced by utilization of various strengths at differing ages of grout. Hence equivalent spring coefficients (JSCE 1996) for ground mass and grout subsidence could be calculated. Referring to Figure 1, uplift force which is acting on rings is obtained for a uplift test on structure of a model ring (Lin et al, 2008).

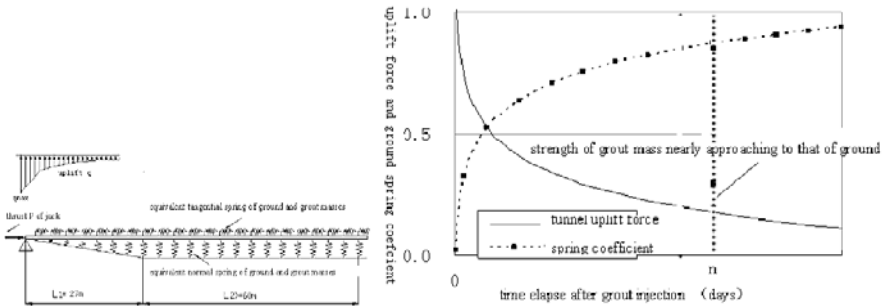


Figure 1. Longitudinal modeling Figure 2. Relation between uplift and strengthen of subsidence

In analysis, uplift force and spring coefficient composed of ground mass and grout mass are assumed as shown in Figure 2. At the moment segments cleared off by shield tail, the maximum uplift is the weight of grout so displaced by the same volume of tunnel. By that time spring coefficient is zero. Based on analysis mentioned above, grout strength (some day after) is quite approaching that of surrounding ground.

### 2.3.2 Calculation in Tunnel Transverse Direction

As shown in Figure 3, upon segment cleared off by shield tail, between the ring just cleared off by shield tail, and the ones still remaining in contact with shield tail, may appear a more significant shear force  $Q$  which magnitude is to be determined by uplift on tunnel. The force necessary to overcome this shear  $Q$  would be the amount of frictions  $F$  caused by the resultant of thrusts from hydraulic jacks plus shear resisting force  $S$  of longitudinal bolts. When  $F+S \geq Q$ , the safety requirement of tunnel is met (Lin et al, 2008).

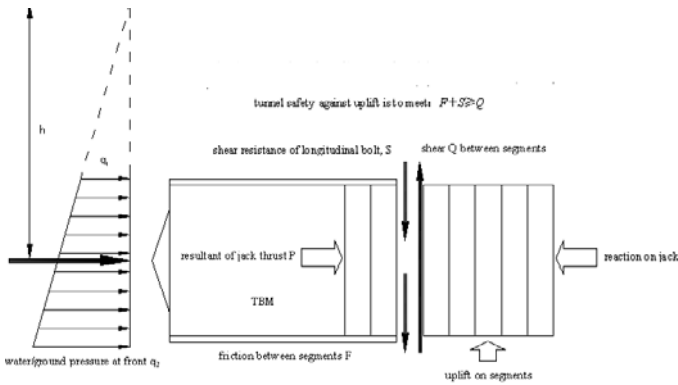


Figure 3. Loading schematics on segments as they are cleared off by shield tail.

From Figure 3, the resultant of hydraulic jacks  $P = (q_1 + q_2) / 2 \times h \times A = \gamma h A$ ; whereby friction of jacks  $F = \mu k_0 P$ , resultant shear resistant force by longitudinal bolts  $S$ , shear  $Q$  between segments produced by tunnel uplift are to be calculated by means of longitudinal float resistance of tunnel. Actual uplift produced is  $N = Q - F$ . If  $N \leq S$ , tunnel is safe for uplift resistant. If  $N \geq S$ , tunnel falls short of uplift resistance pending structural measures to be taken. From the formula,  $\gamma$  is average specific weight of ground in front of shield;  $A$  is the area to be excavated by shield;  $k_0$  is coefficient of lateral ground pressure;  $\mu$  is the friction coefficient between segments.

### 3 Project Application against Uplift of Tunnel during Tunnelling

#### 3.1 Project Introduction

Tunnel A is bored by shield tunnelling which is through ground with the minimum overburden of 7.23m near launching shaft. The tunnel section has inner diameter of 5.84m and outer diameter of 6.8m with tapered RC segmental ring composed of 6 segments of 1.5m wide and staggered joints.

### 3.2 Analysis of Influence on Compression Strength of Simultaneous Grout Injection

The compression strength (3 day) of a single grout subsidence has reached 59kPa, basically greater than the confined compression strength of ground in shallow cover section (the strength of ground is 50kPa). It is therefore to be believed that 3d after segments cleared off by shield tail; uplift acting upon tunnel by the grout has become relatively smaller.

### 3.3 Verification in Tunnel Longitudinal Direction

The data for calculation are longitudinal curved bolts M30, Grade 5.8 ( $\alpha=30^\circ$ ) 16pcs. For longitudinal rigidity, based on “Structure Design Code of Japan Railway”, equivalent rigidity (EA)eq, (EI)eq for tunnel longitudinal can be calculated.

Figure 4 shows simulated calculation results for tunnel longitudinal at the time of tunnelling rate of 6ring/d. As shown in the figure, the maximum uplift force loaded on segments by grout, upon segments cleared off by shield tail is 2248kN, then following shield tunnelling forward, grout strength surrounding the segments gains with less uplift loaded on segments, to reach that of ground mass strength after 3d or uplift on tunnel tending to zero.

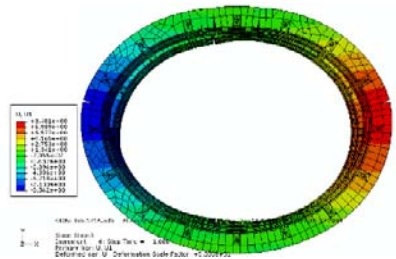
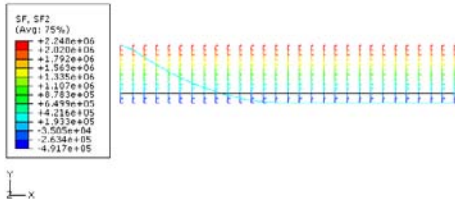


Figure 4. results in longitudinal direction.

Figure 5. Staggering between segmental rings.

The verification results indicate that near at shield break-out section, only when advance rate is controlled below 6ring/d, segments could meet uplift resistance requirement. When its uplift force over shear strength of longitudinal bolts as tested on segments is equal to 2.54 (as its safety coefficient).

### ***3.4 Verification in Tunnel Transverse Direction***

For transversal calculation modelling, two full rings 3-d solid tunnel calculation modelling is taken. Via transversal numerical calculation, segment deformation under action of uplift is obtained to verify fissure width of segment structure, deformation of segment joint and staggering between segments (see Figure 5).

From calculation results on converged deformation, it is then known that given shield advance at a rate of 6ring/d, the maximum shear force produced between rings caused by tunnel uplift is 2248kN. By when max converged deformation is 16.9mm, basically controlled within 3‰D allowance. Whereas the maximum Mises stress of the bolt is 162MPa, basically controlled within an allowance of 480MPa as design criteria. The maximum deformation at joints as calculated is 1.07mm against design tolerance 4.0mm, meeting design requirement for deformation of joints, The maximum staggering between segmental rings is 2.4mm which is less than the allowed value of 5.5mm as stated in “A Full Ring Lining Structural Test for Changjiang Tunnel in Shanghai Under Tunnel Uplift Regime” (Yang et al, 2007). Therefore it is believed that the tunnel is safe.

## **4 Conclusions**

Overburden near at shield break-out section of the Tunnel A is about 7.23m. Given shield advance is controlled below 6ring/d, segment seam width can meet design requirement within allowance, i.e. 2.54 safety coefficient against tunnel uplift.

Therefore, uplift of tunnel must be paying a high degree of attention, and take effective measures in construction technology and construction requirements, in order to ensure quality works. Control of tunnel construction technology uplift measures and structural requirements are as follows:

1. Simultaneous grouting age 3 days yield strength must be met 0.059Mpa; and in accordance with the actual situation, as far as possible to improve the early strength grout.
2. Encountering other special conditions during the construction will need to make other tunnel structure checked.

Shield across the shallow soil, it is recommended to control the construction speed to 10ring/d below the convergence of tunnel deformation, if the deformation is too large (more than allowed value), it is proposed to set the construction speed to 6ring/d.

## Acknowledgements

The authors wish to acknowledge the financial support from Hi-tech Research and Development Program (863 Program) of China (No. 2006AA11Z118) and Technology Center of STEC for test data.

## References

- Lin J.X., Yang F.Q., Shang T.P. and Xie B. (2008). Study on tunnel stability against uplift of super-large diameter shield tunnelling, *The Shanghai Yangtze River tunnel, theory, design and construction*: 267-274. Shanghai: Talor & Francis.
- Lin J.X., Duan C.F., Zhao Y.P. and Xie B. (2008). Study of new mortar anti-floating model experiment of tunnel, *Urban Roads Bridges & Flood Control*, 8(8): 157-160.
- Yang G.X., Lin J.X. & Yang F.Q. (2007). Study on safeness of lining structure during super large diameter shield tunneling. *Underground Construction and Risk Prevention – Proceedings of the 3rd International Symposium on Tunneling*. Shanghai, Tongji University Press: 597-606.

*“This page left intentionally blank.”*

# Effects of Concentrated Initial Stresses on Global Buckling of Plates

A.Y.T. Leung<sup>1</sup> and Jie Fan<sup>1\*</sup>

<sup>1</sup>Department of Building and Construction, City University, Hong Kong

**Abstract.** Buckling is an instability phenomenon that can occur if a slender and thin-walled plate – plane or curved – is subjected to axial pressure (e.g. inplane compression). At a certain given critical load the plate will buckle very sudden in the out-of-plane transverse direction. The destabilizing force could come from pure axial compression, bending moment, shear or local concentrated loads, or by a combination of these. If the structural element is bulky, the load-carrying capacity is governed by the yield stress of the material, rather than the buckling strength. If instead the element is slender and/ or thin-walled, the buckling strength is governed by the so-called slenderness ratio – the buckling length over the radius of gyration for global buckling of a column or a strut, or the loaded width over the thickness of the plate for local buckling. A special form of instability, that has to be considered with great care in design, is the combined global and local buckling risk of a slender and thin-walled axially loaded plated column – the capacity could be much lower than the two buckling effects analyzed separately. Conventionally, averaged initial stresses due to compression or shear are considered in a plate buckling analysis. Unfortunately, the analytical solutions of initial stresses for a cantilever square plate subject to uniform compression that the initial stresses concentrated at corners and cannot be considered uniform at all. The paper will report on the effects of concentrated initial stress on the global buckling of plates.

**Keywords:** global buckling, concentrated initial stresses, cantilever plates, skew plates, trapezoidal plates

## 1 Introduction

The elastic buckling of rectangular plates or skew plates have been widely considered by Kitipornchai et al (1993). Conventionally, averaged initial stresses due to compression or shear are considered in a plate buckling analysis. However, the distributed initial stresses when the plate is subjected to uniform compressive

---

\* Corresponding author, e-mail: jiefan@student.cityu.edu.hk

loads or shear stresses on the edges are not necessarily uniform as assumed. The initial stress concentration is very considerable and may have great influence on the buckling of the plates. Moreover, trapezoidal shaped plates are used in many structural applications such as aircraft wings. Due to the complexity of the trapezoidal shapes, studies focused on trapezoidal plates are seldom investigated. The stresses in the internal of the trapezoid considered by Kelvin (1956), Saadatpour et al (1998) and Herdi et al (2000) are cursorily assumed to vary linearly along with the height of the trapezoid, which are very different from what actually happen. In fact, the concentration at the corners for the clamped trapezoidal plates is much greater when compared with rectangular plates.

In this paper, the initial stresses buckling of clamped rectangular plates are obtained by ANSYS. The results of rectangular plates are compared with buckling results that the initial stresses are considered to be uniform. New results of buckling loads for trapezoidal plates clamped on one parallel side will be compared with those given by p-element (Leung and Fan, 2008).

## 2 Methodology

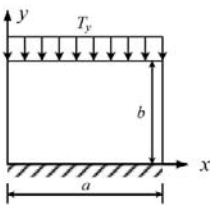
In this paper, the critical buckling load of a flat plate by eigenvalue buckling analysis will be studied by ANSYS. Eigenvalue buckling analysis predicts the theoretical buckling strength of an ideal linear elastic structure. Eigenvalue buckling analysis in ANSYS has four steps: 1) Build the model; 2) Obtain the static solution, that is, obtain the initial stress distribution in the plates; 3) Obtain and expand the eigenvalue buckling solution, i.e. obtain the buckling loads and buckling mode shapes of the plates; 4) Interpret the results. Since the plate will develop out-of-plane displacements, a shell element type, named 'Elastic 8node 93' in ANSYS, is chosen for the eigenvalue buckling of the plates. 2821 nodes and 900 elements are used in the ANSYS analysis.

## 3 Numerical Examples

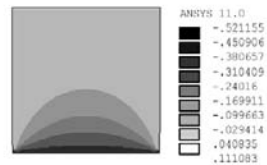
Buckling problems of rectangular plates, skew plates and trapezoidal plates with one side clamped and the other three sides free will be considered. Two types of uniaxial compressive loads on different sides are studied: 1) act on the two sides normal to the clamped side; 2) act on the side parallel to the clamped side. The aspect ratio  $a$ ,  $b$ ,  $c$  and inclination angle  $\alpha$ ,  $\theta$  for plates with different shapes are shown in Figure 1 (a) – 6 (a) respectively. The geometric parameters for the plates are: for the rectangular plate,  $a=b=10$ ; for the skew plate,  $a=b=10$  and  $\alpha=45^\circ$  and for the trapezoidal plate,  $a=30$ ,  $b=c=10$  and  $\theta=45^\circ$ . The thickness  $t$  of the plates is chosen as 1. The buckling load intensity factors for a plate under uniaxial com-

pression is defined as  $K_b = T_x(b_f)^2 / (\pi^2 D)$ , where  $D = Et^3 / [12(1 - \nu^2)]$ , the material properties are 200Gpa for Young's modulus  $E$  and 0.3 for Poisson's ratio  $\nu$ , and  $b_f$  is the average loading length. Two loading cases for each of the three types of plates, rectangle, skew and trapezoidal, are investigated. 1) For a rectangular plate under loading case 1,  $b_f = a$ ; and under loading case 2,  $b_f = b$ . 2) For a skew plate under loading case 1,  $b_f = a$ ; and under loading case 2,  $b_f = b$ . 3) For a trapezoidal plate under loading case 1,  $b_f = (a+c)/2$ ; and under loading case 2,  $b_f = b$ .

Buckling loads for the rectangular plates, skew plates and trapezoidal plates are considered in this Section. The initial distribution of the normal stress  $\sigma_{xx}$ ,  $\sigma_{yy}$  and shear stress  $\sigma_{xy}$  are shown in the corresponding figures. Buckling intensity factors comparison with results of p-element (Leung and Fan, 2008) for the three types of plates are given in Table 1. In Table 1, the results of p-elements considering that the loading are uniform for all the cases besides of a trapezoidal plate under loading case 1, but assuming that the loading varies linearly along with the height of the trapezoid. It is shown in Table 1 that the results of rectangular plate, skew plate (under loading case 2), trapezoidal plate (under loading case 2) obtained by ANSYS are very close to those by p-elements. It suggests that the initial normal stress concentration when under loading case 2 have little influence on the buckling results. While for a trapezoidal plate, the result under loading case 1 is 0.37818, which is larger than the result of p-elements 0.33924. It means the buckling capacity is underestimated when assuming initial stress varying linearly along the height of the trapezoid. Moreover, for a skew plate under loading case 1 (as shown in Figure 3), since the high stresses concentration on the right-bottom corner of the plate, great relative error reaching to 27.87% is produced. The great difference of the buckling results given by ANSYS and p-elements shows that the initial stresses concentration caused by loading case 1 has a great effect on the buckling loads of skew plates and trapezoidal plates. Meanwhile, for a rectangular plate, though the maximum stress of case 2 (1.37, as shown in Figure 2 (b)) is less than that of case 1 (1.994, as shown in Figure 1 (c)), the relative errors of the buckling loads with results of p-elements under loading case 2 (0.87%) is larger than the error under loading case 1 (0.03%). This phenomenon maybe caused by the size of the covering area of the stress concentration and hence the internal energy. The cover area of high normal stress  $\sigma_{xx}$  for case 2 is much larger than the area for high normal stress  $\sigma_{yy}$  of case 1.



(a) Loading case 1



(b) Normal stress  $\sigma_{xx}$

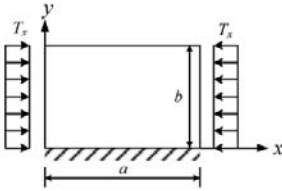


(c) Normal stress  $\sigma_{yy}$

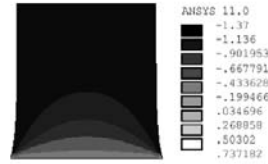


(d) Shear stress  $\sigma_{xy}$

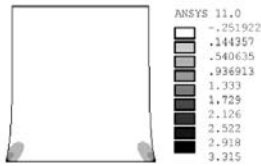
Figure 1. Stress distribution for a square plate under loading case 1



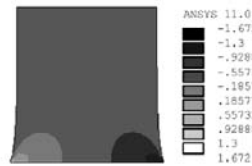
(a) Loading case 2



(b) Normal stress  $\sigma_{xx}$

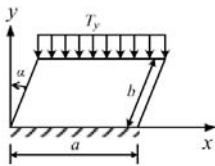


(c) Normal stress  $\sigma_{yy}$

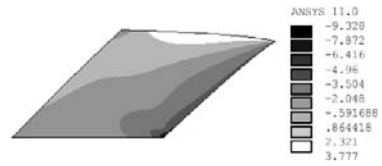


(d) Shear stress  $\sigma_{xy}$

Figure 2. Stress distribution for a square plate under loading case 2



(a) Loading case 1



(b) Normal stress  $\sigma_{xx}$



(c) Normal stress  $\sigma_{yy}$



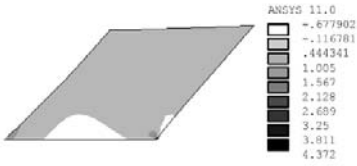
(d) Shear stress  $\sigma_{xy}$

Figure 3. Stress distribution for a skew plate under loading case 1



(a) Loading case 2

(b) Normal stress  $\sigma_{xx}$



(c) Normal stress  $\sigma_{yy}$

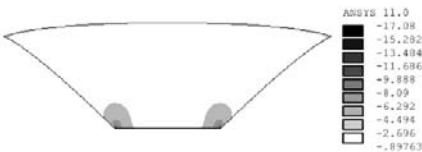
(d) Shear stress  $\sigma_{xy}$

Figure 4. Stress distribution for a skew plate under loading case 2



(a) Loading case 1

(b) Normal stress  $\sigma_{xx}$



(c) Normal stress  $\sigma_{yy}$

(d) Shear stress  $\sigma_{xy}$

Figure 5. Stress distribution for a trapezoidal plate under loading case 1



(a) Loading case 2

(b) Normal stress  $\sigma_{xx}$

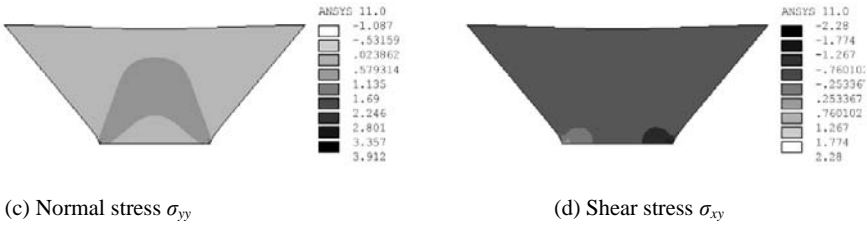


Figure 6. Stress distribution for a trapezoidal plate under loading case 2

Table 1. Buckling load intensity factors for rectangular plates, skew plates and trapezoidal plates

	Loading case 1			Loading case 2		
	Present	P-element	Relative Error	Present	P-element	Relative Error
Rectangular plate	0.23752	0.23747	0.03%	0.54807	0.55284	0.87%
Skew plate	0.23620	0.32742	27.87%	0.45057	0.45150	0.21%
Trapezoidal plate	0.37818	0.33924	11.48%	0.22320	0.22435	0.52%

### 4 Conclusions

The initial stresses buckling of cantilevered rectangular plates, skew plates and trapezoidal plates are studied by ANSYS, and compared with the results of p-elements. The results of the three types of plates under loading case 2 agree well with those assuming uniform initial stresses. Buckling loads of skew plates and trapezoidal plates under loading case 1 have a great different from the results assuming uniform initial stress for skew plates and varying linearly along the height for the trapezoidal plates, and further study should be undertaken.

### Acknowledgement

The research is supported by SGR #7002120 of City University of Hong Kong.

### References

Herdı M., Tutuncu N. (2000). A parametric stability analysis of composite plates tapered in planform. *Journal of Strain Analysis*, 35, 59-64.  
 Kitipornchai S., Xiang Y. (1993). Buckling of thick skew plates. *International Journal for Numerical Methods in Engineering*, 36, 1299-1310.

- Klein B. (1956). Buckling of simply supported plates tapered in planform. *Journal of Applied Mechanics*, 23, 207-213.
- Leung A.Y.T., Fan J. (2008). Buckling problems of Mindlin plates by analytical quadrilateral p-elements. *Proceeding of the 8<sup>th</sup> World Congress on Computational Mechanics*, Venice, Italy.
- Saadatpour M.M., Azhari M. and Bradford M.A. (1998). Buckling of arbitrary quadrilateral plates with intermediate supports using the Galerkin method. *Computer Methods in Applied Mechanics and Engineering*, 164, 297-306.

*“This page left intentionally blank.”*

# Application of a Thin-Walled Structure Theory in Dynamic Stability of Steel Radial Gates

Zhiguo Niu<sup>1\*</sup> and Shaowei Hu<sup>1</sup>

<sup>1</sup>Department of Materials and Structural Engineering, Nanjing Hydraulic Research Institute, Nanjing 210024, P.R. China

**Abstract.** With the increasing shortage of water resources in the whole earth, many diversion projects have been constructed to make a better use of water resources in many water-shorting places and the radial gates are need to operate partly for adjustment of discharge in these projects. However, the low head steel gate accident emerges increasingly one after another, due to the instability of radial gate arms under dynamic loading action. In this article, the space frame composed of main cross beams, vehicle beams, arms and some other components is taken as one analytical model, based on the perturbation method and thin-walled structure theory, the dynamic instability region can be calculated by the finite element method. Finally, the method is validated by a comparison with existing project data.

**Keywords:** hydraulic structure, thin-walled structure, radial gate, dynamic stability

## 1 Introduction

The radial gate is one kind of the most widely applied steel gates in hydraulic engineering. But a lot of engineering projects show that radial gates have vibration of different degree caused by water flow action during gate operation in dynamic water or gate partial opening. Under some special working conditions, the vibration of radial gate is so serious that the dynamic instability of arms may happen. Therefore, the dynamic stability problems of radial gates have been being the important problems that should be solved in the design and practical operation of radial gates. Based on the radial gates' characteristics of structural and acting forces, research work of steel radial gates is focused on the dynamic instability of arms. In 1980s, Professor Yan Shiwu, Professor Zhang Jiguang recognized parametric vibration was one of reasons caused dynamic instability of arms and presented a

---

\* Corresponding author, e-mail: niuzhiguo@yahoo.cn

simple analytical method, in recent years, a series of investigations have been widely seen in some literatures.

This paper presents a computational method which is used to analyze the dynamic instability of radial gates. By Thin-walled Structure Theory, a new method combining with the physical and numerical model to predict the dynamic stability of radial gates' arms is described in detail.

## 2 The Elastomer Perturbation Equation

The structure is likely to subject to be dynamic instability because of axially periodic force when the structure is acted on by vibration load. Equation (1) is applied in analyzing dynamic stability of structure.

$$[M] \cdot \{\ddot{Y}\} + [ [K] - [K_{gs}] - [K_{gt}] \sin(\theta t) ] \cdot \{Y\} = \{0\} \tag{1}$$

If the structure is damped, the equation can be written as:

$$[M] \cdot \{\ddot{Y}\} + [C] \cdot \{\dot{Y}\} + [ [K] - [K_{gs}] - [K_{gt}] \sin(\theta t) ] \cdot \{Y\} = \{0\} \tag{2}$$

The term of damping is added in Equation (2), where  $[C]$  is the damping matrix.  $[M]$  is the mass matrix and  $[K]$  is the elastic stiffness matrix of the structure respectively;  $[K_{gs}]$  and  $[K_{gt}]$  are the static and time dependent components of the geometric stiffness matrices; and  $\theta$  is the frequency of the vibration load. This equation is a governing equation for parameter vibration. To solve the Equation and to analyze the dynamic stability of the structure is more complicated than to solve Equation (1). By means of a concrete analysis of the character of the governing equation, it is known that the condition of structure instability is the equation with periodic solution of periods  $T$  and  $2T$ , where  $T=2\pi/\theta$ . When there is a periodic solution with Period  $2T$  in the equation, the instability of structure can be excited very easily. The regions with periodic solution of  $2T$  are the main regions of dynamic instability, that is,  $\theta=2\omega_j$  is taken as disturbing frequency, where  $\omega_j$  is  $j$ th natural frequency of structure, and the main regions of  $j$ th dynamic instability can be calculated. The boundaries of a main unstable region can be determined with Equation (3).

$$\begin{vmatrix} [K_e] - [K_{gs}] + 0.5[K_{gt}] - [M] \frac{\theta^2}{4} & -[C] \frac{\theta}{2} \\ [C] \frac{\theta}{2} & [K_e] - [K_{gs}] - 0.5[K_{gt}] - [M] \frac{\theta^2}{4} \end{vmatrix} = 0 \tag{3}$$

$[K_{gs}]$  and  $[K_{gt}]$  can be determined when the external load is given. Therefore, the range of  $\theta$  can be obtained. The structure is unstable when  $\theta$  is in this range. By increasing the value of the external load, the boundaries of regions of dynamic instability can be achieved. The axial force can be determined directly when the structure is subjected to vertical loads at joints. For the structure, it is necessary to analyze the structure dynamically before the geometric stiffness matrix is obtained,  $[K_{gt}]$  is related to  $\theta$ , but the calculation indicates that if the value of  $\theta$  is changed in a quite small range, there will be no significant change of dynamic axial force in the structure which is subjected to the vertical dynamic load, such as  $P_0 \sin \theta t$ . This can be attributed to the large difference between the disturbing frequency and longitudinal natural vibration frequency of the structure. The dynamic coefficient, which does not change much, can be regarded as constant. Thus the  $j$ th main dynamic unstable regions can be determined by means of the axial disturbing force with frequency  $2\omega_j$ . From the above analysis, Equation (3) can be solved by means of perturbation method.

### 3 Beam Element Model of the Thin-walled Structure

It is observed in the thin-walled structure that warping which is caused by restrained torsion have a significant effect on the strain and stress of the structure. In order to consider the effect of the warping of the thin-walled beam, an improved displacement model is adopted to simulate the arms of the radial gates.

If we accept that in an element two nodes (i.e., 14 variables) define the deflected shape, we can assume these to be given by a cubic.

$$\begin{aligned}
 u &= a_1 + a_2 x ; v = a_3 + a_4 x + a_5 x^2 + a_6 x^3 ; \omega = a_7 + a_8 x + a_9 x^2 + a_{10} x^3 \\
 \theta_x &= a_{11} + a_{12} x + a_{13} x^2 + a_{14} x^3 ; \theta_y = a_8 + 2a_9 x + 3a_{10} x^2 \quad \theta_z = a_4 + 2a_5 x + 3a_6 x^2 ; \\
 \phi &= \theta'_x + \lambda \theta''_x = a_{12} + 6\lambda a_{14} + 2a_{13} x + 3a_{14} x^2
 \end{aligned}$$

where  $\varphi$  is the warping angle,  $\lambda$  is the warping coefficient which is dependent upon the beam cross-section shape. These displacement functions can be represented as following:

$$U = N \cdot A \tag{4}$$

$$\begin{aligned}
 U &= [u \quad v \quad \omega \quad \theta_x \quad \theta_y \quad \theta_z \quad \phi] \\
 A &= [a_1 \quad a_2 \quad a_3 \quad a_4 \quad a_5 \quad a_6 \quad a_7 \quad a_8 \quad a_9 \quad a_{10} \quad a_{11} \quad a_{12} \quad a_{13} \quad a_{14}]
 \end{aligned}$$

The strain formula of thin-walled beam element can be given by

$$\epsilon = \begin{bmatrix} -y \frac{\partial \theta_z}{\partial x} & -z \frac{\partial \theta_y}{\partial x} & -\omega \frac{\partial \phi}{\partial x} & + \frac{\partial u}{\partial x} \end{bmatrix} \quad (5)$$

$$\gamma_p = \rho \cdot \frac{\partial \theta_x}{\partial x} + \phi \cdot (\psi - \rho) \quad (6)$$

where  $\psi$  is a torsion function, finally, a new stiffness matrix, a new static geometric stiffness matrices and a new static geometric stiffness matrix of thin-walled beam elements are derived, which is applicable to thin-walled beams with cross-sections of any shape (either open, or closed). The possible patterns of the deformation of thin-walled arms are taken into account in.

### 4 Example

In order to further study on the dynamic stability of radial gate arms, a simplified frame model of radial gates (Figure 2) and a working gate of a hydropower project (Figure 1). The simplified space frame composed of main cross beams, vehicle beams, arms and some other components is taken as one analytical model. When the radial gate remaining to water head is 90.0m, the main regions of dynamic instability have been obtained by the method proposed in the paper and is shown in Figure 4. In addition, the main regions of dynamic instability have been obtained by traditional method is shown in Figure 3.

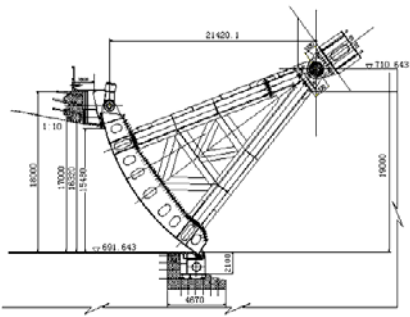


Figure 1 Structure of radial gate

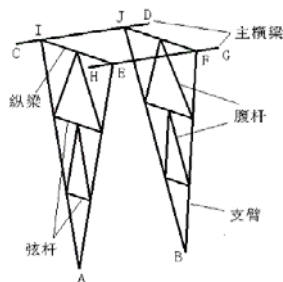


Figure 2 Space frame model of radial gate

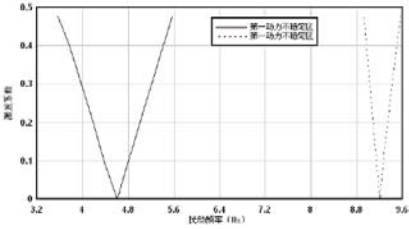


Figure 3 Main instability regions of traditional method

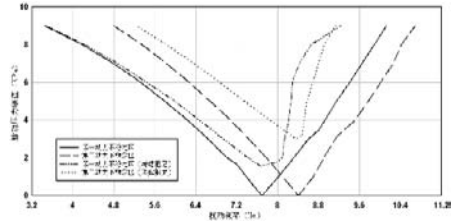


Figure 4 Main instability regions

By hydraulics experiments, the information of flow fluctuating pressure in radial gate is achieved, the flow fluctuant pressure on radial gate can be treated as stationary random process going through all of states in the case of certain opening, so we make use of Fourier transform, the random load can be expressed a series of harmonic load, if the main frequency region and the corresponding amplitudes lie in the dynamic instability region, the radial gate will occur to dynamic instability; otherwise, the gate is safe.

### 5 Conclusions

In this paper, based on the simplified model of the radial gate, a method which is used to obtain the dynamic instability region is proposed, the method takes account of the space effect, it also can consider the possible patterns of the deformation of thin-walled beam, such as tension or compression, shear, bending, torsion and warping. In order to make the method be applied in real project, with the physical and numerical models, a method recognizing the parameter resonates of steel radial gate is proposed. Finally, it is shown that the method is correct by analyzing of a project. The method is not only an improvement for the radial gate parametric vibration computational method, but also lays a solid foundation for further study to the dynamic stability of radial gate structure.

### Acknowledgements

The authors gratefully acknowledge the financial support of Youth Fund of Nanjing Hydraulic Research Institute (No. Y40805).

## References

- Lin J.H., Qu N.S. and Sun H. CH. (1990). *Computational Structural Dynamics*. Beijing: Higher Education Publishing House.
- Nie G.J. and Qian R.J. (2002). Beam element analytical model of thin-walled beam structure. *Chinese Quarterly of Mechanics*, 23(1):87–91 [in Chinese].
- Niu Z.G. and Li T.CH. (2008). Finite element analysis for parametric vibration of radial gate. *Journal of Hydroelectric Engineering*, 27 (6):101–105 [in Chinese].
- Wu J.k. and Su X.Y. (1994). *The Stability of Elastic Systems*. Beijing: Science Press.
- Zhang J. and Liu G.R. (1992). Analysis and study of accidents of lightweight hydraulic steel radial gate. *Journal of Hydroelectric Engineering*, 2 (3):49–57 [in Chinese].
- Zhang J.G. (1985). Summary on the study of gate vibration in China, *Water Power*, 4(1):36–42[in Chinese].

# Research on the Difference between the Linear and Nonlinear Analysis of a Wing Structure

Ke Liang<sup>1\*</sup> and Qin Sun<sup>1</sup>

<sup>1</sup>School of Aeronautics, Northwestern Polytechnical University, Xi'an 710072, P.R. China

**Abstract.** The nonlinear stability analysis of the short box, the long box and the whole wing structure were compared by MARC2003 nonlinear finite element calculation software. The results indicated they were not appropriate to substitute the important part for the whole structure and use the node displacements of the linear calculation as the boundary conditions of the nonlinear analysis. This technique should not be used for the stability design. By comparing the differences of the deflection and the torsion angle between the linear and nonlinear analysis, it was concluded that the nonlinearity seldom influenced the deflection whereas it could remarkably influence the torsion angle. In conclusion, the nonlinear impact must be considered in the torsion stiffness and aeroelastic designs of the wing.

**Keywords:** nonlinear stability, nonlinear finite element, boundary condition, deflection, torsion angle

## 1 Introduction

The wing under the aerodynamic force will deform largely, which is a typical kind of geometry nonlinear problem (Zhou, 1997). Due to the complexity of the nonlinear calculation and the wing structure, the analytical methods often used in engineering field are replacing the whole structure by the important part and using the node displacements of linear calculation as the boundary conditions of nonlinear analysis at present. Although the methods solve problems of the convergence and the calculation efficiency, the veracity of the calculation is still doubtful (Shao et al., 2006; An, 2007; Zhao et al., 2008).

With the loading increasing, the nonlinear feature of the structure is more obvious. If the feature is not obvious in the extreme, the simpler method (linear calculation) can be adopted. For the wing structure, the deflection and torsion are the most important places which should be paid attention to. Hence, by researching the change of their difference between the linear and nonlinear calculation with

---

\* Corresponding author, e-mail: liangke.nwpu@163.com

the loading increasing, we can know when the difference becomes obvious (Satoru and Minsu, 2008; Teters, 2007; Barski, 2006; Crisfield, 1997).

The investigations have been carried on into the forenamed problems. The results are valuable in engineering.

## 2 Influence of the Boundary Condition

Based on HyperMesh finite element software, the finite element model of the wing structure which is shown in Figure 1 has been established. In order to model the real exterior condition of the wing, the proper constrain is used on the wing root and the precise aerodynamic force is used on the wing surface. The overload coefficient is introduced and multiplied by aerodynamic force as the total loading. In this section, the overload coefficient is equal to 3.2. During the nonlinear calculation, the arc-length method is used to ensure convergence (Ling and Xu, 2004).

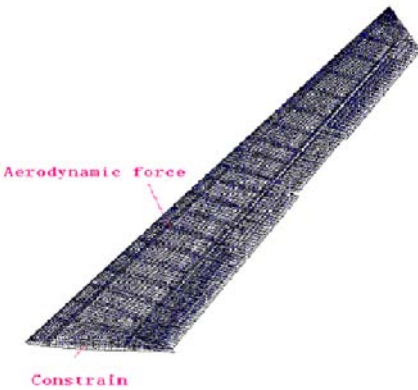


Figure 1. Finite element model of wing

For the shell structure, the instability often occurs on the pressing surface. In the wing structure, the instability is represented as the buckling pits which often occur near the wing root. In order to check the veracity of the method which is often used in engineering, the models of the short box and the long box are picked up from the wing root and the node displacements of the linear calculation are used as the boundary condition of A and B section. The models are observed from Figures 2 to 4. Tables 1 to 3 show the results of the comparison of nonlinear stability analysis of the short box, the long box and the whole wing structure.



Figure 2. Short box



Figure 3. Long box

Table 1. Comparison of the time when pits occur

Model	Percent of the load (%)
Short box	29
Long box	25
Whole wing	22

Table 2. Comparison of the pit deep

Model	Deep/mm
Short box	8.9
Long box	9.6
Whole wing	10.8

Table 3. Comparison of the pit radius

Model	Radius/mm
Short box	74.4
Long box	82.3
Whole wing	87.5

From the above tables, it is concluded that if the whole wing structure is used to do nonlinear stability analysis, the time is earlier as the deep and size are larger when pits occur. Compared with the short box, the deviation has reached to 15%, which is not acceptable in engineering. The results indicate that they were not proper to substitute important part for the whole structure and use the node displacements of linear calculation as the boundary conditions of nonlinear analysis.

In order to find out the reason, the node displacements of nonlinear calculation on A and B sections can be obtained in the whole wing structure and the difference between the liner and nonlinear calculation should be compared. The com-

parison shows in Table 4. In this table, UX is represented as the displacement in the X direction.

Table 4. Comparison of the node displacements between the linear and nonlinear calculation %

Section	Section A	Section B
Difference of UX	8	21
Difference of UY	15	6.4
Difference of UZ	93	85

From Table 4, it is obvious that the error results from using the node displacements of linear calculation as the boundary condition of nonlinear calculation. Therefore nonlinear stability analysis must be carried on the whole structure when the structure is obviously possessed of nonlinear feature.

### 3 Course of Nonlinear Behaviour

As stated above, it is known that the difference between the linear and nonlinear analysis is very obvious, when the overload coefficient is equal to 3.2. In this section, the difference of the deflection and the torsion angle between the linear and nonlinear calculation should be paid close attention to. In addition, the investigation also concentrates on the change of difference with the overload coefficient increasing.

Firstly, seven nodes along the wing span are picked up. Their displacements are denoted by the y-axis while their locations are denoted by x-axis. The deflection curves under different overload coefficients are shown in Figure 4 to Figure 6. In order to make comparison, the linear and nonlinear curves are shown in one figure.

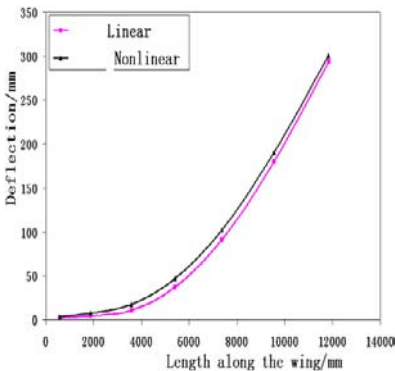


Figure 4. Deflection curve (overload = 1)

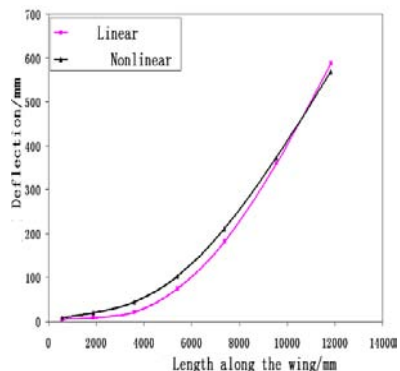


Figure 5. Deflection curve (overload = 2)

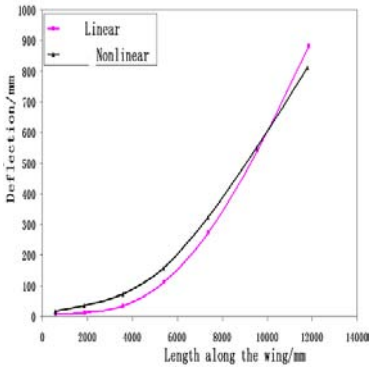


Figure 6. Deflection curve (overload = 3.2)

From the figures, it is concluded that the differences of the linear and nonlinear deflection curves become greatly obvious when the overload coefficient is equal to 2.0. At the moment, the two curves have a point of intersection which indicates that the structure nonlinear behavior starts occurrence. This conclusion can be used for the overload coefficient design of wing structures.

Secondly, the difference of the wing tip deflection value between linear and nonlinear analysis is calculated on condition that the overload coefficient is increasing (shown in Table 5). Results show that the difference become more and more obvious with the overload coefficient increasing,

Table 5. Comparison of the deflection between the linear and nonlinear calculation

Overload( m / s <sup>2</sup> )	1	2	3.2
Difference of the deflection in the wing tip (%)	1.7	4	9.37

Lastly, the difference of the wing tip torsion angle between linear and nonlinear is calculated on the condition that the overload coefficient is increasing (shown in Table 6). Results show that the nonlinear influence on torsion angle is much wider than that on deflection. The reason is that the bending moment can be beared by the beam when the skin becomes buckling. However, the torsion stiffness has been diminished when the skin buckling because the torsion moment is balanced by the shear force which is on the skin. Therefore the nonlinear impact must be considered in the torsion stiffness design and the aeroelastic design of the wing (Chen, 2004).

Table 6. Comparison of torsion angle between the linear and nonlinear calculation

Overload( $m / s^2$ )	1	2	3.2
Difference of the torsion angle in the wing tip (%)	23.9	37.5	47

## 4 Conclusions

The results of nonlinear stability analysis of the short box, the long box and the whole wing structure suggested that they was not appropriate to using the important part in place of the whole structure and use the node displacements of the linear calculation as the boundary conditions of the nonlinear analysis. Therefore this technique should not be used for the stability design. By comparing the differences of the deflection and the torsion angle between the linear and nonlinear analysis, it was concluded that the differences of the linear and nonlinear deflection curves became very obvious when the overload coefficient was equal to 2.0 and the nonlinear influence on torsion angle was much wider than that on deflection. Therefore the nonlinear impact must be considered in the torsion stiffness and the aeroelastic design of the wing.

## Acknowledgment

The project is supported by the Aviation Science Foundation of China (No. 20060953013).

## References

- An Y. (2007). *Research of design optimization and stability analysis of composite shell structure*. Xi'an, Northwestern Polytechnical University: 1-86 [in Chinese].
- Barski M. (2006). Optimal design of shells against buckling subjected to combined loadings. *Structural and Multidisciplinary Optimization*, (31): 146-154.
- Chen G. (2004). *The foundation of aeroelastic design*. Beijing: Beihang University Press, 1-200 [in Chinese].
- Crisfield M.A. (1997). *Nonlinear finite element analysis of solids and structures. Advanced topics*, Vol. 2. UK, Wiley: 1-150.
- Ling D. and Xu X. (2004). *Nonlinear FEM and program*. Hangzhou, Press of ZJU: 1-5 [in Chinese].
- Satoru S. and Minsu J. (2008). Evaluation of short-term stability for sea-wall structure at Kobe Airport. (12): 26-31.

- Shao X., Yue Z., Zhou L., et al. (2006). Study of stability of moderately thick composite laminates under axial compression loading and shear loading. *Journal of Mechanical Strength*, 28(5): 716-720 [in Chinese].
- Teters G. (2007). Multicriteria optimization of a rectangular composite plate subjected to longitudinal thermal stresses and buckling in shear loading. *Mechanics of Composite Materials*, (1): 45-51.
- Zhou C. (1997). *Elastoplastic and stability theory of the thin shell*. Beijing: National Defence Industry Press: 1-152 [in Chinese].
- Zhao X., Liu G. R. and Dai K. Y. (2008). Geometric nonlinear analysis of plates and cylindrical shells via a linearly conforming radial point interpolation method. *Computational Mechanics*, (4): 41-49.

*“This page left intentionally blank.”*

# A New Slice Method for Seismic Stability Analysis of Reinforced Retaining Wall

Jianqing Jiang<sup>1,2\*</sup> and Guolin Yang<sup>1</sup>

<sup>1</sup> School of Civil Engineering and Architecture, Central South University, Changsha Hunan 410075, P.R. China

<sup>2</sup> School of Civil Engineering, Hunan City University, Yiyang Hunan 413000, P.R. China

**Abstract.** According to retaining walls reinforced by extensible reinforcements such as geogrids and geotextiles, a new slice analysis methodology was developed to analyze its internal stability under horizontal and vertical seismic loads. The slide failure wedge of the reinforced retaining wall was divided into a number of soil slices parallel to the reinforcements. Based on the single line shape assumption for the critical slip surface of the wall, the equilibrium equations for horizontal forces, vertical forces and moments of each soil slice were established. And then, the recurrence formulas for horizontal and vertical inter-slice forces, reinforcement tensile forces were derived consequently, in which the relationship between the inter-slice forces and the safety factor  $FS$  of the wall was included. The safety factor  $FS$  and the vertical bearing capacity  $q_{max}$  at the wall top were obtained by solving those recurrence formulas. This proposed slice method was applied to analyze the seismic stability of one reinforced retaining wall whose height was 10m, and the results were compared with those of strength reduction method. The results show that: this method is simple, practical and good precision in calculation, so it can be used in actual seismic stability design of reinforced walls; the simplified critical slip surface is more feasible and convenient for engineering application than the log-spiral failure surface.

**Keywords:** new slice method, reinforced soil, retaining wall, seismic, stability

## 1 Introduction

Applications of reinforced soil walls are mostly in non-earthquake regions at present (Jiang and Zou, 2006). So it is significant to study on its seismic stability in order to apply this economical structure in earthquake area reasonably.

---

\* Corresponding author, e-mail: lh201314@163.com

The anti-seismic design for reinforced retaining walls is usually based on limit equilibrium and pseudo-static technique (Ling et al., 1997; Ling and Leshchinsky, 1998; Michalowski, 1998; Jiang and Zou, 2007). The conventional approaches exist obvious disadvantages due to inclusion of reinforcement tensile force in stability analysis. Therefore, the idea of horizontal slice means is introduced into analyze reinforced structures (Shahgholi et al., 2001; Nouri et al., 2006). Whereas, these methods are inconvenient in application because of being carried out using optimization program and assuming a log-spiral failure surface when the wall are destroyed.

Hence in this paper an attempt has been made to investigate the stability of reinforced retaining walls under horizontal and vertical seismic conditions by using a new slice method, which considers a single line shape for the critical slip surface of the wall with respect to extensible reinforcements. The recurrence formulas for horizontal and vertical inter-slice forces are derived consequently. The safety factor and the ultimate vertical load at the wall top are obtained.

## 2 New Slice Theoretical Method

### 2.1 Basic Assumption

According to Mechanically Stabilized Earth Walls and Reinforced Soil Slopes Design & Construction Guidelines (FHWA-NHI-00-043 2001), the critical slip surface is approximately linear in case of the retaining wall reinforced by extensible reinforcements (Figure 1).

The slip failure wedge is divided into  $n$  soil slices parallel to reinforcements, one layer reinforcement is included in each slice (Figure 1). The force system acted on each slice is shown in Figure 2. Where,  $W_i$  is the weight of the  $i^{\text{th}}$  slice;  $F_{N,i}$ ,  $F_{N,i+1}$ ,  $F_{t,i}$ ,  $F_{t,i+1}$  are the normal and tangential inter-slice forces at the upside and underside respectively;  $N_{N,i}$  and  $N_{t,i}$  are the normal and tangential reaction forces at the  $i^{\text{th}}$  critical slip surface;  $T_i$  is the tensile force of the  $i^{\text{th}}$  reinforcement;  $F_{EH,i}$  and  $F_{EV,i}$  are the horizontal and vertical seismic inertia forces at the mass center of the  $i^{\text{th}}$  slice.

### 2.2 Equilibrium Equations for Each Slice

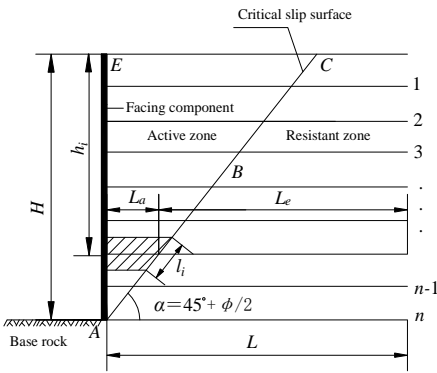
From Figure 2,  $\sum F_x = 0$  (for each slice) and  $\sum F_y = 0$  (for each slice),

$$\left. \begin{aligned} T_i + N_{t,i} \cos \alpha_i - N_{N,i} \sin \alpha_i - F_{EH,i} + F_{t,i+1} - F_{t,i} &= 0 \\ F_{N,i+1} - F_{N,i} - W_i - F_{EV,i} + N_{t,i} \sin \alpha_i + N_{N,i} \cos \alpha_i &= 0 \end{aligned} \right\} \quad (1)$$

where in accordance with mohr-coulomb criterion,

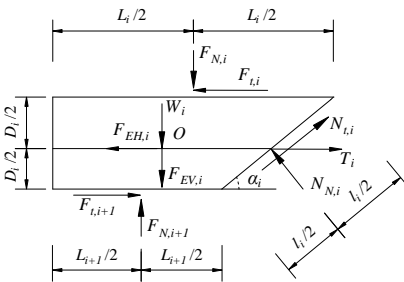
$$\left. \begin{aligned} N_{t,i} &= (c_l + N_{N,i} \tan \phi) / FS \\ F_{t,n} &= (cD_n \cot \alpha + F_{N,n} \tan \phi) / FS \end{aligned} \right\} \quad (2)$$

where  $c$  and  $\phi$  is cohesion and internal friction angle of the fill respectively.



$H$  – Height of the wall;  $h_i$  – Distance of the  $i^{\text{th}}$  reinforcement below the wall top;  $L$  – Total length of reinforcement;  $L_e$  – Embedment length in the resistive zone behind the failure;  $L_a$  – Length of reinforcement in the active zone; 1~ $n$  – Sequence number for reinforcements;  $l_i$  – Intersecting line Length of the  $i^{\text{th}}$  soil slice and the critical slip surface

Figure 1. Simplified critical slip surface for extensible reinforcements and division for its slide failure wedge



$D_i$  – Depth of the  $i^{\text{th}}$  soil slice;  $\alpha_i$  – Angle between the critical slip surface and horizontal plane;

$V_i, V_{i+1}, H_i, H_{i+1}, EH_i, EV_i, W_i, N_i, S_i, T_i$  – Force system acted on the  $i^{\text{th}}$  soil slice

Figure 2. Schematic diagram for force system of the  $i^{\text{th}}$  soil slice

For the whole slide failure wedge  $ABCE$ , the sum of its horizontal applied forces is zero,

$$\sum_{i=1}^n T_i + \sum_{i=1}^n N_{t,i} \cos \alpha_i - \sum_{i=1}^n N_{N,i} \sin \alpha_i - \sum_{i=1}^n F_{EH,i} = 0 \tag{3}$$

Moment equilibrium is satisfied for each slice with respect to the moment center (point O in Figure 2),

$$(F_{N,i+1} + F_{N,i}) \frac{D_i}{4 \tan \alpha_i} - (N_{t,i} \sin \alpha_i + N_{N,i} \cos \alpha_i) \frac{H-h_i}{2 \tan \alpha_i} - (F_{t,i+1} + F_{t,i}) \frac{D_i}{2} = 0 \tag{4}$$

### 2.3 Safety Factor of the Wall and Vertical Ultimate Load

Combining Equation 1 with Equation 2, 3, 4, the recurrence formulas for horizontal and vertical inter-slice forces can be derived,

$$\left. \begin{aligned} F_{N,i+1} &= \left\{ F_{N,i} \left[ \frac{2(H-h_i) - D_i}{4 \tan \alpha_i} \frac{(\tan \phi / FS) \cos \alpha_i - \sin \alpha_i}{(\tan \phi / FS) \sin \alpha_i + \cos \alpha_i} \right] + \frac{(W_i + F_{EV,i})(H-h_i)}{2 \tan \alpha_i} + \left[ \frac{2F_{t,i} - T_i}{FS} \frac{c_i \cos \alpha_i}{(\tan \phi / FS) \sin \alpha_i + \cos \alpha_i} \right] \times \right. \\ &\quad \left. \left( \frac{W_i + F_{EV,i}}{FS} \frac{c_i \sin \alpha_i}{FS} + F_{EH,i} \right) \times \frac{D_i}{2} \right\} \left/ \left[ \frac{2(H-h_i) + D_i}{4 \tan \alpha_i} \frac{(\tan \phi / FS) \cos \alpha_i - \sin \alpha_i}{(\tan \phi / FS) \sin \alpha_i + \cos \alpha_i} \times \frac{D_i}{2} \right] \right. \\ F_{t,i+1} &= \left\{ F_{t,i} \left( \frac{(\tan \phi / FS) \sin \alpha_i + \cos \alpha_i}{(\tan \phi / FS) \cos \alpha_i - \sin \alpha_i} \times \frac{D_i + 2(H-h_i)}{4 \tan \alpha_i} + \frac{D_i}{2} \right) \left( 2F_{N,i} + W_i + F_{EV,i} \frac{c_i \sin \alpha_i}{FS} \right) \times \frac{D_i}{4 \tan \alpha_i} + \frac{c_i \sin \alpha_i}{FS} \times \frac{H-h_i}{2 \tan \alpha_i} + \right. \\ &\quad \left. \left( \frac{F_{EH,i} - T_i}{FS} \frac{c_i \cos \alpha_i}{(\tan \phi / FS) \cos \alpha_i - \sin \alpha_i} \right) \times \frac{D_i + 2(H-h_i)}{4 \tan \alpha_i} \right\} \left/ \left[ \frac{(\tan \phi / FS) \sin \alpha_i + \cos \alpha_i}{(\tan \phi / FS) \cos \alpha_i - \sin \alpha_i} \times \frac{D_i + 2(H-h_i)}{4 \tan \alpha_i} \right] \right. \end{aligned} \right\} \tag{5}$$

Given the boundary load conditions at the wall top:  $F_{N,1} = q$ ,  $F_{t,1} = 0$ . The safety factor and the vertical ultimate load can be obtained by solving Equation 10 using iterative method according to the following steps,

Step 1: Assume iterative initial value of the safety factor  $FS$  to be  $FS^*$ .

Step 2: The iterative calculation start from the 1<sup>st</sup> slice, and then its underside inter-slice forces  $F_{N,2}$  and  $F_{t,2}$  can be solved from Equation 10. Thereafter,  $F_{N,2}$  and  $F_{t,2}$  are used as recurrence initial value for the 2<sup>nd</sup> slice. So  $F_{N,n}$  and  $F_{t,n}$  can be attained in sequence from the 1<sup>st</sup> slice to the end slice.

Step 3: Substitute  $F_{N,n}$  and  $F_{t,n}$  into Equation 3, the safety factor  $FS^{**}$  is obtained.

Step 4: When  $|FS^{**} - FS^*| \leq 2\%$ , the last iterative initial value  $FS^*$  is the true value for safety factor.

Step 5: When solving for the vertical ultimate load  $q_{max}$ , the initial value  $q_{max}^*$  and  $FS=1$  could be given. Similar to step 2,  $F_{N,n}$  and  $F_{t,n}$  can be attained. Substitute  $F_{N,n}$  into Equation 3,  $F_{t,n}^*$  is calculated. If  $|F_{t,n} - F_{t,n}^*| \leq 2\%$ , it indicates that the initial value  $q_{max}^*$  is the true value for  $q_{max}$ .

### 3 Verification for the Slice Method

Verification has been undertaken by the following Example through comparing results obtained using the proposed method with those obtained using two published procedures.

Example: A reinforced retaining wall is 10m in height, the basic physical and mechanical properties for the fill soil and the reinforcements are shown in Table 1. Variations of parameters considered in this example are as follows:  $k_h = 0.0, 0.1g$ ,  $k_v = 0.0$ , and the vertical space for geogrids layers is  $0.05H$  or  $0.1H$ . The safety factor results by the proposed method and the strength reduction method (Dawson 1999) are listed in Table 2.

From the example, it is evident that comparisons the proposed slice method with conventional method yielded satisfactory agreement.

Table 1. Basic physical and mechanical properties of soil and geogrids

Internal friction angle /°	Cohesion /kPa	Soil			Geogrids	
		Unit weight /Kn/m <sup>3</sup>	Elastic module /MPa	Poisson's ratio	Length /m	Elastic module /GPa
35	20	20	33	0.3	10	26

Table 2. Calculation results for safety factor

$k_h$	Vertical space of geogrids layers 0.1H		Vertical space of geogrids layers 0.05H	
	slice method	Strength reduction method	slice method	Strength reduction method
0.0	1.28	1.30	1.33	1.35
0.1g	1.16	1.19	1.20	1.23

## 4 Conclusions

The seismic stability of reinforced retaining wall has been investigated using a new slice method. In this slice method, the sliding wedge is divided into several slices, which are parallel to the reinforcement layers. With respect to the extensible reinforcements and based on the single line shape assumption for the critical slip surface of the wall, the recurrence formulas for horizontal and vertical inter-slice forces and reinforcement tensile forces are derived consequently. The safety factor and the ultimate vertical load at the wall top are obtained. The slice method is validated by comparing with the conventional method through one Example. Moreover, the present study shows that the simplified critical slip surface is more feasible and convenient for engineering application than the log-spiral failure surface.

## Acknowledgments

The work is supported by Hunan Provincial Department of Education Project (08c199) of China.

## References

- Dawson E.M., Roth W.H. and Drescher A.. (1999). Slope stability analysis by strength reduction. *Geotechnique*, 49(6): 835-840.
- FHWA-NHI-00-043. (2001). Mechanically Stabilized Earth Walls and Reinforced Soil Slopes Design & Construction Guidelines. National Highway Institute Office of Bridge Technology, Washington D.C.
- Jiang J.Q. and Zou Y.S. (2006). Numerical Simulation of Reinforced Retaining Walls under Dynamic Loads. *Journal of Hunan City University (Natural Science)*, 15(4): 12-14 [in Chinese].
- Jiang J.Q. and Zou Y.S. (2007). Interior stability analysis of reinforced earth retaining wall under complicated dynamical loads. *Journal of Central South Highway Engineering*, 32(1): 51-54 [in Chinese].
- Ling H.I., Leshchinsky D. and Perry E. (1997). Seismic design and performance of geosynthetic reinforced soil structures. *Geotechnique*, 47(5): 933-952.
- Ling H.I. and Leshchinsky D. (1998). Effects of vertical acceleration on seismic design of geosynthetic reinforced soil structures. *Geotechnique*, 48(3): 347-373.
- Michalowski R.L. (1998). Soil reinforcement for seismic design of geotechnical structures. *Computers and Geotechnics*, 23(1): 1-17.
- Nouri H., Fakher A., Jones C.J.F.P. (2006). Development of horizontal slice method for seismic stability analysis of reinforced slopes and walls. *Geotextiles and Geomembranes*, 24(5): 175-187.
- Shahgholi M., Fakher A., Jones C.J.F.P. (2001). Horizontal slice method of analysis. *Geotechnique*, 51(10): 881-885.

# Hysteretic Response and Energy Dissipation of Double-Tube Buckling Restrained Braces with Contact Ring

Zhanzhong Yin<sup>1\*</sup>, Xiuli Wang<sup>1</sup> and Xiaodong Li<sup>1</sup>

<sup>1</sup>School of Civil Eng., Lanzhou Univ. of Technology, Lanzhou 730050, China

**Abstract:** The buckling restrained braces (BRBs) might yield but would not buckle whether compressed or tensioned. Thus, BRBs could dissipate in advance the energy of weak earthquake action and protect the structure of main complex from destruction. Meantime, under the action of strong earthquake the BRBs could absorb its energy in large amount, so that the structural safety was improved. The double-steel tube BRBs with was remodeled with additional contacting in the middle of their inner tube and at their ends. Finite element numeric simulation was conducted for this kind of BRBs and its result showed that it exhibited fine ability of energy dissipation and force performance.

**Keywords:** buckling restrained braces, contact ring, finite element analysis

## 1 Introduction

Since Kimura etc. had put forward Buckling-Restrained Braces (BRBs) in 1976, it had got many scholars' attention. Since buckling-restrained braces (BRBs) can yield in both tension and compression without buckling, the disadvantages of the conventional braced frame system can be overcome. It can also absorb higher energy under earthquake action, so the safety of structure was enhanced. In China, most of the regions were located on earthquake region, so the influence of ground motion should be considered in seismic design. From the above aspect, a kind of brace namely double-tube buckling restrained brace with contact-ring was proposed in this paper, whose performances were analyzed in details.

---

\* Corresponding author, e-mail: yinzhanzhong-1@163.com

## 2 Geometry Parameters of Component

According to the results of the analysis of document (Yin et al., 2008), in this paper, some discontinuous steel rings were set between the inner tube and the outer tube, namely the contact rings (see Figure 1). So the lateral supporting roles were provided by the contact rings to improve the bearing capacity of the component. Geometry parameters of component see table 1. The finite element analysis presented in this study was conducted using available commercial software (ANSYS) and a three-dimension non-linear analysis was also applied. Furthermore, the ideal elastoplastic model was adopted. Both material and contact non-linearity was also considered in the analysis. The average values of ultimate yield strength and elastic modules were 235MPa and 210GPa respectively, and Poison ratio is about 0.3.

Table 1 Geometric dimension table.

Numbers of Brace	length/m		Component specifications /mm				Defect %
	outer tube	inner tube	outer tube①	inner tube②	the contact rings		
					Num- ber	Specificat- ions ③④	
TBRBs-1	1.2	1.0	Φ89×4	Φ60×3.5	2	Φ80×10.0	1
TBRBs-2	1.2	1.0	Φ89×4	Φ60×3.5	3	Φ80×10.0	1
TBRBs-3	1.2	1.0	Φ89×4	Φ60×3.5	5	Φ80×10.0	1
TBRBs-4	1.2	1.0	Φ89×4	Φ60×3.5	5	Φ80×10.0	3
TBRBs-5	1.2	1.0	Φ76×4	Φ60×3.5	5	Φ68×4.0	3
TBRBs-6	1.2	1.0	Φ108×5	Φ60×3.5	5	Φ100×20	3

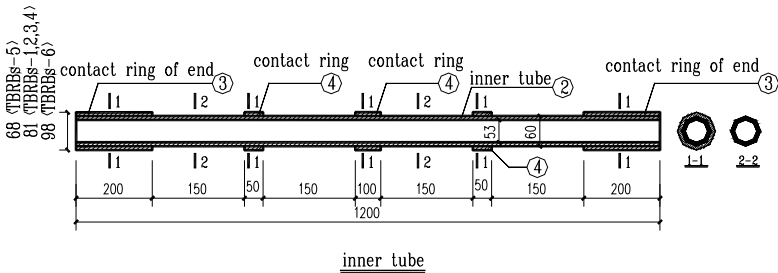


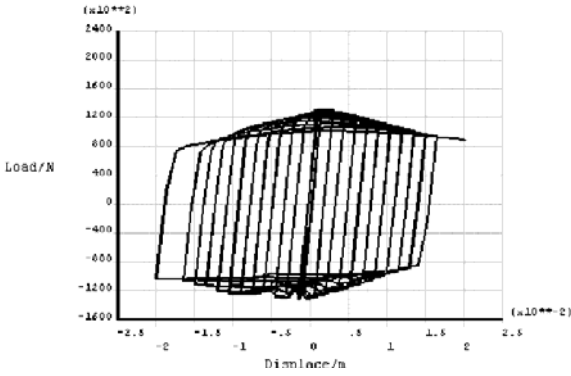
Figure 1. Different structures of BRBs.

### 3 Analysis of Hysteretic Performance

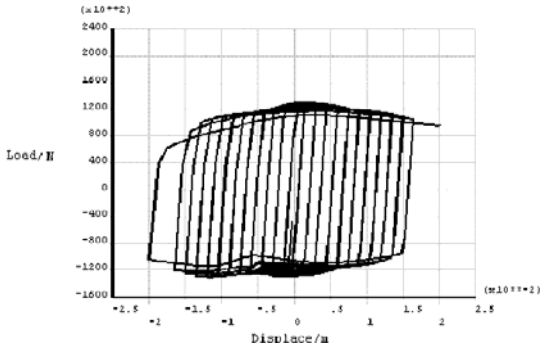
Hysteresis loop was load-deformation curve of structure and component under a cycle loading. Areas of hysteresis loop exemplified energy dissipation capacity of structure and component. The more areas of hysteresis loop, the more ability of dissipating energy. So on the view of macroscopic, hysteresis curve shape can show the seismic mechanism of structures or component.

In order to discuss capacity of energy dissipation of buckling-restrained braces, cycle loading was carried out for double-tube buckling restrained braces with contact ring listed in table 1, and hysteresis curves were obtained as shown in figure 2. In this paper the parameter analysis of BRBs with contact ring were carried out. The effect of the number of contact ring was discussed. For example, in the same conditions the number of contact ring of component TBRBs-1, TBRBs-2 and TBRBs-3 was from 2 to 5, and the following results were obtained from hysteresis curves of BRBs with contact ring.

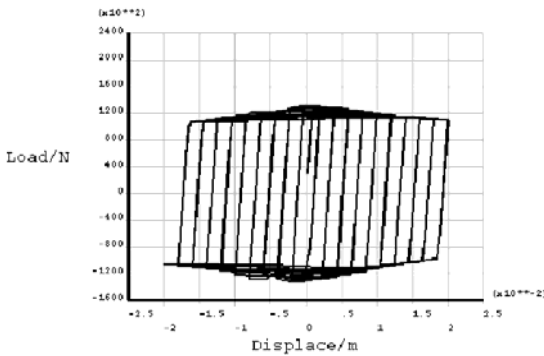
1. From the full extent of hysteresis curves, TBRBs-2 and TBRBs-3 were all full (see Fig 2(b) and (c)). The shape of those hysteresis curves shows square or rectangle approximatively. It indicated that Energy dissipation capacity of TBRBs-2 and TBRBs-3 was better and more stable. The bearing capacity of TBRBs-1 began decreasing since the second cycle, and hysteretic curves of TBRBs-1 become instable. It indicated that hysteretic performance observably improved with the increase of the contacting ring.
2. The peakload was stable under circulating load, but peak of displacement increased with the increase of cycling times. Results from numerical simulation show that rigidity degradation behavior occurred beyond the peak displacement.
3. As we can see from Figure 2(a,b,c) below, strength degradation of material in the fatigue process occurred too, but the degree of strength degradation decreased with the increase of number of contacting ring. For component TBRBs-3, strength degradation did not happen; one major reason is that constrains of inner tube increased and defect was avoided after the increase of number of contacting ring.



(a) Hysteresis loop of TBRBs-1



(b) Hysteresis loop of TBRBs-2



(c) Hysteresis loop of TBRBs-3

Figure 2. Hysteresis loop of TBRBs.

## 4 Analysis of Stress and Deformation

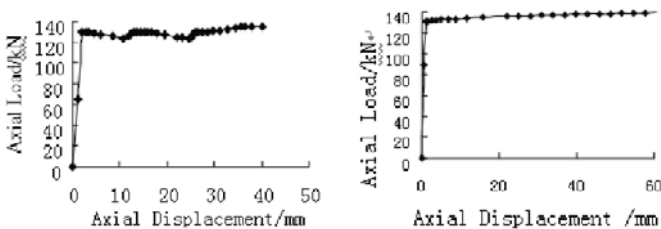
In order to get more reliable result of settlement, initial deflections were taken into account, such as initial bending. Based on characteristic value buckle analysis method of finite elements theory, initial bending of member was obtained. The value of initial bending was one-in-a-thousand or three-in-a-thousand times wider than initial bending.

As can be seen from the figure of stress (see Figure 3), when axial displacement of inner tube of TBRBs reached 1~2mm, the stress of inner tube reached the yield point. From this phenomenon we can see that inner tube BRBs were starting to dissipated energy. Combining with load-displacement curve (see Figure 4), the Buckling-Restrained Braces (BRBs) show the same load-deformation behavior in both compression and tension, and ideal elastic-plastic model was drawn. And elastic-plastic model become perfect with the increase of number of contacting ring. Load-displacement curve from Figure 4(a) suggests that plastic segment of curve had significant volatility. This is primarily caused by limited numbers of contacting ring. These results imply that the capacity of BRBs with contact ring to absorb energy increased with the increase of number of contacting ring.



(a) TBRBs-4 stress figure (b) TBRBs-5 stress figure (c) TBRBs-6 stress figure

Figure 3. Stress figure.



(a) double-tube BRBs with contact ring (b) double-tube BRBs with contact ring

Figure 4. Axial load-displacement curve.

Maximum lateral displacement of inner tube of all TBRBs reached clearance distance between inner tube and outer tube respectively. It means that deformation of inner tube was constrained on outer. And according to Figure 3, the larger the clearance distance was, the larger the deformation was. But when the clearance distance was too small, failure which is caused by local buckling of inner tube was possible.

Moreover, it was clear that minimum strain of BRBs with contact ring reached 2.25%, and maximum strain of that reached 16.67%. This value exceeded maximum strain of yielding stage in ideal elastoplastic model. This means deformation capacity of inner tube was very good. It was that BRBs can absorb higher energy under earthquake action, so the safety of structure was enhanced.

## 5 Results

Based on the theory of the finite element method, the finite element entity model of Double-Tube Buckling Restrained Brace with Contact-Ring was built and analyzed. Then the strength, the stiffness and the dissipative characteristics of BRBs were obtained.

1. Double-tube buckling restrained brace with contact-ring had very good performance of absorbing energy. Buckling-restrained braces (BRBs) with contact ring can yield in both tension and compression without buckling, and performance of this brace was very stable in compression.
2. Under unidirection loading, load-displacement curve of buckling-restrained braces (BRBs) with contact ring was close to ideal elastoplastic model. The value of deformation exceeded maximum strain of yielding stage in ideal elastoplastic model, and maximum strain of that reached 16.67%. This indicated that plastic deformation of BRBs with contact ring was very good. But the capacity of BRBs with contact ring to absorb energy increased with the increase of number of contacting ring.
3. Compared with ordinary BRBs, double-tube buckling restrained brace with contact ring was more reliable and its characteristic was dexterous and light. The connection was reliable and convenient with other members.
4. Overall, under cyclic loadings Energy dissipation capacity of double-tube buckling restrained brace with contact ring was quite good. But hysteretic performance observably improved with the increase of the contacting ring. Rigidity degradation of BRBs with contact ring was obvious. At the same time, strength degradation occurred, but the degree of strength degradation decreased with the increase of number of contacting ring.

## References

- Cai K.Q., Chen J.H., Wang H.Y. (2001). Earthquake-resistant behavior of moment resisting frame with supplemental shear panels made of low yield strength steel [J]. *Earthquake Engineering and Engineering Vibration*, 21(4):88-93.
- Hu O.H., Onoda J. (2002). An experimental study of a semiactive magneto-rheological fluid variable damper for vibration suppression of truss structures. *Smart Materials and Structures*, 11(1):156-162.
- Nakamura, Maeday, Sasaki, et al. (2000). Fatigue properties of practical scale unbounded braces. *Nippon Steel Technical Report*, 82:51-57.
- Nakaxhima M., Iwai S., Iwata M., et al. (1994). Energy Dissipation Behavior of Shear Panels Made of Low-Yield steel. *Earthquake Engineering and Structural Dynamics*, 23:1299-1313.
- Tsai K.C., Hwang Y.H., Weng C.S. (2005). Seismic Performance and Applications of Double-Tube Buckling-Restrained Braces. *Progress in Steel Building Structures*, 7(3):1-8.
- Wang C.M., Nakashima M. (2005). The Practice and Research Development of Buckling-Restrained Braced Frames. *Progress in Steel Building Structures*, 7(2):1-11.
- Wang X.L., Su C.J. (2007). Analysis of mechanical behavior and high-order mode of buckling-restrained brace [J]. *Journal of Lanzhou University of Technology*, 5:105-108.
- Yin Z.Z., Wang X.L., Li X.D. (2008). Finite element analysis of double-steel-tube buckling restricting braces with contact-ring. *Journal of Lanzhou University of Technology*, 5:122-126.

*“This page left intentionally blank.”*

# **SEISMIC ENGINEERING**

*“This page left intentionally blank.”*

# Numerical Simulation and Analysis for Collapse Responses of RC Frame Structures under Earthquake

Fuwen Zhang<sup>1\*</sup>, Xilin Lu<sup>1</sup> and Chao Yin<sup>1</sup>

<sup>1</sup>State Key Laboratory for Disaster Reduction in Civil Engineering, Tongji University, Shanghai 200092, P.R. China

**Abstract.** In this paper, a discrete element model for collapse simulation of RC frame structure is constructed by discretizing the structure into a few elements and spring groups. This model introduces special hysteretic models of connected springs for arbitrary loading path, and also takes into account reasonable failure criteria for springs considering coupling effect of shear and axial force. Based on the discrete element model, a computer program is developed to simulate the whole process of RC frame structures from initial state to collapse under earthquakes. Particularly, the contact-impact problem between discrete elements has been treated with effective measures. Then the program is employed to study the collapse mechanism of a real building in Wenchuan earthquake-hit area, the result of which shows that the simulation program developed based on the new model can realistically simulate the seismic collapse process of RC frame structures.

**Keywords:** discrete element method, failure criteria, contact-impact, simulation program

## 1 Introduction

Wenchuan earthquake of 2008 was the strongest earthquake in China since 1949, causing considerably heavy casualties and enormous damage to buildings. Many experts in the field of structural engineering rushed to the disaster area for investigation immediately after the earthquake, and accomplished statistical analysis for seismic damage of different styles of structures. Statistical data showed that overall performance of RC frame structures was rather good during the earthquake (Civil and Structural Groups of Tsinghua University, 2008), but in magistoseismic area and high intensity region there were still quite a few collapsed examples (Sun

---

\* Corresponding author, e-mail: 2004\_zhang@mail.tongji.edu.cn

et al., 2008; Sun et al., 2008). Taking Yingxiu Town located in the epicenter for example, once it had more than ten reinforced concrete frame buildings but 40% of them were completely ruined and 40% partly collapsed during Wenchuan earthquake (Sun et al., 2008). The frame structures collapsed in this earthquake also include a considerable number of school buildings and other public buildings, which made a severe impact on society. Therefore, when realities cannot agree with the principle of no collapsing with strong earthquake, it will be of great social value and practical significance to conduct further research on failure process of reinforced concrete frame structure during strong earthquake.

In the past, macroscopic survey of seismic damages and model test study of structures were adopted as main research methods for mechanism of structural collapse, however the both methods had certain deficiencies. The former can not describe whole process of structural collapse and for the latter, test models designed according to building codes are difficult to collapse in the laboratory due to the limited capacity of shaking table. With the development of computer simulation technology, constitutive models and failure criteria of structural materials, and numerical methods such as explicit finite element, discrete element, etc., it is possible to obtain the whole process of structural collapse by numerical simulation analysis and some progress having been made so far (Utagawa et al., 1992; Hakuno, 1996; Tagel-Din and Meguro, 2000; Wang et al., 2008; Katahira et al., 2008). In this paper, a simulation program based on discrete element method and segment-multi-spring model is developed to simulate the response of RC frame structures including collapse process under earthquakes. An example illustrated in the paper successfully displays the whole process of structural response under strong earthquake, and to some extent, provides a probable explanation of failure process and collapse mechanism for RC frame structures.

## **2 Numerical Model for Collapse Analysis of RC Frame Structure**

Basic discrete element model of RC frame structure in the paper is similar to which was presented in (Huang, 2006): First divide all the columns and beams along the longitudinal direction into several rigid rectangular elements, and then connect every two adjacent elements with a spring group. The spring group is established to model the mechanical properties of components within the length of mass center of two adjacent elements, and it consists of a sectional shear spring, several concrete axial springs and steel springs.

To guarantee both computational efficiency and accuracy, cross-section of the beam or column is divided into seven uniform stripes parallel to centroidal axis. Each strip contains a concrete axial spring, and three more steel springs are respectively attached to the central and two marginal strips of the cross-section. Besides, the element numbers of beams or columns also directly influence on compu-

tational accuracy. In (Huang, 2006), deformation calculations of a RC cantilever column with different element numbers were carried out, and the results of analysis compared to finite element method showed that satisfying accuracy could be achieved when the element number was not less than five. Therefore, element division method will be adopted in the model as follows: plastic hinge at the end of a beam or column is modeled by one element, the middle zone by three elements and beam-column joint by one element.

### 3 Constitutive Relations and Failure Criteria of Spring Group

#### 3.1 Hysteretic Model and Failure Criterion of Concrete Axial Spring

For concrete axial spring, its cross sectional area is the same as the strip it represents and its length is the centroidal distance between the two adjacent elements. Various cyclic deformations of the structure may occur under earthquakes. Meanwhile stress path of concrete is arbitrary, loading and unloading may occur at any possible time. Considering the effect of cracked section in the hysteretic model proposed by (Huang, 2006), a new concrete constitutive relation is presented in Figure 1  $\varepsilon_w$  denotes the width of crack which just triggers the effect of cracked section, and  $\varepsilon_{\max}$  denotes the corresponding strain of maximum crack width when reloaded. Their relationship can be determined as follows:

$$\varepsilon_w = \varepsilon_{\max} \left( 0.1 + \frac{0.9\varepsilon_0}{\varepsilon_0 + \varepsilon_{\max}} \right) \quad (1)$$

The spring is assumed to fail permanently when its strain exceeds ultimate compressive strain. Whereas, the force of spring turns to zero when ultimate tensile strain is reached, but the spring will work again when its strain is less than  $\varepsilon_w$ . Coupling effect of concrete axial springs and sectional shear spring will be described in section 3.3.

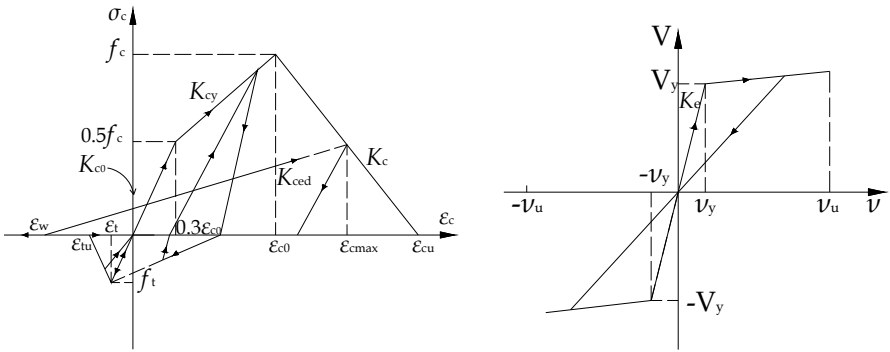


Figure 1. Restoring force model for concrete      Figure 2. Restoring force model for shear spring

### 3.2 Hysteretic Model and Failure Criterion of Steel Spring

Based on reasonable simplification, only three steel springs are placed in the central and two marginal strips of the cross-section. The steel spring represents the area of reinforcement in corresponding strip and its length is the centroidal distance between its adjacent elements. Hysteretic model of steel spring is the same as illustrated in (Huang, 2006) and its details are not mentioned here.

Steel spring is assumed to fail when its compressive or tensile strain is greater than ultimate strain. Moreover, the total spring group will not resist any force or moment when all the steel springs get failed.

### 3.3 Hysteretic Model and Failure Criterion of Sectional Shear Spring

Compared with constitutive relations of concrete and steel, the research on constitutive relation of structural members is far from mature. It is neither necessary nor economic to accurately simulate the shear behavior since its influence is not very significant. Therefore a simple bilinear origin-pointed model in Figure 2 is adopted to describe the shear hysteretic behavior of structural members. The expressions of symbols in Figure 2 can be referred to (Wang and Lu, 2007).

Taking into account the coupling effect of sectional shear spring and concrete axial spring, failure criteria are presented as follows: When deformation of shear spring exceeds the ultimate deformation, shear spring and all the concrete axial springs are assumed to fail; when failures of some concrete axial springs in the

spring group occurred, linear elastic stiffness  $K_e$  of the skeleton curve in Figure 2 should be adjusted by

$$K_e := K_e (7 - n_d) / 7 \quad (2)$$

where  $n_d$  represents the number of concrete axial springs with compressive failure. Steel springs still work normally after the failure of sectional shear spring, so after sectional concrete crushed the behavior of steel bars can be well considered for studying failure patterns of columns or beams.

## 4 Treatments for Contact and Impact between Discrete Elements

During collapse process of the structure, contacts and impacts between discrete elements are inevitable. If neglecting impacts, irrational phenomena such as one element passing through another element will occur. In order to obtain reasonable result, impacts should be considered and before that, contacts between any two elements have to be detected first. Contact detection between two polygons is easy to be solved and related methods will not be given here. For improving computational efficiency, a key point is to determine the moment to trigger contact detection. Contact detection is triggered at the moment when spring group of the elements get failed in (Huang, 2006), but there are a lot of limitations in that way. When only one spring group adjacent to an element failed, the element may not fall, while the adjacent spring groups of a falling element may not get failed, for example, when a whole beam is falling, spring groups of the middle elements have no failures at all. Taking into account that only falling elements may impact other elements, an element can be defined as failure element when it meets the following requirement:

$$y_{ccu} - y_{cin} > \varepsilon_{cu} y_{cin} \quad (3)$$

where  $y_{cin}$  and  $y_{ccu}$  are central vertical coordinates of the element at original time and a particular time during calculation,  $\varepsilon_{cu}$  represents the ultimate compressive strain of concrete. Contact detections between the element and other elements will be triggered when it becomes failure element.

When two elements are judged to be collided with each other, kinestates of the elements will be determined by their pre-impact information such as masses, velocities, material properties and so on. According to the impact tests with 30 pairs

of non-reinforce concrete blocks, (Hou et al., 2007) proposed the impulse model of impact between concrete blocks as follows:

$$I = 1.3 \times 10^{-3} mv(f_c + 246.4) \left[ 1 - \frac{1}{1 + (n/1.075)^{1.158}} \right] [\exp(-\theta/1.358) + 3.986] \quad (4)$$

where  $I$  represents the impact impulse,  $m$  represents the mass of striking block,  $v$  represents the initial impact velocity of string block,  $f_c$  represents the prismatic compressive strength of concrete,  $n$  represents the mass ratio of striking block and struck block,  $\theta$  represents the initial impact angle and  $0^\circ \leq \theta \leq 5^\circ$ . When computing effect influence between failure elements, the impulse model will be adopted because its foundation is the tests of impact between concrete blocks. Apparently, it is not suitable for dealing with impact between failure element and the ground. According to the results of perfect elastic collision and perfect inelastic collision between falling beams and ground, the beams were almost in the same position finally (Zhang and Liu, 2001), therefore perfect elastic collision is used for simple when computing impact effect between failure element and the ground.

## 5 Development of Simulation Program of Structural Collapse

Simulation program for structural collapse of planar RC frame developed in the paper adopts Visual C++ 6.0 language as the compiling platform. Class libraries of MFC in the language, which encapsulate device context classes and graphic tools classes, can help to realize the visualization of the program. Numerical model and constitutive relations of the springs in the program are as mentioned above, and synchrony dynamic relaxation method is adopted as the numerical algorithm of discrete element method. In addition, values of damping ratio and calculating time step are the same as presented in (Wang and Lu, 2006).

## 6 Numerical Example

A simulation analysis has been carried out for collapse response of frame structure under earthquake, which is based on Art Building of Dujiangyan Beijie Experimental Foreign Language School – an actual building in Wenchuan earthquake-stricken area. This building is a four-storey and three-bay reinforced concrete structure, from which a plane frame is chosen for research. Figure 3 shows the load applied and dimension of beams and columns. Reinforcement of this numerical model is determined according to the practice, and the further details are not mentioned here.

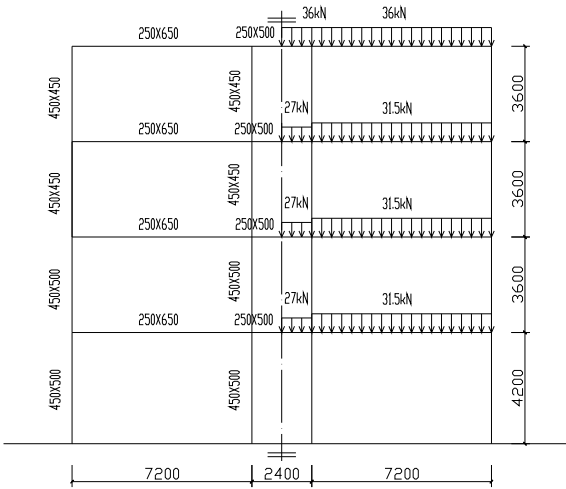
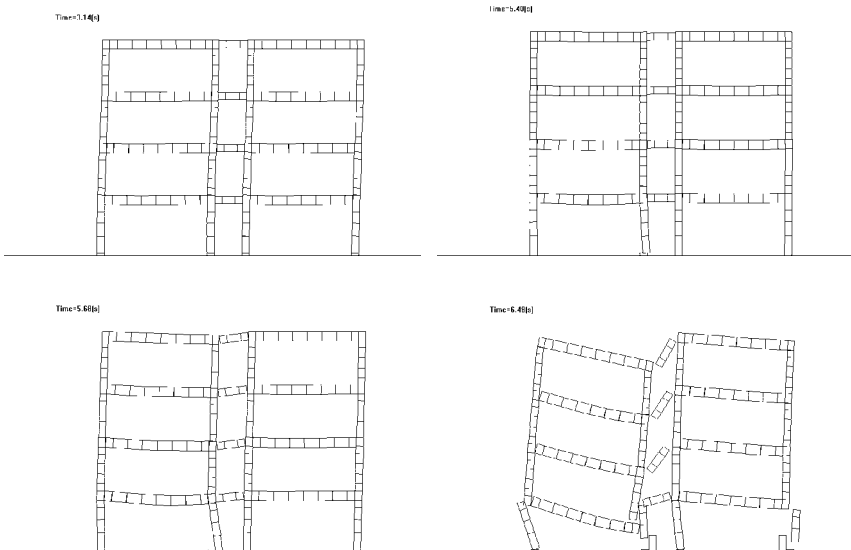


Figure 3. Dimension and load of the frame

The building suffered moderate damage which mainly presented as concrete crush at ends of columns during Wenchuan earthquake. The program developed in the paper is employed to simulate collapse process of the plane frame by inputting El Centro seismic wave (1940, N-S). Collapse occurs when peak acceleration was raised to  $1.7g$ , and frame states in several representative moments are obtained from the whole process, as shown in Figure 4.



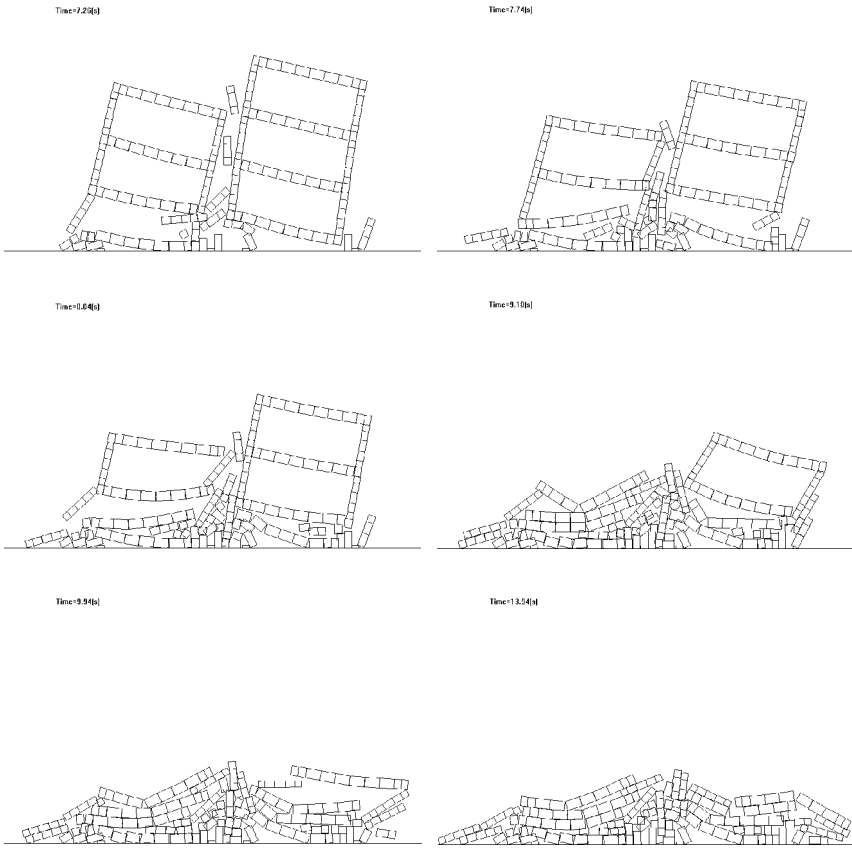


Figure 4. Simulation of seismic collapse process for RC frame structure

Figure 4 directly illustrates the whole collapse process of this frame under earthquake. Although the amplitude of earthquake acceleration is relatively higher in the first several seconds, the cumulative damage of the structure is not severe and plastic hinges at the end of columns has not fully developed. At about 5.40s, the bottom of column in the left-middle of ground floor crushed and the entire structure began to collapse, but there were no obvious signs of frame beams. Later, both ends of side columns of ground floor crushed, followed by the sharply falling upper frame. The mid-bay beam was pulled off and fell freely due to the non-uniform displacement between left and right bays, while beams of side bays kept relatively intact. The whole collapse process took almost 8.54s and terminated at about 13.94s.

Although the actual building did not collapse during Wenchuan earthquake, the damage part shows very good agreement with that of simulation results. Sun et al. (2008) provides a variety of actual collapse examples of frame structures, some

damages of which match well with the results of simulation illustrated in this section.

## 7 Conclusions

In this paper, a computer program was developed to simulate the whole process of planar frame structures from initial state to collapse under earthquakes with the method of discrete element. Then a series of computation works were conducted with this program on a real structure in Wenchuan earthquake-hit area, the result of which leads to the following conclusions:

1. The simulation on the whole process of frame structures under earthquake approximately matches the real seismic damage and basically meets the expectation. Thus, the accuracy of computation method and reliability of simulation program is verified.
2. The peak acceleration of earthquake demanded to cause structural collapse in these computation works largely exceeds the expectation. There are two reasons for this: firstly, the bond slip between bars and concrete and the change of damping ratio in the collapse process have not given careful consideration; the other is that frame structures definitely have excellent anti-collapse capacity.
3. As a non-continuum numerical algorithm method, discrete element method can be successfully applied to structural collapse analysis on the premise of meeting engineering accuracy requirement. The factors that influence the computation accuracy include the size of elements, the number of concrete springs, the selection of hysteric model of each spring and the definition of failure criterion.

## References

- Civil and Structural Groups of Tsinghua University, Xinan Jiaotong University and Beijing Jiaotong University. (2008). Analysis on seismic damage of buildings in the Wenchuan earthquake. *Journal of Building Structures*, 29(4):1-9 [in Chinese].
- Hakuno M. (1996). Simulation of 3-D concrete-frame collapse due to dynamic loading. In: *Proceedings of 11th WCEE* (CD).
- Huang Q.H. (2006). Study on spatial collapse responses of reinforced concrete frame structures under earthquake. Shanghai: Tongji University, School of Civil Engineering.
- Hou J. and Lin F. et al. (2007). Impulse model of impact between concrete blocks. *Journal of Vibration and Shock*, 26(10):1-5 [in Chinese].
- Katahira N. and Isobe D. et al. (2008). Development of macro-model seismic collapse simulator for framed structures using ASI-Gauss technique. In: *Proceedings of 14th WCEE* (CD).
- Sun B.T. and Yan P.L. et al. (2008). Overview on seismic damage to different structures in Yingxiu Town during Wenchuan earthquake. *Journal of Earthquake Engineering and Engineering Vibration*, 28(5):1-9 [in Chinese].

- Sun J.J. and Ma Q. et al. (2008). Building damage in cities and towns located in higher intensity areas during Wenchuan earthquake. *Journal of Earthquake Engineering and Engineering Vibration*, 28(3):7-15 [in Chinese].
- Tagel-Din H. and Meguro K. (2000). Analysis of small scale RC building subjected to shaking table test using applied element method. In: *Proceedings of 12th WCEE* (CD).
- Utagawa N. and Kondo I. et al. (1992). Simulation of demolition of reinforced concrete buildings by controlled explosion, *Microcomputers in Civil Engineering*, 7:151-159.
- Wang F. and Chaudat T. et al. (2008). Seismic collapse tests and simulation of reinforced concrete frames with not confined beam-column joints. In: *Proceedings of 14th WCEE* (CD).
- Wang Q. and Liu X.L. (2006a). Simulation analysis of seismic collapse process for frame structures by DEM. *Journal of Earthquake Engineering and Engineering Vibration*, 26(6):77-82.
- Wang Q. and Liu X.L. (2006b). Numerical algorithm of distinct element method. *Journal of Tongji University(Natural Science)*, 34(12):91-93 [in Chinese].
- Wang Q. and Liu X.L. (2007). The improvement of segment-multi-spring model of DEM. *Journal of Shenyang Jianzhu University*, 23(2):91-93 [in Chinese].
- Zhang L.M. and Liu X.L. (2001). Some issues in the collapse analysis of frame structures. *Journal of Shanghai Jiaotong University*, 35(10):1578-1582 [in Chinese].

# High-Order Spring-Dashpot-Mass Boundaries for Cylindrical Waves

Xiuli Du<sup>1\*</sup> and Mi Zhao<sup>1</sup>

<sup>1</sup>The Key Laboratory of Urban Security and Disaster Engineering, Ministry of Education, Beijing University of Technology, Beijing 100124, China

**Abstract.** An accurate local time-domain transmitting boundary, called high-order spring-dashpot-mass boundary (HSDMB), is proposed for modeling the propagation of cylindrical waves in infinite elastic medium. HSDMB is a high-accuracy approximation to the exact analytical transmitting boundary, which can be easily implemented into finite element method and even commercial software, leading to stable and efficient computation. Numerical examples are given to indicate the effectiveness of HSDMB.

**Keywords:** soil-structure interaction, transmitting boundary, cylindrical wave, finite element method

## 1 Introduction

Finite element analysis of dynamic foundation and soil-structure-interaction problems requires the use of transmitting (also called nonreflecting, absorbing, or radiation) boundary to model dynamic behavior of truncated infinite medium, i.e., the propagation of waves from near field through artificial boundary into far field (where such waves are called outgoing waves). The transmitting boundary should be applicable to time-domain analysis, so that the finite element method can solve any possible nonlinearity in the near field. For the cylindrical wave propagation in infinite elastic medium, which can be derived from many engineering problems such as pile foundation under dynamic loads, the transmitting boundary at a cylindrical artificial boundary is local in space. Exact analytical transmitting boundary for such problem is a nonlocal temporal convolution of interaction stress and displacement on cylindrical artificial boundary, which results from their frequency-domain analytical dynamic-stiffness relation. It will therefore lead to computational complexity with large costs and storages. As an alternative, several mechanical-model-based boundaries (Lysmer and Kuhlemeyer, 1969; Underwood and

---

\* Corresponding author, e-mail: duxiuli@bjut.edu.cn

Geers, 1981; Deeks and Randolph, 1994; Kellezi, 2000; Liu and Li, 2005; Du and Zhao, 2006), consisting of spring-dashpot-mass elements with frequency-independent parameters and containing auxiliary internal degrees of freedom, have been developed due to the following advantages: (1) conceptual clarity with physical insight; (2) good compatibility with the interior finite element method because the finite-element model is actually a generalized spring-dashpot-mass system, leading to that the total dynamic soil-structure-interaction system can be solved stably by a standard dynamics program; and (3) simple and easy implementation even into commercial finite-element software. However, the accuracy of these transmitting boundaries may be insufficient in many cases, due to using only a dashpot and possibly a spring and a mass to simply represent the dynamic behavior of the truncated infinite medium. Note that the (consistent or systematic) lumped-parameter models (Wolf, 1994; Wu and Lee, 2002; Wu and Lee, 2004) for foundation vibration analysis contains more spring-dashpot-mass elements and internal degrees of freedom, therefore leading to higher accuracy. The lumped-parameter models can actually be applied to the case of cylindrical wave, but note that their spring, dashpot and mass parameters are real but not necessary positive constants. In a word, it is an effective way to improve accuracy of the mechanical-model-based boundary by increasing the number of spring-dashpot-mass elements and internal degrees of freedom. This paper develops a new accurate mechanical-model-based boundary called high-order spring-dashpot-mass boundary (HSDMB) for cylindrical waves.

## 2 Exact Analytical Transmitting Boundaries

Exact analytical transmitting boundaries for outgoing cylindrical waves at a cylindrical artificial boundary ( $r = R$ ) are the dynamic-stiffness relations in the frequency domain

$$f_j(\omega) = S_j(\omega)u_j(\omega) \quad (1)$$

where  $\omega$  is frequency;  $j = r, \theta, z$  denote the radial, circumferential, and axial boundaries, respectively, for the cylindrical P, SV, and SH waves;  $u_j$  are displacements at artificial boundary;  $f_j$  are interaction stresses of finite domain to infinite medium;  $S_j(\omega)$  are dynamic stiffness of infinite medium, listed in Table 1. Applying the convolution theorem to Equation (1) will result in the nonlocal exact analytical transmitting boundaries as temporal convolutions in the time domain.

### 3 High-Order Spring-Dashpot-Mass Boundaries (HSDMBs)

High-order spring-dashpot-mass boundaries (HSDMBs) shown in Figure 1 are proposed as accurate alternative to the exact analytical transmitting boundaries. For clarity and simplicity, the subscript  $j$  is omitted in this section. The time-domain Equations of motion of HSDMB are

$$(c_0 + c_1)\dot{u} + k_0u = c_1\dot{u}_1 + f \tag{2a}$$

$$m_l\ddot{u}_l + (c_l + c_{l+1})\dot{u}_l = c_l\dot{u}_{l-1} + c_{l+1}\dot{u}_{l+1} \quad l = 1, \dots, N \tag{2b}$$

with  $u_0 = u$  and  $c_{N+1} = u_{N+1} = 0$ , where  $u_l$  are displacements of the internal degrees of freedom; a dot over the variable denotes the derivative to time; and  $k_0$ ,  $c_l$ , and  $m_l$  are spring, dashpot, and mass parameters, respectively. Performing Fourier transformation to Equation (2) leads to the dynamic stiffness of HSDMB

Table 1. Dynamic stiffness of infinite medium for cylindrical waves

Radial dynamic stiffness for cylindrical P wave	$S_r(\omega) = S_r(\omega_s, \eta);$	$S_r(\omega_s, \eta) = S_r^0[k_r(\omega_s, \eta) + i\omega_s c_r(\omega_s, \eta)]$
static stiffness $S_r^0$ ;	dimensionless spring and damping coefficients $k_r(\omega_s, \eta)$ and $c_r(\omega_s, \eta)$	$S_r^0 = \frac{2G}{R}$ $k_r(\omega_s, \eta) = 1 - \frac{\eta^2 \omega_p}{2} \frac{J_0(\omega_p)J_1(\omega_p) + Y_0(\omega_p)Y_1(\omega_p)}{J_1^2(\omega_p) + Y_1^2(\omega_p)}$ $c_r(\omega_s, \eta) = \frac{\eta}{\pi\omega_p} \frac{1}{J_1^2(\omega_p) + Y_1^2(\omega_p)}$
Circumferential dynamic stiffness for cylindrical SV wave	$S_\theta(\omega) = S_\theta(\omega_s);$	$S_\theta(\omega_s) = S_\theta^0[k_\theta(\omega_s) + i\omega_s c_\theta(\omega_s)]$
static stiffness $S_\theta^0$ ;	dimensionless spring and damping coefficients $k_\theta(\omega_s)$ and $c_\theta(\omega_s)$	$S_\theta^0 = \frac{2G}{R}$ $k_\theta(\omega_s) = 1 - \frac{\omega_s}{2} \frac{J_0(\omega_s)J_1(\omega_s) + Y_0(\omega_s)Y_1(\omega_s)}{J_1^2(\omega_s) + Y_1^2(\omega_s)}$ $c_\theta(\omega_s) = \frac{1}{\pi\omega_s} \frac{1}{J_1^2(\omega_s) + Y_1^2(\omega_s)}$
Axial dynamic stiffness for cylindrical SH wave	$S_z(\omega) = S_z(\omega_s);$	$S_z(\omega_s) = S_z^0[k_z(\omega_s) + i\omega_s c_z(\omega_s)]$
high-frequency-limit stiffness $S_z^0$ ;	dimensionless spring and damping coefficients $k_z(\omega_s)$ and $c_z(\omega_s)$	$S_z^0 = \frac{G}{2R}$ $k_z(\omega_s) = 2\omega_s \frac{J_0(\omega_s)J_1(\omega_s) + Y_0(\omega_s)Y_1(\omega_s)}{J_0^2(\omega_s) + Y_0^2(\omega_s)}$ $c_z(\omega_s) = \frac{4}{\pi\omega_s} \frac{1}{J_0^2(\omega_s) + Y_0^2(\omega_s)}$

In Table 1,  $R$  is radius of cylindrical artificial boundary;  $G$  is shear modulus;  $\eta = c_p/c_s$  is ratio of P-wave velocity to S-wave velocity;  $\omega_s = R\omega/c_s$  is S-wave dimensionless frequency;  $\omega_p = R\omega/c_p = \omega_s/\eta$  is P-wave dimensionless frequency;  $J_0, J_1$  are the first kind Bessel functions of order zero and one;  $Y_0, Y_1$  are the second kind Bessel functions of order zero and one; and  $H_0^{(2)}, H_1^{(2)}$  are the second kind Hankel functions of order zero and one.

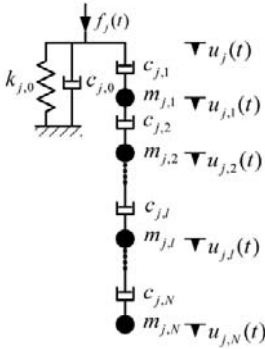


Figure 1. High-order spring-dashpot-mass boundaries (HSDMBs) for cylindrical waves.

The first subscripts  $j = r, \theta, z$  denote radial, circumferential and axial boundaries, respectively, for cylindrical P, SV and SH waves.

$$\bar{S}(\omega) = \frac{f(\omega)}{u(\omega)} = k_0 + i\omega(c_0 + c_1) + i\omega A_1 \tag{3a}$$

$$A_l = -\frac{c_l^2}{c_l + c_{l+1} + i\omega m_l + A_{l+1}} \quad l = 1, \dots, N \tag{3b}$$

with  $A_{N+1} = c_{N+1} = 0$ , where  $A_l = -c_l u_l(\omega) / u_{l-1}(\omega)$  are auxiliary variables.

Introduce dimensionless spring parameter  $d$ , dashpot parameters  $a_l$ , and mass parameters  $b_l$ , all of which are independent of the material constants of infinite medium and the location of cylindrical artificial boundary, and satisfy

$$k_0 = Sd ; \quad c_l = \rho c a_l \quad l = 0, \dots, N ; \quad m_l = \rho R b_l \quad l = 1, \dots, N \tag{4}$$

where  $\rho$  is mass density;  $S = S_j^0 (j = r, \theta, z)$ ; and  $c = c_p$  or  $c_s$ . These dimensionless parameters are obtained by identifying rational approximation of exact dynamic stiffness of infinite medium using penalty genetic-simplex optimization algorithm, and then by comparing continued-fraction expansion of the resulting

rational approximation with continued-fraction dynamic stiffness of HSDMB. The parameters are listed in Tables 2 and 3 for practical application. The HSDMB with these parameters is dynamically stable due to that all poles of rational form of its dynamic and flexibility have negative real parts. The dynamic-stiffness of radial boundary for cylindrical P wave is shown in Figure 2.

Table 2. Dimensionless parameters for radial and circumferential HSDMBs

	N=1	N=2	N=3
$d$	1.0000000 E+00	1.0000000 E+00	1.0000000 E+00
$a_0$	2.7562626 E-01	1.1295445 E-01	5.4651680 E-02
$a_1$	7.2437374 E-01	8.8704555 E-01	9.4534832 E-01
$b_1$	1.0627400 E+00	1.5764527 E+00	1.7880150 E+00
$a_2$	—	2.7396532 E-01	3.8929369 E-01
$b_2$	—	3.8650309 E-01	5.1546393 E-01
$a_3$	—	—	1.7193378 E-01
$b_3$	—	—	3.9127731 E-01

Table 3. Dimensionless parameters for axial HSDMB

	N=2	N=3	N=4
$d$	0.0000000 E+00	0.0000000 E+00	0.0000000 E+00
$a_0$	1.1592342 E+02	3.0845686 E+02	5.4214908 E+02
$a_1$	-1.1192342 E+02	-3.0445686 E+02	-5.3814908 E+02
$b_1$	-6.3013868 E+03	-4.6434336 E+04	-1.4489398 E+05
$a_2$	-1.1852790 E+03	-1.0573972 E+04	-3.4818684 E+04
$b_2$	-3.5559404 E+03	-2.0100788 E+04	-5.4576248 E+04
$a_3$	—	-3.2529318 E+03	-1.8125074 E+04
$b_3$	—	-2.9352973 E+04	-6.5761264 E+04
$a_4$	—	—	-3.7727035 E+03
$b_4$	—	—	-8.2104268 E+04

## 4 Numerical Examples

This section analyzes a plane-strain infinite medium with a cavity of radial 1 m, where the radial, circumferential, or axial uniform triangular-impulse loads (with peak value of  $5 \times 10^5$  N/m and acting time of 0.02 s) act on the internal radial to form the corresponding cylindrical P, SV, or SH wave. The shear modulus of medium is 45 MPa, and the mass density 2000 kg/m<sup>3</sup>. To investigate the effect of the boundary location, the artificial boundary is placed at  $R = 2$  m and even directly at

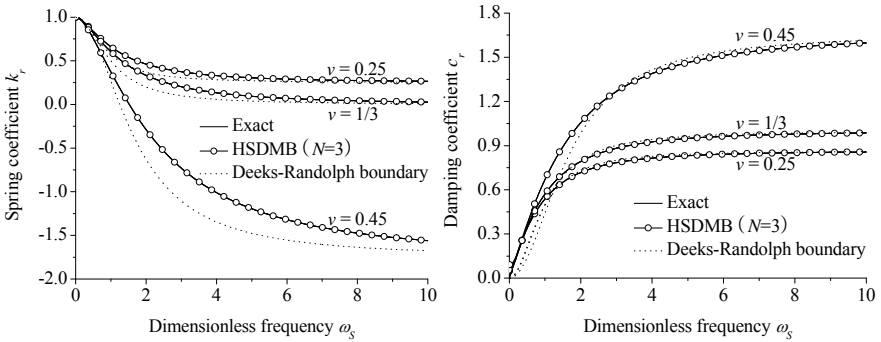


Figure 2. Dynamic stiffness of radial boundaries for cylindrical P wave with several typical Poisson's ratio  $\nu$

the radius  $R = 1$  m of the cavity for a more severe test, respectively. The extended mesh solution is used as an exact reference for each case. Comparisons are made with Deeks-Randolph boundary (Deeks and Randolph, 1994) which have been validated to be more accurate for cylindrical waves than the viscous boundary and the doubly-asymptotic boundary. The implicit average acceleration method of Newmark family and the explicit method by Du and Wang (2000) are respectively used as the time-integration solver.

Only the radial displacement solutions at the internal radius of the cavity for cylindrical P wave with Poisson's ratio of 0.45 are given in Figure 3. It is clear that the solution using HSDMB coincides with the extended mesh solution in each case, so that the former is indistinguishable from the later. Although the Deeks-Randolph boundary gives an accurate result, the deviation from the extended mesh solution can be seen clearly, and it increases as the artificial boundary moves towards the source. The same observations can be obtained for cylindrical SV and SH waves.

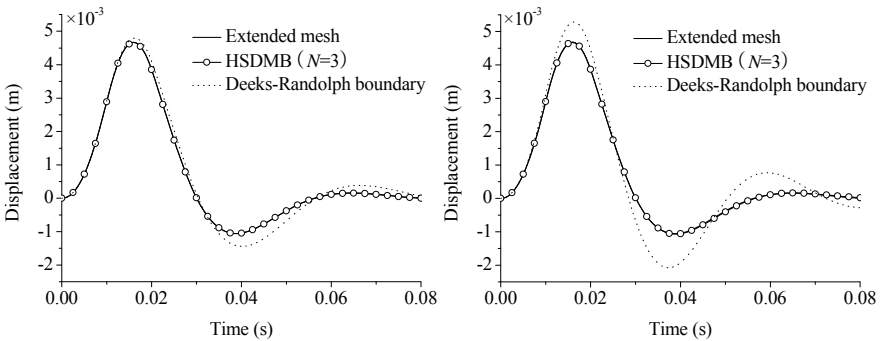


Figure 3. Radial displacements at internal radius for cylindrical P wave (Poisson's ratio  $\nu=0.45$ ) using radial boundaries with artificial boundary at  $R = 2$  m (left) and  $R = 1$  m (right)

## 5 Conclusions

High-order spring-dashpot-mass boundary (HSDMB) is an effective method modeling the propagation of outgoing cylindrical waves. The radial and circumferential HSDMBs with  $N=3$  for the cylindrical P and SV waves, and axial HSDMB with  $N=4$  for the cylindrical SH wave have very sufficient accuracy and are recommended to use. Although HSDMB is proposed only for the cylindrical waves, it can also be applied to many problems which may be approximately simplified as such model, just as done by viscous boundary, viscous-spring boundary, and so on. These extended applications will be studied in future.

## Acknowledgements

This work was supported by the National Basic Research Program of China (2007CB714203) and the Major Research Plan of the National Natural Science Foundation of China (90715035, 90715041, 90510011).

## References

- Deeks A.J. and Randolph M.F. (1994). Axisymmetric time-domain transmitting boundaries. *Journal of Engineering Mechanics*, 120(1), 25–42.
- Du X. and Wang J. (2000). An explicit difference formulation of dynamic response calculation of elastic structure with damping. *Engineering Mechanics*, 17(5), 37–43 [in Chinese].
- Du X. and Zhao M. (2006). A stress artificial boundary in FEA for near-field wave problem. *Chinese Journal of Theoretical and Applied Mechanics*, 38(1), 49–56 [in Chinese].
- Kellezi L. (2000). Local transmitting boundaries for transient elastic analysis. *Soil Dynamics and Earthquake Engineering*, 19, 533–547.
- Liu J. and Li B. (2005). A unified viscous-spring artificial boundary for 3-D static and dynamic applications. *Science in China Ser. E*, 48(5), 570–584.
- Lysmer J. and Kuhlemeyer R.L. (1969). Finite dynamic model for infinite media. *Journal of the Engineering Mechanics Division*, 95(EM4), 859–877.
- Underwood P. and Geers T.L. (1981). Doubly asymptotic boundary-element analysis of dynamic soil-structure interaction. *International Journal of Solids and Structures*, 17, 687–697.
- Wolf J.P. (1994). *Foundation vibration analysis using simple physical models*, Prentice Hall, Englewood Cliffs, NJ.
- Wu W.H. and Lee W.H. (2002). Systematic lumped-parameter models for foundations based on polynomial-fraction approximation. *Earthquake Engineering and Structural Dynamics*, 31, 1383–1412.
- Wu W.H. and Lee W.H. (2004). Nested lumped-parameter models for foundation vibrations. *Earthquake Engineering and Structural Dynamics*, 33, 1051–1058.

*“This page left intentionally blank.”*

# Unified Formulation for Real Time Dynamic Hybrid Testing

Xiaoyun Shao<sup>1\*</sup> and Andrei M. Reinhorn<sup>2</sup>

<sup>1</sup>Department of Civil and Construction Engineering, Western Michigan University, Kalamazoo, MI 49008, USA

<sup>2</sup>Department of Civil, Structural and Environmental Engineering, University at Buffalo, The State University of New York, Buffalo, NY 14260, USA

**Abstract.** This paper proposes a unified formulation for Real time dynamic hybrid testing (RTDHT), which is a structural seismic response simulation method combining the numerical simulation of the *computational substructure* and the physical testing of the *experimental substructure*. By introducing a set of splitting coefficient matrices to the general equation of motion of the structural model subjected to investigation, various seismic testing methods can be formulated, including real time pseudo-dynamic substructure testing, effective force testing and shake table testing. This paper first reviews the seismic testing methods currently used in earthquake engineering with a brief introduction about the RTDHT. Then the unified formulation is presented with a detailed discussion of the splitting coefficient matrices. Hardware components necessary to implement the unified formulation RTDHT are integrated into a unified test platform. While a number of tests were performed in medium scale, a small-scale pilot setup was used in the verification tests. Test results which validated the concept of the proposed unified formulation and the feasibility of the corresponding platform for RTDHS are discussed at last.

**Keywords:** seismic testing, hybrid testing, real time, unified formulation

## 1 Introduction

Laboratory seismic testing of civil structural components and systems includes Quasi-static testing (QST), Pseudo dynamic testing (PSD), Shake table testing (STT), Effective force testing (EFT) and the newly developed Real time dynamic hybrid testing (RTDHT). RTDHT shown in Figure 1 combines the use of shake tables, actuators, and computational engines for the seismic response simulation of structures. The structure to be simulated is divided into a physical experimental substructure and one or more computational substructures. The interface forces between the substructures are imposed by the actuators and resulting displace-

---

\* Corresponding author, e-mail: xiaoyun.shao@wmich.edu

ments and velocities are fed back to the computational engine. The earthquake ground motion, or motion of other computational substructures, is applied to the experimental substructure by the shake tables (for more details see Reinhorn et al., 2005).

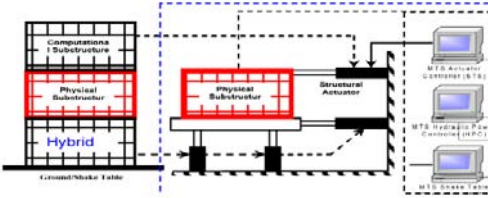


Figure 1 Real time dynamic hybrid testing (RTDHT) system

Table 1 Summary of laboratory seismic testing methods

	<i>Fast / Real time</i>	<i>Sub-structure</i>	<i>Dynamic effect</i>	<i>Loading Device</i>	
				Actuator	Shake Table
QST	No	Yes	Actuator imposes predefined displacement or force quasi-statically, no dynamic effect.	Displ. / force	N/A
PSD	Slow	No	Dynamic response including interface interaction with the computation substructure is numerically simulated from the equation of motion and applied by actuator in displacement.	Displ.	N/A
	Fast	Yes	Yes	Realistic dynamic effect achieved in the structural assembly.	N/A
EFT	Yes	Yes	Effective force directly applies to the lumped mass of the structural model.	Force	N/A
<b>RTDHT</b>	Yes	Yes	Realistic inertial force achieved in the experimental substructure and interface force between substructures applied by actuator.	Force	Accel.

Table 1 summarizes the speed of applying load, compatibility with substructure techniques, achieved dynamic effects and loading devices used in various laboratory seismic testing methods. QST does not include any dynamic effect while EFT is limited to test structural model with lumped mass. STT is not suitable for testing of large scale model. Although both fast PSD and RTDHT testing methods use substructure techniques involving both physical testing and online computations to obtain the seismic response of the global system. The latter method produces real inertial effects in the physical structural assembly while the former method only computationally simulates such effect. Therefore RTDHT allows a researcher to focus on specific problems represented in the experimental substructure under the most realistic dynamic loading conditions using the emerging computational pow-

er in tandem with the state-of-the-art control systems. Moreover, the testing capability of RTDHT are extended significantly by the proposed unified formulation in that various seismic testing methods in Table 1 can be conducted by the developed RTDHT system without individual numerical algorithm and control system modifications.

## 2 Unified Formulation of RTDHT

A derivation for substructure formulation in the Real time dynamic hybrid testing (RTDHT) can be obtained by partitioning the equation of motion describing the global structural model, the equation of motion for the experimental substructure then becomes (Shao, 2006):

$$\mathbf{M}_e \ddot{\mathbf{x}}_e + \mathbf{C}_e \dot{\mathbf{x}}_e + \mathbf{f}_e(\mathbf{x}_e, \dot{\mathbf{x}}_e) = -\mathbf{M}_e \mathbf{R} \ddot{\mathbf{u}}_g + \mathbf{T}_e \quad (1)$$

where  $\mathbf{M}_e$ ,  $\mathbf{C}_e$  are the mass and damping matrices,  $\mathbf{f}_e(\mathbf{x}_e, \dot{\mathbf{x}}_e)$  represents the inelastic response of the experimental substructure.  $\ddot{\mathbf{x}}_e$ ,  $\dot{\mathbf{x}}_e$  and  $\mathbf{x}_e$  are vectors of experimental substructure's acceleration, velocity and displacement/rotation associated with each degree-of-freedom relative to the ground reference frame. Terms on the left side of Equation (1) are the idealized model of the experimental substructure that will actually be physically replicated from the prototype structure during an RTDHT. The input to the experimental substructure in Equation (1) consists of the base acceleration  $\ddot{\mathbf{u}}_g$  and the interface force vector  $\mathbf{T}_e$ , resulting from the interaction between the computational and experimental substructures.  $\mathbf{R}$  is the ground motion scale and direction vector. When RTDHT was first proposed, the base acceleration input was designated to be applied by the shake table and the interface forces applied by the force controlled dynamic actuators. Alternative loading configurations were identified with the progress of RTDHT development. These alternatives can be generalized in one unified formulation Equation (2) that will generate the same boundary effects to the experimental specimen as formulated in Equation (1) representing various testing methods.

$$\mathbf{M}^p_e \ddot{\mathbf{x}}_e + \mathbf{C}_e \dot{\mathbf{x}}_e + \mathbf{f}_e(\mathbf{x}_e, \dot{\mathbf{x}}_e) = -\mathbf{M}^p_e \mathbf{R} (\mathbf{E} - \boldsymbol{\alpha}_l) \ddot{\mathbf{u}}_g + (\mathbf{T}_e - \boldsymbol{\alpha}_m \mathbf{M}_e (\mathbf{R}_e \ddot{\mathbf{u}}_g + \ddot{\mathbf{x}}_e) - \mathbf{M}^p_e \mathbf{R} \boldsymbol{\alpha}_l \ddot{\mathbf{u}}_g) \quad (2)$$

in which  $\boldsymbol{\alpha}_m$  and  $\boldsymbol{\alpha}_l$  are *mass and load splitting coefficient matrices*. By setting different values of these matrices, a variety of loading cases are formulated and listed in Table 2.

In a conventional dynamic testing such as EFT, STT, full mass  $\mathbf{M}_e$  is usually required to be comprised in the physical specimen. The inertia forces are therefore developed naturally during the testing. However, for structures that are large with respect to the loading devices, such masses may be difficult to be built and sup-

ported. To overcome these limitations, a portion of the mass can then be modeled numerically in a computer to reduce the size of the physical mass being fabricated, installed and tested (see also Kausel, 1998 and Chen et al., 2006). The mass that is modeled analytically is defined as *virtual mass*. A mass splitting coefficient matrix  $\alpha_m$  is then defined as a diagonal matrix consisting of the ratio of the virtual mass ( $M_e^v$ ) to the total mass of the experimental substructure ( $M_e$ ) required in the simulation.

$$\alpha_m = M_e^v \cdot M_e^{-1} = (M_e - M_e^p) \cdot M_e^{-1} \tag{3}$$

The physical mass matrix  $M_e^p$  can then be expressed as  $M_e^p = (\mathbf{E} - \alpha_m)M_e$ , in which  $\mathbf{E}$  is a diagonal identity matrix.  $T_e'' = -\alpha_m M_e (R_e \ddot{u}_g + \ddot{x}_e) + T_e$  is the new force vector which must be applied to the boundaries of the reduced mass specimen during the experiment, which includes the additional inertial force related to the virtual mass of the experimental substructure. Note that the force vector contains either all, or a portion of the inertia forces, depending of the magnitude of  $\alpha_m$  and different test methods are formulated: 1)  $\alpha_m = \mathbf{E}$  represents the case of a massless specimen; all the inertia force is numerically simulated in the computer and applied to the physical substructure as an external force, known as the PSD test but conducted in real time speed; 2)  $\alpha_m = \mathbf{0}$  defines that full mass is included in the physical substructure without virtual mass in the numerical model. This test condition, with full physical mass, is defined as the Dynamic testing as compared to PSD where the inertia effects within the experimental substructure are developed physically (or “naturally”) during the RTDHT; 3)  $\mathbf{0} < \alpha_m < \mathbf{E}$  (not all the diagonal entries in  $\alpha_m$  equal to zero or unity), the required mass is divided between the physical mass attached to the specimen and the virtual mass. This is defined as a Quasi-dynamic testing (a hybrid testing method combining the dynamic and the PSD testing). Part of the inertia effects are simulated numerically while the remaining developed naturally. This method allows application of part of the dynamic loading to the physical substructure when the loading devices have limited capacities.

Table 2 Experimental substructure loading cases in RTDHT

STRUCTURAL TEST MODEL		TOTAL DYNAMIC LOAD		
$M_e^p \ddot{x}_e + C_e \dot{x}_e + f_e(x_e, \dot{x}_e)$		$-M_e^p R (\mathbf{E} - \alpha_m) \ddot{u}_g + (T_e - \alpha_m M_e (R \ddot{u}_g + \ddot{x}_e)) - M_e^p R \alpha_m \ddot{u}_g$		
Test type	Test model	Load splitting	Table accel.	Actuators forces
Pseudo-Dynamic Testing ( $\alpha_m = \mathbf{E}$ )	$C_e \dot{x}_e + f_e(x_e, \dot{x}_e)$	$\alpha_m = \mathbf{E}$	0	$T_e - M_e (R \ddot{u}_g + \ddot{x}_e)$
Dynamic Testing ( $\alpha_m = \mathbf{0}$ )	$M_e \ddot{x}_e + C_e \dot{x}_e + f_e(x_e, \dot{x}_e)$	$\alpha_m = \mathbf{E}$	0	$T_e - M_e R \ddot{u}_g$
		$\alpha_m = \mathbf{0}$	$\ddot{u}_g$	$T_e$

		$\mathbf{0} < \alpha_i < \mathbf{E}$	$(\mathbf{E} - \alpha_i) \ddot{\mathbf{u}}_g$	$\mathbf{T}_e - \mathbf{M}'_e \mathbf{R} \ddot{\mathbf{u}}_g$
Quasi-Dynamic		$\alpha_i = \mathbf{E}$	0	$-\mathbf{M}'_e \mathbf{R} \ddot{\mathbf{u}}_g + \mathbf{T}'_e$
Testing	$\mathbf{M}'_e \ddot{\mathbf{x}}_e + \mathbf{C}'_e \dot{\mathbf{x}}_e$	$\alpha_i = \mathbf{0}$	$\ddot{\mathbf{u}}_g$	$\mathbf{T}'_e$
$(\mathbf{0} < \alpha_m < \mathbf{E})$	$+\mathbf{f}'_e(\mathbf{x}_e, \dot{\mathbf{x}}_e)$	$\mathbf{0} < \alpha_i < \mathbf{E}$	$(\mathbf{E} - \alpha_i) \ddot{\mathbf{u}}_g$	$\mathbf{T}'_e - \mathbf{M}'_e \mathbf{R} \alpha_i \ddot{\mathbf{u}}_g$

During an RTDHT test the dynamic loading formulated by the right side of Equation (1) is simultaneously applied with shake tables and actuators with the load sharing that can be determined by the load splitting coefficient matrix  $\alpha_i$  in Equation (2). The ground acceleration is separated into two components, with one component assigned to the base excitation (shake table) and the other to the actuators. Several cases are notable: 1)  $\alpha_i = \mathbf{0}$ , the shake table (or base) does not move and the entire dynamic loading is applied to the experimental substructure using the actuators attached to the structure at the effective interface degrees of freedom (DOFs). This is the EFT substructure method; 2)  $\alpha_i = \mathbf{E}$ , the ground motion is applied at the base without contribution from effective forces. For substructure testing, the interface forces with the complementary computational substructure can be introduced by actuators at the appropriate interface DOFs shown by term  $\mathbf{T}_e$  in Equation (1). This is the conventional RTDHT; 3)  $\mathbf{0} < \alpha_i < \mathbf{E}$ , the ground acceleration or its effects are applied in part by shake table (or another form of base movement) and in part by actuators. Several strategies may be used for splitting the driving function between the shake table and the dynamic actuators as proposed by Kausel (1998). In fact, the characteristics of the splitting coefficients can be chosen to optimize the total power needed by the testing system or to achieve other mechanical advantages.

Therefore, Equation (2) represents the unified formulation defining the load configurations applied to the experimental substructure during the RTDHT. The three types of tests (pseudo-dynamic, dynamic and quasi-dynamic), and the associated load application splitting between the shake tables and the actuators, are identified and listed in Table 2. All seven cases shall produce the same response of the global structural model including both computational substructure and experimental substructure when subjected to ideal real time loading conditions.

### 3 Verification Test

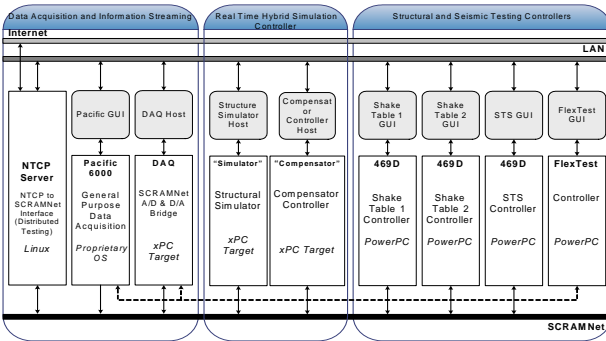


Figure 2 Hardware Components of Real Time Dynamic Hybrid Simulation test platform

The test platform developed to implement the unified formulation for RTDHT is a force-based test platform as illustrated in Figure 2 (Shao, 2006). The platform uses multiple physical and computational systems including: (i) high-performance servo-hydraulic Structural and seismic testing controllers; (ii) Data acquisition and information streaming; (iii) Real time hybrid simulation controller that includes a computational model based Real time structure simulator to perform substructure numerical simulation; and a force based System compensation controller. The System compensation controller has two functions. One is to conduct the necessary compensation of the hydraulic loading devices (i.e. time delay in response) and the other is to perform the load command calculation based on the unified formulation Equation.(2). The intent of this test platform design was to integrate and coordinate various hardware components during an RTDHT and the modularized configuration makes it flexible for future development of individual components without modifying the platform architecture.

The concept of the proposed unified formulation for RTDHT and the corresponding test platform was then experimentally verified using a small-scale pilot test setup as is shown in Figure 3, including a SDOF frame structure, a force controlled actuator (Sivaselvan et al., 2008) and a unidirectional shake table. The full mass of the structure is 79.1kg. By removing the lead bricks, a reduced mass specimen was obtained which was used for the quasi-dynamic testing where the specimen contained only 23% of the full mass. The white noise acceleration time history input was created by a function generator, using a frequency range of 0.1~10Hz and unity amplitude. Seven loading cases were conducted as listed in Table 3 defined by the unified formulation and the measured structural responses are presented in Figure 4 compared with the numerical simulation result (the thinner line). All the displacement responses exhibit a good match to the simulated response, showing that different loading cases derived from the unified formulation produce similar response in the specimen during the RTDHT.

Table 3 RTDHT loading cases

TEST NAME	$\alpha_i$	TABLE ACCELERATION	ACTUTOR FORCES
Shake Table Test		$\ddot{ii}_g$	None
Dynamic Test	$\alpha_l = 0$	0	$-M\ddot{ii}_g$
	$\alpha_m = 0$	$\ddot{ii}_g$	0
	$\alpha_l = 0.5$	$0.5\ddot{ii}_g$	$-0.5M\ddot{ii}_g$
Quasi-Dynamic Test	$\alpha_l = 0$	0	$-M(\ddot{ii}_g + \alpha_m \ddot{x})$
	$\alpha_m = 0$	$\ddot{ii}_{eq} = (\ddot{ii}_s + \alpha_m \ddot{x}) / (1 - \alpha_m)$	0
	$\alpha_l = 0.5$	$0.5\ddot{ii}_g$	$-0.5M(\ddot{ii}_g + \alpha_m \ddot{x})$



Figure 3 RTDHT test setup

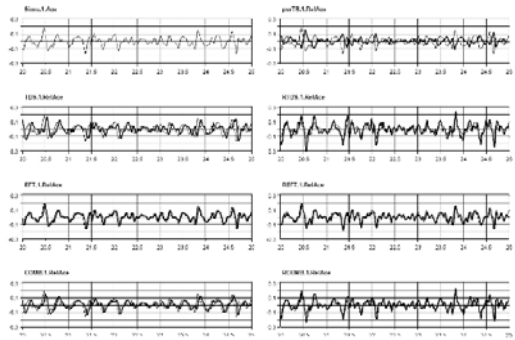


Figure 4 RTDHT verification test results

### 4 Concluding Remarks

A unified formulation is proposed for Real time dynamic hybrid testing (RTDHT), which is a seismic laboratory testing method combining the shake tables, dynamic actuators and numerical simulation in one test procedure. Using the two splitting coefficient matrices in the equation of motion of the experimental substructure, the unified formulation broadens the application range of RTDHT to include all the current modern seismic simulation methods. A corresponding test platform was developed to implement the unified formulation. Both the concept of the unified

formulation and the test platform were verified experimentally by a simple one degree of freedom specimen hybrid simulation.

## References

- Chen C. and Ricles J. M. (2006). Effective force testing method using virtual mass for real-time earthquake simulation. 8th US National Conference of Earthquake Engineering, San Francisco.
- Kausel E. (1998). New seismic testing method. I: Fundamental concepts. *Journal of Engineering Mechanics, ASCE*, 124, (5):565-570.
- Mathworks (2006). Using Simulink (Version 6). The Mathworks Inc., Natick MA.
- MTS (2003). Real Time Hybrid Structural Test System User's Manual. MTS Systems Corporation, Eden Prairie, Minnesota.
- Reinhorn A.M., Bruneau M., Chu S.Y., Shao X., and Pitman M.C. (2003). Large scale real time dynamic hybrid testing technique-shake tables substructure testing. Proceedings of ASCE Structures Congress. Seattle WA, 587.
- Reinhorn A. M., Sivaselvan M. V., Weinreber S. and Shao X. (2004). A novel Approach to dynamic force control. Proceedings of Third European Conference on Structural Control. Vienna, Austria.
- Reinhorn A.M., Shao X., Sivaselvan M.V., Pitman M. and Weinreber S. (2006). Real time dynamic hybrid testing using shake tables and force-based substructuring, Proceedings of ASCE 2006 Structures Congress St. Louis, Missouri, May 18-20, 2006.
- Shao X., Reinhorn A.M. and Sivaselvan M.V. (2006). Real time dynamic hybrid testing using force-based substructuring. 8th US National Conference of Earthquake Engineering, April 17-23, 2006, San Francisco.
- Shao X. (2006). Unified control platform for Real Time Dynamic Hybrid Simulation. Ph.D. Dissertation, University at Buffalo – State University of New York (SUNY).
- Sivaselvan M.V., Reinhorn A.M., Shao X., and Weinreber S. (2008). Dynamic force control with hydraulic actuators using added compliance and displacement compensation. *Earthquake Engineering & Structural Dynamics*, 37(15): 1785-1800.

# Research on Seismic Response Reduction of Self-Anchored Suspension Bridge

Meng Jiang<sup>1</sup>, Wenliang Qiu<sup>1\*</sup> and Baochu Yu<sup>2</sup>

<sup>1</sup> School of Civil & Hydraulic Engineering, Dalian University of Technology, Dalian 116024, P.R. China

<sup>2</sup> Department of Civil Engineering, Dalian Fishery University, Liaoning, Dalian 116023, P.R. China

**Abstract.** Because self-anchored suspension bridge is a floating system, some seismic reduction devices are installed between tower and stiffening girder to reduce the displacements and forces induced by longitudinal seismic wave. Using time history analysis method, the pounding process of a concrete self-anchored suspension bridge with main span of 180m is studied in detail. The influences of different stiffness, free gap, damping coefficient of the device and different frequency spectrum characteristics of seismic wave were considered in the analysis. The parameter analysis reveals that the pounding may increase or decrease the seismic response which is mainly depend on the free gap between the tower and the main girder. The frequency spectrum characteristics of seismic wave have great influence on the displacement, forces and times of pounding. Compared with pounding device, viscous dampers are also researched to reduce the seismic responses of self-anchored suspension bridge and the main influential factors are considered in detail. The conclusions of the study are useful for the practical design of self-anchored suspension.

**Keywords:** suspension bridge, self-anchored, anti-seismic analysis, pounding, viscous damper

## 1 Introduction

According to traditional anti-seismic methods, a structure is generally improved in anti-seism performance by strengthening the structure, enlarging cross section, and adding reinforcement. The structure stores and consumes seismic energy through its deformation and damages of varying degrees. Appropriate and effective anti-seismic means include adding an anti-seismic device to the structure so that the device and structure can work together against earthquake, in other words,

---

\* Corresponding author, e-mail: qwl2002@263.net

store and dissipate seismic energy. This helps regulate and mitigate seismic response of the structure, protect the main structure and members from damage. There are many available shock absorption measures. Popular practices include the adopting of elastic restraint, pounding bearings and dampers between the girder and piers (Fan, 1997).

Because of the difference of anchorage of main cable, the seismic responses of self-anchored suspension bridge are very different from earth anchored suspension bridge (Zhang, 2005). For the main cables are anchored to the ends of stiffening girder, which makes self-anchored suspension bridge to be a floating system, the anchor blocks and the tops of tower move with the girder, and the longitudinal displacement of girder and moment of tower are very large when strange earthquake happens. So some seismic reduction devices are installed between tower and girder to reduce the displacements and forces induced by longitudinal seismic wave. In this paper, detailed analysis, with the aid of time history analysis, is made on the shock absorption performance and influencing factors of limiting devices and dampers installed between the pylon and the girder of a 180m-span self-anchored suspension bridge under construction. The results of study are useful for the shock absorption of this type of bridges.

## 2 Engineering Background and Analysis Model

Chaoyang Huanghelu Bridge in Liaoning province is a self-anchored concrete suspension bridge (Figure 1). The spans are  $73+180+73=326\text{m}$ . The bridge has a width of 31.5m and the main cable of the main span has a rise ratio of 1/5.5. Sliding bearings are adopted at the pylons and the anchor piers. Between the pylon and the girder, a restraint rubber bearings are installed, which is fixed on the pylon. There is 15cm gap between the bearing and the girder. This bridge is of box girder structure, made of cast-in-situ pre-stressed concrete.

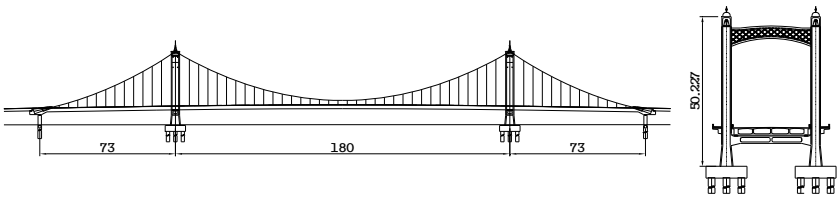


Figure 1. Chaoyang Huanghelu bridge (unit: meter)

Ridge beam model shown in Figure 2(a) is employed for dynamic analysis of this bridge (Fan, 1997). Beam element is used to simulate girder, pylons, piers and pile foundations. The main cables and hangers are treated with cable elements, the influence of the initial internal stresses of the main cables upon the main cable

stiffness is also considered. Spring elements are used to simulate the restraint of the soil around the piles.

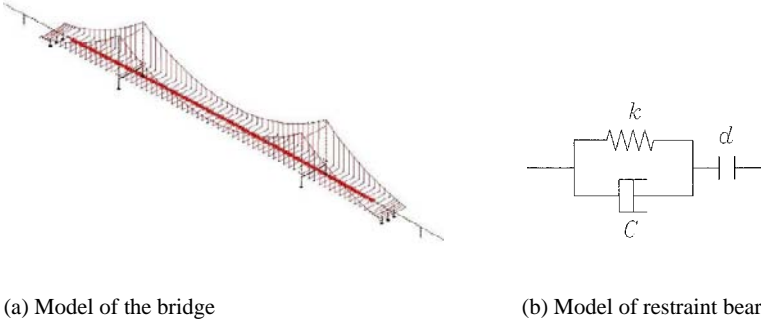


Figure 2. Dynamic analysis model

In this paper, contact elements illustrated in Figure 2(b) are used to simulate the pounding between the girder and the pylon. In the contact element model, the spring stiffness  $k$  assumes the value of the axial compression stiffness of the stop bearing, and it is  $5.12 \times 10^6$  kN/m for the rubber bearings of this bridge. The gap  $d$  in the contact element model represents the gap between the girder and the restraint bearing, and the initial gap is 0.15m for this bridge. The damping coefficient  $C$  of the model is:

$$C = 2\xi \sqrt{k \frac{m_1 m_2}{m_1 + m_2}}, \quad \xi = \frac{-\ln e}{\sqrt{\pi^2 + (\ln e)^2}} \quad (1)$$

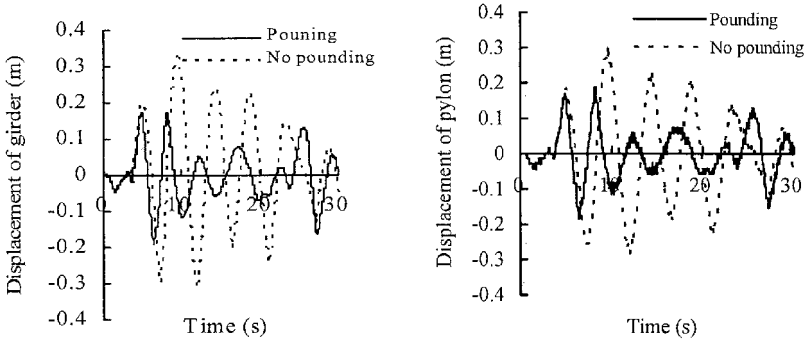
Where  $k$  is the pounding stiffness,  $m_1$  and  $m_2$  are the mass of two bodies respectively,  $\xi$  is the damping ratio,  $e$  stands for the recovery factor of energy dissipation during pounding. Considering the fact that the pounding bearing is rubber plate and remains elastic during pounding, the factor  $e$  takes a value of 1.0.

Time-history analysis method is employed for seismic response analysis. Ten artificial seismic waves fitted to normative response spectra and produced by artificial seismic wave generation program, are used. The final result of seismic response analysis is the average seismic response value of all the seismic waves.

### 3 Study on Pounding Shock Absorption

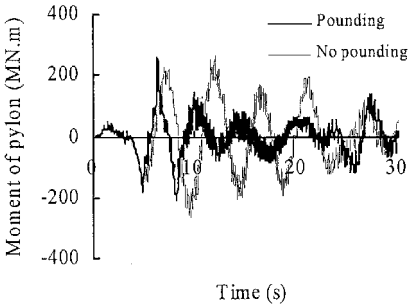
Time history analysis method is used based on the above finite element models. Artificial waves are input in longitudinal direction. The peak accelerations of the

seismic waves are 0.2g. Simulation of the pounding process of Huanghelu Bridge is performed. Seismic response time history of longitudinal displacement of the girder, longitudinal displacement of pylon top, and moment at the pylon root are obtained respectively as shown in Figure 3. The analysis results in case of non-pounding are also given in the same graphs.



(a) Longitudinal displacement of the girder

(b) Longitudinal displacement of the pylon top



(c) Moment of the pylon root

Figure 3. Time history of seismic responses

From Figure 3, it is known that when the pounding effect is considered the maximum longitudinal displacements of the pylon and the girder reduce from 0.325m and 0.299m to 0.191m and 0.186m respectively, namely a reduction of 58.7% and 62.2% when compared with the case of no pounding considered. Additionally, the moment at the pylon root reduces from  $3.24 \times 10^5$  kN.m to  $2.55 \times 10^5$  kN.m, or a reduction of 78.6% compared with a non-pounding case. So the restraint bearings play a significant role in reducing the longitudinal displacement of the girder and pylon top and in reducing the moment of the pylon.

The principal parameters influencing upon pounding response include gap  $d$ , contact stiffness  $k$ , seismic intensity and the recovery factor. The parameters that can be chosen by the designer are mainly the initial gap  $d$  and the contact stiffness  $k$ . Hence, in this article analysis focuses on the influences of these two parameters upon the pounding.

Since the deformation caused by shrinkage, creep and temperature must be considered, the initial gap must not be too small. Four values of the gap 0.05m, 0.15m, 0.25m, and 0.35m are considered for comparison in this article. The results are presented in Table 1. Judging from the data given in the table, it can be concluded that an excessively large initial gap is not performing in restraining displacement of the girder, rather it increases the moments of the pylons. With a too small initial gap, both the times and pounding force will rise quickly, which will inevitably result in local damage at the pounding portion and be harmful to seismic performance of the structure.

Table 1. Influence of initial gap  $d$  upon pounding effect

Initial gap $d$ (cm)	Moment of pylon (kN.m)	Pounding times	Pounding force (kN)
5	$2.38 \times 10^5$	15	21630
15	$2.55 \times 10^5$	3	15300
25	$3.10 \times 10^5$	2	11700
35	$3.24 \times 10^5$	0	0

For this bridge, the axial compressive stiffness of the restraint bearing is  $5.12 \times 10^6$  kN/m. In this study, three contact stiffness values  $5.12 \times 10^5$  kN/m,  $5.12 \times 10^6$  kN/m, and  $5.12 \times 10^7$  kN/m are considered in order to have a comparison analysis. The results are given in Table 2. It can be inferred from the computation results that too large or small contact stiffness reduces shock absorption performance. Therefore, at design stage the compressive stiffness of a bearing should be decided after calculation. In case of a rubber bearing, its compressive stiffness can be adjusted by changing the height of the bearing or the thickness of the rubber layers.

Table 2. Influence of contact stiffness  $k$  upon pounding effect

Contact stiffness $k$ (kN/m)	Moment of pylon (kN.m)	Pounding times	Pounding force (kN)
$5.12 \times 10^5$	$3.07 \times 10^5$	6	14800
$5.12 \times 10^6$	$2.55 \times 10^5$	3	15300
$5.12 \times 10^7$	$2.58 \times 10^5$	3	15940

## 4 Study on Seismic Reduction of Viscous Damper

### 4.1 Design of Viscous Dampers

Most of the mass of a self-anchored suspension bridge concentrated in the decking system. The seismic inertia forces of the decking system are transferred through the main cables and bearings to the pylons and anchor piers. To reduce the seismic response, viscous dampers can be installed in a longitudinal arrangement between the pylon and the girder. The dampers at these locations will not only diminish the pounding effect between a pylon and the girder, but also a portion of inertial forces can be transferred to a pylon from the girder height and thus reduces the height of the action point of inertia forces, which benefits the stress condition at the root of pylon.

In order to have a correct understanding of the influence of viscous dampers upon structure seismic performance, the model of viscous damper is established as the following expression:

$$F = C v \quad (2)$$

where  $C$  is the equivalent linear damping coefficient. The damping coefficient of viscous dampers has a direct influence upon the seismic response of a structure. With a too small value of the damping coefficient, the dampers will not have any practical purposes, too large, stringent demanding must be imposed on the dampers, in which case the economic performance may be poor.

According to analysis of the seismic response, the first order vibration mode is longitudinal floating with frequency of 0.218Hz, and the effective mass of the first order is  $2.94 \times 10^7$ kg, that is 76.9% the total mass. Apparently, under longitudinal excitation the main response of a self-anchored suspension bridge is the longitudinal floating of the first order. During primary decision of the damping coefficient, if the original damping coefficient of the structure is neglected and assuming the damping coefficient of the first order vibration mode is completely contributed by the dampers, the damping coefficient can be estimated by the following formula:

$$C = 2m\omega\xi \quad (3)$$

So we can obtain  $C=2m\omega\xi=16060$  kN.s/m. It is planned to install 8 longitudinal viscous dampers, each one having an initial damping coefficient of 2000kN.s/m.

## 4.2 Influences of the Dampers upon Seismic Response

Table 3 presents the analysis results of the moments of the pylons and the pounding forces with the input of different longitudinal waves with the same peak acceleration 0.2g. Evidently, longitudinal viscous dampers reduce the moment at the pylon root and the pounding force. Specifically for the artificial seismic wave, the moment at the pylon root is reduced from  $2.55 \times 10^5$  kN.m to  $1.85 \times 10^5$  kN.m, namely a reduction of 72.5% as compared against the case without viscous dampers. The pounding force becomes 3790kN, about 24.7% of the value in case of no dampers. The pounding is only one time. Apparently, dampers help reduce pounding force greatly.

Table 3. Influence of viscous dampers upon longitudinal seismic responses

Seismic wave	Moment of pylon (kN.m)		Pounding force (kN)	
	Damper	No damper	Damper	No damper
Artificial wave	$2.55 \times 10^5$	$1.85 \times 10^5$	15300	3790
Taft wave	$1.63 \times 10^5$	$6.30 \times 10^4$	4075	0
El Centro wave	$8.61 \times 10^4$	$6.04 \times 10^4$	0	0
Northridge wave	$6.66 \times 10^4$	$3.89 \times 10^4$	0	0

Longitudinal damping coefficient  $C$  is changed and the ten artificial waves and three recorded natural earthquake waves are input to Huanghelu Bridge longitudinally. Their time history analysis results are averaged and Figure 4 presents the average results. It can be known that with increasing damping coefficients, the moment of the pylon at root descends. However, after the damping coefficient exceeds a certain value, this descending tendency becomes less. With the damping coefficient increasing from 1500kN.s/m to 2000kN.s/m, the moment of the pylon diminishes merely 6.4%.

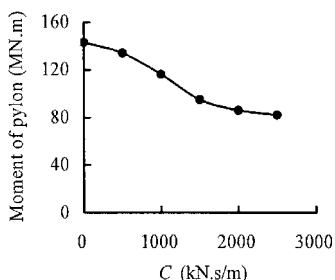


Figure 4. Influence of damping coefficient upon the moment of pylon

## 5 Conclusions

This article takes Huanghelu Bridge, a self-anchored suspension bridge, as a case in analyzing the influence of pounding among bridge members caused by earthquake. The performances of viscous damper shock absorption and energy dissipation are also studied. Based on the study, the following conclusions are arrived:

1. For a self-anchored suspension bridge, girder-pylon pounding effects can be both favorable and unfavorable to the stress conditions of the pylon. The determining factor is found to be the initial gap between the pounding bodies. With the gap increasing, the anti-seismic performance becomes less effective, and the displacement of girder and the moment of pylon increase. On the other hand, an excessively small gap increases the pounding force and times greatly, which cause local damages, this is not favorable to anti-seismic performance of the structure.
2. Not relying on any external energy input, viscous dampers are able to consume a large quantity of vibration energy without causing any supplementary static stiffness to bridge structure. Under longitudinal earthquake action, the provision of longitudinal viscous dampers at the pylon-girder jointing places reduces remarkably the moment and pounding force of the pylon. The choice of damping coefficient must consider both the shock absorption performance desired and the cost of dampers.

## References

- Deng Y. L., Peng T. P. and Li J. Z. (2007) Pounding model of bridge structure and parameter analysis under transverse earthquakes. *Journal of Vibration and Shock* 26(9):104-107 [in Chinese].
- Fan L. C. (1997) *Seismic of bridge*. Tongji University Press, Shanghai [in Chinese].
- Jamkowski R., Kezysztow W. and Fujino Y. (2000) Reduction of pounding effects in elevated bridges during earthquakes. *Earthquake Engineering and Structural Dynamics* 29:195-212.
- Li J. Z. and Fan L. C. (2005) Longitudinal seismic response and pounding effects of girder bridge with unconventional configurations, *China Civil Engineering Journal* 38(1):84-90 [in Chinese].
- Zhang Z. (2005) *Concrete suspension bridge*. People Communication Press, Beijing [in Chinese].

# Seismic Responses of Shot Span Bridge under Three Different Patterns of Earthquake Excitations

Daochuan Zhou<sup>1\*</sup>, Guorong Chen<sup>1</sup> and Yan Lu<sup>2</sup>

<sup>1</sup>Department of Civil Engineering, Hohai University, Nanjing 210098, P.R. China

<sup>2</sup>School of Water Conservancy & Environment, Zhengzhou University, Zhengzhou 450001, P.R. China

**Abstract.** This paper presents a study of the influence of three different types of seismic input methods on the longitudinal seismic response of a short, three-span, variable cross-section, reinforced concrete bridge. Research progress of the seismic model is introduced briefly. Finite element model is created for the bridge and time history analysis conducted. Three different types of illustrative excitations are considered: 1) the EI-Centro seismic wave is used as uniform excitations at all bridge supports; 2) fixed apparent wave velocity is used for response analysis of traveling wave excitations on the bridge; 3) conforming to a selected coherency model, the multiple seismic excitation time histories considering spatially variable effects are generated. The contrast study of the response analysis result under the three different seismic excitations is conducted and the influence of different seismic input methods is studied. The comparative analysis of the bridge model shows that the uniform ground motion input can not provide conservative seismic demands-in a number of cases it results in lower response than that predicted by multiple seismic excitations. The result of uniform excitation and traveling wave excitation shows very small difference. Consequently, multiple seismic excitation needs to be applied at the bridge supports for response analysis of short span bridge.

**Keywords:** seismic model, uniform excitation, traveling wave excitation, coherency model, multiple seismic excitation, time history analysis

## 1 Introduction

Seismic input is the weakest part in seismic design of long-span bridges for its uncertainties and errors. Uniform excitation and traveling wave excitation are com-

---

\* Corresponding author, e-mail: zdcpara@yahoo.com.cn

monly used currently. But they are different from the actual seismic input. The seismic excitation in each support point differ greatly for the traveling wave effect, site effect, partial coherence effect and attenuation effect during the seismic process. Thus, multiple seismic excitation method must be considered in analysis. The spatial variation of earthquake ground motions may have a significant effect on the seismic response of both long and short span bridges as indicated in many studies: Bogdanoff, Goldberg, and Schiff(1965) and Werner et al. (1977) examined traveling wave effects on the seismic response of structures; Abdel-Ghaffar and Rubin(1982) and Abdel-Ghaffar and Nazmy (1988) studied the seismic response of suspension and cable-stayed bridges; Zerva (1990) and Harichandran and Wang (1990) examined the effect of spatial variability on the response of bridge models; Zerva (1994) studied the quasi-static and dynamic response of bridge models using different coherency expressions; Harichandran, Hawwari, and Sweidan (1996) analyzed the response of long-span bridges to spatially varying excitations; Monti, Nuti, and Pinto (1996) conducted nonlinear seismic analysis of bridges subjected to multiple support excitations; Price and Eberhard (1998) examined an idealized two-span symmetric beam bridge model to non-uniform excitation; Deodatis, Saxena, and Shinozuka (2000) and Kim and Feng (2003) analyzed the effect of spatially variable ground motions on fragility curves for bridges; and Lou, Zerva, and Deodatis (2002) analyzed the effect of multiple support excitations on the linear response of two bridge models.

All aforementioned studies indicate that uniform excitations at the structures' supports cannot always predict the critical seismic demand for structural members. The present analysis is a first step in attempting to quantify effect of the spatial variation of seismic ground motions on the response of realistic bridge models, result compared with the uniform excitation and traveling wave excitation.

## 2 Bridge Model

The bridge selected for this evaluation is a reinforced concrete bridge with three spans of 45m, 76m and 45m. The plan of the bridge is shown in Figure 1. Its superstructure is a cast-in-place reinforced concrete box girder, the bent has a cross beam integrated with the box girder and column that pinned at the top of spread footing foundations. Linear elastic is created to investigate the effect of the spatial variation of ground motions on the seismic response of the bridge, and 5% Rayleigh damping is utilized in the seismic analyses. For illustration purposes, the first four modes obtained from the free vibration analysis of the model are presented in Figure 2.

### 3 Multiple Seismic Excitation Model

In this study, the ground motions are adopted from EI-Centro seismic record, the simulation technique proposed by Deodatis (1996) and Saxena et al. (2000) was employed. The ground motion time history curve and the power spectrum curve are shown in Figure 3. The seismic ground motions are simulated as non-stationary, conforming to a selected coherency model.

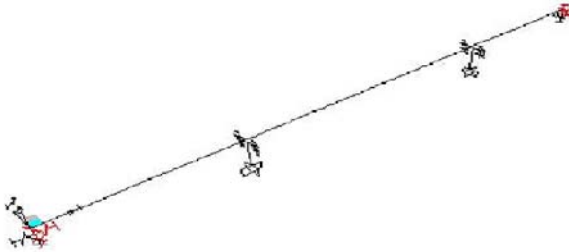
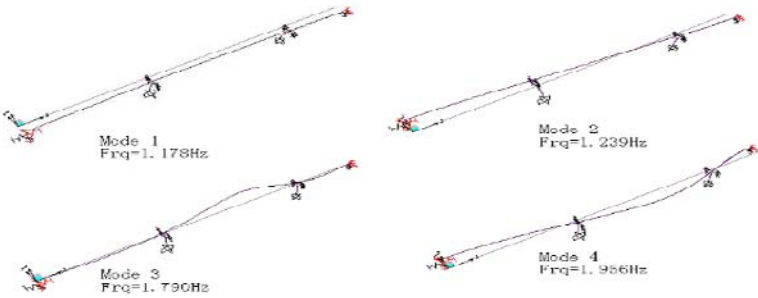


Figure 1. The 3-D bridge model



(a)Time history curve

(b)Power spectrum curve

Figure 2. First four modes of the bridge model

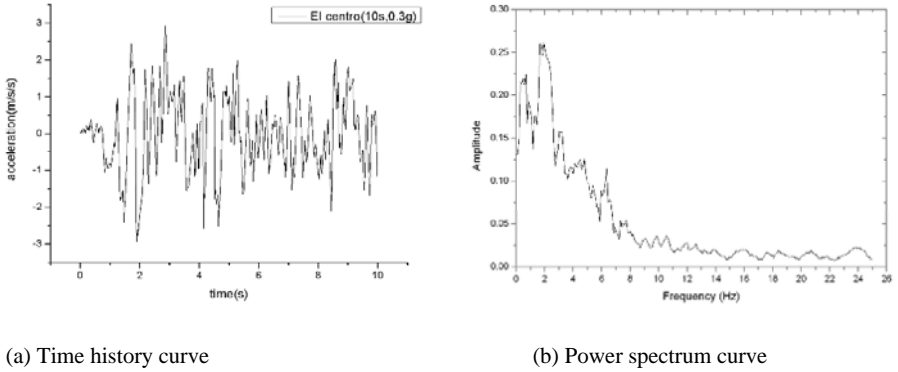


Figure 3. The ground motion information

The approach, described in detail in Deodatis (1996) and Saxena et al. (2000) is summarized in the following: the cross-spectral density matrix of the stationary process  $S_0(\omega)$ , with  $\omega$  indicating frequency, has as diagonal elements the power spectral densities of the seismic motions at each station  $S_{jj}(\omega)$ , and as off-diagonal terms the corresponding cross spectral densities:

$$S_{jk}(\omega) = \sqrt{S_{jj}(\omega)S_{kk}(\omega)}\gamma_{jk}(\omega)\exp(-i\omega\xi_{jk}/v) \tag{1}$$

with  $\gamma_{jk}(\omega)$  being the coherency between stations having a separation distance of  $\xi_{jk}$ , and the exponential term reflecting the apparent propagation of the motions with velocity  $v$ .  $S_0(\omega)$  is then factorized into the following product:

$$S_0(\omega) = H(\omega)H^{T*}(\omega) \tag{2}$$

with  $T$  indicating transpose and  $*$  complex conjugate, using, e.g. Cholesky decomposition. The elements of  $H(\omega)$  can be written in polar form as:

$$H_{jk}(\omega) = |H_{jk}(\omega)|\exp[i\theta_{jk}(\omega), j > k] \tag{3}$$

$$\theta_{jk}(\omega) = \tan^{-1}\left(\frac{\text{Im}(H_{jk}(\omega))}{\text{Re}(H_{jk}(\omega))}\right)$$

The seismic ground motions at a set of  $n$  locations on the ground surface are generated as:

$$g_j(t) = 2 \sum_{n=1}^n \sum_{l=1}^N |H_{jm}(\omega_l)| \sqrt{\Delta\omega} \cos[\omega_l t - \theta_{jm}(\omega_l) + \Phi_{ml}] \tag{4}$$

with  $j = 1, 2, \dots, n$  and  $N \rightarrow \infty$ . To generate a sample, the random phase angles  $\Phi_{ml}$  are generated randomly in the range  $(0, 2\pi)$ . The corresponding non-stationary process is obtained through the multiplication of the above equation by a modulating function [19].

The coherency model of Harichandran and Vanmarcke (2005) is utilized:

$$\gamma(\xi, \omega) = A \exp\left[-\frac{2\xi}{\alpha\theta(\omega)}(1 - A + \alpha A)\right] + (1 - A) \exp\left[-\frac{2\xi}{\theta(\omega)}(1 - A + \alpha A)\right]$$

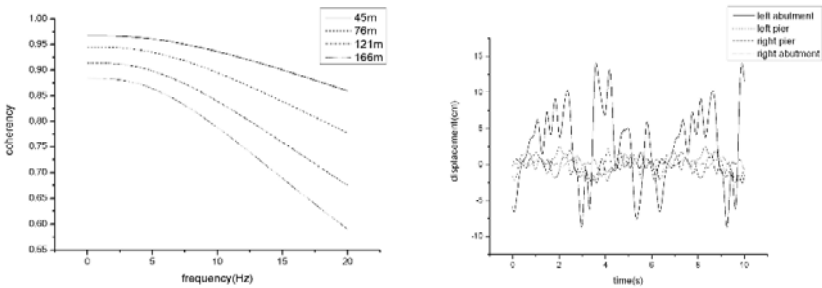
$$\theta(\omega) = k \left[ 1 + \left( \frac{\omega}{\omega_0} \right)^b \right]^{-1/2} \tag{5}$$

where  $\xi$  indicates separation distance in m,  $\omega$  represents frequency in rad/s, and the parameters of the equation assume the values:

$$A = 0.736, \alpha = 0.147, k = 5210m, \tag{6}$$

$$\omega_0 = 6.85rad/s, b = 2.78$$

which correspond to data recorded during Event 20 at the SMART-1 array, Lo-tung, Taiwan. Figure 4(a) presents the decay with frequency of the Harichandran and Vanmarcke coherency model (2005) for separation distances pertinent to the bridge. In the simulations, an apparent propagation velocity of  $v = 750m/s$  was used. The target peak ground acceleration was 0.3 g. Figure 4(b) presents the time histories of the spatially variable ground motions at the bridge’s supports used in this study.



(a) Coherency model

(b) Seismic ground motions

Figure 4. Coherency model and seismic ground motions (displacements) for the bridge.

## 5 Results and Analysis

### 5.1 Force Response Analysis

The seismic response analysis results of the bridge subjected to uniform excitations, traveling wave excitation and multiple seismic excitation are compared in terms of seismic force demand.

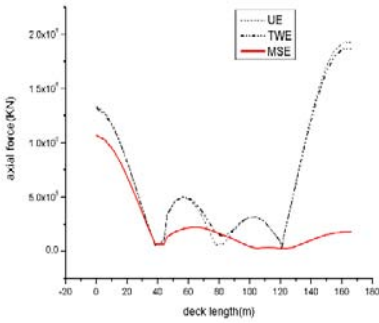


Figure 5. Axial force demand envelopes

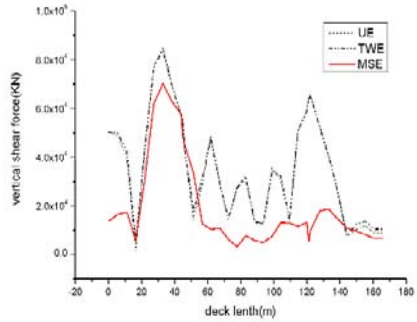


Figure 6. Vertical shear force demand envelopes

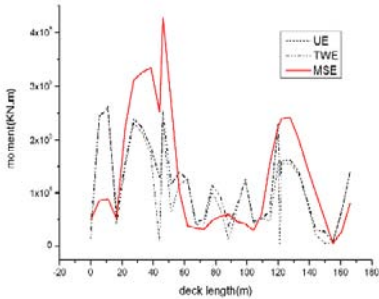


Figure 7. Moment demand envelopes

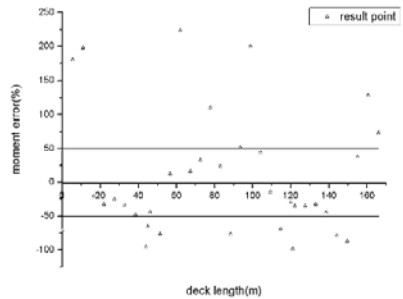


Figure 8. Moment error of the uniform excitation

Figures 5-7 show the absolute seismic force demand envelopes of the bridge deck. In all subsequent figures, ‘MSE’ denotes response quantities induced by multiple seismic excitation; ‘UE’ denotes response quantities induced by uniform excitation; ‘TWE’ denotes response quantities induced by traveling wave excitation; Figures 5-7 suggest that the response along the deck is not symmetric absolutely, even for the uniform excitation.

For axial forces (Figure 5), multiple seismic excitation produce the higher response than the uniform excitation along the middle span, the same value in the left and right pier as the uniform excitation, whereas multiple seismic excitation produce lower value than the uniform excitation in other place along the span. Traveling wave excitation produces the higher response along the middle span but the lower response along the right abutment than the uniform excitation scenario, whereas traveling wave excitation produces very small difference to the uniform excitation in other place along the span, the two result curves almost coincide with each other. The uniform excitation produces the lowest response along the middle span, whereas the multiple seismic excitation produces lower response along the span except the middle span and the piers. The axial force demand is decreased most in the right abutment when consider spatially variable effect of the ground motion.

For vertical shear forces (Figure 6), traveling wave excitation almost has the same result with the uniform excitation except very small difference in the left pier and the right abutment. Multiple seismic excitation produce lower response than the uniform excitation and the traveling wave excitation mostly along the span. The vertical shear force demand is decreased mostly when consider spatially variable effect of the ground motion.

For bending moments (Figure 7), basically all three input motion scenarios produce similar results that the higher response along the piers and lower response along other places. The multiple seismic excitation produces lower response along the middle span and higher response along the two piers than the other two seismic input method. Along the two piers, the uniform excitation and the traveling wave excitation typically underestimate the seismic demand for the bridge bending moments and that the multiple seismic excitation predicts the higher demand. Bending moments are significantly higher when spatially variable effect is considered.

## ***5.2 Error Analysis***

From the figures, the response curves of uniform excitation and traveling wave excitation almost coincide with each other. The difference is very small. This is because the span is not so long that the traveling wave effect is not obvious, also in this paper, the apparent wave velocity is determined by experience which might be different from the actual velocity. Therefore results under different velocity of traveling wave excitation need to be calculated in further study comparing to the results of uniform excitation to determine the influence of traveling wave effect.

As great differences exist in the results of the multiple seismic excitation and the other two seismic input methods, compare the result of the uniform excitation to the result of the multiple seismic excitation, the multiple seismic excitation result is used as a benchmark, taken the moment response as an example, the error

of the uniform excitation is calculated, see figure 8. If taken 50 percentage as a limit, most of the error data are within this scope except the data around the abutments, piers and the middle span which are more than 50 percentage. Therefore, the influence of different seismic input methods for bridge response is mainly around the abutments, piers middle span, the results of different seismic input methods in these locations will be of great difference.

## 6 Conclusions

In this study, the influences of three different types of seismic input methods on the seismic force demand of a short, three-span, reinforced concrete bridge are studied. In order to quantify the effect of the spatial variation of seismic ground motions on the bridge response for the particular model analyzed, three different types of excitations are considered: the first case is the multiple seismic excitation utilizing spatially variable ground motions incorporating the effects of loss of coherency and wave passage as input motions at the structures' supports, the latter two are uniform excitation and traveling wave excitation. Based on these analyses, the following conclusions are taken:

1. from the axial force envelope analysis and vertical shear force envelope analysis, the uniform excitation, correspond to uniform motions at the structures' supports, produce too large value, while multiple seismic excitation produce lower value than the uniform excitation.
2. the difference between response curves of uniform excitation and traveling wave excitation is very small.
3. multipling seismic excitation result in highest bending moment may be the controlling input motion for the design of the bridge deck.
4. the influence of different seismic input methods for bridge response is mainly around the abutments, piers and the middle span, and the results of different seismic input methods in these locations will be of great difference.
5. the present results indicate that there is difficulty in establishing uniform input motions that would have the same effect on bridge models as the spatially variable ones. Consequently, the multiple seismic excitation method should be applied at the bridge supports in analysis.

It is noted that the present analysis dealt with excitations only in the longitudinal direction of the bridge. Realistic input motions in three directions (along and normal to the bridge, and the vertical direction) need to be considered in analyses. Additionally, a suite of simulated motions needs to be applied as input excitations at the bridge supports to get the exact results. However, this study indicates that the multiple seismic excitation introduce certain features in the response of realistic models of bridges that are not captured by uniform excitation. Hence, additional research needs to be conducted in this area, so that the effects of spatially varia-

ble ground motions are further quantified and incorporated into seismic design criteria for bridges.

## References

- Abdel-Ghaffar A.M., Nazmy A.S. (1988). 3D nonlinear seismic behavior of cable-stayed bridges. *Struct Eng, ASCE*, 117:3456–77.
- Abdel-Ghaffar A.M., Rubin L.I. (1982). Suspension bridge response to multiple support excitations. *Eng Mech Div, ASCE*, 108:419–35.
- Bogdanoff J.L., Goldberg J.E., Schiff A.J. (1965). The effect of ground transmission time on the response of long structures. *Bull Seismol Soc Am*, 55:627–40.
- Deodatis G. (1996). Non-stationary stochastic vector processes: seismic ground motion applications. *Probab Eng Mech*, 11:149–67.
- Deodatis G., Shinozuka M. (1989). Simulation of seismic ground motion using stochastic waves. *ASCE EngMech*, 115(12):2723–2737.
- Deodatis G., Saxena V., Shinozuka M. (2000). Effect of spatial variability of ground motion on bridge fragility curves. Proceedings of the eighth specialty conference on probabilistic mechanics and structural reliability, University of Notre Dame, IN.
- Harichandran R.S., Vanmarcke E. (1986). Stochastic variation of earthquake ground motion in space and time. *Eng Mech Div, ASCE*, 112:154–74.
- Harichandran R.S., Wang W. (1990). Response of indeterminate two-span beam to spatially varying earthquake excitation. *Earthquake Eng Struct Dyn*, 19:173–87.
- Harichandran R.S., Hawwari A., Sweidan B.N. (1996). Response of long-span bridges to spatially varying ground motion. *Struct Eng, ASCE*, 122:476–84.
- Jennings P.C., Housner G.W., Tsai N.C. (1968). Simulated earthquake motions. California Institute of Technology: Earthquake Engineering Research Laboratory.
- Kim S.H., Feng M.Q. (2003). Fragility analysis of bridges under ground motion with spatial variation. *Int Non-Linear Mech*, 38(5):705–21.
- Lou L., Zerva A., Deodatis G. (2002). Seismic response of bridge models to spatially variable multiple support excitations. Proceedings of the fifth European conference on structural dynamics, Eurodyn2002, Munich, Germany.
- Monti G., Nuti C., Pinto P.E. (1996). Nonlinear response of bridges under multisupportexcitation. *Struct Eng, ASCE*, 122:1147–59.
- Price T.E., Eberhard M.O. (1998). Effects of varying ground motions on short bridges. *Struct Eng, ASCE*, 124:948–55.
- Ronalds. H., Erikh V. (1986). Stochastic vibration of earthquake ground motion in space and time. *ASEC, Eng Mech*, 112(2):173–87.
- Saxena V., Deodatis G., Shinaozuka M., Feng M.Q. (2000). Development of fragility curves for multi-span reinforced concrete bridges. Proceedings of the international conference on Monte Carto Simulation, Principality of Monaco.
- Shinozuka M., Deodatis G. (1988). Stochastic process models foe earthquake ground. *Probabilistic Eng Mech*, 3(3):114–23.
- Werner S.D., Lee L.C., Wong H.L., Trifunac M.D. (1977). An evaluation of the effects of traveling seismic waves on the three-dimensional response of structures, Agbajian Associates, El Segundo, CA, Report No. R-7720-4514.
- Zerva A. (1990). Response of multi-span beams to spatially incoherent seismic ground motions. *Earthquake Eng Struct Dyn*, 19:819–32.
- Zerva A. (1994). On the spatial variation of seismic ground motions and its effects on lifelines. *Eng Struct*, 16:534–46.

*“This page left intentionally blank.”*

# Seismic Response Analysis on a Steel-Concrete Hybrid Structure

Zeliang Yao<sup>1\*</sup> and Guoliang Bai<sup>2</sup>

<sup>1</sup>Department of Civil Engineering, Xi'an Technological University, Xi'an 710032, P.R. China

<sup>2</sup>School of Civil Engineering, Xi'an University of Architecture & Technology, Xi'an 710055, P.R. China

**Abstract.** The steel-concrete hybrid structure is mainly designed by foreign companies because of its complexity and China backward technology. Its stiffness and mass is non-uniform at vertical direction. The structural model is established with software SAP2000. Its dynamic behavior is studied with mode method. Results show that its mode is complicated. Its torsion response is obvious. Its one way, both way and vertical seismic response is analyzed with response spectrum method. Results show that the shear of its foundation bottom by different seismic action is similar. Its vertical seismic response should be analyzed based on the codes. Its one way and both way seismic response is analyzed with elastic time history method by three seismic waves. Results show that structural torsion response by one way and both way seismic action is similar. The shear average with three time history curves is smaller than that with response spectrum method.

**Keywords:** steel-concrete hybrid structure, seismic analysis, torsion coupling mode division response spectrum method, time history method

## 1 Introduction

The hybrid structure belongs to a new industrial structure in large thermal power plants (Dong, 2006; Cui, 2004). This structure has a wide application future in north area of China having rich coal and lacking water because of its water-efficient production technique. The structure is composed of a steel truss and steel-concrete tubular columns. On account of production needs, "A" shape structure, air cooled equipments and tens of large-diameter fans are installed on the top. Its stiffness and mass is highly non-uniform at vertical direction. Its span and suspension part is long. Its top part is rigid, its lower part is flexible, and its form is

---

\* Corresponding author, e-mail: wangzhua@163.com

like a thin-stemmed drumstick (Figure 1). Its dynamic behaviour and seismic response is complicated.

This structure is mainly designed by foreign companies until now because of its complexity and China backward technology. Foreign companies mainly use STAAD program to design it. This structure is mainly built in high seismic intensity zonings of China (Ding, 1992; Bai and Zhao, 2006). Until now, be not certain whether the foreign design is safe, whether it is accordant with China codes, whether it is economical. For one reason or another there are few references on this structure. Some electric power designing institutes of China try to design this structure based on the foreign data, but they feel blindfold in the design process because there aren't any codes relating to this structure. China electric power investment aggregative company organizes north-west electric power designing institute etc. to tackle key problem on this structure and do some basic research (Knirsch, 1990; Bai and Li, 2006). Seismic response on a steel-concrete hybrid structure is studied with finite element method in this paper. Its dynamic behaviour is studied. Its one way, both way and vertical seismic response is analyzed with response spectrum method. Its one way and both way seismic response is analyzed with elastic time history method.



Figure 1. Structural form.

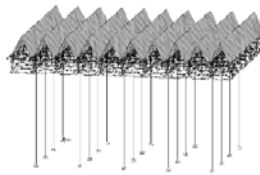


Figure 2. Computation model.

## 2 Modelling Introduction and Mode Analysis

There are twenty columns, their height is 47.8 meters. Truss height is 7.2 meters. "A" shape structure is fourteen-meter high. There are eighty fans on the truss top. Middle span is 22.62 meters. Suspension part length is 11.31 meters. Design earthquake group belongs to the first group. Seismic intensity is eight degrees. Site kind is category III. The structural model is established with software SAP2000 (Figure 2). The columns and truss members are simulated with framework elements. The joints of columns and the truss are simulated with hinges.

The structural 1st to 12th modes and periods are calculated in order to study its mass and stiffness distribution. According to the results, the 1st to 3rd periods are 1.87 to 1.95 seconds. So the structural basic period is about 1.9 seconds. The 1st to 3rd mode coupling action of is evident. The 1st mode is torsion. The 2nd mode is

X-direction horizontal movement. The 3rd mode is Y-direction horizontal movement. The modes and periods are changed from the fourth mode. So the structural main vibration mode is the vibration in two main axis directions.

### **3 Structural Seismic Response Analysis**

#### ***3.1 Torsion Coupling Mode Division Response Spectrum Analysis***

As already stated in the previous paper, the structural stiffness and mass is highly non-uniform at vertical direction, its previous several steps modes are similar, and its torsion effect is evident. So the structural seismic response can't be studied with bottom shear method. Response spectrum method can study the structural seismic response on the basis of the seismic response on a single body elastic system (Wei, 1991, China building aseismatic design standard, 2001). The dynamic relation between the structural dynamic behaviour and seismic vibration is considered with the method. Many countries use the response spectrum method because of its simple computation and rational concept (Hu, 1988). According to the standard (Hu and Jin, 2003), the structural torsion effect under one way and both way seismic action can be studied with the torsion coupling mode division response spectrum method.

##### **3.1.1 One Way Seismic Response Analysis**

Seismic acceleration is loaded on the structural X-direction and Y-direction respectively. The modes are composed with CQC and SRSS method respectively. According to the results, X-direction deformation maximum under X-direction seismic action is 46.5 mm. Y-direction deformation maximum under Y-direction seismic action is 43.9 mm. Foundation counterforce difference between these two methods is about fifteen percent because of the structural torsion effect and its previous several step mode coupling action.

##### **3.1.2 Both Way Seismic Response Analysis**

According to statistical analysis on strong earthquake observation records, seismic acceleration maximum on two directions is different. The proportion of the two is 1 to 0.85. The maximum on two directions is not certain to occur at the same time (Hu and Jin, 2003). Seismic acceleration is loaded on the structural X-direction and Y-direction at the same time. Its modes are composed with CQC method, their direction is composed with SRSS method. According to the results, X-direction

displacement maximum is 46.6 mm. Y-direction displacement maximum is 45.2 mm.

Table 1. Foundation bottom counterforce under one way and both way seismic action

Seismic effect	Foundation bottom counterforce					
	$F_x/\text{kN}$	$F_y/\text{kN}$	$F_z/\text{kN}$	$M_x/\text{kN.m}$	$M_y/\text{kN.m}$	$M_z/\text{kN.m}$
Both way	7878.8	8066.7	27.9	430001.0	420108.0	438994.7
X-direction	7866.9	204.2	27.7	11043.5	420006.1	266014.4
Y-direction	204.2	8054.8	3.2	429898.5	10881.8	376283.9

Main results on one way and both way seismic action are shown in Table 1. According to the results, the structural column bottom shear difference maximum between under X-direction seismic action and under bidirectional seismic action is 0.3%. Its column bottom shear difference maximum between under Y-direction seismic action and under both way seismic action is 2.5%. So the structural torsion effect can be analyzed with a single direction horizontal seismic action.

### 3.1.3 Structural Vertical Seismic Response Analysis

According to the standard (Hu and Jin, 2003), vertical seismic response on large span structure and long projecting structure in seismic intensity zone 8 and 9 and high-rise structure in seismic intensity zone 9 should be analyzed. According to the results on strong motion acceleration record peaks, vertical average response spectrum in all kinds of fields is basically the same as horizontal average response spectrum. Vertical seismic influence coefficient is about 0.65 times as much as horizontal seismic influence coefficient. The structural high steps vibration modes are the vibration outside the truss itself plane and local member vibration. The number of vertical vibration modes is doubtful. It is taken to 800 steps in this paper. According to the results, the vertical mass accumulative participation coefficient at 800 steps vertical vibration mode is 76.3%, and calculated vertical seismic force is about 0.035 times as much as the whole structure gravity load central value. So it is doubtful to use the response spectrum method to analyze the structural vertical seismic effect and its distribution law. It is suggested that the structural vertical seismic effect should be directly valued based on the standard (Hu and Jin, 2003).

## 3.2 Analysis with Time History Method

The often meeting seismic effect on especially irregular buildings, category A buildings and high buildings within regulated height limits should be calculated

with time history method, the average value of several time history curves is compared with the response spectrum analysis result, the often meeting seismic effect should be valued based on the larger. There are some regulations on the results as follows. The structural foundation shear with every time history curve should not be less than 65 percent of its foundation shear with the response spectrum analysis method. The average value of its foundation shear with several time history curves should not be less than 80 percent of its foundation shear with the response spectrum analysis method. Time history analysis method is a method using gradual integral method to directly calculate the integral of a structural dynamic equation based on its recovery capacity property curve and chosen seismic waves. A structural instantaneous displacement, speed and acceleration response can be obtained with the method. Its internal force change from elastic stage to inelastic stage, its whole destructive process from its member split, damage to the whole damage can be observed during a strong earthquake.

It is necessary to analyze the structural seismic effect with the elastic time history method because it is given a complicated force, it belongs to lifeblood engineering, and there aren't any relevant professional design standards and relevant earthquake historical materials in China now. According to field soil grade and design seismic classification, the structural seismic effect is analyzed with the elastic time history method by three seismic waves (Hu and Jin, 2003; Yang and Li, 2000). The waves are Lanzhou wave, Emc-fairview ave wave and a man-made wave reformed from Cpc-topanga canyon wave. Lanzhou wave form is shown in Figure 3. The structural time history curve is shown in Figure 4 when North-south Lanzhou wave is loaded on X-direction. Main results are shown in Table 2.

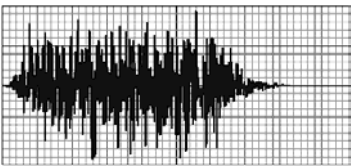


Figure 3. North-south Lanzhou wave

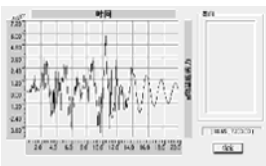


Figure 4. Foundation shear X

Table 2. Foundation bottom counterforce with three seismic waves

Seismic effect			Foundation bottom counterforce					
			$F_x/kN$	$F_y/kN$	$F_z/kN$	$M_x/kN.m$	$M_y/kN.m$	$M_z/kN.m$
Lanzhou	Both way	X max.	5702	4877	11	144846	199425	419183
		X min.	-4294	-3663	-13.4	-169712	-169534	-320329
	One way	X max.	5691	31.2	11.2	1797	199 063	198834
		X min.	-4286	-33.9	-12.3	-1758	-169216	-157076
	Both way	Y max.	4480	5723	11.5	170056	165358	405374
		Y min.	-4885	-4306	-11.6	-199396	-123030	-298422
Emc fairview ave	One way	Y max.	31.9	5721	2.2	170007	1695	259213
		Y min.	-33.0	-4299	-1.8	-199290	-1754	-192047
	One way	X max.	3862	38.1	43.5	2579	111175	128869
		X min.	-5192	-37.8	-43.3	-2216	-116443	-180304
		Y max.	38.1	3865	5.1	116436	2030	176874
		Y min.	-37.8	-5196	-7.9	-112061	-2019	-235270
Man-made	One way	X max.	9381	156.5	23.2	8540	496740	359318
		X min.	-10567	-158.5	-20.1	-8449	-489524	-375892
		Y max.	156	9398	4.0	492885	8373	423020
		Y min.	-158	-10671	-5.1	-500756	-8478	-485866

According to the results, the structural foundation shear difference maximum between under X-direction seismic action and under both way seismic action is 0.94%, its foundation shear difference maximum between under Y-direction seismic action and under both way seismic action is 4.0%. The foundation shear with every time history curve isn't less than 65 percent of the shear with the response spectrum method, the average value of the foundation shear with three curves isn't less than 80 percent of the shear with the response spectrum method, the average value of the foundation shear with three time history curves is less than the shear with the response spectrum method. So the foundation shear can be valued based on the results with the response spectrum method.

## 4 Conclusions

The structural stiffness and mass is highly non-uniform at vertical direction. Its seismic response is very complicated. The structural seismic response is analyzed with the torsion coupling mode division response spectrum method and time history method respectively. Main conclusions are shown as follows.

1. The structural basic period is about 1.9 seconds. Its mode is complicated. The 1st mode is torsion. The 2nd and 3rd modes are the vibration on two main axis directions. Its torsion effect is evident. The 1st to 3rd mode coupling action is evident. Its seismic effect should be analyzed with response spectrum method.
2. The structural torsion effect difference maximum between one way and under both way seismic action is not much. The structural torsion effect can be analyzed based on the one way seismic action. The structural vertical seismic effect can be valued based on the standard (Hu and Jin, 2003) .
3. The results with three time history curves meet the standard (Hu and Jin, 2003). The average value of the structural foundation shear with three time history curves is less than the results with the response spectrum method. The structural foundation shear can be valued based on the results with the response spectrum method.

## References

- Bai G.L. and Li H.X. (2006). Test on 600MW Air Cooled Support Structure in Large Thermal Power Plant. Xi'an: Civil Engineering School Data Room of Xi'an Architecture & Technology University [in Chinese].
- Bai G.L. and Zhao C.L. (2006). Study on 1000MW Air Cooled Support Structure in Large Thermal Power Plant. Xi'an: Civil Engineering School Data Room of Xi'an Architecture & Technology University [in Chinese].
- China Aseismic Design Standard Management Office (2001). *China Building Aseismic Design Standard*. Beijing: China Building Industry Press [in Chinese].
- Cui Y.X. (2004). Technique of Air Cooled Condenser and Stratagem of Continuous Development. *Proceedings of Learning Communion Conference of Dynamic Engineering*, Beijing, China: 39-42.
- Ding E.M. (1992). *Air Cooled Technology on Electric Power Plant*. Beijing: Water Resources and Electric Power Press [in Chinese].
- Dong J. (2006). China Development Strategy Formal Transform. *South Weekend*, 12(2), 3-9 [in Chinese].
- Hu J.X. (1988). *Earthquake Engineering*. Beijing: Earthquake Press [in Chinese].
- Hu W.Y. and Jin H. (2003). Study on Earthquake Wave Choice in Time History Analysis Method. *Journal of South Metallurgical Academy*, 15(3), 16–20 [in Chinese].
- Knirsch H. (1990). Design and Construction of Large Direct Dry Cooled Units for Thermal Power Plants. ASME 90-JPGC/Pwr-26.
- Wei L. (1991). *Structures Aseismic Design*. Beijing: Universal Academic Press [in Chinese].
- Yang B. and Li Y.M. (2000). Study on Control Indexes for Earthquake Wave in Time History Analysis Method. *Journal of Civil Engineering*, 8(4): 23–27 [in Chinese].

*“This page left intentionally blank.”*

# Seismic Behavior and Structural Type Effect of Steel Box Tied Arch Bridge

Jin Gan<sup>1\*</sup>, Weiguo Wu<sup>1</sup> and Hongxu Wang<sup>1</sup>

<sup>1</sup>School of Transportation, Wuhan University of Technology, Wuhan 430063, P.R. China

**Abstract.** This paper took the railroad through tied-arch bridge with steel box ribs as engineering background. Author established 3-D finite element model of this whole bridge with the ANSYS FEM software, and calculated its seismic response by time-history analysis. Then, changed the bridges' type, such as the number of struts, parallel ribs or X ribs and the type of suspenders, analyzed their seismic responses and structural type effect of steel box tied arch bridge to seismic excitation. The results should be used to guide the aseismatic design of the steel box tied arch bridge.

**Keywords:** steel box tied arch bridge, seismic response analysis, structural type effect, finite element method, ANSYS

## 1 Introduction

Arch bridges are characterized by their beautiful appearance, easily constructed and relative lower cost, and their span can be increased when the ribs of arch are made of the steel box or truss of steel box, so it can be considered as a most competitive style among the long-span bridges. However, similar studies concerning the seismic response analysis of arch bridges have been scarce. Thereby, this paper took the railroad through tied-arch bridge with steel box ribs as engineering background. Author analyzed its seismic behavior and discussed the structural type effect of steel box tied arch bridge to seismic excitation. The results should be used to guide the aseismatic design of the steel box tied arch bridge.

---

\* Corresponding author, e-mail: ganjin82@yeah.net

## 2 Description of the Arch Bridge

The steel box tied arch bridge is a railroad through tied-arch bridge with steel box ribs. The bridge superstructure consists of a 140m arch span and a 30m wide roadway. At the middle of the arch span, the height of the arch ribs is 33m from the deck level. The arch bridge, shown in Figure 1, consists of two tiebeams, floorbeams, stringers, deck slab, two arch ribs and their struts, and a set of suspenders. The arch ribs consist of two rectangular steel box girders spaced 16m apart and hinged to the tiebeams at the ends of the arch span. The concrete slab is spliced along the centerline of the bridge, and the continuity of each end-floor-beam is broken at the middle of the beam.

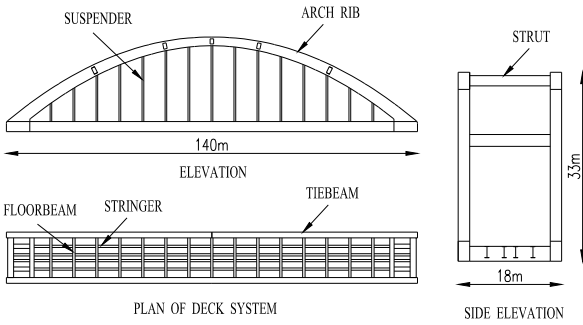


Figure 1. Typical view of the arch bridge.

## 3 Analytical Model

In this bridge modeling, according to the pattern and mechanical characteristic of the components, selected the appropriate element type in the ANSYS software to simulate the components accurately. The element types were used in the analytical modeling as follows:

The arch elements, tiebeams, floorbeams, stringers and rigid suspenders were modeled by the element BEAM188. BEAM188 is suitable for analyzing slender to moderately stubby/thick beam structures. This element is based on Timoshenko beam theory. It has six or seven degrees of freedom at each node. Shear deformation effects are included. This element is well-suited for linear, large rotation, and/or large strain nonlinear applications.

The reinforced concrete deck slab was modeled by the element SHELL63. SHELL63 has both bending and membrane capabilities. Both in-plane and normal loads are permitted. The element has six degrees of freedom at each node: transla-

tions in the nodal x, y, and z directions and rotations about the nodal x, y, and z-axes. Stress stiffening and large deflection capabilities are included. A consistent tangent stiffness matrix option is available for use in large deflection (finite rotation) analyses.

A three-dimensional model of the arch bridge, shown in Figure 2, was built to analyze its dynamic characteristics and seismic response analysis.

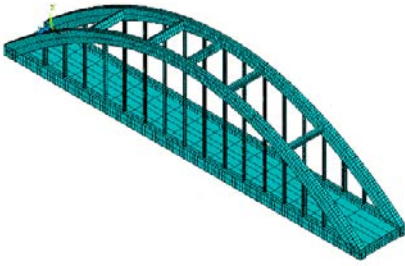
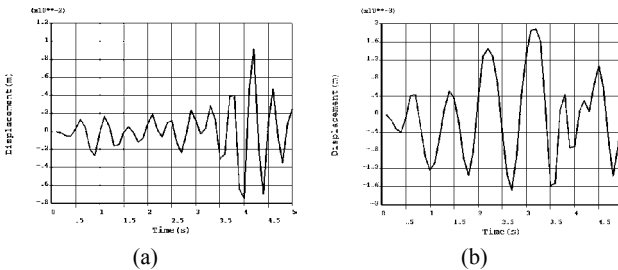


Figure 2. Three-dimensional modal of the arch bridge.

### 4 Seismic Response Analysis

The Tianjin earthquake of 1976 was chosen to calculate the seismic responses using the time-history analysis method. The input was considered two kind of situations, namely the vertical ground motion record was used as vertical inputs while the horizontal ground motion were used as longitudinal or lateral inputs. The seismic responses under the combination of vertical and longitudinal seismic motion inputs were shown in Figure 3, and the seismic responses under the combination of vertical and lateral seismic motion inputs were shown in Figure 4.



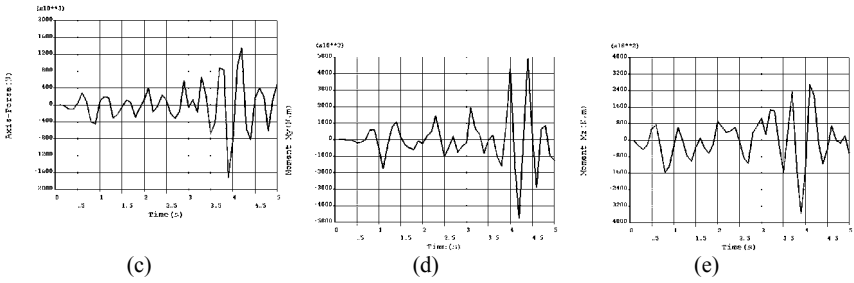


Figure 3. (a) Vertical displacement at arch crown section; (b) Longitudinal displacement at arch crown section; (c) Bending moment at arch abutment section (normal: y); (d) Bending moment at arch abutment section (normal: z); (e) Axial force at arch abutment section.

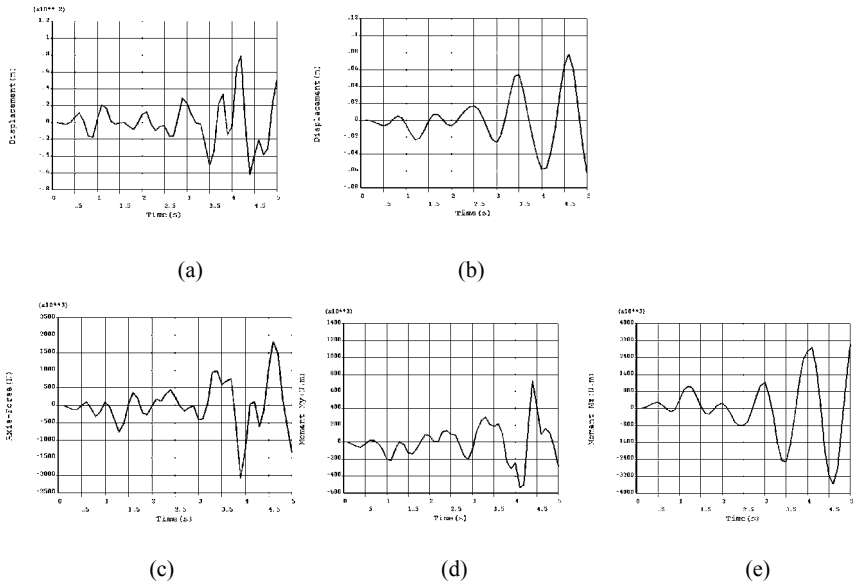


Figure 4. (a) Vertical displacement at arch crown section; (b) Lateral displacement at arch crown section; (c) Bending moment at arch abutment section (normal: y); (d) Bending moment at arch abutment section (normal: z); (e) Axial force at arch abutment section.

As shown in Figure 3 and Figure 4, the results of this analysis are as follows:

1. Under the function of vertical and longitudinal seismic inputs, the longitudinal displacement at arch crown section was very small, the maximum value was approximately 1.9mm, and its maximum value of vertical displacement was 9.1mm. Under the function of vertical and lateral seismic inputs, the maximum value of lateral displacement at arch crown section was 78.3mm, and its maximum value of vertical displacement was 7.9mm. The results show that the lat-

eral rigidity of this bridge was small, so some methods must be used to enhance the lateral rigidity of the arch bridge in design process.

2. Comparing the function of vertical and lateral seismic inputs with the function of vertical and longitudinal seismic inputs, the maximum values of axial force and bending moment at arch abutment section were larger, so the combination of vertical and lateral seismic loads must be considered in the design of steel box tied arch bridge.

## 5 Structural Type Effect

Different types of steel box tied arch bridge have different aseismatic capabilities, so author discussed the structural type effect of steel box tied arch bridge by building different types of model to analyze their seismic responses. The combination of vertical and lateral seismic motion inputs (Tianjin earthquake) were chosen to calculate the seismic responses using the time-history analysis method.

1. The arrangement of struts (shown in Figure 5)

Modal 1: retain all the struts

Modal 2: retain strut A

Modal 3: retain strut A, strut B and strut C

Modal 4: retain strut D and strut E

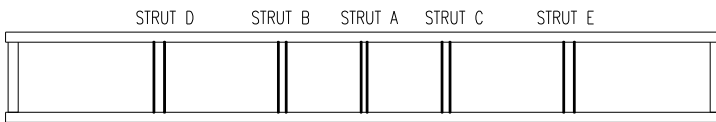


Figure 5. Strut layout of the arch bridge

Comparing with the results of the seismic responses of four modals, the analysis is as follows:

Setting struts at arch crown area, reduced the lateral displacement values of arch ribs and increased the internal force values of arch ribs at the same time. The more struts number, the larger internal force values of arch ribs at arch abutment area. Comparing setting struts at arch abutment area with setting struts at arch crown area, the internal force values of arch ribs were smaller.

In order to enhance the aseismatic capabilities of steel box tied arch bridge, the arrangement of struts should do the overall evaluation, and find a balance point to enable the struts to exert the greatest effect in earthquake.

2. The inclination angle of arch ribs

Modal 1: parallel arch ribs, inclination angle is  $0^\circ$  (shown in Figure 2)

Modal 2: X arch ribs, inclination angle is  $10^\circ$  (shown in Figure 6a)

Comparing with the results of the seismic responses of two modals, the analysis is as follows:

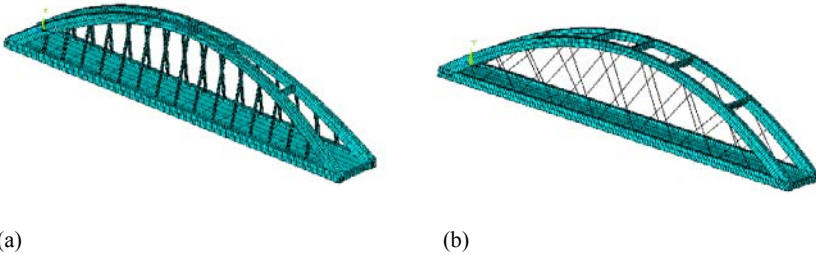


Figure 6. Three-dimensional modals of arch bridge

The maximum seismic response values of arch bridge with X ribs were smaller than the one with parallel ribs. It is because that instead of parallel arch ribs, X arch ribs could enhance the rigidity of arch bridge and make the centre of gravity of arch bridge down. So the structural type of steel box tied arch bridge should first consider X arch ribs in earthquake-prone areas.

### 3. The type of suspenders

Modal 1: Rigid parallel suspenders (shown in Figure 2)

Modal 2: Flexible parallel suspenders, modelled by the element LINK10

Modal 3: Flexible X suspenders (shown in Figure 6b)

Comparing with the results of the seismic responses of three modals, the analysis is as follows:

Setting rigid suspenders, comparing with setting flexible suspenders, reduced the vertical displacement values of arch ribs and increased the lateral displacement values of arch ribs at the same time. For the internal force responses of arch ribs, setting rigid suspenders could enhance the link between arch ribs and tiebeams, and reduce the structural internal force responses effectively. Comparing setting flexible X suspenders with setting flexible parallel suspenders, the maximum seismic response values of arch ribs changed little.

## 6 Conclusions

In order to assess the seismic behavior and the structural type effect of steel box tied arch bridge, a certain bridge was chosen for study. Conclusions based on the findings of seismic responses made during the study are:

1. According to the results of seismic response analysis, it was confirmed that the lateral rigidity of this bridge was small. Thus, the lateral rigidity of the steel box tied arch bridge should be enhanced in design process.

2. Since the responses of the bridge modal were larger under the combination of vertical and lateral seismic loads, the combination of vertical and lateral seismic loads must be considered in the design of steel box tied arch bridge.
3. For steel box tied arch bridges, their structural types affected their aseismatic capabilities much, such as arrangement of struts, inclination angle of arch ribs and type of suspenders.
4. Based on our results, it seems that steel box tied arch bridges should design as X arch ribs, rigid suspenders and less struts in earthquake-prone areas.

## References

- Lee H. E. and Torkamani M.A.M. (1998). Dynamic response of tied arch bridges to earthquake excitations. Research Rep. ST-3, Dept. of Civil Engineering, Univ. of Pittsburgh, Pittsburgh.
- Li G. H. (1983). Theory of bridges and structures, Shanghai Science and Technology Publishing House, China.

*“This page left intentionally blank.”*

# The Seismic Behavior Analysis of Steel Column-Tree Web Connection with Bolted-Splicing

Yuping Sun<sup>1,2\*</sup> and Liping Nie<sup>1,2</sup>

<sup>1</sup>School of Civil Engineering, Lanzhou University of Technology, Lanzhou 730050, P.R. China

<sup>2</sup>Engineering Research Center of Disaster Mitigation in Civil Engineering, Ministry of Education, Lanzhou 730050, P.R. China

**Abstract.** Five different splicing design methods are used to design the column-tree web connection, and a method called S-F which has characters of transmits force directly, simple calculation, economic materials consumption is obtained by theories and finite element simulation analysis. In order to consider the influence of several factors such as the thickness of beam and column flange and web, friction coefficient and so on, a series of specimen are obtained by change the parameters of S-F design method with which as the BASE specimen. Finite element simulation analysis in monotonic and cyclic load of these specimen are carried out, at the same time ,mechanical behavior of BASE specimen and failure mechanism of connections are analyzed, and the result provides a reference for design and construction of this connection.

**Keywords:** splice design method, column-tree web connection, influence factors failure mechanism

## 1 Introduction

Steel column-tree connection is a kind of steel frame joint with cantilever beam welded to the column and the beam spliced, it is a recommended type for Technical specification for steel structure of tall buildings (JGJ 99-98) and Code for seismic design of buildings (GB50011-2001) in China (Li et al., 2004), especially it is commonly used in steel frame web connection. But the beam-to-column welded connection is used accurate method to design for a long time, and the beam splicing joint seismic design always according to the equal strength of beam (Li et al., 2004), so it leads to the flexural capacity of beam splicing joint higher than the beam-to-column welded connection (Xia and Hong, 2005) and the seis-

---

\* Corresponding author, e-mail: hhyy707@lut.cn

mic design requirements “stronger joint with weaker beam” cannot meet, it can easily cause the beam-to-column welded connection brittle fracture under earthquake action. There are many kinds of beam splicing design methods, the splicing joint mechanical behavior vary with the design methods, so it is necessary to find out a design method which is simple calculation, transmits force directly, economic materials consumption, at the same time, provides a reference for design and construction of this connection.

## 2 Splicing Design for Column-Tree Connection

### 2.1 Calculation Principle of Splicing Joint

At present, there are mainly several following methods (Li et al., 2004): equal strength design method, practical design method, accurate design method and simplified design method. Equal strength design method is spliced according to the net cross-sectional area equal strength condition of the beam flange and web which are connected. The beam flange splicing of practical design method is conducted according to the net cross-sectional area equal strength condition of the beam flange, in addition to the web connection should calculate the shear force in the splice-site, should according 1/2 of the web net cross-sectional area shear capacity design values or the shear force which is the moment at both ends of the beam divided by the net cross-beam length to determine. Accurate design method is based on the beam flange and web which are connected to share the moment  $M$  in the splice-site respectively, in other words, the beam flange bears the moment  $M_f$ , the web bears the moment  $M_w$  and all of the shear force, at the same time, the beam flange and web bolts force coordination should considered. Simplified design method is assumed that the moment  $M$  in the splice-site fully borne by the flange, and the shear force  $V$  fully borne by the web, at the same time, the web connection should according to the practical design method to determine. In overseas, through theoretical analysis and experimental verification of its correctness, Sheikh-Ibrahim and Frank (1998) put forward that because of the beam flange in the lateral cross-section, in the limit stress state, it will always achieve its maximum carrying capacity, if it unable to achieve this state under the action of moment, then the flange also have to bear the shear force. At the same time, according to the splicing design method of literature (Li, 2003), we put forward that the beam flange splicing should bear the moment which leads the net-cross section of flange to yield, and the web splicing bears the remainder moment, shear force, and the eccentric moment which is caused by the shear force. And the eccentric distance defined as one side of the group bolts center to the centerline of splicing, in this paper, the method called as the S-F method.

## 2.2 Design of Splicing Joint

The shape of the column-tree web connection is showed in Figure 1.

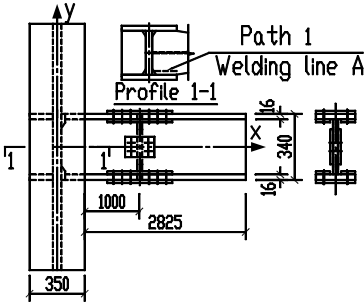


Figure 1. The shape of column-tree connection.

Applied 150kN of point load in the beam end where the length from loading point to the location of splicing is 1.825m. Internal force of the splicing place is: Moment:  $M_n^b = 150 \times 1.825 = 273.75 \text{ kN}$ ; shear force:  $V_n^b = 150 \text{ kN}$ ; using level 10.9 M22 high strength bolts for friction type connection, friction coefficient is 0.35. The results of splicing design are shown in Table 1.

Table 1. High strength bolt amount on one side after adjustment of friction coefficient in the location of beam splicing

Design method	Flange bolts	Web bolts	Flange friction coef- ficient	Web friction coeffi- cient
Equal strength	6	3	0.375	0.375
Practical	6	2	0.375	0.375
Accurate	6	3	0.375	0.35
Simplified	6	2	0.4	0.35
S-F	6	2	0.35	0.35

## 3 Finite Element Analysis of Splicing Joint

### 3.1 Selection of Basic Parameters

In order to compare mechanical behavior of these five kinds of splicing node, made monotonic and cyclic loading finite element simulation to treelike column node by using ANSYS software. Material constitutive relation used trilinear mod-

el including descent segment. According to the test data, elastic modulus are all for  $E = 206000 \text{ MPa}$ , poisson ratio are all for 0.3; performance index of various steel are shown in Table 2.

Table 2. The performance index of steel

Performance index class	$\sigma_y$ (MPa)	$\epsilon_y$	$\sigma_u$ (MPa)	$\epsilon_u$	$\sigma_{st}$ (MPa)	$\epsilon_{st}$
Q235 steel	235	0.00114	415	0.15	340	0.21
welding line	330	0.0016	460	0.12	410	0.17
Bolt	940	0.00456	1130	0.10	960	0.13

Sections of beam and column and bolts were adopted entity elements to mesh generation, using elements of Solid45, Solid92, Solid95. When splicing joints were under load, effect of contact and extrusion existed between nuts and splice bars, splice bars and threaded holes. There are a lot of contact problems. The contact between nuts and splice bars, beam flange web and splice bars, bolt bars and threaded holes. Contact elements were selected Targe170 and Contac174. In addition prestressed element Prets179 was selected for applying prestress in bolt bars. Considering symmetry, only used half model to calculate. Finite element model is shown in Figure 2.

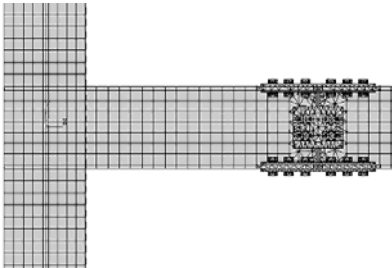


Figure 2. Finite element model.

### 3.2 Finite Element Analysis Results and Analysis of Seismic Performance

The yield displacement  $\Delta_y$  and yield load  $P_p$  at the beam end are determined by the method shown in Figure 3. Through numerical analysis, it gives each series of specimen  $P/P_p - \Delta/L$  curve under monotonic loading, and  $P/P_p -$

$\Delta / \Delta_y, P / P_p - \theta_p$  hysteretic curves under cyclic loading. In order to conveniently compare the results, use the S-F design method specimen as the base specimen, the load-displacement curve in monotonic force is shown in Figure 4.

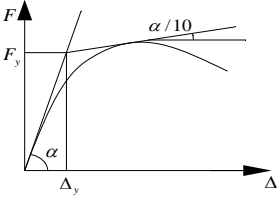
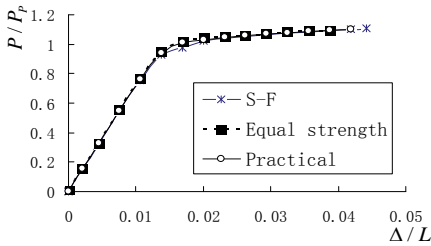
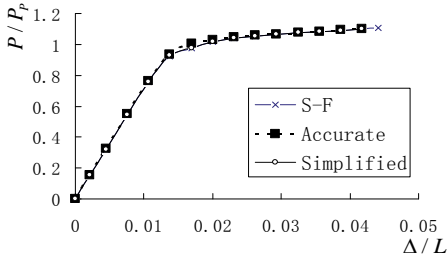


Figure 3. Beam end yield displacement determination



(a) Equal strength, practical design method specimens



(b) Accurate, Simplified design method specimens

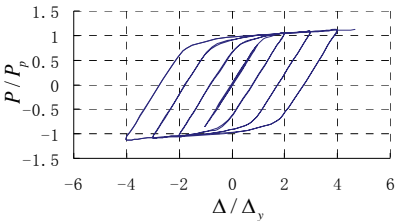
Figure 4. Load-displacement curve in monotonic load

It can be seen from Figure 4 that the yield load of S-F method specimen was 146.28kN. The starting and final displacement of each method when slip are shown in Table 3.

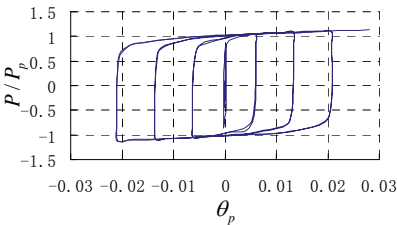
Table 3. The starting and final displacement of each method when slip

Design method	starting displacement ( $\Delta / L$ )	Final displacement ( $\Delta / L$ )
Equal strength	—	0.038
Practical	0.019	0.041
Accurate	0.017	0.042
Simplified	0.014	0.042
S-F	0.014	0.044

Because the curves of these types of design methods are very close, in order to facilitate comparison, only use the methods which have bigger difference such as equal strength and S-F method to compare. The hysteretic curve of S-F design method specimen as seen in Figure 5. And the equal strength design method as seen in Figure 6.



(a)  $P/P_p - \Delta/\Delta_y$  hysteretic curve



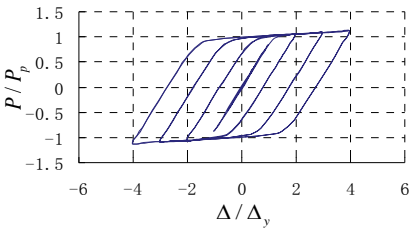
(b)  $P/P_p - \theta_p$  hysteretic curve

Figure 5. Hysteretic curves of S-F design method specimen

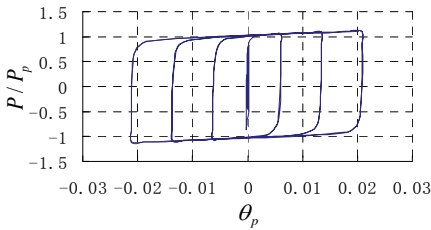
When the S-F specimen reaches  $4 \Delta_y^- \sim 4 \Delta_y^+$  cycle, and the load reaches  $0.88 P/P_p$ , the splicing connection appeared slip. Eventually destroyed in the side seam beam-to-column connection when the specimen reaches the cycle of

$4\Delta_y \sim 5\Delta_y$ . It can be seen from the chart that the hysteretic curve are full, stability, and the strength, stiffness without apparent degeneration in every cycle. When destruction the whole plastic deflection is 0.028rad,  $P/P_p$  reached 1.13, performed good seismic behavior.

Equal Strength design method specimen (Figure 6) in the cycle load without slipping phenomena appeared. Destruction is still in the side seam beam-to-column connection when the specimen reached the cycle of  $4\Delta_y^- \sim 4\Delta_y^+$ , the whole plastic deflection reached 0.028rad,  $P/P_p$  reached 1.14. The ultimate bearing capacity is almost as the same with S-F specimen, but the whole plastic deflection is lower than S-F specimen 25%, so the S-F design method shows better seismic performance. This is mainly because the splicing of the slip zone enhances the seismic performance of beam-column connections.



(a)  $\Delta/\Delta_y - P/P_p$  hysteretic curve



(b)  $P/P_p - \theta_p$  hysteretic curve

Figure 6. Hysteretic curves of equal strength design method specimen

## 4 Conclusions

From the five different splicing design methods described above, it can be concluded that:

1. The flange in the connection only bears the moment which the net section of flange reaches to yield, the other moment must be load by web plate. So, after reach to yield loads of net section which load by bolts of flange, it can not be improved the load capacity by increase the number of flange bolt or increase the friction coefficient of flange. If the moments which bear by web plate do not be considered, the splicing design will be over-conservative. The seismic performance of connection will be reduced because the bolts can not sliding.
2. It basically do not have influence to ultimate capacity of splicing specimen of the number of web plate bolts, and to reduce the number of web plate bolts can increase the ductility of specimen.
3. The difference of ultimate capacity of the five means is very small. The equal strength design method specimen doesn't appear sliding under the load, and the ultimate displacement when it destroyed is minimum. The sliding of S-F method appears earliest, the ultimate displacement of S-F method when it is destroyed is 13.6% bigger than the minimum, and it appears good semi-rigid connection performances.
4. The five specimens have good seismic performance. The hysteretic curve is plumping and stability, the strength and stiffness do not have degraded obviously under the circulation, when the specimen is destroyed, the whole plastic angle is minimum at the methods of equal strength design, but it is maximum at the method of S-F which is 25% larger than that minimum. The specimen of S-F method have better seismic performance because the friction sliding and squeezing action of bolts of contact area can dissipated the seismic energy and increase the rotation capacity .
5. The stress distribution of the side welding line is not uniform, it is maximum at the edge of beam column connection, it will be decreased when it moves to inner, at last the specimens destroy will occur at the longitudinal fillet of beam column connection.

## References

- Li Q.C. (2003). Splicing of a cantilever beam with end-column connections under cyclic loading in the failure mechanism and seismic design countermeasures. Xi'an: Xi'an University of Science and Technology Building Dissertation.
- Li X.R., Wei C.A., Ding Z.K., et al. (2004). *Steel connections design manual* (second edition). Beijing: China Building Industry Press.
- Li Y.C., Gao M. (2005). Steel frame beam-column web connections Butt Weld Flange failure mechanism. *Building Technology Development*, 32(8): 24-57.

- Sheikh-Ibrahim F.I. and Frank K.H. (1998.) The ultimate strength of symmetric beam bolted splices. *Engineering Journal*, AISC, 3rd Qtr.: 106-118.
- Sun Y.P., Wang Y, Wang W.Z., et al. (2008). Steel frame beam-column weak axis connecting nodes in the fracture behavior under earthquake . *Gansu Science Journal*, 20(2): 53-56.
- JGJ99-98. Technical Specification for Steel Structures of Tall Buildings (1996). Beijing: China Building Industry Press.
- Xia J.W., Hong F. (2005). Cantilever steel frame columns with spliced segment the node elastic-plastic analysis. *Progress in Building Steel Structure*, 7(3): 49-51.

*“This page left intentionally blank.”*

# Direct Displacement-Based Seismic Design Method of High-Rise Buildings Considering Higher Mode Effects

Xiaoling Cui<sup>1,2\*</sup>, Xingwen Liang<sup>1</sup> and Li Xin<sup>1</sup>

<sup>1</sup>Key Laboratory for Structural Engineering and Earthquake Resistance of China Education Ministry, Xi'an University of Architecture and Technology, Xi'an 710055, China

<sup>2</sup>Department of Civil Engineering, Faculty of Water Resources and Hydraulic Power, Xi'an University of Technology, Xi'an 710048, China

**Abstract.** Direct displacement-based Seismic design of high-rise buildings considering higher mode effects is realized. The structural natural periods and corresponding modes are obtained by free vibration analysis. Based on the periods, the equivalent displacement of single-degree-of-freedom system for each mode is obtained by displacement response spectra, and the structural lateral elastic displacement of each mode could be determined by "Equivalence Principle". So the structural lateral elastic displacement can be deduced by SRSS rule. Then, based on allowable storey drift ratio, the structural target lateral displacement of each mode could be determined, and the storey shear is obtained by SRSS rule. The design example shown in Table 3 demonstrates that the base shear considering higher mode effect in serviceability performance level is 2212kN, that is larger than 1975kN which only considering the first mode, so the design results will be more safety. The elasto-plastic time history analysis proves that this method is accurate enough to practical application in building design.

**Keywords:** high-rise buildings, higher mode effects, direct displacement-based seismic design, elasto-plastic time-history analysis

## Introduction

Over the last decade, an important advancement in earthquake engineering has been the elaboration of performance-based concepts for the seismic design of structures. This approach, based on the coupling of multiple performance limit states and seismic hazard levels, overcomes several of the shortcomings of the traditional force-based seismic design procedure. The first step in Direct

---

\* Corresponding author, e-mail: cuixl4953@sina.com

Displacement-based Seismic Design (DDBSD) procedure is the definition of the target displacement that the building should not exceed under a given seismic hazard level. At present, the structural target lateral displacement curve is mostly determined by its first mode displacement without considering the higher mode effects (Medhekar and Kennedy, 2000; Luo and Qian, 2003; Liu and Zhou, 2003; Liang and Huang, 2005), so it fails to evaluate the high-rise building’s performance accurately.

In this paper, based on uncoupling vibration theory of dynamics, an analysis procedure of each mode’s contribution to the target displacement, and each mode’s target displacement is presented. The multi-degree-of-freedom system is transformed into equivalent single-degree-of-freedom system, and the base shear of each mode is obtained by displacement response spectra theory. Then the total base shear could be determined by SRSS rule. It provides a valuable thought to DDBSD method of high-rise buildings.

### 1 Performance Levels

DDBSD method needs to determine the relationship between performance levels and displacement. The structural performance is divided into three levels: “serviceability, life-safety and collapse prevention” in accordance with the “three levels” of Chinese code (Code for seismic design of buildings, 2001). Storey drift ratio is a key parameter for the control of damage in RC buildings, it is rational to examine a procedure wherein displacements are considered at the beginning of the seismic design process. This paper offers the high-rise structural storey drift ratio for different performance level based on Liang’s work (Liang et al., 2006), as shown in Table 1.

Table 1. The allowable storey drift ratio for each performance

Performance level	Structural type		
	Frames	Frame-shearwall structures	Shearwall structures
Serviceability	1/500	1/800	1/1000
Life safety	1/200	1/220	1/250
Collapse prevention	1/50	1/100	1/120

## 2 Target Lateral Displacement Curve of Each Mode

### 2.1 The Natural Modes and Periods

If the preliminary design scheme of the structure has determined, the natural periods and corresponding modes of the structure can be obtained by means of computer analysis.

### 2.2 The Position of Maximum Story Drift

The structure's target lateral displacement is an indispensable variable in DDBSD method, and it needs to locate the position of maximum story drift in the structure. The first mode of vibration plays a dominant role in the structural seismic design, so the position of maximum story drift ratio for the 1st mode can be regarded as a substitute for the structure. Two methods are usually used to solve this problem. First, the 1st mode shape could be determined by virtue of computer analysis. Second, some experimental formulas are used to calculate the fundamental mode of structures. MU Cuiling (Mu et al, 2003) offers the fundamental mode's expression and the position of maximum story drift of frame-shearwall structure, LIANG Xingwen (Liang and Huang, 2005) offers the lateral displacement pattern of frames, supposes one of the bottom floors reaches storey drift ratio limits. The storey drift ratio is determined by displacement difference of floors in this paper.

### 2.3 The Structural Lateral Displacement Curve

The mass is distributed throughout the building, but we will idealize it as concentrated at the floor levels, the floor systems are rigid in their plane. The vibration of each mode is regarded as uncoupling (Chopra and Goel, 2002) (Figure 1). The calculation procedure of target lateral displacement is described as follows:

(1) Transform the multi-degree-of-freedom system (MDOF) into equivalent single-degree-of-freedom system (ESDOF).

The structure's elastic lateral displacement demand of each mode is expressed as

$$X_{ji} = d_{jn} x_{ji} \quad (1)$$

In which  $X_{ji}$  is the elastic lateral displacement demand of the  $j$ th mode at the  $i$ th floor level,  $d_{jn}$  is the elastic lateral displacement of the  $j$ th mode at the roof floor

level,  $x_{ji}$  is relative displacement of the  $j$ th mode at the  $i$ th floor level,  $n$  is the number of stories.

Based on Liang’s work (Liang and Huang, 2005), the equivalent displacement of ESDOF system is deduced as follows:

$$X_{j\text{eff}} = \frac{\sum_{i=1}^n m_i (d_{jn} x_{ji})^2}{\sum_{i=1}^n m_i d_{jn} x_{ji}} = d_{jn} \frac{\sum_{i=1}^n m_i x_{ji}^2}{\sum_{i=1}^n m_i x_{ji}} = d_{jn} / \gamma_j \tag{2}$$

In which  $X_{j\text{eff}}$  is the equivalent displacement of ESDOF system for the  $j$ th mode,  $m_i$  is the mass at the  $i$ th floor level,  $\gamma_j$  is the modal participation factor.

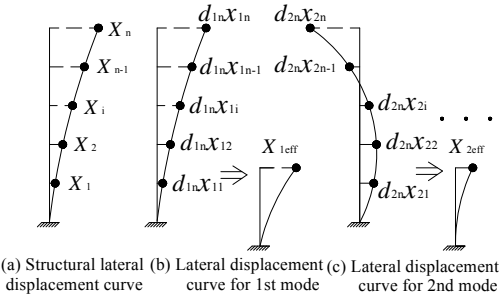


Figure 1. Lateral displacement curve for each mode and the ESDOF system

(2) Converting the acceleration response spectra of current code (Code for seismic design of buildings, 2001) into displacement response spectra according to follow equation:

$$S_d = \left( \frac{T}{2\pi} \right)^2 S_a \tag{3}$$

(3) Let  $S_{dj} = X_{j\text{eff}} = d_{jn} / \gamma_j$ ,  $d_{ij} = \gamma_j S_{dj}$ , the elastic lateral displacement of the structure is obtained by SRSS rule, that is

$$X_i = \sqrt{\sum_{j=1}^m X_{ji}^2} = \sqrt{\sum_{j=1}^m (\gamma_j S_{dj} x_{ji})^2} \tag{4a}$$

(4) Supposing that the structural lateral displacement curve in inelastic range is similar to that in the elastic range, the structural target lateral displacement curve satisfying the performance level could be expressed as follows:

$$u_i = DX_i = D \sqrt{\sum_{j=1}^m (\gamma_j S_{dj} X_{ji})^2} \quad (4b)$$

where  $D$  is constant.

If the storey in the maximum story drift is determined, and the  $[\theta]$  is known,  $D$  could be calculated by follow formula:

$$D = \frac{[\theta] h_i}{X_i - X_{i-1}} \quad (5)$$

In which  $h_i$  is a height of  $i$ th storey which storey drift is the max;  $X_i$ ,  $X_{i-1}$  is the floor displacement demand at  $i$ th and  $(i-1)$ th floor level respectively, it could be calculated by Equation (4a).

(5) Based on Jan's work (Jan and Liu, 2004) it can be assumed that the displacement proportion contributed by each mode is invariable, so  $DX_j$  is the structure's target lateral displacement of the  $j$ th mode, as given by the following expression:

$$u_j = DX_j \quad (6)$$

where  $u_j$  is the structural target lateral displacement for the  $j$ th mode.

### 3 Equivalent Parameters of ESDOF System and Earthquake action of Structure

After the target lateral displacement for each mode is determined, the equivalent parameters of the ESDOF system and the base shear could be obtained by following equations (Liang and Huang, 2005):

$$u_{j\text{eff}} = \frac{\sum_{i=1}^n m_i u_{ji}^2}{\sum_{i=1}^n m_i u_{ji}} \quad (7)$$

$$M_{j\text{eff}} = \left( \sum_{i=1}^n m_i u_{ji} \right) / u_{j\text{eff}} \tag{8}$$

$$K_{j\text{eff}} = \left( \frac{2\pi}{T_{j\text{eff}}} \right)^2 M_{j\text{eff}} \tag{9}$$

$$V_{bj} = K_{j\text{eff}} u_{j\text{eff}} \tag{10}$$

in which  $u_{ji}$  is target lateral displacement for the  $j$ th mode at the  $i$ th floor level,  $V_{bj}$  is the base shear of the structure for the  $j$ th mode,  $u_{j\text{eff}}$ ,  $M_{j\text{eff}}$ ,  $K_{j\text{eff}}$  and  $T_{j\text{eff}}$  are the equivalent displacement, equivalent mass, equivalent stiffness and equivalent period for the  $j$ th mode respectively.

$T_{j\text{eff}}$  could be deduced by inversion formula of Equation (3) for “serviceability” performance, but for “life safety” and “collapse prevention” performance level, the structure has been in inelastic range, the equivalent damping ratio should be determined. Gulkan and Sozen’s equation (Miranda and Garcia, 2002) is cited in this paper:

$$\zeta_{\text{eff}} = 0.05 + 0.2 \left( 1 - 1/\sqrt{\mu} \right) \tag{11}$$

where  $\mu$  is displacement ductility ratio demand.

The lateral load at the  $i$ th floor level for the  $j$ th mode could be expressed by Equation (12), the storey shear in the  $i$ th storey for the  $j$ th mode, and the storey shear in the  $i$ th storey are expressed by Equation (13) and Equation (14)

$$F_{ji} = \frac{m_i u_{ji}}{\sum_{k=1}^n m_k u_{jk}} V_{bj} \tag{12}$$

$$V_{ji} = \sum_i^n F_{ji} \tag{13}$$

$$V_i = \sqrt{\sum_{j=1}^m V_{ji}^2} \tag{14}$$

### 4 Pushover Analysis

The evaluation method in this paper is described as follows:

The base shear  $V$  and lateral displacement at roof level  $u_t$  for each performance are expressed in  $V-u$  coordinate, like  $A, B$  and  $C$  in Figure 2,  $OABC$  represents demand curve.  $V$  is determined by Equation (13) when  $i=1$ , and  $u_t$  could be obtained by following equation:

$$u_t = \sqrt{\sum_{j=1}^m (\gamma_j u_{jeff})^2} \tag{15}$$

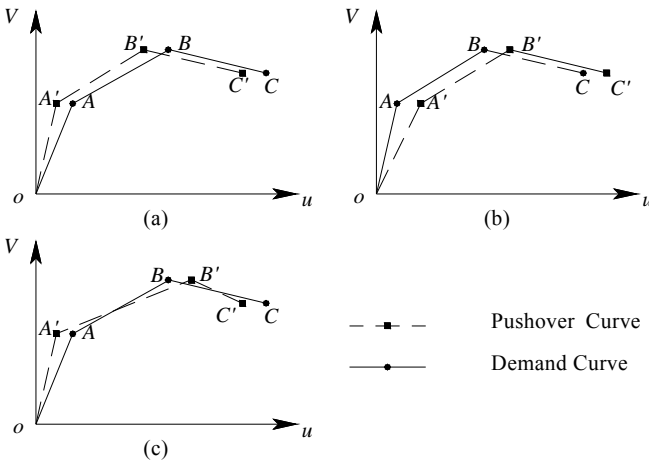


Figure 2. The pushover curve and demand curve

The capacity curve  $OA'B'C'$  are obtained by modal Pushover analysis (Chopra and Goel, 2002) in order to considering higher mode effects. Applied lateral load pattern for the  $j$ th mode is  $S = [m]x_{ji}$ . The base shear  $V$  for each performance is the controlling parameter. The lateral displacement at roof of each performance could be obtained. Increasing the lateral load till the base shear is equal to  $V$ , then the structural lateral displacement at roof level  $u_t$  should be obtained by SRSS rule.

Putting the demand curve and capacity curve in a same coordinate, there are three conditions occurring generally. If the capacity curve exceeds or match together with demand curve (Figure 2a), it illustrates that the actual displacement of the structure under design earthquake action is less than or equal to anticipating displacement, and the structure satisfies the requirements of fortification objective.

If not (Figure 2b), more revision or a repeating design is needed. In addition, The point *B* of capacity curve fall behind *B'* of demand curve is the third condition, and it presents that the performance objective under moderate earthquake is over-estimate. Adjusting performance objective or designing again are two selections.

### 5 Example

Figure 3 shows the structural arrangement scheme of a 12-story frame. The height of the first storey is 4.5m, and others are 3.0m. The seismic fortification intensity is VIII; the characteristic period ( $T_g$ ) of the adopted elastic response spectrum is 0.55s. The member details are as follows. 1-6 stories: concrete grade is C35; column section is 700mm×700mm; girder section is 250mm×550mm; other beams section is 200mm×500mm; and slab thickness is 120mm. 7-12 stories: concrete grade-C30; column section is 500mm×500mm; girder section is 250mm×550mm; other beams section is 200mm×500mm; and slab thickness is 120mm. As an example, this paper analyzes the structural performance under transverse earthquake only. The structural natural periods and modes are obtained by means of ETABS. The first three periods are as follows:  $T_1 = 1.33s$ ,  $T_2 = 0.44s$ ,  $T_3 = 0.24s$ . And it can be learned that the storey which story drift is max is the 3rd storey. The mass of each mode is shown in Table 2.

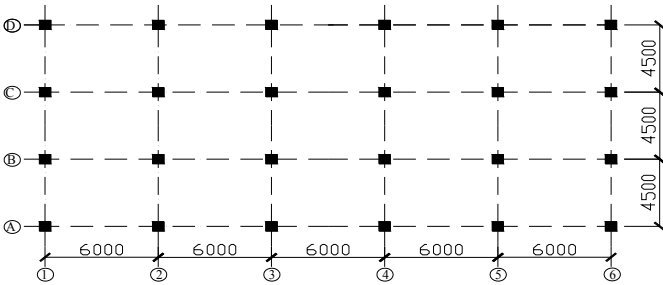


Figure 3. Structural arrangement scheme

Table 2. The mass of each story

Floor	1	2~5	6	7~11	12
Mass (kg)	401736	369595	358356	348373	317250

## 5.1 Serviceability Performance Level ( $I_0=1/500$ )

### 5.1.1 Target Lateral Displacement Curves for Each Mode

According to the first three structural natural periods and Equation (3) (damping ratio takes 0.05,  $\alpha_{\max}=0.16$ ), the ESDOF system's equivalent displacement are obtained:  $S_{d1}=31.8\text{mm}$ ,  $S_{d2}=7.7\text{mm}$ ,  $S_{d3}=2.3\text{mm}$ . The modal participation factors are  $\gamma_1=1.322$ ,  $\gamma_2=0.491$ ,  $\gamma_3=0.291$ . Substituting these parameters to Equation (2), the roof displacement for each mode are  $d_{1n}=42.0\text{mm}$ ,  $d_{2n}=3.8\text{mm}$ ,  $d_{3n}=0.7\text{mm}$ . It can be deduce that  $D=1.29$  based on Equation (5),  $D$  is a little larger than 1, so the initial design scheme is feasible, and the target lateral displacement curves for each mode are determined by Equation (6).

### 5.1.2 The Shear in Each Story

According to the target lateral displacement curves for each mode, the structure can be transformed into ESDOF system, and the equivalent parameters are shown in Table 5.2. The lateral earthquake forces and shear in each story of each mode could be determined respectively based on Equation (12) and Equation (13). If each mode is combined by the SRSS rule, the shear force in each story is obtained by Equation (14). The procedure is outlined in Table 3.

Table 3. The equivalent parameter of SDOF system for each mode (serviceability)

Modes	Equation displacement/ mm	Equation mass/ kg	Equation period/ s	Base shear/ kN
1	41.02	3446007	1.68	1975
2	9.93	466881	0.5	731
3	2.97	164635	0.27	264

Internal forces by earthquake loads, wind loads and gravity loads are combined and regarded as the design criteria, the structure can be designed.

## 5.2 Life-Safety Performance Level ( $I_0=1/200$ )

The structure has been in elasto-plastic range for "Life safety" Performance Level, and it needs to determine ductility coefficient  $\mu$  in order to calculating damping ratio  $\zeta_{\text{eff}}$ . The frames' yield lateral displacement at roof level is 2.5~2.7 times larger than that under minor earthquakes, and 2.6 times is taken in this paper. The structural lateral displacement at roof level under minor earthquakes could be ex-

pressed by  $d_{jn}$  in Equation (1), based on the relationship between  $d_{jn}$  and  $X_{j\text{eff}}$ , the ductility ratio demand  $\mu_j$  for  $j$ th mode can be determined by

$$\mu_j = u_{jn} / (2.6X_{jn}) \tag{16}$$

The design procedure is similar to “serviceability” performance except for  $\alpha_{\text{max}} = 0.45$ . The results are outlined in Table 5.

### 5.3 Collapse Prevention Performance Level ( $[\theta] = 1/50$ )

Taking  $\alpha_{\text{max}} = 0.90$ , the results are outlined in Table 5.

Table 4. The shear in each story (serviceability)

Floor	1 <sup>st</sup> mode		2 <sup>nd</sup> mode		3 <sup>rd</sup> mode		$V_i$ (kN)
	$F_{1i}$ (kN)	$V_{1i}$ (kN)	$F_{2i}$ (kN)	$V_{2i}$ (kN)	$F_{3i}$ (kN)	$V_{3i}$ (kN)	
12	240.19	240.19	-243.77	-243.77	147.77	147.77	372.76
11	256.30	496.49	-216.99	-460.76	83.98	231.75	715.90
10	245.29	741.78	-141.24	-602.00	-18.06	213.69	978.93
9	230.30	972.08	-46.49	-648.49	-109.77	103.92	1173.15
8	211.44	1183.52	53.92	-594.57	-154.98	-51.06	1325.46
7	188.94	1372.46	144.90	-449.67	-135.43	-186.49	1456.24
6	168.11	1540.57	215.58	-234.09	-62.29	-248.78	1577.99
5	145.94	1686.51	253.11	19.02	29.02	-219.76	1700.87
4	116.88	1803.39	252.23	271.25	108.72	-111.04	1827.05
3	86.69	1890.08	218.83	490.08	149.30	38.26	1952.96
2	56.14	1946.22	153.39	643.47	138.13	176.39	2057.41
1	28.75	1975	87.54	731	87.61	264	2122.42
$\Sigma$	1975		731		264		

### 5.4 Pushover Analysis

The modal pushover analysis is used to evaluate the structure that is designed by “serviceability” performance’s results, and the procedure is described in Section 4 of this paper. The demand curve and capacity curve are expressed in V-u coordinate (Figure 4).

Table 5. The equivalent parameter of SDOF system for each mode (life safety and collapse prevention)

mode	Equation disp./mm		Equation mass/kg	Equation period/s		Base shear/kN		Total base shear/kN	
	life safety	collapse prevention	life safety and collapse prevention	life safety	collapse prevention	life safety	collapse prevention	Life safety	collapse prevention
1	102.55	410.31	3446007	1.75	3.19	4551	5480		
2	24.83	99.28	466881	0.50	1.08	1829	1567	4949	5838
3	7.49	29.72	164635	0.27	0.39	667	1268		

Figure 4 shows that the capacity curve exceeds the demand curve in each performance level, and it illustrates that the designed structure satisfies performance objective.

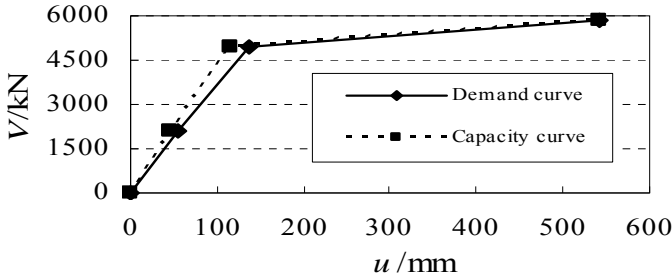


Figure 4. Comparison of demand and Pushover curve

### 5.5 Elasto-plastic Time-history Analysis

Elasto-plastic time-history analysis is used to examine the designed structure. Lanzhou wave 1, Elcentro wave and CPC-TOPANGA CANYON-16-nor wave are selected, and the peak acceleration of the waves is defined by seismic code (Code for seismic design of buildings, 2001). The floor displacement envelopes for “collapse prevention” are showed in Figure 5.

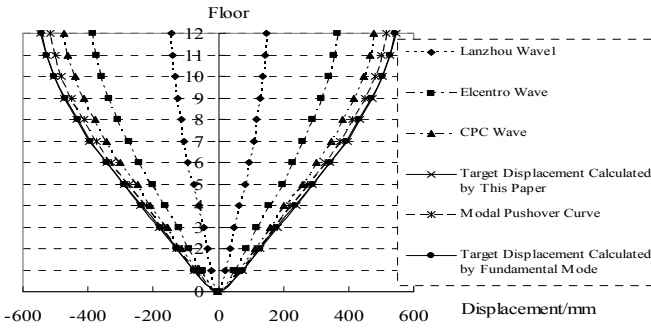


Figure 5. The floor displacement envelopes for “collapse prevention”

The analysis results indicate that the lateral displacement distribution throughout building calculated by this paper is identical to the modal pushover curve and time-history analysis curve approximately, and the results of different waves have great differences. The displacement envelopes obtained by time-history analysis are less than the target displacement calculated by this paper, and it implies that the structure satisfies the performance requirements of “collapse prevention”. The evaluation results coincidence with the modal pushover analysis.

## 6 Conclusions

1. The proposed method in this paper obtains most possible accurate target lateral displacement and therefore can be applied in DDBSD method of high-rise buildings.
2. The target lateral displacement curve considering higher mode effects is identical to the target lateral displacement curve calculated by fundamental mode approximately, so the position of maximum story drift for the fundamental mode can be regarded as a substitute for the global structure. The design example shows that the earthquake action excited by higher modes can not be neglect.
3. The displacement response spectra converted by acceleration response spectra of current code is not so accurate in longer period (>1.3s), so it fails to anticipate the performance of the structure which has longer period or the structure which is in inelastic range. It's urgent to perfect the displacement response spectra theory for DDBSD method.

## References

- Chopra A.K., Goel R.K. (2002). A modal pushover analysis procedure to estimate seismic demands for buildings. *Earthquake Engineering and Structural Dynamics*, 31: 561-582.
- GB 50011-2001, Code for seismic design of buildings. Beijing, China Architecture & Building Press [in Chinese].
- Jan T.S., Liu M.W. (2004). An Upper-bound pushover analysis procedure for estimating the seismic demands of high-rise buildings. *Engineering Structure*, 26: 11-128.
- Liang X.W., Deng M.K., and Li X.W. (2006). Research on displacement-based seismic design method of R.C. high-rise structure. *Building Structure*, 36(7): 15-22 [in Chinese].
- Liang X.W., Huang Y.J. (2005). Research on displacement-based seismic design method of RC frames. *China Civil Engineering Journal*, 38(9): 53-60 [in Chinese].
- Luo W.B., Qian J.R. (2003). Displacement-based seismic design for RC frames. *China Civil Engineering Journal*, 36(5): 22-29 [in Chinese].
- Liu Y.J., Zhou J.M. (2003). Study of displacement -based seismic design for RC frame structures. *Structural Engineers*, (3): 1-6 [in Chinese].
- Miranda E., Garcia J.G. (2002). Evaluation of approximate methods to estimate maximum inelastic displacement demands. *Earthquake Engineering and Structural Dynamics*, 31: 539-560.
- Medhekar M.S., Kennedy D.T.L. (2000). Displacement-based seismic design of building theory. *Engineering Structures*, 22: 201-209.
- Mu C.L., Wang W.J., and Chen C.E. (2003). Optimal criteria of frame-shear wall structures, *World Earthquake Engineering*, 19(1): 154-157 [in Chinese].
- Yang P., Li Y.M. (2005). Study on the comparison of different methods of simplifying capacity spectrum. *Journal of Chongqing Jianzhu University*, 27(4): 59-63 [in Chinese].

*“This page left intentionally blank.”*

# Rotational Components of Seismic Waves and Its Influence to the Seismic Response of Specially-Shaped Column Structure

Xiangshang Chen<sup>1\*</sup>, Dongqiang Xu<sup>1</sup> and Junhua Zhang<sup>1</sup>

<sup>1</sup>Institute of Civil Engineering, Hebei University of Technology, Tianjin 300132, P.R. China

**Abstract.** In this article, the rotational components of Ninghe wave was obtained through the translational components of it using the procedure of Matlab software developed by author, and time history analysis was carried on when the rotational component and the translational components were input to the specially-shaped column frame's space elastoplasticity model which establishes through the ANSYS software simultaneously. The result indicated that the specially-shaped column structure is very sensitive to the rotational seismic component, the effect's enlargement by rotational components should be considered fully when the specially-shaped column structure was designed, and enlarge the frame's seismic safety.

**Keywords:** seismic waves, rotational accelerate components, specially-shaped column, frame, seismic response, time history analysis

## 1 Introduction

Special-shaped column is reinforced concrete column whose section shape is T, +, L, Z. It has the advantage such as light weight, no arris in the house and disposing of furniture easily, increasing the usable floor area, saving energy and so on. It is very suitable for residential building and has rapidly used widely at present.

Because of the property of the special-shaped column section, the special-shaped column is sensitive to oblique load and torsion stress, and it appears very important to carry out the experiments and analysis on special-shaped column structure under the multi-dimensional seismic including the torsional component of seismic wave.

Due to the current level of observation to strong earthquake, we can not pick up the seismic wave's torsional acceleration component. In this paper, we use the principle of Frequency Domain Method to do Fourier transform to the horizontal

---

\* Corresponding author, e-mail: chenxiangshang@hebut.edu.cn

component of seismic wave (Newmark, 1969). Use the Matlab software to get the torsional component of EI Centro wave and Ninghe wave. Then import this component into the ANSYS finite element model of specially-shaped column frame, and carry out time-history analysis to it.

## 2 Solution of the Seismic Wave's Torsional Acceleration Component

### 2.1 The Solution Method of the Seismic Wave's Torsional Acceleration Component

It has been proved that seismic wave contained not only translational components, but also three rotational components which around three main axis.

It was assumed that the propagation medium is isotropic uniform elastic half-space or layered elastic half-space. When the incident wave is SH wave ( $S_{SH}$ ), the reflected wave is only SH wave ( $S_{SH}$ ). For the SH incident wave ( $S_{SH}$ ) whose frequency is  $\omega$ , displacement function is (Sun and Chen, 1998):

$$S_{SH}(x, z, t) = A_{SH} \exp i \omega \left( t - \frac{\sin \theta_0}{\beta} x + \frac{\cos \theta_0}{\beta} z \right) \quad (1)$$

The displacement components which are on the y out-plane direction are:

$$v = 2S_{SH} \quad (2)$$

Define the torsional component turning around z-axis, and get the torsional component according to the elastic wave theory as follow:

$$\varphi_{gz} = \frac{1}{2} \left( \frac{\partial v}{\partial x} - \frac{\partial u}{\partial y} \right)_{z=0} = \frac{1}{2} \frac{\partial v}{\partial u} \Big|_{z=0} \quad (3)$$

We can substitute equation (1) and equation (2) into equation (3), get:

$$\varphi_{gz} = -i\omega \frac{\sin \theta_0}{2\beta} v \quad (4)$$

According to the equation (4), we can get the Fourier spectrum relationship between torsional component and translational motion component (when the incident wave is SH wave):

$$\Phi_2(\omega) = i\omega u_3(\omega) / 2c \tag{5}$$

In the equation,  $\Phi_2$  is the torsional component  $\varphi_{gz}$  of equation (4),  $i = -1$ ,  $\omega$  is circular frequency,  $c$  is apparent velocity ( $c = -\frac{\beta}{\sin \theta_0}$ ),  $u_3$  is the  $v$  of equation (2).

### 2.2 The Time-History Curve of the Seismic Wave's Torsional Acceleration Component

Using the above method and the Matlab calculating program developed by the author, the torsional acceleration component of EI Centro wave was get. The result is basically matched with that in the literature (Li Hongnan, 1998).

Since the very wide range of applications of Ninghe wave, we calculate its torsional acceleration component, and the calculated time-history curve of torsional acceleration is shown in Figure 1.

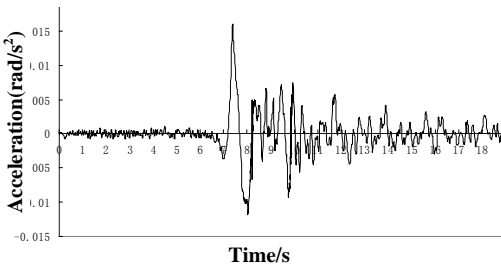


Figure 1. Time-history curve of torsional acceleration of Ninghe wave

Power spectrum of torsional acceleration and horizontal acceleration of NingHe wave are shown in Figure 2. In Figure 2, frequency for abscissa and power for ordinate. We can see that the frequency of torsional acceleration were greater than the frequency of horizontal acceleration, that is, the high frequency components of time-history curve of torsional acceleration is very rich, and the decay is more slowly.

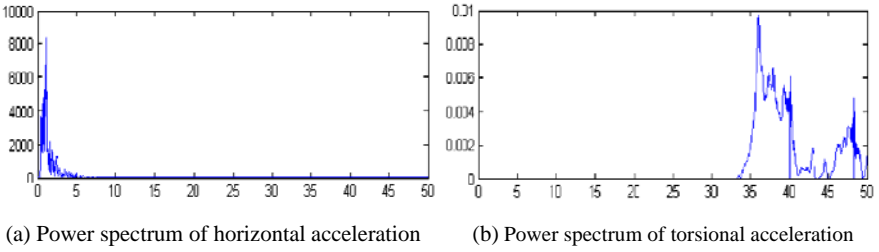


Figure 2. Power spectrum of acceleration of NingHe wave

### 3 Establishment of Finite Element Model of Special-Shaped Column Frame

Because this text focus on the solution to the macroreaction of structural members and system under external load, so bar element is selected to the beam and column, shell element is selected to floor to establish space finite element model.

In this paper, the special-shaped columns frame model is, and the has six layers, and the standard floor plan is shown in Figure 3.

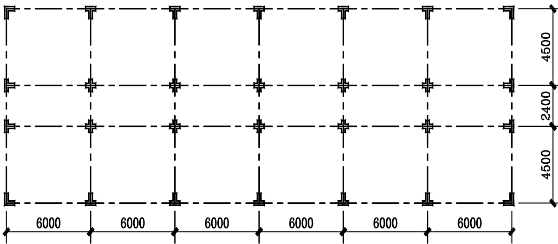


Figure 3. The standard floor plan of special-shaped

### 4 Analysis of the Reaction of the Special-Shaped Column Structure under Multi-Dimensional Seismic

Input the unidirectional Ninghe seismic wave and multi-dimensional seismic wave to finite element model above and carry out the time-history analysis separately.

Analyze the influence of multi-dimensional seismic wave to frame structure through compare the differences of displacement response between the two.

Figure 4 shows the increasing ratio of structure's displacement curve which compared seismic action of three-way (including torsional acceleration component) to seismic action of one-way. We can see from Figure 5, the displacement of all floors increase more 13%. It shows that the multiway acceleration component has large effect to frame structure and we can't ignore it. Besides, its displacement response of first floor increased more than 20%.

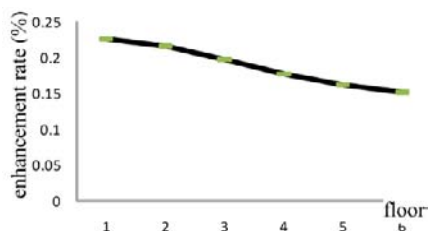


Figure 4. Increasing proportion of structure's displacement of bidirectional and torsional seismic action

In order to analyze the similarities and dissimilarities between special-shaped column frame and rectangular column frame structure under torsional seismic wave, this article establish the rectangular column frame structure model, and the section of its column is selected as square column whose lateral stiffness is the same as the special-shaped column. The structure arrangement and other calculation condition is the same as special-shaped column, and compare the two with the calculation results. The increasing rate of the most displacement responses of different structure when inputting bidirectional and torsional seismic wave compared to the unidirectional seismic wave is shown as in Figure 5. We can see that the influence of torsional seismic wave on special-shaped column structure is more than on the rectangular column frame structure, and the special-shaped column structure is the sensitive structure system to the torsional seismic wave.

In addition, to analyze the structure model of various spans and various storey heights, we can know that the increscent proportion on displacement response under multi-dimensional seismic wave is averages about 22%.

Because the structure in this text is symmetric regular, the seismic response under multi-dimensional seismic wave is larger about one-fifth than under unidirectional seismic wave. So the response of irregular and asymmetric special-shaped column structure under torsional seismic will be more. The increasing influence should be considered when designing the special-shaped column structure especially irregular structure. It is best to consider the torsional seismic effect when calculating.

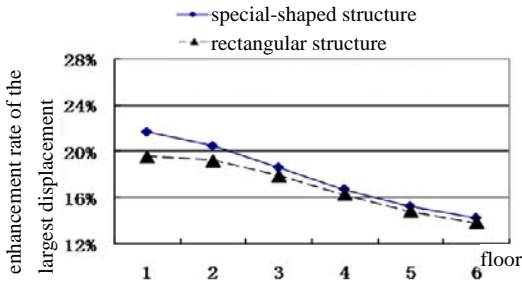


Figure 5. Enhancement rate of displacement of different structure when import multi-dimensional seismic wave

## 5 Conclusions

1. The torsional acceleration is plentiful in high frequency components, and the decay of it is slower than horizontal acceleration.
2. Through the elastic-plastic time-history analysis for finite element model of special-shaped column frame structure, we obtain special-shaped column structure have the large earthquake response than the rectangular column structure under multidimensional seismic wave. That is, special-shaped column frame structures are very sensitive to torsional component of seismic wave.
3. The displacement effect of the first floor of regular special-column frame structure under multidimensional seismic should increase about 20%, and the seismic response of irregular frame structure should increase more. So during the design, we should consider the influence of the torsional seismic wave.

## References

- Li Hongnan (1998). *Multidimensional aseismic theory of structure*. Beijing: Science Press [in Chinese].
- Newmark N. M. (1969). Torsion in symmetrical buildings. *Proc. 4thWCEE*, (A 23): 19-30.
- Sun S. J., Chen G. X. (1998). The synthetic method of rotational component of ground motion. *Journal of Seismology*, 1:19-24 [in Chinese].

# Seismic Assessment for a Subway Station Reconstructed within High-Rise Building

Zhengkun Lin<sup>1\*</sup>, Zhiyi Chen<sup>1</sup> and Yong Yuan<sup>1,2</sup>

<sup>1</sup>Department of Geotechnical Engineering, Tongji University, Shanghai 200092, P.R. China  
Tongji University, Shanghai 200092, P.R. China

<sup>2</sup>Key Laboratory of Geotechnical and Underground Engineering of Ministry of Education

**Abstract.** Underground construction at densely populated downtown may confront with reconstruction in existing building. Therefore, mechanical performance of building structure after such reconstruction is the main issue, especially under earthquake. In this present paper, SSI effect is discussed. Dynamic models are built to investigate whether the existing substructure can behavior as the fixed foundation to support the up-structure. Seismic assessment based on dynamic analysis of these structures in two situations, that is, before reconstruction and after it. To account for the response of complicated building structure, software package ETABS are applied to set up three-dimension numerical model. Investigation focuses on typical structural members and drift of reformed structural under seismic inputs.

**Keywords:** SSI effect, high-rise structure, seismic assessment, FEM, reconstruction

## 1 Introduction

It is well known that soil-structure interaction (SSI) could play a significant role on the structural seismic response, yet the effects of SSI on the seismic response of structures had not been taken into account until the 1970s when Wong and Luco (1976) published their journal papers. In 1980s and 1990s, research progress have been made by Spyrakos and Beskos (1986), Gazetas (1991), and Wolf (1985). As far as those high-rise buildings with basement are concerned, when should the SSI effect taken into account and the depth effect of the embedment was recognized by Todorovska (1992).

The setting of basement can increase the depth of foundation, and largely enhanced the stability of the structure. According to the Code for seismic design

---

\*Corresponding author, e-mail: ktongji@gmail.com

of buildings of China, when the lateral stiffness of the basement is not less than double of the lateral stiffness of the level up to the basement, the basement can be regarded as the fixed foundation of the up-ground structure, thus the SSI effect can be ignored. But some research (Li and Lu, 2004) shows that when the high-rise building adopt the box foundation, the variance of structure natural frequency can not be ignored. In this present paper, further studies are made to investigate when the basement can be regarded as the fixed foundation for different type of structures.

## 2 Dynamic Model

The complicated high-rise structural system can be simplified into a multi-particle series model, and the eigenperiod as well as the basic vibration mode play a determined role in seismic design and assessment. In order to investigate when can the basement can be regarded as the fixed foundation of the up-ground structure, this paper adopt a simple 10-level structure with a single basement model as a case.

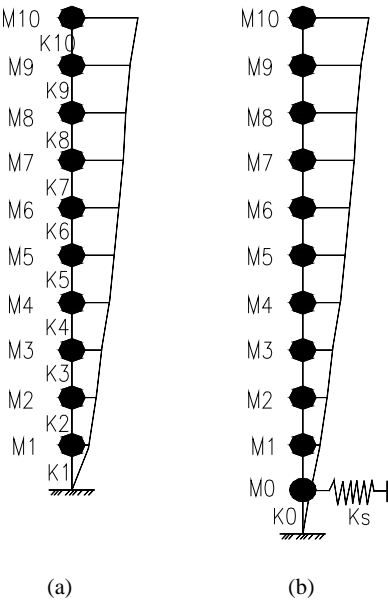


Figure 1. Sketch for calculating model

As shown in Figure 1, (a) depicted the situation when the basement can be regarded as the fixed foundation of the up-ground structure and (b) is the situation

when the SSI effect is taken into account. According to the free vibration equation:

$$[M]\ddot{\{x\}} + [K]\{x\} = 0$$

where the indices [M] represent structural mass matrix, and [K] represent structural stiffness matrix

$$[M] = \begin{bmatrix} m_1 & \mathbf{0} & \cdots & \mathbf{0} \\ \mathbf{0} & m_2 & \cdots & \mathbf{0} \\ \vdots & \vdots & \ddots & \vdots \\ 0 & 0 & \cdots & m_n \end{bmatrix}_{n \times n}; [K] = \begin{bmatrix} k_{00} & k_{01} & \cdots & k_{0n} \\ k_{10} & k_{11} & \cdots & k_{1n} \\ \vdots & \vdots & \ddots & \vdots \\ k_{n0} & k_{n1} & \cdots & k_{nn} \end{bmatrix}_{n \times n}$$

And we assume the mass and lateral stiffness of each up-ground level is m and k respectively, i.e.  $m_1=m_2=m_3\dots=m_{10}=m, k_1=k_2=k_3\dots=k_{10}=k$ , the mass and lateral stiffness of the basement is  $m_0=A \times m$  as well as  $k_0=B \times k$  respectively, and the number n equal to 10 and 11 respectively.

According to static calculation manual for structure design, the number:

$$B = \frac{k_0}{k} = \frac{10 \left[ 4(\beta + 10)^3 - 3439 \right]}{9 \left[ 3(\beta + 10)^4 + 40(\beta + 10)^3 + 10^4 \right]}$$

where the indices  $\beta$  represent the ratio of story height between the basement and the standard floor.

Table 1. Calculating Result of different B Value

B	$\beta$	A=1	A=2	A=3	A=4
		u %	u %	u %	u %
4	0.8	15.8	15.8	15.8	15.8
6	0.6	11.7	11.7	11.7	11.7
11	0.4	7.9	7.9	7.9	7.9
18	0.3	5.8	5.8	5.8	5.8
36	0.2	3.9	3.9	3.9	3.9

In Table 1, the indices  $u = [T(A, B) - T_1] / T_1$ , which T(A,B) represent the eigenperiod corresponding to the situation when the basement taken into account as shown in (a) of Figure1, and T1 represent the eigenperiod corresponding to the

situation the basement regarded as the fixed foundation of the up-ground structure as shown in (b) of Figure1. When  $u\% < 5\%$ , the base-isolated model can satisfy the engineering precision and the SSI effect can be ignored. But, as shown in Table 1, only when  $B > 25$ , the value of  $u\%$  is less than 5%. Actually, for most high-rise structures, the value of  $B$  is range from 1 to 4. Thus, we can come to a conclusion that for most high-rise structures, the SSI effect can not be ignored, and can not regarded the basement to be the fixed foundation of the up-ground structure.

### 3 Seismic Responses

#### 3.1 Case History

Xujiahui district is the most famous CBD of Shanghai, and it is also the urban center of the city's overall plan. In order to improve the intergrated-transport-hub function of Xujiahui, three metro lines were planed to be connected in the ground floor of Grand Gateway Plaza, which is located in the center of Xujiahui district. And the ground floor of Grand Gateway Plaza will be reconstructed to be a distribute hall of metro line 1, metro line 9, metro line 11 of Shanghai, thus the transfer between the three lines can be made in the basement of Grand Gateway Plaza.

Three-dimensional model considering SSI effect are established to assess the seismic performance. There are two high-rise buildings, as depicted in Figure2, named OT1 and OT2 respectively. OT1 and OT2 are frame-corewall structures consist of 53 levels including 3 underground levels.

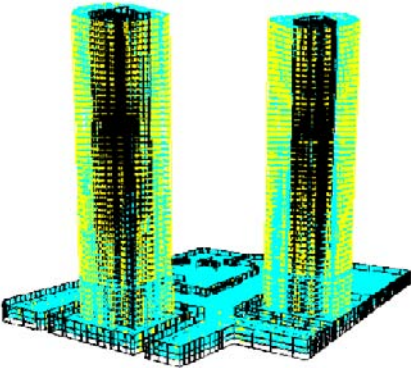


Figure 2. Three-dimensional model

### 3.2 Modeling Assumption

In the present case study, the finite element method software package ETABS was chosen for several reasons (Berkeley, 2002): (1) the code has been extensively verified for static and dynamic analyses of structures; (2) there is extensive experience with the code in the structural fields.

In the present case study, it is assumed that the structure to exhibit an elastic behavior throughout the entire analysis, no elastoplastic behavior was assigned to the structure.

It is assumed that all beam-column joints are fully rigid and possess resistance which are sufficiently large in comparison with their connected members to prevent the occurrence of yield, connection flexibility is therefore not taken into account. Each floor diaphragm is assumed rigid in its own plane but flexible out of it, because of the rigidity, each floor has three common degrees of freedom: two translations and one rotation.

The basic seismic parameters are summarized in Table 2.

Table 2. Basic seismic parameter

Serial Number	seismic parameter	Content
1	Security level	Level I
2	Seismic fortification intensity	7
3	Earthquake acceleration	0.1g
4	The maximum of seismic coefficient	0.08
5	Site classification	IV
6	Site eigenperiod	0.9s
7	Damping ratio	0.05
8	Liquefaction of the soil	No

As far as soil is concerned, most soils exhibit a pronounced nonlinear behavior, and there are two basic approaches in present seismic design of underground structures. One approach is to carry out dynamic, nonlinear soil–structure interaction analysis using finite element methods. The second approach assumes that the seismic ground motions induce a pseudostatic loading condition on the structure. This approach allows the development of analytical relationships to evaluate the magnitude of seismically induced strains in underground structures.

In the present paper, the soil spring is adopted to simulate the interaction between the underground diaphragm and the surrounding soil.

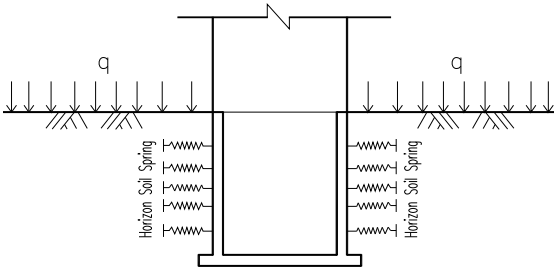


Figure 3. Schematic of horizon soil spring

The stiffness coefficient of horizon soil spring  $K_h$  is determined by:

$$K_h = m \cdot z \cdot b \cdot h$$

where the indices “m” represent horizon coefficient of subgrade reaction; the indices “z” represent value of the vertical distance between soil spring and the ground surface; the indices “b” and “h” represent horizontal and vertical space of soil spring respectively, in the present paper,  $m=5000\text{kN/m}^3$ ,  $b=3.8\text{m}$  and  $h=1.9\text{m}$ .

## 4 Seismic Assessment

In this section, results of the analysis are presented and discussed. Comparisons are made of predicted by ETABS program elastic story drifts, structure eigenperiod, base shear to compare the seismic behavior of the structure before and after the reconstruction.

The comparisons are summarized in Table 3, Table 4, and Table 5. The dynamic characteristics and maximum elastic story drift angle after reconstruction still satisfied the regulation of the Code, thus the reconstruction plan is feasible and reliable.

Table 3. Dynamic characteristic comparison

Mode of vibration	Before Reconstruction			After Reconstruction		
	eigenperiod (s)	Moving participation coefficient(x+y)	Torsion participation coefficient	eigenperiod (s)	Moving participation coefficient(x+y)	Torsion participation coefficient
1	4.3061	0.96 ( 0.91+0.05)	0.04	4.3068	0.96 ( 0.91+0.05)	0.04
2	4.1872	0.99 (0.05+0.95)	0.01	4.1876	0.99 ( 0.05+0.95)	0.01
3	3.4234	0.04 ( 0.04+0.00)	0.96	3.4234	0.04 ( 0.04+0.00)	0.96
4	1.0402	0.71 ( 0.68+0.03)	0.29	1.0403	0.71 ( 0.68+0.03)	0.29
5	1.0085	1.00 ( 0.03+0.97)	0.00	1.0086	1.00 ( 0.03+0.97)	0.00
6	0.8906	0.29 ( 0.28+0.00)	0.71	0.8905	0.29 ( 0.28+0.00)	0.71
7	0.4998	0.57 ( 0.50+0.07)	0.43	0.4998	0.57 ( 0.50+0.07)	0.43
8	0.4728	0.98 ( 0.06+0.92)	0.02	0.4728	0.98 ( 0.06+0.92)	0.02
9	0.4251	0.45 ( 0.44+0.01)	0.55	0.4251	0.45 ( 0.44+0.01)	0.55

Table 4. The ratio of moving vibration mode period and torsion vibration mode

	First moving vibration mode period $T_m$ (s)	First torsion vibration mode period $T_t$ (s)	$T_m/T_t$
Before Reconstruction	4.3061	3.4234	0.795
After Reconstruction	4.3068	3.4234	0.795

Table 5. Maximum elastic story drift angle

Conditions	Maximum elastic story drifts angle		Remarks
	$\frac{D_{xi,max}}{H_i}$	$\frac{D_{yi,max}}{H_i}$	
Before Reconstruction	1/1115	1/1166	The X Axis maximum elastic story drifts angle occurred in story 34, and Y Axis in story 35.
After Reconstruction	1/1115	1/1166	

## 5 Conclusions

In this paper, dynamic calculation models are built to investigate whether the basement can behavior as the fixed foundation of the up-ground structure. And we found that only when the lateral stiffness of the basement is 25 times larger the lateral stiffness of the first up ground level of the structure, the SSI effect can be ignored and the basement can behavior as the fixed foundation of the up-ground structure. But for most high-rise structures, the value of  $B$  is range from 1 to 4. Thus the SSI effect can not be ignored for majority high-rise buildings. Seismic assessment of structures in Xujiahui district under two situations (before and after the reconstruction) are numerical three-dimensionally investigated considering SSI effect, the result showed that the reconstruction plan is feasible and reliable.

## Acknowledgements

The authors would like to acknowledge the support from MOST, China on 'Hazard Prevention for Urban Underground' (Grant Number: 2006BAJ27B04) for which Professor Yuan serves as the primary investigator, and thanks also are extended to Science and Technology Committee of Shanghai Municipal.

## References

- DBJ08-61-97 (2001), Foundation pit design code of Shanghai [in Chinese].
- ETABS2000 Berkeley (2002). CA: CSI: Computers and Structure Inc.
- Gazetas G. (1991). *Foundation vibrations. Foundation engineering handbook*, 2nd ed. London: Chapman & Hall.
- GB50011-2001 (2001). Code for seismic design of buildings of China [in Chinese].
- Group of static calculation manual for structure design, static calculation manual for structure design (1974). Beijing Industrial Press of China [in Chinese].
- Li P.Z. and Lu X.L. (2004). Numerical analysis of tall buildings considering dynamic soil-structure interaction. *Earthquake Engineering and Engineering Vibration*, 24(3): 130-138.
- Spyrakos C.C. and Beskos D.E. (1986). Dynamic response of flexible strip-foundations by boundary and finite elements. *Soil Dynamic and Earthquake Engineering*, 5(2): 84-96.
- Todorovska M.I. (1992). Effects of the depth of the embedment on the system response during building-soil interaction. *Soil Dynamic Earthquake Engineering*, 11: 111-123.
- Wolf J.P. (1985). *Dynamic soil-structure interaction*. New Jersey: Prentice-Hall.
- Wong H.L. and Luco J.E. (1976). Dynamic response of rigid foundations of arbitrary shape. *Earthquake Engineering and Structure Dynamic*, 4: 587-597.
- Zhen Y.L., Yang D.L. et al. (2005). *Seismic design and analysis of underground structures*. Shanghai, Tongji University Press [in Chinese].

# A Simplified Method for Estimating Target Displacement of Pile-Supported Wharf under Response Spectrum Seismic Loading

Pham Ngoc Thach<sup>1,2,3\*</sup> and Shen Yang<sup>1,2</sup>

<sup>1</sup> Key Laboratory of Ministry of Education for Geomechanics and Embankment Engineering, Hohai University, Nanjing 210098, China

<sup>2</sup> Research Institute of Geotechnical Engineering, Hohai University, Nanjing 210098, China

<sup>3</sup> Faculty of Construction Engineering, University of Transport in Hochiminh, Vietnam

**Abstract.** A single wharf segment tends to behave as a simple 1-DOF structure under transverse component of seismic excitation. Main complexities arise from the significant torsional behavior under longitudinal component of seismic excitation. The objective of seismic analysis is to estimate target displacement at critical piles under transverse and longitudinal components of seismic excitation applied simultaneously. This demand can be done by using Multi-mode Spectral Method (MSM) which is a standard one used in most seismic codes. This paper presents a simplified method, called Equivalent Single mode Spectral Method (ESSM). This method determines target displacement by multiplying the displacement induced by transverse component of seismic excitation and a factor, called Displacement Amplification Factor ( $F_a$ ), which accounts for torsional components of response and multi-directional effects of seismic excitation. The proposed equations of  $F_a$  were from a parametric study using 2520 wharf examples with different conditions of soil and structure. In this parametric study, pile-soil interaction was represented by the Winkler spring model, nonlinear force-deformation response of springs was determined based on Matlock's p-y model for soft clay under cyclic loading and MSM was used as a main tool for seismic analysis. The study showed very good fits between displacements resulted from ESSM and that resulted from MSM.

**Keywords:** pile, wharf, seismic analysis, target displacement

---

\* Corresponding author, e-mail: phamngocthach091@yahoo.com

### 1 Introduction

Wharves considered in this study are single wharf segments which are composed of a deck supported by vertical piles (Figure 1). The free lengths of piles in a transverse line of piles vary from landward to seaward because of the sloping dike as shown in Figure 1b and that in a longitudinal line of piles are uniform. The objective of seismic analysis is to estimate target displacement at critical piles, as circled in Figure 1, under transverse and longitudinal components of seismic excitation applied simultaneously which is known as Multi-directional Effects of seismic excitation (PIANC, 2001). This demand can be done by using Multi-mode Spectral Method (MSM) which is a standard one used in most seismic codes.

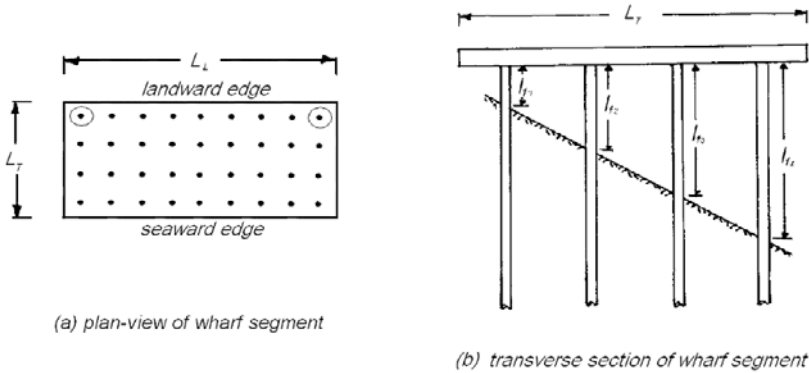


Figure 1. Plan view and transverse section of a wharf segment

Although such 3D analysis can give a good estimate of target displacement, however, for wharf structures having a large number of piles, the computational cost may become much more expensive. A way that significantly reduces the computational cost is using Equivalent Single mode Spectral Method (ESSM). This method is an approximation of MSM, which estimates the target displacement by

$$\Delta_{3D} = F_a \cdot \Delta_{2D} \tag{1}$$

where  $\Delta_{3D}$  is Target Displacement at critical pile;  $\Delta_{2D}$  is Displacement under pure transverse component of seismic excitation;  $F_a$  is Displacement Amplification Factor which accounts for torsional components of response and the multi-directional effects of seismic excitation. Based on the opinion that MSM is referred to be standard for design, a parametric study on displacement amplification

factor was performed in order to find trends for displacement amplification factor, which is presented in the next section.

## 2 Finding Trends for Displacement Amplification Factor (Fa)

### 2.1 Soil, Structural and Seismic Parameters

Tables 1 to 6 define cases of soil, pile, transverse length, longitudinal length, slope and layout of pile, respectively. Five cases of soil in Table 1 reflect soft clay conditions and were based on the statistical study by Dinh (2005) using a large number of soil samples at different sites of ports around Southern Vietnam. In general, the cases selected in Tables 2 to 6 were intended to provide a wide range of structural stiffness and dimensions. There were thus  $5 \times 3 \times 6 \times 7 \times 2 \times 2 = 2520$  wharf examples combined in the cases, detail on each can be found in Pham (2008). Figure 2 shows the displacement design spectrum from TCXDVN375 (2006) which was used in this study with a value of 0.1g for peak ground acceleration. Seismic mass at the deck level included a uniform load of  $40\text{kN/m}^2$  representing dead and live loads and tributary mass of piles, each pile tributary mass was determined by  $1/3(l_f + 5D)\bar{m}$  (PIANC 2001, pages 221 and 226), where:  $\bar{m}$ ,  $l_f$  and  $D$  are mass per unit length, free length and diameter, respectively.

Table 1. Soil properties

Case	$\gamma'$	Cu	Site
1	5.0	1.01z + 4.33	port of Caimep
2	5.1	0.9z + 5.59	port of Thivai
3	5.2	0.87z + 8.2	port of Nhontrach
4	5.1	0.53z + 8.18	port of Hiepphuoc
5	5.1	1.81z + 3.34	port of Catlai

where  $\gamma'$  is average unit weight ( $\text{kN/m}^3$ ),  $C_u$  is undrained shear strength ( $\text{kN/m}^2$ )

Table 2. Pile properties

Case	D	EI	$\bar{m}$	$M_p$
1	0.406	$2.426 \times 10^4$	41.2	180.8
2	0.508	$6.298 \times 10^4$	78.4	291.4
3	0.610	$13.578 \times 10^4$	117.7	523.1

where  $D$  is pile diameter (m),  $EI$  is elastic stiffness ( $\text{kN/m}^4$ ),  $\bar{m}$  is mass per unit length of pile ( $\text{kg/m}$ ),  $M_p$  is plastic moment ( $\text{kN.m}$ ) and elastic-full plastic behavior was assumed to piles

Table 3. Transverse dimensions

Case	1	2	3	4	5	6
$L_T / \Delta L$	3	4	5	6	7	8

Table 4. Longitudinal dimensions

Case	1	2	3	4	5	6	7
$L_L / L_T$	1	2	3	4	5	6	7

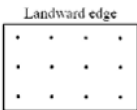
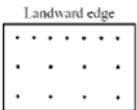
In Tables 3 and 4:  $L_L$  and  $L_T$  are longitudinal and transverse lengths of wharf (m);  $\Delta L$  is span length of wharf (m) which was assumed as follows:  $\Delta L = 4\text{m}$  for the case 1 of pile properties in Table 2,  $\Delta L = 5\text{m}$  for the case 2 of pile properties in Table 2 and  $\Delta L = 6\text{m}$  for the case 3 of pile properties in Table 2. It was also assumed that longitudinal and transverse span lengths are equal.

Table 5. Slope of ground surface

Case	Slope	$L_{f1}$
1	1.75/1.0	2.0m
2	3.5/1.0	10.0m

$L_{f1}$  is the free length of the most landward pile

Table 6. Layout of piles

Case	1	2
Layout		

## 2.2 Methodology

This study focused on lateral seismic responses of wharf due to inertia force at the deck level, it means accepting the assumption that the deformations of soil are small compared to that of structure. Pile-soil interaction was represented by the Winkler spring model, nonlinear force-deformation response of springs was determined based on Matlock’s (1970) p-y model for soft clay under cyclic loading, this has been widely applied in seismic analysis of wharf and pier such as Werner (1998), Ferritto et al (1999), PIANC (2001), CSCL (2003), etc. Wharf deck was assumed to be infinitely rigid, both in-plane and out of plane, as consequence, individual pile pushover analysis could be independently carried out based on full fixity at the top of pile in order to estimate lateral elastic stiffness for piles.

SAP2000 (CSI, 2005), which has special facilities to perform pushover analysis, was used for pile pushover analysis in this study. After a wharf model has been established, seismic analysis proceeds using MSM. 5% damping was assumed to structure. Torsional inertia of deck mass was correctly modeled from deck dimensions with reference to center of mass. Structural stiffness was calculated using the Direct Stiffness Method given by Chopra (2001). CQC rule (Wilson, 1981) was used for modal combination and the Scale Absolute Sum Method with a directional combination factor of 0.3 was applied as recommended by PIANC (2001) to account for the multi-directional effects of seismic excitation. For some wharf examples, the analysis resulted in the target displacement that falls into the inelastic range of the pile pushover curve, in these cases, the “Equal Displacement Approximation” were used i.e. target displacement of inelastic system is equal to that of elastic system, this approximation has been successfully applied to wharf analysis such as Priestley (2000) and CSCL (2003). There were two nondimensional parameters recorded for each analysis which are: 1/ ratio of eccentricity and longitudinal length of wharf ( $e/L_L$ ) and 2/ ratio of target displacement and peak displacement under transverse component of seismic excitation ( $\Delta_{3D} / \Delta_{2D} = F_a$ ), this is just displacement amplification factor. It is also noted that, due to the linear nature of MSM, the ratio  $\Delta_{3D} / \Delta_{2D}$  is independent of peak ground acceleration this study was therefore used a representative value of 0.1 for peak ground acceleration.

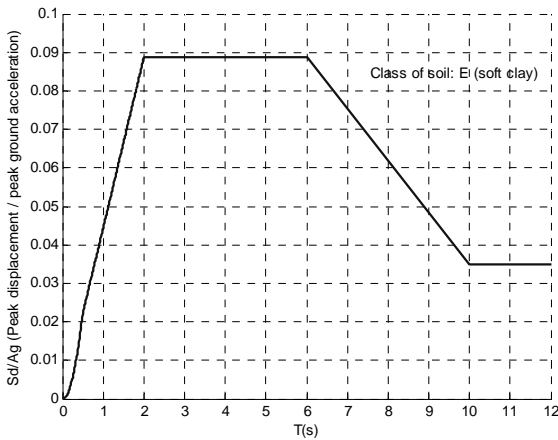


Figure 2. Design displacement spectrum

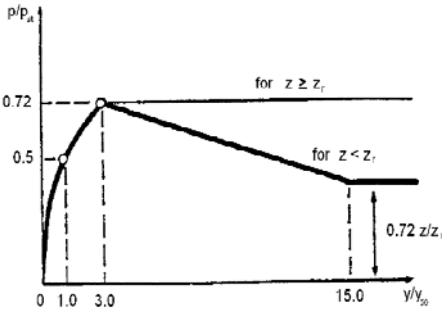


Figure 3. Matlock's (1970) p-y model

### 2.3 Proposed Relations for Displacement Amplification Factor

A statistical study was conducted which showed that the results of  $(\epsilon/L_L, F_a)$  could be divided into three cases corresponding to  $L_L/L_T = 1$ ,  $L_L/L_T = 2$  and  $L_L/L_T \geq 3$  as shown in Figures 4 to 6, respectively. The proposed curves for the cases are also shown in the Figures and their equations are presented in Table 7. In addition, trial analyses by Pham (2008) showed that for intermediate values of  $L_L/L_T$ , approximations by linear interpolation of the cases in Table 7 can provide good representations to  $F_a$ . The upper bound curve for the case  $L_L/L_T \geq 3$ , dashed line in Figure 6, implies that ESSM using this curve will provide a conservative value of target displacement. The statistical parameters in Table 7, determined by equations (2a, b, c), show that the proposed relations, on average, did not underestimate  $F_a$  and provided good fits to the data points with small values of standard deviation ( $\sigma_E$ ).

$$E_i = \frac{(F_{a,app})_i}{(F_{a,ex})_i} \tag{2a}$$

$$\bar{E} = \frac{1}{N} \sum_{i=1}^N E_i \tag{2b}$$

$$\sigma_E = \frac{1}{N-1} \sum (E_i - \bar{E})^2 \tag{2c}$$

where  $F_{a,app}$  is the value from the proposed curves;  $F_{a,ex}$  is the value from MSM;  $E$  is the error;  $N$  is the number of wharf examples in the case under consideration;  $\bar{E}$  and  $\sigma_E$  are mean and standard deviation of the errors

Table 7. Summary of the proposed relations for displacement amplification factor

$L_L/L_T$	Displacement amplification factor $F_a$	$\bar{E}$	$\sigma_E$
1	For $0 \leq e/L_L \leq 0.0705$ , $F_a = 4.6 e/L_L + 1.044$	1.0002	0.0533
	For $e/L_L \geq 0.0705$ , $F_a = 1.287(e/L_L)^{-0.025}$		
2	For $0 \leq e/L_L \leq 0.0409$ , $F_a = 9.5 e/L_L + 1.044$	1.0083	0.0281
	For $e/L_L \geq 0.0409$ , $F_a = 1.67(e/L_L)^{0.048}$		
$\geq 3$	For $0 \leq e/L_L \leq 0.0245$ , $F_a = 14.303 e/L_L + 1.044$	1.0001	0.0187
	For $e/L_L \geq 0.0245$ , $F_a = 2.043(e/L_L)^{0.103}$		
• The upper-bound curve:			
	For $0 \leq e/L_L \leq 0.045$ , $F_a = -172.4(e/L_L)^2 + 18.8 e/L_L + 1.044$	1.0277	0.0201
	For $e/L_L \geq 0.045$ , $F_a = 2.101(e/L_L)^{0.1}$		

where  $L_L$  and  $L_T$  are longitudinal and transverse lengths of wharf (m);  $e$  is eccentricity between centers of mass and rigidity;  $\bar{E}$  and  $\sigma_E$  are mean and standard deviation of the errors.

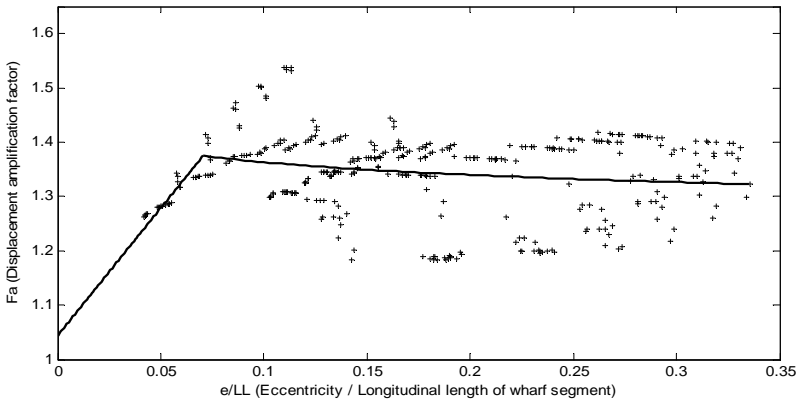


Figure 4. 360 resulting points and the proposed approximate curve in the cases  $L_L/L_T = 1$

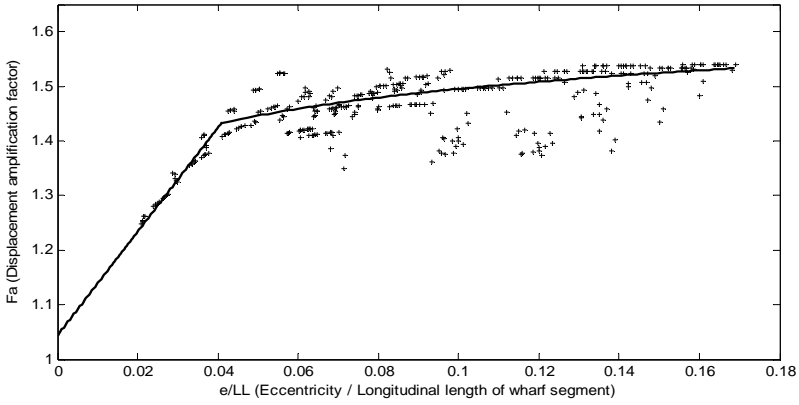


Figure 5. 360 resulting points and the proposed approximate curve in the cases  $L_L/L_T = 2$

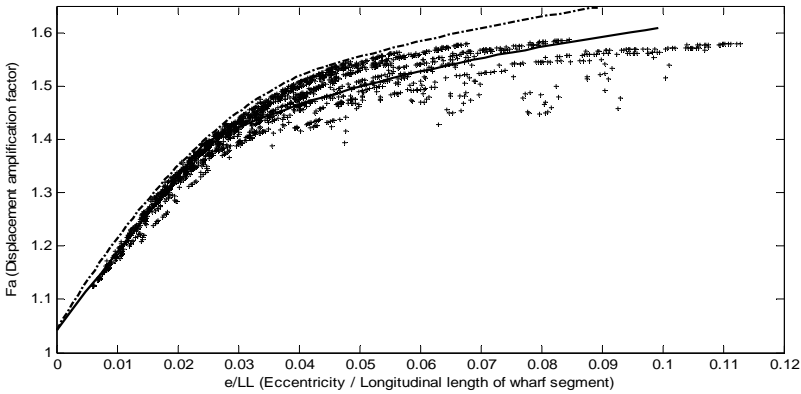


Figure 6. 1800 resulting points, the approximate and upper-bound curves in the cases  $L_L/L_T \geq 3$

### 3 Conclusion

Based on the opinion that the Multi-mode Spectral Method (MSM) is most reliable in code-based design and on the system parameters assumed, this study used MSM to perform a parametric study on displacement amplification factor ( $F_a$ ). The results were fitted by the relations given in Table 7 or Figures 4 to 6. The Equivalent Single mode Spectral Method (ESSM) with three proposed relations of  $F_a$  corresponding to the cases  $L_L/L_T = 1$ ,  $L_L/L_T = 2$  and  $L_L/L_T \geq 3$  can be effective-

ly applied to preliminary design works before a detail analysis of MSM is carried out. In addition, for a wharf having  $L_L/L_T \geq 3$ , an upper-bound value of target displacement can be obtained by ESSM using the upper-bound curve (the dashed line in Figure 6 with the corresponding equation in Table 7). This upper-bound value can be directly applied to final design because of conservatism.

In practice, the computational cost can be further reduced by applying ESSM on a transverse unit-frame of wharf in place of the whole structure and this thus reflects the 2D nature of ESSM. Once ESSM applied in conjunction with the Equivalent Fixity Model of pile, i.e. the pile is considered fully fixed at some depth below the ground surface and the soil is ignored, designers will quickly and readily obtain an estimation of target displacement to the preliminary design process.

## Acknowledgement

This work was supported by National Science Foundation of China (No. 50639010) and Qing Lan Project of Jiangsu Province, China.

## References

- Chopra A.K. (2001). Dynamics of structures: theory and applications to earthquake engineering. Pearson education, Inc
- CSI (2005). SAP2000 version 10. Computer and Structure Inc.
- CSLC (2003). Marine Oil Terminal Engineering and Maintenance Standards (MOTEMS). California State Lands Commission
- Dinh M. C. (2005). Calculation of piles under lateral loading in thick soft clay ground. Ms thesis, University of Technology, Hochiminh, Vietnam. [in Vietnamese]
- Ferritto J.M., Dickenson S.E., Priestley M.J.N., Werner S.D. and Taylor C.E. (1999). Seismic Criteria for California Marine Oil Terminals. Technical Report TR-2103-SHR, Naval Facilities Engineering Service Center, Port Hueneme
- Matlock H. (1970). Correlations for design of laterally loaded piles in soft clay. Paper No. OTC 1204, *Proceedings, Second annual offshore technology conference*, Houston, Texas, 1: 577-594
- Pham N.T. (2008). Research on Response Spectrum Procedures for Seismic Analysis of Pile-Supported Wharf. Msc thesis, Hohai University, China
- PIANC (2001). Seismic Design Guideline for Port Structures. Balkema
- Priestley M.J.N (2000). Seismic Criteria for California Marine Oil Terminals, volume 3: Design Example. TR-2103-SHR, Naval Facilities Engineering Service Center, Port Hueneme
- TCXDVN375 (2006). Vietnamese Code: Design of structures for earthquake resistances.
- Werner S.D. (1998). Seismic Guideline for Port Structures. Technical Council on Lifeline Earthquake Engineering. Monograph No.12, ASCE
- Wilson E.L, Der K.A. and Bayp E.P. (1981). A replacement of the SRSS method in seismic analysis. *Earthquake engineering and structural dynamics*, 9: 187-194

*“This page left intentionally blank.”*

# The Fractal Dimensionality of Seismic Wave

Lu Yu\* and Zujun Zou

Research Institute of Structural Engineering and Disaster Reduction, Tongji University,  
Shanghai 200092, P.R. China

**Abstract.** As a new nonlinear science, fractal theory is investigated and applied widely in many complex fields, such as seismology. Today there have been many research results to prove that seismic waves have fractal characteristics, while the influence and significance of the fractal is neglected calculating earthquake action of practical engineering design. Seismic wave is fractal time series data, and the fractal dimensionality of it is a magnitude which can characterize the degree of the data enriching the time amplitude plane. In this paper, it was pointed out that the fractal dimensionality value also should be as one of the parameters of the seismic waves from researching on the design response spectrum curve. Using an improved ‘box counting method’, this study was carried out to calculate fractal dimensionalities of a set of famous ground motion records in different site conditions and basic intensities. And some characteristics of fractal dimensionalities were introduced though contrasting and analyzing. Furthermore, four influencing factors were illustrated, which can impact the magnitudes of fractal dimensionalities of seismic waves.

**Keywords:** fractal, seismic wave, box counting method, fractal dimensionality

## 1 Introduction

In ‘Code for seismic design of buildings’ (GB 50011-2001, 2001), when considering about earthquake action, some response spectra are obtained at first, which are corresponding with ground motion acceleration time history curves under the same site condition in strong earthquake. Then these spectra are analyzed statistically and a representative average response spectrum curve is presented at last. To be expressed and employed more convenient and simpler, this curve is smoothed by some reasonable methods. The final spectrum curve is named design response spectrum curve which can be used as basis for seismic design. Though it is brief and fast in computing earthquake action quantitatively through this way, there has

---

\* Corresponding author, e-mail: ylgrace85@hotmail.com

a question. In the process of acquiring that spectrum curve, the earthquake action was simplified artificially. That is to say, only the magnitude of peak acceleration was considered, while the distribution and duration were neglected, also the secondary peak value. That spectrum curve was just lay on high frequency components of ground motion, so it was depicted local characteristics merely and can not reflect the whole situation of ground motion. Thus fractal dimensionality of seismic wave was also should be taken into account besides acceleration peak value, duration and frequency spectrum which are characteristic parameters of seismic wave in describing properties of it. Seismic wave is fractal time series data, and the fractal dimensionality of it is a magnitude which can characterize the degree of the data enriching the time amplitude plane. Not only absorptive capacity of different seismic wave on each stratum can be reflected, but also time information of seismic wave itself. The main purpose of this paper was to illustrate that seismic wave was fractal, and fractal dimensionality also should be confirmed as one of characteristic parameters by investigating and calculating. Only by doing this, can the understanding of information of seismic wave be more accurate and detailed, and in practical engineering design, can the consideration of earthquake action be more precise and reasonable.

## 2 Determination of the Fractal Dimensionality

Fractal is one of seismic wave attributes. Basing on the improved “Box counting method” (Benoit, 1977, 1982; Paul, 1998), in this paper, fractal dimensionality was measured quantitatively. Above all, the scaling range of a given earthquake curve was determined by “self-similarity ratio” method, then, the fractal dimensionality of that range can be measured by numerically fitting a straight line to data sets on log-log scales with least square method. The whole calculation process was implemented by a MATLAB program edited by the author.

### 2.1 Calculation Examples

The first example was to estimate fractal dimensionality of an arbitrarily assumed line, which was  $y=1.6x+0.5$ , where  $x$  ranged from 0 to 24 (Figure 1). After running the program, a fitting line was obtained (Figure 2). The fractal dimensionality is just the linear slope in the graphic chart of  $\log N$  versus  $\log e$ . In Figure 2, it can be seen clearly that it is fitted quite well and the slope of the line is 1.003, which is only bigger than topological dimension about 0.003, and the error value is 3%. So it is proved that the whole MATLAB program edited is effective with high solution precision which can be used as a practical approach to the measurement of the fractal dimensionality of “self-similar” structures.

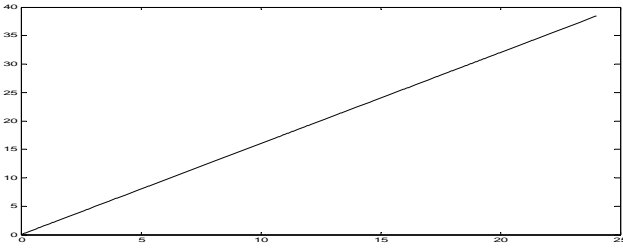


Figure 1. Straight line:  $y=1.6x+0.5$

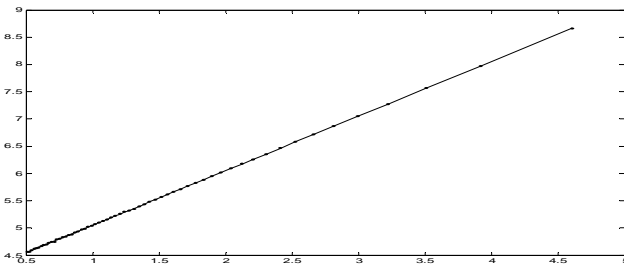


Figure 2. Fitting line with slope of 1.003

Taking NS direction component of Qian'an wave as the other example, in which time interval was 0.01s, duration was 23.19s and peak acceleration was  $-158.62 \text{ cm/s}^2$ . It was employed to calculate the fractal dimensionality of time history curve in the 7-degree seismic intensity zone where peak ground acceleration (PGA) of the design spectrum is considered to be  $0.15g$ . In interval  $[-\ln 0.6, -\ln 0.05]$  of scaling range, fitting all the points between it by least square method, a fitting line was obtained with slope of 1.7218, which indicated that the fractal dimensionality was 1.7218. The fractal dimensionality ( $D$ ) is an indicator that takes value between 1.0000 and 2.0000 and reveals how effectively the curve fills the 2-dimensional time amplitude space. So the  $D$  can be recommended as an index representing the irregular and complex extent of an earthquake wave. And the more irregular the earthquake wave is, the bigger the  $D$  becomes. The Qian'an wave and corresponding fitting line are depicted in Figure 3 and Figure 4, respectively.

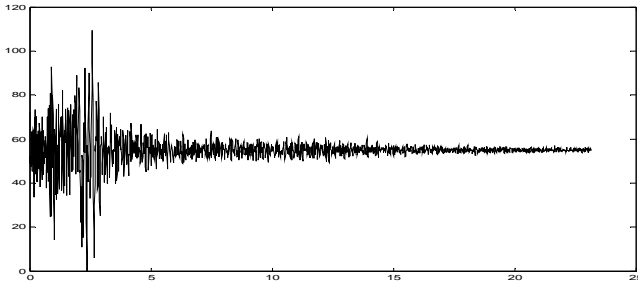


Figure 3. NS direction component of the Qian'an wave

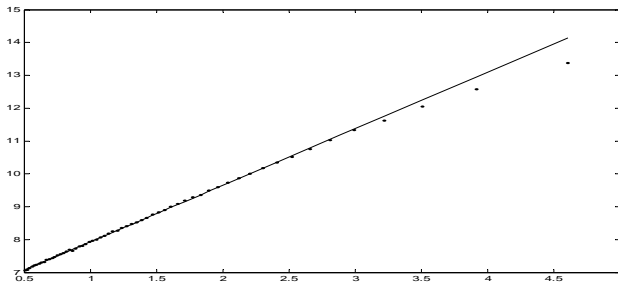


Figure 4. Fitting line with slope of 1.7218

## 2.2 Calculation Results

Measuring fractal dimensionalities of some famous earthquake waves according to different site conditions and seismic intensities by the aforementioned method, calculation results are presented from Table 1 to Table 4.

Table 1. Fractal dimensionalities of earthquake waves in the first class site

Wave	Intensity Direction	Intensity					
		6(0.05g)	7(0.10g)	7(0.15g)	8(0.20g)	8(0.30g)	9(0.40g)
Qian'an wave (No.1)	N-S	1.6989	1.7150	1.7218	1.7241	1.7277	1.7288
	E-W	1.7042	1.7221	1.7296	1.7328	1.7363	1.7379
	U-D	1.7171	1.7336	1.7399	1.7428	1.7461	1.7474
Qian'an wave	N-S	1.7157	1.7308	1.7367	1.7394	1.7424	1.7437
	E-W	1.7083	1.7211	1.7262	1.7282	1.7308	1.7318

(No.2)	U-D	1.7119	1.7278	1.7339	1.7367	1.7398	1.7411
	N-S	1.6039	1.6201	1.6269	1.6292	1.6326	1.6336
Lancang wave	E-W	1.5898	1.6045	1.6099	1.6121	1.6152	1.6162
	U-D	1.7089	1.7239	1.7302	1.7326	1.7354	1.7365
Guangzhou wave	No.1	1.7326	1.7370	1.7387	1.7393	1.7401	1.7405
	No.2	1.7294	1.7340	1.7359	1.7362	1.7374	1.7376
	No.3	1.7517	1.7564	1.7661	1.7670	1.7679	1.7684

Table 2. Fractal dimensionalities of earthquake waves in the second class site

Wave	Intensity Direction	6(0.05g)	7(0.10g)	7(0.15g)	8(0.20g)	8(0.30g)	9(0.40g)
		Gengma wave	N-S	1.4586	1.4758	1.4830	1.4858
	E-W	1.4459	1.4709	1.4790	1.4807	1.4847	1.4860
(No.1)	U-D	1.5774	1.5852	1.5786	1.5799	1.5818	1.5823
Beijing wave	N-S	1.3622	1.3701	1.3730	1.3743	1.3758	1.3765
	E-W	1.3937	1.4011	1.4043	1.4055	1.4072	1.4078
	U-D	1.5942	1.6010	1.6037	1.6048	1.6061	1.6068
Lanzhou wave	No.1	1.7418	1.7468	1.7492	1.7499	1.7510	1.7514
	No.2	1.7387	1.7442	1.7467	1.7474	1.7407	1.7409
	No.3	1.7412	1.7464	1.7485	1.7490	1.7502	1.7505
	No.4	1.7453	1.7506	1.7528	1.7534	1.7540	1.7549
Taft wave	N-S	1.5237	1.5358	1.5417	1.5434	1.5461	1.5471
	E-W	1.5392	1.5555	1.5610	1.5632	1.5662	1.5677
	U-D	1.5840	1.5970	1.6027	1.6045	1.6071	1.6085
El-Centro wave	N-S	1.5208	1.5396	1.5443	1.5476	1.5507	1.5521
	E-W	1.5854	1.5990	1.6047	1.6065	1.6095	1.6102
	U-D	1.6406	1.6727	1.6680	1.6716	1.6757	1.6775
Chichi wave	N-S	1.3524	1.3574	1.3592	1.3600	1.3609	1.3613
	E-W	1.3469	1.3523	1.3543	1.3551	1.3561	1.3566

Table 3. Fractal dimensionalities of earthquake waves in the third class site

Wave	Intensity Direction	6(0.05g)	7(0.10g)	7(0.15g)	8(0.20g)	8(0.30g)	9(0.40g)
		Gengma wave	N-S	1.5309	1.5471	1.5538	1.5563
	E-W	1.5477	1.5463	1.5539	1.5778	1.5608	1.5620
(No.2)	U-D	1.5955	1.6049	1.6093	1.6100	1.6119	1.6127
Lanzhou wave	No.1	1.7519	1.7572	1.7590	1.7597	1.7607	1.7610
	No.2	1.7656	1.7704	1.7723	1.7731	1.7740	1.7744

Hollywood wave	N-S	1.5482	1.5662	1.5774	1.5804	1.5871	1.5893
	E-W	1.5256	1.5567	1.5680	1.5719	1.5783	1.5804

Table 4. Fractal dimensionalities of earthquake waves in the forth class site

Wave	Intensity Direction	6(0.05g)	7(0.10g)	7(0.15g)	8(0.20g)	8(0.30g)	9(0.40g)
		Tianjin wave	N-S	1.3559	1.3635	1.3665	1.3680
	E-W	1.3933	1.4011	1.4052	1.4062	1.4082	1.4088
	U-D	1.6385	1.6464	1.6498	1.6508	1.6524	1.6532
Shanghai artificial wave	No.1	1.3698	1.3751	1.3778	1.3784	1.3798	1.3801
	No.2	1.4187	1.4244	1.4270	1.4063	1.4292	1.4297
	No.3	1.2727	1.2656	1.2680	1.2684	1.2697	1.2698
	No.4	1.4174	1.4250	1.4280	1.4288	1.4304	1.4307
	No.5	1.4809	1.4875	1.4901	1.4909	1.4923	1.4927
Olympia wave	N-S	1.5274	1.5464	1.5509	1.5572	1.5610	1.5622
	E-W	1.5929	1.5854	1.6014	1.6056	1.6117	1.6143
	U-D	1.5658	1.5863	1.5943	1.5969	1.6009	1.6020
Treasure wave	N-S	1.3282	1.3447	1.3501	1.3531	1.3561	1.3573
	E-W	1.3173	1.3152	1.3253	1.3267	1.3313	1.3320

After analyzing those data from the above tables, statistical results are presented in Table 5.

Table 5. Mean values of fractal dimensionalities in different site conditions and seismic intensities

Wave	Intensity	6-degree	7-degree	7-degree	8-degree	8-degree	9-degree
		(0.05g)	(0.10g)	(0.15g)	(0.20g)	(0.30g)	(0.40g)
The 1st class site		1.688	1.701	1.706	1.708	1.711	1.712
The 2nd class site		1.576	1.585	1.589	1.590	1.591	1.592
The 3rd class site		1.649	1.660	1.666	1.667	1.670	1.672
The 4th class site		1.396	1.404	1.407	1.406	1.411	1.412

### **2.3 Results Analysis**

As observed from the data given in above tables, some results are revealed as follows.

1. Fractal dimensionalities of earthquake waves in different site conditions are different.
2. In the same class site, there is a strong correlation can be observed between fractal dimensionality and seismic intensity. With the intensity becoming bigger and bigger, the fractal dimension increases.
3. Although seismic intensities are different, the corresponding scaling ranges are almost unchanged to the same earthquake wave.
4. To different seismic records, fractal dimensionalities are similar in the same site conditions with the same earthquake focus.
5. To different acceleration curves in different site conditions with the same earthquake focus, sometimes the fractal dimensions are similar, while sometimes they are various.
6. Earthquake waves extracted from existing records of Chinese and other countries are different, so there are differences in calculated dimensionalities although they are according to the same site condition. It means that different records should be considered comprehensively in computing earthquake effects. Thus the results presented here would help researchers and practitioners in the selection of ground motions for certain applications.

### **3 Influencing Factors**

Earthquake wave possesses property of self-similar, so it is a fractal structure (Jens, 1988; Donald and Turcotte, 1997). Fractal dimensionality is another parameter different from the three ground motion parameters which describe properties of earthquake wave (Ahmet and Hazim, 2008; Roberto, 2007). The original meaning of fractal dimensionality is to characterize the degree of irregularity or filling degree in space of a curve. In earthquake wave propagation, because of the influence of various external factors, recorded wave becomes complicated. It contains not only ground motion information during the development and occurrence of earthquake, but also relevant information in propagation process. Different earthquake curve has different complex degree, which indicates that each wave has its own fractal dimensionality, and in most time, they are different from each other. So fractal dimensionality also should be confirmed as a characteristic parameter of earthquake wave. In practical engineering design, fractal of earthquake wave should be taken into account adequately in calculating effects of ground motion on buildings and structures.

Some influencing factors of dimensional magnitudes of earthquake waves were analyzed as follows.

1. Influence of peak acceleration value. It can be seen clearly from Table 1 to Table 5 that the dimensionality increases with the growth of peak value.

2. Influence of frequency of earthquake wave. Taking NS direction component of Beijing wave as an example, in which peak acceleration was 55.4868cm/s<sup>2</sup> and duration was 59.92s. Comparing fractal dimensionalities of the whole records with another two modified waves of which time-periods were the front of 20s and the following time from 20s to 40s respectively in different seismic intensities, the results were presented in Table 6. As can be observed from Table 6, the dimensionality increases with frequency growing in the same intensity.

Table 6. Fractal dimensionality of waves with different frequency

Wave	Intensity 6-degree amax=18 cm/s <sup>2</sup>	7-degree amax=35 cm/s <sup>2</sup>	8-degree amax=70 cm/s <sup>2</sup>	9-degree amax=140 cm/s <sup>2</sup>	Main frequency (Hz)
Wave recorded from 0-20s	1.4024	1.4181	1.4276	1.4324	2.002
Wave recorded from 20-40s	1.3445	1.3479	1.3501	1.3512	1.124
The whole records	1.3622	1.3701	1.3743	1.3765	1.111

3. Influence of comparative ratio of peak value. Also taking NS direction component of Beijing wave as an example, in 8-degree seismic intensity, extending the amplitude locally of the middle period from 20s to 40s by amplifying a constant value in different stretching units, the comparison results were given in Table 7. It is indicated that dimensionalities increase with extending units decreasing. That is to say, while comparative ratio of peak value grows, the dimensionality becomes bigger.

Table 7. Fractal dimensionality of waves with different extending units

		Fractal dimensionality	Comparative rise degree
Original wave		1.3743	—
Local extending time unit	0.8s	1.3786	0.313 %
	0.4s	1.3972	1.666 %
	0.2s	1.4384	4.664 %
	0.1s	1.5026	9.336 %
	0.05s	1.5185	10.493 %

4. Influence of symbols alternation. Still taking NS direction component of Beijing wave (8-degree intensity) as an example. Modifying the acceleration curve

to some new ones, of which the positive or negative signs of several continuous recorded points are inconsistent, the calculation results were presented in Table 8. It is shown that fractal dimensionality increases with the number of continuous points decrease, which means that, with the frequency of signs alteration becomes higher, fractal dimension also jumps.

Table 8. Fractal dimensionality in different symbols alternation

		Fractal dimensionality	Comparative rise degree
Original wave		1.3743	—
	5	1.5929	15.906 %
Number of continuous points	4	1.5973	16.226 %
	3	1.7367	26.370 %
	2	1.7386	26.508 %

From the above analysis, a conclusion can be drawn reasonably. Fractal dimensionality will be changed when earthquake wave is extended or compressed vertically, or the wave is extended or compressed locally in the constancy of peak value. And what's more, it also will be different when the frequency of symbols alteration is modified. In each case, the changing degree is inconstant. So it should be distinguished in the course of studying.

## 4 Conclusions

Through study on the calculation process of earthquake action, in this paper, it was pointed out that distribution and duration of peak or secondary peak acceleration had stochastic property because of randomness of earthquake. But in fact, the seismic influence coefficient curve employed widely was just a concrete and determined one, so there had contradiction between them. To remedy this defect, an advice was proposed in this paper, which fractal dimensionality should be applied in calculation of earthquake action as another characteristic parameter of earthquake wave. By calculating and analyzing, a statistic table of fractal dimensionalities of earthquake waves in different site conditions and seismic intensities was presented, and some influencing factors of the magnitude of fraction dimensionality were also investigated.

## References

- Ahmet Yakut and Hazım Yılmaz (2008). Correlation of deformation demands with ground motion intensity. *Journal of Structural Engineering*, Vol. 134(12):1818-1828.

- Benoit B. and Mandelbrot (1977). *Fractal: Form, chance, and dimension*. San Francisco: W.H. Freeman.
- Benoit B. and Mandelbrot(1982). *The fractal geometry of nature*. San Francisco: W. H. Freeman.
- Donald L. and Turcotte (1997). *Fractals and chaos in geology and geophysics*. Cambridge, U.K.: Cambridge University Press.
- GB 50011-2001: Code for seismic design of buildings.
- Jens Feder (1988). *Fractals*. New York: Plenum Press.
- Paul Meakin (1998). *Fractals, scaling and growth far from equilibrium*. Cambridge, U.K.: Cambridge University Press.
- Roberto Villaverde (2007). Methods to assess the seismic collapse capacity of building structures: State of the art. *Journal of Structural Engineering*, Vol. 133(1):57-66 [in Chinese].

# Chaotic Time Series Analysis of Near-Fault Ground Motions and Structural Seismic Responses

Dixiong Yang<sup>1,2\*</sup> and Pixin Yang<sup>1,2</sup>

<sup>1</sup>Department of Engineering Mechanics, Dalian University of Technology, Dalian 116023, China

<sup>2</sup>State Key Laboratory of Structural Analysis for Industrial Equipment, Dalian 116023, China

**Abstract.** Nonlinear dynamics theory and chaotic time series analysis are suggested to investigate the nonlinear characteristic of near-fault ground motions and structural seismic responses in this paper. Based on the power spectrum analysis and principal component analysis, it is illustrated qualitatively that the acceleration time series of ground motions have chaotic property. Then, the chaotic time series analysis is applied to calculate quantitatively the nonlinear characteristic parameters of 30 acceleration time histories of near-fault ground motions. Numerical results show that the correlation dimension of these ground motions is fractal dimension with the value 1.0-4.0, and their maximal Lyapunov exponent is in the interval 0-2.0. The average maximum Lyapunov exponents between the ground motions with rupture forward directivity and fling-step effect are close, while those values of non-pulse ground motions are smaller. Moreover, the earthquake ground motions present the chaotic characteristic rather than the pure random signal. Finally, the chaotic feature of seismic responses of single degree of freedom systems subjected to ground motions is revealed by using chaotic time series analysis.

**Keywords:** near-fault ground motions, chaotic time series analysis, correlation dimension, maximal Lyapunov exponent, structural seismic responses, chaotic characteristic

## 1 Introduction

The engineering characteristics of near-fault ground motions are an important research topic in engineering seismology and earthquake engineering. Since 1947, when earthquake ground motion was firstly viewed as random process by Housner, the random vibration analysis of seismic response of structure has been implemented popularly. There are several random process models of ground mo-

---

\* Corresponding author, e-mail: yangdx@dlut.edu.cn

tion such as white noise model, filter noise model and harmonic wave model as well as non-stationary model, which represent the stochastic property of ground motions. Undoubtedly, it is reasonable to certain degree that the aggregation of ground motion samples is regarded as a random process for the convenience of structural random response analysis. However, do earthquake ground motions have other properties besides their randomness? Is there an intrinsic law for the ground motion recordings which is covered by the superficial irregularity and disorder?

In fact, another side of the earthquake ground motion's complexity has been ignored for a long time, namely nonlinear property, because the nonlinear dynamics theory and nonlinear time series analysis to solve highly nonlinear problems had not developed until 1980s. The nonlinear characteristic of ground motions is reflected in two aspects: (1) the waveform of ground motion time series is nonlinear, which cannot be linearly represented by harmonic waves; (2) the ground motions depend sensitively on the initial conditions including site conditions, the initial and boundary value condition of nonlinear dynamical equations and so on. Recently, nonlinear science and nonlinear time series analysis based on chaos theory are developing quickly (MaCauley, 1993; Kantz and Schreiber, 1997). It inspires us to explore the nonlinear character of ground motion time series in the dynamical state space, which completely differs from the probabilistic approach for random process. The chaotic time series analysis uses the dynamical modeling instead of probabilistic modeling, and applies the phase space reconstruction to replace time and frequency domain analysis, which is a deterministic analysis method.

This paper investigates the chaotic character of near-fault ground motion by the qualitative method and especially the quantitative method. Firstly, the qualitative methods such as power spectrum analysis and principal component analysis are introduced. Next, chaotic time series analysis to quantitatively calculate the nonlinear characteristic parameters are suggested. Moreover, the nonlinear properties in acceleration time histories of near-fault ground motions are analyzed. Finally, the seismic dynamic responses of single degree of freedom (SDOF) systems subjected to ground motions are examined by using chaotic time series analysis.

## 2 Methods to Identify Chaos

The methods to distinguish chaos include three kinds such as qualitative method, quantitative method and hybrid method combining the two methods. Qualitative method mainly differentiates the periodic, chaotic or random character of the system via showing the spatial structure and frequency property of the nonlinear time series in time domain or frequent domain, in which the familiar approaches are power spectrum analysis, principal component analysis and Poincare section analysis etc. Quantitative method mainly characterizes the chaos and chaotic level

through computing the correlation dimension, Kolmogorov entropy and Lyapunov exponent of nonlinear time series, which are the invariant of chaotic attractors and are very important to identify the chaos (Kantz and Schreiber, 1997).

Power spectrum analysis is an important method to study a system evolving from periodic bifurcation to chaos. Power spectrum expresses the statistical properties of various frequency components of system's motion, in which the periodic motion corresponds to a sharp peak, chaos shows the background noise and wide frequency, and the pure white noise represents a straight line. However, in the actual calculation, the data is limited and the spectral analysis is also performed by limited resolution factor. Hence, there are no clear boundary lines between a very long periodic solution and a chaotic solution from the viewpoint of physical experiments and numerical simulation, which is also the major drawback of the power spectrum analysis.

The principal component analysis method (also known as singular value decomposition) is proposed in recent years, which is an effective method to identify the chaos and noise. The principal components spectrum of the noise is a line almost parallel to X-axis, while that of chaotic signal is a straight line which passes the vertex and has negative slope. Consequently, the standard deviation of principal component distribution can distinguish chaos and noise.

Chaotic time series analysis based on nonlinear dynamics has been developed since 1980s. Researchers discovered that there was randomness in some deterministic nonlinear systems, which is caused by the chaos of the system rather than its random factors. Therefore, for this time series it is not appropriate to apply stochastic approach to deal with them. Whereas, the chaotic time series analysis is suitable for this kind of time series, which is a nonlinear dynamical method in essence. It is applied to study the chaotic property of the system based on single variable time series which reflects the system's evolution, further calculate the attractor's nonlinear characteristic parameters: correlation dimension, Kolmogorov entropy and Lyapunov exponents.

### 3 Verification of Chaotic Time Series Analysis Procedure

Studying chaos from time series is based on the phase space embedding theory. In 1981 Takens proposed the delay-coordinate method which is the most common method to reconstruct the phase space, and to analyze the single variable time series in the nonlinear system and resume the nonlinear dynamical properties (Kantz and Schreiber 1997). This method uses the system's single variable time series  $x=\{x_i|i=1,2,\dots,N\}$ , after embedding phase space the time series becomes

$$Y=\{y_j|y_j=[x_j,x_{j+\tau},\dots,x_{j+(m-1)\tau}]^T, \quad j=1,2,\dots,M\} \quad (1)$$

where  $m$  denotes the embedding dimension,  $\tau$  is the time lag,  $M = N - (m - 1)\tau$  is the number of points in the state space.

To verify the procedures for nonlinear time series analysis, this paper introduces Gaussian white noise as random signal, and the chaotic time series from classical chaotic system as chaotic signal. Specifically, the periodic signal is taken as sine wave of which the period is 0.02 s, namely,  $\sin(100\pi x)$ . The chaotic signal is taken from Lorenz system in the reference (MaCauley, 1993). Figure 1 shows the power spectrum of three kinds of series, from which there is significant difference between chaotic and random series. The chaotic series presents continuous power spectrum, while white noise's power spectrum approximately exhibits a straight line. Figure 2 illustrates the principal component of the chaos and noise. It is seen that the principal component spectrum of chaotic signal is a straight line with a negative slope, while that of the noise is a horizontal line.

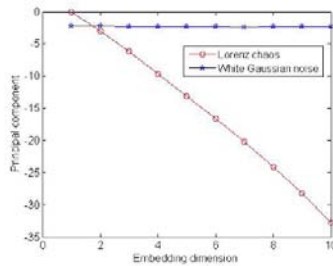
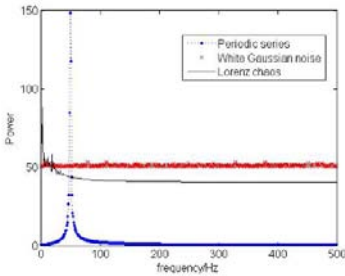


Figure 1. power spectrum of three series.      Figure 2. principal component of chaos and noise.

Thereafter, the correlation dimension and maximal Lyapunov exponent of several chaotic systems including Lorenz equations, Logistic map, Henon map, Duffing equations and Rossler equations are calculated based on phase space embedding and characteristic parameter computation. The error between the results of this paper and the references (MaCauley 1993; Kantz and Schreiber 1997) are compared, which is in the range of 1% and 13% indicating that the procedure of chaos time series analysis in this paper is viable and effective.

### 4 Chaotic Time Series Analysis of Near-Fault Ground Motions

In recent years, severe structural damages caused by near-fault ground motion have been intensively concerned and investigated in earthquake engineering. Dynamic rupture forward directivity and static fling-step effect produce two different long period velocity pulses (Yang et al. 2009), which input the high energy into the structure at the beginning of the earthquake to damage the structure. Herein, 30 near-fault ground motion recordings are selected from the great earthquakes in-

cluding Chi-Chi earthquake in Taiwan, China (1999, 9, 21,  $M_w=7.6$ ) and Northridge earthquake in USA (1994, 1, 17,  $M_w=6.7$ ). These records are classified to three groups such as velocity pulses with rupture forward directivity, fling-step and without pulses listed in Table 1. For all the records,  $PGA>100$  gal,  $PGV>30$  cm/s and distance close to fault is less than 20 km. Moreover, the mean correlation dimension  $D$  and maximal Lyapunov exponent  $\lambda_1$  of the acceleration time series of the three groups of records are shown in this table.

According to the numerical results, some observations can be obtained as follows. (1) The correlation dimension of these acceleration time series is fractal dimension with the value 1.0-3.8, illustrating that these ground motions present fractal characteristic. Further, the nonlinear time series of ground motions can be considered as a 7 dimensional dynamical system in terms of the formula for calculating the embedding dimension. (2) The maximal Lyapunov exponents of these time series are in the interval 0.0665-1.0861. Combining with these two parameters, it is concluded that these ground motions do present chaotic characteristic. (3) The maximal Lyapunov exponents amongst ground motions show the significant difference, which indicates that the chaotic level of them is different. In light of Table 1, the mean of maximal Lyapunov exponents of near-fault ground motions with rupture forward directivity is close to that of ground motions with fling-step effect, while that value of non-pulse ground motions is smaller.

Table 1. Mean nonlinear parameters of near-fault ground motion

Acceleration responses	Correlation dimension $D$	Maximal Lyapunov exponent $\lambda_1$
Pulses with forward directivity	2.4968	0.4956
Pulses with fling step	2.7797	0.5052
Without velocity pulses	2.7443	0.4862

## 5 Chaotic Time Series Analysis of Responses of SDOF Systems

The chaotic feature of seismic responses of elastic and bilinear SDOF systems subjected to near-fault ground motions from Chi-Chi earthquake, including 5 records with forward directivity pulses and 5 records without pulses, is revealed by using chaotic time series analysis herein.

According to the results of SDOF systems with representative periods  $T=0.3$  s, 1.0 s and 3.0 s in Table 2, it is observed that: (1) the acceleration responses of SDOF systems subjected to near-fault ground motions retain the chaotic characteristic; (2) the correlation dimension of these responses is fractal dimension with the value 0.8-4.0, but the correlation dimension of responses of bilinear systems are larger; (3) the maximal Lyapunov exponent is in the interval 0.0361-

1.6732 which shows that there is chaotic property; (4) the mean maximal Lyapunov exponents of acceleration of systems subject to non-pulse ground motions are bigger, and those exponents of responses of elastic systems are greater.

Table 2. Mean correlation dimension and maximal Lyapunov exponents of seismic responses of SDOF systems

	$T=3$ s, elastic	$T=3$ s, bilinear	$T=1$ s, elastic	$T=1$ s, bilinear
Correlation dimension $D$				
Impulsive ground motions	1.7219	1.7231	2.1351	2.1492
Non-pulse ground motions	1.8508	1.9400	1.8355	2.1868
Maximal Lyapunov exponent $\lambda_1$				
Impulsive ground motions	1.0489	0.5323	0.3680	0.3093
Non-pulse ground motions	0.9389	0.6191	0.7378	0.5266

## 6 Conclusions

In the past several decades, earthquake ground motions have been considered as a random process, this paper attempts to investigate the irregularity and complexity of ground motions from the perspective of nonlinear dynamics. There are lots of chaotic systems in various disciplines, of which the output response is chaotic time series. Similarly, the ground motion recordings as the output of the complicated nonlinear geophysical systems may be also the chaotic time series.

The numerical results illustrate that the near-fault ground motions and seismic responses of elastic and bilinear SDOF systems present the chaotic characteristic instead of pure random signal, in which the chaotic time series can be viewed as pseudorandom process originated from the deterministic nonlinear systems.

## Acknowledgements

Supports of the National Natural Science Foundation of China (Grant nos. 10672030, 90815023) are highly appreciated.

## References

Housner G. W. (1947). Characteristics of strong motion of earthquakes. *Bulletin of the Seismological Society of America*, 37(1): 19-31.

- Kantz H., Schreiber T. (1997). *Nonlinear Time Series Analysis*. Cambridge University Press, Cambridge.
- MaCauley J. L. (1993). *Chaos, Dynamics and Fractals*. Cambridge University Press, Cambridge.
- Yang D.X., Pan J. W., Li G. (2009). Non-structure-specific intensity measure parameters and characteristic period of near-fault ground motions. *Earthquake Engineering and Structural Dynamics*, 38: 889.

*“This page left intentionally blank.”*

# Parameters Observation of Spatial Variation Ground Motion

Yanli Shen<sup>1,2\*</sup>, Qingshan Yang<sup>2</sup> and Lingyan Xuan<sup>1</sup>

<sup>1</sup>College of Civil Engineering, Hebei Engineering University, Handan 056038, P.R. China

<sup>2</sup>School of Civil Engineering, Beijing Jiaotong University, Beijing 100044, P.R. China

**Abstract.** The procedure of random vibration analysis of linear structure subjected to spatial variation ground motion was deduced. A linear continuous beam subjected to spatial variation ground motion was established; By using the Claugh-Penzien self power spectrum model and Harichandran-Vanmarcke coherence function model, the influences of distance between supports, system damping ratio, and site condition on structural mean square response were researched, the results of parameters studies are useful for further studies.

**Keywords:** random vibration, spatial variation ground motion, means square response, parameter study

## 1 Introduction

For large engineered structures such as dams, bridges, pipelines, etc, their seismic responses are determined by spatial variation earthquake ground motion (SVEGM) (Loh and Ku, 1995). The design of those structures must consider the spatial variation of ground motion. However, there are less as-recorded SVEGM, so the seismic design of structures with large span has to use simulated records. To generate simulated records, there will be many input parameters, such as passage velocity, coherence coefficient, and so on. The selection of these parameters is important for the simulated SVEGM.

It has been shown that the causes of SVEGM are (Zerva and Zervas, 2002):  
a. *Wave passage effect*: Seismic waves arrive at different times at different stations.  
b. *Incoherence effect*: Differences in the manner of superposition of waves (a) arriving from an extended source, and (b) scattered by irregularities and inhomogeneities along the path and at the site, causes a loss of coherency.  
c. *Local site effect*: Differences in local soil conditions at each station may alter the amplitude and frequency content of the bedrock motions differently. To describe the spatial

---

\* Corresponding author, e-mail: caseyshen@sina.com

variation, there are many parameters involved. To observe the influence of these parameters on structural response, this study will adopt random vibration theory.

In this paper, the procedure of random vibration response of linear structure subjected to SVEGM will be deduced; and parameters study will be performed by using the cross spectrum matrix established by using Claugh-Penzien power spectrum model and Harichandran-Vanmarcke coherence function model.

## 2 Random Vibration Response of Structure Subjected to SVEGM

The dynamic response equation of linear system with  $n$  degrees of freedom and  $m$  supports is:

$$\begin{bmatrix} \mathbf{m} & \mathbf{m}_g \\ \mathbf{m}_g^T & \mathbf{m}_{gg} \end{bmatrix} \begin{Bmatrix} \ddot{\mathbf{u}}^t \\ \ddot{\mathbf{u}}_g \end{Bmatrix} + \begin{bmatrix} \mathbf{c} & \mathbf{c}_g \\ \mathbf{c}_g^T & \mathbf{c}_{gg} \end{bmatrix} \begin{Bmatrix} \dot{\mathbf{u}}^t \\ \dot{\mathbf{u}}_g \end{Bmatrix} + \begin{bmatrix} \mathbf{k} & \mathbf{k}_g \\ \mathbf{k}_g^T & \mathbf{k}_{gg} \end{bmatrix} \begin{Bmatrix} \mathbf{u}^t \\ \mathbf{u}_g \end{Bmatrix} = \begin{Bmatrix} \mathbf{0} \\ \mathbf{P}_g(t) \end{Bmatrix} \quad (1)$$

where  $\mathbf{m}$ ,  $\mathbf{c}$  and  $\mathbf{k}$  are mass matrix, damping matrix and stiffness matrix of upper structure respectively;  $\mathbf{m}_{gg}$ ,  $\mathbf{c}_{gg}$  and  $\mathbf{k}_{gg}$  are mass matrix, damping matrix and stiffness matrix of support structure respectively;  $\mathbf{m}_g$ ,  $\mathbf{c}_g$  and  $\mathbf{k}_g$  are coupled matrix;  $\mathbf{u}^t$  and  $\mathbf{u}_g$  are displacement vectors of upper and support structure respectively;  $\mathbf{P}_g(t)$  is excitation.

Using pseudo-static method, the structural displacement response is divided into two parts:

$$\begin{Bmatrix} \mathbf{u}^t \\ \mathbf{u}_g \end{Bmatrix} = \begin{Bmatrix} \mathbf{u}^s \\ \mathbf{u}_g \end{Bmatrix} + \begin{Bmatrix} \mathbf{u} \\ \mathbf{0} \end{Bmatrix} \quad (2)$$

where  $\mathbf{u}^s$  is displacement vector corresponding to  $\mathbf{u}_g$  which is induced by pseudo static support force at support.

$$\begin{bmatrix} \mathbf{k} & \mathbf{k}_g \\ \mathbf{k}_g^T & \mathbf{k}_{gg} \end{bmatrix} \begin{Bmatrix} \mathbf{u}^s \\ \mathbf{u}_g \end{Bmatrix} = \begin{Bmatrix} \mathbf{0} \\ \mathbf{P}_g^s \end{Bmatrix} \quad (3)$$

where  $\mathbf{P}_g^s$  is the pseudo static support force;  $\mathbf{u}^s$  is dynamic displacement.

Expanding all first partition matrixes in equation (1), there is the new equation,

$$\mathbf{m}\ddot{\mathbf{u}}' + \mathbf{m}_g \ddot{\mathbf{u}}_g + \mathbf{c}\dot{\mathbf{u}}' + \mathbf{c}_g \dot{\mathbf{u}}_g + \mathbf{k}\mathbf{u}' + \mathbf{k}_g \mathbf{u}_g = \mathbf{0} \quad (4)$$

Substituting equation (2) into equation (4), then,

$$\mathbf{m}\ddot{\mathbf{u}} + \mathbf{c}\dot{\mathbf{u}} + \mathbf{k}\mathbf{u} = \mathbf{P}_{eff}(t) \quad (5)$$

where  $\mathbf{P}_{eff}(t)$  is effective force vector,

$$\mathbf{P}_{eff}(t) = -(\mathbf{m}\ddot{\mathbf{u}}^s + \mathbf{m}_g \ddot{\mathbf{u}}_g) - (\mathbf{c}\dot{\mathbf{u}}^s + \mathbf{c}_g \dot{\mathbf{u}}_g) - (\mathbf{k}\mathbf{u}^s + \mathbf{k}_g \mathbf{u}_g) \quad (6)$$

According to equation (3),  $\mathbf{k}\mathbf{u}^s + \mathbf{k}_g \mathbf{u}_g = \mathbf{0}$ , then,  $\mathbf{u}^s = \boldsymbol{\iota}\mathbf{u}_g$ , where,  $\boldsymbol{\iota} = -\mathbf{k}^{-1}\mathbf{k}_g$ . Therefore, equation (6) becomes

$$\mathbf{P}_{eff}(t) = -(\mathbf{m}\boldsymbol{\iota} + \mathbf{m}_g)\ddot{\mathbf{u}}_g - (\mathbf{c}\boldsymbol{\iota} + \mathbf{c}_g)\dot{\mathbf{u}}_g \quad (7)$$

For ordinary structures, the damping components in equation (7) can be neglected, and  $\mathbf{m}_g$  is usually blank matrix (Chopra, A. K. 2001). Thus the effective force  $\mathbf{P}_{eff}(t) = -\mathbf{m}\ddot{\mathbf{u}}_g$ .

In frequency domain, it is assumed that  $\ddot{\mathbf{u}}_g$  is expressed as  $\ddot{\mathbf{u}}_g(j\omega)$  and the cross spectrum matrix is  $\mathbf{S}(\omega)$ , then, equation (5) can be expressed as

$$\left[ -\omega^2\mathbf{M} + j\omega\mathbf{C} + \mathbf{K} \right] \mathbf{u}(j\omega) = -\mathbf{M}\ddot{\mathbf{u}}_g(j\omega) \quad (8)$$

For linear systems, equation (8) can be decoupled by mode superposition method. For structure with  $n$  DOFs, there are  $n$  natural frequencies  $\omega_1^2, \omega_2^2, \dots, \omega_n^2$  and  $n$  orders modal matrix  $\Phi = [\Phi_1, \Phi_2 \dots \Phi_n]$ . The  $l$ th modal damping ratio and corresponding equation are

$$\xi_l = \frac{1}{2\omega_l \Phi_l^T \mathbf{M} \Phi_l} \Phi_l^T \mathbf{C} \Phi_l; (\omega_l^2 - \omega^2 + 2j\omega_l \xi_l \omega) u_l(j\omega) = \frac{\Phi_l^T \mathbf{M} \ddot{\mathbf{u}}_g(j\omega)}{\Phi_l^T \mathbf{M} \Phi_l} \quad (9)$$

Then,  $\mathbf{u}(j\omega)$  is the displacement response in frequency domain,

$$\mathbf{u}(j\omega) = \Phi \left[ \text{diag}(H_l(\omega)) \right] \Phi^T \frac{\Phi^T \mathbf{M} \ddot{\mathbf{u}}_g(j\omega)}{\Phi^T \mathbf{M} \Phi} = \mathbf{H}(\omega) \mathbf{L} \ddot{\mathbf{u}}_g(j\omega) \quad (10)$$

where  $H_l(\omega) = (\omega_l^2 - \omega^2 + 2j\omega_l\zeta_l\omega)^{-1}$ , which is the frequency response function of  $l$  mode;  $\mathbf{H}(\omega)$  is frequency response matrix;  $\mathbf{L} = \frac{\Phi^T \mathbf{M} \mathbf{l}}{\Phi^T \mathbf{M} \Phi}$  is the influence matrix of excitations. Having the cross spectrum matrix  $\mathbf{S}(\omega)$  of excitations, the displacement response spectrum matrix is

$$\mathbf{S}_u(\omega) = \mathbf{H}(\omega)^* \mathbf{L} \mathbf{S}(\omega) \mathbf{L}^T \mathbf{H}(\omega)^T \tag{11}$$

By integrating  $\mathbf{S}_u(\omega)$  in frequency domain, the displacement mean square response can be obtained (Soong and Grigoriu, 1993).

As for the excitation model, the self power spectrum of each support adopts Clough-Penzie model.

$$S(\omega) = S_0 \cdot \frac{1 + 4\zeta_g^2 (\omega/\omega_g)^2}{\left[1 - (\omega/\omega_g)^2\right]^2 + 4\zeta_g^2 (\omega/\omega_g)^2} \times \frac{(\omega/\omega_f)^4}{\left[1 - (\omega/\omega_f)^2\right]^2 + 4\zeta_f^2 (\omega/\omega_f)^2} \tag{12}$$

where  $S_0$  is the constant about the acceleration intensity;  $\omega_g, \zeta_g$  are natural frequency and damping ratio of SDOF soil model;  $\omega_f, \zeta_f$  are parameters of the specified filter.

The cross power spectrum between supports is expressed by coherence function. Based on the Harichandran-Vanmarcke (1986) model, the retarded coherence function between support  $i$  and support  $j$  is

$$\gamma_{ij}(\omega) = [A \exp(-\frac{2d_{ij}}{\alpha\theta(\omega)}(1 - A + \alpha A)) + (1 - A) \exp(-\frac{2d_{ij}}{\theta(\omega)}(1 - A + \alpha A))] \times \exp(-\frac{i\omega d_{ij}}{v}) \tag{13}$$

where  $\theta(\omega) = k / \sqrt{1 + (\omega/\omega_0)^b}$ ;  $d_{ij}$  is the distance between  $i$  and  $j$ ;  $A, \alpha, k, \omega_0, b$  are regressive coefficients,  $A=0.626, \alpha=0.022, k=19700\text{m}, \omega_0=12.692\text{rad/s}, b=3.47$ ;  $v$  is the wave passage velocity.

### 3 Parameter Study

#### 3.1 The Numerical Model

As shown in Figure 1, a simple two-span continuous beam model is established. In Figure 1,  $EI$  is flexural stiffness;  $L$  is span length;  $m_1$  and  $m_2$  are lumped mass at span 1 and span 2 respectively, and if the linear mass density is  $m_0$ ,  $m_1=m_2=m_0L/2$ .

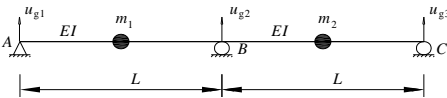


Figure 1. Numerical analytical model

The parameters to be studied are: (1)  $L$ , assuming that  $EI/m_0$  is a constant,  $\zeta=0.05$ , the change of mean square response of model with the change of span will be observed; (2)  $\zeta$ , assuming that  $EI/m_0$  and  $L$  are constants,  $\zeta=0.02,0.05,0.08,0.10,0.20$ , the change of mean square response of model will be observed; (3) site condition, three kinds of site condition will be observed, which are soft soil, hard soil and rock, and the corresponding parameters of each kind of site condition can be seen in Table 1; (4)  $\nu$ , the effect of passage wave will be observed.

Table 1. Value of parameters at given site

Site condition	$S_0$ $m^2/s^3$	$\omega_g$ rad/s	$\zeta_g$	$\omega_f$ rad/s	$\zeta_f$
Rock	0.006	$8.0\pi$	$0.8\pi$	0.60	0.60
Hard soil	0.010	$5.0\pi$	$0.5\pi$	0.60	0.60
Soft soil	0.018	$2.4\pi$	$0.24\pi$	0.85	0.85

#### 3.2 Analytical Results

##### 3.2.1 Parameter Study of L

It is assumed that linear mass density is  $m_0$ ;  $EI=5 \times 10^4(m_0)$ ;  $\zeta=0.05$ , soft soil;  $\nu=3000m/s$ ;  $L=50m, 60m, 70m, 80m, 90m, 100m, 120m, 200m$ . The results are shown in Figure 2.

It can be seen form Figure 2 that the mean square response decreases with increasing of  $L$ , which is because the stiffness will decrease with increasing of  $L$  and

the relativity between supports will decrease too. The results show that with increasing of  $L$ , structural responses are more stable, and the structural reliability is more controllable.

### 3.2.2 Parameter Study of $\xi$

It is assumed that linear mass density is  $m_0$ ;  $EI=5 \times 10^4(m_0)$ ;  $L=100m$ ; soft soil;  $v=3000m/s$ ;  $\xi=0.02, 0.05, 0.08, 0.10, 0.20$ . The results are shown in Figure 3.

As shown in Figure 3, the mean square response decreases with increasing of  $\xi$ , which is identical to the behavior of structural response due to increasing of  $\xi$ . At the same time, the decrease of  $m_1$  is less than  $m_2$ , which means that variation of  $\xi$  will influence either span of the model more.

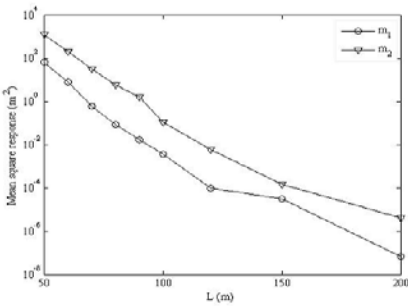


Figure 2. Influence of  $L$  on displacement mean square response

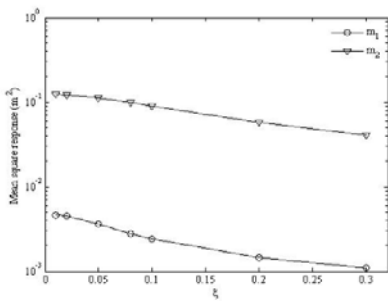


Figure 3. Influence of  $\xi$  on displacement mean square response

### 3.2.3 Parameter Study of Site Condition

For observing the influence of site condition on mean square response and the error induced by substituting identical excitation for SVEGM, two load cases was designed. Case 1: multiple support excitations; case 2: identical excitation. It is assumed that linear mass density is  $m_0$ ;  $EI=5 \times 10^4(m_0)$ ;  $L=100m$ ;  $v=3000m/s$ ; soft soil;  $\xi=0.05$ . The results are shown in Figure 4.

As shown in Figure 4, harder the site is, less mean square response is, which is because frequency components are relatively simple after wave traveled through site soil.

Figure 4 also shows that mean square responses induced by identical excitation are smaller than the one due to SVEGM, which shows that the mean square response results would be conservative if incoherence effect be neglected (identical excitation).

### 3.2.4 Parameter Study of $v$

It is assumed that linear mass density is  $m_0$ ;  $EI=5 \times 10^4(m_0)$ ;  $L=100m$ ;  $\xi=0.05$ ;  $v=200m/s, 400m/s, 600m/s, 800m/s, 1000m/s, 2000m/s, 3000m/s, 4000m/s$ . The results are shown in Figure 5.

As shown in Figure 5, for all site conditions, the influences of  $v$  on mean square response are very small, and mean square response takes on trend of increase with passage velocity only if  $v$  is relatively small. According to these results, the contribution of passage wave velocity to variation of structural response could be neglected when estimating seismic performance of structures.

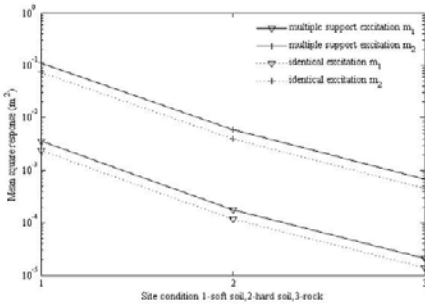


Figure 4. Influence of site conditions on displacement mean square response

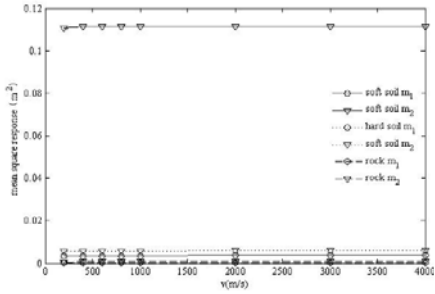


Figure 5. Influence of v on displacement mean square response

### 4 Conclusions

The procedure of random vibration response of linear structure subjected to SVEGM was developed; the parameters studies were performed by using the cross spectrum matrix established based on Clough-Penzien power spectrum model and Harichandran-Vanmarcke coherence function model. And, some useful conclusions are list as below.

1. With the increase of span length L, the displacement mean square response of structure decreases, this is because the decrease of structural stiffness and relativity between supports. This means that with increasing of L, structural responses are more stable, and the structural reliability is more controllable.
2. Mean square response decreases with increase of damping ratio, which is identical to structural response due to increasing of  $\xi$ . The decrease of m1 is less than the one of m2, which means that variation of  $\xi$  will influence either span of the model more.
3. Harder the site is, smaller mean square response is. This is because frequency components of wave are relatively smaller after filtered by site soil. It is also shown that mean square responses due to identical excitation are smaller than the one due to SVEGM, which shows that the mean square response would be conservative if incoherence effect be neglected.
4. The influences of passage wave velocity on mean square response are very small. Therefore, the contribution of passage wave velocity to structural response variation could be neglected.

The conclusions of this study can provide reference for simulating spatial variation ground motion while determining input parameters.

## References

- Chopra A.K. (2001). *Dynamics of Structures: Theory and Applications to Earthquake Engineering*, 2nd Edition, Prentice Hall, Englewood Cliffs, New Jersey.
- Loh Chin-Hsiung and Ku B.D. (1995). An efficient analysis of structural response for multiple-support seismic excitations. *Engng Struct*, 17(1):15-26.
- Soong T.T. and Grigoriu M. (1993). *Random Vibration of Mechanical and Structural Systems*. Prentice-Hall, Englewood Cliffs, New Jersey.
- Zerva A. and Zervas V. (2002). Spatial variation of seismic ground motions. *Appl Mech Rev*, 55(3):271-297.

*“This page left intentionally blank.”*

# Inelastic Response Spectra for Bi-directional Earthquake Motions

Feng Wang<sup>1,2\*</sup>

<sup>1</sup> College of Architecture & Civil Engineering, Dalian Nationalities University, Dalian 116600, Liao ning, China

<sup>2</sup>State Key Laboratory of Coastal and Offshore Engineering, Dalian University of Technology, Dalian 116024, Liao ning, China

**Abstract.** The strength reduction factor spectra of constant ductility factor for bi-directional ground motions is developed by considering the multi-component earthquake excitation and coupled characteristics of structural response, which is defined as the ratio of the maximum displacement response in the same principal axes direction of a single-mass-system with two translational freedoms along its perpendicular principal axes when subjected to two-and one-dimensional ground motions respectively. The effects on nonlinear response of systems under bi-directional earthquake excitations are discussed based on statistic analysis of 178 recordings for hard site, medium site and soft site. By the sufficient statistic analysis, the simplified model of strength reduction factor design spectra of constant ductility factors is established, which is the foundation for forming the inelastic design demand spectra for structures subjected to bi-directional ground motions.

**Keywords:** bi-directional earthquake ground motions, strength reduction factor, inelastic response spectra, ductility factor

## 1 Introduction

In the design procedures of current code, there are uncertainties concerning the seismic demand and seismic capacity of the structure. Performance-based seismic design (PBSD) is a more general design philosophy in which the design criteria is expressed in terms of achieving pre-set performance objectives for the structure subjected to expected seismic levels. In PBSD theories, inelastic response spectrum plays a central role.

Both theoretical studies and seismic disasters indicate that the torsional response can aggravate the destroying of asymmetry-plan structures (Li et al., 2004;

---

\* Corresponding author, e-mail: win\_0803@163.com

Fajfar and Gaspersis, 1996). The torsionally coupled response is essentially spatial vibration that can't be solved in two dimensional (2D) analysis. Although the theories of inelastic response spectrum are increasing rapidly, most of current researches (Newmark and Hall, 1982; Krawinkler and Nassa, 1982; Vidic et al., 1994; Ordaz and Perez-Rocha, 1998; Borzi et al., 2001; Riddell et al., 2002) focus on 2D analysis. Therefore, it is necessary to develop strength reduction factor spectra of constant ductility factors for multi-directional earthquake motions.

## 2 Inelastic Response Spectrum under Bi-directional Ground motions

### 2.1 Dynamic Equation of SMBDF System

The equations of motion for the single-mass bi-degrees of freedom (SMBDF) system with two translational freedoms subjected to orthogonal bi-directional earthquakes can be expressed as:

$$\begin{cases} m\ddot{x}(t) + c_x\dot{x}(t) + f(x,t) = -m\ddot{x}_g(t) \\ m\ddot{y}(t) + c_y\dot{y}(t) + f(y,t) = -m\ddot{y}_g(t) \end{cases} \quad (1)$$

where  $x(t)$  and  $y(t)$  are instantaneous displacements of SMBDF system along x and y direction, respectively;  $\ddot{x}_g(t)$  and  $\ddot{y}_g(t)$  are acceleration histories of bi-directional ground motions in x and y direction;  $m$  is the mass of the system;  $c_x$  and  $c_y$  are damping coefficients (without considering non-linear behavior) in x and y direction, respectively;  $f(x,t)$  and  $f(y,t)$  are elastic-plastic restoring forces of the system in x and y direction, respectively, which are determined by two-dimensional yield-surface plasticity rule (Wang et al., 2005). The restoring force characteristics of SMBDF system include two parts, one of which is linear elastic part representing the initial elastic behavior of the two independent elastic Single-Degree-of Freedom (SDOF) systems, and another one of which is non-linear part representing the yielding behavior of the system with two coupled response components. The yield displacements of uncoupled systems with two independent SDOFs are defined as  $x_y$  and  $y_y$ , and the corresponding yield force can be determined by  $f_{x,y} = k_x x_y$  (or  $f_{y,y} = k_y x_y$ ) in which  $k_x$  (or  $k_y$ ) is the linear stiffness of elastic SDOF system. If define  $\mu_x(t) = x(t)/x_y$  and  $\mu_y(t) = y(t)/y_y$ , Equation (1) can be normalized as:

$$\left\{ \begin{array}{l} \ddot{\mu}_x(t) + 2\xi\omega_x\dot{\mu}_x(t) + \omega_x^2 \frac{f(x,t)}{f_{x,y}} = -\frac{\omega_x^2 \cdot R_x}{\beta_x(\omega_x, \xi)} \frac{\ddot{x}_g(t)}{\max(|\ddot{x}_g|)} \\ k\ddot{\mu}_y(t) + 2k\xi\omega_y\dot{\mu}_y(t) + k\omega_y^2 \frac{f(y,t)}{f_{y,y}} = -k \frac{\omega_y^2 \cdot R_y}{\beta_y(\omega_y, \xi)} \frac{\ddot{y}_g(t)}{\max(|\ddot{y}_g|)} \end{array} \right. \quad (2)$$

where the maximal value of  $\mu_x(t)$  ( $\mu_y(t)$ ) is ductility factor defined as a ratio between the maximal displacement and the yield displacement;  $\omega_x = \sqrt{k_x/m}$ ,  $\omega_y = \sqrt{k_y/m}$  are natural vibration frequency of elastic SDOF system in x direction and y direction, respectively;  $\xi_x = c_x/2\sqrt{mk_x}$ ,  $\xi_y = c_y/2\sqrt{mk_y}$  are damping ratio of elastic SDOF system in x direction and y direction, respectively; The values of damping ratio  $\xi_x$  and  $\xi_y$  are assumed to be 5% for RC Structures or 2% for steel structures;  $\beta_x(\omega_x, \xi)$  and  $\beta_y(\omega_y, \xi)$  are values in the elastic amplification coefficient spectrum of the system subjected to bi-directional earthquakes; The strength reduction factors of x and y components can be respectively expressed as:

$$R_x = f_{x,e} / f_{x,y}; \quad R_y = f_{y,e} / f_{x,y} \quad (3)$$

where  $f_{x,e}$  and  $f_{y,e}$  are elastic force; The parameter  $k$  is defined as:

$$k = \frac{S_{dy}}{S_{dx}} \cdot \frac{R_x}{R_y} \quad (4)$$

in which  $S_{dx}$  and  $S_{dy}$  are displacement spectrum values of the system subjected to perpendicular.

## 2.2 Restoring Force Characteristics

The yield rule of SMBDF system is determined by two-dimensional yield-surface plasticity function (Wang et al., 2005) which can be expressed as:

$$F(f(x,t), f(y,t)) = \left| \left( \frac{f(x,t)}{f_{x,y}} \right) \right|^2 + \left| \left( \frac{f(y,t)}{f_{y,y}} \right) \right|^2 = 1.0 \tag{5}$$

The responses of SMBDF system are assumed to have ideal elastic-plastic restoring force characteristics which the rules of loading and unloading are given as follows:

$$F(f(x,t), f(y,t)) < 1.0 \quad \text{elastic phase} \tag{6a}$$

$$F(f(x,t), f(y,t)) = 1.0 \begin{cases} dF = 0 \rightarrow \text{loading} \\ dF < 0 \rightarrow \text{unloading} \end{cases} \tag{6b}$$

The function  $F(f(x,t), f(y,t)) < 1.0$  means a linear elastic phase, in which the tangent stiffness matrix of SMBDF system is:

$$[K_t] = [K_e] \tag{7}$$

where  $[K_e] = \text{Diag}(\omega_x^2, k\omega_y^2)$  is the elastic stiffness matrix of system. The expressions  $f_{x,y} = \omega_x^2$  and  $f_{y,y} = k\omega_y^2$  can be introduced to simplify Equation (2). The function  $F(f(x,t), f(y,t)) = 1.0$  represents coupled yielding responses for two perpendicular components, in which the tangent stiffness matrix of SMBDF system is given as:

$$[K_t] = [K_e] - \frac{[K_e] \left\{ \frac{\partial F}{\partial \{f\}} \right\} \left\{ \frac{\partial F}{\partial \{f\}} \right\}^T [K_e]}{\left\{ \frac{\partial F}{\partial \{f\}} \right\}^T [K_e] \left\{ \frac{\partial F}{\partial \{f\}} \right\}} \tag{8}$$

where  $\left\{ \frac{\partial F}{\partial \{f\}} \right\}$  is the partial derivative vector defined as the instantaneous rate of change of a function  $F$  with respect to its variable vector  $\{f\} = \{f(x,t) \quad f(y,t)\}^T$ .

### 2.3 Presumptive Relationship between $R_x$ and $R_y$

A consensus has been reached that intensities and spectral characteristics of the earthquake ground motions with same seismic locus but different input direction are approximately identical. The lateral strength of an existing structure is generally obtained from the value of seismic influence coefficient design spectrum of seismic code (Figure 1), and then lateral strength ratio of two perpendicular components,  $y$  and  $x$  axes, can be approximately determined as:

$$\eta = \frac{f_{x,y}}{f_{y,y}} \approx \frac{\bar{\beta}(T_x)}{\bar{\beta}(T_y)} \quad \text{or} \quad \eta = \frac{f_{x,y}}{f_{y,y}} \approx \frac{\alpha(T_x)}{\alpha(T_y)} \quad (9)$$

where  $\bar{\beta}$  and  $\alpha$  are mean amplification coefficient spectrum and seismic influence coefficient design spectrum, respectively. The values of  $\bar{\beta}$  and  $\alpha$  are the the function of periods  $T_x$ ,  $T_y$  (or  $\omega_x$ ,  $\omega_y$ ) and damping ratio  $\xi$ . The relations between  $R_x$  and  $R_y$  are deduced as follows:

$$\frac{R_x}{R_y} = \frac{\bar{\beta}(T_x)}{\eta \cdot \bar{\beta}(T_y)} \quad \text{or} \quad \frac{R_x}{R_y} = \frac{\alpha(T_x)}{\eta \cdot \alpha(T_y)} \quad (10)$$

To compute the raw  $R_x$  ( $R_y$ ) data for given bi-directional ground motions and initial vibration periods,  $T_x$  and  $T_y$ , Equations (2) are iterated until the absolute value of the difference between the calculated displacement ductility factor and a specified value of  $\mu_x$  (or  $\mu_y$ ) is within 0.025. The non-linear dynamic time history analysis of SMBDF system can be finished by the Wilson- $\theta$  method with an adaptive step size control scheme (with maximum step size,  $\Delta t = 0.01\text{sec}$ ). During the iterations, if more than one value of  $R_x$  (or  $R_y$ ) have been obtained for the same ductility ratio, the minimum value of  $R_x$  (or  $R_y$ ) will be considered.

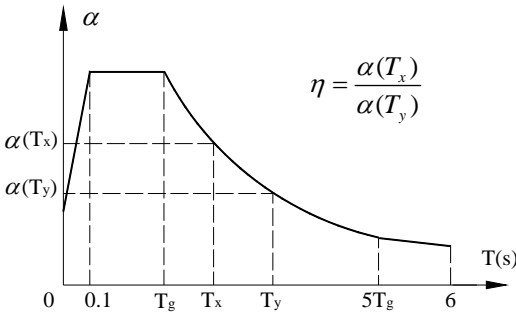


Figure 1. The approximate relation of yield strength between x and y component of existing structures

### 2.4 Statistical Rule of Strength Reduction Factor Design Spectrum for Bi-directional Earthquake Motions

The relation between inelastic maximal response  $S_{d,x,e}^{(i)}$  and elastic maximal response  $S_{d,x,p}^{(i)}$  for x component of SMBDF system under the bi-directional earthquakes:

$$\frac{S_{d,x,p}^{(i)}}{S_{d,x,e}^{(i)}} = \frac{\mu_x}{R_x^{(i)}} \tag{11}$$

where “i” is the sequence number of bi-directional earthquakes. The expectation of  $S_{d,x,p}^{(i)}$  can be derived from above equation:

$$E(S_{d,x,p}^{(i)}) = \mu_x E\left(\frac{S_{d,x,e}^{(i)}}{R_x^{(i)}}\right) \tag{12}$$

The strength reduction factor spectrum of x component,  $\bar{R}_x$ , is defined as:

$$\bar{R}_x = E(S_{d,x,p}^{(i)}) / E\left(\frac{S_{d,x,e}^{(i)}}{R_x^{(i)}}\right) \tag{13}$$

Let  $\bar{S}_{d,x,p} = E(S_{d,x,p}^{(i)})$  be inelastic displacement spectrum and  $\bar{S}_{d,x,e} = E(S_{d,x,e}^{(i)})$  be linear elastic displacement spectrum of x component, the equation of inelastic constant ductility factor design spectrum can be written as:

$$\bar{S}_{d,x,p} = \mu_x \frac{\bar{S}_{d,x,e}}{\bar{R}_x} \tag{14}$$

This computation of strength reduction factors of constant ductility factors for x (or y) component under given ground motion records pair are repeated for 30 initial periods  $T_x$  from 0.1 to 3.0 sec, with  $T_y/T_x = 0.4, 0.6, 0.8, 1, 1.25, 1.66, 2.5,$  and  $\mu_x = 2, 3, 4, 5, 6$ . The strength reduction factor spectra of constant ductility along x direction are created by considering 178 horizontal seismic acceleration records for three kinds of soil sites (hard, medium and soft) with magnitude ranging from 6 to 8 and distance from the horizontal projection of the causative fault from 15 to 45 km, approximately (see the work of Feng Wang, 2007, for further details).

### 2.5 Simplified Expressions of Strength Reduction Factor Design Spectrum for Bi-directional Earthquake Motions

A simplified expression of strength reduction factor spectrum needs to be derived to facilitate a rapid assessment of the strength demand. As a result of tradeoff between accuracy and simplicity, the following equations are established for strength reduction factor spectrum of constant ductility based on 178 earthquake records:

$$T_x \leq T_0, \quad R_x = \gamma \frac{(\mu_x - 1)^{0.95}}{\mu_x^{c_1}} \frac{T_x}{T_0} + 1 \tag{15}$$

$$T_x > T_0, \quad R_x = \gamma \frac{(\mu_x - 1)^{0.95}}{\mu_x^{c_1}} + 1 \quad \text{soft site} \tag{16a}$$

$$R_x = \gamma \frac{(\mu_x - 1)^{0.95}}{\mu_x^{c_1}} \cdot c_m + 1 \quad \text{medium hard (soft) site} \tag{16b}$$

$$\left. \begin{aligned}
 R_x &= \gamma \frac{(\mu_x - 1)^{0.95}}{\mu_x^{c_1}} + 1, \quad T_x \leq T_1 \\
 R_x &= \left( \gamma \frac{(\mu_x - 1)^{0.95}}{\mu_x^{c_1}} + 1 \right) \cdot (T_1/T_x)^{c_2 \cdot \mu}, \quad T_x > T_1
 \end{aligned} \right\} \text{hard site} \tag{16c}$$

in which  $T_0 = 0.75\mu^{c_T} T_c \leq T_c$ ;  $T_1 = 0.16$  sec is the characteristic period of bi-directional strength reduction factor design spectrum; and

$$c_m = \begin{cases} 1 & T_y/T_x = 0.4 \\ \text{interpolation} & \\ 1 + 0.01\mu(T - T_0) & T_y/T_x \geq 0.8 \end{cases} \tag{17}$$

where  $T_c$  is the characteristic period of acceleration spectrum of SDOF system. Constant coefficients  $\gamma$ ,  $c_1$ ,  $c_2$ ,  $c_T$  are summarized in Table.1, in which the period ratios are given interruptedly, such as  $T_y/T_x = 0.4, 1, 2.5$  for hard soil-site, and the interpolation method can be adopted to obtain the uninterrupted results of constant coefficients in the given range of period ratios discussed in this paper.

Table 1. The parameter table for simplified formula of strength reduction factor design spectra

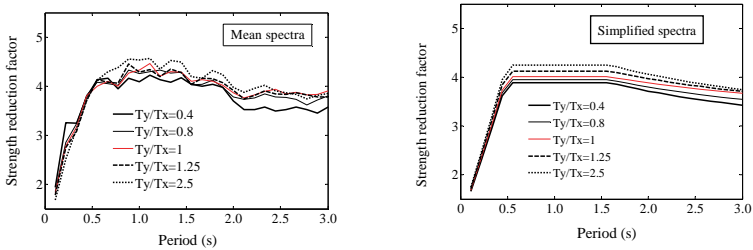
Coefficient	Hard soil (I)			Intermediate(II, III)		Soft soil (IV)	
	$T_y/T_x$	0.4	1	2.5	0.4	0.8~2.5	0.4~2.5
$\gamma$		1.2	1.25	1.35	1.13	1.18	1.3
$C_1$		0.12	0.12	0.12	0.1	0.1	0.25
$C_T$		0.3	0.3	0.3	0.1	0.1	0.2
$C_2$		0.05	0.035	0.05	—	—	—

### 3 Analysis of Strength Reduction Factor Design Spectrum for Bi-directional Earthquake Motions

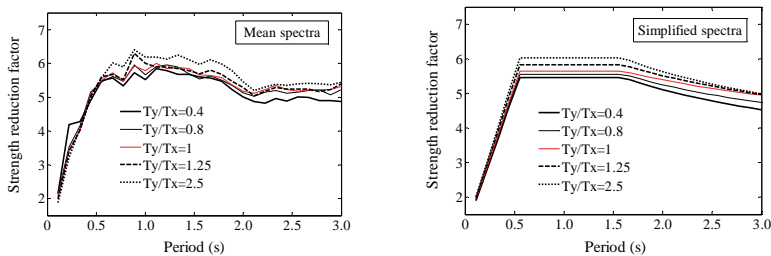
The influence of period ratios on strength reduction factor spectrum for bi-directional earthquakes is assessed at different soil-site conditions. For hard site, mean spectra of constant ductility strength reduction factor and corresponding

simplified design spectra obtained by Equation (15), (16c), (17) are compared in Figure 2. It can be observed that as the period ratio  $T_y/T_x$  increases in the range of period more than 0.5 second, strength reduction factor increases. This implies that, for a fixed value of strength, the period ratio  $T_y/T_x$  has significant influence on non-linear displacement demands of the system.

The influence of period ratio  $T_y/T_x$  on strength reduction factor is illustrated in Figure 3 and Figure 4 for soft soil and medium hard (soft) soil, respectively. From the spectra shown in Figure 3 and Figure 4, it can be seen that the influences of period ratios  $T_y/T_x$  on soft site and medium hard (soft) site are comparatively less than those for hard soil class. For medium hard (soft) site, the spectral values of  $T_y/T_x=0.4$  are obviously less than those of other period ratios (Figure 3). For soft site, the spectral values of  $T_y/T_x=1$  are minimum for all the given ranges of period ratios. According to the phenomena described in the previous description, the influences of period ratios on spectral values are reflected on the simplified spectral models. Compared the spectral shape of mean spectra with that of simplified design spectra in Figure 3 and Figure 4, it can be seen that the trends for them are approximately identical and simplified design spectra always lie below mean spectra, which indicates that simplified design spectra developed in this paper is relatively safe for structural design.

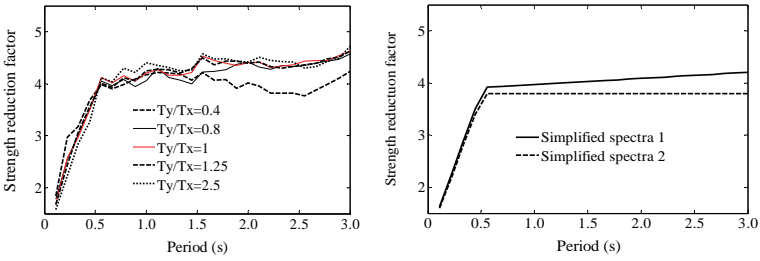


(a) Ductility factor  $\mu_x=4$

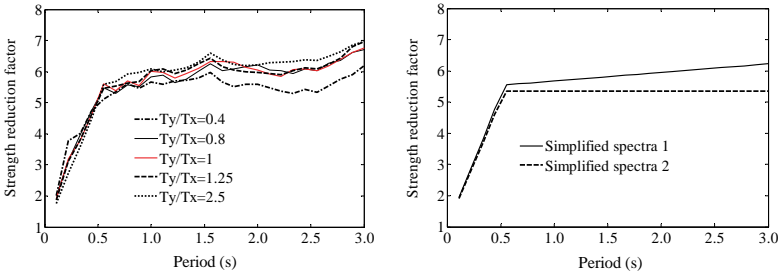


(b) Ductility factor  $\mu_x=6$

Figure 2. Influences of period ratios for constant ductility factors spectra of x component in hard soil site

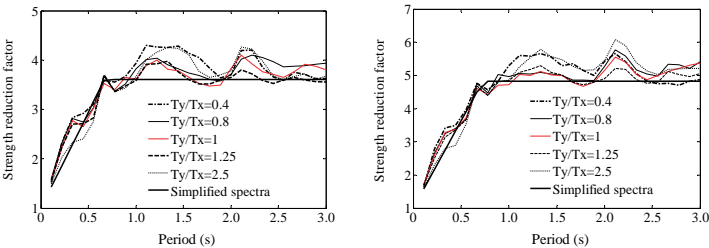


(a) Ductility factor  $\mu_x=4$



(b) Ductility factor  $\mu_x=6$

Figure 3. Influences of periods ratios for constant ductility factors spectra of x component in medium hard (soft) soil site



(a) ductility factor  $\mu_x=4$

(b) ductility factor  $\mu_x=6$

Figure 4. Influences of period ratios for constant ductility factors spectra of x component in soft soil site

The results discussed in the previous sections suggest that the strength reduction factor mean spectrum (or design spectrum) of constant ductility for bi-directional earthquakes depends strongly on the period ratio of  $T_y/T_x$ , and period of SMBDF system, ductility factor and the site conditions, etc.

## 4 Conclusions

For creating multi-dimensional PBSDF methods for estimating seismic demands of asymmetric-plan structures, the strength reduction factor spectra for systems subjected to bi-directional earthquakes are presented and the rules of those spectra are analyzed in detail. The simplified design spectrum equations are established based on analysis results. Furthermore, two useful conclusions are drawn as follows:

1. The strength reduction factor mean spectrum of constant ductility for bi-directional earthquake motions is affected strongly by vibration period of SMBDF system, ductility factor and soil-site conditions, especially period ratio of system.
2. The simplified design spectrum presented in the paper is convenient in engineering application. Every influence factor of statistical mean spectrum is almost reflected on the formula of simplified design spectrum. The trends and shapes of simplified design spectra are similar to those of statistical mean spectra and the results from simplified design spectra are comparatively safe in design.

## References

- Borzi B., Calvi G.M., Faccioli E. and Bommer J.J. (2001). Inelastic spectra for displacement-based seismic design. *Soil Dynamics and Earthquake Engineering*, 21: 47-61.
- Fajfar P. and Gaspersis P. (1996). The N2 method: The seismic damage analysis of RC buildings. *Earthquake Engineering and Structural Dynamics*, 25: 31-46.
- Krawinkler H. and Nassar A.A. (1992). Seismic design based on ductility and cumulative damage demands and capacities. *Nonlinear Seismic Analysis and Design of Reinforced Concrete Buildings*. Elsevier Applied Science, London and New York: 23-29.
- Li H.N., Sun L.Y. and Wang S.Y. (2004). Improved approach for obtaining rotational components of seismic motion. *Nuclear Engineering and Design*, 232(2): 131-137.
- Newmark N.M. and Hall W.J. (1982). Earthquake spectra and design. EERI, Berkeley, California.
- Ordaz M. and Perez-Rocha L.E. (1998). Estimation of strength-reduction factors for elastoplastic systems: A new approach. *Earthquake Engineering and Structural Dynamics*, 27: 889-901.
- Riddell R., Garcia J.E. and Garces E. (2002). Inelastic deformation response of SDOF systems subjected to earthquake. *Earthquake Engineering Structural Dynamics*, 31(3): 515-538.
- Vidic T., Fajfar P. and Fishinger M. (1994). Consistent inelastic design spectra: Strength and displacement. *Earthquake Engineering and Structural Dynamics*, 23: 507-521.
- Wang D.S., Li H.N. and Wang G.X. (2005). Research on inelastic response spectra for bi-directional ground motions. *Journal of Dalian University of Technology*, 45(2): 248-254.
- Wang F. (2007). Studies on performance-based seismic design methods of structures subjected to multi-dimensional earthquake excitations. Dalian University of Technology, Dalian, China.

*“This page left intentionally blank.”*

# Seismic Dynamic Reliability Analysis of Gravity Dam

Xiaochun Lu<sup>1\*</sup> and Bin Tian<sup>2</sup>

<sup>1</sup>State Key Laboratory of Water Resources and Hydropower Engineering Science, Wuhan University, Wuhan 430072, P.R. China

<sup>2</sup>College of Civil and Hydroelectric Engineering, Three Gorges University, Yichang 443002, P.R. China

**Abstract.** A great many large dams with high seism have been built and will be built in the northwest and southwest regions in China. As large dams have great significance for the national economic development, the aseismic safety evaluation of large dams is an important part of earthquake engineering. The aseismic safety assessment criteria of dams based on the probabilistic method has been an important trend in the safety research of hydraulic structure in recent ten years. Based on the gravity dam, the linear elastic mode-superposition response spectrum method is used in the seismic response; the dynamic and static combination method is discussed. The method of seismic dynamic reliability analysis of gravity dam is also established using the stress coefficient method and Monte-Carlo simulation method. The point strength reliability in the dam and the seismic sliding stability reliability can be calculated via this method. It is simple, convenient and efficient.

**Keywords:** gravity dam, dynamic reliability, safety assessment, stress coefficient method, Monte-Carlo simulation method

## 1 Introduction

The use of underground structures such as subway stations is increasing in both developed and developing countries. After the Great Hanshin earthquake on 17 January 1995, which brought about serious damage to some subway stations, the safety of these facilities during operation in areas with seismic activities has been questioned. Supported by the strategic decision of the western region development and west-to-east power transmission, a great many large dams have been built and will be built in high seismic areas of China. The Xiaowan arch dam with a height of 292m, the Xiluodu arch dam with a height of 278m and the Jinping arch dam

---

\* Corresponding author, e-mail: luxiaochun1014@163.com

with a height of 305m exceed the highest Inguri arch dam ( $H=271.5\text{m}$ ). The design seismic acceleration of Xiaowan arch dam is  $0.308g$ , the one of Xiluodu arch dam is  $0.321g$  and the one of Jinping arch dam is  $0.197g$ . In addition, the one of Dagangshan arch dam on the Dadu River is  $0.5575g$ , the one of Tiger Leaping Gorge arch dam on the Jinshajiang River is  $0.407g$ . All are larger than the design seismic acceleration of the existing dams in china. For the building dams, the aseismic safety for dams is an important problem which is necessary to be solved, and the method of aseismic safety evaluation for dams is an important aspect in the earthquake-resistance safety evaluation.

Compared with the other loads, the time, place and intensity of earthquake have more random factors. So, the dynamic reliability analysis and anti-seism design with the seismic random and the variation of other loads and resistances based on the probability method will be the certain trend in the development of analysis and design theory for the hydraulic structure in the future.

The analysis method of aseismic safety for dams is mainly linear elastic dynamic (Gao, 2006). Thus, the dynamic analysis based on the linear elastic mode destructive response spectrum is investigated in this paper, the dynamic and static combination method is discussed. The method of seismic dynamic reliability analysis of gravity dam is also established using the stress coefficient method and Monte-Carlo simulation method (Wu, 1990), and is applied in the overflowing section of Silin hydropower station.

## 2 The Gravity Dam of Silin Hydropower Station

The hydro project of Silin hydropower station is located in the middle of the Wujiang River in Guizhou province, whose main function is power generation; the other functions include preventing or controlling flood, shipping, and irrigation. The elevation of normal water level is  $440\text{m}$ , the reservoir capacity is 1.205 billion cubic meters, the installed capacity is  $1000\text{MW}$ , the water retaining dam section is RCC gravity dam, and the whole length of the dam crest is  $310\text{m}$ . According to the Seismic Intensity Regionalization Map (1990), the basic seismic intensity is 6 degree intensity and the seismic peak acceleration is  $0.05g$  in the project region. According to the Specifications for seismic design of hydraulic structures (DL5073-2000), the aseismic design intensity should be enhanced to 7 degree for the water retaining dam section, the representative value of horizontal design acceleration  $a_h$  is  $0.1g$ , the maximum value of design response spectrum  $\beta_{\max}$  is 2.00, the dam foundation is the type of site, the characteristic period is  $0.20\text{s}$ , the damping ratio of concrete is 8% (DL5073-2000, 2001).

In this paper, dam section no.8 of overflow section in Silin hydro project is analyzed; the 3-D finite element model is established and analyzed via reliability theory. Dead load, static water pressure, uplift pressure, dynamic water pressure,

silt pressure, wave pressure and earthquake action are considered in the computing model. Dynamic water pressure is calculated by the additional mass method of Westergaard formula. The seismic loading includes the horizontal earthquake function and the vertical earthquake function. According to the specifications for seismic design of hydraulic structures (DL5073-2000), the mode destructive response spectrum is used in dynamic analysis; the design response spectrum is obtained from the DL5073-2000. The mode combination method under earthquake is SRSS. The dam foundation is elastic and massless, the perimeter of foundation is constrained. Figure 1 shows the mesh, in which the element number is 16580, the node number is 19358.

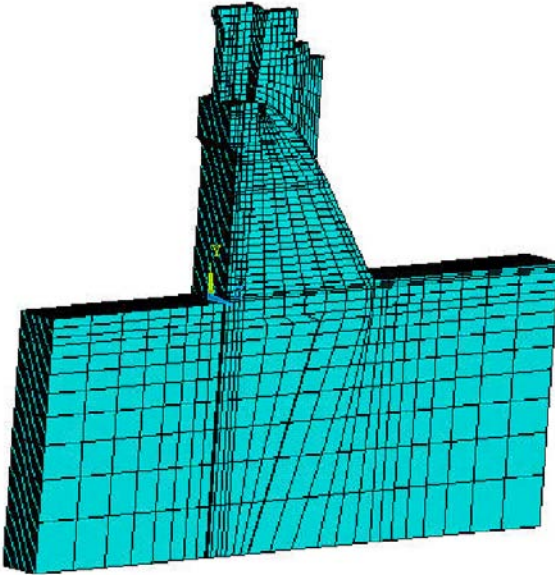


Figure 1. The finite element meshes of dam and its foundation.

### 3 The Combination Method of Dynamic and Static Response

In the specifications for seismic design of hydraulic structures (SDJ10-78), the general influence coefficient  $C_z = 0.25$  is used to combine dynamic response with static response, because some factors are uncertain under earthquake excitation such as seismic failure mechanism and actual safety margin under the static load and so on in that period. But, the result using the  $C_z$  cannot express the real aseismic safety, so it is difficult to evaluate the safety. The specifications for seismic design of hydraulic structures (DL 5073-2000) cancel the general influence

coefficient  $C_z$  (Hou et al., 2001). The seismic design is performed by using the partial factors and the bearing capacity under extreme condition. It provides a flat to reflect the real stress condition for dynamic analysis, but it does not give the specific combination method of dynamic and static response.

Because the mode combination method is SRSS when the dynamic response is analyzed by using the response spectrum, the results of stress and displacement are positive. But stress and displacement are vectors and should be combined with the static result. So they should be combined via a combination method. Moreover, the combination of both the static response and the dynamic response is made with the principle for extreme condition (Chang et al., 2005).

The method of displacement combination is: for the same node in the dam, if the static displacement of X axis (Y axis, Z axis) is positive, we can treat the dynamic value as positive value for the combination; if the static displacement of X axis (Y axis, Z axis) is negative, we can treat the dynamic value as negative value for the combination. The combination displacement is in the extreme condition.

The method of stress combination is: for the same node in the dam, if a certain static component of stress is tensile stress, the corresponding dynamic component of stress is regarded as tensile stress; if a certain static component of stress is compressive stress and the absolute value is less than the value of corresponding dynamic component of stress, the corresponding dynamic component of stress can be regarded as tensile stress; if in the other cases, the dynamic component of stress is regarded as compressive stress. Under the combination method of dynamic and static response, the stress and the displacement are in the extreme condition.

## 4 Dynamic Reliability Analysis

The Monte-Carlo simulation method is used to calculate the Reliability index. This method is a relative accurate method in the reliability analysis. The limitary condition has little effect on the analysis process and the convergence has nothing to do with the nonlinearity of state equation, non-normal distributions of random variables, etc. It is adaptable, reliable and easy to use.

### 4.1 Random Variables

The difference between the reliability analysis and the determinacy analysis is that the reliability analysis regards the design variables as random variables. As the volatility of some variables is minor, we can regard these variables as determined value. Then we regard the upstream level, peak acceleration, concrete strength, friction coefficient and cohesion as the random variables.

According to the scientific research achievements of hydraulic structure reliability research team in Hohai University (Wu et al., 1988), the upstream level can be regarded as the normal distribution, the mean value  $u_H = 0.935H_n - 0.330$ , coefficient of variation  $V_H = 0.063$ ,  $H_n$  is the normal pool level. Based on the references (Chen, 2006; GB50199-1994, 1994; Chen and Liang, 1994) and the characters of Silin hydropower station, the characteristic values of the other random variables are determined. The values are listed in Table 1.

Table 1. Characteristic value of random variables

Random variable		Numerical characteristic		Distribution
		Mean value	Cov	
Load	Upstream level H (m)	411.07	0.063	Normal
	Peak acceleration $a_h$ ( $m/s^2$ )	0.1g	1.38	Extremal type II
Resistance	Compressive strength of concrete $R_y$ (MPa)	27.75	0.20	Logarithm normal
	Tensile strength of concrete $R_t$ (MPa)	2.775	0.25	Logarithm normal
	friction coefficient $f'$	1.0	0.2	normal
	Cohesion $c'$	1.0	0.35	Logarithm normal

## 4.2 The Stress Regression Coefficients

For the stress regression coefficients, the calculation includes:

1. Only the load of upstream level H, the separate value is 449m, 444m, 440m, 435m, 431m;
2. The dynamic response under the horizontal design acceleration value: 0.06g, 0.08g, 0.10g, 0.12g, 0.14g;
3. Only the dead weight load;
4. Only the uplift pressure;
5. Only the slit pressure.

The stress under the 13 kinds of loads is calculated. The relationship curve between the stress  $\{\sigma_x, \sigma_y, \sigma_z, \tau_{xy}, \tau_{yz}, \tau_{zx}\}$  and the water level  $H$ , horizontal de-

sign Acceleration value  $a_h$  can be obtained. These curves are similar with the line. So the linear regression is used for getting the regression coefficients.

The regression equation is

$$y = a + bx \quad (1)$$

Where

$$b = \frac{\sum_{i=1}^n (x_i - \bar{x})(y_i - \bar{y})}{\sum_{i=1}^n (x_i - \bar{x})^2} \quad (2)$$

$$a = \sum_{i=1}^n \frac{y_i}{n} - b \sum_{i=1}^n \frac{x_i}{n} \quad (3)$$

The correlation coefficient is

$$\rho = \frac{\sum_{i=1}^n (x_i - \bar{x})(y_i - \bar{y})}{\sqrt{\sum_{i=1}^n (x_i - \bar{x})^2 \sum_{i=1}^n (y_i - \bar{y})^2}} \quad (4)$$

Where  $n$  is the sample number,  $\bar{x}, \bar{y}$  are the average of  $x_i, y_i$  ( $i = 1, \dots, n$ ), respectively.

If the water level  $H$  and the representative value of horizontal design acceleration are respectively expressed as  $x_H$  and  $x_{a_h}$ , after the regression, we can get

$$\begin{cases} \sigma_x = a_{11}x_H + a_{12}x_{a_h} + a_{13} \\ \sigma_y = a_{21}x_H + a_{22}x_{a_h} + a_{23} \\ \sigma_z = a_{31}x_H + a_{32}x_{a_h} + a_{33} \\ \tau_{xy} = a_{41}x_H + a_{42}x_{a_h} + a_{43} \\ \tau_{yz} = a_{51}x_H + a_{52}x_{a_h} + a_{53} \\ \tau_{zx} = a_{61}x_H + a_{62}x_{a_h} + a_{63} \end{cases} \tag{5}$$

The matrix form is expressed as follows

$$\begin{bmatrix} \sigma_x \\ \sigma_y \\ \sigma_z \\ \tau_{xy} \\ \tau_{yz} \\ \tau_{zx} \end{bmatrix} = \begin{bmatrix} a_{11} & a_{12} & a_{13} \\ a_{21} & a_{22} & a_{23} \\ a_{31} & a_{32} & a_{33} \\ a_{41} & a_{42} & a_{43} \\ a_{51} & a_{52} & a_{53} \\ a_{61} & a_{62} & a_{63} \end{bmatrix} \begin{bmatrix} x_H \\ x_{a_h} \\ 1 \end{bmatrix} \tag{6}$$

The three principal stresses  $\{\sigma_1 \ \sigma_2 \ \sigma_3\}$  can be solved form the formula (7) based on the elastic mechanics theory.

$$\begin{vmatrix} \sigma_x - \sigma & \tau_{xy} & \tau_{zx} \\ \tau_{xy} & \sigma_y - \sigma & \tau_{yz} \\ \tau_{zx} & \tau_{yz} & \sigma_z - \sigma \end{vmatrix} = 0 \tag{7}$$

In the paper, the tensile stress is positive, the maximum tension stress is  $\sigma_1$ , the maximum compressive stress is  $\sigma_3$ .

### 4.3 The Limit State Equation

The limit state equations of dam seismic sliding stability and the concrete allowable stress are established in this paper.

For the dam sliding stability extreme condition, the performance function can be obtained from the stress which is calculated by the linear regression. The formula is as follows

$$g(H, a_h) = R - S = \sum_{i=1}^m \sigma_y A_i f' + \sum_{i=1}^m A_i C' - \sum_{i=1}^m \tau_i A_i \quad (8)$$

where  $m$  is the element number of dam foundation plane,  $\sigma_y$  is the vertical element stress of dam foundation plane;  $\tau_i$  is the element shear stress of dam foundation plane;  $A_i$  is the element surface area of dam foundation plane;  $f'$  is the coefficient of friction;  $C'$  is the cohesion.

Based on the concrete allowable stress, for every node  $i, i = 1, \dots, n$  if  $\sigma_{1i}$  or  $\sigma_{3i}$  is greater than zero, then it is tensile stress, the performance functions are as follows

$$G_{1i} = K_2 R_l - \sigma_{1i} \quad (9)$$

$$G_{2i} = K_2 R_l - \sigma_{3i} \quad (10)$$

If  $\sigma_{1i}$  or  $\sigma_{3i}$  is less than zero, then it is compressive stress, the performance functions are as follows

$$G_{1i} = K_1 R_y - |\sigma_{1i}| \quad (11)$$

$$G_{2i} = K_1 R_y - |\sigma_{3i}| \quad (12)$$

So the tensile and the compressive strength limit state equations exist for every point in the dam.

#### 4.4 The Dynamic Reliability Analysis Result

The reliability in the key locations is calculated by using the Monte-Carlo simulation method.

Through the computation, the safety index trends to be changeless when the sample number reaches 70-80 thousand. The minimum strength reliability index and the reliability of sliding stability are listed in Table 2.

Table 2. The minimum reliability index and corresponding reliability

Safety index	Locations			Sliding stability
	Dam heel	Dam toe	Upper broken line slope	
Reliability $P_s$	0.9098	>0.9999	>0.9999	0.9997
Reliability index $\beta$	1.34	4.53	3.42	3.51

The result shows the reliability of dam heel is least, only 90.98%, the corresponding reliability index is 1.34. The reliability of other places in an ultimate limit state is greater than the dam heel, which reaches 99.9%, and the corresponding reliabilities are greater than 3. The dynamic reliability probability of sliding stability reaches 0.9997, the corresponding reliability reaches 3.51. It shows the safety margin for sliding stability is great. In the document (Chen et al., 1993), the dynamic reliability analysis of 22 gravity dams with a height of 30m-190m above different rock foundation were calculated. The result shows under 7° earthquake, the seismic sliding stability reliability index is about 2.5, but the minimum tear strength reliability index is about 1.0. Based on the result, dynamic reliability indexes are conforming to the law. Except the dam heel, other reliability indexes are above 95%.

## 5 Conclusions

Taking the dynamic movement and seismic response as the random process is accordant with the fact. Combining the seismic response and the static response, and then, taking them into consideration of the dynamic reliability analysis for gravity dam has larger theoretical and practical significance. The whole slide-resistant extreme condition and the bearing capacity under extreme condition are considered. A method for analyzing aseismic reliability of gravity dam is put forward in this paper, which is applied to the Silin hydropower station. The result indicates that this method is practice and simple, and can be used into the reliability assessment of gravity dams.

## References

- Chang X.L., Wei M. and Gao Z.P. (2005). Dynamic analysis on Jin'anqiao RCC Gravity Dam under high seismic intensity. *Water Resources and Hydropower Engineering*, 7:57-59 [in Chinese].
- Chen H.Q. et al. (1993). Aseismic reliability design of concrete dams. *Journal of China Institute of Water Resources and Hydropower Research*, 1:1-6 [in Chinese].
- Chen H.Q and Liang A.H. (1994). *The special papers of unified design standard for reliability of hydraulic engineering structures*. Sichuan Science Press, Chengdu [in Chinese].
- Chen H.Q. (2006). Mechanics problems of seismic study on concrete large dams. *Mechanics and Practice* 2:1-8 [in Chinese].
- DL5073-2000 (2001). Specifications for seismic design of hydraulic structures [in Chinese].
- Gao L. (2006). Developing tendency of the seismic safety evaluation of large concrete dams. *Journal of Disaster Prevention and Mitigation Engineering*, 1:1-12 [in Chinese].
- GB50199-1994 (1994). Unified design standard for reliability of hydraulic engineering structures [in Chinese].
- Hou S.Z., Li D.Y. and Liang A.H. (1998). The dynamic analysis and seismic safety evaluation of Three Gorges Dam. *Hydroelectric Engineering*, 12:40-43 [in Chinese].
- Wu S.W., et al. (1988). *The papers of structural safety and reliability analysis*. Hehai University Press, Nanjing [in Chinese].
- Wu S.W. (1990). *Structural reliability analysis*. Publishing House of People Traffic, Beijing [in Chinese].

# Application of Iterative Computing of Two-Way Coupling Technique in Dynamic Analysis of Sonla Concrete Gravity Dam

Trinh Quoc Cong<sup>1\*</sup> and LiaoJun Zhang<sup>1</sup>

<sup>1</sup>College of Water conservancy and Hydropower Engineering, Hohai University, Nanjing, China

**Abstract.** Dam-Reservoir system subjected to earthquake is a nonlinear system regardless of the dam body model used (linear or nonlinear) because the fluid equations are always nonlinear. Therefore, transient analysis of Dam-reservoir system subjected to earthquake ground acceleration is necessary for realistic analysis. In this study, Dam-reservoir interaction under earthquake load is modeled by utilizing couple finite element equation. The iterative computing of two-way coupling method is used to solve this couple equation. In this solution, the fluid and solid solution variables are fully coupled. The fluid equations and solid equations are solved individually in succession, using the latest information provided from another part of the coupled system. Following from this, the method was applied in analysis of Sonla concrete gravity dam constructed in Sonla province, Vietnam. The methodology introduced is very convenient and can be easily implemented in the finite element program ADINA with regard to fluid-structure interaction modules.

**Key words:** dam-reservoir interaction, time domain, two-way coupling, ADINA Sonla dam

## 1 Introduction

Dam-reservoir systems are fluid-structure interaction problems. Most fluid-structure analyses are based on one of two approaches; Eulerian approach and Lagrangian approach (Olson and Bathe, 1983). In Eulerian approach, displacements are the variables in the solid zone and pressures are the variables in fluid zone and in Lagrangian approach, displacements are the variables in both the fluid and solid zone. Dynamic responses of dam-reservoir systems have been investi-

---

\* Corresponding author, e-mail: Quoccongdtl@yahoo.com

gated using the Eulerian and Lagrangian approaches by many researches (Finn and Varoğlu, 1973).

When subjected to earthquake ground motion, the analysis of the dam-reservoir interaction effects is a complex problem. Traditionally, the linear dynamic response of the dam is obtained in the frequency domain. However, these methods are limited to linear dynamic analysis and do not reflect the behaviour of Dam during an earthquake period. Another approach to determine the linear and nonlinear response of the dam-reservoir system is to approximate the reservoir effects by a number of masses that are added to the dam equation. This is known as the added mass approach. But there is evidence that the added mass approximation may not be suitable for problems such as those involving the analysis of cracking in the dam structure (Ghaemian and Ghobarah, 1998).

Dam-Reservoir system subjected to earthquake is a nonlinear system regardless of the dam body model used (linear or nonlinear) because the fluid equations are always nonlinear. Therefore, transient analysis of Dam-reservoir system subjected to earthquake ground acceleration is necessary for realistic analysis. In this paper, formulation of fluid systems based on the Eulerian approach is obtained by using the finite element method. And the couple equation of water-dam interaction is solved by utilizing the iterative computing of two-way coupling method. Following from this, Sonla gravity dam was analyzed in time history domain based on this technique.

## 2 The Couple Finite Element Equation of Dam-Reservoir System

The dam-reservoir interaction is a classic coupled problem, which contains two differential equations of the second order. The equations of the dam structure and the reservoir can be written in the following form (Ghaemian and Ghobarah, 1998):

$$[M]\{\ddot{U}\} + [C]\{\dot{U}\} + [K]\{U\} = \{f_i\} - [M]\left\{\ddot{U}_s\right\} + Q\{P\} \tag{1}$$

$$[G]\left\{\ddot{P}\right\} + [C']\left\{\dot{P}\right\} + [K']\{P\} = \{F\} - \rho[Q]^T\left(\left\{\ddot{U}\right\} + \left\{\ddot{U}_s\right\}\right) \tag{2}$$

where [M], [C] and [K] are the mass, damping and stiffness matrices of the structure respectively and [G], [C'] and [K'] are matrices representing the mass, damping and stiffness of the reservoir, respectively. [Q] is the coupling matrix (Zienkiewicz and Taylor, 2000); {f<sub>i</sub>} is the vector of body force and hydrostatic force;

and  $\{P\}$  and  $\{U\}$  are the vectors of hydrodynamic pressures and displacements.  $\{\ddot{U}_g\}$  is the ground acceleration and  $\rho$  is the density of the fluid. The over-dot represents the time derivative.

### 3 Iterative Computing of Two-Way Coupling

The coupled fluid-structure equation is a nonlinear system regardless of the solid model used (linear or nonlinear), since the fluid equations are always nonlinear. An iteration procedure must therefore be used to obtain the solution at a specific time. In this solution, the fluid and solid solution variables are fully coupled. The fluid equations and the solid equations are solved individually in succession, always using the latest information provided from another part of the coupled system. This iteration is continued until convergence in the solution of the coupled equations is reached. The computational procedure can be summarized as follows:

To obtain the solution at time  $t + \Delta t$ , we iterate between the fluid model and the solid model. For iterations  $k = 1, 2, \dots$ , the following iteration is performed to obtain the solution at time step  $t + \Delta t$ .

1. Prescribing solid displacement  $\{U\}$
2. Solving the equation (2) to obtain the fluid solution  $\{\bar{P}\}; \{\dot{P}\}; \{P\}$
3. Substituting vector  $\{P\}$  in to equation (1) to calculate the solid solution  $\{\ddot{U}\}; \{\dot{U}\}; \{U\}$
4. Using these criteria as following to check for convergence of the iterations

$$\frac{|U^k - U^{k-1}|}{|U^k|} \leq \varepsilon_U \text{ and } \frac{|P^k - P^{k-1}|}{|P^k|} \leq \varepsilon_P \quad (3)$$

where  $\varepsilon_U$  and  $\varepsilon_P$  are tolerances for stress and displacement convergence, respectively.

If the criteria (3) is satisfied, solutions at time step  $t + \Delta t$  are obtained. If the criteria (3) has not been satisfied, the solving process goes back to step 2 and continues for the next iteration.

### 4 Application in Seismic Analysis of Sonla Dam

Sonla Dam is located in the Da river, Sonla province, Vietnam This dam is 130 meters high, 95 meters width at bottom of the dam. The analysis of dam-reservoir

interaction has been implemented in to ADINA using iterative computing of two-way coupling algorithm above. The accuracy and efficiency of this software has been tested with many numerical examples (ADINA R & D. 2005).

### 4.1 Selected Model

The analysis of Sonla dam is considered as a two dimensional model which is well accepted for a typical gravity dam. This mean, a section of Dam-reservoir-foundation system is considered with unit thickness (Figure 1). The 4-nodes plane solid finite element is used for the dam and foundation domain. The 4-nodes plane fluid finite element is used for reservoir domain. The model consists of a total of 897 nodes and 1794 degrees of freedom and the mesh includes 376, 72 planes solid and fluid elements, respectively. The water level is considered at the height of 122 meters above the base. The length of the reservoir is 350m. Fluid-structure interaction boundary condition is applied at the upstream of the dam and at the bottom of the reservoir. The massless-foundation input model is used in this study (Bayraktar et al., 2005)

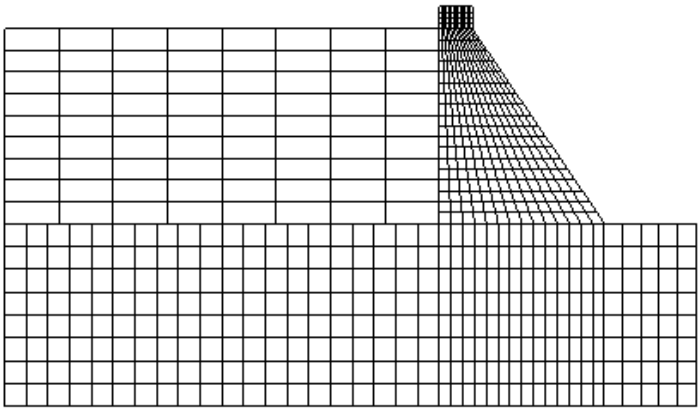


Figure 1. Finite element mesh of Sonla Dam-Reservoir system

### 4.2. Basic Parameters and Loads

The concrete is assumed to be homogeneous and isotropic with the following basic properties:

- Elastic modulus  $E = 25.5 \text{ GPa}$
- Poisson's ratio  $\nu = 0.167$
- Unit weight  $\gamma = 24 \text{ kN/m}^3$

The water is taken as potential-based fluid with weight density of  $10 \text{ kN/m}^3$ . The Rayleigh damping matrix is applied and the corresponding coefficients are determined such that equivalent damping for the frequencies close to the first and the third modes of vibration would be 5%.

The dam is subjected hydrostatic load, hydrodynamic load, self weight and earthquake load caused by ground excitation. The dynamic excitation considered in this paper is the acceleration spectrum given by the Vietnam code for seismic design of construction (TCXDVN 375, 2006). The history artificial acceleration curve is computed from the acceleration spectrum correlatively by utilizing SIMQKE program. Response spectrum at Son la dam location and artificial acceleration are showed in figure 2 and figure 3 respectively.

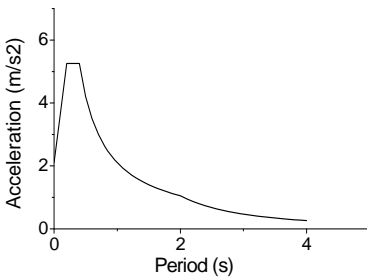


Figure 2. Response spectrum

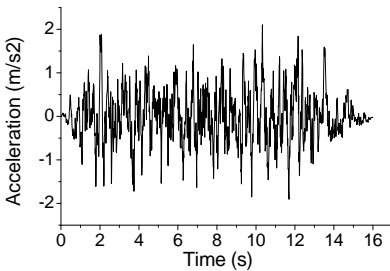


Figure 3. Time history acceleration

### 4.3 Analysis Results

The model is analyzed and the result corresponding to the maximum stress\_Z is illustrated in figure 4. The time histories of stress\_Z at dam heel and displacement at dam crest are illustrated in figure 5 and figure 6. From figure 6 we know that the maximum displacement occurs at t=2.16s.

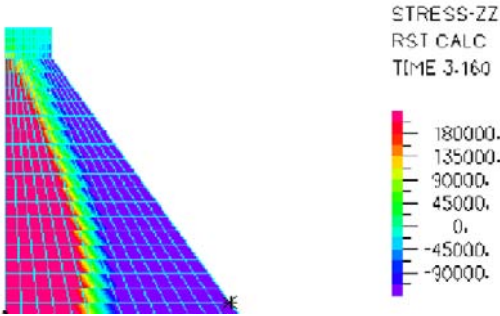


Figure 4. Envelop of stress Z-Z at t = 2.16(Sec)

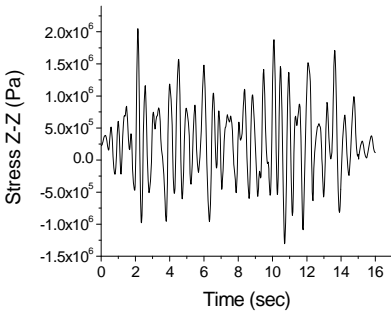


Figure 5. Stress Z-Z history at dam heel

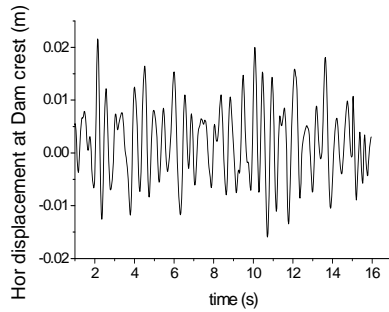


Figure 6. Displacement history at dam crest

## 5 Conclusions

A technique is proposed for the dynamic analysis of concrete gravity dams. The couple finite element equation of Dam reservoir interaction was solved by utilizing iterative computing of two-way coupling technique. A two-dimensional mod-

el of Sonla dam was analyzed. The results satisfy safety critical in Vietnamese building code.

The methodology introduced is very convenient and can be easily implemented in the finite element program ADINA with regard to fluid-structure interaction modules.

## References

- ADINA R&D, Inc. ADINA. 2005. ADINA verification manual.
- Bayraktar A., Hançer E. and Akköse M. (2005). Influence of base-rock characteristics on the stochastic dynamic response of dam-reservoir-foundation systems, *Eng. Struct.*, 27(10):1498–1508.
- Finn W.D.L. and Varoğlu E. (1973) Dynamics of gravity dam-reservoir systems, *Comput. Struct.*, 3: 913–924.
- Ghaemian M. and Ghobarah A. (1998). Nonlinear seismic response of concrete gravity Dams with dam-reservoir interaction, *Eng. Struct.*
- Olson L.G. and Bathe K.J. (1983). A study of displacement-based fluid finite elements for calculating frequencies of fluid and fluid-structure systems. *Nucl. Eng. Design*, 76:137–151.
- TCXDVN 375 (2006). Design of Structures for Earthquake Resistance: 28–32.
- Zienkiewicz O.C. and Taylor R.L. (2000). *The Finite Element Method*. 5th Edition, Butterworth-Heinemann, Oxford, UK.

*“This page left intentionally blank.”*

# Full 3D Numerical Simulation Method and Its Application to Seismic Response Analysis of Water-Conveyance Tunnel

Haitao Yu<sup>1\*</sup>, Yong Yuan<sup>1,2</sup>, Zhiyi Chen<sup>1,2</sup>, Guangxi Yu<sup>1</sup> and Yun Gu<sup>3</sup>

<sup>1</sup>Department of Geotechnical Engineering, Tongji University, Shanghai 200092, P.R. China

<sup>2</sup>Key Laboratory of Geotechnical and Underground Engineering of Ministry of Education, Tongji University, Shanghai 200092, P.R. China

<sup>3</sup>Shanghai Qingcaosha Investment Construction & Development Co., Ltd, Shanghai 201206, P.R. China

**Abstract.** In order to depict seismic response of a newly-built shield tunnel used for water supply and its extinct features during earthquake, a three-dimensional numerical simulation method for large-scale seismic response of tunnel structure is proposed with the character of fully approximating to the reality. The development of appropriate crucial theories and methods are briefly described, including explicit finite element algorithm, time step control and equivalent connecting method between local refined model and integral model. Then the three-dimensional analytical object is set up from geometrical model to finite element model, which consists of surrounding soils, shield tunnel segments, bolts, and many other entities. This model could consider dynamic hysteretic nonlinear behaviors of soil, contact interface between soil and tunnel, contact interface between bolts and segments; and the contact interfaces between segments. Final calculation is successfully completed on a high-performance computer. According to the calculation results, the whole dynamic tendency of shield tunnel are achieved, which reveals the interaction and distortion of the foundation soil-shield tunnel system under seismic loading. Consequently, it provides a practical method and meaningful data for the seismic design and analysis of tunnel structure.

**Keywords:** earthquake engineering, underground structure, water-conveyance tunnel, large-scale computation, numerical method

---

\* Corresponding author, e-mail: yuhaitaobest@163.com

## 1 Introduction

The Great Hanshin Earthquake of January 1995 caused great damage to underground structures, highlighting the need for seismic design and analysis which takes into account the dynamic behavior of underground structures.

As a special underground structure, tunnel has the feature of significant length, passing through different stratum, tortuous direction and complex configuration like shield tunnel, which make the research on mechanical property and flexibility of tunnel structure subjected to earthquake very important and much valuable. Response displacement method and other underground seismic analysis methods are basically pseudo-static methods, with the limitations to deal with heterogeneity and nonlinearity of medium as well as complex geometry configuration and boundary condition. Comparatively, the most overall and widely used seismic analysis method for tunnel structure is dynamic finite element method (Hashash et al., 2001).

In the past, the seismic research on tunnel structure was productive, but with both the limitations of numerical calculation and computing capacity of computer, these research mainly on 2-D analysis with many simplifications and assumptions (Gil et al. 2001; Mohammad and Akbar, 2005). Even if some research accomplished with the 3-D soil-structure analysis, they were restricted to small-scale space area, which made difficult to fully reflect the complex spatial features of large-scale tunnel structure motion (Xiao, 1997; Dobashi et al., 2007). With the appearance of high-performance computer and its increasing application, it is possible that three-dimensional dynamic FEM can be a chance for the large-scale seismic response analysis of long-distance tunnel structure with its supercomputing and mass storage capability.

This research provides a full 3D numerical simulation method for seismic response analysis and its corresponding application to a recently built long-distance double line shield tunnel used for water supply in Shanghai. The structure of the paper is as follows: the methodology used for analysis is briefly introduced in Section 2 (such as the explicit time integration scheme and dynamic nonlinear hysteretic model for soil); the analytical model is described in Section 3; the results and the corresponding discussion are shown in Section 4; the conclusion and direction for potential future work are given in Section 5.

## 2 Principle and Methods

### 2.1 Dynamic Explicit Algorithm

Generally, the motion equation of a deformed body for nonlinear dynamic behavior (Hallquist, 1998) can be described as:

$$M\ddot{x}(t) = P - F + H - C\dot{x} \quad (1)$$

where  $M$  is the global mass matrix,  $P$  accounts for the global load vector (nodal load, body force, surface force, etc.),  $C$  is the damping matrix,  $H$  is the global hourglass resisting force vector handling the hourglass deformation modes,  $F$  is the assembly of equivalent nodal force vectors from all the elements.

The explicit central differential method (CDM) is adopted to solve the motion equation by time integration:

$$\dot{x}(t_{n+1/2}) = \dot{x}(t_{n-1/2}) + (\Delta t_{n+1/2} + \Delta t_{n-1/2})\ddot{x}(t_n)/2 \quad (2)$$

$$x(t_{n+1}) = x(t_n) + \Delta t_{n+1/2}\dot{x}(t_{n+1/2}) \quad (3)$$

where  $\dot{x}(t_{n+1/2})$  is the nodal velocity vector at time  $t_{n+1/2}$ ,  $x(t_{n+1})$  is the nodal displacement vector at time  $t_{n+1}$ .

After the nodal location and the nodal acceleration at time  $t_n$  are acquired together with the nodal velocity at time  $t_{n+1/2}$ , the nodal displacement at time  $t_{n+1}$  can be calculated by Equation (3). In time domain, the displacement, velocity and acceleration of each discrete point can be calculated through such integral recursive formulae.

### 2.2 Time Step

Because the explicit CDM is conditionally stable, it is necessary to guarantee a small time step for modeling wave propagation. In fact, the time step size depends on the minimum natural period of the whole mesh to guarantee the calculation stability of the central difference method. Hence, during the solution, a new time step size is determined by taking the minimum value over all elements:

$$\Delta t^{n+1} = \alpha \cdot \min\{\Delta t_1, \Delta t_2, \dots, \Delta t_N\} \quad (4)$$

where  $\alpha$  is a scale factor,  $N$  is the number of elements,  $\Delta t$  is the critical time step size.

### 2.3 Dynamic Hysteretic Model of Soil

Several soil layers close to the tunnel mainly influence the seismic response of the underground tunnel. Here, the soil’s behavior is assumed to be governed by a non-linear dynamic hysteretic constitutive relation based on Ramberg-Osgood (R-O) model. This model allows a simple rate independent representation of the hysteretic energy dissipation observed in soils subjected to cyclic shear deformation. For monotonic loading, the stress-strain relationship is given by (Hallquist, 1998):

$$\left. \begin{aligned} \frac{\gamma}{\gamma_y} &= \frac{\tau}{\tau_y} + \alpha \left| \frac{\tau}{\tau_y} \right|^r & \text{if } \gamma \geq 0 \\ \frac{\gamma}{\gamma_y} &= \frac{\tau}{\tau_y} - \alpha \left| \frac{\tau}{\tau_y} \right|^r & \text{if } \gamma < 0 \end{aligned} \right\} \quad (5)$$

where  $\gamma$  is the shear strain,  $\tau$  is the shear stress,  $\gamma_y$  is the reference shear strain,  $\tau_y$  is the reference shear stress,  $\alpha$  is stress coefficient, and  $r$  is stress exponent.

In the soil-tunnel analytical model, some parts that contact each other will possibly have extrusion and sliding behaviors under seismic loading. To handle this problem, it finally comes down to the search for contact objects and the calculation of contact forces as a nonlinear boundary condition.

Such a contact problem is often solved by the symmetrical penalty method (Hallquist, 1998), which consists of placing normal interface springs between all penetrated nodes and the contact surface. First, the penetration between the slave node  $n_i$  and the master segment  $s_i$  is judged within each time step. If there is no penetration, there is no treatment; otherwise, a normal contact force  $f_s$  will be calculated:

$$f_s = mk_i n_i \quad (6)$$

where  $m$  is the amount of penetration,  $n_i$  is the normal to the master segment at the contact point,  $k_i$  is the stiffness factor for the master segment.

Friction is based on a Coulomb formulation, and the maximum frictional force  $F_v$  is defined as:

$$F_v = \mu |f_s| \quad (7)$$

where  $\mu$  is the coefficient of friction,  $f_s$  is the normal force at slave node  $n_s$ .

## ***2.4 Equivalent Connecting Method***

Generally, if the whole tunnel structure constructed of refined model including bolts and joints, the finite element model will be huge and hardly solved, even with most advanced supercomputer in the world. Hence, equivalent connecting method is put forward to solve this problem. It mainly consists of two steps: (1) based on axial direction of the whole tunnel, establish 3D finite element model of soil and equivalent tunnel structure without bolts and joints, but consider dynamic coupling relationship between soil and tunnel, then carry out numerical simulation of this model and identify seismic response characteristics of the integral system as well as dangerous area of tunnel; (2) replace equivalent tunnel model with refined model including bolts and joints in dangerous sections or other interested districts, with no change of other parts, then perform numerical simulation of the hybrid model under the same condition.

This equivalent connecting method can not only cover adequately wide simulation area of the whole tunnel-soil system, but also consider large extent of detailed key position of tunnel. Furthermore, the number of finite element would be controlled in the range of calculation capacity of supercomputer.

## **3 Computation Model**

The Qingcaosha Water-conveyance Tunnel is a newly built double-line shield tunnel used for water supply in the city of Shanghai, China. It contains three parts: island region, cross-river region and land region, with total length of 14km. The inner diameter and outer diameter of tunnel segment for cross-river region are 5.84m and 6.8m respectively, in addition to other regions with 5.5m and 6.4m respectively.

The principal part of foundation soil-tunnel system is double-line shield tunnel composed of approximately 1000 rings of segment lining, respectively. Each ring consists of six segments, with the length of 1.5m. Stagger-jointed assembling mode is adopted between segment linings. In addition, three working shafts are contained in the whole analytical model. The surrounding soil model (300m deep into the local bedrock) has also been constructed according to the geological exploration data, which includes 10 layers of earth with different thickness. All of the entity is plotted with physical dimension, which could fully express tunnel and soil on the part of actual space figure, traversing direction of strike and fluctuant characteristic on height. Figure 1 shows tunnel structure model of the whole analytical system.

The global finite-element model of this soil-tunnel system is illustrated in Figure 2. The finite element model of equivalent tunnel structure including three working shafts (Figure 3) has been built with the eight-node hexahedron solid element. The surrounding soil is meshed by both of eight-node hexahedron and four-node tetrahedral element, because the 3D solid model of the surrounding soil is divided into 10 layers with various geometrical configurations. The final 3D size of this soil-tunnel system model is  $12660\text{m} \times 2509\text{m} \times 300\text{m}$ , with the number of nodes and elements reaching 1,323,978 and 4,785,026, respectively.

For the hybrid model, equivalent tunnel model is replaced with refined model including bolts and joints, which has been built with mainly eight-node hexahedron element (Figure 4). Of which, six segments in each ring are connected by M36 circumferential bolts with total number of 24; the joints between two adjacent segment rings are composed of M30 longitudinal bolts with total number of 16.

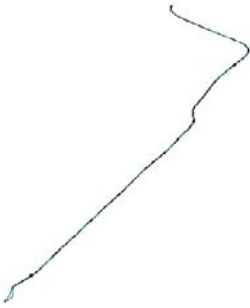
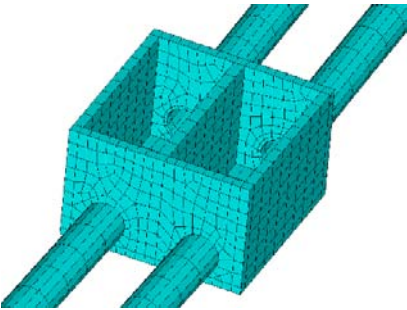


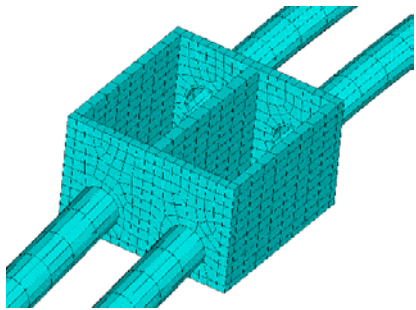
Figure 1. Tunnel structure model of the whole analytical system



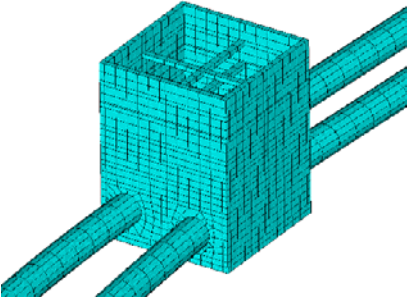
Figure 2. The mesh of the whole soil-tunnel system



(a) Working shaft of island region

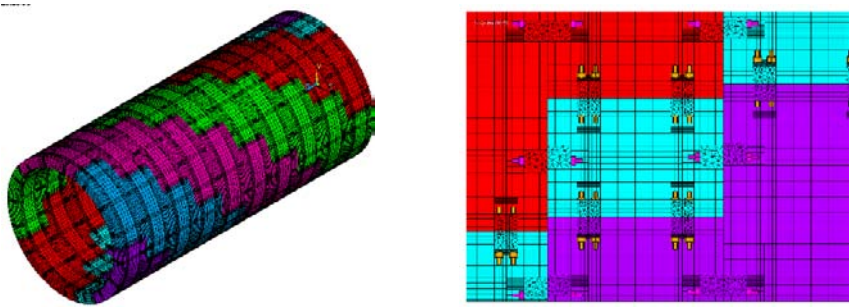


(b) Working shaft of cross-river region



(c) Working shaft of land region

Figure 3. The mesh of three working shafts



(a) Global mesh effect

(b) Local mesh effect

Figure 4. The mesh of multi-ring refined model

The elastic material model is assumed for tunnel segments and working shafts, with material parameters shown as follows: Young's modulus, 35.5GPa; density, 2500kg/m<sup>3</sup>; Poisson's ratio, 0.2. Material parameters of bolts include: Young's modulus, 206GPa; density, 7850kg/m<sup>3</sup>; Poisson's ratio, 0.3.

As has been mentioned, the seismic response of a tunnel is mainly affected by the layers of surrounding soil closer to the tunnel. Material property data for 10 layers of soil through which this tunnel is excavated are illustrated in Table 1 as an emphasis.

Considering contact and relative sliding between interfaces of different structural parts, surface-to-surface contact form has been located among segments of each liner ring, joints of adjacent liner rings, tunnel-soil interface and shaft-soil interface.

Table 1. Material parameters of soil layers surrounding tunnel

Soil layer	Reference shear strain	Reference shear stress (kPa)	Stress coefficient	Stress exponent	Elastic bulk modulus (MPa)
Drab sandy silt	$4.1 \times 10^{-4}$	10.98	1.34	2.00	58.02
Gray silty clay	$4.1 \times 10^{-4}$	14.53	1.30	2.00	86.43
Gray mucky silty clay	$4.2 \times 10^{-4}$	18.32	1.30	2.00	97.04
Gray mucky clay	$4.2 \times 10^{-4}$	20.45	1.30	2.00	110.34
Gray silty clay	$4.3 \times 10^{-4}$	37.46	1.26	1.80	188.76
Gray sandy silt	$3.8 \times 10^{-4}$	55.12	1.36	2.05	314.25
Gray sandy silt	$3.8 \times 10^{-4}$	55.41	1.36	2.05	315.94
Gray silty sand	$4.0 \times 10^{-4}$	59.58	1.33	2.08	322.75
Gray silty sand	$4.0 \times 10^{-4}$	94.08	1.03	2.10	509.60
Gray fine sand	$4.1 \times 10^{-4}$	137.84	1.45	1.85	728.43

### 4 Calculation and Results

In seismic calculation, El-Centro seismic wave record has been applied as ground motion at the bedrock (Figure 5). According to the exceeding probability of 10% in 50 years and the designed 7-degree preventive intensity of the tunnel, amplitude modulation has been applied to make the maximum ground acceleration value of this seismic wave equal 0.1g.

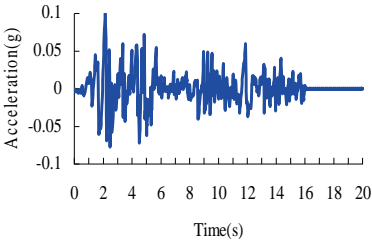


Figure 5. El-Centro seismic wave acceleration time history

The seismic wave has been input at the bedrock surface under the condition of propagating along the transverse direction, while the longitudinal and vertical displacements are constrained. Meanwhile, the lateral boundary surfaces of the surrounding soil have been modeled with free boundary, due to the large size of the soil model.

Seismic response calculation of the tunnel-soil system has been finished with 64 CPUs on the Dawning 4000A supercomputer in Shanghai Supercomputer Center, which costs about 70 hours.

Final calculation has produced plenty of data describing the response of the shield tunnel under seismic excitation, where the results can be post-processed in several styles. Take cross-river region as an example, Figure 6 shows the resultant displacement in the transverse direction as the seismic wave propagates along the transverse direction. It can be seen that the maximum displacement value is about 70mm at time 5.8s, which indicates the behavior of tunnel belongs to small deformation compared to the whole tunnel length. Figure 7 illustrates the maximum principal stress response in a lining segment, which provides a direct understanding of the tunnel segment's stress condition.

From full 3D seismic response calculation results, three working shafts and other special structures can also be further understood and analyzed. Because of limited length, this would not be discussed in this paper.

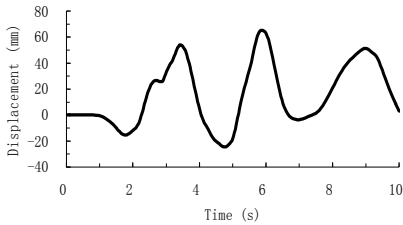


Figure 6. The resultant displacement of cross-river region in the transverse direction

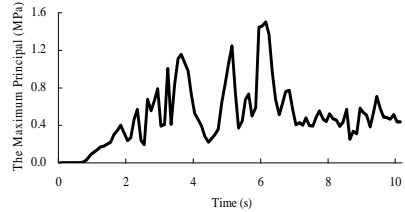


Figure 7. Example of the maximum principal stress variation with time in lining segments

## 5 Conclusions

This paper presents a novel and reliable simulation method for estimating the seismic response of a long-distance shield tunnel used for water supply in the city of Shanghai. Based on tunnel-foundation soil dynamic interaction system subjected to earthquake, the three-dimensional large-scale FEM model consisting of soil and tunnel structure is constructed; the corresponding numerical simulation methods are presented. Meanwhile, several important and necessary factors such as material nonlinearity and contact nonlinearity are also taken into consideration. The analytical model put forward in this study fully depicts the real three-dimensional configuration of the water-conveyance shield tunnel and geological features of the construction site, overcoming the deficiency that seismic response analysis could not be performed from full 3D view due to the limitation of computational capacity in the past. The calculation has been accomplished successfully

using LS-DYNA MPP on the “Dawning 4000A” supercomputer. Finally, there are some detailed and meaningful results with respect to the tunnel segments, as well as an overall understanding of the behavior of this tunnel, which could provide reference for seismic design and analysis of tunnel structures.

Future work will include a more in-depth analysis of the current abundant results, research on the influence of different seismic input directions and inconsistent excitation on the final dynamic response of tunnel structure.

## Acknowledgements

The authors gratefully acknowledge the Shanghai Tunnel Engineering & Rail Transit Design and Research Institute for support and cooperation, and the Shanghai Supercomputing Center for offering access to the Dawning 4000A supercomputer with LS-DYNA 971 MPP. The authors also wish to express special thanks to Zong-zhao Qiao, Wen-hong Cao and Dr. Jun-hong Ding for helpful advice. This research is supported financially by the National Key Technology R&D Program of the People’s Republic of China (Serial Number: 2006BAJ27B02-02).

## References

- Dobashi H., Ochiai E., Ichimura T. et al. (2007). 3D FE analysis of seismic response of complicated large-scale ramp tunnel structure. *ECCOMAS Thematic Conference on Computational Methods in Structural Dynamics and Earthquake Engineering*, Rethymno, Crete, Greece, 13-16 June 2007.
- Gil L.M., Hernandez E, et al. (2001). Simplified transverse seismic analysis of buried structures. *Soil Dynamics and Earthquake Engineering*, 21: 735-740.
- Hallquist J.O. (1998). *LS-DYNA Theoretical Manual*. Livermore: Livermore Software Technology Corporation.
- Hashash Y.M.A., Jeffrey J., Hook et al. (2001). Seismic design and analysis of underground structure. *Tunneling and Underground Space Technology*, 16(4): 247-293.
- Housner G.W. (1954). Earthquake pressures on fluid containers. *Pasadena: California Institute of Technology*.
- Mohammad C.P., Akbar Y. (2005). 2-D Analysis of circular tunnel against earthquake loading. *Tunnelling and Underground Space Technology*, 20: 411-417.
- Westergaard H.M. (1933). Water pressures on dams during earthquakes. *ASCE Trans.*, 98: 418-434.
- Xiao M. (1997). Three-dimensional nonlinear finite element analysis of shield tunnel prefabricated linings. *Chinese Journal of Geotechnical Engineering*, 19(2): 106-111 [in Chinese].

# **DYNAMIC INTERACTIONS**

*“This page left intentionally blank.”*

# Comparison of Different-Ordered Polynomial Acceleration Methods

Changqing Li<sup>1\*</sup> and Menglin Lou<sup>1</sup>

<sup>1</sup> State Key Laboratory for Disaster Reduction in Civil Engineering, Tongji University, Shanghai 200092, China

**Abstract.** The polynomial interpolation acceleration method for time history analysis is presented, in which accelerations between several equal neighboring time steps are assumed to be polynomial function of time. In term of Taylor deployment theorem, with the increase of degree of polynomial, higher order precision of the solution of dynamic equation can be achieved thus wider time step can be used to solve the dynamic equation with truncation error in the acceptable limit. However, when higher degree of polynomial is used, the stabilization field of the method narrow down, which leads to restriction of the time step size. Once time step is larger than the limit of smaller convergence field, the transferred error will be magnified many times and results in the failure of solution. Numerical analysis shows that the higher order polynomial interpolation acceleration method unnecessarily leads to wider acceptable time step. Stabilization field and convergence accuracy taken into account, the square acceleration method is superior to linear and third-degree polynomial acceleration method.

**Keywords:** acceleration, time history analysis, polynomial, convergence, stabilization field, spectral radius

## 1 Introduction

In time history analysis, time step size directly affects the efficiency of solution procedure. If time step is too small, it will lead to enormous cost of computation time. Otherwise, large time step may cause great loss of solution accuracy. Thus, how to choose a feasible maximum time step is very important, which is determined not only by solution efficiency but also by solving algorithm itself.

Between neighboring time points, acceleration is assumed to be  $n$ -ordered polynomial of time, which is called  $n$ -ordered polynomial acceleration method. Based on known motion state of the system at the first time point, its motion state at the

---

\* Corresponding author, e-mail: 0610020029@smail.tongji.edu.cn

next time points can be achieved through formula derivation. Repetition of this kind of work can get the solution result at the whole time domain. Therefore, the question is raised to be determined that how much is the value of time steps  $n$  when in the  $n$ -ordered polynomial acceleration method widest time step can be chose with acceptable accuracy. To answer this question, this paper presents the evaluation of polynomial acceleration method at first, and then gives a simple numerical model. At last compares the solution results using different-ordered polynomial acceleration method with the accurate theory solution to draw a conclusion.

## 2 Evaluation of Polynomial Acceleration Method

The Equation of motion for a linear single-degree-of-freedom system is:

$$m\ddot{v}(t) + c\dot{v}(t) + kv(t) = p(t) \tag{1}$$

where  $m$  the mass of system,  $c$  the damping coefficient,  $k$  the stiffness of system,  $v(t)$   $\dot{v}(t)$  and  $\ddot{v}(t)$  are displacement, velocity and acceleration of the system respectively.  $p(t)$  is external force.

In the  $n$ -ordered polynomial acceleration method, it is assumed that acceleration is  $n$ -ordered polynomial of time between  $n$  neighboring time points, as

$$\ddot{v}(\tau) = \ddot{v}_i + a_1\tau + a_2\tau^2 + \dots + a_n\tau^n \quad 0 \leq \tau \leq nh \tag{2}$$

where  $\ddot{v}_i$  is the known initial acceleration,  $\tau$  is time and  $a_1, a_2, \dots, a_n$  are the coefficients to be determined,  $h$  is the time step.

When  $n=1$ , the method is called linear acceleration method (LAM), when  $n=2$ , the method is called quadratic acceleration method (QAM), when  $n=3$ , the method is called third-degree polynomial acceleration method (TPAM), and so on.

Applying integration to Equation (2), one obtains

$$\dot{v} = \dot{v}_i + \ddot{v}_i\tau + \frac{a_1}{2}\tau^2 + \frac{a_2}{3}\tau^3 + \dots + \frac{a_n}{n+1}\tau^{n+1} \tag{3}$$

where  $\dot{v}_i$  is the known initial velocity

Applying integration to Equation (3) again, one obtains

$$v=v_i+\dot{v}_i\tau+\frac{\ddot{v}}{2}\tau^2+\frac{a_1}{6}\tau^3+\dots+\frac{a_n}{(n+1)(n+2)}\tau^{n+2} \tag{4}$$

where  $V_i$  is the known initial displacement.

Substituting  $\tau=h, 2h, \dots, nh$  in Equation2,Equation3,Equation4,one obtains

$$\begin{bmatrix} \ddot{v}_{i+1} \\ \dot{v}_{i+1} \\ v_{i+1} \end{bmatrix} = \begin{bmatrix} \ddot{v}_{i+1}(a_1, a_2, \dots, a_n) \\ \dot{v}_{i+1}(a_1, a_2, \dots, a_n) \\ v_{i+1}(a_1, a_2, \dots, a_n) \end{bmatrix} = \begin{bmatrix} \ddot{v}_i+a_1h+a_2h^2+\dots+a_nh^n \\ \dot{v}_i+\dot{v}_i h+\frac{a_1}{2}h^2+\frac{a_2}{3}h^3+\dots+\frac{a_n}{n+1}h^{n+1} \\ v_i+\dot{v}_i h+\frac{\ddot{v}}{2}h^2+\frac{a_1}{6}h^3+\dots+\frac{a_n}{(n+1)(n+2)}h^{n+2} \end{bmatrix} \tag{5.1}$$

$$\begin{bmatrix} \ddot{v}_{i+2} \\ \dot{v}_{i+2} \\ v_{i+2} \end{bmatrix} = \begin{bmatrix} \ddot{v}_{i+2}(a_1, a_2, \dots, a_n) \\ \dot{v}_{i+2}(a_1, a_2, \dots, a_n) \\ v_{i+2}(a_1, a_2, \dots, a_n) \end{bmatrix} = \begin{bmatrix} \ddot{v}_i+a_1(2h)+a_2(2h)^2+\dots+a_n(2h)^n \\ \dot{v}_i+\dot{v}_i(2h)+\frac{a_1}{2}(2h)^2+\frac{a_2}{3}(2h)^3+\dots+\frac{a_n}{n+1}(2h)^{n+1} \\ v_i+\dot{v}_i(2h)+\frac{\ddot{v}}{2}(2h)^2+\frac{a_1}{6}(2h)^3+\dots+\frac{a_n}{(n+1)(n+2)}(2h)^{n+2} \end{bmatrix} \tag{5.2}$$

... ..

$$\begin{bmatrix} \ddot{v}_{i+n} \\ \dot{v}_{i+n} \\ v_{i+n} \end{bmatrix} = \begin{bmatrix} \ddot{v}_{i+n}(a_1, a_2, \dots, a_n) \\ \dot{v}_{i+n}(a_1, a_2, \dots, a_n) \\ v_{i+n}(a_1, a_2, \dots, a_n) \end{bmatrix} = \begin{bmatrix} \ddot{v}_i+a_1(nh)+a_2(nh)^2+\dots+a_n(nh)^n \\ \dot{v}_i+\dot{v}_i(nh)+\frac{a_1}{2}(nh)^2+\frac{a_2}{3}(nh)^3+\dots+\frac{a_n}{n+1}(nh)^{n+1} \\ v_i+\dot{v}_i(nh)+\frac{\ddot{v}}{2}(nh)^2+\frac{a_1}{6}(nh)^3+\dots+\frac{a_n}{(n+1)(n+2)}(nh)^{n+2} \end{bmatrix} \tag{5.n}$$

To satisfy motion equation at every time point, substituting equation sets (from Equation (5.1) to Equation (5.n)) into Equation (1), a linear Equation including  $n$  unknowns ( $a_1, a_2, \dots, a_n$ ) can be obtained:

$$\begin{aligned} m\ddot{v}_{i+1}(a_1, a_2, \dots, a_n) + c\dot{v}_{i+1}(a_1, a_2, \dots, a_n) + kv_{i+1}(a_1, a_2, \dots, a_n) &= p(t_{i+1}) \\ m\ddot{v}_{i+2}(a_1, a_2, \dots, a_n) + c\dot{v}_{i+2}(a_1, a_2, \dots, a_n) + kv_{i+2}(a_1, a_2, \dots, a_n) &= p(t_{i+2}) \\ \dots\dots\dots \\ m\ddot{v}_{i+n}(a_1, a_2, \dots, a_n) + c\dot{v}_{i+n}(a_1, a_2, \dots, a_n) + kv_{i+n}(a_1, a_2, \dots, a_n) &= p(t_{i+n}) \end{aligned} \tag{6}$$

Solving above linear Equation (6), the value of  $a_1, a_2, \dots, a_n$  can be determined. Then substituting the known  $a_1, a_2, \dots, a_n$  back into Equation (5), the motion state of system at time point  $t_{i+1}, t_{i+2}, \dots, t_{i+n}$  is determined.

Taking third-degree polynomial acceleration method as an example: First, divide the time domain to multiplication of number 3 (time steps is not as much as multiplication of number 3, zero force time step can be added). Then assuming that acceleration within three neighboring time steps from  $t_i$  to  $t_{i+3}$  is third-degree polynomial function of time (Clough and Penzien, 1993) as shown in Figure 1.

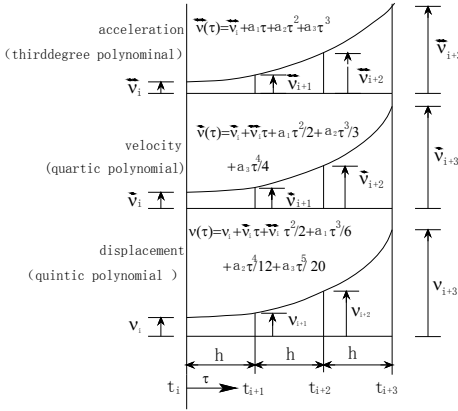


Figure 1. Third-degree polynomial acceleration method

$$\ddot{v}(\tau) = \ddot{v}_i + a_1\tau + a_2\tau^2 + a_3\tau^3 \quad (0 \leq \tau \leq 3h) \tag{7}$$

From Equation (7), one can obtain

$$\dot{v}(\tau) = \dot{v}_i + \ddot{v}_i\tau + \frac{a_1}{2}\tau^2 + \frac{a_2}{3}\tau^3 + \frac{a_3}{4}\tau^4 \quad (0 \leq \tau \leq 3h) \tag{8}$$

And from Equation (8), one obtains

$$v(\tau) = v_i + \dot{v}_i\tau + \frac{\ddot{v}_i}{2}\tau^2 + \frac{a_1}{6}\tau^3 + \frac{a_2}{12}\tau^4 + \frac{a_3}{20}\tau^5 \quad (0 \leq \tau \leq 3h) \tag{9}$$

Substituting  $\tau=h, \tau=2h, \tau=3h$  into Equations (7), (8) and (9) respectively, nine following formulas can be obtained:

$$v_{i+1} = v_i + \dot{v}_i h + \frac{\ddot{v}_i}{2} h^2 + \frac{a_1}{6} h^3 + \frac{a_2}{12} h^4 + \frac{a_3}{20} h^5 \tag{10.1}$$

$$v_{i+1} = v_i + \dot{v}_i h + \frac{\ddot{v}_i}{2} h^2 + \frac{a_1}{6} h^3 + \frac{a_2}{12} h^4 + \frac{a_3}{20} h^5 \tag{10.2}$$

$$\ddot{v}_{i+1} = \ddot{v}_i + a_1 h + a_2 h^2 + a_3 h^3 \tag{10.3}$$

$$v_{i+2} = v_i + 2\dot{v}_i h + 2\ddot{v}_i h^2 + \frac{4a_1}{3} h^3 + \frac{4a_2}{3} h^4 + \frac{8a_3}{5} h^5 \tag{11.1}$$

$$\dot{v}_{i+2} = \dot{v}_i + 2\ddot{v}_i h + 2a_1 h^2 + \frac{8a_2}{3} h^3 + 4a_3 h^4 \tag{11.2}$$

$$\ddot{v}_{i+2} = \ddot{v}_i + 2a_1 h + 4a_2 h^2 + 8a_3 h^3 \tag{11.3}$$

$$v_{i+3} = v_i + 3\dot{v}_i h + \frac{9\ddot{v}_i}{2} h^2 + \frac{9a_1}{2} h^3 + \frac{27a_2}{4} h^4 + \frac{243a_3}{20} h^5 \tag{12.1}$$

$$\dot{v}_{i+3} = \dot{v}_i + 3\ddot{v}_i h + \frac{9a_1}{2} h^2 + 9a_2 h^3 + \frac{81a_3}{4} h^4 \tag{12.2}$$

$$\ddot{v}_{i+3} = \ddot{v}_i + 3a_1 h + 9a_2 h^2 + 27a_3 h^3 \tag{12.3}$$

Substituting Equations (10), (11) and (12) into Equation (1) gives

$$\begin{aligned} & (mh + \frac{1}{2}ch^2 + \frac{1}{6}kh^3)\ddot{v}_i + (\frac{1}{2}mh^2 + \frac{1}{6}ch^3 + \frac{1}{24}kh^4)\ddot{v}_i + (\frac{1}{6}mh^3 + \frac{1}{24}ch^4 + \frac{1}{120}kh^5)\ddot{v}_i \\ & = \Delta p_{i+1} - (ch + \frac{k}{2}h^2)\ddot{v}_i - (kh)\dot{v}_i \end{aligned} \tag{13.1}$$

$$\begin{aligned} & (2mh + 2ch^2 + \frac{4}{3}kh^3)\ddot{v}_i + (2mh^2 + \frac{4}{3}ch^3 + \frac{2}{3}kh^4)\ddot{v}_i + (\frac{4}{3}mh^3 + \frac{2}{3}ch^4 + \frac{4}{15}kh^5)\ddot{v}_i \\ & = \Delta p_{i+2} - (2ch + 2kh^2)\ddot{v}_i - (2kh)\dot{v}_i \end{aligned} \tag{13.2}$$

$$\begin{aligned}
 & (3mh + \frac{9}{2}ch^2 + \frac{9}{2}kh^3)\ddot{v}_i + (\frac{9}{2}mh^2 + \frac{9}{2}ch^3 + \frac{27}{8}kh^4)\ddot{v}_i + (\frac{9}{2}mh^3 + \frac{27}{8}ch^4 + \frac{81}{40}kh^5)\ddot{v}_i \\
 & = \Delta p_{i+3} - (3ch + \frac{9}{2}kh^2)\ddot{v}_i - (3kh)\dot{v}_i
 \end{aligned} \tag{13.3}$$

where

$$\Delta p_{i+1} = p_{i+1} - p_i, \quad \Delta p_{i+2} = p_{i+2} - p_i, \quad \Delta p_{i+3} = p_{i+3} - p_i.$$

The value of a1, a2 and a3 can be determined by solving Equation (13). And then substituting them into Equations (9), (10) and (11), the value of  $V_{i+j} \dot{V}_{i+j} \ddot{V}_{i+j}$  (j=1,2,3) can be obtained. Repeating the procedure above, and taking  $V_{i+3} \dot{V}_{i+3} \ddot{V}_{i+3}$  as the known starting point, the value of  $V_{i+j} \dot{V}_{i+j} \ddot{V}_{i+j}$  (j=4,5,6) can be gotten. This computing procedure is done repeatedly until the values at all discrete time points are obtained.

### 3 Stabilization Analysis

Stabilization of an algorithm is important since it determines whether the transferred error will be magnified with the iteration procedure going on. An ideal undamped single degree of freedom system (Li and Lou, 2008) is considered here to analyze the stabilization filed of polynomial acceleration method. The third-degree polynomial acceleration method is taken still as an example.

Let  $r=\omega h$ , where  $\omega$  is natural vibration frequency of system and  $\beta = 1 + \frac{1}{3}r^2 + \frac{13}{240}r^4 + \frac{1}{40}r^6$  for writing simplicity and substituting  $k=\omega^2m$ ,  $c=0$  in Eqs (13), then solving the Equation gives:

$$\begin{aligned}
 a_1 = & \frac{1}{mh\beta}(3 + \frac{27}{20}r^2 + \frac{9}{20}r^4)\Delta p_1 - \frac{1}{mh\beta}(\frac{3}{2} + \frac{3}{5}r^2 + \frac{9}{160}r^4)\Delta p_2 + \frac{1}{mh\beta}(\frac{1}{3} + \frac{11}{180}r^2 + \frac{1}{180}r^4)\Delta p_3 \\
 & + \frac{1}{h\beta}(\frac{1}{4}r^4 - \frac{11}{80}r^6)\ddot{v}_i - \frac{1}{h^2\beta}(r^2 + \frac{1}{3}r^4 + \frac{17}{48}r^6)\dot{v}_i
 \end{aligned} \tag{14}$$

$$\begin{aligned}
 a_2 = & \frac{1}{2mh^2\beta}(-5 - \frac{13}{4}r^2 - \frac{3}{2}r^4)\Delta p_1 + \frac{1}{2mh^2\beta}(4 + 2r^2 + \frac{3}{10}r^4)\Delta p_2 - \frac{1}{2mh^2\beta}(1 + \frac{1}{4}r^2 + \frac{1}{30}r^4)\Delta p_3 \\
 & + \frac{1}{2h^2\beta}(-r^2 - \frac{5}{4}r^4 + \frac{3}{10}r^6)\ddot{v}_i + \frac{1}{2h^3\beta}r^6\dot{v}_i
 \end{aligned} \tag{15}$$

$$\begin{aligned}
 a_3 = & -\frac{1}{6mh^3\beta}(3+\frac{7}{4}r^2+\frac{3}{2}r^4)\Delta p_1 + \frac{1}{6mh^3\beta}(3+\frac{7}{4}r^2+\frac{3}{8}r^4)\Delta p_2 - \frac{1}{6mh^3\beta}(1+\frac{1}{4}r^2+\frac{1}{18}r^4)\Delta p_3 \\
 & + \frac{1}{6h^3\beta}(-\frac{3}{2}r^4+\frac{1}{4}r^6)\ddot{v}_i + \frac{1}{6h^4\beta}(-r^4+\frac{11}{12}r^6)\dot{v}_i
 \end{aligned}
 \tag{16}$$

Substituting Equations (14), (15) and (16) into Equations (10), (11) and (12), gives iteration format

$$\begin{bmatrix} v_{i+1} \\ \dot{v}_{i+1} \\ \ddot{v}_{i+1} \\ v_{i+2} \\ \dot{v}_{i+2} \\ \ddot{v}_{i+2} \\ v_{i+3} \\ \dot{v}_{i+3} \\ \ddot{v}_{i+3} \end{bmatrix} = \begin{bmatrix} A & & \\ & B & \\ & & C \end{bmatrix} \begin{bmatrix} v_i \\ \dot{v}_i \\ \ddot{v}_i \\ v_i \\ \dot{v}_i \\ \ddot{v}_i \\ v_i \\ \dot{v}_i \\ \ddot{v}_i \end{bmatrix} + \begin{bmatrix} D & & \\ & E & \\ & & F \end{bmatrix} \begin{bmatrix} \Delta p_{i+1} \\ \Delta p_{i+2} \\ \Delta p_{i+3} \\ \Delta p_{i+1} \\ \Delta p_{i+2} \\ \Delta p_{i+3} \\ \Delta p_{i+1} \\ \Delta p_{i+2} \\ \Delta p_{i+3} \end{bmatrix}
 \tag{17}$$

where

$$\begin{aligned}
 A = & \begin{bmatrix} 1 & \frac{720+120r^2-7r^4+11r^6}{720\beta}h & \frac{120+30r^2+r^4+r^6}{240\beta}h^2 \\ 0 & \frac{720-120r^2-111r^4+38r^6}{720\beta} & \frac{240+40r^2-22r^4+4r^6}{240\beta}h \\ 0 & \frac{-720r^2-360r^4+215r^6}{720\beta} \frac{1}{h} & \frac{240-40r^2-137r^4+19r^6}{240\beta} \end{bmatrix} \\
 B = & \begin{bmatrix} 1 & \frac{1420-480r^2-434r^4+352r^6}{720\beta}h & \frac{4320-1710r^4+288r^6}{2160\beta}h^2 \\ 0 & \frac{2160-3600r^2-2763r^4+2724r^6}{2160\beta} & \frac{480-160r^2-494r^4+82r^6}{240\beta}h \\ 0 & \frac{-1440r^2-1440r^4+1810r^6}{720\beta} \frac{1}{h} & \frac{240-400r^2-947r^4+164r^6}{240\beta} \end{bmatrix} \\
 C = & \begin{bmatrix} 1 & \frac{720-840r^2-807r^4+891r^6}{240\beta}h & \frac{1080-450r^2-1413r^4+243r^6}{240\beta}h^2 \\ 0 & \frac{240-1000r^2-1157r^4+1446r^6}{240\beta} & \frac{720-840r^2-2256r^4+396r^6}{240\beta}h \\ 0 & \frac{-720r^2-1320r^4+1815r^6}{240\beta} \frac{1}{h} & \frac{240-1000r^2-2777r^4+501r^6}{240\beta} \end{bmatrix} \\
 D = & \frac{1}{4320m\beta} \begin{bmatrix} (1152+324r^2)h^2 & (-252-9r^2+27r^4)h^2 & (24-10r^2-4r^4)h^2 \\ (2340+261r^2-378r^4)h & (180+459r^2)h & -(180+93r^2+22r^4)h \\ -(2448r^2+2376r^4) & 4320+2988r^2+675r^4 & -(1440+456r^2+88r^4) \end{bmatrix}
 \end{aligned}$$

$$E = \frac{1}{2160m\beta} \begin{bmatrix} -(288+1800r^2+1728r^4)h^2 & (3168+2160r^2+486r^4)h^2 \\ (-5760-6048r^2-4536r^4)h & (9360+5688r^2+1161r^4)h \\ -(17280+13248r^2+8856r^4) & 19440+11088r^2+2133r^4 \end{bmatrix}$$

$$\begin{bmatrix} -(1056+328r^2+64r^4)h^2 \\ -(2880+816r^2+152r^4)h \\ -(5760+1536r^2+280r^4) \end{bmatrix}$$

$$F = \frac{1}{480m\beta} \begin{bmatrix} -(4536+4050r^2+2916r^4)h^2 & (6156+3645r^2+729r^4)h^2 \\ (-9180-6939r^2-4698r^4)h & (10260+5859r^2+1134r^4)h \\ -(12960+8856r^2+5832r^4) & 12960+7236r^2+1377r^4 \end{bmatrix}$$

$$\begin{bmatrix} -(1872+516r^2+96r^4)h^2 \\ -(3060+813r^2+150r^4)h \\ -(3840+992r^2+184r^4) \end{bmatrix}$$

The stabilization field of iteration format is decided by spectral radius of block diagonal iteration matrix which is formed by three diagonal matrixes A, B, C shown in Equation (17). Based on the definition of spectral radius (Li et al., 2001), the spectral radius of matrix A,B,C is only correlated with  $r$ , where  $r$  is the multiplication of time step  $h$  and natural vibration frequency  $\omega$ . Thus, the stabilization field of the third-degree polynomial acceleration method is just dependent of  $r$ .

Numerical analysis plot the change of spectral radius of matrix A,B,C along with  $r$  in Figure 2c. Solution results show that stability field of matrix A is  $r \leq 1.85$  ( $r = \omega h$ ), of matrix B is  $r \leq 0.092$  and of matrix C is  $r \leq 0.062$ . To satisfy stability condition of three matrixes, matrix field of third-degree polynomial acceleration method is  $r \leq 0.062$ , which can be transformed to be  $h/T \leq 0.0099$ , where T is natural vibration period of system.

For the iteration matrix of linear acceleration method, let  $r = \omega h$ ,  $\beta = 1 + \frac{1}{6}r^2$ , the iteration matrix can be obtained by using similar manner above,

$$[v_{i+1} \quad \dot{v}_{i+1} \quad \ddot{v}_{i+1}]^T = K [v_i \quad \dot{v}_i \quad \ddot{v}_i]^T + \frac{1}{6m\beta} p_{i+1} [h^2 \quad 3h \quad 6]^T \tag{18}$$

where

$$K = \begin{bmatrix} \frac{6}{6\beta} & \frac{6}{6\beta}h & \frac{2}{6\beta}h^2 \\ -\frac{r^2}{2\beta} \frac{1}{h} & \frac{2-\frac{2}{3}r^2}{2\beta} & \frac{1-\frac{1}{6}r^2}{2\beta}h \\ -\frac{r^2}{\beta} \frac{1}{h^2} & -\frac{r^2}{\beta} \frac{1}{h} & \frac{-\frac{1}{3}r^2}{\beta} \end{bmatrix}$$

For the quadratic acceleration method, let  $r = \omega h, \beta = 1 + \frac{1}{4}r^2 + \frac{1}{18}r^4$ , the iteration matrix can be obtained by using similar manner above,

$$[v_{i+1} \ \dot{v}_{i+1} \ \ddot{v}_{i+1}]^T = G[v_i \ \dot{v}_i \ \ddot{v}_i]^T + \begin{bmatrix} \frac{(6+\frac{4}{3}r^2)p_{i+1}-p_{i+2}}{24m(1+\frac{1}{4}r^2+\frac{1}{18}r^4)}h^2 & \frac{(4+\frac{2}{3}r^2)p_{i+1}+(\frac{-1}{2}+\frac{1}{24}r^2)p_{i+2}}{6m(1+\frac{1}{4}r^2+\frac{1}{18}r^4)}h & \frac{2p_{i+1}+(2+\frac{1}{4}r^2)p_{i+2}}{2m(1+\frac{1}{4}r^2+\frac{1}{18}r^4)} \end{bmatrix}^T \tag{19}$$

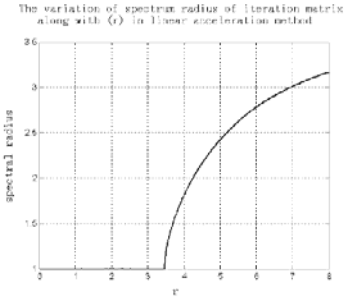
$$[v_{i+2} \ \dot{v}_{i+2} \ \ddot{v}_{i+2}]^T = H[v_{i+1} \ \dot{v}_{i+1} \ \ddot{v}_{i+1}]^T + \begin{bmatrix} \frac{4p_{i+1}-\frac{1}{6}p_{i+2}}{3m(1+\frac{1}{4}r^2+\frac{1}{18}r^4)}h^2 & \frac{(4-\frac{4}{3}r^2)p_{i+1}+(1+\frac{5}{12}r^2)p_{i+2}}{3m(1+\frac{1}{4}r^2+\frac{1}{18}r^4)}h & \frac{\frac{4}{3}p_{i+1}+(1+\frac{1}{4}r^2)p_{i+2}}{m(1+\frac{1}{4}r^2+\frac{1}{18}r^4)} \end{bmatrix}^T \tag{20}$$

where

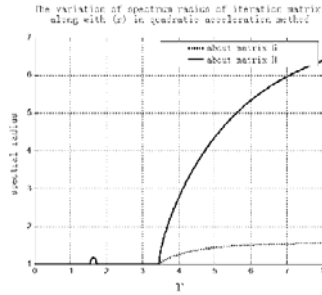
$$G = \begin{bmatrix} \frac{24+r^2}{24\beta} & \frac{24+2r^2}{24\beta}h & \frac{7+\frac{2}{3}r^2}{24\beta}h^2 \\ -\frac{7}{2}r^2-\frac{17}{24}r^4 & \frac{6-\frac{3}{2}r^2-\frac{5}{12}r^4}{6\beta} & \frac{5-\frac{5}{24}r^2-\frac{1}{12}r^4}{6\beta}h \\ -\frac{2r^2-\frac{1}{12}r^4}{2\beta} & \frac{-2r^2-\frac{1}{6}r^4}{2\beta} \frac{1}{h} & \frac{-\frac{7}{12}r^2-\frac{1}{18}r^4}{2\beta} \end{bmatrix}$$

$$H = \begin{bmatrix} \frac{3-\frac{13}{4}r^2}{3\beta} & \frac{6-\frac{5}{2}r^2}{3\beta}h & \frac{2-\frac{2}{3}r^2}{3\beta}h^2 \\ -\frac{4r^2+\frac{11}{12}r^4}{3\beta} \frac{1}{h} & \frac{3-\frac{21}{4}r^2+\frac{2}{3}r^4}{3\beta} & \frac{1-\frac{19}{12}r^2+\frac{1}{6}r^4}{3\beta}h \\ -\frac{r^2+\frac{13}{12}r^4}{\beta} \frac{1}{h^2} & \frac{-2r^2+\frac{5}{6}r^4}{\beta} \frac{1}{h} & \frac{-\frac{2}{3}r^2+\frac{2}{9}r^4}{\beta} \end{bmatrix}$$

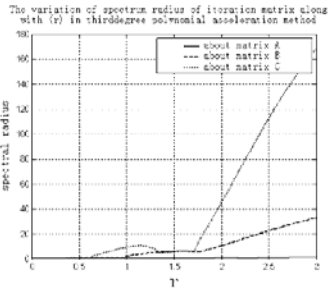
Through numerical analysis, the stabilization fields of linear and quadratic acceleration method are shown in Figures 2(a) and 2(b), which shows the variation of spectral radius of the two polynomial acceleration methods along with  $r$ . Stabilization field of the three different-ordered polynomial acceleration methods are listed in Table 1 numerically.



(a) Linear acceleration method



(b) Quadratic polynomial acceleration method



(c) Third-degree polynomial acceleration method

Figure 2. The variation of spectrum radius along with  $r$

Table 1. Stabilization field of three different acceleration methods

method	Linear polynomial acceleration method	quadratic polynomial acceleration method	Third-degree polynomial acceleration method
Stability field	$\omega h \leq 3.46$	$\omega h \leq 1.54$	$\omega h \leq 0.062$

The results shown in Table 1 shows that as higher ordered polynomial used, the stability filed of algorithm decreased, from  $\omega h \leq 3.46$  in linear acceleration method to  $\omega h \leq 1.54$  in quadratic acceleration method. When third-degree polynomial acceleration is used, the stabilization field narrow down rapidly to be  $\omega h \leq 0.062$ . That

is to say, with higher order polynomial is used, the stabilization filed of the algorithm becomes narrow.

### 4 Numerical Example

A single degree of freedom is shown in Figure 3. The mass weighing 1kg is excited by an external force  $p(t)$ , where  $p(t)=\sin(0.5t)N$  ( $t\leq 60s$ ), the spring stiffness  $k$  is 1N/m and damp coefficient  $c$  is 0.1N·s/m. The initial condition of motion of mass is:  $v_0 = \dot{v}_0 = 0$ .

When taking different time step, the solution results obtained from three different polynomial acceleration methods compared with accurate theory solution result are shown in Figure 4 respectively.

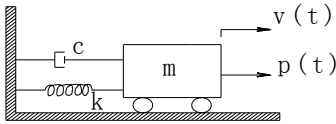
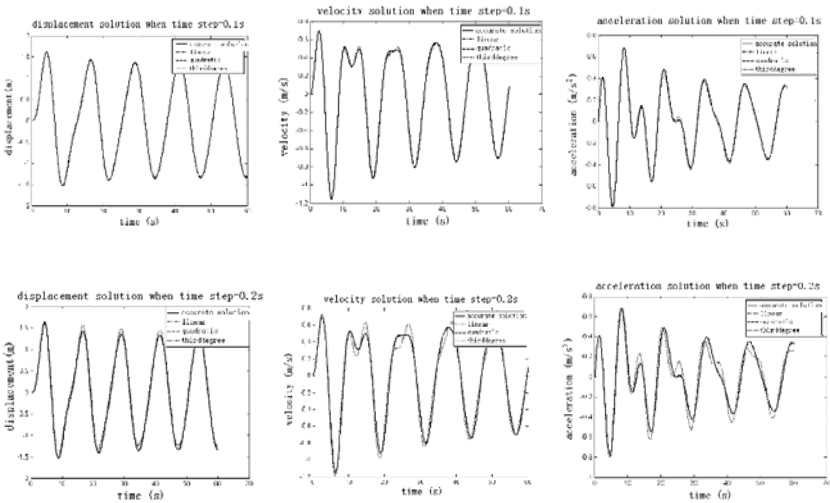


Figure 3. Ideal system of single degree of freedom



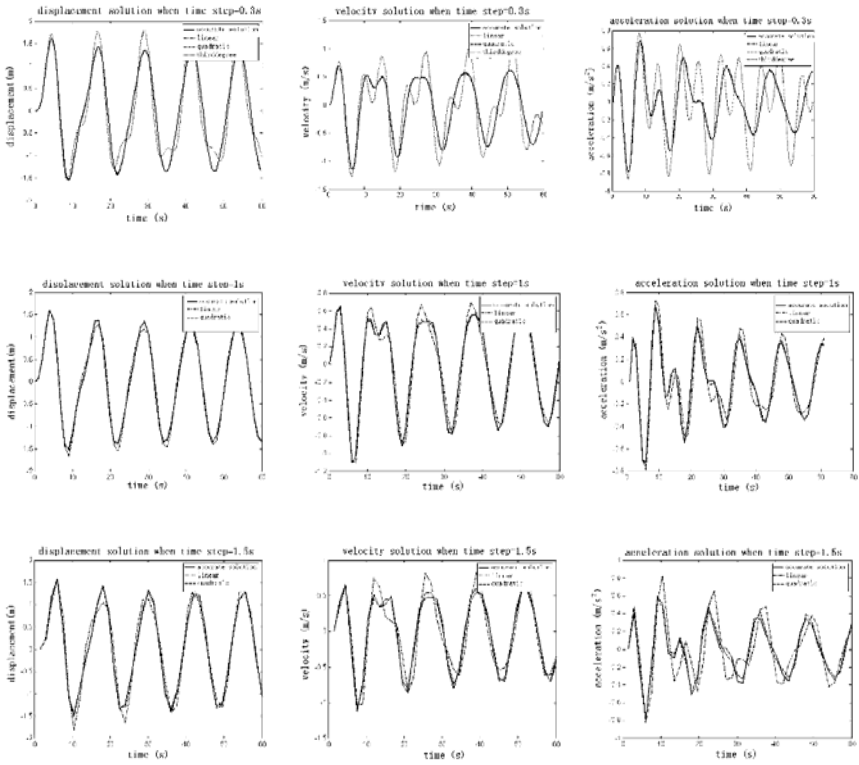


Figure 4. Solution results of time history analysis

In last two rows in Figure 4, only solution of linear and quadratic acceleration method compared with theory solution are shown when time step is taken as 1s and 1.5s. The reason is that when the time step  $h$  equal to 1s and 1.5s, the calculation error of third-degree polynomial acceleration method is too big to show the solution results of linear and quadratic acceleration method, as shown in Figure 5.

The other solution results that are not listed in this paper also show that when time step  $h=0.06s$  all the solution results fit theory solution very well because  $h$  is small and is within the three different methods' stability field. When time step equal to 0.1s, which is outside the stabilization field of third-degree polynomial acceleration method, the spectral radius of algorithm is 1.0003 and the transferred error magnification factor at 600th time point is 1.2 (see Table 2), and by virtue of the algorithm's high converging accuracy one the other side, the solution results still fit the theory solution well. However, When  $h=0.2s$ , the error magnification factor being 5.0 (Table 2) at 300th time point leads to the apparent deviation of solution results from accurate theory solution. When  $h=0.3s$  the enormous error occurred leads to the complete failure of third-degree polynomial acceleration

method. It can be seen that the size of time step in third-degree polynomial acceleration method is controlled by its stabilization field.

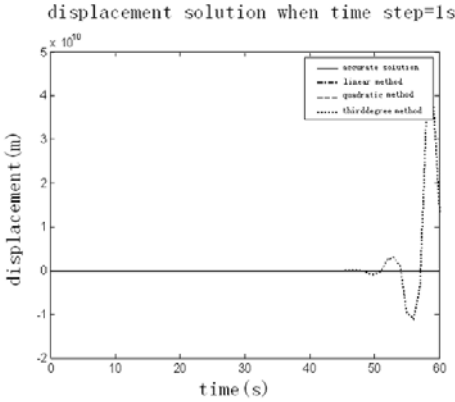


Figure 5. Displacement solution of time history (time step=1 sec)

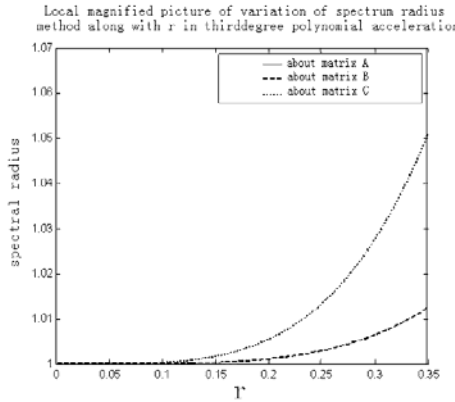


Figure 6. Local magnification of variation of spectrum radius of third-degree polynomial acceleration method along with  $r$

When  $h=0.1s, 0.2s, 0.3s$ , the solution results agree with theory solution well for linear and quadratic acceleration method. Because of its low converging efficiency, obvious error occurs in linear acceleration method despite of its wide stabilization field ( $\omega h=1 \leq 3.46$ ) when  $h=1s$ . For quadratic acceleration method, the solution results fit the ideal solution well even when  $h=1.5s$  due to its wide stabilization field ( $\omega h=1.5 \leq 1.54$ ) and its higher converging accuracy than the linear acceleration methods.

Table 2. Error magnification in third-degree polynomial acceleration method

Time step	Step number	Spectral radius	Error magnification factor =spectral radius <sup>(step number)</sup>
0.1	600	1.0003	1.2
0.2	300	1.0054	5.0
0.3	200	1.0275	227

## 5 Conclusions

To get correct results and to guarantee high efficiency of the solution of the equation of motion, advisable maximum time step size in low-ordered polynomial acceleration method such as linear acceleration method is controlled by algorithm’s converging accuracy rather than the algorithm’s stability field. But the conclusion is reverse in high-ordered polynomial acceleration method. For example, in third-degree polynomial acceleration method, advisable maximum time step is controlled by algorithm’s narrow stability field rather than its high converging accuracy. Only from the point of high converging accuracy, maximum time step size in third-degree polynomial acceleration method can be taken wider than the lower-ordered polynomial acceleration method, but as its stability field narrows rapidly to  $\omega h \leq 0.062$ , the maximum value of  $h$  is much smaller than that used in lower-ordered polynomial acceleration method. It is impressive that quadratic acceleration method gives attention to both stabilization field and converging accuracy at the same time and to obtain a maximum acceptable time step, where  $h$  can be 1.5s in this paper’s numerical model computation.

As a conclusion, it is not advisable to use algorithm with too high converging accuracy in time history analysis since its stabilization field becomes too small. Converging accuracy and stability field taken into consideration, quadratic acceleration method is superior to linear and third-degree polynomial acceleration method.

## References

Clough R., Penzien J. (1993). *Dynamics of Structures*. New York: McGraw-Hill.  
 Li C.Q., Lou M.L. (2008). Analysis of the stabilization field of linear acceleration method in time history. *Protective Engineering*, 30(2):35-38 [in Chinese].  
 Li Q.Y. et al. (2001). *Numerical Analysis*. Beijing: Tsinghua University Press.

# An Effective Approach for Vibration Analysis of Beam with Arbitrary Sections

Shuang Li<sup>1</sup>, Changhai Zhai<sup>1\*</sup>, Hongbo Liu<sup>1,3</sup> and Lili Xie<sup>1,2</sup>

<sup>1</sup>School of Civil Engineering, Harbin Institute of Technology, Harbin 150090, P.R. China

<sup>2</sup>Institute of Engineering Mechanics, China Earthquake Administration, Harbin 150080, P.R. China

<sup>3</sup>School of Civil Engineering and Architecture, Heilongjiang University, Harbin 150080, P.R. China

**Abstract.** An approach to analyze vibration of beam with arbitrary sections is presented. This element formulation employs element equilibrium relationship to obtain an accurate representation to internal forces of a beam. The stiffness matrix and mass matrix are derived for the proposed beam element. Verification example demonstrates the accuracy of this formulation and its ability to vibration analysis of beams.

**Keywords:** beam element, vibration analysis, arbitrary section, mass matrix

## 1 Introduction

The needs to predict the accurate response of structures have been the main motivation behind the development of new analytical methods in the recent years. Beam elements are an economical and accurate solution for the dynamic response analysis of structures. A wide variety of approaches have been proposed in literature for the derivation of finite element models for beams. One of the popular methods, called stiffness-based method, has been used in derivation of the beam element with polynomial interpolation functions based on assumed displaced shapes in element (Bathe 1996; Wang 2003). The method often utilizes linear functions and three-order polynomials for axial and flexural displacement, respectively, which present exact solution for a prismatic beam member with uniform elastic material properties. However, these assumed displaced shapes lead to a limitation of constant axial strain and linear curvature along the element. Higher-order polynomial interpolation functions or several elements in per beam member are often employed to overcome the limitation. There are cases of beams with arbitrary sec-

---

\* Corresponding author, e-mail: zch-hit@hit.edu.cn

tions. In these cases, poor results are obtained with beam elements derived by stiffness-based method. Starting from an alternative point of view, in several works (Spacone et al. 1996; Petrangeli and Ciampi 1997), beam elements are derived by approach which interpolates internal force fields along the elements. Although there are differences in formulations of derivation of the beam elements, the same foundation of the elements is that firstly guaranteed the equilibrium relationship between element nodal forces and section forces. The better performances of these elements have been demonstrated in researches (Neuenhofer and Filippou 1997; Huang and Chen 2003) in the presence of material nonlinearity. Parallel researches, geometrically nonlinear problem have been studied (Neuenhofer and Filippou 1998; De Souza 2000; Chen and Huang 2005), which illustrated that more accurate of these elements than traditional three-order beam elements can be achieved.

The aim of this paper is to develop a general-purpose beam element model. This beam element, which is one of the element models using interpolation internal force fields along the element, can be employed to model generic beam members and beam members with arbitrary sections. Numerical example is presented to assess the performance of the proposed element.

## 2 Beam Formulations

### 2.1 Stiffness Matrix

The plane beam element model is based on the theory of Euler-Bernoulli beam. The beam element formulation consists of interpolation of generalized nodal forces with the element equilibrium relationship, as shown in Figure 1. The  $ox(I \rightarrow J)$ ,  $\mathbf{Q} = [Q_1 \ Q_2 \ Q_3]^T$  are the axis parallel to geometric centroids of sections at nodes I and J, generalized nodal forces, respectively. The section forces are defined by generalized nodal forces and internal force interpolation functions. With the element equilibrium relationship, equilibrium is stated in the form

$$\mathbf{S}(x) = \mathbf{e}(x)\mathbf{Q} \tag{1}$$

in which  $\mathbf{S}(x) = [N(x) \ M(x)]^T$  is the section forces. The matrix  $\mathbf{e}(x)$  contains interpolation functions for the section forces in terms of generalized nodal forces

$$\mathbf{e}(x) = \begin{bmatrix} 1 & 0 & 0 \\ 0 & \frac{x-L}{L} & \frac{x}{L} \end{bmatrix} \tag{2}$$

in which  $L$  is the length of the element.

The matrix  $\mathbf{e}(x)$  is independent of the sectional area and the moment of inertia of the section. Comparing with traditional three-order beam elements, the discretization approach of equation (1) directly predefines element equilibrium relationship rather than compatible relationship.

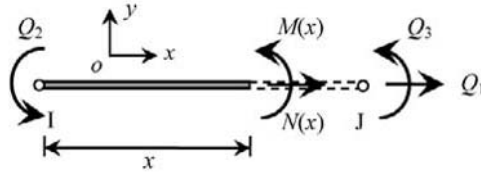


Figure 1. The beam in the generalized coordinate system: generalized nodal forces and section forces

The section deformations of the element are

$$\mathbf{d}(x) = [\varepsilon(x) \quad \kappa(x)]^T \tag{3a,b}$$

in which  $\varepsilon(x)$  is axial strain and  $\kappa(x)$  is the curvature respect to  $x$ .

According to the principle of virtual force and application of the boundary conditions of generalized beam system, the relationship between section deformations and generalized nodal deformations may be express as

$$\mathbf{D} = \int_0^L \mathbf{e}(x)^T \mathbf{d}(x) dx \tag{4}$$

in which  $\mathbf{D} = [D_1 \ D_2 \ D_3]^T$  are generalized nodal deformations.

The element flexibility matrix  $\mathbf{F}$  in generalized coordinate system is then obtained by the usual formula that differentiation of  $\mathbf{D}$  with respect to  $\mathbf{Q}$ . Then, the stiffness matrix is

$$\mathbf{K} = \mathbf{F}^{-1} = \left( \frac{\partial \mathbf{D}}{\partial \mathbf{Q}} \right)^{-1} \tag{5}$$

It is worth to note that the sectional area and the moment of inertia of the section are variables and the  $\mathbf{K}$  is accurate if the error of numerical integration is neglected. The stiffness matrix in generalized coordinate system is transformed to global coordinate system and then assembled to global matrix.

### 2.2 Mass Matrix

The boundary conditions in generalized coordinate system are same as those in a simple supported beam. The transverse deformation  $u(x)$  and axis deformation

$v(x)$  respect to  $x$  can be obtained by unit force method. The expressions of these are given by

$$u(x) = \int_0^L \frac{\bar{N}(x_0, x)N(x_0)}{EA(x_0)} dx_0, \quad v(x) = \int_0^L \frac{\bar{M}(x_0, x)M(x_0)}{EI(x_0)} dx_0 \tag{6a,b}$$

in which  $N(x_0)$  and  $M(x_0)$  are section axial force and moment respect to  $x_0$ . And

$$\bar{N}(x_0, x) = H(x - x_0) \tag{7a}$$

$$\bar{M}(x_0, x) = \left(-1 + \frac{x}{L}\right)x_0 H(x - x_0) + \left(-1 + \frac{x_0}{L}\right)x H(-x + x_0) \tag{7b}$$

where  $H(\cdot)$  is the Heaviside function.

Replacing  $\mathbf{Q}$  with  $\mathbf{K} \cdot \mathbf{D}$  and considering the equations (1) and (6), yields the following relationships

$$u(x) = \left[ \int_0^L \frac{\bar{N}(x_0, x)\mathbf{e}_1(x_0)}{EA(x_0)} dx_0 \mathbf{K} \right] \mathbf{D}, \quad v(x) = \left[ \int_0^L \frac{\bar{M}(x_0, x)\mathbf{e}_2(x_0)}{EI(x_0)} dx_0 \mathbf{K} \right] \mathbf{D} \tag{8a,b}$$

in which  $\mathbf{e}_1(x_0)$  and  $\mathbf{e}_2(x_0)$  are the first and second row of equation (2), respectively.

Transforming the equation (8) to local element coordinate system, leads to

$$u^e(x) = \left[ \int_0^L \frac{\bar{N}(x_0, x)\mathbf{e}_1(x_0)}{EA(x_0)} dx_0 \mathbf{K} \cdot \mathbf{T}(0) \right] \mathbf{D}^e + D_1^e \tag{9a}$$

$$v^e(x) = \left[ \int_0^L \frac{\bar{M}(x_0, x)\mathbf{e}_2(x_0)}{EI(x_0)} dx_0 \mathbf{K} \cdot \mathbf{T}(0) \right] \mathbf{D}^e + \frac{D_5^e - D_2^e}{L} x + D_2^e \tag{9b}$$

in which  $\mathbf{D}^e = [D_1^e \ D_2^e \ D_3^e \ D_4^e \ D_5^e \ D_6^e]^T$  is nodal displacements in local element coordinate system, where  $D_i^e$  are axis, transverse and rotation displacements at nodes I and J.

The equation (9) can be rewritten in the following form

$$u^e(x) = N_1 D_1^e + N_4 D_4^e, \quad v^e(x) = N_2 D_2^e + N_3 D_3^e + N_5 D_5^e + N_6 D_6^e \tag{10a,b}$$

in which

$$N_1 = 1 - \gamma_1 \mathbf{K}(1,1), N_2 = 1 - \frac{x}{L} + \gamma_2 [\mathbf{K}(2,2) + \mathbf{K}(2,3)] + \gamma_3 [\mathbf{K}(3,2) + \mathbf{K}(3,3)]$$

$$N_3 = \gamma_2 \mathbf{K}(2,2) + \gamma_3 \mathbf{K}(3,2), N_4 = 1 - N_1, N_5 = 1 - N_2, N_6 = \gamma_2 \mathbf{K}(2,3) + \gamma_3 \mathbf{K}(3,3)$$

$$\gamma_1 = \int_0^L \frac{H(x-x_0)}{EA(x_0)} dx_0$$

$$\gamma_2 = \int_0^L \frac{\left(1 - \frac{x_0}{L}\right) \left[ \frac{x_0}{L} \left(1 - \frac{x}{L}\right) H(x-x_0) + \frac{x}{L} \left(1 - \frac{x_0}{L}\right) H(-x+x_0) \right]}{EI(x_0)} dx_0$$

$$\gamma_3 = \int_0^L \frac{-\frac{x_0}{L} \left[ \frac{x_0}{L} \left(1 - \frac{x}{L}\right) H(x-x_0) + \frac{x}{L} \left(1 - \frac{x_0}{L}\right) H(-x+x_0) \right]}{EI(x_0)} dx_0$$

It can be seen that  $N_1 \sim N_6$  are similar as the element polynomial displacement interpolation functions in three-order beam elements. Thus, the element mass matrix in local element coordinate system is given by the usual formulation

$$\mathbf{M} = \int_0^L \rho(x) A(x) \mathbf{N} \mathbf{N}^T dx \tag{11}$$

in which  $\rho(x)$  is the material density. The matrix  $\mathbf{N}$  is the interpolation function matrix which can be readily found in many references including Wang (2003).

Because the  $\mathbf{N}$  matrix is dependent with  $A(x_0)$  and  $I(x_0)$ , the element mass matrix proposed in this paper is suitable for beam with arbitrary sections. The  $\mathbf{M}$  matrix is then transformed from local element coordinate system to global coordinate systems.

### 3 An Example

The example is a vertical cantilever column shown in Figure 2. The section width  $b = 0.5\text{m}$  and section height varies as  $h(y) = h_0 - 2y/25$ , where  $h_0 = 1\text{m}$  is the section height at the fixed end. The material modulus  $E = 2.1 \times 10^8 \text{ kN/m}^2$ . The mass density  $\rho$  is  $7.8 \times 10^3 \text{ kg/m}^3$ . Figure 3 shows the first model frequency. The result of

three-order beam element with variable section is also presented for comparison. It can be seen that several three-order beam elements with variable section are required to achieve comparable accuracy with the presented element.

### 4 Conclusions

In this study, formulations based on element equilibrium relationship for vibration analysis of beam with arbitrary sections are derived. Detailed forms of element stiffness matrix and mass matrix, which are accurate for beam with arbitrary sections if the error of numerical integration is neglected, are presented. The approach shows higher accuracy in vibration analysis of beams than the traditional three-order beam element

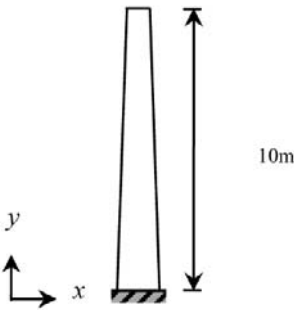


Figure 2. Cantilever column

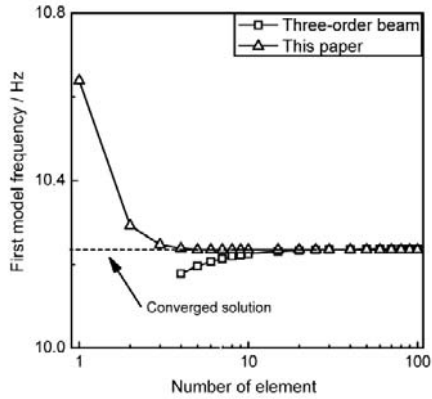


Figure 3. Comparison of the natural frequency of vibration

### Acknowledgments

The writers acknowledge the financial supports provided by the National Natural Science Foundation of China (Grant No. 50538050, 90815014 and 90715021).

### References

Bathe K.J. (1996). *Finite element procedures*. New Jersey: Prentice-Hall.

- Chen Tao, Huang Zong-Ming (2005). Comparison between flexibility-based and stiffness-based geometrically nonlinear beam-column elements. *Engineering Mechanics* 22(3): 31-38 [in Chinese].
- De Souza R.M. (2000). Force-based finite element for large displacement inelastic analysis of frames. PhD Dissertation, California: University of California, Berkeley.
- Huang Zong-Ming, Chen Tao (2003). Comparison between flexibility-based and stiffness-based nonlinear beam-column elements. *Engineering Mechanics*, 20(5): 24-31 [in Chinese].
- Neuenhofer A., Filippou F.C. (1997). Evaluation of nonlinear frame finite-element models. *Journal of Structural Engineering*, 123(7): 958-966.
- Neuenhofer A., Filippou F.C. (1998). Geometrically nonlinear flexibility-based frame finite element. *Journal of Structural Engineering*, 124(6): 704-710.
- Petrangeli M., Ciampi V. (1997). Equilibrium based iterative solutions for the non-linear beam problem. *International Journal for Numerical Methods in Engineering*, 40(3): 423-437.
- Spacone E., Filippou F.C., Taucer F.F. (1996). Fiber beam-column model for non-linear analysis of R/C frames: Part I. Formulation. *Earthquake Engineering and Structural Dynamics*, 25(7): 711-725.
- Wang Xu-Cheng (2003). *Finite element method*. Beijing: Tsinghua University Press [in Chinese].

*“This page left intentionally blank.”*

# Analyses on Vortex-Induced Vibration with Consideration of Streamwise Degree of Freedom

Changjiang He<sup>1\*</sup>, Zhongdong Duan<sup>1</sup> and Jinping Ou<sup>1</sup>

<sup>1</sup>School of Civil Engineering, Harbin Institute of Technology, Harbin 150090, China

**Abstract.** By applying overlapping mesh, this work simulated vortex-induced vibrations (VIV) of low-mass-damping cylinder. Because of no need to re-mesh on the whole computational domain, but to find donors for nodes on the boundary of sub-domain, time and CPU resources were saved dramatically. We found that the transverse amplitudes increased by approximately 30% in the resonance area when took streamwise degree of freedom into account. But the transverse amplitudes had no change outside of the resonance area. In the range  $m^* = 1.0 \sim 40$ , the ratios of streamwise amplitudes to those of transverse increased as  $m^*$  decreased, especially as  $m^* < 2.6$ , the ratios would be greater than around 10%; moreover, the phase angles between streamwise displacements and transverse displacements descended as  $m^*$  ascended.

**Keywords:** vortex-induced vibration, streamwise degree of freedom, transverse vibration, overlapping grid, phase angle, numerical simulation

## 1 Introduction

Vortex-induced vibrations (VIV) are much concerned issues in many engineering fields. In ocean engineering, riser is typical “VIV-body” (Sarpkaya, 2004). Generally, this kind of cylindrical structure has the same mass-ratios ( $m^*$ , of order 1 or 10) and natural frequencies at streamwise and transverse directions. However, almost of the researches has been focused on structures restricted to vibrations only transverse to a free stream, these works were reviewed by Sarpkaya (2004), Williamson and Govardhan (2004), Gabbai and Benaroya (2005).

There are few researches concerned about VIV at two directions (streamwise,  $X$  and transverse,  $Y$ ). Jong and Vandiver (1985), Vandiver and Jong (1987) find that motions at  $X$  and  $Y$  directions have strong quadratic relationship. In the case of Sarpkaya (1995), dimensionless amplitudes ( $A^* = A/D$ ) and lock-in range (ac-

---

\* Corresponding author, e-mail:changjianghe@yahoo.cn

counted as  $f_{st}/f_{ex}$ ,  $f_{st}$  = Strouhal frequency,  $f_{ex}$  = excitation or vibration frequency) increased by 20% when  $X$  direction concerned. Experiment ( $Re = 3 \times 10^4$ ,  $m^* = 3.0$ ,  $\zeta = 0.035$ ) done by Triantfyllou (2003) shows that no jumps happening, but the peak amplitude ( $A^* \approx 1.5$ ) is larger than that of  $Y$ -only case ( $A^* \approx 1.0$ ), and the location of reduced velocity where peak amplitude occurs is postponed ( $V_r \approx 7 > V_r \approx 5.6$ ). At the same time, in  $XY$  motion, peak amplitude ( $A^* \approx 0.5$ ) at  $X$  direction appearing as  $V_r \approx 5.5$ , ahead of that at  $Y$  direction.

Jauvtis and Williamson (2003; 2004a, b) states that in moderate case ( $m^* > 6.0$ ), the streamwise freedom, as well as transverse, hardly changes the dynamics of elastically mounted cylinders. However, for very small mass ratios ( $m^* < 6.0$ ), there exists a ‘super-upper’ branch of response, that is huge amplitudes of vibration, whereby the vortex wake is so-called ‘2T’. This is a dramatic departure from  $Y$ -only cases.

This paper applied numerical simulations on two-direction VIV, comparisons with Jauvtis and Williamson (2004a, b) and analyses were taken.

## 2 Computational Model

For 2-dimensional case, assume a rigid cylinder was mounted elastically at two directions, as **Error! Reference source not found.a)** shows. The traditional treatment of dynamic mesh is to generate new mesh on the whole computational domain at each time step, which wastes a large amount of CPU time, and spreads computational errors due to dissatisfaction of mesh-movement-conservation on the whole domain.

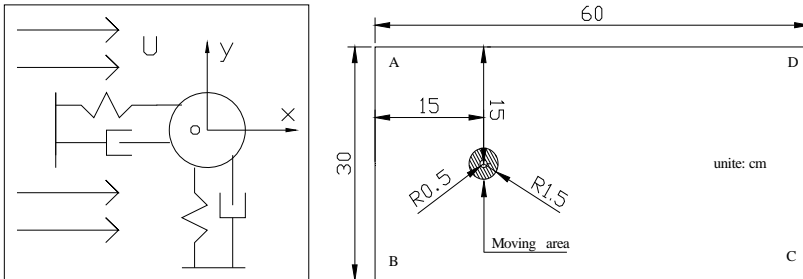
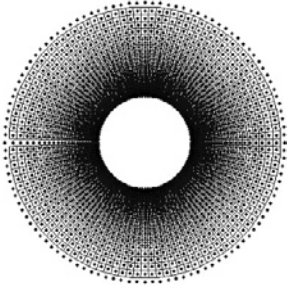


Figure 1. (a) Schematic diagram

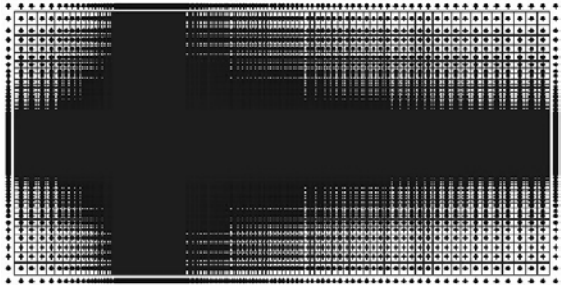
(b) Computational domain and overlapping part

This paper applied overlapping mesh and the total domain was split into two parts, as **Error! Reference source not found.b** shows: 1) an area of proper size around the cylinder was generated (Figure 1a), the mesh in this area would move simultaneously with cylinder, while the other mounted; 2) donor volumes of boundary nodes of moving mesh were found on the background mesh (covering

the whole computational domain, Figure 1b), then interpolations between boundary nodes and their donor volumes were taken to make sure information communicate between the two areas. In Figure 1, star point stands for node and small rectangle stands for finite control volume. The convergence number of the total mesh is 26258 (22755+3503), and the radial size of the first layer of mesh is 0.008D.



(a) the moving domain



(b) the background domain

Figure 1. Computational mesh

### 3 Control Functions

#### 3.1 CFD Functions

According to Arbitrary Lagrangian-Eulerian (ALE) method, the general control function of fluid on a volume  $V$  (with boundary  $\partial V$ ) with velocity  $\mathbf{u}_g$  reads

$$\frac{d}{dt} \int_V \phi dV + \int_{\partial V} \phi (\mathbf{u} - \mathbf{u}_g) \cdot \mathbf{n} dA = \int_{\partial V} v \nabla \phi \cdot \mathbf{n} dA + \int_V s_\phi dV \tag{1}$$

where  $\phi$  is general variable, here it is component of Eulerian velocity  $\mathbf{u}$ ,  $u$  or  $v$ ;  $s_\phi$  is material source term.

#### 3.2 Structural Control Function

The fluid stress tensor reads

$$\boldsymbol{\sigma} = p\mathbf{I} + 2\mu\boldsymbol{\varepsilon}(\mathbf{u}), \quad \boldsymbol{\varepsilon}(\mathbf{u}) = \frac{1}{2}\left((\nabla\mathbf{u}) + (\nabla\mathbf{u})^T\right) \tag{2}$$

where  $p$  is fluid pressure,  $\mu$  is dynamic viscosity. Define fluid load coefficients

$$C_D = \frac{1}{\frac{1}{2}\rho_f U^2 D} \int_{\Gamma_{\text{wall}}} \boldsymbol{\sigma} \cdot \mathbf{n}_x \, d\Gamma, \quad C_L = \frac{1}{\frac{1}{2}\rho_f U^2 D} \int_{\Gamma_{\text{wall}}} \boldsymbol{\sigma} \cdot \mathbf{n}_y \, d\Gamma \tag{3}$$

In which  $\mathbf{n} = (n_x, n_y)$  is the outer unite normal vector of cylinder surface  $\Gamma_{\text{wall}}$ .

Dynamic functions of cylinder under the action of fluid are

$$m \frac{\partial^2 x}{\partial t^2} + c \frac{\partial x}{\partial t} + kx = \frac{1}{2} \rho_f D U^2 C_D, \quad m \frac{\partial^2 y}{\partial t^2} + c \frac{\partial y}{\partial t} + ky = \frac{1}{2} \rho_f D U^2 C_L \tag{4}$$

where  $m$ ,  $c$  and  $k$  are structural mass, damping and stiffness respectively,  $D$  is diameter of cylinder.

### 4 Results and Analyses

Results at  $m^* = 6.9$  were firstly given. In all computations,  $\zeta = 0.15\%$ ,  $f_N = 2.0$ , which consulted to corresponding parameters in the case of Jauvtis and Williamson (J&W, 2003). As shown in Figure 2, they get three-branch responses whether streamwise degree of freedom (DOF) was constricted or not. However, huge amplitudes didn't appear. When streamwise DOF was constrained, present data match J&W well in upper branch, peak value  $A_Y = 0.83$ . When streamwise DOF was allowed, peak amplitude  $A_Y = 1.24$ , increased by 37%, the corresponding reduced velocity value  $V_r \approx 6.7$ . But amplitudes were almost the same out of the lock-in range.

In most range of reduced velocities, streamwise peak amplitudes collapsed that of Jauvtis and Williamson (2004b) well except around  $V_r \approx 3.0$ , where they get 'large' peak values which are of the same order with corresponding transverse amplitudes.

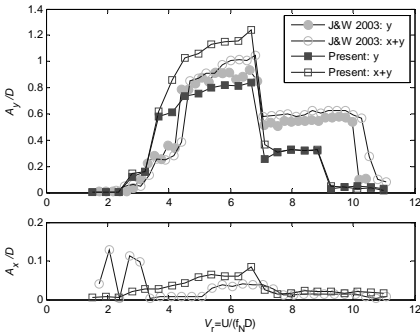


Figure 2. Amplitudes as  $m^* = 6.9$

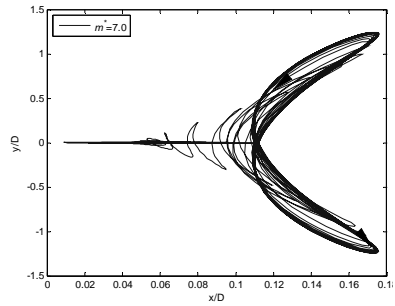


Figure 3. XY trajectory as  $V_r = 6.7$

The  $XY$  trajectory at  $V_r \approx 6.7$  was plotted in Figure 3. According to the schematic plot in Jauvtis and Williamson (2004b), phase angle between  $X$ - and  $Y$ -displacements was in the range  $270^\circ \sim 315^\circ$ .

Table 1. Amplitudes of each case as  $V_r \approx 6.7$

$m^*$	1.0	2.6	6.9	12.8	29.0	40.0
$A_y$ only/D	0.94	0.86	0.83	0.81	0.78	0.34
$A_x$ /D	0.48	0.11	0.06	0.03	0.012	0.01
$A_y$ /D	1.37	1.29	1.24	1.17	1.004	0.48
$A_y$ only/ $A_y$	68.61%	66.67%	66.73%	69.23%	68.76%	70.83%
$A_x$ / $A_y$	34.66%	8.81%	5.02%	2.73%	1.23%	2.08%

In order to observe the change of phase angles between  $X$ - and  $Y$ -displacements, several cases were calculated at  $V_r \approx 6.7$ , and  $m^* = 1.0 \sim 40.0$ . As shown in Table 1. Peak amplitudes decreasing as  $m^*$  increasing, which may be self-evident. And we found that the ratios of  $X$ - to  $Y$ -displacements lessening as  $m^*$  largening in two-direction motions, while ratios of transverse displacements in  $Y$ -only motions to those in corresponding  $XY$  motions maintained around 70%, that is to say,  $Y$ -displacements increased by 30% when  $X$ -DOF was allowed.

As shown in Figure 4, phase angles between  $X$ - and  $Y$ -displacements decreased as  $m^*$  increased in the range of  $1.0 \sim 40$ . Jauvtis and Williamson (2004a, b) find a super-upper branch of responses and a corresponding new vortex wake mode ‘2T’ firstly in two-direction experiments at  $m^* = 2.6$ , but the present results shown ‘2P’ mode (as shown in Figure 5).

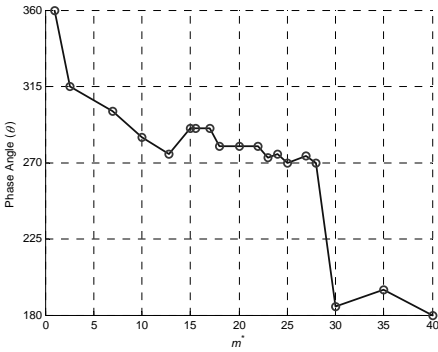


Figure 4.

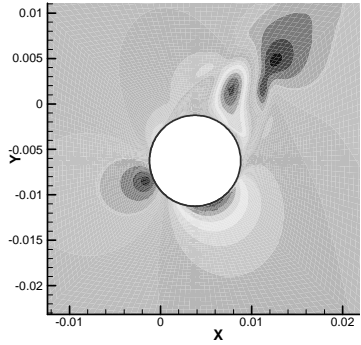


Figure 5. “2P” mode of wake flow

## 5 Conclusion

In conclusion, the analyses and discussions above educed

1. In lock-in range, the ratios of  $Y$ -only displacements to that of  $XY$  motions maintained about 70%, but remained almost the same out the range.
2. As  $m^*$  descended, the ratios of streamwise amplitudes to that at transverse direction ascended. Especially as  $m^*$  was less than about 2.6, this ratio would be larger than 10%.
3. Phase angles between  $X$ - and  $Y$ - displacements decreased as  $m^*$  increased.
4. As  $m^*$  was smaller than around 2.6, rather than ‘2T’ vortex wake mode, ‘2P’ mode corresponding to ‘super-upper’ branch of responses was found in this work.

## Acknowledgement

The authors gratefully acknowledge the support from National Natural Science Foundation of China (NSFC, No. 50538050).

## Reference

Evangelinos C, Lucor D and Karniadakis G E (2000). DNS-derived force distribution on flexible cylinders subject to VIV. *Journal of Fluids and Structures*, 14: 429-440.  
 Gabbai R D, Benaroya H (2005). An overview of modeling and experiments of vortex-induced vibration of circular cylinders. *Journal of Sound and Vibration*, 282: 575-616.

- Jauvtis N, Williamson C H K (2004a). A high-amplitude 2T mode of vortex -induced vibration for a light body in XY motion. *European Journal of Mechanics B/Fluids*, 23: 107-114.
- Jauvtis N, Williamson C H K (2004b). The effects of two degrees of freedom on vortex-induced vibration. *Journal of Fluid Mechanics*, 509: 23-62.
- Jauvtis N, Williamson C H K (2003). Vortex-induced vibrations of a cylinder with two degrees of freedom. *Journal of Fluids and Structures*, 17: 1035-1042.
- Sarpkaya T (2004). A critical review of the intrinsic nature of vortex-induced vibrations. *Journal of Fluids and Structures*, 19: 389-447.
- Williamson C H K and Govardhan R (2004). Vortex-induced vibrations. *Annual Review of Fluid Mechanics*, 36: 413-455.

*“This page left intentionally blank.”*

# Equivalent Static Loading for Ship-Collision Design of Bridges Based on Numerical Simulations

Junjie Wang<sup>1\*</sup> and Cheng Chen<sup>1</sup>

<sup>1</sup>Department of Bridge Engineering, Tongji University, 1239 Siping Road, Shanghai 200092, China

**Abstract.** The numerical simulation technology for structural impacts is used to develop the equivalent static loading for design of bridges against ship collisions. FEM models of five ships whose DWT vary from 3000T-50000T have been developed for numerical collision simulations using the software, LS-DYNA. Time histories for ship-rigid wall collisions are obtained and three kinds of equivalent static loading, the maximum collision force, the local average collision force and the global average collision force are defined. The relationship between the equivalent static loading and DWT, the collision velocity of a ship are established. Modification factors are introduced to consider the effects of geometry of a bridge foundation on the equivalent static loading.

**Keywords:** equivalent static loads, ship-bridge collision, numerical simulation, modification factors

## 1 Introduction

The design against vessel collisions for the bridges crossing these waterways is a core component of a design process. First of all, it is required that the lateral impact loads by vessels be quantified. According to most of the vessel-bridge collision scenarios, an errant vessel generally collided with a bridge by its bow. While elements of a bridge other than the piers may also be subjected to impact loads, most bridge collapses attributable to vessel collision occur as the result of impact load on a pier.

The loads on a bridge due to a vessel's collision are fundamentally dynamic in nature. The peak load generated and the rate of load oscillation during the impact are functions of the type, structural configuration, mass, and initial velocity of the

---

\* Corresponding author, e-mail: jjqxu@tongji.edu.cn

impacting vessel; the structural configuration and mass of the pier; and the soil conditions, etc.

Due to the complex nature of such dynamic events and the degree of scatter found in the loads generated (Knott 2000), bridge design specifications generally provide simplified procedures for deciding equivalent static loads as an alternative to conducting fully dynamic impact analyses.

The AASHTO's (the American Association of State Highway and Transportation Officials) bridge design specifications (AASHTO, 1991, 2004) provide procedures for estimating equivalent static loads for ship collision,

$$P = 0.122\sqrt{DWT} \cdot V \quad (1)$$

where  $P$  is the equivalent static loads for ship collision in  $MN$ ;  $V$  is ship impact velocity in  $m/s$ .

In the Part 2.7 of the Eurocode 1 (Henrik Gluwer, 1998), the design collision force is estimated as

$$P = V\sqrt{KM} \quad (2)$$

Where  $K$  is the equivalent stiffness and  $M$  is the impact mass.  $V=3m/s$ ,  $K=5MN/m$  for the inland waterways, and  $V=3m/s$  and  $K=15MN/m$  for sea going vessels.

In General Code for Design of Railway Bridges and Culverts (the Railway Ministry of China, 1999, TB10002.1-99), the design collision load is estimated as:

$$P = \gamma V \sqrt{\frac{W}{c_1 + c_2}} \sin \alpha \quad (3)$$

where  $\gamma$  is the reduction coefficient of kinetic energy in the unit of  $s/m^{1/2}$ ;  $\gamma=0.3$  for head-on bow collision, and  $\gamma=0.2$  for other collision cases;  $W$  is the weight of the vessel;  $c_1$  is elastic deformation coefficient of vessel;  $c_2$  is elastic deformation coefficient of collided bridge component. If there is no data to refer to, TB10002.1-99 specified  $c_1 + c_2 = 0.0005m/kN$ .

Although there are many other empirical formulas for the estimate of the design collision loading, the above three equations are widely used for the design of bridges in China.

## 2 Numerical Simulations of Ship-Bridge Collisions

The numerical simulation technology for structural impacts is now mature for practical applications. The estimate of impact contact force for ship-bridge colli-

sions may be obtained by the numerical simulation technology (Consolazio and Cowa, 2003; Wang, et al., 2005). FEM models of five ships, with *DWT* of 3,000, 5,000, 10,000 and 50,000, are developed using software LS-DYNA (Version970, 2003) in this paper.

Ship-bridge collision is a strong nonlinear process. The head part will undergo buckling and crashing. To obtain a reasonable simulation of ship-bridge collision, the head part of the ships should be modeled carefully, an example was shown in Figure 1 for a ship with *DWT* of 10,1000.

The elastic-plastic area of a ship is divided into three parts. For the first part, the size of mesh in is about 10cm; for the second part, the size of mesh is in the range of 10-15cm; and for the third part, the size of mesh is about 40cm. Rigid elements are used to model the rest part of a ship to reduce the time consumption in simulation computation.

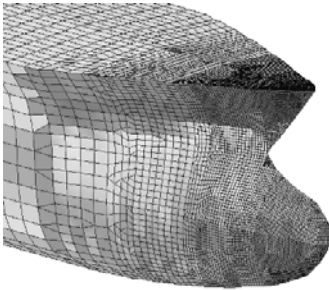


Figure 1 FEM models of a ship with *DWT* of 10,000 for collision simulations

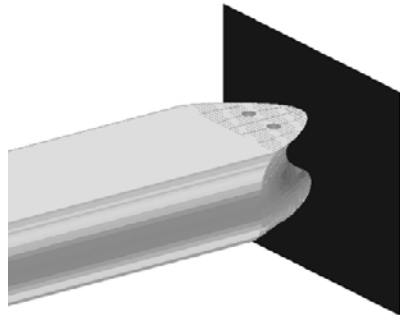


Figure 2 Model for ship-rigid wall collisions (head-on bow collision)

For the collision calculation, strain rate effect should be taken into account, and the Cowper-Symonds strain rate model (Jones, 1989) is used.

To develop the basic formulas for equivalent static loading, the dynamic processes for ship-rigid wall collisions have been computed, shown in Figure 2.

### 3 Basic Formulas for Equivalent Static Loading

#### 3.1 Basic Observations

Many factors affect the time history of collision force for a ship. Two of the most important factors are collision velocity,  $V$ , and the size of colliding ship presented by *DWT*. To obtain the basic relationships, numerical simulation computations for various velocities and for various ships were carried on for head-on bow collisions on rigid wall. Figure 3 shows the  $P_m$ - $V$  relationship, and Figure 4 shows the  $P_m$  -

DWT relationship. A linear relationship between  $P_m$  and collision force is observed, and then a nonlinear relationship is observed between  $P_m$  and DWT.

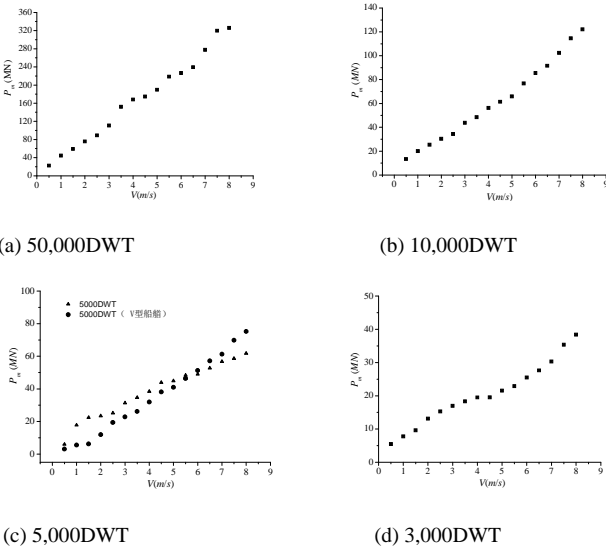


Figure 3  $P_m$  - $V$  relationship

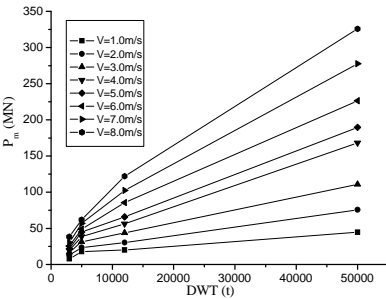


Figure 4  $P_m$  - $DWT$  relationship

### 3.2 Basic Formulas for Equivalent Static Loading

From Figure 4, the relation of  $P_m$  - $DWT$  may be fitted by a power function,  $y=ax^b$ .

A three-step fitting method is used to obtain the basic formulas for equivalent static loading.

**First step:** by fitting  $P_m$ -DWT data pair for various velocities,  $a$  and  $b$  may be obtained; and calculate the mean value of  $b$  to obtain a constant value, denoting as  $b_m$ ;

**Second step:** for given  $b_m$ , refitting  $P_m$ -DWT data pair to obtain new values of  $a$ ;

**Third step:** to obtain the  $a$ - $V$  relation.

Follow the above procedures and one can obtain the following equations:

$$P_m = 0.031(DWT)^{0.66}V \quad (4)$$

## 4 Modifications of the Basic formulas for Equivalent Static Loading

In the previous formulas of equivalent static loading,  $DWT$  of ships and collision velocity are two factors to determine the collision force. However, geometry of a bridge foundation may also significantly affect the value of collision force. According to the design practice of bridge foundations, and for the common use in design practice and for simplicity, a ideal geometry are considered in this section, i.e., a rectangular block, as shown in Figure 5.

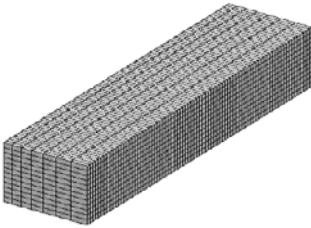


Figure 5. Ideal shapes of bridge foundations (especially for the pile-caps)

It is assumed that the width of ships is less than the width of the ideal rectangular block. Theoretically, the collision force on rigid wall is larger than that for rectangular block. To include the effects of the height of an ideal rectangular block, three factors,  $\eta$ , is introduced as,

$$\eta = P_{im} / P_m \quad (5)$$

where  $P_{im}$  is the maximum collision force, local average collision force and global average collision force on a rectangular block.

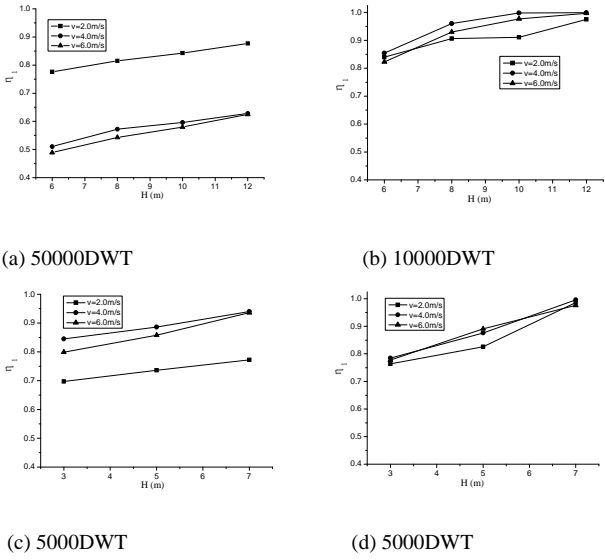


Figure 6.  $\eta_1$ - $H$  Relationship

Figure 6 shows the results for the ships of 50000DWT and 10000DWT, colliding on a rectangular block with height of 6m, 8m, 10m and 12m; and for the ships of 5000DWT and 3000DWT, colliding on a rectangular block with height of 3m, 5m and 7m. From these figures, one can observe that  $\eta_1$  increases with the height of rectangular block,  $H$  for a given collision velocity,  $V$ . But  $\eta_1$  does not increase monotonously with  $V$  from 2.0m/s to 6.0m/s. This means  $\eta_1$  depends on the bow structures of a ship in a complicated way. Further, one can observe that  $\eta_1$  takes its values in the range of 0.48 to 1.0, and fluctuates with collision velocity, especially for large ships, e.g., ships of 50000DWT and 10000DWT.

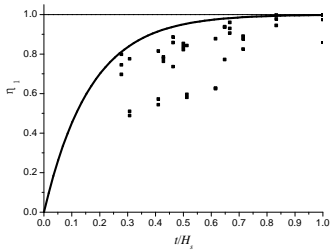


Figure 7. Envelope for  $\eta_1$

Because of the spread of  $\eta_1$ , a statistical prediction formulation can not be reached with reasonable accuracy. However, the fact is that  $\eta_1$  increases with  $H$ , and approaches unity (corresponding to collides with rigid wall). From the manner

of engineering design, an envelope function is proposed for  $\eta$ , as shown in Figure 7. The expression of the envelope function is,

$$\eta_1 = \begin{cases} 1 - \exp\left(-\frac{6H}{H_s}\right), & \text{for } H/H_s \leq 1.0 \\ 1.0, & \text{for } H/H_s > 1.0 \end{cases} \quad (6)$$

where  $\eta$  is called the modification factor for height of rectangular block;  $H$  is the height of rectangular block (m);  $H_s$  is the height of ship's bow(m).

By introducing the modified factors,  $\eta$ , the basic formulas of equivalent static loading may be modified as,

$$P_m = 0.031 \cdot \eta \cdot (DWT)^{0.66} \cdot V \quad (7)$$

## 6 Results

The numerical simulation technology for structural impacts is used to develop the equivalent static loads for design of bridges against ship collisions. FEM models of five ships whose  $DWT$  vary from 3,000-50,000 have been developed for numerical collision simulations using the software, LS-DYNA. The following results are reached in this paper:

Three definitions of equivalent static loading,  $P_m$ , is proposed and their meanings are explained based on the dynamic time histories from numerical simulations of ship-rigid wall collisions;

The basic formulas for,  $P_m$ , is developed following the rules of simplicity and easy to use in design;

Geometrical modification factors for rectangular block and circular block are introduced to consider the effects of geometry of a bridge foundation on the equivalent static loading, and the modified formulas for equivalent static loading are developed.

Finally it should be mentioned that the proposed formulas in this paper may be improved with the increase of the numbers of ships included in the numerical simulations.

## Acknowledgements

This paper is supported by NSFC, under No. 90715022 and supported by Chinese high-tech R&D Program (863 Program, No. 2006AA11Z120).

## References

- AASHTO (1991), Guide Specifications and Commentary for Vessel Collision Design of Highway Bridges, American Association of State Highway and Transportation Official, Washington DC .
- AASHTO (2004), LRFD bridge design specifications and commentary. American Association of State Highway and Transportation Officials.
- Consolazio G.R., Cowa D.R. (2003), Nonlinear analysis of barge crush behavior and its relationship to impact resistant bridge design, *Computers and Structures*, 81: 547–557.
- Jones N. (1989), *Structural Impact*, Cambridge University Press.
- Knott M., Prucz Z. (2000), *Vessel collision design of bridges: Bridge engineering handbook*. CRC Press LLC.
- Railway Department of China (2000), The Primary Code for Railway Bridges (TB10002.1-99), Beijing.
- Vrouwenvelder A.C.W.M. (1998), Design for ship impact according to Eurocode 1, part 2.7, *Ship Collision Analysis*. A.A. Balkema, Rotterdam.
- Wang Junjie, Yan Haiqun, Qian Hua (2005), Comparisons of design formula of ship collision for bridges based on FEM simulations, *Journal of Technology of Highway Transportation*, 23(2): 68–73.

# Signature Turbulence Effect on Buffeting Responses of a Long-span Bridge with a Centrally-Slotted Box Deck

Ledong Zhu<sup>1,2,3\*</sup>, Chuanliang Zhao<sup>3</sup>, Shuibing Wen<sup>3</sup> and Quanshun Ding<sup>1,2,3</sup>

<sup>1</sup>State Key Laboratory for Disaster Reduction in Civil Engineering, Tongji University, Shanghai 200092, P.R. China

<sup>2</sup>Key Laboratory for Wind Resistance Technology of Bridges (Ministry of Transport), Tongji University, Shanghai 200092, P.R. China

<sup>3</sup>Department of Bridge Engineering, Tongji University, Shanghai 200092, P.R. China

**Abstract.** Shanghai Bridge over Yangtze River is a steel cable-stayed bridge with a main span of 730m and a centrally-slotted twin-box deck. The equivalent aerodynamic admittances with and without signature turbulence effect were identified at first for the windward and leeward deck boxes, respectively, via sectional model wind tunnel tests of force measurement, and fitted using proposed model functions of fraction (series). The buffeting responses of the bridge with and without signature turbulence effect were then analyzed using a CQC method in frequency domain, where, the buffeting forces on the windward and leeward deck boxes were separately modeled. The analyzed responses were then compared with those obtained via full bridge aeroelastic model test. The results show that the calculated buffeting responses using measured aerodynamic admittances approach well to the tested results, and the signature turbulence exerts almost no effect on the buffeting responses at the wind speeds higher than 10m/s, but fairly significant influence that at lower wind speeds about 7m/s. This means that the signature turbulence will not prick up the strength issue of bridge structure, but may significantly aggravate the fatigue issue of bridge structure due to buffeting and vortex-excited resonance at lower wind speeds.

**Keywords:** long-span bridge, signature turbulence, buffeting response, aerodynamic admittance

---

\* Corresponding author, e-mail: ledong@tongji.edu.cn

## 1 Introduction

Buffeting is one of important types of wind-induced vibration of long-span bridges due to their flexibility and lower fundamental natural frequencies, and has been paid great attentions to in both wind engineering and bridge engineering fields. Up to now, apart from wind tunnel test means, various analysis methods have been developed for predicting buffeting responses of long-span bridges. In the early sixties of the last century, Davenport (1962) pioneered the application of the statistical concepts of the stationary time series and random vibration theory to the buffeting analysis of long-span bridges in frequency domain. Quasi-steady theory was employed to establish the buffeting forces on the bridge and aerodynamic admittance functions were introduced to consider the unsteadiness and spatial variation of wind turbulence surrounding bridge deck cross sections. Aerodynamic strip assumption was adopted to simplify the 3-dimensional flow issue in to 2-dimensional one, and joint acceptances were introduced to consider the temporal and spanwise cross correlation of buffeting forces. However, the effects of motion-dependent aerodynamic forces and aerodynamic coupling were not fully taken into account in this theory. In the seventies of the last century, Scanlan and his co-workers introduced their linear self-excited aeroelastic force model, which was already used successfully in bridge flutter analysis, into the buffeting analysis to include the influenced of aerodynamic damping and stiffness and aerodynamic coupling (Scanlan and Gade 1977; Scanlan 1978). While the frequency-domain method was applied to bridge buffeting analysis, Lin and his co-workers presented the time-domain method for the prediction of bridge response to turbulent wind using Ito's stochastic differential equations (Lin 1979; Lin and Ariarantnam 1980).

The above-mentioned classical methods for buffeting analysis have been continuously refined by various researchers with the increasing demand for more accurate prediction of buffeting response of modern long-span bridges as well as the development of techniques of finite element and computer. Nowadays, not only the effects of multi-modes, inter-mode coupling and aerodynamic coupling but also the interaction among major bridge components can be included in either the time domain (Diana et al. 1999; Boonyapinyo et al. 1999; Chen 2000a) or the frequency domain (Jain et al. 1996; Xu et al. 1998; Katsuchi et al. 1999; Chen et al. 2000b; Xu et al. 2000). Furthermore, to carry out more reasonable verification of buffeting analysis through field measurements of bridge responses to strong winds with arbitrary incident directions, Zhu and Xu presented a finite element approach for analyzing the buffeting responses of long-span bridges und skew (yawed and inclined) winds, and found that the direction normal to the bridge span is not necessary to be the most dangerous wind direction to the buffeting responses (Zhu and Xu 2005; Xu and Zhu 2005).

However, the buffeting forces in most of the current buffeting analyses are determined based on the quasi-steady theory, where, only the turbulence of incident

wind is included. The signature turbulence caused by the interaction between structure and flow around it is normally ignored. Up to now, the extent of signature turbulence effect on the bridge buffeting responses has not been understood yet and has rarely been investigated, although this issue was already regarded as one of major challenges in the prediction of long-span bridge response to wind (Jones 1999).

In this connection, the signature turbulence effect on bridge buffeting responses are investigated in this study using finite element analyses of buffeting responses with equivalent aerodynamic admittances including/excluding the signature turbulence effect, which are measured via force measurement wind tunnel tests of sectional model in turbulence flow. Because the signature turbulence is regarded to be much more significant for bridge decks with separate boxes than other types of decks, Shanghai Bridge over Yangtze River, which is a steel cable-stayed bridge with a main span of 730m and a centrally-slotted twin-box deck (see Figure 1), is thus taken as an engineering background in this study. The details of the research are to be introduced in the following sections.

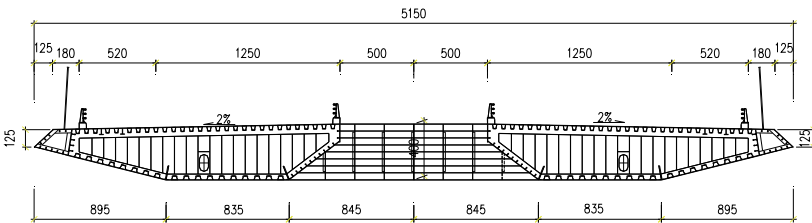


Figure 1. Deck cross section of Shanghai Bridge over Yangtze River

## 2 Brief Description of Sectional Model and Installation

The sectional model tests for the equivalent aerodynamic admittances of the bridge deck were carried out in the TJ-2 Boundary Layer Wind Tunnel at a length scale of 1/80. Grid-generated the turbulent flow fields with turbulent intensities of 6%, 10%, 15% and 20% adopted in the test.

Figure 2 shows the model mounted on a five-component force balance in the wind tunnel. The sectional model was designed in such a way that the fluctuating forces could be separately measured in the test for the windward and leeward boxes. Therefore, the sectional model was comprised of a measured segment, an upper compensatory segment and a side compensatory segment. The measured segment and upper compensatory segment simulated the aerodynamic shape of one box of the twin-separate box deck, and the side compensatory segment simulated the shapes of another box and transverse beams linking the two boxes.

The measured segment was made of wood and an aluminum link endplate, which was used to connect the measured segment to the balance. The measured segment was 0.4m long (excluding the end plate), and its total mass was 1.1kg. The aluminum end plate had a basic shape as same as the cross section shape of the measure segment, but its middle part was circular with a diameter as same as the force balance. The upper and side compensatory segments were 0.4m and 0.8m long, respectively, and were made of Perspex plates and used to simulate compensatively the aerodynamic shape of the bridge deck surrounding the measured one.

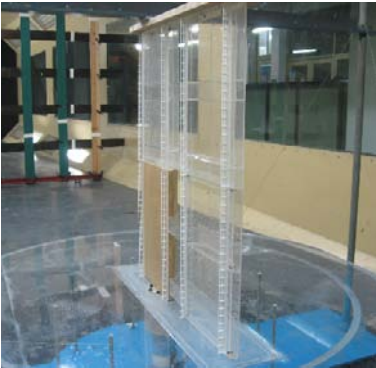


Figure 2. Sectional model in TJ-2 Boundary Layer Wind Tunnel.

Before the test, a steel frame for the installation of compensatory segments was mounted on the turntable at first. The five-component force balance was then fixed at the center of the turntable with its surface being 0.3m from the tunnel floor through a steel pipe support. Afterwards, to depress the disadvantageous effects of boundary layer above the tunnel floor and 3D flow around the lower end of the sectional model, a circular separating plate with a diameter of 1.5m and made of Perspex was then mounted at on the turntable with its bottom surface level a little bit lower than the top surface level of the force balance. In the middle region of the circular plate, there was an opening with a shape similar to the aluminum end plate of the measured segment, but a little bit larger than the latter. The separating plate must keep no touch to the top perceptual surface of the force balance. In the next step, the measured segment was vertically mounted on the force balance through the preset opening of the circular separating plate without any contact, and the upper compensatory segment was installed on the steel frame at its top end and was kept a narrow gap of 1-2mm from the measured segment at its bottom end. Then, the top end of the side compensatory segment was also connected the steel frame while its bottom end was connected to the circular separating plate. Finally the upper and side compensatory segments were connected to each other through the transverse link beam model to increase their stiffness. As a result, the fundamental natural frequencies of the model-balance system were

73Hz, 68Hz in the directions in and out of the deck plane, respectively, and 113Hz in torsional direction.

In the test, only the fluctuating aerodynamic forces on the measured segment were measured, and by rotating the turntable at 180°, the position of the measured segment could be switched between the windward and leeward positions.

### 3. Results of Equivalent Aerodynamic Admittances

The buffeting forces on the bridge deck can be expressed with the following equations according to the quasi-steady theory (Chen et al. 2001)

$$D_b = \frac{1}{2} \rho U^2 B \left[ 2C_D \chi_{Du}^{(K)} \frac{u(t)}{U} + (C'_D - C_L) \chi_{Dw}^{(K)} \frac{w(t)}{U} \right] \quad (1b)$$

$$L_b = \frac{1}{2} \rho U^2 B \left[ 2C_L \chi_{Lu}^{(K)} \frac{u(t)}{U} + (C'_L + C_D) \chi_{Lw}^{(K)} \frac{w(t)}{U} \right] \quad (1b)$$

$$M_b = \frac{1}{2} \rho U^2 B \left[ 2C_M \chi_{Mu}^{(K)} \frac{u(t)}{U} + C'_M \chi_{Mw}^{(K)} \frac{w(t)}{U} \right] \quad (1c)$$

where  $C_D$ ,  $C_L$  and  $C_M$  are the aerodynamic coefficients of mean drag, lift and torsion moment, respectively;  $C'_D = dC_D / d\alpha$ ,  $C'_L = dC_L / d\alpha$ ;  $\alpha$  is the wind attack angle;  $u(t)$ ,  $w(t)$  are the alongwind and vertical fluctuating wind speed;  $U$  is the mean wind speed;  $\chi_{Du}$ ,  $\chi_{Dw}$ ,  $\chi_{Lu}$ ,  $\chi_{Lw}$ ,  $\chi_{Mu}$  and  $\chi_{Mw}$  are the aerodynamic admittances, respectively;  $K = \omega B / U$  is reduced frequency,  $B$  is the whole width of the deck in this paper. Then, the spectra of buffeting drag ( $S_{DD}$ ), lift ( $S_{LL}$ ) and torsion moment ( $S_{MM}$ ) can be written as follows:

$$\begin{aligned} S_{DD} &= (\rho UB/2)^2 \left[ 4C_D^2 |\chi_{Du}|^2 S_{uu} + (-C_L + C'_D)^2 |\chi_{Dw}|^2 S_{ww} \right. \\ &\quad \left. + 2C_D (-C_L + C'_D) (\chi_{Du}^* \chi_{Dw} S_{uw} + \chi_{Du} \chi_{Dw}^* S_{uw}^*) \right] \quad (2a) \\ &= (\rho UB/2)^2 \left[ 4C_D^2 S_{uu} + 4C_D (-C_L + C'_D) C_{uw} + (-C_L + C'_D)^2 S_{ww} \right] |\chi_D|^2 \end{aligned}$$

$$\begin{aligned}
 S_{LL} &= \left(\frac{\rho UB}{2}\right)^2 \left[ 4C_L^2 |\chi_{Lu}|^2 S_{uu} + (C_D + C'_L)^2 |\chi_{Lw}|^2 S_{ww} \right. \\
 &\quad \left. + 2C_L (C_D + C'_L) (\chi_{Lu}^* \chi_{Lw} S_{uw} + \chi_{Lu} \chi_{Lw}^* S_{uw}^*) \right] \\
 &= (\rho UB/2)^2 \left[ 4C_L^2 S_{uu} + 4C_L (C_D + C'_L) C_{uw} + (C_D + C'_L)^2 S_{ww} \right] |\chi_L|^2
 \end{aligned}
 \tag{2b}$$

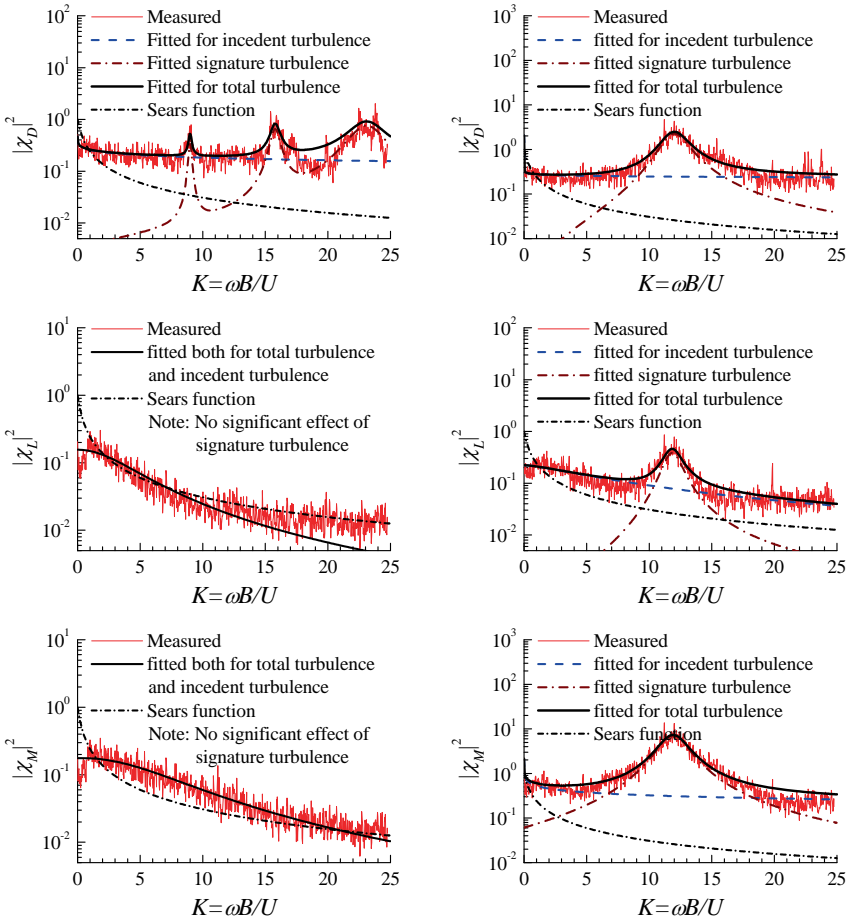
$$\begin{aligned}
 S_{MM} &= \left(\frac{\rho UB}{2}\right)^2 \left[ 4C_M^2 |\chi_{Mu}|^2 S_{uu} + C_M'^2 |\chi_{Mw}|^2 S_{ww} \right. \\
 &\quad \left. + 2C_M C'_M (\chi_{Mu}^* \chi_{Mw} S_{uw} + \chi_{Mu} \chi_{Mw}^* S_{uw}^*) \right] \\
 &= (\rho UB/2)^2 \left[ 4C_M^2 S_{uu} + 4C_M C'_M C_{uw} + C_M'^2 S_{ww} \right] |\chi_M|^2
 \end{aligned}
 \tag{2c}$$

where the superscript \* indicates the conjugate operation;  $S_{uu}$  and  $S_{ww}$  are auto spectra of fluctuating wind components  $u$  and  $w$ , respectively;  $S_{uw}$  and  $C_{uw}$  are the cross spectrum and co-spectrum between  $u$  and  $w$ , respectively;  $|\chi_D|^2$ ,  $|\chi_L|^2$  and  $|\chi_M|^2$  are the square of modules of equivalent aerodynamic admittances of drag, lift and torsion moment, respectively, considering the joint contribution of  $u$  and  $w$ .

Figure 2 shows the results of  $|\chi_D|^2$ ,  $|\chi_L|^2$  and  $|\chi_M|^2$  of the windward and leeward boxes measured in the turbulence flow field with the intensity of 10% and the mean attack angle of zero. The measured data are then fitted using the following target functions of fraction series of Eq. (3) for the incident turbulence contribution and of Eq. (4) for the signature turbulence contribution, respectively, and the corresponding fitted curves are also plotted in Figure 2.

$$|\chi_i|^2 = \frac{\alpha}{1 + \beta K^r}
 \tag{3}$$

$$|\chi_s|^2 = \sum_{i=1}^n \frac{c_{1i} + c_{2i} K}{(K - c_{3i})^2 + c_{4i}}
 \tag{4}$$



(a) Windward box

(b) Leeward box

Figure 2. Measured and fitted equivalent aerodynamic admittances.

From Figure 2, it can be seen that for the windward box, the effect of signature turbulence makes the  $|\chi_D|^2$  curve of having three significant peaks at about  $K=9$ , 16 and 23, but doesn't influence the  $|\chi_L|^2$  and  $|\chi_M|^2$  curves. For the leeward box, the effect of signature turbulence exerts remarkable influence on all the three equivalent aerodynamic admittances within the reduced frequency zone between 10 and 15, and makes each of the curves having a peak with a value much higher than 1.0 at about  $K=12$ . Furthermore, the measured equivalent aerodynamic admittances are generally smaller than Sears function for  $K < 1$ . For  $K > 1$ , all the three equivalent aerodynamic admittances of the leeward box as well as the values of  $|\chi_D|^2$  of the windward box are generally much larger than Sears function whilst the  $|\chi_L|^2$  of

the windward box is mostly somewhat smaller than Sears function and  $|\chi_M|^2$  of the windward box is generally larger than Sears function.

### 4 Effect of Signature Turbulence on Buffeting Responses

The buffeting responses of Shanghai Bridge over Yangtze River were analyzed in frequency-domain using the method presented in Zhu and Xu (2005), where the buffeting forces on the windward and leeward boxes were separately modelled. In all, 30 natural modes were considered in the analysis. The fundamental vertical, lateral and torsional frequencies are 0.252Hz, 0.325Hz and 0.665Hz, respectively. The damping ratios were set to be 0.5% for all 30 modes. The aerodynamic coefficients obtained used is measured via the above-mentioned sectional model test. Four cases of aerodynamic admittances were considered, including unit, Sears function, fitted admittances including solely the incident turbulent contribution, and fitted admittances including both the incident and signature turbulence contributions. Lacking in the measured aerodynamic derivatives of the windward and leeward boxes, the self-excited aeroelastic forces were approximately determined using the measured aerodynamic coefficients according to the quasi-steady theory. The Simiu spectra were used for  $S_{uu}$  and  $S_{vv}$  while the Panofsky Spectrum and Kaimal spectrum were used for  $S_{wv}$  and  $C_{iw}$  (Simiu and Scanlan 1996). The roughness length  $z_0$  was taken as 0.05, which was determined with the following equation:

$$z_0 = \frac{k(z - \bar{H})}{ke^{k\beta_u/I_u} - 1} \tag{5}$$

where von Karman constant  $k=0.4$ ; The mean height of upwind obstacles  $\bar{H}=0$ ;  $\beta_u=2.5$ ;  $z=62.5\text{m}$  is the height of deck mid-span above water level;  $I_u$  is the turbulent intensity at deck level and is taken as 14%, the measured value in the wind tunnel test of the full bridge aeroelastic model.

Figure 3 shows the variation of the calculated vertical, lateral and torsional RMS responses at mid-span with wind speed, and Figure 4 gives a close-up view of the vertical response at lower wind speed region.

It can be seen from Figure 3 that the vertical RMS responses calculated using measured admittances agree well with the tested results, whilst the corresponding calculated lateral and torsional responses are much smaller than the tested ones. One of the reasons may be that the lateral and torsional responses are too small so that the ratios of noise to signal in the measured responses are remarkable. The other reasons may come from the approximation of the used empirical wind spectra and the used quasi-steady aerodynamic derivatives.

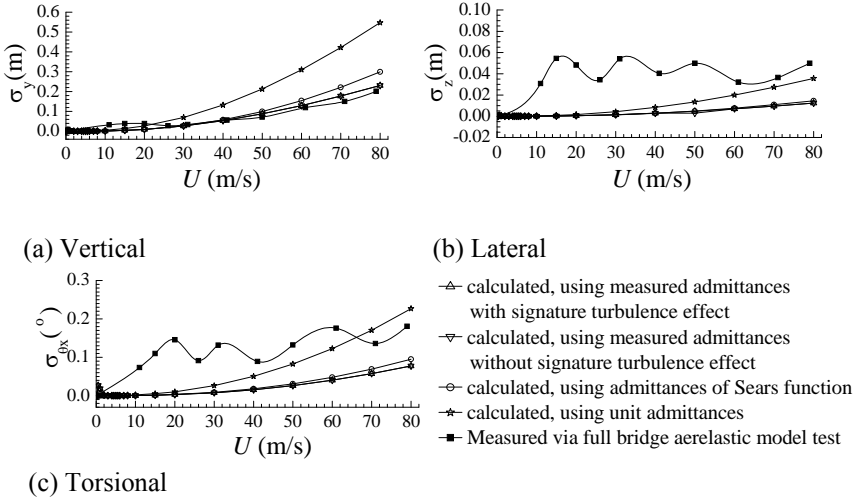


Figure 3. RMS responses at mid-span vs. wind speed at deck level.

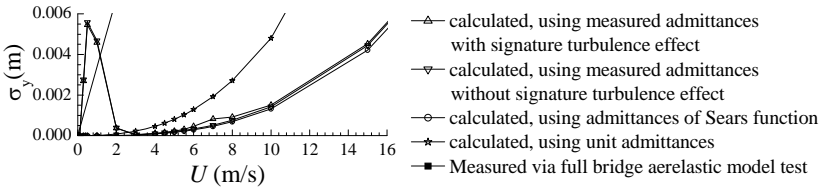


Figure 4. Vertical RMS responses at mid-span for lower wind speeds

From Figure 3 and Figure 4, it can further be found that the signature turbulence effect exerts very limited influence on the buffeting responses when wind speed is higher than 10m/s. However, for the wind speed about 7m/s, the effect of signature turbulence is evident on the vertical buffeting responses, and the RMS response may be doubled in this occasion. This is similar to the phenomenon of vortex-excited resonance which occurs often at lower wind speeds. Actually, like vortex-induced force, the signature turbulence is also caused by the vortex shedding. Nevertheless, because of the existence of the incident turbulence, signature turbulence shows itself more random and wider in frequency-band compared with the vortex-induced force. From Figure 2, it one can see that the eminent reduce frequency of signature turbulence is very high. On the other hand that the natural frequencies of fundamental modes of long-span bridges, which provide major contributions to the buffeting responses of the bridge, are rather lower. Therefore, the signature turbulence can exert significant influence on the bridge buffeting re-

sponses only at lower region of wind speed, where the reduced frequencies of the fundamental modes may approach to the eminent one of signature turbulence.

Moreover, the calculated vertical responses using measured admittances are remarkably smaller than those calculated using unit admittances, and also smaller than those calculated using Sears function, and much closer to the tested one. The lateral and torsional responses calculated using measured admittances are also much smaller than those obtained using unit admittance, but quite close to those got using Sear function. This means that Sears function is not necessary to be the low bound of the aerodynamic admittance functions of separate-box cross sections.

## 5. Concluding Remarks

The effect of signature turbulence on the buffeting responses of long-span bridges with twin-separate box decks is discussed in this paper. From the discussion, it can be concluded that the eminent reduced frequencies of the signature turbulence acting on twin-separate box deck are very higher and may close or exceed 10. This leads to that the signature turbulence can play fairly significant influence on the buffeting responses of long-span bridges only at lower wind speeds, for instance, less than 10m/s. This is similar to the phenomenon of vortex-excited resonance. Therefore, the signature turbulence effect will not prick up the strength issue of bridge structure, but may significantly exacerbate the fatigue issue of bridge structure due to buffeting and vortex-excited resonance at lower wind speeds.

## Acknowledgments

The work described in this paper was jointly supported the Program for New Century Excellent Talents in University of China (Grant No. NCET-05-0381), the National Natural Science Foundation of China (Grant No. 50538050) and the National High-tech R&D Program (863 Program) of China (Grant No.: 2006AA11Z120), to which the writers are most grateful. Any opinions and concluding remarks presented here are entirely those of the writers.

## References

- Boonyapinyo V., Miyata T. and Yamada H. (1999). Advanced aerodynamic analysis of suspension bridges by state-space approach. *Journal of Structural Engineering, ASCE*, 125(12), 1357-1366.

- Chen X., Matsumoto M. and Kareem A. (2000a). Time domain flutter and buffeting response analysis of bridges. *Journal of Engineering Mechanics, ASCE*, 126(1), 7-16.
- Chen X., Matsumoto M. and Kareem A. (2000b). Aerodynamic coupled effects on flutter and buffeting of bridges. *Journal of Engineering Mechanics, ASCE*, 126(1), 17-26.
- Chen X., A. X. and Matsumoto M. (2001). Multimode coupled flutter and buffeting analysis of long span bridges. *Journal Wind Engineering and Industrial Aerodynamics*, 89, 649-664.
- Davenport A.G. (1962). Buffeting of a suspension bridge by storm winds. *Journal of the Structural Division, ASCE*, 88(ST3), 233-268.
- Diana G., Cheli F. and Bocciolone M. (1999). Suspension bridge response to turbulent wind: Comparison of a new numerical simulation method results with full scale data. *Proceedings of the Tenth International Conference on Wind Engineering: Wind Engineering into 21st Century*, Copenhagen, Denmark, 871-878.
- Jain A., Jones N.P. and Scanlan R. H. (1996). Coupled buffeting analysis of long-span bridges. *Journal of Structural Engineering, ASCE*, 122(7), 716-725.
- Jones N.P. and Scanlan R.H. (1998). Advances (and challenges) in the prediction of long-span bridge response to wind. *Proc. of International Symposium on Advances in Bridge Aerodynamics: Bridge Aerodynamics*, Copenhagen, Denmark, 131-143.
- Katsuchi H., Jones N.P. and Scanlan R.H. (1999). Multimode coupled flutter and buffeting analysis of the Akashi-Kaikyo Bridge. *Journal of Structural Engineering*, 125(1), 60-70.
- Lin Y.K. (1979). Motion of suspension bridges in turbulent winds. *Journal of the Engineering Mechanics Division, ASCE*, 105(EM6), 921-932.
- Lin Y.K. and Ariaratnam S.T. (1980). Stability of bridge motion in turbulent winds. *Journal of Structural Mechanics*, 8(1), 1-15.
- Scanlan R.H. (1978). The action of flexible bridge under wind, II: Buffeting theory. *Journal of Sound and Vibration*, 60(2), 201-211.
- Scanlan R.H. and Gade R.H. (1977). Motion of suspension bridge spans under gusty wind. *Journal of the Structural Division, ASCE*, 103(ST9), 1867-1883.
- Simiu E. and Scanlan R.H. (1996). *Wind Effects on Structures: Fundamentals and Applications to Design*, 3rd Edition, John Wiley & Sons, New York.
- Xu Y. L., Sun D.K., Ko J.M., Lin J.H. (1998). Buffeting analysis of long span bridges: A new algorithm. *Computers and Structures*, 68, 303-313.
- Xu Y.L., Sun D.K., Ko J.M. and Lin J.H. (2000). Fully coupled buffeting analysis of Tsing Ma suspension bridge. *Journal of Wind Engineering and Industrial Aerodynamics*, 85(1), 97-117.
- Xu Y.L. and Zhu L.D. (2005). Buffeting response of long cable-supported bridges under skew winds – Part 2: Case study. *Journal of Sound and Vibration*, 281(3-5), 675-697.
- Zhu L.D. and Xu Y.L. (2005). Buffeting response of long cable-supported bridges under skew winds – Part 1: Theory. *Journal of Sound and Vibration*, 281(3-5), 47-673.

*“This page left intentionally blank.”*

# Simulation of Flow around Truss Girder with Extended Lattice Boltzmann Equation

Tiancheng Liu<sup>1\*</sup>, Gao Liu<sup>1</sup>, Hongbo Wu<sup>1</sup>, Yaojun Ge<sup>2</sup> and Fengchan Cao<sup>2</sup>

<sup>1</sup>CCCC Highway Consultants Co., Ltd., Beijing 100010, China

<sup>2</sup>Tongji University, Shanghai 200092, China

**Abstract.** Based on the theory of turbulence and molecule kinetics, an extended Lattice Boltzmann equation (ELBE) is derived to solve turbulent flow, in which sub-grid turbulence model is introduced to simulate vortex viscosity as well as turbulence relaxation time to modify the normal LBGK equation. Further more, the ELBE is applied to predict aerodynamic forces and vortex shedding frequency of bridge truss girder, and an equivalent two-dimensional model is studied to solve truss girder considering block ratio.

**Keywords:** extended lattice Boltzmann equation, turbulence flow, truss girder, aerodynamic force, block ratio

## 1 Introduction

Numerical fluid dynamic (CFD) models and computer capacity have been developed over the past two decades to a stage where assessment of the effect of practical cross-section shapes on structure response is possible (Tamura, 2006). In particular, numerical simulations appear well suited for design studies of the effect of cross-section shape on structure response to wind loading. In general, the direct numerical simulation (DNS), Reynolds averaged Navier-Stokes (RANS) and large eddy simulation (LES) are applied to expect the turbulence flow, which are on the basis of coarse grained model: Navier-Stokes (NS) equations (Spalart, 2000). However, the solution of these basic coarse-grained equations becomes mathematically difficult in the presence of turbulence. The simplified turbulence model used to modify the underlying coarse-grained equations still can not reliably reproduce many physical effects.

Here, we will analyze molecule kinetic-based Lattice Boltzmann (LB) method, a new approach with different conception (Chen, 1998). The LB method is an effective numerical scheme for solving complex fluid dynamics problems, which

---

\* Corresponding author, e-mail: liutcmal@163.com

was proposed by McNamara and Zanetti (1988), and it has gained rapid progress in development and application in the last two decades (Chen, 2003 and Liu, 2007, 2008). In solving turbulent flow problems by DNS based on LB method, one should resolve all these relevant excited degrees of freedom, and this is a virtually impossible task when  $Re \gg 1$ . It is thought that turbulence flow consists of two components: large-scale flows and small-scale fluctuations (Spalart, 2000). In this way, an extended Lattice Boltzmann equation (ELBE) is developed combined with the turbulence model and the Smagorinsky sub-grid model is employed to represent the contribution of small-scale flow. Further more, the ELBE is applied to simulate flows around bridge truss girder with an equivalent method in two-dimensions considering block ratio. Finally, a summary of the computational results and discussion is concluded.

## 2 Extended Lattice Boltzmann Equation

It is thought that flows are consisted of lots of particles in heat motion, and the motions of many particle kinetic systems can be expressed as Boltzmann equation governing single particle motions (Chen, 2003), namely,

$$\frac{\partial f}{\partial t} + \mathbf{v} \cdot \frac{\partial f}{\partial \mathbf{x}} = \Omega(f) \quad (1)$$

where  $f=f(x,v,t)$  is particle distribution function;  $v$  is particle velocity vector;  $x$  is spatial position;  $t$  is time variable. The left side of this equation represents free streaming of molecules in space while the right side expresses intermolecular interactions or collisions. On the assumption that the details of collision operator are immaterial, an effective collision operator represented by BGK (Bhatnagar, Gross, and Krook) expression is introduced as follows:

$$\frac{\partial f}{\partial t} + \mathbf{v} \cdot \nabla f = -\frac{1}{\lambda} (f - f^{(eq)}) \quad (2)$$

where  $\lambda$  is relaxation time;  $f^{(eq)}$  is equilibrium distribution function. In order to solve  $f$  numerically, Eq. (2) is discretized in velocity space with a finite set of velocity vectors  $\{\mathbf{e}_\alpha\}$  in the content of conservation laws as shown in figure 1, and then a completely discretized equation is derived with time step  $\Delta t$  and space step  $\Delta \mathbf{x}$ , namely LB equation, as

$$f_\alpha(\mathbf{x}_i + \mathbf{e}_\alpha \Delta t, t + \Delta t) = f_\alpha(\mathbf{x}_i, t) - \frac{1}{\tau} [f_\alpha(\mathbf{x}_i, t) - f_\alpha^{(eq)}(\mathbf{x}_i, t)] \quad (3)$$

where  $f_\alpha$  is the particle distribution function associated with the  $\alpha$ th discrete velocity  $\mathbf{e}_\alpha$ ;  $\mathbf{x}_i$  is the location of spatial points;  $\tau = \lambda / \Delta t$  is the dimensionless relaxation time.

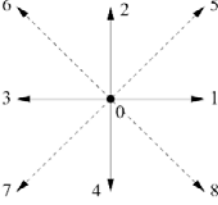


Figure 1. Topological structure of nine velocity two-dimensions model.

Particle distribution function  $f$  and equilibrium distribution function  $f^{(eq)}$  describe large-scale turbulent flows. In order to consider unresolved small-scale fluctuations, an eddy viscous turbulence should be used in LB equation. As a result, relaxation time  $\tau$  can be replaced by total relaxation time  $\tau_{total}$ , and the ELBE is derived as

$$f_\alpha(\mathbf{x} + \mathbf{e}_\alpha \Delta t, t + \Delta t) = f_\alpha(\mathbf{x}, t) - \frac{1}{\tau_{total}} (f_\alpha - f_\alpha^{(eq)}) \quad (4)$$

where  $\tau_{total} = \tau_0 + \tau_t$  is the total relaxation time depending on space and time;  $\tau_0$  and  $\tau_t$  represent the contribution of the molecule viscosity  $\nu_0$  and turbulence viscosity  $\nu_t$ , respectively.  $\tau_t$  includes the effect of sub-grid scale flow, so that Eq. (4) keeps the large-scale eddies, but keeps out the small-scale eddies.

The remaining problem is to define the effective turbulent relaxation time  $\tau_{total}$  describing dynamics of turbulent fluctuations. Indeed,  $\tau_{total}$  should depend on the variety of different turbulent physics, which includes molecule relaxation time  $\tau_0$  and turbulent relaxation time  $\tau_t$ .

$$\tau_{total} = \tau_0 + \tau_t = 3 \frac{\Delta t}{\Delta x^2} (\nu_0 + \nu_t) + \frac{1}{2} \quad (5)$$

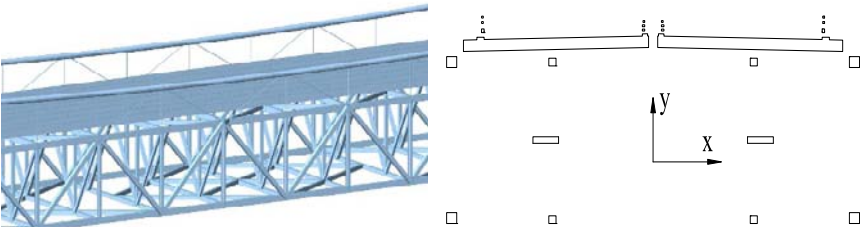
The turbulence viscosity  $\nu_t$  is governed by Smagorinsky model, in this paper, as  $\nu_t = (C_s \Delta)^2 |\bar{S}|$ , in which  $C_s$  is Smagorinsky constant;  $\Delta$  is the filter size;  $|\bar{S}| = \sqrt{2 \bar{S}_{ij} \bar{S}_{ij}}$  is the magnitude of the strain-rate tensor  $\bar{S}_{ij}$ . The quantity of  $\bar{S}_{ij}$  can be calculated with resolved-scales non-equilibrium momentum tensor  $\Pi_{ij} = \sum_\alpha e_{\alpha i} e_{\alpha j} (f_\alpha - f_\alpha^{eq})$ , as

$$\bar{S}_{ij} = -\frac{3}{2\bar{\rho}\tau_{total}\Delta t} \prod_{ij}^{(1)} = -\frac{3}{2\rho\tau_{total}\Delta t} \sum_{\alpha} e_{\alpha i} e_{\alpha j} (f_{\alpha} - f_{\alpha}^{eq}) \tag{6}$$

### 3 Simulation of Flow around Bridge Truss Girder

Based on above-mentioned ELBE, a parallel algorithm which is suitable for muster-computers is developed, and the parallel computation code (namely CWT-LB) is compiled using C++ computer language. The simulation of flow around bridge truss girder is performed by CWT-LB as follows.

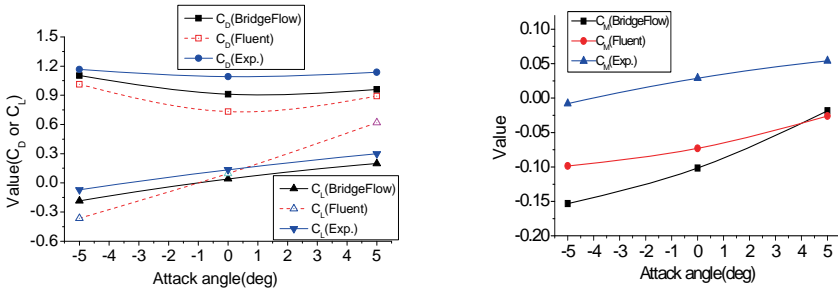
The truss girder shown as in Figure 2(a) has been widely used for long span bridge and possesses strong aerodynamic three-dimensional (3D) effects. Besides wind tunnel experiment, the more appropriate way to predict its aerodynamic force is numerical simulation with 3D model. However, the 3D numerical simulation needs a great number of points and time which is often inaccessible for engineer. Here, an equivalent two-dimensional (2D) model of truss girder is established shown as in figure 2(b), in which the block rates and position of truss members in direction x, y are determined by the averaged values of 3D truss girder of unit-length. The computational domain covers 20B in stream-wise direction (x), 20H in normal direction, in which B and H are the width and height of truss, respectively. The velocity boundary condition is applied for inlet; the pressure boundary condition for outlet; the non-slip wall boundary conditions for the surface of obstacles and outer-wall of flow field.



(a) Prototype of bridge truss girder (b) Equivalent 2D model of truss girder section

Figure 2. Geometry model of bridge truss girder.

The present computational aerodynamic forces of truss girder are shown as figure 3 comparing with that of Fluent and wind tunnel experiment, in which  $C_D$ ,  $C_L$  and  $C_M$  are drag coefficient, lift coefficient and moment coefficient, respectively. From figure 3, we can find that the present computational results agree well with that of experiment.

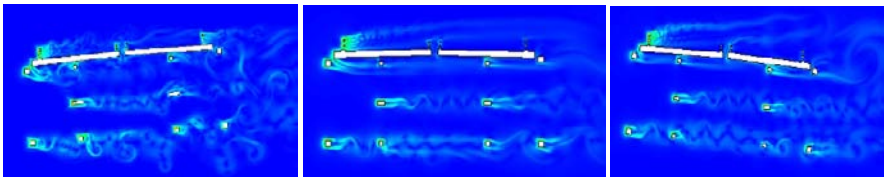


(a) Drag and lift coefficients

(b) Lift coefficients

Figure 3. Aerodynamic forces of truss girder depending on attack angle.

Figure 4 depicts the distribution of vortex viscosity around truss, in which the vortex structures including large-scales and small-scales are identified clearly. It is visible that the vortices are separating, re-attaching and shedding around truss, and the Karman vortex street is occurred along the leeward of truss member. Otherwise the wake of upstream obstacle has great interference effects on downstream obstacle.

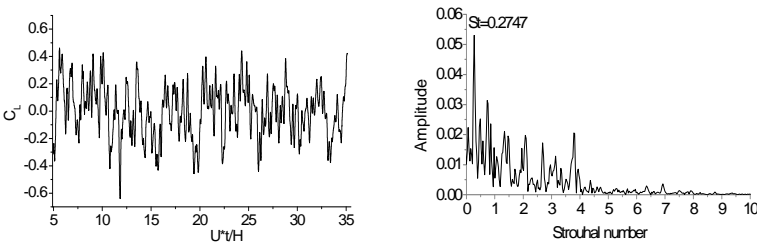


(a) Attack angle  $\alpha = -5$  deg.

(b) Attack angle  $\alpha = 0$  deg

(c) Attack angle  $\alpha = +5$  deg.

Figure 4. Distributions of vortex viscosity around truss girder.



(a) Time history of lift coefficient

(b) Amplitude spectrum of lift coefficient

Figure 5. Time history and amplitude spectrum of lift coefficient.

The vortex shedding frequency can be represented by Strouhal number ( $St$ ) with Fast Fourier Transform spectrum analysis of lift time-history. Figure 5(a) de-

picts the lift time-history of truss model at attack angle of 0 degree and its Strouhal number is equaled to 0.2747 corresponding to the dominant frequency of vortex shedding as shown in figure 5(b). In addition, there exist more than one order frequencies shown in amplitude spectrum of lift, which describe vortex shedding frequencies with different scales like in figure 4.

## 4. Concluding Remarks

The extended lattice Boltzmann equation is derived based on molecule kinetic theory and turbulence theory, which is verified by the simulation of flow around bridge truss girder. The aerodynamic force and vortex shedding frequency of truss girder can be predicts correctly by simplified 2D computational model with ELBE. Otherwise, both large-scales and small-scales vortexes structure can be identified clearly.

## Acknowledgements

The authors are grateful to the financial support by the National High-Tech Research and Development Plan of China (No. 2007AA11Z101) and the Western Region Science & Technology Development Projects, Ministry of Communication, China (No.2006318 49426).

## References

- Chen H., Satheesh K., Steven O., et al. (2003). Extended Boltzmann kinetic equation for turbulent flows. *Science*, 301, 633-636.
- Chen S., Doolen G.D. (1998). Lattice Boltzmann method for fluid flows. *Ann. Rev. Fluid. Mech.*, 30, 329-364.
- Liu Tian-Cheng, Ge Yao-Jun, Cao Feng-Chan (2007). Turbulence flow simulation based on the lattice-Boltzmann method combined with LES. *Proceeding in ICWE12*, Cairns, Australia, 8
- Liu Tian-Cheng, GE Yao-Jun, CAO Feng-Chan, et al. (2008). Simulation of flow around square cylinder based on lattice Boltzmann method. *J. of Tongji University (National Science)*, 36(8), 1028-1033.
- McNamara GR., Zanetti G. (1988). Use of the Boltzmann equation to simulate lattice automata. *J. Phys. Rev. Let.*, 61, 2332-2335.
- Spalart P.R. (2000). Strategies for turbulence modeling and simulations. *Int. J. Heat Fluid Flow*, 21, 252-263.
- Tamura T. (2006). Towards practical use of LES in wind engineering. *Proc. in CWE2006*, Yokohama, 1-8.

# Computational Comparison of DES and LES in Channel Flow Simulation

Zhigang Wei<sup>1,2</sup> and Yaojun Ge<sup>1,2\*</sup>

<sup>1</sup>Department of Bridge Engineering, Tongji University, Shanghai 200092, China

<sup>2</sup>State Key Laboratory for Disaster Reduction in Civil Engineering, Shanghai 200092, China

**Abstract.** As two computational fluid dynamics (CFD) simulation methods, detached-eddy simulation (DES) and large-eddy simulation (LES) are compared in a turbulent channel flow simulation at  $Re_b=2800$ . The Navier–Stokes equations are solved with three different grid resolutions by using a co-located finite-volume method. Spalart–Allmaras model dynamic model and are implemented in DES and LES, accordingly. DES acts as a wall-modeling of LES and functions powerfully as a near-wall treatment for LES technique, though it failed to predict the near wall turbulent structure as expected. The results of LES with the finest mesh compared well with direct numerical simulation (DNS).

**Keywords:** detached-eddy simulation, large-eddy simulation, direct numerical simulation, channel flow, Reynolds number

## 1 Introduction

Detached-eddy simulation (DES) can be used in two ways. In its original purpose, DES is designed for massively separated flow by Spalart 1997 (hereafter denoted by DES97). Its derivative use as wall modeling of LES initialized by Nikitin in 2000 has showed its capability in a “LES grid”. The term “LES grid” is used against “DES grid” that has to be carefully designed for DES97. “DES grid” refers to creating a “RANS grid” with a large spacing  $\Delta_{\parallel}$  parallel to the wall, compared with a boundary-layer thickness:  $\Delta_{\parallel}/\delta$ . In the separated regions, good accuracy is expected once the grid spacing in all directions is far smaller than the size of the region:  $\Delta/\delta$ . But when DES97 is applied to a “LES grid” with  $\Delta_{\parallel}/\delta$ , it behaves as a subgrid-scale (SGS) model with built-in wall modeling. In the core region of the channel we have  $\Delta_{\parallel}\approx\Delta_{\perp}$ . In this communication, DES97 is applied in the latter way. Different from quasi-DNS in the near wall region which is most used in LES

---

\* Corresponding author, e-mail:yaojunge@tongji.edu.cn

simulation with proposals for near-wall SGS improvements, the current application of DES97 aims to have a larger  $\Delta_{\parallel}^+$ , provided  $\Delta_{\parallel}/\delta$  is small. Regarding the fidelity of the fields, it is believed that any type of wall modeling will produce unrealistic coherent structures in a kind of “super-buffer layer” at the bottom of the LES region.

Channel flow is selected as test case, for as a wall-bounded flow, channel flow serves as a basic test for direct numerical simulation (DNS), LES and DES. Smagorinsky first derived an eddy viscosity subgrid-scale model based on a Boussinesq approximation. Deardorff computed a fully turbulent channel flow by using the Smagorinsky model, Smagorinsky constant in his simulation is lowered. Moin and Kim later applied a van Driest damping function to reduce the near-wall viscosity even further. The Smagorinsky model is absolutely dissipative and it is based on resolved strains. With gradient flows, non-zero residual stresses are predicted even for laminar flows. Germano *et al.* introduced a model that computed the coefficient as the calculation progresses. No *ad hoc* damping functions were needed. Numerous simulations have been devoted to near-wall modeling in LES for a channel flow these years. Piomelli has given a detailed description for near-wall modeling in LES. A general trend was that the addition of the SGS models decreased the wall stress.

Channel flow is now well understood by both DNS and LES, but most of the large-eddy simulations over the past years have been performed by using spectral methods, where the idea of filtering is realized ideally. This study aims to compare DES97 with LES for channel flow based on finite-volume methods. The results from simulations with the constant and the dynamic Smagorinsky SGS models are compared to a non-modelled simulation. The effect of the grid resolution on the results is studied with and without the SGS model. A fully turbulent channel flow at Reynolds numbers 2800 (based on the bulk velocity) is the test case in the study of large-eddy simulation with a co-located finite volume technique. In the next section, the numerical methods and the configurations of channel flow simulation are described. In Section 3, the results are discussed. The conclusions are drawn in Section 4.

## 2 Numerical Methods and Configuration

Firstly, the definition of the length scale  $\tilde{d}$  is:

$$\tilde{d} \equiv \min(d, C_{DES} \Delta) \quad , \quad \Delta \equiv \sqrt[3]{V} \quad (1)$$

where  $d$  is the distance to the nearest wall and expresses the (inviscid) confinement of the eddies by that wall. Note  $\Delta$  is the cube root of the cell volume, the original DES97 defines  $\Delta \equiv \max(\Delta x, \Delta y, \Delta z)$ .

The channel flow case is a fully developed turbulent flow in a channel with a bulk Reynolds number of 2800 defined as  $Re_b = U_b \delta / \nu = 2800$ , where  $U_b$  is the bulk velocity and  $\delta$  is half of the channel height  $H$ . This approximately equals a wall shear velocity based Reynolds number:  $Re = U_\tau \delta / \nu = 180$ , where  $U_\tau = (\tau_w / \rho)^{1/2}$  is the wall shear velocity and  $\tau_w$  is the wall shear stress. The parameters have the following values:  $H = 1\text{m}$ ,  $U_b = 1\text{m/s}$  and  $\nu = 1.786 \times 10^{-4} \text{m}^2/\text{s}$ .

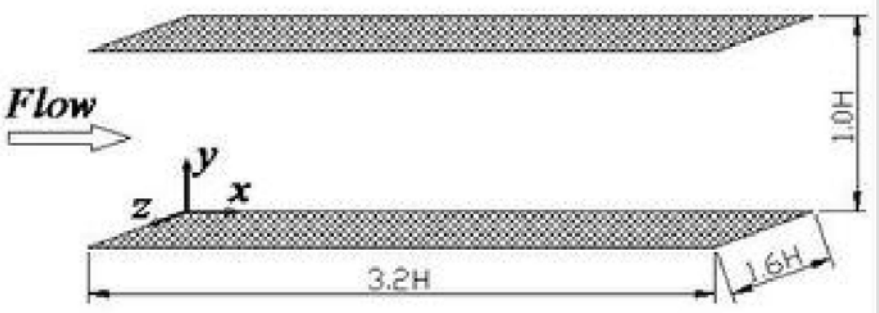


Figure 1. The computational domain in the channel flow. Periodic boundary conditions are applied in the streamwise ( $x$ ) and the spanwise directions ( $z$ ). Solid walls restrict the inhomogeneous direction ( $y$ ).

Figure 1 shows a schematic picture of the channel. Periodic boundary conditions are applied in the streamwise and in the spanwise directions, where the lengths of the domain are  $3.2H$  and  $1.6H$ , respectively. These distances are actually half of those used by Kim et al., in their direct numerical simulation. They utilized a spectral method and  $192 \times 129 \times 160$  grid points in the  $x$ -,  $y$ - and  $z$ -directions, respectively. In the wall normal direction, 64 cells are used and the height of the two closest cells next to the walls is  $y^+ = 1$  in dimensionless units. This height can be approximated from the logarithmic law

$$\frac{U_b}{u_\tau} = \frac{1}{\kappa} \ln \left( \frac{u_\tau \delta}{\nu} \right) + B - \frac{1}{\kappa} = \frac{1}{\kappa} \ln \left( \frac{U_b \delta}{\nu} \frac{u_\tau}{U_b} \right) + B - \frac{1}{\kappa} \quad (2)$$

where the relation  $(U_b/u_\tau) = (1/c_f)^{1/2}$  has been used. Here,  $c_f$  is the skin-friction coefficient, which can be solved from Equation (2) after introducing the values  $\kappa = 0.41$  and  $B = 5.0$ . Hence,  $u_\tau$  is solved from Equation (2) and the dimensional distance from the wall in terms of  $y^+$  can be solved from  $y_n = y^+ \nu / u_\tau$ .

Table 1. The parameters of the grids used.

Case	Grid	$N_x$	$N_y$	$N_z$	$\Delta x^+$	$\Delta y_{\min}^+$	$\Delta y_{\min}^+$	$\Delta z^+$
LES-C	Coarse	16	64	16	71	1.0	16.8	36
LES-M	Medium	32	64	32	36	1.0	16.8	18
LES-F	Fine	64	64	64	18	1.0	16.8	9
DES-C	Coarse	16	64	16	71	1.0	16.8	36

The stretching ratio of the cells is 1.10 in the wall direction. The cell height next to the centre line is  $16.8\Delta y_{\min}^+$ . Calculations are carried out with three different grids, whose streamwise and spanwise cell densities vary.

The parameters are given in Table 1. The streamwise length of the box in dimensionless units is approximately  $1140\Delta x^+$ . The periodic boundary condition is set for all the variables.

### 3 Results and Discussion

The initial velocity profile for the simulation is

$$U_{ini} = U_b (1 - \cos(4\pi y/H)) \quad (3)$$

A false steady solution seems to be found in flow computation, unless it is provoked with an initial condition that produces a lot of vorticities. This causes an earlier transition to turbulence and reduces the computation time. LES with the coarse, medium and fine grids are called LES-C, LES-M and LES-F, DES with the coarse grids are called DES-C. The CFL numbers are controlled to below 0.1, 0.1 and 0.2 in the coarse, medium and fine grids, respectively. The corresponding time-step sizes are then  $0.008T$ ,  $0.0048T$  and  $0.0058T$ , where  $T = H/U_b$ . The mean data is collected along one line. The averaging was done over the plane.

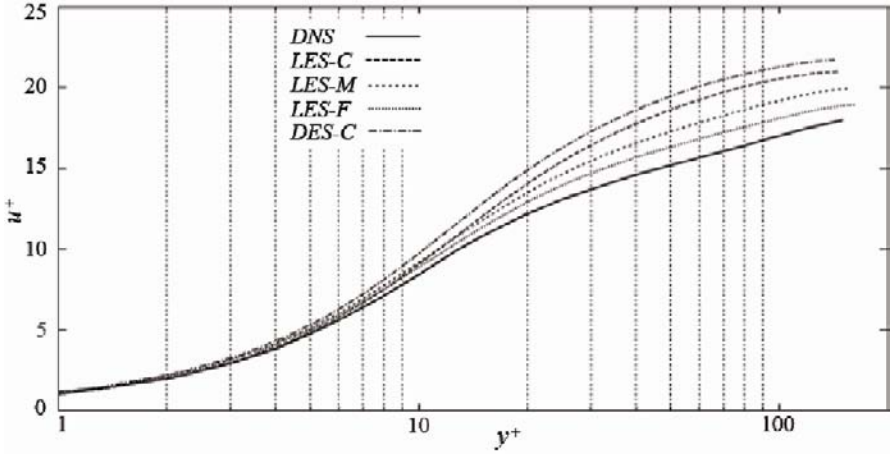


Figure 2. The dimensionless velocity profiles.

The dimensionless velocity profiles are shown in Figure 2. All simulations do not predict as proper logarithmic region as LES-F does, although it does show some offset to the reference result.

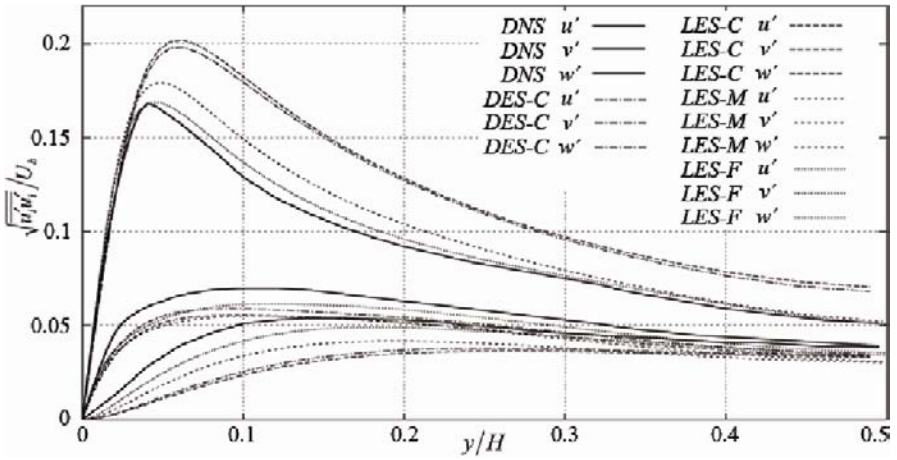


Figure 3. The rms fluctuations of  $(\overline{u'_i u'_i})^{1/2}/U_b$ .

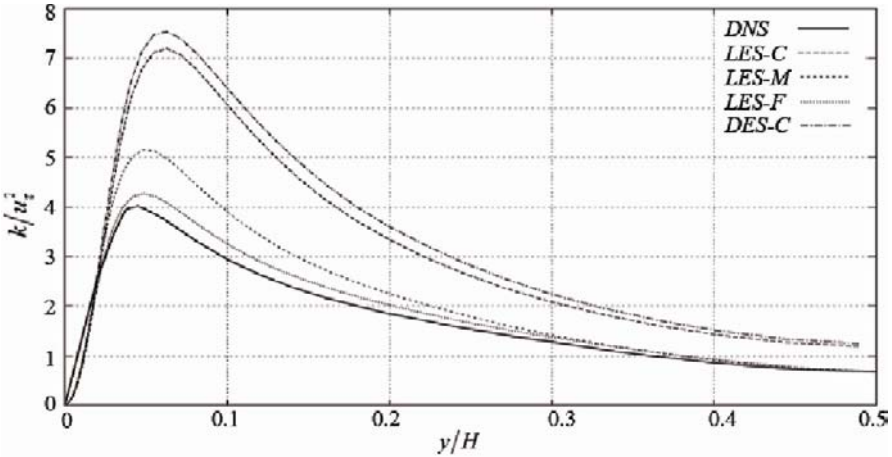


Figure 4. The kinetic energy normalized by the shear velocity  $k/u_\tau^2$

Figure 3 show the resolved rms fluctuations;  $(\overline{u'_i u'_i})^{1/2}/U_b$ , and Figure 4 the kinetic energy normalized by the shear velocity,  $k/u_\tau^2 = (\overline{u' u'} / 2) / u_\tau^2$ ; Figure 5 the normalized Reynolds stress  $\overline{u' v'} / U_b^2$ . The computations with the coarse and themedium grid (DES-C, LES-C and LES-M) overpredict the peak of the kinetic energy as shown in Figure 4 and underpredict the wall stress. The reason for this is likely an inadequate grid resolution. If the near-wall flow structures are not properly resolved, the effective shear stress on the wall is reduced. This is also the case of DES-C, the fluctuations normal to the wall (vrms) are underpredicted, as shown in Figure 4, even worse than LES-C, which decreases the momentum transfer between the wall and the core flow. The dominant streamwise fluctuations (urms) grow and so does the resolved turbulent kinetic energy. The fine-grid simulation predicts all the monitored quantities quite well, so it probably catches most of the eddies present in the flow. In this case, the largest deviations of the turbulent fluctuations are located in  $y/H=0.12$ , when compared to the DNS results. It is probably because the stretching need to be lowered so as to increase the near-wall grids number.

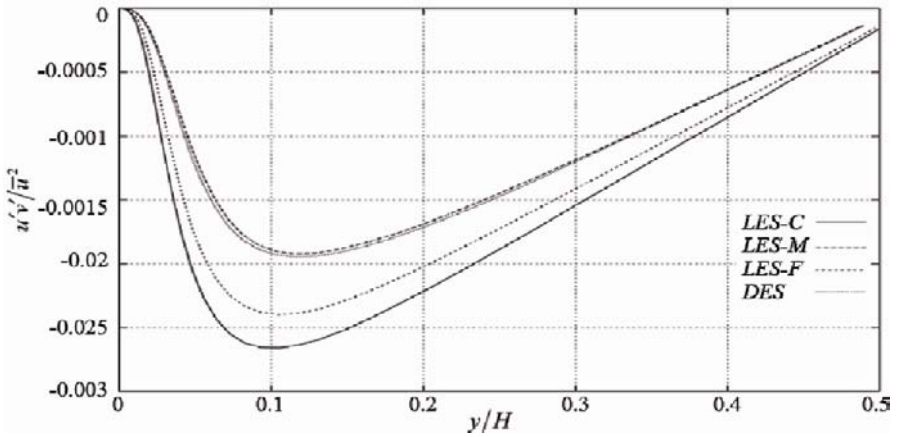


Figure 5. The dimensionless Reynolds stress  $\overline{u'v'}/U_b^2$ .

## 4 Conclusions

1. Both LES and DES are able to simulate the channel flow at  $Re_b=2800$ ;
2. Compared to LES, DES is a more grid-saving turbulence modeling method, and the near-wall velocity profile is also well resulted;
3. It is authors' belief that DES is very capable for wall-bounded flow at higher Reynolds numbers.

## Acknowledgements

The research work described in this paper is partially supported by the NSFC under the grants of 50538050 and 90175039 and the MOST under the grants of 2006AA11Z108 and 2008BAG07B02.

## References

- Kim J, Moin P, Moser R. Turbulence statistics in fully developed channel flow at low Reynolds number. *J. Fluid Mech.*, 177:133–166.
- Petri Majander, Timo Siikonen (2002). Evaluation of Smagorinsky-based subgrid-scale models in a finite-volume computation. *Int. J. Numer. Meth. Fluids*, 40:735–774.

# A Micro-Plane Model for Reinforced Concrete under Static and Dynamic Loadings

Junjie Wang<sup>1\*</sup>, Bifeng Ou<sup>1</sup>, Wei Cheng<sup>1</sup> and Mingxiao Jia<sup>1</sup>

<sup>1</sup>Department of Bridge Engineering, Tongji University, Shanghai 200092, China

**Abstract.** A dynamic constitutive model for reinforced concrete based on microplane model M4 for plain concrete was presented. The model is established based on two hypotheses as strain being parallel coupling and macro stress being superposition of those on all microplanes. The constitutive model of Cowper-Symonds considering strain rate effect is adopted for steel. This model is adapted for explicit computational algorithm. This model is calibrated and verified by comparison with test data.

**Keywords:** reinforced concrete, microplane, constitutive model, strain parallel coupling.

## 1 Introduction

A proper constitutive model of reinforced concrete is crucial for nonlinear structural analysis problems. Till now, there have been mainly three kinds of classical constitutive model of reinforced concrete for the finite element analysis of reinforced concrete, i.e., detached model, combined model and integral model (Guo, *et al.*, 2003). These classical models, in which the mechanical properties of material is formulated directly in terms of stress and strain tensors and/or their invariants, have been extensively investigated and programmed for FEM computation. But as mentioned by (Bažant *et al.*, 2000), these classical approaches has probably entered a period of diminishing returns, since a great effort yields only minor and insufficient improvements. Much more promising and conceptually transparent is the microplane model, in which the constitutive law is formulated in terms of vectors rather than tensors—as a relation between the stress and strain components on a plane of any orientation in the material microstructure, called the microplane (Bažant *et al.*, 1984).

Compared with the classical tensorial constitutive models based on tensorial invariants, nine potent advantages of microplane model were stated (Bažant *et al.*,

---

\* Corresponding author, e-mail: jjqxu@gmail.com

1996). However, microplane models (M1-M5) have been developed only for plain concrete, not for reinforcement concrete so far. As we know, reinforcement concrete is more commonly used than plain concrete in structures. It is needed to improve the microplane model to consider the effects of reinforcement steel. A dynamic constitutive model for reinforced concrete based on microplane model M4 for concrete (Bažant et al., 1996) is presented in this paper.

## 2 Reinforced Concrete Microplane Model

### 2.1 Hypotheses of Strain Parallel Coupling

In order to consider the effect of steel, we assume steel and concrete on the microplane have the same strain or strain increment. This method has been used to build steel fiber concrete model in Bažant et al. (1996) as,

$$\epsilon_{ij}^s = \epsilon_{ij}^c = \epsilon_{ij} \tag{1}$$

Where  $\epsilon_{ij}^s$  and  $\epsilon_{ij}^c$  are steel and concrete strain tensors respectively.

### 2.2 The Orthogonal Disposing Method for Steel

A set of three orthogonal directions are chosen according to the arrangements of the reinforcement bars in concrete structures (Figure 1a), and then the area of a reinforcement bar can be projected to the set of three orthogonal direction (Figure 1b),

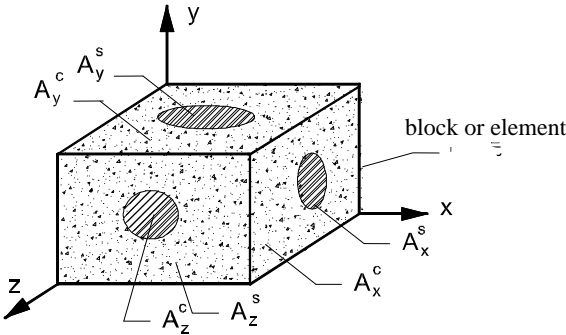


Figure 1. (a) Three orthogonal directions for steel and concrete

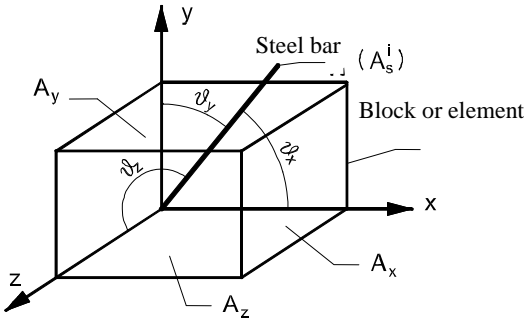


Figure 1(b) Three orthogonal directions and projection relations

Let the reinforcement ratio of the three directions are  $p_x$ ,  $p_y$  and  $p_z$  respectively. Based on projection relations and modified elastic modulus, we obtain:

$$p_x = \frac{1}{A_x} \sum_{i=1}^N \frac{E_s^i}{E_x} A_s^i \cos \theta_x^i, \quad p_y = \frac{1}{A_y} \sum_{i=1}^N \frac{E_s^i}{E_y} A_s^i \cos \theta_y^i, \quad p_z = \frac{1}{A_z} \sum_{i=1}^N \frac{E_s^i}{E_z} A_s^i \cos \theta_z^i \quad (2)$$

where  $p_x$ ,  $p_y$  and  $p_z$  are equivalent area reinforcement ratio in three main direction  $x$ ,  $y$  and  $z$ .  $N$  is reinforcement number;  $\theta_x^i$ ,  $\theta_y^i$  and  $\theta_z^i$  are direction angles for reinforcement with  $x$ ,  $y$  and  $z$  axes respectively;  $A_s^i$  is the area of  $i$ -th reinforcement bar;  $A_x$ ,  $A_y$  and  $A_z$  are element section area in  $x$ ,  $y$  and  $z$  directions respectively;  $E_s^i$  is the elastic modulus of  $i$ -th reinforcement bar;  $E_x$ ,  $E_y$  and  $E_z$  are elastic modulus in  $x$ ,  $y$  and  $z$  directions respectively.

### 2.3 Constitutive Theory for Reinforcement Concrete

The effects of reinforcement bars are mainly: (1) increases the normal stress on the microplane; (2) improve the ductility after the crack of concrete; (3) change the mechanic behavior of concrete, such as crack form of concrete is changed due to the bond-slip performance (which is beyond the content of this paper). The affection of reinforcement bars to the normal stress on the microplane and to the crack can be presented through the reinforcement area projected to the normal vector (Figure 1).

The stress contribution of steel and concrete to the whole stress should be calculated when considering the affection of steel. The stress equilibrium equation

can be written as  $A\sigma = A_c\sigma_c + A_s\sigma_s$  ( $A = A_c + A_s$ ;  $A$ ,  $A_c$ ,  $A_s$  are whole area, concrete area and steel area respectively), and can be written as  $\sigma = p_c\sigma_c + p_s\sigma_s$  using area ratio ( $p_c, p_s$  are area ratio of concrete and steel and can be written as  $p_s = A_s / A$ ,  $p_c = 1 - p_s$  respectively). In order to keep the symmetry of stress tensors, we can also use the square root of area ratio matrix. The stress contribution of the two kinds of materials can be written as:

$$\sigma_{ij}^s = P_{ik}^s \sigma_{kn}^{s0} P_{nj}^s, \quad \sigma_{ij}^c = P_{ik}^c \sigma_{kn} P_{nj}^c \tag{3}$$

where  $\sigma_{ij}^s, \sigma_{ij}^c$  are the stress contribution to the whole stress of steel and concrete,  $\sigma_{kn}^{s0}, \sigma_{kn}$  are stress of steel and concrete ( $\sigma_{kn}$  can be calculated according to

M4 and  $\sigma_{kn}^{s0}$  will be discussed later),  $P_{ij}^s = \begin{cases} \sqrt{p_i}, i = j \\ 0, i \neq j \end{cases}$ ,

$P_{ij}^c = \begin{cases} \sqrt{1 - p_i}, i = j \\ 0, i \neq j \end{cases}$  are reinforcement area ratio square root matrix of steel and

concrete respectively.  $p_1, p_2$  and  $p_3$  are reinforcement area ratio along coordinate direction of  $x_1, x_2$  and  $x_3$  and  $p_i = A_s^i / A^i$  ( $A_s^i$  and  $A_c^i$  are the whole area of steel and concrete in direction  $i$ ).

Taking the contributions of both steel and concrete into account, the whole stress can be superposed by stress of steel and concrete, i.e.

$$\sigma_{ij} = \sigma_{ij}^s + \sigma_{ij}^c \tag{4}$$

where  $\sigma_{ij}^s, \sigma_{ij}^c$  are steel and concrete strain and stress tensors respectively.

### 2.4 The Constitutive Model of Steel

Proper stress and strain relation for steel should consider the following aspects: tensile and compress behavior, yield and strengthen behavior, fracturing rate hardening behavior. The classical Cowper-Symonds rate dependent kinematic plasticity constitutive model, called EPKH (which means elastic-plastic behavior with kinematic hardening), was first presented by Krieg et al. (1976) will be used in this paper.

### 2.5 Rate Dependent Effect

Recent research results (3, 12) show that there are two types of rate effect in the nonlinear triaxial behavior of concrete: rate dependent of fracturing (microcrack growth) associated with the activation energy of bond ruptures and creep (or viscoelasticity). The former is mainly under high strain rate. Microcrack growth when softening occurs, so the fracturing rate effect is reflected by modifying stress boundaries in M4. After considering fracturing, the stress boundaries can be modified as:

$$F_N(\varepsilon_N) = F_N^0(\varepsilon_N)[1 + c_{R2} \operatorname{asinh}(\dot{\gamma} / c_{R1})] \tag{5a}$$

$$F_D^-(\varepsilon_D) = F_D^{0-}(\varepsilon_D)[1 + c_{R2} \operatorname{asinh}(\dot{\gamma} / c_{R1})] \tag{5b}$$

$$F_D^+(\varepsilon_D) = F_D^{0+}(\varepsilon_D)[1 + c_{R2} \operatorname{asinh}(\dot{\gamma} / c_{R1})] \tag{5c}$$

$$F_T(-\sigma_N) = c_{10} \langle \sigma_N^0 - \sigma_N \rangle \left\{ 1 + \frac{c_{10} \langle \sigma_N^0 - \sigma_N \rangle}{E_T k_1 k_2 [1 + c_{R0} \operatorname{asinh}(\dot{\varepsilon} / c_{R1})]} \right\}^{-1} \tag{5d}$$

As for creep effect, the research results by Bažant et al. (1984, 2005) shows that the creep response is basically viscoelasticity, and a nonaging Maxwell spring-dashpot model can fit well test data of short time loading such as shock. The explicit stress increment expression can be written as following when considering creep effect:

$$\sigma_D^{ve} = \sigma_D^i + E_D^n \Delta \varepsilon_D - \Delta \sigma_D^n, \quad E_D^n = \frac{1 - e^{-\Delta t / \tau}}{\Delta t / \tau} E_D^i, \quad \Delta \sigma_D^n = (1 - e^{-\Delta t / \tau}) \sigma_D^i \tag{6a}$$

$$\sigma_V^{ve} = \sigma_V^i + E_V^n \Delta \varepsilon_V - \Delta \sigma_V^n, \quad E_V^n = \frac{1 - e^{-\Delta t / \tau}}{\Delta t / \tau} E_V^i, \quad \Delta \sigma_V^n = (1 - e^{-\Delta t / \tau}) \sigma_V^i \tag{6b}$$

$$\sigma_L^{ve} = \sigma_L^i + E_L^n \Delta \varepsilon_L - \Delta \sigma_L^n, \quad E_L^n = \frac{1 - e^{-\Delta t / \tau}}{\Delta t / \tau} E_L^i, \quad \Delta \sigma_L^n = (1 - e^{-\Delta t / \tau}) \sigma_L^i \tag{6c}$$

$$\sigma_M^{ve} = \sigma_M^i + E_M^n \Delta \varepsilon_M - \Delta \sigma_M^n,$$

$$E_M^n = \frac{1 - e^{-\Delta t / \tau}}{\Delta t / \tau} E_M', \quad \Delta \sigma_M^n = (1 - e^{-\Delta t / \tau}) \sigma_M^i \tag{6d}$$

In equations (5a-6d), definitions of the mathematical symbols can be found in references (Bažant and Gambarova, 1984; Bažant et al., 1996; Bažant et al., 2005).

### 3 Calibration and Comparison with Classical Test Data

The present model has been calibrated and compared to the typical test data available in the literature. They included (1) uniaxial compression tests by Salim Razvi (1995) for different section types and ratio of steel bar, shown in Figure 2 and 3, note that the member label is the same as in the references. (2) tests of reinforced concrete slabs under impact loading by Zineddina (2002, 2007), shown in Figures 4, 5, and 6. The parameters value adopted for Figure. 2 and 3 are listed in Table 1, and for Figures 4, 5, and 6 are listed in Table 2, respectively.

Table 1 Parameters value adopted in axial compression test

$E_c=31.0\text{GPa}$		$\nu_c=0.18$	
$k_1=0.18 \times 10^{-4}$	$k_2=110$	$k_3=12$	$k_4=38$
$c_1=0.62$	$c_2=2.76$	$c_3=4.0$	$c_4=70$
$c_5=3.45$	$c_6=1.30$	$c_7=50$	$c_8=10.5$
$c_9=0.60$	$c_{10}=0.60$	$c_{11}=0.20$	$c_{12}=7000$
$c_{13}=0.20$	$c_{14}=0.50$	$c_{15}=0.02$	$c_{16}=0.01$
$c_{17}=0.40$	$c_{18}=0.04$		

Table 2 Parameters value adopted in impact test

$E_c=32.5\text{GPa}$		$\nu_c=0.18$	
$k_1=1.35 \times 10^{-4}$	$k_2=110$	$k_3=12$	
$c_1=0.62$	$c_{18}=0.4$	$k_4=38$	
$c_{R0}=1.0$	$c_{R1}=1.0 \times 10^{-6}/\text{s}$	$c_{R2}=0.011$	

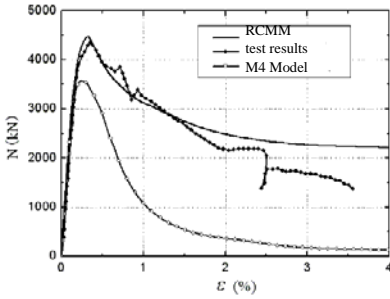


Figure 2. Axial compress curves for member CS22

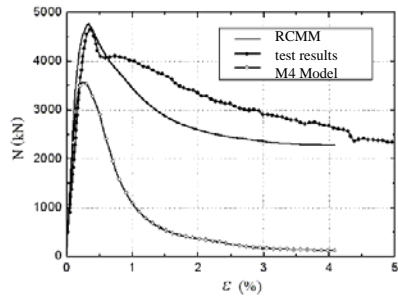


Figure 3. Axial compress curves for member CS24

As seen from Figures 2 and 3, the comparisons are quite good. In general, the fitting are quite good for reinforced member at the beginning. The main differences are at the peak and post-peak. The fitting can be better if we know more about the concrete performance in the test. Compared with plain concrete member, the strength and ductile performances are better for the reinforced concrete member.

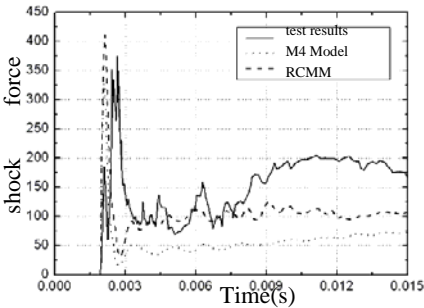


Figure 4. Shock force time history diagram

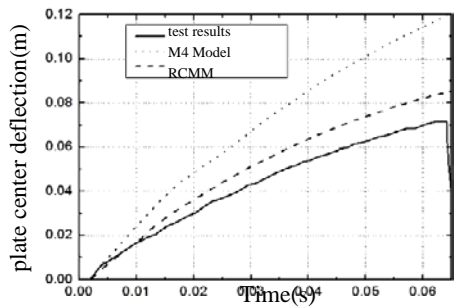


Figure 5. Plate center deflection time history diagram

As seen from Figure 4, there is an obvious pulse in the shock force history and then decline to even. As we can see from Figures 4 and 5, the impact resistance capacity and ductile performance are strengthened for the reinforcement concrete plate and give closer descriptions of the test data. Compared with test data in Figure 6, the computation results are basically similar although differences exist.

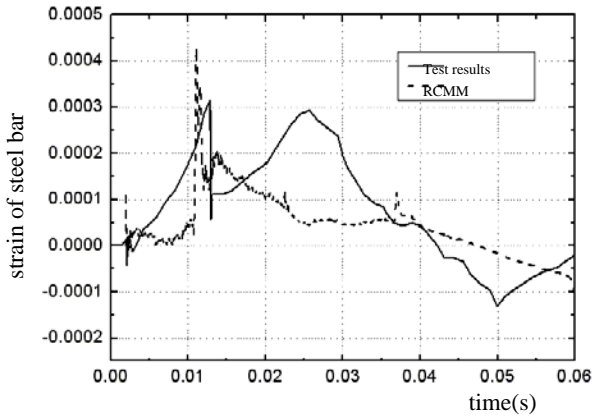


Figure 6. Strain of steel bar in the bottom layer along the short side of the plate

## 4. Conclusions

A dynamic constitutive model for reinforced concrete based on microplane model M4 is presented, which is founded by two hypotheses of strain parallel coupling and stress contribution according to area ratio, and superposition principle of deformation energy. This model can predict steel effect and rate effect based on microplane model for concrete. So it can be used to analyze static or dynamic problems. Although there are a lot of parameters in the model, but it's easy to determine them. The calibration and comparison with classical test data shows that the RCMM model presented in this paper can predict various mechanic property of reinforcement concrete properly.

## Acknowledgement

This paper is supported by NSFC, under No. 90715022 and supported by Chinese high-tech R&D Program (863 Program, No. 2006AA11Z120).

## References

- Bažant Z.P. and Gambarova P. (1984). Crack shear in concrete: Crack band microplane model. *J. Struct. Engrg., ASCE*, 110(9), 2015-2035.
- Bažant Z.P., Xiang Y. and Prat P.C. (1996). Microplane model for concrete. I: Stress-strain boundaries and finite strain. *J. Engrg. Mech., ASCE*, 122(3), 245-254.
- Bažant Z.P., *et.al.*(2000), Microplane model M4 for concrete, I: Formulation with work-conjugate deviatoric stress, *J. Engrg. Mech.*, 126(9), 944-953.

- Bažant Z.P., Ferhun C. and Caner (2005). Microplane model M5 with kinematic and static constraints for concrete fracture and anelasticity. I: Theory, *J. Engrg. Mech.*, 131(1), 31-40.
- Guo Z., Shi X. (2003). *Reforced Concrete Principle and Analysis*. Beijing, Tsinghua Publisher, pp. 319.
- Krieg R.D., Key S.W. (1976). Implement of time dependent plastic theory into structural computer programs. Constitutive equations in viscoplasticity. *Computational and Engineering Aspects, ASME*, 20, 125-137.
- Salim Razvi. (1995). Confinement of normal and high-strength concrete columns (D). University of Ottawa, Ottawa, Canada.
- Zineddina M. (2002). Behavior of structure concrete slabs under impact loading (D). The Pennsylvania State University.
- Zineddina M. and Krauthammer T. (2007). Dynamic response and behavior of reinforced concrete slabs under impact loading. *Int. J. Impact Engrg.*, 34, 1517-1534.

*“This page left intentionally blank.”*

# Behavior Optimization of Flexible Guardrail Based on Numerical Simulation

Peng Zhang<sup>1,2\*</sup>, Deyuan Zhou<sup>2</sup> and Yingpan Feng<sup>3</sup>

<sup>1</sup>China State Construction Engineering Corporation, Beijing 100037, P.R. China

<sup>2</sup>Research Institute of Structural Engineering and Disaster Reduction of Tongji University, Shanghai 200092, P.R. China

<sup>3</sup>Beijing Benz-Daimler-Chrysler Automotive Co. Ltd, Beijing 100022, P.R. China

**Abstract.** In this paper, finite element models which couple Ford F800, semi-rigid and flexible guardrail together in program ANSYS/LS-DYNA were established in order to probe into the feasibility of applying cable flexible guardrail learning from the structural type of semi-rigid guardrail on East-sea bridge to bridge. The result of numerical simulation shows that it is feasible to apply the flexible guardrail structure to bridge guardrail, while guide behavior and safety of flexible guardrail is worse than semi-rigid guardrail.

**Keywords:** flexible guardrail, impacting, ANSYS/LS-DYNA, numerical simulation, optimization

## 1 Introduction

Chinese highway cause has entered the fast-growing stage since 1998. By the end of 2005, China has owned 41 thousand kilometers and ranked second all over the world. According to “National Highway Traffic Network Planning” formulated by Ministry of Transport, Chinese government will invest 2 trillion RMB to construct 51 thousand kilometers highway from 2005 to 2030, and China will own 85 thousand kilometers highway. However, safety issues are increasingly apparent with the development of highway cause. Based on the statistics on traffic accidents by Ministry of Public Security, falling car is the major pattern of serious traffic accidents, and there are 47 and 38 serious traffic accidents in 2005 and 2006 separately throughout China, in which serious traffic accidents account for 44.7% and 60.5%. Therefore, more attention should be paid to the study of road safety, and more efforts should be make to study the behavior of all kinds of guardrails.

There are two main study methods of safety behavior of guardrail, which are real collision test and numerical simulation. Although real collision test is recog-

nized as the most basic and effective way to study the interaction between guardrail and vehicle, it has obvious disadvantages such as expensive cost. In e contrast, numerical simulation has a great advantage in the economy.

Flexible guardrail is a ductile structure with larger buffer capacity than rigid guardrail. Cable guardrail is a typical form of flexible guardrail, which consists of posts and cables tensioned initially. Tensile stress in cable can resist the impact from vehicles, and vehicles out of control change their direction with energy dissipation during the course of collision between flexible guardrail and vehicle. Compared with rigid guardrail and semi-rigid guardrail, flexible guardrail has the larger deformability and energy dissipation capacity. Cables work in elastic stage, so it is easy to be modified after collision. Flexible guardrails are often used on scenic highway because of its convenience to clear snow. However, Flexible guardrails are seldom applied on bridge. Up to now, there are few studies on crashworthiness of flexible guardrail at home and abroad (Lei, 2002; Huang, 1996; Xianrong Chen, 1994; Chenhu Wang, 2007), code JTJ074-94 describes cable flexible guardrail (abb. CFG) in details, but there is no provision on bridge flexible guardrail. Therefore, referring to the structure of semi-rigid guardrail (Zhang, 2008), based on the results of numerical simulation in ANSYS/LS-DYNA, the feasibility of cable flexible guardrail used as bridge guardrail is discussed in this paper.

## 2 Model Descriptions

### 2.1 Guardrail Model

The geometry of CFG guardrail is showed in Figure 1. CFG models are divided into whose section area is 135 mm<sup>2</sup> and whose section area is 180 mm<sup>2</sup> according to the section area of cables. The geometry of WBSG guardrail is showed in Figure 2. Referring to the geometry of east-sea bridge, the two guardrail FEM were established as shown in Figure 3 and Figure 4. In the two models, the distance between posts is 3 m, and link160 was used to model cable. Shell163 was used to model post whose element thickness was 4.5 mm and block whose element thickness is 3 mm. Solid65 was used to model guarding round and bridge floor. The sizes of shell elements were designed to about 15 mm, and link elements were designed to about 20 mm. Material model of steel constituting guardrails except cables was \*MAT\_PIECEWISE\_LINEAR\_PLASTIC, which can take elastoplastic behavior and strain rate stiffness into account. The real relationship between stress and strain of steel is shown in Figure 5. Material model of cable was elastic model because cables should be kept in elastic stage in real collision. No.5 hourglass formulation (Flanagan-Belytschko stiffness form with exact volume integration) was use to control hourglass energy caused by single point gauss integration used

in solid element, while No.4 hourglass formulation (Flanagan-Belytschko stiffness form) was use to control hourglass energy caused by shell element (Zhang, 2007, 2008).

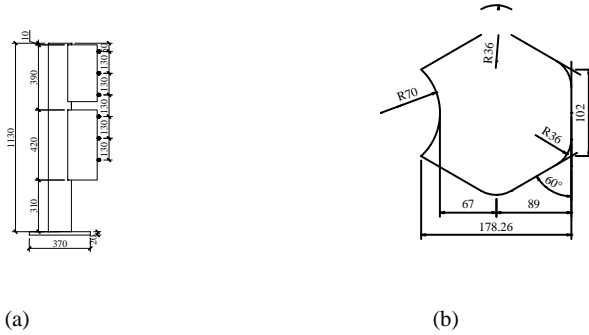


Figure 1. Geometry of CFG

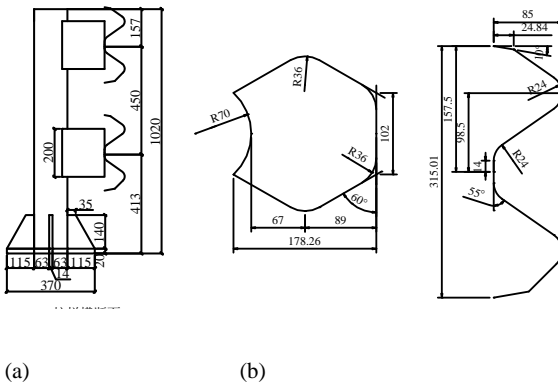


Figure 2. Geometry of WBSG

## 2.2 FEM of Vehicle

FEM of Ford F800 is shown in Figure 6 whose total mass is 7.792t. Outline dimension of Ford F800 is 8582mm×2445mm×3276mm. The formulations of beam, shell and solid are Hughes-Liu, Belytschko-Tsay and constant stress separately. In FEM of the vehicle, there are 21383 elements totally, and AUTOMATIC\_SINGLE\_SURFACE is employed to model contact between parts. RIGID\_BODY, SPOTWELD, NODAL\_RIGID\_BODY and so on are introduced to model connection between parts.

### 2.3 Coupled FEM of Vehicle and Guardrail

The coupled FEM of vehicle and guardrail is shown in Figure 7, in which AUTOMATIC\_SURFACE\_TO\_SURFACE is used to model the contact between wheels and bridge floor, and friction coefficient is set to 0.4. It needs to be emphasized that AUTOMATIC\_SURFACE\_TO\_SURFACE is of no effect to contact between edges, so AUTOMATIC\_GENERAL is employed to model the contact between vehicle and cables. According to the design condition in code, impacting angle is set to  $15^\circ$ , and initial velocity of vehicle is set to 80km/h.

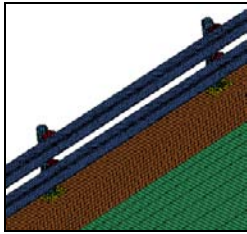
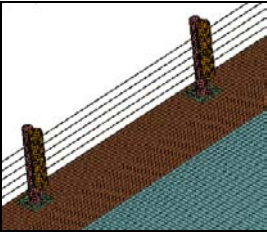


Figure 3. Finite element model of CFG

Figure 4. Finite element model of WBSG

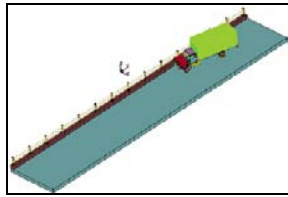
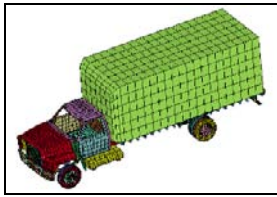
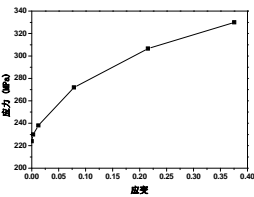


Figure 5. Stress-strain curve of steel

Figure 6. Ford F800 model

Figure 7. Whole model

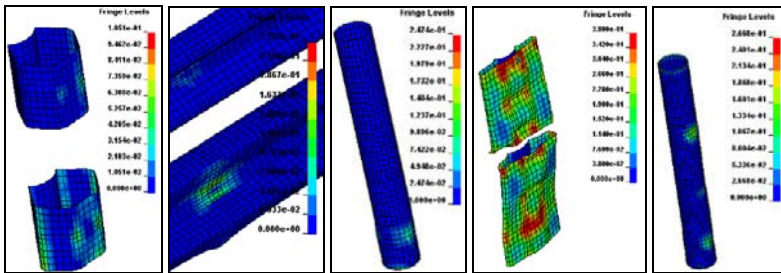
## 3 Analysis of Calculation Results

It is shown in previous studies that WBSG guardrail has better crashworthiness than rigid guardrail, so WBSG guardrail is regarded as a criterion to estimate the crashworthiness of CFG I and II. The animation of simulation results shows that the collision process between vehicle and flexible guardrail can be divided into the following three stages: the front of vehicle impacts guardrail, and then the trailer sways to impact guardrail, finally vehicle departs from guardrail and returns to normal status. The strength and deformation of guardrail, impacting force, nodal acceleration near driver and the track of the vehicle centroid will be the focuses to study in order to estimate the crashworthiness of flexible guardrail.

### 3.1 Strength and Deformation of Guardrail

The plastic strain contours of blocks, W beams and posts constituting WBSG which is impacted by vehicle are shown in Figure 8(a)-(c). Maximum plastic strains are 0.1051, 0.2333 and 0.2474 separately, and in the range of ultimate strain, so these parts don't fail. The simulation results show that WBSG can satisfy bearing capacity requirements, and vehicle can't cross the guardrail. The crashworthiness of WBSG is so good that vehicle doesn't impact posts and move out smoothly.

The plastic strain contours of blocks and posts constituting CFG I which is impacted by vehicle are shown in Figure 8 (d) and (e). It can be seen that blocks deform largely and the top block fail after impacted by vehicle. In contrast, the deformation of posts is smaller than blocks, and concentrates relatively, because posts are not impacted by vehicle directly. The damage extent of CFG I is smaller than WBSG because cables make CFG bear external action uniformly. The relationships between cable stress and time of CFG I and II are shown in Figure 9, and it is obvious that the cable stress of CFG I is beyond the allowing stress. It is necessary that cables don't fail, so it is suggested that the areas of cables should be raised and a 4-unit-7-core cable is recommended for the sake of safety.



(a) (b) (c) (d) (e)

Figure 8. Effective plastic strain

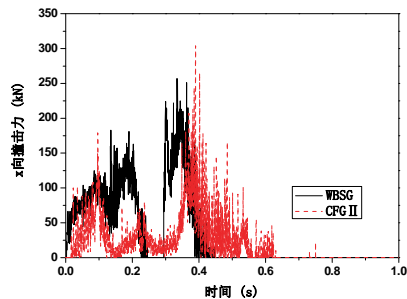
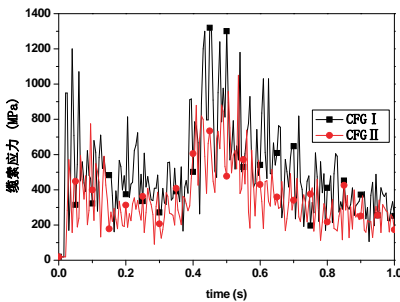


Figure 9. Cable stress-time curve Figure 10 Impacting force between guardrail and vehicle

### 3.2 Comparison of Impacting Force

The relationships between lateral impacting force and time of WBSG and CFG II are shown in Figure 10. The two peak impact force display the three stage of collision course. The peak value of impacting force and maximum displacement of cables are shown in Table 1. It can be seen from Table 1 that there is little difference between peak values of impacting force of the two guardrails while there is large difference between the lateral displacements. The contact time between vehicle and CFG II is 0.2 second longer than that between vehicle and WBSG, which reveals the worse guide behavior of CFG II. Figure 11 gives the time history curve between impacting force of guarding round and vehicle, which shows that vehicle sways more seriously in the collision course with CFG II because of its larger impact to guarding round.

Table 1. Peak value of impacting force, acceleration and displacement

Guardrail type	The first peak value (kN)	The second peak value (kN)	Peak value of acceleration ( $10^3\text{m/s}^2$ )	Peak value of X-displacement (mm)
WBSG	183	257	1.85	200
CFG I	179	270	4.50	296.8
CFGII	173	304	4.53	270.3

### 3.3 The Track of Vehicle

Figure 12 gives the tracks of vehicle centroid in the three cases, which shows that the track transition of CFG is rougher than WBSG, and the X-displacement is larger. Therefore, CFG has worse vehicle guide behavior than WBSG. Figure 13 gives the three stages of collision course between vehicle and guardrail. It is seen clearly from Figure 14 that vehicle has larger deformation in the collision with CFG than with WBSG, which reveals that CFG is more dangerous than WBSG. Figure 15 and 16 give the curves of X-velocity and Y-velocity of vehicle centroid. Centroid Y-velocity in the condition of CFG has larger change than in the condition of WBSG, which shows it is more difficult for vehicle to move out from CFG than WBSG.

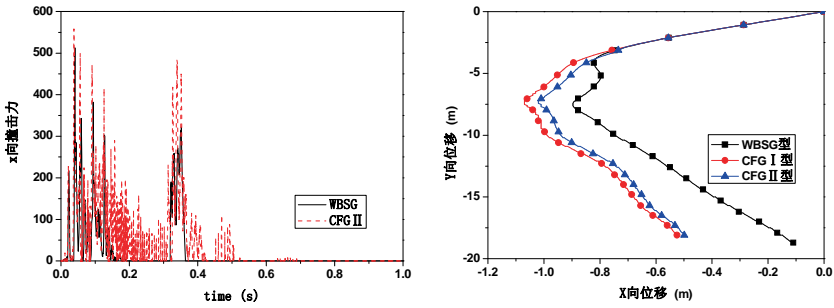


Figure 11. Impacting force between rail guard and vehicle Figure 12 Track of vehicle centroid

### 3.4 Nodal Acceleration near Driver

Resultant acceleration of node 93148 near driver is selected in order to study the safety of driver. Figure 17 gives the relationship between the nodal acceleration and time, and peak value of acceleration is shown in Table 1. It can be seen that the peak value of acceleration in the condition of CFG is higher than in the condition of WBSG, which reveals CFG is more dangerous than WBSG.

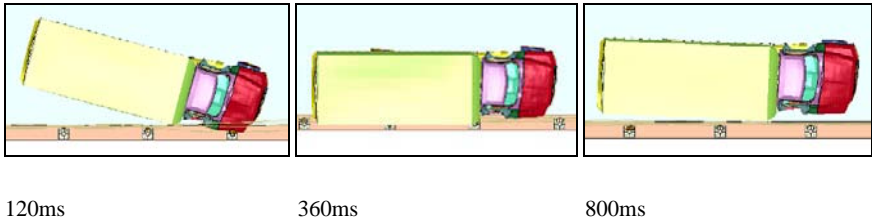
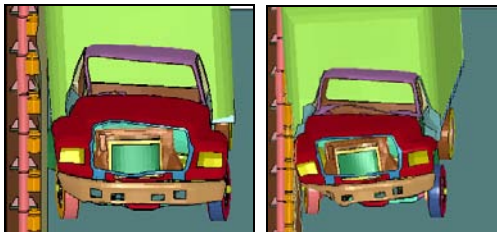


Figure 13. Movement process of vehicle



(a) WBSG (b) CFG II

Figure 14. Deformation of vehicle

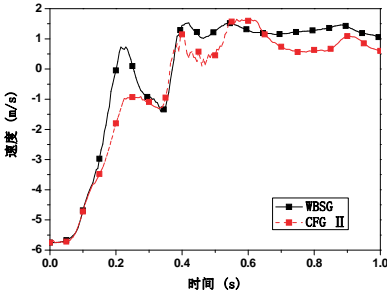


Figure 15. X-Velocity of gravity center of vehicle

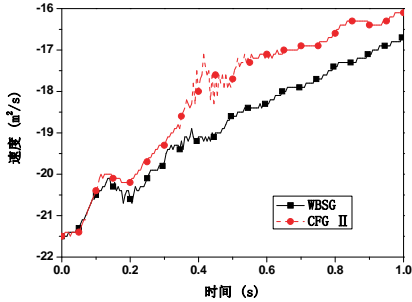


Figure 16. Y-Velocity of gravity center of vehicle

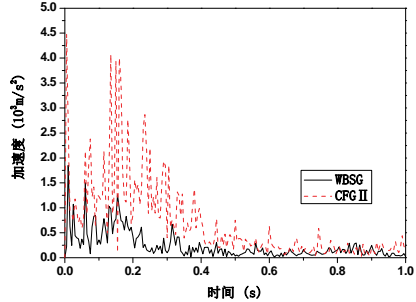


Figure 17. Resultant acceleration of node 93148

## 4 Conclusion and Suggestion

The following conclusions and inspiration through the analysis of calculation results about the collision between vehicle and guardrail based on ANSYS/LS-DYNA:

- (1) Though CFG has worse crashworthiness than WBSG, vehicle can move out from CFG successfully. Therefore CFG combining upper cable-post with nether concrete guarding round can be applied to bridge guardrails.
- (2) CFG I can not be used because cable area is not enough to ensure safety. It is suggested that CFG II should be used as bridge guardrails.
- (3) The design chart of CFG II can be used as the reference of real collection test, and its practicability should be tested.

## Acknowledgements

Project supported by fund: National Natural Science Foundation (50538050).

## References

- Chenhu Wang, Zhiwei Zhou et al. (2007). A study on cable guardrail safety. *Road traffic technology*, 24(7):52-55.
- Shuqin Huang (1996). Road guardrail abroad. *Road Abroad*, 16(4):10-11.
- Xianrong Chen, Ke Wang (1994). The introduce of guardrail design method in America. *Traffic Technology of Henan*, 58(2):28-40.
- Zhang Peng, Zhou Deyuan (2007). A research on the LS-DYNA hourglass formulations. *2nd International Conference on Advances in Experimental Structural Engineering*, 2(2):641-648.
- Zhang Peng, Zhou Deyuan (2007). Comparison and analysis about elastic and elastoplastic dynamic response of multi-story frame. *Earthquake Engineering and Engineering Vibration*, 27(5):40-47.
- Zhang Peng, Zhou Deyuan, Feng Yingpan (2008). Behavior optimization of semi-guardrail guardrail based on numerical simulation. *Journal of Tongji University*, 28(6):56-62.
- Zhang Peng, Zhou Deyuan (2008). A research on analysis accuracy of guardrail impacting simulation based on ANSYS/LS-DYNA. *Journal of Vibration and Shock*, 27(4):147-152+163.
- Zhengbao Lei (2002). Research on the new mechanism of collision protection for semi-rigid fences. *Journal of Vibration and Shock*, 21(1):1-6.

*“This page left intentionally blank.”*

# A Stochastic Finite Element Model with Non-Gaussian Properties for Bridge-Vehicle Interaction Problem

S.Q. Wu<sup>1\*</sup> and S.S. Law<sup>2</sup>

<sup>1</sup> Civil and Structural Engineering Department, Hong Kong Polytechnic University, Hunghom, Kowloon, Hong Kong, People's Republic of China

<sup>2</sup> Civil and Structural Engineering Department, Hong Kong Polytechnic University, Hunghom, Kowloon, Hong Kong, People's Republic of China

**Abstract.** A new Bridge-Vehicle interaction model based on finite element method with considerations on both the randomness of excitation forces and system parameters is given in this paper. The random properties included in the proposed model are assumed to be non-Gaussian. The Karhunen-Loève expansion and polynomial chaos expansion are employed to form a framework for the non-Gaussian processes and the stochastic equation of motion of system is transformed into a set of deterministic differential equations which can be easily solved by using a numerical method. The proposed method is compared with Monte Carlo method in numerical simulations with good agreements. The mean value and variance of the structural responses are found very accurate even for the case with large system uncertainties and excitation randomness.

**Keywords:** bridge-vehicle interaction, stochastic finite element, Karhunen-Loève expansion, polynomial chaos, non-Gaussian

## 1 Introduction

The dynamic responses of a bridge structure subject to moving vehicular loads have been studied for decades. The research on the bridge-vehicle interaction (BVI) problem can be mainly categorized into two kinds according to the technique employed to solve the equation of motion of the bridge-vehicle system: (1) methods based on modal superposition technique (Zhu and Law, 2003); (2) methods based on finite element method (Henchi, 1998). The latter is capable of handling more complex bridge-vehicle models with complex boundary conditions in dynamic analysis compared with the former which needs mode shapes in solving of system equations.

---

\* Corresponding author, e-mail: 06902055r@polyu.edu.hk

The above methods are deterministic with deterministic system parameters of the bridge and the excitation due to moving vehicle. The effect of road surface roughness is considered as deterministic samples of irregular profile according to its power spectral density defined in the ISO standard (1995), moreover, the randomness exists in the system parameters and excitation forces in bridge-vehicle interaction problem. A stochastic analysis should be adopted to study the bridge-vehicle interaction problem. The research on the dynamic response of a bridge deck under random moving forces has been carried out by many researchers (Da Silva, 2004, Seetapan and Chucheeepsakul, 2006) while for the stochastic analysis of the bridge-vehicle system including random system parameters, very few papers can be found (Fryba et al., 2003; Wu and Law, 2008).

In this paper, a new Bridge-Vehicle interaction model based on spectral stochastic finite element method (SSFEM) (Ghanem and Spanos, 1991, Ghanem, 1999) with considerations on both the randomness of excitation forces and system parameters is given. The random properties included in the proposed model are assumed to be non-Gaussian. The Karhunen-Loève (K-L) expansion (Schenk and Schuëller, 2005) and polynomial chaos (PC) expansion (Ghanem and Spanos, 1991) are employed to form a framework for the non-Gaussian processes and the stochastic equation of motion of system is transformed into a set of deterministic differential equations which can be easily solved by using a numerical method. The proposed method is compared with Monte Carlo method in numerical simulations with good agreements. The mean value and variance of the structural responses are found very accurate even for the case with large system uncertainties and excitation randomness.

## 2 System Modelling with Non-Gaussian Properties

The mass per unit length  $\rho(x,\theta)$ , Young’s modulus  $E(x,\theta)$  and damping  $c(x,\theta)$  are assumed as non-Gaussian random processes. The system equation of motion of the structure with random material properties and randomness in the excitations can be rewritten as

$$\rho(x,\theta)A\frac{\partial^2}{\partial t^2}u(x,t,\theta)+c(x,\theta)\frac{\partial}{\partial t}u(x,t,\theta)+E(x,\theta)I\frac{\partial^4}{\partial x^4}u(x,t,\theta)=\sum_{j=1}^{N_F}F_{j1}(t,\theta)\delta(x-v_{j1}t) \tag{1}$$

where  $A$  is the cross-sectional area,  $I$  is the moment of inertia of the beam and  $\theta$  denotes the random dimension.  $u(x,t,\theta)$  denotes the random deflection. Employing the Hermitian cubic interpolation shape functions and with the assumption of Rayleigh damping, the equation of motion of the bridge can be rewritten as

$$M\ddot{R}(t,\theta)+C\dot{R}(t,\theta)+KR(t,\theta)=H_bF(t,\theta) \tag{2}$$

where,  $R$ ,  $\dot{R}$  and  $\ddot{R}$  are the nodal displacement, velocity and acceleration vectors of the structure respectively.  $M$ ,  $C$  and  $K$  are the random mass matrix, damping matrix and stiffness matrix, respectively.  $NN$  is the number of total degrees-of-freedom of the structure.  $H_b$  is a  $NN \times N_F$  location matrix which can be found in Ref (Law *et al* 2004).

$$R = \{R_1(t, \theta), R_2(t, \theta), \dots, R_{NN}(t, \theta)\}^T, \quad F(t) = \{F_1 \quad F_2 \quad \dots \quad F_{NN}\}^T.$$

The non-Gaussian system parameters can be represented according to the framework established by using the K-L expansion and PC expansion, thus the random system matrices can be expressed as follows after truncation,

$$K = \sum_{i1=0}^{K_E} \xi_{i1}(\theta) K_{i1} = \sum_{i1=0}^{K_E} \left( \sum_{k1=0}^{p_1} \Psi_{i1,k1}(\theta) c_{1,k1}^{(i1)} \right) K_{i1} = \sum_{j1=0}^{P_E} \Psi_{j1}(\theta) K'_{j1} \quad (3)$$

$$M = \sum_{i1=0}^{K_\rho} \xi_{i1}(\theta) M_{i1} = \sum_{i1=0}^{K_\rho} \left( \sum_{k1=0}^{p_2} \Psi_{i1,k1}(\theta) c_{2,k1}^{(i1)} \right) M_{i1} = \sum_{j1=0}^{P_\rho} \Psi_{j1}(\theta) M'_{j1} \quad (4)$$

$$C = \sum_{i1=0}^{K_c} \xi_{i1}(\theta) C_{i1} = \sum_{i1=0}^{K_c} \left( \sum_{k1=0}^{p_3} \Psi_{i1,k1}(\theta) c_{3,k1}^{(i1)} \right) C_{i1} = \sum_{j1=0}^{P_c} \Psi_{j1}(\theta) C'_{j1} \quad (5)$$

where  $M_{i1}$  and  $K_{i1}$  are the deterministic matrices calculated from the K-L components of the mass per unit length  $\rho(x, \theta)$  and the Young's modulus  $E(x, \theta)$ .  $C_{i1}$  is calculated based on the assumption of Rayleigh damping.  $\xi_{i1}(\theta)$  and  $\Psi_{j1}(\theta)$  denote the random variables in K-L expansion and PC expansion respectively.

The relationship between the number of K-L components  $K_s$  and the number of Polynomials  $P$  required for a complete expansion of order  $p$  becomes

$$P = 1 + K_s \times p \quad (6)$$

The random nodal displacements and the random excitation forces which are also considered as non-Gaussian process can be derived similarly as the random system parameters respectively by truncating after  $p$  terms as

$$R_i(\theta, t) = \sum_{j2=0}^{P_R} \Psi_{j2}(\theta) u_{j2}(t), \quad F_i(\theta, t) = \sum_{j2=0}^{P_F} \Psi_{j2}(\theta) v_{j2}(t) \quad (7a,b)$$

Take the first and second derivatives of equation (7a) with respect to  $t$  to obtain the expressions for the nodal velocity and acceleration, substitute which into equation (2) together with equation (3), (4), (5) and (7). Then take inner product of both side of equation (2) with  $\Psi_k$  and employ the orthogonal property of Homogenous Chaos (Ghanem and Spanos 1991), results in

$$\sum_{j_2=0}^P \sum_{j_1=0}^{P_\rho} \langle \Psi_{j_1} \Psi_{j_2} \Psi_k \rangle M'_{j_1} \ddot{u}_k(t) + \sum_{j_2=0}^P \sum_{j_1=0}^{P_c} \langle \Psi_{j_1} \Psi_{j_2} \Psi_k \rangle C'_{j_1} \dot{u}_k(t) + \sum_{j_2=0}^P \sum_{j_1=0}^{P_E} \langle \Psi_{j_1} \Psi_{j_2} \Psi_k \rangle K'_{j_1} u_j(t) = H_b \langle \Psi_k^2 \rangle v_k(t) \tag{8}$$

Let

$$K^{(j_2,k)} = \sum_{j_1=0}^{P_E} \frac{\langle \Psi_{j_1} \Psi_{j_2} \Psi_k \rangle}{\langle \Psi_k^2 \rangle} K'_{j_1}, M^{(j_2,k)} = \sum_{j_1=0}^{P_\rho} \frac{\langle \Psi_{j_1} \Psi_{j_2} \Psi_k \rangle}{\langle \Psi_k^2 \rangle} M'_{j_1}, C^{(j_2,k)} = \sum_{j_1=0}^{P_c} \frac{\langle \Psi_{j_1} \Psi_{j_2} \Psi_k \rangle}{\langle \Psi_k^2 \rangle} C'_{j_1}$$

The values of inner product of polynomial chaos  $\langle \bullet \rangle$  are constants and they can be obtained analytically (Ghanem and Spanos 1991).

### 5 Numerical Simulations

The following properties of the bridge model are used in the simulation: length of bridge deck  $L=40\text{ m}$ ; cross-sectional area  $A=4.8\text{ m}^2$ ; second moment of inertia of cross-section  $I=2.5498\text{ m}^4$ ; damping ratio  $\zeta_i=0.02$  for all modes; elastic modulus  $E$  and the mass density  $\rho$  are assumed as random variables with mean value  $5 \times 10^{10}\text{ m/s}^2$  and  $2.5 \times 10^3\text{ kg/m}^3$  respectively and a coefficient of variation denoted as  $COV_\rho$  and  $COV_E$ , respectively. The first five natural frequencies of the bridge deck are 3.9, 15.6, 35.1, 62.5 and 97.6 Hz. Rayleigh damping is assumed. The bridge-vehicle model is shown in Figure 1.

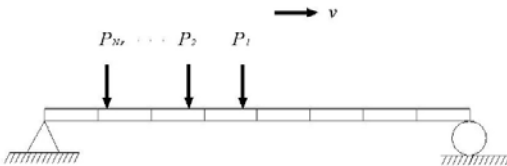


Figure 1. The Bridge-Vehicle System

The random time-varying moving forces are generated with the following mean values,

$$\begin{aligned} F_1 &= 20000(1 + 0.1\sin(10\pi t) + 0.05\sin(40\pi t)) \\ F_2 &= 20000(1 - 0.1\sin(10\pi t) + 0.05\sin(40\pi t)) \end{aligned} \quad (10)$$

using different coefficients of variation (COV) at each time instance. The two loads are moving at a specific speed four meters apart.

The errors between the calculated and reference responses are denoted as

$$RE = \frac{\|R^{calculated} - R^{reference}\|_2}{\|R^{reference}\|_2} \times 100\% \quad (11)$$

In the proposed SSFEM, a kernel for the random field of system parameter has to be defined. The bridge model is divided into eight equal Euler-Bernoulli finite elements of 5 m long each. The lognormal distributed stochastic system parameters in the simulation studies are assumed to have the spatial correlation represented by an exponential auto-covariance function as:

$$C(x_1, x_2) = \sigma^2 \exp\left(-\frac{|x_1 - x_2|}{a}\right) \quad (12)$$

where  $\sigma$  is the standard deviation of system parameter  $E$  or  $\rho$ . A positive dislocation of two points in a spatial domain of interest is set to 0.5m and  $a$  is the correlation length set as unity in the following study. The sampling rate for all the simulations is 200Hz. The proposed SSFEM algorithm is verified with the Monte Carlo simulation with 10000 samples.

Third order polynomial chaos is used to represent the random processes of both the non-Gaussian system parameters and the non-Gaussian excitation forces. The Percentage Error of Mid-span displacement statistics due to different level of excitation randomness by using the SSFEM and the Monte Carlo simulation are compared in Table 1 when  $COV_E = COV_\rho = 20\%$ . Results show that the mean value and variance calculated from the proposed non-Gaussian model and the Monte Carlo simulation respectively are very close to each other.

It may be concluded that the proposed model can accommodate large uncertainties in the system randomness and excitation forces with good performance in the response statistics prediction. The proposed algorithm can obtain accurate results with a COV of system parameter up to 0.3 which is superior to the perturbation method which is only good for small deviations from the center value. With the ability to reduce the number of polynomials  $P$  according to equation (6), the proposed algorithm will be more powerful than existing SSFEM (Ghanem and

Spanos 1991) in engineering application whereby a relative large number of K-L components can be used to represent the stochastic process with a higher frequency of random fluctuations.

Table 1. Percentage Error of Mid-span displacement statistics due to different level of excitation randomness

$COV_E=COV_\rho=20\%$						
$COV_F$	5%	10%	20%	30%	40%	50%
Mean Value	1.81	1.79	1.84	1.84	1.82	1.93
Variance	6.64	3.93	8.27	4.88	5.92	8.45

## 6 Conclusions

The stochastic analysis of the bridge-vehicle interaction problem with non-Gaussian system parameters and excitation forces is presented in this paper. The mathematic model of the bridge-vehicle system is established based on the spectral stochastic finite element method. A new framework is established using finite element method to discretize a second order random field with non-Gaussian property into a multi-dimensional continuous random process. Such process is then represented by both the Karhunen-Loève expansion and the Polynomial Chaos expansion. A reduction in the number of polynomial chaos is proposed enabling a more powerful analytical technique than existing SSFEM in engineering application. Numerical simulations with the proposed method and the Monte Carlo method show good agreement in the results for cases with high level of uncertainties in the excitation and system parameters.

## Acknowledgments

The work described in this paper was supported by a research grant from the Hong Kong Polytechnic University.

## References

- Da Silva J.G.S. (2004). Dynamical performance of highway bridge decks with irregular pavement surface. *Computers and Structures*, 82(11-12), 871-881.
- Fryba L., Nakagiri S. and Yoshikawa N. (2003). Stochastic finite elements for beam on a random foundation with uncertain damping under a moving force. *Journal of Sound and Vibration*, 163(1), 31-45.
- Ghanem R. and Spanos P.D. (1991). *Stochastic Finite Elements: A Spectral Approach*, Springer-Verlag, New York.
- Ghanem R. (1999). Ingredients for a general purpose stochastic finite elements implementation. *Computer Methods in Applied Mechanics and Engineering*, 168(1-4), 19-34.
- Henchi K., Fafard M., Talbot M. and Dhatt G. (1998). An efficient algorithm for dynamic analysis of bridges under moving vehicles using a coupled modal and physical components approach. *Journal of Sound and Vibration*, 212(4), 663-683.
- ISO 8606:1995(E) (1995). Mechanical vibration—road surface profiles—reporting of measured data.
- Law S.S., Bu J.Q., Zhu X.Q. and Chan S.L. (2004). Vehicle axle loads identification on bridges using finite element method. *Engineering Structures*, 26(8), 1143-1153.
- Schenk C.A. and Schuëller G.I. (2005). *Uncertainty Assessment of Large Finite Element Systems*. Springer-Verlag, Berlin/Heidelberg.
- Seetapan P. and Chucheepsakul S. (2006). Dynamic responses of a two-span beam subjected to high speed 2DOF sprung vehicles. *International Journal of Structural Stability and Dynamics*, 6(3), 413-430.
- Wu S.Q. and Law S.S. (2008). Dynamic analysis of bridge-vehicle system with uncertainties based on spectral stochastic finite element. *Computer Methods in Applied Mechanics and Engineering* (under review).
- Zhu X.Q. and Law S.S. (2003). Dynamic behavior of orthotropic rectangular plates under moving loads. *Journal of Engineering Mechanics*, 129(1), 79-87.

*“This page left intentionally blank.”*

# Numerical Analysis on Dynamic Interaction of Mega-Frame-Raft Foundation-Sand Gravel Soil Structure

Bin Jia<sup>1,2\*</sup>, Ruheng Wang<sup>1,2</sup>, Wen Guo<sup>2</sup> and Chuntao Zhang<sup>2</sup>

<sup>1</sup> Department of Civil Engineering, ChongQing University, Chongqing 400044, P.R. China

<sup>2</sup> Department of Civil Engineering and Architecture, Southwest University of Science and Technology, Mianyang 621010, P.R. China

**Abstract.** More and more mega-frame structures are extensively adopted by the whole world, because it has the good flexible layout and the good whole space property. But study on dynamic interaction of mega-frame structure is not systematical. This paper calculates the dynamic interaction of the mega-frame-raft foundation-sand gravel soil structure under seismic waves with finite element method. And the numerical calculation includes five projects and contraposes all kinds of factor including: the interaction, the hypo-frame, the model about raft foundation and the thickness of raft foundation. The natural vibration frequency of mega-frame structure and the maximum displacement of all levels are studied. The interaction action change the dynamic characteristic of the whole mega-frame structure, for example, the natural vibration period is extended, the vibration mode is altered and the maximum displacement of the top floor is increased. The results given by the paper might be a significant guide for the interaction theoretical analysis and the engineering of mega-frame structure.

**Keywords:** mega-frame, interaction, numerical analysis

## 1 Introduction

The earthquake response of the high-rise building is an important issue for it has numerous floors. In addition, the high-rise building is composed of ground, foundation and superstructure, each part has own function and research method, so it's very difficult to analysis the earthquake response because the three parts have complicated relationship and restriction (1981). The mega-frame structure is a widespread structural style in the skyscrapers, which are requested by more height structures. At the same time, a precise computation-model must be suitable for the

---

\* corresponding author, e-mail:jiabin216@126.com

mega-frame structure for that a very small error of the computation-model will be enlarged by the highness to reduce the veracity of the result about static analysis or dynamic analysis (2008). So it is extremely significative to research the dynamic properties and the internal mechanism of mega-frame which has three parts in engineering (2001). The article will carry on the numerical simulation of the mega-frame structure and analysis the internal mechanism of the three parts to create a calculating method that could reflect the dynamic mechanism accurately.

## 2 Numerical Model

A numerical model of the mega-frame-raft foundation-sand gravel soil structure is built by using ANSYS soft. The ground is the sand gravel soil layer which is calculated with solid 45 as a computing element. And boundaries of the ground are intercalated by the 3D visco-elastic artificial boundaries which are simulated by the element named COMBINE 14(2004). The raft foundation on sand gravel is analyzed by the thin plate theory, the moderately-thick plate theory and the space elastic theory, which was simulated by three numerical model elements: SHELL63, SHELL43 and SOLID45. The super mega-frame is simulated consulting the actual project, for example, geometry size and concrete strength. And the modulus about the numerical model are follows: the elastic modulus “E” as  $3.0 \times 10^{10}$ Pa, Poisson’s ratio as 0.2, denty “ $\rho$ ”as 2500Kg/m<sup>3</sup>, gravity acceleration as 10.0 KN/kg, live load as 2.0 KN/m<sup>2</sup>. The numerical models of mega-frame-raft foundation-sand gravel soil structure are showed in the Figure 1. The dynamic analysis adopts the Ninghe earthquake wave to vibration model. Five kinds of plan computations are processed according to Table 1.

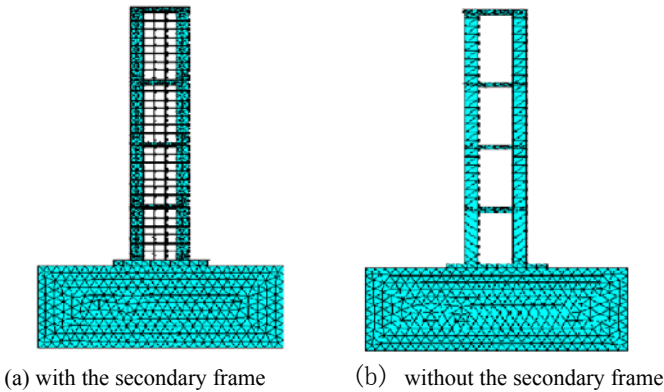


Figure 1. Finite element model of mega frame.

Table 1. Project of numerical calculation

	Ground	Foundation	Superstructure
Plan1	——	the bottom of super-structure is fixed	Mega-frame without the secondary frame
Plan2	——	the bottom of super-structure is fixed	Mega-frame with the secondary frame
Plan 3	Solid45, sand gravel soil parameter	Solid 45, 3m	Mega-frame with the secondary frame
Plan 4	Solid45, sand gravel soil parameter	Solid 65, 3m	Mega-frame with the secondary frame
Plan 5	Solid45, sand gravel soil parameter	Solid 65, 5m	Mega-frame with the secondary frame

### 3 Dynamic Interaction Analysed by Periods

For foundation was hypothesized to be rigid by consuetude, the periods of structure is approximate during dynamic analysis. After relating to the movement of soil, the flexibility of the whole structure is higher and rigidity is lower although the movement of soil is comparatively faint. Table 2 showed that the periods considering the dynamic interaction increases. Thus it is distinct that the interaction between superstructure and foundation would changes the dynamic characteristic of the mega-frame structure.

The primary period of the Mega-frame with secondary frame which was calculated by the plan 2 is delayed 0.155 seconds than the plan 1, for which the stiffness of Mega-frame connected with secondary frame increases. Meanwhile, the primary period of the Mega-frame considering the dynamic interaction by the plan 4 is delayed 0.148 seconds than the plan 1. So the increasing stiffness by secondary frame is quite to the reducing stiffness by interaction. But the conclusion is likely to fit the structure whose ground is the sand gravel soil which has high rigidity, whether other soil layers have this character need more study. Finally, the thickness of raft foundation increase 2 meters by the plan 5, comparing to the plan 4, the periods decrease during the dynamic interaction.

SOLID45 is used for the 3-D modeling of solid structures which has plasticity, creep, swelling, stress stiffening, large deflection, and large strain capabilities. And SOLID64 is similar to the SOLID45 which is capable of cracking in tension and crushing in compression. The most important aspect of this element is the treatment of nonlinear material properties. The element may be used to model geological materials (such as rock). The two elements were used to model raft foundation both considering the interaction, and the calculation results have the accordant nature periods. Thus dynamic interaction would take the SOLID45 element to simulate raft foundation in order to economize computation time during numerical model.

Table 2. Period about all calculation projects (Unit: s)

Vibration modes	Plan1	Plan2	Plan3	Plan4	Plan5
1	2.000	1.845	1.868	1.852	1.853
2	1.920	1.744	1.766	1.791	1.793
3	0.791	0.605	0.611	0.630	0.630
4	0.545	0.491	0.496	0.494	0.494
5	0.483	0.433	0.438	0.443	0.444

#### 4 Dynamic Interaction Analysed by the Maximum Displacement

The most horizontal displacements of each mega-frame layer are shown by Table 3 after the time history analysis. The maximum displacement of the top story in the mega-frame considered the interaction is bigger than that assuming the foundation rigid. Therefore the influence of raft foundation and sand gravel soil can not be ignored during the displacement analysis of superstructure, and the maximum displacement of the top story in the mega-frame is composed of the movement of foundation and the deformation of structure during the interaction. At the same time, the maximum displacement of the top story in the mega-frame without secondary frame increase, for example, the calculation results by the Plan 1. So the maximum displacement of the top story by Plan 2 is the smallest in all calculation projects. By comparing results which were shown by Table 2, it can be concluded that the higher stiffness which is engendered by secondary frame under seismic load is significant, and it is distinct that the interaction can change the dynamic behavior of the mega-frame structure.

Table 3. Maximum displacements of each part with all calculation projects (Unit: m)

Mega-frame		Plan1	Plan2	Plan3	Plan4	Plan5
Top floor	Top	0.0293	0.0271	0.0281	0.0287	0.0289
	Bottom	0.0206	0.0211	0.0206	0.0206	0.0205
Third floor	Top	0.0185	0.0171	0.0183	0.0182	0.0181
	Bottom	0.0152	0.0133	0.0154	0.0153	0.0151
Second floor	Top	0.0134	0.0126	0.0132	0.0133	0.0132
	Bottom	0.0106	0.0104	0.0107	0.0106	0.0106
Ground floor	Top	0.0061	0.0065	0.0063	0.0062	0.0062
	Bottom	0.0024	0.0020	0.0028	0.0026	0.0026

## 5. Conclusion

The dynamic interaction of mega frame-raft foundation-sand gravel soil was analyzed by numerical calculation. The calculation model about the upper part of the mega-frame structure is researched, and the secondary frame can change the dynamic response of mega-frame structure. Among these work, the conclusions that the increasing stiffness by secondary frame is quite to the reducing stiffness by interaction is innovative.

## References

- Wang R.H., Guo W. et al. (2008). Study on dynamic characteristics of mega-frame structure based on cooperative effect theory. *Journal of Huazhong University of Science and Technology (Urban Science Edition)*, 25(4), 61-63 [in Chinese].
- Zhao M. (2004). Study on the viscous-spring boundary and the transmitting boundary. Master's degree paper. Beijing University of Technology, 37-68 [in Chinese].
- Zhou X.F. (2001). Static, aseismic and wind-resistant analysis of steell mega-frame. Doctor's degree paper. Zhejiang University, 15-18 [in Chinese].
- Zhu B.L., Cao M.B. et al. (1981). Numerical analysis of framed structure-foundation-soil interaction, with linear and non-linear soil behavior models. *Journal of Tongji University*, 4), 15-31 [in Chinese].

*“This page left intentionally blank.”*

# **FLUID AND STRUCTURES**

*“This page left intentionally blank.”*

# Structural Static Performance of Cable-Stayed Bridges with Super Long Spans

Jinxin Cao<sup>1,2</sup>, Yaojun Ge<sup>1,2\*</sup> and Yongxin Yang<sup>1,2</sup>

<sup>1</sup>State Key Laboratory for Disaster Reduction in Civil Engineering, Shanghai 200092, China

<sup>2</sup>Department of Bridge Engineering, Tongji University, Shanghai 200092, China

**Abstract.** The ultimate span length of cable-stayed bridge has been an interesting issue among bridge engineers for a long time. Although knowledge about the span limitation is growing, little is known about the difference of structural mechanical performances among cable-stayed bridges with even larger spans. Four bridges with main span length from 1,000 to 2,500m were preliminarily designed and calculated, with their components and main parameters adopted based on existing long-span cable-stayed bridges such as Sutong Bridge. The bridge models with the spans from 1,000m to 2,000m can meet requirements of strength, rigidity and stability, but in-plane stability of the 2,500m model can not be ensured.

**Keywords:** cable-stayed bridge, ultimate span length, trial design, numerical calculation, static performance

## 1 Introduction

The evolution of modern cable-stayed bridges has experienced only half a century since the completion of the first modern cable-stayed bridge, Stromsund Bridge in Sweden with a main span of 183m in 1956. However, the main span length has jumped to almost 6 times longer, from less than 200m to 1,088m of Sutong Bridge, presenting utterly different ways from other bridge types.

For such a short period, the span length of cable-stayed bridges has grown into the reasonable span range for suspension bridge which was widely recognized not long ago. Besides, in China and in the world, cable-stayed bridges with longer spans are still required to be planned and constructed. This situation makes it a necessity to answer the question how long the span length of cable-stayed bridge can be extended.

Guohao Li (1987) predicted the maximum span length could reach 3,600m from the perspective of nonlinear effect of cable's elastic modulus. Muller (1990)

---

\* Corresponding author, e-mail: yaojunge@tongji.edu.cn

proposed a Bi-stayed system which helped to reach 3,000m as a reasonable limit. N.J. Gimsing (2002) thought 5,000m may be realistic with present cable materials while 20km may be possible if new materials and structural systems were adopted. Bohui Wang (2003) and M. C. Tang (2006) pointed out the limitation of span length was the allowable stress of the girder, and their recommended spans are 2,510m and 5,000m, respectively. Nagai (2004) gave a rational span of 1,400m as the span limit considering both mechanical and economical issues.

In this paper, the feasibility of the 2,500m main span, which was nearly the technical limit of cable stayed bridge was investigated and trial designs of bridges with the main span from 1,000m to 2,000m were compared.

## 2 Bridge Models

### 2.1 Design Conditions

Four cable-stayed bridges with the main span length of 1,000, 1,500, 2,000, 2,500m were preliminarily designed under the following conditions:

1. Material grade Q345qD (for 1000m model), Q420qD (for 1500m and 2000m model) and Q460qD (for 2500m model) were used in girder. The tower adopted concrete degree C55 or C60. The allowable stress and stress amplitude of cables are 708, 250MPa.

2. The dead load per unit length ( $W_D$ ) is calculated by:  $W_D=1.4\gamma_s A_s+60$  (KN/m), where  $\gamma_s$  is the weight density of steel;  $A_s$  is cross-sectional area of girder; a coefficient of 1.4 is used to taken into account the weight of diaphragms, cross beams and other components; and 60KN/m, the superimposed dead load, accounts for pavement, handrails, curbs and attachments, etc according to Sutong Bridge.

3. The uniform live load ( $W_L$ ) is calculated by:  $W_L=10.5\times 8\times 0.5\times 0.93=39$  (KN/m), where 10.5KN/m is the standard value of uniform lane loading according to the Chinese Code, 0.5 and 0.93 is multi-lane reduction factor and longitudinal discount factor for long span bridge, respectively, and 8 is the number of lane. Similarly, concentrated load ( $P_L$ ) is:  $P_L=360\times 8\times 0.5=1440$  (KN/m).

### 2.2 Main Parameters

Except for design of structural components, general parameters such as the cross-sectional shape of girder, the ratio of main span to side span, the ratio of tower height (from the deck level) to main span length may influence the structural performance of cable-stayed bridges.

1. The ratio of main span to side span affects the structural deformation property and the fatigue performance of cables. For most typical steel cable-stayed bridges, this ratio lies between 2 to 3 (Zhou et al 2004). In this paper, the ratio of all bridge models is 2.5. For the side span, two (1000m and 1500m model) or three (2000m and 2500m model) auxiliary piers are installed at a distance of 100m in order to increase in-plane flexural rigidity of the models.

2. The span-to-width ratio of the girder cross section is the ratio of main span to girder width which is widely believed to be less than 40 in order to ensure out-plane stability. Nagai (2004) discussed the feasibility of a 1,400m span steel cable-stayed bridge with the span-to-width ratio of 56. In order to study key problems of these models with larger spans from the perspective of static performance, the same girder configuration as Sutong Bridge was used in the current investigation and the maximum span-to-width ratio of the 2,500m model is 70.6. (See Table 2)

3. The span-to-depth ratio is the ratio of main span to girder depth which is considered to lie between 40 and 130 in order to ensure the in-plane global stability. However, this ratio of Tataru Bridge is up to 330 and Nagai (2008) pointed out that in-plane global instability problem need not considering if this ratio was less than 600-700. Designs in this paper adopt 4m depth for girders of all models with the maximum span-to-depth ratio of 625.

4. The tower height from deck level for all models is one fifth of their main span lengths which typically lies between one fourth and one sixth of the main span length (Lin 2004).

Table 1. Main parameters of bridge models

Span/m	Side span $L_1$ /m ( $L/L_1$ )	Girder width/m (span to width ratio)	Girder depth/m (span to depth ratio)	Tower height(from deck) H/m ( $H/L$ )
1088	500 (2.2)	35.4 (30.7)	4 (272)	230 (1/4.7)
1000	400 (2.5)	35.4 (28.2)	4 (250)	200 (1/5)
1500	600 (2.5)	35.4 (42.4)	4 (375)	300 (1/5)
2000	800 (2.5)	35.4 (56.5)	4 (500)	400 (1/5)
2500	1000 (2.5)	35.4 (70.6)	4 (625)	500 (1/5)

Table 2. Cross sectional properties

Model	Steel grade	$A/m^2$	$I_z/m^4$	$I_y/m^4$	$J/m^4$	$t_u/mm$	$t_b/mm$	$t_w/mm$
Sutong	Q345qD	1.73~2.48	4.73~7.20	219.85~293.51	13.20~20.58	14~22	12~22	30
1000	Q345qD	1.73~2.32	4.73~6.57	219.85~282.04	13.20~18.63	14~20	12~18	30
1500	Q420qD	1.73~3.46	4.73~10.24	219.85~405.91	13.20~31.54	14~36	12~34	30~40
2000	Q420qD	1.73~5.28	4.73~15.88	219.85~618.56	13.20~50.53	14~58	12~56	30~60
2500	Q460qD	1.73~5.43	4.73~16.35	219.85~633.76	13.20~52.13	14~60	12~58	30~60

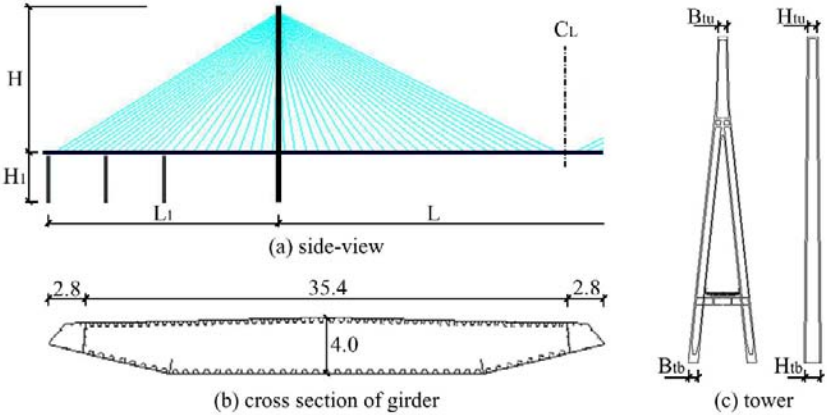


Figure 1. Bridge model

Table 3. Tower parameters

Model	$H(H_1)$ /m	$B_{tw}$ /m	$B_{tb}$ /m	$H_{tw}$ /m	$H_{tb}$ /m
Sutong	236(64)	8	8	9	15
1000	250(80)	8	8	9	15
1500	300(80)	11	11	12	20
2000	400(80)	14	14	16	24
2500	500(80)	17	17	20	28

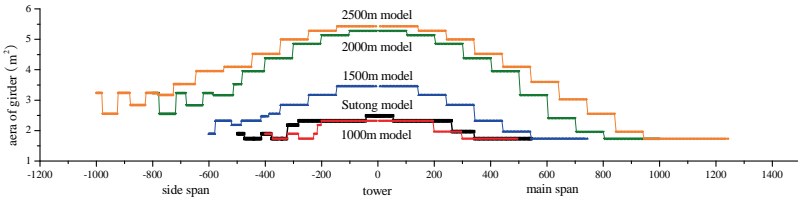


Figure 2. Area of girder

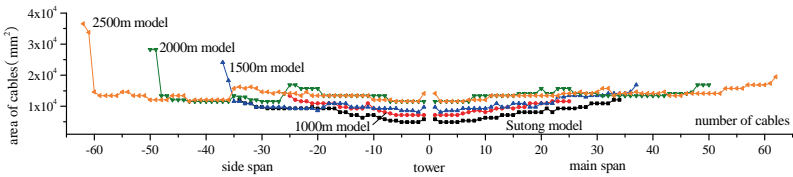


Figure 3. Area of cables

## **2.3 Component Areas**

### 1. Girder

The girder areas of trail designs are shown in Figure 2.

### 2. Cable

The cable areas of trail designs are shown in Figure 3.

### 3. Tower

The configuration of concrete towers of bridge models are shown in Figure 1 and Table 3 provides the parameters.

## **3 Static Analysis**

The structural static analysis of above bridge models was carried out by using Finite Element Analysis (FEA) software ANSYS. In FEA, the girder and the pylon were simulated by beam elements, while cables were simulated by tension-only truss elements. Nonlinear factors, large deformation, initial internal force and sag of the cable, were taken into consideration. The first and dominant issue of the design is to compute and achieve the ideal state, followed by the calculation of live load.

### **3.1 Stress**

Because of the effects of temperature change, base movement, impact effect and so on have not been explicitly considered in the preliminary design, the allowable stress of the girder is adopted from the stress level of Sutong Bridge in relevant state besides the requirement of material allowable stress. For example, the maximum stress of Sutong Bridge in the complete state is about 110MPa, thus the allowable stress under dead load of 1000m model (Q345qD) should be less than 110MPa, and 1500m and 2000m model 130MPa (Q420qD), 2500m model 150MPa (Q460qD).

The response under dead load and live load in the complete state is shown in Figures 4 and 5.

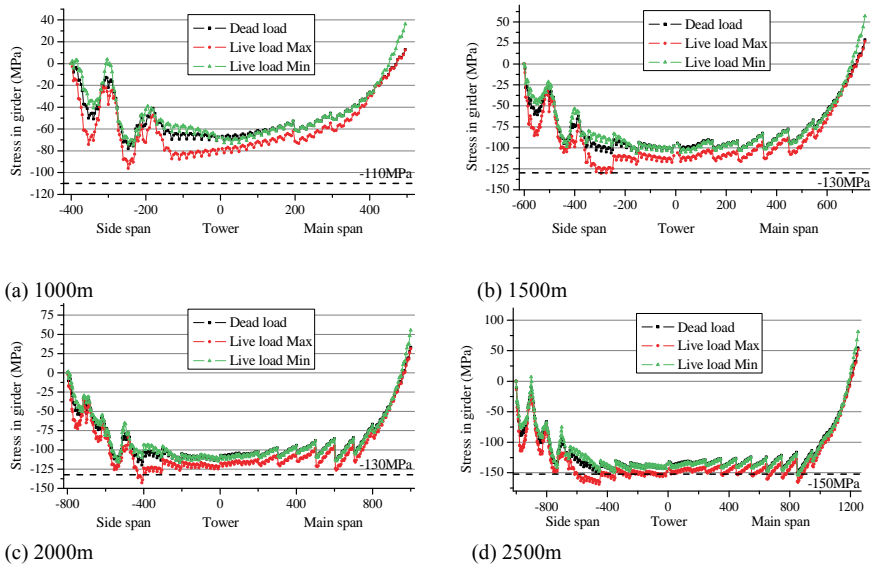


Figure 4. Stress combination in girder

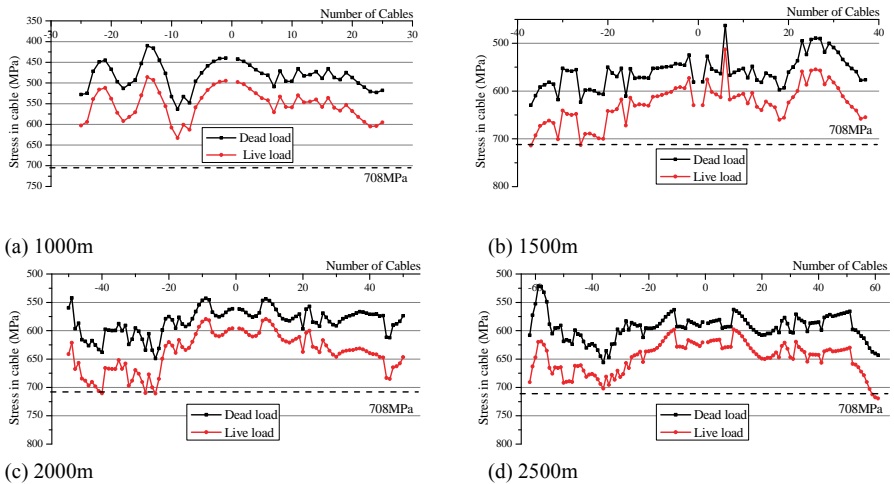


Figure 5. Stress combination in cable

### 3.2 Deformation

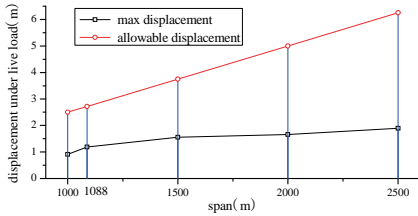


Figure 6. Displacement under live load

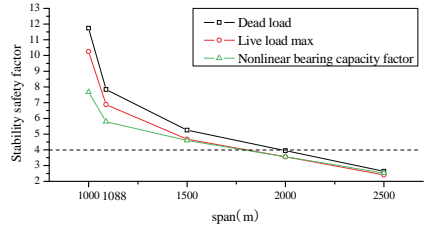


Figure 7. Stability safety factor

Displacements under live load of all models are less than the allowable one,  $L/400$  (see Figure 6), according to the Chinese Code.

### 3.3 In-plane Stability

A critical point will be reached at which the determinant of the total stiffness matrix is zero if the loads that cause the initial stress keep increasing. Such a bifurcation stability problem can be solved as an eigenvalue problem. Figure 7 shows the values under different load cases.

Then the stability analysis can be combined with the nonlinear analysis, which was required for long-span cable-stayed bridges. A step-by-step nonlinear static analysis method was used to obtain the critical load which makes the structure to unstable (also see Figure 7).

Considering the requirement of the Chinese code, 2000m model seems to reach the in-plane stability limit using box girder with 4m depth while the 2500m model can not meet the requirement.

## 4 Conclusions

1. Referring to the existing longest cable-stayed bridge, Sutong Bridge, bridge models with main span from 1,000m to 2,500m were preliminarily designed and analyzed from the perspective of structural static performance.
2. By adopting steel grade Q345qD and Q420qD and the same girder configuration as Sutong Bridge, the bridge models with the main spans of 1,000m, 1,500m and 2,000m can meet all requirements of strength, rigidity and in-plane stability.

3. Even with steel grade Q460qD, the 2,500m bridge model fails to ensure the safety of in-plane stability although strength and rigidity are good enough.
4. The dynamic properties and aerodynamic characteristics still need to be further investigated to help the practices of super long-span cable-stayed bridges.

## Acknowledgements

The research work described in this paper is partially supported by the NSFC under the grant of 90175039 and the MOC under the grant of 2006-318-494-26.

## References

- Chongqing Communications Research & Design Institute (2007). *Guidelines for Design of Highway Cable-stayed Bridge*. Beijing: China Communications Press [in Chinese].
- CCCC Highway Consultants (2004). *General Code for Design of Highway Bridges and Culverts*. Beijing: China Communications Press [in Chinese].
- Gimsing N.J. (2002). *Cable-Supported Bridge-Concept and Design*. Beijing: China Communications Press [in Chinese].
- Lin Yuanpei (2004). *Cable-Stayed Bridge*. Beijing: China Communications Press [in Chinese].
- Nagai M., Fujino Y. et al. (2004). Feasibility of a 1400 m Span Steel Cable-Stayed Bridge. *Journal of Bridge Engineering*, 9(5), 444-452.
- Wang Bohui (2004). *The Development of Cable-Stayed Bridges and Chinese Experiences*. Beijing: China Communications Press [in Chinese].
- Yin Delan (2006). *Man-Chuang Tang and Bridges-Section of China*. Beijing: Qsinghua University Press [in Chinese].
- Zhou Mengbo (2004). *Cable-Stayed Bridge Handbook*. Beijing: China Communications Press [in Chinese].

# Parametric Oscillation of Cables and Aerodynamic Effect

Yong Xia<sup>1\*</sup>, Jing Zhang<sup>1</sup> and Youlin Xu<sup>1</sup>

<sup>1</sup>Department of Civil and Structural Engineering, The Hong Kong Polytechnic University, Kowloon, Hong Kong, China

**Abstract.** This paper addresses the aerodynamic effect on the nonlinear oscillation, particularly parametric vibration of cables in cable-stayed bridges. A simplified 2-DOF model including a beam and a stayed cable is formulated first. Response of the cable under global harmonic excitation which is associated with wind speed is obtained using multiple scales method. Via numerical analysis, the stability condition of the cable in terms of wind speed is derived. The method is applied to a numerical example and a real cable-stayed bridge at Hong Kong to analyze all the cables of the bridge. It is demonstrated that very large vibration at one of the longest cables in the middle span of the bridge can be parametrically excited when the wind speed is over around 140 km/h.

**Keywords:** parametric vibration, cables, cable-stayed bridge, nonlinear

## 1 Background

Increase in span of cable-stayed bridges generally makes the bridge more flexible and prone to vibrate under environmental and operational loadings such as wind, rain, traffic and earthquake. Large cable vibrations have been observed in practice. For example, significant vibrations of cables in Meiko-Nishi cable-stayed bridge in Japan were first discovered during the construction of the bridge and subsequently investigated in wind-tunnel tests (Hikami 1986). The vibration amplitude of nine cables in the Ben-Ahin Bridge in Belgium was up to 1m in 1988. Similar phenomenon occurred in Wander Bridge in the same year (Lilien and Pinto da Costa 1994).

These cable vibrations are considered to be local nonlinear vibrations of the cables due to excitation of the supports at bridge deck and towers. Several studies have addressed this problem, for example, Yamaguchi and Fujino (1998), Gattulli and Lepidi (2003), and so on. Generally, large-amplitude vibrations of cables can be induced when one natural frequency of the global modes of a cable-stayed

---

\* Corresponding author, e-mail: ceyxia@polyu.edu.hk

bridge is either close to one natural frequency of the local modes of the cable or twice that of the cable. Fujino et al. (1993) and Xia and Fujino (2006) studied auto-parametric vibration of a simple yet practical 3-DOF model under harmonic loading and random loading, respectively. Wilde et al. 1996) have studied the auto-parametric vibration of Tataru Bridge. It is found that the first torsional frequency of the bridge falls in the range which can excite the cable parametrically. Wind tunnel testing also confirmed this.

Wind-induced vibration of deck in a cable-stayed bridge may induce large-amplitude motion of cables. On the other hand, aerodynamic damping may mitigate the vibration of the cables. However, the aerodynamic damping effect on parametric vibration of cables has been rarely investigated. This paper investigates the aerodynamic effect on nonlinear oscillation of stay cables. In particular, cables in a real cable-stayed bridge at Hong Kong are analyzed from the aspect of vibration stability at different wind speeds. It is demonstrated that the cables close to the middle of the main span of the bridge can be parametrically excited when the wind speed is over 140 km/h (about 38.5 m/s).

## 2 Analytical Model

For simplicity, a 2-DOF model including one cable and one beam is considered as shown in Figure 1. The following general assumptions are made for the cable when deriving the governing differential equation of motion:

- (i) flexural rigidity is small which can be ignored;
- (ii) axial motion is neglected;
- (iii) only vertical motion is considered.

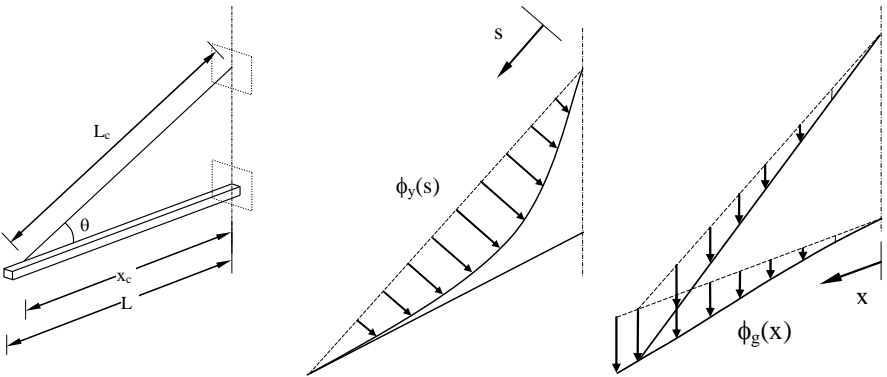


Figure 1. Cable-stayed beam model and vibration mode

The vibration of the system is thus described by the global vertical motion  $\phi_g$  and the local vertical motion of the cable  $\phi_y$ . The corresponding generalized coor-

dinates are  $g$  and  $y$ , respectively. The beam displacement is denoted as  $w_b(x, t)$  for the vertical. For the cable,  $w_c(s, t)$  and  $u_c(s, t)$  stand for the component perpendicular and parallel to the cable axis, respectively, in the vertical plane. Therefore, the following equations are obtained

$$w_b(x, t) = \phi_g(x)g(t) \tag{1a}$$

$$u_c(s, t) = \phi_g(x_c)g(t)\sin\theta\frac{s}{L_c} \tag{1b}$$

$$w_c(s, t) = \phi_g(x_c)g(t)\cos\theta\frac{s}{L_c} + \phi_y(s)y(t) \tag{1c}$$

where  $\phi_g$  is the global mode of the entire model which is mass normalized satisfying  $\phi_g(L) = 1$ , and  $\phi_y$  is set to the first mode of the cable, i.e.,  $\phi_y(s) = \sin(s\pi/L_c)$ . With Lagrange's approach, the governing equation can be acquired

$$\tilde{y}'' + 2\xi_y\tilde{y}' + \tilde{y} + \zeta_g\tilde{g}'' + \eta_g\tilde{y}\tilde{g} + \alpha\tilde{y}^3 = 0 \tag{2}$$

$$\tilde{g}'' + 2\xi_g\frac{f_g}{f_y}\tilde{g}' + \frac{f_g^2}{f_y^2}\tilde{g} + \zeta_y\tilde{y}'' = \tilde{P}(\tau) \tag{3}$$

via the nondimensionalization parameters

$$\tilde{y} = \frac{y}{u_0}, \quad \tilde{g} = \frac{g}{u_0}, \quad \tau = \sqrt{\frac{\pi^2 E_c A_c u_0}{L_c^3 \mu_c}} t = ct \tag{4}$$

where  $\mu_c$  and  $\mu_b$  are the uniform mass per unit length of the cable and beam, respectively;  $E_c$  = Young's modulus,  $A_c$  = the cross sectional area,  $L_c$  = the chord length,  $\theta$  = the cable inclination angle,  $\xi_y$  and  $\xi_g$  are viscous damping ratios of the cable and beam, respectively;  $f_y$  and  $f_g$  are local and global natural frequencies, respectively;  $c$  is the circular natural frequency of the cable,  $\tilde{P}(\tau)$  is the nondimensionalized external forces at the beam, and the prime denotes differentiation with respect to  $x$ . Detailed description of the parameters can refer to Fujino et al. (1993).

We can assume the global motion as the form of

$$\tilde{g} = G \cos \omega_g \tau \tag{5}$$

where  $\omega_g = f_g / f_y$  and  $G$  is the amplitude of the normalized global vibration.

Wind-tunnel tests have shown that  $G$  and wind speed  $V$  are generally in a linear manner in the typical wind speed range as,  $G = \beta V$ , where  $\beta$  is a coefficient that can be determined from a wind-tunnel test. The damping of a stay cable  $\xi$  is considered as the summation of the aerodynamic damping  $\xi_{ae}$  and the structural damping  $\xi_{in}$  which depends on the cable technology very much

$$\xi = \xi_{in} + \xi_{ae} \tag{6}$$

For transverse winds, the aerodynamic damping coefficients in mode  $k$  for vertical vibration are given by

$$\xi_k = \frac{\rho V D C_D}{4 \mu_c \omega_k} = \xi_a V \tag{7}$$

where  $\rho$  is the air density ( $1.23 \text{ kg/m}^3$ ),  $D$  is the cable diameter,  $\omega_k$  is the pulsation of the stay cable of mode  $k$  and  $C_D$  is the drag coefficient which depends on Reynolds number. Here only vertical motion of the first mode is considered. Therefore, the governing equation considering the aerodynamic effect is obtained as

$$\tilde{y}'' + 2(\xi_{in} + \xi_a V)\tilde{y}' + (1 + \eta_g \beta V \cos \omega_g \tau)\tilde{y} + \alpha \tilde{y}^3 = \zeta_g \beta V \omega_g^2 \cos \omega_g \tau \tag{8}$$

The steady-state solution of the cable can be obtained with multiple scales method (Nayfeh and Mook, 1979). Although there are two possibilities that  $\omega_g \approx 1$ , and  $\omega_g \approx 2$ , this paper will investigate the wind effect on the principal parametric resonance of the cable, i.e.,  $\omega_g \approx 2$ , the ratio of the global frequency to the cable's frequency is around 2.

### 3 Solutions with Multiple Scales Method

In the case of  $\omega_g \approx 2$ , the detuning parameter  $\sigma_g$  is introduced

$$\omega_g = 2 + \varepsilon\sigma_g \quad (9)$$

which quantitatively describes the nearness of  $\omega_g$  to 2, and  $\varepsilon$  is a small, dimensionless parameter. With the method of multiple scales (Nayfeh and Mook, 1979), the solution of Equation (8) is obtained as

$$\tilde{y}_0 = a \cos \frac{1}{2}(\omega_g \tau - \gamma) \quad (10)$$

where  $\gamma$  is the phase of the oscillation,  $a$  is the amplitude as

$$a = \sqrt{\frac{1}{1.5\alpha} \left[ 2\sigma_g \pm \sqrt{(\eta_g \beta V)^2 - 16(\xi_m + \xi_a V)^2} \right]} \quad (11)$$

Depending on the parameters, number of non-zero solutions of Equation (11) can be 0, 1 and 2.

## 4 A Numerical Example

A numerical example used in Xia and Fujino (2006) is employed here to investigate the nonlinear response and stability properties of the system. Figure 2 shows the classification of the steady-state solution of the parametrically excited system. When the wind speed is less than 3.4 m/s, the cable cannot be parametrically excited. When the wind speed is larger than 3.4 m/s, vibration of the cable depends on how the frequency ratio approaches to 2. In Region I, there is no non-zero solution, say, only trivial solution exists. In Region II, the trivial solution is unstable, and the only realizable solution is given by Equation (11). In Region III, both trivial and non-trivial solutions are realizable depending on the initial condition. Figure 3 shows the response curve of the cable with respect to wind speed when the global frequency is 19.81 Hz. When the wind speed is less than 3.4 m/s, only trivial solution exists. When the wind speed is larger than 3.4 m/s but smaller than 58.5 m/s, both trivial and non-trivial solutions are realizable depending on the initial condition. When the wind speed is larger than 58.5 m/s, only the non-trivial solutions is realizable, that is, any disturbance will excite the cable to a large vibration. The critical wind speed depends on the global frequency. If the global frequency is close to twice of the cable, 19.32 Hz, the critical wind speed approaches to 3.4 m/s, which is easy to be realized in practice.

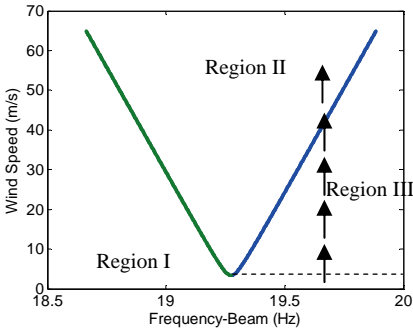


Figure 2. The various regions in parameter space for the classification of the steady-state solutions

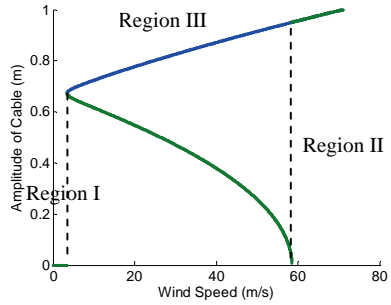


Figure 3. Response curve at different wind speed ( $f_g=19.81$  Hz)

### 5 Application to a Practical Bridge

The bridge investigated here is one of the world’s longest cable-stayed bridges with a main span of about 1000 m, which consists of 56 pair of double-side cables in the east and west ends as shown in Figure 4. Wind-tunnel testing discovered that torsional mode is prone to be excited in the presence of wind. Consequently, only the first torsional mode with frequency of 0.496 Hz is considered in the global vibration. The cables with frequency of around 0.248 Hz can be likely parametrically excited. It is noted that these cables are the longest ones staying over the central deck, i.e., No. 225~228 and 325~328. The response curve of No. 226 and 326 is shown in Figure 5.

The Figure clearly shows three regions regarding stability: 1) when wind speed is less than 15.4 m/s, parametric vibration cannot be excited and only the trivial solution exists (stable); 2) when wind speed is over 15.4 m/s but less than 38.5 m/s, two steady-state solutions are possible and stable. The large vibration of the cable is realizable only when the initial vibration is large, which is not very likely; 3) when the wind speed is over 38.5 m/s (about 140 km/h), the trivial solution is unstable and the large motion of the cable is excited and stable. Parametric vibration of the other cables cannot be excited under the range of design wind speed.

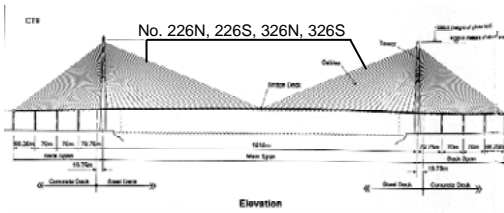


Figure 4. Configuration of the Bridge

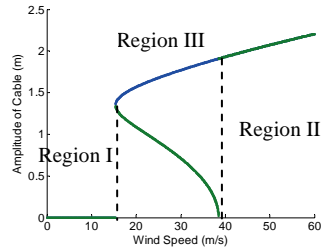


Figure 5. Response curve of cables No. 226N, 226S, 326N and 326S under different wind speeds

## 6 Conclusions

The aerodynamic effect on the nonlinear oscillation of cables has been analyzed and applied to a numerical example and a practical cable-stayed bridge at Hong Kong. It shows that one set of long cables in the middle span can be parametrically excited when the wind speed is over 140 km/h.

## Acknowledgements

The work described in this paper is partially supported by a grant from the Research Grants Council of the Hong Kong SAR (Project No. PolyU 5306/07E) and partially by University Niche Areas programme (Project No. A-BB6G).

## References

- Fujino, Y., Warnitchai, P. and Pacheco, B. M. (1993) An experimental and analytical study of autoparametric resonance in a 3DOF model of cable-stayed-beam, *Nonlinear Dynamics*, 4, 111-138.
- Gattulli, V. and Lepidi, M. (2003) Nonlinear interactions in the planar dynamics of cable-stayed beam, *International journal of solids and structures*, 40(18), 4729-4748.
- Hikami, Y. (1986) Rain vibration of cables in cable-stayed bridges, *Journal of Wind Engineering and Industrial Aerodynamics*, 27(3), 23-34.
- Lilien, J. L. and Pinto da Costa, A. (1994) Vibration amplitudes caused by parametric excitation of cable stayed structures, *Journal of Sound and Vibration*, 174(1), 69-90.
- Nayfeh, A. H. and Mook, D. T. (1979) *Nonlinear Oscillations*, John Wiley & Sons.
- Wilde, K., Fujino, Y. and Masukawa, T. (1996) Time domain modeling of bridge deck flutter, *Journal of Structural Engineering and Earthquake Engineering*, 13, 93-104.

Xia, Y., and Fujino, Y. (2006) Auto-parametric vibration of a cable-stayed-beam structure under random excitation, *Journal of Engineering Mechanics*, 3, 279-286.

Yamaguchi, H. and Fujino, Y. (1998) Stayed cable dynamics and its vibration control, in *Bridge aerodynamics*, A. A. Balkema, Rotterdam, the Netherlands, 235-253.

# CFD Numerical Simulation of Vortex-Induced Vibration of a Stay Cable under a Wind Profile

Wenli Chen<sup>1\*</sup> and Hui Li<sup>1</sup>

<sup>1</sup>School of Civil Engineering, Harbin Institute of Technology, Harbin 150090, P.R. China

**Abstract.** VIV (Vortex-induced vibration) of a stay cable subjected to a wind profile is numerically simulated through combining CFD (Computational Fluid Dynamics) code CFX 10.0 and CSD (Computational Structural Dynamics) code ANSYS 10.0. A stay cable with the inclined angle of  $30^\circ$  is used as the numerical model. Under a profile of mean wind speed, unsteady aerodynamic lift coefficients of the cable have been analyzed in both time-domain and frequency-domain when VIV occurs. The results indicate that the lift coefficient wave response of the stay cable under a wind profile is different from that of an infinitely long cable under a uniform flow in water (i.e. without consideration of profile) obtained by direct numerical simulation. Cable oscillations can severely influence the unsteady aerodynamic frequencies, and change flow field distribution near the cable and influence the vortex shedding in the wake.

**Keywords:** stay cable, fluid-structure interaction, numerical simulation, vortex-induced vibration

## 1 Introduction

Cables are key components of long-span bridges, such as cable-stayed and suspended-cable bridges, and the increasing span makes the cables easily oscillate under wind, rain, traffic and seismic loadings. Vortex-induced vibration (VIV) of a cable is easy to occur when subject to a wind field. Carbon Fiber Reinforced Polymer (CFRP) is a novel cable material and has merits of high strength, light weight and corrosion resistance compared with steels; therefore, CFRP cables will be more and more employed in the long-span bridges in the future. Since CFRP cables are lighter than traditional steel cables with uniform cross-sections or uniform tensions which induce smaller mass ratio (structure to fluid), VIV of a CFRP cable will may occur with larger amplitude. So it is necessary to investigate the VIV of a CFRP cable.

---

\* Corresponding author, e-mail: cwl\_80@hit.edu.cn

In spite of a number of experiments for VIV carried out, investigation of VIV as a fully coupled problem is far from completely solved. An alternative to experimental approaches for study of VIV phenomenon is to perform numerical simulation of the Navier-Stokes equation. At the present time, there have been several different computational approaches toward describing the flow field for this problem. These include the discrete vortex method (DVM), direct numerical simulation (DNS), Reynolds-averaged Navier–Stokes (RANS), Large Eddy Simulation (LES), and combinations of the four.

DNS is the only method that is capable of capturing all aspects of turbulence characteristics. However the up-to-date computational hardware is not powerful enough to perform DNS for a high Reynolds number ( $Re$ ) turbulent flow, which occurs much more frequently in the reality. Newman and Karniadakis (1997) and Evangelinos and Karniadakis (1999) carried out a DNS of flow-induced vibrations of a flexible cable in water at  $Re=100$  and  $Re=1000$ , respectively. The traveling wave cable response is the main response, although a standing wave response will occur at some conditions. The maximum lift force coefficients of the standing wave were significantly larger than that of the traveling wave. Dong and Karniadakis (2005) investigated turbulent flows past a rigid cylinder undergoing forced oscillations at  $Re=10000$  adopting a DNS method incorporating with a multilevel-type parallel algorithm. The parallel performance was demonstrated by a Compaq Alpha cluster with 1536 processors for the cylinder flow at  $Re=10000$  with a problem of 300,000,000 freedom degrees.

Al-Jamal and Dalton (2004) uses a 2-D LES method to simulate VIV at a moderate Reynolds number of  $Re=8000$  for a range of damping ratios and natural frequencies. Tutar and Holdo (2000) used LES in incorporation with the finite element method to numerically simulate a cylinder subjected to forced oscillations at  $Re=24000$ . The 3-D simulations were compared with the 2-D results and experimental data in order to assess the relative performance of the 3-D LES simulations. The results show that three-dimensional representation was necessary to obtain accurate enough results.

Zhou et al. (1999) and Meneghini et al. (2002) use a DVM method to study a uniform flow past an elastic circular cylinder at  $Re=200$  and 10000, respectively. Their simulations did not obtained an ‘Upper branch’. The case of a cantilever yielded similar results. Their single riser simulations provided the expected vibration modes and the comparisons with the quasi-steady analysis were quite encouraging. Guilmineau and Queutey (2001) used a 2-D  $k-\omega$  RANS solution to represent the flow past a cylinder with a low mass-damping. The calculated results were compared with the experimental results of Khalak and Williamson (1999) over the range of  $Re$  from 900 to 15000. The results correctly predict the maximum amplitude of oscillation with the mass ratio of 2.4.

At present, the computer is not powerful enough to perform DNS for VIV numerical simulations at a high Reynolds number. Few other methods discussed above ensure sufficient generality for characterizing the problem of VIV.

Thus, researchers may hope for the prediction of some aspects of VIV through the use of RANS (with suitable turbulence models) and LES (with suitable sub-grid models). The above investigations of VIV for cylinders or cables are carried out under a uniform flow in water or air. In present paper, numerical simulation of VIV of a CFRP cable is carried out using a RANS method incorporating ANSYS and CFX codes under a profile of mean wind speed.

## 2. Cable/Fluid Models

### 2.1 Structural Finite Element Model (FEM)

The diameter and length of the CFRP cable are respectively  $D = 0.05$  m, and  $L = 10.0$  m, resulting in a length to diameter ratio  $L/D = 200$ . The density of the CFRP cable is  $\rho_c = 1500 \text{ kg/m}^3$  and the air density is chosen to be  $\rho = 1.20 \text{ kg/m}^3$  at the temperature  $20^\circ\text{C}$ . The mass ratio  $M^* = m_c / \rho D^2$  ( $m_c$  is mass of the CFRP cable per unit length) is about 983, which is much larger than the condition of VIV of marine cables in water. Geometric model building and grid partition are realized in ANSYS as shown in Figure 1 (a). The endpoints of the CFRP cable are pinned. The Young's modulus of the CFRP cable is  $E_c = 140 \text{ GPa}$  and the cable tension is  $T = 50 \text{ kN}$ . Modal analysis is independently accomplished for the CFRP cable before fluid-structure interaction analysis. The first natural frequency of the CFRP cable obtained in vacuum is  $6.49 \text{ Hz}$ . The FSI interface of structural FEM is the side surface of the cable. Data transmission is accomplished through this interface.

### 2.2 Fluid Model

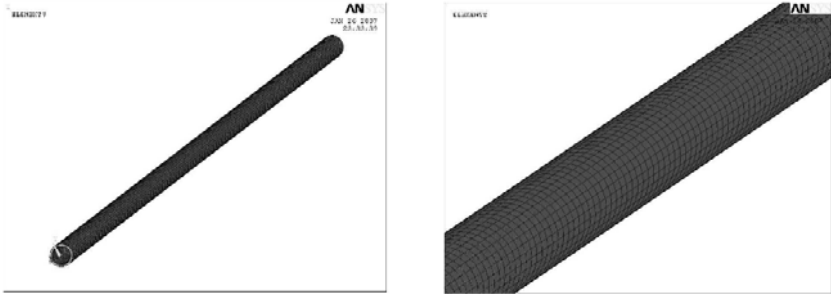
In the present paper, the shear stress transport (SST)  $k - \omega$  model (Menter, 1993) is employed. This model is a two equation turbulence model which solves one equation for the turbulent kinetic energy  $k$  and the other equation for the turbulent frequency  $\omega$ .

Figure 1(b) shows the flow field model and grid partition. The structural mesh is chosen in the discretizational process, the domain diameter and length of flow field are  $30D$  and  $L$ , respectively. An inlet and opening boundary conditions are used for the flow entering into/outflow the domain. No slip wall boundary condition is used for the surface of the cable. The surface between the CFRP cable and flow field domain is defined as a FSI interface. The mean wind speed profile of the bridge cable is not uniform influenced by the atmosphere boundary layer. Ac-

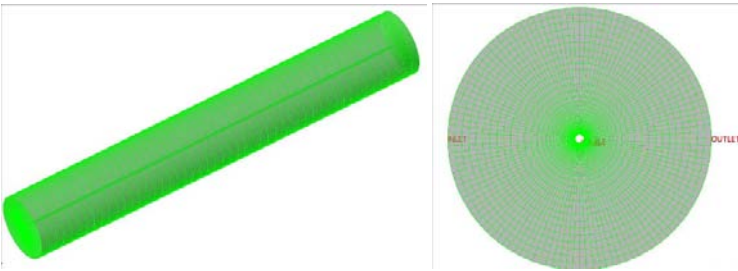
According to the log law, the mean wind speed profile in atmosphere boundary layer is defined as:

$$U(z) = U_b \left( \frac{z}{z_b} \right)^\alpha \tag{1}$$

where  $z_b$  is the roughness length which is a measure of the roughness of the ground surface and equals 10m, and the height of lowest point of the cable is supposed to be  $z_b$  in the present paper;  $z$  is any height above sea level;  $U_b$  is the mean wind speed at the height  $z_b$ , and  $\alpha$  is the terrain roughness index, and equals 0.16 for *B* terrain.



(a) FEM of the CFRP cable



(b) Model of flow field and grid partition

Figure 1. Cable/flow field models

### 3. Results and Discussion

VIV of the CFRP cable is numerically simulated with an inclined angle of  $30^\circ$  as shown in Figure 2. The profile of mean wind speed in Equation (1) is adopted.

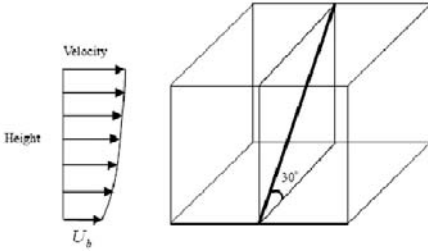


Figure 2. A CFRP cable with an inclined angle of  $30^\circ$

Numerical simulation results of flow around a static cable indicate that the vortex shedding frequency is close to the first natural frequency of the CFRP cable when the mean wind speed is 1.58 m/s if the Strouhal number,  $St$ , is chosen to be 0.203 for a circular cylinder (Dong and Karniadakis, 2005). So the mean wind speed of  $U_b = 1.5$  m/s at the lowest position of the cable is adopted. The mean wind speeds at other positions of the CFRP cable can be determined according to Equation (1). The reduced velocities ( $V_r = U/fD$ ) is calculated to be 4.62 – 4.93 corresponding to the profile of the mean wind speed.

#### 3.1 VIV Response of the CFRP Cable

The time histories of cross-flow displacement at 0.1, 0.3 and 0.5  $L$  are shown in Figure 3 where the maximum cross-flow displacement reaches 0.189  $D$  at 0.5  $L$ . The frequency response of the cable along its overall length is shown in Figure 4. The curves show that large amplitudes are centralized near 6.5 Hz (which is close to the first natural frequency) and symmetrical along span of the cable.

The normalized first mode shape of VIV of the cable is shown in Figure 5(a). For comparison, the first mode shape of the cable in vacuum is also depicted in Figure 5(a). The two curves are almost the same except the little computation error. We may conclude that the additional aerodynamic mass and stiffness have slight influence on the mode shape and frequency for a larger the mass ratio ( $M^*=983$ ).

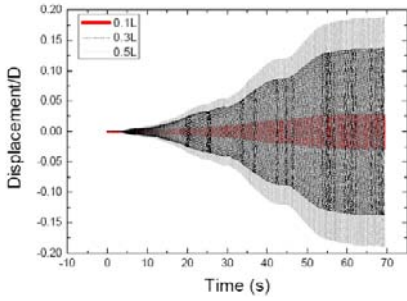


Figure 3. Time histories of cross-flow displacement at 0.1 L, 0.3 L and 0.5 L

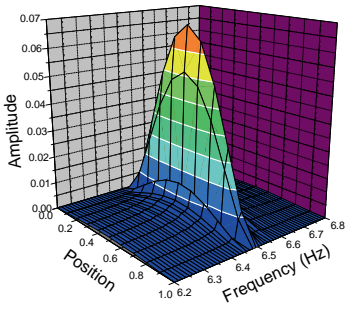
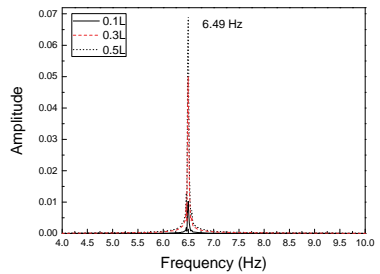
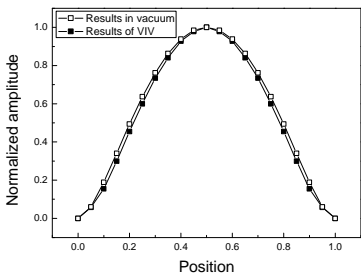


Figure 4. Amplitudes along the cable span versus frequency through FFT



(a) Normalized amplitude versus position

(b) At 0.1 L, 0.3 L and 0.5 L

Figure 5. Spectra of cross-flow displacement

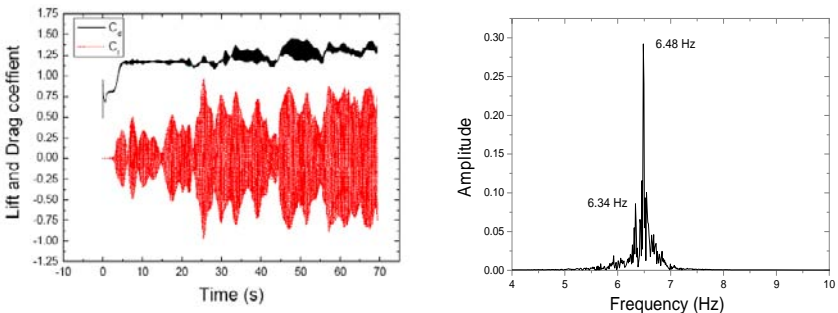
### 3.2 Variation of Lift Coefficient in Both the Time Domain and Frequency Domain

The unsteady aerodynamic forces acting on the CFRP cable are classified into: lift force which is perpendicular to the undisturbed flow direction and whose frequency equals to the vortex shedding frequency; and drag force, which is along flow direction and whose frequency is two times of the vortex shedding frequency. The lift coefficient and drag coefficient are obtained through dimensionless analysis:

$$C_l = \frac{F_L}{\frac{1}{2}\rho U^2 D}, \quad C_d = \frac{F_D}{\frac{1}{2}\rho U^2 D} \quad (2)$$

where  $F_L$  and  $F_D$  are the lift force and drag force, respectively;  $C_l$  and  $C_d$  are the lift coefficient and drag coefficient, respectively.

The time histories of sum lift and drag coefficients along the cable span are obtained as shown in Figure 6 (a) when VIV of the stay cable will occur under a profile of mean wind speed. It can be seen that the lift coefficient amplitude remarkably fluctuates and the average drag coefficient gradually increases with time. Spectrum of the sum lift coefficient is shown in Figure 6 (b) in which two main frequencies of 6.34 and 6.48 Hz appear. 6.34 Hz is the vortex shedding frequency, while 6.48 Hz is approximately identical to the 1<sup>st</sup> natural frequency of the cable.



(a) Time histories of sum lift and drag coefficients (b) Spectra of sum lift coefficient of the cable

Figure 6. Responses of aerodynamical coefficients

For further investigation of local characteristics of lift coefficient along axial direction of the cable, time histories and corresponding spectrum of lift coefficient at nine observation locations with the space interval of  $0.1 L$  are shown in Figure 7 (a) and (b). Figure 7 (a) indicates that the amplitudes of lift coefficient vary with time when the VIVs occur, and the amplitudes of lift coefficient between  $0.4 - 0.9 L$  are larger than that between  $0.1 - 0.3 L$ . The phenomenon above is much

different from that without consideration of profile of wind speed. The results in Figure 7 (b) indicate that the main frequency of lift coefficient between 0.1 – 0.3  $L$  is 6.34 Hz which is the vortex shedding frequency unlocked to the 1<sup>st</sup> natural frequency of the cable and keeps constant. While the frequencies of lift coefficient between 0.4 – 0.8  $L$  and at location of 0.9  $L$  are 6.48 Hz and 6.51 Hz, respectively, which are very close to the 1<sup>st</sup> natural frequency of the cable; so the range of 0.4 – 0.9  $L$  is named frequency lock-in region where the vortices alternately sheds from the cable at the 1<sup>st</sup> natural frequency.

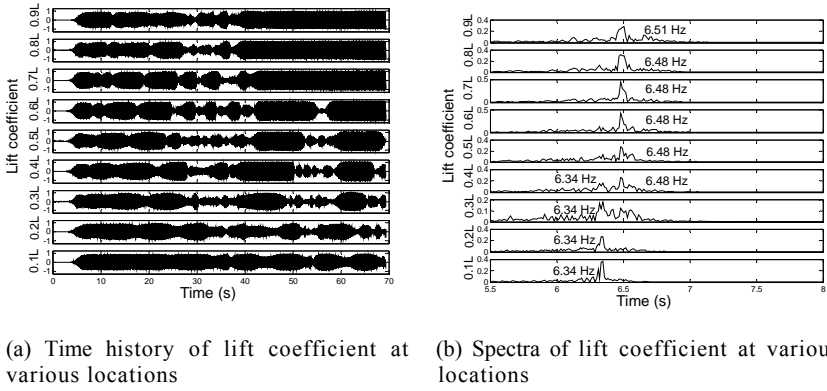


Figure 7. Response of lift coefficient in the time domain and frequency domain

The lift coefficient contours along the span of the CFRP cable versus time are shown in Figure 8 where the horizontal axis denotes observing locations along span direction and the vertical axis denotes time. The lift coefficient response is a modulated traveling wave (10 – 10.5 s) at first, then becomes a modulated standing wave (20 – 20.5 s) response, at last, is transformed into a new wave response (40 – 40.5 s and 50 – 50.5 s) without variety along the span direction in the frequency lock-in region, incorporating with a modulated standing wave response in the frequency unlock-in region. The variety of lift coefficient along the span is different with results of uniform flow field by a DNS method (Newman and Karniadakis 1997).

### 3.3 Wake of the CFRP Cable

The cable oscillation can induce pressure redistributions of flow field near the and also influence the vortex shedding in the wake. Figure 9 indicates total pressure contours at the plane of  $Y = 0$  with the inclined angle of  $30^0$  ( $X$ -axis denotes the flow direction,  $Y$ -axis denotes across flow direction and  $Z$ -axis denotes the axial direction of the cable). As time shifts, the pressure synchronous regions are gradu-

ally formed. At  $t = 50$  s, two pressure synchronous regions in the wake are formed and homologous to the frequency lock-in regions shown in Figure 7(b).

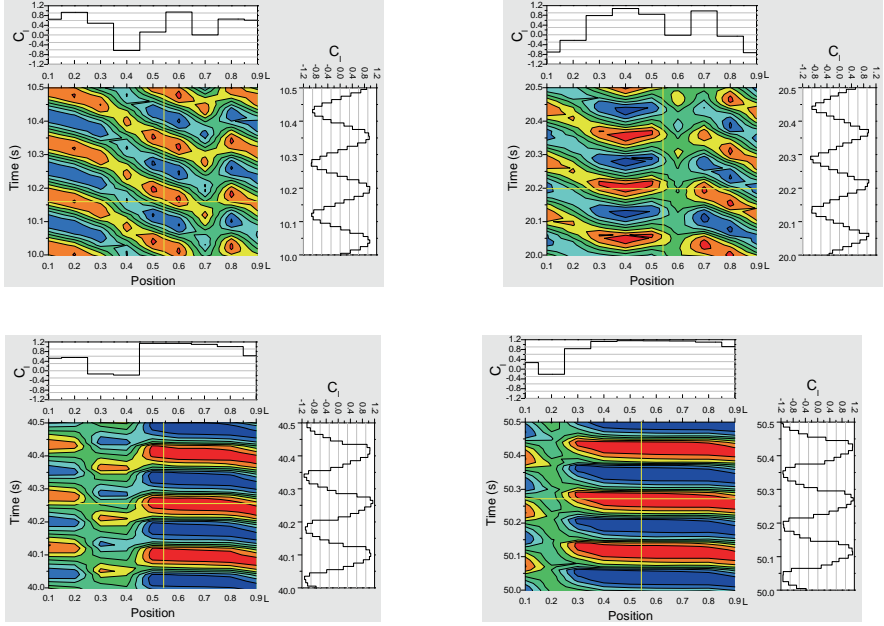


Figure 8. Lift coefficient contours versus time and span distance along cable

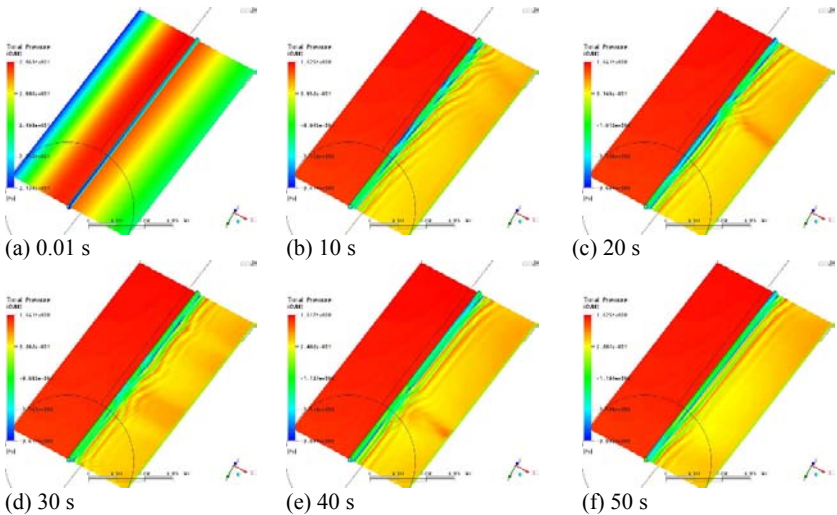


Figure 9. Total pressure contours of  $Y = 0$  plane for the cable with the inclined angle of  $30^\circ$

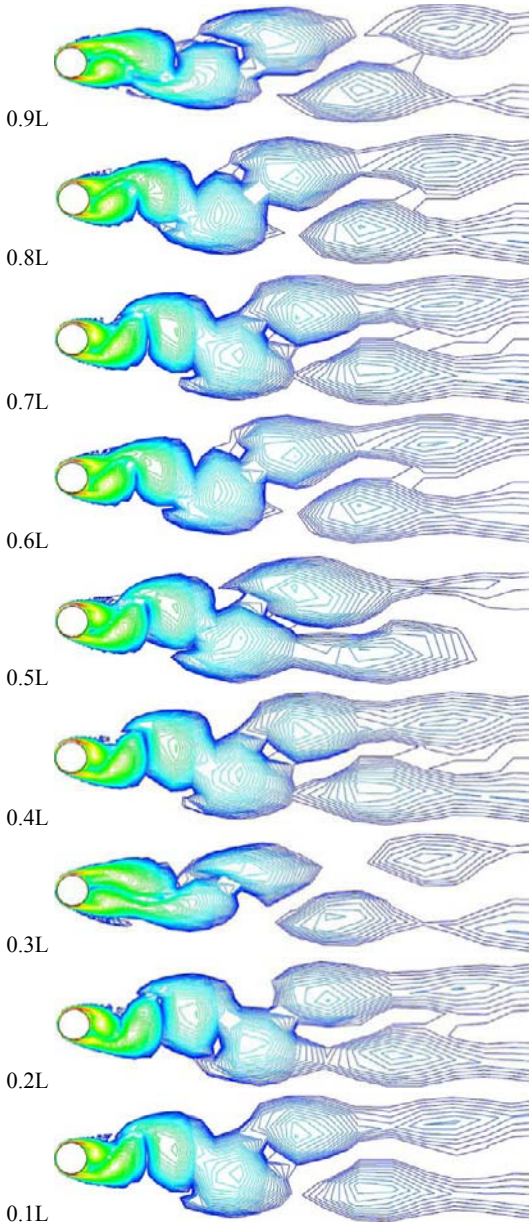


Figure 10. Vorticity contours at time  $t = 50$  s along the span of the cable

The instantaneous vorticity fields at time  $t = 50$  s along the span of the cable are shown in Figure 10. In the span region  $0.1 - 0.2 L$ , the vortex shedding keeps in synchronism,  $0.3 L$  is transition position where the vortex shedding is anti-phase

to that of  $0.1 - 0.2 L$ ; and the vortex shedding is almost in phase in the region  $0.4 - 0.9 L$ . Comparing with Figure 9 (f), the two regions of vortex shedding in phase is similar to the two pressure synchronous regions.

## 4 Conclusion

The VIV of a CFRP cable is numerically simulated through combination of the CSD code ANSYS and CFD code CFX. The following conclusions are obtained: Cable oscillation can influence the vortex shedding frequencies and form the frequency lock-in and unlock-in regions along span direction of the CFRP cable.

The lift coefficient response is a modulated traveling wave at first, then becomes a modulated standing wave, at last, is transformed into a new wave response without variety along the span direction in the frequency lock-in region, incorporating with a modulated standing wave response in the frequency unlock-in region. The pressure distribution and vortex shedding are synchronous in the frequency lock-in and unlock-in regions, respectively.

## Acknowledgements

This research is financially supported by National Excellent Young Scientists Fund (50525823), NSFC of China (50738002) and (90715015).

## References

- Al-Jamal H., Dalton C. (2004). Vortex induced vibrations using large eddy simulation at a moderate Reynolds number, *Journal of Fluids and Structures*, 19:73-92.
- Chen M.Z. (2002). *Fundamentals of Viscous Fluid Dynamics*, Beijing: Higher Education Press.
- Dong S.J., Karniadakis G.E. (2005). DNS of flow past a stationary and oscillating cylinder at  $re=10000$ , *Journal of Fluids and Structures*, 20:519-531.
- Evangelino C., Karniadakis G.E. (1999). Dynamics and flow structures in the turbulent wake of rigid and flexible cylinders subject to vortex-induced vibrations, *Journal of Fluid of Mechanics*, 400:91-124.
- Guilmineau E., Queutey P. (2001). Numerical simulations in vortex-induced vibrations at low mass-damping, *AIAA paper 2001-2852*, Anaheim.
- Khalak A., Williamson C.H.K. (1999). Motions, forces, and mode transitions in VIV at low mass damping, *Journal of Fluids and Structures*, 13:813-851.
- Meneghini J.R., Bearman P.W. (1995). Numerical simulation of high amplitude oscillatory flow about a circular cylinder, *Journal of Fluids and Structures*, 9:435-455.
- Menter F.R. (1993). Zonal two-equation  $k - \omega$  turbulence models for aerodynamic flows. *AIAA 24th Fluid Dynamics Conference*, AIAA Paper 93-2906, Orlando, USA.

- Newman D.J., Karniadakis G.E. (1997). A direct numerical simulation study of flow past a freely vibrating cable, *Journal of Fluid of Mechanics*, 344:95-136.
- Sarpkaya T. (2004). A critical review of the intrinsic nature of vortex-induced vibrations, *Journal of Fluids and Structures*, 19:389-457.
- Tutar M., Holdo A.E. (2000). Large eddy simulation of a smooth circular cylinder oscillating normal to a uniform flow, *ASME, Journal of Fluids Engineering*, 122:694-702.
- Zhou C.Y., So R.M.C., Lam K. (1999). Vortex induced vibrations of an elastic circular cylinder, *Journal of Fluids and Structures*, 13:165-189.

# Aerodynamic Interference Effect between Large Wind Turbine Blade and Tower

Nianxin Ren<sup>1</sup> and Jinping Ou<sup>1,2\*</sup>

<sup>1</sup>School of Civil Engineering, Harbin Institute of Technology, Harbin 150090, China

<sup>2</sup>School of Civil and Hydraulic Engineering, Dalian University of Technology, Dalian 116024, China

**Abstract.** The aerodynamic interference effect between wind turbine blade and tower is very common in the wind turbine structure, so the study of the physical mechanism of the interference effect is both of important practical interest and profound academic interest. Firstly, the full two-dimensional Navier–Stokes algorithm and the  $k-\omega$  SST turbulence model were used to investigate incompressible viscous flow past the wind turbine NACA 63-430 airfoil and tower in detail. The flow physics in the two-dimensional analysis was clarified by the aerodynamic loads acting on the wind turbine tower. The numerical results under the blade-tower interference effect and the results under a single tower were compared in view of lift and drag coefficient time histories. Furthermore, the effect of the three-dimensional blade rotation on the wind turbine tower was simulated based on the rotational sliding mesh technique and the effective large eddy simulation (LES) methods. The force perturbation acting on the tower under the blade rotational effect was clearly studied. As a result, the numerical results are very used for understanding the physical mechanism of the aerodynamic interference effect between the wind turbine blade and tower, which will be helpful for guiding the structural design of the wind turbine tower.

**Keywords:** aerodynamic interference effect, wind turbine, large eddy simulation, rotational effect

## 1 Introduction

As is known to all, the worldwide energy crisis and environment problem are more and more serious. Wind energy, as one kind of clean renewable energy resources, has been paid more and more attentions. As the size of the wind turbine is growing bigger and bigger, the safety of wind turbine tower is becoming more and

---

\* Corresponding author, e-mail: oujnping@dlut.edu.cn

more important. The aerodynamic interference effect between wind turbine blade and tower is very common in the wind turbine structure, which can strongly influence the flow field around the wind turbine tower and excite the complex unsteady loads acting on the tower. However, most of the present standards, such as IEC 61400, DNV-OS-J101 and GL, haven't taken the interference effect between wind turbine blade and tower into consideration. So far, few researchers have done very deep study on this issue.

Because the large wind turbine blade is very close to the tower, the aerodynamic interference effect between them is very significant. Therefore, it is both of practical and academic interests to clearly understand the physical mechanism of interference effect. In this paper, as the first step, the simplified two-dimensional stationary NACA 63-430 airfoil with the circle tower numerical model has been studied, based on Navier–Stokes algorithm and the  $k-\omega$  SST turbulence model. Then, the flow interaction effect was compared with the tower model with no airfoil interference. Furthermore, the three-dimensional blade rotational effect was taken into consideration for better understanding the interference of the blade and tower, which was based on the effective large eddy simulation method and the rotational sliding mesh technique.

## 2 Two-Dimensional Stationary Numerical Model

The flow past the airfoil and tower was modeled by the full Navier–Stokes equation for two-dimensional, viscous and incompressible flow. The continuity equation and Momentum equation based on Reynolds averaged N-S equations are as follows:

$$\frac{\partial u_i}{\partial x_i} = 0 \quad (1)$$

$$\frac{\partial(\rho \bar{u}_i)}{\partial t} + \frac{\partial(\rho \bar{u}_i \bar{u}_j)}{\partial x_j} = -\frac{\partial \bar{p}}{\partial x_i} + \frac{\partial}{\partial x_j} \left( \mu \frac{\partial \bar{u}_i}{\partial x_j} - \overline{\rho u_i' u_j'} \right) \quad (2)$$

where  $i, j=1, 2$ ;  $\rho=1.255\text{kg/m}^3$ ;  $\mu=1.7894 \times 10^{-5} \text{ kg/(m}\cdot\text{s)}$

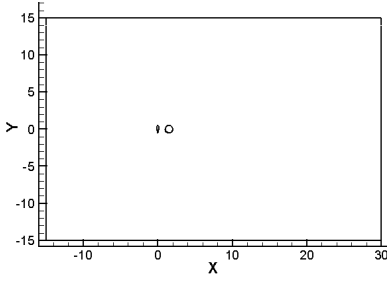


Figure 1. The whole computational zone

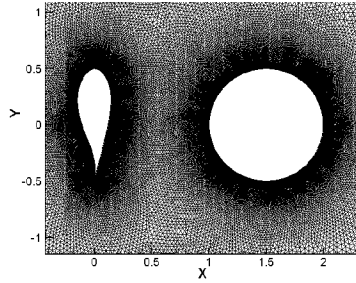


Figure 2. Unstructured grids near the airfoil and tower.

The whole computational zone is a rectangle with the width of 30m and the length of 42m. The NACA 63-430 airfoil with the chord length of 1m and the circle tower with the diameter of 1m locate in the middle of the rectangle (Figure 1). The topologic unstructured grids near the airfoil and the circle are shown in Figure 2.

### 3 Two-Dimensional Stationary Numerical Results

First of all, the complex unsteady flow field of the wind turbine tower with frontal airfoil interference was simulated with the inlet velocity of 25m/s, based on the full two-dimensional Navier–Stokes algorithm and the  $k-\omega$  SST turbulence model. Then, the results of the airfoil-tower interference effect were compared with the results of a single circle tower without front airfoil interference. The comparison of the tower drag coefficients time history and the lift coefficients time history under the two conditions are shown in Figure 3 and Figure 4, respectively.

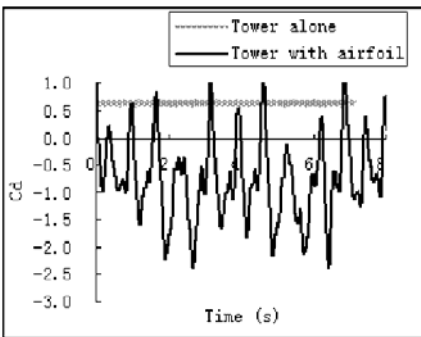


Figure 3. The comparison of Cd time history.

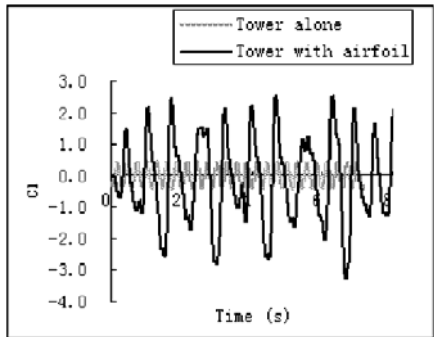


Figure 4. The comparison of Cl time history.

In Figure 3, it can be seen that the drag coefficient value of the tower with no airfoil interference is around 0.6 and its fluctuation is rather small, while the drag coefficient value of the tower with airfoil interference changes from -2.3 to 1 and its fluctuation is very significant. What's more, from the Figure 4, it is clear that the lift coefficient value of the tower without airfoil interference periodically changes with the amplitude of 0.32 and with the frequency of about 2.92Hz, which was obtained by the FFT transformation of the lift coefficient time history. The frequency of a single tower lift force calculated by numerical simulation is very close to empirical value of 3Hz, considering the empirical Strouhal number of the circle configuration is about 0.2. Therefore, it can be verified that the two-dimensional numerical simulation results are satisfying. However, the lift coefficient fluctuation of the tower with airfoil interference is more serious than that of no airfoil interference, which changes quasi-periodically form -3.2 to 2.3. On the whole, it can be concluded that the aerodynamic loads acting on the tower with the interference of the airfoil is much higher than that of no airfoil interference, which is meaningful and benefit for guiding the design of large wind turbine tower.

To further clarify the physical mechanism of the airfoil and tower flow interaction, the more detailed information of the airfoil-tower interaction flow is shown in Figure5 and Figure6. From the two pictures, it is obvious that the tower is just in the serious wake of the airfoil, that's the right reason, why the aerodynamic loads acting on the tower with the airfoil interference is more complex and larger than that of no airfoil interference.

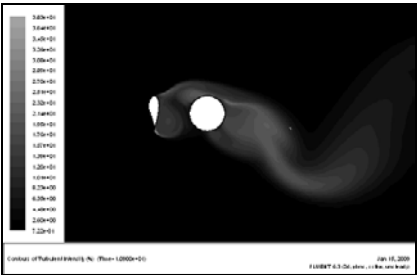
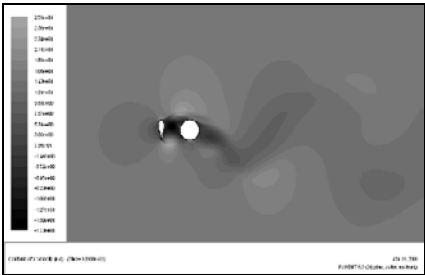


Figure 5. Velocity distribution in the flow field.

Figure 6. Turbulence distribution of the flow field.

### 4 Three-Dimensional Rotational Numerical Model

In this section, the blade rotational effect on the flow interaction of the wind turbine tower was taken into consideration. Filtering the Navier-Stokes equations, the governing equations in the large eddy simulation (LES) are as follows:

$$\frac{\partial(\rho\bar{u}_i)}{\partial t} + \frac{\partial(\rho\bar{u}_i\bar{u}_j)}{\partial x_j} = -\frac{\partial\bar{p}}{\partial x_i} + \frac{\partial}{\partial x_j} \left( \mu \frac{\partial\sigma_{ij}}{\partial x_j} \right) - \frac{\partial\tau_{ij}}{\partial x_j} \quad (3)$$

where  $\sigma_{ij}$  is the stress tensor due to molecular viscosity and  $\tau_{ij}$  is the subgrid-scale stress defined by

$$\tau_{ij} = \overline{\rho u_i u_j} - \rho \bar{u}_i \bar{u}_j = \frac{1}{3} \tau_{kk} \delta_{ij} - 2\mu_t \bar{S}_{ij} \quad (4)$$

where  $\mu_t$  is the subgrid-scale turbulent viscosity. The isotropic part of the subgrid-scale stresses  $\tau_{kk}$  is not modeled, but added to the filtered static pressure term.  $S_{ij}$  is the rate-of-strain tensor for the resolved scale.

The whole computational zone is a cube with the width of 1000m, the length of 2000m and the height of 700m. The diameter of the wind turbine rotor is 80 m and the height of the tower is 80m. The whole three-dimensional numerical model is shown in Figure 7, and the grids in the vicinity of the blade and the tower are tightened. The total grid size is nearly 2 millions.

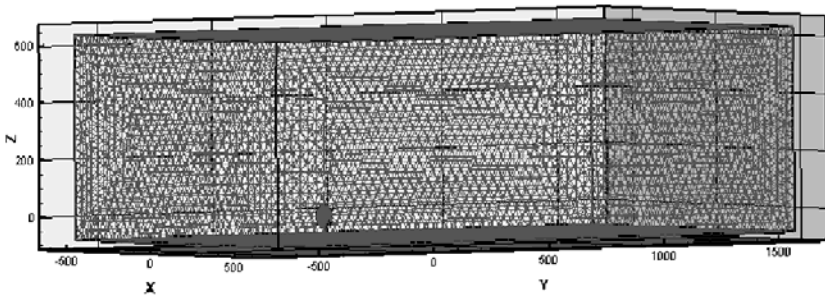


Figure 7. The whole computational zone for three-dimensional numerical simulation.

## 5 Three-Dimensional Rotational Numerical Results

In calculation the rotational sliding mesh technique of cylinder zone containing the wind turbine rotor is involved, and the effective large eddy simulation turbulence model is adopt for the investigation of the flow interference between wind turbine rotor and the tower. In the simulation, the wind speed is 15m/s and the angular velocity of the rotor is 2rad/s. The tower aerodynamic loads time history with the blade rotational effect is shown in Figure 8.

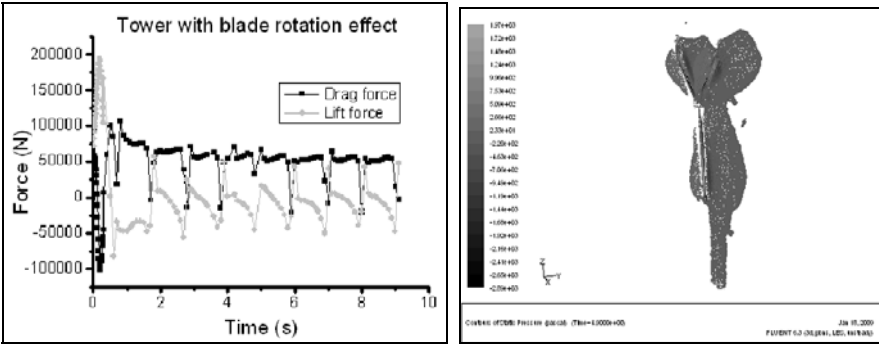


Figure 8. Tower aerodynamic loads time histories. Figure 9. Static pressure contour distribution.

It can be seen that, when blades just rotate across the downstream tower, the lift force (across-wind direction) experiences a sudden increase from the minimum to the maximum, while the drag force (along-wind direction) experiences a sudden decrease from the normal value to the minimum. That’s because that, when the rotating blade is crossing the downstream tower with a relative high speed, the downstream tower is just in the complex unsteady wake of the rotating blade. The wake can strongly influence the aerodynamic loads acting on the tower. Therefore, the lift force time history and the drag force time history clearly reflect the wake effect of the rotating blades. The interactional flow field of the rotating blades and the stationary tower is shown in Figure 9, in the case of one of the blades just crossing the downstream tower. It can be observed that the top half of the tower is obvious in the wake of the blade and the flow between the blade and the tower is so complex. As a result, the complex unsteady wake of the rotating blades can lead to the unfavorable influence on the wind turbine tower fatigue life.

### 6 Conclusion

Firstly, the full two-dimensional Navier–Stokes algorithm and the  $k-\omega$  SST turbulence model were used to investigate incompressible viscous flow past the stationary wind turbine NACA 63-430 airfoil with the downstream tower. The aerodynamic loads acting on the wind turbine tower with the airfoil flow interference are much higher than the single tower without the interference. Therefore, in the case that the rotor blade just stops at the front of the tower over the cut-out wind speed, the flow interference effect on the dynamic loads of the tower must be taken into consideration.

Furthermore, the rotational sliding mesh technique and the effective large eddy simulation turbulence model is adopt for the investigation of the three-dimensional

flow interference between wind turbine rotor and the tower. The rotational effect of the rotor on the aerodynamic loads of the tower is clearly clarified, which can strongly influence the fatigue life of the wind turbine tower.

## Acknowledgements

Foundation: The National Science Foundation of China under project No. 50538020 and the National Science and Technology Planning under project No. 2006BAJ03B00.

## References

- Awad E sam, Toorman Erik and Lacor Chris (2008). Large eddy simulations for quasi-2D turbulence in shallow flows: A comparison between different subgrid scale models, *Journal of Marine Systems*, in press, corrected proof, available online.
- Cao Renjing and Hu Jun (2006). Flow interaction between HAWT Rotor wake and downstream circular tower, *Acta Energiæ Solaris Sinica*, 27(4): 326-330 [in Chinese].
- Fluent Inc (2005). FLUENT 6.2 User's Guide. Fluent Inc.
- Hu Danmei, Ouyang Hua and Du Zhaohui (2006). A study on stall-delay for horizontal axis wind turbine, *Renewable Energy*, 31: 821-836.
- Jeon W. P., Park T. C. and Kang S.H. (2002). Experimental study of boundary layer transition on an airfoil induced by periodical passing wake. *Exp Fluids*, 32(2): 229-241.
- Menter F. R. (1993). Zonal two-equation model k- $\omega$  models for aerodynamic flows. In: 24th Fluid Dynamics Conference. Orlando, Florida.
- Palau-Salvador G., Stoesser T., Rodi W. (2008). LES of the flow around two cylinders in tandem, *Journal of Fluids and Structure*, 24: 1304-1312.
- Tsubokura Makoto (2009). On the outer large-scale motions of wall turbulence and their interaction with near-wall structures using large eddy simulation, *Computers & Fluids*, 38: 37-48.
- Timmer W. A. and Rooij R. Van (2001). Some aspects of high angle-of attack flow on airfoils for wind turbine application. In: EWEC 2001. Copenhagen, Denmark.

*“This page left intentionally blank.”*

# Windborne Debris Damage Prediction Analysis

Fangfang Song<sup>1\*</sup> and Jinping Ou<sup>1,2</sup>

1 Department of Urban & Civil Engineering, Harbin Institute of Technology Shenzhen Graduate School, Shenzhen 518055, China

2 School of Civil and Hydraulic Engineering, Dalian University of Technology, Dalian 116024, China

**Abstract:** Windborne debris is one of the most important causes of the envelop destruction according to the post-damage investigations. The problem of windborne debris damage could be summarized as three parts, including windborne debris risk analysis, debris flying trajectories, and the impact resistance of the envelopes analysis. The method of debris distribution was developed. The flying trajectories of compact and plate-like debris were solved by using numerical method according to the different aerodynamic characteristics. The impact resistance of the envelopes was analyzed. Besides, the process of windborne debris damage analysis was described in detail. An example of industrial building was given to demonstrate the whole method by using the observed data of typhoon CHANCHU (2006). The method developed in this paper could be applied to risk assessment of windborne debris for structures in wind hazard.

**Keywords:** typhoon, windborne debris, structural envelopes, damage estimation

## 1 Introduction

Lots of wind disaster investigations have revealed that the typhoon-induced debris is the main reason for damage of structural envelopes. According to the damage reports of hurricane Alicia (Houston, Tex., 1983), hurricane Hugo (Carolina, 1989) and hurricane Andrew (Florida, 1992), the loss caused by windborne debris was the important part of the total loss (Minor, 2005). Fast-flying debris may penetrate envelopes and threaten human life and property. Debris penetration also induces internal pressurization, approximately doubling the net loading on roofs, side walls, and leeward walls (Lin et al., 2007). The problem of windborne debris damage could be summarized as three parts, including windborne debris risk analysis, debris flying trajectories, and the impact resistance of the envelopes analysis.

---

\* Corresponding author, e-mail: qingtiansong@163.com

Potential debris includes roof gravel, roof members, and other building components, as well as tree limbs and vehicles.

### 2 Windborne Debris Risk Analysis

The number of the windborne debris could be calculated by using equations (1) and (2), where  $A_{deb}$  is the area of debris source region,  $L_s$  is the length of the structure,  $R$  is the radius of debris region,  $\alpha_{UH}$  is the wind direction angle,  $N_{deb}$  is the total number of the debris, and  $\rho_{deb}$  is the distribution density of the debris region. For wind direction  $\alpha_{UH}$  varies with time, and then  $N_{deb}$  is not a constant but a variable. A schematic drawing of the dimensions of debris source region and structure is shown in Figure 1.

$$A_{deb} = L_s \cdot R \cdot \sin \alpha_{UH} \tag{1}$$

$$N_{deb} = \rho_{deb} \cdot A_{deb} \tag{2}$$

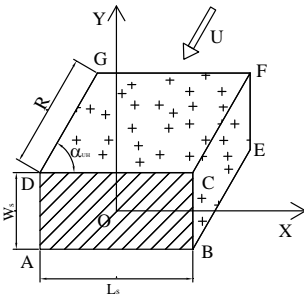


Figure 1. The debris distribution around the structure

### 3 Windborne Debris Flying Trajectories

Wills et al. classified debris into three generic types: compact, plate-like, and rod-like (Wills et al., 2002). The different shapes of debris have different flying trajectories because of their different dynamical characteristics. Windborne debris fly-

ing trajectories depend on the shape, density and dimension of the debris, the constraint form, initial wind attack angle, wind speed and the air density etc.

(a) Plate-like debris flying trajectories

The forces acting on the plate-like debris include wind load, gravity, and frictional drag of the air. Through calculating the dynamical trajectory equations (3)-(5) of the debris by numerical method, both velocities and distances of horizontal and vertical could be achieved (Tachikawa, 1983).

$$m \frac{d^2 x}{dt^2} = m \frac{du_m}{dt} = \frac{1}{2} \rho_a A [(U - u_m)^2 + v_m^2] (C_D \cos \beta - C_L \sin \beta) \quad (3)$$

$$m \frac{d^2 z}{dt^2} = m \frac{dv_m}{dt} = \frac{1}{2} \rho_a A [(U - u_m)^2 + v_m^2] (C_D \sin \beta + C_L \cos \beta) - mg \quad (4)$$

$$I_m \frac{d^2 \theta}{dt^2} = \frac{1}{2} \rho_a A l [(U - u_m)^2 + v_m^2] C_M \quad (5)$$

where  $m$ =debris mass;  $l$ =reference length (along-wind dimension for a plate or rod);  $A$ =reference debris area (usually taken as the largest face area);  $I_m$ =mass moment of inertia;  $x$ = horizontal displacement of debris;  $z$ =vertical displacement of debris;  $\theta$ = angular rotation;  $u_m$ =horizontal debris velocity;  $v_m$ =vertical debris velocity;  $U$ =wind speed;  $\rho_a$ =air density;  $C_D$ ,  $C_L$ ,  $C_M$ =drag, lift, and moment force coefficients, respectively;  $\beta$ =angle of the relative wind vector to the horizontal;  $g$ =acceleration due to gravity; and  $t$ =time.

(b) Compact debris flying trajectories

The kinematics of compact debris accelerated in a steady horizontal wind stream is assumed to have drag forces and gravity given by equations (6) and (7).

$$\frac{d^2 x}{dt^2} = \frac{\rho_a C_D (U - u_m) \sqrt{[(U - u_m)^2 + v_m^2]}}{2 \rho_m l} \quad (6)$$

$$\frac{d^2 z}{dt^2} = \frac{\rho_a C_D (-v_m) \sqrt{[(U - u_m)^2 + v_m^2]}}{2 \rho_m l} - g \quad (7)$$

where  $l$  is the characteristic length of the object equal to the ratio of the volume to the frontal area, which in the case of a sphere is equal to two-thirds of the diameter (Holmes 2004).

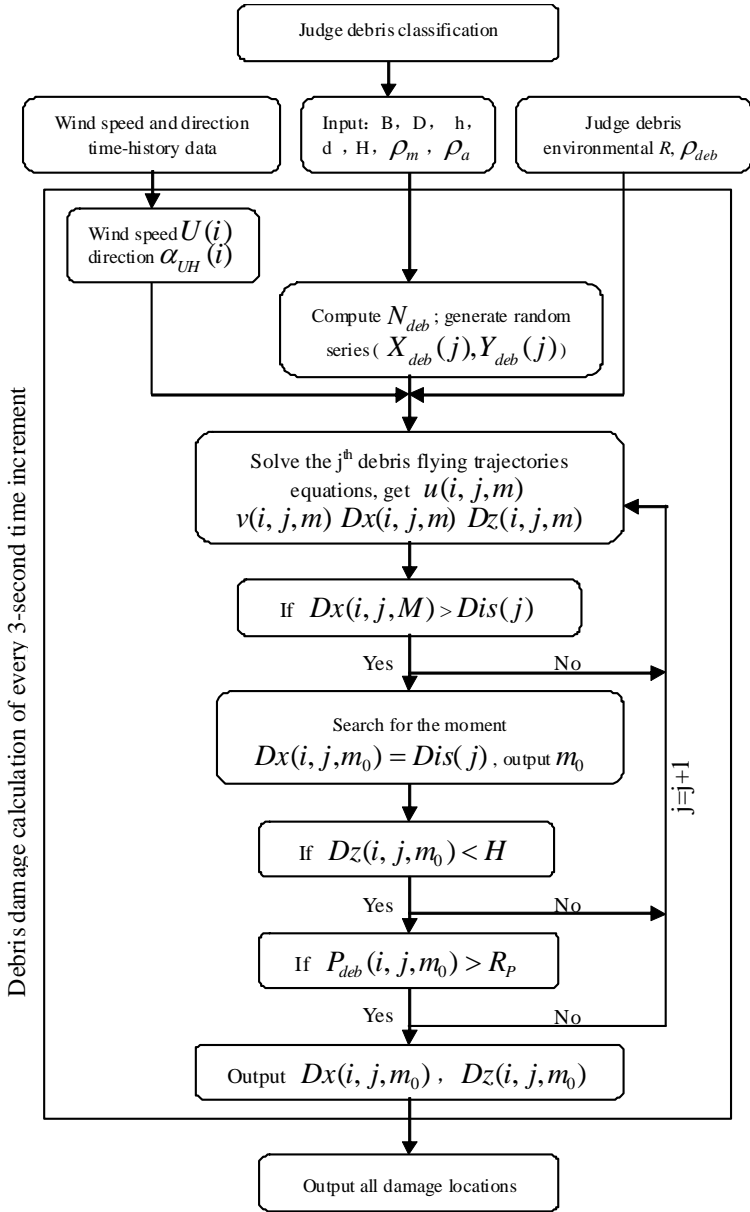


Figure 2. The flowchart of windborne debris damage estimation of structural envelopes

## 4 Impact Resistance of Structural Envelopes Analysis

Glass is the one of the most common vulnerable structural envelope materials in strong wind events. The destruction of glass under windborne debris is typical kind of impact brittle damage, which related to many aspects including the thickness and dimension of glass, the processing style, and the supporting way etc. According to method mentioned in the reference [HAZUS-MH 2006], the impact resistance of the glass is the critical momentum value. The impact momentum of the debris is the product of the mass and the speed of debris. If the impact momentum of the debris is larger than the impact resistance of glass, the glass was broken up, otherwise the glass is safe and the debris fell down.

## 5 Debris Damage Analyses of Structural Envelopes

The damage estimation method of structural envelopes caused by windborne debris is shown in Figure 2 as a flowchart. 3-second gust speed is used here instead of 10-minute mean wind speed for the purpose of damage prediction.  $u(i, j, m)$ ,  $v(i, j, m)$ ,  $Dx(i, j, m)$ , and  $Dz(i, j, m)$  are horizontal and vertical speed and displacement of the  $j^{\text{th}}$  debris at time step  $i$  at the substep  $m$  respectively.

## 6 An Application Example

An example of steel structure of light-weight with gabled frames was given to demonstrate the whole process of windborne debris damage estimation. The number of 11 windows distribute uniformly on each windward and leeward walls with dimension of 3m×3.6m. The schematic drawing of structural dimension and wind direction is shown in Figure 3. The window glass is 6mm thick fully tempered monolithic glass that provides an estimated threshold average breakage momentum of 0.1kg-m/s (Behr et al. 1994). Assume that gravel is the debris around the model with the radius of debris region ( $R=30$ ) and the distribution density of the debris region ( $\rho_{deb}=2$ ). The diameters of the gravel vary from 5mm to 15mm with uniform distribution, and the density of the gravel is 2000 kg/m<sup>3</sup>.

Typhoon Chanchu (No. 0601) was chosen to be the present wind load original data. First, the original data was treated properly, then the wind speed was transformed from 325m to the average roof height (here 8.625m). For the time interval is ten minutes, the gust speed envelope value was obtained through 10 minutes mean value multiplied by gust factor. The time-history curves of wind speed were shown in Figure 4.

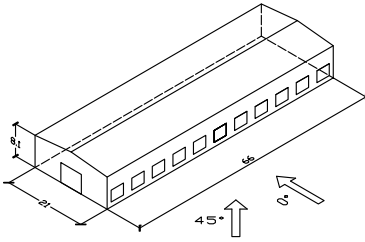


Figure 3. Schematic drawing of structural dimension and wind direction

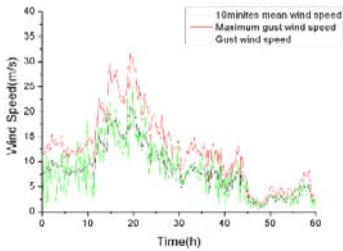


Figure 4. Gust speed time-history of typhoon Chanchu

The damage estimation application of the model was coded in terms of Matlab functions according to the process previous described. The necessary parameters of every time step were calculated according to the diameter and the density of the debris, the dimension and the distribution density of the debris region, and time-history data of the wind speed and direction etc. The trajectory of debris at every moment was obtained by solving the equations (3)-(7) through numerical method. Judging the glass was safe or destroyed by using the method shown in Figure 5 and output the damage locations at the same time. Finally, the final damage rate was achieved after a series of computing. When the gravel was on the ground and the impact resistance of glass is 0.1 kg-m/s, the windows are all safe in the model. If the window glass was laminated glass with resistance 0.05 kg-m/s, and all gravels were at the height of 8m, there are 3 pieces of glasses are broken, the damage rate is equal to 13.6%.

## References

Behr R. A., Minor J. E. (1994). A survey of glazing system behavior in multi-story buildings during Hurricane Andrew. *Structural Design of Tall Buildings*, 3(3), 143-161.  
 HAZUS-MH Hurricane Technical Manual (2006), Vol. 1, 5-12.

- Holmes J. D. (2004). Trajectories of spheres in strong winds with application to wind-borne debris. *J. Wind. Eng. Ind. Aerodyn.*, 92, 9-22.
- Lin N., Holmes J. D., Letchford C. W. (2007). Trajectories of wind-borne debris in horizontal winds and applications to impact testing. *Journal of Structural Engineering*, 274-282.
- Minor J. E. (2005). Lessons learned from failures of the building envelope in windstorms. *Journal of Architectural Engineering*, March, 10-13.
- Tachikama M. (1983). Trajectories of flat plates in uniform flow with applications to wind-generated missiles. *J. Wind. Eng. Ind. Aerodyn.*, 14(1-3), 443-453.
- Wills J. A. B., Lee B. E., Wyatt T. A. (2002). A model of wind-borne debris damage. *J. Wind. Eng. Ind. Aerodyn.*, 90, 555-565.

*“This page left intentionally blank.”*

# Engineering Characteristics Analysis of Typhoon Wind Field Based on a Mesoscale Model

Xing Tang<sup>1\*</sup> and JinPing Ou<sup>1,2</sup>

<sup>1</sup>School of Civil Engineering, Harbin Institute of Technology, Harbin 150090, P.R. China

<sup>2</sup>School of Civil & Hydraulic Engineering, Dalian University of Technology, Dalian 116024, P.R. China

**Abstract.** In the current civil engineering field, the characteristics of typhoon wind field are chiefly studied through field measurements and simple numerical simulation of typhoon engineering model. This paper will bring in the sophisticated non-hydrostatic version 3.7 of American Pennsylvania State University (PSU) – National Center for Atmospheric Research (NCAR) Fifth-Generation Mesoscale Model MM5 in meteorology to simulate typhoon in order to apply in disaster prevention and reduction of civil engineering. Taking the strong typhoon Wipha (0713) as a example, the quadrupled nesting grid with spacing of 27 km, 9 km, 3 km and 1 km in MM5 is applied to the typhoon to obtain the high-resolution, three-dimensional wind field. Meanwhile the effectiveness and applicability of MM5 model are evaluated by the typhoon yearbook of China Meteorological Administration. Then the engineering characteristics of typhoon wind field in the boundary layer, such as horizontal wind speed and wind profile are presented and briefly analyzed from the respect of physics essence.

**Keywords:** typhoon wind field in the boundary layer, mesoscale model MM5, numerical simulation, engineering characteristics

## 1 Introduction

In the last several decades, as the fast development of computer technology and numerical computation method, the wind engineering field gradually forms computing wind engineering (CWE) – a new interdisciplinary. Besides traditional theory research, wind tunnels experiment and field measurements (Bienkiewicz, 1996) computing wind engineering becomes another very effective study method in wind engineering (Murakami, 1997). Among these means, the most outstanding

---

\* Corresponding author, e-mail: tangxing627@163.com

one is computational fluid dynamics (CFD), which mainly studies the small-scale flow phenomenon in engineering, and it has been widely applied in the problems of wind-induced vibration about the high-rise structure and bridge structure in civil engineering.

However, as for mesoscale or microscale disastrous weather phenomena, such as typhoon (hurricane), thunderstorm and downburst, which cause great damage in the engineering, computational fluid dynamics (CFD) cannot directly make numerical simulation with them. Because the CFD model does not consider complex geophysical process and effect, which include atmospheric cumulus, precipitation, radiation, boundary layer, topography and air-sea-land interaction. As a result, in the current civil engineering field, the study on wind field characteristics of disastrous weather phenomena primarily depends on field measurements and simple numerical simulation of engineering model. Taking the problem of typhoon numerical simulation as an example, the famous experiential model like Batts (Batts et al., 1980), Shapiro (Shapiro, 1983 and Vickery et al., 1995a and 1995b) and Yan-Meng (Meng et al., 1995 and 1997) model have been widely used in the typhoon engineering field. Nevertheless, these typhoon engineering models which usually use simplification of the dynamical governing equation have fairly obvious limitations. They are really feasible and convenient from the aspect of computational quantity, but not considering the complex effect of atmospheric physics detailedly, they simulate the structure of typhoon wind field which has quite differences with reality situation. More complex the terrain and underlying surface are, more obvious the difference is, especially in atmospheric surface layer. So the simulated results of engineering models can hardly satisfy the fine need of modern engineering. Just like the successful and fine numerical simulation of CFD technique in small scale flow, it is necessary to bring in a new numerical simulation means to civil engineering to study the temporal and spatial distribution characteristics of wind field of disastrous weather phenomena at high resolution, which cause the great damage to engineering structures.

In 1922, L. F. Richardson firstly proposed the method of numerical integration to forecast the future weather condition (Kimura, 2002), namely numerical weather prediction (NWP). Similarly, accompanying with advances in computers technique and atmospheric observation technique, numerical weather prediction (NWP) has acquired the significant increase in the degree of complexity and applicability. Now the meteorological centers of most countries in the world already have independently developed the numerical weather models which include from macroscale to microscale, and established an integrated numerical weather prediction system in operation, for instance, China Meteorological Administration (CMA), American Environmental Prediction Centre (NCEP) and Japan Meteorological Agency (JMA) etc. In the essence, numerical weather prediction (NWP) and computational fluid dynamics (CFD) have the same root and source. Both of them apply the method of numerical simulation to study atmosphere flow phenomenon and based on the same fluid governing equation (Navier-Stokes equation). The major differences are their different emphases, the former one studies atmos-

phere flow from the view of meteorology, while the latter one from engineering (Pielke et al., 1997). Due to the huge success of numerical weather prediction, especially the rapid growth of mesoscale numerical model in 1980s, after 1990s, some mesoscale simulating systems have developed fairly sophisticatedly and complicatedly, and there are many famous mesoscale models – MM5, WRF, RAMS and ARPS etc. springing up. Mesoscale numerical simulation models are no longer limited to macroscale weather forecast, and develop toward fine direction. With the precision ceaselessly increases, mesoscale models can meet the need of engineering to some degree, and have been widely used in urban heat island (Kondo et al., 2008), environment pollution (Niewiadomski et al., 1999), and wind energy prediction (Murakami et al., 2003) such engineering field.

The common study method of the typhoon characteristic in engineering is field measurements (Li et al., 2005 and Cao et al., 2008), but field measurements which waste a great deal of human and material resources, usually have small observational range and short observational time, and only can get the partial information of typhoon wind field. Therefore, reconstruction of high-resolution, three-dimensional typhoon wind field in the boundary layer by numerical simulation is indispensably. Typhoon is one of the extreme mesoscale weather phenomena (strong wind and heavy rain). Different from applying simple numerical simulation of typhoon in civil engineering, this paper will take the strong typhoon Wipha (0713) which made landfall in Zhejiang province of south China in 2007 as an example, and employ mesoscale model MM5 to simulate it with high degree of accuracy. Then the mean wind characteristics associated with civil engineering (such as horizontal wind speed and wind profile) in the boundary layer are finely analyzed by the simulated result of MM5 model, which can cast a new viewpoint to the structure of typhoon wind field at the perspective of engineering.

## **2 The MM5 Model and Setting Up**

### ***2.1 Overview of Typhoon Wipha***

Tropical storm Wipha (0713), which originated from the northeast sea of Philippines, moved steadily northwestward and strengthened gradually. At 2100 UTC 17 September 2007, the system upgraded to supper strong typhoon intensity and maintained this intensity for 9 hours. Subsequently the typhoon with a maximum wind speed of 45 m/s and a minimum central pressure of 950 hPa make landfall in the Cangnan county of Zhejiang province at 1830 UTC 18 September 2007. During its landfall, the wind speeds of coastal region in Zhejiang and Fujian province generally exceeded 24.5 m/s, and the maximum wind speed reaching to 55.3 m/s was recorded at Cangnan observation station in Zhejiang province. Strong wind

associated with landfall of typhoon Wipha brings the great damages to the engineering structures especially in Zhejiang and Fujian province etc.

### 2.2 Model Configuration

The Fifth-Generation Mesoscale Model MM5, which is developed by American Pennsylvania State University (PSU) and National Centre for Atmospheric Research (NCAR) together, has become to one of the most essential mesoscale dynamical models after several years improvement. MM5 model is a non-hydrostatic primitive equation mesoscale model with three velocity components ( $u, v, w$ ), pressure perturbation ( $p'$ ), temperature ( $T$ ), and specific humidity ( $q$ ) as the main prognostic variables, which are based on terrain following sigma coordinates and solved in the Arakawa B grid. MM5 model has already been employed to simulate various typhoons of the Northwest Pacific by many operational and research institution, which has already been shown to have very reasonable accuracy. A detailed description of the model is available in Dudhia (1993) and Dudhia et al (2005).

Table 1. The domain design and parameter description of MM5 model. PBL Planetary Boundary Layer, NCEP National Centre for Environmental Prediction, USGS United States Geological Survey.

Model domain	D01	D02	D03	D04
Dynamics	Primitive equation, Non-hydrostatic			
Grid centre	27.2°N, 120.5°E			
Grid dimension	121×121	121×121	121×121	121×121
Horizontal grid spacing	27 km	9 km	3 km	1 km
Integration time step	75 s	25 s	8.3 s	2.8s
Vertical level number	37 sigma levels (18 levels in the lowest 1 km)			
Terrain elevation and land-use/vegetation	USGS 25-category global dataset			
Initial and lateral boundary conditions	NCEP final analysis data (1°×1°)			
Cumulus parameterization	Grell	Grell	None	None
PBL scheme and diffusion	High-resolution Blackadar PBL			
Radiation scheme	Cloud-radiation			
Surface layer scheme	Five-layer soil model			
Explicit Moisture scheme	Simple ice			
Initial position of bogus typhoon	27.1°N, 120.6°E			

In order to obtain high-resolution, three-dimensional wind field, we present a numerical simulation of typhoon Wipha using the version 3.7 of PSU/NCAR MM5 in this study (Liu et al. 1997 and 1999). Table 1 describes the main paramete-

trical scheme and setup of simulation used in this study, and the domain of quadrupled nested grid model simulated in MM5 model is shown in Figure 1. This study utilizes the NCAR (National Center for Atmospheric Research) – AFWA (Air Force Weather Agency) synthetic vortex scheme which is now available as part of MM5. The basic parameters are determined by the yearbook of typhoon. In the synthetic vortex scheme, the wind speeds below the 850 hPa level (~1500 meters) are fixed at the maximum wind speed from the yearbook of typhoon identically, which may cause the underestimate of surface wind speed. So the maximum wind speed used in synthetic vortex scheme is amplified to keep large wind speed near typhoon center in the boundary layer.

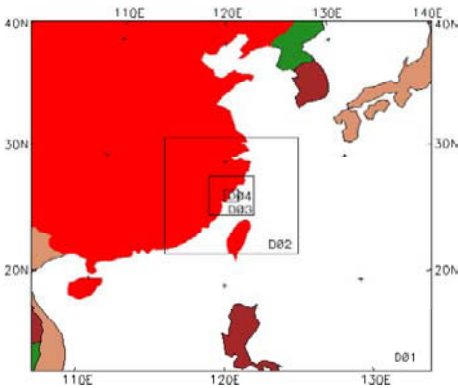


Figure 1. The model domains of quadrupled nested grids.

Model vertical level number	Height above ground level (m)
1st level	~ 10
3rd level	~ 50
8th level	~ 150
10th level	~ 225
13th level	~ 450
18th level	~ 1000

Table 2. The convert relation between model  $\sigma$  level and height above ground level.

The vertical output of MM5 model is defined at the  $\sigma$  coordinate, which has a certain transformational relation with the common height above ground level ( $z$  coordinate) in the engineering. Table 2 tells the relation between model  $\sigma$  level and height above ground level, which will be used in subsequent analyses.

### 3 Validation of Simulation

Figure 2 shows the comparison between the observed and simulated track of typhoon Wipha from 1800 UTC 18 September to 1800 UTC 19 September 2007. The typhoon center from MM5 model is located at the position of the minimum central pressure, and the observed one is determined according to the yearbook of typhoon (2007) published by CMA. From Figure 2 we can see that MM5 model basically reproduces the track of typhoon Wipha in 24 hours. The simulated typhoon translates a little faster than the observed at first 6 hours and a littler slower at last 6 hours. The mean track error is about 50 km which we can accept.

Figure 3 shows the observed and simulated maximum wind speed and minimum central pressure of typhoon. The horizontal wind speeds of MM5 model which are considered about several minutes or tens of minutes interval, are transformed to compare with the ones of typhoon yearbook which are recorded by two minutes interval by empirical formula. At the beginning, the simulated maximum wind speed of typhoon is bigger than the observed one and then smaller later, which makes a difference within 5 m/s. The simulating central pressure agrees well with the observed one in Figure 3, which is only a bit lower than observation, and the maximum error is about 10 hPa. The agreement of observed and simulated typhoon can preliminarily prove that inserting bogus typhoon vortex in the NCEP first guess field is very important for keeping typhoon intensity and MM5 model is feasible for the simulated typhoon Wipha to some extents. In this study, only three key parameters of typhoon—typhoon track, central pressure and maximum wind speed, have been examined. Admittedly, further inspection and applicability study are needed because of the complexity of typhoon.

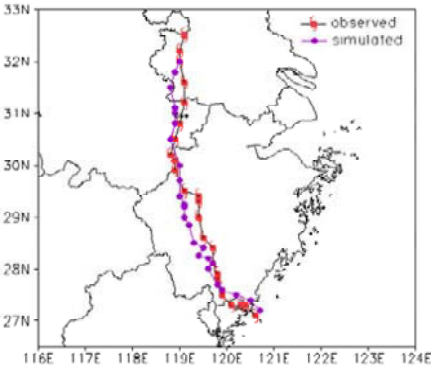


Figure 2. The simulated and observed track of Wipha every 1 hour.

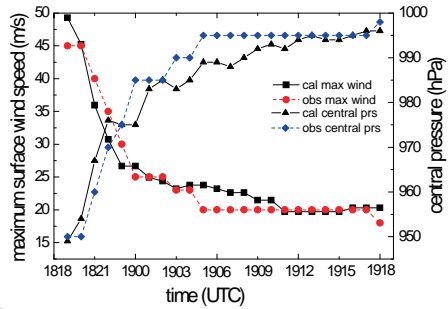


Figure 3. The simulated and observed maximum surface wind speed and minimum central pressure of typhoon Wipha every 1 hour.

The reasons which are responsible for discrepancies between the observed and simulated typhoon are mainly as follow. Firstly, the good or bad quality of large-scale initial guess field determines the accuracy of simulation very badly. Due to shortage of observation, the global analyzing field data provided by NCEP may not contain sufficient small scale flow information near typhoon centre correctly. Secondly, the synthetic vortex scheme employed in the simulation which contains some actual and simple information of typhoon, such as centre position and the maximum wind speed etc., greatly affects the prediction of the track and intensity of typhoon. But the incorporation of artificial vortex into the initial conditions may occur somewhat contradiction between the storm and its larger-scale environment physically and dynamically. And the optimization of parameters is obviously necessary. Thirdly, the output result of MM5 model which represents the

average value of time and space, has different property with the observation, and the translating relation with them is needed to study further.

## 4. Characterises of Typhoon Wind Field

When typhoon make landfall, the boundary layer is the most intensively affected vertical atmospheric layer. The distribution of typhoon wind field in the boundary layer is closely associated with the disaster of engineering structure, because the height of high-rise structure is lower than 1000 meters presently. A lot of investigations about the damage of typhoon indicate that the places near the typhoon eyewall suffer the most serious disaster and the greatest loss in engineering, which relate to the maximum wind speed and strong vertical convection current occurring at these places closely. Influenced by the complicated factors of underlying surface, terrain and free troposphere, the three-dimensional structure of typhoon boundary layer is rather complex, which cannot be described by simple engineering typhoon model correctly. Advanced high-resolution mesoscale numerical model is applied to civil engineering absolutely necessary. The followings will analyze the mean wind speed characteristics of typhoon Wipha in the boundary layer respectively.

### 4.1 *Horizontal Wind Field of Wipha*

Our attention will be paid mostly to the simulations at the typhoon centre. Figure 4 illustrates the spatial distribution of simulated wind speed near eye region of typhoon Wipha at 1900 UTC 18 September 2007. All the contours of horizontal wind speed are greater than 20 m/s which may begin to cause damage to engineering structure and given at very 5 m/s in Figure 4. We can clearly see some sophisticated structures of typhoon eyewall from the figures. At present the storm which has made landfall for about half hour, has half part on the landmass and half on the sea. Figure 4a shows the wind speed distribution at about 10 meters elevation above the ground. It appears that the distribution of wind speed presents obvious anomaly and asymmetry, which has some relations with the specific topographic forcing on landmass. The contours of wind speed on the landmass are dense and the values are comparatively small, especially at the southwest quadrant of typhoon where the maximum wind speed does not overpass 20 m/s. While on the sea the wind speeds change gently and keep relatively large value (more than 40 m/s). The vicinity of typhoon eyewall has very fierce air motions and the extreme wind speed of typhoon occurs at the northeast quadrant of typhoon in Figure 4a. The wind speed distribution of the other four figures is similar to Figure 4a, but

the extreme wind speed gradually increases as height, and the region where the wind speeds are more than 20 m/s gradually enlarge.

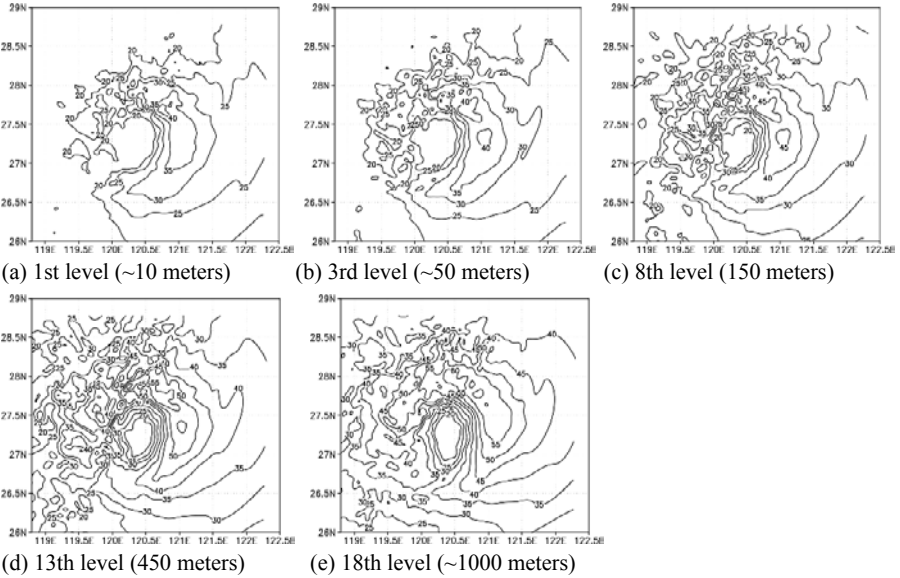


Figure 4. The horizontal distribution of wind speed (great than 20 m/s) near the typhoon eye region, 1900 UTC 18 September 2007.

In the engineering application, the standard height of wind load has some arbitrariness, which means the value changes with the different codes used. For example, the architectural structure load standards of China is defined as 10 meters height, while the railway code as 20 meters height. As we all know, the wind speeds near the surface which are influenced by local topography and land-use significantly have obvious shortage and limitation. Air motions at the high levels which have little relation with local terrain condition, are chiefly controlled by mesoscale circulation of typhoon and macroscale environmental wind field. MM5 Model can reproduce the wind speeds at the top of boundary layer detailed. Thus in engineering design, establishing the standard based on the wind speed of boundary layer top (such as 1000 meters) and reversely calculating the surface wind speeds (wind profile) by considering the influence of terrain and vegetation, may be more reasonable for wind-resistant design of high-rise structure. This method also can make up the deficiency that MM5 model smoothes steep terrain by average to result in the inaccuracy of simulated wind speed behind high mountains and hills.

Typhoon Wipha weakens rapidly after landfall and makes the damages to engineering structure gradually reduced. Figure 5 shows the temporal variations of horizontal wind speeds near typhoon Wipha eyewall at 10th  $\sigma$  level (~225 meters) from 1900 UTC 18 September to 0000 UTC 19 September 2007. Owing to cut

off energy source and friction drag of the ground, typhoon intensity ceaselessly weakens in the first six hours after landfall. The maximum wind speed changes from initial 50 m/s to 25 m/s in Figure 5. Due to the complicated factors like underlying surface, the typhoon cannot keep axisymmetric shape unlike the mature stage on the sea, which has approximately axisymmetric pressure and velocity field. The distributions of pressure and velocity field are more complex, which are associated with irregular terrain and air-sea interaction. It is pointed out that engineering models only have better simulation with the mature typhoon on the sea. Because when typhoon make landfall, the location of lowest central pressure no longer coincides with the minimum wind speed, which shows some baroclinicity of atmosphere flow and cannot satisfy the basic assumption of engineering model. And people in wind disaster prevention and reduction of civil engineering emphasize on concerning the irregular wind field of typhoon after landfall, which attack coastal region directly. Three-dimensional non-hydrostatic MM5 model which considers more complete physical process can get the phenomena mentioned above and agree well with observational data. The engineering model cannot satisfy the fine analyze of typhoons obviously.

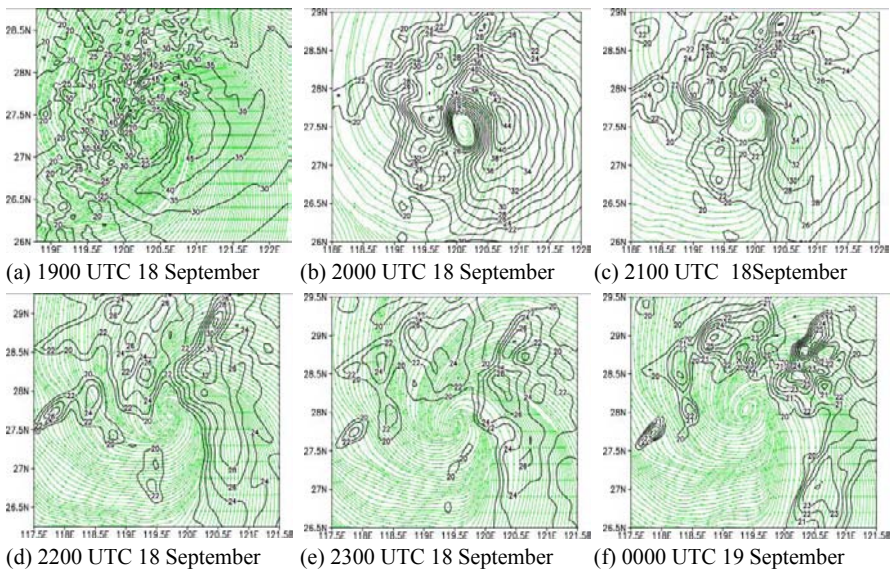


Figure 5. The time evolutions of the wind speed (great than 20 m/s) and streamline (solid line with arrows) at 10th level (~225 meters) near the typhoon eye.

### 4.2 Wind Time Variation of Grid Points

Figure 6 and Figure 7 respectively show the temporal variations of wind speed and wind direction (north wind is 0°, and clockwise is positive) of grid point A (27.2°N, 120.5°E) and grid point B (28.0°N, 119.0°E) from 1900 UTC 18 September to 1800 UTC 19 September 2007. There are five vertical levels having been presented in Figure 6 and Figure 7, which are 1st  $\sigma$  level (~10 meters), 3rd  $\sigma$  level (~50 meters), 8th  $\sigma$  level (~150 meters), 13th  $\sigma$  level (~450 meters) and 18th  $\sigma$  level (~1000 meters). The simulated data are substituted by the nearest grid points of MM5 model approximately.

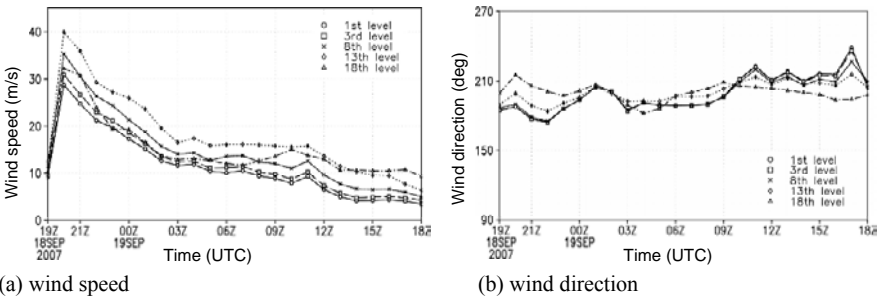


Figure 6. The time evolutions of wind speed and wind direction of point A (27.2°N, 120.5°E), 1900 UTC 18 September 2007.

In Figure 6, grid point A is located at the place where typhoon make landfall and has been strongly affected by typhoon. In Figure 6a, the wind speeds of grid point A are very strong at first, then increase suddenly due to the rapid approach of typhoon centre, and subsequently weaken gradually later because the typhoon has moved away to the northwest. In the low levels near surface, the wind speeds increase with height. But the law is not kept all along in the whole boundary layer. The maximum wind speed occurs at 13th  $\sigma$  level (~450 meters), but not at 18th  $\sigma$  level (~1000 meters), which shows obviously supergradient wind phenomenon (Kepert et al., 2001). Figure 6b shows the wind direction of grid point A slowly varies from around 180° to 240°, which indicates that the edge region not the eye region of typhoon has passed through grid point A.

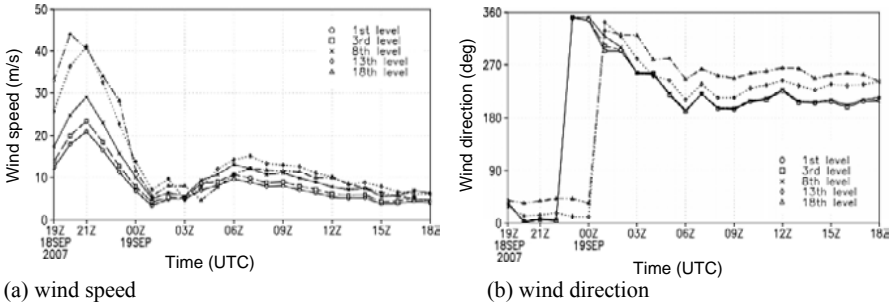


Figure 7. The time evolutions of wind speed and wind direction of point B (28.0°N, 119.0°E), 1900 UTC 18 September 2007.

In Figure 7a, with approach of typhoon, the wind speeds come to increase and then reach the maximum at 2100 UTC 18 September 2007. It can be explained that the eyewall region of the typhoon has reached grid point B. Subsequently the wind speed curves reach an obvious low value when the typhoon eye region has traversed across grid point B. At the same time, the wind direction makes a sudden change from less than 50° to more than 300°, then decreases gradually and finally keeps the fixed value about 240° in Figure 7b. The wind directions in Figure 6 and Figure 7 are almost coincident in the lowest three levels near ground, which is consistent with conclusion that wind direction does not vary with the height in the surface layers. Generally speaking, the wind speed and wind direction of grid points mainly depend on the relative position and distance from the typhoon centre.

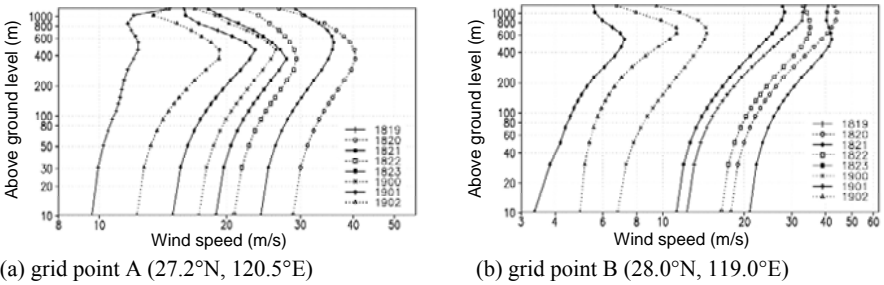


Figure 8. The time evolutions of wind speed profiles.

Figure 8 shows the temporal evolutions of wind speed profiles of grid point A (27.2°N,120.5°E) and grid point B (28.0°N, 119.0°E) at each one hour from 1900 UTC 18 September (namely 1819 in Figure 8) to 0200 UTC 19 September (namely 1902 in Figure 8) 2007 respectively.

In Figure 8a, the wind speeds of grid point A are small at 1900 UTC 18 September, due to the position located probably near and even in the typhoon eye region. The wind speeds strengthen suddenly when the eyewall region of typhoon

moved over grid point A. The wind speeds are close to 30 m/s, and the maximum wind speeds in the boundary layer can reach 40 m/s at around 400 meters height above the ground. We can easily find that the supergradient wind phenomena are universal existence in the inner region of typhoon. Most curves of wind profile in Figure 8a have a turning point at about 400 to 600 meters in the vertical direction which Yoshida et al. (2008) have pointed out. The special phenomena have a great distinct from normal monsoon wind and may be a remarkable characteristic of typhoon wind profiles. Finally the wind speeds weaken gradually with typhoon gone far.

In Figure 8b, the wind speeds of grid point B at 10 meters elevation gradually increased from 12.3 m/s at 1900 UTC 18 September to the maximum value about 21.0 m/s at 2100 UTC 18 September. The reduced distance between grid point B and the typhoon centre leads to the change of wind speeds gradually. The wind speeds cannot reach the value of grid point A, because the typhoon intensity weakens rapidly after landfall. Although from 1900 UTC 18 September to 2300 UTC 18 September grid point B is located at the inner region of typhoon, the wind speeds increase with height monotonically until the top of the boundary layers, and do not present supergradient wind phenomenon like in Figure 8a. The wind profiles have some similarities with the monsoon wind. The reason is not clear, but may associate with the rapid weakening of typhoon and local terrain.

The wind profiles approximately increase linearly within the lowest 200 meters as shown in Figure 8, which illustrates it perfectly meet logarithmic law and power law in the surface layers. Some previous studies (Moss et al., 1975) have pointed out that without the fierce vertical convective motion, the mechanical friction rather than the buoyancy will really work significantly, especially occurring in the observed strong wind of typhoon, and the atmosphere will always maintain neutral stratification condition. According to the aforementioned reason, the weather of strong wind can satisfy the theoretical assumption (logarithmic law and power law) of wind profile in the surface layers. The average power exponent  $\alpha$  ( $U = (z/10)^\alpha$ ) of wind profiles is about 0.13 in Figure 8a, while in Figure 8b,  $\alpha$  is about 0.20.

### 4.3 Wind Profile of Wipha

Figure 9 shows the radial distribution of typhoon wind profiles at 1900 UTC 18 September 2007. Figure 9a and Figure 9b are cross sections along longitude (toward west) and latitude (toward north) though the storm respectively. There are eight curves which denote different distances (5-500 km) from the typhoon centre, and the wind speeds present the same tendency with distance from the typhoon center in each subfigure of Figure 9. Firstly, from the change of wind profiles denoted 5km and 10 km, we can see that in the typhoon eye region the wind speeds are smaller and the air flow is very calm. Then the atmosphere begins to fiercely

flow intensely influenced by typhoon until 30 km from the centre, which have quite different flow property from the typhoon eye region. The maximum wind speed appears between 50 km and 100 km from the typhoon centre, and the radius of maximum wind is about 70 km. The supergradient wind phenomenon generally exists inside the typhoon eyewall, which maybe originates from the unique warm core structure of typhoon. Finally, the wind speeds will quickly decrease, and the wind profiles have no difference with the normal monsoon, when the distance reaches a threshold value at the outer vortex region. Comparing with Figure 9a and Figure 9b, the wind speeds of west cross-section are smaller than the north one, especially in strongly influenced region of typhoon. The asymmetry distribution is affected by the complicated terrain as precious analysis. From Figure 9, the wind profiles also satisfy the power law in the low levels near ground approximately, and the average power exponent  $\alpha$  of wind profiles in Figure 9a is about 0.20, while in Figure 9b,  $\alpha$  is about 0.16.

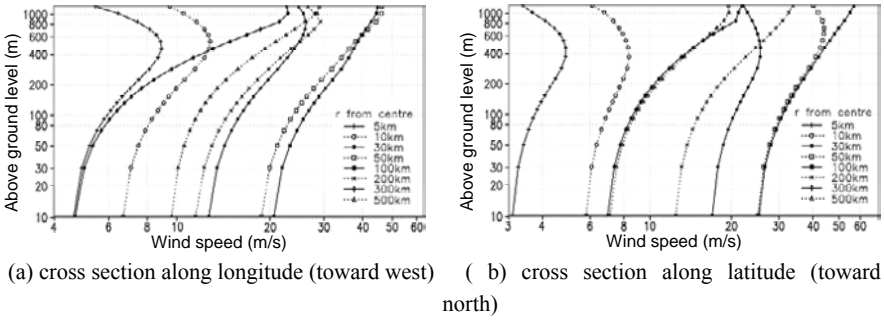


Figure 9. The radial distribution of wind speed profiles, 1900 UTC 18 September 2007.

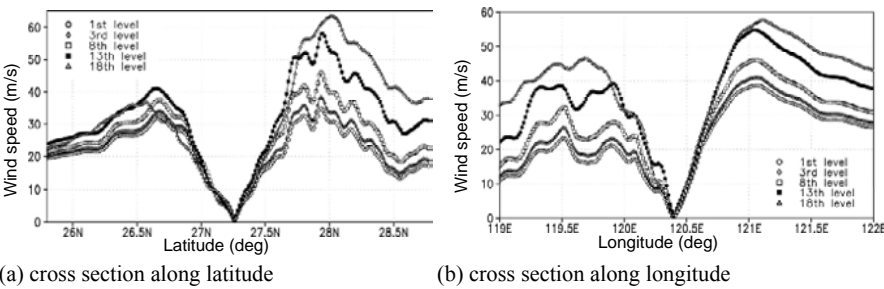


Figure 10. The cross sections of asymmetric wind speed through the typhoon centre, 1900 UTC 18 September 2007.

Figure 10 shows the latitude-height and longitude-height cross sections of asymmetric wind speed through typhoon centre at 1900 UTC 18 September 2007. The simulated distribution of wind speeds near the typhoon centre in Figure 10 shows a typical “funnel type”. The wind speeds are relatively small even approach

0 m/s and keep constant with different levels at very close to the typhoon centre. The eyewall region of typhoon exists clearly, which can distinctly divide typhoon into the inner region with the width about 70 km and outer vortex region. The thickness of typhoon eyewall is comparatively small, but the gradient of wind speed is quite great. Usually the maximum wind speed occurs at the typhoon eyewall region. At the inner region and eyewall region, the wind speeds of 13th  $\sigma$  level (~450 meters) are bigger than the 18th  $\sigma$  level (~1000 meters) which indicates remarkable supergradient wind phenomenon. On the contrary, at outer vortex region which are far from typhoon center, the wind speeds of 13th  $\sigma$  level (~450 meters) will be less than the 18th  $\sigma$  level (~1000 meters), which accords with the previous result of normal wind. It should be pointed out that the critical value (supergradient wind phenomenon) approximately equals to the radius of maximum wind.

In Figure 10a, the wind speeds in the west part of typhoon are smaller than the east, because the western section of typhoon has made landfall and been blocked by coastal terrain, while the eastern section still maintains on the sea and subject little friction. Compared with Figure 10a, in Figure 10b the difference between southern part and northern part of typhoon flow is fairly small, and the wind speeds of low levels like 1st  $\sigma$  level present more asymmetric than the high levels like 18th  $\sigma$  level in the boundary layer. The distribution of wind speed varies irregularly in southern part, while gentle variation in northern part, which we have analyzed in previous paper. Generally speaking, the wind field of typhoon after landfall exhibits apparent asymmetric and intricate. Even if the location has the same distances off typhoon center, the wind speeds will take different value. In summary, the flow of typhoon at northern and eastern part performs more intense than south and west, and the west part is the weakest, which perhaps associates with the moving direction of typhoon and intensive influence of terrain.

## 5 Conclusions

In this study, we used the non-hydrostatic MM5 model to simulate typhoon Wipha after landfall. By comparing the simulated data with the typhoon yearbook, the research result preliminarily demonstrates MM5 model performed reasonably well on simulating this rare event. Subsequently we analyze the engineering characteristics of typhoon wind field in boundary layer, which civil engineering concerns such as the temporal and spatial distributions of horizontal wind speeds and wind profiles. These results from our simulation are more realistic than any previously obtained in civil engineering field.

Comparing with the engineering typhoon model, High-resolution MM5 model can reproduce the three-dimensional structure and some other basic features of the typhoon after landfall, which can help to understand the three-dimensional structure and evolution law of typhoon wind field from the perspectives of engineering,

and provide much more useful wind field physical parameters, which can solve the problem of scarce observations in some sense. Under the current conditions – imperfect typhoon observational system and the deficiency of typhoon observational data, using mesoscale model like MM5 to reconstruct typhoon by high resolution numerical simulation is a feasible and effective method to study the engineering characteristics of typhoon wind field.

This paper made a preliminary exploration and attempt to apply meteorological mesoscale model to the typhoon disaster prevention and reduction field in civil engineering. Many works are required further investigations, like applying four-dimensional data assimilation method, and combining mesoscale model with CFD to achieve the precision of engineering. Meanwhile, further validation and applicability study are also necessary. Finally it should be pointed out that applying the high resolution meteorological model to simulate the extreme disastrous weathers such as typhoon (hurricane), thunderstorm and downburst etc., may be the promising and feasible method to investigate the engineering characteristics of extreme wind to prevent and reduce wind disaster in civil engineering.

## Acknowledgement

This research work was supported by Nation Key Technology R&D Program of China under Grant No. 2006BAJ03B04.

## References

- Batts M. E., Russell L. R. et al. (1980). Hurricane wind speeds in the United States. *Journal of the Structural Division*, 106, 2001–2016.
- Bienkiewicz B. (1996). New tools in wind engineering. *Journal of Wind Engineering and Industrial Aerodynamics*, 65, 279–300.
- Cao S., Tamura Y. et al. (2008). Wind characteristics of a strong typhoon. *Journal of Wind Engineering and Industrial Aerodynamics*, 97, 11–21.
- Dudhia J. (1993). A non-hydrostatic version of Penn State–NCAR mesoscale model: validation tests and simulation of an Atlantic cyclone and cold front. *Monthly Weather Review*, 121, 1493–1513.
- Dudhia J., Gill D. et al. (2005). PSU/NCAR mesoscale modeling system tutorial class notes and user's guide: MM5 Modeling System Version 3.
- Keprt J., Wang Y. (2001). The dynamics of boundary layer jets within the tropical cyclone core. Part II: Nonlinear enhancement. *Journal of Atmospheric Sciences*, 58, 2485–2501.
- Kimura R. (2002). Numerical weather prediction. *Journal of Wind Engineering and Industrial Aerodynamics*, 90, 1403–1414.
- Kondo H., Tokairin T. et al. (2008). Calculation of wind in a Tokyo urban area with a mesoscale model including a multi-layer urban canopy model. *Journal of Wind Engineering and Industrial Aerodynamics*, 96, 1655–1666.

- Li Q. S., Xiao Y. Q. et al. (2005). Full-scale monitoring of typhoon effects on super tall buildings. *Journal of Fluids and Structures*, 20, 697–717.
- Liu Y., Zhang D. L. et al. (1997). A multiscale numerical study of hurricane Andrew (1992). Part I: Explicit simulation and verification. *Monthly Weather Review*, 125, 3073–3093.
- Liu Y., Zhang D. L. et al. (1999). A multiscale numerical study of hurricane Andrew (1992). Part II: Kinematics and inner-core structures. *Monthly Weather Review*, 127, 2597–2616.
- Meng Y., Matsui M. et al. (1995). An analytical model for simulation of the wind field in a typhoon boundary layer. *Journal of Wind Engineering and Industrial Aerodynamics*, 56, 291–310.
- Meng Y., Matsui M. et al. (1997). A numerical study of the wind field in a typhoon boundary layer. *Journal of Wind Engineering and Industrial Aerodynamics*, 67, 437–448.
- Moss M. S., Rosenthal S. L. (1975). On the estimation of boundary layer variables in mature hurricanes. *Monthly Weather Review*, 103, 980–988.
- Murakami S. (1997). Current status and future trends in computational wind engineering. *Journal of Wind Engineering and Industrial Aerodynamics*, 67&68, 3–34.
- Murakami S., Mochida A. et al. (2003). Development of local area wind prediction system for selecting suitable site for windmill. *Journal of Wind Engineering and Industrial Aerodynamics*, 91, 1759–1776.
- Niewiadomski M., Leung D.Y.C. et al. (1999). Simulations of wind field and other meteorological parameters in the complex terrain of Hong Kong using MC2 – A mesoscale numerical model. *Journal of Wind Engineering and Industrial Aerodynamics*, 83, 71–82.
- Pielke R. A., Nicholls M. E. (1997). Use of meteorological models in computational wind engineering. *Journal of Wind Engineering and Industrial Aerodynamics*, 67&68, 363–372.
- Shapiro L. J. (1983). The asymmetric boundary layer flow under a translating hurricane. *Journal of Atmospheric Sciences*, 40, 1984–1998.
- Vickery P. J., Twisdale L. A. (1995a). Prediction of hurricane wind speeds in the United States. *Journal of Structural Engineering*, 121, 1691–1699.
- Vickery P. J., Twisdale L. A. (1995b). Wind field and filling models for hurricane wind-speed prediction. *Journal of Structural Engineering*, 121, 1700–1709.
- Yoshida M., Yamamoto M. et al. (2008). Prediction of typhoon wind by Level 2.5 closure model. *Journal of Wind Engineering and Industrial Aerodynamics*, 96, 2104–2120.

# Geometrical Nonlinearity Analysis of Wind Turbine Blade Subjected to Extreme Wind Loads

Guoqing Yuan<sup>1\*</sup> and Yu Chen<sup>1</sup>

<sup>1</sup>School of Aerospace Engineering and Applied Mechanics, Tongji University, Shanghai 200092, P.R. China

**Abstract.** Modern wind turbine blades become more and more flexible with its increasing size. Under extreme wind excitations, the considerable blade deformation may result in large deflection at blade tip. This paper proposes a Variable Step Deformation Difference Method (VSDDM) to analyze the nonlinear blade structure. The VSDDM has the advantages of distinct concept, easy to understand, and simple to program. Owing to the linear solution always bigger than the nonlinear solution, the design would be conservative based on the linear solution.

**Keywords:** large-scale wind turbine blade, large deflections, cantilever beams, variable step deformation difference method (VSDDM)

## 1 Introduction

Wind turbines have been growing in size in recent years for larger energy generation. The world's biggest wind turbine generator is currently undergoing testing in the North Sea 15 miles off the East coast of Scotland near the Beatrice Oil Field. It has a power output of 5 Megawatts with a 126-meter rotor diameter and 61.5-meter-long turbine blades. Offshore wind turbines with a nominal power output up to 10MW and a rotor diameter of 175m, and to be placed on water depths as deep as 20m, are under serious consideration (Larsen and Nielsen, 2006). With their increasing size, the blades become more and more flexible. Furthermore, mechanical properties of the blade material are characterized with high strength and relatively low Young's modulus. Thus the blade will deform considerably when subjected to extreme wind loads. In theory, geometrical nonlinearity should be taken into account for such cases. However, most of the available commercial programs for numerical analysis of wind turbines use simplified linear structural

---

\* Corresponding author, e-mail: gqyuan@tongji.edu.cn

models, which cannot be applied to structures with considerable deformations. Thus it is necessary to understand the various nonlinear interactions thoroughly and develop a geometrical nonlinear analysis method for such wind turbine blades.

Different approaches have been used to deal with large deflection problems, such as elliptic integral formulation, numerical integration with iterative shooting techniques, incremental finite element method, incremental finite differences method, method of weighted residual (MWR), perturbation method etc. (Larsen and Nielsen, 2006; Mohammad Dado and Samir Al-Sadder, 2005; Chien, 2002).

Based on the differential equation of large deflection cantilever beams, an approximate deflection equation for moderate large deflection problems is developed with Newton binomial theorem in this paper. The large deflection equation in difference form is given by applying 3-nodes difference formulas and an explicit recurrence formula of calculating the nodes deflections can be obtained so that there is no need to solve non-linear equation. This yields high calculation efficiency. The proposed VSDDM has been used to analyze the nonlinear large deflection of the blades. Several conclusions have been reached by comparing its solution with nonlinear finite element analysis.

## 2 Development of VSDDM

### 2.1 Approximation of Beam Deflection Equation

The basic equation of beams with large deflection (Chien, 2002) is

$$\frac{\frac{d^2 y}{dx^2}}{\left[1 + \left(\frac{dy}{dx}\right)^2\right]^{\frac{3}{2}}} = \frac{M(x)}{EI} \tag{1}$$

where  $x$  is horizontal axis,  $y(x)$  is the vertical deflection,  $EI$  is the flexural rigidity of the beam, and  $M(x)$  is the bending moment.

According to the Newton binomial theorem, when  $\left|\frac{dy}{dx}\right| < 1$ , whether  $m$  is positive integer or not, there is

$$\left[1 + \left(\frac{dy}{dx}\right)^2\right]^{\frac{3}{2}} = 1 + \frac{3}{2}y'^2 + \frac{3}{8}y'^4 + \dots \tag{2}$$

With moderate deflection, the first two terms of the right-side expression of Eq. (2) may possess sufficient precision. Thus for moderate flexible elements such as

wind turbine blades, this approximation may be permitted. Consequently Eq. (1) can be written approximately as follows:

$$\frac{y'''}{1 + \frac{3}{2}y'^2} = \frac{M(x)}{EI} \tag{3}$$

### 2.2 VSDDM Details

The beam axis can be divided into n equal segments initially. Thus there will be (n+2) nodes in total with the virtual node, which can be denoted as -1, 0, 1, 2, ..., and n, respectively. Considered the changing of projection position of nodes on x-axis due to the deformation, variable step-size differences are introduced to analyze the large deflection. The step sizes are denoted by  $h_0, h_1, \dots, h_1, \dots,$  and  $h_n$ , in which  $h_0$  is the virtual step.

The 3-node difference formulas are employed for the node i

$$\left\{ \begin{aligned} \left(\frac{dy}{dx}\right)_i &= \frac{y_{i+1} - y_{i-1}}{h_i + h_{i+1}} \\ \left(\frac{d^2y}{dx^2}\right)_i &= \frac{\frac{y_{i+1} - y_i}{h_{i+1}} - \frac{y_i - y_{i-1}}{h_i}}{\frac{h_i + h_{i+1}}{2}} \end{aligned} \right. \tag{4}$$

Substituting (4) into (3) yields the follow large deflection equation in difference form

$$\frac{\frac{y_{i+1} - y_i}{h_{i+1}} - \frac{y_i - y_{i-1}}{h_i}}{\frac{h_i + h_{i+1}}{2}} = \frac{M_i}{EI_i} \left( 1 + \frac{3}{2} \left( \frac{y_{i+1} - y_{i-1}}{h_i + h_{i+1}} \right)^2 \right) \tag{5}$$

The boundary conditions for a cantilever beam are

$$y_{x=0} = 0, \quad y'_{x=0} = 0$$

Since  $y_1 = y_{-1}$

And let  $h_0 = h_1$

Then

$$y_i = \frac{M_0}{EI_0} h_i^2 / 2 = y_{i-1} \quad (6)$$

$$\text{Let } \frac{M_i}{EI_i} \left( \frac{h_i + h_{i+1}}{2} \right) = s, \quad h_i + h_{i+1} = r, \quad a = \frac{3s}{2r^2}, \quad b = \frac{3s}{r^2} y_{i-1} + \frac{1}{h_{i+1}},$$

$$c = ay_{i-1}^2 + s + \frac{y_i - y_{i-1}}{h_i} + \frac{y_i}{h_{i+1}} \quad (7)$$

Then Eq. (5) becomes

$$ay_{i+1}^2 - by_{i+1} + c = 0 \quad (8)$$

Thus

$$y_{i+1} = \frac{b \pm \sqrt{b^2 - 4ac}}{2a} \quad (9)$$

Because a, b and c only relate to  $y_i, y_{i-1}$ , and  $y_0, y_1$  can be determined directly by the boundary conditions,  $y_2, \dots, y_n$  can be successively calculated by Eq. (9).

The accurate deflection curve can be obtained by an iterative procedure described next. First, the bending moments at each node can be calculated based on the initial nodal coordinates and the load position. Then the deflection of every node is calculated by Eqs. (6) and (9). But the calculation results are not the accurate nodal deflection because of the change of projection position of nodes on x-axis by deformation. By assuming the length of the axis of the deformed beam remain the same, projection lengths of each segment on x-axis can be deduced with the deflections from last iteration by following formula

$$(h_i)_k = ((h_i)_0^2 - ((y_{i+1})_{k-1} - (y_i)_{k-1})^2)^{1/2} \quad (10)$$

where  $(h_i)_k$  denotes the i-th segment size in the k-th iteration step,  $(h_i)_0$  denotes the initial size of the i-th segment, and  $(y_{i+1})_{k-1}$  and  $(y_i)_{k-1}$  denote deflections at the (i+1)-th and i-th nodes, respectively, after the (k-1)-th iteration calculation.

Furthermore, x coordinate of each node of the deformed beam can be calculated by the following formula and  $(x_0)_k \equiv 0$ .

$$(x_i)_k = (h_i)_k + (x_{i-1})_k \quad (11)$$

Thus the more and more realistic bending moments at each node can be obtained after the second, the third, (and so on) iteration calculation. It is considered that the accurate deflections have been obtained once the deflections of each node stay close enough to these by previous iteration.

### 3 Analysis of Geometrical Nonlinear Deformation of Large Wind Turbine Blade Subjected to Extreme Wind Load

A 200KW wind turbine blade (Yuan Guoqing, 1993; Zhang Jinnan, 1997) was analyzed in this paper. The technical specifications of the blade are as follows – nominal power 200KW, rotor diameter 23m, cut-in wind speed 4.5m/s, rated wind speed 14m/s, cut-out wind speed 28m/s, extreme wind speed 60m/s ( 2 minuets average), blade length 10.8m, weight 800kg, safe life 20 years, three-bladed, up-wind, horizontal.

The extreme 10-minute mean wind speed is 45m/s and the turbine shuts down when it meets the extreme wind load. The impact factor can be taken 3 conservatively. The limit design wind load (linear load in N/m, y' direction) is taken as

$$P(r) = 7361(1.715 - 0.1r) \tag{12}$$

where r denotes the distance from the rotation center to any section in meters.

The blades are constructed from fiberglass reinforced epoxy. The blade tips can be turned 90 degrees respectively to the main blade, thereby acting as aerodynamic brakes. Figure 1 is the conceptual diagram of the blade and the cross section. Table 1 shows the geometrical properties of every cross section.

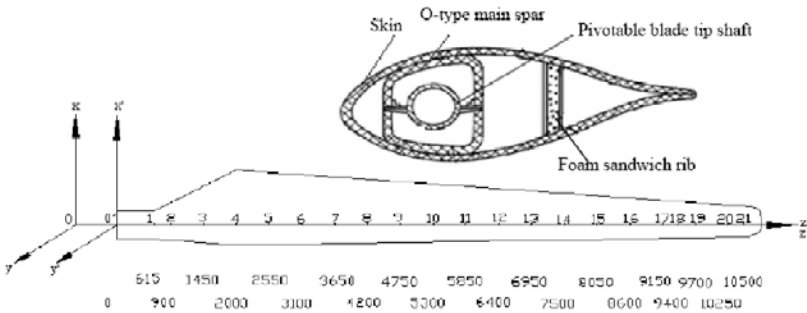


Figure 1. Conceptual diagram of the blade and its cross section

Table 1. Geometrical properties of each cross section of the 200KW wind turbine blade

Section position Z'(mm)	Aera (mm <sup>2</sup> ×10 <sup>3</sup> )	J <sub>x</sub> (mm <sup>4</sup> ×10 <sup>8</sup> )	Section position Z'(mm)	Aera (mm <sup>2</sup> ×10 <sup>3</sup> )	J <sub>x</sub> (mm <sup>4</sup> ×10 <sup>8</sup> )
0	59.45	18.54	5850	16.14	0.98
615	59.45	18.54	6400	15.07	0.72
900	51.06	26.77	6950	12.71	0.47
1450	52.87	32.57	7500	11.07	0.32
2000	41.19	13.13	8050	10.21	0.22
2550	33.89	8.63	8600	9.38	0.16
3100	27.42	5.50	9150	8.57	0.12
3650	24.41	3.86	9400	8.21	0.10
4200	20.31	2.53	9700	5.44	0.05
4750	18.54	1.81	10250	4.99	0.03
5300	17.36	1.34	10500	4.54	0.03

Table 2 lists the tip deflections of the blade by variable step deformation difference method (VSDDM) and nonlinear finite elements beam3 and shell 93 of the multi-purpose computer program ANSYS. It also compares the nonlinear and linear solutions. Table 3 shows that the proposed method provides accurate prediction of the blade tip deflection, and is effective to solve such non-prismatic cantilever beams with variable stiffness, large deflection, and subjected to complicate loads. Figure 2 is the comparison of the deflection curves.

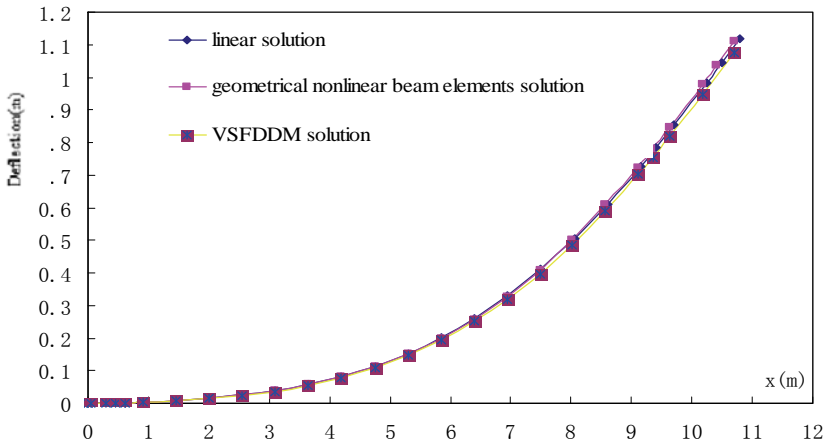


Figure 2. Comparison of the deflection curves of the blade in y direction

Table 2 Comparison of tip deflections of the blade (units: mm)

	VSFDDM	FEM (beam element)	FEM (shell element)
Geometrical non-linear solution	1074.5	1110.0	1072.0
Error of the linear beam elements (%)	4.09	0.76	4.33

Note: The tip deflection solved by linear beam elements is 1111.84mm.

When subjected to extreme wind load, the 200KW wind turbine blade will have very large deflection not only at the tip, but also the rare blade part of approximately 1/10 total length of the blade and 2 times maximum thickness of blade cross section. In theory, geometrical nonlinearity should be taken into account to analyze and design the blade structure for such a load case, and the small deflection beam theory is not accurate. However, this study shows that the difference between the geometrical nonlinear solution and linear solution is small (less than 5 percent). Thus the linear solution has enough precision for the design of these wind turbine blades. Moreover, it is conservative to ignore their geometrical nonlinearity as the solution from geometrical nonlinear theory is always smaller than the one from linear theory.

It is worth of noting that the geometrical nonlinearity of wind turbine blades may be significant and must be considered in their design. For example, when the loads are doubled or the blade stiffness is reduced to half, the results will change as list in Table 3. Obviously the errors from linear solution have become big, which should not be neglected.

Table 3 Comparison of tip deflections of the blade with doubled loads (units: mm)

	VSFDDM	FEM (beam element)
Geometrical non-linear solution	1994.8	2107.7
Error of the linear beam elements (%)	12.14	6.13

Note: The tip deflection solved by linear beam elements is 2236.9mm.

## 4. Conclusions

A new scheme to solve large deflection problem of cantilever beams, VSDDM, is presented in this paper. This method is based on an approximate deflection equation developed with Newton binomial theorem from the Euler-Bernoulli beam theory. VSDDM is effective as nonlinear finite element methods to solve non-prismatic cantilever beams with variable stiffness, large deflection and subjected to complicate loads. VSDDM has the advantage that its concept is easy to under-

stand and its program is easy to write. The convergence speed of iterative calculation is rapid.

Though the deformation of the 200KW wind turbine blade is belong to large deflection, it is revealed by analyzing that the large wind turbine blades possess better stiffness still and the difference between the geometrical nonlinear solution and linear solution is small. Owing to the linear solution bigger than the nonlinear solution it is inclined to safety to design based on it.

Certainly if the blade becomes more flexible, or the loads become bigger, it should be paid attention to analyze the geometrical nonlinear effects from the results of Table 2 and 3. The errors will become so big that it should not be neglected. The results showed in table 3 have justified it. To obtain optimal design, nonlinear analysis is extremely necessary.

## Acknowledgements

This research work is supported by Shanghai Leading Academic Discipline Project (No. B302).

## References

- Chien W. Z. (2002). Second order approximation solution of nonlinear large deflection problem of Yongjiang railway bridge in Ningbo. *Applied Mathematics and Mechanics*, 23, 441-451 [in Chinese]
- Larsen J. W., Nielsen S.R.K. (2006). Non-linear dynamics of wind turbine wings. *Int. J. Non-linear Mechanics*. 41,629-643
- Mohammad Dado, Samir Al-Sadder (2005). A new technique for large deflection analysis of non-prismatic cantilever beams. *Mechanics Research Communications*, 32, 692-703
- Yuan G. Q. (1993). The calculation report of the 200KW wind turbine blade structure design. Shanghai: Tongji University [in Chinese].
- Zhang J. N. (1997). 200KW wind turbine blade. *Solar energy*, (3), 23-24 [in Chinese].

# Dynamic Response and Reliability Analysis of Wind-Excited Structures

Zhangjun Liu<sup>1,2\*</sup> and Jie Li<sup>2</sup>

<sup>1</sup>College of Civil & Hydroelectric Engineering, China Three Gorges University, Yichang 443002, P.R. China

<sup>2</sup>School of Civil Engineering, Tongji University, Shanghai 200092, P.R. China

**Abstract.** This paper proposes a new procedure for simulation of random wind velocity field with only a few random variables. The procedure starts with decomposing the random wind velocity field into a product of a stochastic process and a random field, which represent the time property and spatial correlation property of the wind velocity fluctuation respectively. Then the stochastic process for wind velocity fluctuations is represented as a finite sum of deterministic time functions with corresponding uncorrelated random coefficients by an innovative orthogonal expansion technology. Similarly, the random field is expressed as a combination form with only a few random variables by the Karhunen-Loeve decomposition. It provides opportunities to use probability density evolution method (PDEM), which had been proved to be of high accuracy and efficiency, in computing the dynamic response and reliability of general linear/nonlinear structural systems. A numerical example, which deals with a MDOF frame structure subjected to wind loads, is given for the purpose of illustrating the proposed approach.

**Keywords:** random wind velocity field, orthogonal expansion method, probability density evolution method, dynamic response, reliability

## 1 Introduction

Wind loading is a typical dynamic load taken into account in the design of structures such as long-span suspended and cable-stayed bridges, towers and tall buildings. However, randomness and uncertainties, which are inherent in both wind loading and structural characteristics, will introduce variability in the dynamic response of wind-sensitive structures. In addition, the dynamic reliability of stochastic structures is usually assessed by the level crossing theory through the Rice formula (Crandall, 1970). It is found that only approximate dynamic reliability can

---

\* Corresponding author, e-mail: liuzhangjun73@yahoo.com.cn

be obtained by the methods because the joint PDF of the response and its velocity required in the Rice formula is usually unavailable. Although the diffusion process theory-based method may give more accurate results, it is still difficult to apply to practical multi-degree of freedom systems.

In recent years, a class of probability density evolution method (PDEM), which had been verified to be applicable to stochastic response and dynamic reliability analysis of general MDOF systems, has been developed (Li and Chen, 2004, 2006; Chen and Li, 2005). Using the approach for evaluation of the extreme-value distribution of a set of random variables and /or a stochastic process (Chen and Li, 2005) and the idea of equivalent extreme-value event (Li et al, 2007), the structural system reliability could be evaluated requiring neither the joint PDF of the response and its velocity, nor the assumptions on properties of the level-crossing events. As a numerical example, a deterministic frame structure subjected to wind loading is investigated.

## 2 Orthogonal Expansion of Wind Velocity Field

Let  $x, y, z$  be a point in space,  $z$  is the height from the ground and  $x$  is the lateral wind direction,  $y$  is assumed to be the along-wind direction. Then the velocity at a given point location can be seen either as a one-variate four-dimensional (1V-4D) random field or a time-dependent 1V-3D stochastic field process. In practice, in order to simplify the concepts, the wind velocity fluctuation can be characterized in the plane  $y = 0$ . Then the time-dependent 1V-2D stochastic field process can be examined. Then wind field velocity can be written as:

$$V(x, z; t) = \bar{V}(z) + \tilde{V}(x, z; t) \quad (1)$$

where  $V(x, z; t)$  is the wind speed of the point  $(x, z)$ ;  $\bar{V}(z)$  is the mean wind speed at the height  $z$ ; and  $\tilde{V}(x, z; t)$  is the fluctuating component of the wind speed, assumed to be a normal zero-mean stationary stochastic process. In the following, the mean wind speed  $\bar{V}(z)$  can be represented by the power-law:

$$\bar{V}(z) = (z/10)^\alpha \bar{V}_{10} \quad (2)$$

where  $\alpha$  is the coefficient of ground roughness degree,  $\bar{V}_{10}$  is the mean wind speed at 10 m above the ground.

For the PSD of wind velocity fluctuations don't vary with height, such as Davenport power spectrum, its fluctuating wind field velocity  $\tilde{V}(x, z; t)$  can be decomposed as:

$$\tilde{V}(x, z; t) = U(x, z)v(t) \quad (3)$$

where  $v(t)$  is the fluctuating wind velocity stochastic process whose complete probabilistic characterization is ensured by the PSD function such as Davenport spectrum. The wind velocity fluctuation process  $v(t)$  can be represented using the orthogonal expansion method as (Liu and Li, 2008):

$$v(t) = \sum_{j=1}^{10} \sqrt{\lambda_j} \xi_j(\theta) f_j(t), \quad f_j(t) = \sum_{k=0}^{600} \chi_{k+1} \varphi_{j,k+1} \dot{\phi}_k(t) \quad (4)$$

where  $\chi_{k+1}$  is the energy equivalence coefficients,  $\lambda_j$  is the  $j$ th eigenvalue of the correlation matrix,  $\varphi_{j,k+1}$  is the  $(k+1)$ th element of the  $j$ th normalized eigenvector of the correlation matrix,  $\phi_k(t)$  is the Hartley orthogonal function;  $\{\xi_j\}$  is a set of independent normalized Gaussian random variables.

In Equation (3),  $U(x, z)$  is the spatial correlation random field which is the stochastic function of spatial coordinates  $x, z$ , and its correlation function can be expressed as:

$$R_U(x_1, x_2; z_1, z_2) = \exp \left[ - \left( \frac{(x_2 - x_1)^2}{L_x^2} + \frac{(z_2 - z_1)^2}{L_z^2} \right)^{1/2} \right] \quad (5)$$

Using a finite Karhunen-Loeve (K-L) series, the two-dimensional homogeneous random field  $U(x, z)$  can be expressed as (Li and Liu, 2008):

$$U(x, z) = \sum_{i=1}^{r_x} \sqrt{\lambda_{xi}} \xi_{xi} f_{xi}(x) \cdot \sum_{j=1}^{r_z} \sqrt{\lambda_{zj}} \xi_{zj} f_{zj}(z) \quad (6)$$

### 3 Stochastic Dynamic Response and Reliability Analysis

#### 3.1 General Evolution PDF Equation of Dynamic Response

Without loss of generality, consider the equation of motion of a deterministic MDOF system subjected to the random excitation as follows:

$$\mathbf{M}\ddot{\mathbf{X}}(t) + \mathbf{C}\dot{\mathbf{X}}(t) + \mathbf{K}\mathbf{X}(t) = \mathbf{F}(\Theta, t) \quad (7)$$

The system has  $n$ -degrees-of-freedom, so that the vector  $\mathbf{X}$  is an  $n \times 1$  displacement response vector, and  $\mathbf{M}$ ,  $\mathbf{C}$  and  $\mathbf{K}$  are  $n \times n$  mass, damping and stiffness matrices, respectively. The overhead dot denotes differentiation with respect to time,  $t$ .  $\mathbf{F}$  is a  $n \times 1$  forcing function vector, and  $\Theta$  is the  $n_\theta \times 1$  random vector with known PDF  $p_\Theta(\theta)$  where  $\Theta = (\xi_1(\theta), \xi_2(\theta), \dots, \xi_{n_\theta}(\theta))$ .

Obviously, the dynamic response  $\mathbf{X}(t)$  is a random vector process dependent on and determined by  $\Theta$ , and can be expressed as:

$$\mathbf{X}(t) = \mathbf{H}(\Theta, t) \tag{8}$$

where  $\mathbf{H}$ , existent and unique for a well-posed problem, is a deterministic operator. Its any component can be written as:

$$X(t) = H(\Theta, t) \tag{9}$$

According to Li and Chen (2004, 2006), the joint PDF of the augmented state vector  $(X, \Theta)$  satisfies the governing partial differential equation:

$$\frac{\partial p_{X\Theta}(x, \theta, t)}{\partial t} + \dot{X}(\theta, t) \frac{\partial p_{X\Theta}(x, \theta, t)}{\partial x} = 0 \tag{10}$$

where  $\dot{X}(\theta, t)$  is the velocity of the response for a prescribed  $\theta$ .

The initial condition of Equation (10) is given as:

$$p_{X\Theta}(x, \theta, t)|_{t=0} = \delta(x - x_0) p_\Theta(\theta) \tag{11}$$

where  $x_0$  is the deterministic initial value of  $X(t)$ .

After the initial-value problem (Equations (10) and (11)) is solved, the PDF of  $X(t)$  could then be evaluated by:

$$p_X(x, t) = \int_{\Omega_\Theta} p_{X\Theta}(x, \theta, t) d\theta \tag{12}$$

where  $\Omega_\Theta$  is the distribution domain of  $\Theta$ .

### 3.2 Dynamic Reliability Evaluation

As well known, the dynamic reliability about the dynamic response  $X(t)$  can be expressed as:

$$R = \Pr\{X(\Theta, t) \in \Omega_s, t \in [0, T]\} \quad (13)$$

where  $\Omega_s$  is the safe domain. In general cases, it is easy to rewrite Equation (13) into

$$R = \Pr\left\{\bigcap_{t \in [0, T]} (G(\Theta, t) > 0)\right\} \quad (14)$$

Here  $G(\cdot)$  is a time dependent limit state function.

According to the idea of equivalent extreme-value event (Li et al, 2007), if one defines an extreme value as:

$$W_{\min} = \min_{t \in [0, T]} (G(\Theta, t)) \quad (15)$$

whose PDF can be captured through the PDEM, then the reliability in Equation(14) equals:

$$R = \Pr\{W_{\min} > 0\} = \int_0^{+\infty} P_{W_{\min}}(W) dW \quad (16)$$

Likewise, if there is more than one limit state function combined together in the dynamic reliability evaluation, say,

$$R = \Pr\left\{\bigcap_{j=1}^m (G_j(\Theta, t) > 0, t \in [0, T_j])\right\} \quad (17)$$

where  $T_j$  is the time duration corresponding to  $G_j(\Theta, t)$ . According to the idea of equivalent extreme-value event, one can define the equivalent extreme value as

$$W_{\text{ext}} = \min_{1 \leq j \leq m} \left( \min_{t \in [0, T_j]} (G_j(\Theta, t)) \right) \quad (18)$$

Therefore, the reliability in Equation (17) can be computed directly by

$$R = \Pr\{W_{\text{ext}} > 0\} \quad (19)$$

### 4 Numerical Examples

The along-wind loading generated by the orthogonal expansion method and associated response of a 100m tall building with 10 DOFs is used for demonstrating the application of PDEM-based dynamic analysis schemes. The lumped mass of each story from the bottom to the top are 2.5, 2.5, 2.2, 2.2, 2.2, 2.2, 2.2, 2.2, 1.8, 1.8 ( $\times 108$  kg), respectively. The stiffness of each story from the bottom to the top are 3.48, 2.93, 2.92, 2.94, 2.92, 2.91, 2.92, 2.92, 2.31, 0.43 ( $\times 104$  kN/mm), respectively. The first and second natural periods of the building are 1.764 and 0.601 sec, respectively. Rayleigh damping is employed, i.e.  $C = aM + bK$ , where  $a = 0.2657 H_z$ ,  $b = 0.0071 \text{sec}$ ,  $M$  is the mass matrix,  $K$  is the stiffness matrix. The modal damping ratio for each mode is assumed to be 0.05.

The external loading vector is  $F(\Theta, t) = \{F_1(\Theta, t), F_2(\Theta, t), L, F_{10}(\Theta, t)\}^T$ , where  $F_j(\Theta, t)$  is the along-wind fluctuating force at the  $j$ th story node, which based on the quasi-steady and strip theories is modeled by:

$$F_j(\Theta, t) = \mu_D \times \frac{1}{2} \rho V^2 B_j \tag{20}$$

where  $\mu_D$  is the drag coefficient and assumed as 1.2;  $\rho$  is the air density;  $B_j$  is the tributary area.

The probabilistic information of the top displacement of the structure is shown in Figures 1-2. Figure 1 is the surface constructed by the PDF at different instants of time while Figure 2 is the contour of the surface, respectively.

The probabilities of reliability of the structure over time interval [0, 600] sec against inter-story drift are listed in Table 1. From Table 1 it is seen that the failure probability of the structural system is equal to the failure probability of the 10th story. It is shown that the failure probability of the weakest link is equivalent to the failure probability of the structural system.

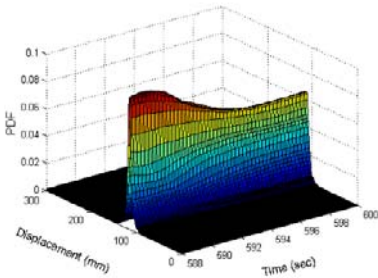


Figure 1. The PDF evolution against time

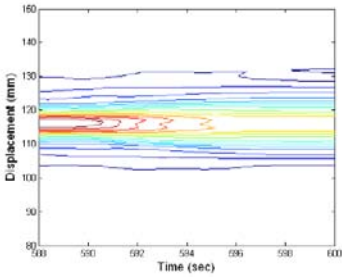
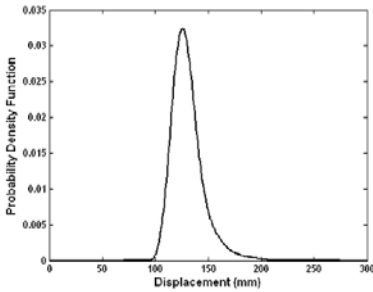
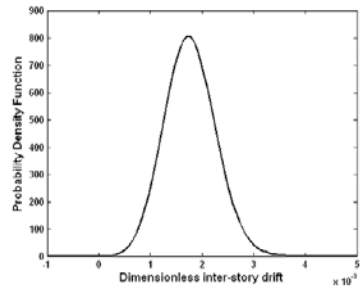


Figure 2. The contour of the PDF surface



(a) Top displacement



(b) Structural system

Figure 3. PDF of the equivalent extreme value

Table 1 the reliability probability of the structure against inter-story drifts

Number of story	Threshold of dimensionless inter-story drift	
	1/500	1/600
10th	0.7067	0.4518
9th	0.7137	0.4586
8th	0.7357	0.4807
7th	0.7793	0.5285
6th	0.8743	0.6230
5th	0.9279	0.7466
4th	0.9858	0.9045
3rd	0.9989	0.9845
2nd	1.0000	1.0000
1st	1.0000	1.0000
The structural system	0.7067	0.4518

## 5 Conclusions

The probability density evolution method is adopted for dynamic response and reliability analysis of wind-excited structures. As a numerical example, a deterministic frame structure subjected to wind loading is investigated. It is founded that the PDEM is feasible and efficient in the dynamic response and reliability analysis of wind-excited structures.

## Acknowledgements

The supports of the National Natural Science Foundation of China for Innovative Research Groups (Grant No.50621062), the National Natural Science Foundation of China for Young Scholars (Grant No.50808113) and China Postdoctoral Science Foundation funded project (Grant No.20080430689) are gratefully appreciated.

## References

- Chen J.B. and Li J. (2005). Dynamic response and reliability analysis of nonlinear stochastic structures. *Probabilistic Engineering Mechanics*, 20(1), 33-44.
- Chen J.B. and Li J. (2005). The extreme value distribution and reliability of nonlinear stochastic structures. *Earthquake Engineering and Engineering Vibration*, 4(2), 275-286.
- Crandall S-H. (1970). First-crossing probability of the linear oscillator. *Journal of Sound and Vibration*, 12, 285-299.
- Li J. and Chen J.B. (2004). Probability density evolution method for dynamic response analysis of structures with uncertain parameters. *Computational Mechanics*, 34, 400-409.
- Li J. and Chen J.B. (2006). The probability density evolution method for dynamic response analysis of non-linear stochastic structures. *International Journal for Numerical Methods in Engineering*, 65(6), 882-903.
- Li J. et al. (2007). The equivalent extreme-value event and evaluation of the structural system reliability. *Structural Safety*, 29, 112-131.
- Li J. and Liu Z.J. (2008). Orthogonal expansion method of random fields of wind velocity fluctuations. *China Civil Engineering Journal*, 41(2), 49-53 [in Chinese].
- Liu Z.J. and Li J. (2008). Orthogonal Expansion of Stochastic Processes for Wind Velocity. *Journal of Vibration Engineering*, 21(1), 96-101 [in Chinese].

# Wind-Induced Self-Excited Vibration of Flexible Structures

Tingting Liu<sup>1\*</sup>, Wenshou Zhang<sup>1</sup>, Qianjin Yue<sup>1</sup> and Jiahao Lin<sup>1</sup>

<sup>1</sup>State Key Laboratory of Structural Analysis for Industrial Equipment, Faculty of Vehicle Engineering and Mechanics, Dalian University of Technology, Dalian, China

**Abstract.** The modern tall buildings, slender and lightly damped, are vulnerable to the dynamic wind action. Vortex induced vibration, a typical crosswind excited vibration, is significant for the flexible structures and complex in the mechanism. In order to predict the vortex induced response of a super tall building with a SDOF empirical model, wind tunnel tests were carried out with an improved aeroelastic model according to the similitude. Based on the experimental data, the vortex-excited force parameters were determined and the characteristics of vortex induced vibration were investigated in some details. The time history of acceleration at the lock-in wind speeds range of the tall building is then obtained through Runge-Kutta method and the results show good agreement with measurements.

**Keywords:** crosswind, vortex induced vibration, flexible structure, wind tunnel test

## 1. Introduction

Crosswind induced vibration of the flexible and lightly damped slender structure is a typical aeroelastic phenomenon which would result in the probability of failure or loss of serviceability. Vortex shedding excitation is considered as a prime problem. The detrimental effects are caused by the fluid passing across a bluff body, separating and forming the vortices in the wake of the structures. When the frequency of vortex shedding approaches or synchronizes the structural natural frequencies, the motion of the structure suddenly increases and persists over a wide range of wind speeds, which is known as the lock-in phenomenon.

In order to describe the vortex induced vibration of the flexible structures, several mathematical models have been developed based on the experimental researches. These models can be divided into two main groups: single-degree-of-freedom (SDOF) model and coupled wake-oscillator model. Coupled wake-

---

\* Corresponding author, e-mail: ttliu44@hotmail.com

oscillator model was confirmed by Bishop and Hassan (1970) that the wake of the cylinder can be treated as an oscillator and then the vortex induced vibration is expressed by two differential equations with constant coefficients. The SDOF model for the aerodynamic computation is mainly proposed by Scanlan and Simiu (1986). The motion of structures is modeled as a solid oscillator that incorporates a nonlinear lift with a single equation. In this SDOF model, three independent parameters should be determined from the wind tunnel test with the aeroelastic models or prototypes. The methods for the parameters identification from the test data and simplifying and solving the nonlinear equation of motion would affect the results and need to be pondered in the application. Ehsan and Scanlan (1990) provided a two-step-process method to predict the vortex induced response of flexible bridges with the SDOF model. The parameters were estimated with the measured data of decay to resonance phenomenon. Vickery and Basu (1983) used the similar model and the stochastic vibration theory for assessment of vortex induced crosswind vibration of chimneys and towers. Larsen (1995) suggested a new SDOF model which was suited for design for non-linear dashpot elements applicable to finite element models of wind sensitive structures.

In this study, the vortex induced response of the tall buildings is obtained with the empirical SDOF model. The aeroelastic model in the wind tunnel test was designed as a multi-section structure according to the aerodynamic features of the tall buildings, which is first used in the vortex induced vibration prediction. Based on the test data, the parameters were identified with measured resonance data at two different damping ratios. The time history of acceleration at the lock-in wind speeds range is then obtained using Runge-Kutta method and the results show good agreement with measurements.

## 2. SDOF Model

In the wind engineering, the vortex induced response of structures is the primary problem, and the details pertaining to fluid-structure interaction are of less concern. Therefore, the SDOF empirical model is suggested. The general form of SDOF model is expressed as:

$$m \left[ \ddot{x}(t) + 2\zeta\omega_n \dot{x}(t) + \omega_n^2 x(t) \right] = F(x, \dot{x}, \ddot{x}, \omega_s t) \quad (1)$$

where  $m$  is the mass of per unit length,  $\zeta$  is the damping ratio,  $\omega_n$  is the structural circular frequency, and  $x$  is the displacement at the crosswind direction.  $F$  is the general function of vortex induced excitation of per unit length. The Simiu and Scanlan (1986) nonlinear force model incorporates aeroelastic damping, stiffness and harmonic force terms.

$$F = \frac{\rho U^2 D}{2} \left[ Y_1(K) \left( 1 - \frac{\varepsilon x^2}{D^2} \right) \frac{\dot{x}}{D} + Y_2(K) \frac{x}{D} + \frac{1}{2} C_L(K) \sin(\omega_s t + \phi) \right] \quad (2)$$

in which  $K = \omega D/U$  is the reduced frequency, where  $\omega$  is the vortex shedding frequency. The aerodynamic parameters  $Y_1$  and  $\varepsilon$  are associated with the linear and nonlinear term, respectively.  $Y_2$  is a linear aeroelastic stiffness and  $C_L$  defines a direct forcing at  $\omega_s$ .

Based on the wind tunnel data, the direct vortex shedding force is small when large amplitude oscillations are taking place. Therefore, the non-dimensional form of SDOF model in the lock-in wind speed range can be expressed as:

$$\ddot{\eta} + 2\zeta K_n \dot{\eta} + K_n^2 \eta = m_r Y_1 (1 - \varepsilon \eta^2) \dot{\eta} + m_r Y_2 \eta \quad (3)$$

where  $\eta = x/D$  is the non-dimensional displacement;  $m_r = \rho D^2/m$  is the mass ratio; and  $K_n = \omega_n D/U$  is the reduced natural frequency of the structure.

The estimation of aerodynamic parameters is based on a solution of the autonomous nonlinear equation with the method of slowly varying parameters (Ehsan and Scanlan, 1990). ‘Decay-to-resonance’ method is suggested when the steady-state amplitude  $\beta$ , the initial amplitude  $A_0$  and the initial phase angle  $\psi_0$  are measured. However, the operations of ‘decay-to-resonance’ method in wind tunnel tests consume much time. In this study, when the steady state amplitudes  $\beta_1$  and  $\beta_2$  at the same wind speed of two closely spaced values of the damping ratios, i.e.  $\zeta_1$  and  $\zeta_2$ , respectively, are obtained; the aerodynamic parameters  $Y_1$ ,  $\varepsilon$  and  $Y_2$  of the same model can be identified.

$$Y_1 = \frac{2K_n}{m_r} \frac{\beta_1^2 \zeta_2 - \beta_2^2 \zeta_1}{\beta_1^2 - \beta_2^2}, \quad \varepsilon = \frac{4}{\beta^2} \left( 1 - \frac{2\zeta K_n}{m_r Y_1} \right), \quad Y_2 = \frac{K_n^2 - K^2}{m_r} \quad (4)$$

### 3. Wind Tunnel Test

The two super towers (ST1 and ST2) of ETON Dalian Center are the tallest high-rise buildings in the city of Dalian. The ratios of the height to the width of the buildings are about 8.3 and 6.9, respectively. The effect of vortex shedding should be considered. Based on the conclusion on the wind tunnel tests with the rigid models of the project, the shape and the location of ST2 are inclined to induce a large dynamic response caused by crosswind excitation. Therefore, wind tunnel tests are carried out with the improved aeroelastic model of ST2.

The height of ST2 is 278.8m, and the cross section approaches to a square section with the length of 40m. The first natural frequencies at the two transverse directions are 0.183Hz and 0.195Hz, respectively, and the mass density is 350kg/m<sup>3</sup>.

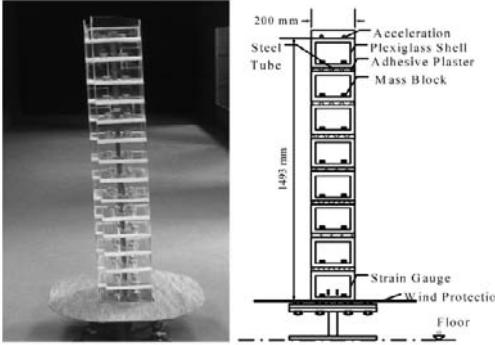


Figure 1. Model from practical experiment and the scheme of aeroelastic model of ST2

The multi-section aeroelastic model is shown in Figure 1. The rigid plexiglass shell, manufactured according to the real figuration of ST2, is attached to a circle shaped steel tube. The shell is divided into several segments and installed with an approximately 2-mm interstice between the adjacent ones. This setting makes the structural stiffness provide only by the steel tube and the motion is simulated properly. Damping is provided by the adhesive plaster which can also block the interstices. The added lumped mass blocks are evenly fixed at the bottom of each shell segment to provide sufficient mass. The whole model is firmly sited on the flange, which is welded on the floor of the wind tunnel.

The aeroelastic model test of ST2 is performed in the boundary layer wind tunnel DUT-1 of Dalian University of Technology. Considering the cross section size of the test section, the length scale is selected to be 1/200. According to the similarity requirement proposed by Themongkorn and Kwok (1999), the other scales of the aeroelastic model, i.e. structural density scale, frequency scale, and etc., can be selected. The mass of the model is determined to be 19.39kg, and the first natural frequency is 2.4Hz. The structural damping ratios adopted in the test are 0.7% and 0.3%. The wind flow is set from the north elevation of ST2, i.e. from the direction perpendicular to one face of the structure. The wake flow can be regularly separated from the symmetrical surface. This situation is supposed to the most potential one to induce the steady state vibration of the vortex shedding. The mean wind speed profile is not taken into account in order to simplify the analysis.

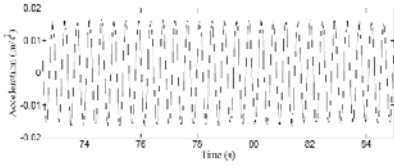


Figure 2. Top acceleration at the reduced wind speed = 33.3 (experimental wind speed = 16m/s) with damping ratio  $\zeta = 0.7\%$ .

The time history of the top acceleration in the lock-in wind speed range with the structural damping ratio 0.7% is shown in Figure 2. The aerodynamic parameters  $Y_1$  and  $\varepsilon$  are estimated with the steady state amplitudes of two separate damping ratios with the method mentioned in the former section. The variation of them with reduced wind speed is shown in Figure 3. The linear aeroelastic stiffness term related with  $Y_2$  can be ignored in the steady state.

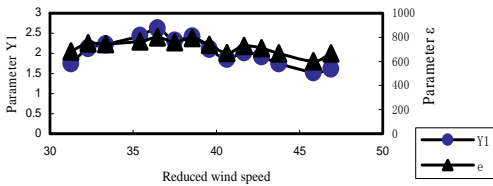


Figure 3. The aerodynamic parameters at different reduced wind speeds:  $Y_1$  and  $\varepsilon$

### 4. Numerical Analysis

The analysis of vortex induced responses of tall buildings should consider the assumption (Simiu and Scanlan, 1986) that: the crosswind response is only dependent on the related fundamental mode shapes which are linear in most cases. Based on the modal superposition method, the numerical solution of the generalized displacement can be obtained with Runge-Kutta method. In this study the parameters  $Y_1$  and  $\varepsilon$  of the structure are assumed as constants. The initial displacement and initial velocity are assumed to be zero.

The computed steady state vibration at the same wind speed in Figure 2 is shown in Figure 4. The simulated time history of the top acceleration is harmonic vibration and the period is matched with the oscillation in the wind tunnel test. The computed amplitude is accord with the one in the experiment at the reduced speed. At the wind speed 15m/s, the wind-structure system experienced a ‘growth-

to-resonance' type vibration process, illustrated in Figure 5a, which can be simulated with the numerical method in Figure 5b.

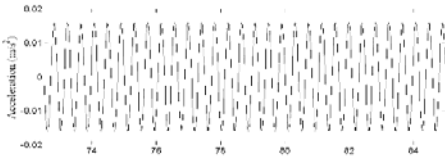


Figure 4. Simulated top acceleration at the reduced speed 33.3 with damping ratio  $\zeta = 0.7\%$

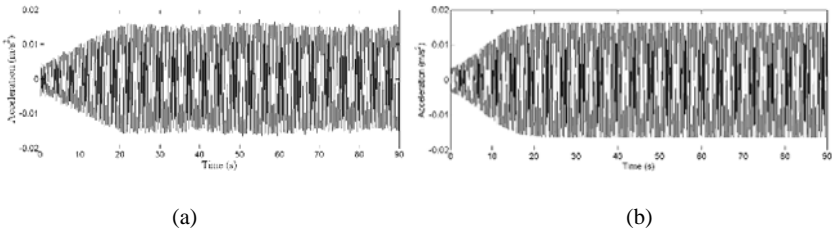


Figure 5. Acceleration of the 'growth-to-resonance' type vibration at the reduced speed 31.25 (experimental wind speed = 15 m/s): (a) measured; (b) simulated acceleration

In the higher wind speed region the vortex shedding becomes unstable because the structural vibration is significantly effected by the linear forcing term. However, the proposed numerical method is focus on the steady state vibration which neglects the contributions of them. The simulation in this case is not as perfect as the one in the lock-in wind speed range.

## 5. Conclusions

The vortex induced response of a practical tall building is obtained through the improved SDOF empirical model in this present paper. The aerodynamic parameters are identified with the measured data in the wind tunnel test with aeroelastic model which is designed as a multi-section structure according to the aerodynamic features of tall buildings. The time history of acceleration at the lock-in wind speed region is then obtained using Runge-Kutta method and the results show good agreement with measurements in the wind tunnel test. It should be noted that the aerodynamic parameters are sensitive to the shape of the structures and the direction of the flow.

## References

- Ehsan F., Scanlan R. H. (1990). Vortex-induced vibration of flexible bridges. *Journal of Engineering Mechanics*, 117(6):1392-1411.
- Hartlen R. T., Currie I. G. (1970). Lift oscillator model of vortex induced vibration. *Proceedings of the American Society of Civil Engineers EM4*: 577-591.
- Larsen A. (1995). A generalized model for assessment of vortex-induced vibration of flexible structures. *Journal of Wind Engineering and Industrial Aerodynamics*, 57: 281-294.
- Simiu E., Scanlan R. H. (1986). *Wind Effects on Structures*. John Wiley, New York.
- Themongkorn S., Kwok K.C.S. and Lakshmanan N. (1999). A two-degree-of-freedom base hinged aeroelastic (BHA) model for response predictions. *Journal of Wind Engineering and Industrial Aerodynamics*, 83: 171-181.
- Vickery B. J., Basu R. I. (1983). Across-wind vibration of structures of circular cross-section. *Journal of Wind Engineering and Industrial Aerodynamics*, 12: 35-73.

*“This page left intentionally blank.”*

# Evaluation of Strength and Local Buckling for Cooling Tower with Gas Flue

Shitang Ke<sup>1,2</sup>, Yaojun Ge<sup>1,2\*</sup> and Lin Zhao<sup>1,2</sup>

<sup>1</sup>State Key Laboratory for Disaster Reduction in Civil Engineering, Shanghai 200092, China

<sup>2</sup>Department of Bridge Engineering, Tongji University, Shanghai 200092, China

**Abstract.** The wind pressure on the surface of a cooling tower with gas flue is compared with the corresponding cooling tower without gas flue through wind-tunnel testing, then the characteristics of wind pressure distribution around the flue is investigated. The strength and buckling nearby the flue are analysed with finite element software. It is found that stress concentration nearby the flue is very obvious, and its safe factor of local buckling is much less than the value without flue, which makes unsafe place to transfers from top of the tower to the area near flue. The corresponding schemes of reinforcement on the basis of this situation are proposed, and static performance of each scheme is compared for selecting the better one.

**Keywords:** cooling tower with gas flue, wind pressure distribution, local buckling

## 1 Introduction

With the development of electric power in our country, the comparatively extensive research works about cooling tower under wind loading have been carried out, Professor Wu ji-ke and Wei Qing-ding of Peking University made the vibration test to research group effect in wind tunnel (Chen and Wei, 2003), seminar of Tongji University proposed aeroelastic model designed by equivalent beam-net method according to the shortages of old methods in actual engineering application, and then research the load characteristic in the wind tunnel (Zhao et al., 2008), Professor Sun Bing-nan of Zhejiang University adopts numerical simulation method to obtain the wind load on large hyperbolic cooling tower (Wang and Huang, 2006). These researches are almost good enough for the corresponding cooling tower without flue on the surface. With the sustainable development of national economy, considering environmental protection cooling towers with gas flue will be the developing direction in electric power, but relevant research stock

---

\* Corresponding author, e-mail: yaojunge@tongji.edu.cn

is insufficient obviously, so this article carries on evaluation of strength and local buckling and its reinforcement.

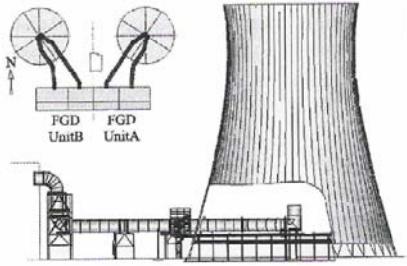
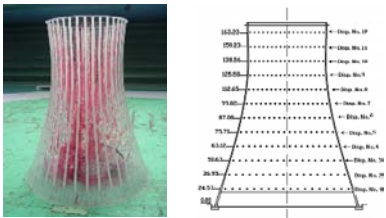


Figure 1. Flow chart of technics for cooling tower with gas flue

The cooling tower with gas flue has the technology of discharging gas after wet desulfuration through natural draft cooling tower. Figure 1 gives the engineering flow sheet of the cooling tower with gas flue, it can be found that the surface of cooling tower needs a hole for discharging gas. The hole destroys the symmetrical characteristic of cooling tower, it is necessary to take wind tunnel test to get the real wind pressure model on the surface of tower; and compare the stress value around the hole with/without hole through finite element analysis, the influence of intensity and buckling under different yaw angle of incoming wind will be gained, the corresponding schemes of reinforcement are proposed.

## 2 Wind Tunnel Testing

The pressure-measured test of cooling tower with gas flue was carried out in the TJ-3 Boundary Layer Wind Tunnel of Tongji University. The pressure-measured model and the measuring points are demonstrated in Figures 2 and 3.



(a) rigid model      (b) Measured taps

Figure 2. Model and its number of tap sensors

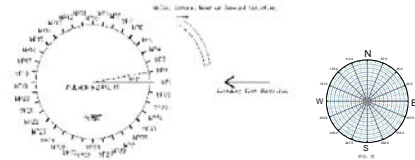


Figure 3. Arrangement for pressure points and relationship of wind and tower

The drag/lift force coefficient measured through pressure-measured test is defined as Equation 1:

$$C_D = \left( \sum_{i=1}^n C_{p_i} A_i \cos(\theta_i) \right) / A_T \tag{1}$$

Where  $A_i$  is the overlapped area about the  $i^{th}$  tap,  $\theta_i$  is angle between  $i^{th}$  tap surface vertical direction and wind axial direction, and  $A_T$  is total projected area about cooling tower structure to wind axial direction.

For normal cooling tower, because of its structural symmetry characteristic, they have the same value of  $C_D$ . The pressure distribution of the three bottom sections of the cooling tower with gas flue and corresponding cooling tower is given in figure 4, and figure 5 provides the characteristic value of  $C_D$  of normal cooling tower and cooling tower with gas flue under different yaw angle of incoming flow. It can be obviously found that  $C_D$  is 0.485 for normal tower; but for tower with gas flue  $C_D$  is variable under different yaw angle of incoming flow, and  $C_D$  is up to the maximum 0.542 under about 45 degrees, it is 1.12 times of the corresponding cooling tower's value, and is minimum in 180 degrees of leeward districts. The effect is obvious in 45 degrees where negative pressure is the largest, when the flue is in the leeward areas, its characteristic is almost similar with corresponding cooling tower.

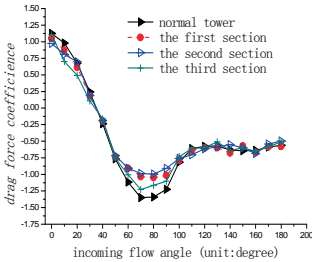


Figure 4. Pressure distribution

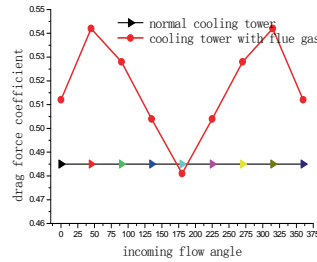


Figure 5. the value of  $C_D$

### 3 Static Analysis

Table 1 gives the main structural characteristics and model.

In order to confirm the influence area with the flue, the stress of the throat area and the area around flue are given in Tables 2 and 3. According to the conclusion, it can be found that the variation of peak value of stress is small, so that the influence caused by the flue of whole strength could be neglect. But it is different with

the area around the flue, the increment after opening the hole is too obvious to neglect, it must cause attention when designing.

Table 1. Main structural characteristics of cooling tower

Compo-	height / m	thick /m	Radius / m	model
Vent sleeve	12.216	1.400	67.347	
	open the hole with a diameter of 10.5m at 40.5m			
	62.594	0.330	51.656	
	100.378	0.310	43.123	
	166.150	0.271	39.543	
Column	Φ 1300mm 52 pairs			C35
Ring base	Section of 7500×2500mm			C30
foundation	312 pringe unit Φ1000mm312			C30

Table 2. The peak value of stress near throat under all loads (unit: Mpa)

Stress Classification	Max stress	With the flue					
		0°		30 °		60°	
	No flue	stress	Variation	stress	Variation	stress	Variation
$\sigma_1$	0.16	0.17	6.30%	0.15	-6.30%	0.174	8.75%
$\sigma_2$	-1.87	-1.93	3.31%	-1.76	-5.88%	-1.98	4.81%
$\sigma_{mises}$	0.76	0.79	3.94%	0.72	-5.26%	0.82	7.89%

Table 3. The peak value of stress near flue under all loads (unit: Mpa)

Stress classification	Peak value of the stress		The position	Variation
	With flue	No flue		
$\sigma_1$	1.78	0.72	Bottom	147.22%
$\sigma_2$	-2.56	-1.24	Flank	106.45%
$\sigma_{mises}$	1.04	0.42	Flank	147.61%

The some buckling must be considered because of its thin shell’s characteristic, and it can be calculated by the formula:

$$0.8 K_B \left( \frac{\sigma_1}{\sigma_{cr1}} + \frac{\sigma_2}{\sigma_{cr2}} \right) + 0.2 K_B^2 \left[ \left( \frac{\sigma_1}{\sigma_{cr1}} \right)^2 + \left( \frac{\sigma_2}{\sigma_{cr2}} \right)^2 \right] = 1 \tag{2}$$

$$\sigma_{cr2} = 0.612E / \sqrt[4]{(1-\nu^2)^3} (h/r_0)^{4/3} K_2$$

$$\sigma_{cr1} = 0.985E / \sqrt[4]{(1-\nu^2)^3} (h/r_0)^{4/3} K_1 \tag{3}$$

where  $\sigma_{cr1}$  is the circumferential critical pressure,  $\sigma_{cr2}$  is the vertical critical pressure,  $\sigma_1$  and  $\sigma_2$  are the circumferential and vertical critical pressure under the combination load,  $h$  and  $r_0$  are the thick and radius,  $K_1=0.15$ ,  $K_2=1.28$ ,  $K_B$  is the safe factor of buckling, it should greater than 5.0 according to the norm.

The minimum buckling factor  $K_B$  of some buckling of the corresponding cooling tower is 7.96 under the combination of wind load and self-weight, which happens in the throat area, the minimum buckling factor  $K_B$  in the area around the hole as the tower with gas flue is 34.05, so the reinforcement should be carried out to avoid the destabilization area transferring from the throat to the area around the hole. Figure 6 gives the value of  $K_{B,min}$  nearby the hole under the different yaw angle of incoming flow.

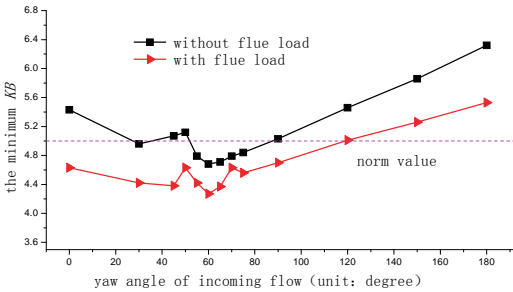
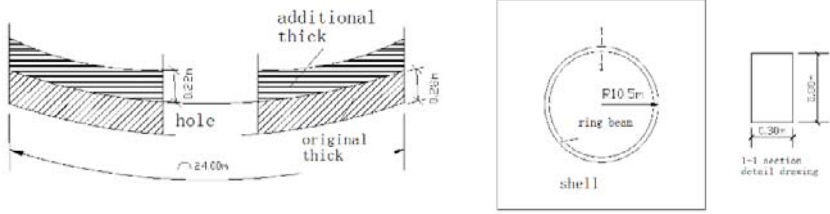


Figure 6. The value of  $K_{B, min}$  nearby the hole under different conditions

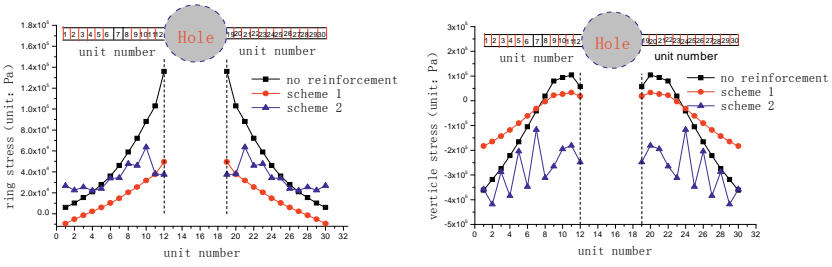
It can be found from Figure 6 that  $K_{B, min}$  of some buckling is 4.27 under the yaw angle of  $60^\circ$ , which is lower than the value fixed by norm. Two reinforcement schemes are put forward to improve the buckling factor under wind load. The first scheme is to change the thickness around the hole up to 0.5m from original 0.28m; the second scheme is to take the ring beam that has the section of  $0.3 \times 0.8m$  (see Figure 7), Figure 8 gives the stress of area around the hole.



a) the first scheme

b) the second scheme

Figure 7. The two schemes of reinforcements



a) ring stress

b) vertical stress

Figure 8. The stress of elements around hole under combined loads

In Figure 8, it is obvious that two schemes could reduce the stress, and the first scheme is effective for the ring stress, the second scheme is more effective for the vertical stress, but the stress concentration is also obvious. So some buckling analysis need to be carried out to determine the better scheme. Table 4 gives the value of  $K_B$  under  $60^\circ$  incoming flow angle.

Table 4. The value of  $K_B$  under  $60^\circ$  of wind loading

Operating mode	Concrete Consump-	No hole	running state		construction state	
			No flue	with flue	No flue	with flue
No reinforce-			4.68	4.27	3.62	3.05
Scheme 1	106.58	34.05	39.36	35.21	28.32	24.41
Scheme 2	7.92		12.02	10.64	9.46	8.85

It is found, in Table 4, that the difference between the buckling considered construction load and the buckling without construction load is small, the effect of the

first scheme is obviously better than the second scheme, and the  $K_B$  under the first scheme is 35.21 in the normal running state, which exceeds the value of  $K_B$  without the hole. However, the second scheme has the advantages of lower cost and convenient construction, it is suggested that the scheme could be applied under the lower tower.

## 4 Conclusions

The following conclusions are arranged on the basis of the wind test and the finite element analysis:

1. Drag force coefficients of the tower with gas flue vary with different yaw angle of incoming flow, and have the maximum 0.542 under the yaw angle of  $45^\circ$ , which is about 1.12 times of the corresponding tower without flue at the  $180^\circ$  yaw angle;
2. The variation of stress near the throat is very small, but the stress increase near the flue is very large, which can not be neglected. Local buckling factor is lower than the value fixed by norm;
3. The reinforcement must be adopted at the surface near gas flue, and the first scheme by changing thickness is more effective than the second one, so that the first one is to be applied in practice.

## Acknowledgement

The research work described in this paper is partially supported by the NSFC under the grant of 50538050 and the 90715039.

## References

- Chen K., Wei Q.D. (2003). Investigation of wind-induced vibration of cooling towers. *The Proceedings of 11th Structural Wind Engineering Conference*, pp.177-182.
- GB/T 50102-2003, Code for design of cooling for industrial recirculating water [in Chinese].
- Kasperski M. (2003). Specification of the design wind load based on wind tunnel experiments, *J. Wind Eng. Ind. Aerodyn.*, 91 527-541.
- Wang M., Huang Z.L. (2006). Finite element analysis of a natural draft cooling tower with flue gas inlets integrated. *Mechanics and Practice*, 26(68): 2-4 [in Chinese].
- Zhao L., Li P.F., Ge Y.J., et al. (2008). Investigation on wind load characteristics for super large cooling tower in wind tunnel. *Engineering Mechanics*, 25(6): 60-67 [in Chinese].

*“This page left intentionally blank.”*

# Numerical Study on Vortex Induced Vibrations of Four Cylinders in an In-Line Square Configuration

Feng Xu<sup>1,3\*</sup>, Jinping Ou<sup>1,2</sup> and Yiqing Xiao<sup>3</sup>

<sup>1</sup>School of Civil Engineering, Harbin Institute of Technology, Harbin 150090, P.R. China

<sup>2</sup>School of Civil & Hydraulic Engineering, Dalian University of Technology, Dalian 116023, P.R. China

<sup>3</sup>Shenzhen Graduate School of Harbin Institute of Technology, Shenzhen 518055, P.R. China

**Abstract.** The two-dimensional numerical simulation of the vortex induced vibrations of four cylinders in an in-line square arrangement is investigated at low Reynolds number in this paper. The mean and fluctuating aerodynamic forces, Strouhal number ( $St$ ) and vortex shedding pattern in the wake for each cylinder are analyzed with the six spacing ratio  $L/D$  changing from 2.5 to 6.0. The results indicate that the mean drag force and the fluctuating lift forces and the transverse displacements of the upstream cylinders are relatively larger than the downstream cylinders, and the downstream cylinders usually undergoing serious fluctuating streamwise displacement. The dominant frequency of drag coefficient is equal to  $St$  of downstream cylinders for all spacing ratio, so the simultaneous resonance in the in-flow and cross-flow directions may occur for downstream structures of multi-body oscillating system. The streamwise oscillation of downstream cylinders which is free to move in two degrees of freedom could be as large as 0.75 diameter, and the maximum transverse amplitude of upstream cylinders may achieve 0.82 diameter, is much higher than the transverse amplitude of flow around a single cylinder at same parameter setting.

**Keywords:** vortex induced vibration, four cylinders, two degree-of-freedom model, numerical simulation

## 1 Introduction

Vortex induced vibration (VIV) of cylinder group is widely exist in many actual engineering related to fluid dynamics, such as high-rise building groups in wind field, offshore platform structures under current and wave loads, and pipeline

---

\* Corresponding author, e-mail: xufeng\_hit@163.com

structures in large cooling system, etc. The transverse and streamwise vibrations might cause a reduction of structure fatigue life and might even lead to the occurrence of severe accidents under some specific conditions. Due to the complexity of flow separation and free shear layers interaction of bluff bodies, the mechanism of fluid-induced forces and their related frequencies is a highly nonlinear characteristic, so the flow pattern and forced characteristics was further complicated in the presence of neighboring body and obviously different from the single body. So far, a number of studies have been experimentally or numerically performed on the flow around single cylinder, see recent review on VIV by Sarpkaya (2004).

Nevertheless, investigations of the flow past more than one or two cylinders are still relatively scarce. The VIV of multi-cylinder system was greatly affected by the incoming flow turbulence, Reynolds number (Re), cylinder arrangement, natural vibration parameters such as natural frequency  $f_n$ , mass ratio  $M^* = m/\rho D^2$  and reduced damping  $S_g = 8\pi^2 S_i^* M^* \zeta$ . Here,  $S_i^* = f_s^* D/U_\infty$  is the Strouhal number,  $f_s^*$  is the vortex shedding frequency, D is the cylinder diameter. Zdravkovich (1987) proposed a classification for the multi-cylinders and categorized the two cylinder arrangements into three types: tandem, side-by-side and staggered arrangements. The results indicate that the mean and fluctuation values of aerodynamical force, pressure coefficients, Strouhal number, and the vortex shedding pattern in the wake are related with Reynolds number, arrangement form and spacing ratio (L/D, L is the center-to-center distance) between two cylinders. At the critical spacing, the deflected flow phenomenon will occur between two side-by-side arrangement cylinders, the wake behaves strong nonlinearity, there is not obvious vortex shedding from the upstream one of two cylinders in tandem arrangement, furthermore the downstream one is in the free shear layer separated from the upstream cylinder and undergoing a force along direction to the upstream. When two cylinders are located out of critical spacing, each cylinder will behave steady vortex shedding for two side-by-side arrangement cylinders; for two tandem arrangement cylinders, the vortices are shedding in the wake of the upstream cylinders and impinging to the downstream one, and the downstream cylinders are normally subjected to more serious fluctuating forces under the influence of unsteady wake vortices (Meneghini 2001; Kang 2003; Mahbub Alam 2003).

The four cylinders in an in-line square configuration combined with two side-by-side and two tandem cylinders are the common arrangement form in the actual engineering, such as in tube array system and offshore structure et al. Some experimental (Sayers 1988; Lam 1995) and numerical studies on the flow around four rigid cylinders in an in-line square configuration have been carried out. Farrant (2000, 2001) carried out 2-D numerical simulation for two side-by-side, tandem and staggered arrangement cylinders and four square arrangement cylinders with L/D=3 and 5 at Re=200 using a cell boundary element method. It is found that there is vortex shedding from four cylinders in the wake for the two spacing ratios through analyzing the vorticity contours. Lam and Li (2003) measured the flow field around four cylinders in a square configuration and obtained vortex shedding

pattern, velocity vector distribution and streamline distribution for four typical attack angles at  $Re=200$  and  $L/D=4.0$ , but didn't measure the aerodynamical forces of each cylinder. Lam and Gong (2008) studied a two- and three-dimensional numerical simulation of flow around four cylinders in square arrangement at low Reynolds number using a finite volume method. Three flow modes were defined and the analysis focuses on the relationship between pressure distribution and flow pattern transformation.

Compared with the flow around the four rigid cylinders, little work, especially numerical simulation, focused on the VIV of the four elastic cylinders in square arrangements. Kubo (1995) studied the wind-induced vibration of more than two cylinders in different arrangements in wind tunnel, which include the two cylinders in tandem, regular triangle arrangement of three circular cylinders and four cylinders in diamond arrangement. The results further shown that the dimensionless response of VIV and galloping of each cylinder, and the optimum configuration of multiple cable systems of cable-stayed bridges is the turning regular triangle arrangement. In the experiment by Lin (2005), a monitored cylinder with two degree of freedom motion was flexibly mounted in a water tunnel, surrounded by one to six identical cylinders elastically mounted in rotated triangular pattern. The effects of the incoming velocity boundary, the number of the surrounding cylinders, and the cylinder's natural frequency on the monitored cylinder's response are analyzed in detail, and it points out that an oval orbit implying that the cylinder behaves like an oscillator with the streamwise and cross-stream responses have the same frequency but with a phase shift. Lam (2006) simulated the flow-induced vibration of a single cylinder row and a staggered cylinder array by a fluid structure interaction model based on the surface vorticity method (SVM) at a Reynolds number  $Re = 2.67 \times 10^4$ . Three combination of structural parameter which include reduced damping, mass ratio and frequency ratio are considered in the computation. It is found that the in-flow vibration has a significant effect on the cross-flow vibration for large-amplitude vortex-induced vibration.

The present work concentrates on the 2-D numerical researches on VIV of four cylinders in an in-line square arrangement at  $Re=200$  using the finite volume method. The spacing ratio  $L/D$  is set as 2.5, 3.0, 3.5, 4.0, 5.0 and 6.0 in turn. The main objective of this study is to examine the effect of  $L/D$  on the flow pattern, aerodynamic forces and response of the four cylinders.

## 2 Numerical Computation Method

### 2.1 Governing Equation and Solution Process of Fluid-Structure Interactions

The unsteady continuity equation and Navier-Stokes equations for an incompressible flow can be written in the following tensor form under the inertia rectangular coordinate:

$$\frac{\partial u_i}{\partial x_i} = 0, \quad i=1, 2 \quad (1)$$

$$\frac{\partial u_i}{\partial t} + u_j \frac{\partial u_i}{\partial x_j} = -\frac{1}{\rho} \frac{\partial p}{\partial x_i} + \nu \frac{\partial^2 u_i}{\partial x_j \partial x_j}, \quad i, j=1, 2 \quad (2)$$

It is assumed that the cylinder is mounted as a mass-spring-damper system, which can be vibrating along x- and y-direction. Thus, the motion of the cylinder can be described by the equation

$$\ddot{\chi} + 2\zeta\omega_0\dot{\chi} + \omega_0^2\chi = F(t)/m \quad (3)$$

where  $u_i$  is velocity component,  $p$  is the average pressure,  $\rho$  is the fluid density,  $\nu$  is the kinematic viscosity;  $\chi = x\mathbf{i} + y\mathbf{j}$ ,  $x$  and  $y$  are the instantaneous displacement of the cylinder in the x- and y-direction, respectively;  $\zeta$  is the damping factor,  $\omega_0$  is the angular natural frequency of the cylinder,  $m$  is the mass per unit length of the cylinder,  $F(t)$  is obtained by integrating the pressure and frictional stress along the cylinder surface, and is decompose into two forces: drag force  $F_d(t) = 1/2 \rho U_\infty^2 D \cdot C_d(t)$  which is along in-flow direction and lift force  $F_l(t) = 1/2 \rho U_\infty^2 D \cdot C_l(t)$  which is along cross-flow direction, where  $C_l(t)$  and  $C_d(t)$  are lift and drag coefficients.

The unsteady flow field is numerically simulated by CFD code (Fluent) based on a finite volume method (FVM) with a pressure-based algorithm. The SIMPLE algorithm is employed for the coupling between pressure and velocity. The format of pressure interpolation is chosen Standard and the second-order upwind scheme is employed for momentum spreads to achieve stability and calculation accuracy. The fluid-structure interaction system was solved by loosely coupled method, and the dimensionless time-step was set as 0.06 for the all computations. Assuming that in each time-step, flow-induced force in the dynamic equation is constant. Firstly, we solved the fluid governing equations and obtained the velocity domain and pressure domain. The lift force  $F_l(t)$  and drag force  $F_d(t)$  were substituted in-

to the structural vibration equations (3) by using the user-defined-function (UDF). Then the Newmark- $\beta$  method is utilized to solve the dynamic response of cylinder. The cylinder velocity is transferred to mesh domain by using the rigid body motion macro of Fluent code, and new position is obtained by iteration of dynamic mesh model. When the mesh iteration converged, the whole fluid domain is updated and the next time-step started. The loop continues until the stable solution is achieved.

## 2.2 Computational Models and Boundary Conditions

The numbering and arrangement form of four equal diameter cylinders are shown in Figure 1. The origin is located at the middle point of the line connecting centers between the upstream cylinders.  $L$  is the distance of two centers of cylinder,  $D$  is the cylinder diameter and equal to 0.01 m, and  $L/D$  is the spacing ratio. The unstructured grids are employed to discretize the flow field and the grids near cylinder surface and in the wake regions where there is a larger variety in the parameter gradients are locally refined (Figure 2). The rectangle computational region is  $50D \times 20D$  with  $15D$  upstream,  $35D$  downstream and  $10D$  on either side, respectively. The flow direction is from left to right, left side is set as velocity-inlet, right side is set pressure-outlet, the relative pressure is set as 0, the upper and lower free slip boundaries are set as symmetry and the model surface is set as wall.

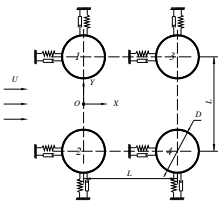


Figure 1. Arrangement form and oscillating model with 2-DOF of four cylinders

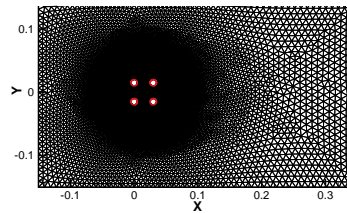


Figure 2. Computational domain and mesh distribution at  $L/D=3.0$

## 2.3 Validation for Single Rigid Cylinder

Firstly, the flow around a single cylinder at  $Re=200$  is carried out in order to ensure the reliability of numerical calculation. Figure 3(a) denotes the dimensionless time histories of lift and drag coefficients of single cylinder. Figure 3(b) indicates spectral analysis of lift and drag coefficients, the peaks are responding to the

Strouhal number and dimensionless frequency of drag force, respectively. The mean drag coefficient calculated is  $\bar{C}_d=1.321$  and the dimensionless frequency is 0.3766 which is two times of  $S_t^*=0.1883$ . The root-mean-square (RMS) value of lift and drag coefficients are  $C'_l=0.3995$  and  $C'_d=0.0231$ , respectively.

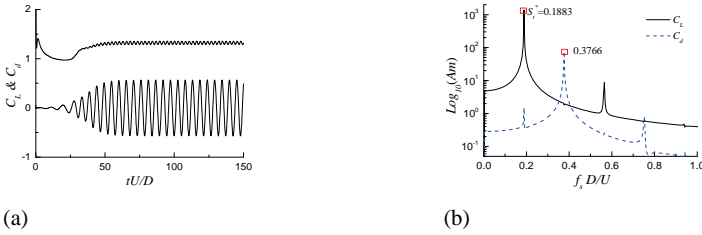


Figure 3. Lift and drag coefficient time histories (a) and spectral analysis (b) for the flow around a single cylinder

The present calculations and the published results are tabulated in Table 1.  $C'_l$  and  $S_t^*$  calculated in this paper are larger the results of the empirical formula summarized by Norberg (2003),  $\bar{C}_d$  is relatively exact and slightly smaller than the result of cell boundary element method by Farrant (2000),  $C'_d, C'_l$  and  $S_t^*$  are smaller than the previous results of simulations and are close to the results of Lam (2008). It is shown that the grid resolution, time step and numerical solving format chosen in present paper are proper for numerical simulation of the flow near the cylinder.

Table 1. Force coefficient and Strouhal number of flow around a single cylinder at Re=200

Investigation	$\bar{C}_d$	$C'_d$	$C'_l$	$S_t^*$
Farrant T. (2000)	1.36	-	0.51	0.196
Meneghini J. R. (2001)	1.30	0.032	0.50	0.196
Norberg C. (2003)	-	-	0.374	0.1815
Lam K. (2008)	1.32	0.026	0.426	0.196
Current work	1.321	0.0231	0.3995	0.1883

### 3 Results and Discussion

Current study results which mostly focus on the flow induced vibration (FIV) of one or two cylinders in the open publications confirm that the ratio between the natural frequency  $f_n$  of elastic cylinder and the natural vortex shedding frequency  $f_s^*$  of flow around rigid cylinder (hereinafter referred to as “frequency ratio  $f_n/f_s^*$ ”), the dimensionless mass ratio  $M^*=m/\rho D^2 l$  and reduced damping

$S_t = 8\pi^2 S_t^* M^* \zeta$  are important parameters which have significant influence on the structural vibration. The physical parameters  $S_t^* = 0.01$ ,  $M^* = 1.0$  and  $f_n / f_s^* = 1.30$  are chosen for any one of the four cylinders in this work, and a single cylinder with the same parameter subjected to VIV confined in the resonance band such as described by Zhou (1999).

### 3.1 Characteristics of Force and Response

The forced characteristics of the cylinders in the flow field are the base of investigation of FIV, which include the mean value, RMS (root mean square) value and correlated frequency characteristics. The program of calculating the lift and drag forces of the cylinder is written in UDF, can solve the problem of obtaining the lift and drag coefficients of multi models at the same time in Fluent, and this is premise and basis of researching on fluid structure interaction of multi-body system. Supposing a infinitely long cylinder, 2-D numerical simulation of flow around the cylinder can greatly save computing time at the low Re, exhibit main flow characteristics and obtain aerodynamic forces which are difficult to measured in the experiments at low Reynolds number.

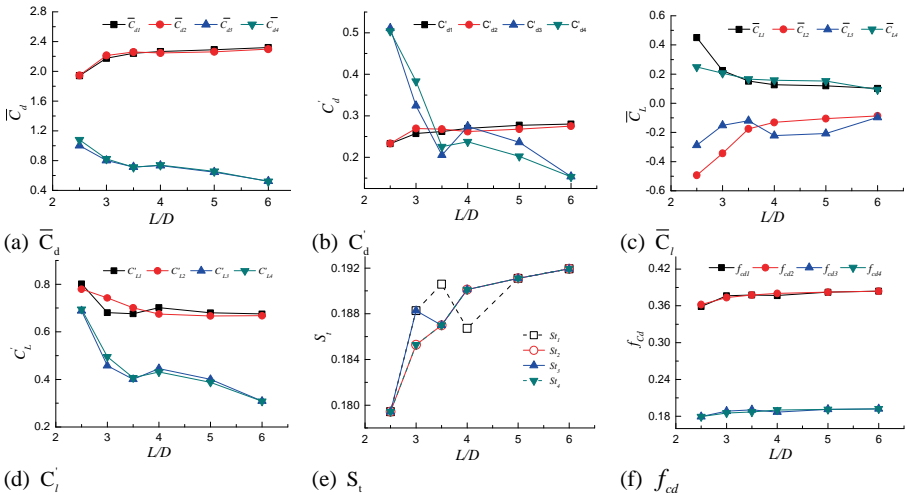


Figure 4.  $\bar{C}_d, C'_d, \bar{C}_l, C'_l, S_t, f_{cd}$  versus  $L/D$  for four cylinders in an in-line square arrangement

Figure 4 shows the force coefficients and corresponding frequency characteristics vary as spacing ratio for four cylinders in an in-line square arrangement, which include the mean and RMS value of drag coefficient  $\bar{C}_d$  and  $C'_d$ , the mean and RMS value of lift coefficient  $\bar{C}_l$  and  $C'_l$ , Strouhal number  $S_t$  and dimensionless frequency of drag coefficient  $f_{cd}$ .

Figure 4(a) indicates that  $\bar{C}_d$  keeps coincidence to each other not only for two upstream cylinders but for downstream cylinders, the  $\bar{C}_{d1}$  and  $\bar{C}_{d2}$  are larger than  $\bar{C}_{d3}$  and  $\bar{C}_{d4}$  for all  $L/D$  range. It is seen that the mean drag coefficients of upstream cylinders increase gradually from 1.94 to 2.30 as the ratio  $L/D$  increases, and the mean drag coefficients decrease gradually from 1.08 to 0.52 as the ratio  $L/D$  increases for the two downstream cylinders. Figure 4(b) shows  $C'_{d1}$ ,  $C'_{d2}$  behave similarly and increase gradually from 0.23 to 0.28 as the ratio  $L/D$  increases. The  $C'_{d3}$ ,  $C'_{d4}$  are basically in coincidence and much larger than the  $C'_{d1}$ ,  $C'_{d2}$  of upstream cylinders when  $L/D < 3.5$ , and the phenomenon is just opposite when  $L/D \geq 3.5$ . When  $L/D$  changes from 2.5 to 3.5,  $C'_{d3}$  and  $C'_{d4}$  rapidly decrease by 60% of original values which is approximately equal to 0.5 at  $L/D=2.5$ . The  $C'_{d3}$  and  $C'_{d4}$  increase slightly when  $L/D$  increases up to 4.0, and decrease gradually as  $L/D$  increases. Finally, the  $C'_{d3}$  and  $C'_{d4}$  are close to 0.15 at  $L/D=6.0$ .

Figure 4(c) indicates that  $\bar{C}_{l1}$  and  $\bar{C}_{l3}$  are approximately symmetrical to  $\bar{C}_{l2}$  and  $\bar{C}_{l4}$ , respectively. The all lift coefficient mean values gradually trend to zero as  $L/D$  increasing, and it indicates that the flow interference effects between upper and lower rows cylinders is gradually weakened as spacing increasing. When  $L/D=2.5\sim 3.5$ , the  $\bar{C}_{l1}$ ,  $\bar{C}_{l2}$  rapidly decrease and reach to 40% of original values, respectively, and decrease gradually when  $L/D > 3.5$ .  $C'_{l1}$  and  $C'_{l2}$  of the upstream cylinders are larger than  $C'_{l3}$  and  $C'_{l4}$  as shown in Figure 4(d).  $C'_{l1}$  and  $C'_{l2}$  gradually decrease with increasing  $L/D$  from 2.5 to 4.0 and keep at 0.7 for  $L/D > 4.0$  which is larger than that of single cylinder.  $C'_{l3}$  and  $C'_{l4}$  rapidly decrease with increasing  $L/D$ , represent a concave characteristic for  $L/D=2.5\sim 4.0$ , reach minimum value at  $L/D=3.5$ , and  $C'_{l3}$  and  $C'_{l4}$  increase to 0.3 at  $L/D=6.0$  which less than that of single cylinder.

The varieties of  $S_t$  and dimensionless frequency of drag coefficient  $f_{cd}$  versus spacing are presented in Figure 4(e) and (f).  $S_t$  of cylinder 2 and cylinder 4 are equal to each other and increase with  $L/D$  increasing, and  $S_t$  of four cylinders are equal to each other at  $L/D=2.5$ .  $S_t$  of cylinder 1 and cylinder 3 are slightly larger than cylinder 2 and cylinder 4 at  $L/D=3.0$ .  $S_t$  of cylinder 1 change from being larger into less than that of cylinder 2, 3 and 4 which are all equal with increasing  $L/D$  from 3.5 to 4.0.  $S_t$  of four cylinders are all equal for  $L/D \geq 5.0$ .  $f_{cd}$  of upstream cylinders are 2 times of downstream cylinders and 2 times of  $S_t$  that is same with flow around single cylinder; but  $f_{cd}$  of downstream cylinders are close to  $S_t$  that indicate the in-flow and cross-flow resonance vibration may occur.

The ratio of cross-flow displacement mean ( $\bar{Y}$ ) to diameter is shown in Figure 5(a) of which the change law is same with that in Figure 4(a). The  $\bar{Y}$  of each cylinder gradually trends to 0 with increasing  $L/D$  that indicates interference between two upstream cylinders and two downstream cylinders decreases with  $L/D$  increasing and  $\bar{Y}_3$  of upside is negative and  $\bar{Y}_4$  of underside is positive.

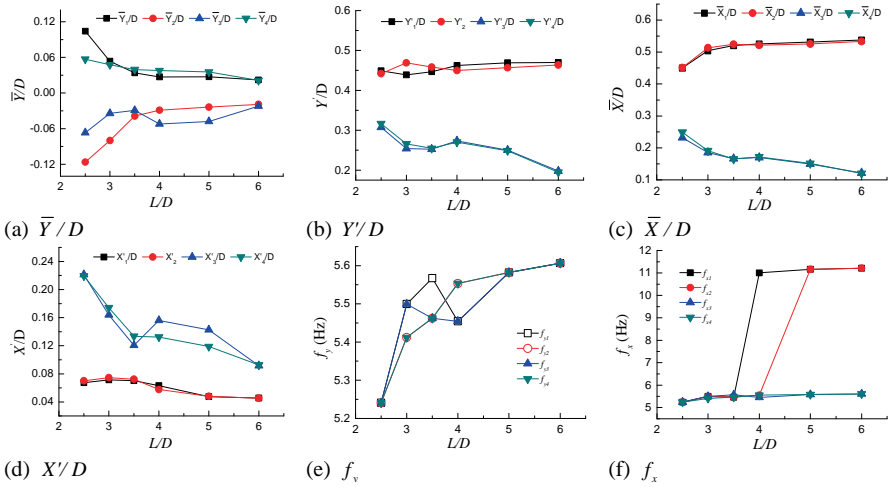


Figure 5.  $\bar{Y}/D, Y'/D, \bar{X}/D, X'/D, f_y, f_x$  versus  $L/D$  for four cylinders in an in-line square arrangement

The ratio of root mean square (RMS) of the cross-flow displacement to diameter is shown in Figure 5(b) in which  $Y'_1$  and  $Y'_2$  of upstream cylinders are larger than  $Y'_3$  and  $Y'_4$  of downstream cylinders for all range of  $L/D$ .  $Y'_1$  of upstream cylinder 1 represents a concave characteristic for  $L/D=2.5\sim 3.5$  and reaches minimum value at  $L/D=3.0$ .  $Y'_2$  of upstream cylinder 2 represents a convex characteristic for  $L/D=2.5\sim 3.5$  and reaches maximum value at  $L/D=3.0$ .  $Y'_1$  and  $Y'_2$  keep invariant are close to 0.45 for  $L/D>4.0$  and  $Y'_1$  is slightly larger than  $Y'_2$ .  $Y'_3$  and  $Y'_4$  represent a concave characteristic for  $L/D=2.5\sim 4.0$  and reaches minimum value at  $L/D=3.5$ , and increase with decreasing  $L/D$  and are close to 0.2 at  $L/D=6.0$ .

The ratio of the in-flow displacement mean to diameter is shown in Figure 5(c) and the ratio of the RMS of the in-flow displacement to diameter is shown in Figure 5(d). The means of the in-flow displacement of upstream cylinders are larger than that of downstream cylinders, and the RMS of the in-flow displacement of upstream cylinders are less than that of downstream cylinders for all range of  $L/D$ .  $\bar{X}_1$  and  $\bar{X}_2$ ,  $\bar{X}_3$  and  $\bar{X}_4$  gradually increase and decrease with increasing  $L/D$ , respectively.  $X'_1$  and  $X'_2$  trend to same with each other in the range of 0.04~0.08.  $X'_3$  and  $X'_4$  rapidly decrease to original 50% for  $L/D$  increasing from 2.5 to 3.5.  $X'_3$  increase and  $X'_4$  keeps invariant for  $L/D$  increasing to 4.0.  $X'_3$  and  $X'_4$  increase with increasing  $L/D$ , and  $X'_3$  is slightly larger than  $X'_4$  when  $L/D=4.0\sim 6.0$ .

The dominant frequencies of the cross-flow displacement and the in-flow displacement are shown in Figure 5(e) and (f), respectively. For  $L/D=2.5\sim 6.0$ , the dominant frequencies of the in-flow displacement equal to each other for two downstream cylinders and approximately equal to the dominant frequencies of the cross-flow displacement. It indicates that both cross-flow and in-flow resonance

vibrations occur. The maximum cross-flow oscillation amplitude occurs for the upstream cylinder 1 and reaches  $0.82D$  which is much larger than  $0.57D$  of the single cylinder by Zhou (1999) using a detached vortex method with the same parameters setting. The maximum in-flow oscillation amplitude occurs for the upstream cylinder 3 and reaches  $0.75D$ . It is indicated that the cross-flow oscillation amplitude of upstream cylinders significantly increased and the in-flow oscillation of downstream cylinders is unneglectable for vortex-induced vibration of multi-cylinder system.

### 3.2 Time Histories of Force and Response

Figure 6 indicate the time histories of lift and drag coefficients, the ratio of the cross-flow displacement to diameter  $D$  and the ratio of the in-flow displacement to diameter  $D$  of every cylinder for different spacing ratio. The force and response histories represent similar changing laws for every cylinder with same geometric dimensions and oscillation parameters along  $X$  and  $Y$  directions for various spacing ratios with only quantitatively differences. So, the results of spacing ratio of 2.5, 3.5 and 5.0 are shown.

The lift coefficients and cross-flow displacement represent in-phase and it is same for the drag coefficients and in-flow displacement. The lift coefficients and cross-flow displacement of upstream cylinders are relatively regular and it indicates that the vortex shedding is controlled by a dominant frequency. The irregularity of the aerodynamical force and response histories of downstream ones indicates there are several frequency components as shown in Figure 6(a), so the intense interference of the upstream cylinders for the downstream cylinders induce complex vortex structures shedding from the downstream cylinders for a small spacing ratio. As the spacing ratio increasing, the weakened interference of the upstream cylinders for the downstream cylinders induce relatively regular lift coefficients and cross-flow response histories of downstream ones as shown in Figure 6(b) and (c).

The motion trajectories of each cylinder centroid for different spacing ratio are shown in Figure 7 in which it can be seen that the amplitude and RMS of the cross-flow displacement are relatively larger and the RMS of in-flow displacement is relatively larger. The motion trajectories of two upstream cylinders represent a half “figure of 8” shape for a small spacing ratio as shown in Figure 7(a), than the orbits change into a full “figure of 8” shape at  $L/D=3.0$  as shown in Figure 7(b) and the “figure of 8” shape is more and more distinct with continuously increasing the spacing ratio as shown in Figure 7(c-f). The reason is the frequency of in-flow is two times of that of cross-flow oscillation of two upstream cylinders; furthermore, the RMS of in-flow vibration is less than RMS of cross-flow vibration, so, the motion trajectory represents a vertical “figure of 8” shape.

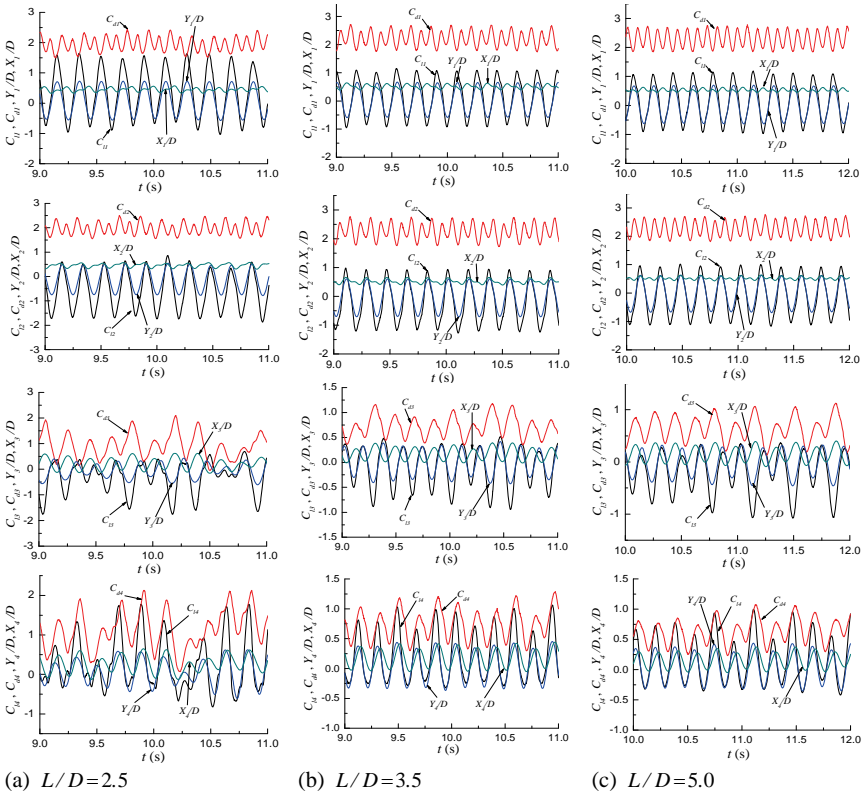


Figure 6. Force and displacement time-histories of four cylinders with 2-DOF at some  $L/D$

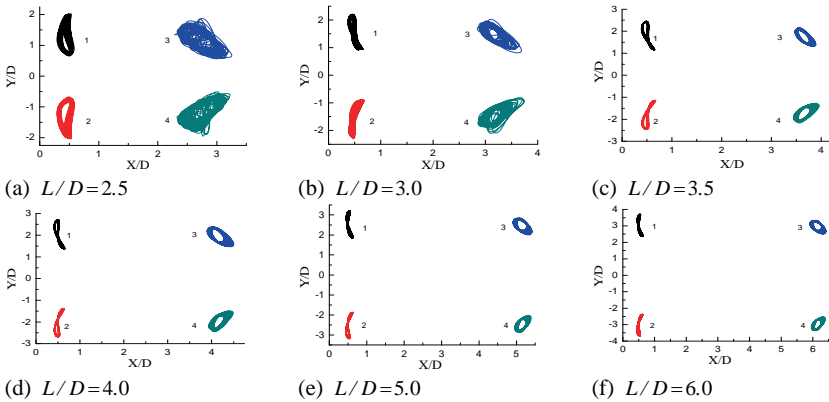


Figure 7. X-Y plot of the four vibrating cylinders versus  $L/D$

The motion trajectories present a distinct oblique ellipse which is same with the results of Lin (2005), and it indicated that the frequency of in-flow oscillation equal to the frequency of the cross-flow oscillation of two downstream cylinders and there is a certain phase difference between two oscillations. The motion trajectories of cylinder 3 and cylinder 4 are downward and upward oblique ellipses, respectively, and it indicated that the cross-flow oscillation lags and leads of the in-flow oscillation for cylinder 3 and cylinder 4, respectively.

### 3.3 Vortex Structure in the Wake

For investigating the influencing of cylinder oscillation to the vortex shedding pattern, the instantaneous vorticity contours in the wake of flow around static and elastic oscillating four circular cylinders in an in-line square arrangement are shown in Figures 8 and 9, respectively.

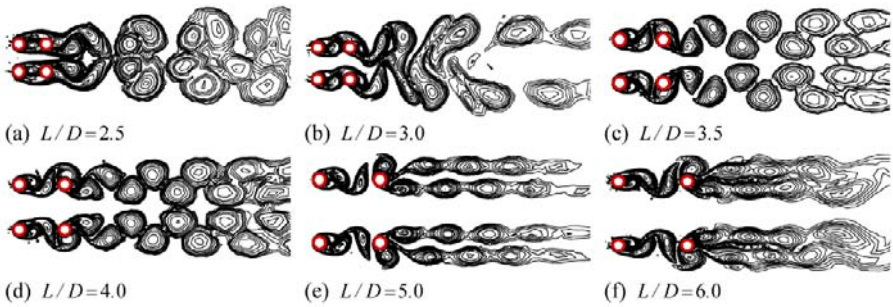


Figure 8. Instantaneous vorticity contours of four static cylinders versus  $L/D$

Figure 8 shows the instantaneous vorticity contours of four cylinders with different spacing ratio at the time when the lift force of downstream cylinder 3 reaches to the positive maximum value. There is no vortex shedding from upstream cylinders as shown in Figure 8(a), the inner side free shear layers of two upstream cylinders reattach to the surfaces of two downstream cylinders while the outer free shear layers don't reattach, but the outer side free layers are alternately wiggling in the wake of the downstream cylinders. As the downstream cylinders are shielded, this flow pattern is named as "shielding anti-phase-synchronized". Figure 8(b) shows that the mature vortices shedding from upstream cylinders and impinge to the downstream cylinder surfaces. The vortex shedding between two upstream cylinders is kept in-phase, and it is same for two downstream ones, so the flow pattern is defined as "in-phase-synchronized". As the interference between upper and lower rows cylinders, pairs of like-signed vortices shedding from downstream cylinder are actively merged, and some distance downstream the merging process

ceases, then a single row vortices with a large spacing are formed. Observed from Figure 8(c)-(f), the flow pattern is transformed again. It is presented a “anti-phase-synchronized” flow pattern for  $L/D \geq 3.5$ . The vortices shedding from upstream cylinders impinge to the surfaces of downstream cylinders and two rows mature vortex streets are formed.

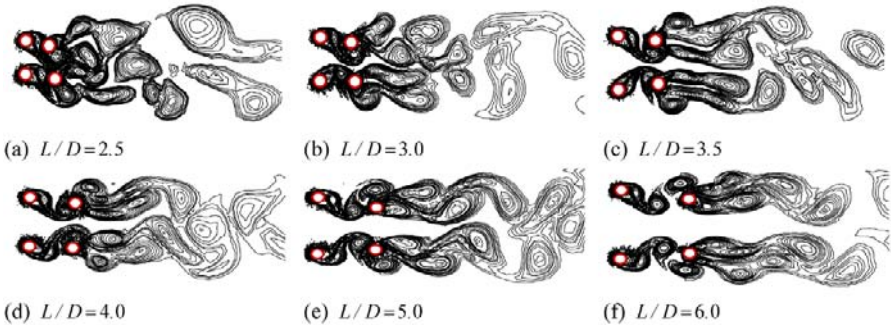


Figure 9. Instantaneous vorticity contours of four elastic cylinders versus  $L/D$

The instantaneous vorticity contour when cylinder 1 reaches the maximum positive displacement is shown in Figure 9. It is obviously different with Figure 8 as the symmetric and antisymmetric modes have disappeared and the vortex structures shedding from downstream cylinders become more complex. There is vortex shedding from two upstream cylinders in Figure 9(a) at  $L/D=2.5$ , but there is no vortex shedding of flow around the static four cylinders in Figure 8(a). The shear layer of upstream cylinders rolls up in the wake, enters into the wake of downstream cylinders, combines with the wake vortex of downstream cylinders and induces the wake of downstream cylinders presenting different scale and disturbed vortices. The across spacing of downstream cylinders gradually tensile for  $L/D > 3.0$  that indicates the wake interference gradually weakens with the spacing ratio increasing as shown in Figure 9(b-f). The wakes of downstream cylinders still collide and combine at  $x=22D$  in downstream for  $L/D=6.0$ ; but the wake interference of flow around the static four cylinders is very small for  $L/D \geq 3.5$  and there is an independent vortex street for each cylinder.

## 4 Conclusions

The 2-D CFD numerical simulation of vortex-induced vibration of four circular cylinders in line square arrangements is investigated in present paper. The fluid domain simulation is completed by Fluent, the structure response is achieved using the Newmark- $\beta$  method and the grid domain updating is accomplished through a dynamic mesh method. The mass ratio, reduced damping and frequency

ratio are kept invariant and the emphasis analysis is carried out for influence of the spacing ratio variety to aerodynamical forces, oscillation responses and wake vortex modes of each cylinder. The following conclusions are obtained from this study:

(1) The mean drag coefficient and fluctuating lift coefficient of upstream cylinders are larger than those of downstream cylinders for all range of spacing ratios. As the spacing ratios increasing, the mean of lift coefficient of each cylinder trends to 0,  $C'_{l1}$  and  $C'_{l2}$  slowly decrease and  $C'_{l3}$  and  $C'_{l4}$  rapidly decrease.  $\bar{C}_{d1}$ ,  $\bar{C}_{d2}$ ,  $C'_{d1}$  and  $C'_{d2}$  slowly increase with increasing the spacing ratio, the  $\bar{C}_{d3}$  and  $\bar{C}_{d4}$  of downstream cylinders decrease with increasing the spacing ratio.  $C'_{d3}$  and  $C'_{d4}$  are larger than  $C'_{d1}$  and  $C'_{d2}$  for  $L/D < 3.5$  and less than  $C'_{d1}$  and  $C'_{d2}$  for  $L/D \geq 3.5$ .

(2) The fluctuation of the cross-flow displacement ( $Y'$ ) and the mean of the in-flow displacement ( $\bar{X}$ ) of upstream cylinders are larger than those of downstream cylinders, and the fluctuation of the cross-flow displacement ( $X'$ ) is less than that of downstream cylinders. The mean of the cross-flow displacement ( $\bar{Y}$ ) of each cylinder trend to 0 with increasing the spacing ratio.

(3) The vortex shedding of flow around four static cylinders as spacing ratio increasing is presented three patterns: “shielding anti-phase-synchronized”, “in-phase-synchronized” and “anti-phase-synchronized”. There are vortex shedding from the upstream cylinders and the regular vortex shedding pattern disappears and becomes more complex for  $L/D=2.5\sim 6.0$  when the vortex-induced vibration occurs.

(4) The motion trajectories of upstream cylinders represent a “figure of 8” shape and the oblique oval orbits of downstream cylinders implying that the resonance occurs both in the x-direction and in the y-direction because of the streamwise and transverse responses have the same frequency but with a phase shift. The maximum cross-flow oscillation amplitude of the upstream cylinders reaches  $0.82D$  which is much larger than that of the single cylinder with the same parameters, and the maximum in-flow oscillation amplitude of the downstream cylinders reaches  $0.75D$ . It is indicated that the in-flow oscillation of downstream cylinders is unneglectable for vortex-induced vibration of multi-cylinder system.

## Acknowledgements

This research is funded by National Natural Sciences Foundation of China (NSFC) (50538020). The authors gratefully appreciate to the High Performance Computing Center (“DAWN TC4000” cluster) of Department of urban and civil engineering of Harbin Institute of Technology Shenzhen Graduate School for their great help in the calculations.

## References

- Alam Md. Mahbub, Moriya M., Takai K., Sakamoto H. (2003). Fluctuating fluid forces acting on two circular cylinders in a tandem arrangement at a subcritical Reynolds number. *Journal of Wind Engineering and Industrial Aerodynamics*, 91, 139–154.
- Farrant T., Tana M., Price W.G. (2000). A cell boundary element method applied to laminar vortex-shedding from arrays of cylinders in various arrangements. *Journal of Fluids and Structures*, 14, 375–402.
- Farrant T., Tana M., Price W.G. (2001). A cell boundary element method applied to laminar vortex shedding from circular cylinders. *Computers & Fluids*, 30, 211–236.
- Kang Sangmo (2003). Characteristics of flow over two circular cylinders in a side-by-side arrangement at low Reynolds numbers[J]. *Physics of Fluids*, 15(9), 2486–2498.
- Kubo Yoshinobu, Nakahara Tomonari, Kato Kusuo (1995). Aerodynamic behavior of multiple elastic circular cylinders with vicinity arrangement. *Journal of Wind Engineering and Industrial Aerodynamics*, 54/55, 227–237.
- Lam K., Fang X. (1995). The effect of interference of four equispaced cylinders in cross flow on pressure and force coefficient. *Journal of Fluid and Structures*, 9, 195–214.
- Lam K., Gong W.Q., So R.M.C. (2008). Numerical simulation of cross-flow around four cylinders in an in-line square configuration. *Journal of Fluids and Structures*, 24, 34–57.
- Lam K., Jiang G.D., Liu Y., So R.M.C. (2006). Simulation of cross-flow-induced vibration of cylinder arrays by surface vorticity method. *Journal of Fluids and Structures*, 22, 1113–1311.
- Lam K., Li J.Y., Chana K.T., So R.M.C. (2003). Flow pattern and velocity field distribution of cross-flow around four cylinders in a square configuration at a low Reynolds number. *Journal of Fluids and Structures*, 17, 665–679.
- Lin Tsun-kuo, Yu Ming-huei (2005). An experimental study on the cross-flow vibration of a flexible cylinder in cylinder arrays. *Experimental Thermal and Fluid Science*, 29, 523–536.
- Meneghini J.R., Saltara F., Soqueira C.L.R., Ferrari J.A. Jr (2001). Numerical simulation of flow interference between two circular cylinders in tandem and side-by-side arrangements. *Journal of Fluid and Structures*, 15, 327–350.
- Norberg C. (2003). Fluctuating lift on a circular cylinder: review and new measurements. *Journal of Fluids and Structures*, 17, 57–96.
- Sarpkaya T. (2004). A critical review of the intrinsic nature of vortex-induced vibrations. *Journal of Fluids and Structures*, 19, 389–447.
- Sayers A.T. (1988). Flow interference between four equispaced cylinders when subjected to a cross flow. *Journal of Wind Engineering and Industrial Aerodynamics*, 31, 9–28.
- Zdravkovich M.M. (1987). The effects of interference between circular cylinders in cross flow. *Journal of Fluids and Structures*, 1, 235–261.
- Zhou C.Y., So R.M.C., Lam K. (1999). Vortex-induced vibrations of an elastic circular cylinder. *Journal of Fluid and Structures*, 13, 165–189.

*“This page left intentionally blank.”*

# Dynamic Response Analysis of TLP's Tendon in Current Loads

Gongwei Yan<sup>1\*</sup>, Feng Xu<sup>1</sup>, Hang Zhu<sup>1</sup> and Jinping Ou<sup>1,2</sup>

<sup>1</sup>School of Civil Engineering, Harbin Institute of Technology, Harbin 150090, P.R. China

<sup>2</sup>School of Civil and Hydraulic Engineering, Dalian University of Technology, Dalian 116024, P.R. China

**Abstract.** The large finite element software ANSYS and the CFD software FLUENT are used to analyze the dynamic response of TLP's tendon in current load effect. ANSYS is used to figure out the hydrodynamic forces of tendon. The hydrodynamic forces are transferred to the tendon through flow field. The tendon is considered as two tips end-fixed and its dynamic response is solved in different pretensions. The results show that the tendon has realizing transverse vibration and little vibration in current direction, but the realizing drift in current direction must be considered.

**Keywords:** TLP, dynamic response, VIV, boundary condition

## 1 Background

Tension leg platform (TLP) is a type of deep-water platform. It has been used in oil production extensive according to its accomplished technology and steady capability. There are many studies about TLP, such as study of TLP's types (Hanna et al. 1987), study of TLP's mounting (Rasmussen et al., 1988), study of TLP's analysis method (Rossit et al., 1996), study of TLP's fatigue and reliability (Arnljot Skogvang et al., 1997), etc. Tendon will have vortex-induced vibration response in current load. Wave load and tension change in tendon will observably influence the VIV response.

Many scholars have studied the VIV of offshore platform. Allen (1998) presented an overview of deepwater riser vortex-induced vibration analysis. Vandiver (1998) presented an overview about the key limiting issues of current research in the prediction of vortex-induced vibration of marine risers. Triantafyllou (1999), Foulhoux (1994) and Halse (2000) presented the methods of calculation and examination which are acceptable for the actual offshore platforms. Dongyao Wang

---

\* Corresponding author, e-mail: yangongwei\_hit@qq.com

et al. (1998) presented a time domain analysis for presented for predicting vortex-shedding induced transverse vibration of TLP tethers which are subject to wave current and oscillatory displacements at their upper end both in horizontal and vertical directions. Weimin Chen et al. (2003) presented an introduction about theories and analysis methods of VIV.

This paper considers the effect of current, numerically simulates tendon's dynamical response using finite element software ANSYS and CFD software FLUENT, and the deflection of different tension in tendon is considered in this simulation based on the classic TLP which is globally designed according to the practical environmental load in south China Sea.

## 2 Analytical Models

The parameters of this analytical model which is modeled from the single tendon of a globally designed classic TLP are as follows:

Table 1. The parameters of the analytical model

Length	Diameter	Thickness	Density of steel	Elastic modulus
978m	1.2m	0.04m	7850kg/m <sup>3</sup>	2.0×10 <sup>11</sup> N/m <sup>2</sup>
Tension	Wave height	Period	Density of water	Coefficient of viscosity
12798kN	15m	10s	1030kg/m <sup>3</sup>	1.205×10 <sup>-3</sup> kg/m·s

There are several conditions to modeling the tendon of TLP:

1. The density of the air locked tendon is the same to water, therefore the gravity of tendon equal to buoyancy force of tendon;
2. The tendon is considered as two tips end-fixed because of the hull's slowly movement;
3. The tendon is slinness element.
4. Based on the steady velocity of current, the tendon can be divided into several cells according to its length, and the distributed force of each cell can be degerated into the force on its middle point.

### 3 Current Load Accounts

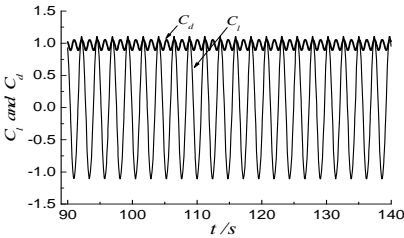
The CFD software Fluent is used to solve current load of tendon.

The boundary conditions are set as follows. Left side: velocity-inlet, uniformity of velocity distribution. Right side: outflow. Upper and lower side: symmetry. Surface of tendon: wall.

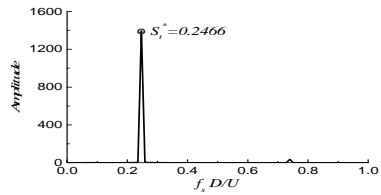
The flow field around cylinder is obtained by Segregated Solver of Fluent software. The SIMPLE algorithm is used to solve the coupling relationship between velocity and pressure in momentum equation. The Standard interpolation scheme of pressure is used in account. The momentum spread adopts QUICK type which is suitable for structured grid.



(a) Vorticity isoline of wake flow behind tendon



(b) Time histories of lift and drag coefficients



(c) Lift coefficient of FFT spectrum analysis

Figure 1. Fixation flow results of the tendon's 33<sup>rd</sup> part in middle point ( $Z=978/33 \times 32.5m$ )

Figure 1(a) is velocity isoline and vorticity isoline of the circle flow field around tendon.

Figures 1(b) and (c) are the dimensionless lift and drag coefficients and the result of spectrum analysis obtained through FFT transform. The average of drag coefficient  $C_{dmean} = 0.9766$ , the amplitude of lift coefficient  $C_l = 1.109$ , Strouhal number  $S_t^* = 0.2466$  is bigger than empirical value 0.2 because of the higher Reynolds number. Yanqiu Dong (2005) shows that  $C_l = 0.6 \sim 2.4$  and  $C_{dmean} = 0.4 \sim 2.0$ .

The lift coefficients  $C_l(t)$  and drag coefficients  $C_d(t)$  of tendon's each part can be figured out, and then the lift and drag of tendon's each part can be figured out according to the equations as follows:

$$F_l(t) = 1/2 \rho U_\infty^2 D \cdot C_l(t) \quad F_d(t) = 1/2 \rho U_\infty^2 D \cdot C_d(t)$$

Table 2 is the detailed results of the vortex-excited force account about the middle point of tendon's each part, where  $C_{l_{rms}}$  is the root mean square value of lift coefficient,  $C_{d_{mean}}$  is the mean value of drag coefficient,  $S_t = f_s D / V$  is Strouhal number,  $f_s$  is the vortex shedding frequency of tendon in wake flow,  $V$  is velocity at each part's middle point of tendon,  $F_l$  is the amplitude of uniform vortex-excited force on each part of tendon.

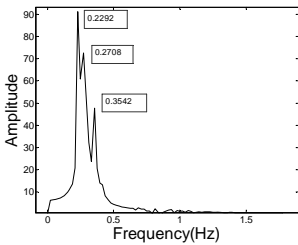
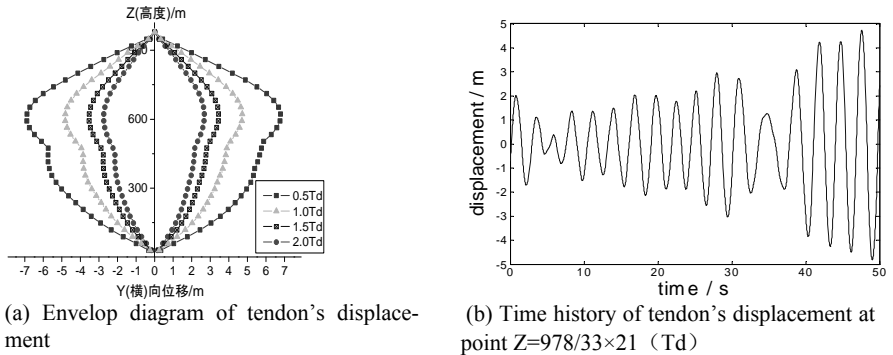
Table 2. Calculation results of vortex-excited force on each part of tendon

	1	2	3	4	5	6	7	8	9	10	11
$V(\text{m/s})$	1.0533	1.0800	1.1067	1.1334	1.1600	1.1867	1.2134	1.2400	1.2667	1.2934	1.3201
$C_{l_{rms}}$	0.6647	0.6988	0.7268	0.8450	0.7284	0.8071	0.8251	0.8609	0.8067	0.8588	0.8519
$C_{d_{mean}}$	1.134	1.133	1.130	1.128	1.123	1.114	1.111	1.104	1.103	1.096	1.090
$St$	0.2509	0.2447	0.2388	0.2543	0.2485	0.2429	0.2376	0.2519	0.2465	0.2415	0.2548
$F_l(\text{N/m})$	881.7	926.5	972.6	1020.0	1061.5	1109.0	1155.0	1201.0	1247.0	1295.0	1344.0
	12	13	14	15	16	17	18	19	20	21	22
$V(\text{m/s})$	1.3467	1.3734	1.4001	1.4268	1.4534	1.4801	1.5124	1.5479	1.5835	1.6191	1.6546
$C_{l_{rms}}$	0.8626	0.8555	0.8517	0.8629	0.8619	0.8592	0.8598	0.8486	0.8412	0.8407	0.8365
$C_{d_{mean}}$	1.087	1.081	1.077	1.071	1.067	1.063	1.055	1.046	1.040	1.036	1.030
$St$	0.2497	0.2449	0.2402	0.2526	0.2479	0.2435	0.2541	0.2483	0.2427	0.2522	0.2468
$F_l(\text{N/m})$	1393.0	1443.0	1493.0	1543.0	1594.5	1646.0	1709.0	1779.0	1851.0	1923.0	1996.0
	23	24	25	26	27	28	29	30	31	32	33
$V(\text{m/s})$	1.6902	1.7257	1.7613	1.7969	1.8324	1.8680	1.9036	1.9391	1.9747	2.0103	2.0458
$C_{l_{rms}}$	0.8340	0.8289	0.8250	0.8205	0.8138	0.8144	0.8057	0.8035	0.8004	0.794	0.7892
$C_{d_{mean}}$	1.026	1.020	1.016	1.010	1.005	1.004	0.995	0.991	0.986	0.981	0.977
$St$	0.2416	0.2506	0.2455	0.2406	0.2491	0.2443	0.2524	0.2478	0.2433	0.2509	0.2466
$F_l(\text{N/m})$	2070.5	2146.0	2223.0	2300.0	2378.0	2458.0	2538.0	2619.0	2702.5	2789.0	2868.0

### 4 Analysis of Dynamic Response

The software Ansys10.0 is used to analyze the dynamic response of tendon under the action of wave and current. This analysis considers several different pretensions' effect of tendon such as  $0.5T_d$ ,  $T_d$ ,  $1.5T_d$  and  $2.0T_d$ , where pretension of tendon  $T_d = 12798kN$ . Tendon is uniformly divided into several sections from below along the depth of water. The element BEAM188 is used to solve the modal of tendon. Pretension is brought to tendon through changing the extension length of tendon in advance.

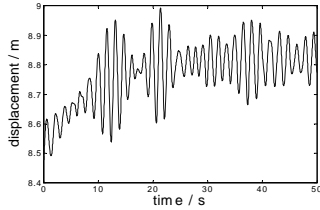
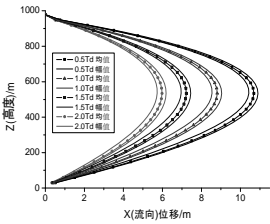
Figure 2 is the results for dynamic response analysis of tendon under the action of transverse lift caused by current.



(c) Spectrum for Y-direction time history of tendon's displacement at point  $Z=978/33 \times 21$  ( $T_d$ )

Figure 2. Y-direction dynamic response analysis for tendon under the action of lift caused by current

Figure 3 is the results for dynamic response analysis of tendon under the action of drag caused by current.



(a) Envelop diagram of tendon's displacement

(b) Time history of tendon's displacement at middle point (Td)

Figure 3. X-direction dynamic response analysis for tendon under the action of drag force

### 5 Conclusions

Based on the results of numerical analysis, the following conclusions are drawn:

1. The vortices are alternant shedding in the near wake region of tendon effecting with current load. The current velocity and diameter of tendon have obvious influence on the value of shedding frequency.
2. The tendon has realizing transverse vibration, maximum responses present to the 2/3 height of tendon away the seabed. The tension of tendon has obvious influence on the response amplitude of tendon.
3. The tendon has little vibration in current direction, but the realizing drift in current direction must be considered.

### Acknowledgments

The authors gratefully acknowledge the support from National Natural Science Foundation of China (NSFC, No. 50538050) and National "863" plans project of China (No. 2006AA09A103, 2006AA09A104).

### References

Allen Donald W. (1998). Vortex-induced vibration of deepwater risers. OTC 8703.  
Chen W.M., Shi Z.M. (2003). The vortex-induced vibration of offshore platform. *Shipbuilding of China*, 44(Special), 480-487 [in Chinese].  
Dong Y.Q. (2005). *Wave loads and response of the oil-extraction platform in deep ocean* [M]. Tianjin: Tianjin University Press, 292-304 [in Chinese].

- Foulhoux L, Saubestre V. (1994). An engineering approach to characterize the lock-in phenomenon generated by a current on a flexible column. *International Journal of Offshore and Polar Engineering*, 4(3), 231-233.
- Halse K. H. (2000). Norwegian deepwater program: improved predictions of vortex-induced vibrations. OTC 11996.
- Hanna S. Y., Thomason W. H. et al. (1987). Influence of tension, weight and hydrostatic pressure on deepwater TLP Tendons. OTC 5610, Houston, Texas.
- Rasmussen J., Karlsson P. et al. (1988). A new and cost-beneficial approach to TLP tethering. OTC 5722, Houston, Texas.
- Rossit C. A., Laura P. A. A. et al. (1996). Bambil. Dynamic response of the leg of a tension leg platform subjected to an axial, suddenly applied load at one end. *Ocean Engineering*, 23(3), 219-224.
- Skogvang A., Vogel H. (1997). Lessons to learn from full scale measurements of snorre TLP tethers. *Proceedings of the Seventh International Offshore and Polar Engineering Conference*, Honolulu, USA.
- Triantafyllou M. (1999). Pragmatic riser VIV analysis. OTC 10931.
- Vandiver J. K. (1998). Research challenges in the vortex-induced vibration prediction of marine risers. OTC 8698.
- Wang D.Y., Ling G.C. (1998). Vortex-induced nonlinear vibrations of TLP tethers under circumstances of platform oscillation. *Acta Oceanologica Sinica*, 20(3), 119-128 [in Chinese].

*“This page left intentionally blank.”*

# Flutter Performance and Surrounding Flow Structures of Central-Slotted Box Girders

Yongxin Yang<sup>1\*</sup>, Yaojun Ge<sup>1</sup> and Wei Zhang<sup>1</sup>

<sup>1</sup>State Key Laboratory for Disaster Reduction in Civil Engineering, Tongji University, Shanghai 200092, China

**Abstract.** Investigation on flutter stabilization and its mechanism of long-span suspension bridges with box girders by using central air vent, which resulted in central-slotted box girders, was introduced in this paper. With the experimental results of wind tunnel tests, the minimum values of critical flutter speeds for certain slot width were always measured at the  $+3^\circ$  angle of attack. Based on the concept of full-degree coupling analysis, stabilization mechanism was found with the references of aerodynamic damping and degree participation. The characteristics of main vortices around the decks in the flow field obtained from Particle Image Velocimetry (PIV) wind tunnel tests and numerical calculations were finally investigated.

**Keywords:** flutter stabilization, flutter mechanism, central-slotted box girder, slot width, particle image velocimetry

## 1 Introduction

With the ever-growing span length of suspension bridges, one of the most challenging problems encountered is aeroelastic stability. Based on the experience gained from existing long-span bridges, the span length of 1,600m seems to be the aerodynamic limit for suspension bridges with a streamlined box girder at the flutter checking speed about 60m/s. It is necessary to seek further improvement on aerodynamic stability when the bridge site is located in typhoon-prone region or a bridge with even longer main span is required.

Theoretical and experimental investigations reported in the literature (Walshe, 1997; Miyata, 2002) support the conclusion that the application of central vent in the box section centre can improve aerodynamic stability of suspension bridges. The effect of location and size of the slot on the aerodynamic characteristics was examined through section model wind tunnel tests (Sato, 1995), and it was found

---

\* Corresponding author, e-mail: yang\_y\_x@tongji.edu.cn

that a slot at the center could enhance flutter onset wind speed and the flutter speed rises with the increase of the slot width (Sato, 2000, 2001). The effectiveness of central slot was further confirmed by a full aeroelastic model wind tunnel test based on an assumed super long-span bridge with the main span of 2800m (Sato, 2002). The feasibility study of Gibraltar Bridge shows that not only there is a clear trend for the slotted-box section to become increasingly aeroelastically stable for increasing deck slot width but also this increase ratio of critical wind speeds with slot width can be fitted to the Power-law expressions by means of the least squares method (Larsen, 1998).

This paper presents the aerodynamic stabilization for long-span suspension bridges with box girders by employing central air vent, which leads to slotted box girders. The experimental investigation through sectional model testing was firstly carried out to detect critical wind speeds corresponding to slot widths and angles of attack. The stabilizing mechanism of central slot for the box girder was revealed through comparison and contrast of aerodynamic damping and degree participation levels among different widths of central slot. The characteristics of vortices around the decks in the flow field obtained from Particle Image Velocimetry (PIV) tests and numerical calculations were finally investigated.

## 2 Flutter Performance

According to previous research results, slot width is a key parameter in determining the aerodynamic performance of a slotted box girder section. Therefore the relationship between structural aerodynamic performance and slot width was investigated first of all. In order to establish the experimental evidence linking slot width to aerodynamic stability, the ratio of slot width  $b$  to the solid box width  $B$  was respectively set to  $b/B = 0, 0.2, 0.4, 0.6, 0.8$  and  $1.0$  (section S00, S01, S02, S03, S04 and S05 respectively) in wind tunnel tests with cross sections described in Figure 1.

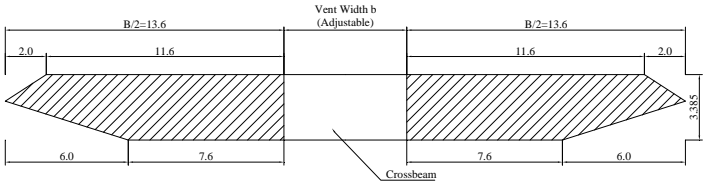


Figure 1. Central-Slotted Cross Section (Unit: m).

## 2.1 Stabilizing Effect

The wind tunnel testing of the slotted box girders was carried out in smooth flow at Tongji University's TJ-1 Boundary Layer Wind Tunnel with the working section of the 1.8m width, the 1.8m height and the 15m length. The flutter critical speeds of sections with different slot widths and under different wind angles of attack are tested and summarized in Figure 2.

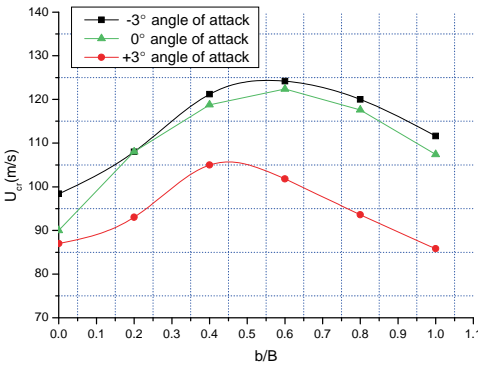


Figure 2. Flutter Critical Speeds of Slotted Girders.

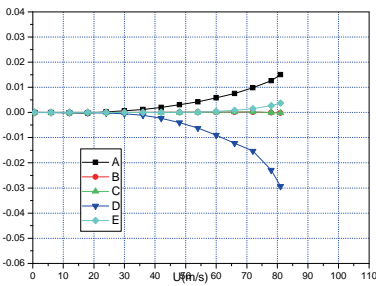
It can be seen from Fig. 2 that the flutter stabilizing effectiveness of slotted box girders generally depends upon two important characteristics including width of central slot and angle of attack. The values of critical wind speeds vary with angle of attack for all cases with various widths of central slot, and the minimum values of critical flutter speeds for certain slot width were always measured at the +3° angle of attack. For each angle of attack, the relationship between flutter performance and slot width is not mono increase, and the evolution trend of flutter critical speed comprises two different regions: the critical wind speed first increases with the relative width of central slot until an optimal point is reached, then decreases.

## 2.2 Stabilizing Mechanism

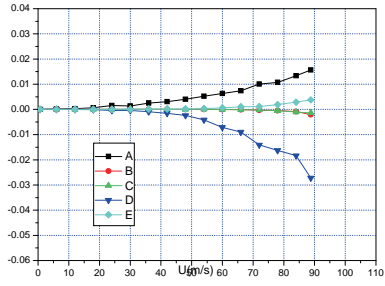
Based on the concept of full-degree coupling analysis, a two-dimensional three-degree-of-freedom flutter analysis method was proposed by the authors to reveal the driven mechanism of flutter oscillation (Yang, 2002, 2003), and was thus applied in the theoretical analysis of stabilizing mechanism of central slotting with the references of aerodynamic damping and degree participation.

According to this method, the aerodynamic damping ratio in torsion can be expressed by the summation of five parts, which are the combination of aerodynamic

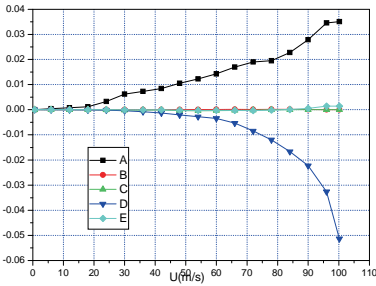
derivatives and phase lags between motions having the same oscillation frequency. Figure 3 describes the evolution of these five parts for section S00, S01 and S02 at the +3° angle of attack. For all three cases, Part A with the reference of  $A_2^*$  is always positive and makes the greatest contribution to aerodynamic stability among five parts for all three cases, while Part D with the reference of  $A_1^*H_3^*$  keeps negative all the way and causes the worst influence on aerodynamic stability. The influence of Part E is helpful to stability but with the smaller effect, and Both Parts B and C have smallest value. Compared with that of section S00, the value of positive aerodynamic damping Part A gets a little larger for central-slotted section S01, while the evolution of Part D is like being controlled to some extent and the absolute value gets smaller. When the slot width increases to  $b/B = 0.4$ , these controlling effects become more evident as the value of Part A gets even larger and the absolute value of Part D gets even smaller. Therefore, the oscillation system becomes more aerodynamically stable.



(a)  $b/B = 0$  (S00)



(b)  $b/B = 0.2$  (S01)



(c)  $b/B = 0.4$  (S02)

$$\begin{aligned}
 A &\Leftrightarrow -1/2 \cdot \rho B^4 / I \cdot A_2^* \\
 B &\Leftrightarrow -\rho^2 B^6 / 2m_h I \cdot \Omega_{h\alpha} \cdot A_1^* H_2^* \cos \theta_1 \\
 C &\Leftrightarrow \rho^2 B^6 / 2m_h I \cdot \Omega_{h\alpha} \cdot A_4^* H_2^* \sin \theta_1 \\
 D &\Leftrightarrow -\rho^2 B^6 / 2m_h I \cdot \Omega_{h\alpha} \cdot A_1^* H_3^* \cos \theta_2 \\
 E &\Leftrightarrow \rho^2 B^6 / 2m_h I \cdot \Omega_{h\alpha} \cdot A_4^* H_3^* \sin \theta_2
 \end{aligned}$$

Figure 3. Aerodynamic damping ratios.

Table 1. DOF participation level.

$b/B$	$U_{cr}(m/s)$	$\alpha$	$h$
0	87.0	0.967	0.254
0.2	93.0	0.949	0.315
0.4	105.0	0.938	0.348
0.6	101.8	0.940	0.341
0.8	93.6	0.942	0.335
1.0	85.8	0.968	0.249

For the above-mentioned six cases in two-degree vibration, the DOF participation level and the corresponding critical wind speed at the flutter onset can be represented in Table 2. The box section with the relative slot width of  $b/B = 0.4$  at the  $+3^\circ$  angle of attack has the highest level of heaving DOF participation and the greatest critical wind speed, while the box section with the relative width of  $b/B = 1.0$  and without slot have almost the same lowest values of both coupling effect of heaving DOF participation and critical wind speed. In general, it can be concluded that the more heaving DOF participate at the flutter onset, the higher critical wind speed can be reached.

### 3 Flow Structures

The emergence of Particle Image Velocimetry (PIV) makes it possible to obtain the velocity maps of the wind field around the decks, in which may exist some important clues to the mechanism of wind-induced vibration of structures. Efforts were made in the current investigation to find the differences of flow structures around central-slotted box girder sections with different slot width.

#### 3.1 PIV System

A PIV system is set up in Tongji University's TJ-4 wind tunnel with the working section of 0.8m width, 0.8m height and 5m length. The dual Nd:YAG laser and the digital CCD camera are set outside of the working section which is made to be transparent for getting the images easily. The dual Nd:YAG laser which provides laser light sheet through a cylinder and a sphere lens are used for illuminating the liquid tracer particles with the diameter of several microns put into the flow. The illuminated particles are taken images by the camera with the location at 90 degrees to the light sheet. Then velocity maps can be obtained using FFT based cross-correlation analysis in two sequential frames of 50% overlapping in each direction with an interrogating window of 32 pixels by 32 pixels. The impulse en-

ergy and the according time delay between two subsequent laser pulses are controlled by the synchronizer based on the wind speed and the area of the field of view.

### 3.2 Flow Structures in the Slots

With this PIV system, ensemble averaged velocity maps and some typical instantaneous velocity maps of section S01, S02 and S03 are shown in Figure 4. As the results shown, flow structures in the slots vary with the slot width. For section S01, two large vortices occupy almost all the spaces in the slot, and the instantaneous velocity map only differs a little with the ensemble averaged velocity map. However, for section S02 and S03, the instantaneous velocity map differs from the ensemble averaged one in which only two small vortices could be found just behind the upstream part of the deck. In the instantaneous velocity map of section S02, two vortices with opposite vorticity can be found in the slot, while the number of vortices increases to four for section S03. The velocity vectors in the slot also vary significantly with the increase of slot width, which implies the variation of aerodynamic forces.

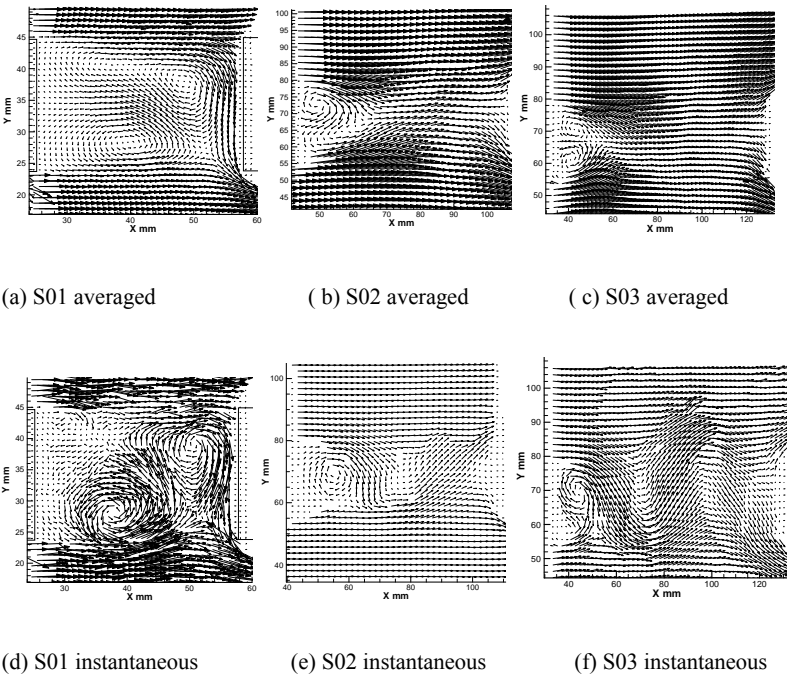


Figure 4. Velocity maps of central slot.

After snapshot Proper Orthogonal Decomposition (POD) (Adrian 2000, Berkooz 1993, Santa Cruz 2005), vortices can be identified more clearly. Figure 5a) to c) shows the different modes of the velocity map for section S02. Energy distribution of different modes is shown in Figure 5d). Obviously the former modes occupy most energy of the total fluctuating structures energy. Then mode 2 to 15 was used to reconstruct the fluctuating velocity maps as shown in Figure 5e).

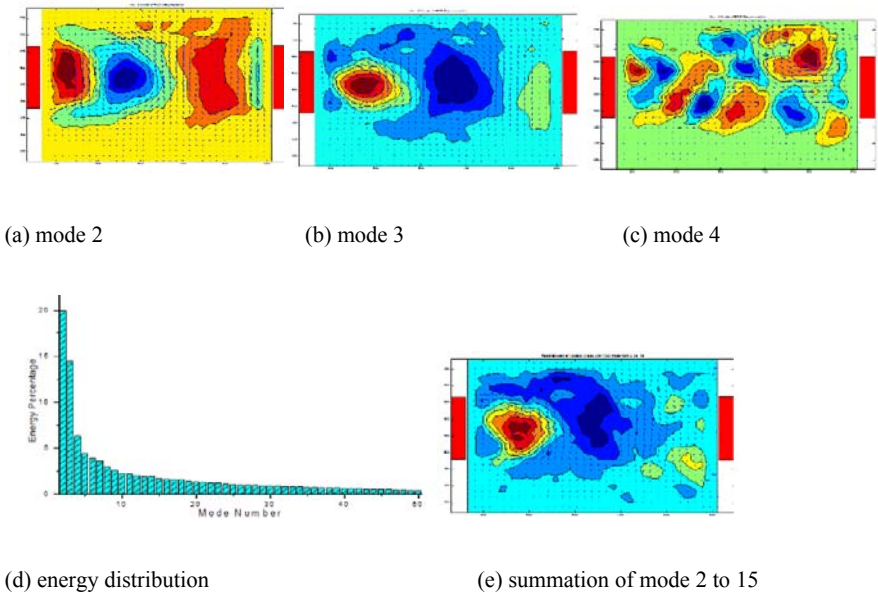


Figure 5. Snapshot POD results for section S02.

### 3.3 Wake Flow Structures

In the PIV results of wake flow velocity map, vortices can not be identified clearly, so numerical method was used to obtain the velocity map with short time intervals. After snapshot POD decomposition, the fluctuating velocity maps were reconstructed using the former 15 modes, which are shown in Figure 6 for section S02 and S04 in four phase angles of  $0$ ,  $\pi/2$ ,  $\pi$  and  $\pi/3/2$ . The phase angle is set to  $0$  when the lift force coefficient increases to its maximum value. In central slot, three vortices can be found for section S02 while four or five vortices for section S04. These vortices will be separated by the downstream part of the deck for both sections. In the case of section S02, the separated upper and lower part of one vortex will reunite again in the wake flow. However, for section S04 the same thing won't happen, the separated two parts will dissipate separately instead. Furthermore, in the case of section S04 the strength of the vortices drops more quickly. It

is proved that there do exist some vortices in the flow field related to aerodynamics of structures which will enlighten us on the discrepancies of the flow structures around central-slotted sections with different slot width and the relationship between the characteristics of flow structures and the aerodynamic performances of bridge decks.

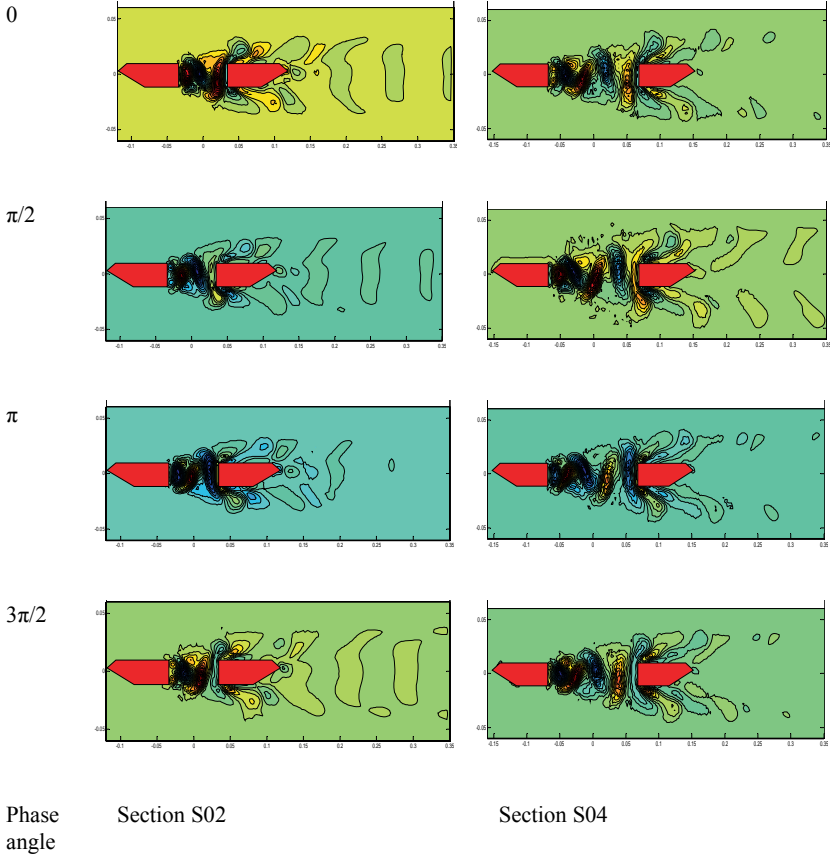


Figure 6. Flow structures for section S02 and S04.

## 4 Conclusions

Aerodynamic stabilization and its mechanism of central slot for long-span suspension bridges with box girders were carefully investigated through experimental investigation and theoretical analysis. The results of sectional model wind tunnel tests indicate that the minimum values of critical flutter speeds for certain slot

width were always measured at the  $+3^\circ$  angle of attack, and the relationship between flutter performance and slot width is not mono increase for each angle of attack. The flutter critical speed first increases with the relative width of central slot until an optimal point is reached, then decreases. Based on the concept of full-degree coupling analysis, theoretical investigation of stabilization mechanism was then carried out with the references of aerodynamic damping and degree participation. Through flow structure analysis based on PIV technique and snapshot POD decomposition, it is proved that typical vortices in the flow field around central-slotted sections can be identified, which is related to the interactive force between structures and surrounding air flow, and the characteristics of these vortices vary significantly with the relative slot width. More efforts still need to find the interrelationship between the dynamics of the decks and the characterization of the vortices in the flow field to discover the inherent mechanism of wind-induced vibration.

## Acknowledgements

The work described in this paper is part of a research project financially supported by the Natural Science Foundation of China under the Grants 50608059, 50538050 and 90715039, and the Hi-Tech Research and Development Program of China under the Grant 2006AA11Z108.

## References

- Adrian R.J., Christensen K.T., and Liu Z.C., 2000. Analysis and interpretation of instantaneous turbulent velocity fields. *Experiments in Fluids*, 29(3), 275-290.
- Berkooz G., Holmes P. and Lumley J., 1993. The proper orthogonal decomposition in the analysis of turbulent flows. *Annual Review of Fluid Mechanics*, 25, 539-575.
- Larsen A., Astiz M.A., 1998. Aeroelastic consideration for the Gibraltar Bridge feasibility study, in: *Bridge Aerodynamics*, Larsen & Esdahl (eds), Balkema, Rotterdam, 165-173.
- Miyata T., 2002. Significance of aero-elastic relationship in wind-resistant design of long-span bridges, *Journal of Wind Engineering and Industrial Aerodynamics* 90, 1479-1492.
- Santa Cruz A., et al., 2005. Characterization by proper-orthogonal-decomposition of the passive controlled wake flow downstream of a half cylinder. *Experiments in Fluids*, Published online.
- Sato H., Hirahara N. et al., 2002. Full aeroelastic model test of a super long-span bridge with slotted box girder, *Journal of Wind Engineering and Industrial Aerodynamics* 90, 2023-2032.
- Sato H., Kusuhara S. et al., 2000. Aerodynamic characteristics of super long-span bridges with slotted box girder. *Journal of Wind Engineering and Industrial Aerodynamics* 88, 297-306.
- Sato H., Toriumi R., Kusakabe T., 1995. Aerodynamic characteristics of slotted box girders, in: *Proceedings of Bridges into the 21st Century*, Hong Kong, 721-728.
- Sato H., Toriumi R., Kusakabe T., 2001. Aerodynamic characteristics of slotted box girders, in: *Bridges into the 21st Century*, 721-728.
- Walshe D.E., Twidle G.G., Brown W.C., 1997. Static and dynamic measurements on a model of a slender bridge with perforated deck, in: *International Conference on the Behaviour of Slender Structures*, The City University, London, England.

- Yang Y.X., Ge Y.J., Xiang H.F., 2002. Coupling effects of degrees of freedom in flutter instability of long-span bridges, in: *Proceedings of the 2nd International Symposium on Advances in Wind and Structures*, Busan, Korea, 625-632.
- Yang Y.X., Ge Y.J. and Xiang H.F., 2007. Investigation on flutter mechanism of long-span bridges with 2d-3DOF method, *Journal of Wind and Structures*, 10(5).

# Dynamic Analysis of Fluid-Structure Interaction on Cantilever Structure

Jixing Yang<sup>1\*</sup>, Fan Lei<sup>1</sup> and Xizhen Xie<sup>1</sup>

<sup>1</sup>Faculty of Transportation, Wuhan University of Technology, Hubei, Wuhan 430063, China

**Abstract.** ANSYS software was used to analyze the influence on nature frequency of cantilever structure with water inside or outside. The calculation frequencies of this paper were compared to those of the theoretical formula, and the results are found to be the same. It comes to a conclusion that the internal and external hydrodynamic pressure has great influence on nature influence of structure. It cannot be neglected especially to slender structure and thin-walled structure.

**Keywords:** fluid-structure interaction, nature frequency, hydrodynamic pressure

## 1 Introduction

Many engineering structures are operating under water or used to store liquid, such as all kinds of bridge pier and liquid storage structure. In fact, the water retaining dam is also regarded as a kind of cantilever beam with water on one side, ordinary (Ju and Zeng, 1983). Therefore, it has practical significance to study the dynamic characteristics of fluid-structure interaction. The fluid-structure interaction of structure can be divided into two situations, one is structure filled with fluid, and the other is structure under fluid. The paper calculates the nature frequency of cylinder cantilever structure with different radius and height by ANSYS, when there is no fluid, when there is fluid inside and when there was fluid outside. By comparing and analyzing, the influence of hydrodynamic pressure on structure nature frequency is found out.

## 2 Calculation Method of ANSYS Software

ANSYS is powerful software of finite element analysis. It can realize the analysis of multi-field and multi-coupled field. Among them, the coupled sound field can

---

\* Corresponding author, e-mail: leifan\_1983@163.com

analyze the interaction of fluid and structure, and the interaction is achieved by applying FSI on their interface.

The paper mainly discusses the fluid-structure interaction of cylinder cantilever structure. Elements uses in the model include FLUID29, FLUID30 (ABSENT), FLUID30 (PRESENT), PLANE42, SOLID45.

### 3 Structure Model

Choosing several cylinder structures of different sizes to calculate, and analyze the influence on structure nature frequency caused by hydrodynamic pressure. Size and material parameters of cylinder: Outer radius  $r_1 = 5m$ , height  $h = 5r_1, 10r_1, 20r_1, 30r_1$ . When there is fluid inside of structure, select inside radius  $r_2 = 0.2r_1, 0.4r_1, 0.6r_1, 0.8r_1$ . Density  $\rho_1 = 2400kg/m^3$ , elastic modulus  $E = 3 \times 10^{10} Pa$ , Poisson's ratio  $\gamma = 0.2$ . Density of fluid  $\rho_2 = 1000kg/m^3$ . Figure 1 shows the simplified models.

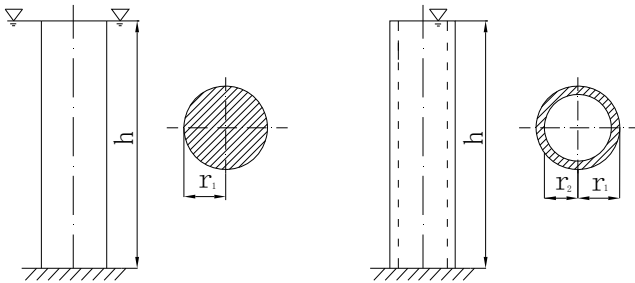
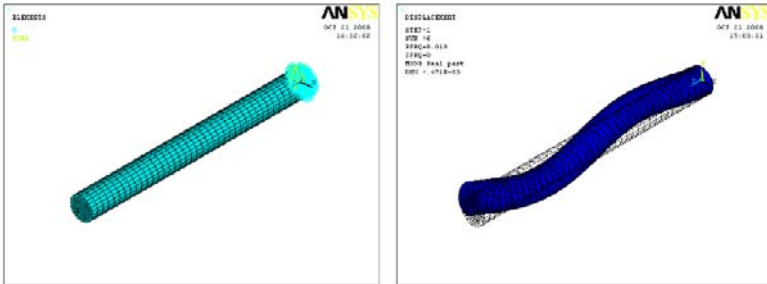


Figure 1. Simplified models

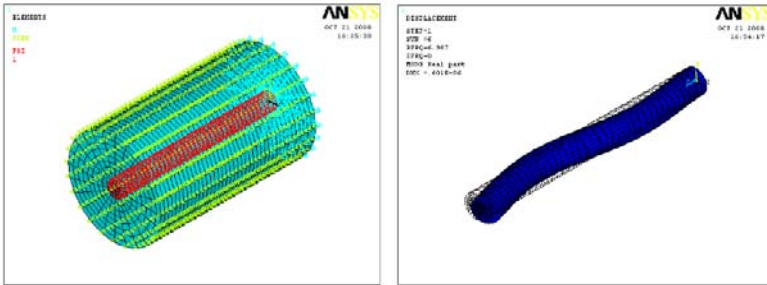
#### 3.1 Structure with Outside Fluid

First, a cylinder model without fluid is built, and the nature frequency of it is calculated. Then the fluid elements are built to surround the cylinder, and its nature frequency is calculated, too. The thickness of the fluid elements was 5 times to the radius of cylinder (Zhang, 2006). Some of computation models and mode shapes

are shown in the following Figure 2 and Figure 3. (Take the situation of  $r_1/h = 1/20$  for example)



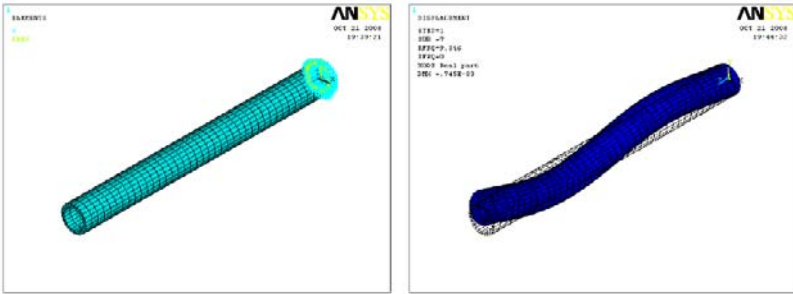
a) b)  
 Figure 2. a) Computation model of cylinder without fluid; b) Mode shape



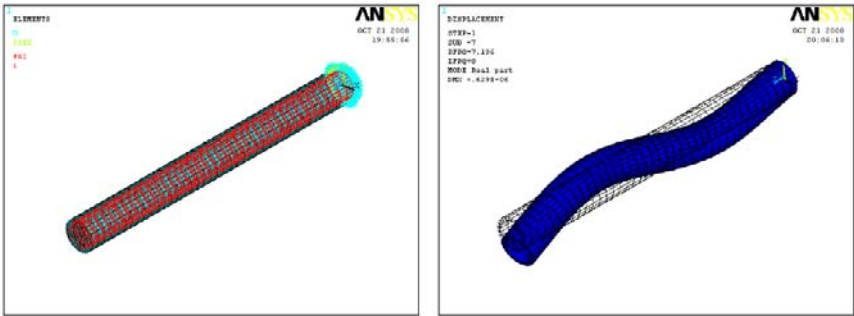
a) b)  
 Figure 3. a) Computation model of cylinder with outside fluid; b) Mode shape

### 3.2 Structure with Inside Fluid

The problems of structure with inside fluid are familiar to the problems of pipe conveying fluid. Computation models and mode shapes are shown in the following Figure 4 and Figure 5 (take the situation of  $r_1/h = 1/20$  and  $r_2/r_1 = 4/5$  for example).



a) b)  
 Figure 4. a) Computation model of cylinder without fluid; b) Mode shape



a) b)  
 Figure 5. a) Computation model of cylinder with inside fluid; b) Mode shape

## 4 Results and Analysis

### 4.1 Calculation Results

Let  $\xi$  be the ratio of radius to height  $\xi = \frac{r_1}{h}$ , let  $\eta$  be the radius ratio  $\eta = \frac{r_2}{r_1}$ , let  $f$  be nature frequencies of cylinder without fluid, let  $f_w$  be the nature frequencies of cylinder with fluid. The calculation results of the models were list in the following tables (fundamental frequency).

Table 1. Nature frequencies of cylinder and cylinder with outside fluid (Hz)

-	$\xi = 1/5$	$\xi = 1/10$	$\xi = 1/20$	$\xi = 1/30$
$f$	7.3281	1.9339	0.4904	0.2185
$f_w$	6.3305	1.6570	0.4183	0.1862

Table 2. Nature frequencies of cylinder and cylinder with inside fluid (Hz)

-		$\xi = 1/5$	$\xi = 1/10$	$\xi = 1/20$	$\xi = 1/30$
$\eta = 4/5$	$f$	7.2241	2.4034	0.6229	0.2788
	$f_w$	5.5335	1.8296	0.4727	0.2114
$\eta = 3/5$	$f$	8.0461	2.2144	0.5691	0.2543
	$f_w$	7.2719	1.9962	0.5125	0.2289
$\eta = 2/5$	$f$	7.6624	2.0643	0.5269	0.2351
	$f_w$	7.3859	1.9880	0.5072	0.2263
$\eta = 1/5$	$f$	7.4135	1.9674	0.4998	0.2228
	$f_w$	7.3522	1.9508	0.4955	0.2209

### 4.2 Result Comparison

Compare the value of  $f_w / f$  in Table 1 and Table 2 to the theoretical calculation results in the literature (Ju and Zeng, 1983), in order to verify the accuracy of numerical calculation method in this paper.

Table 3.  $f_w / f$  (structure with outside fluid)

-	$\xi = 1/5$	$\xi = 1/10$	$\xi = 1/20$	$\xi = 1/30$
Theoretical value	0.9039	0.8710	0.8512	0.8430
Numerical value	0.8639	0.8568	0.8530	0.8522

We can see that the numerical values are very close to the theoretical values in above Tables. The maximum error of the values is 4.43% in Table 3 and 1.77% in

Table 4. The errors in Table 3 are larger than Table 4; it is related to the fluid range outside the structure and proximate calculation of theoretical formula. On the whole, the results of numerical calculation in this paper are accurate.

Table 4.  $f_w / f$  (Structure with inside fluid)

		$\xi = 1/5$	$\xi = 1/10$	$\xi = 1/20$	$\xi = 1/30$
$\eta = 4/5$	Theoretical value	0.775	0.775	0.772	0.770
	Numerical value	0.7660	0.7613	0.7589	0.7582
$\eta = 3/5$	Theoretical value	0.907	0.907	0.905	0.902
	Numerical value	0.9038	0.9015	0.9005	0.9001
$\eta = 2/5$	Theoretical value	0.965	0.965	0.963	0.960
	Numerical value	0.9639	0.9630	0.9626	0.9625
$\eta = 1/5$	Theoretical value	0.991	0.991	0.989	0.987
	Numerical value	0.9917	0.9916	0.9914	0.9914

### 4.3 Results Analysis

In order to study the influence on structure vibration characteristic cause by fluid, the numerical values in Table 3 and Table 4 are drawn in the following Figures after appropriate complement.

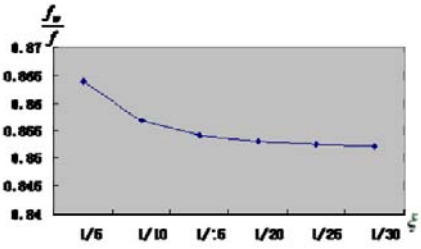


Figure 6.  $f_w / f$  change with  $\xi$  when cylinder with outside fluid

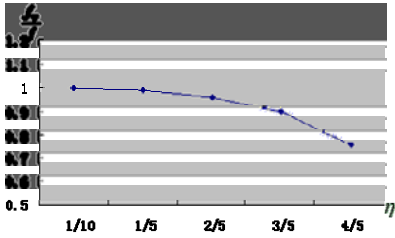


Figure 7.  $f_w/f$  change with  $\eta$  when cylinder with inside fluid and  $\xi = 1/20$

Figure 6 shows that as the ratio of radius to height  $\xi$  decrease, the ratio  $f_w/f$  decrease, too. In other words, the influence of external hydrodynamic pressure on structure increases as the value of  $\xi$  decrease. That is external hydrodynamic pressure has greater influence on nature frequency of slender structure. A cylinder of  $\xi = 1/20$  is analyzed in Figure 7. The value of  $f_w/f$  decrease as the radius ratio increases. Namely the internal hydrodynamic pressure on structure increase when  $\eta$  increase, that is the internal hydrodynamic pressure has great influence on nature frequency of thin-walled structure.

## 5 Conclusions

The nature frequencies of cylinder structure with outside fluid and inside fluid have been calculated and analyzed by numerical method in the paper, and the results have been compared to the theoretical calculation results, it comes to the conclusion that the numerical calculation method in the paper is a simple and accurate way to do structure analyzing, and it is proved that the internal and external hydrodynamic pressure has great influence on nature influence of structure. It cannot be neglected especially to the slender structure and thin-walled structure.

## Acknowledgements

Acknowledge the finance support of 863 Project (2007AA11Z107) of the Chinese Ministry of Science and Technology.

## References

- Cao L. (2004). *Characteristic Analysis of Fluid Structure Interaction in Liquid-filled Pipe*. Kunming University of Technology, 1-10.
- Cheng H.M. (2006). Dynamic analysis of the interaction between the prestressed egg-shaped digester and liquid. *Engineering Mechanics.*, 10.23(10).
- Ju R.C. and Zeng X.Z. (1983). *Coupled Vibration Theory of Elasticity Structure and Fluid*. Earthquake Press.
- Zhang M. (2006). *Vibration Analysis of Solid-Fluid Interaction for the Pier-River Water*. Dalian University of Transportation.

# **MECHANICAL MODELING OF WOOD AND WOOD PRODUCTS**

*“This page left intentionally blank.”*

# A Computational Approach for the Stress Analysis of Dowel-Type Connections under Natural Humidity Conditions

Stefania Fortino<sup>1</sup> and Tomi Toratti<sup>1\*</sup>

<sup>1</sup>VTT Technical Research Centre of Finland, P.O. Box 1000, FIN-02044 VTT, Finland

**Abstract.** In this paper a computational method for evaluating moisture induced stresses in timber connections is proposed. A 3D orthotropic-viscoelastic-mechanosorptive model for wood is implemented in the Umat subroutine of the FEM code Abaqus and a moisture-stress analysis is performed. Some dowel-type connections are computationally analyzed under sustained mechanical loads and natural humidity conditions.

**Keywords:** timber connections, moisture transfer, creep, natural humidity, stress analysis, FEM, Abaqus

## 1 Introduction

The combination of moisture history and mechanical loading is an important topic for the serviceability of timber connections (Sjödin, 2004). In the presence of moisture content changes, the shrinkage can cause relatively high deformations of the wood elements but the stiffness of the steel components makes the connections rigid and may produce high values of the stresses, particularly in the cross grain direction. When wood is extremely dry the risk of cracking on the wood surface is strongly increased, especially if gradients of moisture content occur between the inner part and the outer part of the timber section. In some extreme cases the induced moisture stresses in timber can also induce the collapse of the structure. In (Frühwald et al., 2007), 23% of the studied failure cases in timber structures were due to joint failures and 57% of them were dowel type connections. As one consequence, new failure modes have been introduced in the joint design of Eurocode 5 to account for timber shear block type failure. However, moisture effects in connections are not deeply understood and need to be further investigated (see Miriamon et al., Part 2, 2008).

---

\* Corresponding author, e-mail: tomi.toratti@vtt.fi

The aim of the present research work is to computationally estimate the levels of moisture induced stresses in timber connections and particularly in dowel-type joints which are often used in long span structures. The computational method is based on the three-dimensional orthotropic viscoelastic-mechanosorptive model for wood proposed and analyzed in (Mirianon et al., Part 1, 2008).

In this paper the moisture-stress analysis of a dowel-type connection under natural humidity conditions measured in Finland is carried out. The results show that variations of moisture content in timber connections can significantly increase the stresses in the direction perpendicular to the grain.

### 3 A Three-Dimensional Moisture-Stress Analysis for Timber Structures

At a macroscopic level, wood is described as a continuum and homogeneous material with cylindrical orthotropy. In this paper the orthotropic viscoelastic-mechanosorptive constitutive model proposed in (Mirianon et al., Part 1, 2008) is used. The rheological model is characterized by five deformation mechanisms (see figure 1) and a thermodynamic formulation is used starting from the Helmholtz free energy expressed in function of temperature, moisture content, total strain, viscoelastic strain and recoverable mechanosorptive strain. The used viscoelastic and mechanosorptive models are an extension of earlier 1D formulations for parallel to grain direction and for cross grain direction. These consist of sums of Kelvin type elemental deformations (see references in Mirianon et al., 2008). The mechanosorptive model contains also an irrecoverable part described through a simple dashpot. The extension of the 1D models to 3D is based on three-dimensional elemental viscoelastic and mechanosorptive matrices.

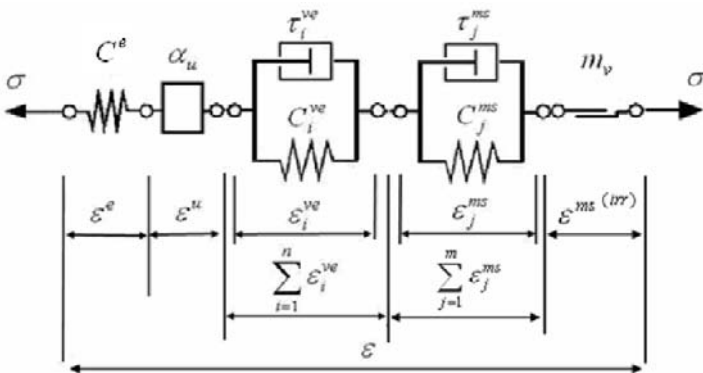


Figure 1. Scheme of the rheological model.  $\tau_i^{ve}$  and  $\tau_j^{ms}$  represent the retardation times of the Kelvin elements,  $\alpha_u$  is the coefficient of hygroexpansion and  $m_v$  the mechanosorptive stiffness.

By integrating the viscoelastic and mechanosorptive creep equations during the time, the following stress increment at the time step  $n+1$  is obtained:

$$\Delta\sigma_{n+1} = C_T \left( \Delta\varepsilon - \Delta\varepsilon_\sigma^e - \Delta\varepsilon^u - \Delta\varepsilon_{n+1}^{ms(irr)} + \sum_{i=1}^p R_i^{ve} + \sum_{j=1}^q R_j^{ms} \right) \quad (1)$$

where  $\varepsilon$  is the total strain,  $\varepsilon_\sigma^e$  the part of the elastic strain depending on the stress state at the beginning of the time increment,  $\varepsilon^u$  the strain due to hygroexpansion,  $\varepsilon_i^{ve}$  the elemental viscoelastic strain,  $\varepsilon_j^{ms}$  the elemental mechanosorptive strain, and  $\varepsilon_j^{ms(irr)}$  the irrecoverable part of the total mechanosorptive strain ( $p$  and  $q$  are the number of viscoelastic and mechanosorptive Kelvin elements, respectively). Furthermore

$$C_T = \left( C^e^{-1} + \sum_{i=1}^p C_{i,n+1}^{ve^{-1}} + \sum_{j=1}^q C_{j,n+1}^{ms^{-1}} \right)^{-1} \quad (2)$$

represents the tangent operator of the full model where  $C^e$  is the elastic operator,  $C_i^{ve}$  the algorithmic viscoelastic tangent operator,  $C_j^{ms}$  the algorithmic mechanosorptive tangent operator,  $R_i^{ve}$  and  $R_j^{ms}$  are functions of stress  $\sigma_n$ , of the elemental viscoelastic strain  $\varepsilon_{i,n}^{ve}$  and of mechanosorptive strain  $\varepsilon_{j,m}^{ms}$  at the previous time step (Mirianon et al., Part 1, 2008).

The moisture transfer is modeled by using the 3D Fick equation and the moisture flow from the air to the surface is given by the following equation proposed by Rosen, Avramidis and Siau (Mirianon et al., 2008):

$$q_n = \rho_0 S (u_{air} - u_{surf}) \quad (3)$$

where  $q_n$  is the flow across the boundary,  $\rho_0$  is the wood density in absolute dry conditions,  $S=3.2 \times \exp(4u)$  m/s is the surface emissivity (being  $u$  the current moisture content). Furthermore  $u_{air}$  represents the equilibrium moisture content of wood corresponding to the air humidity defined as in (Mirianon et al., 2008) and  $u_{surf}$  is the moisture content on the wood surface.

The routine for the viscoelastic-mechanosorptive creep is implemented into the user subroutine UMAT of the Abaqus FEM code while Equation (3) is implemented into the Abaqus user subroutine DFLUX. A coupled moisture-stress gradient analysis is performed by using the Abaqus/Standard program. The constitutive model was compared in (Mirianon et al., 2008) with experimental results of small scale wood specimens and small glulam sections under mechanical loading in both cases of constant and variable humidity conditions. The temperature is not taken into account because its effect in service conditions of buildings is considered to be very small if compared to the moisture content effect.

### 4 Computational Results and Future Work

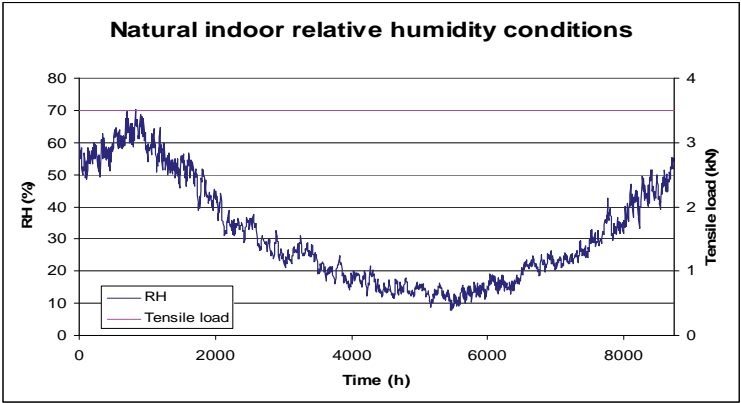


Figure 2. Applied natural indoor relative humidity conditions under constant tensile load.

A simple connection previously analyzed in (Sjödin, 2008) has been studied (figure 3). The connection is loaded with a constant 7kN tensile load ( $F = 3.5\text{kN}$ ) which corresponds to about 25% of the experimental elastic limit of the connection. The relative humidity values used in the calculation are as measured in the Sibelius hall (Finland) under service building conditions during one year (Koponen 2002).

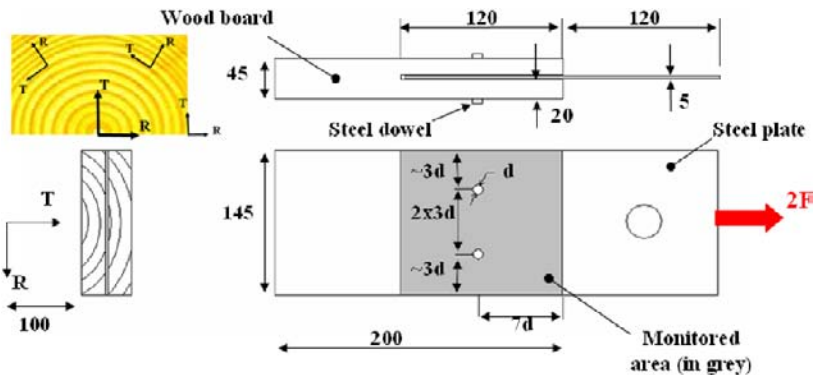


Figure 3. Cylindrical coordinate system (R=radial direction, T=tangential direction) and scheme of the 2-dowel connection (dimensions in mm,  $d = 12\text{mm}$ ).

The measurements of moisture in the “Forest Hall” of the Sibelius hall showed that in a heated room, the relative humidity can be very low. In this case, during the winter time, the indoor average relative humidity is around RH15% while, at

the same time, the outdoor average relative humidity is around RH85%. The initial moisture content of wood was taken as 12%. For the calculations carried out in the present work, the starting of the test corresponds to the beginning of July. Figure 2 shows the natural load case applied to the studied connection. The parameters for *Norway spruce* in the analysis and the other parameters values for creep and moisture diffusion can be found in (Mirianon et al., Part 1, 2008).

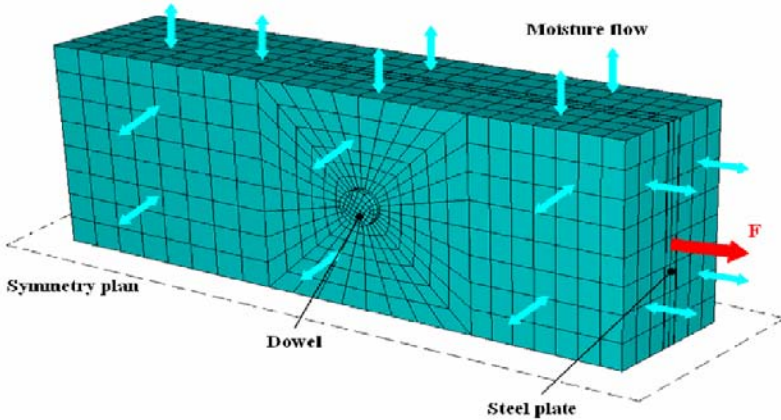


Figure 4. Numerical model of the connection done with ABAQUS CAE. Hexagonal C3D8T elements have been used to mesh the wood part and C3D8 elements for the plate and the dowel.

ABAQUS 6.5-3 has been used for the simulation. The contacts are modelled by using a hard contact pair with a penalty method in the tangential direction and a 0.4 penalty factor. The stress state of the connection at time 5550 hours, which corresponds to an instant in the middle of the winter, is drawn in figure 5. The results show that the stresses perpendicular to grain in points 2 and 4 exceed the characteristic strength levels of glulam beams GL28c (Eurocode 5).

The obtained numerical results suggest that, by using the proposed constitutive model, the stresses perpendicular to grain can exceed the material strength, especially during the winter time, when the buildings are heated and the conditions are dry. This could cause splitting of wood and lead to further failures. For the moment, the proposed computational method has been compared with experimental results on real-scale dowel joints under constant humidity conditions only (Mirianon et al., Part 2, 2008). In order to validate the method for general environmental conditions, further experimental work is required. Because of the lack of experiments on timber connections in presence of variable moisture conditions, the results obtained by using the proposed method could provide some suggestions on the possible experimental tests to be carried out for improving the current knowledge on the subject. There is a need to develop methods on how the humidity environment affects the behavior of the connections, and how this should be con-

sidered in connection design and in detailing in general. Coating for instance might be very beneficial in this respect.

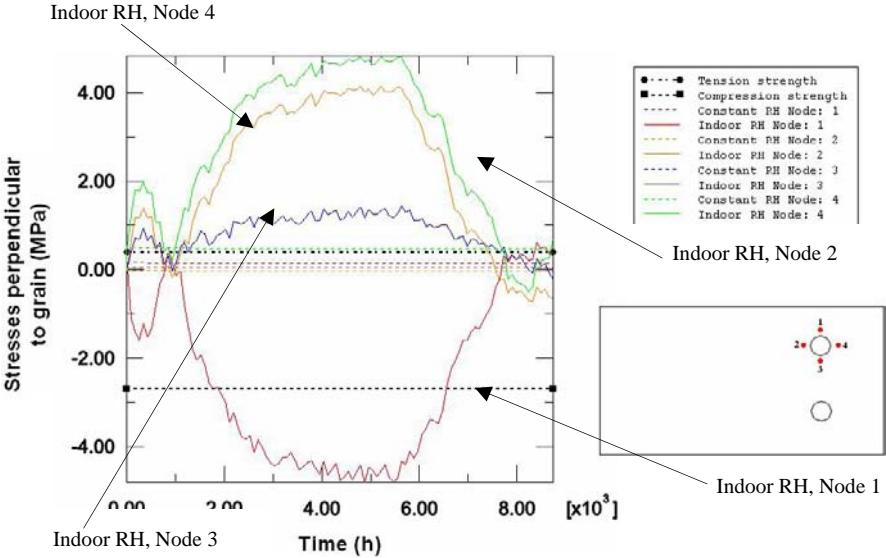


Figure 4. Stresses perpendicular to grain in four points around the dowel. The arrows indicate the stress-time curves in four points around the dowel in the case of indoor conditions.

## References

Abaqus version 6.5 documentation.

Eurocode 5 (2002). Design of timber structures. Part 1-1 General rules and rules for building. Document CEN/TC 250/SC 5: N 195. prEN 1995-1-1. Final draft 2002-10-09.

Frühwald E., Serrano E., Toratti T., A. Emilsson and S. Thelandersson (2007). Design of safe timber structures – How can we learn from structural failures in concrete, steel and timber Report TVBK-3053, Lund Institute of Technology, Lund University.

Koponen S. (2002). Puurakenteiden kosteudenhallinta rakentamisessa. Raportti 1-0502. Teknillinen Korkeakoulu. (In Finnish).

Mirianon F., Fortino S., Toratti T. (2008). A method to model wood by using ABAQUS finite element software. Part 1. Constitutive model and computational details. VTT publication nr. 687.

Mirianon F., Fortino S., Toratti T. (2008). A method to model wood by using ABAQUS finite element software. Part 2. Applications to dowel-type connections. VTT, Espoo. VTT publication nr. 690.

Sjödin J. (2008). Strength and Moisture Aspects of Steel-Timber Dowel Joints in Glulam Structures. An Experimental and Numerical Study. Doctoral Thesis. Växjö University.

# FE-Based Strength Analysis of Penglai Pavilion

Jingsi Huo<sup>1\*</sup>, Biyong Xiao<sup>1</sup>, Hui Qu<sup>2</sup> and Linan Wang<sup>3</sup>

<sup>1</sup>China Ministry of Education Key Laboratory of Building Safety and Energy Efficiency, College of Civil Engineering, Hunan University, Yuelu Mountain, Changsha 410082, China

<sup>2</sup>College of Civil Engineering, Yantai University, Yantai 264005, China

<sup>3</sup>China Academy of Cultural Heritage, Beijing 100029, China

**Abstract.** This paper focuses on a strength analysis of the timber structure of Penglai Pavilion. A finite element model is presented to evaluate the dynamic characteristics and strength of the timber frame structure. Some constructive suggestions are presented to be a basis for strengthening the ancient timber Pavilion.

**Keywords:** finite element, strength analysis, dynamic analysis, timber structure

## 1 Introduction

China is one of the oldest countries in which timber was used in ancient buildings and constructions. Many kinds of timber frame structures had been ever widely used in great Pavilions, temples, common folk houses and multi-storey pavilions. Most existing ancient timber structures were built in Ming and Qing Dynasty. Few ancient timber structures built before Tang Dynasty can be found in China. It had attracted the government and people's attention that most of the existing ancient timber structures are in danger. Penglai Pavilion, one of the important historical structures with conservation required in Mainland, may possibly collapse at any moment because of man-made damage or long-term natural aging and corrosion. The corridors and other parts of the Pavilion are suffering remarkable deformations and distortions. It is very difficult to carry out experimental researches on the mechanical behaviors of traditional historical structures because of scarcity and historical value of ancient timber structures. A finite element method was used to conduct the strength analysis of a typical ancient timber frame structure of Penglai Pavilion in order to provide us a basis to repair and maintain the Pavilion.

---

\* Corresponding author, e-mail: jingsihuo@gmail.com

## 2 Finite Element Modeling

Penglai Pavilion, which was built in Song Dynasty (1061), lies on the top of the Red-brown cliff of Bohai Sea. The Pavilion is a two-storey timber frame structure, a typical beam-lifted structural system, with a Chinese hip-and-gable roof and an ambulatory on the four sides and 16 open columns. The Pavilion is facing southwards, 15-meter high, 14.8 meter by 9.65 meter long for the first storey and 13.5 meter by 8.55 meter long for the second storey. The Chinese traditional timber frame structural system is used as the load-bearing skeleton. The timber frame was assembled and erected by joining the structural components with tenon-and-mortise joints and corbel bracket. No nails or bracing are used in the frame. The exterior-protected construction was built with brick enclosure at the first floor, while the exterior-protected construction was built with wood partition. At the first floor, a *sui-liang-fang* beam, which can be used to reinforce the connection between peripheral column and principal column, was added to the bottom of the *bao-tou* beam.



Figure 1. Penglai Pavilion

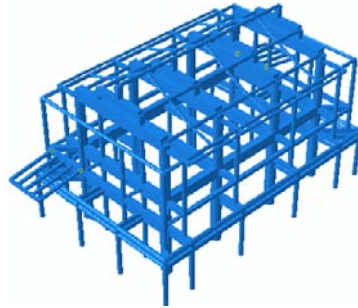


Figure 2. 3D Model of Penglai Pavilion

The Pavilion's main body frame except the corbel brackets under the eaves purlins at the sub-step at the first floor was built with timber columns, beams and girders. The Penglai Pavilion's 3-D finite element structural model, as shown in Figure 2, was constructed using beam elements according to the structural characteristics. Because the corbel brackets under the eaves purlins are used to transfer the load from eaves purlins to the decorated tie-beams, they are modeled as beam elements to simulate the supporting function.

### 2.1 Material Properties

Wood is characterized by a particularly significant anisotropy of physical and mechanical properties. The wood strength along the grain is the highest strength val-

ue, and that perpendicular to the grain is the lowest one among the mechanical strength indexes. Compared with new wood, the mechanical behaviors of old wood of ancient structures present variability to some degree. An anisotropic material model “Engineering Constant” (ABAQUS, 2006) was adopted in the FE model to simulate the mechanical properties of wood. The timber was approved to be Northeast Korean pine. Some wooden specimens were cut from a northwest principal column and a cantilevered corner beam and made into some clear wood samples which were tested to determine the mechanical behaviors of the Pavilion’s timber. The wood density is  $0.42\text{g/cm}^3$ , the modulus of elasticity, Poisson’s ratio and strength parameters are shown in Table 1.

Table 1. Material Properties of wood

$E_1$ (MPa)	$E_2$ (MPa)	$E_3$ (MPa)	$\nu_{12}$	$\nu_{13}$	$\nu_{23}$	$G_{12}$ (MPa)	$G_{13}$ (MPa)	$G_{23}$ (MPa)
7532	314	566	0.0	0.3	0.03	275	650	210
			2		5			

## 2.2 Tenon and Mortise Joint

The beam-column joints typically used in the timber frame structure of Penglai Pavilion are tenon and mortise joints (plug-slot type connection), which are composed of the tenons and the mortises. The tenon joint has a relatively excellent flexibility and a good resistance to horizontal force. The tenon joints can be regarded as semi-rigid connections (Dong et al., 2006). Horizontal forces or actions, such as wind load and earthquake action, can result in horizontal slipping movement and rotation between tenon component and mortise component. The friction between tenon component and mortise component can absorb some earthquake energy and alleviate the structural response.

Based on the mechanical behaviors of the tenon joints, a coupling joint element “Slide-Plane-Rotation: CONN3D2” (ABAQUS, 2006) was used to tie the beams and columns. The 3D 2-node semi-rigid connector element is suggested to simulate the behavior of tenon joints and the connection joint has neither mass nor dimension. To obtain the equivalent stiffness parameters of CONN3D2 without high accuracy, it was assumed that all six degrees of freedom are uncoupled. Accordingly, the beams and columns will have a relative motion depended on the equivalent stiffness parameters.

As shown in Figure 3, connection type Slide-plane keeps node  $b$  on a plane defined by the orientation of node  $a$  and the initial position of node  $b$ . The normal direction distance from node  $a$  to the plane is constant. The orientation 2 of global coordinate is specified as the normal direction which coincides with the axes of



Fang et al. (2001), the following parameters were introduced into the FE model:  $k_y = k_z = 2 \times 10^9 \text{ N} \cdot \text{m}$ ,  $k_{\theta_x} = k_{\theta_y} = k_{\theta_z} = 90000 \text{ N} \cdot \text{m}/\text{rad}$ .

### 2.3 Selection of Finite Element's Type

A 3D 2-node linear beam element (B31) was adopted to model the structural beams and columns. Timoshenko beams (B31) allow for transverse shear deformation. It can be used for thick as well as slender beams. The cross-sectional dimensions can be defined by specifying geometric data in Profile tool in ABAQUS. For the beam section selected in ABAQUS will calculate the transverse shear stiffness values required in the element formulation.

### 2.4 Boundary Conditions

The timber frame columns are placed on the mirror surfaces of plinth stones. The plinth stone, which is mainly in compression and little in tension and bending, is used to support the column and supply some horizontal friction force. Therefore, it is generally thought that the columns are simply supported by plinth stones and the connections between column and plinth stone are regarded as hinged (Fang et al. 2001). As the roof has been proven to be rigid, its stiffness can be enlarged by adding diagonal elements in the roof to turn into a three triangular trusses in the roof so that the roof can provide the structure with great lateral force resistance. The wood slabs are flexible and loosely connected with beams and their stiffness effects were ignored in the computational model. Considering the fact that the timber columns on the first floor, which are embedded in the enclosure wall, are laterally supported by the wall to a certain degree, four beams similar to a kind of structural member *Fang* were added into the FE model to take the wall's lateral resistant effect into consideration.

## 3. FE Analysis Results

### 3.1 Dynamic Characteristics of Penglai Pavilion

With the above equivalent stiffness parameters integrated into the stiffness matrix of the FE model and the most unfavorable manner for analysis determined, the first four natural frequencies of the Penglai Pavilion structure were computed us-

ing ABAQUS program. They were 0.679, 1.543, 3.297 and 4.515 Hz, respectively. The vibration configurations of the first four modes are shown in Figure 3. The first mode is lateral vibration, the second and third modes are torsion vibrations, and the fourth mode is the combination of vertical vibration and torsion vibration.

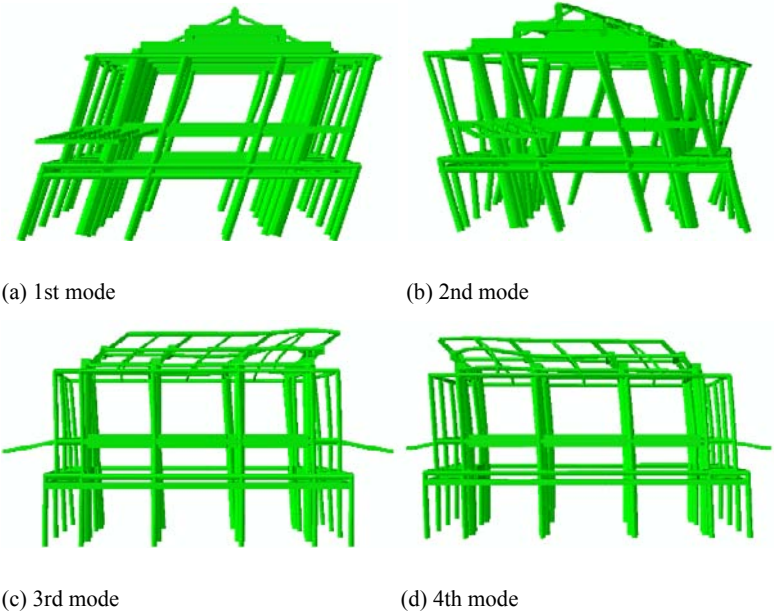


Figure 3. First four modes of Penglai Pavilion

### 3.2 Strength Analysis

In FE-based strength analysis, load combinations are considered according to the Chinese Loading Code. Load combinations related to the roof, floor and main structural components' weight, wind, snow and visitors are the main loads for the structure, which were applied in the most unfavorable manner for analysis. The mass of roof and slabs are distributed to adjacent members, and a concentrated mass method is adopted to obtain the mass matrix. The live load (the visitors) was distributed on different parts, including the hall at the second floor and eaves gallery. Design loads as follows:

Table 2. Summary of strength analysis

No.	Maximum deflection (mm)	Position of maximum deflection	Maximum stress (MPa)	Stress ratio (%)			Position of maximum stress
				Cantilevered corner beam at lower eaves	Northwest principal column	Non-labeled material	
1	25.52	Centre girder	6.72	14.5	19.8	25.94	Centre girder, intersection of second floor <i>bao-tou</i> beam and peripheral column
2	19.28	Centre girder	41.02	87.8	90.1	118	ground floor <i>sui-liang-fang</i> and top of second floor principal column
3	19.36	Centre girder	41.76	89.4	91.8	120	ground floor <i>sui-liang-fang</i> and top of second floor principal column
4	19.42	Centre girder	42.24	90.4	92.8	121	ground floor <i>sui-liang-fang</i> and top of second floor principal column
No.	Maximum deflection (mm)	Position of maximum deflection	Maximum stress (MPa)	Stress ratio (%)			Position of maximum stress
				Cantilevered corner beam at lower eaves	Northwest principal column	Non-labeled material	
5	13.23	Central part of eaves purlin	42.14	90.2	92.6	121	ground floor <i>sui-liang-fang</i> and top of second floor principal column
6	9.21	Central part of eaves purlin	6.235	13.4	18.3	23.97	intersection of second floor <i>bao-tou</i> beam and peripheral column
7	12	Central part of purlins	41.4	88.6	91.0	119	ground floor <i>sui-liang-fang</i> and top of second floor principal column
8	13.23	Central part of eaves purlin	42.14	90.2	92.6	121	ground floor <i>sui-liang-fang</i> and top of second floor principal
9	13.49	Central part of eaves purlin	42.24	90.4	92.8	121	ground floor <i>sui-liang-fang</i> and top of second floor principal column
10	13.25	Central part of eaves purlin	42.28	90.5	92.9	122	ground floor <i>sui-liang-fang</i> and top of second floor principal column

1. *Roof weight.* The traditional hip-and-gable roof was built with nine ridges and six kinds of decorative tiles. The dead load of tile is  $191.8\text{kg/m}^2$ , and that of the rafter  $45\text{kg/m}^2$ .
2. *Floor and wall weight.* The line load of brick wall and floor are  $12.4\text{kN/m}$ , and the eave load of floor  $1\text{kN/m}^2$ .
3. *Wind.* The wind load is determined according to the design wind load specified by the Chinese Loading Code.
4. *Live load.* The live load is 70 visitors ( $70\text{kg}$  per person) determined by site survey.

According to different distributions of visitors, static analysis on ten cases was computed by using the FE model. The stress and displacement analyses were made and the theoretical results are shown in Table 2.

## 4 Discussion and Conclusion

The structure would not suffer such significant deflections in the ten selected cases that generally it can be thought safe. When it subjects to great wind or heavy snow, the principal columns on the second floor and the secondary beams on the first floor would have little emergency capacity, while the other structural members would be relatively safe.

It can be concluded from the comparisons between the timber beam's maximum stress of  $40\text{MPa}$  under wind loading and that less than  $7\text{MPa}$  without considering wind load that wind load has significant effect on structure's safety. It can be concluded from the stress ratio that the *bao-tou* beam, *sui-liang-fang* beam and eaves purlin are the building's weak part, which needs reinforcement.

The first mode is lateral vibration, the second and third modes are torsion vibrations. The ratio of the first two mode's frequencies is 0.44.

The parameter values used in the FE model was based on the sampling check and completed works on Chinese ancient timber architecture. The deformation and stress in floor gallery wasn't strong in the FE mode, which doesn't coincide with obvious deformation appeared in floor gallery of the Penglai Pavilion, and without considering the damage of the wood in the FE mode maybe give an explanation for that.

## References

- ABAQUS (2006). ABAQUS 6.5, Theory manual and users Manual. Pawtucket USA: HKS-Hibbitt, Karlsson & Sorensen Inc.

- Dong Y.P., Zhu R.X., Yu M.H., Yu R.L. (2003). Study on the north inclination of the main hall of Ningbo Baoguo Temple. *Sciences of Conservation and Archaeology*, 15(4): 1-5 [in Chinese].
- Fang D.P., Iwasaki S., Yu M.H., Shen Q.P., Miyamoto Y. and Hikosaka H. (2001). Ancient Chinese timber architecture. II: Dynamic characteristics. *Journal of Structural Engineering*, 127(11): 1358-1364.
- Fang D.P., Yu M.H., Miyamoto Y., Iwasaki S. and Hikosaka H. (2001). Numerical analysis on structural characteristics of ancient timber architectures. *Engineering Mechanics*, 17(2): 137-144 [in Chinese].
- Yao K., Zhao H.T., Ge H.P. (2006). Experimental studies on the characteristic of mortise-tenon joint in historic timber buildings. *Engineering Mechanics*, 23(10): 168-173 [in Chinese].

*“This page left intentionally blank.”*

# Transient Simulation of Coupled Heat, Moisture and Air Distribution in Wood during Drying

Zhenggang Zhu<sup>1\*</sup> and Michael Kaliske<sup>1</sup>

<sup>1</sup>Institute for Structural Analysis, Technische Universität Dresden, D-01062 Dresden, Germany

**Abstract.** An approach to the numerical simulation of wood drying based on the finite element method is presented. Wood, as a hygroscopic, strongly anisotropic porous material, must be dried before being used for a practical purpose. Wood drying leads to a combination of vapor, bound water, and free water movement. A numerical simulation of the drying process of wood involves three fundamental phenomena: heat transfer, movement of moisture, and mechanical deformation. Liquid flow due to capillarity, water vapor and air (diffusing and convection in bulk gas flow), and bound liquid diffusion are basic mechanisms of mass transfer in wood. The aim of the paper is to present a numerical model of coupled heat, moisture and air transfer in pores of wood subjected to high temperature drying conditions. Heat and moisture exchange take place between wood and drying medium, and coupled problems can be described from a macroscopic viewpoint of continuum mechanics. Benchmark tests of a 3-D model under Dirichlet and mixed type of boundary conditions are used to account for the coupling among temperature, moisture content and gas pressure.

**Keywords:** wood drying, numerical simulation, moisture diffusion, coupling

## 1 Introduction

As a highly ecological material, wood has been used widely as building material for a long time. Before being employed in a practical purpose, wood needs to be dried. Mass transfer in wood during drying is governed by various processes. Wood drying is a combination of vapor, bound water, and free water movement (Fyhr and Rasmuson, 1997, Simpson and Liu, 1997). Adsorption of water vapor onto the cell wall constituents attributes to its hygroscopicity (Wadso, 1994). The cells communicate via small openings (pits) in the cell walls (Turner, 1996). The degree of the pits' aspiration governs permeability to liquid flow which becomes very low once pits are aspirated (Pang, 1996).

---

\* Corresponding author, e-mail: zhenggang.zhu@mailbox.tu-dresden.de

The Luikov model of coupled heat and mass transfer is commonly adopted. Following Luikov's approach (Kocafe et al., 2006, Turner, 1996, Younsi et al., 2006), the ratio of vapor diffusion to total moisture transfer of red pine sapwood drying is determined experimentally (Tremblay et al., 1999). Heat transfer takes place due to conduction (Fourier law), phase change and moisture transfer (Dufour effect). Similarly, mass transfer is governed by diffusion (Fick's law), temperature gradient (Soret effect), convective flow and flux of air due to a convective flow driven by the gradient of gas pressure. However, the theory based on a coupled Luikov model and air transfer are rarely used modeling the thermal treatment of wood at high temperature using variable thermo-hygro-physical properties. In this paper, a coupled Luikov model and air transfer are applied to simulate heat, moisture and pressure in wood subjected to high temperature.

## 2 Mathematical Models

During wood drying, heat, moisture and air transfer affect each other. Heat flux due to the gradient of moisture content (Dufour effect) is usually neglected though Soret effect (moisture flow due to thermal gradient) plays an important role in mass transfer of moisture content. Convective flow of air, governed by the gradient of pressure, also contributes to mass transfer.

### 2.1 Assumptions

The presented modeling of coupled heat and moisture transfer is based on the following assumptions:

1. Mass of vapor, compared to that of liquid water, is negligible.
2. Dufour effect is ignored.
3. Temperature, moisture content and pressure of the liquid, vapor and the dry body are equal at coincident points.
4. Chemical reactions associated with water loss are not taken into account.
5. Dimensional changes in wood are infinitesimally small.
6. Diffusional flow of air in vapor is neglected.

### 2.2 Governing Equations

Three unknowns (temperature, moisture content, and gaseous pressure) are selected as basic degrees of freedom of the finite element model of heat, moisture

and air transfer of wood drying. Both, heat conduction and enthalpy change of water from liquid to gas, contribute to the energy balance

$$\rho C \frac{\partial T}{\partial t} = -\nabla \cdot (-\lambda \nabla T) + \varepsilon \Delta H_v a_m \rho \nabla \cdot (\nabla X + \delta \nabla T) \quad (1)$$

where  $\rho$  is density,  $C$  heat capacity,  $\lambda$  heat conductivity,  $\varepsilon$  ratio of diffusion coefficient of vapor to that of total moisture,  $\Delta H_v$  enthalpy of phase change,  $a_m$  diffusion coefficient of moisture,  $X$  moisture content,  $\delta$  coefficient of Soret effect and  $\nabla$  gradient operator.

The Soret effect, namely mass transfer caused by thermal gradient, is considered. Mass balance of both liquid water and vapor can be described by

$$\frac{\partial X}{\partial t} = \nabla \cdot a_m (\nabla X + \delta \nabla T). \quad (2)$$

The air flow in the pores of solid structure is given by

$$\frac{\partial m_a}{\partial t} = -\nabla \cdot \left( -m_a \frac{KK_g}{\mu_g} \nabla P_g \right) \quad (3)$$

where  $K$  is permeability,  $K_g$  relative permeability,  $\mu_g$  viscosity, and  $P_g$  pressure.

Both, equation (1) and equation (2), can be rearranged respectively to

$$C_{11} \frac{\partial T}{\partial t} = \nabla \cdot (K_{11} \nabla T + K_{12} \nabla X); \quad C_{22} \frac{\partial X}{\partial t} = \nabla \cdot (K_{21} \nabla T + K_{22} \nabla X). \quad (4)$$

Mass of the air, according to the ideal gas law and the Dalton's law of partial pressure, is a function of four unknowns, namely the temperature, the volume (related to the moisture content), the gaseous pressure and the vapor pressure, which cannot be solved by three equations (equation (1), equation (2), and equation (3)). However, the vapor pressure, derived from the sorption isotherm, is a function of the temperature and the moisture content. Therefore, mass balance of the air (equation (3)) can be simplified as

$$C_{31} \frac{\partial T}{\partial t} + C_{32} \frac{\partial X}{\partial t} + C_{33} \frac{\partial P_g}{\partial t} = \nabla \cdot (K_{33} \nabla P_g). \quad (5)$$

The model of coupled heat, moisture and air transfer (equation (4), and equation (5)) can be solved with the finite element method for the geometry and the fi-

nite difference method in the time scale. A backward finite difference method is selected to discretize the time dimension due to its unconditionally stable feature.

### 2.4 Initial and Boundary Conditions

In the subsequent considerations, initial conditions of temperature and moisture content are set to 25°C and 22%, respectively. Gas pressure is initially atmospheric and kept constant. For Neumann type boundary conditions, the normal gradient of the pressure on the surface is zero.

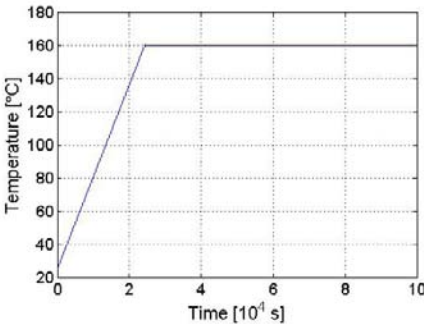


Figure 1. Environmental temperature

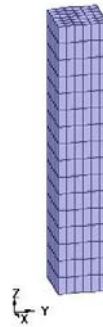


Figure 2. 3-D discretization

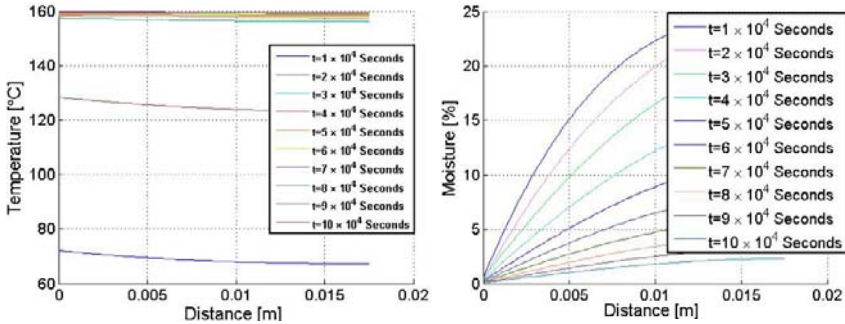
## 3 Results

A 3-D model of coupled heat and moisture transfer with anisotropic physical coefficients of wood with the size of  $0.0175\text{m} \times 0.025\text{m} \times 0.1\text{m}$  (figure 2) is simulated. The left, front and upper side are set as Neumann type boundary conditions for heat and moisture transfer, though air pressure is kept constant and set by Dirichlet boundary conditions. The other surfaces are planes of symmetry, where heat and moisture flow are zero.

The model is strongly nonlinear due to anisotropic, nonlinear physical properties, such as heat conductivity, heat capacity, diffusion coefficient of moisture or moisture conductivity, and thermo-gradient coefficient of Soret effect, dependent on temperature and moisture content.

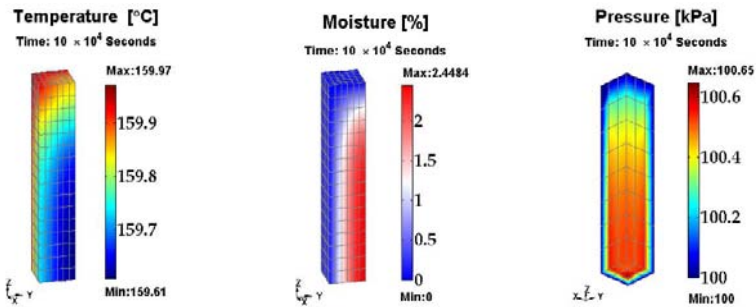
The time history of temperature and moisture (figure 3) on the boundary ( $x = 0.0175\text{m}$ ) show that the temperature decreases from the surface towards the centre. Moisture content decreases from the centre towards the surface. All of these

trends are in very good agreement with the experimental observations of (Kocaefe et al. 2006). Contour plots of both temperature (figure 4) and moisture (figure 5) show that wood is totally dried after  $10^5$  seconds.



(a) Temperature (b) Moisture content

Figure 3. Time history along central line of specimen



(a) Temperature (b) Moisture content (c) Pressure

Figure 4. Contour plots of the degrees of freedom

The mesh of the model is refined doubly in order to determine the influence of mesh size on the final results. Only a slight difference is found compared to those of the coarse mesh. Therefore, a refined mesh is not required, time-consuming and even may cause numerical problems due to the ill-conditioned Jacobian matrix. The gradient of the total pressure of the gaseous phase (figure 4(c)) is small due to the boundary conditions of pressure set to be atmospheric. However, an overpressure is observed. The Dirichlet boundary condition prevents the pressure from increasing in the vicinity of the exchange faces.

## 4 Conclusions

A 3-D model of heat, moisture, and air flow in wood during drying is developed. Temperature, gas pressure, and moisture of wood subjected to high temperature are numerically simulated. The benchmark test of a 3-D model shows that the approach simulates the distribution of temperature, moisture content and pressure successfully. Numerical results are in good agreement with the findings of (Kocaeffe et al., 2006). The model presented in this paper can be used as a reliable and useful numerical tool to analyze a wide range of engineering situations dealing with heat and moisture transfer in porous media.

The successful simulation of numerical models depends on the selected physical coefficients. The model may fail and the numerical process will be not convergent if some decisive parameters, such as sorption isotherm used in the model, cause a badly conditioned stiffness matrix.

Modeling of coupled heat, moisture, air movement and mechanics are challenging. Further research work needs to be done to investigate the mutual effect of heat, moisture, air in combination with the mechanical characterization.

## Acknowledgements

The authors gratefully acknowledge the financial support of the German Academic Exchange Service (DAAD).

## References

- Fyhr C., Rasmuson A. (1997). Some aspects of the modelling of wood chips drying in superheated steam. *International Journal of Heat and Mass Transfer*, 40(12), 2825–2842.
- Kocaeffe D., Younsi R., Chaudry B., Kocaeffe Y. (2006). Modeling of heat and mass transfer during high temperature treatment of aspen. *Wood Science and Technology*, 40, 371–391.
- Pang S. (1996). Moisture content gradient in a softwood board during drying: Simulation from a 2-d model and measurement. *Wood Science and Technology*, 30, 165–178.
- Simpson W. T., Liu J. Y. (1997). An optimization technique to determine red oak surface and internal moisture transfer coefficients during drying. *Wood Fiber Sci.*, 29(4), 312–318.
- Thomas H. R., Morgan K., Lewis R. W. (1980). A fully nonlinear analysis of heat and mass transfer problems in porous bodies. *International Journal for Numerical Methods in Engineering*, 15, 1381–1393.
- Tremblay C., Cloutier A., Grandjean B. (1999). Experimental determination of the ratio of vapor diffusion to the total water movement in wood during drying. *Wood Fiber Sci.*, 31(3), 235–248.
- Turner I. W. (1996). A two-dimensional orthotropic model for simulating wood drying processes. *Applied Mathematical Modelling*, 20(1), 60–81.
- Wadso L. (1994). Describing non-fickian water-vapour sorption in wood. *Journal of Materials Science*, 29, 2367–2372.
- Younsi R., Kocaeffe D., Kocaeffe Y. (2006). Three-dimensional simulation of heat and moisture transfer in wood. *Applied Thermal Engineering*, 26, 1274–1285.

# Three-Dimensional Numerical Analysis of Dowel-Type Connections in Timber Engineering

Michael Kaliske<sup>1\*</sup> and Eckart Resch<sup>1</sup>

<sup>1</sup>Institute for Structural Analysis, Technische Universität Dresden, D-01062 Dresden, Germany

**Abstract.** Dowel-type connections of wood are characterized by a complex load-bearing behavior and failure mechanism. For prediction and understanding of this behavior, numerical simulations of double shear dowel-type connections are introduced. The failure of the wood components and the steel fasteners are modeled and appropriate material formulations are introduced. The analysis of the numerical calculation and verification shows the suitability of the model to predicting the load-carrying capacity and the failure mechanism.

**Keywords:** Dowel-type connection, wood failure, material modeling

## 1 Motivation

In timber engineering, dowel-type connections are a significant part of many constructions. Experiments determining the load-carrying capacity of dowel-type connections show a complex load bearing behavior. Regarding the load transfer, dowel-type connections are characterized by the interaction of the fasteners, different failure mechanisms – with specifications ranging from ductile to brittle – as well as a large numbers of influencing factors. Experiments yield an important contribution to understanding the load bearing behavior. At the same time, the results of these investigations and the information obtained are limited due to the uncertainty of wood properties and boundary conditions.

Therefore, it is of importance to carry out additional numerical analyses of the load bearing behavior of dowel-connections. In comparison to the experiment, the advantage of the analyses is the potential to investigate or to exclude the influence of the uncertainty of different factors (scattering wood properties, wood inhomogeneities, and geometry imprecision). Furthermore, numerical experiments allow to conduct a broader spectrum of experiments at lower costs.

In comparison to two-dimensional formulations, three-dimensional numerical approaches consider the stress field realistically (Patton-Mallory et al., 1997) and

---

\* Corresponding author, e-mail: michael.kaliske@tu-dresden.de

do not overestimate the load-carrying capacity (Ju and Rowlands, 2001). However, only a few numerical 3D-studies have been carried out to analyze the behavior of dowel-type connections (Ju and Rowlands, 2001; Patton-Mallory et al., 1997; Santos et al., 2009). None of these approaches takes into consideration softening material behavior and the interaction of the fasteners, the structure failure cannot be simulated.

The aim of the numerical model introduced here is the realistic 3D-simulation of a double shear multiple dowel-type connection of wood including the post-failure domain. The required steps for constitutive modeling of wood and aspects of the generation of the FE-model are outlined.

## 2 Constitutive Modeling

To simulate the mechanical behavior of wood of Norway Spruce realistically, material models regarding elasticity, ductile failure and brittle failure are introduced. All these formulations are using the cylindrical definition of material directions of wood. For further information about transferring stem and growth information to the definition of the cylindrical coordinate system see Resch and Kaliske (2005).

### 2.1 Elasticity

The cylindrical anisotropic elastic behavior of wood bases on the standard strain-energy-density function

$$\Psi = \frac{1}{2} \underline{\underline{\varepsilon}} : \underline{\underline{C}} : \underline{\underline{\varepsilon}}, \tag{1}$$

defines the elasticity tensor

$$\underline{\underline{C}}^{-1} = \begin{bmatrix} \frac{1}{E_r} & -\frac{\nu_{rt}}{E_t} & -\frac{\nu_{rl}}{E_l} & 0 & 0 & 0 \\ -\frac{\nu_{rt}}{E_t} & \frac{1}{E_t} & -\frac{\nu_{tl}}{E_l} & 0 & 0 & 0 \\ -\frac{\nu_{rl}}{E_l} & -\frac{\nu_{tl}}{E_l} & \frac{1}{E_l} & 0 & 0 & 0 \\ 0 & 0 & 0 & \frac{1}{G_{rt}} & 0 & 0 \\ 0 & 0 & 0 & 0 & \frac{1}{G_{tl}} & 0 \\ 0 & 0 & 0 & 0 & 0 & \frac{1}{G_{rl}} \end{bmatrix} \tag{2}$$

including the Young’s moduli  $E_r, E_t, E_l$ , the shear moduli  $G_{rt}, G_{tl}, G_{rl}$  and the Poisson’s ratios  $\nu_{rt}, \nu_{tl}, \nu_{rl}$ . The indices ( $r$  - radial;  $t$  - tangential;  $l$  - longitudinal) represent the cylindrical material directions of wood. With the relation  $E_i/E_j = \nu_{ji}/\nu_{ij}$ , the stress tensor

$$\underline{\sigma} = \underline{C} : \underline{\varepsilon} \quad (3)$$

is determined.

## 2.2 Ductile Failure

To simulate the ductile behavior of wood under compression loading, a multi-surface plasticity model with a  $C_I$ -continuous yield condition ( $C_I$ -MSP) is developed. In order to provide a robust path-following procedure, the  $C_I$ -MSP model takes into consideration pressure failure exclusively in combination with hardening for post-failure. The softening behavior and the brittle failure due to shear and tension perpendicular to fibre will be simulated using cohesive elements (see Section 2.3). The  $C_I$ -MSP model is developed for continuum-elements and requires only engineering parameters without using any shape-parameters depending on the wood species.

**Yield condition.** The  $C_I$ -MSP model defines an elastic and a plastic domain in the stress space. The bounding surface between these domains is described by the yield condition

$$f = \underline{\sigma} : \underline{b} : \underline{\sigma} + q - 1 \leq 0, \quad (4)$$

which bases on the TSAI/WU-failure criterion . There, the strength tensor

$$\underline{b} = \underline{b}_s \otimes \underline{b}_f \quad (5)$$

is assembled by the factor

$$\underline{b}_s = \frac{1}{2} \cdot \underline{1} - \frac{1}{2} \cdot \text{sign}(\underline{\sigma}), \quad (6)$$

which stands for the quadrant of stress space, for which the yield condition has to be defined depending on the stress state, and the factor

$$\underline{b}_f = \begin{bmatrix} \frac{1}{f_{G'}^2} & 0 & 0 \\ 0 & \frac{1}{f_{G'}^2} & 0 \\ 0 & 0 & \frac{1}{f_{G'}^2} \end{bmatrix}, \quad (7)$$

which contains the strength information. To achieve the  $C_I$ -continuous yield criterion, the condition

$$\frac{df}{d\sigma_i}(\sigma_i = 0) = 0 \tag{8}$$

has to be fulfilled. For this, the linear term of the TSAI/WU-failure criterion is neglected in Equation (4). The hardening behavior in post-failure is defined by the function  $q(\alpha)$ . With the conditions  $q(0) = 0$  and  $dq/d\alpha \leq 0$  softening is excluded. Figure 1 shows the yield surface of the  $C_I$ -MSP model. The light-grey face presents the combination of all three pressure failure modes, the middle-grey faces the combination of two modes and the dark-grey faces only one failure mode. All surfaces are coupled  $C_I$ -continuously.

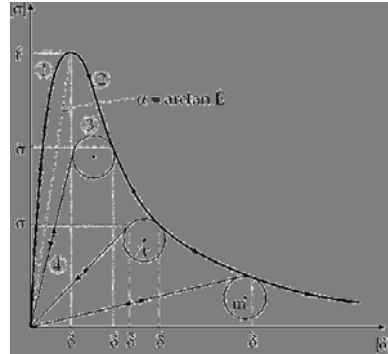
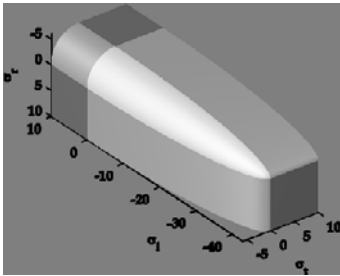


Figure 1. Yield condition for  $f_{cr} = f_{ct} = 6 \text{ N/mm}^2$ ,  $f_{cl} = 43 \text{ N/mm}^2$  and  $q = 0$  in intervals  $\sigma_r = \sigma_t = [6;10] \text{ N/mm}^2$  and  $\sigma_l = [43;10] \text{ N/mm}^2$

Figure 2. Stress-displacement relationship of the coupled interface-material model with status 1 to 4

### 2.3 Brittle Failure

Wood shows brittle failure behavior due to shear loading or tension loading perpendicular to fibres. Therefore, so-called cohesive elements as well as a suitable material model are developed. These types of elements allow an appropriate modelling of the fracture surface resulting from cracking.

To simulate brittle failure of wood and aligned to the interface-element formulation, a coupled material-model is introduced. Basically, this model is characterized by a stress-deformation-relation. Using the input parameters, the stress-deformation function (see figure 2) is composed of a sinusoidal function in the elastic range (status 1) and the function, which describes the softening behaviour in the damage area status 2). In case of unloading after softening or hardening, the path is defined by a spherical surface (status 3) and linear function to the starting point (status 4). The material formulation can be continuously differentiated in the domain of definition due to the fact that all transitions are  $C_I$ -continuous. The ma-

terial formulation takes into consideration the anisotropy and, therefore, the not coaxial orientation of the displacement and stress-vector. For further information about the material law and its numerical implementation see Schmidt and Kaliske (2007, 2009).

## 2 Numerical Simulation

The FE-model developed here represents a double shear dowel-type connection with unstaggered fasteners. With the assumptions of a symmetric loading and a fibre orientation parallel to the loading direction, two planes of symmetry are defined (see figure 3). To limit the size of the FE-model, further divisions into parts are carried out. With the assumption that part C shows nearly the same behavior as part B, two parts (A and B) will be discretized and simulated. These components are defined by the symmetric boundary conditions and suitable element and material formulations. The  $C_I$ -MSP model is used in the area around the fasteners for simulating ductile failure of wood. The interface-elements are located in two planes (see figure 3) to take into consideration the shear and tension failure. The fasteners are modelled using VON MISES-plasticity. The wood-steel contact is defined by BEZIER-contact-elements.

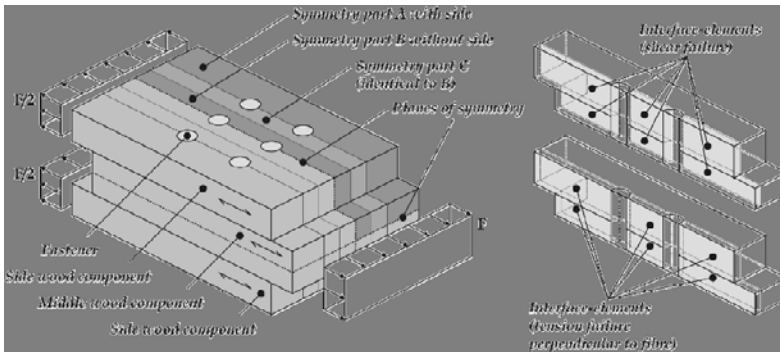


Figure 3. Geometry of double-shear multiple dowel-type connection – planes of symmetry, definition of parts, assembly of interface-elements

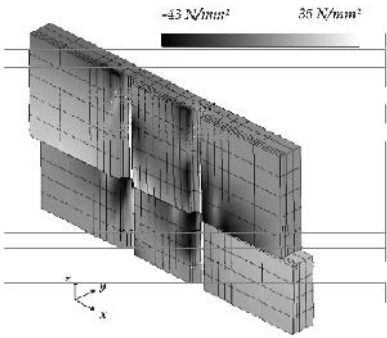


Figure 4. Distribution of stress in the direction of fibres for the wood components

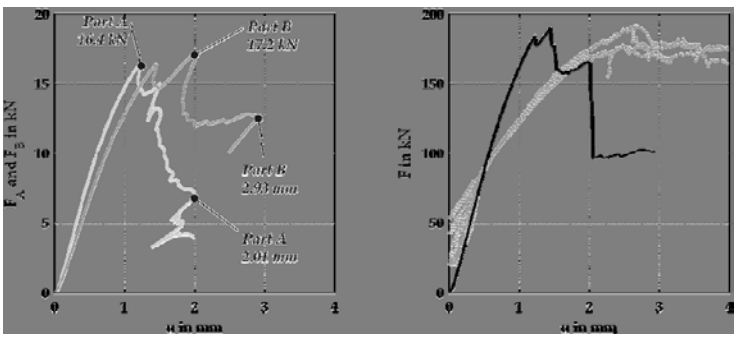


Figure 5. Force-displacement-dependency of part A and B (left) and comparison of the global numerical force-displacement-dependency (black) to Ehlbeck and Werner (1989) (right)

The verification has been carried out by comparing test results of Ehlbeck and Werner (1989) with the numerical simulation. On the left hand side, figure 5 shows the force-displacement-dependency of the numerical model for part A and B. The geometrical boundary conditions are selected from the tests. By adding the results  $4 \cdot F_A + 8 \cdot F_B = F$  analogously to figure 3, the force-displacement-dependency of the multiple dowel-type connection is determined (see figure 5). In comparison to the test, the load-bearing capacity is predicted precisely as well as the failure mechanism. The stiffness of the numerical model is nearly identical to the path under reloading, but differs for first loading. Finally, figure 4 shows the 3D distribution of stress in the direction of fibres for maximum loading of part B.

## References

- Ehlbeck J., Werner H. (1989). Tragverhalten von Stabdübeln in Brettschichtholz und Vollholz verschiedener Holzarten bei unterschiedlichen Risslinienanordnungen [Load bearing behavior of wooden dowel-type connections considering different crack-line-configurations]. Forschungsbericht T2145, IRB-Verlag, Stuttgart.
- Ju S.H., Rowlands R.E. (2001). A three-dimensional frictional stress analysis of double-shear bolted wood joints. *Wood and Fiber Science* 33, 550–563.
- Patton-Mallory M., Cramer S.M., Smith F.W., Pellicane P.J. (1997). Nonlinear material models for analysis of bolted wood connections. *Journal of Structural Engineering* 123, 1063–1070
- Resch E., Kaliske M. (2005). Bestimmung des Faserverlaufs bei Fichtenholz [Determination of the fibre orientation for Norway Spruce]. *LACER* 10, 117–130.
- Santos C.L., Jesus A.M.P., Morais J.J.L., Lousada J.L.P.C. (2009). Quasi-static mechanical behaviour of a double-shear single dowel wood connection. *Construction and Building Materials* 23, 171–182.
- Schmidt J., Kaliske M. (2007). Simulation of cracks in wood using a coupled material model for interface elements. *Holzforschung* 61, 382–389.
- Schmidt J., Kaliske M. (2009). Models for numerical failure analysis of wooden structures. *Engineering Structures* 31, 517–579.

*“This page left intentionally blank.”*

# Aseismic Character of Chinese Ancient Buildings by Pushover Analysis

Qian Zhou<sup>1,2\*</sup> and Weiming Yan<sup>1</sup>

<sup>1</sup>Beijing University of Technology, Beijing 100022, China

<sup>2</sup>Imperial Palace Museum, Beijing 100009, China

**Abstract.** In order to protect Chinese ancient buildings, Shen-Wu Gate in the Forbidden City is taken as an example to study its aseismic character under 8-degree of seldomly occurred earthquake by pushover analysis. Based on constitution of tenon-mortise joint and tou-kung, finite model of the structure is built. By modal analysis main mode of the structure is obtained, based on which level loads is applied to the structure to carry out pushover analysis. Results show that mode 1 in y direction is main mode of the structure. Under 8-degree of seldomly occurred earthquake the structure produces displacement which is less than permissible value. Under earthquake plastic hinges mainly appear near bottom tenon-mortise joints. However the upper part remains intact because of isolation of tou-kung.

**Keywords:** wooden constitution, pushover curve, demand spectrum; aseismic character, Shen-Wu Gate

## 1 Introduction

Chinese ancient buildings are mainly made of wood and are worth protecting for their historical, artistic and scientific values. For thousands of years they have experienced sorts of earthquakes but remain intact, a good example is the Shen-Wu Gate in the Forbidden City (Figure 1). The building was built in 1420 A.D with the plan size of 41.74×12.28m (length×width). The good aseismic character of Shen-Wu Gate is related to its constitution (Zhou, 2007): Tenon-mortise joints between beams and columns can absorb vibration by friction between each other, tou-kungs like springs which can isolate vibration, heavy roof can increase base shear to reduce earthquake responses and so on.

There are many aseismic assessment methods for structures, such as assessing by experience, response spectrum analysis, time-history analysis, vibration tests, pushover analysis and so on. Thereinto, pushover method has been widely applied

---

\* Corresponding author, e-mail: zy\_7225@yahoo.com.cn

for steel structure, concrete structure and masonry structure and so on (Yang et al., 2007, Wang et al., 2004, Qu and Xie, 2007). However it has very seldom been applied to Chinese ancient wooden constitutions until now.



Figure 1. Shen-Wu Gate in the Forbidden City

In order to protect Chinese ancient buildings, the Shen-Wu Gate is taken as an example to study its aseismic characters by pushover method based on capacity-demand spectrum curves under 8-degree of seldomly occurred earthquake. Results will be helpful for aseismic strengthening for ancient buildings.

## 2 Capacity Spectrum and Demand Spectrum Curves

### 2.1 Spectrum Curves

In this paper capacity spectrum method is taken for pushover analysis on Shen-Wu Gate. The capacity spectrum curve transformed by pushover curve is shown in Figure 2. The demand spectrum curve transformed from acceleration response spectrum curve is shown in Figure 3. If there is an intersection point between the two curves above, the point will be “target displacement point” which will be compared with permissible displacement value of the structure to assess its aseismic capacity.

The pushover curve is transformed to capacity spectrum curve by the following equation:

$$S_{ai} = \frac{V_i / G}{\alpha_1}, S_{di} = \Delta / (\gamma_1 \varphi_1) \quad (1)$$

In equation (1),  $V_i$  represents base reaction,  $\Delta$  represent top displacement,  $G$  represents equivalent weight of the structure,  $S_{di}$  represents spectral displacement,  $S_{ai}$  represents spectral acceleration,  $\alpha_1$  represents mass participation coefficient for mode 1,  $\gamma_1$  represent modal participation coefficient for mode 1,  $\varphi_1$  represents top displacement for mode 1.

The acceleration response spectrum is transformed to demand curve by the following equation:

$$S_{di} = (T^2 / 4\pi^2) S_{ai} g \tag{2}$$

In equation (2),  $T$  represents period,  $g$  represents gravity acceleration.

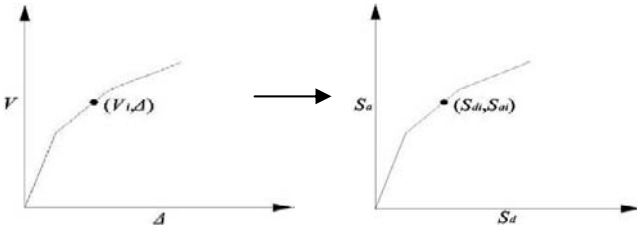


Figure 2. Capacity spectrum curve by transformation

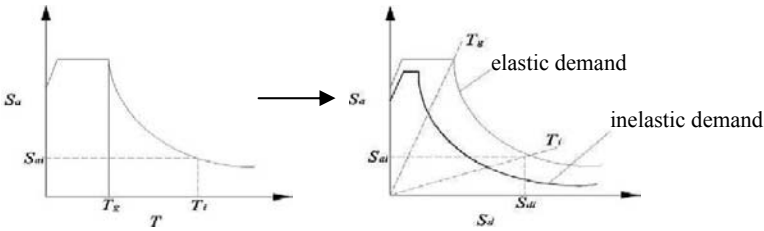


Figure 3. Demand spectrum curve by transformation

### 2.2 Reduction of Demand Spectrum

To consider inelastic character of the structure, demand spectrum curve is usually reduced by introducing equivalent damping ratio  $\zeta_e$  which can be expressed as following:

$$\zeta_e = E_D / (4\pi E_S) \tag{3}$$

In equation (3),  $E_D$  represents energy dissipation by hysteretic damping which also is area of parallelogram in Figure 4;  $E_S$  represents maximum strain energy which also is area of shadow part in Figure 4. On the other hand  $d_y$  and  $d_p$  represent yielding and maximum displacement of equivalent SDOF system.

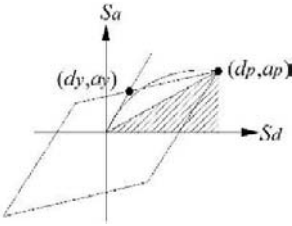


Figure 4. Damping transformation

### 3 Mechanical Model

#### 3.1 Tenon-mortise Joints

Beams and columns of the palace are connected by tenon-mortise joints, as shown in Figure 5(a). For each joint, under seismic forces energy dissipation occurs by friction between tenon and mortise, which is just like a damper fixed on the joint to reduce the structure’s response.

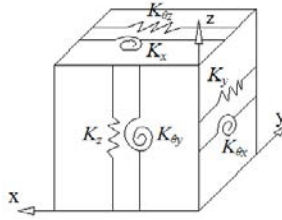
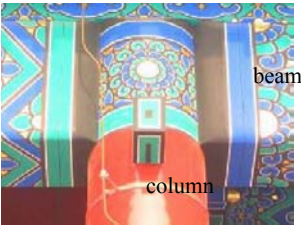


Figure 5(a). Photo of tenon-mortise joint      Figure 5(b). Simulation method

Considered as a semi-rigid joint, a tenon-mortise joint can be simulated as a 2-node spatial spring element which is composed of 6 uncoupled springs, as shown in Figure 5(b). Thereinto,  $K_x$ ,  $K_y$  and  $K_z$  represent axial stiffness in x, y and z directions;  $K_{\theta x}$ ,  $K_{\theta y}$  and  $K_{\theta z}$  represent rotational stiffness about x, y and z directions. The simulation method is like adding axial and rotational springs to the joint.

By experimental achievements of Xi’An University of Architecture and Technology (Yao et al., 2006, Zhang, 2003), stiffness values for the spring element can be obtained as following:

$$K_x=K_z=1.69 \times 10^6 \text{N/m}, K_y=0, K_{\theta x}=K_{\theta y}=K_{\theta z}=1.5 \times 10^5 \text{N/m}$$

### 3.2 Tou-kung

On top of side columns of the palace there are layers of tou-kungs. Each tou-kung is composed by layers of wooden members in cross and longitudinal directions, as shown in Figure 6(a). Under seismic forces, the tou-kungs are tensed and compressed just like springs which produces isolation.

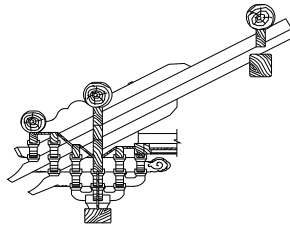


Figure 6(a). Photo of tou-kung

Figure 6(b). Constitution of tou-kung

As Tou-Kung can isolate vibration in x,y and z directions, it can also be simulated by a 2-node spring element just as that of Figure 5(b). However, it does not produce torsion. According to obtained experimental achievements (Sui, 2006), stiffness values for Tou-Kung are:

$$K_x=K_z=0.3 \times 106 \text{N/m}, K_y=5.5 \times 106 \text{N/m}, K_{\theta x}=K_{\theta y}=K_{\theta z}=0$$

### 3.3 Finite Element Model

The height of each side-column of the Shen-Wu Gate is 4.3m, whose root has to be pushed outside 0.01 times of the height size (0.043m) according to construction code for Chinese ancient buildings; The roof mass is considered as even loads which can be simulated by even mass elements; Roots of all columns are restricted as swivel joints. Considering conditions all above finite element model of the structure is built, as shown in Figure 7, which includes 5091 beam and column elements, 671 roof mass elements, 160 Tou-Kung elements and 48 Tenon-Mortise joint elements.

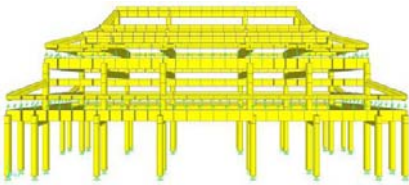


Figure 7. Finite element model

### 4 Modal Analysis

In order to study vibration characters of the palace, modal analysis is carried out before pushover analysis. Table 1 shows the first 10 frequencies as well as modal ratios, where x represents lengthwise direction, y represents cross direction.

Table 1. Vibration results

Num	Fre (Hz)	Modal ratio		Num	Fre (Hz)	Modal ratio	
		x	y			x	y
1	1.07	0.01	1.00	6	3.87	0.69	0.02
2	1.20	0.05	0.02	7	4.42	0.01	0.12
3	1.33	0.01	0.02	8	5.09	0.40	0.05
4	2.40	0.01	0.02	9	5.29	1.00	0.03
5	3.36	0.24	0.05	10	5.43	0.41	0.04

From Table 1 it is obvious that basic frequency of the structure is 1.07Hz. Mode 1 is the main mode which is of translation in y direction, as shown in Figure 8. So pushover analysis can be applied to y direction of the structure.

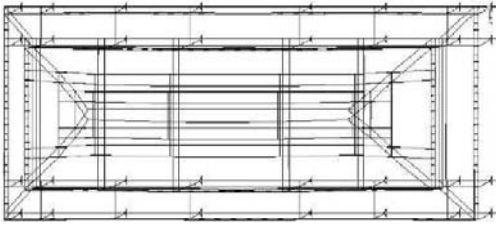


Figure 8(a). Plan view of mode 1

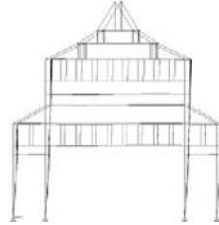


Figure 8(b). Side view of mode 1

### 5 Pushover Analysis

Shen-Wu Gate has regular layout as well as low natural vibration period. Since under earthquake its main mode focuses on mode 1, level loads based on which is applied to the structure which is expressed by the following equation:

$$F_i = \frac{W_i \phi_i}{\sum_{i=1}^n W_i \phi_i} V \tag{4}$$

In equation (4),  $F_i$  represents floor shear forces,  $W_i$  represents floor weight,  $\varphi_i$  represents floor mode,  $V$  represents base reaction.

Figure 9(a) shows curve of base-reaction vs top displacement. According to pushover results, when top displacement reaches 0.23m, the first set of plastic hinges appear; as top displacement reaches 0.36m, the structure begins to be collapse. Figure10 shows plastic hinges of operational and collapse prevention status, from which it can be seen that plastic hinges mainly appear near bottom tenon-mortise joints. On the other hand, the upper part of the structure remains intact because of isolation of tou-kung.

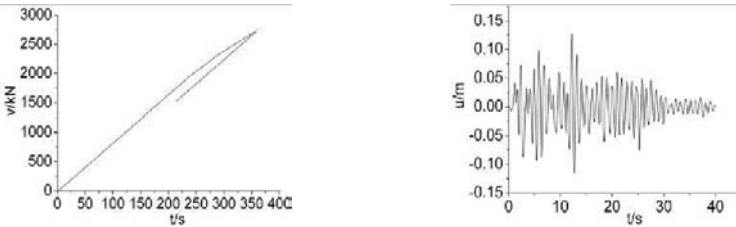


Figure 9(a). Top displacement vs base reaction      Figure 9(b). Displacement response

By pushover analysis, under 8-degree of seldomly occurred earthquake the performance point of the structure is:  $S_a=0.297$ ,  $S_d=0.137m$ . After transformation by equation (1),it can be obtained that  $V=1179kN$  and  $\Delta=0.144m$ .On the other hand,  $\Delta < 0.46m(H_0/30)$  which is the permissible value of the structure (Liang et al., 1992).

Figure 9(b) shows response of top displacement under 8-degree seldomly occurred earthquake (400gal) in y direction by time-history analysis. It is clear that maximum value is 0.127m which is similar to that of pushover analysis result, but the latter method tends to be more safe.

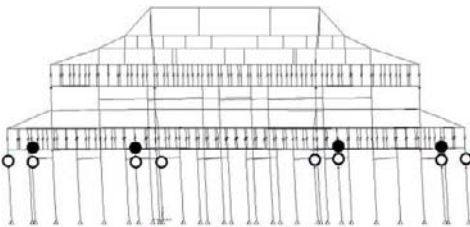


Figure 10. Plastic hinges (O :operational    ● :collapse prevention)

## 6 Conclusions

1. Main mode of Shen-Wu Gate is mode 1 in y direction.
2. By pushover analysis under 8-degree of seldomly occurred earthquake the structure produces displacement which is within permissible value.
3. Plastic hinges of the structure mainly appear near bottom tenon-mortise joints, however the upper part of the structure remains intact because of isolation of tou-kung.

## References

- Liang T. et al. (1992). *Technical code for maintenance and strengthening of ancient timber buildings*. Chinese Building Industry Press, Beijing [in Chinese].
- Qu C. Z. and Xie L. L. (2007). Pushover analysis on middle-rise and high-rise block masonry structures. *China Safety Science Journal*, 17(11), 124-129 [in Chinese].
- Sui L. (2006). Study on aseismic mechanics and analysis on Tou-Kung of Chinese ancient buildings. ME Thesis of Xi'an Univ. of Arch. & Tech, Xi'an [in Chinese].
- Wang Da-sui, He Jun-li et al. (2004). The basic principle and a case study of pushover analysis. *World Earthquake Engineering*, 20(1), 45-53 [in Chinese].
- Yang Jun, Liu Hong-bing et al (2007). Research on seismic assessment of existing structures under the action of earthquake. *Earthquake Resistant Engineering and Retrofitting*, 29(6), 86-90 [in Chinese].
- Yao K. et al. (2006). Experimental studies on the characteristic of mortise-tenon joint in the historic timber buildings. *Engineering Mechanics*, 23(10), 168-172 [in Chinese].
- Zhang P.C. (2003). Study on structure and its seismic behavior development of Chinese ancient timber structure buildings. PhD Thesis of Xi'an Univ. of Arch. & Tech, Xi'an [in Chinese].
- Zhou Q. (2007). Study on antiseismic constitution of Shen-Wu Gate in the Palace Museum. *Earthquake Resistant Engineering and Retrofitting*, 29(6), 91-98 [in Chinese].

# Aseismic Effects of Masonry Walls Embedded in Chinese Ancient Wooden Buildings by Wen-chuan Earthquake

Qian Zhou<sup>1,2\*</sup> and Weiming Yan<sup>1</sup>

<sup>1</sup>Beijing University of Technology, Beijing 100022, China

<sup>2</sup>Imperial Palace Museum, Beijing 100009, China

**Abstract.** In order to protect Chinese ancient buildings, a wooden building in Guangyuan city in China is taken as an example to study aseismic effects of masonry walls to wooden constitution by Wenchuan earthquake. By ANSYS PROGRAM, semi-rigid character of tenon-mortise joint as well as contact between wooden constitution and walls are simulated. Then finite element model of the building is built. By comparison method, vibration modal as well as dynamic responses of the structure before and after considering wall effects are studied. Results show that after considering embedding effects of masonry walls, main mode of the ancient building is mode 1 in x direction. Under Wenchuan earthquake the wooden constitution produces lower displacement but higher acceleration values.

**Keywords:** embedded masonry wall, Chinese ancient building, aseismic effects, tenon-mortise joint, Wenchuan earthquake

## 1 Introduction

Chinese ancient buildings are mainly made of wood, whose beams and columns are connected by tenon-mortise joints. On May 12th, 2008, an earthquake measuring 8 Richter scale occurred in Wenchuan district in China which caused lots of loss of money and life. Several places nearby were also affected by the earthquake including an ancient building which is 189 km far way from epicenter. The building was built in Qing Dynasty whose size is 45.0×8.2×7.0m (length×width×height). Figure1 shows its plan view. The building was repaired in 2005 with all incline members corrected, slack tenon-mortise joints strengthened by iron hooks and roof tiles repaved. So the ancient building remains intact except for some cracks in intersect positions of wooden beams and the back walls.

---

\* Corresponding author, e-mail: zy\_7225@yahoo.com.cn

From research results by now, damage study on Chinese ancient buildings by earthquakes are mainly focused on description and lack of numerical analysis (Yang et al., 2000, He et al., 2006). On the other hand, present researches on dynamic responses of Chinese ancient buildings always omit the embedding effects of masonry walls, which is not consistent with actual results (Cang et al., 2004, Zhao et al., 2000). In this paper the problems will be solved. By comparison method and by modal and dynamic analysis, embedding effects of masonry walls to aseismic character of Chinese ancient wooden buildings will be studied, results will be helpful for aseismic strengthening for Chinese ancient buildings.

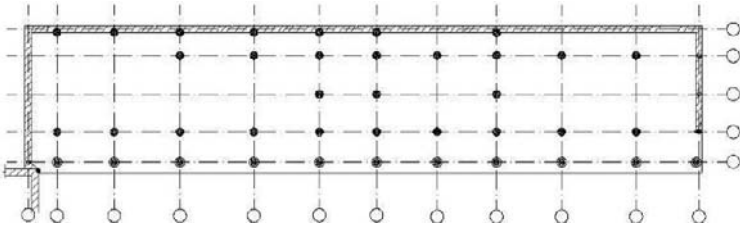
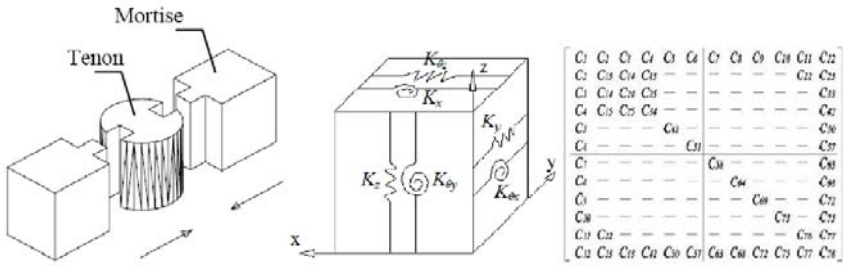


Figure 1. Plan view of the ancient building

## 2 Finite Element Model

### 2.1 Tenon-Mortise Joint

In this paper ANSYS PROGRAM is used for analysis on damage of the ancient building by Wenchuan earthquake. Considered as a semi-rigid joint, tenon-mortise joint can be simulated by a 2-node virtual spatial spring element. The element is composed of 6 uncoupled springs, as shown in Figure 2(b). Stiffness of the spring element includes 3 of translation ( $K_x, K_y, K_z$ ) and 3 of rotation ( $K_{\theta_x}, K_{\theta_y}, K_{\theta_z}$ ). In ANSYS PROGRAM stiffness matrix of the spring element can be simulated by element MATRIX27, which has no shape but can reflect stiffness matrix characters by 2 nodes. Figure 2(c) shows output results of element MATRIX 27.



(a) Tenon-mortise joint      (b) 2-node spatial spring element      (c) Stiffness matrix

Figure 2. Simulation of tenon-mortise joint

In Figure 2(b), matrix elements for  $K_x$  are:  $C_1, C_7$  and  $C_{58}$ ; For  $K_y$  are:  $C_{13}, C_{19}$  and  $C_{64}$ ; For  $K_z$  are:  $C_{24}, C_{30}$  and  $C_{69}$ ; For  $K_{\theta x}$  are:  $C_{34}, C_{40}$  and  $C_{73}$ ; For  $K_{\theta y}$  are:  $C_{43}, C_{49}$  and  $C_{76}$ ; For  $K_{\theta z}$  are:  $C_{51}, C_{57}$  and  $C_{78}$ . By reference of obtained research results (D.P. Fang et al., 2001), stiffness values are:  $K_x=K_y=1.0 \times 10^9 \text{KN/m}$ ,  $K_z=2.1 \times 10^8 \text{KN/m}$ ,  $K_{\theta x}=5.8 \times 10^{13} \text{KN}\cdot\text{m}$ ,  $K_{\theta y}=6.3 \times 10^{12} \text{KN}\cdot\text{m}$ ,  $K_{\theta z}=3.1 \times 10^{11} \text{KN}\cdot\text{m}$ .

### 2.2 Wall Embedding Simulation

For Chinese ancient buildings, masonry walls among wooden columns and under wooden beams are usually thick (about 0.5-1.0m) and used for filler function. When embedding effects of the walls are simulated by ANSYS PROGRAM, face-to-face contact element can be used to build wall-wooden constitution contact pairs, as shown in Figure 3, where, the column side and beam bottom faces act as “contact face” which can be simulated by element CONTA174. The side and top faces of walls act as “target face” which can be simulated by element TARGE170. On the other hand, friction coefficient between wall and wooden constitution is 0.5 (Wang, 1987).

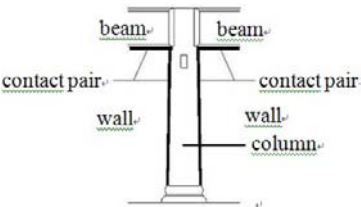


Figure 3. Wall embedding simulation

### 2.3 Finite Element Model

The height of each side-column of the building is 4.1m, whose root has to be pushed outside 0.01 times of the height size (0.041m) according to construction code for Chinese ancient buildings; The roof mass is considered as even loads which can be simulated by element MASS21; Beams and columns are simulated by element BEAM189; walls are simulated by element SHELL63; roots of all columns are restricted as swivel joints. Considering conditions all above finite element model of the structure is built, as shown in Figure 4, which includes 2102 beam and column elements, 611 roof mass elements, 1580 wall elements and 84 tenon-mortise joints elements.

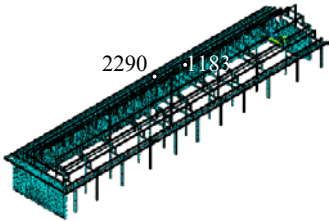


Figure 4. Finite element model

### 3 Modal Analysis

In order to study embedding effects of the 0.5m thick walls to the wooden constitution, two cases are considered: Case 1 only considers the wooden constitution vibration; Case 2 considers both wall and wooden constitution vibration. By modal analysis the first 10 frequencies as well as modal participation ratios for both cases are shown in Tables 1-2, main modes are shown in Figures 5-6. Thereinto, x represents lengthwise direction, y represents cross direction and z represents vertical direction.

Table 1. Vibration results for case 1

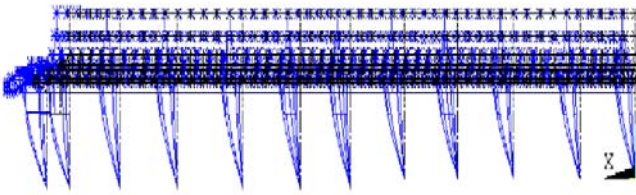
Num	Fre (Hz)	Participation ratio		Num	Fre (Hz)	Participation ratio	
		x	y			x	y
1	1.38	104.25	-3.08	6	5.21	-0.17	4.24
2	2.44	5.18	55.17	7	5.74	-0.52	0.38
3	3.24	-0.49	0.24	8	6.86	-0.55	0.40
4	4.11	1.10	0.13	9	6.95	0	-2.63
5	4.69	1.23	10.06	10	7.23	-0.56	0

Note: Modal participation ratio for z direction is zero.

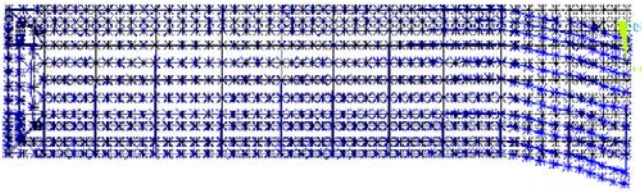
Table 2. Vibration results for case 2

Num	Fre (Hz)	Participation ratio		Num	Fre (Hz)	Participation ratio	
		x				x	
1	1.59	195.59		6	3.79	2.47	
2	2.87	1.90		7	4.11	-5.16	
3	3.04	-6.06		8	4.39	22.46	
4	3.38	8.32		9	4.60	18.91	
5	3.50	-15.90		10	5.83	19.91	

Note: Modal participation ratios for y and z direction are zero.



(a) Front view of mode 1



(b) Plan view of mode 2

Figure 5. Main modes for case 1

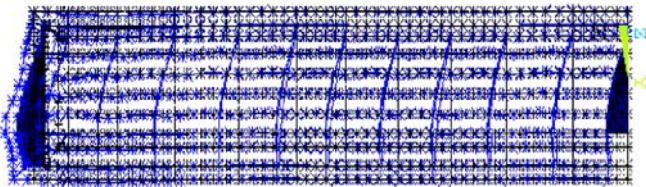


Figure 6. Plan view of mode 1 for case 2

From Table 1 it is obvious that basic frequency of the structure for case 1 is 1.38Hz, whose main modes are mode 1 in x direction and mode 2 in y direction.

On the other hand, from Figure 5 it is known that the structure vibrates with the back columns swing toward x direction which led to the left side part of the wooden constitution distorted; in y direction the structure vibrates with part of the right side wooden constitution distorted. Neither of the above is consistent with the actual damage symptoms.

From Table 2 it is obvious that basic frequency of the structure for case 2 is 1.59Hz, whose main mode is only mode 1. On the other hand, from Figure 6 it is clear that the structure vibrates with its front part swing toward left side of the structure, while the back columns keep stable because of the embedding effect of the walls. According to actual damage symptoms, no serious damage appeared during the earthquake for the ancient building, as shown in Figure 7(a). Only a few cracks in intersect positions of wooden beams and the back walls appear, as shown in Figure 7(b). Thus vibration results for case 2 really accord the actual damage symptoms of the building, which also reflects the restraining effect of the walls to the wooden constitution.



(a) Intact wooden constitution



(b) cracks on the wall

Figure 7. Photos of the building after earthquake

## 4 Earthquake Response

According to damage symptoms of the ancient building as well as data of obtained intensity scale, Wenchuan earthquake waves in x, y and z directions are modulated. Peak value of acceleration in each direction is 100gal after modulation, the duration time is 10s with spacing of 0.005s. Damper ratio of the structure is 0.05 (Liu and Du, 2005). In order to study embedding effects of the walls to aseismic character of the wooden constitution, two typical nodes are selected: Node 1183 (in the middle of roof) and node 2290 (in the middle of contact position of back wall and wooden beam), as shown in Figure 4, Figures 8-9 are displacement response comparison curves; Figures 10-11 are acceleration response comparison curves. Thereinto, n represents no wall effect, y represents considering wall effects.

From Figures 8-9, it is clear that after considering wall effects, displacement responses of both nodes decrease. For node 2290, its peak value in x direction nearly falls to zero, which is far less than that of case 1(0.015m); for node 1183, after considering wall effects, peak values of displacement response fall from 0.014m to 0.007m in x direction, from 0.036m to 0.019m in y direction. On the other hand, from displacement response curves of both nodes, it is obvious that they vibrate basically based on balance location. So it can be deduced that for both case1 and case 2 the structure keeps stable vibration status.

From Figures 10-11, it is clear that after considering wall effects, acceleration responses of both nodes increase. For node 1183, its peak values of acceleration response increase from 1.12m/s<sup>2</sup> to 2.27 m/s<sup>2</sup> in x direction, from 1.27 m/s<sup>2</sup> to 2.14 m/s<sup>2</sup> in y direction; For node 2290, its peak values of acceleration response increase from 1.23 m/s<sup>2</sup> to 2.06 m/s<sup>2</sup> in x direction, from 1.69 m/s<sup>2</sup> to 3.04 m/s<sup>2</sup> in y direction. From data above it is obvious that after considering wall effects, displacements of the structure decrease but inner forces increase.

Liu (Liu, 1988) provided curve of earthquake force ( $F$ ) vs displacement ( $\Delta$ ) for different structures under earthquakes, as shown in Figure 12, which is consistent with analysis results above.

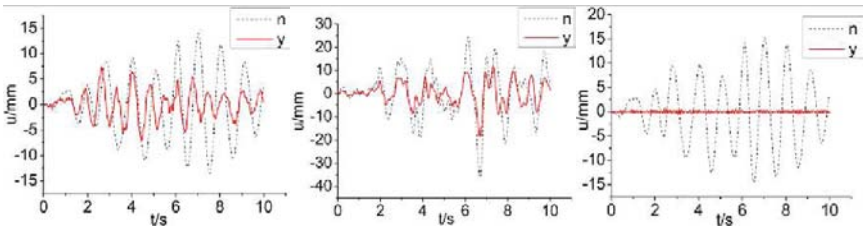


Figure 8(a).  $U_x$  for node 1183    Figure 8(b).  $U_y$  for node 1183    Figure 9(a).  $U_x$  for node 2290

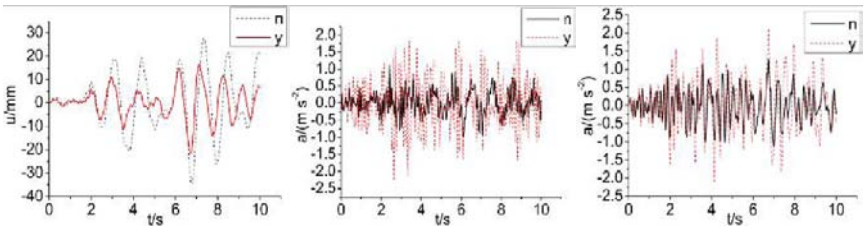


Figure 9(b).  $U_y$  for node 2290    Figure 10(a).  $A_x$  for node 1183    Figure 10(b).  $A_y$  for node 1183

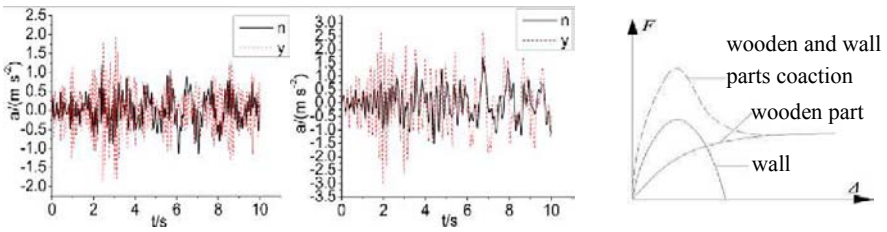


Figure 11(a). Ax for node 2290      Figure 11(b). Ay for node 2290      Figure 12. Curve of F- $\Delta$

## 5 Conclusions

1. By simulation, after considering embedding effects of walls, vibration mode of the ancient building focuses on x direction, which accords its actual damage symptoms.
2. Under Wenchuan earthquake the building keeps stable vibration status whether considering wall effects or not.
3. After considering wall effects, peak value of displacement response of the structure decreases but of acceleration response increases.

## References

- Cang S. et al. (2004). Dynamic analysis of ancient wood structures with mortise and tenon connection. *Journal of Ningbo University (NSEE)*, 17(3), 332-335 [in Chinese].
- Fang D.P., Iwasaki S. and Yu M.H. (2001). Ancient Chinese timber architecture-II: Dynamic characteristics. *Journal of Structural Engineering*, 11(1), 358-1364.
- He L., Pan W. and Yang Z.H. (2006). Seismic damage of rural wooden constitutions and their aseismic methods. *Earthquake Resistant Engineering and Retrofitting*, 28(6), 94-101 [in Chinese].
- Liu J.B. and Du X.L. (2005). *Structural Dynamics*. Mechanical Industrial Press, Beijing [in Chinese].
- Liu X.D. (1988). Study on aseismic character of Chinese ancient wooden constitution. M.E. Paper of Xi'an Jiaotong University, Xi'an [in Chinese].
- Wang Q.C. (1987). Determination of slide friction ratio. *Teaching Instruments and Experiments*, 3, 15-16 [in Chinese].
- Yang Y.D., Du J.L. and Li G.R. (2000). Analysis of the earthquake disaster characteristics of ancient building structures. *World Information on Earthquake Engineering*, 16(3), 12-16 [in Chinese].
- Zhao J.H., Yu M.H. and Yang S.Y. (2000). Dynamic analysis for the ancient superstructure of the east city gate of Xi'An by FEM. *China Civil Engineering Journal*, 33(1), 32-35 [in Chinese].

# Numerical Simulation of Semi-Rigid Element in Timber Structure Based on Finite Element Method

Yunkang Sui<sup>1</sup>, Jingya Chang<sup>1\*</sup> and Hongling Ye<sup>1</sup>

<sup>1</sup> Numerical Simulation Center for Engineering, Beijing University of Technology, Beijing 100124, China

**Abstract.** In each traditional timber structure in China, the mortise and tenon are one of the most important parts, because they connect differential components as a whole more big component. Of course, they made also beam and column as a frame. To conveniently utilize FEM for computing timber structure, mortise and tenon are considered as relative independent configurations, as well as the part which should be paid more attention. Because the connection between mortise and tenon is semi-rigid deformation behavior, rather than full rigid or ideally pinned connection, it is a key to accurately approach property of semi-rigid stiffness of mortise and tenon during the numerical simulation, for expressing the property of whole actual wooden structure. This study summarizes the research of the development of semi-rigid element and establishes easy computing and analytic finite element model of mortise and tenon. In addition, parameters of the model have been obtained by comparing numerical result applied MSC FEM software and the consequence of crossing timber frame experiment, based on the response surface method and optimize interactive theory. The analysis and the result mentioned above could be applied on the study of other entire large-scale ancient wooden architecture.

**Keywords:** mortise and tenon connection, semi-rigid node, timber structure, response surface method, FEM

## 1 Introduction

During the long history of China, ancient wooden architectures in China undoubtedly are the shining precious treasure in the world and also manifest the wisdom of Chinese. However, those ancient timber architectures have suffered from natural or man-made, such as seism, corrosion, war or material ageing, damaging,

---

\* Corresponding author, e-mail: jingya\_cn@yahoo.com.cn

therefore, taking action to carry out security evaluation and appraisal, predict potential danger, protect and maintain them is definitely necessary for us. Using FEM theory, static analysis and dynamic analysis for the timber architecture model can be taken. It is not only able to reduce the destruction caused by the experiment, but also extremely decrease the consuming of labor power and resources. What is the more, simulation is also able to complete tests, which the experiment can not do. How to accurately and effectively simulate ancient timber structure? Establishing reasonable and exact FEM model is the key.

Mortise-tenon connection is the main joints for the Chinese ancient timber architectures, most of which do not use one nail or pin, as showed in Figure 1. While modern timber structure usually utilize finger, hollow steel dowel, nail, and screw bolt or other steel type fasters as timber joints (Guan et al., 2001). Mortise-tenon joint unlike other kinds of modern timber joints, composed by mortise and tenon, can bear load of definite magnitude and resist horizontal thrust as well (Yao et al., 2006). On incipient stage, when applying load on mortise-tenon structure, the gap of joint is jam-packed, and slipping generates between timber component parts, while the property of mortise-tenon connection approximates like a hinge. With continually increasing load, girder suffers from improving load and then axial force of mortise-tenon joint increase, the moment of flexion and shear appear and at the same time the stiffness of timber connection rises, as mortise and tenon squeeze to each other. This period shows semi-rigid property and the mortise-tenon joint is able to stand moment of flexion and also has certain deformation, which forms striking angle. As the augmenting of burden, the stiffness of mortise-tenon connection will decrease obviously, and then the mortise will disengage from tenon and finally timber structure will be broken. However, though the construction may be broken, the material of the timber structure probably does not broken, so it is vital to research and improve the property of mortise-tenon joint to avoid the breakage of architecture (Wang, 2008). On the other hand, during the process presented above, the deformation and relative displacement of the mortise-tenon joint are generated, which can readjust the distribution of endogen force of the entire wooden structure and then absorb most of energy (Zhu et al., 2006). Especially when the seismic shock happens, the friction between the mortise and tenon will play an important role in resisting seismic loading and enhance energy-absorption capability. In short, to intensely research the characteristic of Chinese ancient timber structure, focus on mortise-tenon connection when establishing timber construction model by FEM is necessary and significant.

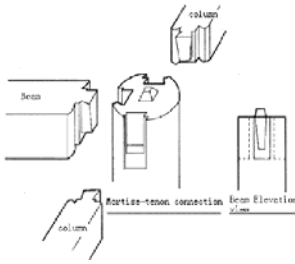


Figure 1. Mortise-tenon connection between the Beam and column

## 2 Finite Element Model of Mortise-Tenon Joint

Mortise-tenon connection displays strong semi-rigid property during the loading period, as discussed above. Presently extensive research works, experimental as well as numerical have been carried out to use for predicting the actual behavior of modern timber joints on abroad (Plannic et al., 2008; Ying et al., 2005; Goto, 1995; Goto et al., 1993), but regarding to the semi-rigid components of Chinese ancient wooden structure few foreign researchers study deeply. In China, the semi-rigid characteristic of the joggle joint and the change rules of stiffness degradation and moment-deflection angle hysteretic curves were obtained by Yao Kan through experiment. However, he does not point out how to realize application of semi-rigid elements in FEM analysis. Considering the complex during the period of contacting and movement of mortise-tenon joints, transition element can deal with this problem to approximately simulate mortise-tenon property, as showed in Figure 2. The researchers, such as Zhao Junhai, Zhao Xuguang, Yu Maohong utilize space dummy spring elements as transition elements to take dynamic analysis (Fang et al., 2001; Zhao et al., 2000; Zhao et al., 2008; Xue et al., 2004; Zhai et al., 2005).



Figure 2. Transition element

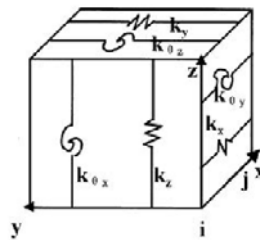


Figure 3. Space dummy spring elements



where  $E_n, A_n, I_{yn}, I_{zn}, G_n, J_n$  is undetermined coefficients. Meanwhile, mechanical property of this transition component will variable as the stiffness combination beams alteration, therefore moment-rotation response of semi-rigid characteristic concerning mortise-tenon connection is able to be expressed by this new element model. We now suppose that  $E_2 = E_4, E_1 = E_3$ , the length of every component of combination beam is same and  $b_1, h_1$  are the section parameters of 1,3 parts, while  $b_2, h_2$  for the 2,4 parts. Then undetermined coefficients of the element model convert to variables,  $E_1, E_2, b_1, h_1, b_2, h_2$ . Through comparison between experimental and numerical study, the property of this transition element can be obtained for predicting the actual behavior of the flexible connection.

### 3 Discussion the Influence and Determine the Variables of the Transition Element

This study based on crossing-timber frame experiment in Reference3. As shown in Figure 6, ‘ac’ is beam, ‘bl’ is column and mortise-tenon joint connects them. Adding displacement load on node ‘I’, 10mm per time until the structure is broken. Establish Finite Element Model. Beam and column use ‘Beam189 element’, which can transfer tension, torsion, bend and contain ‘section’ command to control dimension, established by MSC. Pantran software. Transition element applies combination beam discussed as above, seen as Figure 7, where,  $E_1, E_2, b_1, h_1, b_2, h_2$  are undetermined coefficient.

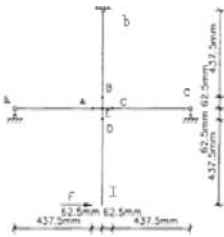


Figure 6. Experiment

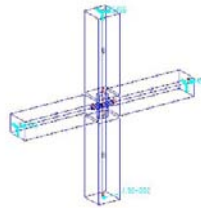


Figure 7. Finite element model

### 3.1 Calculation the Variables – Using Response Surface Method to Find the Optimum Solution

Based on the response surface method, establish linear response surface equation and then using optimize iteration search the optimum solution.

1) Establish response surface.

First, build a series of sample models under every displacement load, and then

choice good samples, which obey the following criterions:  $\frac{(M_j^{(k)}) - M_j}{M_j} = \varepsilon \leq 0.1$

and  $\frac{(\theta_j^{(k)}) - \theta_j}{\theta_j} = \eta \leq 0.1$ , where  $M_j$  and  $\theta_j$  are experimental moment and rotation data

(Wang, 2008), while  $\tilde{M}_j^{(k)}$  and  $\tilde{\theta}_j^{(k)}$  are numerical analysis data using MSC.Nastran.

How to build sample models? As Figure 8 shown, the middle points is the initial point and other sample points are acquired through floating around the middle one, and then corresponding sample models can be created based on those sample points.

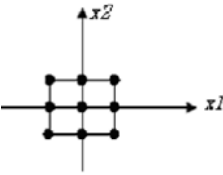


Figure 8. Sample points

$\tilde{M}_j = \sum_{i=1}^6 a_i x_{ij}$  and  $\tilde{\theta}_j = \sum_{i=1}^6 b_i x_{ij}$  are linear response surface moment equation and rotation equation separately and are compiled through C++ program. Then set up target function and coefficients  $a_j, b_j$  are obtained through minimize the target function.

2) Optimized iteration for searching optimum solution (Sui, 2005).

Applying optimize iteration to fine optimum solution for the average stiffness of transition element. Optimum model is shown as formula (3).

$$\begin{cases} find x_i \\ f = \sum_j (M_j - \tilde{M}_j)^2 + (\theta_j - \tilde{\theta}_j)^2 \rightarrow \min \\ \text{s.t. } \underline{x}_j \leq x_j \leq \overline{x}_j \end{cases} \quad (3)$$

Where  $x_i$  are design variables ( $E_1, E_2, b_1, h_1, b_2, h_2$ ),  $M_j$  and  $\theta_j$  are experimental moment and rotation data, while  $\tilde{M}_j$  and  $\tilde{\theta}_j$  are numerical analysis data using MSC.Nastran. Put response surface formulas  $\tilde{M}_j = \sum_{j=1}^6 a_j x_{ij}$  and  $\tilde{\theta}_j = \sum_{j=1}^6 b_j x_{ij}$  into target function  $f = \sum_j (M_j - \tilde{M}_j)^2 + (\theta_j - \tilde{\theta}_j)^2$ , plus minimize it to get the new property  $x_i$ . Condition of convergence is expressed as following.

$$\sum \frac{|x^{(k)} - x^{(k+1)}|}{x^{(k)}} \leq \varepsilon_1, \quad \varepsilon_1 = 0.01, \quad \frac{|f^{(k)} - f^{(k+1)}|}{f^{(k)}} \leq \varepsilon_2, \quad \varepsilon_2 = 0.01$$

Compile optimized program and flow process chart shown as Figure 10.

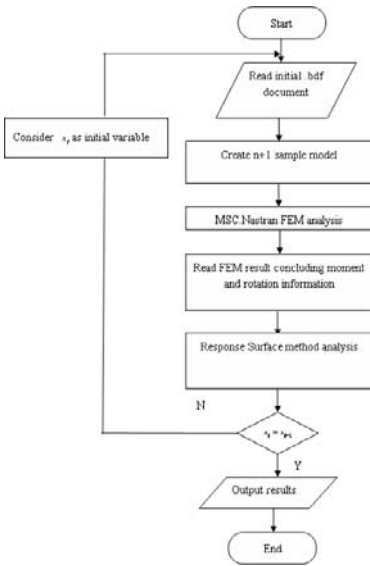


Figure 10. Flow process chart

3) Result and analysis, as shown in Figures 11-13.

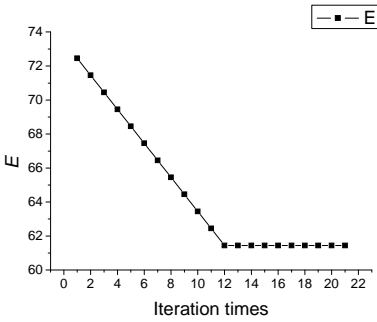


Figure 11. Mean Young's modulus

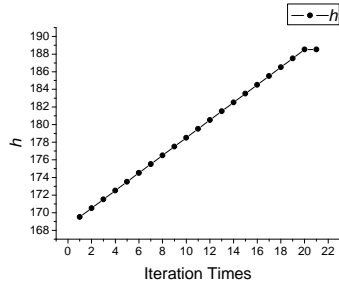


Figure 12. Mean section parameters

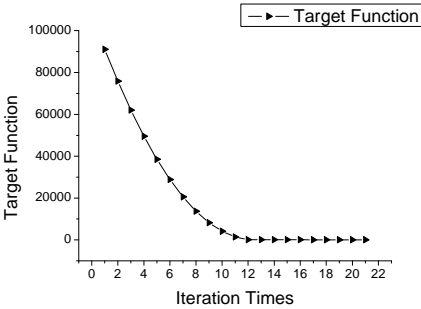


Figure 13. Target function

Using optimize iteration method adjusts coefficients of response surface and get the optimum solution faster. As shown in Figure 13, the target function falls down 99.9261%, from 91068.7548 to 67.273 after twenty times iteration. At the meantime, the variables  $E_1, E_2, b_1, h_1, b_2, h_2$  converge separately at 58.5739, 61.4496, 188.514, 30, 20.5 and 11.2. Moreover, mean stiffness of semi-rigid element can be obtained by formula1. Comparing Figure 11 and Figure 12, convergence of  $E$  is quicker than  $h$  obviously, which indicates that material coefficients play less role when section parameters change to certain extent. And then the section parameters become stable later. It is shown that the method deduced by this paper can easily get the target values through iteration. In short, this study obtains the average stiffness of transition element to approximately simulate mortise-tenon connection through computing every single variable. This status can express the moment-rotation characteristic of semi-rigid element, and finally could be used to the FEM analysis of large size Chinese ancient wooden architectures.

### 3.2 Verification and Comparison

Compare numerical result and experimental data concerning the moment and rotation curves, as shown in Figure 14 and Figure 15.

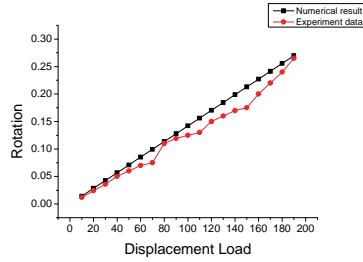
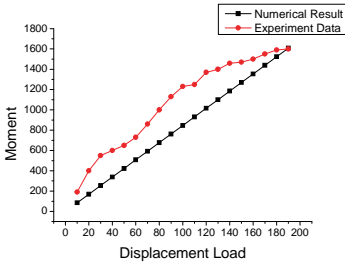


Figure 14. Moment-load curves comparison    Figure 15. Rotation-load curves comparison

From the pictures, it concludes that numerical consequence is close to the experimental result, though there have some difference between them since after all the Finite element model not 100 percent accuracy simulate actual structure. However, this conclusion is still available under the acceptable extent.

## 4. Summary and Conclusions

Mortise-tenon joint is the crucial part in the Chinese ancient architectures and it shows strong semi-rigid characteristic and high energy-absorption capability. This study describes the mechanical property of mortise-tenon connection and summary the recently research of semi-rigid element applied for timber joints. Considering the complex of the loading process of mortise-tenon joints, this research presents using transition element to simulate semi-rigid property and a new semi-rigid Finite Element Model has been established for researching Chinese ancient timber structure. Through response surface method and optimized theory obtain optimum parameters and the mean stiffness of this semi-rigid element. It required twenty iterations, which clear indicates the superiority of this method. In short, the consequence and method of this paper could be used to analyze large size Chinese ancient timber architectures.

## References

- Chui Y.H. and Li Y.T. (2005). Modeling timber moment connection under reversed cyclic loading. *J. Struct. Engrg.*, 131(11): 1757-1763.
- Fang D.P., Yu M., Miyamoto Y., Iwasaki S., Hikosaka H. (2001). Numerical analysis on structural characteristics of an ancient timber architecture. *Journal of Engineering Mechanics*, 18(1): 137-144 [in Chinese].
- Goto Y., Suzuki S. and Chen W.F. (1993). Stability behavior of semirigid sway frames. *Engineering Structures* 15(3) 209-219.
- Goto Y. and Miyashita S. (1995). Validity of classification systems of semirigid connections. *Engineering Structures*, 17(8): 544-553.
- Guan Z.W. and Rodd P.D. (2001). Hollow steel dowels – A new application in semi-rigid timber connections. *Engineering Structures* 23: 112-119.
- Planinc I., Schnabl S., Saje M., Lopatic J., Cas B. (2008). Numerical and experimental analysis of timber composite beams with interlayer slip. *Engineering Structures* 30: 2959–2969.
- Sui Y.K. (1996). *Modeling Transformation and Optimization New Developments of Structural Synthesis Method*. Dalian University of Technology Press [in Chinese].
- Wang J.X. (2008). *Static and Dynamic Analysis of Mortise-Tenon Connection Timber Structure*. College of Architecture Engineering [in Chinese].
- Xue J.Y., Zhao H.T. and Zhang P.C. (2004). Study on the seismic behaviors of Chinese ancient wooden building by shaking table test. *China Civil Engineering Journal*, 37(6): 6-11 [in Chinese].
- Yang Q.S. (2002). FEM-theory, implementation and development. Beijing University of Technology graduate teaching material [in Chinese].
- Yao K., Zhao H.T. and Ge H.P. (2006). Experimental studies on the characteristic of mortise-tenon joint in history timber building. *Engineering Mechanics*, 23(10), 168-173 [in Chinese].
- Zhai H.J. (2005). Research on elastoplastic finite element on the timber and rampart of Xi'an east city gate. Chang'an University, 19-22 [in Chinese].
- Zhao J.H., Yu M.H., Yang S.Y. and Sun J.J. (2000). Dynamic analysis for the ancient superstructure of the east city gate of Xi'an by FEM. *China Civil Engineering Journal*, 33(1): 32-35 [in Chinese].
- Zhao X.G. (2008). Aseismic performance analysis of Xi'an bell tower in FEM. Xi'an Architecture Science University [in Chinese].
- Zhu X.D. and Zhang Tongle (2006). Aseismic technique of Chinese traditional architecture. *Shan xi Architecture*, 32.

# **STRUCTURAL DYNAMICS**

*“This page left intentionally blank.”*

# Numerical Investigation of Blasting-Induced Damage in Concrete Slabs

Yuan Wang<sup>1</sup>, Zheming Zhu<sup>1\*</sup>, Zhangtao Zhou<sup>1</sup> and Heping Xie<sup>1</sup>

<sup>1</sup>College of Architecture and Environment, Sichuan University, Chengdu, Sichuan 610065, P.R. China

**Abstract.** Concrete slabs are among the most common structural elements and their stability under blasting load has received the most attention recently. Therefore, to investigate the concrete slab response to blasting loads is a very significant project. In this paper, 2D dynamic numerical models for concrete slabs subjected to explosive loading are developed through the use of AUTODYN code and the following two issues are investigated: (1) material statuses of concrete slab as a function of time from the exploding source; (2) slabs with different layers of materials under dynamic loading. The objective is to compare their behaviors and find out useful tips to improve the blast-resistant capacity of concrete slabs. In the simulation, RHT failure model which considers damage accumulation, strain-hardening and strain rate are employed to determine concrete material statuses. The simulation results shows that two damage zones of different characters occur in the plain concrete slab and the damage statuses of layered slabs are extensively different from that of plain slabs.

**Keyword:** concrete slab, blasting, damage, layered slab

## 1 Introduction

Usually explosions can release a large amount of energy within microseconds, under such circumstances, the concrete material undergoes high pressures in the gigapascal range including thermodynamic influences (Gebben et al., 2006). Short duration dynamic loads often exhibit strong spatial and time variations, resulting in sharp stress gradients in the structures and a varying strain rate (Krauthammer, 1999). Thus the study on the damage of a structure under blasting loads is very difficult. Under this scenario, it is essential to implement both experimental study (David et al. 1998; Lan et al. 2005; Gebben et al., 2006; Schenkera and Antebya, 2008) and numerical study (Krauthammer, 1999; Luccioni et al., 2004; Xu

---

\* Corresponding author, email: zhemingzhu@hotmail.com

and Lu, 2006; Zhou et al., 2008; Zhu et al., 2007; Zhu et al., 2008). The experimental study could generate an experimental database, however, explosive blasting tests are also quite costly, dangerous and difficult to instrument. The numerical study could simulate the processes of concrete fracture and fragmentation through the use of numerical models so as to obtain a better understanding of the dominant parameters that control concrete slab stability.

Gebbeken et al. (2006) have developed a set of full-scale detonation experiments and flyer-plate impact tests to determine the equation of state properties of concrete. Lu and Xu (2004) developed a constitutive model stemmed from the continuum fracture mechanics to describe the behavior of concrete under blast loading. Riede et al. (2008) studied the shock properties of conventional and high strength concrete by experimental and mesomechanical analysis. Zhou et al. (2008) developed 3D numerical models of an ordinary reinforced concrete slab and a high strength steel fiber concrete slab. Schenkera and Antebya, (2008) performed full-scale experiments to investigate the behavior of the aluminum foam as the external protection layer of the concrete slab. However, as the author indicated that a definitive conclusion as to its efficiency for practical purposes requires more tests and analyses.

There are many forms of composite concrete slabs which have been applied in a variety of constructions. It is of interest to investigate the behavior of those slabs under explosive loading to find out a relatively effective blast-resistant slab structure. Lan et al. (2005) carried out an extensive large-scale test program on a set of composite slabs including conventional reinforced concrete slabs, steel fiber reinforced concrete slabs, profiled steel sheeting reinforced concrete slabs, steel-air-steel sandwich slabs and steel-concrete-steel sandwich slabs. A lot of useful tips have been elicited. Silva and Lu, (2007) investigated the feasibility of using carbon and steel fiber to improve the blast resistance capacity of one-way reinforced concrete (RC) slab and they have developed a displacement based method to predict the explosive charges weight and standoff distances required to impose a given damage level. Razaqpur et al. (2007) studied the behavior of RC slabs retrofitted with glass fiber reinforced polymer composite under blast loading. Although many significant results have been published, it is far from complete for the numerical study of concrete slab fragmentation under blasting load.

In this paper, a concrete slab subjected to explosive loading is developed through the use of AUTODYN code. And by using this model, the issue of concrete material statuses as a function of time is first analyzed, and then the issue of layered slabs is investigated. Throughout the paper, tensile stress is positive and compressive stress is negative.

## 2 Numerical Model

The slab considered here is a disk-like plate which measures 1200 mm in diameter and 300 mm in thickness. The TNT explosive is placed in the center of the top surface (see Figure 1). Because the model is central symmetric, a 2D axial symmetrical model is employed in the calculation. The dashed lines in Figure 1 represent transmit boundary in which the stress waves are not allowed to reflect back, which essentially is an analog of an infinitely large concrete slab. In the top and bottom free surfaces, stress waves can reflect back which could cause tensile or spalling cracks near the free surface, depending on the stress wave's magnitude and material tensile strength. In order to analyze the concrete damage mechanics later, four target points are selected to record the damage and stress histories.

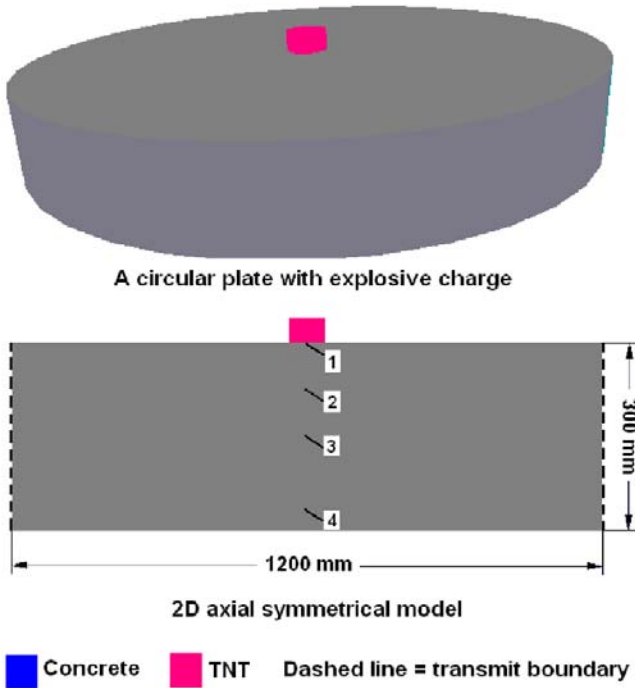


Figure1. Sketch of a slab with explosive charge on the top surface.

## 2.1 Material Model of Concrete

In the model shown in Figure 1, the concrete material is CONC140. In the layered concrete model which will be studied later, concrete material CONC35 will be employed too.

Concrete has porosity, thus, the parameter  $\alpha$  is introduced expressing the porosity

$$\alpha = \frac{v}{v_s} \quad (1)$$

where  $v$  is the specific volume of the porous material and  $v_s$  is the specific volume of the material in the solid state under the same pressure and temperature. When the material compacts to a solid,  $\alpha$  becomes unity.

The polynomial equation of state is employed for the concrete materials. For the solid concrete materials, in the case of compression, i.e.  $\mu = \frac{\rho}{\rho_0} - 1 \geq 0$ , the equation of state is

$$P = A_1\mu + A_2\mu^2 + A_3\mu^3 + (B_0 + B_1\mu)\rho_0 \cdot e \quad (2)$$

And in the case of tension, i.e.  $\mu = \frac{\rho}{\rho_0} - 1 < 0$ , it is

$$P = T_1\mu + T_2\mu^2 + B_0\rho_0 \cdot e \quad (3)$$

where  $P$  is pressure,  $\rho$  is current density,  $\rho_0$  is initial density,  $e$  is specific internal energy. For the porous material, only change the  $\rho$  to  $\alpha\rho$ . The constants  $A_1 = 35.27\text{GPa}$ ,  $A_2 = 39.58\text{GPa}$ ,  $A_3 = 9.04\text{GPa}$ ,  $B_0 = B_1 = 1.22$ ,  $T_1 = 35.27\text{GPa}$ ,  $T_2 = 0.0$ . The two concrete materials, i.e. CONC140 and CONC35, will use the same polynomial equation of state (EOS).

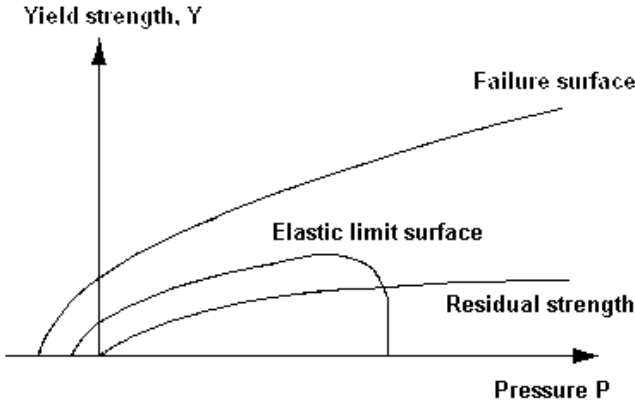


Figure 2. RHT strength model used for concrete material [Riedel (2000), cited by Leppänen, 2006].

For the concrete material CONC140, the solid concrete density is 2.75 g/cc; the porous concrete density is 2.52 g/cc, and the porous soundspeed is 3.242 km/s. For the concrete material CONC35, the solid concrete density is 2.75 g/cc; the porous concrete density is 2.314 g/cc, and the porous soundspeed is 2.92 km/s.

The RHT strength model is applied which was developed by Riedel (2000). The RHT model, which consists of three strength surfaces, namely an elastic limit surface, a failure surface and a strength surface for the remaining crushed concrete, as shown in Figure2, includes pressure hardening, strain hardening and strain rate hardening. For the concrete material CONC140, the concrete shear modulus is 22.06 GPa, the compressive strength is 140 MPa, the tensile strength is 14 MPa, the shear strength is 25.2 MPa. For the concrete material CONC35, the concrete shear modulus is 16.7 GPa, the compressive strength is 35 MPa, the tensile strength is 3.5 MPa, the shear strength is 6.3 MPa.

In this model, the damage is generated by activation and growth of cracks due to tension, shear and compression. A variable,  $D$ , is defined to express the degree of damage.  $D = 0$  represents the material without damage, and  $D = 1$  represents fully damaged, and  $0 < D < 1$  corresponds to various degree of damage states. After damaged, the elastic modulus and yield strength of materials can be expressed as

$$E_{dam} = E(1 - D) \quad \text{and} \quad Y_{dam} = Y(1 - D) \quad (4)$$

where  $E$  and  $Y$  are the elastic modulus and yield strength for the material without damage. The RHT model has been applied in several numerical simulations to study the penetration and perforation of concrete targets under impact (Leppänen, 2005; 2006; Tham, 2005) and the response of concrete under blasting load (Zhou et al. 2008). The major problems come from uncertainties about some of the pa-

rameters in the concrete model. However, fairly good quantitative agreements between numerical predictions and experimental results can be achieved through careful parametric analyses and model validations (Leppänen, 2006).

## 2.2 Material Model of Explosive

In this simulation, the EOS of Johns-Wilkins-Lee (JWL) is employed for TNT explosive which can be expressed as

$$P = C_1 \left( 1 - \frac{\omega}{r_1 v} \right) e^{-r_1 v} + C_2 \left( 1 - \frac{\omega}{r_2 v} \right) e^{-r_2 v} + \frac{\omega e}{v} \quad (5)$$

The JWL equation is suited for hydrodynamic of detonation product expansions to pressures down to 1 kbar. Where  $P$  is hydrostatic pressure,  $v$  is specific volume,  $e$  is specific internal energy,  $C_1$ ,  $r_1$ ,  $C_2$ ,  $r_2$  and  $\omega$  are constants determined from dynamic experiments.

After blasting, the explosive TNT will convert to ideal gas which is strengthless and will never fail.

## 2.3 Material Model of Steel

Steel material is employed in the layered slab model which will be simulated later. Linear EOS and Johnson and Cook (1985) strength model are applied to the steel material. Some parameters of the steel material are: density is 7.83; bulk modulus is 159 GPa; shear modulus is 81.8 GPa; yield stress is 792 MPa. The steel material we designed will not fail because the failure of the steel material is not focused and also no failure model can fit the damage of the steel material very well.

## 3 Simulation Results

In order to investigate some of the key aspects of concrete damage, numerical simulations are implemented by employing the suggested numerical model, the equation of state, the failure criterion, and the related parameters in Section 2.

### 3.1 Damage Process

In order to illustrate concrete slab damage mechanism under blasting loads, the calculation results of material statuses as a function of time after initiation of the explosive are presented in Figure 3. The explosive charge is 30 mm in height and 60 mm in diameter, and located on the top surface of the slab. In order to clearly express the concrete statuses, the explosive products are not fully presented in Figure 3. In the four gauge points, the damage and the stress histories are recorded in order to analyze the damage mechanism later. It can be seen that the material statuses change with time. An intense damage zone has developed near the explosive charge, and in this intense damage zone, the rock is severely crushed, and beyond this zone, the damage extent reduces progressively. Finally a crater shaped damage zone has developed, and near the slab bottom gauge 4, a small damage zone (damage variable  $D$  is about 0.3) occurs.

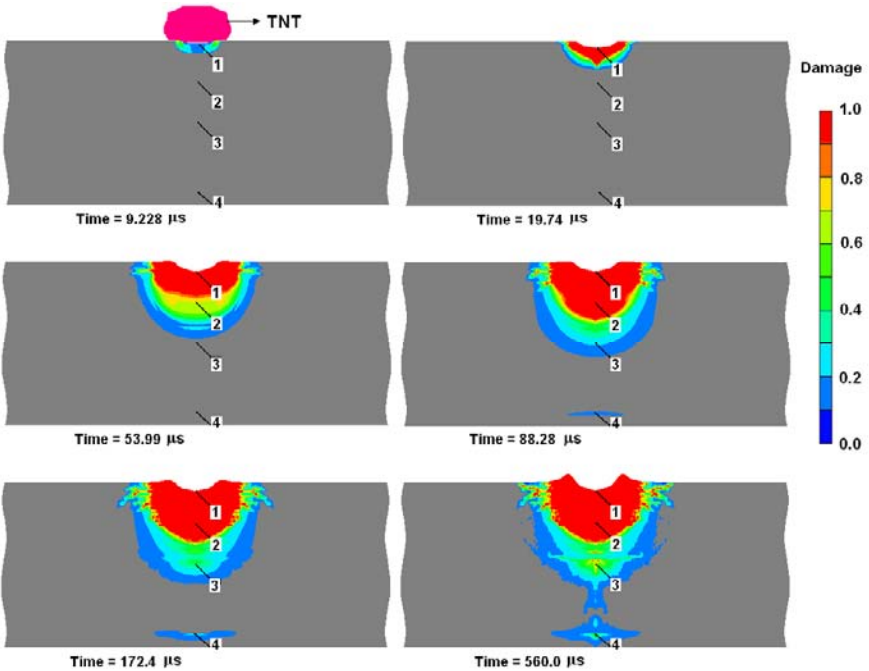


Figure 3. Material statuses as a function of time after initiation of the explosive.

### 3.2 Damage History

The damage histories in the elements containing gauges 1-4 are plotted in Figure 4. It can be seen that the damage extent reduces as the distance from the charge to the gauges increases. Gauge 1 is near the charge, the damage variable  $D$  reaches 1.0 immediately after the shock wave reached. Gauge 2 is 75 mm away from the charge, and its damage variable  $D$  reaches 1.0 in about 70  $\mu\text{s}$  after detonation. Gauge 3 is 150 mm away from the charge, and its damage variable reaches 0.573 after 532  $\mu\text{s}$  since detonation. Gauge 4 is 280 mm away from the charge and only 20 mm away from the bottom free surface, in which stress waves can reflect back resulting in tensile cracks or spalling cracks in target 4. The spalling cracks usually occur some distance away from the free boundary (Zhu et al. 2007; 2008). It should be noted that the extent of spalling would depend on the dynamic tensile strength of the target concrete and the distance traveled by the stress waves. For a very thick concrete slab or with a much higher tensile strength, it is possible not to have any spalling cracks.

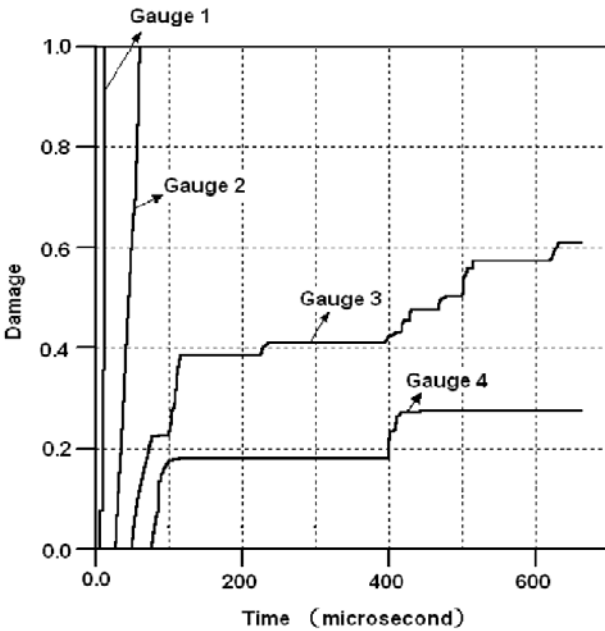


Figure 4. Calculation results of the damage histories in the elements containing targets 1-4.

### 3.3 Stress History

Figure 5 shows the curves of dynamic stresses  $\sigma_x$ ,  $\sigma_y$  and  $\tau_{12}$  versus time for the element containing gauge 2. It can be seen that both  $\sigma_x$  and  $\sigma_y$  are compressive before 60  $\mu\text{s}$  since detonation, and at the time of 24.1  $\mu\text{s}$ , both  $\sigma_x$  and  $\sigma_y$  reach their maximum values, 218.08 MPa and 549.62 MPa, respectively. The difference between  $\sigma_y$  and  $\sigma_x$  is 331.54 MPa, which is very large.  $\sigma_y$  is the stress causing from the stress wave directly impacting the concrete slab, whereas  $\sigma_x$  is the horizontal stress and it is passive. The big difference between  $\sigma_y$  and  $\sigma_x$  can induce a large shear stress according to the theory of Mohr's circle. The maximum shear stress  $\tau_{12}$  shown in Figure 5 is 169.72 MPa which is much larger than the concrete shear strength 25.2 MPa, therefore, the concrete material at gauge 2 is severely damaged in shear. From Figure 3, it can be seen that a severely damaged zone developed near the explosive charge, and this crater-shaped zone is shear crushed zone.

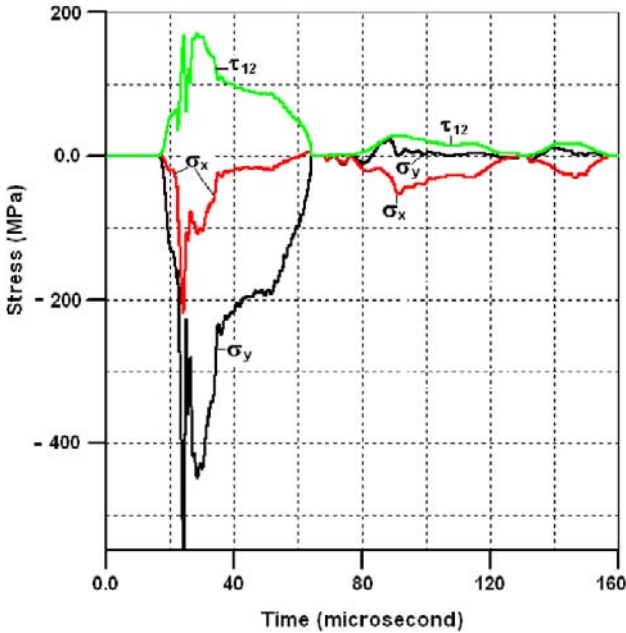


Figure 5. Relationship of the dynamic stresses (i.e. normal stress  $\sigma_x$  and  $\sigma_y$ , and maximum shear stress  $\tau_{12}$ ) versus time for the element containing target 2.

Figure 6 shows the curves of dynamic stresses  $\sigma_x$  and  $\sigma_y$  versus time for the element containing gauge 4. It can be seen that  $\sigma_y$  at the time of 78.89  $\mu\text{s}$  reaches its maximum tensile stress 31.10 MPa, which is larger than the concrete tensile strength 14 MPa, thus, the element containing gauge 4 is damaged in tension. At the time about 400  $\mu\text{s}$ , the stress  $\sigma_x$  and  $\sigma_y$  both change from compression to tension again and reach large values, which causes the element at gauge 4 to damage again. This can be confirmed from Figure 4, where after 400  $\mu\text{s}$ , the damage variable D of gauge 4 jumps up to a high level.

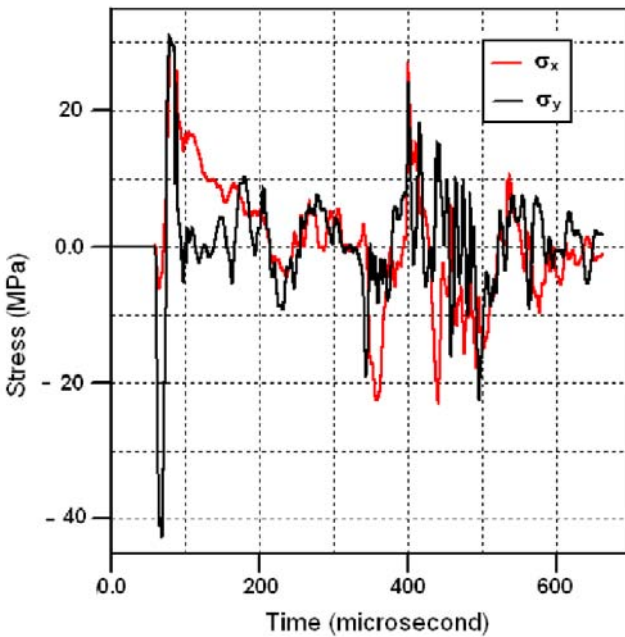


Figure 6. Relationship of the dynamic stresses (i.e.  $\sigma_x$  and  $\sigma_y$ ) versus time for the element containing target 4.

## 4 Layered Slabs

Because of the threats of terrorist attacks or explosion accidents, some concrete structures are required to have the capacity to resist blast-induced damage. A cost-effective way to resist concrete damage is to use composite slabs. The designs of

such composite slabs depend on the knowledge of detonation properties of explosive and the responses of concrete. In this study, six different layered slab numerical models, shown in Figure 7, are set up. Two concrete materials CONC35 (weak) and CONC140 (strong), and a steel material are employed as the materials of the slabs. The dimensions of all the six models are the same and they are 1200 mm in length and 300 mm in width. Model -1 shown in Figure 7 consists of only one concrete plate; model - 2 and model - 3 both consist of two concrete sublabs, but the sequences of strong layer and weak layer are different; model - 4 consists of one steel plate and two concrete sublabs; model - 5 consists of two strong concrete sublabs and one weak sublabe; and model - 6 consists of two weak sublabs and one strong sublabe.

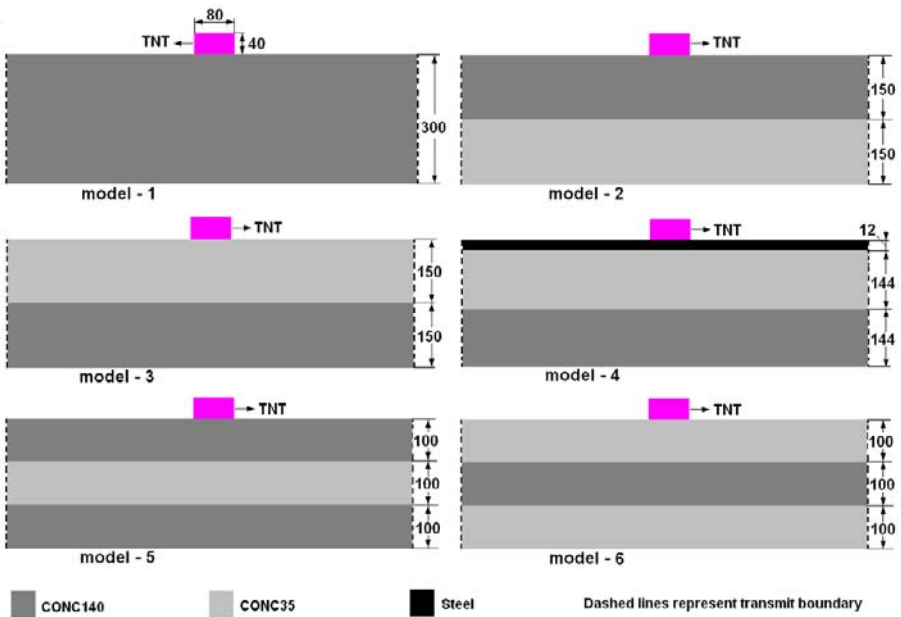


Figure 7. Six different slab models.

By employing the suggested numerical model, the equation of state, the failure criterion, and the related parameters in section 2, the numerical simulations are implemented and the results of the material damage statuses at the time of 508  $\mu$ s are presented in Figure 8. It can be seen that the difference of the damage statuses for the slabs with different layering structures are significant. The capacity to resist blast-induced damage of model - 2 is much larger than that of model - 3; comparing model - 3 with model - 4, one can find that using steel plate can reduce the concrete plate damage significantly. The damage of the third layer in model - 5 is much slighter than its counterpart in model - 6, and the spalling zone near the slab

bottom in model – 5 is smallest in all the six models, thus, the layering structure of model – 5 has the most capacity to resist blast-induced damage. Figure 8 shows that along the interfaces between layers, intense damage occurs. This is to be expected as the interfaces between layers are the natural weak surface for the layered structures.

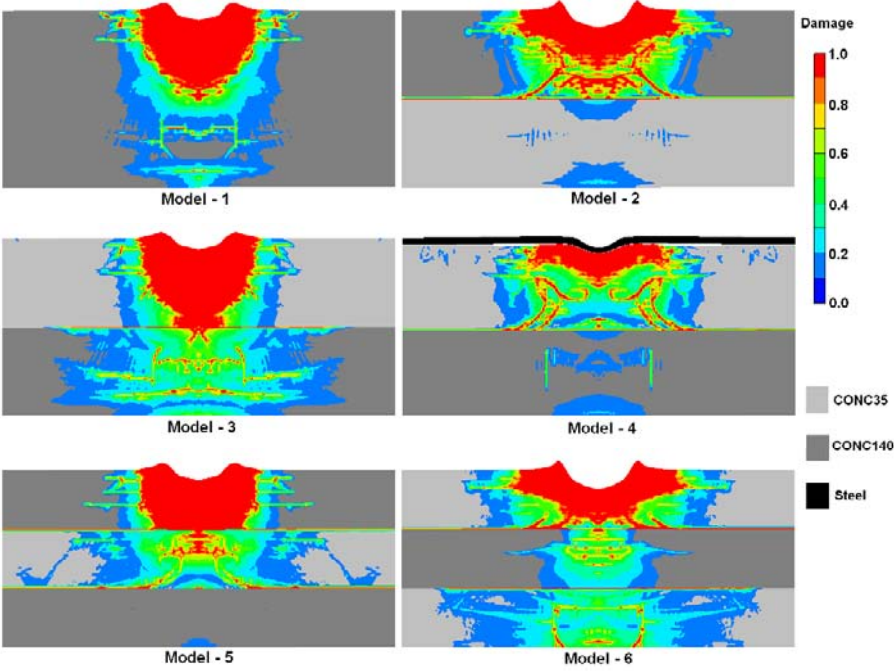


Figure 8. Material damage statuses of the six layered slabs shown in Figure7; the time is 508μs.

### 5 Conclusions

A numerical model for a concrete slab under blasting loads has been developed in this paper. By using this model, the damage statuses, damage history and stress history of a concrete slab under blasting loads are investigated. The results show that an intense damage zone ( $D=1.0$ ) develops near the explosive charge, and beyond this intense damage zone, the damage extent reduces progressively. Near the slab bottom, because of the reflection of the stress waves from the free bottom, a small damage zone may occur, depending on the stress wave’s magnitude and concrete dynamic tensile strength.

Using layers in concrete slab not only can improve slab capacity to resist blast-induced damage but also can save cement in producing concrete slabs. From Figure 8, it can be seen that the layering structure of model – 5 should be applied to the concrete structures as they are often subjected to dynamic loads.

## Acknowledgements

This work has been funded in part by Sichuan Sciences and Technology Project 2008JY0041; The Project of SRF for ROCS, SEM 2008890-19-19; NSFC-50639100; NSFC-50620130440.

## References

- David Z., Yankelevsky U., Itzhak A. (1998). Autoclaved aerated concrete behavior under explosive action. *Construction and Building Materials*, 12: 359-364.
- Gebbeken N., Greulich S., Pietzsch A. (2006). Hugoniot properties for concrete determined by full-scale detonation experiments and flyer-plate-impact tests. *International Journal of Impact Engineering*, 32: 2017-2031.
- Johnson G.R., Cook W.H. (1985). Fracture characteristics of three metals subjected to various strains, strain rates, temperatures and pressures, *Engng. Frac. Mech.*, 21: 31-48.
- Lan S., Lok T.S., Heng L. (2005). Composite structural panels subjected to explosive loading. *Construction and Building Materials*, 19: 387-395.
- Leppänen J. (2005). Experiments and numerical analyses of blast and fragment impacts on concrete. *International Journal of Impact Engineering*, 31: 843-860.
- Leppänen J. (2006). Concrete subjected to projectile and fragment impacts: Modelling of crack softening and strain rate dependency in tension. *International Journal of Impact Engineering*, 32: 1828-1841.
- Lu Y., Xu K. (2004). Modelling of dynamic behaviour of concrete materials under blast loading. *International Journal of Solids and Structures*, 41: 131-143.
- Luccioni B.M., Ambrosini, R.D., Danesi, R.F. (2004). Analysis of building collapse under blast loads. *Engineering Structures*, 26: 63-71.
- Krauthammer T. (1999). Blast-resistant structural concrete and steel connections. *International Journal of Impact Engineering*, 22: 887-910.
- Razaqpur A.G., Tolba A., Contestabile E. (2007). Blast loading response of reinforced concrete panels reinforced with externally bonded GFRP laminates. *Composites, Part B*, 38: 535-546.
- Riedel W. (2000). Beton unter dynamischen Lasten: Meso- und makromechanische. Doctoral thesis, Universität der Bundeswehr. Munchen, Freiburg, Germany.
- Riedel W., Wicklein M., Thoma K. (2008). Shock properties of conventional and high strength concrete: Experimental and mesomechanical analysis. *International Journal of Impact Engineering*, 35: 155-171.
- Schenker A., Antebya I. (2008). Full-scale field tests of concrete slabs subjected to blast loads. *International Journal of Impact Engineering*, 35: 184-198.
- Silva P.F., Lu B. (2007). Improving the blast resistance capacity of RC slabs with innovative composite materials. *Composites, Part B*, 38: 523-534.
- Tham C.Y. (2005). Reinforced concrete perforation and penetration simulation using AUTODYN-3D. *Finite Elements in Analysis and Design*, 41: 1401-1410.

- Xu K., Lu Y. (2006). Numerical simulation study of spallation in reinforced concrete plates subjected to blast loading. *Computers and Structures*, 84: 431-438.
- Zhou X.Q., Kuznetsov V.A., Hao H., Waschl J. (2008). Numerical prediction of concrete slab response to blast loading, *Int. J. Impact*, doi: 10.1016/j.ijimpeng.2008.01.004.
- Zhu Z., Mohanty B., Xie H. (2007). Numerical investigation of blasting-induced crack initiation and propagation in rocks. *Int. J. Rock Mech. Min. Sci.*, 44: 412-424.
- Zhu Z., Xie H., Mohanty B. (2008). Numerical investigation of blasting-induced damage in cylindrical rocks. *Int. J. Rock Mech. Min. Sci.*, 45: 111-121.

# Research on Analysis Method for Concrete Column to Resist Vehicle Bomb

Jianyun Sun<sup>1\*</sup>, Guoqiang Li<sup>2,3</sup>, Chunlin Liu<sup>1,2</sup> and Suwen Chen<sup>2</sup>

<sup>1</sup>K&C Protective Technologies Pte Ltd, 159361, Singapore

<sup>2</sup>College of Civil Engineering, Tongji University, Shanghai 20092, China

<sup>3</sup>State Key Laboratory for Disaster Reduction in Civil Engineering, Shanghai 20092, China

**Abstract.** The analysis method about concrete column to resist vehicle bomb is proposed in this paper. The example how to use this method is shown using LS-DYNA software. The loading rate and boundary condition's effects on the analysis result are studied. The concrete columns can not be destroyed totally because of the vehicle bomb's blast load, there is the residual capacity in the column after the blast loading. The method provided in this paper is suitable to study the concrete's residual capacity and damage factor because of vehicle bomb. The calculated residual capacity can be affected by the loading rate, but the damage factor is almost the same if the loading rate is kept unchanged when the original capacity and the residual capacity are calculated. The simple single column model can be used when studying the column to resist vehicle bomb. The study result in this paper can be taken as the reference for analyzing and researching the column to resist vehicle bomb.

**Keywords:** vehicle bomb, blast loading, concrete column, damage factor

## 1 Introduction

The vehicle bombs are the main attack method used by terrorist since 1980s, which make thousands of people injured and died. The building's progressive collapse due to blast loading is the main issue that can kill most of the persons in the building. The Oklahoma City Bomb (Corley, et al., 1998; Mlkar, et al., 1998; Sozen, et al., 1998; Norville, et al., 1999) and the 911 event (Bažant and Zhou, 2002; Corley, 2004) are two well-known examples. The key column or structure's critical members' failure under blast loading can make the whole structure be progressive collapse. So the key structure's elements such as the columns designed to resist blast loading is an important method for structure to resist terrorist attack.

---

\* Corresponding author, e-mail: sun.jian.yun@kcpt.com.sg

According to Europe and American design codes, it is necessary to take some measures in design process to prevent the progressive collapse for critical building. One well-known and widely used code is “UFC 4-023-03 Design of Buildings to Resist Progressive Collapse” (UFC, 2005), the another is “GSA Progressive Collapse Analysis and Design Guidelines for New Federal Office Buildings and Major Modernization Projects” (GSA, 2003). In these two design codes, the critical column is assumed to be destroyed totally and suddenly. Based on the assumption mentioned above, dynamic or equivalent static method are used to calculate the whole structure’s response and capacity to resist progressive collapse.

Actually the concrete columns can not be destroyed totally on the blast load. There is the residual capacity in the column after resisting the blast loading, which is very useful to protect the whole building from progressive collapse. So it is necessary to consider residual capacity in design the structure to prevent progressive collapse.

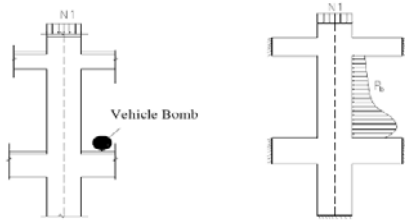
In this paper, the analysis method about concrete column to resist vehicle bomb is proposed. The method provided in this paper is suitable to study the concrete’s residual capacity and damage factor because of vehicle bomb. The example how to use this method is shown using LS-DYNA software. The conditions affected the simulation result are discussed.

The study results in this paper can be taken as the reference for analyzing and researching the column to resist vehicle bomb.

## 2 Analysis Method for Concrete Column to Resist Vehicle Bomb

The analysis method of concrete column to resist vehicle bomb is shown in Figure 1, Figure 2 and Figure 3.

Dislike the earthquake, there is serious local dynamic response for structure under the vehicle bomb’s blast loading. The blast loading on the column induced by vehicle bomb is uneven. The overpressure near the blast charge is bigger than that far away from the blast charge as shown in Figure 1. In the simulation model, the different blast loading curves must be used because of the uneven blast loading on the column.



(a) Location of vehicle bomb (b) Blast load

Figure 1. Demonstration of column under vehicle bomb’s blast loading

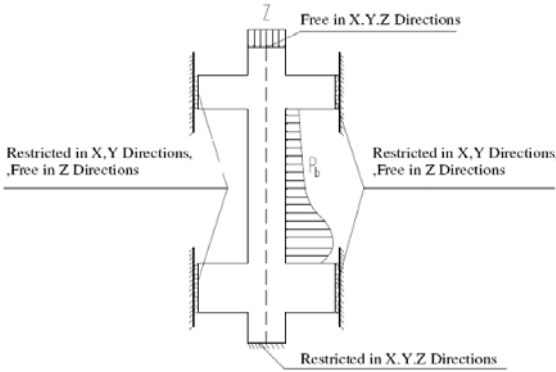


Figure 2. Boundary condition of analysis model

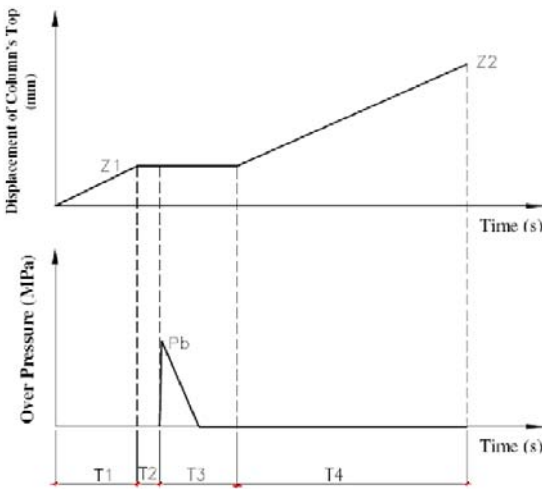


Figure 3. Loading curve used in the simulation

In order to consider the beam's restriction to the column, part lengths of beams are built up in the model. The ends of beam are restricted in horizontal direction and are free in vertical direction. The bottom of column is restricted, and the top of column is free as shown in Figure 2.

At the beginning of simulation process, the column's top displacement is increased from 0 to  $Z_1$  which is to simulate the column's original axial force induced by the dead load and live load. As shown in Figure 3, the duration is  $T_1$  when the column top's displacement is from 0 to  $Z_1$ . In the duration  $T_2$ , the column top's displacement is kept unchanged in order to get the axial force in the

column stable. The blast loading is added on the column in the duration T3, the T3 is longer than the actual blast load’s duration usually. In the duration T4, the column top’s displacement is increased to Z2 until the column is failure. The loading curve is shown and explained in Table 1 and Figure 3.

The residual capacity of column under vehicle bomb blast loading can be got from the curve of column’s axial force which is provided from the LS-DYNA simulation result. Assuming the maximum value in the column’s displacement-axial force curve is N1 which is also the residual capacity of the column. The column’s original capacity N0 can be got by the above method too. The difference between calculating the original capacity and calculating the residual capacity is that there is not blast loading in the duration T3. So, the column’s damage factor because of vehicle bomb blast loading can be defined as  $\omega = 1 - (N1 / N0)$ .

Table 1. Description of loading curve

Time Duration	Loading Curve Phases	Description
T1	Increasing the column’s top displacement from 0 to Z1	In order to simulate the original axial force in the column induce by the dead and live loading
T2	Keeping the column’s top displacement unchanged	In order to get the axial force in the column to be stable
T3	Applying blast load on the column	Analysis the column’s response under the blast loading
T4	Increasing the column’s top displacement to Z2	In order to calculate the residual capacity N1 of the column

### 3 Demonstration of Analysis Method’s Usage

In order to demonstrate the analysis method introduced above, a simulation model is made up using LS-DYNA soft ware (refer to Figure 4). The details of column’s properties are specified in Table 2 and Figure 5.

In the simulation model, \*MAT\_CONCRETE\_DAMAGE\_REL3 is used to simulate the concrete, the \*MAT\_PIECEWISE\_LINEAR\_PLASTICITY is used to simulate the rebar under blast loading separately (Hallquist, 1988; Livermore Software Technology Corporation, 2003; Malvar, 1997; Malvar, 2002). The simulation results under different conditions are listed in Table 3.

According to the analysis method introduced before, the column’s original capacity is N0=175000KN (refer to Figure 6), and the residual capacity of column under blast loading is N1=80000KN (refer to Figure 7). So the damage factor of column under this kind of vehicle bomb is  $\omega = 1 - (N1 / N0) = 0.543$  (refer to CASE-2 in Table 3).

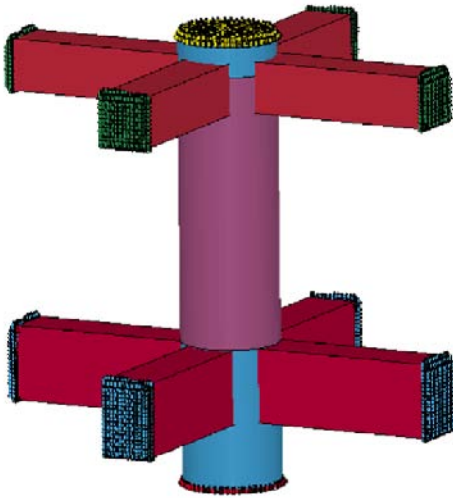
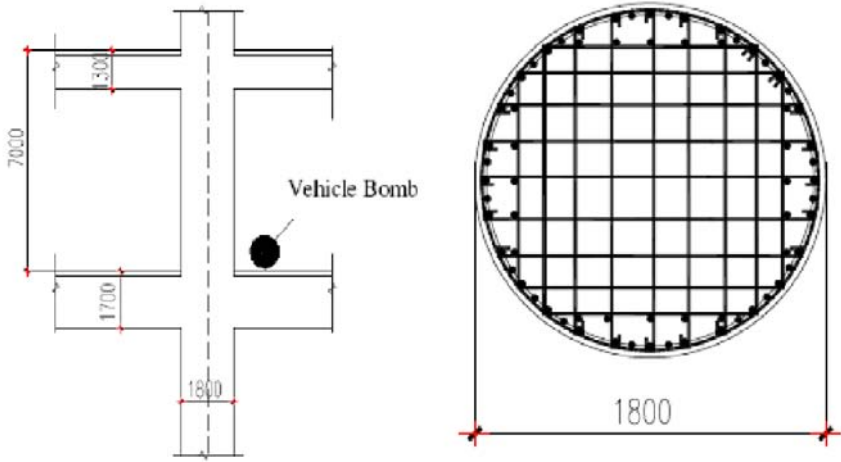


Figure 4. LS-DYNA analysis model (1)-Beam-Column Model

Table 2. Material properties of concrete column

Material Name	Material Model in LS-DYNA	Properties of Materials
Hoop	*MAT_PIECEWISE_LINEAR_PLASTICITY	Density $\rho = 78.50 \text{ KN/m}^3$ ; Modulus of Elastic $E=200000.0 \text{ MPa}$ ; Poisson Ratio $\nu = 0.30$ ; Yield Strength $\sigma_y = 335.0 \text{ MPa}$
Rebar	*MAT_PIECEWISE_LINEAR_PLASTICITY	Density $\rho = 78.50 \text{ KN/m}^3$ ; Modulus of Elastic $E= 200000.0 \text{ MPa}$ ; Poisson Ratio $\nu = 0.30$ ; Yield Strength $\sigma_y = 400.0 \text{ MPa}$
Concrete (C60)	*MAT_CONCRETE_DAMAGE_REL3	Density $\rho = 24 \text{ KN/m}^3$ ; Compress Strength $\sigma_c = 38.5 \text{ MPa}$



(a) Column elevation

(b) Column section

Figure 5 Details of the concrete column

Table 3 Simulation results in different conditions (continued)

Case Number	T1 (ms)	T2 (ms)	T3 (ms)	T4 (ms)	Z1 (mm)	Z2 (mm)
CASE-1	100	0	0	300	5.1	100
CASE-2	100	50	200	300	5.1	100
CASE-3	100	0	0	1900	5.1	40
CASE-4	100	50	200	4650	5.1	97
CASE-5	100	50	200	300	5.1	100
CASE-6	100	50	200	350	5.1	142
CASE-7	100	50	200	350	5.1	130

Table 3 Simulation results in different conditions

Case Number	Blast Loading	Analysis Model	N0 (KN)	N1 (KN)	Damage Factor $\omega$
CASE-1	NO	Model 1	175000	—	—
CASE-2	YES	Model 1	—	80000	0.543
CASE-3	NO	Model 1	165000	—	—
CASE-4	YES	Model 1	—	77000	0.533
CASE-5	YES	Model 2	—	82000	0.531
CASE-6	YES	Model 3	—	76000	0.566
CASE-7	YES	Model 4	—	81000	0.537

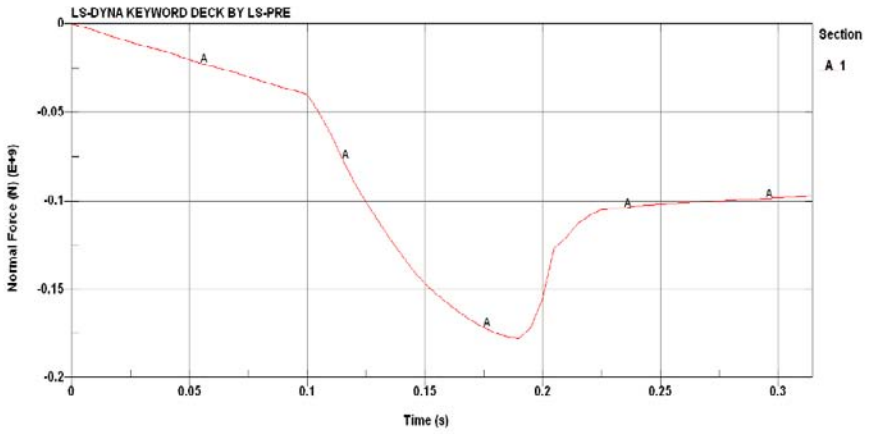


Figure 6. Time history curve of column's axial force (CASE-1)

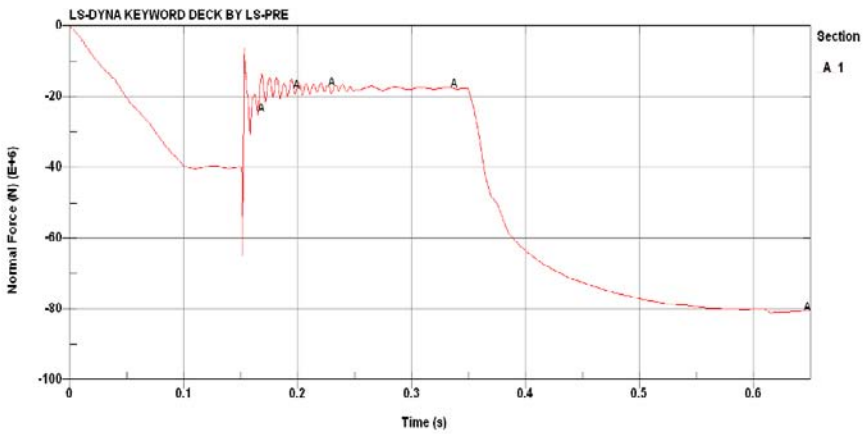


Figure 7. Time history curve of column's axial force (CASE-2)

#### 4 Effect of Loading Rate on Analysis Result

The significant difference of concrete and steel under the dynamic loading from that of under static loading is that the strength of steel and concrete under dynamic loading is more than that of under static loading. This is also called the strain-rate

effect of steel and concrete. So the capacity of column is changed because of the different loading rate. The loading rate is controlled by the rate of column top's displacement in the analysis model in this paper.

In order to consider the effect of strain rate, the CASE-3 and CASE-4 are analyzed. The other conditions in CASE-3 and CASE-4 are similar to CASE-1 and CASE-2 except that the duration T4 and displacement Z2 are different as shown in Table 3. The loading rate in CASE-3 and CASE-4 is about 20 (mm/s), which is smaller than 320 (mm/s) in the CASE-1 and Case2. From the simulation results shown in Figure 8, Figure 9 and Table 3, it can be seen that the original capacity of column in CASE-3 is  $N_0=165000\text{KN}$  which is smaller than the  $N_0=175000\text{KN}$  in CASE-1. The residual capacity of column in Case 4 is  $N_1=77000\text{KN}$  which is also smaller than the  $N_1=80000\text{KN}$  in CASE-2. But the damage factor deduced from Case 3 and Case 4 is  $\omega=0.533$  which is similar to the  $\omega=0.543$  deduced from Case 1 and Case 2.

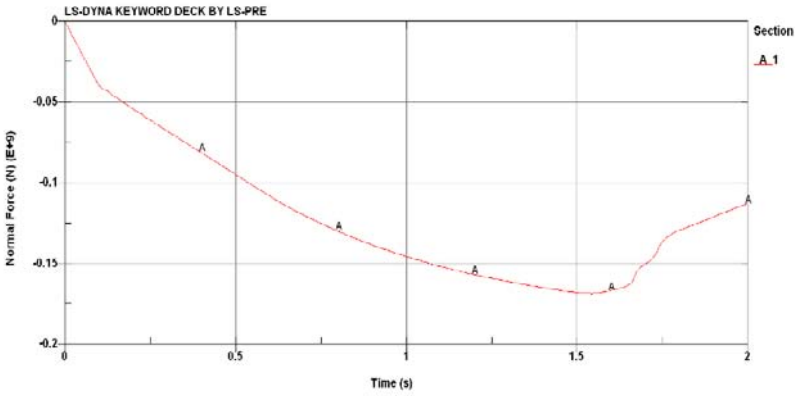


Figure 8. Time history curve of column's axial force (CASE-3)

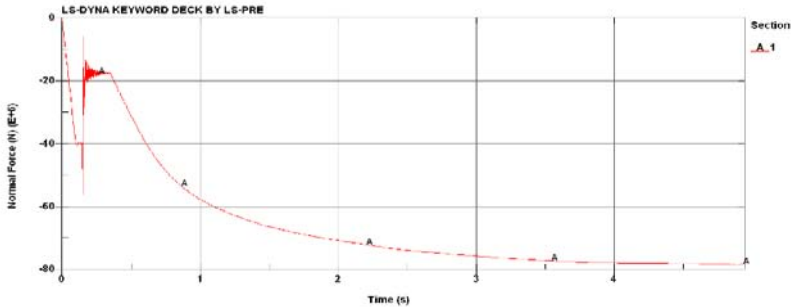


Figure 9. Time history curve of column's axial force (CASE-4)

## 5 Boundary Conditions' Effects on Analysis

The Model 1 shown in Figure 4 includes parts of column which is complicated than the simple single Model 2 shown in Figure 10, but is simpler than the sub-frame Model 3 shown in Figure 11. In order to research the simulation result because of the different condition, some different analysis models are studied in the paper as shown in the Table 3 and Table 4.

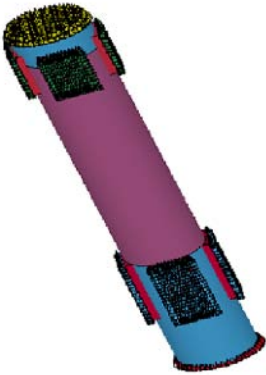


Figure 10. LS-DYNA analysis model (2)-Single Column Model

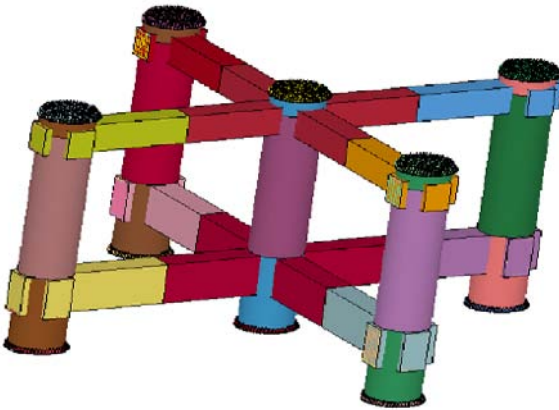


Figure 11. LS-DYNA analysis model (3)-Sub-Frame Model

The simulation results are shown in Figure 6,7,8,9,12,13,14 and summarized in Table 3 for CASE-1, CASE-2, CASE-3, CASE-4, CASE-5, CASE-6 and CASE-7.

The sub-frame model is used in CASE-5, the displacements are applied on the top of all columns until they are failure, so the CASE-5 is most similar to the actual condition. In CASE-6, the displacement is only applied on the top of column which will resist the vehicle bomb blast loading. The simple single column model is used in the CASE-7 which is often used in the actual project analysis in order to save the analysis time.

Table 4. Description of analysis model

Model Types	Description	Reference
Model 1	The beam-column model. The length of beam connected to column is about 3500 mm which is used to simulate the restriction of beam to column	Figure 4
Model 2	Sub-frame model. The displacement is applied on the top of all columns at the same time until the columns is failure.	Figure 11
Model 3	Sub-frame model. The displacement is only applied on the top of column which is under the blast loading until the column is failure	Figure 11
Model 4	Simply single column model.	Figure 10

From the analysis results summarized in Table 3, it can be seen that the damage factors deduced from CASE-2, CASE-5 and CASE-7 are very similar, and the discrepancies of them are less than 3%. But the damage factor in CASE-6 is larger than the others. The reason is that there will be large tension in the beams connected with the analyzed column when the column is close to be failure in CASE-6, the tension force have a bigger effect on the column’s residual capacity as shown in Figure 13, which will make the column’s damage factor analyzed be more.

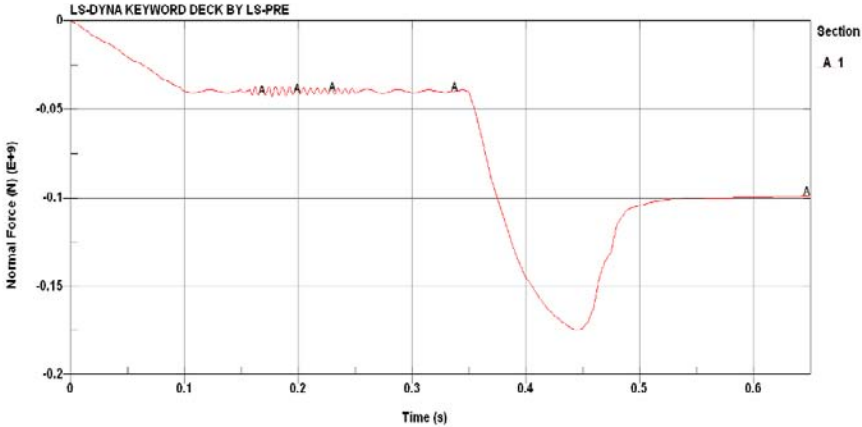


Figure 12. Time history curve of column’s axial force (CASE-5)

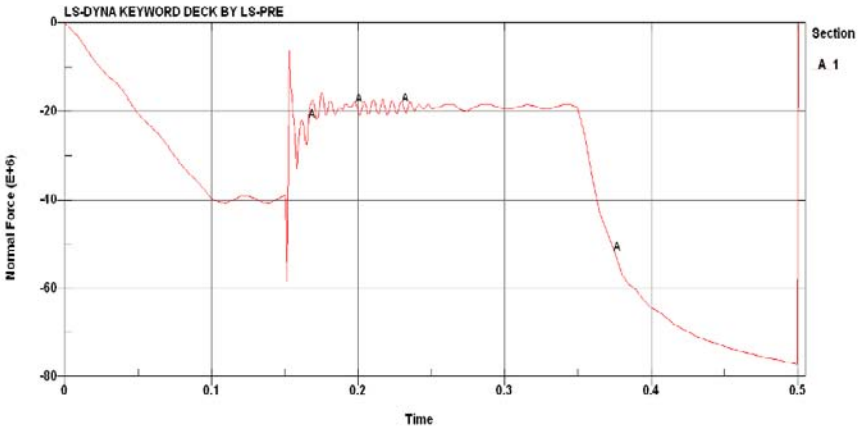


Figure 13. Time history curve of column's axial force (CASE-6)

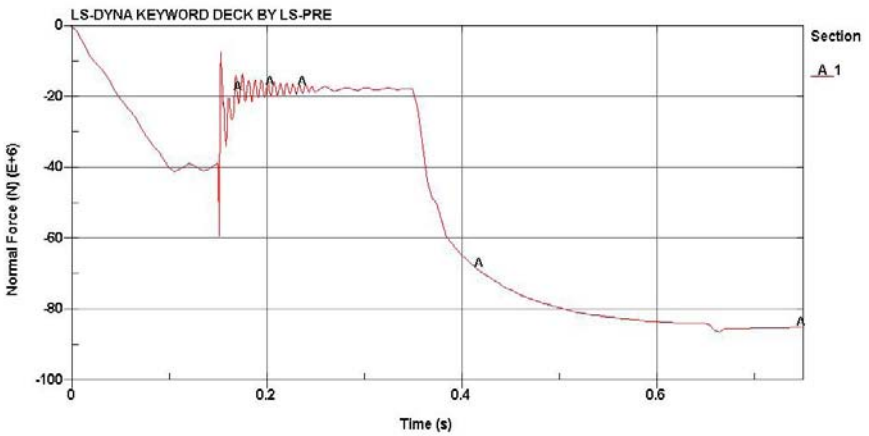


Figure 14. Time history curve of column's axial force (CASE-7)

## 6 Conclusions

In this paper, a new analysis method used to study the concrete column to resist vehicle bomb is developed. The example how to use this method is demonstrated. The loading rate and boundary condition's effects on the analysis result are studied.

The findings from this study may be concluded as follows:

1. The concrete columns can not be destroyed totally under vehicle bomb, there is the residual capacity in the column after resisting the blast loading.
2. The method introduced in this paper is suitable to calculate the concrete's residual capacity and damage factor because of vehicle bomb.
3. The loading rate has effects on the concrete column's residual capacity because of blast loading. But the damage factors are almost the same if the same loading rate is used when the column's residual capacity and the original capacity are analyzed.
4. The concrete column can be simplified as the simple single column when studying the column to resist blast loading.

## References

- Bazant Z. P. and Zhou Y. (2002). Why Did the World Trade Center Collapse – Simple Analysis. *ASCE: Journal of Engineering Mechanics*, 128(1):2-6.
- Corley W. G. (2004). Lessons Learned on Improving Resistance of Building to Terrorist Attacks. *ASCE: Journal of Performance of Constructed Facilities*, 18(2):68-78.
- Corley W. G., Mlaker P. F., et al. (1998). The Oklahoma City Bombing: Summary and Recommendations for Multihazard Mitigation. *ASCE: Journal of Performance of Constructed Facilities*, 12(3):100-112.
- GSA. (2003). Progressive Collapse Analysis and Design Guidelines for New Federal Office Buildings and Major Modernization Projects. Us General Services Administration.
- Hallquist, J. Q. (1988). LS-DYNA Theoretical Manual. California, USA: Livermore Software Technology Corporation.
- Livermore Software Technology Corporation (2003). LS-DYNA Keyword User's Manual (970V). California, USA: Livermore Software Technology Corporation.
- Malvar L. J., Morrill K. B., et al. (2002). Numerical Modeling of Concrete Confined by Fiber. *Mechanical Sciences*, (44):1985-1998.
- Malvar L. J., and Crawford J. E. (1997). A Plasticity Concrete Material Model for DYNA3D. *Int. J. Impact.*, 19(9-10):847-873.
- Mlaker P. F., Corley W. G., et al. (1998). The Oklahoma City Bombing: Analysis of Blast Damage to the Murrah Building. *ASCE: Journal of Performance of Constructed Facilities*, 12(3):113-119.
- Norville H. S., Harvill N., et al. (1999). Glass-Related Injuries in Oklahoma City Bombing. *ASCE: Journal of Performance of Constructed Facilities*, 13(2):50-56.
- Sozen M. A., Thornton C. H., et al. (1998). The Oklahoma City Bombing: Structure and Mechanisms of the Murrah Building. *ASCE: Journal of Performance of Constructed Facilities*, 12(3):120-136.
- United Facilities Criteria (2005). UFC 4-023-03: Design of Buildings to Resist Progressive Collapse. The United Department of Defense.

# Numerical Analysis of Blast Loads inside Buildings

Xiaojing Yin<sup>1\*</sup>, Xianglin Gu<sup>1</sup>, Feng Lin<sup>1</sup> and Xinxin Kuang<sup>1</sup>

<sup>1</sup>Department of Building Engineering, Tongji University, Shanghai 200092, P.R. China

**Abstract.** The determination of pressure produced by blast loads was carried out with the aid of hydrocode LS-DYNA. The simulations of the blast wave both in air and encountering a solid target were discussed. Numerical results were compared with those obtained from the empirical expressions for different scaled distances. The material parameters of explosive and air were studied. In order to accurately evaluate the incident pressure distributions within building structures, the Arbitrary Lagrangian Eulerian (ALE) coupling was adopted to simulate the blast loading and its interaction with the structure. The blast wave was predicted by the Jones-Wilkins-Lee (JWL) equation of state for high explosives. The effect of mesh size on pressure evaluation and the appropriate boundary conditions were also studied. The results show that the material parameters and the numerical algorithm are applicable for the blast loads determination.

**Keywords:** blast load, pressure distribution, wave reflection, numerical analysis

## 1 Introduction

The blast phenomenon is a large-scale, rapid and sudden release of energy, and can damage or destroy building structures. In recent years, blast loads have received more and more attention due to different accidental or intentional events related to important structures all over the world. Many researches have been done on structural blast protection and the responses of building structures under explosive loads (Baker et al., 1983).

In order to achieve these objectives, the assessment of blast loads on structures is the prior stage. The accurate evaluation of the pressure distribution on structures is required for the analysis. Unlike other kinds of loads, the blast wave propagates within a very short time, and experiments have shown that the blast phenomena is quite complex involving some important effects such as multiple blast wave reflections, the Mach effect, rarefactions, and the negative phase of the blast wave.

---

\* Corresponding author, e-mail: rex.yxj@gmail.com

Simplified analytical and semi-empirical techniques usually ignore such phenomena. To precisely evaluate the shock propagation around a structure, numerical models have to be used (Smith and Rose, 2002).

Numerical simulations can help to minimize the number of required tests that are very costly, and also help to interpret test results. Once simulations are validated by test results, it can be used as an analysis or a design tool for the responses investigation of building structures subjected to blast loads as well as the improvement or optimization of structural systems.

The distribution of pressures generated by a high explosive charge is described in this paper. The effect of mesh size is also addressed in this paper.

## 2 Blast Wave Propagation

When a high explosive is detonated, a blast wave is generated. It can be described by a sudden pressure increase at the shock front, followed by a quasi-exponential decay back to ambient pressure and a negative phase in which the pressure is less than ambient pressure as shown in Figure 1.

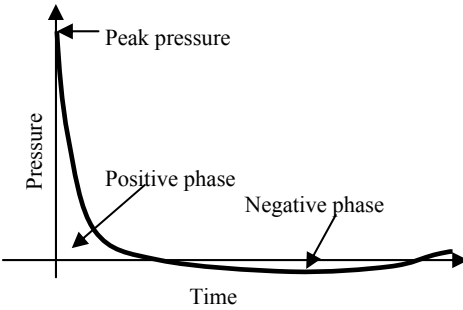


Figure 1. Blast wave pressure – time history curve

All blast parameters are primarily dependent on two factors: the amount of released energy of detonation and the distance from the explosion. A universal normalized description of the blast effects can be given by scaling distance relative to  $(E/p_0)^{1/3}$  and scaling pressure relative to  $p_0$ , where  $E$  is the energy release, and  $p_0$  is the ambient pressure. The most widely used approach for blast wave scaling is Hopkinson's law which establishes that similar explosive waves are produced at identical scaled distances when two different charges of the same explosive and with the same geometry are detonated in the same atmosphere (Mays and Smith, 1995). Thus, any distance  $R$  from explosive charge can be transformed into a characteristic scaled distance  $Z$  shown in Equation 1.

$$Z = R / W^{1/3} \quad (1)$$

where  $W$  is the explosive charge mass expressed in kilograms of TNT. The use of  $Z$  allows a wide range of situations. By using the scaled distance  $Z$ , the free air blast overpressure can be expressed as Equation 2 conveniently (Henrych, 1979).

$$\begin{cases} \Delta p_s = \frac{1379.96}{Z} + \frac{543.26}{Z^2} - \frac{35.03}{Z^3} + \frac{0.613}{Z^4} \quad (\text{kPa}), & 0.05 \leq Z \leq 0.3 \\ \Delta p_s = \frac{607.40}{Z} - \frac{31.99}{Z^2} + \frac{209.12}{Z^3} \quad (\text{kPa}), & 0.3 \leq Z \leq 1.0 \\ \Delta p_s = \frac{64.92}{Z} + \frac{397.17}{Z^2} + \frac{322.44}{Z^3} \quad (\text{kPa}), & 1.0 \leq Z \leq 10 \end{cases} \quad (2)$$

Other researchers also present different equations for the determination of blast overpressure (Baker et al., 1983), which can be illustrated in Figure 2.

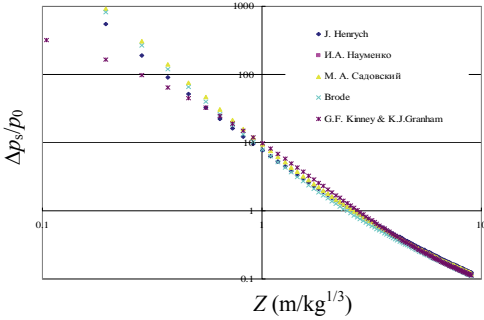


Figure 2. Blast overpressure under different scaled distances

When the blast waves encounter an infinite large wall on which they impinge at zero angle of incidence, they are normally reflected. All flow behind the wall is stopped and the pressures are considerably greater than the incident overpressure.

The peak reflected overpressure  $\Delta p_r$  can be obtained from Rankine-Hugoniot relationships for an ideal gas (Equation 3).

$$\Delta p_r = 2\Delta p_s + \frac{6\Delta p_s^2}{\Delta p_s + 7p_0} \quad (3)$$

where  $\Delta p_s$  is the overpressure in free air,  $p_0$  is the ambient atmosphere pressure.

For angles of incidence between  $0^\circ$  and  $90^\circ$ , either regular or Mach reflection occurs depending on incident angle and shock strength. The evaluation of reflected pressures resulting from multiple reflections on surfaces with different incidence angles is rather complicated and difficult to perform with empirical equations. In this case, the use of numerical methods is more appropriate.

### 3 Numerical Analysis

The numerical analysis was carried out using the finite element program LS-DYNA, which uses finite difference, finite volume, and finite element techniques to solve non-linear problems in solid, fluid and gas dynamics. It is particularly suited to the modeling of impact, blast and explosion events.

There are two key points during the numerical simulation: one is the determination of material parameters, and the other is the adoption of the computational method for the blast wave propagation as well as the interaction between the wave and the solid objects.

In this paper, two situations were treated. The first one is dealing with the propagation of the air blast wave in free space. The second concerns the reflection of the shock wave by a rigid wall. In both cases, a spherical high explosive TNT is surrounded by air and the ignition point is placed at the centre of the explosive.

#### 3.1 Computational Model

When the spherical explosive charge detonates in an infinite air domain, a gas bubble forms and expands. Consequently, air elements are pushed in front of the bubble. A high velocity shock front departs from the ignition point to the surrounding air. In order to simulate such phenomenon, the air and explosive were modeled by 1/8th of sphere with three symmetric planes.

The ignition point is placed at the centre of the sphere. The spherical explosive charge is surrounded with the air mesh such that there is one-to-one node match at the boundary between the explosive model and the air models (Figure 3).

According to the expansion characteristic of detonation, finer mesh resolution would be required for the explosive element and the air elements near the spherical charge.

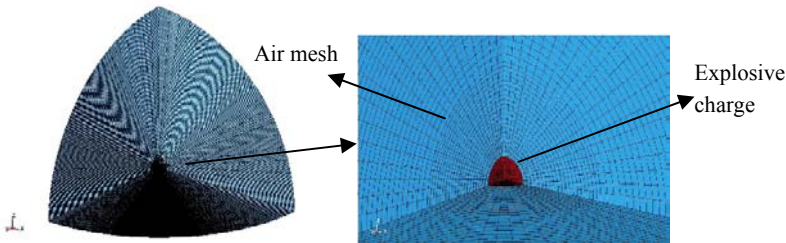


Figure 3. Computational model of blast wave free propagation

When investigating the reflected shock wave, the rigid wall should be introduced into the finite element model, as shown in Figure 4.

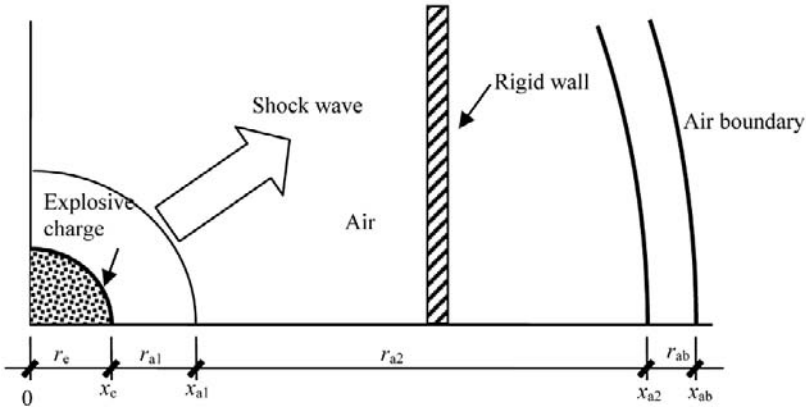


Figure 4. Computational model of blast wave encounter a rigid wall

### 3.2 Material Parameters

There are several materials need to be considered when studying the blast phenomenon: the explosive charge and the air.

The numerical model of material consists of two parts: the characteristic parameters and the equation of state (EOS), which can describe the relationship among the volume, energy and pressure of detonation products.

Air is modelled with 8 node finite elements using the hydrodynamic material model. The model requires an equation of state, density, and pressure cut-off and viscosity coefficient to be defined. The viscosity and pressure cut-off are set to zero, because pressure cannot be negative and the viscosity forces are negligible. The ideal gas law is used as the equation of state for air. This polytropic equation of state is given by considering the general linear polynomial equation of state (Equation 4).

$$p = C_0 + C_1\mu + C_2\mu^2 + C_3\mu^3 + (C_4 + C_5\mu + C_6\mu^2) E \tag{4}$$

For ideal gas, this equation can be reduced using appropriate coefficients ( $C_0 = C_1 = C_2 = C_3 = C_6 = 0$ ,  $C_4 = C_5 = \gamma - 1$ ), and the pressure is

$$p = (\gamma - 1) E \rho / \rho_0 \tag{5}$$

where  $\mu = \rho / \rho_0 - 1$ ,  $\rho_0$  and  $\rho$  are the initial and current densities of air, and  $E$  is the specific internal energy and  $\gamma$  is the ratio of specific heats.

The parameters adopted in this paper are listed in Table 1.

Table 1. Parameters of air

$\rho$ (g·cm <sup>-3</sup> )	$C_0$ (×10 <sup>11</sup> Pa)	$E_0$ (×10 <sup>11</sup> Pa)
1.29×10 <sup>-3</sup>	0	2.5×10 <sup>-6</sup>

$C_0$  is the parameter in EOS,  $E_0$  is the internal energy of air.

The explosive material model requires density  $\rho$ , detonation velocity  $v_d$ , Chapman-Jouguet pressure  $p_{CJ}$ , and an equation of state for pressure. Chapman-Jouguet pressure generally refers to the detonation pressure, which is somewhat lower than the initial shock front pressure. Among various types of equations, Jones-Wilkins-Lee (JWL) EOS shown in Equation 6 is widely used because of its simplicity and accuracy.

$$p = A \left( 1 - \frac{\omega}{R_1 V} \right) e^{-R_1 V} + B \left( 1 - \frac{\omega}{R_2 V} \right) e^{-R_2 V} + \frac{\omega E_0}{V} \tag{6}$$

where  $p$  is the pressure,  $V$  is the specific volume,  $E_0$  is the internal energy,  $A$ ,  $B$ ,  $R_1$ ,  $R_2$ , and  $\omega$  are constants listed in Table 2.

Table 2. Parameters of explosive

$\rho$ (g·cm <sup>-3</sup> )	$v_d$ (cm·μs <sup>-1</sup> )	$p_{CJ}$ (×10 <sup>11</sup> Pa)	$A$ (×10 <sup>11</sup> Pa)	$B$ (×10 <sup>11</sup> Pa)	$R_1$	$R_2$	$\omega$	$E_0$ (×10 <sup>11</sup> Pa)
1.63	0.700	0.281	3.712	0.0374	4.15	0.90	0.35	0.10

The high explosive process is divided in two stages, the detonation process, and the interaction between the produced gas and the surrounding air. The detonation process consists of burning effects and propagation of reactive wave with constant velocity inside the explosive, this process is very fast. It only takes few microseconds for the explosive to be burned. Two different detonations can be used, programmed burn based on time, or compression burned where detonation is based on material compression, and the former is adopted in the following numerical tests. After the completion of the detonation process, the interaction process takes place. A produced gas with high pressure and temperature expands outward by generating a pressure wave.

### 3.3 ALE Method

As mentioned above, the explosion is a complex phenomenon, which requires good finite element modelling techniques. The blast shock wave and air are fluids

which are especially difficult to model because they undergo large deformations, and element shapes and sizes can change considerably.

Classical Lagrangian finite element methods cannot resolve such large deformations very accurately. The ALE formulations can overcome the difficulties due to large mesh distortion. For explosion problem, an element may contain one or two different materials, air and gas produced from explosive detonation. The ALE is a method allowing the finite mesh to move independently from the material flow and where each element in the mesh can contain a mixture of two or more different materials.

### 3.4 Free Field Explosion

In order to study the free propagation of blast waves in air, 7 numerical tests have been studied by changing the explosive weight and the distance from the target to the ignition point. Flow out of air was allowed in all the model borders, so that the infinite air space can be simulated. As mentioned above, the initial internal energy of the air is non-zero, so the air can leak out of the air boundary. To avoid such phenomenon, 1 atmosphere pressure is applied on the air boundary.

Numerical results for the peak overpressure related to the ambient pressure  $p_s/p_0$  are compared with those obtained with empirical equations for different scaled distances from the explosive charge (Figure 5).

The result shows good agreement among numerical and empirical results.

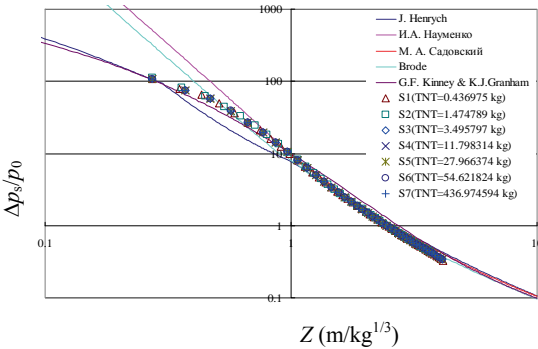


Figure 5. Comparison among numerical tests and empirical methods

The accuracy of predictions and measurements in the near field is lower than in the far field, probably due to the complexity of blast phenomena.

The mesh size effect upon the accuracy of numerical simulation is studied through 5 numerical tests (Table 3).

Table 3. Numerical tests for the study of mesh size effect

Test number	S1-1	S1-2	S1-3	S1-4	S1-5
Mesh size (cm)	1.0	1.5	2.0	3.0	6.0

The TNT weight is 436.98 g.

The investigation for the blast pressure at the same scaled distance with different mesh sizes shows that 2.0 cm is accurate enough for the blast loads evaluation (Figure 6).

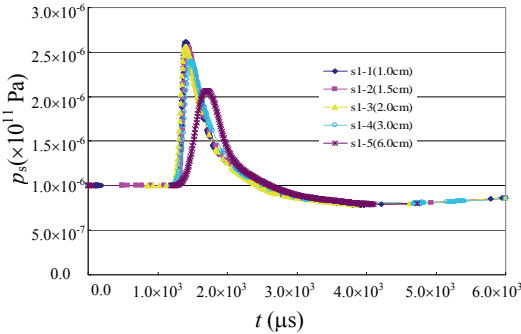


Figure 6. Pressure-time history curves under different mesh sizes

The time cost for computing increase significantly with the decrease of mesh size as shown in Figure 7.

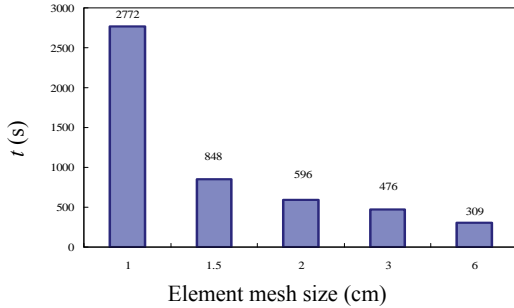


Figure 7. Computing cost under different mesh sizes

In the explicit time integration, the time step length is determined by the smallest element size in the model. Therefore, the mesh should be as uniform as possible. Unnecessarily small elements should be avoided, which can lead to unbearable computing time increasing. Extremely large elements should be avoided as

they may decrease accuracy. So the appropriate mesh size should be chosen, and 2.0 cm is adopted in this paper.

### 3.5 Normal Reflection

In this application, the impinge angle of incidence is zero, and 18 numerical tests were studied (Table 4).

Table 4. Normal reflection numerical tests

Test number	$Z$	$p_s$ (kPa)	$p_r$ (kPa)	$p_r^N$ (kPa)	error %
r1	0.26	11270.31	86159.82	71044.00	17.54
r2	0.53	2465.03	16415.80	18803.01	14.54
r3	0.79	1140.13	6497.61	5376.52	17.25
r4	1.05	694.16	3448.43	2561.78	25.71
r5	1.32	418.92	1771.07	1497.04	15.47
r6	1.58	281.48	1042.64	1120.00	7.43
r7	1.84	203.21	678.10	754.00	11.20
r8	2.11	154.52	475.02	535.00	12.64
r9	2.37	122.16	351.97	394.00	12.0
r10	2.64	99.46	272.21	246.22	9.56
r11	2.90	82.91	217.87	240.01	10.19
r12	3.16	70.42	179.03	159.22	11.10
r13	3.43	60.82	150.40	162.00	7.71
r14	3.69	53.27	128.61	136.01	5.73
r15	3.95	47.19	111.70	95.10	14.82
r16	4.22	42.02	98.22	100.01	1.86
r17	4.48	37.90	87.21	87.00	0.26
r18	4.74	34.48	78.28	77.53	0.92

$Z$  is the scaled distance,  $p_s$  is calculated based on equation (2),  $p_r$  is calculated based on equation (3),  $p_r^N$  is the numerical result of reflected pressure, error =  $|p_r^N - p_r|/p_r \times 100$

The results show that the reflected overpressure can be estimated through the numerical model, but the results are more stable at large scaled distances because of the complicated reflection in the near field.

## 4 Conclusions

Two different situations have been calculated, a free air blast wave, and the blast wave with rigid wall reflection. Good agreements between the numerical results and the empirical data are obtained and major explosion physical phenomenon can be well simulated using the ALE method.

The material behaviour of air and explosive are presented and the appropriate parameters consisted in the EOS are determined. The mesh size of finite element has a significant effect on the accuracy of simulation results, which is determined based on both the dimensions of the model and the computer capacity.

Further studies will be focused on the accurate pressure determination under more complex structural conditions.

## Acknowledgement

The financial support by National Natural Science Foundation of China (No. 50538050) is gratefully acknowledged by the authors.

## References

- Baker W.E., Cox P.A., Westine P.S. et al. (1983). *Explosion hazards and evaluation*. Elsevier, Amsterdam.
- Beshara F.B.A. (1994a). Modeling of blast loading on aboveground structures – I. General phenomenology and external blast. *Computers & Structures*, 51(5): 585-596.
- Beshara F.B.A. (1994b). Modeling of blast loading on aboveground structures – II. Internal blast and ground shock. *Computers & Structures*, 51(5): 597-606.
- Department of the Army (1990). Structures to resist the effects of accidental explosions, TM 5-1300.
- Henrych J. (1979). *The dynamics of explosion and its use*. Elsevier, Amsterdam.
- Jacinto A.C., Ambrosini R.D. and Danesi R.F. (2001). Experimental and computational analysis of plates under air blast loading. *International Journal of Impact Engineering*, 25: 927-947.
- Kinney G.F., Graham K.J. (1985). *Explosive shocks in air*, 2nd edn. Springer-Verlag, Berlin.
- Li Z.X., Du H. and Bao C.X. (2006). A review of current researches on blast load effects on building structures in China. *Proceeding of 1st International Conferences on ADSEI*, 36-41.
- Mays G.C., Smith P.D. (1995). *Blast effects on buildings – Design of buildings to optimize resistance to blast loading*. Thomas Telford, London.
- Plotzitz A., Rabczuk T. and Eibl J. (2007). Techniques for numerical simulations of concrete slabs for demolishing by blasting. *Journal of Engineering Mechanics*, 133(5): 523-533.
- Smith P.D., Rose T.A. (2002). Blast loading and building robustness. *Progress in Structural Engineering and Materials*, 4(2): 213-223.

# Numerical Simulation for Responses of Reinforced Concrete Slabs under Blast Loads

Xinxin Kuang<sup>1\*</sup>, Xianglin Gu<sup>1</sup>, Feng Lin<sup>1</sup> and Xiaojing Yin<sup>1</sup>

<sup>1</sup>Department of Building Engineering, Tongji University, Shanghai 200092, P.R. China

**Abstract** The numerical simulation for responses of reinforced concrete slabs under blast loads with the finite element program LS-DYNA was performed. A quarter of the three-dimensional solid model was established for the reinforced concrete slab. Blast loads were imposed on the surface of the slab. The H-J-C model for concrete was employed, taking into account the damage and the strain rate effect. The J-C model was employed to model the steel bar, taking strain effect into account. And the parameters of J-C model were derived by means of regressive analysis of experimental data conducted in our research group. The erosion technique was adopted to model the spallation process. The comparison result between numerical simulation and the test shows that the numerical simulation is an appropriate way for the study of responses of reinforced concrete components under blast loads.

**Keywords:** numerical simulation, blast load, reinforced concrete slab, strain rate effect

## 1 Introduction

Due to different accidental or intentional events, related to important structures, the behaviors of structural components subjected to blast loads have received considerable attention in recent years. For studying, there are some insufficiencies in experimental method such as that it is difficult to simulate the real boundary condition in tests. Besides, the explosion test is not only expensive but also dangerous.

In recent years, many efforts have been devoted to the development of reliable methods and algorithms for a more realistic analysis of structural components subjected to high dynamic loading. Some techniques, such as specialized contact algorithms and adaptive meshing or erosive techniques exist nowadays in computer codes such as the transient dynamic code LS-DYNA used in present study

---

\* Corresponding author, kuangxinxin2006@163.com

(Livermore Software Technology Corporation, 2003). With such techniques, it is possible to carry out three-dimensional computations for reinforced concrete structures concerning a realistic reproduction of the blast load effects. On this basis, numerical results may be generated to supplement experimental studies for analyzing the behavior of structures under blast loads.

The objective of this paper is to determine all parameters in the numerical simulation by comparing the simulation result with the experimental data for the further research, particularly focus on the material constitutive models. A realistic blast load was considered in the simulation. The dynamic fracture criterion for concrete was employed in the implementation of the erosion technique to capture the fracture and material separation process.

## 2 Test Study

A 1300mm×1300mm×50mm slab shown in Figure1 was cast with 30 MPa concrete and reinforced with bottom steel mesh of designation HPB235, which had bar cross-sectional diameter 10mm.

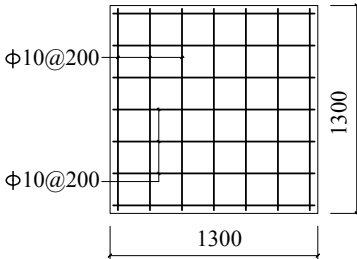


Figure 1. Details of the slab

The blast test was conducted in an explosion pressure simulator shown in Figure 2 which was used to simulate even short duration shock waves originating from an air blast. Two pressure gauges were applied to measure the reflected pressure. Strain foils on the concrete surface and on the rebar were also in the test. The slab was simply supported with a span of 1.2 m.

The slab was failure, with ‘X’ fracture and square bottom fracture. The remained deformation of the midspan reached 4.5 cm. The steels were yield.

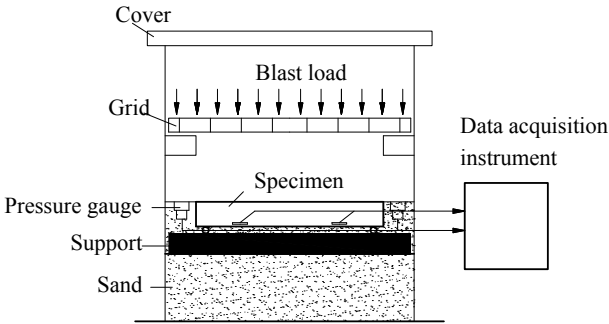


Figure 2. Experimental set-up

### 3 Numerical Simulation

#### 3.1 Element Type

The finite element program LS-DYNA was selected for the simulation. The Solid164 element type and the Link160 element type were employed for the model of concrete and steel, respectively. The slippage between concrete and steel was not taken into account.

#### 3.2 Material Model

##### 3.2.1 Concrete Constitutive Model

In the present study, the H-J-C model (Holmquist and Johnson, 1993) was employed to model the concrete. This model provides necessary elements needed to describe the concrete behavior under high dynamic. The equivalent strength is expressed as a function of the pressure, strain rate, and damage. The pressure is expressed as a function of the volumetric strain and includes the effect of permanent crushing. The damage is accumulated as a function of the plastic volumetric strain, equivalent plastic strain. The material constants are  $A$ ,  $B$ ,  $N$  and  $C$ . The specific expression is

$$\sigma^* = [A(1 - D) + BP^{*N}](1 + C \ln \dot{\epsilon}^*) \quad (1)$$

$$D = \sum \frac{\Delta \varepsilon_p + \Delta \mu_p}{D_1 (P^* + T^*)^{D_2}} \tag{2}$$

$$\sigma^* = \sigma / f'_c, P^* = P / f'_c, \dot{\varepsilon}^* = \dot{\varepsilon} / \dot{\varepsilon}_0, T^* = T / f'_c \tag{3}$$

where  $P^*$  is the normalized pressure (where  $P$  is the actual pressure), and  $\dot{\varepsilon}^*$  is the dimensionless strain rate (where  $\dot{\varepsilon}$  is the actual strain rate and  $\dot{\varepsilon}_0$  is the reference strain rate). The normalized maximum tensile hydrostatic pressure is  $T^*$ , where  $T$  is the maximum tensile hydrostatic pressure the material can withstand. The damage is  $D$ , where  $\Delta \varepsilon_p$  and  $\Delta \mu_p$  are the equivalent plastic strain and plastic volumetric strain, respectively.  $D_1$  and  $D_2$  are constants.

### 3.2.2 Steel Constitutive Model

The J-C model (Livermore Software Technology Corporation, 2003) strain sensitive plasticity was used for problems where the strain rates vary over a large range. In this model, thermal effect is ignored. The specific expression is

$$\sigma = [A + B(\varepsilon^p)^n][1 + C \ln \frac{\dot{\varepsilon}^p}{\dot{\varepsilon}_1}] \tag{4}$$

where  $A$ ,  $B$ ,  $n$  and  $C$  are material parameters,  $\varepsilon_p$  and  $\dot{\varepsilon}_p$  are plastic strain and plastic strain rate, respectively.

### 3.2.3 Simulation of Fracture by Erosion Algorithm

In order to simulate the physical fracture or crushing of concrete in the numerical model, the so-called erosion algorithm was implemented. When the material response in an element reaches certain critical value, the element is immediately deleted. There may be a variety of criteria governing the “erosion” of the material. Typically, the material fracture and failure under tension and compression may be defined by the magnitude of the effective plastic strain and volumetric tensile strain, respectively. In the present study, the failure criteria were defined on an empirical basis. Typical concrete strain at peak tensile stress under static loading is around 0.0002. Considering the softening phase, the concrete at fracture with practically complete loss may be assumed as  $5 \times 0.0002 = 0.001$ . For the explosion cases under consideration, the maximum strain rate is generally on the order of  $10s^{-1}$ - $100s^{-1}$ . For this magnitude of strain rate, the corresponding dynamic strength enhancement factor can reach 5.0 or above. Taking this influence into account and

in conjunction with trial parameter simulation, it is found that the dynamic tensile fracture strain should be around 0.001 for spallation with the concrete material. Thus, the principal tensile fracture strain reaching 0.001 was adopted as the primary criterion in the implementation of the erosion algorithm in the numerical simulation.

### 3.3 Finite Element Model

#### 3.3.1 Mesh

Assuming the uniformity of the blast load, a quarter of the slab was used in the numerical model considering symmetry. The total number of solid elements in the model was 676,000 for the slab dimension with a uniform element size of 5mm×5mm×5mm (Figure 3).

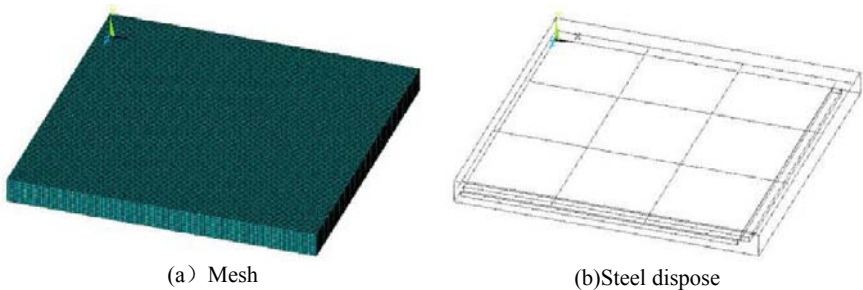


Figure 3. Finite element model

#### 3.3.2 Boundary Condition

According to the test mentioned above, a rigid material in which strain is ignored was employed to model the support. The vertical freedom of the support was constrained. The contact between the slab and the support was defined as automatic single surface contact, with the friction factor sampled 0.8.

#### 3.3.3 Material Parameters

According to the method determining the parameters of H-J-C model offered by Zhang and Li (Zhang and Li, 2001), Table 1 gives the concrete parameters in the study (unit: g-cm- $\mu$ s).

The parameters of steel constitutive model are given in Table 2, derived by means of regressive analysis of experimental data conducted in our research group (Lin et al., 2008) (unit: g-cm- $\mu$ s).

Table 1. Parameters for concrete model

<i>A</i>	<i>B</i>	<i>C</i>	<i>N</i>	$f'_c$	<i>T</i>
0.79	1.6	0.007	0.61	$2.58 \times 10^{-4}$	$3.15 \times 10^{-5}$
$\dot{\epsilon}_0$	$EF_{\min}$	$SF_{\max}$	$P_c$	$\mu_c$	$P_{\text{lock}}$
$1.0 \times 10^{-6}$	0.01	7.0	$8.60 \times 10^{-5}$	$5.97 \times 10^{-4}$	0.010
$\mu_{\text{lock}}$	$D_1$	$D_2$	$K_1$	$K_2$	$K_3$
0.1	0.034	1.0	0.85	-1.71	2.08

Table 2. Parameters for steel model

$\rho$	$\gamma$	<i>E</i>	<i>A</i>	<i>B</i>	<i>N</i>
7.83	0.3	2.0	$4.55 \times 10^{-3}$	$1.34 \times 10^7$	11.50
<i>C</i>	<i>PSFAIL</i>	<i>SIGMAX</i>	<i>SIGSAT</i>	$\dot{\epsilon}^p$	
0.02	0.13	$6.32 \times 10^{-3}$	$6.86 \times 10^{-3}$	$1.0 \times 10^{-6}$	

### 3.3.4 Blast Load

The load-time curve was obtained from the test (Figure 4). The load lasted about 1s, with peak value around 72 kPa.

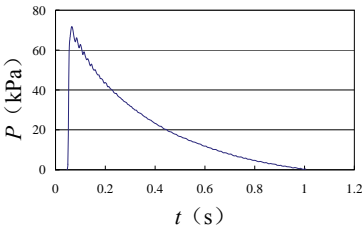


Figure 4. Blast load curve

## 4 Numerical Simulation Results

Figure 5 and Figure 6 illustrate the simulation result as compared to the experimental result. The slab was failure, with ‘X’ fracture and square bottom fracture. The details of the fracture are revealed from the simulation in a rather realistic manner. The steels were yield. Comparison of the strain-time curves also show a favorable agreement.

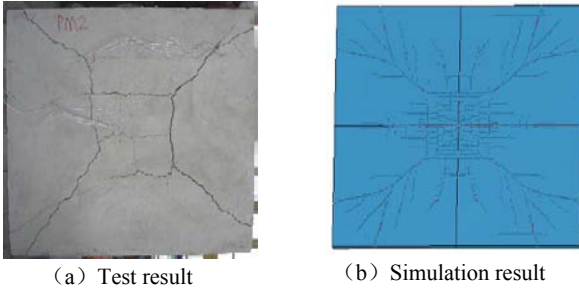


Figure 5. Comparison of the failure mode

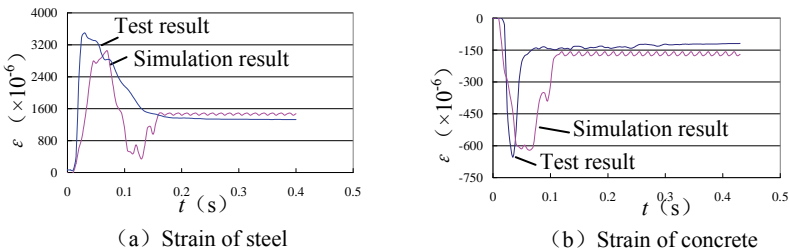


Figure 6. Strain-time curve

## 5 Conclusions

The reinforced concrete slab subjected to the blast loads was analyzed with the finite element program LS-DYNA. Numerical simulation result was presented to compare the experimental data. The result shows that the H-J-C model and the J-C model are adaptive for modeling concrete and steel bar, respectively, and the uniform element size of 5mm×5mm×5mm is precise enough. The material separation process was well demonstrated by the erosion technique. The further researches for the behavior of structural components under blast loads will be developed on the basis of the result got in this paper.

## Acknowledgement

The financial support from the National Natural Science Foundation of China (No. 50538050) is gratefully acknowledged by the authors.

## References

- Holmquist T. J., Johnson G. R. (1993). A computational constitutive for concrete subjected to large strains, high strain rates, and high pressures. *4th International Symposium on Ballistics*, Canada, 1993, 9(1): 1-10.
- Lin F., Gu X. L., Kuang X. X. et al. (2008). Constitutive models for reinforcing steel bars under high strain rates. *Journal of Building Material*, 11(1): 14-20 [in Chinese].
- Livermore Software Technology Corporation (2003a). LS-DYNA Theory Manual. Livermore.
- Livermore Software Technology Corporation (2003b). LS-DYNA Keyword User's Manual (970v). Livermore.
- Zhang F. G., Li E. Z. (2001). A method to determine the parameters of the model for concrete impact and damage. *Journal of Ballistics*, 13(4): 12-16 [in Chinese].

# Numerical Simulation of Internal Blast Effects on a Subway Station

Qiuyun Hu<sup>1\*</sup> and Yong Yuan<sup>1,2</sup>

<sup>1</sup>Department of Geotechnical Engineering, Tongji University, Shanghai 200092, P.R. China

<sup>2</sup>Key Laboratory of Geotechnical and Underground Engineering of Ministry of Education, Tongji University, Shanghai 200092, P.R. China

**Abstract.** Due to the confined space in a station, the internal blast effects are obviously different from the air blast. In order to design and retrofit a subway station to resist an internal blast, the distribution of blast loading and its effects on structures should be acquired firstly. The explicit dynamic nonlinear finite element software —ANSYS/LS-DYNA was used in this study. It briefly introduced the material constitutive models and boundary conditions used in the simulation. The numerical model of a typical two-layer and three-span frame subway station is established. Then two cases of different location of explosives were considered to analyze the dynamic responses of the structure. The effective plastic strain, displacement and total energy of the structure in the two cases were presented and discussed.

**Keywords:** internal blast loading, subway station, location of explosives, dynamic response

## 1 Introduction

Once an internal explosion happens to a subway station, it might result in deaths or injures to people, collapse or damage to subway station, and adverse vibration to surrounding buildings nearby. The harmful effects are no less than those of an up-ground blast. That is just the reason why subway station becomes one of the targets for terrorists. With the rapid development of underground construction and to the potential threaten of terrorism, engineers and researchers have made extensive efforts on the research of underground structures to resist blast loadings. Since it's hard to conduct a full scale in-site experiment, numerical techniques are usually applied to simulate blast events. A number of researches have done plenty of work to analyze the wave propagation (Rigas and Sklavounos, 2005; Zhou et

---

\* Corresponding author, e-mail: huqiuyun112@163.com

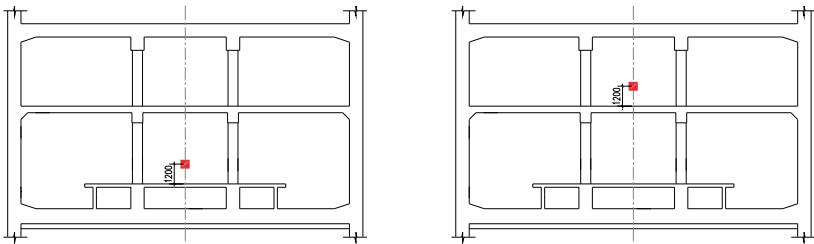
al., 2007) and dynamic responses of underground structures (Feldguna et al., 2008; Li et al., 2006; Hu et al., 2008) subjected to blast loading. However, there is few work focus on complex underground structures such as subway stations, and the structures subjected to internal blast.

In this paper, with the available commercial software ANSYS/LS-DYNA, the numerical model of a typical two-layer and three-span frame subway station is established. Two different locations of explosives are assumed to analyze the dynamic responses of the structure under different explosion loadings. The TNT charge of 10kg is considered. The dynamic responses of effective plastic strain, displacement and total energy of the structure in the two cases were presented and discussed.

## 2 Numerical Model

### 2.1 Model of the Subway Station

The subway station in this study is a typical two-layer station of 21.2m in width (X-axis), 12.02m in height (Y-axis) and about 200m in length (Z-axis). The depth of soil above the top surface of the station is 3.5m. The thickness of the roof plate, side walls, bottom plate, middle plate and platform is 0.8m, 0.8m, 0.9m, 0.4m and 0.2m respectively. The section size of columns is 0.6m×0.9m, and space distance between them is 5.7m in X-axis and 8.5m in Z-axis. Two cases of the location of TNT are assumed. Case 1: TNT situates in the middle of the cross section and at 1.2m height above the platform; Case 2: TNT situates in the middle of the cross section and at 1.2m height above the middle slab. The layout of the subway station and the location of TNT are shown in Figure 1. The numerical model of the subway station is shown in Figure 2.



(a) Case1

(b) Case 2

Figure 1. Layout of the subway station and the location of TNT

The FEM model consists of reinforced concrete structure (side walls, roof plate, bottom plate, middle plate, beams, columns and platform), surrounding soil, TNT and air (as shown in Figure2). The element type of SOLID164 defined by eight nodes is adopted for the 3D model. The bound of soil is assumed as 6m below the bottom plate and 6m beyond the side walls. The whole domain is assumed to be axial symmetric, so 1/4 of the model is established in this study. The calculated length of the station is 30m away from the explosive point. The opening in the middle plate represents the hatch for stairs between the two layers.

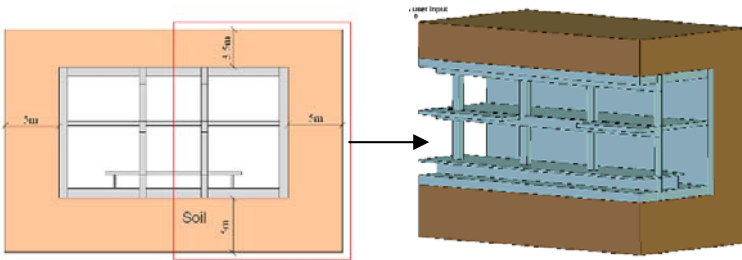


Figure 2. FEM model of the subway station

The nodes transitional displacement normal to the symmetry planes (XY and YZ planes) is constrained, which forms the symmetry boundary condition. The ground surface adopts free boundary condition. Non-reflected boundary condition was considered in all the else boundaries.

## 2.2 Material Constitutive Models

The response of concrete under shock loading is a complex nonlinear and rate-dependent process. A number of dynamic constitutive models for concrete have been proposed in the past (Ning et al., 2006). In this study, the interaction of steel bars and concrete is not considered. The Concrete Damage model (LS-DYNA keyword user’s manual, 2003) was employed to describe the concrete, which is suited to model reinforced concrete with the option of rate effects, damage accumulation, strain softening and hardening effects (Malvar, 1997). The main parameters of this model are listed in Table 1.

Table 1. Main parameters of concrete model (\*MAT\_CONCRETE\_DAMAGE)

Mass density ( $kg/m^3$ )	Maximum principle stress for failure (Pa)	Poisson’s ratio (concrete)	Yield stress (steel) (Pa)	Tangent modulus (steel) (Pa)	Elastic modulus (steel) (Pa)	Poisson’s ratio (steel)
$2.5 \times 10^3$	$1.43 \times 10^{10}$	0.21	$3 \times 10^8$	$2.1 \times 10^9$	$2.1 \times 10^{11}$	0.3

The dynamic behavior of surrounding soil is described by Soil\_and\_Foam model (LS-DYNA keyword user’s manual, 2003). The main parameters of this model are listed in Table 2.

Table 2. Main parameters of soil model (\*MAT\_SOIL\_AND\_FOAM)

Mass density (kg/m <sup>3</sup> )	Shear modulus (Pa)	Bulk modulus (Pa)	A0	A1	A2
1.88×10 <sup>3</sup>	5.14×10 <sup>7</sup>	2.4×10 <sup>10</sup>	6.2×10 <sup>8</sup>	1.67×10 <sup>4</sup>	0.1126

The HIGH EXPLOSIVE BURN and the Jones-Wilkins-Lee (JWL) equation of state (EOS) (LS-DYNA keyword user’s manual, 2003) are used to model the detonation of the TNT. The JWL equation of state defines the pressure as

$$P = A \left( 1 - \frac{\omega}{R_1 V} \right) e^{-R_1 V} + B \left( 1 - \frac{\omega}{R_2 V} \right) e^{-R_2 V} + \frac{\omega E_0}{V} \tag{1}$$

where the parameters are assumed as  $A = 3.74 \times 10^{11} \text{Pa}$ ,  $B = 3.23 \times 10^9 \text{Pa}$ ,  $R_1 = 4.15$ ,  $R_2 = 0.95$ ,  $\omega = 0.38$  and  $E_0 = 7 \times 10^9 \text{J/m}^3$ . The mass density of TNT  $\rho = 1630 \text{kg/m}^3$ , detonation velocity  $D = 6930 \text{m/s}$  and Chapman-Jouget pressure  $PCJ = 2.1 \times 10^{10} \text{Pa}$ .

Air is modeled by Null material model and the LINEAR\_POLYNOMIAL equation of state (LS-DYNA keyword user’s manual, 2003), which defines the pressure as

$$P = C_0 + C_1 \mu + C_2 \mu^2 + C_3 \mu^3 + (C_4 + C_5 \mu + C_6 \mu^2) E_0 \tag{2}$$

where the parameters are assumed as  $C_0 = -1 \times 10^5$ ,  $C_1 = 0$ ,  $C_2 = 0$ ,  $C_3 = 0$ ,  $C_4 = 0.4$ ,  $C_5 = 0.4$  and  $C_6 = 0$ . The mass density of air  $\rho = 1.2929 \text{kg/m}^3$  and the initial internal energy per unit reference specific volume  $E_0 = 2.5 \times 10^5 \text{J/m}^3$ .

### 3 Numerical Results and Discussions

Considering the quantity of explosive which a terrorist could take with won’t be much too large, the charge of TNT is assumed as 10kg.

### 3.1 Blast Wave Propagation

The maximum pressure values in different time for the both cases are listed in Table 1.  $P_{max1}$  is the maximum pressure of air in case1, while  $P_{max2}$  is the maximum pressure of air in case2. It can be found that, in the same time,  $P_{max2}$  is larger than  $P_{max1}$ . It implies that the pressure attenuation in case 2 is slower than case 1, which because the upper layer is of narrower space than lower layer.

Table 1. The maximum pressure in different time and different cases

	Pressure (Mpa)					
	5ms	10ms	20ms	40ms	60ms	80ms
$P_{max1}$	0.476	0.228	0.207	0.062	0.054	0.048
$P_{max2}$	0.484	0.295	0.212	0.069	0.061	0.055
a	1.6%	6%	2%	10%	13%	14%

$$a = (P_{max2} - P_{max1}) / P_{max1}$$

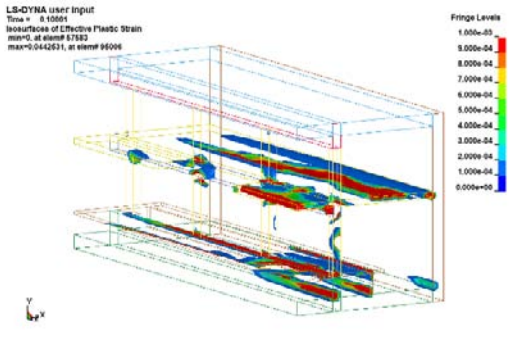
### 3.2 Effective Plastic Strain

In this study, the erosion algorithm of concrete isn't conducted. Therefore, the fracture or crushing of concrete can't be simulated. However, the failure area of structure can be reflected by the effective plastic strain. Figure 3 shows the isosurfaces of effective plastic strain in the both two cases. The following results can be drawn:

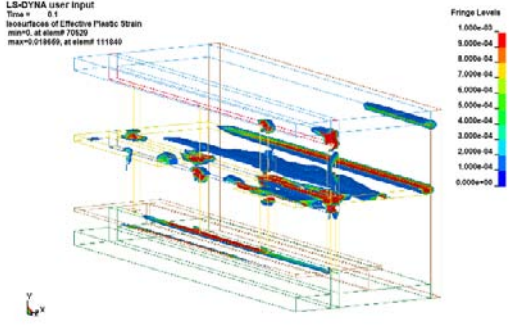
- (1) In case 1, the platform, middle slab and bottom beam are of extensive damage; while in case 2, the damage area is almost in the upper layer besides the connecting part between the platform and bottom beam.
- (2) The junctions of members are the vulnerable parts.

### 3.3 Response of Displacement

Point A on the platform and point B on the middle slab are the points of shortest distance (1.2m) to the explosion point in case 1 and case 2 respectively. The thickness of platform and middle slab is 200mm and 400 mm respectively. Curves in Figure 4 are the time histories of vertical displacement of the two points.



(a) Case 1



(b) Case 2

Figure 3. Isosurfaces of effective plastic strain

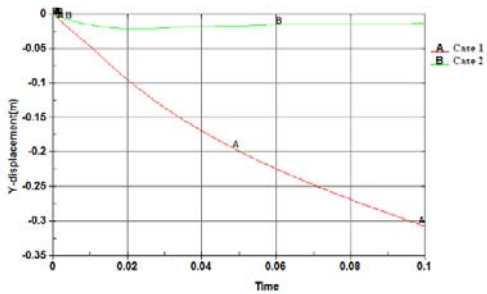


Figure 4. Time histories of vertical displacement

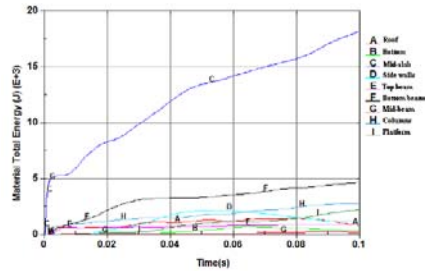
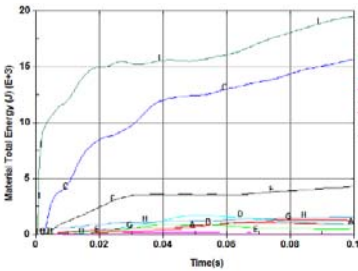
In the two cases, the charges of TNT are equivalent (10kg) and the distance to the explosives of the two points are the same. However, the maximum values of displacement of the two points are very different from each other. The maximum displacement of point A in case 1 is about 310mm in 100ms, and it may be in-

creased. While in case 2, the maximum displacement of point B is about 21mm in 20ms, and it declines to 13mm in 100ms. This phenomenon implies that the thickness of slab has a great deal to do with the vertical displacement.

### 3.4 Dissipation of Total Energy

When explosion happens, the chemical energy of the TNN converts into explosive energy, most of which propagates and dissipates in the air and some of which acts on structures. Figure 5 shows the time histories of total energy of each member.

In case 1, the middle slab and platform consumed more energy than other members, which implies that the two members experienced larger deformation than others. Comparing with case 2, the total energy in case 1 is larger, which because the members in case 1 experienced more plastic strain than those in case 2.



(a) Case 1

(b) Case 2

Figure 5. Time histories of total energy of each member

## 4 Conclusions

Two cases of explosion are simulated to study the different responses of structures. From the numerical results, the following conclusions can be drawn:

1. When explosion happens in the upper layer of the subway station, the pressure attenuation is slower than explosion happens in the lower layer.
2. When explosion happens in the lower layer of the subway station, the area of plastic strain is larger and the total energy of structure is more than explosion happens in the upper layer.
3. The junctions of members are the vulnerable parts of the subway station.
4. The thickness of slab has a great deal to do with the vertical displacement.

In order to acquire more precise results, the models of materials and structures should be improved. Further studies on blast-resistant factors for a subway station will be carried on.

## Acknowledgements

The supports by National Key Technology R&D Program (Grant No.: 2006BAJ27B04) and International Science and Technology Cooperation Foundation of Shanghai (Grant No.: 08210705700) are gratefully acknowledged by the authors.

## References

- Feldguna V. R., Kochetkov A. V., Karinskia Y. S. and Yankelevsky D. Z. (2008). Internal blast loading in a buried lined tunnel. *International Journal of Impact Engineering*, 35: 172-183.
- Hu Q. Y., Yu H. T. and Yuan Y. (2008). Numerical simulation of dynamic response of an existing subway station subjected to internal blast loading. *Transactions of Tianjin University*, 14(B10): 563-568.
- Livermore Software Technology Corporation. LS-DYNA keyword user's manual (Version 970), Livermore, CA, 2003.
- Li Z. X., Liu Y., Tian L. (2006). Dynamic response and blast-resistance analysis of double track subway tunnel subject to blast loading within one side of tunnel. *Journal of Beijing University of Technology*, 32(2): 173-182 [in Chinese].
- Malvar L. J., Crawford J. E., Wesevich J. W., et al. (1997). A plasticity concrete material model for DYNA3D. *International Journal of Impact Engineering*, 19: 847-873.
- Ning J. G., Shang L., Sun Y. X. (2006). The developments of dynamic constitutive behavior of concrete. *Advances in Mechanics*, 36(3): 389-405 [in Chinese].
- Rigas F. and Sklavounos S. (2005). Experimentally validated 3-D simulation of shock waves generated by dense explosives in confined complex geometries. *Journal of Hazardous Materials*, A121: 23-30.
- Zhou X. Q., Hao H. and Li Z. X. (2007). Numerical simulation of an underground structure under a hypothetic terrorist bombing. *Journal of PLA University of Science and Technology (Natural Science Edition)*, 8(6): 567-572 [in Chinese].

# Quantitative Study on Frequency Variation with Respect to Structural Temperatures

Yong Xia<sup>1\*</sup>, Zelong Wei<sup>1</sup> and Youlin Xu<sup>1</sup>

<sup>1</sup>Department of Civil and Structural Engineering, The Hong Kong Polytechnic University, Kowloon, Hong Kong, China

**Abstract.** The present paper aims to quantify the relation between structural temperatures and its natural frequencies via thermodynamic approach. A simply-supported beam was tested in laboratory. The temperature values at different points were recorded continuously in one day, together with a series of forced modal testing to extract its frequencies. A thermodynamic model is established to estimate the temperature distribution of the slab and compared with the measurement data. The frequencies of the slab are calculated, and the variation of frequency with respect to temperature is established and verified by the experiment. The present study provides a new approach to investigate the environmental effect on structural responses.

**Keywords:** vibration property, temperature, thermodynamics

## 1 Background

In structural condition monitoring (Doebbling et al., 1996; Sohn et al., 2003), a practical difficulty exists because the structural responses vary with the changing environmental conditions, particularly the temperature. Some studies have found that the changes in structural responses due to temperature variation could be more significant than the changes due to normal structural damage (Salawu, 1997). Pioneer study of the topic may attribute to Adams et al. (1978) who investigated the relation between the temperature and axial resonant frequency of a bar. During the last 20 years, more and more studies in this field have been carried out on real structures. Askegaard and Mousing (1988) studied a three-span RC footbridge and observed a 10% seasonal change in frequency over a three-year period. Researchers from Los Alamos National Laboratory (Cornwell, 1999) found that the first three natural frequencies of the Alamosa Canyon Bridge varied about 5% during a 24 hour period as the temperature of the bridge deck changed by approximately 22°C. Peeters and De Roeck (2001) continuously monitored the Z24-Bridge for nearly a year and they reported that the frequencies decreased with the tempera-

---

\* Corresponding author, e-mail: ceyxia@polyu.edu.hk

ture increase. Xia et al. (2006) have conducted experiments on a continuous concrete slab for nearly two years. Not only temperature changes, but also humidity effect on variation of frequencies, mode shapes and damping were investigated.

Most of these studies however, focused on developing empirical correlation between the temperature measured at limited points (or more simply, air temperature) and the structural responses. Although a few researchers attempted to accommodate the temperature effect in abnormality detection, the analysis is far from mature due to the following issues:

1. The temperature is usually measured at a few limited points while the temperature distribution in the structure is generally non-uniform and time-dependent. As the structural responses are associated with the temperature distribution of the entire structure, using the surface temperature alone cannot capture the realistic relation between the structural responses and temperature.
2. Without quantitative analysis of the temperature effect, it is very difficult to reliably explain the structural responses, assess the structural conditions and avoid false identification.

To overcome the difficulties, this study provides a new framework to study the quantitative relation between structural temperatures and responses. First, the thermal field distribution of a structure will be obtained through thermodynamic analysis. The temperature data measured at some critical points at different times will be employed to calibrate the numerical results. Second, with the temperature data at different members and thermal properties of materials, the structural dynamic properties will be calculated. Next, the relation between the temperature and structural responses will be established quantitatively and calibrated with the measurement data. The proposed techniques will be verified through a laboratory tested slab.

## 2 Tests and Results

### 2.1 Description of the Slab

The slab constructed for this study measures 3200 mm×800 mm×120 mm with 100 mm overhang at each end, as shown in Figure 1a. Under sunshine, the temperature in the longitudinal direction and horizontal direction are assumed uniformly distributed, which implies only temperature gradient exists along the height direction of the slab. Therefore, 7 thermocouples were embedded into the slab at interval of 20 mm along the thickness direction to measure the temperature distribution along thickness direction. 7 strain gauges were also placed adjacent to the thermal sensors to measure the strain. Figure 1b shows the sensors embedded in the slab. The data logger automatically recorded the data at every minute.

The specimen was tested in one day from 7:30 am to 22:00 pm. Due to space limitation in campus of The Hong Kong Polytechnic University, the slab can be exposed to sun irradiation in the morning only and shaded by buildings in the afternoon. Accelerometers were mounted firmly on the surface of the slab to extract the frequencies and mode shapes, via instrumented hammer impact testing every 15 minutes.



Figure 1a. RC slab

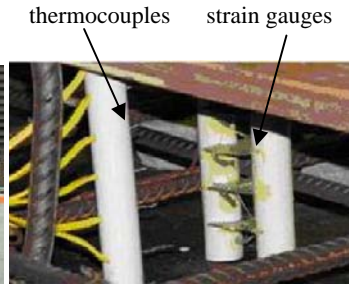
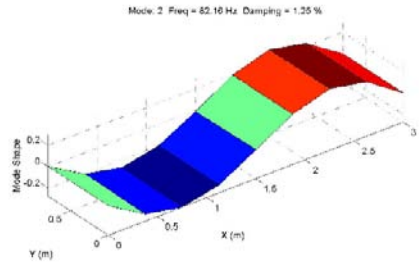
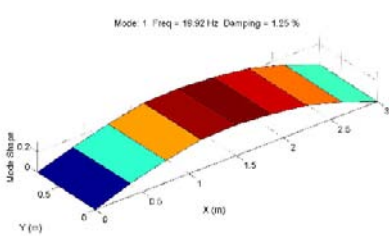


Figure 1b. Embedded sensors

## 2.2 Dynamic Testing

Typical mode shapes for the first four modes are shown in Figure 2. Modes 1, 2 and 4 are bending modes and mode 3 is a torsional mode.



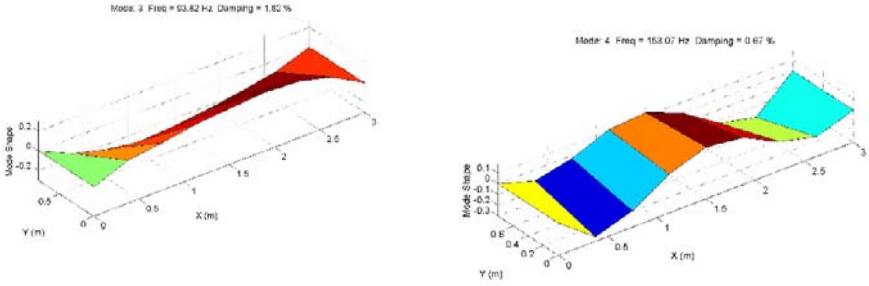


Figure 2. The first four mode shapes of the slab identified from impact testing

### 2.3 Temperature Measurement

Figure 3 shows the variation of the temperature measured from the 7 thermal sensors. We can find that the temperature of the slab increase fast from 10 am to 12 pm. After that, the temperature decrease as the irradiation is blocked. It also shows that the upper surface temperature increases more significantly than other points while decrease faster than others as well. The temperature within the slab changes in a smaller range, due to thermal inertia. This is a general phenomenon as expected.

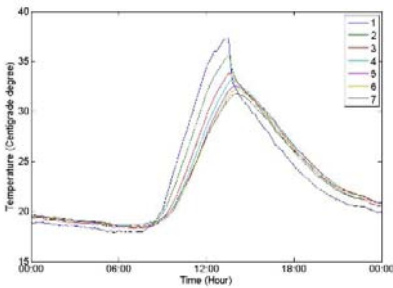


Figure 3. Temperature variation of the slab in 24 hours

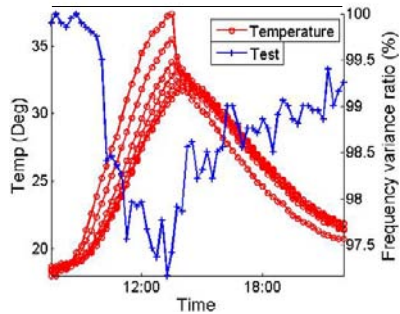


Figure 4. Variation of the first frequency vs. temperature

Figure 4 draws the variation of frequency with respect to temperature in different time. It clearly illustrates that when temperature increases, the frequency of the structure generally decreases. In contrast, when temperature decreases in the afternoon, the frequency goes up.

As commonly accepted, the variation of frequency is based on a fact that the mechanical properties are temperature dependant. In particular, Young's modulus decreases as temperature rises up. Although structural dimensions are temperature dependant as well, variation of Young's modulus with respect to temperature is much more significant than thermal expansion (Xia et al., 2006).

### 3 Analysis and Verification

#### 3.1 Thermodynamic Analysis

Usually full temperature field of a structure is not available, a thermodynamic model can be used to predict the temperature distribution throughout the structure. In the present study, the boundary temperature data (upper surface and bottom of the slab) measured at different time are input into a FE model to conduct thermal transient analysis. As we assume the temperature only varies along the thickness direction, a simple 1-D thermodynamic model is established in ANSYS. The temperature within the slab can be calculated and compared with the measurement, which illustrated in Figure 5. In the analysis, the thermal conductivity of the concrete is  $1.74 \text{ W}/(\text{m}\cdot^\circ\text{C})$ , specific heat  $960 \text{ J}/(\text{kg}\cdot^\circ\text{C})$ , and density  $2316.3 \text{ kg}/\text{m}^3$ . Only two points are shown here for brevity. From the figure, it can be found that the numerical simulation results agree well with the measurement, thus the numerical model is verified.

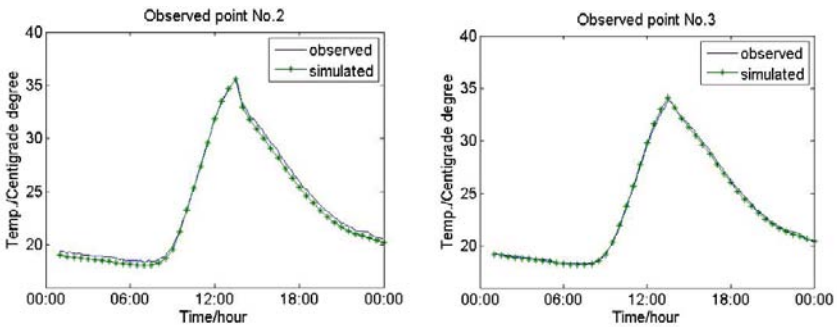


Figure 5. Temperature comparison – model prediction vs. measurement

### 3.2 Eigenvalue Analysis

Given temperature distribution throughout the slab, the mechanical properties of different elements can be estimated. According to the Model Code 90 issued by C.E.B in 1991, the relation between Young's modulus and temperature of concrete is suggested as,

$$E(T) = E_{20^{\circ}C} (1.06 - 0.003T) \quad (1)$$

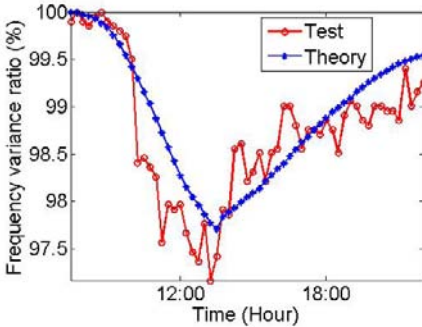


Figure 6. Comparison of the first frequency of the slab between the analysis and measurement

The Young's modulus of each element is inputted into the ANSYS model and then the natural frequencies of the slab can be calculated. To compare with the experimental counterparts, both are normalized with the maximum value. The comparison is illustrated in Figure 6 and shows a good agreement.

## 4 Conclusions

The paper studied the variation of frequencies with respect to structural temperature via a new thermodynamic approach in the first time. Although thermodynamics has been well developed quite a long time, it hasn't been applied to study the temperature effect on structural dynamic properties. From a thermodynamic model, the thermal distribution of a whole structure can be predicted. Then based on material thermal property, the natural frequency of the structure can be estimated. The results will be more accurate than usual correlation exercises as temperatures are only recorded at a few points. Therefore this study provides a new approach to investigate the environmental effect on structural behaviors and thus condition monitoring.

## Acknowledgements

The work described in this paper is supported by University Niche Areas programme (Project No. A-BB6G).

## References

- Adams R. D., Cawley P., Pye C. J. and Stone B. J. (1978). A vibration technique for non-destructively assessing the integrity of structures. *Journal of Mechanical Engineering Science* 20 (2): 93-100.
- Askegaard V. and Mossing P. (1988). Long term observations of RC-bridge using changes in natural frequency. *Nordic Concrete Research* 7: 20-27.
- CEB-FIP Model Code. (1991). Thomas Telford.
- Cornwell P., Farra, C. R., Doebling S. W., and Sohn H. (1999). Environmental variability of modal properties. *Experimental Techniques* 23 (6): 45-48.
- Doebling S. W., Farrar C. R., Prime M. B. and Shevitz D. W. (1996). Damage identification and health monitoring of structural and mechanical systems from changes in their vibration characteristics: a literature review. Los Alamos National Laboratory Report LA-13070-MS.
- Peeters B. and Roeck G. D. (2001). One year monitoring of the Z24-bridge: environmental effects versus damage events. *Earthquake Engineering and Structural Dynamics* 30 (2): 149-171.
- Salawu O. S. (1997). Detection of structural damage through changes in frequency: a review. *Engineering Structures* 19 (9): 718-723.
- Sohn H., Farrar C. R., Hemez F. M., Shunk D. D., Stinemates S. W., Nadler B. R. and Czarnecki J. J. (2003). A review of structural health monitoring literature form 1996-2001. Los Alamos National Laboratory report LA-13976-MS.
- Xia Y., Hao H., Zanardo G. and Deeks A. J. (2006). Long term vibration monitoring of a RC slab: temperature and humidity effect. *Engineering Structures* 28 (3): 441-452.

*“This page left intentionally blank.”*

# Experimental Study on Vibration Behavior of Cold-Form Steel Concrete Composite Floor

Ziwen Jia<sup>1\*</sup> and Xuhong Zhou<sup>1,2</sup>

<sup>1</sup>School of Civil Engineering, Chang'an University, Xi'an 710064, P.R. China

<sup>2</sup>School of Civil Engineering and Mechanics, Lanzhou University, Lanzhou 730000, P.R. China

**Abstract.** This paper introduces the experimental study on vibration behavior of 4 full scale cold-formed steel composite floors. The research is focused on the fundamental frequency of composite floor, which considering the influence of screw spacing and rigid blocking under different loading cases during normal use. The test apparatus and methods are introduced in details. The finite element analysis model of cold-formed steel composite floors is set up to study the vibration behavior. Finite element analysis results are close to those of the experiments. The results show that the flexural rigidity of composite floor can be improved by changing the spacing of screws. The fundamental frequency of composite floor with large spacing of screws, that connect profiled steel sheet and the flange of joists, is smaller than the composite floor with small screw spacing. The flexural rigidity and frequency of composite floor can be increased by setting rigid blocking at mid-span of adjacent joist of the composite floor and bearing rigid support. It is suggested that the fundamental frequency of cold-formed steel concrete composite floor should be more than 8 Hz.

**Keywords:** composite floor, cold-formed steel, fundamental frequency, experimental study, finite element analysis

## 1 Introduction

Vibrations caused by human activities have long been recognized as a major serviceability concern for residential floor systems. Cold-formed steel composite steel concrete slab residential floor systems provide an alternative for traditional residential floor systems. Steel framed floors are lighter, with high-strength and have less damping than traditional floors. However, lightweight floors will be more easily to vibrate under human activities, such as walking, running and jumping. The research on vibration behavior of cold-formed steel concretes composite

---

\* Corresponding author.

floor due to walking in light-frame construction is carried out in this paper. Several acceptability criteria have been developed for such kinds of floor systems based on the static deflection of the floors. The Australian Standard Domestic Metal Framing Code (1993), Johnson's criterion (1994), Onysko's criterion (1998), Ohlsson's Criterion (1998), ATC Design Guide (1999), which suggests the natural frequency of light-frame floor should be greater than 8Hz. If the natural frequency is less than 8Hz, resonance occurs. In addition, Xu (2007) and Kraus (1997), put forward a different Construction method to the floor frequency's effects. In this paper, an experimental study on vibration behavior of 4 full scale cold-formed steel composite floors is carried out. The research of the fundamental frequency of composite floor, which considering the influence of screw space and rigid blocking under different loading cases during normal use is carried out in this paper. Then, a finite element analysis model of cold-formed steel composite floors is presented to study their vibration behaviour.

## 2 Summary of Test

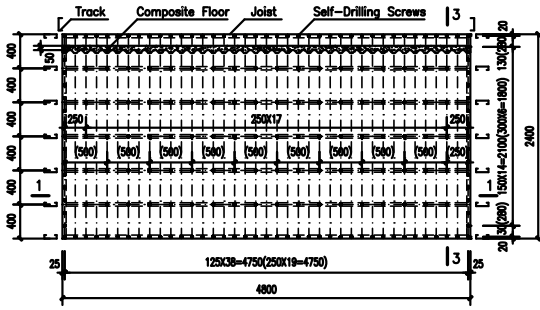
### 2.1 Specimens Design

Four composite floors, with consideration in the different spacing of self-drilling screws and the existence of the blockings, are designed in Figure 1. The research on the fundamental frequency of composite floor, which considers the influence of screw spacing and rigid blocking under different loading cases during normal use is carried out. The configurations of specimens are described in Table 1.

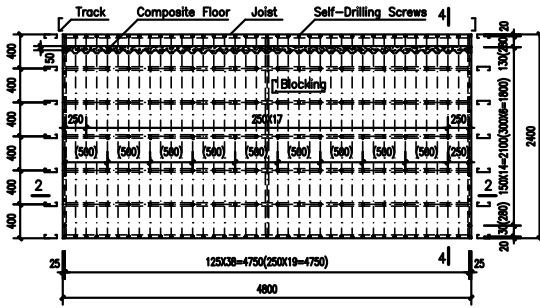
The framework of composite floor is composed of 7 joists (C305×41×14×1.6mm) and 2 tracks (U307×35×1.6mm). The length of each joist is 4800mm, and that of track is 2400mm. The spacing of each joist is 400mm. The section of web stiffener, which connects the web of joist and track by self-drilling screws, is C305×41×14×1.6mm with a length of 255mm. The section of blocking is C305×41×14×1.6mm and with a length of 380mm. The connectors are self-drilling screws and their numbers and arrangements are determined according to the Standard (JG/T 182—2005).

The sheeting-concrete composite slabs are composed of profiled steel sheet and concrete with grade C30, whose thickness is 0.74mm and 50mm, respectively. The rib of slab is vertical to the joist, and connects to the flange of joist with self-drilling screws ST4.2. There are no shear resistance studs and reinforcing steel bars between profiled steel sheet and concrete.

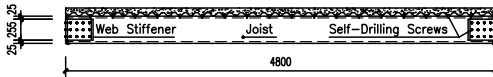
The thickness and loading cases of specimens are shown in Table 2. According to "Loading Code for the Design of Building Structures" (GB 50009—2001), 2.0 kN/m<sup>2</sup> is adopted as the live load in this paper, quasi-permanent value of variable load is 0.8 kN/m<sup>2</sup>, and 0.0 kN/m<sup>2</sup> when considering no live load.



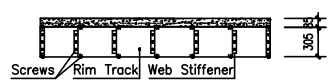
(a) FL-1 (3) layout chart (The data in the bracket belong to FL-3)



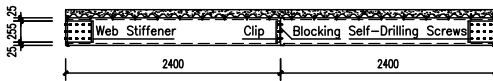
(b) FL-2 (4) layout chart (The data in the bracket belong to FL-4)



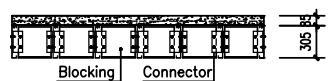
(c) Section 1-1



(d) Section 3-3



(e) Section 2-2



(f) Section 4-4

Figure 1. Construction details of FL-1~4.

According to the material experiments, it is known that the material properties of the specimens are as following: the yielding strength of cold-formed steel is

330N/mm<sup>2</sup>, Young’s modulus is 2.06 × 10<sup>5</sup>N/mm<sup>2</sup>, passion ratio is 0.3; the yielding strength of steel slab is 382N/mm<sup>2</sup>, Young’s modulus is 2.06 × 10<sup>5</sup> N/mm<sup>2</sup>, passion ratio is 0.3; the standard compression strength of concrete is 23.9 N/mm<sup>2</sup>, Young’s modulus is 3.0 × 10<sup>4</sup> N/mm<sup>2</sup>, passion ratio is 0.2.

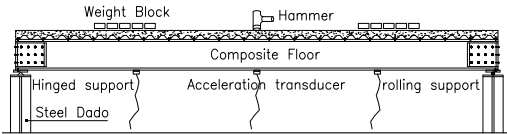
Table 1. Configuration of specimens

Load cases	Screw space /mm	Blocking	Live load /mm <sup>2</sup>	Bearing support
FL-1-A-1-A-0.0			0.0	
FL-1-A -1-A-0.8			0.8	1: Simple support
FL-1-A -1-A-2.0			2.0	_____
FL-1-A -2-A-0.0		A: No	0.0	
FL-1-A -2-A-0.8	A: 150 along the direction of tracks, 125 at the side joists and 250 in the middle field of floor		0.8	2: Rigid support
FL-1-A -2-A-2.0			2.0	_____
FL-2-A -1-B-0.0			0.0	
FL-2-A -1-B-0.8			0.8	1: Simple support
FL-2-A -1-B-2.0			2.0	_____
FL-2-A -2-B-0.0		B: Yes	0.0	
FL-2-A -2-B-0.8			0.8	2: Rigid support
FL-2-A -2-B-2.0			2.0	_____
FL-3-B -1-A-0.0			0.0	
FL-3-B -1-A-0.8			0.8	1: Simple support
FL-3-B -1-A-2.0			2.0	_____
FL-3-B -2-A-0.0		A: No	0.0	
FL-3-B -2-A-0.8	B: 300 along the direction of tracks, 250 at the side joists and 500 in the middle field of floor		0.8	2: Rigid support
FL-3-B -2-A-2.0			2.0	_____
FL-4-B -1-B-0.0			0.0	
FL-4-B -1-B-0.8			0.8	1: Simple support
FL-4-B -1-B-2.0			2.0	_____
FL-4-B -2-B-0.0		B: Yes	0.0	
FL-4-B -2-B-0.8			0.8	2: Rigid support
FL-4-B -2-B-2.0			2.0	_____

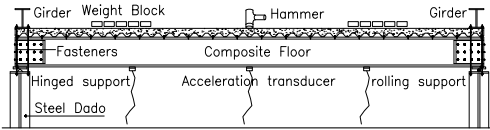
Note: FL-1-A-1-A-0.0 denotes floor specimen FL-1, screw spacing A, bearing support 1, blocking A, live load 0.0 N/mm<sup>2</sup>.

## 2.2 Experiment Program

There are two kinds of supporting conditions for composite floor: simply supported slabs and rigid supported slabs as shown in Figure 2 (a) and (b). The hinged support is adopted in one supporting boundary, and the other is rolling support. In order to simulate the rigid support boundary, a steel girder weighted 200kg is used on one edge of composite floor, and the steel girder is fixed to dado tightly. Many weight blocks are placed on the composite floor, in order to considering the influence of live load on floor.



(a) Simply supported slab



(b) Rigid supported slab

Figure 2. Test set-up

The equipment for shock excitation is impact hammer. Many acceleration transducers are arranged on the bottom flange of cold-formed steel joists, and they can record the dynamic response of the composite floor. All the test dates were collected by LMS (Test. Lab Modal Impact) data collector. The measuring points of acceleration transducer are shown in Figure 3. The measuring point No.11 is shocking point.

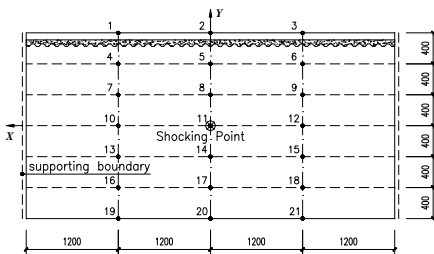


Figure 3. Layout of measuring points

### 2.3 Experimental Results and Analysis

The test results of fundamental frequency in different loading conditions are listed in Table 2. The fundamental frequency of these given four specimens, which have the same length-width ratio but different structural mode, are more than 8 Hz. the vibration frequency of light floor should be over 8Hz in references ATC Design Guide (1999).

Table 2. Thickness of specimens and the comparisons of test results and numerical results

Load cases	Thickness /mm	Test Frequency /Hz	FEM Frequency /Hz	FEM/Test
FL-1-A-1-A-0.0	50	12.4	12.76	1.03
FL-1-A -1-A-0.8		11.3	11.86	1.05
FL-1-A -1-A-2.0		10.4	10.14	0.98
FL-1-A -2-A-0.0		12.8	12.93	1.01
FL-1-A -2-A-0.8		11.8	12.74	1.08
FL-1-A -2-A-2.0		11.3	12.01	1.06
FL-2-A -1-B-0.0		50	12.3	14.31
FL-2-A -1-B-0.8	11.3		12.34	1.09
FL-2-A -1-B-2.0	10.5		10.31	0.98
FL-2-A -2-B-0.0	12.5		15.18	1.21
FL-2-A -2-B-0.8	12.8		14.56	1.14
FL-2-A -2-B-2.0	11.5		13.19	1.15
FL-3-B -1-A-0.0	52		13.2	11.92
FL-3-B -1-A-0.8		12.2	11.20	0.92
FL-3-B -1-A-2.0		11.3	9.74	0.86
FL-3-B -2-A-0.0		13.8	12.04	0.87
FL-3-B -2-A-0.8		12.5	11.76	0.95
FL-3-B -2-A-2.0		11.5	11.17	0.97
FL-4-B -1-B-0.0		52	13.3	13.46
FL-4-B -1-B-0.8	12.3		11.87	0.97
FL-4-B -1-B-2.0	11.3		9.97	0.88
FL-4-B -2-B-0.0	14.5		13.95	0.96
FL-4-B -2-B-0.8	12.4		13.48	1.09
FL-4-B -2-B-2.0	11.5		12.41	1.08

Note: Thickness is the actual value of floor.

There exist differences with the regulations in Technical specification for Steel structures of Tall Buildings (JGJ99—98). However, they meet requirements that

the fundamental frequency comparison of these four specimens in different loading conditions are summarized as:

1. With the increase of the floor live loads, the fundamental frequency of the specimens gradually decreases in the same constraint condition.
2. The bigger the screw spacing of specimens FL-3 (4) are, the bigger the fundamental frequency is. The largest difference between them is 1 Hz. The fundamental frequency of thicker profiled steel sheet and bigger joist flange screw spacing is less than that of the smaller. The FEM shows that changing screw spacing can improve flexural rigidity of composite floors; it is the same with test results in Xu (2007). With the decreasing of screw spacing, associative effects becomes more obvious, also the flexural rigidity and vibration frequency become larger. The causes for larger frequency are as follows: these four composite floors are site concreting in the process of fabrication. Because of the unevenness concrete surface and the difference of thickness, the mass of these four composite floors show an uneven distribution, and the real thickness of the floor has some difference with the design. So it shows the fundamental frequency becomes larger with the screw spacing increasing.
3. The profiled steel sheet and joist flange screw spacing of FL-1 is the same as FL-2, just like FL-3 as FL-4. The changing of rigid boundary has little effects on the frequency increasing of composite floors. The corresponding fundamental frequency in different working conditions is basically identical to each other. The FEM shows the fundamental frequency of the composite floors with rigid blocking is somewhat larger than that without rigid blocking. Rigid blocking not only can improve the lateral stability of joist, but also increase the flexural rigidity of composite floors. Rigid blocking is always assembled after the joist frame fastness. As the small torsion stiffness of joists with open sections can easily lead to torsion deformation, and the construction space is also small, the installation precision and fastening degree of rigid blocking are always problems in practice, which become the obstacles to fully provide the lateral supports and improve greatly the flexural rigidity of composite floors. So this paper suggests using bolt instead of self-drilling screws, and setting flat steel belts to link the bolts at the joist bottom flanges.
4. The fundamental frequency become bigger if the end restraints are enhanced in the corresponding working conditions. It shows steel girder simulating end restraint of wall frame stud can limit the joist-end rotation, improve flexural rigidity of composite floor and increase frequency. The strength of the end restraint simulated by steel girder is related to girder mass, fastening degree between girder and pedestal, and levelling degree. Therefore the improvement of measured fundamental frequency is not obvious.
5. The acceleration response of composite floors is related to energy under impact hammer effect. PSD means how the energy distributes in vibration frequency domain. Maximum of power spectrum density means the fundamental frequency of composite floors. The acceleration and PSD in different measuring

points are different, but the fundamental frequency and frequency domain are unrelated to different measuring points. The FL-1-A-1-C-0.0 measuring point distribution of PSD is showed in Figure 4 and 5. It includes obvious peak value, which always represents the fundamental frequency of composite floors. It means most of energy concentrates in fundamental frequency limits. As shown in Figure 4, the distribution value of PSD is changing with the measuring points varying. However, all the measuring points are distributed under one joist, so the PSD distribution forms are similar. Energy in point 11 is max, which gradually decreased far from impact point. The distribution value of PSD in different joists is a little different, shown in Figure 5, as the deformation of every joist is unified, when hammering on composite floor. Different structural composite floors have different PSD distribution forms and fundamental frequency, which is like FL-1-A-1-C-0.0.

In addition, we cannot feel vibration of composite floors when the author walks on the floor. However, when we hop on it we can feel a little vibration. In order to avoid resonance caused by walking and jumping, this paper suggests that the controlled fundamental frequency should be more than 8Hz, referred to the measured results and references ATC Design Guide (1999).

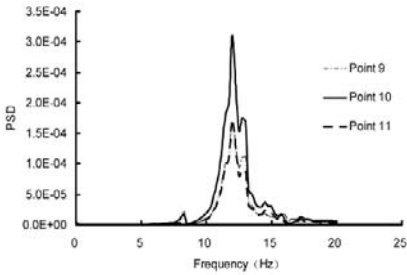


Figure 4. FL-1-A-C-0.0 along Y-axis PSD

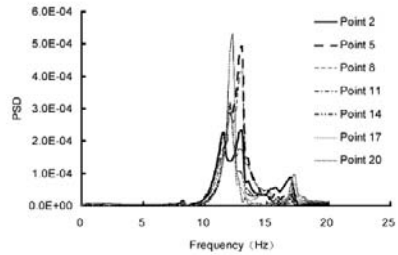


Figure 5. FL-1-A-C-0.0 along X-axis PSD

### 3 Numerical Study

In order to compare with the test results of the finished four specimens under 24 kinds of loading case, the numerical analysis is executed for each loading case of the composite floor by ANSYS finite element program. The following assumptions are used:

1. Profiled steel sheets and concrete are completely bonded. The slip is not considered if there is any. The steel and concrete are considered to be elastic materials in numerical analysis.

2. The relative slip is allowed for the composite floor. Profiled Steel Sheet - concrete composite floor and the flange of joists could impinge on the position of no screws under gravity load and live load.
3. The live load is converted to the equivalent density of floor board to consider its influence in the finite element analysis.

### ***3.1 Finite Element Model***

The plastic shell element shell181 is used to simulate the C-section joists, U-section tracks, profiled steel sheets, support stiffening members and rigid blockings. The element solide65 is used to simulate the concrete; the screws that connect the profiled steel sheets and the flanges of joists are simulated by element beam188. At the positions with no screws they are simulated by 3-D contact element contac52; the screws among the support stiffening members, joists and tracks are simulated by coupling, the screws between rigid blocking and joist webs. When building a model, the real measured concrete thickness is used.

### ***3.2 Results of Finite Element Model Analysis***

The finite model analysis is executed for four specimens under 24 kinds of loading cases by ANSYS finite element program, the fundamental frequency of numerical simulation is shown in Table 2.

The numerical simulation method used by this paper can reflect the vibration behavior of composite floor exactly, and has high precision and calculation efficiency. The calculated fundamental frequency agrees well with experimental model fundamental frequency. The results between experiment and finite element simulation have some difference under individual loading cases because of the fabrication error of the specimens, the discrimination of boundary constraint, and the fastening degree of rigid support connections.

## **4 Conclusions**

In this paper, the experimental research has been carried out for the vibration behavior of composite floor with different configuration modes, and by setting up numerical models the tested specimens have been analyzed with finite element program ANSYS. Comparison of the results from tests and finite element numerical analysis, the feasibility of precise frequency calculation by ANSYS finite ele-

ment program is verified. The obtained results allow the following conclusions to be drawn:

1. Under the same boundary constraints, the measured fundamental frequency of one specimen under different loading cases gradually decreases with the increase of floor live loads. The assumption that the live load is converted to the equivalent density of floor board in the finite element analysis is reasonable.
2. The flexural rigidity of composite floor can be improved by changing the spacing of screws. The fundamental frequency of composite floor with large spacing of the screws, that connect profiled steel sheets and the flange of joists, is smaller than the composite floor with small spacing. The lateral stability of joists can be strengthened and the flexural rigidity and frequency of composite floor will be increased by setting rigid blocking at mid-span of adjacent joist of composite floor. The fundamental frequency of composite floor is increasing if the end restraints are enhanced.
3. Different measuring points have different acceleration and PSD value, but the fundamental frequency and frequency domain are unrelated to different measuring points.
4. It is suggested that the construction quality should be strictly controlled and the fundamental frequency should be more than 8 Hz.

## References

- AS3623, Australian Standard (1993). Domestic metal framing code. Standards Association of Australia, Homebush, NSW.
- ATC, Applied Technology Council (1999). Design Guide 1: Minimizing Floor Vibration. Redwood, California, USA.
- Canadian Wood Council et al. (1996). Development of design procedures for vibrations controlled spans using engineered wood members. *Final Report Prepared for Canadian Construction Material Centre and Industry Partnership Consortium*.
- GJ 99-98 (1998). Technical specification for steel structure of tall buildings [in Chinese].
- GB 50009-2001 (2001). Load code for the design of building structures [in Chinese].
- JG/T 182-2005 (2005). Technical requirements for low-rise assembled residential buildings with light-weight steel framing [in Chinese].
- Johnson J.R. (1994). Vibration Acceptability of Floor Under Impact Vibration, Department of Civil Engineering, Virginia Polytechnic Institute and State University, Blacksburg, Virginia, USA.
- Kraus C.A. (1997). Floor vibration design criterion for cold-formed C-Shaped supported residential floor systems, Virginia Polytechnic Institute and State University, Blacksburg, Virginia, USA.
- Ohlsson S.V. (1988). Springiness and human-induced floor vibrations – A design guide. D12, Swedish Council for Building Research, Stockholm, Sweden.
- Xu, L., Tangorra F.M. (2007). Experimental investigation of lightweight residential floors supported by cold-formed steel C-shape joists. *Journal of Constructional Steel Research*, Vol. 63, 422-435.

# Method of Reverberation Ray Matrix for Dynamic Response of Space Structures Composed of Bar Elements with Damping Effect

Guoqiang Cai<sup>1</sup>, Guohua Nie<sup>1\*</sup> and Huiyuan Zhang<sup>2</sup>

<sup>1</sup> School of Aerospace Engineering and Applied Mechanics, Tongji University, Shanghai 200092, P.R. China

<sup>2</sup> Institute of Taiyuan Architectural Design and Research, Taiyuan 030002, P.R. China

**Abstract.** A method of reverberation ray matrix (MRRM) is developed for transient response analysis of space structures composed of bar elements taking into account of damping effect. Based on the forms of exact solution in frequency domain for axial, bending and twisting wave motions in beam structure, displacements and internal forces in the beam can be expressed by arriving and departing vectors, which are determined by evaluating a reverberation ray matrix. The IFFT algorithm is finally used to derive transient response of the structures. As an application, a framed structure under impact load is considered as computational model. Comparison with results from FEM shows a high precision in computation for the method. The result shows that high-frequency portions of the response are weakened by effect of damping.

**Keywords:** space structure composed of bar elements, method of reverberation ray matrix (MRRM), hysteretic damping, transient response

## 1 Introduction

Recently a method of reverberation ray matrix has been proposed by Pao *et al.* for analysis of static and dynamic response of two-dimension framed structure (Pao, Keh and Howard, 1996, 1999; Pao and Sun, 2003; Howard and Pao, 1998). More recently, a corresponding reverberation matrix method has been developed for the static analysis of three-dimension framed structure (Cao and Nie, 2005; Cai and Nie, 2008).

---

\* Corresponding author, e-mail: ghnjie@tongji.edu.cn

There is no doubt that the dynamic responses are influenced by various damping effects. This paper aims to develop a method of reverberation ray matrix (MRRM) for transient response analysis of space structures composed of bar elements taking into account of hysteretic damping effect. Based on the forms of exact solution in frequency domain for axial, bending and twisting wave motions in beam structure, displacement and rotational angle, axial force, shear force, bending moment and twisting moment at any location in the beam can be expressed by arriving and departing vectors as well as location functions. The two kinds of unknown vectors for entire structure can be determined analytically by constructing corresponding relations between them using the relation between the displacements of two ends of each beam expressed under the prescribed dual local coordinates, and establishing propagation matrix, scattering matrix and reverberation matrix on the basis of the dynamic equilibrium and compatibility conditions for displacements of each joint. The IFFT algorithm is finally used to derive transient response of the structures. As an application, a framed structure under impact load is considered as computational model. Comparison with results from FEM shows a high precision in computation for the model. The result shows that high-frequency portions of the response are weakened by effect of hysteretic damping.

## 2 Mathematical Formulation for Reverberation Ray Matrix

### 2.1 Steady-State Solutions for Axial, Twisting and Bending Wave Motions in Members

It is assumed that the number of joints for a structure is  $n$ , the number of members is  $m$ , and the number of members meeting at the same joint  $J$  is  $m'$ . For the axial wave in a member  $JK$ , solutions for steady-state wave equation can be expressed by

$$\hat{u}_x(x, \omega) = a_1(\omega)e^{ik_1x} + d_1(\omega)e^{-ik_1x}, \quad \hat{F}_x(x, \omega) = E(1 + i\eta_u)Aik_1(a_1e^{ik_1x} - d_1e^{-ik_1x}) \quad (1)$$

where  $a_1(\omega)$  and  $d_1(\omega)$  are two components of arriving and departing wave vectors.  $\eta_u$  and  $k_1$  are the hysteretic damping coefficient and complex wave number, and  $i = \sqrt{-1}$ . For the twisting wave, the formulae of angular displacement and twist moment are

$$\hat{\phi}_x(x, \omega) = a_2e^{ik_2x} + d_2e^{-ik_2x}, \quad \hat{M}_x(x, \omega) = G(1 + i\eta_\phi)I_xik_2(a_2e^{ik_2x} - d_2e^{-ik_2x}) \quad (2)$$

The solution for bending wave motion in  $x$ - $y$  plane can be written as

$$\hat{u}_y(x, \omega) = (1 + \alpha_3)(a_3 e^{ik_3 x} + d_3 e^{-ik_3 x}) + (1 + \alpha_4)(a_4 e^{ik_4 x} + d_4 e^{-ik_4 x}) \quad (3)$$

$$\hat{\phi}_z(x, \omega) = ik_3(a_3 e^{ik_3 x} - d_3 e^{-ik_3 x}) + ik_4(a_4 e^{ik_4 x} - d_4 e^{-ik_4 x}) \quad (4)$$

$$\hat{F}_y(x, \omega) = i\kappa AG(1 + i\eta_\phi) \left[ k_3 \alpha_3 (a_3 e^{ik_3 x} - d_3 e^{-ik_3 x}) + k_4 \alpha_4 (a_4 e^{ik_4 x} - d_4 e^{-ik_4 x}) \right] \quad (5)$$

$$M_z(x, t) = -E(1 + i\eta_u) I_z \left[ k_3^2 (a_3 e^{ik_3 x} + d_3 e^{-ik_3 x}) + k_4^2 (a_4 e^{ik_4 x} + d_4 e^{-ik_4 x}) \right] \quad (6)$$

where  $\alpha_i$  ( $i=3,4$ ) are constants concerning the complex wave numbers  $k_i$  ( $i=3,4$ ). The solution for bending wave motion in  $x$ - $z$  plane can be expressed by replacing the indices 3,4 and subscript  $z$  with 5,6 and subscript  $y$ , respectively. Combing the above equations, displacements and internal forces in member  $JK$  can be expressed in a form of matrix below

$$\hat{\mathbf{U}}^{JK}(x, \omega) = \mathbf{C}_{+u}^{JK} \mathbf{P}^{JK}(+k_j x) \mathbf{a}^{JK}(\omega) + \mathbf{C}_{-u}^{JK} \mathbf{P}^{JK}(-k_j x) \mathbf{d}^{JK}(\omega) \quad (7)$$

$$\hat{\mathbf{F}}^{JK}(x, \omega) = \mathbf{C}_{+F}^{JK} \mathbf{P}^{JK}(+k_j x) \mathbf{a}^{JK}(\omega) + \mathbf{C}_{-F}^{JK} \mathbf{P}^{JK}(-k_j x) \mathbf{d}^{JK}(\omega) \quad (8)$$

where  $\mathbf{P}^{JK}(\pm k_j x)$  is a diagonal matrix of  $6 \times 6$ , which is composed of six elements:  $e^{\pm ik_j x}$  ( $j=1 \dots 6$ );  $\mathbf{C}_{\pm u}^{JK}$  and  $\mathbf{C}_{\pm F}^{JK}$  are modal factor matrixes of  $6 \times 6$ , and

$$\hat{\mathbf{U}}^{JK}(x, \omega) = [\hat{u}_x, \hat{u}_y, \hat{u}_z, \hat{\phi}_x, \hat{\phi}_y, \hat{\phi}_z]^T, \quad \hat{\mathbf{F}}^{JK}(x, \omega) = [\hat{F}_x, \hat{F}_y, \hat{F}_z, \hat{M}_x, \hat{M}_y, \hat{M}_z]^T,$$

$$\mathbf{a}^{JK}(\omega) = [a_1, a_2, a_3, a_4, a_5, a_6]^T, \quad \mathbf{d}^{JK}(\omega) = [d_1, d_2, d_3, d_4, d_5, d_6]^T.$$

## 2.2 Scattering Matrix and Reverberation Ray Matrix

The scattering matrix of joint  $\mathbf{S}^J$  and source wave vector of joint  $\mathbf{s}^J$  might be derived from the equilibrium equations and compatibility conditions for displacements

$$\mathbf{d}^J = \mathbf{S}^J \mathbf{a}^J + \mathbf{s}^J \quad (9)$$

For a structure composed of  $n$  joints and  $m$  members, we assemble all  $\mathbf{S}^J$  and  $\mathbf{s}^J$  into global  $\mathbf{S}$  and  $\mathbf{s}$

$$\mathbf{d} = \mathbf{S}\mathbf{a} + \mathbf{s} \quad (10)$$

where  $\mathbf{d}_{12m \times 1} = [\mathbf{d}^1, \mathbf{d}^2, \dots, \mathbf{d}^n]^T$  is called the global departing wave vector in all members while  $\mathbf{a}_{12m \times 1} = [\mathbf{a}^1, \mathbf{a}^2, \dots, \mathbf{a}^n]^T$  is global arriving wave vector.  $\mathbf{s}_{12m \times 1} = [\mathbf{s}^1, \mathbf{s}^2, \dots, \mathbf{s}^n]^T$  represents the global source wave vector; and  $\mathbf{S}_{12m \times 12m}$  is global Scattering matrix containing  $\mathbf{S}^1, \mathbf{S}^1, \dots, \mathbf{S}^n$  along its main diagonal.

For each member  $JK$ , two right-hand systems of coordinates are introduced, i.e.,  $(x, y, z)^{JK}$  with origin at  $J$  and  $(x, y, z)^{KJ}$  at  $K$  (Cao and Nie, 2005). For one member, the relation between the arriving and departing wave vectors can be derived as  $a_j^{JK} = \pm e^{-ik_j l^{JK}} d_j^{KJ}$ . It might be written in the form of matrix as

$$\mathbf{a}^{JK}(\omega) = \mathbf{P}^{JK}(l, \omega) \mathbf{d}^{KJ}(\omega) \quad (11)$$

where  $\mathbf{P}^{JK}(l, \omega)$  is a  $6 \times 6$  diagonal matrix, whose elements in main diagonal are  $(-e^{-ik_1 l}, -e^{-ik_2 l}, -e^{-ik_3 l}, -e^{-ik_4 l}, e^{-ik_5 l}, e^{-ik_6 l})$ . Assembling the Equation (11) to form the global equation for the entire structure as  $\mathbf{a} = \mathbf{P}\tilde{\mathbf{d}}$ , where the column matrix  $\tilde{\mathbf{d}}$  and  $\mathbf{d}$  contain the same elements but in different permutation (i.e.,  $JK$  and  $KJ$ ). We may express this relation by a permutation matrix  $\mathbf{U}$  as  $\tilde{\mathbf{d}} = \mathbf{U}\mathbf{d}$ , then there is another relation between  $\mathbf{a}$  and  $\mathbf{d}$

$$\mathbf{a} = \mathbf{P}\mathbf{U}\mathbf{d} \quad (12)$$

Substituting Equation (12) into Equation (10) yield

$$\mathbf{d} = [\mathbf{I} - \mathbf{S}\mathbf{P}\mathbf{U}]^{-1} \mathbf{s} = [\mathbf{I} - \mathbf{R}]^{-1} \mathbf{s} \quad (13)$$

where  $\mathbf{R} = \mathbf{SPU}$  is called the reverberation ray matrix. Substituting the resulting  $\mathbf{d}$  into Equation (12) or Equation (10) results in  $\mathbf{a}$ . Using the inverse fast Fourier transform (IFFT), the dynamic response of structure could be obtained finally.

### 3 Example Analysis

As shown in Figure 1, a framed structure is chosen as computational model, and material parameters are listed in Table 1. In calculation, we choose  $l_0$  as unit length,  $t_0 = l_0/c_0$  as unit time, where  $c_0$  is the velocity of axial wave. A horizontal rectangle impact load during a time period of  $30t_0$  has been assumed to act at joint 2 with amplitude of  $F_0 = El_0^2$ . All of internal forces and moments can be normalized by  $F_0$  and  $F_0l_0$  while the time by  $t_0$ .

The transient response for of the axial force in member 32 at joint 3 is displayed in Figure 2 using present method (MRRM) and finite element method (FEM) based on ANASYS code. In computation, the damping coefficients are chosen as  $\eta_u = \eta_\phi = 0.04$ . Three non-solid lines marked by ANSYS(1), (2) and (3) represent the results using element length of  $0.2l_0$ ,  $0.5l_0$ , and  $l_0$  respectively in FEM. The results show that the present model (MRRM) agrees with FEM model with the smallest element. It reveals that the present method is valid.

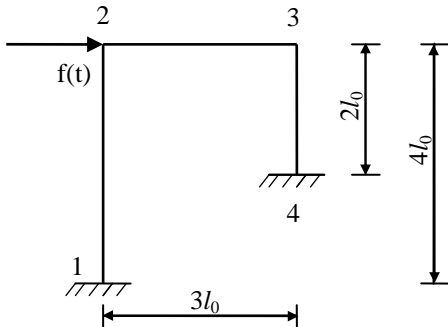


Figure 1. Computational model

Table 1. Parameters of the model

E (Pa)	$\nu$	$\rho(\text{kg/m}^3)$	A	$\kappa$	$I_x$	$I_y$	$I_z$
$2e11$	0.3	7800	$0.1963 l_0^2$	0.8225	$6.1359e-3 l_0^4$	$3.0680e-3 l_0^4$	$3.0680e-3 l_0^4$

The transient responses for axial force of member 32 at joint 3 with and without damping effect are illustrated in Figure 3 using MRRM. It is observed that

there is no response for the axial force before  $t=3t_0$ , which is, theoretically, the earliest arrival time for the fastest (axial) wave from source joint 2 to joint 3. The result indicates MRRM has high accuracy in computation for prediction of first arrival times of signals in such structures. Furthermore, it is seen that the dash line (no damping) presents a violent change due to high-frequency induced by impact. In contrast, the solid line (damping effect) is smoother, which shows that high-frequency portions of the response are weakened by effect of damping.

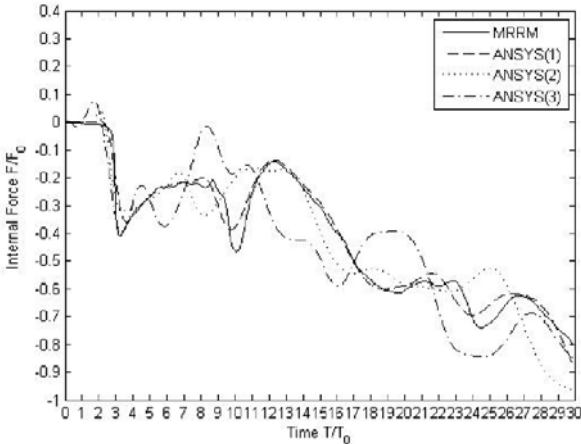


Figure 2. Comparison between MRRM and FEM for axial force in member 32

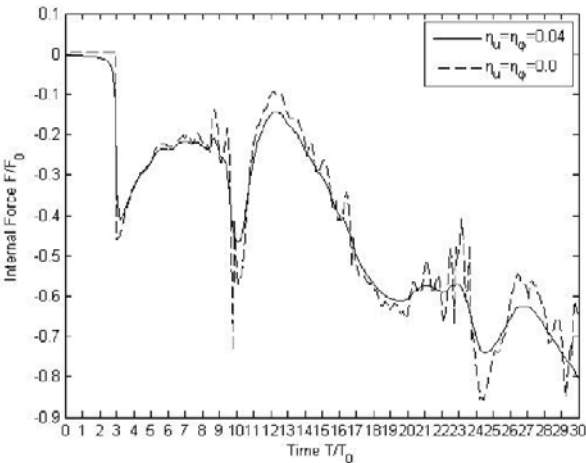


Figure 3. Response for axial force at joint 3 in member 32

## 4 Conclusions

A method of reverberation ray matrix (MRRM) has been developed for transient response analysis of space structures composed of bar elements taking into account of hysteretic damping effect. Comparison with results from FEM shows a high precision in computation for MRRM. The result shows that high-frequency portions of the response are weakened by effect of damping.

## References

- Cai G.Q., Nie G.H. (2008). Reverberation matrix method for static analysis of space structures composed of bar elements under arbitrary connection and constraint conditions. *Chinese Quarterly of Mechanics*, 29(4):544-555 [in Chinese].
- Cao L.W., Nie G.H. (2006). Reverberation matrix method and its application to static analysis of framed structures. *Chinese Quarterly of Mechanics*, 26(4):687-691 [in Chinese].
- Howard S.M., Pao Y.H. (1998). Analysis and experiments on stress waves in planar trusses. *ASCE Journal of Engineering Mechanics*, 124(8):884-891.
- Pao Y.H., Keh D.C. (1996). Moment-distribution method and re-distribution matrix analysis of frame structures. *The Chinese Journal of Mechanics*, 12(1):157-165.
- Pao Y.H., Keh D.C., Howard S.M. (1999). Dynamic response and wave propagation in plane trusses and frames. *AIAA Journal*, 37(5):594-603.
- Pao Y.H., Sun G. (2003). Dynamic bending strain in planar trusses with pinned or rigid joints. *Journal of Engineering Mechanics*, 129(3):324-332.

*“This page left intentionally blank.”*

# A Study of Bending-Bending-Torsional Coupled Vibrations of Axially-Loaded Euler-Bernoulli Beams Including Warping Effects

Fang Zhang<sup>1\*</sup> and Guoyan Wang<sup>1</sup>

<sup>1</sup>School of Aerospace Engineering and Applied mechanics, Tongji University, Shanghai 200092, P.R. China

**Abstract.** The bending-bending-torsional coupled undamped free vibrations of axially-loaded Euler-Bernoulli beams with bi-asymmetric cross sections are studied in this paper; and the warping effect is considered. The reference point is chosen coincident with the mass center of the cross sections of the beam and reference axes are chosen parallel to the geometric axes of the cross sections; geometric parameters of the cross-sections of the beam are determined with respect to geometric axes. The numerical results show the accuracy and effectiveness of the present method, and the effects of axial load and warping rigidity on natural frequencies are discussed.

**Keywords:** bending-bending-torsional coupled vibrations, Euler-Bernoulli beams, axial-load, warping effect

## 1 Introduction

It is well known that, when the cross sections of a beam have two symmetric axes so that the mass center and the shear center are coincident, the bending motion and the torsional motion of the beam are independent and the classical Euler-Bernoulli and/or Timoshenko beam theory are valid (Li, 2004a). However, for many practical beams, the mass center and the shear center of the cross-sections are obviously not coincident due to some certain geometric properties. In these cases, the bending motion of the beams are coupled with the torsional motion (Li, 2004b); and then, the classical beam theories are invalid.

In recent years, a number of studies dealing with bending-torsional coupled vibrations of beams were developed. For example, Banerjee (1992, 1994) derived some analytical expressions for the coupled bending-torsional dynamic stiffness

---

\* Corresponding author, e-mail: zhangxw5566@163.com

matrix of an axially-loaded uniform beam element with mass center and shear center not coincident. The influences of axial force on the coupled bending-torsional frequencies of a cantilever beam with thin-walled section were demonstrated by numerical results, but the warping rigidity was not included. Hashemi (2000) presented a new dynamic finite element for calculating the natural frequencies and mode shapes of coupled bending-torsional vibrations of axially loaded beams, by means of the closed form solutions of the governing equations of motion based on the Euler-Bernoulli and St.Venant beam theories; but the warping effect was also not considered. According to the state-of-art literatures, ignoring warping rigidity could lead to large errors when calculating the natural frequencies of thin-walled beams with open sections. Li (2002, 2004a, 2004b) studied the bending-torsional coupled vibrations of Timoshenko/Euler-Bernoulli beams with one symmetric axis, using exact dynamic stiffness matrix method. In their studies, the exact dynamic stiffness matrixes were developed and the effect of axial force, warping rigidity, shear deformation and rotary inertia were considered. Kaya (2007) investigated an axially-loaded Timoshenko beam with closed cross-sections using differential transform method; the effects of the bending-torsional coupling, the axial force and the slenderness ratio on natural frequencies were investigated with the help of the Mathematica.

In all of the above reported researches, the reference points of the cross sections of the beams coincide with the shear centers and the reference axes coincide with the principal axes of inertia of the cross sections, the parameters used in these studies are about the principal axis of inertia of the cross sections. Generally speaking, the geometric parameters of a beam with respect to principal axes of inertia are calculated by means of geometric parameters with respect to geometric axes; that is, when the product of inertia equals to zero, the corresponding axes are the principal axes of inertia. Therefore, the process of calculation in the above researches would be a little bit more complicated. In order to simplify the process of calculation, the reference points are chosen coincident with the mass centers of the beam and the reference axes are chosen coincident with the geometric axes of the cross sections in the present study. So, the geometric parameters of the cross-sections of the beam are determined with respect to geometric axes. The warping effect is considered in the present study.

## 2 Governing Differential Equations of Motion

A uniform straight elastic Euler-Bernoulli beam with bi-asymmetric cross sections is shown in Figure 1. The length of the beam is  $L$ ; the shear center and the mass center are denoted by  $S$  and  $C$ , respectively; the origin of the coordinate system coincides with the mass center  $C$  and the  $x$  axis is chosen coincident with the longitudinal elastic axis of the beam. The coordinates of the shear center  $S$  are  $(-e_y, e_z)$ . The bending translations of the mass center in  $Y$  and  $Z$  directions and

the torsional rotation about the X axis are denoted by  $v(x, t)$ ,  $w(x, t)$  and  $\varphi(x, t)$ , where  $x$  and  $t$  denote the distance from the origin and the time, respectively. A constant axial compression force  $P$  is applied at the mass center of the cross section at an end of the beam. At the beginning of the vibration, due to bending-torsional coupling, the mass center  $C$  moves to  $C^1$  and shear center  $S$  moves to  $S^1$ , and the cross section rotates by the angle  $\varphi$  about the longitudinal axis through the shear center, and the final position of the mass center  $C$  is  $C^2$ .

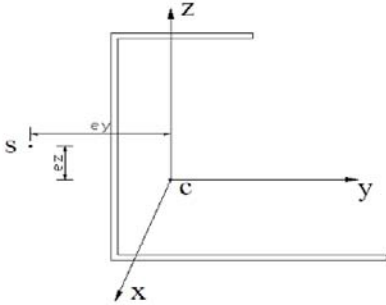


Figure 1. Cross section of the beam

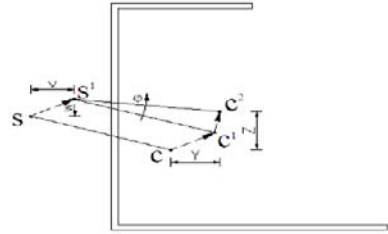


Figure 2. Movement of Shear center and mass center

The final displacements of the shear center  $S$  are  $v_s = v + \varphi e_z$ ,  $w_s = w - \varphi e_y$ ,  $v_s$  and  $w_s$  are the displacements of  $S$  along  $y$  and  $z$  axes, respectively.

The governing differential equations in the two bending directions are:

$$\frac{\partial^2 M_z}{\partial x^2} = -w_y = -m \frac{\partial^2 v}{\partial t^2} - P \frac{\partial^2 v}{\partial x^2}, \quad \frac{\partial^2 M_y}{\partial x^2} = -w_z = -m \frac{\partial^2 w}{\partial t^2} - P \frac{\partial^2 w}{\partial x^2} \tag{1}$$

On the other hand, the bending moment and curvature in the two directions have the following relations:

$$M_z = EI_z \frac{d^2 Y}{dx^2} + EI_{yz} \frac{d^2 Z}{dx^2} = EI_z \frac{d^2 (v + \varphi e_z)}{dx^2} + EI_{yz} \frac{d^2 (w - \varphi e_y)}{dx^2} \tag{2a}$$

$$M_y = EI_y \frac{d^2 Z}{dx^2} + EI_{yz} \frac{d^2 Y}{dx^2} = EI_y \frac{d^2 (w - \varphi e_y)}{dx^2} + EI_{yz} \frac{d^2 (v + \varphi e_z)}{dx^2} \tag{2b}$$

Therefore, the governing differential equations of motion in the two bending directions are:

$$EI_z \frac{\partial^4 (v + \varphi e_z)}{\partial x^4} + EI_{yz} \frac{\partial^4 (w - \varphi e_y)}{\partial x^4} + m \frac{\partial^2 v}{\partial t^2} + P \frac{\partial^2 v}{\partial x^2} = 0 \tag{3a}$$

$$EI_y \frac{\partial^4 (w - \varphi e_y)}{\partial x^4} + EI_{yz} \frac{\partial^4 (v + \varphi e_z)}{\partial x^4} + m \frac{\partial^2 w}{\partial t^2} + P \frac{\partial^2 w}{\partial x^2} = 0 \tag{3b}$$

where  $EI_y$  ,  $EI_z$  are the flexural rigidities about geometric axes;  $EI_{yz}$  is the product of inertia about geometric axes;  $m$  is the mass per unit length.

To establish the governing equation of the torsional vibration, let T be the intensity of the distributed torque applied to the beam along the longitudinal axis through the shear centers. According to Saint-Venant’s theory, warping rigidity is assumed to be the same along the beam. The given torque is then balanced at any cross-section partially by shearing stresses due to twist and partially by shearing stresses due to bending. So,  $T = EI_w \frac{\partial^4 \varphi}{\partial x^4} - GJ \frac{\partial^2 \varphi}{\partial x^2}$  , and  $EI_w$  is the warping rigidity ,  $GJ$  is the torsional rigidity.

The governing differential equations of motion of torsional vibration can be derived by substituting the inertia torque into the corresponding equations of D’Alembert’s principle. Since the axial forces P are applied at the mass center of the cross sections at two end of the beam, so

$$T = -P \left( \frac{I_c}{m} \frac{\partial^2 \varphi}{\partial x^2} + e_y \frac{\partial^2 w}{\partial x^2} - e_z \frac{\partial^2 v}{\partial x^2} \right) + me_z \frac{\partial^2 v}{\partial t^2} - me_y \frac{\partial^2 w}{\partial t^2} - I_c \frac{\partial^2 \varphi}{\partial t^2} \tag{4}$$

where  $I_c$  is the polar moment of inertia per unit length of beam about x axis.

Then, the governing differential equation of motion in torsional direction is:

$$GJ \frac{\partial^2 \varphi}{\partial x^2} - P \left( \frac{I_c}{m} \frac{\partial^2 \varphi}{\partial x^2} + e_y \frac{\partial^2 w}{\partial x^2} - e_z \frac{\partial^2 v}{\partial x^2} \right) + me_z \frac{\partial^2 v}{\partial t^2} - me_y \frac{\partial^2 w}{\partial t^2} - I_c \frac{\partial^2 \varphi}{\partial t^2} - EI_w \frac{\partial^4 \varphi}{\partial x^4} = 0 \tag{5}$$

Finally, the governing differential equations of motion of axially-loaded bending-torsional coupled vibrations of Euler-Bernoulli beams are:

$$\begin{cases} EI_z \frac{\partial^4 v}{\partial x^4} + EI_{yz} \frac{\partial^4 w}{\partial x^4} + EI_z e_z \frac{\partial^4 \varphi}{\partial x^4} - EI_{yz} e_y \frac{\partial^4 \varphi}{\partial x^4} + P \frac{\partial^2 v}{\partial x^2} + m \frac{\partial^2 v}{\partial t^2} = 0 \\ EI_y \frac{\partial^4 w}{\partial x^4} - EI_{yz} e_y \frac{\partial^4 \varphi}{\partial x^4} + EI_{yz} e_z \frac{\partial^4 v}{\partial x^4} + P \frac{\partial^2 w}{\partial x^2} + m \frac{\partial^2 w}{\partial t^2} = 0 \\ GJ \frac{\partial^2 \varphi}{\partial x^2} - P \left( \frac{I_c}{m} \frac{\partial^2 \varphi}{\partial x^2} + e_y \frac{\partial^2 w}{\partial x^2} - e_z \frac{\partial^2 v}{\partial x^2} \right) + me_z \frac{\partial^2 v}{\partial t^2} - me_y \frac{\partial^2 w}{\partial t^2} - I_c \frac{\partial^2 \varphi}{\partial t^2} - EI_w \frac{\partial^4 \varphi}{\partial x^4} = 0 \end{cases} \tag{6}$$

### 3 The Solution of the Governing Differential Equations of Motion

Following the similar solution procedure given by Li jun (2002, 2004a, 2004b), we get the solution of Equation (6) as follows:

$$\begin{aligned}
 V(\xi) &= t_1^v C_1 \operatorname{ch} \alpha \xi + t_1^v C_2 \operatorname{sh} \alpha \xi + t_2^v C_3 \operatorname{ch} \beta \xi + t_2^v C_4 \operatorname{sh} \beta \xi + t_3^v C_5 \cos \gamma \xi + t_3^v C_6 \sin \gamma \xi \\
 &+ t_4^v C_7 \cos \delta \xi + t_4^v C_8 \sin \delta \xi + t_5^v C_9 \cos \eta \xi + t_5^v C_{10} \sin \eta \xi + t_6^v C_{11} \cos \chi \xi + t_6^v C_{12} \sin \chi \xi \\
 W(\xi) &= t_1^w C_1 \operatorname{ch} \alpha \xi + t_1^w C_2 \operatorname{sh} \alpha \xi + t_2^w C_3 \operatorname{ch} \beta \xi + t_2^w C_4 \operatorname{sh} \beta \xi + t_3^w C_5 \cos \gamma \xi + t_3^w C_6 \sin \gamma \xi \\
 &+ t_4^w C_7 \cos \delta \xi + t_4^w C_8 \sin \delta \xi + t_5^w C_9 \cos \eta \xi + t_5^w C_{10} \sin \eta \xi + t_6^w C_{11} \cos \chi \xi + t_6^w C_{12} \sin \chi \xi \\
 \Theta(\xi) &= \alpha C_1 \operatorname{sh} \alpha \xi + \alpha C_2 \operatorname{ch} \alpha \xi + \beta C_3 \operatorname{sh} \beta \xi + \beta C_4 \operatorname{ch} \beta \xi + \gamma C_5 \operatorname{sh} \gamma \xi + \gamma C_6 \operatorname{ch} \gamma \xi \\
 &- \delta C_7 \sin \delta \xi + \delta C_8 \cos \delta \xi - \eta C_9 \sin \eta \xi + \eta C_{10} \cos \eta \xi - \chi C_{11} \sin \chi \xi + \chi C_{12} \cos \chi \xi
 \end{aligned}$$

where

$$t_j^v = \frac{(b_3 e_z - e_y) a_3 \tau j^4 - (e_z - a_3 e_y) [\tau j^4 + (b_1 - b_2) \tau j^2]}{[\tau j^2 + (a_1 - a_2)] [\tau j^2 + (b_1 - b_2)] - a_3 b_3 \tau j^4},$$

$$t_j^w = \frac{(e_z - a_3 e_y) b_3 \tau j^4 - (b_3 e_z - e_y) [\tau j^4 + (a_1 - a_2) \tau j^2]}{[\tau j^2 + (b_1 - b_2)] [\tau j^2 + (a_1 - a_2)] - a_3 b_3 \tau j^4}, \quad j = 1, 2, \dots, 6$$

$\alpha = \sqrt{\tau_1}, \beta = \sqrt{\tau_2}, \gamma = \sqrt{\tau_3}, \delta = \sqrt{\tau_4}, \eta = \sqrt{\tau_5}, \chi = \sqrt{\tau_6}$  are the six roots of the following equation:

$$\begin{aligned}
 &(a_3 b_3 - 1) c_4 \tau^6 + [(1 - a_3 b_3)(1 + c_3 - c_1 d) + (a_2 - a_1 - b_1 + b_2) c_4 + \\
 &(1 - a_3 b_3)(c_2 - c_1)(e_y^2 + e_z^2)] \tau^5 + [(a_1 - a_2 + b_1 - b_2)(1 + c_3) + (a_2 + a_1)(b_1 - b_2) c_4 + \\
 &(b_2 - a_1 - b_1) c_1 d + (a_2 - a_1)(c_1 - c_2)] e_y^2 + (a_3 b_1 - a_3 b_2 + a_1 b_3 - a_2 b_3)(c_1 + c_2) e_y e_z + \\
 &(c_1 - c_2)(b_2 - b_1) e_z^2 \tau^4 + (a_1 b_1 - a_2 b_1 - a_1 b_2 + a_2 b_2)(1 + c_3 - c_1 d) \tau^3 = 0
 \end{aligned} \tag{7}$$

$$a_1 = \frac{P}{EI_z} L^2, a_2 = \frac{m\omega^2}{EI_z} L^4, a_3 = \frac{I_{yz}}{I_z}, b_1 = \frac{P}{EI_y} L^2, b_2 = \frac{m\omega^2}{EI_y} L^4,$$

$$b_3 = \frac{I_{yz}}{I_y}, c_1 = \frac{P}{GJ}, c_2 = \frac{m\omega^2}{GJ} L^2, c_3 = \frac{I_C\omega^2}{GJ}, c_4 = \frac{EI_w}{GJL^2}, d = \frac{I_C}{m}$$

### 4 Boundary Conditions

In this study, we adopt the boundary conditions given by (Tanaka, 1999).

1. For clamped end:  $V = V' = 0, W = W' = 0, \Theta = \Theta' = 0$
2. For free end:  $V'' = V''' = 0, W'' = W''' = 0, \Theta'' = GJ\Theta' - EI_w\Theta''' = 0$
3. For Simply-Supported end:  $V = V'' = 0, W = W'' = 0, \Theta = \Theta'' = 0$

For a beam with each of the above boundary conditions, there are four boundary conditions in each direction, so 12 linear homogeneous equations are obtained, which can be written in matrix form:  $[D][C] = 0$ , where  $[C] = [C_1, C_2, \dots, C_{12}]^T$  contains 12 constants,  $[D]$  is a  $12 \times 12$  matrix.

For nontrivial solutions of  $[C]$ , there must be  $Det[D] = 0$  which is the characteristic equation of the problem or the frequency equation of the beam. Obviously the resulting frequency equation is a transcendental one, there are an infinite number of natural frequencies and mode shapes of the beam. The method adopted in the present study is: first, find the small frequency intervals in which a solution of the frequency equation lies with the functional digraph using the software Mathematica; then, solve the frequency equation in those small intervals.

### 5 A numerical example

A thin-walled uniform Euler-Bernoulli beam with bi-asymmetric axes is considered. The geometric and physical properties of the beam are given below:

$$m = 21.62kg / m, L = 5m, e_y = 35.7mm, e_z = 53.69mm, P = 2500N, GJ = 3710Nm^2,$$

$$EI_y = 4995534Nm^2, EI_z = 385625Nm^2, EI_{yz} = -433956Nm^2, EI_w = 2461.2m^6, I_C = 0.20Nm$$

In order to investigate and validate the correctness and accuracy of the present method, the software Ansys is used in the example, in which the element type beam188 is adopted and the warping rigidity is considered. To investigate the ef-

fect of axial force on the frequencies, the situation  $P=0$  and  $P=2500N$  are considered, respectively. Also, the situations with and without warping rigidity are considered to investigate the effect of warping rigidity on the frequencies.

The first six natural frequencies of the axially unloaded beam ( $P=0$ ) and loaded beam ( $P=2500N$ ) are calculated for three types of end conditions by ignoring and including the effect of warping rigidity.

It can be seen from Table 1 that the results obtained by the present method coincide well with the results obtained by Ansys, in the situation of axially loaded beam ( $P=2500N$ ) with warping included. The maximum error between the two results is less than 5%. The differences can be attributed to the fact that the present method is based on Euler-Bernoulli beam theory, in which the shear deformation is ignored, while the element type beam188 is based on Timoshenko beam theory in which the effect of shear deformation is taken into account.

Table 1. Natural frequencies of the beam with Free-Free, Clamp-Free, Simply-Supported boundary conditions (Hz)

	Free-Free						Clamp-Free						Simply-Supported					
	P=0			P=2500			P=0			P=2500			P=0			P=2500		
	A	B	C	A	B	C	A	B	C	A	B	C	A	B	C	A	B	
1	14.33	13.57	14.20	14.21	13.40	2.80	2.76	2.78	2.79	2.75	7.56	7.43	7.53	7.53	7.35			
2	17.08	16.79	17.01	17.07	16.42	7.28	6.17	7.22	7.24	6.05	14.50	13.20	14.42	14.45	13.15			
3	31.93	27.05	31.76	31.84	26.89	12.32	11.82	12.27	12.29	11.80	26.76	21.08	26.61	26.67	20.97			
4	42.32	32.05	42.04	42.28	31.93	16.55	15.18	16.42	16.53	15.13	33.62	33.07	33.29	33.59	32.92			
5	66.80	44.35	66.35	66.72	44.16	27.65	21.60	27.50	27.57	21.53	42.28	33.46	42.05	42.23	33.44			
6	77.10	54.32	73.79	74.75	54.14	40.91	28.58	40.55	40.84	28.43	55.01	37.66	54.60	54.91	37.60			

Note: "A" represents "warping included", "B" represents "warping ignored", and "C represents Ansys".

The results shown in Table 1 indicate that, although the effect of warping rigidity on the first two natural frequencies is insignificant, it has a significant influence on higher natural frequencies for all conditions under investigation. It can be seen that with the frequencies getting higher and higher, the effect of warping rigidity becomes more and more significant and therefore the errors can be unacceptably large if the warping effect is ignored in these situations. So, it is clear that warping rigidity should be taken into account when higher frequencies are required.

On the other hand, it can be seen from Table 1 that, with the frequencies getting higher and higher, the effect of axial force on natural frequencies becomes smaller quickly. The effects of axial load on higher natural frequencies are insignificant for all the three end conditions.

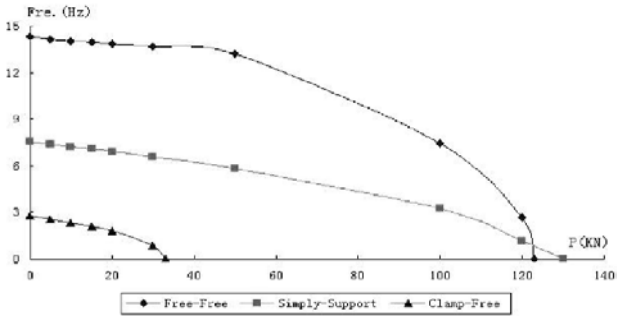


Figure 3. The varying trend of the first order frequency with axial loads

In order to investigate the effect of axial load on the natural frequencies of the beam, the varying trend of the first order frequency with axial loads in the three boundary conditions are listed in Figure 3. It's easy to know that, with the load increasing, the frequencies in all the three boundary conditions decrease, and the decreasing speed become more quickly when the axial force close to the buckling load. Finally, the frequencies become zero when the load coincides with the buckling load of the beam, which means the buckling of the beams can be regarded as a degenerate case of zero frequency vibration. The buckling loads in the three boundary conditions are  $P = 123\text{kN}$ ,  $33.2\text{kN}$ ,  $130\text{kN}$ , respectively.

## 6 Conclusions

In this paper, the bending-bending-torsional coupled vibration of axially-loaded uniform Euler-Bernoulli beams with bi-asymmetric cross sections is studied. During the research, the origin of the coordinate system of each cross section is located at the mass center and the coordinate axes are chosen coincident with the geometric axes of the cross sections, so that geometric parameters of the cross-sections of the beam are determined with respect to geometric axes. Warping effect is considered in this study.

It is shown from the calculation of the numerical example that the present method can simplify the process of calculation for the situations in which geometric parameters of the cross sections need to be determined for the specifically. The numerical results show the accuracy and effectiveness of the present method.

## References

- Banerjee J.R., Fisher S.A. (1992). Coupled bending-torsional dynamic stiffness matrix for axially loaded beam elements. *International Journal for Numerical Methods in Engineering*, 33(4): 739-751.
- Banerjee J.R., Williams F.W. (1994). Coupled bending-torsional dynamic stiffness matrix of an axially loaded Timoshenko beam element. *International Journal of Solids and Structures*, 31(6): 749-762.
- Kaya, Ozgumus O. (2007). Flexural-torsional coupled vibration analysis of axially loaded closed-section composite Timoshenko beam by using DTM. *Sound and Vibration*, 30(6): 495-506.
- Li J., Li W.Y., Shen R.Y., Hua H.X., Jin X.D. (2004a). Coupled bending and torsional vibration of axially loaded Bernoulli-Euler beams including warping effects. *Applied Acoustics*, 65(2): 153-170.
- Li J., Hua H.X., Shen R.Y., Jin Xianding (2004b). Dynamic response of axially loaded monosymmetrical thin-walled Bernoulli-Euler beams. *Thin-walled Structures*, 42(12): 1689-1707.
- Li J, Jin X.D. (2002). Theoretical analysis on natural vibration and stability of axially-loaded Timoshenko thin-walled beam. *Structure & Environment Engineering*, 29: 18-23.
- Mohammad H.S., Richard M.J. (2000). Free vibrational analysis of axially loaded bending-torsion coupled beams: a dynamic finite element. *Computers and Structures*, 77: 711-724.
- Tanaka M., Bercin A.N. (1999). Free vibration solution for uniform beams of nonsymmetrical cross section using Mathematica. *Computers and Structures*, 71: 1-8.

*“This page left intentionally blank.”*

# Damage Analysis of 3D Frame Structure under Impulsive Load

Julin Wang<sup>1\*</sup> and Taisheng Yang<sup>1</sup>

<sup>1</sup>Institute of Building Structures, Shanxi Architectural Technical College, Taiyuan 030006, P.R. China

**Abstract.** In this article, we utilized the lumped damage mechanics method to implement the damage analysis to the 3D frame structure under impulsive load. First, take the damage parameters as the interior variable of the system, and based on the finite unit, combine continuum mechanics, fracture mechanics and plastic hinge to analyze the mechanical behaviors of the structure, and finally implement numerical simulation analysis to the frame structure with two layers, and compare the result with the computation result of ABAQUS to validate the feasibility.

**Keywords:** lumped damage mechanics, impulsive load, damage

## 1 Introduction

Since the twin towers of the World Trade Center were stroke by terrorists, the nonlinear analysis and damage computation of structure under sudden impulsive loads are more and more concerned by people. The relative researches cannot only establish more reasonable structure design theory, but offer necessary theoretic base for the reliability evaluation and reinforce design of damaged structure.

In recent years, many deep researches about the reaction analysis and damage mechanism of structure under sudden impulsive loads occur and some reasonable methods are put forward one by one (Taucer, 1991; Zhu 1991; Bolzon 1996; Cipollina, 1995; Marante, 2002; Mazza, 1998; Xue, 1999 and Perera, 2000). Based on former researches, we utilize the method of lumped damage mechanics to directly solute the damage of 3D frame structure under the impulsive loads, and implement numerical simulation analysis to one frame structure with two layers, and compare the result with the computation result of ABAQUS to validate the feasibility.

---

\* Corresponding author, e-mail: wangjl\_tj@163.com

## 2 The Dynamic Equation of 3D Structure

Suppose there are  $m$  frame members and  $n$  nodes, and the dynamic equation in the time range of  $[0, T]$  is

$$\sum_{e=1}^m [B]_e^T [M]_e + \sum_{e=1}^m [m]_e \left\{ \ddot{U} \right\} = \{P\} \quad \forall \left\{ \dot{U}^* \right\} \tag{1}$$

where the matrix  $[B]$  is the node displacement function, and the concrete form is

$$[B] = \begin{bmatrix} -\frac{m_1}{L} & -\frac{m_2}{L} & -\frac{m_3}{L} & n_1 & n_2 & n_3 & \frac{m_1}{L} & \frac{m_2}{L} & \frac{m_3}{L} & 0 & 0 & 0 \\ -\frac{m_1}{L} & -\frac{m_2}{L} & -\frac{m_3}{L} & 0 & 0 & 0 & \frac{m_1}{L} & \frac{m_2}{L} & \frac{m_3}{L} & n_1 & n_2 & n_3 \\ -t_1 & -t_2 & -t_3 & 0 & 0 & 0 & t_1 & t_2 & t_3 & 0 & 0 & 0 \\ \frac{n_1}{L} & \frac{n_2}{L} & \frac{n_3}{L} & m_1 & m_2 & m_3 & -\frac{n_1}{L} & -\frac{n_2}{L} & -\frac{n_3}{L} & 0 & 0 & 0 \\ \frac{n_1}{L} & \frac{n_2}{L} & \frac{n_3}{L} & 0 & 0 & 0 & -\frac{n_1}{L} & -\frac{n_2}{L} & -\frac{n_3}{L} & m_1 & m_2 & m_3 \\ 0 & 0 & 0 & -t_1 & -t_2 & -t_3 & 0 & 0 & 0 & t_1 & t_2 & t_3 \end{bmatrix} \tag{2}$$

where  $t$ ,  $m$  and  $n$  respectively are the unit vectors of  $x$ ,  $y$  and  $z$  axis, and  $L$  is the length of the frame member.

$M_e^T$  is the interior force of the unit  $e$ ,  $M_e^T = (m_{iy}, m_{jy}, N, m_{iz}, m_{jz}, m_x)$ .

where  $N$  is the axial force,  $m_x$  is the torque,  $m_{iy}$  and  $m_{jy}$  are the flexural moments of  $i$  and  $j$  ports in the face of  $xz$ ,  $m_{iz}$  and  $m_{jz}$  are the flexural moments of  $i$  and  $j$  ports in the face of  $xy$ .

$\{U\}^T$  is the displacement matrix of the whole structure,  $\{U\}^T = (\{u\}_1, \{u\}_2, \dots, \{u\}_n)$ .

$\{P\}$  is the node exterior force of the structure.

### 3 Model of Lumped Damage Mechanics

#### 3.1 The Damage Constitutive Equation (Maria, 2003)

For the lumped damage mechanics model, the unit is composed by one elastic girder and two plastic hinges on two ends, and suppose the dissipation of all energies is centralized on the plastic hinges.

Suppose the distortion of the hinge is composed by the plastic distortion and the distortion induced by the damage, i.e.

$$\{\Phi^h\} = \{\Phi^p\} + \{\Phi^d\} \tag{3}$$

where  $\Phi^p$  denotes the plastic distortion of the hinge and  $\Phi^d$  denotes the distortion induced by the damage.

$$\{\Phi^p\} = (\phi_{iy}^p, \phi_{jy}^p, \delta^p, \phi_{iz}^p, \phi_{jz}^p, \phi_x^p)^T \tag{4}$$

in the frame structure of RC, the plastic corner is mainly induced by the reinforcing steel bar yield, and the fracture of the concrete can be described by following two damage matrixes.

$$\{D^+\} = (d_{iy}^+, d_{jy}^+, d_{iz}^+, d_{jz}^+) \tag{5}$$

$$\{D^-\} = (d_{iy}^-, d_{jy}^-, d_{iz}^-, d_{jz}^-) \tag{6}$$

where + and - respectively denote the damages induced by positive and negative flexural moments (seen in Figure 1).

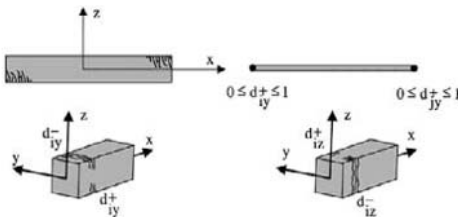


Figure 1. Cracking in a RC frame member via damage variables

The constitutive equation of the plastic hinge is

$$\{\Phi - \Phi^p\}_e = [F(D^+)]_{e,+} [M]_{e,+} + [F(D^-)]_{e,-} [M]_{e,-} \tag{7}$$

where + and - respectively denote the damages induced by positive and negative flexural moments,  $[F(D)]$  denotes the flexibility matrix of the damage unit, and the concrete expressions are

$$F(D^+) = F^0 + C(D^+) \tag{8}$$

$$F(D^-) = F^0 + C(D^-) \tag{9}$$

In the equation (8) and equation (9),  $F^0$  denotes the flexibility matrix of the unit in the flexible stage,  $C(D^+)$  and  $C(D^-)$  denotes the flexibility matrix induced by the damage of concrete, and the concrete expressions are

$$[C(D^+)] = \begin{bmatrix} \frac{d_{iy}^+ F_{11}^0}{1 - d_{iy}^+} & 0 & 0 & 0 & 0 & 0 \\ 0 & \frac{d_{jy}^+ F_{22}^0}{1 - d_{jy}^+} & 0 & 0 & 0 & 0 \\ 0 & 0 & 0 & 0 & 0 & 0 \\ 0 & 0 & 0 & \frac{d_{iz}^+ F_{44}^0}{1 - d_{iz}^+} & 0 & 0 \\ 0 & 0 & 0 & 0 & \frac{d_{jz}^+ F_{55}^0}{1 - d_{jz}^+} & 0 \\ 0 & 0 & 0 & 0 & 0 & 0 \end{bmatrix} \tag{10}$$

$$[C(D^-)] = \begin{bmatrix} \frac{d_{iy}^- F_{11}^0}{1 - d_{iy}^-} & 0 & 0 & 0 & 0 & 0 \\ 0 & \frac{d_{jy}^- F_{22}^0}{1 - d_{jy}^-} & 0 & 0 & 0 & 0 \\ 0 & 0 & 0 & 0 & 0 & 0 \\ 0 & 0 & 0 & \frac{d_{iz}^- F_{44}^0}{1 - d_{iz}^-} & 0 & 0 \\ 0 & 0 & 0 & 0 & \frac{d_{jz}^- F_{55}^0}{1 - d_{jz}^-} & 0 \\ 0 & 0 & 0 & 0 & 0 & 0 \end{bmatrix} \quad (11)$$

### 3.2 Damage Evolvement Rate (Marante, 2002)

Marante regarded the damage rule of Rankine as the function of the plastic hinge energy release rate, and Figure 2 explains the rule.

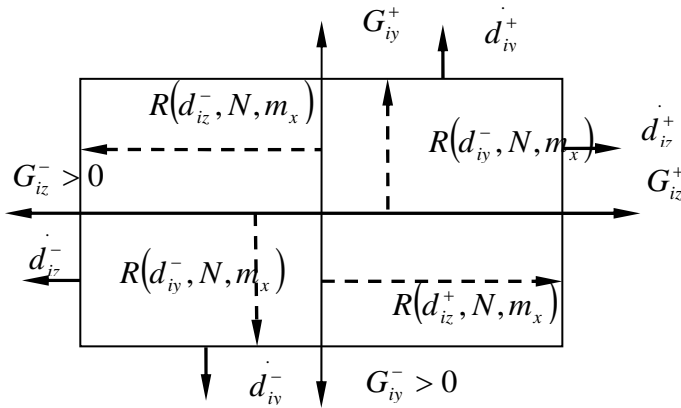


Figure 2. Damage criterion in the energy release rate space

From the figure, we can see that the undamaged is confirmed by the following equations.

$$\begin{aligned}
 G_{iy}^+ &= R_{iy}^+(d_{iy}^+; N, m_x) \quad ; \quad G_{iy}^- = R_{iy}^-(d_{iy}^-; N, m_x) \\
 G_{iz}^+ &= R_{iz}^+(d_{iz}^+; N, m_x) \quad ; \quad G_{iz}^- = R_{iz}^-(d_{iz}^-; N, m_x)
 \end{aligned}
 \tag{12}$$

The function of  $R(\ )$  is used to describe the anti-cracking ability of the plastic hinge  $i$ , and it is related with the axial force, torque and damage parameters, and it can be confirmed in the experiment. Cipollina et al obtained the expression of  $R(\ )$  according to the experiment.

$$R = G_{cr}(N, m_x) + q(N, m_x) \frac{\ln(1-d)}{1-d}
 \tag{13}$$

where  $G_{cr}$  and  $q$  respectively denote the anti-cracking parameters before and after the crack occurs, and both parameters are related with the axial force and torque, and they are confirmed by the following formulas.

$$G_{cr} = \frac{1}{2} F_0 m_{cr}^2(N, m_x)
 \tag{14}$$

$$\begin{aligned}
 \frac{F_0 m_u^2(N, m_x)}{2} &= (1-d_u)^2 G_{cr} + q(1-d_u) \ln(1-d_u) \\
 &\quad - 2(1-d_u) G_{cr} + q[\ln(1-d_u) + 1] = 0
 \end{aligned}
 \tag{15}$$

In above two formulas,  $m_{cr}$  denotes the flexural moment when the crack occurs,  $m_u$  denotes the maximum flexural moment, and  $d_u$  denotes the maximum damage value.

### 3.3 Yield Function

The effective flexural moments of the plastic hinge,  $m_{iy}^-$  and  $m_{iz}^-$  are

$$m_{iy}^- = \begin{cases} \frac{m_{iy}}{1-d_{iy}^+} & d_{iy}^+ > 0 \\ \frac{m_{iy}}{1-d_{iy}^-} & d_{iy}^- > 0 \end{cases} \quad (16)$$

$$m_{iz}^- = \begin{cases} \frac{m_{iz}}{1-d_{iz}^+} & d_{iz}^+ > 0 \\ \frac{m_{iz}}{1-d_{iz}^-} & d_{iz}^- > 0 \end{cases} \quad (17)$$

Replace the actual flexural moment by the effective flexural moment, and the yield function of the plastic hinge  $i$  is

$$f_i = f_i \left( m_{iy}^-, m_{iz}^-, m_x, N, \phi_{iy}^p, \phi_{iz}^p, \delta_i^p \right) \quad (18)$$

So the plastic distortion evolvement rate of the plastic hinge is

$$\begin{aligned} \dot{\phi}_{iy}^p &= \dot{\lambda}_i \frac{\partial f_i}{\partial m_{iy}} \quad ; \quad \dot{\phi}_{iz}^p = \dot{\lambda}_i \frac{\partial f_i}{\partial m_{iz}} \\ \dot{\phi}_x^p &= \dot{\lambda}_i \frac{\partial f_i}{\partial m_x} \quad ; \quad \dot{\delta}_i^p = \dot{\lambda}_i \frac{\partial f_i}{\partial N} \end{aligned} \quad (19)$$

and the axial plastic distortion evolvement rate and the plastic corner evolvement rate of the unit are

$$\dot{\delta}_x^p = \dot{\lambda}_i \frac{\partial f_i}{\partial N} + \dot{\lambda}_j \frac{\partial f_j}{\partial N} \quad (20)$$

$$\dot{\phi}_x^p = \dot{\lambda}_i \frac{\partial f_i}{\partial m_x} + \dot{\lambda}_j \frac{\partial f_j}{\partial m_x} \quad (21)$$

## 4 Numerical Computation of the Example

### 4.1 Description of the Example

The example is one single span RC frame structure with two layers. The span is 3.5m, the height of the layer is 2m, the Poisson ratio is 0.3, the elastic modulus is 2.633GPa and the density is  $2.5t/m^3$ . When the pole section is  $0.3 \times 0.3m$ , the reinforcement assembly is  $4\Phi 10$ , and when the girder section is  $0.4 \times 0.4m$ , the reinforcement assembly is  $4\Phi 12$ . The top suffers the impulsive load, which is seen in Figure 5.

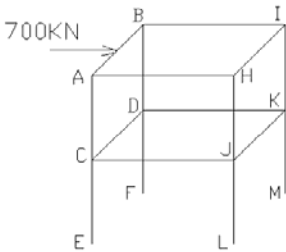


Figure 3. Finite element model of the frame structure

In 1ms, the pressure will increase from zero to the max. 700KN, and then the pressure will keep at the constant in 9ms, and in the later 10ms, the pressure will reduce to zero. And the pressure will keep at zero in later analysis (seen in Figure 6).

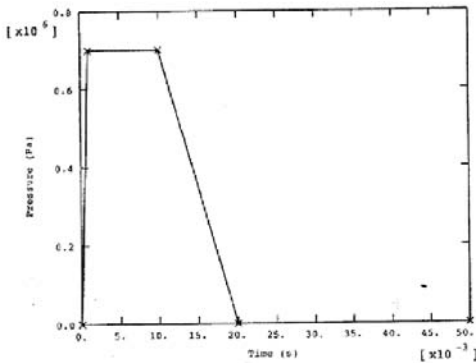


Figure 4. The impulsive load as the function of time

### 4.2 Numerical Analysis (Chopra, 2000)

The time interval  $[0, T]$  is dispersed into a series of discontinuous time  $(0, t_1, t_2 \dots, T)$ , and we use the finite difference method and the Newmark method to denote the node displacement acceleration by the node displacement, and structure can be analyzed in  $[0, T]$ . In the appointed time  $t_s$ , the equation (1) can be wrote as

$$\{L(U)\} = \sum_{e=1}^m [B]_e^T [M]_e + \sum_{e=1}^m [m]_e \left\{ \ddot{U} \right\} - \{P\} = 0 \tag{22}$$

to obtain the displacement at the time  $t_s$ , we can solve it by the following equation.

$$\{L(U)\} \cong \{L(U_0)\} + \left[ \frac{\partial L}{\partial U} \right]_{\{U\}=\{U_0\}} \{U - U_0\} = 0 \tag{23}$$

where  $\{U_0\}$  denotes the displace matrix obtained by the computation before the time  $t_s$ , and  $\{U\}$  denotes the displace matrix of the time  $t_s$  which we want to beg.

We utilize the center difference method to implement explicit time integral to the above motion equation, and offer the acceleration which can fulfill the dynamical balance condition when the increment step begins. To obtain the acceleration, we explicitly deduce the speed and displacement on time. The computation of the unit includes confirming the constitutive relation between unit strain and applied materials and the unit stress, and further computing the interior force and obtaining the damage value of the unit finally. The concrete approaches include

1. According to the strain rate  $\dot{\varepsilon}$ , compute the unit strain increment  $d\varepsilon$ .
2. According to the constitutive relation, compute the stress  $\sigma$ .
3. Integrating node internal force  $I_{(t+\Delta t)}$ .
4. Computing the damage value of the unit.

### 4.3 Parameter Setting

Take the time increment as  $3.0 \times 10^{-5} s$ . According the design principle of RC, compute and obtain the flexural moment of the girder and pole in various stages.

Pole:  $m_{cr} = 0.28 \times 10^5 KN mm$ ,  $m_u = 1.61 \times 10^5 KN mm$ .

Girder:  $m_{cr} = 0.69 \times 10^5 KN mm$ ,  $m_u = 2.53 \times 10^5 KN mm$ .

### 4.4 Computation and Analysis

Take the sub-module VUMAT of ABAQUS as the interface, adopt Fortran to compile and define the above model of the lumped damage mechanics, and run the program, and the computation result is seen in Figure 5. Use the fixed subprogram EXPLICIT modeling and compute the example, the result is seen in Figure6.

From Figure 5 and Figure 6, both the method in the article and the commercial software ABAQUS can compute the damage of structure under the impulsive load, but the obvious difference is that the method can compute the damage values of the two ends of the frame member, but ABAQUS can compute the damage value of the whole unit. In fact, the place that damage easily occurs in RC is the joint among frame members, i.e. the end part of the frame members. So, the method in the article more accords with the requirement of the actual engineering.

For the computation of the damage value, because of different damage meanings both express, so we can not directly compare, but it is consistent to judge whether the frame member is damaged and the damage degree. For example, for the frame member AB, comparing with other pole members, the damage values computed by two sorts of method are maximum values, and for the frame member DK, the former computation results are 0.06 and 0.09, and the later computation results are 0.09, which indicates the frame member DK is not damaged basically.

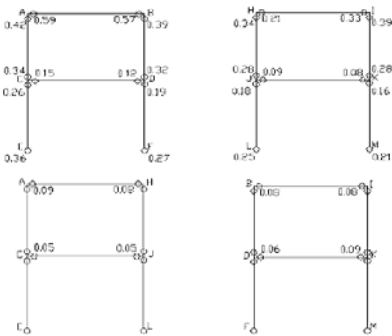


Figure 5. Result of lumped damage mechanics

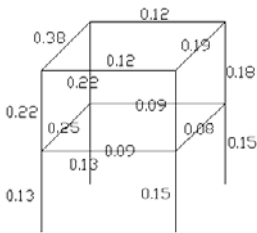


Figure 6. Result of EXPLICIT

## 5. Conclusions

From the above analysis, we can obtain two conclusions.

First, because the method in the article can be used to directly analyze the damage value of the two ends of the frame member, it can be extensively applied in diagnosing the damages because of earthquake or other sudden loads or evaluation the surplus credibility.

Second, the mature interface of the finite unit commercial software can be utilized to realize the mechanical model in the method and develop applied program conveniently.

## References

- Bolzon G. (1996). An approximate method for fatigue-life prediction of framed structures. *Fatigue Fract. Engng Mater. Struct.*, 19(12):1481–1491.
- Chopra A.K. (2000). *Dynamics of Structures: Theory and Applications to Earthquake Engineering*. Prentice Hall.
- Cipollina A., López-Inojosa A. and Flórez-López J. (1995). A simplified damage mechanics approach to nonlinear analysis of frames. *Comput. Struct.*, 54(6):1113–1126.
- Marante M.E. and Flórez-López J. (2002). Model of damage for RC elements subjected to biaxial bending. *Engng Struct.*, 24(9):1141–1152.
- Marante M.E. and Flórez-López J. (2003). Three-dimensional analysis of reinforced concrete frames based on lumped damage mechanics. *International Journal of Solids and Structures*, 40:5109–5123.
- Mazza, F. (1998). Modelli di danneggiamento nell'analisi sismica non lineare di strutture intelaiate in C.A. Tesis. Università degli Studi della Calabria Cosenza, Italy [in Italian].
- Perera A., Carnicero, Alarcón E. and Gómez S. (2000). A fatigue damage model for seismic response of RC structures. *Comput. Struct.*, 78:293–302.
- Taucer F., Enrico F. and Spacone (1991). *A fiber beam-column element for seismic response analysis of reinforced concrete structures*. Earthquake Engineering Research Center.

- Xue W.C. and Zhang Z.T. (1999). Nonlinear full range analysis methods of steel concrete structures and its application. *Chinese Journal of Computational Mechanics*, 16(3):334–342.
- Zhu Bolong and Yu Andong (1991). Nonlinear full-range analysis of R.C. frames. *Journal of Tongji University*, 83(3):21–30.

# Experimental and Numerical Approach to Study Dynamic Behaviour of Pavement under Impact Loading

Cherif Asli<sup>1,2\*</sup>, Zhiqiang Feng<sup>1</sup>, Gérard Porcher<sup>1</sup> and Jean Jacques Rincent<sup>2</sup>

<sup>1</sup>Laboratoire de Mécanique et d'Energétique d'Evry, Université d'Evry-Val d'Essonne, 40 rue du Pelvoux, 91020 Evry, France

<sup>2</sup>Rincent BTP Services, 39 rue Michel Ange, 91026 Evry, France

**Abstract.** This paper is devoted to investigate the dynamic response of a semi-rigid pavement under impact loading. Both experimental and numerical approaches are proposed. The experimental approach is conducted using a suitable instrumentation of the pavement. For numerical modelling, the finite element method is applied to simulate the elasto-dynamic response of the pavement.

**Keywords:** pavement, impact, measurement, finite element modeling

## 1 Introduction

These last years, the increase in the density of traffic on the roadway networks, as well as the speed and the weight of the vehicles, raised a polemic about the reliability of mechanistic and empirical methods to evaluate the performances of the pavements. The roadway managers and the local authorities are still searching for a reliable tool which allows them to make a feasible rehabilitation and to establish an appropriate strategy for the maintenance.

The development of the non-destructive testing techniques (NDT) for parameter identification and structural condition evaluation of the roadways grows more and more since these parameters are widely used to establish a diagnostic and assess the performance of pavements. According to the methods employed to quantify the response of the pavement to a solicitation, the NDT can be classified in two categories: deflection basin methods and wave propagation methods (Roesset, 1998; Hildebrand, 2002). Among the deflection basin methods, the falling weight deflectometer (FWD) has currently seen the most widespread use, while the spectral analysis of surface wave (SASW) is the most used among the wave propaga-

---

\* Corresponding author, e-mail: Feng@iup.univ-evry.fr

tion methods. If the later provides material properties because of the low strain level induced within the pavement, the former, gives rather material parameters because of its ability to impose the real dynamic loads or similar to those induced by heavy vehicle (Hildebrand, 2002). However, these parameters (elastic moduli, e.g.) are often obtained using backcalculation methods which are based on the static assumptions (Goktepe et al., 2006). The time history of the vertical displacements or actual velocities recorded in one or different points on the surface of the pavement are not entirely exploited. Only peak values which are assumed to be caused by a static load are used to backcalculate the elastic moduli of the layers although these peak values do not occur in fact at the same time. Hence, the use of elasto-static analyses instead of an elasto-dynamic analysis leads to inaccurate evaluation of the mechanical parameters since important frequency-dependent response information would be missing potentially when neglecting the inertia of the system ( Picoux et al., 2009; Stolle and Hein, 2002; Ji et al., 2006).

The dynamic behaviour of the pavement under an impact load can be investigated rigorously with numerical methods. In this paper, the computational program FER/Impact developed in our laboratory is used for this purpose. The finite element model established in the code is characterized by the combination of the bi-potential method for the solution of the contact problem and the first order integration scheme for the temporal discretization (Feng et al., 2005; 2006).

## 2 Experimental Study

The tests are performed on a semi-rigid pavement composed of a bituminous surfacing laid on a cement treated layer and both rest on the in-place subgrade (Figure 1). The instrumentation of the pavement is carried out using a circular loading plate and, at its axis, a velocity sensor is glued to the pavement. Via the loading plate, a load mass, endowed with a force sensor, impacts the road surface. The applied force and the induced pavement surface motion are simultaneously monitored (Figure 1). The geometrical and material properties of the pavement structure established by the designers are listed in Table 1 (Simonin, 2005).

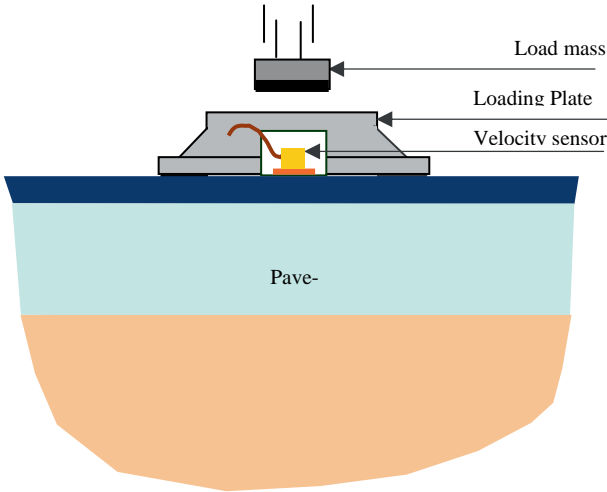
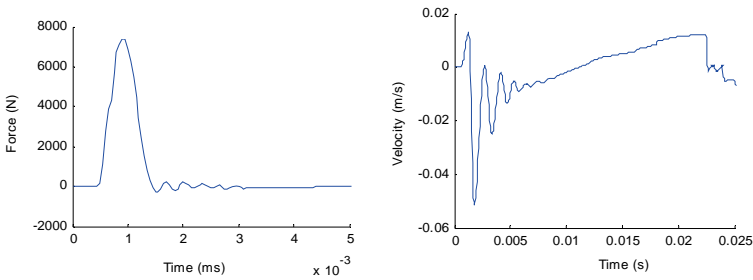


Figure 1. Instrumentation

Table 1. Geometrical and material proprieties

	E [MPa]	$\rho$ [kg/m <sup>3</sup> ]	$\nu$	Vp [m/s]	h[m]
Surfacing layer (AC)	5200	2300	0.35	1900	0.05
Base layer (BC)	23000	2350	0.25	3450	0.25
Subgrade	150	1200	0.35	448	infinite

During field tests, the acquisition is performed via two filtered digitalisation channels. The signals are sampled with a cadence of 20 kHz and the sampling interval time is 5 10<sup>-5</sup> s. This allows acquiring 2000 samples during the entire time acquisition of 100 ms. Force and velocity signals are recorded in the time domain. A typical time history of a recorded signal is illustrated in Figure 2.



(a) Force

(b) Velocity

Figure 2. Experimental results

Fourier transform is the most conventional signal processing tool used for spectral analysis. The signals are translated from the time domain to the frequency domain.

$$F(f) = \sum_{n=1}^N f(n).e^{j2\pi(k-1).(\frac{n-1}{N})} \qquad V(f) = \sum_{n=1}^N v(n).e^{j2\pi(k-1).(\frac{n-1}{N})}$$

where  $1 \leq k \leq N$  and  $N$  is the number of samples.

By performing Fourier transform, signals are decomposed into sinusoidal functions of various amplitudes and frequencies. This representation enables examination of the frequency content of the complete duration of the signals as illustrated in Figure 3.

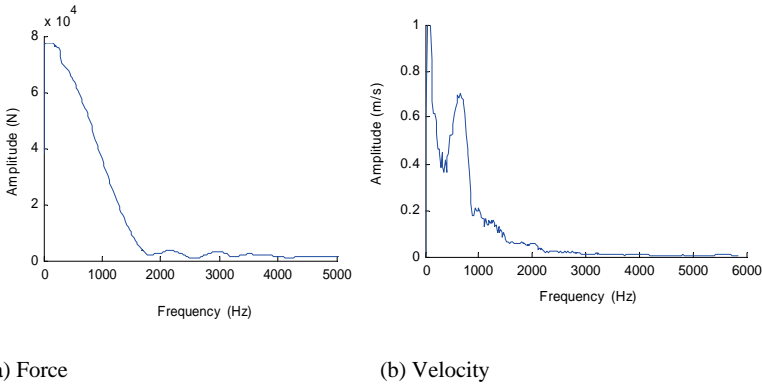


Figure 3. Spectral analysis

The spectral analysis of transient data makes use of a frequency response function (FRF) namely Mobility  $M(f)$  which is defined as the ratio between the Fourier transform of the velocity  $V(f)$  and the Fourier transform of the force  $F(f)$  (Figure 4). The analysis of the mobility enables to extract material and geometrical properties.

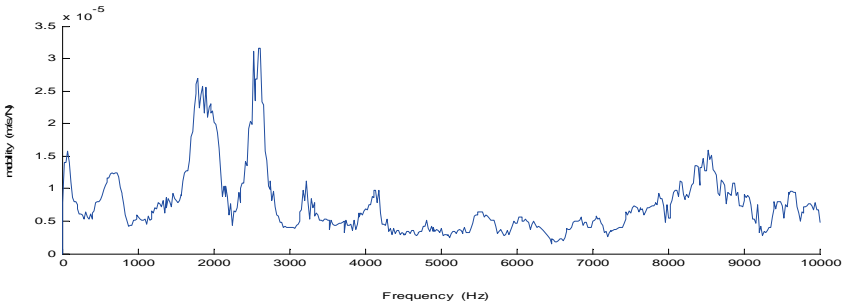


Figure 4. Mobility

### 3 Numerical Model

In the present work, the main goal of numerical simulations is not to reproduce exactly the field measurements but to support and explain the experimental results. Thus, a simplified axisymmetric model is used. In the numerical model, the pavement is considered as a multi-layer linear elastic system. The finite element mesh with boundary conditions is shown in Figure 5a. Four-node axisymmetric elements are used. Each layer is assumed to be homogeneous and isotropic. The model has a radius of 1.5 m and a height of 1.8 m. This choice restricts the influence of the boundaries. We use a variable mesh density to increase the accuracy of the numerical solution (Figure 5a). The other characteristics of this model are given in Table 1. Under the impact load, the stress propagates in the pavement. Figure 5b shows the evolution of von Mises stress near the impact zone. It is worth noting that an elasto-static analysis does not take into account the impact phenomena and, consequently, it will not allow for such distribution of the stress.

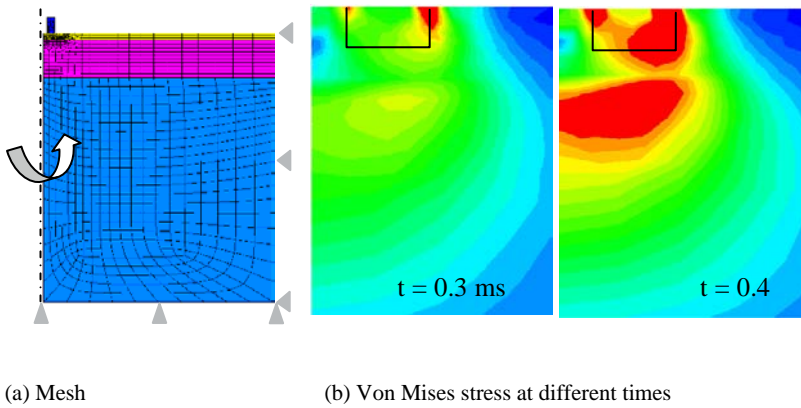


Figure 5. Finite element modelling

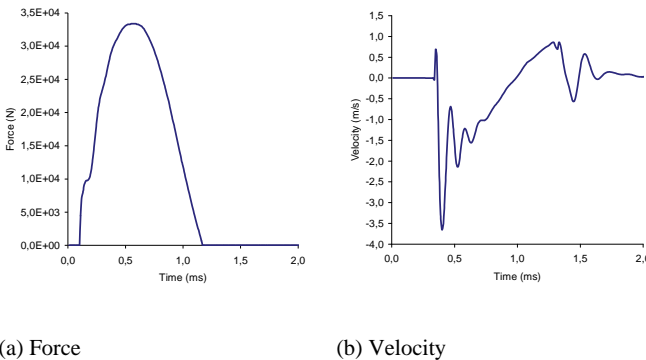


Figure 6. Numerical results

Figure 6 shows the evolution of the impact force and the velocity on the centre point of the pavement. These results reproduce, in a qualitative manner, the measured signals as shown in Figure 2. For the moment, the measurement is carried out onto a pavement which does not have the same characteristics listed in Table 1. In addition, a hammer is used to obtain the signals. So the initial conditions are different. That is why we did not obtain the same results.

## 4 Conclusions

In this paper, we have presented experimental and numerical approaches applied to the elasto-dynamic analysis of the pavement under impact loadings. Numerical results demonstrated that our model could match better the reality when compared to other existing elasto-static solutions. Qualitatively, the experimental and numerical approaches lead to similar results in terms of impact forces and velocity. Our on-going work concerns the correlation of experimental and numerical results in a quantitative way.

## References

- Feng Z.Q., Joli P., Cros J.M. and Magnain B. (2005). The bi-potential method applied for the modeling of dynamic problems with friction. *Comput. Mech.*, 36(5):375-383.
- Feng Z.Q., Magnain B. and Cros J.M. (2006). FER/Impact: Logiciel de simulation numérique des problèmes d'impact, *Revue Européenne de Mécanique Numérique*, 15:175-186
- Goktepe A. B., Agar E. and Hilmi Lav A. (2006). Advances in backcalculating the mechanical properties of flexible pavements. *Advances in Engineering Software*, 37(7):421-431.
- Hildebrand G. (2002). Verification of flexible pavement response from a field test. VI Report 121, Danish Road Institute.
- Ji Y., Wang F., Luan M. and Guo Z. (2006). A simplified method for dynamic response flexible pavement and applications in time domain backcalculation. *Journal of American Science*, 2(2):70-81
- Picoux B., Ayadi A. El. and Petit C. (2009). Dynamic response of a flexible pavement submitted by impulsive loading. *Soil Dynamics and Earthquake Engineering*, 29(5):845-854.
- Roesset J. M. (1998). Non-destructive dynamic testing of soils and pavements. *Journal of Science and Engineering*, 1(2):61-81.
- Simonin J. M. (2005). Contribution à l'étude d'auscultation des chaussées par méthode d'impact mécanique pour la détection et la caractérisation des défauts d'interface, PhD thesis, INSA de Rennes, France.
- Stolle D. F. E. and Hein D. K. (2002). Assessment of the impact of layer moduli on measured surface deflections. Conference of the FWD and Road Profilers User Groups.

# Dynamic Analysis of Vertical Loaded Single Pile in Multilayered Saturated Soils

Jun Yu<sup>1,2\*</sup>, Haiming Chen<sup>1,2</sup>, Zhao Yang<sup>1,2</sup> and Cheng Liu<sup>1,2</sup>

<sup>1</sup>Department of Geotechnical Engineering, Tongji University, Shanghai 200092, P.R. China

<sup>2</sup>Key Laboratory of Geotechnical and Underground Engineering of Ministry of Education, Tongji University, Shanghai 200092, P.R. China

**Abstract.** This paper presents a method for the elastic analysis of vertical loaded single pile in multilayered saturated soil. Based on Biot's consolidation equation, plane strain assumption is applied to research pile-soil interaction in saturated soil. The analytical solution of impedance function of soil is obtained. Combining with a transfer-matrix formulation in the case of multi-layered saturated soil, the analytical solution of vertical impedances of pile are determined. The results of this method are compared well with the existing solutions in the literature. A parametric study for a two-layered saturated soil is further presented to show the effects of layered soils on the behavior of a single pile.

**Keywords:** saturated soil, soil-pile interaction, plane strain assumption, vertical vibration

## 1 Introduction

A thorough understanding of load transfer of a single pile under vertical loads is essential for analysis and design of pile foundations. Therefore, a number of analytical and numerical methods have been developed for analyzing vertical loaded piles. They include two methods: (1) the overall analysis methods, such as finite element methods (Cheung and Zhao, 1991), finite layer methods (Guo et al., 1987, Cheung et al., 1989), boundary element methods (Banerjee and Davis, 1977, 1978); (2) the simplified analytical approach as the Winkler-type subgrade method (Lee et al, 1987 and Chin et al., 1990). Using these solutions for two-layered elastic medium, Banerjee and Davis (1977, 1978) analyzed piles in non-homogeneous soils. Lee et al. (1987) and Chin et al. (1990) gave the results of piles in layered soils by utilizing the analytical layered solutions. A good compilation of used techniques is the one presented by Novak (1991).

---

\* Corresponding author, e-mail: jjyy1017@163.com

The above studies were based on single-phase soil medium, and studies based on saturated soil medium were rarely. Very few studies exist whereby the two-phase character of these soils has been taken into account according to Biot's theory (1956, 1962). Zeng and Rajapakse (1999) presented the first dynamic studies of a pile in a poroelastic medium. Many authors extended the classical elastostatic Muki and Sternberg formulation (1970) to analyze steady-state dynamic response of an axially loaded cylindrical elastic bar partially embedded in a homogeneous poroelastic half-space. In a similar way Jin et al. (2001) extended the method proposed by Pak and Jennings (1987) to study the dynamic lateral response of a single pile. This paper presents a method for the elastic analysis of vertical loaded single pile in multilayered saturated soil. The paper adopts plane strain assumption based on Biot's consolidation equation, and then combining with a transfer-matrix formulation in the case of multi-layered saturated soil, the analytical solution of vertical impedances of pile are determined. It is found that the analytical solution can be used with ease for the analysis and prediction of piles in layered saturated soil.

## 2 Governing Equations and General Solution

The problem studied in this paper is the vertical vibration of a pile embedded in multilayered saturated soil medium and the geometric model is shown in Figure 1. The main assumptions adopted in this paper are: (1) The pile is vertical, elastic, end bearing, circular in cross section and has a perfect contact with the surrounding soil; (2) the soil is a linearly elastic, homogeneous and isotropic layer, and the soil medium is a two-phase material consisting of soil grains and fluid, the layer overlies a rigid bedrock; (3) the soil is accord with plane strain assumption, which can be assumed to compose with much of the hole radius  $r_0$  infinite thin elastic layers, these thin layers are independent of each other, that is the vertical displacements are independent of  $z$ ; (4) the vibration is harmonic; (5) only the vertical displacements are considered; (6) the pile and soil layer have no separation.

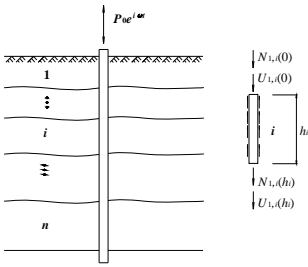


Figure 1. Model of soil-pile interaction

### 2.1 Dynamic Soil Reactions for the Saturated Soil

According to the dynamic consolidation theory of Biot (1956, 1962) for a completely saturated medium and the assumptions above, the dynamic equilibrium equation for the saturated soil layers in polar coordinate system can be expressed as:

$$G\nabla^2 u_z = \rho \frac{\partial^2 u_z}{\partial t^2} + \rho_f \frac{\partial^2 w_z}{\partial t^2} \tag{1}$$

$$0 = \frac{1}{k_d} \frac{\partial w_z}{\partial t} + \rho_f \frac{\partial^2 u_z}{\partial t^2} + \frac{\rho_f}{n} \frac{\partial^2 w_z}{\partial t^2} \tag{2}$$

where  $u_z$ ,  $w_z$  are the displacement components of the solid and of the fluid relative to the solid in the cylindrical polar coordinate system;  $n$  is the porosity;  $G$  is the Lamé's constants;  $\rho = (1-n)\rho_s + n\rho_f$  is the mass density of bulk material, where  $\rho_s$  and  $\rho_f$  are the mass density of fluid and of grains, respectively;  $kd'$  is dynamic coefficient of permeability.  $\nabla^2 = \frac{\partial^2}{\partial r^2} + \frac{1}{r} \frac{\partial}{\partial r}$  is the Laplace operator.

Due to the symmetry of the pure torsional vibration of medium about the vertical axis, the motion is independent of angle  $\theta$ . For the harmonic motion,  $u_z(r, t) = u_z(r)e^{i\omega t}$ , where  $i = \sqrt{-1}$ ,  $\omega$  is circular frequency of excitation and  $t$  is time.

Substituting Equation (2) into Equation (1), the equilibrium equation can be written as:

$$(\nabla^2 - h^2)u_z(r) = 0 \tag{3}$$

where

$$h^2 = -\frac{\rho\omega^2}{G} - \frac{\rho_f^2\omega^4}{G(\frac{i\omega}{k_d} - \frac{\rho_f\omega^2}{n})} \tag{4}$$

It is not difficult to show that the general solution of Equation (3) can be expressed as:

$$u_z(r) = A_0K_0(hr) + B_0I_0(hr) \tag{5}$$

where  $I_0(hr)$  and  $K_0(hr)$  are the modified Bessel functions of the first and second kind of the zero order, respectively;  $A_0$  and  $B_0$  can be obtained from the boundary conditions.

Referring to Figure 1, it can be observed that the boundary conditions of the soil layer can be written as:

$$u_z(r \rightarrow \infty) = 0 \tag{6}$$

$$u_z(r) \Big|_{r=r_0} = u_1 \tag{7}$$

where  $u_1$  is vertical displacement of the pile.

Then the solution of Equation (1) and Equation (2) can be written as :

$$u_z(r, t) = u_1 e^{i\omega t} K_0(hr) / K_0(hr_0) \tag{8}$$

The shear stress amplitude  $\tau_{rz}$  corresponding to Equation (8) can be expressed as:

$$\tau_{rz} \Big|_{r=r_0} = G \frac{\partial u_z(r, t)}{\partial r} \Big|_{r=r_0} = -Ghu_1 e^{i\omega t} K_1(hr) / K_0(hr_0) \tag{9}$$

The resisting moment  $q_n$  per unit of length of the pile can be expressed respectively

$$q_n = - \int_0^{2\pi} \tau_{rz} \cdot 1 \cdot d(r_0\theta) = 2\pi hGr_0 u_1 e^{i\omega t} \frac{K_1(hr_0)}{K_0(hr_0)} = C_1(hr_0) u_1 e^{i\omega t} \tag{10}$$

where

$$C_1(hr_0) = 2G\pi hr_0 K_1(hr_0) / K_0(hr_0) = k_z + ic_z \tag{11}$$

### 2.2 Impedance of a Pile

A single circular cylindrical pile is embedded in a multilayered elastic saturated soil. The pile is loaded with an axial force  $P$  at its head. Its length is  $h$  and its shaft radius is  $r_0$ . The pile material has a constant Yang’s modulus  $E_p$ . The pile has a cross-section area  $A$ . The pile shaft is embedded a rigid bedrock. The pile is mod-

eled as an elastic  $n$ -section pile unit system of infinite horizontal extent. The displacement of the  $i$ th segment pile  $u_{1,i}(z,t) = U_{1,i}(z)e^{i\omega t}$  is governed by the following one-dimensional equation of motion:

$$\frac{d^2U_{1,i}(z)}{dz^2} - \xi_i^2 U_{1,i} = 0 \tag{12}$$

where  $\xi_i^2 = (k_z + ic_z - \rho_p A_p \omega^2) / (E_p A_p)$ ,  $k_z, c_z$  can be given as Equation (11)

The solution of Equation (12) is

$$U_{1,i}(z) = A_{1,i} \cosh(\xi_i z) + B_{1,i} \sinh(\xi_i z) \tag{13}$$

where  $A_{1,i}$  and  $B_{1,i}$  are the coefficients which remain to be determined later from the boundary conditions.

We can obtain the axial force of the  $i$ th segment:

$$N_{1,i} = E_p A_p \frac{dU_{1,i}}{dz} = E_p A_p \xi_i [A_{1,i} \sinh(\xi_i z) + B_{1,i} \cosh(\xi_i z)] \tag{14}$$

The axial force and displacement between the both ends of the segment  $i$  can be written as:

$$\begin{bmatrix} U_{1,i}(h_i) \\ N_{1,i}(h_i) \end{bmatrix} = S_{1,i} \begin{bmatrix} U_{1,i}(0) \\ N_{1,i}(0) \end{bmatrix} \tag{15}$$

where

$$S_{1,i} = \begin{bmatrix} \cosh(\xi_i h_i) & \frac{\sinh(\xi_i h_i)}{E_p A_p \xi_i} \\ E_p A_p \xi_i \sinh(\xi_i h_i) & \cosh(\xi_i h_i) \end{bmatrix} \tag{16}$$

Coordinated by the interface conditions:

$$U_{1,i+1}(0) = U_{1,i}(h_i), N_{1,i+1}(0) = N_{1,i}(h_i) \tag{17}$$

By using transfer matrix method, the relationship of displacement and axial force between the end and the top of  $i$ th segment can be expressed as:

$$\begin{bmatrix} U_{1,n}(h_n) \\ N_{1,n}(h_n) \end{bmatrix} = S_{1,n} \begin{bmatrix} U_{1,1}(0) \\ N_{1,1}(0) \end{bmatrix} \tag{18}$$

where

$$S_{1,n} = \prod_{k=1}^n S_{1,k} \tag{19}$$

Because  $S_{1,n}$  is a 4×4 matrix, we can assume:

$$S_{1,n} = \begin{bmatrix} S^1_{1,n} & S^2_{1,n} \\ S^3_{1,n} & S^4_{1,n} \end{bmatrix} \tag{20}$$

So that the Impedance function at the top end of the pile is given by:

$$K_z = -\frac{S^1_{1,n}}{S^2_{1,n}} \tag{21}$$

### 3 Numerical Result and Discussion

#### 3.1 Compared with the Existing Solutions in the Literature

In this paper, the results of the method are compared well with the degradation of the solution to the single-phase is compared well with the solution of Novak (1991). By compare with Novak’s solution from Equation (3) and Equation (4), we can obtain that the solution of this paper in saturated soil is added an effects of one fluid factor, That is  $\frac{\rho_f^2 \omega^4}{G(\frac{i\omega}{k_d} - \frac{\rho_f \omega^2}{n})}$ , from which we can learn that the fluid

factor is closely related to the properties of saturated soils  $k_d'$ , when  $k_d'$  is small, the fluid factor is near zero, then can be ignored. Thus we can replace the saturated soil solution whit Novak’s solutions when  $k_d'$  is smaller than  $10^7$ .

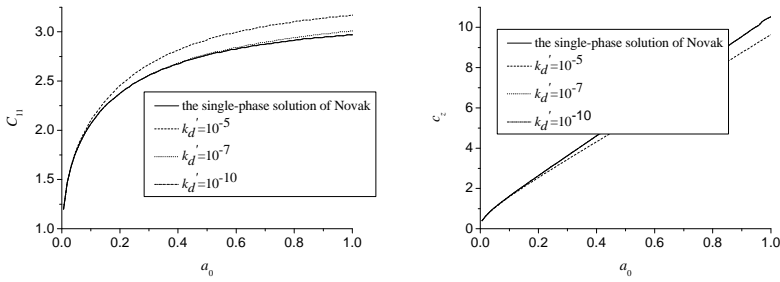


Figure 2. Comparison with Novak’s solution

### 3.2 Impedance of End Bearing Pile

In the analysis of structures supported by pile foundations, the complex impedance at the pile head is often used to gauge the vibration characteristics of the pile–soil system. The real part of the complex impedance represents the real stiffness, while the imaginary part of the complex impedance represents the radial damping of the system. The complex impedance is influenced by the frequency of excitation  $\omega$ , pile slenderness ratio  $H/r_0$ , pile modulus ratio  $E_p$ ,  $k'_d$  and other material properties. Now, a parametric study for a two-layered saturated soil is further presented to show the effects of layered soils on the behavior of a single pile. The parameters used in calculation are:  $v_{s1}=100\text{m/s}$ ,  $v_{s2}=200\text{m/s}$ ,  $h_1=4\text{m}$ ,  $h_2=6\text{m}$ ,  $r_0=0.5\text{m}$ ,  $\rho_1=1850\text{ kg/m}^3$ ,  $\rho_2=1950\text{ kg/m}^3$ ,  $a_1=\omega r_0/v_{s1}$ .

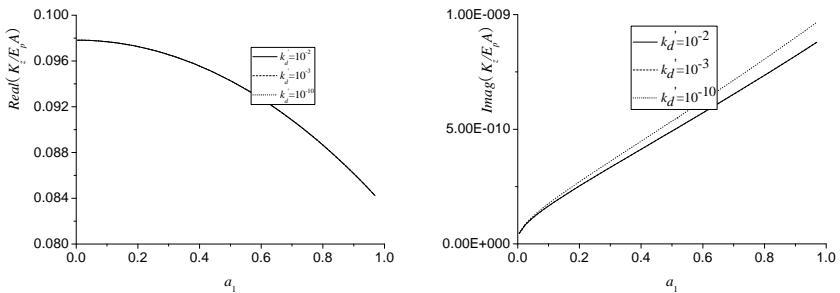


Figure 3. Variation of vertical impedance of pile in two-layered saturated soil with  $k'_d$

Figure 3 shows the variations of vertical impedance of single pile in two-layered saturated soil with the different dynamic coefficient of permeability  $k_d'$ . It can be seen that the stiffness parameter  $\text{Real}(K_z/E_pA)$  is almost unchanged with the different  $k_d'$ , and the damping parameter  $\text{Imag}(K_z/E_pA)$  is almost unchanged when  $k_d'$  is less than  $10^{-3}$ .

Figure4 shows variation of vertical impedance of pile in two-layered saturated soil with different thickness ratio of layer. It can be seen that the thickness ratio of layer has a significant influence on the response. The stiffness parameter  $\text{Real}(K_z/E_pA)$  is decrease with the thickness ratio of layer decreased, and the damping parameter  $\text{Imag}(K_z/E_pA)$  is increase with the thickness ratio of layer decreased.

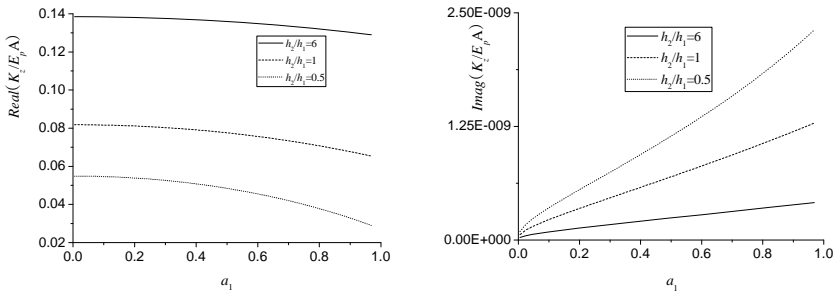


Figure 4. Variation of vertical impedance of pile in two-layered saturated soil with thickness ratio of layer

### 4 Conclusions

By considering the end bearing pile embedded in a multilayered saturated soil as a pile-soil dynamic interaction problem, an analytical solution for the vertical impedance of the saturated soil layer and pile has been derived. An extensive parameters study has been conducted to investigate the influence of major parameters. The results of the method are compared well with the existing solutions in the literature. We can replace the saturated solution with Novak's soil solutions when  $k_d'$  is smaller than  $10^{-7}$ . From the numerical results, conclusions can be drawn that both the real and imaginary parts of the torsional impedance of the soil depend much on the thickness ratio of layer. The stiffness parameter  $\text{Real}(K_z/E_pA)$  is decreased with the thickness ratio of layer decreased, and the damping parameter  $\text{Imag}(K_z/E_pA)$  is increased with the thickness ratio of layer decreased. The stiffness parameter  $\text{Real}(K_z/E_pA)$  is almost unchanged with the different  $k_d'$ , and the damping parameter  $\text{Imag}(K_z/E_pA)$  is almost unchanged when  $k_d'$  is less than  $10^{-3}$ .

## Acknowledgments

This research is supported by China Postdoctoral Science Foundation (Grant No. 20080440652).

## References

- Banerjee P.K., Davis T.G. (1977). Analysis of pile groups embedded in Gibson soil, *Proc. 9th Int. Conf. Soil Mech. Found. Eng.*, Tokyo 1:381–386.
- Banerjee P.K., Davis T.G. (1978). The behavior of axially and laterally loaded single piles embedded in non-homogeneous soils, *Geotechnique* 28(3).
- Biot M.A. (1956). Theory of propagation of elastic waves in a fluid-saturated porous solid. I: Low frequency range. *J. Acoust. Soc. Am.*, 28(2):168–78.
- Biot M.A. (1962). Mechanics of deformation and acoustic propagation in porous media. *J. Appl. Phys.*, 33:1482–98.
- Cheung Y.K., Tham L.G., Guo D.J. (1988). Analysis of pile group by infinite layer method, *Geotechnique*, (3):415–431.
- Cheung Y.K., Zhao W.B. (1991). Elastoplastic analysis of soil-pile interaction, *Comput. Geotechn.*, 12(2):115–132.
- Chin J.T., Chow Y.K., Poulos H.G. (1990). Numerical analysis of axially loaded vertical piles and pile groups, *Comput. Geotechn.*, 9(4):273–290.
- Guo D.J., Tham L.G., Cheung Y.K. (1987). Infinite layer for the analysis of a single pile, *Comput. Geotechn.*, 3(4):229–249.
- Jin B., Zhou D., Zhong Z. (2001). Lateral dynamic compliance of pile embedded in poroelastic half space, *Soil Dyn. Earthquake Eng.*, 21:519–25.
- Lee S.L., Kog Y.C., Karunaratne G.P. (1987). Axially loaded piles in layered soils, *J. Geotech. Eng. Div. ASCE* 113(4):366–381.
- Muki R., Sternberg E. (1970). Elastostatic load transfer to a half-space from a partially embedded axially loaded rod. *Int. J. Solids Struct.*, 6:69–90.
- Novak M. (1991). Piles under dynamic loads. *2nd Int. Conf. Recent Adv. Geotech. Earthquake Eng. Soil Dyn., St Louis, Missouri*, 22(3):250–73.
- Pak R.S.Y., Jennings P.C. (1987). Elastodynamic response of the pile under transverse excitation, *J. Eng. Mech. ASCE*, 113(7):1101–16.
- Randolph M.F., Wroth C.P. (1978). Analysis of the deformation of vertically loaded piles, *J. Geotech. Eng. Div., ASCE* 104(12):1465–1488.
- Randolph M.F., Wroth C.P. (1979). An analysis of the vertical deformation of pile groups, *Geotechnique* 29(4):423–439.
- Zeng X., Rajapakse R.K.N.D. (1999). Dynamic axial load transfer from elastic bar to poroelastic medium, *J. Eng. Mech. ASCE*, 125(9):1048–55.

*“This page left intentionally blank.”*

# Local Dynamic Response in Deck Slabs of Concrete Box Girder Bridges

Jianrong Yang<sup>1\*</sup> and Jianzhong Li<sup>1,2</sup>

<sup>1</sup>Faculty of Civil Engineering and Architecture, Kunming University of Science and Technology, Kunming 650224, China

<sup>2</sup>Department of Bridge Engineering, Tongji University, Shanghai 200092, China

**Abstract:** With the effect of vehicle-bridge coupling considered, the local dynamic response in deck slabs of concrete box girder bridges are analyzed. The mathematical model assumes a finite element representation of the slabs with shell elements. And the vehicle simulation uses a 3 dimensional linear vehicle model with 7 independent degrees of freedom. A well-known power spectral density of road pavement profiles defines the deck surface roughness for Good and Poor roads respectively. Response data are produced on concrete highway bridge decks made of straight box section girder. In this way, a parametric study is conducted to analyze the effects of factors such as road surface roughness, vehicle speed, and bridge damping on the bridge dynamic amplification factors (DAFs). Results are presented to verify the extension of the local dynamical effects on concrete box girder decks with different working condition. From these results some general conclusions have been drawn.

**Keywords:** vehicle-bridge coupling, deck slab, local dynamic effect, concrete box girder

## 1 Introduction

In recent years, heavy vehicles have become larger and have increased in number. At the same time, new materials and improved design methods have resulted in lighter and more flexible bridges. Therefore highway bridges are increasingly susceptible to vibration. Vibration of large amplitude may introduce into the bridges structural damage and increase their retrofitting expenses. Damage in some local elements of bridge, such as deck slabs, hangers, and expansion joints, could be dangerous to highway transportation. Thus the research on local vibration of highway bridges becomes a necessity.

---

\* Corresponding author, e-mail: carpenter\_y@sina.com

It is found that the behaviour of concrete box girder is essentially complex and that there is no simple indicator that may be used to identify impactive vehicles. Generally, bridge engineer use the dynamic amplification factor (DAF) to a design or evaluation of bridge capacity. The DAFs defined in codes have classically been derived from the measurement or simulation of global traffic action effects in the main structural elements of bridges. On the other hand, local dynamic effects in deck slabs have not yet been studied in detail. The local impact on some elements may be much larger than the global ones for certain situations. With only global DAFs, one can hardly describe the local impact effects on different structural elements. Hence a better understanding of the dynamic behaviour of deck slabs under vehicle loading will lead to the definition of more appropriate dynamic amplification factors and avoid the use of values that are too conservative (Broquet et al., 2004).

For concrete box girder bridges, deck slab is an important structural element. The dynamic behaviour of deck slabs under traffic action may be vital for the safety or serviceability of the bridges. Research works in this field are mainly concentrated on the global vibration of the structures. Few references have been found dealing with deck slabs in particular. A detailed review of the literature and an extensive list of references are omitted here as they can be found in the references (Broquet et al., 2004; Bazi et al., 2005; Green and Cebon, 1994).

This paper develops a generalized procedure for the resolution of the dynamic interaction problem between a bridge and a dynamic system of vehicles running at a prescribed speed. A parametric study, based on the simulation of bridge-vehicle interaction, is carried out to investigate characteristic properties of the dynamic behaviour of the bridge deck slabs of concrete box girder bridges and to deduce the distribution of DAFs throughout the deck slab.

## **2 Vehicle and Bridge Models**

### ***2.1 Bridge Model***

To obtain general dynamic characteristics of box girder bridge, a prestressed concrete box girder bridge presented by Dongzhou Huang et al. (1995) is chosen in this study and shown in Figure 1. The bridge is simply supported and has a span length of 45.72 m. The bridge is modelled with shell element. The first frequency of the bridge model is 3.278 Hz. Local modes of vibration in the deck slab have frequencies greater than 27 Hz.

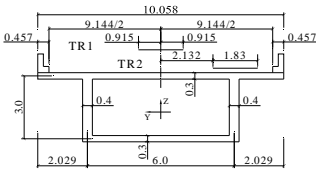


Figure 1. Cross section of the bridge.

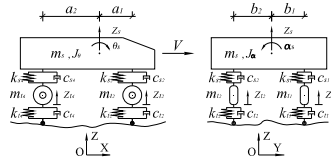


Figure 2. Vehicle model.

## 2.2 Vehicle Model

As shown in Figure 2, the mathematical vehicle model is composed of a vehicle body and four wheel bodies. The tires and suspension systems are idealized as linear elastic spring elements and dashpots. The vehicle body has three degrees of freedom, including  $z$  displacement, rolling, and pitching; each wheel has only one degree of freedom, namely  $z$  displacement. Therefore, each vehicle has a total of 7 degrees of freedom.

Here, the mass of vehicle body  $m_s=2.55E4$  kg; the pitching ( $J_0$ ) and rolling ( $J_\alpha$ ) moment of inertia of vehicle body are  $5.53E4$  kg  $\cdot$  m<sup>2</sup>/rad and  $56.89E3$  kg  $\cdot$  m<sup>2</sup>/rad respectively; the damping coefficients of vehicle suspension ( $c_{s1}$ ,  $c_{s2}$ ,  $c_{s3}$ ,  $c_{s4}$ ) are  $2.00E4$  N  $\cdot$  s/m; the spring stiffness coefficient of vehicle suspension for the front ( $k_{s1}$ ,  $k_{s2}$ ) and rear ( $k_{s3}$ ,  $k_{s4}$ ) axles are  $4.00E6$  and  $8.00E6$  N/m respectively; the mass of each front axle tires are 445 kg; the mass of each rear axle tires are 890 kg; the damping coefficient for each tires ( $c_{t1}$ ,  $c_{t2}$ ,  $c_{t3}$ ,  $c_{t4}$ ) is  $2.00E4$  N  $\cdot$  s/m; the spring stiffness coefficient of tires for the front ( $k_{t1}$ ,  $k_{t2}$ ) and rear ( $k_{t3}$ ,  $k_{t4}$ ) axles are  $2.25E6$  and  $8.00E6$  respectively; distance  $\alpha_1$ ,  $\alpha_2$ ,  $b_1$ , and  $b_2$  are 3.479, 1.021, 0.915, 0.915 m respectively. The 7 frequencies of the vehicle are calculated as 2.03, 3.22, 4.27, 18.91, 19.77, 21.41 and 21.63 Hz respectively with Stodola (Bhatt, 2002) method.

## 3 Vehicle-Bridge Dynamic System

### 3.1 Vehicle-Bridge Model

The modal equations of a bridge can be expressed as

$$[M_B]\{\ddot{A}\}+[C_B]\{\dot{A}\}+[K_B]\{A\}=\{F_B\} \quad (1)$$

where  $\{A\}$ =modal displacement vector;  $[M_b]$ =modal mass matrix;  $[C_b]$ =modal damping matrix; and  $[K_b]$ =modal stiffness matrix of the bridge;  $\{F_b\}$ =modal wheel-bridge contact force vector on the bridge. The equations of motion for the vehicle model presented in Figure 2 are Lagrange’s formulation as

$$[M_v]\{\ddot{Z}\} + [C_v]\{\dot{Z}\} + [K_v]\{Z\} = \{F_v\} \tag{2}$$

where  $\{F_v\}$  is the interaction force vector applied on the vehicle;  $[M_v]$ ,  $[C_v]$  and  $[K_v]$  are, respectively, the mass, damping and stiffness matrices of the vehicle. And  $\{Z\}$  is the vertical displacement vector of the vehicle degrees of freedom.

### 3.2 Interaction of Vehicle and Bridge

The interaction force between the bridge and the vehicle on  $i$ th wheel is given by

$$F_{ii} = -k_{ii}(Z_{ii} - U_{bi} - r_i) - c_{ii}(\dot{Z}_{ii} - \dot{U}_{bi} - U'_{bi}V - r'_i V) \tag{3}$$

$k_{ii}$  and  $c_{ii}$  are, respectively, the tire stiffness and tire damping of the  $i$ th wheel;  $Z_{ii}$  is the vertical displacement of the  $i$ th wheel;  $U_{bi}$  and  $r_i$  are, respectively, the bridge vertical displacement and the road surface roughness under the  $i$ th wheel; and  $V$  is the speed of the vehicle. Based on the  $j$ th modal displacement under the  $i$ th wheel  $\phi_j^i$ ,  $U_{bi}$  can be expressed with modal linear superposition technique as

$$U_{bi} = \sum_{j=1}^N \phi_j^i A_j \tag{4}$$

where  $N$ =dimension of the modal space. The force acted on bridge deck by  $i$ th wheel is expressed as  $F_{bi}=F_{Gi}-F_{ii}$ , in which  $F_{Gi}$  is the vehicle gravity under the  $i$ th wheel. While the  $n$ th to  $m$ th wheel of the vehicle is located on the deck, the  $L$ th modal force in Equation (1) can be derived as

$$F_{BL} = \sum_{i=n}^m \phi_L^i F_{bi} \tag{5}$$

Substituting Equation (5) into Equation (1) for all modes, then it becomes

$$\begin{aligned}
 & \begin{bmatrix} [M_V] & [0] \\ [0] & [M_B] \end{bmatrix} \begin{Bmatrix} \{\ddot{Z}_V\} \\ \{\ddot{A}\} \end{Bmatrix} + \begin{bmatrix} [C_V] & [C_{Bt}] \\ [C_{Bt}]^T & [C_B + C_{BV}] \end{bmatrix} \begin{Bmatrix} \{\dot{Z}_V\} \\ \{\dot{A}\} \end{Bmatrix} \\
 & + \begin{bmatrix} [K_V] & [K_{Bt1}] \\ [K_{Bt2}] & [K_B + K_{BV}] \end{bmatrix} \begin{Bmatrix} \{Z_V\} \\ \{A\} \end{Bmatrix} = \{F\}
 \end{aligned} \tag{6}$$

where the additional terms  $C_{Bt}$ ,  $C_{BV}$ ,  $K_{Bt1}$ ,  $K_{Bt2}$ ,  $K_{BV}$  are due to the contact (interaction) force. They are all functions of bridge properties, vehicle properties and the positions of vehicle-bridge contact points. This indicates that the additional terms in Equation (6) are time-dependent terms and will change as the vehicle moves across the bridge.

### 3.3 Road Surface Profile

The typical road surface may be described by a periodically modulated random process. One method of characterizing a random function is by use of the power spectral density (PSD) function. C.J. Dodds et al. (1973) have developed a typical PSD function that can be approximated by an exponential function as

$$S(f) = \begin{cases} S(f_0)(f/f_0)^{-\alpha_1}, & f \leq f_0 \\ S(f_0)(f/f_0)^{-\alpha_2}, & f \geq f_0 \end{cases} \tag{7}$$

where  $S(f)$  =PSD function for the road surface elevation;  $f$ = wave number;  $f_0$ = the discontinuity frequency; the values of  $\alpha_1$ ,  $\alpha_2$  are taken as 2 and 1.4;  $S(f_0)$  =roughness coefficient, and its value is chosen depending on the road condition.

### 4 Effect of Parameters

Most frequently, the DAF is defined as the ratio of maximum dynamic response to maximum static response. C. Broquet et al. (2004) suggested a more appropriate definition of the dynamic amplification factor for deck slabs. The DAF is the peak dynamic effect for a given vehicle trajectory  $R_{Dmax}$  divided by the peak static effect from the envelope for all vehicle trajectories  $R_{Emax}$ :  $DAF = R_{Dmax} / R_{Emax}$ .

The action effects in the deck slab due to static traffic loading are determined by static analysis. Effects including vertical deflection ( $U_z$ ), the longitudinal moment ( $M_x$ ) and the transverse moment ( $M_y$ ) are captured at eleven locations within the bridge deck for five sections as illustrated in Figure 3. These locations are

numbered with its section ID plus a number. For instance, C7 means the seventh location from section C-C.

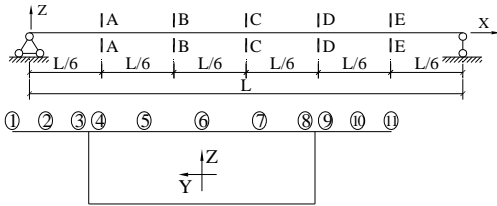


Figure 3. Definition of the key sections and data points.

To get the initial displacements and velocities of the vehicle DOFs while the vehicle enter the bridge, the vehicle run starts at a distance of 20 m away from the left end of the bridge and continues moving until the entire vehicle leave the right end of the bridge. The same class of road surface is assumed for both the approach roadway and bridge decks.

### 4.1 Influence of Road Roughness

The influence of the road profile on the DAF is shown for the box girder bridge in Figure 4. The truck passes over the bridge with a speed range of 10~40 m/s. Still is the bridge damped moderately  $\zeta=0.03$ . In order to analyze the effect of road roughness three road conditions are considered as inputs to the vehicle-bridge coupled model: (1) road surface condition is good; and (2) road surface condition is poor. They are labelled hereafter as good, and poor, respectively.

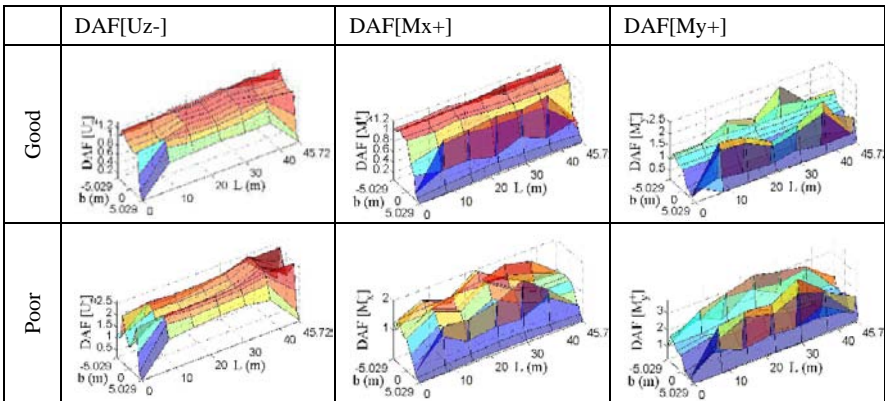


Figure 4. Effects of road roughness on DAFs in deck slab.

As shown in Figure 4, road roughness of a bridge seriously affects the vehicle vibration, thus affecting the vehicle-bridge interaction. An increase in road surface roughness causes an increase in DAFs. Poor road surface condition not only influences the bridge's normal operation but also creates vertical acceleration that can make the driver uncomfortable. Therefore maintenance of a bridge road surface in good condition is very important to reduce the impact effect (Zhang, 2006).

## ***4.2 Influence of Vehicle Speed***

Vehicle speed of 10, 20, 30, and 40 m/s are considered in the simulation. The results demonstrate that there is no critical speed or clear relationship between the DAF and Speed. However, vehicle speed effect is more pronounced when the road surface condition is poor than when it is good.

## ***4.3 Influence of Bridge Damping***

Field experiments have demonstrated a large variation of damping for conventional highway bridges. Damping ratio values of 1%~5% are commonly recommended for conventional bridges in the literature. In addition to the moderately damping of 3%, simulations are carried out with modal damping of 1% and 5% respectively. The influence of vehicle damping is shown in Table 1 for road surface condition: good. The truck passes over the bridge with a speed range of 10~40 m/s. The DAF values come from envelope for all trajectories.

As shown in the table, damping does not affect the location at which the maximum DAFs appear, but affects the values. Higher damping can reduce the DAFs on the slab effectively and helps the bridge damp out the vibration quicker.

## **5 Conclusions**

A general procedure for determining the local dynamic response in deck slabs of concrete box girder bridges under moving vehicles has been presented. Based on the results obtained from the parametric study, the following conclusions can be drawn with respect to dynamic amplification factors in road bridge deck slabs:

1. Three amplitudes of road surface roughness are considered in the simulations representing perfect, good and poor conditions. The results indicate that an increase in road surface roughness leads to higher DAFs.

2. Four vehicle speeds varying between 10 and 40 m/s are considered in the study. It is found that there is no critical speed or clear relationship between the DAFs and speed. The dynamic amplification factors specified in the design codes can be exceeded by a large margin in a situation with an unfavourable combination of some of the parameters.
3. Simulations are carried out with a bridge model damped at three different levels. The results show that bridge damping does not affect the location at which the maximum DAFs appear. However, damping can reduce the impact effect from the vehicles effectively and helps the bridge damp out the vibration quicker.

The conclusions above are drawn from purely numerical simulation results, and should be verified by field testing. The information presented in this research may be used to deduce dynamic amplification factors for bridge deck slabs, and to increase the accuracy of safety evaluations of concrete deck slabs.

Table 1. Effect of bridge damping on DAFs in deck slab.

DAF	Location	$\xi=0.01$	$\xi=0.03$	$\xi=0.05$	Ratio	
		(1)	(2)	(3)	(2)/(1)	(3)/(1)
DAF[ $U_z^-$ ]	D11	1.24	1.21	1.19	98%	96%
DAF[ $M_x^+$ ]	B6	1.08	1.08	1.08	100%	100%
DAF[ $M_x^-$ ]	C11	1.14	1.13	1.12	99%	98%
DAF[ $M_y^+$ ]	B6	1.15	1.16	1.16	101%	101%
DAF[ $M_y^-$ ]	C9	1.17	1.17	1.17	100%	100%

## Acknowledgements

This paper is supported by Yunnan Natural Science Foundation (2005E0023M), and the Natural Science Foundation of Kunming University of Science and Technology (2008-044).

## References

- Bazi G.M., Hajj E.Y. and Itani A.M. (2005). Analysis of R/C decks in multi-cell box girder bridges under rational wheel load distributions. *Bridge Structures*, 1(2), 68–80.
- Bhatt. P. Programming the dynamic analysis of structures (2002). Spon Press, 11 New Fetter Lane, London EC4P 4EE.
- Broquet C. et al. (2004). Dynamic behavior of deck slabs of concrete road bridges. *Journal of Bridge Engineering*, 9(2), 137–146.
- Dodds C.J. (1973). BSI proposals for generalized terrain dynamic inputs to vehicles. ISO/TC/108/WG9, Document No.5, Int. Org. for Standardization.

- Dodds C.J. and Robson J.D. (1973). The description of road surface roughness. *Journal of Sound and Vibration*, 31(2), 175–183.
- Green M.F. and Cebon D. (1994). Dynamic response of highway bridges to heavy vehicle load: Theory and experimental validation. *Journal of Sound and Vibration*, 170(1), 51–78.
- Huang D.Z., Wang T.L. and Shahawy M. (1995). Vibration of thin-walled box-girder bridges excited by vehicles. *Journal of Structural Engineering*, 121(9), 1330–1337.
- Standard of People's Republic of China. JTG D60-2004 General Code for Design of Highway Bridges and Culverts [S]. Beijing: China Communications Press, 2004-06-28 [in Chinese].
- Zhang Y. et al. (2006). Vehicle-induced dynamic performance of FRP versus concrete slab bridge. *Journal of Bridge Engineering*, 11(4), 410–419.

*“This page left intentionally blank.”*

# Steady-State Response of a Beam on an Elastic Foundation Subjected to a Moving Structure

Zhang Tao<sup>1\*</sup> and Gangtie Zheng<sup>1</sup>

<sup>1</sup>School of Astronautics, Beihang University, Beijing 100191, P.R. China

**Abstract.** The steady-state response of a beam on an elastic foundation subjected to a moving structure with constant speed is studied. The moving structure is assumed as an elastic Euler-Bernoulli beam with distributed stiffness and inertial effect considered in the analysis. The integral transforms methods are introduced to transform the partial differential equations to algebraic equations. Then parametric analyses by numerical examples are performed.

**Keywords:** vibration analysis; moving elastic beam; elastic foundation; integral transform method

## 1 Introduction

The dynamic response of a beam on an elastic foundation subjected to moving structures has been an important topic in engineering for a very long time. The moving structure is generally taken as moving loads (Thambiratnam and Zhuge 1996; Mallik et al, 2006) or oscillators (Zheng and Fan, 2002; Yang and Lin, 2005). However, in some other cases, the stiffness of the moving structure should be taken into consideration (Cojocaru et al, 2004).

In the present paper, the steady-state response of a beam on an elastic foundation subjected to a moving structure with constant speed is investigated. The moving structure is assumed as an elastic Euler-Bernoulli beam with distributed stiffness and inertial effect considered in the analysis. In addition, to take the elasticity of the suspension into consideration, the interface between the beam and moving structure is modeled as flexible springs at several discrete points. The analysis of interaction vibration basically requires writing two sets of motion equations. Due to the connection forces existing at the contact points, these equations are coupled and characterized by time-dependent coefficients. The integral transforms methods are introduced to transform the partial differential equations to algebraic eq-

---

\* Corresponding author, e-mail: zt8718167@163.com

uations, and the spatial variables go with the Fourier transform while the temporal variables demand the Laplace transform. Then numerical examples are performed and influence factors on the dynamic response of the simply supported beam are discussed in details.

## 2 Formulations

The model is shown in Figure 1. The moving structure is conceived as a moving elastic beam, and the infinite beam is resting on the elastic foundation. Subscript (*v*) and subscript (*r*) are used to denote the corresponding mechanical entities of the moving structure and the infinite beam. In the following,  $E_v, I_v, \bar{m}_v$  and  $L_v$  are the Young's modulus, the second moment of inertia of the cross-sectional area, the mass of per unit length and the length of the moving structure, respectively. Furthermore,  $E_r, I_r$ , and  $\bar{m}_r$  are the Young's modulus, the second moment of inertia of the cross-sectional area and the mass of per unit length of the infinite beam, respectively. The connections between the moving structure and the infinite beam are assumed as linear springs at several discrete points, and their stiffness parameter is taken as  $k_v$ .

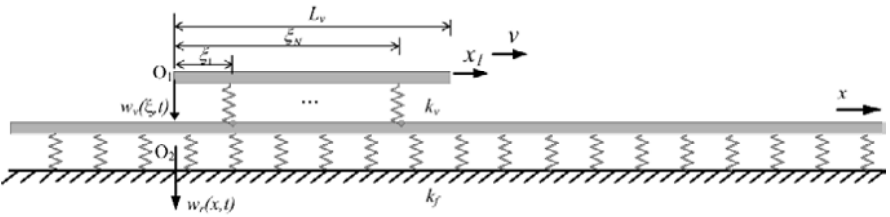


Figure 1. Infinite beam on elastic foundation subjected to moving structure

The motion governing equations of the transverse vibration of the beams are the following fourth-order partial differential equations:

$$E_v I_v \frac{\partial^4 w_v(\xi, t)}{\partial^4 \xi} + \bar{m}_v \frac{\partial^2 w_v(\xi, t)}{\partial^2 t} = - \sum_{j=1}^N f_j(t) \delta(\xi - \xi_j) \tag{1}$$

$$E_r I_r \frac{\partial^4 w_r(x, t)}{\partial^4 x} + \bar{m}_r \frac{\partial^2 w_r(x, t)}{\partial^2 t} + k_f w_r(x, t) = \sum_{j=1}^N \left[ f_j(t) + \frac{\bar{m}_v L_v g}{N} \right] \delta(x - x_j) \tag{2}$$

where  $k_f$  is the stiffness of the foundation per unit length.  $w_v$  is the vertical deflection of the moving structure and measured from its equilibrium position, and  $w_r$

is the vertical deflection of infinite beam.  $\delta(\cdot)$  is the Dirac delta function;  $N$  is the number of the connection springs. The deflection  $w_r(\xi, t)$  under consideration are described as a function of the axial coordinate  $\xi$  measured in the co-ordinate system  $\xi o_r w_r$  together with the moving structure traveling at a constant speed  $v$  along the infinite beam, which has the origin at the left end. The deflection of the infinite beam  $w_r(x, t)$  are described as the axial coordinate  $x$  measured in the inertial co-ordinate system.

The contact force can be given as

$$f_j(t) = k_v \left( w_v(\xi_j, t) - w_r(x_j, t) \right) \quad (3)$$

where  $\xi_j$  is the length between the left end of the moving structure and  $j$ -th springs, which are constant in the moving-structure-fixed co-ordinate system;  $x_j$  is the distance between the  $j$ -th springs and the origin.

To solve the equations, the coordinate transformation is adopted:

$$x = \xi + vt, \tau = t \quad (4)$$

The governing differential Equation (2) can be rewritten as

$$E_r I_r \frac{\partial^4 w_r(\xi, \tau)}{\partial^4 \xi} + \bar{m}_r v^2 \frac{\partial^2 w_r(\xi, \tau)}{\partial^2 \xi} - 2\bar{m}_r v \frac{\partial^2 w_r(\xi, \tau)}{\partial \xi \partial \tau} + \bar{m}_r \frac{\partial^2 w_r(\xi, \tau)}{\partial^2 \tau} + k_j w_r(\xi, \tau) = \sum_{j=1}^N \left[ f_j(\tau) + \frac{\bar{m}_v L_v g}{N} \right] \delta(\xi - \xi_j) \quad (5)$$

According to Ritz method, the deflections of moving structure are then calculated with superposition of  $m$  terms of modes. Then utilizing the orthogonality condition, and assuming that there is no coupling among different vibration mode of the moving structure, Equation (1) is rearranged as

$$M_v \ddot{q}_k(\tau) + C_v \dot{q}_k(\tau) + K_v q_k(\tau) = \sum_{j=1}^N \left[ k_v w_r(\xi_j, \tau) + c_v \dot{w}_r(\xi_j, \tau) \right] X_k(\xi_j) \quad (6)$$

$$M_v = \bar{m}_v \int_0^L X_k(\xi) X_k(\xi) d\xi, \quad C_v = \sum_{j=1}^N c_v X_k(\xi_j) X_k(\xi_j), \quad (7)$$

$$K_v = \left[ \sum_{j=1}^N k_v X_k(\xi_j) X_k(\xi_j) + E_v I_v \int_0^L X_k(\xi) X_k^{IV}(\xi) d\xi \right]$$

where  $X_k(\xi)$  is the assumed vibration modes satisfying the boundary conditions,  $q_k(\tau)$  is the generalized coordinates.

Now applying the Laplace transform to Equation (5) and(6), yields

$$M_v s^2 \bar{q}_k(s) + C_v s \bar{q}_k(s) + K_v \bar{q}_k(s) = \sum_{j=1}^N \left[ k_v \bar{w}_r(\xi_j, s) + c_v s \bar{w}_r(\xi_j, s) \right] X_k(\xi_j) \tag{8}$$

$$E_r I_r \frac{\partial^4 \bar{w}_r(\xi, s)}{\partial \xi^4} + \bar{m}_r v^2 \frac{\partial^2 \bar{w}_r(\xi, s)}{\partial \xi^2} - 2\bar{m}_r v s \frac{\partial \bar{w}_r(\xi, s)}{\partial \xi} + \bar{m}_r s^2 \bar{w}_r(\xi, s) + k_f \bar{w}_r(\xi, s) = \sum_{j=1}^N \left[ k_v \left( \sum_{i=1}^m \bar{q}_i(s) X_i(\xi) - \bar{w}_r(\xi_j, s) \right) + c_v s \left( \sum_{i=1}^m \bar{q}_i(s) X_i(\xi) - \bar{w}_r(\xi_j, s) \right) + \frac{\bar{m}_v L_v g}{Ns} \right] \delta(\xi - \xi_j) \tag{9}$$

then  $\bar{q}_k(s)$  can be obtained from Equation (8). Substituting the expression  $\bar{q}_k(s)$  into Equation(9), and then applying the Fourier transform into Equation (9) gives

$$D(\omega, s) \hat{w}_r(\omega, s) = \sum_{j=1}^N \left[ E_j(s) \bar{w}_r(\xi_j, s) + \frac{\bar{m}_v L_v g}{Ns} \right] e^{-i\omega \xi_j} \tag{10}$$

then applying inverse Fourier transform to Equation (10) yields

$$\bar{w}_r(\xi, s) = \sum_{j=1}^N \left[ E_j(s) \bar{w}_r(\xi_j, s) + \frac{\bar{m}_v L_v g}{Ns} \right] \frac{1}{2\pi} \int_{-\infty}^{+\infty} \frac{e^{-i\omega(\xi - \xi_j)} d\omega}{D(\omega, s)} \tag{11}$$

From Equation(11),  $\bar{w}_r(\xi_j, s)$  can be solved as

$$\bar{w}_r(\xi_j, s) = \mathbf{A}^*(s) \frac{B_j(s)}{|\mathbf{A}(s)|} \quad , (j=1, \dots, N) \tag{12}$$

Substituting expression (12) into Equation (11)

$$\bar{w}_r(\xi, s) = \sum_{j=1}^N \left[ E_j(s) \mathbf{A}^*(s) \frac{B_j(s)}{|\mathbf{A}(s)|} + \frac{\bar{m}_v L_v g}{Ns} \right] \frac{1}{2\pi} \int_{-\infty}^{+\infty} \frac{e^{-i\omega(\xi - \xi_j)} d\omega}{D(\omega, s)} \tag{13}$$

For the steady vibration response  $w_r^s(\xi)$  of the infinite beam (Zhu, 1999)

$$w_r^s(\xi) = w_r(\xi, \tau) \Big|_{\tau \rightarrow \infty} = \lim_{s \rightarrow \infty} s \bar{w}_r(\xi, s) \tag{14}$$

Substituting Equation (13) into Equation(14), then the steady-state vibration response  $w_r^s(\xi)$  can be obtained.

### 3 Numerical Results and Conclusions

In order to illustrate the effects of some parameters on the deflection of the infinite beam, numerical examples are performed. The following values of the parameters are considered in the numerical calculations: the elastic modulus of the infinite beam  $E_r I_r = 1.75e6 \text{ Nm}^2$ ,  $\bar{m}_r = 25 \text{ kg/m}$ ,  $\bar{m}_v = 100 \text{ kg/m}$ ,  $L_v = 20 \text{ m}$ ,  $N=4$ .

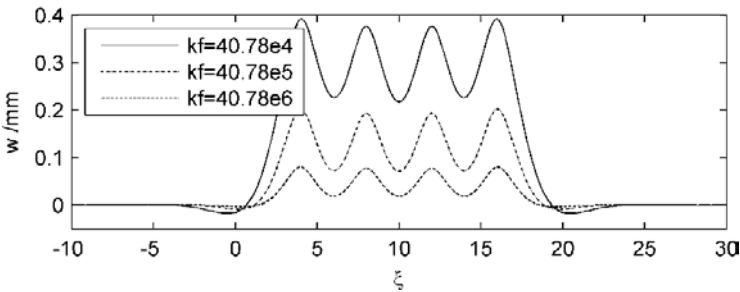


Figure 2. The effect of foundation stiffness on the steady-state vibration response

The influence of the foundation stiffness  $k_f$  on the steady-state vibration response of the infinite beam with the given moving speed  $v = 40 \text{ m/s}$  are illustrated in Figure 2. It can be seen that the dynamic response decreases as the foundation stiffness  $k_f$  increases. The value of response for  $k_f = 40.78e4 \text{ N/m}^2$  is about 4 times as the value for  $k_f = 40.78e6 \text{ N/m}^2$ . The results indicate that when a moving structure travels along a beam, the dynamic responses are greatly influenced by the foundation stiffness.

Figure 3 provides the influence of moving speed on the steady-state vibration response of infinite beam with the stiffness  $k_f = 40.78e4 \text{ N/m}^2$ . From the figure, it is noticeable that the values of the moving speed have no significant effect on the steady-state vibration response, as the responses are nearly constant for different moving speed.

The similar results are shown in Figure 4, in which the steady-state vibration responses are plotted with respect to the moving speed. However, as can be seen

for lower values of foundation stiffness the steady-state vibration responses increase slightly as the speed increase.

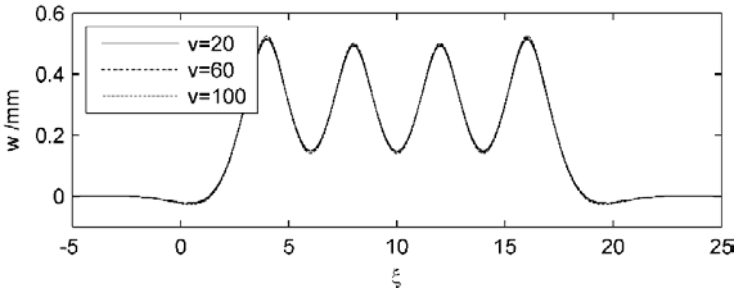


Figure 3. The effect of moving speed on the steady-state vibration response

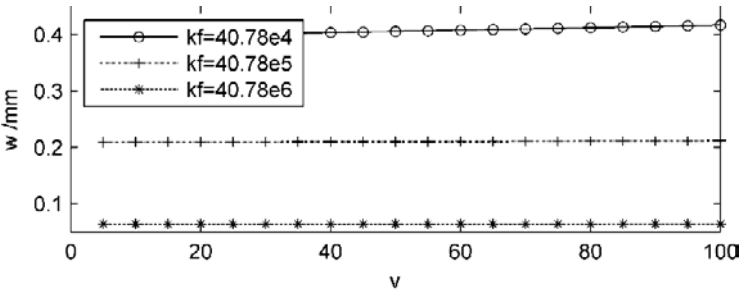


Figure 4. Dependence of steady-state vibration responses with respect to moving speed

## References

Cojocaru E.C., Irschik H. and Schlacher K. (2003). Concentrations of pressure between an elastically supported beam and a moving timoshenko-beam. *J. Eng. Mech.*, 129(9):1076-1082.

Cojocaru E.C., Irschik H. and Gattringer H. (2004). Dynamic response of an elastic bridge due to a moving elastic beam. *Comput. Struct.*, 82(11-12):931-943.

Mallik A.K., Chandra S. and Singh A.B. (2006). Steady-state response of an elastically supported infinite beam to a moving load. *Journal of Sound and Vibration*, 291(3-5):1148-1169.

Thambiratnam D. and Zhuge Y. (1996). Dynamic analysis of beams on an elastic foundation subjected to moving loads. *Journal of Sound and Vibration*, 198(2):149-169.

Yang Y.B. and Lin C.W. (2005). Vehicle-bridge interaction dynamics and potential applications. *Journal of Sound and Vibration*, 28 (1-2):205-226.

Zheng D.Y. and Fan S.C. (2002). Instability of vibration of a moving-train-and-rail coupling system. *Journal of Sound and Vibration*, 255(2):243-259.

Zhu T.J. (1999). *Engineering Mathematics – Integral Transforms*. Higher Education Press: Beijing [in Chinese].

# Building Structures Vibration Differential Equations under Random Excitation

Bin He<sup>1,2\*</sup>

<sup>1</sup> School of Civil Engineering, Xi'an University of Architecture and Technology, Xi'an 710055, P.R. China

<sup>2</sup> College of Hydraulic and Architectural Engineering, Northwest Sci-technology University of Agriculture and Forestry, Shanxi, Yangling 712100, P.R. China

**Abstract.** Applied the stochastic optimal strategy to introduce building structure response to wind and earthquake excitation. First deduced the wind load model in the frequency domain and the wind load model in the time domain, then listed a set of stochastic differential equations based on the power spectral matrix of the discredited fluctuating wind field. For earthquake, represented random processes in the frequency domain by their power spectral density functions. For a structure involving many degrees of freedom, the mode-superposition method is usually adopted for determining the dynamic response of the structure under all random excitation.

**Keywords:** wind, earthquake, random excitation, structure response

## 1 Introduction

Wind and Earthquake are the important design loads. The loads acting on buildings have many types for civil engineering structures. For long span bridges, and some of them are altered with time and some are not. Environmental load such as earthquakes and strong winds are often modeled as random processes represented in the frequency domain by their power spectral density functions and in the time domain. If a structure involves many degrees of freedom, the mode-superposition method is usually adopted for determining the dynamic response of the structure under random excitation.

---

\* Corresponding author, e-mail: ylhebin@163.com

## 2 Structure Responses to Wind Excitation

It is well known that strong wind may induce severe vibration of buildings, discomfort to the occupants and damages of sensitive equipments in the buildings. Since wind excitation is random, it is natural and reasonable to apply stochastic optimal control theory to wind-excited buildings. Because wind excitation can hardly be modeled as Gaussian white noise, to apply the stochastic optimal strategy, it is necessary to establish a set of stochastic differential equations for random wind loading based on the power spectral matrix of the discredited fluctuating wind velocity field.

### 2.1 The Wind Load Model in the Frequency Domain

The wind field acting on a building structure is usually discredited as wind velocity vector, which is often modeled as a vector of stationary Gaussian processes. The wind velocity vector consists of two parts: a deterministic vector for mean wind velocity and a stationary Gaussian random process vector  $v(t)$  with zero mean for fluctuating wind velocity. The fluctuating wind velocity vector averaged is often described in the frequency domain by using a power spectral density matrix  $S_v(x)$ , whose  $ij$ th element is of the form (Zhang, 2000)

$$S_{v_i v_j}(\omega) = \sqrt{S_{v_i v_i}(\omega) S_{v_j v_j}(\omega)} \exp[-f_{ij}(\omega)] \tag{1}$$

where  $v_i$  and  $v_j$  denote the  $i$ th and  $j$ th element of vector  $v(t)$ , respectively;  $f_{ij}(x)$  is the coherence function;  $S_{v_i v_i}(\omega)$  is the one-side power spectral density of random process  $v_i(t) = v(z_i, t)$ .

### 2.2 The Wind Load Model in the Time Domain

The wind load is considered in the following analysis. The wind speed at level  $z$  above the ground,  $v(z, t)$  can be written as (Zhang, 2000)

$$v(z, t) = \bar{v}(z, t) + \hat{v}(z, t) \tag{2}$$

where  $\bar{v}(z, t)$  and  $\hat{v}(z, t)$  denote the average wind speed and fluctuating wind speed, respectively. The mean wind speed at a different level,  $\bar{v}(z)$ , may be calculated according to the power law (Zhang, 2000)

$$\bar{v}(z) = \bar{v}(z') \left( \frac{z}{z'} \right)^\alpha \quad (3)$$

in which  $z'$  and  $\bar{v}(z')$  are the reference height and average wind speed at the reference level, respectively.  $z$  and  $\bar{v}(z)$  are the arbitrary height and its corresponding average wind speed. The power law exponent  $\alpha$  is determined from the terrain roughness. The aerodynamic forces due to wind turbulence are expressed as follows with no lifting effect in the present case of vertical cantilever structure. The fluctuating wind load  $F(z, t)$  on the structure at level  $z$  can be written as

$$F(z, t) = \frac{1}{2} \rho \mu_s(z) A(z) v^2(z, t) \quad (4)$$

where  $\rho$  is the density of air,  $A(z)$  is the orthogonal exposed wind area at level  $z$  and  $\mu_s(z)$  is the drag coefficient of the structure at level  $z$ .

### 2.3 Structure Response

The equation of motion of a structure subjected to wind gust excitation can be written as

$$M \ddot{x}(t) + C \dot{x}(t) + Kx(t) = f(t) = Rp(t) \quad (5)$$

in which  $p(t)$  is an  $m$ -dimensional stationary random excitation vector with the power spectral density matrix  $S_{pp}(w)$  given, which include the spatial and temporal coherence between multi point excitation.  $R$  is an  $N \times m$  matrix consisting of 0 and 1 which expands the  $m$ -dimensional vector  $p(t)$  into the  $N$ -dimensional vector  $f(t)$ . Various fluctuating wind speed (or force) spectra, for different wind directions will lead to different  $S_{pp}(w)$ , but the equation itself is quite general.

Assume the degree of freedom of the structure under consideration, denoted, as  $N$  is very high, so that the mode-superposition scheme is adopted to reduce the computational effort. Based on the first  $q$  ( $q \ll N$ ) normalized modes  $\Phi$ , the structural displacement vector  $x$  can be expressed by the normal co-ordinates vector  $z$  as

$$x(t) = \Phi z(t) \quad (6)$$

and equation (5) can be accordingly transformed into

$$\ddot{z}(t) + C^0 \dot{z}(t) + \Omega^2 z(t) = f^0(t) \tag{7}$$

in which

$$C^0 = \Phi^T C \Phi, f^0(t) = \Phi^T f(t) = \Phi^T R p(t) \tag{8}$$

Because  $p(t)$  has been assumed to be a stationary random excitation vector .if the system is linear  $f^0(t)$  and  $z(t)$  are also stationary random vectors. Therefore, the cross-spectral density matrix of  $z(t)$  can be found from the power spectral density matrix  $f^0(t)$  based on equation (7) .

$$S_{zz}(\omega) = H^*(\omega) S_{f^0 f^0}(\omega) H^T(\omega) \tag{9}$$

in which

$$H(\omega) = (-\omega^2 I + \Omega^2 + i\omega C^0)^{-1} \tag{10}$$

$S_{f^0 f^0}(\omega)$  is the power spectral density matrix of  $f^0(t)$  . From equations (6) and (8) one obtains

$$S_{xx}^1(\omega) = \Phi S_{zz}(\omega) \Phi^T \tag{11}$$

$$S_{f^0 f^0}(\omega) = \Phi^T S_{ff}(\omega) \Phi = \Phi^T R S_{pp}(\omega) R^T \Phi \tag{12}$$

Substituting equations (9) and (12) into equation (11) yields

$$S_{xx}^1(\omega) = \Phi H^*(\omega) \Phi^T S_{ff}(\omega) \Phi H^T(\omega) \Phi^T \tag{13}$$

or

$$S_{xx}^1(\omega) = \Phi H^*(\omega) \Phi^T R(\omega) S_{ff}(\omega) R^T(\omega) \Phi H^T(\omega) \Phi^T \tag{14}$$

if  $C$  is a proportionally damped matrix, both  $C^0$  and  $H(\omega)$  will be diagonal, and equation (14) can be reduced into the following form.

$$S_{xx}^l(w) = \sum_{i=1}^q \sum_{j=1}^q H_i^*(w) H_j(w) \phi_i \phi_i^T R S_{pp}(w) R^T \phi_j \phi_j^T \quad (15)$$

Equation (15) is the complete quadratic combination method for computing the spectral density matrix of structural displacement responses under wind excitation (Zhu et al., 2004).

### 3. Structural Response to Earthquake Excitation

Consider the equation of motion of an elastic structure subjected to ground acceleration  $\ddot{x}_g(t)$  with its power spectral density function  $S_g(t)$  given.

$$M \ddot{x}(t) + C \dot{x}(t) + Kx(t) = -M_e \ddot{x}_g(t) \quad (16)$$

in which  $m$ ,  $c$  and  $k$  are the  $N \times N$  mass damping and stiffness matrices of the structure.  $x(t)$ ,  $\dot{x}(t)$  and  $\ddot{x}(t)$  are the displacement, velocity and acceleration vectors. Respectively  $e$  is an  $N$ -dimensional index vector of inertial forces. For a complex structure,  $N$  is very large, and the mode superposition method is usually used. To this end, the problem is first resolved (Lawa, 2005).

$$K \Phi = M \Phi \Omega^2, \Phi M \Phi = I \quad (17)$$

in which  $I$  is an identity matrix. Then the structural displacement vector  $x$  is decomposed into

$$x(t) = \Phi z(t) = \sum_{i=1}^q \phi_i z_i(t) \quad (18)$$

Finally, equation (3-1) can be reduced into

$$\ddot{z}(t) + C^0 \dot{z}(t) + \Phi z(t) = -\gamma \ddot{x}_g(t) \quad (19)$$

in which

$$C^0 = \Phi^T C \Phi, \gamma = \Phi^T M_e \quad (20)$$

If the structure related to damping matrix C is proportionally damped. Equation (19) can be reduced and uncoupled into the q single-degree-of-freedom equations

$$\ddot{z}_i(t) + 2\xi_i \omega_i \dot{z}_i(t) + \omega_i^2 z_i(t) = -\gamma_i \ddot{x}_g(t) \tag{21}$$

in which  $\xi_i$  and  $\omega_i$  are the ith modal damping ration and angular frequency respectively; and  $\gamma_i$  is the ith modal participation factor<sup>[4]</sup>.

The solution of equation (21) is

$$z_i(t) = -\int_{-\infty}^{\infty} \gamma_i h(\tau) \ddot{x}_g(t - \tau) d\tau \tag{22}$$

in which  $h(\tau)$  is the impulse response function and so

$$x(t) = -\sum_i^q \phi_i \int_{-\infty}^{\infty} \gamma_i h(\tau) \ddot{x}_g(t - \tau) d\tau \tag{23}$$

its correlation matrix is (Benfratello and Muscolino ,1999)

$$R(\tau) = E[x(t)x(t + \tau)] \\ = \sum_{i=1}^q \sum_{j=1}^q \gamma_i \gamma_j \phi_i \phi_j^T \int_{-\infty}^{\infty} \int_{-\infty}^{\infty} R_{x_g x_g}(\tau + \tau_1 - \tau_2) h(\tau_1) h(\tau_2) d\tau_1 d\tau_2 \tag{24}$$

Transforming the above equation into the frequency domain<sup>[4]</sup> gives

$$S_{xx}^2(\omega) = \sum_{i=1}^q \sum_{j=1}^q \gamma_i \gamma_j H_i^*(\omega) H_j(\omega) \phi_i \phi_j^T S_g(\omega) \tag{25}$$

in which  $H_i(\omega) = (\omega_i^2 - \omega^2 + i2\xi_i \omega_i \omega)^{-1}$

Equation (25) is the tradition complete quadratic combination method for computing the spectral density matrix of structural displacement responses under earthquake excitation. It is exact because all the cross-modal terms have been included. When both N and q are big, the computational efforts required are very large because equation (25) involves the double summation operations, for example, when q=10, the operation after the summation symbols must be repeated 100 times<sup>[5,6]</sup>.

## 4 Two Random Excitation Superposition

Suppose two random loads (wind and earthquake) are acting simultaneously. When the system is assumed to be linearly elastic, the response of the system to these loads can be calculated by superposition.

$$S_{xx}(\omega) = \sum_{i=1}^q \sum_{j=1}^q [H_i^*(\omega) H_j(\omega) \phi_i \phi_j^T R S_{pp}(\omega) R^T \phi_j \phi_j^T + \gamma_i \gamma_j H_i^*(\omega) H_j(\omega) \phi_i \phi_j^T S_g(\omega)] \quad (26)$$

## References

- Benfratello S., Muscolino G. (1999). Filter approach to the stochastic analysis of MDOF wind-excited structures. *Probability Engineering Mechanics*, 14(2), 311–321.
- Chen J., Li J. (2001). Study on the inverse wind load identification of tall building. *Chinese Quarterly of Mechanics*, 22(1), 72–77 [in Chinese].
- Lawa S.S., Bub J.Q., Zhua X.Q. (2005). Time-varying wind load identification from structural responses. *Engineering Structures*, 27(5), 1586–1598.
- Zhang W.S. (2000). Generalized pseudo-excitation method and its application for vibration control of wind seismic resistant buildings. A Dissertation for the Degree of Philosophy. Hong Kong Polytechnic University.
- Zhang X.T. (1998). *A handbook for wind load computation in engineering design*. Chinese Construction Publishing House [in Chinese].
- Zhu W.Q., Luo M., Ying Z.G. (2004). Nonlinear stochastic optimal control of tall buildings under wind loading. *Engineering Structures*, 26(5), 1561–1572.

*“This page left intentionally blank.”*

**STRUCTURAL DIAGNOSIS,  
CONTROL AND OPTIMIZATION**

*“This page left intentionally blank.”*

# On the Tapping-Scan Method Designed for the Damage Detection of Bridge Structures

Xiaowei Dai\*, Yao Zhang and Zhihai Xiang

Failure Mechanics Laboratory, Department of Engineering Mechanics, Tsinghua University, Beijing 100084, P.R. China

**Abstract.** Inspired by the hunting behavior of woodpeckers, a new tapping-scan method is proposed for the damage detection of bridge structures with high accuracy. The whole detecting system is a scanning vehicle integrated with tapping devices. With this system, the damage detection can be applied without disturbing the traffic on the bridge. To enhance the detection sensitivity, an analytical solution is firstly deduced to unveil the relation between the vehicle acceleration and the damage. Then numerical simulations are carried out for different damage scenarios. The obtained spectrum of vehicle acceleration is used to locate the damage.

**Keywords:** damage detection, vehicle-bridge interaction, tapping-scan method

## Introduction

Damages, such as cracks, corrosion, loose of anchor force, etc., probably exist in old bridges after a long time service, which may lead to disasters one day. Some damages inside the bridge are quite difficult to discover in the early time for the complexity of this kind of large scale structures. Therefore, developing damage detection methods for bridge structures has been an active topic in the past several decades. These methods can be generally classified into two types: the *local method* just uses naked eyes observation or some non-destructive instruments to detect damage; the *global method* tries to obtain the damage information from the response of the entire structure. The local method can indicate the damage type, location and severity with certain acceptable accuracy. But one disadvantage of such method is the need of prior knowledge about the damage location, otherwise it would take a long time to scan all possible locations and often miss important defects. The global method does not need scanning and can be used for online monitoring, but it usually has less accuracy than local methods 0

---

\* Corresponding author, E-mail: daixw03@mails.tsinghua.edu.cn

It seems that the difficulty always exists to balance the accuracy and the efficiency of damage detection methods. However, this problem could be partially solved by the woodpecker in its hunting activities. By tapping with its beak at high frequency while scanning around the tree, a woodpecker could pinpoint the location of the caterpillar hidden in the trunk. Inspired by this, we know there are two factors that are critical to the success of damage detection methods, i.e., the high frequency tapping and the scanning. This is because the damage is a local phenomenon that will mainly bring changes in the high frequency spectrum. Moreover, the scanning separates the location searching from the judgment of the existence of damage, which would greatly simplify the data analyzing.

Based on the above analysis, a tapping-scan system is proposed to detect damage for bridge structures in this paper. This system is characterized with the integration of the excitation device and the sensor on a moving vehicle. The most important advantages of this damage detection method are not disturbing the normal traffic and the strong anti-interference ability. To our knowledge, a similar testing system has been proposed by Yang et al. to obtain the fundamental bridge frequencies. Although it is difficult to detect the damage only from fundamental frequencies, Yang’s method does mimic the scanning manner of the hunting behavior of woodpeckers and avoids the problems of mounting sensors on bridges. The main difference of our new system is adding an external tapping load on the vehicle, which will excite high frequency responses that contain damage information.

The theoretical model of the proposed system is simplified as a vehicle-bridge interaction problem with external loading produced by a tapping mechanism. Based on the analytical solution of this model, some system parameters can be carefully chosen so that the recorded vehicle acceleration is sensitive to damage. Then, numerical simulations are carried out for different damage scenarios. With these data, damage detection can be conducted through a well-designed pattern recognition method.

### Theoretical Model

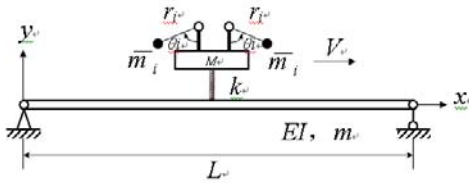


Figure 1. The bridge-vehicle interaction model of the tapping scan system.

Taking the bridge and the vehicle as a simply supported beam and a mass block mounted on a spring, respectively, the whole model can be described as a bridge-vehicle interaction problem shown in Figure 1, in which  $EI$  is the bending stiffness of the bridge;  $m$  is mass in unit length of bridge;  $k$  is the stiffness of the spring; and  $M$  is the mass of vehicle. The scanning vehicle is equipped with a tapping device and moves from one bridge end to the other at a constant speed  $V$ . By changing the tapping device, different type of loadings can be applied on the system, in order to get a rich component in high frequency. In this paper, we would use  $N$  pairs of opposite cycling eccentric mass  $\bar{m}_i$  ( $i = 1, 2, \dots, N$ ) to generate tap excitation, both of which share the same phase so that no force will disturb the horizontal movement. With such a loading system, the force applied on the vehicle should be sinusoidal vertically. Taking all the forces involved in the system into consideration, the equilibrium equations of vehicle can be easily obtained according to the Newton's second law:

$$k[\Delta - (y_V - y_B|_{x=Vt})] = 2 \sum_{i=1}^N F_{\bar{m}_i} + M \ddot{y}_V + Mg \tag{1}$$

where  $\Delta = \left( 2 \sum_{i=1}^N \bar{m}_i + M \right) g / k$  presents the static vehicle displacement;  $y_B$  and  $y_V$  are the bridge and vehicle deflections, respectively;  $F_{\bar{m}_i}$  denotes the force produced by the  $i$ th eccentric mass:

$$F_{\bar{m}_i} = \bar{m}_i \bar{\omega}_i^2 r_i \cos(\bar{\omega}_i t + \theta_{0i}) + \bar{m}_i g \tag{2}$$

$g$  is the acceleration of gravity;  $N$  is the number of eccentric masses;  $\bar{\omega}_i$ ,  $r_i$  and  $\theta_{0i}$  are the angular velocity, eccentric distance and the initial phase of the  $i$ th eccentric mass, respectively.

Substitute (2) into (1), the equation for the moving vehicle can be written as:

$$M \ddot{y}_V + k(y_V - y_B|_{x=Vt}) = -2 \sum_{i=1}^N \bar{m}_i r_i \bar{\omega}_i^2 \cos(\bar{\omega}_i t + \theta_{0i}) \equiv F(t) \tag{3}$$

Taking the bridge as an Euler-Bernoulli beam, its governing equation is:

$$m \ddot{y}_B + EI y_B^{(iv)} = f(t) \delta(x - Vt) \tag{4}$$

where  $\delta$  is the Kronecker delta function; and  $f(t)$  is the force applied on the beam through the suspension spring:

$$f(t) = k(y_v - y_B|_{x=Vt}) - k\Delta = -M \ddot{y}_v(t) + F(t) - Mg - 2\sum_{i=1}^N \bar{m}_i g \tag{5}$$

So the instantaneous stiffness of the beam can be obtained as follows:

$$Z = \frac{f(t)}{y_B(t)} \delta(x - Vt) = \frac{-M \ddot{y}_v(t) + F(t) - \left(2\sum_{i=1}^N \bar{m}_i + M\right)g}{y_B(t)} \tag{6}$$

Hence, the vehicle acceleration can be expressed as:

$$\ddot{y}_v = -\frac{y_B(t)}{M} Z(x) + \frac{F(t)}{M} - \frac{2\sum_{i=1}^N \bar{m}_i + M}{M} g \tag{7}$$

where the damage information is contained in  $Z$ . Equation (7) also implies that the sensitivity of damage detection can be enhanced by maximizing the magnitude of bridge deflection  $y_B$ , which can be obtained from equation (4) by modal superposition method together with Duhamel integration 0.

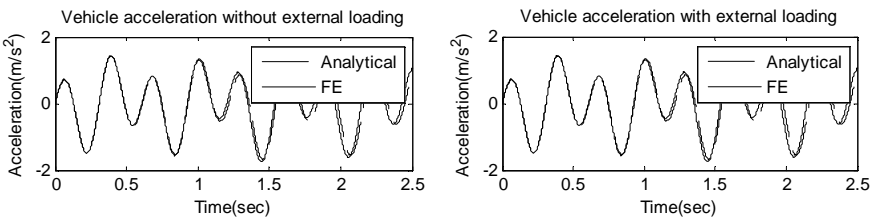


Figure 2. The comparison between the FE results and the analytical results

To evaluate the validity of the analytical solution, a Finite Element (FE) analysis is conducted by using ABAQUS package. Here just take the same FE model used in reference 0, so that the simulation should get the same result when no external tapping force presented. The bridge properties are: cross-sectional area  $A = 2.0\text{m}^2$ , moment of inertia  $I = 0.12\text{m}^4$ , length  $L = 25\text{m}$ , elastic modulus  $E = 2.75 \times 10^{10} \text{N/m}^2$ , and mass per-unit-length  $m = 4800\text{kg/m}$ . The vehicle with the mass of  $M = 1200\text{kg}$  and the spring of  $k = 500000\text{N/m}$  passes through the

bridge at a constant speed  $V = 10\text{m/s}$ . The external tapping force generation system has eccentric mass  $\bar{m} = 10\text{kg}$  with an arm length  $r = 1\text{m}$ , which will rotate at  $\bar{\omega} = 10\text{rad/s}$  with the initial phase angle  $\theta = \pi/2$ . For simplicity, only one pair of eccentric mass is introduced in this simulation, preventing the squeezed waveform. As Figure 2 shows, the numerical results agree very well with the analytical solution not only in the special case free of tapping load but also in the case with external loading applied on the vehicle. This FE model will be used in the following damage detection after introducing the damage into the bridge.

## Damage Identification

The vehicle acceleration on a damaged bridge is used to locate the exact position of the defect. The whole bridge is firstly divided into several segments according to the vehicle speed and the sampling rate. Then the short time Fourier transformation is used to transform the data into the frequency spectrum. Finally, the Modal Assurance Coefficient (MAC) index between the spectrum profiles of each segment is calculated (Allemang, 1982). Since the MAC index can indicate the similarity between the two vectors, and the damaged segment brings a great change in the spectrum, the damage will lead to a sharp decrease in MAC index between damaged and intact segments. All in all, the whole damage detection process is formulated in the manner of pattern recognition.

The damage identification result for that two dimensional beam model presented in above section is shown in Figure 3, in which the x and y axis presents the position along the bridge, while the z axis means the MAC index between two segments. Because the damage is introduced by cutting half the section area in the middle of the bridge, a deep channel appears at the exact position in Figure 3.

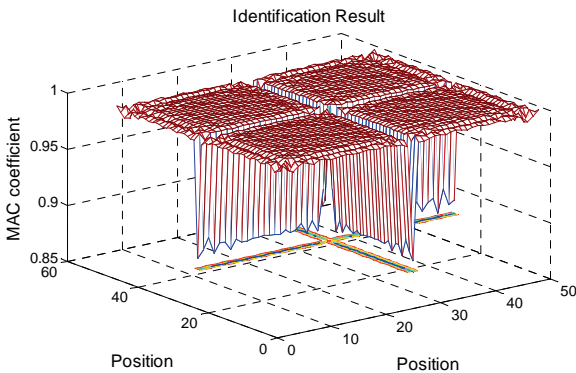


Figure 3. Identification result (2D)

However, in the real structure most damage occurs at local places rather than through the whole cross-section. Therefore, a three dimensional (3D) FE model would be necessary to describe these small flaws. In this model, a box bridge is modeled by shell elements. The damage at the middle span is introduced by reducing the elastic modulus of some elements on one side of the girder.

Figure 4 shows the identification result only from the vehicle acceleration in vertical direction. The result does have a small decrease in MAC index when the vehicle passes the damaged region, but it is difficult to confirm the exact location. This is because only one side of the box section is damaged while the other side can still sustain most of the vertical loading. Considering such an open thin-walled beam is vulnerable to torsion, the angular acceleration of the vehicle is used to detect the damage instead of the vertical translational acceleration. As Figure 5 shows, a channel appears at the exact location at this time.

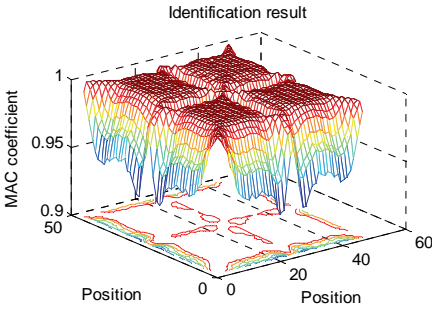


Figure 4. The identification using the vertical acceleration (3D)

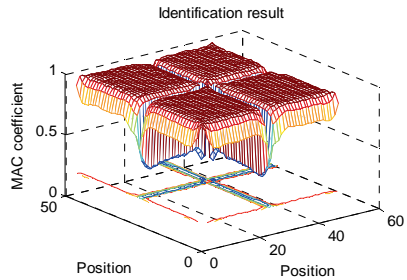


Figure 5 The identification using the angular acceleration (3D)

## Conclusion

In this paper, a tapping-scan method is proposed to detect damage for bridge structures. This new method can achieve good accuracy without the requirement of blocking the traffic. Taking the whole system as a vehicle-bridge interaction problem, the analytical solution of the vehicle response is obtained. Based on this analytical solution, the damage identification is presented as a pattern recognition process. Numerical examples prove that such a tapping-scan method is very effective for damage detection. Of interest is the fact that in 3D case, the angular acceleration is more sensitive to damage than the translation if the damage happens in local regions.

## References

- Allemang R.J. and Brown D.L. (1982). Correlation coefficient for modal vector analysis. In: *Proceedings of the 1st International Modal Analysis Conference*, Society for Experimental Mechanics, Orlando, pp. 110-116.
- Carden E.P. and Fanning P. (2004). Vibration based condition monitoring: a review. *Structural Health Monitoring*, Vol. 3, 355-377.
- Li Y.Q., Xiang Z.H. and Zhou M.S., et al. (2008). An integrated parameter identification method combined with sensor placement design. *Communications in Numerical Methods in Engineering*, Vol. 24, 1571-1585.
- Wu Shiwei, et al. (1988). *The papers of structural safety and reliability analysis*. Hehai University Press, Nanjing [in Chinese].
- Yang Y.B., Lin C.W. and Yau J.D. (2004). Extracting bridge frequencies from the dynamic response of a passing vehicle. *Journal of Sound and Vibration*, Vol. 272, 471-493.

*“This page left intentionally blank.”*

# Structure Damnification Diagnose System by Radial Basis Function Neural Network

Keqin Yan<sup>1,2\*</sup> and Tao Cheng<sup>2</sup>

<sup>1</sup> State Key Laboratory for Disaster Reduction in Civil Engineering, Tongji University, Shanghai 200092, P.R. China

<sup>2</sup> School of Civil Engineering, Huangshi Institute of Technology, Huangshi, 435003, P.R. China

**Abstract.** A structure damnification diagnose system method based on radial basis function (RBF) network is put forward which is composed of three networks from finding damaged position to ensuring damaged extent. Preference of remainder force matrix based on vibration equation is bring forward. Its feasibility and validity of the damnification diagnose system are proved through mode simulate analyzing. Take the discontinuity of concrete structure, better modulus parameter can be chosen as input parameter according to different structure of its dynamic characteristic.

**Keywords:** RBF network, damnification diagnose system, dynamical character, modal analyze, simulation

## 1 Introduction

Recently, more and more damnification diagnose methods of structure are investigated (Peng et.al, 2008; Jeyasehar and Sumangalaa, 2006), in which the uppermost method is to identify the damage status of the structure through the dynamic characteristics parameters (such as free vibration, frequency, vibration mode, frequency response function, etc.) of actually test. These methods suffer a major shortcoming in that the fine error of structure dynamic characteristics will cause a large variation in the indication result.

ANN interlinked by large quantity of simply-disposed unit has been widely applied to the fields such as “pattern recognition”, “automatic control”. And some applications using ANN in civil engineering are investigated such as “optimum structure design” (Lu and Wang, 1999), “numerical modeling of geomaterial” (Cheng et al., 2008), etc. By virtue of good self-adaptive ability, fault-tolerant ability and robustness, ANN is prior to the traditional methods for structure dam-

---

\* Corresponding author, e-mail: drkqyan@yahoo.com.cn

nification diagnosing. In this article, a damnification diagnosing system by RBF neural network introduced from finding damaged position to ensuring damaged extent.

## 2 Theory of Checking

The characteristic equation free vibration of the structure is widely known (Clough and Penzien, 2006)

$$([K]_0 - \omega_{0i}^2 [M]_0) \varphi_{0i} = 0 \quad (1)$$

In consideration of the vibration perturbation equation of damaged structure (Li and Li, 2002):

$$[(K]_0 + \Delta[K]) - (\omega_{0i}^2 + \Delta\omega^2)([M]_0 + \Delta[M])](\varphi_{0i} + \Delta\varphi) = 0 \quad (2)$$

## 3 The Basis Principle of RBF

The model that used widely at present is BP net model (Wu et al., 1992, Saluwu, 1997). Every data input and output will be adapted. But BP network has some shortcomings, such as slow computation speed, merely catching region minimum, etc. The defects above can be overcome by RBF network. An implication neural layer will be added every time during its study. And the data can be adapted accordingly until the error point is acceptable or the maximum training number is reached. Therefore, RBF network is prior to BP network at several aspects such as numerical approximation ability, specialty and study speed etc.

RBF network' structure is divided into three layers showed as Figure 1. The first layer is input layer. The second layer is implicit layer. The transfer function of it is RBF non-linear function. And it's a non-negative and non-linear function. The third layer is output layer. The transfer function of it is liner function.

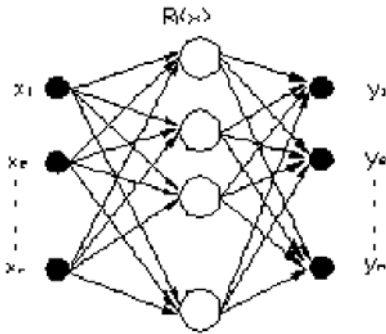


Figure 1. RBF network framework

The action function of implicit layer's node will respond locally to the input signal. That is to say, when the input signal is nearing the central place of the basic function, bigger output will be caused in the implicit layer. So the network is locally approximating. The calculate process of the RBF network is showed as Figure 1. Non-linear mapping  $x \rightarrow R_i(x)$  is carried out in input layer. And linear mapping  $R_i(x) \rightarrow y$  is carried out in output layer. That is:

$$y_k = \sum_{i=1}^m w_{ik} R_i(x) \quad (k = 1, 2, \dots, m) \quad (8)$$

In which,  $k$  is the number of outside nodes.

#### 4 Damnification Diagnosing System and Choice of Parameters

The deformation of element can be expressed by several stages vibration modes. So some-order vibration mode has higher sensibility to some element about its message of damnification whereas it has lower sensibility to other element of its damage of this message. From above, it can be said that the damage degree of every element is implied in the variation of kinds-order of frequency. It is proved theoretically that higher-order vibration mode is easier to distinguish structure damage compared with lower-order vibration mode. But it is difficult to get the higher-order vibration mode. And if  $\beta_i$  is used as network input parameter, it also implied the message of vibration. And it's rational theoretically. It is proved by the calculator principle of  $\beta_i$  that the disturb factor identification error in different element of kinds-order of vibration can be eliminated.

From the analysis above, it can be said that they both can be used as network input parameters.  $\beta_i$  as input parameter is discussed predominating in the article.

The merits of the method that  $\beta_i$  used as input parameter is hoped get in the comparison.

The damnification diagnosing system structure by RBF network is shown as Figure 2

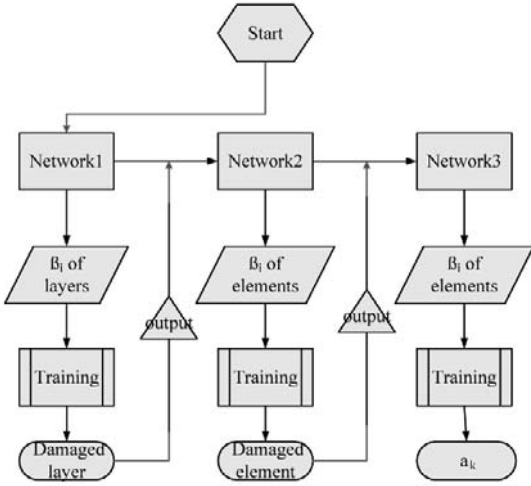


Figure 2. Damnification diagnosing system structure

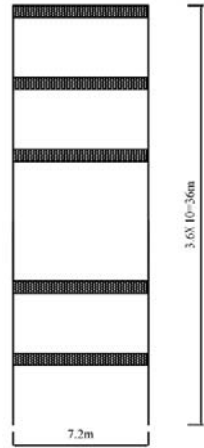


Figure 3. Frame structure sketch

### 4.1 Damaged Position of Damaged Structure

To explain the problem, a single span concrete frame structure is adapted as an example shown as Figure 3.

Parameter of material and geometry is as following:

Elastic modulus  $E = 3.0 \times 10^4 MP_a$ ; Poisson ratio  $\nu = 0.3$ ; material density  $\rho = 2400 kg / m^3$ ; geometric parameter ( $mm$ ): beam section  $250 \times 600$ ; column section of 1~6 layer:  $600 \times 600$ ; column section of 7~10 layer:  $500 \times 500$ .

#### 4.1.1 Sample Parameter

The sections of No.1–No.6 column are cut down one by one to  $250 \times 500$  to imitate the damnification of the elements this layer. The sections of No.7–No.10 column are cut down one by one to  $200 \times 400$  to imitate the damnification of the elements this layer. The perfect structure is added together, there are eleven modes. To make the imitate modulus analysis with analysis, the forth six-order frequency of

every mode can be get. The frequencies are put in the calculate formulations about the two parameter. The ten samples gotten are used as input parameter to train a RBF network. Part of input data are given out as diagram one. (The network parameter input according to normalization frequency variety rate is neglected.)

### 4.1.2 Checking of Training

The sample parameters above are used to train its RBF network. The target error are both Assumed as 0.0001.

The two networks are both convergent normally. But the latter convergence speed is faster. There are only 64 steps before its convergence. The No.7 element section is cut down to 200×400, No.8 to 500×250. They are used as the damaged elements to be identified. The network in which the regularized frequency variety rate is used as input parameter result with bigger error.

Table 1. Maximum vector of residual matrix

mem ber	$\beta_i$									
1	1.9285	15.6889	54.7669	72.9331	13.3865	11.3192	48.2629	71.6473	75.2955	75.6808
2	2.4877	1.3037	12.0187	67.4909	12.7286	8.7438	55.7626	120.6308	136.5111	138.3321
3	4.5137	0.1204	0.0653	0.5704	0.4434	0.3341	1.9198	3.6545	4.0175	4.0578
4	1.8846	1.7133	0.1217	0.0654	0.2055	0.2274	1.0306	1.5933	1.6853	1.6951
5	0.9600	0.8727	0.8648	0.1244	0.1183	0.1663	0.6086	0.8292	0.8604	0.8636
6	0.9840	0.8946	0.8865	0.8857	0.1500	0.2617	0.7151	0.8650	0.8835	0.8854
7	15.9489	14.4990	14.3684	14.3554	0.2872	0.0885	0.0594	0.5728	4.2145	11.5703
8	2.0613	1.8739	1.8570	1.8554	0.3343	0.3997	0.0832	0.0517	0.4136	1.3757
9	1.1019	1.0017	0.9927	0.9918	0.3196	0.3298	0.8259	0.0766	0.0500	0.3438
10	0.1603	0.1458	0.1444	0.1443	0.0552	0.0549	0.1241	0.1420	0.0529	0.0783

This may be owing to the effect of its disturbing message's eliminating is not remarkable. At the same time, the imitate degree of the mode in the imitating modulus is not so high. But if the maximum residual vector of residual matrix  $\beta_i$  is used as input parameter, the damaged element can be identified normally. The identify result is given out in the following table.

Table 2. Result of test

input value										antic- ipant	actual output
2.0613	1.8739	1.8570	1.8554	0.3343	0.3997	0.0832	0.0517	0.4136	1.3757	8	8.000
15.9489	14.4999	14.3684	14.3554	0.2872	0.0885	0.0594	0.5728	4.2145	11.5703	7	7.000

## 4.2 Damaged Element of the Damaged Layer

### 4.2.1 Sample Selection

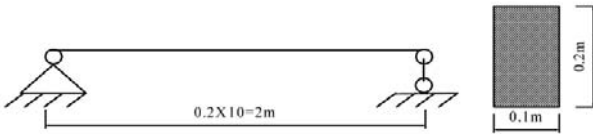


Figure 4. Structure unit and cross section sketch

There are eleven concrete beams what are all 2m long (Figure 3). Section size:  $0.2 \times 0.1(m \times m)$ ; material parameter: elastic modulus  $E_c = 3.0 \times 10^4 MPa$ ; density:  $\rho = 2400kg / m^3$ ; every beam is divided into ten units. One or several units of some beams is made as damaged section. Take the symmetry consideration, sample can be chosen as the following:

Table 3. Damaged element sample

detecting sample	beam1	beam 2	beam 3	beam 4	beam 5	beam 6	beam 7	beam 8	beam 9
Damaged units	intact	unit1	unit2	unit3	unit4	unit5	unit2、 6	unit4、 8	unit1、 7
Section dimen- sion	$0.2 \times 0.1$	$0.15 \times 0.1$	same as beam2	same as beam2	$0.1 \times 0.1$	same as beam5	Unit $0.15 \times 0.1$ unit6 $0.1 \times 0.1$	unit4 $0.1 \times 0.1$ unit8 $0.1 \times 0.1$	unit1 $0.15 \times 0.1$ unit7 $0.1 \times 0.1$

Use the above damaged sample to train the network. That is to say, every beam is divided into ten units, eleven nodes. Ansys is adopted to make its modulus

analysis. The forth three-order vibration mode and free vibration frequency are gotten. Regularized frequency varied rate and residual vector  $\beta_i (i = 1, 2, \dots, 9)$  are used to represent input parameter. The output parameter is the position of damaged unit.

### 4.2.2 Test by Network

Let allowable error  $e=0.0001$ . And the parameters above are used to train the network until it is convergent. To make the modulus imitating experiment with the other two jaggging beams. The third unit of beam I is damaged. The damaged section size is  $0.12 \times 0.1$ . The second and sixth units of beam II are damaged. The damaged sections size are: the second unit equals  $0.12 \times 0.1$ ; the sixth  $0.1 \times 0.1$ . The data are input into the RBF network used two different parameter as input parameter. Similar to example one, the network used residual vector  $\beta_i$  as input parameter has better result. It is especially perfect to forecast the position of single damage unit. The examine output is given out as following:

Table 4. Result of test by network using parameter  $\beta$

Inspected beam 1									
Anticipant output	0.0000	0.0000	1.0000	0.0000	0.0000	0.0000	0.0000	0.0000	0.0000
Actual output	0.0000	0.0000	1.0000	0.0000	0.0000	0.0000	0.0000	-0.0000	0.0000
Inspected beam 2									
Anticipant output	0.0000	1.0000	0.0000	0.0000	0.0000	1.0000	0.0000	0.0000	0.0000
Actual output	-4.9446	1.1374	0.0000	10.1918	-5.6216	1.3005	12.4251	10.2170	6.0200
		0.0000							

### 4.3 Damage Extent of the Damaged Element

The sample selection is same as the example 2. And the parameter  $\beta_i$  is also chosen to be the input parameter for network. But the output data is  $\alpha_N$ , because the parameter  $\alpha_N$  can present damage degree as expression (8) above. So a network can be set up by using data couple:  $\beta_i$  and  $\alpha_N$ . After trained, the network can forecast the damaged extent of the unit. The examine output is given out as following:

Table 5. Result of test on damaged extent by network using parameter

Inspected sample	Unit 3 of beam1	Unit 2 of beam2	Unit 6 of beam2
Anticipant output	0.4000	0.4000	0.5000
Actual output	0.4235	0.3892	0.5211
Relative error(%)	5.88	2.70	4.22

Conclusion can be drawn from the above diagram that the specific damage position and damage extent of structure even to element can be imitated effectively. Perfect result can be gotten in the network with less samples. And it can be said that perfect effect can be gotten if the network is used to identify the symmetry structure about its damaged part.

## 5 Conclusions

1. The difficulties caused by reverse-analysis about its un-posed character can be overcome effectively by the method of ANN. The difficulties of solution caused by parameter choice can be overcome by ANN.
2. The limitation of BP network that it's calculate speed is slow and only the local minimum is gotten can be overcome by RBF network. And it can be used to diagnose the defect of structure effectively. The
3. Choice of parameter plays an important role. The essential parameters that imply quantity of message and can represent the structure to checking should be adopted during training.
4. The structure damnification diagnose has clear physical meanings. Take the discontinuity of concrete structure, better modulus parameter can be chosen as input parameter according to different structure of its dynamic characteristic

## Acknowledgements

The authors would like to thank Hubei Provincial Education Departments (Q200830002) for research funding support. The authors would also like to thank Huangshi Institute of Technology (07yjz03R) for research funding.

## References

- Cheng T., Wang J.T., Yan K.Q. (2008). Coupling analysis method for elastoplastic consolidation of clay considering stress paths. *Chinese Journal of Rock Mechanics and Engineering*, 27(2): 403-409.
- Clough R., Penzien J. (2006). *Structure Dynamics*, Higher Education Press.
- Jeyasehar C.A., Sumangalaa K. (2006). Damage assessment of prestressed concrete beams using artificial neural network (ANN) approach. *Computers & Structures*, 84(26): 1709-1718.
- Li G.Q., Li J. (2002). *Theory and Application of Structure Dynamical Investigation*, Science Press.
- Lu D.G., Wang G.Y. (1999). Structural intelligent optimum design – A new research direction. *J. of Harbin Univ. of Civil Eng. and Arch.*, 32(4): 7-12.
- Peng Z.K., Lang Z.Q., Chu F.L. (2008). Numerical analysis of cracked beams using nonlinear output frequency response functions. *Computers & Structures*, 86(18): 1809-1818.
- Saluwu (1997). Detection of Structural damage through in frequency: A review, *Engineering Structures*, 19(9): 718-723
- Wu X., Ghaboussi J., Garrett J.H. (1992). Use of neural networks in detection of structural damage, *Computers & Structures*, 42(4): 649–659.

*“This page left intentionally blank.”*

# Study on Curvature Modal Shapes of the Damage Reinforced Concrete Beams

Gang Xue<sup>1\*</sup>, Xiaoyan Guo<sup>1</sup> and Zhenhua Dong<sup>1</sup>

<sup>1</sup>Department of Architecture and Civil Engineering, Inner Mongolia University of Science and Technology, Baotou 014010, P.R. China

**Abstract.** The basic principle of curvature modal is discussed, and a mathematical comparison between the vibration mode relative variable quantity and the modal curvature is given. Dynamic test is carried on 9 pieces of RC beams, in which the beam is subjected to an increasing static load in the middle to introduce cracks. After each load step, unloading, and an experimental dynamic monitoring is performed on the beam. Test data is analyzed by means of the system of Data Acquisition Signal Process, and the displacement modal is obtained. The curvature modal is gained from the displacement modal with second order differentiation method. The results show that curvature modal can identify the damage of RC simple-supported beam more accurately, and it is more sensitive to tiny damage. Based on the concept of function total differential, the error transmission formulas from vibration mode to the curvature mode are derived.

**Keywords:** curvature modal, damage detection, RC beams, error transmission

## 1. Introduction

With the development of society, people pay more attention to the safety, durability and normal usage function of the engineering structures. Structural Health Monitoring becomes focus problems for many researchers. In the recent years, some scholars studied the damage detection methods with the curvature mode difference. At present, the research on dynamic inspection by curvature modal has obtained phase achievements. Pandey et al. (1991) compute the influence degree of the local damage to the different orders of curvature modal, and it is shown that Curvature modal is sensitive to local damage. Curvature modal can be used to detection not only damage positions but also damage degrees. Deng Yan (Deng and Yan, 2000; Deng, 2000) compared the simulation results of Reinforced Concrete T-Beams under damage and no damage situations. It is difficult to detect

---

\* Corresponding author, e-mail: xuegang-2008@126.com

some tiny damages with displacement mode, while the same damage can be detected by the change of the modal curvature. Li et al. (2002) illustrated the orthogonality and superposition of the modal curvature, and pointed out the curvature is more sensitive to local damage. Abdel and Roeck (1999) applied the curvature to the damage monitoring of the practical engineering. The curvature modal can be obtained only depending on present modal information, which is convenience for the engineering application. Many researchers (Chang, 2002; Zhao and Lu, 2002; Dutta and Talukdar, 2004; Juan, 2005) studied the question mainly by finite element analysis with computers. In this thesis, damage inspections are carried on nine pieces of simple supported RC beams by means of modal curvatures, and the transmission error is studied, which is generated by second order differentiation calculation.

## 2 Basic Fundamentals of the Modal Curvature

Simulation results (Chang, 2002; Zhao and Lu, 2002; Dutta and Talukdar, 2004; Juan, 2005) all demonstrated that modal curvature can be used to detect damages more easily than vibration mode difference. The Research Results can be explained in a mathematical point of view. In accordance with Taylor's median value Theorem, it is known that if function  $y = f(x)$  have  $(n+1)$  orders of derivatives on interval of  $(a,b)$  which includes  $x_0$ , for given an arbitrary  $x \in (a,b)$ , then:

$$f(x) = f(x_0) + f'(x_0)(x - x_0) + \frac{f''(x_0)}{2!}(x - x_0)^2 + \dots + \frac{f^{(n)}(x_0)}{n!}(x - x_0)^n + R_n(x) \tag{1}$$

If  $n = 2$ ,

$$f(x) = f(x_0) + f'(x_0)(x - x_0) + \frac{f''(x_0)}{2!}(x - x_0)^2 + o(x - x_0)^3 \tag{2}$$

Only take the second differential terms,  $f''(x_0)$  can be expressed as:

$$f''(x_0) \approx \frac{2[f(x) - f(x_0)]}{(x - x_0)^2} \tag{3}$$

From Equation (3), we know that, if one function has a mini increment about certain point, its second differentials will be far more greater than function increment, that is  $f''(x_0) \gg f(x) - f(x_0)$ . We can take the  $f(x) - f(x_0)$  as mode incre-

ment function, and take  $f''(x_0)$  as modal curvature, and absolute value of modal curvature is greater than that of the vibration mode relative change rate.

### 3 Experimental Study on Modal Curvature

In the test, beam is subjected to an increasing static load in the middle to introduce cracks, the last loadstep corresponds to failure. Test procedures for each loadstep are as follows: (1) Sustained loading for 2-3 min, and then check the bar strain of the particular section with static strain checking systems(DH3816), checking crack position, width and the height; (2) Unloading to 0; (3) Arrange compression beam upper side of the beam support to make simply-supporting conditions and restrict vertical displacements; (4) Carrying on the dynamic test of the beam; (5) Remove compression beam upper side of the beam support and reloading. Dynamic signal is picked and processed by DASP system, which is composed of signal-collector, signal-amplifier and signal-processor. In the dynamic test, one accelerometer is placed about 0.6m from one support, the excitation is done by impacting the beam with an instrumented hammer DFC-2, which hardness of the tip is chosen in order to generate a reasonable spectrum in the frequency range of interest. By modal analysis, the more precise vibration modes are obtained. Using the center differential principle, the curvature mode of the beam can be obtained from the vibration mode.

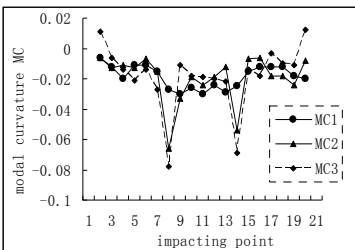


Figure 1. The first order modal curvature of beam 6

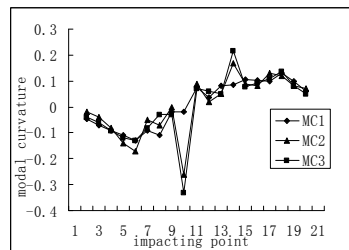


Figure 2. The second order modal curvature of beam 6

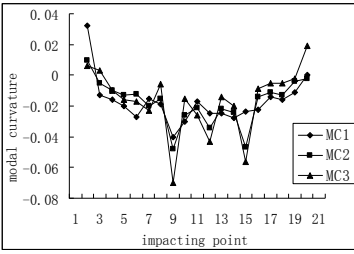


Figure 3. The first order modal curvature of beam 7

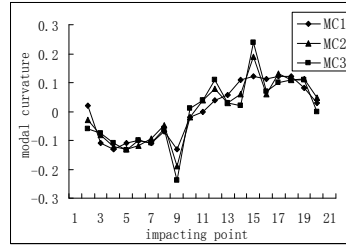


Figure 4. The second order modal curvature of beam 7

Modal curve is relative smooth for the initial stage, demonstrating no abrupt change points. With the development of beam damages, the cusp index displayed on the curvature mode increases constantly. Under successive loading, three main cracks appear on the bottom of beam 7, which locate in the measuring point 9, 12 and 15 respectively. Figure 1 to Figure 2 are the first two orders modal curvature graphs of two test elements, cuspidal point can be observed at cracking positions. The cusp index displayed on the second-order curvature mode is bigger than the one on the first-order curvature mode, so it is easier to identify the structural damages.

According to experiment studies (Xue, 2009), some tiny damages can not be found by means of the vibration mode relative change rate, but being marked on the curvature mode graph. The curvature mode includes damage information more completely, and can effectively avoid the careless judges and misjudge in the damage identifications. As for 2m span simple supported beam with 10 impacting points, if two damage's position is to be close, the modal curvature variation characteristics of small damages can be covered up by the one of big damages. When the number of impacting points increase to 20, identification precision are then improved effectively, and multi-position damages can be identified.

More numbers of the impacting point's numbers are not always necessary. The more the number of impacting points is, the greater the data collect quantity become, and analysis time will last longer. As for single damage, identification can be done with less number of impacting points. Setting for 10 impacting points on the 2m span beam, the precision of the first three order modal curvatures is guaranteed, and single damage can be recognised accurately. Multi-position damages can be identified by increasing the measuring point numbers properly. Spacing of two adjacent impacting point is 1/20 to 1/15 of beam span, damage localization can be determined. In practical application, non-equidistance can be used between measuring points according to actual condition, that is, in damageable areas, the number of measuring points is increased properly, while in other areas, measuring points number can be decreased appropriately.

## 4 The Error Transmission Analysis

Curvature mode is sensitive to damages. At present, sensors which can be used to obtain curvature directly are not invented yet. Curvature is second derivative of the displacement. Using the central differential principle, the curvature mode of the beam can be obtained from the vibration mode. There are transmission error between displacement mode and curvature mode.

In order to represent function standard deviation with measured values standard deviation, measurements with equal precision are done for  $n$  times:

$$y_i = f(x_{1i}, x_{2i}, \dots, x_{mi}) \quad (i = 1, 2, \dots, n) \quad (4)$$

According to whole differential definition and the sufficient condition of whole differential existence, each measurement error is:

$$\delta y_i = \frac{\partial f}{\partial x_1} \delta x_{1i} + \frac{\partial f}{\partial x_2} \delta x_{2i} + \dots + \frac{\partial f}{\partial x_m} \delta x_{mi} \quad (i = 1, 2, \dots, n) \quad (5)$$

Each formula in Equation Group (5) is squared:

$$\delta y_i^2 = \left(\frac{\partial f}{\partial x_1}\right)^2 \delta x_{1i}^2 + \left(\frac{\partial f}{\partial x_2}\right)^2 \delta x_{2i}^2 + \dots + \left(\frac{\partial f}{\partial x_m}\right)^2 \delta x_{mi}^2 + 2 \sum_{1 \leq p \leq q} \frac{\partial f}{\partial x_p} \frac{\partial f}{\partial x_q} \delta x_{pi} \delta x_{qi} \quad (i = 1, 2, \dots, n) \quad (6)$$

Superpose every Equation in (6) and collation:

$$\sigma_y^2 = \left(\frac{\partial f}{\partial x_1}\right)^2 \sigma_{x_1}^2 + \left(\frac{\partial f}{\partial x_2}\right)^2 \sigma_{x_2}^2 + \dots + \left(\frac{\partial f}{\partial x_m}\right)^2 \sigma_{x_m}^2 + 2 \sum_{1 \leq i \leq j} \left[ \frac{\partial f}{\partial x_i} \frac{\partial f}{\partial x_j} \frac{\sum_{m=1}^n \delta x_{im} \delta x_{jm}}{n} \right] \quad (7)$$

given  $K_{ij} = \frac{\sum_{m=1}^n \delta x_{im} \delta x_{jm}}{N}$ ,  $\rho_{ij} = \frac{K_{ij}}{\sigma_{x_i} \sigma_{x_j}}$ , Equation (7) is as follows:

$$\sigma_y^2 = \left(\frac{\partial f}{\partial x_1}\right)^2 \sigma_{x_1}^2 + \left(\frac{\partial f}{\partial x_2}\right)^2 \sigma_{x_2}^2 + \dots + \left(\frac{\partial f}{\partial x_n}\right)^2 \sigma_{x_n}^2 + 2 \sum_{1 \leq i \leq j} \left[ \frac{\partial f}{\partial x_i} \frac{\partial f}{\partial x_j} \rho_{ij} \sigma_{x_i} \sigma_{x_j} \right] \quad (8)$$

where  $\rho_{ij}$  is correlation coefficient between the  $i$ th measurement and the  $j$ th measurement. Since  $x_1, x_2, \dots, x_m$  are mutually independent, its correlation moment is 0, that  $\rho_{ij} = 0$ . Equation (8) can be simplified as:

$$\sigma_y^2 = \sum_{i=1}^n \left(\frac{\partial f}{\partial x_i}\right)^2 \sigma_{x_i}^2 \tag{9}$$

According to Equation (9), we can compute function standard deviation with measured values standard deviation. Equation (9) is random error formula, and  $\partial f / \partial x_i$  ( $i = 1, 2, \dots, n$ ) is error transmission coefficient of the measurements.

Given that the mode error between measuring value and true value is  $\pm \Delta y_{i-1}$ ,  $\pm \Delta y_i$ ,  $\pm \Delta y_{i+1}$ , and the error has a bit of randomness and some probability distribution. Based on the formula (9), the curvature function error is:

$$\Delta v_j(i) = \Delta(y_j''(i)) = \pm \sqrt{\sum_{i=i-1}^{i+1} \left(\frac{\partial y}{\partial x_i} \cdot \Delta y_j(i)\right)^2} \tag{10}$$

According to the differential relationship between curvature and mode, the upper equation is expressed by:

$$\begin{aligned} \Delta v_j(i) &= \pm \sqrt{\left(\frac{\Delta y_j(i+1)}{\Delta l^2}\right)^2 + \left(-\frac{2\Delta y_j(i)}{\Delta l^2}\right)^2 + \left(\frac{\Delta y_j(i-1)}{\Delta l^2}\right)^2} \\ &= \pm \frac{1}{(\Delta l)^2} \sqrt{(\Delta y_j(i+1))^2 + 4(\Delta y_j(i))^2 + (\Delta y_j(i-1))^2} \end{aligned} \tag{11}$$

### 5 Conclusions

1. As for the same damage, the cusp index on curvature graph is several times as the one on mode graph, and so curvature is easier to detect damages, recognizing the tiny damage.
2. Compared with other damage marking quantities, modal curvature has the advantage of demanding incomplete initial reference, and can be used to detect damages by real time information.
3. Modal curvature can be used to identify multi-position damages. Multi-position damages identification can be carried out by increasing the measuring point

- number properly. Spacing of two adjacent impacting point is 1/20 to 1/15 of beam span, damage localization can be determined.
4. From displacement to curvature is a process of differentiation, and the error in displacement is consequently enlarged. According to whole differential fundamentals, the transmission error formulation of modal curvature is derived.
  5. High order modal is relatively more sensitive to damage than low order modal. Under equal loading, the impacted energy of high order amplitude is far lower than that of the low order amplitudes (inversely proportional to the square of the circular frequency  $\omega$ ). Low amplitudes may result in bad signal noise ratio, and the error is thereupon increased. Damage detection of practical engineering should be proceeded with low order modal.

## References

- Abdel W.M.M. and Roeck G. (1999). Damage detection in bridges using modal curvatures application to a real damage scenario. *Journal of Sound and Vibration*, 226(2): 217-235.
- Chang J. (2002). Methods and research of structural damage location by curvature mode. Kunming: Kunming University of Science and Technology [in Chinese].
- Deng Y. (2000). Dynamical testing techniques and system for bridges. Beijing: Tsinghua University [in Chinese].
- Dutta S. and Talukdar (2004). Damage detection in bridges using accurate modal parameters. *Finite Elements in Analysis and Design*, 40: 287-304.
- Deng Y. and Yan P.C. (2000). New approach for strain modal measurement and damage detection of bridges. *Tsinghua Univ (Sic & Tech)*, 40(11): 123-127 [in Chinese].
- Juan C.H.S. (2005). Evaluation of structural damage identification methods based on dynamic characteristics. Civil Engineering University of Puerto Rico Mayaguez.
- Li D.B., Lu Q.H., and Qin Q. (2002). Curvature modal analysis for bending structures. *Tsinghua Univ (Sic & Tech)*, 42(2): 224-227 [in Chinese].
- Pancley A.K., Biswas M., and Samman M.M. (1991). Damage detection from changes in curvature mode shapes, *Sound and Vibration*, 145(2): 321-332.
- Xue G. (2009). Study on dynamic inspections and damage involvement regulations of the reinforced concrete beams. Beijing: University of Science and Technology [in Chinese].
- Zhao Y. and Lu Q.H. (2002). Multiple damage detection of simply supported beam bridges. *Tsinghua Univ (Sic & Tech)*, 42(4): 434-438 [in Chinese].

*“This page left intentionally blank.”*

# Direct Index Method of Damage Degree Identification Based on Local Strain Mode Shape Area of Damage Structure

Peiying Gu<sup>1,2\*</sup>, Chang Deng<sup>1,2</sup> and Fusheng Wu<sup>1,2</sup>

<sup>1</sup>Nanjing Hydraulic Research Institute, Nanjing 210029, P.R. China

<sup>2</sup>Key laboratory of Water Science and Engineering, Ministry of Water Resources, Nanjing 210029, P.R. China

**Abstract.** The vibrotechnique may be applied to damage identification in civil engineering, but there are some technical problems. The identification precision of displacement mode shape is low; however it of strain mode shape is high. Although the present methods of strain modal parameters can be applied to detect damage location, only very few can rough detect damage degree. Furthermore, the precondition of the methods is that the modal parameters of original structure and damage structure must be obtained. It is very difficult for the original structure. Therefore, the direct index method of damage degree identification (the abbreviation is  $I_{LSMSA}$ ) is advanced in the paper. It is based on local strain mode shape area of the damage structure. The strain modal parameters of original structure needn't be provided. The polynomial is applied to fit strain mode shape of the original structure. The mathematics models of optimization polynomial degree and  $I_{LSMSA}$  are founded. According to theoretical derivation and statistical analysis of numerical simulations, the four characteristics of  $I_{LSMSA}$  are obtained. First,  $I_{LSMSA}$  presents monotone increasing tendency with increasing damage degree. Secondly, it is independent of damage location. Thirdly, it is independent of the order of strain mode shape. Fourth, it is independent of normalization.

**Keywords:** vibration, strain mode shape of damage structure, damage identification, local strain mode shape area, direct index method

## 1 Introduction

The present index methods can be applied to damage identification in civil engineering, but the precondition of them is that the modal parameters of original

---

\* Corresponding author, e-mail: pygu@nhri.cn

structure and damage structure must be obtained. The modal parameters may be obtained through finite element analysis and modal test. According the variation of the modal parameters, the location and degree of the damage can be detected. The most of index methods are based on modal parameters of displacement mode shape (DMS). They include coordinate modal assurance criterion of displacement, modal curvature, modal flexibility and modal strain energy.

The damage index methods based on displacement mode shape are insensitive to damage, but ones of strain mode shape (SMS) are very sensitive to it. Therefore, the indexes of SMS are superior to ones of DMS for damage identification. In recent years, five damage index methods based on SMS were advanced. They are absolute variation index of SMS, relative variation index of SMS, change rate index of SMS difference, coordinate modal assurance criterion of strain and generalized strain energy density.

According to absolute value of SMS difference between original structure and damage structure, the principle of comparing magnitude is followed for absolute variation index of SMS. The method was applied to detect the bridge damage by Deng. Zhou attempted to detect the damage location of reinforced concrete structure with relative variation index of SMS. There is an abrupt change about change rate index of SMS difference at the damage location. The method was applied to detect the damage of head conduit by Ren. Coordinate modal assurance criterion of strain is based on correlation theory. Because SMS is sensitive to local damage, modified coordinate modal assurance criterion of strain was advanced by Dong. Liu advanced the method of generalized strain energy density to detect damage location. If test data is adequate, damage degree can be approximately detected with the method.

Although the damage index methods of strain are sensitive to damage, most of them can only detect damage location. Furthermore, the precondition of the methods is that the modal parameters of original structure and damage structure must be obtained. Because of some factors, such as design data deficiency, construction discreteness and material deterioration, it is very difficult to obtain the modal parameters of original structure. Therefore, it is difficult to apply the methods to detect engineering damage. In the paper, the direct index method of damage degree identification (the abbreviation is  $I_{LSMSA}$ ) is advanced. It is based on local strain mode shape area (LSMSA) of the damage structure. The strain modal parameters of original structure needn't be provided. The method is suitable for the field of offshore platform, machine, bridge and construction.

## 2 SMS Fitting Method in Undamaged State

### 2.1 Least Square Method of Fitting Curve

There is abrupt variation at the damage location in SMS curve, but SMS curve vary slightly away from the damage location. Applying SMS data of the unaffected region by damage, SMS curve is fitted in undamaged state. At present, least square method is main method of fitting curve. There are three procedures for fitting SMS curve. First, the damage location is detected based on direct index method of SMS difference. Second, the scope of affected zone by damage is determined. It is formed by three lines around the symmetric center of the damage location. Third, SMS curve is fitted in undamaged state.

The key of least square method is to found and solve normal equations set. It depends on the choice of primary function  $\phi_k$ . Elementary function, spline function and Bezier function can be as primary function. According to preliminary analysis, polynomial is suited to fit SMS curves in undamaged state. At least in small zone, polynomial can arbitrarily approach any continuous function. The advantages of polynomial are that the expression is simple and computing speed is fast. The primary function of polynomial is showed as follows:

$$\{\phi_0, \phi_1, \phi_2, \dots, \phi_m\} = \{1, x, x^2, \dots, x^m\}$$

Polynomial is showed as:

$$s^*(x) = a_0^* + a_1^*x + a_2^*x^2 + \dots + a_m^*x^m = \sum_{k=0}^m a_k^*x^k$$

Where  $(a_0^*, a_1^*, \dots, a_m^*)$  is a coefficient set of least error;  $m$  is degree of polynomial;  $x$  is argument symbol.

The normal equation set is showed as Equation (1).

$$\begin{bmatrix} \sum \rho_i & \sum \rho_i x_i & \dots & \sum \rho_i x_i^m \\ \sum \rho_i x_i & \sum \rho_i x_i^2 & \dots & \sum \rho_i x_i^{m+1} \\ \vdots & \vdots & \ddots & \vdots \\ \sum \rho_i x_i^m & \sum \rho_i x_i^{m+1} & \dots & \sum \rho_i x_i^{2m} \end{bmatrix} \begin{bmatrix} a_0 \\ a_1 \\ \vdots \\ a_m \end{bmatrix} = \begin{bmatrix} \sum \rho_i y_i \\ \sum \rho_i x_i y_i \\ \vdots \\ \sum \rho_i x_i^m y_i \end{bmatrix} \tag{1}$$

Where  $\rho_i$  is weight function,  $\rho_i = \rho(x_i)$  ( $i=1, 2, \dots, n$ );  $n$  is total number of data,  $n>m$ ;  $\sum$  is the abbreviation of  $\sum_{i=1}^n$ ;  $x_i$  is argument value of node  $i$ ;  $y_i$  is dependent variable value of it, usually by testing or computing.

Equation (1) is ill-conditioned system when  $m \geq 7$ , so  $m$  is not suitable to choose great value.

### 2.2 Fitting SMS Curve in Undamaged State

Taking two simple beams with the damage in middle span and quarter span respectively as examples, the size of beams is 75mm×150mm×2100mm. Dynamical modulus of elasticity, density and Poisson’s ratio are 1495MPa、1154kg/m<sup>3</sup>、0.2 respectively. Damage degree of the beam with middle span damage is 5%~35% of effective sectional height, and it of another beam is 5%~50%. The numerical simulation results of SMS were detailed in reference. The degree of polynomial between 3 and 6 is discussed, where  $\rho(x_i) = 1$ . Comparing curve shape and coefficient of determination  $R^2$  respectively, optimization degree of polynomial is founded.  $R^2$  shows the consistency of trial or calculated value with fitted value.

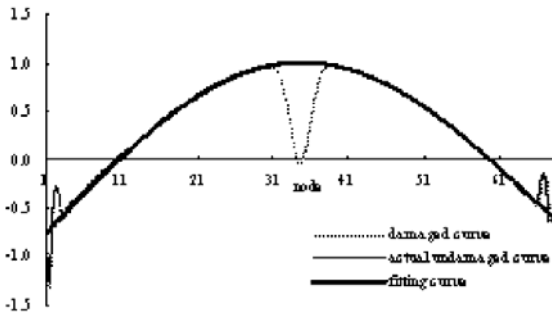
The expression of  $R^2$  is showed as follows:

$$R^2 = 1 - \frac{\sum_{i=1}^n (y_i - \hat{y}_i)^2}{\sum_{i=1}^n (y_i - \bar{y})^2} \tag{2}$$

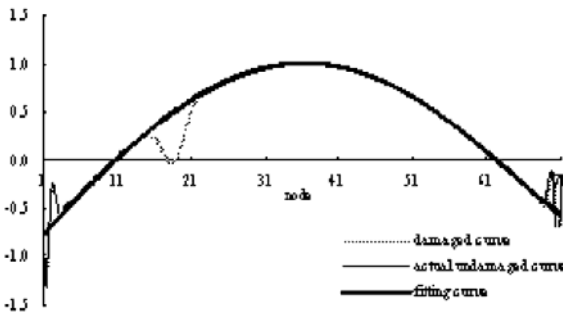
Where  $\hat{y}_i$  is the fitted value of it;  $\bar{y}$  is the average value of  $y_i$  or  $\hat{y}_i$ .

The range of  $R^2$  is 0~1. When  $R^2$  is equal or approaches to 1, reliability of fitting is good.

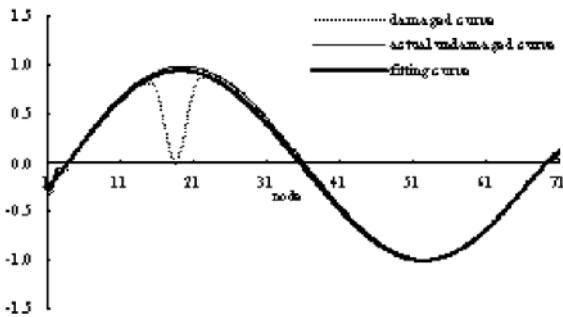
Figure 1 shows the comparison of three type SMS curves, including fitting SMS curve in undamaged state based on the data of unaffected region (fitting curve for short), actual numerical simulation SMS curve in undamaged state (actual undamaged curve for short) and SMS curve in damaged state (damaged curve for short), where normalization method of maximum is applied except supports. The results show mean value of  $R^2$  is equal to 0.9774. It approaches to 1, so fitting SMS curve is fine. Relationships between determinative coefficient and degree of polynomial are shown in Figure 2.



(a) The first-order SMS with middle span damage



(b) The first-order SMS with quarter span damage



(c) The second-order SMS with quarter span damage

Figure 1. Comparison of three type SMS curves, including fitting curve, actual undamaged curve

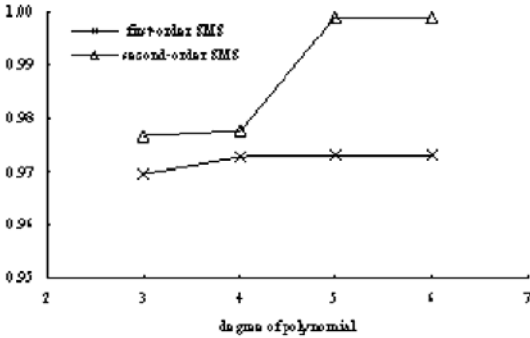


Figure 2. Relationships between determinative coefficient and degree of polynomial

For the first-order SMS, when the degree of polynomial is equal to 4,  $R^2$  approaches stable stage. Therefore fourth polynomial is applied to fitting the first-order SMS curve in undamaged state. The mean value of  $R^2$  is equal to 0.9727. According to Figures 1(a) and (b), fitting SMS curve is consistent with numerical simulation SMS curve in undamaged state and SMS curve in damaged state beyond affected region by damage except supports.

For the second-order SMS, though determinative coefficient is greater than that of the first-order SMS, the deviation between fitting SMS curve and numerical simulation SMS curve is greater when the degree of polynomial is low. When the degree of polynomial is equal to 5,  $R^2$  approaches stable stage. The mean value of  $R^2$  is equal to 0.9990, almost 1. Therefore fifth polynomial is applied to fitting the second-order SMS curve in undamaged state. According to Figure 1(c), fitting SMS curve is consistent with damaged state SMS curve beyond affected region, except the slight deviation between it and numerical simulation SMS curve in undamaged state.

### 3 Damage Degree Identification of Local Strain Mode Shape Area

According to Figure 1, and the relationships between damage degree and SMS curve, three conclusions are given. First, affected region of damage enlarges along with increase of damage degree. Second, the area surrounded by fitting SMS curve in undamaged state and damaged state SMS curve is defined SMS damage area. When damage degree is not more than 25%, the SMS damage area enlarges along with increase of damage degree. When damage degree is more than 25%, the change of SMS damage area is slight if increasing damage degree. Third, SMS damage area is related with damage location even if damage degree keeps con-

stant. Therefore, three factors must be considered. They are affected region of damage, SMS damage area and damage location.

The direct index of damage degree identification must be monotone function of damage degree. According to the results about SMS damage area where mentioned above, it is not suitable to be the direct index of damage degree identification. The expression of the direct index should be simple and easy to apply. It is best to be independent of damage location. Now, the reason which SMS damage area is dependent of damage location would be explained as follows. First, it is apparent that SMS is the function of damage location. Although the change of fitting SMS curve based on the data of unaffected region is slight for different damage location, the change of SMS curve in damaged state is great. Therefore, SMS damage area of different damage location is unequal. The area surrounded by fitting SMS curve around affected region and horizontal axis is defined SMS undamaged area. The SMS undamaged area is smaller, the SMS damage area is smaller for same damage degree. Therefore, the SMS undamaged area can reflect the factor of damage location.

If the ratio of SMS damage area to SMS undamaged area is defined direct index of damage degree identification based on local strain mode shape area, the expression is  $I_{LSMSA}$ . There is good relationship between  $I_{LSMSA}$  and damage degree. The area surrounded by SMS curve in damaged state around affected region and horizontal axis is defined SMS residual area. SMS undamaged area is equal the sum of SMS damage area and SMS residual area.

Then, some symbols are explained as follows. The meaning of  $\Phi_r^\epsilon(x)$  is r-order SMS function. The meanings of  $\Phi_r^{\epsilon u}(x)$  and  $\Phi_r^{\epsilon d}(x)$  are r-order SMS function in undamaged state and in damaged state respectively. The meaning of  $[x_1, x_2]$  is affected region of damage. There are formulas like these:

$$A_r^{\epsilon u} = \int_{x_1}^{x_2} \Phi_r^{\epsilon u}(x) dx, \quad A_r^{\epsilon d} = \int_{x_1}^{x_2} \Phi_r^{\epsilon d}(x) dx$$

Where  $A_r^{\epsilon u}$  and  $A_r^{\epsilon d}$  are SMS undamaged area and SMS residual area of r-order, respectively.

Assume the symbol of  $\Delta A_r^\epsilon$  is r-order SMS damage area. The expression of  $I_{rLSMSA}$  is showed as:

$$I_{rLSMSA} = \frac{\Delta A_r^\epsilon}{A_r^{\epsilon u}} = \frac{A_r^{\epsilon u} - A_r^{\epsilon d}}{A_r^{\epsilon u}} = 1 - \frac{A_r^{\epsilon d}}{A_r^{\epsilon u}} = 1 - \frac{\int_{x_1}^{x_2} \Phi_r^{\epsilon d}(x) dx}{\int_{x_1}^{x_2} \Phi_r^{\epsilon u}(x) dx} \tag{3}$$

Where  $I_{rLSMSA}$  is r-order direct index of damage degree identification based on local strain mode shape area.

The formula (3) shows that direct index  $I_{LSMSA}$  is equal to the ratio of SMS damage area to SMS undamaged area, or one minus the ratio of SMS residual area to SMS undamaged area.

### 4 Computing Example

Taking the beams of middle span damage and quarter span damage for instance, the results of direct index  $I_{LSMSA}$  are shown in Table 1.

According to the results of Table 1, direct index  $I_{LSMSA}$  shows a tendency to increase along with increase of damage degree, but the tendency of increase slows along with it. For the first-order SMS of middle span damage beam and the first two orders SMS of quarter span damage beam, the values of  $I_{LSMSA}$  change slightly under same damage degree. The average error of  $I_{LSMSA}$  is 4.2%. The maximal error is 7.6%. The four characteristics of  $I_{LSMSA}$  are obtained. First,  $I_{LSMSA}$  presents monotone increasing tendency with increasing damage degree. Secondly, it is independent of damage location. Thirdly, it is independent of the order of strain mode shape. Fourth, it is independent of normalization. Therefore, the method which local strain mode shape area is applied to damage identification is simple and effective.

Table 1. Results of direct index  $I_{LSMSA}$

Category	Damage degree									
	5%	10%	15%	20%	25%	30%	35%	40%	45%	50%
first-order direct index $I_{1LSMSA}$ of middle span damage beam	0.1835	0.2789	0.3439	0.3791	0.4055	0.4236	0.4409			
first-order direct index $I_{1LSMSA}$ of quarter span damage beam	0.2120	0.3146	0.3834	0.4158	0.4503	0.4771	0.4945	0.5122	0.5267	0.5437
second-order direct index $I_{2LSMSA}$ of quarter span damage beam	0.2002	0.2958	0.3693	0.4135	0.4381	0.4589	0.4744	0.4879	0.4927	0.4911
average $I_{LSMSA}$	0.1986	0.2964	0.3655	0.4028	0.4313	0.4532	0.4699	0.5000	0.5097	0.5174

According to the average values of direct index  $I_{LSMSA}$ , fourth polynomial is applied to fitting the relationship between direct index  $I_{LSMSA}$  and damage degree. The fitting curve of it is shown in Figure 3. It shows the actual average values distributing around the fitting curve.  $R^2$  is equal to 0.9960, almost 1. Therefore reliability of fitting is good.

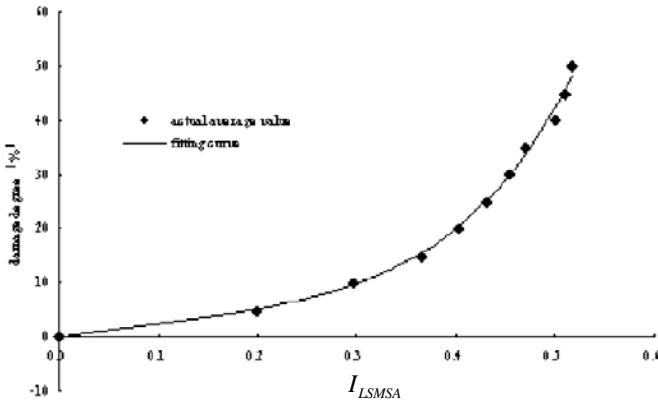


Figure 3. Fitting curve of relationship between direct index  $I_{LSMSA}$  and damage degree

## 5 Conclusions

Conclusions are summarized as follows:

1. The direct index method  $I_{LSMSA}$  of damage degree identification is advanced in the paper. It can be applied to identify damage degree only based on local strain mode shape area of the damage structure. The strain modal parameters of original structure needn't be provided.
2. Applying SMS data of the unaffected region by damage, SMS curve in undamaged state is fitted by least square method. The mathematics models of optimization polynomial degree are founded. The degree of polynomial is equal to 4 and 5 for the first-order and second-order SMS, respectively. Coefficient of determination  $R^2$  is equal or approaches to 1, reliability of fitting is good.
3. According to the results of simple beams with the damage in middle span and quarter span respectively, direct index  $I_{LSMSA}$  shows a tendency to increase along with increase of damage degree, but the tendency of increase slows along

with it. The relationship between direct index  $I_{LSMSA}$  and damage degree is shown. Based on statistical analysis of numerical simulations, the four characteristics of  $I_{LSMSA}$  are obtained. First,  $I_{LSMSA}$  presents monotone increasing tendency with increasing damage degree. Secondly, it is independent of damage location. Thirdly, it is independent of the order of strain mode shape. Fourth, it is independent of normalization. Therefore, the method which local strain mode shape area is applied to damage identification is simple and effective.

## References

- Deng Yan, Yan Puqiang (2000). New approach for strain modal measurement and damage detection of bridges. *J Tsinghua Univ (Sci & Tech)*, 40(11), 123–127 [in Chinese].
- Dong Cong, Ding Hui, Gao Song (1999). The basic principle and method for recognition and location of structural damage. *China Railway Science*, 20(3), 89–94 [in Chinese].
- Gu Peiyong, Chen Houqun et al. (2005). Application of strain mode in diagnosing damage to beam. *Earthquake Engineering and Engineering Vibration*, 25(4), 50–53 [in Chinese].
- Gu Peiyong, Chen Houqun et al. (2006). Direct index method of damage location detection based on difference theory of strain mode shapes. *Journal of Vibration and Shock*, 25(4), 13–17 [in Chinese].
- Gu Peiyong, Ding Weinong (2004). Application of modal test in diagnosing damage of beam. *Journal of Vibration and Shock*, 23(3), 60–63.
- Liu Wenfeng, Liu Chuntu (2003). Numerical research of identify structural damage by generalized strain energy density. *Journal of Mechanical Strength*, 25(2), 159–162 [in Chinese].
- Ren Quan, Li hongsheng, Guo Xinglin (2001). Undamaged detection of pipe based on modal varied quotiety of strain. *Journal of Dalian University of Technology*, 41(6), 648–652 [in Chinese].
- Zhou Xianyan, Shen Pusheng (1997). Study of damage assessment of concrete structures by strain model method. *Journal of Hunan University*, 24(5), 69–74 [in Chinese].

# Improved Genetic Algorithm for Structural Damage Detection

Jose E. Laier<sup>1\*</sup> and Jesus D.V. Morales<sup>1</sup>

Department of Structural Engineering, Engineering School of São Carlos, University of São Paulo, 13566-590 São Carlos, Brazil

**Abstract.** Structural damage detection consists of determining the location and severity of damage in civil structures by using measured parameters. Genetic algorithm is a meta-heuristic computing method for finding approximated global minimums in large optimization problems and has the advantage of probabilistic hill climbing. In this work the improved genetic algorithm is employed to solve damage detection problem in truss type structures using vibration data (natural frequencies and mode shapes). The formulation of the objective function for the optimization procedure is based on natural frequency and vibration mode shapes. Present structural damage-identification scheme is confirmed and assessed using a Finite Element Model formulation (FEM) of truss structure. Results are presented in tables.

**Keywords:** genetic algorithm, vibration parameters, damage detection

## 1 Introduction

As already well established, the methods for structural assessment from dynamic responses can be classified in two groups in accordance with its dependence on a structural model: the methods based on signals (experimental method) is the first one and the second are the methods based on finite element models (Zou et al., 2000).

Novelty Detection (Worden et al., 2002) is a typical signal based method, whose principal objective is to extract features from dynamic data that characterize the state of the structure. This technique permits only to detect the damage in the lowest level that is to decide whether the damage occurred. The other methods based signals as Eddy's currents technique, acoustic emission, X rays, ultrasonic methods, thermal and magnetic field methods and visual inspection (Goch et al., 1999) need an a priori knowledge of damage's location and that the access to any

---

\* Corresponding author, e-mail: jelaier@sc.usp.br

part of the structure be available. More than these limitations, these methods can only permit to detect damage near the structure's surface and work relatively well in small size structures. The advantages of these methods are that they avoid modelling errors and time consuming computational calculations. However, these methods are inefficient when applied to large structural systems, for which the techniques based in the structure's dynamic response are promising due its global character.

In this paper, an improved genetic optimization algorithm using real code version is developed to solve structural damage detection problems; that is, determining the location and severity of damage by using dynamic measured characteristics (natural frequencies and corresponding mode shapes). The formulation of the objective function for the optimization is based on the natural frequencies and mode shapes obtained by using a classical Finite Element Model of truss structures. In order to study the structural damage detection the damage is considered by a reduction in stiffness at the damaged location on the structure.

## 2 Theoretical Backgrounds

When a damage event has occurred in the structure, the stiffness matrix will change and consequently, the natural frequencies and mode shapes will change. Assuming that the mass and damping matrices are constant (not affected by the damage) the stiffness of the  $k^{\text{th}}$  damaged element is given by:

$$[K]_k^d = \alpha_k [K]_k \quad (1)$$

in which  $0 \leq \alpha_k \leq 1$  is a damage variable: the value of unity indicates that the element is undamaged whereas a damage element would cause the stiffness reduction factor for that location to take on a fractional value (decrease in modulus of elasticity) or zero, and constitutes the design variables of our problem;  $d$  as exponent indicates damaged element. Notation  $[K]_k$  indicates the stiffness matrix of the  $k^{\text{th}}$  undamaged element.

The equation of motion for the structural system under free vibration can be written as:

$$[M] \{\ddot{u}\} + [K] \{u\} = \{0\} \quad (2)$$

where  $[M]$ , and  $[K] = \sum_{k=1}^p [K]_k^d$  are the structure mass and stiffness matrices, respectively,  $p$  is the number of elements in the finite element model,  $\{u\}$  is the vector of the displacements. Assuming the undamped free vibration solution for equation (2), one has

$$([K] - \omega^2 [M])\{u\} = \{0\} \tag{3}$$

where  $\omega$  is the eigen-value and  $\{u\}$  is the eigen-vector.

In this paper the objective function is based on the following expression

$$F = \sum_1^{nm} \left| \frac{\omega_j^{ga} - \omega_j^{ex}}{\omega_j^{ex}} \right| + W \sum_1^{nm} \sqrt{\frac{\sum_1^{nc} (u_{ij}^{ga} - u_{ij}^{ex})^2}{\sum_1^{nc} (u_{ij}^{ex})^2}} \tag{4}$$

where  $nm = 8$  refers to number of vibration modes considered, superscript  $ga$  refers to finite element model results using the genetic algorithm, superscript  $ex$  indicates experimental results,  $\omega_j^{ga}$  and  $\omega_j^{ex}$  are the natural frequency of the finite element model and corresponding experimental one, respectively;  $u_{ij}^{ga}$  and  $u_{ij}^{ex}$  are the  $i^{th}$  mode shape magnitude of the degree  $j$  and  $W = 0.1$  is the weight factor. It is important to note that this objective function takes into account a combination involving natural frequency and mode shapes. Since the measured mode shapes are less accurate than natural frequencies, the weight of the mode shapes is usually of a small magnitude. The objective function to be maximized by using genetic algorithm is given by

$$G_{obj} = \frac{c_1}{c_2 + F} \tag{5}$$

where  $c_1 = 20000$  and  $c_2 = 1$  are adopted constants.

### 3 Real-Coded Genetic Algorithms

Genetic Algorithms are based on principles of evolutionary theory such as natural selection and evolution (Mares and Surace 1996). In this paper only the improved version of the real-coded Genetic Algorithm is briefly introduced.

The term chromosome refers to a candidate solution to a defined problem, fitness is the objective function and the gene is component of the chromosome. The proposed genetic algorithm starts with an initial randomly generated population of 100 chromosomes, namely  $x_1, x_2, \dots, x_{100}$ . The length of each chromosome is the dimension of the solution space, ie:  $x_i = [\alpha_1, \alpha_2, \dots, \alpha_m]$ , where  $m$  is the number of element (bars) on structure. As in most practical case the damage occurs in one or two elements, in order to generate the initial population the following heuristic is adopted: if  $rand[0-1] \leq 0.4$  one consider  $\alpha_i = rand[0-0.6]$ , if not it is assumed  $\alpha_i = 0$  (undamaged).

Selection is a process in which individual chromosomes are chosen according to their fitness. The chromosomes with a higher fitness have a higher probability to survive in the next generation. The selection is performed using Tournament operator with  $n=2$  (Goldberg and Deb 1991). The crossover is implemented using BLX- $\alpha$  technique (Eshelman et al. 1993) with  $\alpha=0.5$  and crossover probability of 0.9 (90%). If no crossover takes place, the two off-springs are exact copies of their respective parents. Random mutation is implemented using mutation probability of 0.05 (5%). The final operation is that of elitism, which consists to reproduce in the new generation the best member of the preceding generation.

Good results are obtained applying the following heuristic: after 300 generation the gene whose damage is lower than 5% is considered undamaged and re-start the process. This is done in order to improve the final result. It is known that the light damage elements are not correct and their presence do not permit the convergence to the exact damage scenario.

### 4 Numerical Example

As numerical simulation it is considered the finite element model of the truss-type structure illustrated in figure 1 (Mares and Surace1996). This structure has twenty one degrees-of-freedom, each member in the truss having the following characteristics: modulus of elasticity  $E=7.03 \times 10^{10}$  N/m<sup>2</sup>; density  $\rho = 2685$  kg/m<sup>3</sup>; cross sectional area  $A=0.001$  m<sup>2</sup>; length of each bay  $\ell = 0.75$  m.

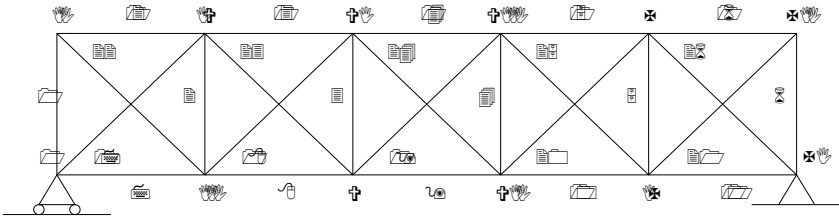


Figure 1. Five-bay truss structure.

The damage scenario considered is given taking into account partial damage of 70% ( $\alpha = 0.7$ ) on members 2, 8 and 23. In this problem, in order to simulate an experimental analysis, random noise given by  $0.01rand[-1,1]\omega_j$  and  $0.03rand[-1,1]\phi_{ij}$  is added to the values of the natural frequencies and mode shapes respectively.

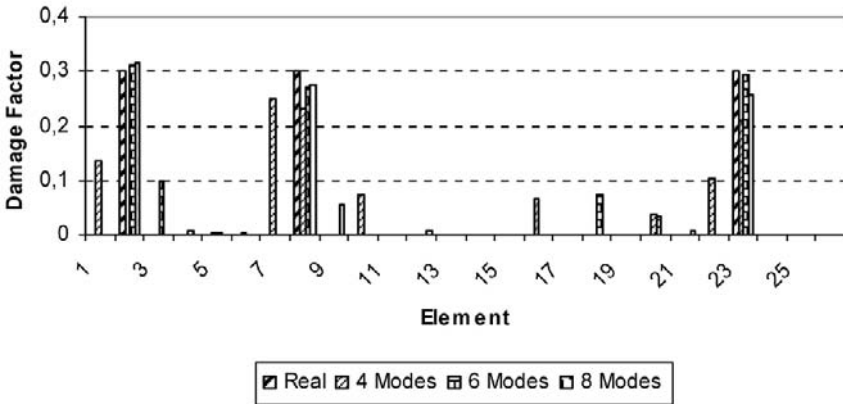


Figure 2. Identified stiffness reduction factor

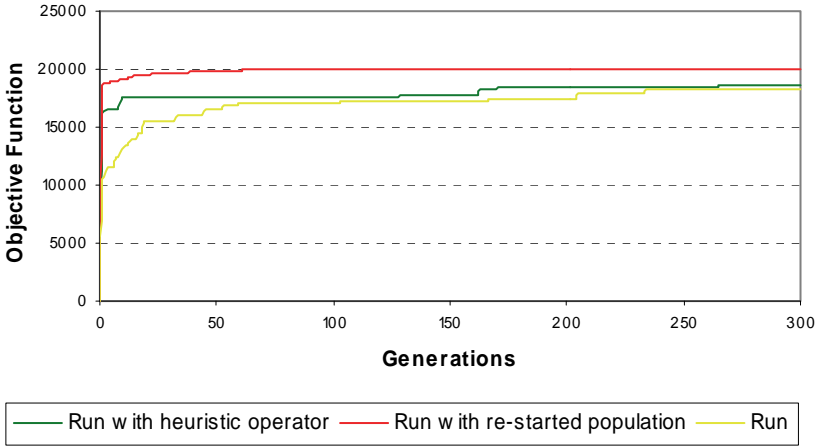


Figure 3. Objective function

Figure 2 shows the results obtained. It is important to note that when 4 modes are used it is not possible to identify correctly the damage scenario. But when 6 modes are considered all three damaged element are captured although the damage of the element 3 is not correct (10%). Good results are clearly obtained using 8 modes. Figure 3 depict the fitness evolution of the best member. One can observe that the proposed heuristic operators are very efficient.

### 5 Conclusions

A genetic algorithm with real number coding is applied to solve the structural damage detection by using free vibration parameters. Numerical results indicate that the proposed heuristics gives better damage detection than the conventional optimization methods.

### Acknowledgments

The author wishes to thank CNPq (Brazilian National Council for Technological and Scientific Development) for their financial support.

## References

- Eshelman L. J. and Schaffer J. D. (1993). Real-coded genetic algorithms and interval-schemata. *Foundation of Genetic Algorithms 2*, L. Darrell Whitley (Ed.), Morgan Kaufmann Publishers, San Mateo, 187-202.
- Goch G., Schmitz B., Karpuschewski B., Geerkens J., Reigl M., Sprongl P. and Ritter R. (1999). Review of non-destructive measuring methods for the assessment of surface integrity: A survey of new measuring methods for coatings, layered structures and processed surfaces. *Precision Engineering*, 23, 9-33.
- Goldberg D. E. and Deb K. (1991). A comparative analysis of selection schemes used in genetic algorithms. *Foundation of Genetic Algorithms 1*, L. Darrell Whitley (Ed.), Morgan Kaufmann Publishers, San Mateo, 69-73.
- Mares C. and Surace C. (1996). An application of genetic algorithms to identify damage in elastic structures. *Journal of Sound and Vibration*, 195(2), 195-215.
- Worden K., Sohn H., Farrar C.R. (2002). Novelty detection in a changing environment: regression and interpolation approaches. *Journal of Sound and Vibration*, 258(4), 741-761.
- Zou Y., Tong L. and Steven P. (2000). Vibration based model dependent damage (delamination) identification on health monitoring for composite structures: A review. *Journal of Sound and Vibration*, 230, 357-378.

*“This page left intentionally blank.”*

# Damage Identification Method for Tunnel Lining Based on Monitoring Stresses Data

Qineng Weng<sup>1\*</sup>

<sup>1</sup>Department of Geotechnical Engineering, Chongqing Jiaotong University, Chongqing 400074, P.R. China

**Abstract.** To concrete structures, the defects such as cracks in this porous-full material are generated naturally. In service life, these defects in tunnel lining concrete will develop to damages under the effect of carbonization, steel corrode, high water pressure, permeability, etc. Incontrovertibly the generation, development and accumulation of these damages will give deterioration to the performance of the structures in service life. The speciality of the tunnel lining structure vary with that of ground structure determines that the normal damage identification method to ground structure such as bridge, building, chimney etc. is not suit for tunnel lining damage identification. Considering of damage expression, material damage model, and damage identification, here a new approach is proposed for damage identification using monitoring stresses data. In this approach, the expression of forces, stresses, and strains under loads is got through analytic method. Considering of possible damages in tunnel lining structure, using substance damage expression and stress damage expression to concrete structure, the difference values of forces, stresses, and strain can be got between those from analytic calculation and those from local monitoring. These values are used as error function; we can get the minimum value through comparing each other. The minimum value of the error function is the representative of damaged state of the lining structure. Then the integral damage and the damage level of the structure can be identified.

**Keywords:** damage, damage identification, tunnel lining, monitoring stress data

## 1 Introduction

The change from loads or temperature, the effect of chemical and circumstances, may cause micro even macro defects in material of the structures, which are known as “Damage”. To concrete structures, the defects such as cracks in this porous-full material are generated naturally. In service life, these defects in tunnel

---

\* Corresponding author, e-mail: qnweng@163.net

lining concrete will develop to damages under the effect of carbonization, steel corrode, high water pressure, permeability, etc. Incontrovertibly the generation, development and accumulation of these damages will give deterioration to the performance of the structures in service life.

The damage to concrete structure will deduce the bearing capacity of the structure. A directly method can be adopted to express the damage to concrete structure that define the macro damage variable as the change of effective loaded area of the structure, and damage stresses can also be expressed by equivalent strain.

The estimation of damage in underground structures such as pile foundations, covered regions of beam-column joints and hidden regions of jacketed members and tunnel lining is even more difficult. The structural response measurements can serve as indicators of damage or degradation and aging process in such situations. Many of the damage detection and evaluation techniques are based on visual inspection. These techniques are often inadequate because of their inability to detect invisible damages; more over it is necessary to quantify the damage rationally.

Structural Health Monitoring is defined as the use of in-situ, non-destructive sensing and analysis of structural characteristics, including the structural response, for the purpose of identifying if damage has occurred, determine the location of damage, estimating the severity of damage and evaluation the consequences of damage on structure. The health monitoring is also emerging as a companion technology to active and passive structural control. The health monitoring is specifically important for (i) maintenance and structural safety of existing structures, (ii) rapid evaluation of condition of damaged structures following an earthquake, (iii) estimating residual life of structures, (iv) repair and retrofitting of structures, and (v) financial planning for renovation and rehabilitation of historical structures.

## 2 Expression of Damage

Scalar damage model, proposed by Kachanov in 1985, is a common model to express many kinds of damage in concrete. The model presume that the damaged part of structure can not hold any loads, so the effective section area of structure will be loss while the load level increase. This loss can be connected with loss of elastic module for elastic material. When the load level increases to the concrete structure, the damage occurred can be expressed by lose of effective section of the material, so

$$A_D = A(1 - D) \tag{1}$$

where D is Damage, AD is effective area of damaged concrete section. There are three possible relations of a damaged section considered: (i) undamaged section, where D=0, in this part of interface there is no damage occurs; (ii) partly damaged

section, where  $0 < D < 1$ , in this part of interface, it is partly damaged; (iii) full-damaged section, where  $D=1$ , in this area, the surface is fully cracked.

Real materials usually exhibit permanent plastic strains as well as the reduction of the stiffness. Consequently, the coupling of elastic-plasticity with damage theory is necessary for a realistic modelling of the structural response. This coupling is accomplished by introducing an effective stress or by introducing damage-induced strains. To any  $(\sigma, \varepsilon_a)$ , the effective area of damaged section can be written as

$$A_D = \frac{1}{E_c} \frac{\sigma}{\varepsilon_a} = A(1-D) \quad (2)$$

The damage can be written as

$$D = 1 - \frac{\frac{\sigma_0}{E_c}}{\frac{\sigma}{E_c}} = \frac{\sigma_0 \varepsilon}{\sigma \varepsilon_{a0}} \quad (3)$$

From Equation (3), the relation of damage and total strain can be deduced and expressed in figure (Figure 1). Use the same method, the “equivalent strain” of the concrete can be determined also, to uniaxial tension condition, the relationship of the stress and strain can be written as

$$\sigma = E(1-D)\varepsilon_a = E' \varepsilon_a \quad (4)$$

To cracked concrete, the assumed thickness is  $b$ . as mentioned above; the damaged area can not hold any load, so the section area loss of the cracked concrete is calculated as

$$A_D = AD = sl \quad (5)$$

where  $l$  is the length of crack. Then the damage caused by crack is

$$D = \frac{A_D}{A} = \frac{s}{b} \quad (6)$$

Accordingly, the damage of the elastic module of the cracked concrete can be expressed with the effective elastic module. This is

$$E_e = (1 - D)E = \left(1 - \frac{s}{b}\right)E \tag{7}$$

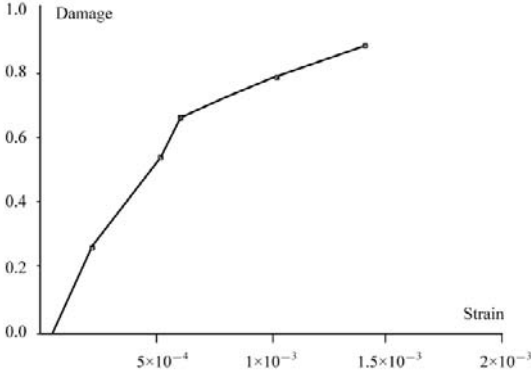


Figure 1. The relationship of the damage and total strain

### 3 Damage Identification Methods

#### 3.1 Review

The features of a scheme of identification (Rytter, 1993) can be classified into four levels:

- Level 1: Determination that damage is present in the structure
- Level 2: Determination of the geometric location of the damage
- Level 3: Quantification of the severity of the damage
- Level 4: Prediction of the remaining service life of the structure

Level 1, Level 2 or Level 3 methods are mostly related to structural dynamics testing and modelling issues. Level 4, prediction is generally categorized with the fields of fracture mechanics and fatigue life analysis. The major developments are yet to take place in Level 3 and Level 4 methods.

The scope of damage identification methods is broad and includes both local and global techniques. Several damage detection methods have been developed. An ideal method is one that can be used to not only detect the damage in structure globally but it should be able to map the localized damage. The majority of the damage detection methods are based in correlating damage with some change in structural property like frequency, mode shape, flexibility coefficient, mode shape curvature, modal energy, stiffness, etc (Doubling, 1996).

The damage detection has been applied to the bridge, tunnel structures in most cases and can be classified into two categories according to the data characteristics: Firstly, dynamic approach is a very powerful tool from the theoretical viewpoint and it can be divided into frequency and time domain analysis again. Various studies have been carried out on the damage assessment techniques using natural frequency (Fabrizio and Danilo, 2000; Lee et al., 2004), but the variation of natural frequencies or modal is not sensitive to the damage of the tunnel. Secondly, static analysis is a convenient tool if the measured data are accurate and the detection algorithm is stable. In this regard, the use of static displacements obtained by a loading that simulates higher modes was suggested. Hjelmstad and Shin (1997) proposed a damage detection and assessment algorithm based on parameter estimation with an adaptive parameter-grouping scheme. Choi and Cho (2003) proposed a damage identification technique using elastic damage load theorem (EDLT) derived from the relationship between damage and displacement. In this case, no loading test or data manipulation is usually required. Jun S. Lee (2005) use the measurement static deformation data obtained from the convergence sensors installed in the inner space of the concrete lining to identify the damage of the structure.

It's difficulty to get the natural frequency or the modal of tunnel lining through vibration test for the existence of rock mass and soil medium, so it's impossible to use the dynamic approach for damage identification and structural health monitoring. The approach proposed here is a new method for damage identification using monitoring stresses data. In this approach, the expression of forces, stresses, and strains under loads is got through analytic method. Considering of possible damages in tunnel lining structure, using substance damage expression and stress damage expression to concrete structure, the difference values of forces, stresses, and strain can be got between those from analytic calculation and those from local monitoring. These values are used as error function; we can get the minimum value through comparing each other. The minimum value of the error function is the representative of damaged state of the lining structure. Then the integral damage and the damage level of the structure can be identified.

### ***3.2 Damage Identification Method of Tunnel Lining Using Monitoring Data***

The performance of tunnel lining structure with loads can be detected through forces, stresses, strains and their relationships in the structure, which can be got through analytic calculation. For example, the calculated stress and strain of structure with loads is  $\sigma_{ij}^c, \varepsilon_{ij}^c$ , where superscript c show the calculated value of the stress and strain under loads. Similarly, the stress and strain of the structure with

loads got from monitoring is  $\sigma_{ij}^M, \epsilon_{ij}^M$ , where superscript M show the monitoring value of the stress and strain under loads. When damage of the structure occurs, the stress and strain in the structure change also. The varied stress (actual stress) is monitoring stress  $\sigma_{ij}^M$ , and the theoretical stress is  $\sigma_{ij}^c$ . From Equation (4) and (7), it is easy to get the relationship of  $\sigma_{ij}^M$  and  $\sigma_{ij}^c$  as

$$\sigma_{ij}^c = (1 - D)\sigma_{ij}^M \tag{8}$$

Then, the damage of structure can be written as

$$D = \frac{\sigma_{ij}^c - \sigma_{ij}^M}{\sigma_{ij}^M} = \frac{\Delta\sigma_{ij}}{\sigma_{ij}^M} \tag{9}$$

### 3.3 Damage Identification Expression to Tunnel Lining

As mentioned above, the expression of forces, stresses, and strains under loads is got through analytic method. Here, taking the ring tunnel as instance, the expression of forces, stresses, and strains of ring tunnel under loads can be got by elastic mechanic solution. Loads type and calculation model of railway tunnel, underground utility tunnel is illustrated in Figure 2. Where, Q is upper vertical uniform soil pressure,  $E_1$  is horizontal uniform soil pressure,  $E_2$  is horizontal triangular soil pressure,  $P_k$ , with a triangular attribution, is elastic resisting force of foundation, W is water pressure on ring tunnel, K is bottom vertical counterforce for balance. Through force method of structural mechanics, the force of the ring with loads can be solved through the summing of force to individual load, which can be written as

$$\begin{aligned} M &= M_g + M_Q + M_K + M_{P_k} + M_W + M_{E_1} + M_{E_2} \\ N &= N_g + N_Q + N_K + N_{P_k} + N_W + N_{E_1} + N_{E_2} \end{aligned} \tag{10}$$

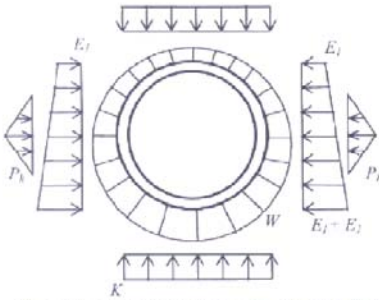


Figure 2. Loads-Structure Calculation Model of Ring Tunnel

Presume a ring tunnel with uniform water pressure, the monitoring external force is  $\sigma_h^M$ , and then stress of any point on the ring tunnel can be written as

$$\begin{cases} \sigma_r^c = \frac{a^2b^2}{b^2-a^2} \cdot \frac{\sigma_h^M}{r^2} - \frac{b^2\sigma_h^M}{b^2-a^2} \\ \sigma_\theta^c = -\frac{a^2b^2}{b^2-a^2} \cdot \frac{\sigma_h^M}{r^2} - \frac{b^2\sigma_h^M}{b^2-a^2} \end{cases} \quad (11)$$

where  $a$  is the inner radius of the ring,  $b$  is outer radius of the ring,  $\sigma_r, \sigma_\theta$  is stress component in radial and circum direction, superscript c, M is the same as mentioned. Another group of stress  $\sigma_r^M, \sigma_\theta^M$  is stress got from monitoring, that is the actual state of the ring. Then we can get the error function  $\Delta\sigma_r, \Delta\sigma_\theta$  between theoretical state and actual state of the ring tunnel as

$$\begin{aligned} \Delta\sigma_r &= \sigma_r^c - \sigma_r^M \\ \Delta\sigma_\theta &= \sigma_\theta^c - \sigma_\theta^M \end{aligned} \quad (12)$$

As the damage theory and damage expression method mentioned above, the effective stress in the ring tunnel damaged can be written as

$$\begin{cases} \overline{\sigma_r} = \sigma_r^M = \frac{\sigma_r^c}{1-D} = \frac{a^2b^2}{(1-D)(b^2-a^2)} \cdot \frac{\sigma_h}{r^2} - \frac{b^2\sigma_h}{(b^2-a^2)(1-D)} \\ \overline{\sigma_\theta} = \sigma_\theta^M = \frac{\sigma_\theta^c}{1-D} = -\frac{a^2b^2}{(1-D)(b^2-a^2)} \cdot \frac{\sigma_h}{r^2} - \frac{b^2\sigma_h}{(b^2-a^2)(1-D)} \end{cases} \quad (13)$$

Equation (13) gives an expression of the effective stress in the ring tunnel damaged. From damage theory of continuum, the substance damage is occurred before the peak stress of the material, while stress damage is relevant to the ultimate state of the material. The substance damage (caused by leaking of water, carbonation, or steel corrosion) is defined as initial damage  $D_0$ , and the stress damage (raise while the stress state exceed ultimate state of the material) is defined as  $\Delta D$ , which can be got by Equation (14).

$$D = 1 - \frac{1}{1 + [a(Y - Y_0)]^b} \tag{14}$$

where  $a, b, Y, Y_0$  is material parameter (Weng et al., 2007).

### 3.3 The Steps of Damage Identification Method to Tunnel Lining

From the tunnel lining concrete structure damage identification model and solution process in this paper, it's clear that the key work of this method is obtain the damage value through comparing calculated stress and monitoring stress of the structure, the steps of stress damage identification method is illustrated in Figure 3.

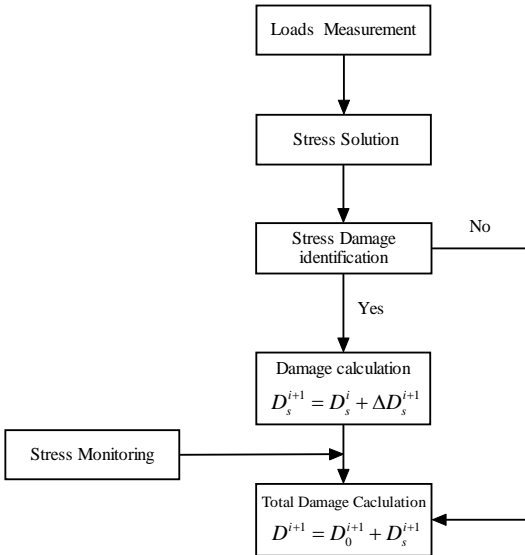


Figure 3. Steps of stress damage identification method to tunnel lining

## 4. Conclusion Remarks

The speciality of the tunnel lining structure vary with that of ground structure determines that the normal damage identification method to ground structure such as bridge, building, chimney etc. is not suit for tunnel lining damage identification. Considering of damage expression, material damage model, and damage identification, here a brief, usable scalar damage expression is proposed for static stress damage identification using monitoring data. The damage identification method can detect the integral damage and the damage level of the structure in service life. The following conclusions may be pointed out:

1. Scalar damage expression, can not only indicate the damage property of concrete, but also have the advantage of simple expression, ease computation.
2. The damage of tunnel lining concrete includes two parts: substance damage and stress damage. The former is occurred about the defects of the material whether the material is under peak state of or not. The latter is relation to the peak state of the material. These two kinds of damage shall be considered individually in damage identification method.
3. The stress damage identification method has the ability to determine the damage level, damage value of the tunnel lining structure, but it can not detect the position of the damage.

## References

- Chen B., Lu X.L. et al. (2002). Modeling of dynamic soil-structure interaction by ANSYS program. *Earthquake Engineering and Engineering Vibration*, 22(1), 126-131 [in Chinese].
- Choi I.Y. (2002). Damage identification techniques for bridges using static response. Ph.D. Dissertation, Hanyang University, Korea.
- Choi I.Y., Cho H.N. (2003). Damage identification technique for bridges using static response. In: *Proceedings of the 7th Korea-Japan Joint Seminar on Steel Bridges*, Daejeon, Korea.
- Doebling S.W., Farrar C.R., Prime M.B. and Shevits D.W. (1996). *Damage Identification and Health Monitoring of Structural and Mechanical Systems from Changes in Their Vibration Characteristics: A Literature Review*, Los Alamos National Laboratory, La-13070-MS, UC-900, New Mexico 87545.
- Hjelmstad K.D., Shin S. (1997). Damage detection and assessment of structures from static response. *J. Eng. Mech.* 123, 568-576.
- Jun S. Lee, Il-Yoon Choi, Hee-Up Lee (2005). Damage identification of a tunnel liner based on deformation data. *Tunnelling and Underground Space Technology*, 20, 73-80.
- Kachanov, L.M. (1986). *Introduction to Continuum Damage Mechanics*. Martinus Nijhoff, Dordrecht, The Netherlands.
- Rytter A. (1993). *Vibration Based Inspection of Civil Engineering Structures*, Ph.D. Dissertation, Department of Building Technology and Structural Engineering, Aalborg University, Denmark.
- Samaha H. and Hover K.C. (1992). Influence of microcracking on the mass transport properties of concrete, *ACI Materials Journal*, 89(4), 416-424.

- St. John C.M., Zahrah T.F. (1987). A seismic design of underground structures. *Tunnelling and Underground Space Technology*, 2(2), 165–197.
- Weng Q.N. Yuan Y. et al. (2007) Damage model of cracking concrete under water permeability. *Materials Review*, 8(5), 104-107.

# A Method of Structure Damage Identification for Shear Buildings

Feng Li<sup>1\*</sup>, Julin Wang<sup>1</sup> and Zeping Zang<sup>2</sup>

<sup>1</sup>Institute of Building Structures, Shanxi Architectural Technical College, Taiyuan 030006, P.R. China

<sup>2</sup>Department of Civil Engineering, Taiyuan University of Technology, Taiyuan 030024, P.R. China

**Abstract.** Based on the easy testability and high measure precision of structural frequency, a damage identification method for shear buildings is presented. With frequency being regarded as the function of damage parameters, the homogeneous linear equations with damage parameters as unknowns can be constructed via Taylor expansion. The equations are solved to locate the whole damage location and quantify the severity of the damage. The data used in the method include frequency and mode shape measurement before and after damage. A numerical simulation example using a three-storey sheer structure is given to validate the present method.

**Keywords:** structural damage identification, homogeneous linear equations, iteration-self

## 1 Introduction

For decades, numerous studies were reported in vibration-based damage identification methods. Their ideas are based on the fact that structural damage usually caused a reduction in structural stiffness which is accompanied by changes in vibration characteristics. Commonly used modal data include the natural frequency and mode shape. Based on the studies of predecessors, this paper has developed a method of structure damage identification for shear buildings. On the basis of structure mode finite element formula, the method regards damage parameters as system variables to construct the homogeneous linear equations with frequency as the function of damage parameters. The equations are solved to locate the whole damage location and quantify the severity of the damage. The first partial derivative of frequency to damage parameters is deduced in the article. Furthermore, the iteration-self modification is proposed to improve the accuracy of damage identi-

---

\* Corresponding author, e-mail: lifeng2634@yahoo.com.cn

fication greatly. Numerical simulation using a three-storey frame structure, confirmed the validity of the proposed damage detection method.

## 2 Constructing the Homogeneous Linear Equations

According to the damage mechanics, the  $i$  th story stiffness of the damaged shear frame is

$$K_d^i = K^i(1 - D_i) \tag{1}$$

where  $D_i$  is the damage parameter of the  $i$  th story.  $D_i$  is from 1 to 0 to describe the severity of the  $i$  th story damage.

Evaluating the natural frequencies and modes, the eigenvalue problem to be solved is

$$K_d \Phi_r = \omega_r^2 M \Phi_r \tag{2}$$

where  $M$  and  $K_d$  respectively, are the mass and stiffness matrix of the damaged structure. We assume that damage is not accompanied by a change in the mass matrix.  $\omega_r$  and  $\Phi_r$ , respectively, are the  $r$  th natural frequency and mode shape.  $\Phi_r$  can be expressed as

$$\Phi_r = [\varphi_{1r}, \varphi_{2r}, \dots, \varphi_{Nr}]^T \tag{3}$$

where  $N$  denotes the number of total stories. The mode shape normalized has the following properties:

$$\begin{cases} \Phi_r^T M \Phi_s = \delta_{rs} \\ \Phi_r^T K \Phi_s = \omega_r^2 \delta_{rs} \end{cases} \tag{4}$$

where  $\delta_{rs} = \begin{cases} 1, & r = s \\ 0, & r \neq s \end{cases}$

With the frequency  $\omega_r$  being regarded as the function of the damage parameter  $D_i$  ( $i = 1, 2, \dots, N$ ), the function is expanded as Taylor series given by:

$$\omega_r = \omega_r^0 + \sum_{i=1}^N \left( \frac{\partial \omega_r}{\partial D_i} \right) D_i + \frac{1}{2} \sum_{i=1}^N \left( \frac{\partial^2 \omega_r}{\partial D_i^2} \right) D_i^2 + \dots \tag{5}$$

where  $\omega_r^0$  is  $r$  th natural frequency of the intact structure. With the item including the first power of  $D_i$  in Equation (5) being only reserved, the frequency difference between the intact structure and the damaged one is

$$\Delta \omega_r = \omega_r^D - \omega_r^0 = \sum_{i=1}^N \left( \frac{\partial \omega_r}{\partial D_i} \right) D_i \quad (r = 1, 2, \dots, N) \tag{6}$$

where  $\frac{\partial \omega_r}{\partial D_i}$  is the constant term.

When  $r$  changes from 1 to  $N$ , the homogeneous linear equations for  $N$  damage parameters as unknowns can be constructed. The whole damage parameters can be found by solving the algebraic equations.

The calculating formula of  $\frac{\partial \omega_r}{\partial D_i}$  is deduced as follows:

Differential to both sides of Equation (2) about the damage parameter  $D_i$  gives

$$\frac{\partial K_d}{\partial D_i} \Phi_r + K_d \frac{\partial \Phi_r}{\partial D_i} - \frac{\partial (\omega_r^2)}{\partial D_i} M \Phi_r - \omega_r^2 M \frac{\partial \Phi_r}{\partial D_i} = 0 \tag{7}$$

Premultiplying both sides of Equation (7) by  $\Phi_r^T$  gives

$$\Phi_r^T \frac{\partial K_d}{\partial D_i} \Phi_r - \Phi_r^T \frac{\partial (\omega_r^2)}{\partial D_i} M \Phi_r + (\Phi_r^T K_d - \omega_r^2 \Phi_r^T M) \frac{\partial \Phi_r}{\partial D_i} = 0 \tag{8}$$

Substituting Equation (2) and (4) into Equation (8) gives

$$\begin{aligned}
 \frac{\partial(\omega_r^2)}{\partial D_i} &= \Phi_r^T \frac{\partial K_d}{\partial D_i} \Phi_r = 2\omega_r \frac{\partial \omega_r}{\partial D_i} \\
 &= \Phi_r^T \left( \sum_{j=1}^N \sum_{k=1}^N \frac{\partial K_d}{\partial k_{jk}} \frac{\partial k_{jk}}{\partial D_i} \right) \Phi_r \\
 &= \sum_{j=1}^N \sum_{k=1}^N \frac{\partial k_{jk}}{\partial D_i} (2 - \delta_{jk}) \phi_{jr} \phi_{kr}
 \end{aligned} \tag{9}$$

where  $k_{ij}$  is the element of the stiffness matrix.

So, the first partial derivative of frequency to  $D_i$  is

$$\frac{\partial \omega_r}{\partial D_i} = \sum_{j=1}^N \sum_{k=1}^N \frac{\partial k_{jk}}{\partial D_i} \left( 1 - \frac{\delta_{jk}}{2} \right) \frac{\phi_{jr} \phi_{kr}}{\omega_r} \tag{10}$$

### 3 Iteration-Self Modification

The homogeneous linear equations being constructed, the first item of Taylor expansion is used, so it greatly debases the effect of diagnose. In order to improve the accuracy of damage identification, the iteration-self modification is proposed.

The procedure is:

**Step 1:** Substituting  $\Delta \omega_r^0 = \omega_r^D - \omega_r^0$  in Equation (6), the approximation of the first-order damage parameter  $D_i^{(1)}$  is obtained.

**Step 2:** Substituting  $D_i^{(1)}$  in Equation (1) and constituting the stiffness matrix to obtain the first-order frequency  $\omega_r^{(1)}$ .

**Step 3:** Substituting  $\Delta \omega_r^{(1)} = \omega_r^D - \omega_r^{(1)}$  in Equation (6) to determine the approximation of the second-order damage parameter  $D_i^{(2)}$ .

**Step 4:** Applying Equation  $1 - D_i^* = (1 - D_i^{(1)})(1 - D_i^{(2)}) \dots (1 - D_i^{(j)})$  gives  $D_i^*$ .

**Step 5:** According to Step3, obtains the approximation of the  $j$ -order damage parameter  $D_i^{(j+1)}$ .

**Step 6:** Repeating Step4 and Step5 for  $j = 2, 3, \dots, p$ , and checking if  $\frac{\Delta\omega_r^{(p)}}{\omega_r^D}$  is in the range of the error requirement. If yes,  $D_i^*$  is accepted as the value of our requirement, otherwise the iterating is kept on.

### 4 Numerical Verification

Numerical simulations for a three-storey shear frame were conducted to confirm the proposed method. Figure shows a shear frame (i.e., rigid beams) and its floor weights and story stiffness. We assume that the damages in 1st, 2nd and 3rd stories are 0.15, 0.3 and 0.35, respectively.

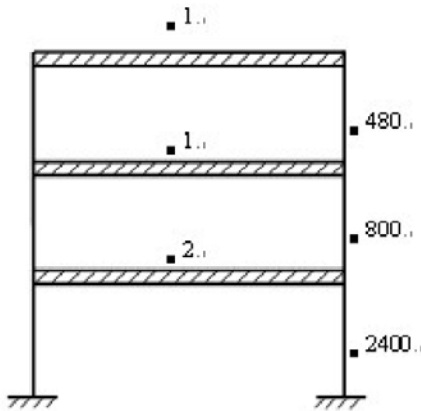


Figure 1. Three-story shear frame

According to Equation (2), the three frequencies and modes of the intact and damaged structure were computed and then substituted in Equation (6) to construct the homogeneous linear equations with three damage parameters as unknowns. By solving the equations and using the iteration-self modification, the values of the damage parameters are shown in Table 1.

We can see from Table that there are errors between the real values and the computing values, but by two time cycles, the computing values approach to the

real values greatly. So this indicates the present method can diagnose synchronously the location and severity of damage.

Table 1. Results of iteration and real values

Number of stories	Solving equations	The first iteration	The second iteration	The real value of $D_i$
1	0.1363301	0.1441241	0.1539512	0.15
2	0.190632	0.3213252	0.3074671	0.30
3	0.3873201	0.3645976	0.3518734	0.35

## 5 Conclusions

1. Solving the homogeneous linear equations based on the change of frequency not only can judge whether the structure is damaged, but also can locate the damage location and quantify the severity of the damage.
2. The iteration modification improved the accuracy of damage identification greatly.
3. Using frequency and mode shape measurement that have easy testability and high measure precision, the method is implemented easily on computer and so can be applied in practice.

## References

- Pandey A.K., Biswas W. and Samman M.M. (1991). Damage detection from changes in curvature mode shapes, *Journal of Sound and Vibration*, (3):505-517.
- Salawu O.S. (1997). Detection of structural damage through changes on frequency: A Review, *Engineering Structures*, 19(9):718-723.
- Yu T.Q. and Qian J.Ch. (1998). *The Theory of Damage and Its Application*. Beijing: National Defence Industry Press.

# Application of Artificial Neural Network for Diagnosing Pile Integrity Based on Low Strain Dynamic Testing

Canhui Zhang<sup>1\*</sup> and Jianlin Zhang<sup>1</sup>

<sup>1</sup>Department of Civil Engineering, Xiamen University, Xiamen 361005, P.R. China

**Abstract.** The artificial neural network (ANN) models are presented for diagnosing pile in this paper based on the pile integrity test (PIT) also known as low strain dynamic test. The back-propagation learning algorithm is employed to train the network for extracting knowledge from training examples. There are fifty-three input neurons in the network including the PIT response and pile length, cross-sectional area and wave velocity. In order to obtain the pile condition in quantity, the novel technique is proposed containing two back-propagation ANN models. The first is to identify the defect patterns while the second to investigate the exact degree of pile defect by computing the change of equivalent cross-sectional area. Training and testing data were drawn from response records of actual piles. The results from the testing phase indicate that the presented method is successful.

**Keywords:** pile integrity diagnosing, artificial neural network, BP algorithm, low strain dynamic testing

## 1 Introduction

Piles are the most significant elements of a building, especially for high-rise structures. The piles with any defect are dangerous for the structure rested above. Any defect of the pile segments can seriously influence the stability and integrity of the building structure. Thus, the assessment of any likelihood of pile failure is necessary before commencement of the construction of the superstructure. Any incorrect estimation of them may result the disaster. However, it is quite difficult to predict the exact defects of the foundation piles because they are hidden into the soil under ground.

A low strain dynamic test or pile integrity test (PIT) is one of the common methods for assessing the condition of piles or shafts (Zhang et al., 2006; Zhang et al., 2005; Yeh et al., 1993). It is cost effective and not very time consuming. How-

---

\* Corresponding author, e-mail: chzhang@xmu.edu.cn

ever, the satisfactory assessment of such pile is by no means an easy task because the data interpretation is always affected by experience, physical and emotional conditions of engineers. So it does demand for an appropriate system without any intervention from the decision-makers. The artificial neural network (ANN) is one of the efficient choices. In most case the researches are focus on the pile defects in quality or their pattern (Yeh et al., 1993; Cai and Lin, 2002). In (Tam et al., 2004; Wang and Zhang, 2003; Gan et al., 2006), the level of accuracy of the model is taken into consideration. However, the improvement for more precision and efficiency is still necessary.

In this paper the novel ANN models based on PIT are presented for pile integrity diagnosis. The actual piles are used to illustrate the process.

## 2 Back-propagation ANN Models Based on PIT

The pile integrity test is based on wave propagation theory. The test is based on wave propagation theory. When a light impact is applied to a pile it produces a compression wave that travels down the pile at a constant wave speed. Changes in cross sectional area - such as a reduction in diameter - or material - such as a void in concrete - produce wave reflections. For homogeneous material in pile, the change in area can be expressed as following:

$$\eta_i = \frac{1 + R_i}{1 - R_i}, R_i = \frac{v_i}{v_0} \quad (1)$$

where  $R_i$  is the reflectance and  $v_i$  is the response of PIT. However, in general it is difficult to obtain the exact reflectance by PIT response.

An Neural networks mimics the cognitive power of human brains in problem-solving. The real power of ANN models is evident when the trained network model is able to produce good results for data, which the network model has never 'seen' before. In this paper, the ANN models based on PIT is presented and the back-propagation learning algorithm is employed to train the network for extracting knowledge from training examples. Back-propagation neural works with a single hidden layer have been shown to be capable of proving an accurate approximation of any continuous function provided there are sufficient hidden neurons. However, there is currently no rule for determining the optimal number of neurons in the hidden layer except through experimentation (Hornik, 1991).

Before the back-propagation ANN model is developed, the variables to be used as the input parameters have to be identified. This requires an understanding of pile engineering and insights from specialists in this field. Generally the reliability of the model improved as the number of input parameters increased. However, it increases the training time. To minimize the number of input parameters for satis-

factory solution, the most significant variables should be determined. The PIT response is always considered to be most reliable. Besides, it is found that the wave velocity and the pile dimensional parameters such as length and cross-sectional area should also be taken into consideration. In this paper, there are fifty-three input neurons including fifty sampling values of the PIT response as well as the wave velocity and the pile length and cross-sectional area.

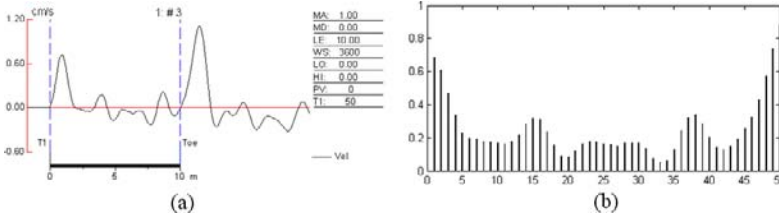


Figure 1. Sampling data of actual pile for network. (a) PIT Record; (b) Sampling data

Preprocessing of the data is usually required before presenting the patterns to the neural network. This is necessary because the sigmoid transfer function modulates the output of each neuron to values between 0 and 1. For the value  $v_k$  of variable, the following normalization procedure is used in this study:

$$x_k = \frac{v_k - v_{\min}}{v_{\max} - v_{\min}}(1 - \alpha) + \alpha x_b \tag{2}$$

where  $x_b = 0.5$ ,  $\alpha = 0.1$ ,  $v_{\max}$  and  $v_{\min}$  are the maximum and minimum of  $v_k$ 's, respectively. A typical response record of actual pile and its corresponding sampling data set for back-propagation ANN models is shown in Figure 1.

Table 1. Output patterns of pile condition.

No.	Pile condition	Output pattern
1	Sound pile	(0,0,0,0,0)
2	Bulge	(1,0,0,0,0)
3	Neck	(0,1,0,0,0)
4	Segregation	(0,0,1,0,0)
5	Crack	(0,0,0,1,0)
6	Multi-defect	(0,0,0,0,1)

In order to find the exact degree of pile defect and its location, the pile has to be discredited into elements. And the defect of every element including bulge, neck, segregation or crack can be determined by finding the reduction or enlarge-

ment of equivalent cross-sectional area. However, the different defect pattern relating to distinct characteristics of response can result the same change in area. Therefore, for every element several patterns should be considered. In this paper, the pile is discredited into fifty elements and the output patterns are listed in Table 1.

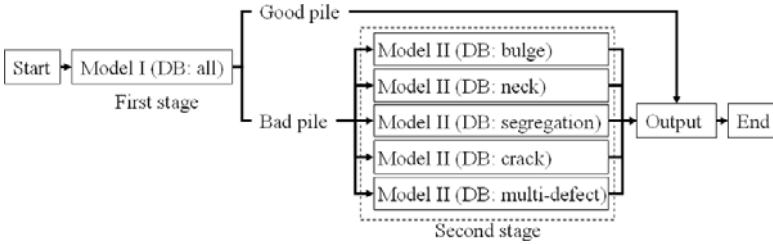


Figure 2. Procedure for diagnosing pile integrity.

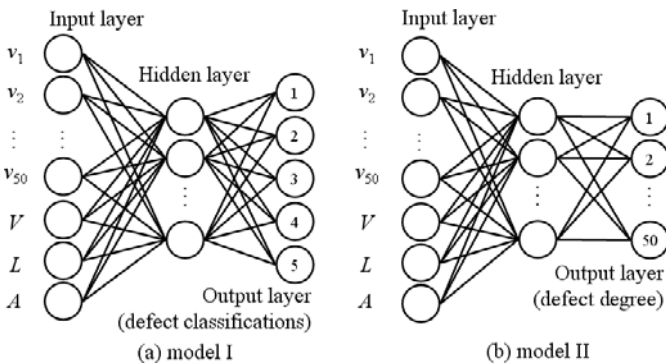


Figure 3. Architecture of networks. (a) Model I: for pile defect classification; (b) Model II: for pile defect degree.

When all the elements for every pattern are taken into consideration, a large number of output neurons are necessary and the training for neural networks are costly. To overcome this issue, the procedure is proposed including two stages with different network model. The presented procedure and architecture of its network models are shown in Figure 2 and Figure 3, respectively, where  $V$  denotes the wave velocity,  $L$  and  $A$  are the length and cross-sectional area of pile.

In the first stage the model I is used to determine the pile condition of different pattern. The database here contains all representative PIT records of the actual piles the neural network is likely to encounter. In the second stage the model II is used to investigate the exact degree of defect and its relating location. For each type of defect, only the corresponding database is necessary. There are fifty output neurons corresponding to different pile element. The values  $a_k, k = 1, \dots, 50$

represent the related change of equivalent cross-sectional area for pile integrity where  $a_k = 0$  stands for sound element without change of area.

### 3 Prediction for Pile Integrity

As discussed in the previous section, the optimal number of neurons in the hidden layer for neural networks usually is determined through experimentation. Using too few neurons impairs the neural network and prevents the correct mapping of input to output. Using too many neurons impedes generalization and increases training time. A common strategy and the one used in this study was to replicate the training several times, starting with two neurons and then increasing the number while monitoring the average sum squared error. Training is carried out until there is no significant improvement in the error. Experiments in this study show that about fifty hidden neurons were found to be the most reliable.

Training and testing data were drawn from records for actual piles. A total of thirty patterns were randomly selected for the training phase and ten patterns for the testing phase. Some of the neural network predictions for the testing sets are shown in Table 2. The results from the testing phase indicate that the neural network was successful in modeling the relationship between foundation pile integrity and the input data set and generally gave the reasonable predictions.

Table 2. Prediction for checking piles

No.	Length/cm	Diameter/cm	Network results	Actual results
1	100.0	3.69	Good pile	Good pile
2	104.5	3.69	Neck in elm 36	Neck in elm 36
3	103.7	3.66	Neck in elm 19	Neck in elm 19
4	101.5	5.57	Segregation in elm 7	Segregation in elm 6
5	102.5	3.66	Crack in elm30	Crack in elm30

### 4 Conclusion

The new method containing two back-propagation ANN models is presented in this paper for the pile integrity prediction. The PIT response records and pile length, cross-sectional area and wave velocity are identified to be the most reliable and are used as the input data set in the network. The defect pattern of pile can be determined using the first model. Then the second model is responsible for the further investigation of the exact degree of pile defect. The numerical examples of actual pile show that the approach is satisfactory and efficient.

## Acknowledgements

The support of this work by the scientific program of Fujian Province of China under grant No. 2007F3096 and the scientific program of Xiamen City of China under grant No. 3502ZZ20073012 is gratefully acknowledged.

## References

- Cai Q.Y. and Lin J.H. (2002). Pile defect diagnosis based on wavelet analysis and neural networks, *Journal of Vibration and Shock*, 21(03).
- Gan H.C., Lu J.H. and Tong J.T. (2006). The application of neural network method in identifying the defect of foundation piles, *Shanghai Geology*, 02: 13-15.
- Hornik K. (1991). Approximation capabilities of multilayer feedforward networks. *Neural Networks*, 4(2): 251-257.
- Tam C.M., Thomas K.L. and Tong et al. (2004). Diagnosis of prestressed concrete pile defects using probabilistic neural networks. *Engineering Structures*, 26: 1155-1162.
- Wang C.H. and Zhang W. (2003). A neural network model for diagnosing pile integrity based on reflection wave method. *Rock and Soil Mechanics*, 24(6): 952-956.
- Yeh Y.C., Kuo Y.H. and Hsu D.S. (1993). Building KBES for diagnosing PC pile with artificial neural network. *Journal of Computing in Civil Engineering*, 7(1): 71-93 [in Chinese].
- Zhang C.H. et al. (2005). The multi-reflected wave analysis on the low strain integrity testing of pile foundation. *Journal of Xiamen University (Natural Science)*, 44(2): 214-216.
- Zhang C.H., Zhang J.L. and Xie J.H. (2006). Nonlinear least squares method for the testing of pile integrity. *Chinese Journal of Applied Mechanics*, 23(1): 142-144 [in Chinese].

# Parametric Study on Damage Control Design of SMA Dampers in Steel Frames

Xiaoqun Luo<sup>1</sup>, Hanbin Ge<sup>2\*</sup> and Tsutomu Usami<sup>2</sup>

<sup>1</sup> Advanced Research Center for Seismic Experiments and Computations, Meijo University, Nagoya 468-8502, Japan

<sup>2</sup> Department of Civil Engineering, Meijo University, Nagoya 468-8502, Japan

**Abstract.** This paper focuses on damage control design of SMA dampers in steel frames. A parametric study based on time history analyses is carried out on a frame bridge pier with axial-type SMA damping devices. The parameters examined are design parameters of strength ratio  $\alpha_F$  and stiffness ratio  $\alpha_K$ . Three JRA recommended Level 2 Ground Type 2 ground motions are used as inputs. Design recommendations are suggested following results of the parametric study.

**Keywords:** damage control design, shape memory alloy, parameter study

## 1 Introduction

The effectiveness of conventional damage control strategies in seismic design has been demonstrated through many numerical and experimental investigations. On the other hand, further improvements can be achieved using new materials and techniques to obtain better seismic performances with respect to the traditional ones. As one of the smart materials, due to their shape memory effect and super-elasticity, shape memory alloys (SMA) show applicable mechanical properties for seismic upgrading performance. Here, a parametric study based on time history analyses are carried out on a frame bridge pier with axial-type SMA damping devices to suggest some useful design recommendations.

---

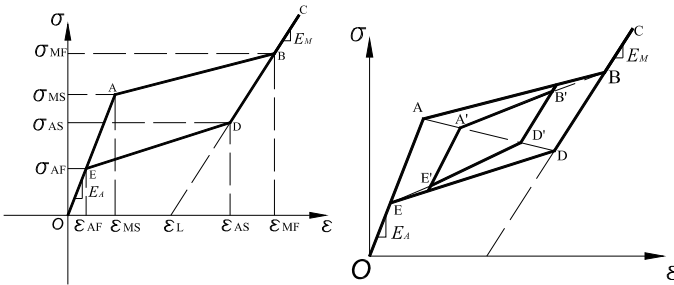
\* Corresponding author, e-mail: [gehanbin@ccmfs.meijo-u.ac.jp](mailto:gehanbin@ccmfs.meijo-u.ac.jp)

## 2 Modelling of Axial-Type SMA Damper

### 2.1 Constitutive Model of SMA Material

In order to simulate material behaviour of SMAs numerically, a simple multi-linear one dimensional constitutive law of SMAs is proposed here. Shown in Figure 1 is the multi-linear bone curve of SMAs in the austenite state at the reference temperature, in which four transformation stresses, i.e.,  $\sigma_{MS}$ ,  $\sigma_{MF}$ ,  $\sigma_{AS}$  and  $\sigma_{AF}$  are known and the elastic moduli in the austenite state and martensite state are  $E_A$  and  $E_M$ , respectively.

An inner hysteretic strategy called diagonal rule is proposed in Figure 1(b). The diagonal rule defines the diagonal line between  $\sigma_{MS}$  and  $\sigma_{AS}$  as a reference line for the phase transformation start point in the inner loop. If unloading occurs before completion of forward transformation, the loading path with a slope of  $E(\xi)$  at the unloading point B' descends from the B' to D' on the diagonal line, and then points to E ( $\sigma_{AF}$ ) which imitates the inner reversal transformation process. This rule is the same in the reloading process before completion of reversal transformation.



(a) Constitutive model of SMA      (b) Diagonal rule assumption of inner hysteretic loop

Figure 1. Multi-linear constitutive model for SMAs.

### 2.2 Modelling of Axial Type SMA Damper

The axial-type SMA damper considered is shown in Figure 2(a) that two blocks (i.e., Part A and Part B) made of steel can slide past each other and two sets of austenite wire systems are kernel material in the damper. The two sets of austenite wire are tension only and react in reverse directions. Combined the two wires together, the corresponding analytical model of the damper is constructed shown as Figure 2(b).

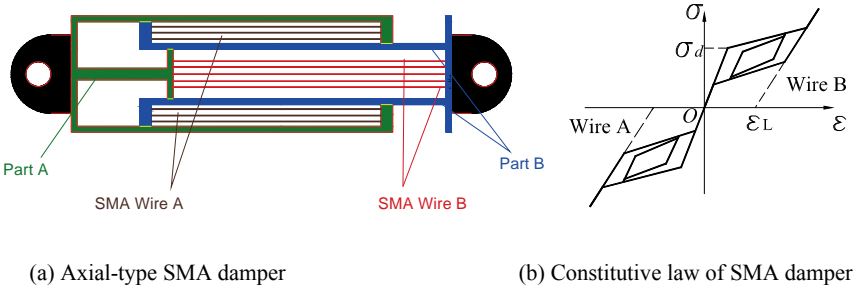


Figure 2. Prototype and stress-strain relationship of SMA damper.

### 3. Seismic Analysis and Results Discussion

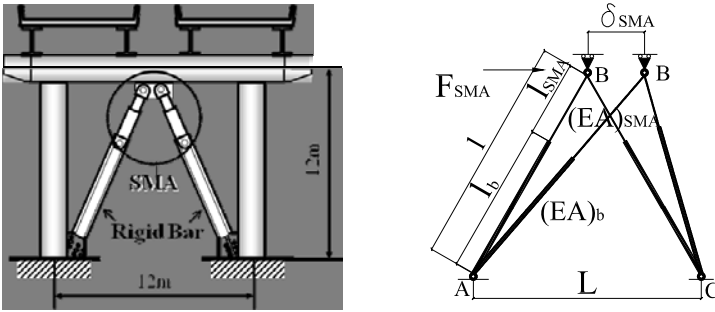
#### 3.1 Design Parameters of SMA Damper

A benchmark frame is a 12×12m square-shaped plane frame as shown in Figure 3(a). The main frame is made of SM490 steel grade and details of the bare frame can be found in a previous study (Chen, et al., 2007a). The SMA damping device consists of two SMA dampers and two steel braces, in which material constants of SMA given in the paper are employed as listed in Table 1. Steel braces are assumed to be rigid for simplicity. The yield shear force and top displacement of the bare main frame given in Table 2 are determined from a pushover analysis.

Three strong ground motions are considered in the analysis, which are recommended in the JRA code (2002), i.e., JRT-EW-M, JRT-NS-M and FUKIAI-M.

As in a previous study of controlled structures (Chen et al., 2007b), three design factors, i.e., the strength ratio  $\alpha_F$ , the stiffness ratio  $\alpha_K$  and the displacement ratio  $\alpha_\delta$ , were proposed as design governing parameters shown below:

$$\alpha_F = \frac{F_{y,d}}{F_{y,f}} \quad \alpha_k = \frac{K_{y,d}}{K_{y,f}} \quad \alpha_\delta = \frac{\delta_{y,d}}{\delta_{y,f}} \tag{1}$$



(a) Frame bridge pier with SMA dampers (b) Schematic diagram for SMA damping device

Figure 3. Multi-linear constitutive model for SMAs.

Table 1 SMA material constants

$E_A$ (GPa)	$E_M$ (GPa)	$\epsilon_L$	$T$ (°C)	$\sigma_{MSCR}$ (MPa)
70	30	0.05	40	100
$\sigma_{MS}$ (MPa)	$\sigma_{MF}$ (MPa)	$\sigma_{AS}$ (MPa)	$\sigma_{AF}$ (MPa)	$\sigma_{MFCR}$ (MPa)
235	325	210	100	170

Table 2 Basic information of the bare frame

Name	$M$ (kg)	$V_y$ (kN)	$\delta_{y,top}$ (m)
FA	2042	6758	0.078

Here,  $F_{y,d}$ ,  $K_{y,d}$  and  $\delta_{y,d}$  are yield strength, elastic stiffness and yield displacement of damping devices, respectively, while  $F_{y,f}$ ,  $K_{y,f}$  and  $\delta_{y,f}$  are those of main structures.

Geometric parameters and basic properties of the SMA damping device are illustrated in Figure 3(b), where  $l$  is the whole length of the damping devices,  $(EA)_{SMA}$  and  $l_{SMA}$  are stiffness and length of the SMA damper, respectively,  $(EA)_b$  and  $l_b$  are stiffness and length of the steel brace, respectively,  $F_{SMA}$ ,  $K_{SMA}$  and  $\delta_{SMA}$  are lateral yield force, elastic stiffness and displacement of the SMA damping devices, respectively.  $\alpha_L$  and  $\beta_L$  are taken as two scale factors on the length ratio and stiffness ratio between the steel brace component and SMA damper listed below:

$$l = l_{SMA} + l_b \quad \alpha_L = l_b / l_{SMA} \quad \beta_L = (EA)_b / (EA)_{SMA} \tag{2}$$

$$F_{SMA} = K_{SMA} \delta_{SMA} \tag{3}$$

$$K_{SMA} = A_{SMA} \cdot \frac{1}{C_1} \frac{E_{SMA} L^2}{l^3} \quad (4)$$

$$\delta_{SMA} = \frac{\sigma_{SMA}}{E_{SMA}} \frac{l^2}{L} C_1 \quad C_1 = \frac{2}{(1 + \alpha_L)} \left( 1 + \frac{\alpha_L}{\beta_L} \right) \quad (5)$$

$$F_{SMA} = \sigma_{SMA} A_{SMA} \frac{L}{l} \quad (6)$$

Parametric study examined here are the strength ratio  $\alpha_F$  and the stiffness ratio  $\alpha_K$  and the ranges of the parameters are listed as Table 3. For a given  $\alpha_F$  and  $\alpha_K$ , the area of SMA is obtained from equation (6), then the length of the damper can be calculated from equation (4) and (2).

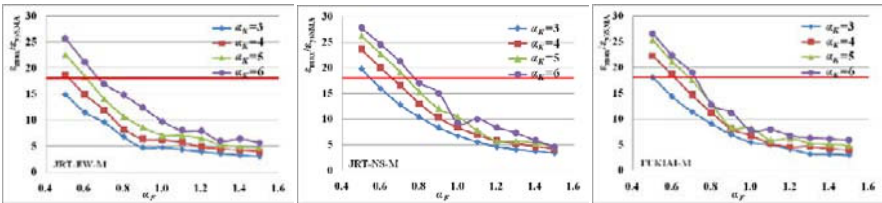
Table 3 Parameters for parametric study

Strength ratio $\alpha_F$	0.5, 0.6, 0.7, 0.8, 0.9, 1.0, 1.1, 1.2, 1.3, 1.4, 1.5
Stiffness ratio $\alpha_K$	3, 4, 5, 6

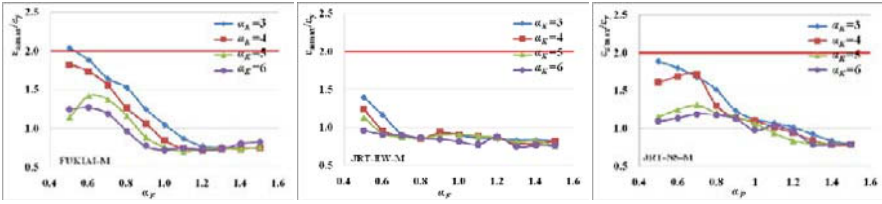
### 3.2 Parametric Study on Damage Control Design of SMA Dampers

The parameters  $\alpha_F$  and  $\alpha_K$  for parametric study are listed in Table 3. Three strong ground motions, i.e., JRT-EW-M, JRT-NS-M and FUKIAI-M, are used here. The strain of SMA dampers over  $\varepsilon_{MF}$ , which occurs after completion of phase transformation of SMA, is not expected because the stress in SMAs increases rapidly and no energy dissipates in the moment, so the  $\varepsilon_{MF}$  is defined as the capacity of SMA dampers. To satisfy the strain based performance level 2 (Usami et al. 2006), the average compressive strains of  $\varepsilon_{a)max} \leq 2.0\varepsilon_y$  at the base of piers are required and reactions are wished as small as possible in the design.

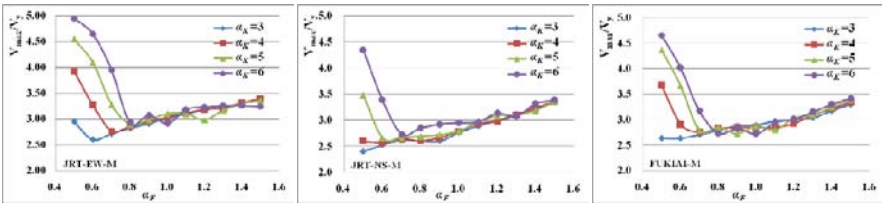
The response results are illustrated in Figure 4. Seismic performances are examined, which include average compressive strains at the base of piers, maximum strains in SMA dampers and maximum shear reactions, and their relationships are also investigated.



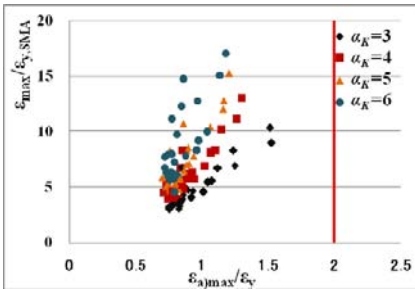
(a) Normalized maximum strain in SMA dampers



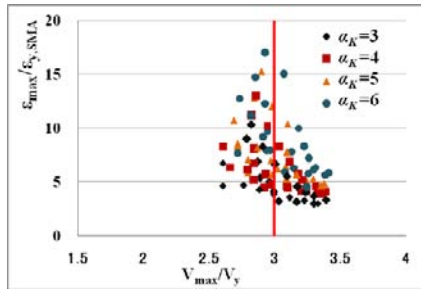
(b) Normalized average compressive strain at the base of piers



(c) Normalized maximum shear reactions



(d) SMA strain - main frame strain relationship



(e) SMA strain - shear reaction relationship

Figure 4. Seismic performance responses

In Figure 4(a), the horizontal line represents the capacity of SMA dampers, i.e.,  $\epsilon_{MF} = 18\epsilon_{y,SMA}$ , which is calculated from SMA material constants given in Table 1 and it is found that demands in all cases are below to the capacity when  $\alpha_F \geq 0.8$  and demands increase as  $\alpha_K$  is increased under three ground motions. In Figure 4(b), the vertical line represents the required performance level 2 of  $\epsilon_{a,max} \leq 2.0\epsilon_y$  and it is shown that all cases are satisfied the requirement and demands of  $\epsilon_{a,max}$  increase with the decrease of  $\alpha_K$ . Figure 4(c) shows that shear reactions decrease

from a high value to a relative low value when  $\alpha_F < 0.8$ , then increase gradually with the growth of  $\alpha_F$  and when  $\alpha_F \geq 0.8$ , no apparent influence on shear reactions is found with varied  $\alpha_K$ .

Shown in Figure 4(d) is the relationship between the strain of SMA dampers and average compressive strain at the base of piers when  $\alpha_F \geq 0.8$  and the vertical line represents the requirement of  $\varepsilon_{a)max} \leq 2.0\varepsilon_y$ . It is indicated that the requirement of  $\varepsilon_{a)max} \leq 2.0\varepsilon_y$  are satisfied in all cases within the range of the capacity of SMA dampers. It is also shown that the demand of  $\varepsilon_{a)max}$  increases with the decrease of  $\alpha_K$ . When  $\alpha_F \geq 0.8$ , the relationship between the strain of SMA dampers and shear reactions in the piers is shown in Figure 4(d) that the shear reactions are controlled in the range of  $2.5\text{-}3.5V_y$  with little influence on  $\alpha_K$ .

## 4. Conclusion

Based on the results in the parametric study, for the given SMA material,  $\alpha_F \geq 0.8$  is recommended for designing to satisfy the performance level 2 and the capacity of SMAs at the same time. Although a bigger  $\alpha_K$  improves the seismic performance, a small  $\alpha_K$  is still recommended not only for economic reasons but also for its relatively little influence on both average compressive strains and shear reactions at the base. A relatively small  $\alpha_F$  is also suggested to reduce shear reactions.

## Acknowledgements

The study was supported in part by grants from the Advanced Research Center for Seismic Experiments and Computations, Meijo University.

## References

- Chen Z. Y., Ge H. B., Kasai A. and Usami T. (2007). Simplified seismic design approach for steel portal frame piers with hysteretic dampers. *Earthquake Eng. and Struct. Dyn.*, 36(4):541-562.
- Chen Z. Y., Ge H. B. and Usami T. (2007). Study on seismic performance upgrading for steel bridge structures by introducing energy-dissipation members. *JSCE, J. of Structural Engineering*, 53(A):573-582.
- JRA (2002). Design specification of highway bridges. Part V: Seismic design. Japan Road Association, Tokyo, Japan [in Japanese].
- Usami T. ed. (2006). Guidelines for seismic and damage control design of steel bridges, *Japanese Society of Steel Construction*, Gihodo Shuppan, Tokyo, Japan [in Japanese].

*“This page left intentionally blank.”*

# Comparison Research of Three Vibration Control Plans on a Super-Tall Building with Connective Structure

Wang Dayang<sup>1\*</sup>, Zhou Yun<sup>1</sup> and Wang Lichang<sup>2</sup>

<sup>1</sup>Department of Civil Engineering of GuangZhou University, Guangzhou 510006, P.R. China

<sup>2</sup>Dalian Architectural Design & Research Institute Co., Ltd, Dalian 116021, P.R. China

**Abstract.** Vibration control of a super-tall frame-shell wall building with connective structure is studied in this paper. According to the natural characteristics of the structure, three kinds of vibration control plans with nonlinear viscous dampers are proposed to proceed vibration control in wind action. The fluctuating wind time-series of the structural forward and reverse Y-direction in 10-year frequency are simulated by improved AR model based on Fourier-transform. The structural dynamic responses of different control plans in wind action are studied, and corresponding vibration control effects are analyzed technically. The results show that the structural wind-induced vibration responses can be controlled effectively by the proposed three control plans, the maximum acceleration reduction of 39.2% can be achieved for point 319 of the top story and then structural comfort induced by wind action is improved greatly. Energy of about 30%-40% input by wind-induced vibration can be dissipated by viscous dampers. So, the effectivity and feasibility of nonlinear viscous dampers in reducing wind-induced vibration responses of high-rise or super-tall structures are fully proved.

**Key Words:** super-tall building with connective structure, AR mode, numerical simulation, wind induced vibration control, viscous damper

## 1 Engineering Survey

In this building, vacation service, fallow service, entertainment service, restaurant service and so on are offered. It has 4 stories underground and 31 stories over-ground. A high building and a low building are connected each other by y. The high building has 31 stories with height of 116.7m and the low building has 20 stories with height of 77.1m. The high building and the low building are designed as a whole under sixth story and then compartmentation from seventh story. Steel truss

---

\* Corresponding author, e-mail: wadaya2006@yahoo.com.cn

is adopted as connective body between the high and low buildings. Frame-shear wall system is adopted and all shear walls are installed in both ends of the structure. The structural three-dimensional model is shown in Figure 1. The plan sketch, axis number and nodal number are shown in Figure 2.

This building located in coastal city and on the east coast of Bohai. According to the code of "port engineering load code (Jt215-98)", the wind pressure in 30-year frequency is  $0.75\text{kN/m}^2$ , which can be transformed to be  $0.62\text{kN/m}^2$  in 10-year frequency. The peak acceleration of the top story of the high building exceeds the limited-value demand of "Technical Specification for Concrete Structures of Tall Building (JGJ3-2002)" according to the tentative calculation. So, nonlinear viscous damper are used to control the responses induced by wind action so as to improve comfort and then meet the demands of both building owner and the code.

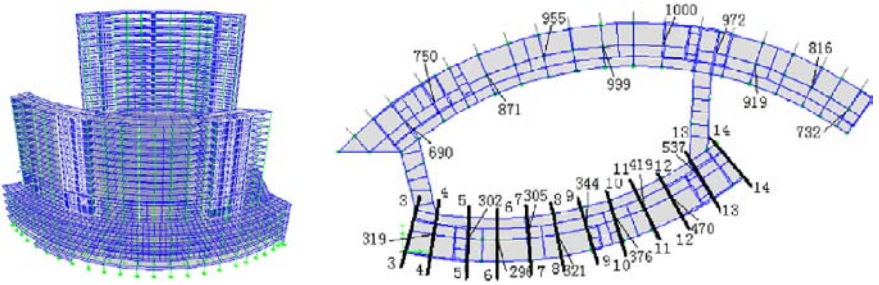


Figure 1. Three dimensional mode figure Figure 2. Plan sketch, axis number and nodal number

## 2 Plan Design of Structural Vibration Control

The Y-direction peak acceleration of upper stories of the high building, except X-direction of the high building and both X-direction and Y-direction of the low building, exceeds the demand of structural comfort according to the tentative calculation. So, vibration control plans are designed mainly to reduce the Y-direction structural responses of the high building induced by wind action. According to natural characteristics of the structure and economical and effective principle, three kinds of vibration control plans are proposed in this paper:

Plan A: Diagonal viscous damping braces (namely viscous damper are installed in diagonal brace) are installed in structural axis 6-6 and axis 11-11. The installation sketch of diagonal viscous damping brace is shown in Figure 3. The installation place is shown in Figure 4(a). 19 nonlinear viscous dampers are installed in axis 6-6 and axis 11-11 separately and 38 dampers in the whole building. The basic parameters of the selected nonlinear viscous damper are list as follows: damping coefficient-300kNs/mm, damping index-0.4, maximum damping force-500kN, stroke- $\pm 50\text{mm}$ , maximum working velocity-350mm/s.

Plan B: Diagonal viscous damping braces are installed in structural axis 6-6, axis 7-7, axis 8-8, axis 10-10 and axis 11-11. The installation location of diagonal viscous damping brace is shown in Figure 4(b). 7 nonlinear viscous dampers are installed in each axis and 35 dampers in the whole building. The basic parameters of viscous damper are same as plan A.

Plan C: Diagonal viscous damping braces are installed in structural axis 6-6, axis 7-7, axis 10-10 and axis 11-11. The installation location of diagonal viscous damping brace is shown in Figure 4(c). 10 nonlinear viscous dampers are installed in each axis and 40 dampers in the whole building. The basic parameters of viscous damper are same as plan A.

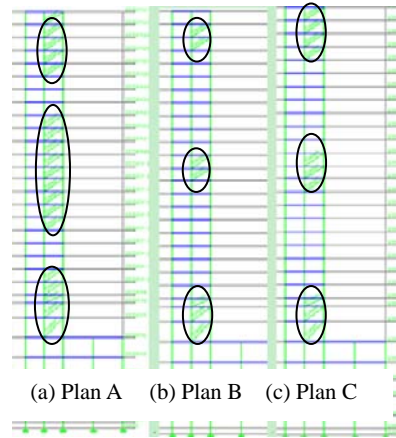
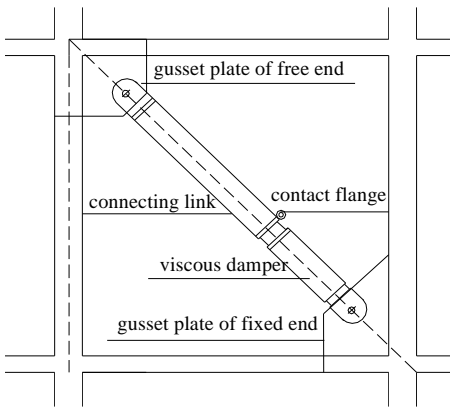


Figure 3. Installation sketch of damping brace

Figure 4. Installation place of damping brace

### 3 Numerical Simulation of Fluctuating Wind Field

Based on the research results (Zhou, 2009), fluctuating wind speed of the structure is simulated by modified AR model (Spanos, 1998; Shinozuka, 1996; Deodatis 1996) using. Darvenport power spectrum is adopted to simulating fluctuating wind speed time-series. Basic parameters of simulating fluctuating wind speed time-series are shown in Table 1. 68 points of the structure are selected as simulation points and their wind speed time-series were then simulated in 0.62kN/m<sup>2</sup> wind pressure. Fluctuating wind speed curves and power-spectrum density figures of forward Y-direction of the 31th story are shown in Figure 5. It can be shown that the fitness of the power-spectrum in median-high frequency is very good and the fitness zone covers the basis frequency of the structure, which verifies that AR model based on is believable and effective to simulate fluctuating wind speed time-series of the super-tall building. So, the validity of using the simulated fluc-

tuating wind to proceed structural analysis and design can be approved by researchers or engineers.

Table 1. Basic parameters of simulating wind speed time-series

Field type	Roughness exponent	Wind pressure	AR model order	Total time	Step
A	0.12	0.62 kN/m	5	600s	0.1s

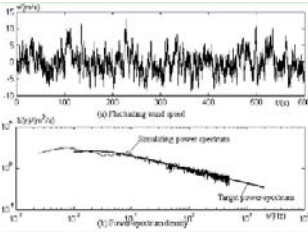


Figure 5. Fluctuating wind speed and power-spectrum density of the 31th story

### 4 Contrast Analysis of Structural Vibration Control Plans

Three-dimensional finite element mode of the super-tall building with connective structure is built by Etabs9.2.0. Shell element, membrane element, bar element are adopted in shear wall, floor, beam-column separately. 21 modes are selected in the structure to proceed mode analysis and results show that mode participation quality exceeds the limit of 90% structural quality. The former 6 periods and mode descriptions of the structure are shown in Table 2. Translation phenomenon is shown in both the first mode and the second mode. Torsion phenomenon is shown in the third mode. The ratio of the first translation period and the first torsion period is less than 0.9, which shows that the torsion effect of the structure is very little.

Table 2. The former 6 periods and mode descriptions of the structure

Mode	1	2	3	4	5	6
Period/s	1.86	1.53	1.16	0.87	0.82	0.75
Mode description	Translation Y-direction	Translation X-direction	Torsion	Translation Y-direction	Translation X-direction	Torsion

Contrasts of inter-story displacement angle in different control plans in forward Y-direction are shown in Figure 6 ("HWIND" means action of fluctuating wind, "JLWIND" means action of static wind, "SUM" means total action of fluctuating and static winds). Contrasts of peak acceleration of point 296 and point 419 in wind action of forward Y-direction are shown in Figure 7. Contrasts of peak ac-

celeration of the top story for the selected points in wind action of forward Y-direction are shown in Figure 8. Contrasts of peak acceleration and vibration control effect of the top story for the selected points in wind action of reverse Y-direction are shown in Table 3. Some results can be obtained: ① Structural story-acceleration increase gradually with height and appear obvious saltation for the structure without control plans. The saltation amplitude of upper stories is greater than lower stories. So, the key factor of reducing wind responses of the structure is to control the greater saltation amplitude of upper stories. ② Relative to the structure without control plans, inter-story displacement angle and story-acceleration of the structure with plans A, B and C have obvious reduction and the change curves of story-acceleration along structural height become continuous and well-proportioned. ③ Wind-induced vibration comfort of the structure is limited strictly. The top peak accelerations of plans A, B and C are all less than the limited value of 0.15m/s<sup>2</sup>. For example, the top peak acceleration in wind action of reverse Y-direction is reduced from 0.209m/s<sup>2</sup> to 0.127m/s<sup>2</sup> and its vibration control efficiency is 39.2%. ④ Structural inter-story displacement angles in wind action for all plans are less than the limited value of 1/800 and the inter-story displacement angles of the three control plans are less than that of the without control plan.

Structural energy figure of plan B is shown in Figure 9. The total energy input by wind-induced vibration increases almost linearly with time, which is coincident with the original assumption of simulating fluctuating wind field "wind load is zero mean stationary white noise" (Wang 2008). 30%-40% energy dissipation can be reached by dampers in plan B, which means that dampers in the structure have great capacity of dissipating energy input by wind and then structural comfort in wind-induced vibration will be improved effectively.

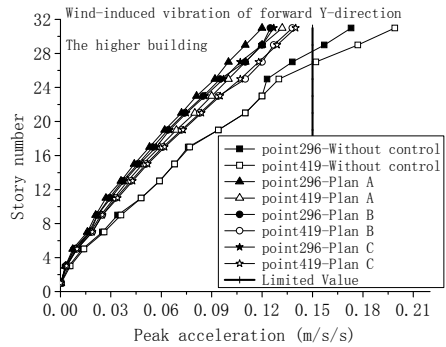
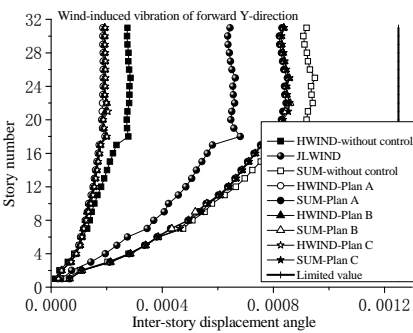


Figure 6. Contrast of inter-story displacement angle      Figure 7. Contrast of peak acceleration

Table 3. Contrast of peak acceleration and vibration control effect of the top story

Point	319	302	296	305	321	344	376	419	470	537
Without control	0.209	0.194	0.196	0.196	0.205	0.214	0.213	0.212	0.211	0.21
Plan A	0.127	0.131	0.134	0.137	0.139	0.142	0.143	0.145	0.146	0.142
Control effect/%	39.2	32.5	31.6	30.1	32.2	33.6	32.9	31.6	30.8	32.4
Plan B	0.133	0.137	0.14	0.143	0.146	0.149	0.15	0.15	0.15	0.149
Control effect/%	36.4	29.4	28.6	27	28.8	30.4	29.6	29.2	28.9	29
Plan C	0.131	0.135	0.138	0.141	0.144	0.146	0.148	0.15	0.15	0.148
Control effect/%	37.3	30.4	29.6	28.1	29.8	31.8	30.5	28.9	28.9	29.5

### 5 Conclusions

According to the comparison research of the proposed control plans on the super-tall building. Some reasonable conclusions can be obtained as follows:

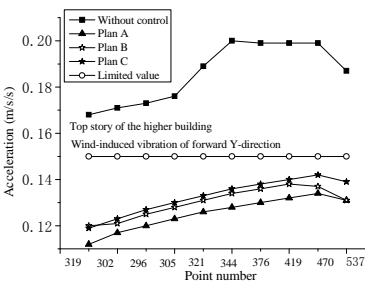


Figure 8. Contrast of peak acceleration

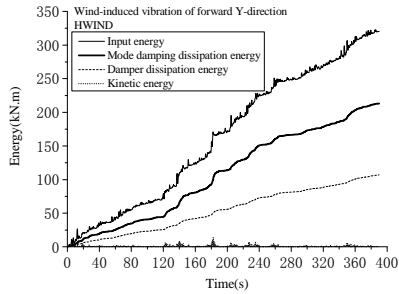


Figure 9. Structural energy figure of plan B

1. AR model modified by is believable and effective to simulate fluctuating wind field of the building and the validity of using the simulated fluctuating wind to proceed structural analysis and design can be approved by researchers or engineers.
2. Structural responses of the connective building induced by wind can be controlled effectively by the three proposed control plans. Energy of about 30%-40% input by wind-induced vibration can be dissipated by viscous dampers.
3. Viscous damper is an effective and feasible devices to reduce structural vibration responses of high-rise or super-tall buildings. Energy input by wind-induced vibration can be dissipated, structural responses induced by wind-induced vibration can be reduced and then structural comfort and reliability can be improved in some certain extent.

## Acknowledgments

This project was granted financial support from Doctor Special Fund Project of Higher School (200810780001) and Team Project of Natural Science Foundation of Guangdong Province (8351009101000001)

## References

- Deodatis G. (1996). Simulation of ergodic multivariate stochastic process. *Journal of Engineering Mechanics, ASCE*, 122(3): 778-787.
- Port Engineering Load Code (Jt215-98) (1998). Beijing: China Communications Press.
- Shinozuka M., Deodatis G. (1996). Simulation of multi-dimensional Gaussian stochastic fields by spectral representation. *Applied Mechanics Review*, 49(1): 29-53.
- Spanos P.D., Zeldin B.A. (1998). Monte Carlo treatment of random fields: Abroad perspective. *Applied Mechanics Review*, 51(3): 219-237.
- Technical Specification for Concrete Structures of Tall Building (JGJ3-2002) [S]. Beijing: China Architecture & Building Press.
- Wang D.Y., Zhou Y., Deng X.S. (2008). Numerical simulation of fluctuating wind field for high-rise buildings considering spatial correlation. *Proceedings of the Tenth International Symposium on Structural Engineering for Young Experts*, Chang Sha, China [in Chinese].
- Zhou Y., Wang D.Y., Deng X.S., et al (2009). Comparison research of three control plans for wind-induced vibration on a super high-rise building. *Journal of Vibration and Shock*, 28(2): 18-23 [in Chinese].

*“This page left intentionally blank.”*

# Amplitude Control of Limit Cycle in Coupled Van Der Pol System

Han Xiao<sup>1\*</sup>, Jiashi Tang<sup>2</sup> and Jianmin Wang<sup>1</sup>

<sup>1</sup> Faculty of Architectural Civil Engineering and Environment, Ningbo University, Ningbo 315211, China

<sup>2</sup> College of mechanics and aerospace, Hunan University, Changsha 410082, China

**Abstract.** To control the amplitude of limit cycle of coupled van der Pol systems, the feedback controllers are designed, the control equations of weakly nonlinear systems are obtained by using the approximate method and the relationship between the amplitude of limit cycle and the control parameter is acquired, hence amplitude of limit cycle can be controlled effectively. The method may also be applied to other coupled van der Pol systems. On some systems, it is difficult to find the function in the amplitude of limit cycle and the control parameter directly. By means of the numerical analysis, we can design effective controllers; therefore can preferably control the amplitude of limit cycle of coupled van der Pol systems.

**Keywords:** coupled van der Pol system, limit cycle, amplitude, feedback controller

## 1 Introduction

Chaos and bifurcation control have caused great interests in recent nonlinear scientific researches (Chen, Moiola et al. 2000). The present interest on bifurcation control is to design a controller to transform the bifurcation behavior of a given nonlinear system into the desirable one (Nayfeh, Harb et al, 1996; Moiola, Berns et al. 1997). The typical bifurcation control can be classified as: defer the bifurcation point, change the bifurcation-chain type, control the amplitude, frequency of a limit cycle, optimize the dynamic behavior around the bifurcation points, etc (Maccari, 2003; Mickens, 2003; Tang, Fu et al., 2002). The main purpose of bifurcation control in engineering is to avoid

Harmful behavior brought by the bifurcation to the system, and so to monitor the system. In bifurcation study, Hopf bifurcation is an important dynamic bifurcation. Van der Pol oscillator is a famous self-oscillates system which first ap-

---

\* Corresponding author, e-mail: xiaohan@nbu.edu.cn

peared in nonlinear electro circuit and had been widely discovered in mechanic, biology, chemistry and so on. The previous researches on van der Pol system mainly concentrated in finding the approximate solutions and numerical solutions in a van der Pol oscillator or a coupled van der Pol system, to analyze the existence of limit cycle and together its stability (Ricardo, 2004; Mickens, Gumel, 2002). The passage mainly concerned on controlling the amplitude of a coupled van der Pol system. This is of great value not only in the theory of bifurcation control but the application (Tang, Chen, 2006).

The following coupled van der Pol system is modeled by differential equations as:

$$\left. \begin{aligned} \ddot{x} + \omega_1^2 x - \varepsilon \alpha_1 (1 - x^2) \dot{x} - \varepsilon \beta_1 x (\eta_1 x^2 + y^2) &= 0 \\ \ddot{y} + \omega_2^2 y - \varepsilon \alpha_2 (1 - y^2) \dot{y} - \varepsilon \beta_2 y (x^2 + \eta_2 y^2) &= 0 \end{aligned} \right\} \tag{1}$$

This system has limit cycle in phase plane, and the amplitude of limit circle can be controlled.

## 2 Amplitude Control of Limit Circle in System (1)

To monitor the amplitude of limit circle of system (1), a feedback controller  $u_i(x, \dot{x}, y, \dot{y})$  ( $i = 1, 2$ ) is needed to be designed. And this controller should not like to change the location of balancing point and bifurcation point. Thus the uncontrolled (1) turned into a controlled system:

$$\left. \begin{aligned} \ddot{x} + \omega_1^2 x - \varepsilon \alpha_1 (1 - x^2) \dot{x} - \varepsilon \beta_1 x (\eta_1 x^2 + y^2) &= u_1(x, \dot{x}, y, \dot{y}) \\ \ddot{y} + \omega_2^2 y - \varepsilon \alpha_2 (1 - y^2) \dot{y} - \varepsilon \beta_2 y (x^2 + \eta_2 y^2) &= u_2(x, \dot{x}, y, \dot{y}) \end{aligned} \right\} \tag{2}$$

The controller can be a linear one or nonlinear one, and among those nonlinear ones, there are quadratic ones and cubic ones. After tried several kind of controllers, the final controller was decided as:

$u_1(x, \dot{x}, y, \dot{y}) = \varepsilon k_1 y^2 \dot{x}$ ,  $u_2(x, \dot{x}, y, \dot{y}) = \varepsilon k_2 x^2 \dot{y}$ , the  $k_1, k_2$  are the control parameters. Hence the original system became

$$\left. \begin{aligned} \ddot{x} + \omega_1^2 x - \varepsilon \alpha_1 (1 - x^2) \dot{x} - \varepsilon \beta_1 x (\eta_1 x^2 + y^2) &= \varepsilon k_1 y^2 \dot{x} \\ \ddot{y} + \omega_2^2 y - \varepsilon \alpha_2 (1 - y^2) \dot{y} - \varepsilon \beta_2 y (x^2 + \eta_2 y^2) &= \varepsilon k_2 x^2 \dot{y} \end{aligned} \right\} \tag{3}$$

If  $\varepsilon$  is a small positive parameter ( $\varepsilon \ll 1$ ), we can find the first-order approximate solution of Equation (3) by using the method of multiple scales, pertur-

bation equations could be gotten with two time-scale  $T_i = \varepsilon^i t$  ( $i = 0, 1$ ) listed as below

$$\left. \begin{aligned} D_0^2 x_0 + \omega_1^2 x_0 &= 0 \\ D_0^2 y_0 + \omega_2^2 y_0 &= 0 \end{aligned} \right\} \tag{4}$$

$$\left. \begin{aligned} D_0^2 x_1 + \omega_1^2 x_1 &= -2D_0 D_1 x_0 + \alpha_1(1 - x_0^2) D_0 x_0 + \beta_1 x_0(\eta_1 x_0^2 + y_0^2) + k_1 y_0^2 D_0 x_0 \\ D_0^2 y_1 + \omega_2^2 y_1 &= -2D_0 D_1 y_0 + \alpha_2(1 - y_0^2) D_0 y_0 + \beta_2 y_0(x_0^2 + \eta_2 y_0^2) + k_2 x_0^2 D_0 y_0 \end{aligned} \right\} \tag{5}$$

The solution of Equation (4) is

$$\left. \begin{aligned} x_0 &= A_1(T_1)e^{i\omega_1 T_0} + \bar{A}_1(T_1)e^{-i\omega_1 T_0} \\ y_0 &= A_2(T_1)e^{i\omega_2 T_0} + \bar{A}_2(T_1)e^{-i\omega_2 T_0} \end{aligned} \right\} \tag{6}$$

After substitute Equation (6) into Equation (5)

$$\left. \begin{aligned} D_0^2 x_1 + \omega_1^2 x_1 &= (-2i\omega_1 A_1' + i\omega_1 \alpha_1 A_1 - i\omega_1 \alpha_1 A_1^2 \bar{A}_1 + 3\beta_1 \eta_1 A_1^2 \bar{A}_1 + \\ & 2\beta_1 A_1 A_2 \bar{A}_2 + 2i\omega_1 k_1 A_1 A_2 \bar{A}_2) e^{i\omega_1 T_0} + (\beta_1 \eta_1 - i\omega_1 \alpha_1) A_1^3 e^{3i\omega_1 T_0} + (\beta_1 + \\ & i\omega_1 k_1) A_1 A_2^2 e^{i(\omega_1 + 2\omega_2) T_0} + (\beta_1 - i\omega_1 k_1) \bar{A}_1 A_2^2 e^{i(2\omega_2 - \omega_1) T_0} + cc \\ D_0^2 y_1 + \omega_2^2 y_1 &= (-2i\omega_2 A_2' + i\omega_2 \alpha_2 A_2 - i\omega_2 \alpha_2 A_2^2 \bar{A}_2 + 3\beta_2 \eta_2 A_2^2 \bar{A}_2 + \\ & 2\beta_2 A_1 \bar{A}_1 A_2 + 2i\omega_2 k_2 A_1 \bar{A}_1 A_2) e^{i\omega_2 T_0} + (\beta_2 \eta_2 - i\omega_2 \alpha_2) A_2^3 e^{3i\omega_2 T_0} + (\beta_2 + \\ & i\omega_2 k_2) A_1^2 A_2 e^{i(2\omega_1 + \omega_2) T_0} + (\beta_2 - i\omega_2 k_2) A_1^2 \bar{A}_2 e^{i(2\omega_1 - \omega_2) T_0} + cc \end{aligned} \right\} \tag{7}$$

Consider the resonance happened when  $\omega_1 \approx \omega_2$ , suppose that

$$\left. \begin{aligned} (2\omega_2 - \omega_1)T_0 &= \omega_1 T_0 + 2\sigma T_1 \\ (2\omega_1 - \omega_2)T_0 &= \omega_2 T_0 - 2\sigma T_1 \end{aligned} \right\} \tag{8}$$

Using the way of eliminating secular terms, the following equations could be inclined

$$\left. \begin{aligned} & -2i\omega_1 A_1' + i\omega_1 \alpha_1 A_1 - i\omega_1 \alpha_1 A_1^2 \bar{A}_1 + 3\beta_1 \eta_1 A_1^2 \bar{A}_1 + 2\beta_1 A_1 A_2 \bar{A}_2 + \\ & \quad 2i\omega_1 k_1 A_1 A_2 \bar{A}_2 + (\beta_1 - i\omega_1 k_1) \bar{A}_1 A_2^2 e^{2i\sigma T_1} = 0 \\ & -2i\omega_2 A_2' + i\omega_2 \alpha_2 A_2 - i\omega_2 \alpha_2 A_2^2 \bar{A}_2 + 3\beta_2 \eta_2 A_2^2 \bar{A}_2 + 2\beta_2 A_1 A_2 \bar{A}_2 + \\ & \quad 2i\omega_2 k_2 A_1 \bar{A}_1 A_2 + (\beta_2 - i\omega_2 k_2) A_1^2 \bar{A}_2 e^{-2i\sigma T_1} = 0 \end{aligned} \right\} \tag{9}$$

Let  $A_1 = \frac{1}{2} a_1(T_1) e^{i\theta_1(T_1)}$ ,  $A_2 = \frac{1}{2} a_2(T_1) e^{i\theta_2(T_1)}$ ,  $\varphi = 2(\theta_2 - \theta_1 + \sigma T_1)$ , and it can be defined that  $\theta_2 - \theta_1 = \varphi - \sigma T_1$ ,  $\theta_2 - \theta_1 + 2\sigma T_1 = \varphi + \sigma T_1$ . Hence Equation (9) can be simplified into:

$$\left. \begin{aligned} & -\omega_1 a_1' + \frac{1}{2} \alpha_1 \omega_1 a_1 - \frac{1}{8} \alpha_1 \omega_1 a_1^3 + \frac{1}{4} \omega_1 k_1 a_1 a_2^2 - \frac{1}{8} \omega_1 k_1 a_1 a_2^2 \cos \varphi + \\ & \quad \frac{1}{8} \beta_1 a_1 a_2^2 \sin \varphi = 0 \\ & \omega_1 a_1 \theta_1' + \frac{3}{8} \beta_1 \eta_1 a_1^3 + \frac{1}{4} \beta_1 a_1 a_2^2 + \frac{1}{8} \beta_1 a_1 a_2^2 \cos \varphi + \frac{1}{8} \omega_1 k_1 a_1 a_2^2 \sin \varphi = 0 \\ & -\omega_2 a_2' + \frac{1}{2} \alpha_2 \omega_2 a_2 - \frac{1}{8} \alpha_2 \omega_2 a_2^3 + \frac{1}{4} \omega_2 k_2 a_1^2 a_2 - \frac{1}{8} \omega_2 k_2 a_1^2 a_2 \cos \varphi - \\ & \quad \frac{1}{8} \beta_2 a_1^2 a_2 \sin \varphi = 0 \\ & \omega_2 a_2 \theta_2' + \frac{3}{8} \beta_2 \eta_2 a_2^3 + \frac{1}{4} \beta_2 a_1^2 a_2 + \frac{1}{8} \beta_2 a_1^2 a_2 \cos \varphi - \frac{1}{8} \omega_2 k_2 a_1^2 a_2 \sin \varphi = 0 \end{aligned} \right\} \tag{10}$$

Suggest that the system has a stable solution, we have  $a_1' = a_2' = \varphi' = 0$ , thus Equation(10) is changed into the following equation:

$$\left. \begin{aligned} & 4\alpha_1 \omega_1 - \alpha_1 \omega_1 a_1^2 + 2\omega_1 k_1 a_2^2 - \omega_1 k_1 a_2^2 \cos \varphi + \beta_1 a_2^2 \sin \varphi = 0 \\ & 4\alpha_2 \omega_2 - \alpha_2 \omega_2 a_2^2 + 2\omega_2 k_2 a_1^2 - \omega_2 k_2 a_1^2 \cos \varphi - \beta_2 a_1^2 \sin \varphi = 0 \\ & 3\omega_2 \beta_1 a_1^2 - 3\omega_1 \beta_2 a_2^2 + 2\omega_2 \beta_1 a_2^2 - 2\omega_1 \beta_2 a_1^2 + (\omega_2 \beta_1 a_2^2 - \\ & \quad \omega_1 \beta_2 a_1^2) \cos \varphi + \omega_1 \omega_2 (k_1 a_2^2 + k_2 a_1^2) \sin \varphi + 8\omega_1 \omega_2 \sigma = 0 \end{aligned} \right\} \tag{11}$$

The above-mentioned equation implied the relationship between the control parameters  $k_1, k_2$  and the amplitudes of system limit cycle  $a_1, a_2$ . If we modify the parameters of the uncontrolled system (1) and controlled system (2) as:  $\varepsilon = 1, \alpha_1 = \alpha_2 = 1, \omega_1 = \omega_2 = 1.0, \beta_1 = \beta_2 = 0.5, \eta_1 = 0.2, \eta_2 = 0.5$ , by using Equation (11), we get these data for  $k_1, k_2, a_1, a_2$  and  $\varphi$ , and the  $k - a$  curve is shown in Figure 1 and Figure 2, the real line indicates Analytical relationship, while the dot line indicates the numerical one:

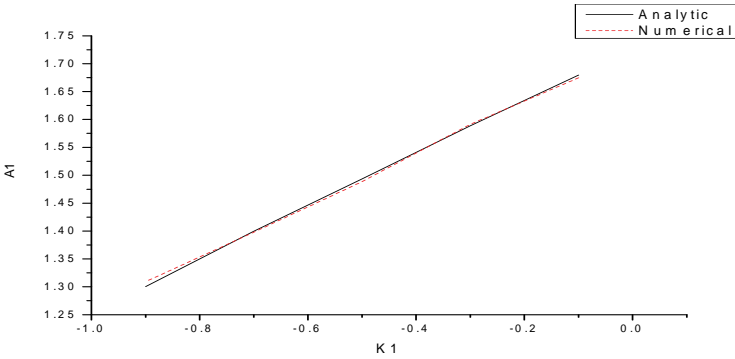


Figure 1. Relationship between control parameter  $k_1$  and amplitude  $a_1$

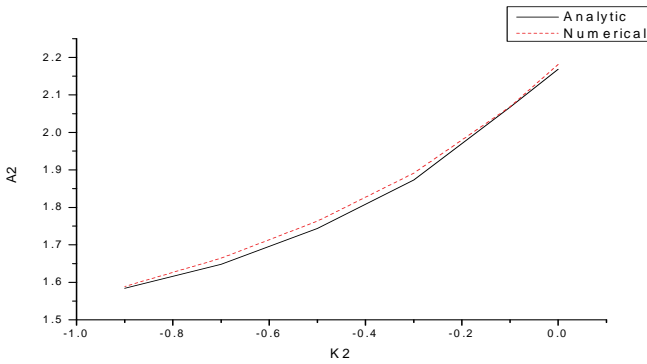


Figure 2. Relationship between control parameter  $k_2$  and amplitude  $a_2$

The controller can also be designed as other nonlinear forms such as:  $u_1(x, \dot{x}, y, \dot{y}) = \varepsilon k_1 (x^2 \dot{y} + y^2 \dot{x})$ ,  $u_2(x, \dot{x}, y, \dot{y}) = \varepsilon k_2 (x^2 \dot{y} + y^2 \dot{x})$ , experiments show that each has well effect, and with high degree of accuracy.

### 3 Conclusions

For coupled van der Pol system, the amplitude of limit cycle can be controlled by designing an appropriate feedback controller. And for some weakly nonlinearity, the relationship between control parameter and amplitude of limit cycle could be obtained by using the approximate method, and this controlling equation can con-

control amplitude of limit cycle effectively. This method can be generalized to other coupled van der Pol systems. To get that relationship, numerical analysis, designing the controller, set appropriate control parameters are needed. To strongly nonlinear systems, the amplitude of limit cycle can also be controlled by designing proper controllers. That would be left to discuss later.

## Acknowledgements

The project supported by the National Science Foundation of China (10672053).

## References

- Chen G.R., Moiola J. L. et al. (2000). Bifurcation control: Theories, methods, and applications. *Int. J. Bifurcation and Chaos*, 10(3): 511-548.
- Moiola J.L., Berns D.W. et al. (1997). Feedback control of limit cycle amplitudes. *Proc. IEEE Conf. Decis. Contr.*, San Diego, CA, 1479-1485.
- Maccari A. (2003). Vibration control for the primary resonance of the van der Pol oscillator by a time delay state feedback. *Int. J. Non-Linear Mechanics*, 38: 123-131.
- Mickens R.E., Gumel A.B. (2002). Numerical study of a non-standard finite-difference scheme for the van der Pol equation. *Journal of Sound and Vibration*, 250(5): 955-963.
- Mickens R.E. (2003). Fractional van der Pol equations. *Journal of Sound and Vibration*, 259(2): 457-460.
- Nayfeh A.H., Harb A.M. et al. (1996). Bifurcations in a power system model. *Int. J. Bifurcation and Chaos*, 6(3): 497-512.
- Qian C.Z., Tang J.S. (2006). Asymptotic solution for a kind of boundary layer problem. *Nonlinear Dynamics*, 45(1-2): 15-24.
- Ricardo L.R. (2004). Symmetry induced oscillations in four-dimensional models deriving from the van der Pol equation. *Chaos, Solitons & Fractals*, 21(1): 55-61.
- Tang J.S. (2000). A method for parameter identification of strongly nonlinear systems. *Journal of Sound and Vibration*, 232(5): 993-996.
- Tang J.S., Fu W.B. et al. (2002). Bifurcations of a parametrically excited oscillator with strong nonlinearity. *Chinese Physics*, 11(10): 1004-1007.
- Tang J.S., Qian C.Z. (2003). The asymptotic solution of the strongly nonlinear Klein-Gordon equation. *Journal of Sound and Vibration*, 268(5): 1036-1040.
- Tang J.S., Liu Z.Y. (2004). The quasi wavelet solution of diffusion problems. *Communications in Numerical Methods in Engineering*, 20(12): 877-888.
- Tang J.S., Chen Z.L. (2006). Amplitude control of limit cycle in van der Pol system. *International Journal Bifurcation and Chaos*, 16(2): 487-495.
- Tang J.S., Qin J.Q. et al. (2007). Bifurcations of a generalized van der Pol oscillator with strong nonlinearity. *Journal of Sound and Vibration*, 306: 890-896.

# Structural Form Intelligent Optimization and Its Data Mining Methods

Shihai Zhang<sup>1,2</sup>, Shujun Liu<sup>2\*</sup>, Jinping Ou<sup>1</sup> and Guangyuan Wang<sup>1</sup>

<sup>1</sup>School of Civil Engineering, Harbin Institute of Technology, Harbin 150090, China

<sup>2</sup>Department of Civil Engineering, Nanyang Institute of Technology, Nanyang 473004, China

**Abstract.** Firstly, we introduced the structural form intelligent optimization (SFIO) basic theory and the methodological framework including the alternative scheme intelligent producing and innovative, intelligent evaluation, intelligent optimization selection and decision-making, knowledge automatic access, intelligent means, laying a foundation for farther study the SFIO theories and methods. Secondly, we gave a more comprehensive overview of DM techniques in SFIO, the important research results and the latest research progress such as Apriori-based, Bayes-based, ID3-based, NN-based, GA-based, RS-based and fuzzy RS-based algorithm, and their characteristics. These methods can mine FO knowledge from a different perspective, and possess a better complementary. This paper gives more comprehensive overview of the data mining technology in the SFIO.

**Keywords:** building structure, intelligent form optimization, knowledge discovery, data mining

## 1 Introduction

Structural optimization can be divided into size optimization, shape optimization, topology (or layout) optimization and form optimization (FO) (Sun, 2002). At present, the study of structure parameter optimization has been mature, and there are many researches already concerning topology and shape optimization (Chai et al., 1999; Luo, 2004; Wang, 1997; Yang, 1999; Guo, 2007), but there are few reports concerning the study of the structural FO design (Zhang, 2003; Xing et al., 2003; Zhang et al., 2006; Zhang et al., 2005; Zhang et al., 2006). FO is the optimization of the most difficult, the most obvious benefits, the most challenging, and cry for strengthening research.

FO is a multi-target, multi-variable, multi-constrained, multi-schemes, multi-solutions and knowledge-intensive integrated intelligent optimization problem, but

---

\* Corresponding author, e-mail: lsj.6290@163.com

also a structural problem with uncertain information, inaccurate, incomplete or limited data, etc. Intelligent design is its development direction and knowledge acquisition is the “bottleneck”. This paper will first briefly introduce the basic theory and the methodological framework of the SFIO, and then sum up the latest research progress of the data mining method and knowledge acquisition in SFIO utilizing in the field of high rise building structure.

## **2 The Basic Theory and the Methodological Framework of the SFIO**

### ***2.1 The Structure of the Basic Theory and the Methodological Framework***

The basic theoretical framework of SFIO mainly composes by the five components: the intelligent producing and innovative theory of the alternative scheme, the intelligent performance evaluation theory of the alternative scheme, the intelligent optimization theory of the alternative scheme, knowledge intelligent acquisition theory, and intelligent support system theory. The above five theoretical framework also includes many of the specific methods to solve the problem; intelligent support system is a tool and means for achieving these methods

### ***2.2 The Intelligent Producing and Innovative Theory and Method of the Alternative Scheme***

For a certain structural scheme, we can often adopt a variety of structure forms. In the process of the structural form optimization design, first of all, we can form or innovate some feasible alternative scheme according to the needs of the consumers and the constraints of the construction and get the alternative scheme set  $u = \{u_i\}_n$ , such laying a foundation for the evaluation and optimal selection. The process of producing  $u$  is a multi-scheme based on multi-target, multi-functional, multi-constrained and this process is a complex creating process with the function of judgment, association, synthesis and decision-making. This theory and methodology include: needs analysis, structural classification, the intelligent production and innovation theory and method of the alternative scheme.

The intelligent production method of the alternative scheme based on RBR, CBR and KDD were presented (Zhang, 2003). The above method integrates the technology and method of pattern identification, fuzzy logic, neural network and GA, synthesizes utilizing expert intelligence, computing intelligence and machine intelligence. The methods are better complementary, and will also be opened to

use different knowledge to reflect the needs and the relationship between the structures. Those have provided a new theory and method for the various types of structural form option, discovery and innovation.

### ***2.3 The Intelligent Performance Evaluation Theory and Method***

After ascertaining the alternative schemes, it will take from a different side of the performance of the schemes to make a comprehensive scientific evaluation in order to provide a reliable scientific basis for scheme optimal selection. The performance intelligent evaluation theory and methods including: performance evaluation process and problem solving strategies, performance index system programming, performance weight ascertaining, evaluation grade, evaluation standard, single performance evaluation, comprehensive performance evaluation theory and methods, etc.. We presented the theory and methodological framework of the SFIO based on improved FIS, FINS and NN by Zhang (2003).

### ***2.4 The Intelligent Optimal Selection Theory and Method***

After evaluating the alternative schemes, we can use experts' experience accumulated in the long-term practice of optimal structural design to select the satisfying scheme. It is a key problem to reducing blindness, improving reliability and effectiveness in constructing appropriate intelligent optimization theory and methods. Intelligent optimization theory and methods include: optimal selection process, method, strategy and means. We presented four intelligent optimal methods such as FIS, FINS and NN etc. in (Zhang et al., 2002).

### ***2.5 The Theory and Method of Knowledge Intelligent Acquisition***

The new knowledge acquisition is the key problem in knowledge-based intelligent form optimization; this process can be regarded as a variety of different types of knowledge transferring in the design of the various nodes between different aspects. Intelligent knowledge acquisition theory and methods include: knowledge classification, characterization, acquisition, storage, management and transport, etc. Data mining and case-based reasoning is the commonly used methods. Papers (Wang et al., 2003 ; Wang et al., 2006; Tu et al., 2004; Zhang et al., 2007; Quinlan et al., 1986; Zhang et al., 2005; Zhang et al., 2009; Zhang et al., 2006a; Zhang et al., 2006b; Wang et al., 2006; Wang et al., 2007) presented eight intelligent knowledge acquisition methods.

### 2.6 Intelligent Support System Theory and Method

In the process of SFIO design, the system need to store, use and generated a lot of information, and to carry out complex analysis, reasoning and numerical computation, therefore, the establishment of intelligent decision support system will be an important means to solve this problem. Intelligent support system theory and methods including: system architecture design, human-machine interface, problem solving strategies, inference engine, knowledge base, method base, database, drawing base, and other aspects of the theory and methods. Common intelligent support system includes expert system, decision support system and integrated intelligent support systems. Zhang (2006) presented FO integrated intelligent system shown in Figure 1.

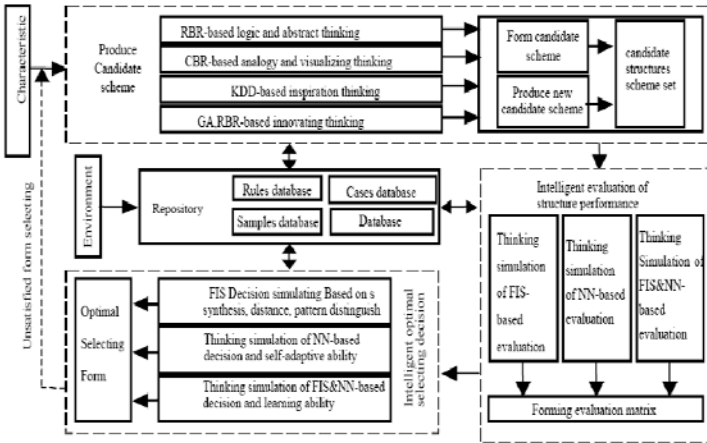


Figure 1. System model of integrated SFIO of high rise buildings

### 3 The Summary of DM Method Utilizing in SFIO

Data mining (DM) is the advanced technique in artificial intelligence, machine learning and database applications. Data mining is to extract hidden, unknown, understandable information from a large number data to provide support for the problem solving. At present, mankind has built the large number of high-rise structures, they contains a wealth of knowledge and information, not been very good development and utilization. Appropriate use of data mining methods, effectively found, access and reuse the information in the past cases to guide the current structure optimal design has become the “bottleneck”. Improving the quality

and efficiency of the design will be a new research direction and effective way. The important research progress of SFIO will be given as following.

### ***3.1 Apriori-based Mining of the Quantitative and Fuzzification Association Rule***

Association rule is to denote a group relationship rules in transaction database. Let  $I = \{i_1, i_2, \dots, i_m\}$  be the itemset,  $D$  the transaction database, where each transaction  $T$  is an item subset ( $T \subseteq I$ ), and has a unique transaction ID. An association rule is expressed as  $X \Rightarrow Y$ , meaning that "IF  $X$ , THEN  $Y$ ." where  $X \subset T$ ,  $Y \subset T$ , and  $X \cap Y = \emptyset$ . Apriori algorithm is a basic method to search the frequent itemset to producing Boolean association rules. Confidence and support are used to measure the accuracy and the importance of the association rule, respectively.

The support of rule  $X \Rightarrow Y$  in database  $D$  is:

$$\text{support}(X \Rightarrow Y) = p(X \cup Y) = \frac{| \{T : X \cup Y \subseteq T, T \in D\} |}{|D|} \quad (1)$$

The support shows how representational the rule is in all transactions. Obviously, the bigger the support is, the greater the association rule is covered by the data. The confidence indicates how accurate the association rule can predict the item  $Y$  given  $X$ . It should be noted that some association rules may have higher confidence but lower support which means that such rules have little data supporting. This may imply that the collected data are not enough or the data are not belonging to this class. Apriori algorithm can be used to mining the association rule that  $X$  is "structural scheme attribute" and  $Y$  is "structural form". At the same time, we name the rule found in the quantitative attributes as quantitative association rule, found in the fuzzy-type attributes as fuzzification association rule. The mining process and method of the quantitative and fuzzification association rule presented (Wang et al., 2003; Zhang et al., 2006; Tu et al., 2004; Zhang et al., 2007).

### ***3.2 ID3-based Mining of the Quantitative and Fuzzification Association Rule***

Decision tree is a flow chart similar to the leaves from the root node to node (classification attributes) of the tree structure, which consists of a range of nodes and branches, each non-leaf node corresponds to a non-category (decision-making) attribute tests, non-leaf node of each branch, the corresponding attributes of a test the test results, each leaf node on behalf of a class. Decision tree learning method

is based on the examples, which get classification rules from the non-order, rule-less cases to classification of the unknown data and prediction.

Most classical decision tree algorithm is ID3 (Interactive Dichotomizer-3) algorithm, the method used entropy or weighted minimum entropy as the selection standard of decision-making attributes(Quinlan J.R., 2005).confirmation of the entropy: Suppose  $w=\{w_i\}_m$  is m different classes in s pending-samples  $X=\{x_j\}_s$ ,  $s_i$  is sample number of class  $w_i$ ,  $A=\{A_k\}_n$  is the set of sample attributes,  $A_k=\{a_{kr}\}_v$  is v different values in sample attribute  $A_k$ , we can divide X into v subset  $\{X_{kr}\}_v$  with  $A_k$ ,  $X_{kr}$  include the samples which value is  $a_{kr}$  in  $A_k$  in X. for a given testing attribute sample  $A_k$ , it is corresponding the dividing branches which node contain set X. the entropy of the  $r^{th}$  sub-set  $X_{kr}$  branch is:

$$H_{kr}(X_{kr}, w) = \sum_{i=1}^m [-p_i(w_i, X_{kr})] \log_2 p_i(w_i, X_{kr}) \tag{2}$$

where  $p_i(w_i, X_{kr})$  is the probability of the samples in  $X_{kr}$  belong to  $w_i$ , estimated by  $s_{kri}/s_{kr}$ ,  $s_{kr}$  is the samples quantity in  $X_k$ , and  $s_{kri}$  is the samples quantity belong to  $w_i$  in  $X_{kr}$ .

Decision tree is an efficient method to mine and found new characteristic rules of form-selection from case base. This process is to gain knowledge from data and to learn. This model is able to represent the result of the data mining directly, and to assorted prediction for newly samples. ID3-based mining process and method of the structural FO assorted rule introduced (Zhang, 2005)

### 3.3 Bayes-based FO Knowledge Mining

Bayes algorithm is the statistical method use of probability and statistics methods to mine knowledge, mainly using Bayes theorem to get the possibilities of the unknown type of a sample X belong to every classes, the most likely chosen one as the forecast class of it. Expression (3) is the simplicity Bayesain assorted post-check formula of X belong to  $C_i$ , where,  $A=\{A_k\}_n$  is attributes set,  $x_k$  is the value of X in  $A_k$ .

$$p(C_i|X) = \left( \prod_{k=1}^n p(A_k = x_k | C_i) p(C_i) \right) / p(X) \tag{3}$$

The premise of the simplicity Bayesian classifier is the value of each attribute should be independent of each other, and the actual circumstances in meeting the conditions are not many, hence its classification accuracy rate will fall. For the DM problem with the correlation between the attributes, people have been proposed a Bayesian Belief Network (BBN). This method does not require a given

category have independent conditions of all the attributes. it has to use a non - DAG visual representation of the dependencies between variables, with nodes representation of the random variables (attributes characteristic value  $\{A_k\}_n$ ), with probability table representation of dependent probability relations between variables. Each node in BBN conditional independent of its predecessors nodes after given its father node, so, for the discrete random variables  $X=\{x_k\}_n$  the joint probability is:  $p(x_1, x_2, \dots, x_n)=\prod p(x_i|f(x_i))$ ,  $f(x_i)$  is the parent node set of node  $A_i$ . The BBN-based structural form selection DM method was presented (Liang B.L et al., 2007).

### ***3.4 NN-based Mining of the Quantitative and Fuzzification Association Rule***

Structure optimization is actually a MIMO complex mapping process from the need space to the feasible structure space through the intellectual resources space, and the input and output of this complex mapping relationship often hidden in people's practice and the construction of the high-rise structure cases. NN is the nonlinear forecasting model through training to learn and consists of the input layer, a number of hidden layer and output layer. They can be used to receive the current conditions information of the input layer through the layers of connection between neurons, the neurons connected strength and function to play the role of receiving, processing, transmission, storage implicit knowledge and information in a large number of cases, Finally, output the form optimization knowledge related to the current conditions. Use of the network, we established BP- based optimization theory and method of data mining in (Zhang, 2006).

### ***3.5 GA-based FO Knowledge Mining***

Genetic Algorithm (GA) is a combinatorial optimization algorithm simulating the biology evolution. Using its random search algorithm and its global optimization function, by the natural evolutionary process such as genetic reproduction, crossover and mutation we can efficiently obtain or create a new structural FO design knowledge. In the implementation of the algorithm, first of all, to code the solving problem to produce initial population, and then calculating individual fitness and then chromosome replication, crossover and mutation, and other operations, until the best solution. Among them, determine the fitness of individual adaptation function is the key step. The fitness function of the FO data mining as following:

$$d_y(RG_y, CG) = \frac{nd(RG_y, DG)}{pd(RG_y, EG)} \quad (4)$$

where,  $pd$ 、 $nd$  is any gene cluster  $RG_y = \{rg_{yi}\}_n$  about a assorted concept  $w_j$  respectively, and is similarity degree of the positive and negative gene case  $DG = \{DG_q\}_s$  and  $EG = \{EG_k\}_m$  respectively.

Mining optimal FO knowledgebase in the entire genome space, in essence, is to search the target function with discontinuous and non-differentiable large-scale combinatorial optimization problem. This method can use adaptive function of the current candidates to evaluate the adaptability of the solution, and the search direction is according to the natural evolution of the survival of the fittest principle, thereby enhances the efficiency of the search. At the same time, this method also implicit parallelism and self-organizing etc. intelligent feature, can mine the knowledge base from the large number of case gene base intelligently and automatically. GA -based of FO process and knowledge mining method is introduced (Zhang et al., 2006a; Zhang et al., 2006b).

### ***3.6 RS-based and Fuzzy RS-based Mining Method***

Rough Set (Rough Set-RS) method can find the implicit knowledge and reveal the potential law from information with the characteristics such as imprecise, uncertain, inconsistent and incomplete. Its main idea is to simplify the decision-making or classification rules under the premise of maintain information systems taxonomic capacity unchanged. Attribute reduction is the core content. Attribute reduction describes each property is necessary or not and how to remove unnecessary knowledge in the attributes set. The main attribute reduction algorithm is based on information entropy, the partition matrix and the correlation matrix.

Rough Set method can only deal with the discrete attributes of information. By discrete the continuous attributes, papers (Wang et al., 2006; Wang et al., 2007) established a RS-based and a fuzzy RS-based knowledge acquisition method of high rise FO respectively. The last method use the partition matrix to simplify the attributes, use the membership function fuzzify the continuous attributes; overcome the irrational attribute mutation occurring at the boundary in the processing of discrete.

In the above data mining methods, the decision making tree method is suitable for high precision a fairly comprehensive case data, other methods are suitable for treatment cases with noise data. They have better complementary. In the process of SFIO knowledge excavation should be integrated using the above methods, mining implicit knowledge in the different type's optimal knowledge of the high rise structure cases from different angles and in different aspects.

## 4 Conclusions

Structural FO design is mainly determined by the experts in the light of experience, the system hasn't yet to see a mature theories and methods. Firstly, we discussed the structural FO problems, and introduced the SFIO theoretical framework including the alternative scheme intelligent producing and innovative, intelligent evaluation, intelligent optimization selection and decision-making, knowledge automatic access, intelligent means, laying a foundation for farther study the SFIO theories and methods. Secondly, we gave a more comprehensive overview of DM techniques in SFIO, the important research results and the latest research progress such as Apriori-based, Bayes-based, ID3-based, NN-based, GA-based, RS-based and fuzzy RS-based algorithm, and their characteristics. These methods can mine FO knowledge from different perspective, and possess a better complementary. All of them can change "information resources" of cases into "wealth of knowledge" of the field of practical guidance, and laid the foundation for full understand and further study SFIO theoretical knowledge and methods.

## References

- Chai S., Shi L.S., Sun H.C. (1999). Topology Optimization of Truss Structures with Discrete Variables Including Two Kinds of Variables. *Acta Mechanica Sinica*, 31(5): 574-583.
- Guo Z.Z., Zhang W.H., Chen Y.Z. (2007). An Overview on the Topological Optimization Design of Structures. *Journal of Machine Design*, 24(8): 1-6.
- Luo Z., Chen L.P., Huang Y.Y., Zhang (2004). Topological Optimization Design for Continuum Structures. *Advances in Mechanics*, 34(4): 463-466.
- Liang B.L., Lu X.L., Wang Z.Z. (2007). Research on Database of High-Rise Buildings Exceeding Some Limits in Codes and Knowledge Discovery Based on Bayesian Network. *Journal of Earthquake Engineering and Engineering Vibration*, 27(1): 72-79.
- Quinlan J.R. (1986). Induction of Decision Trees. *Machine Learning*: 1-356.
- Sun H.C., Cai S., Wang Y.F. (2002). *Structural Optimization Design of Discrete Variables*. Dalian University of Technology Publishing Company, China: 1-5.
- Tu Qing, Huang Qi. (2004). Research and Application of Fuzzy Association Rules Based on Highbuilding Structure Databases. *Computer Engineering and Applications*, 20: 224-226, 232.
- Wang G.Y., Zhang S.H., Liu X.Y., Ou J.P. (2003). A Case-based System for Highrise Building Structure Schemes and Its Application to Structure Intelligence From-Selection. *Engineering Mechanics*, 20(4) 1-8.
- Wang Li, Yuan C.C., Lu D.G., Zhang S.H. (2006). Application of Rough Sets in High-rise building Structure's Knowledge Discovery. *Journal of Harbin Institute of Technology*, 38(12): 2073-2076.
- Wang Li, Yuan C.C., Lu D.G., Zhang S.H. (2007). Knowledge Discovery Method in Scheme Design of High-rise Building Structures. *Journal of Harbin Institute of Technology*, 39(2): 177-180.
- Wang J., Cheng G.D. (1997). Optimal Topology Design of Thin Plate with Stress Constraints. *Acta Mechanica Solida Sinica*, 18(4): 317-322.
- Xing F.L., Wang G.Y. (2003). Selection of Target Structures Based on Self-organizing-feature-map. *Engineering Mechanics*, 20(1): 1-6.

- Yang D.Q. (1999). *Continuous Variables of the Structure Shape and its Topology Optimization Design Theory and Method*. Dalian: Dalian University of Technology.
- Zhang S.H. (2003). *Study of the High-Rise Building Form Intelligent Selection Theories and Methods*. Harbin: Harbin Institute of Technology.
- Zhang S.H., Liu X.Y., Ou J.P., Wang G.Y. (2006). A High-rised Structural Intelligent Form Optimization Method and Support System Based on Fuzzy Inference Network. *Chinese Journal of Computational Mechanics*, 23(6): 647-650, 658.
- Zhang S.H., Liu S.J., Liu X.Y., Ou J.P. (2006). NN Based KDD for High-rise Structures Intelligent Form Selection. *Proceeding of the Ninth International Symposium on Structural Engineering for Young Experts (ISSEYE '09)*, Science Press, vol. 1: 489-494.
- Zhang S.H., Liu S.J., Ou J.P., Wang G.Y. (2006). Data Mining and Its Applications for High-rise Structure Intelligent Form-optimization Based on Genetic Algorithm. *IEEE The 6th World Congress on Intelligent Control and Automation (WCICA'06) Conference Proceedings*, Vol. 11 of 12: 8779-8784.
- Zhang S.H, Liu S.J., and Ou J.P. (2007). KDD Method of Structure Intelligence Form-selection Based on High-rising Case-base and Associate-analysis. *The 11th Pacific-Asia Conference on Knowledge Discovery and Data Mining (PAKDD'07 Industrial Track)*, 72~83
- Zhang S.H., Ou J.P., Wang G.Y. (2006). Case-Genelibrary and Genetic Algorithm Based Knowledge Discovery in Databases for Intelligent Form Selection of High-Rise Structures. *Engineering Mechanics*, 23(1) 87-92.
- Zhang S.H., Liu X.Y., Tu Q., Ou J.P. (2005). Decision Trees Based Knowledge Discovery in Databases for High-rise Structures Intelligent form Selection. *Journal of Harbin Institute of Technology*, 37(4): 451-454.
- Zhang S.H., Shujun Liu, Dong Wang, J.P. Ou, Guangyuan Wang (2006). Knowledge Discovery of Improved Apriori-based High-rise Structure Intelligent Form Selection. *Sixth International Conference Intelligent Systems Design and Applications (ISDA'06)*. Published by the IEEE Computer Society: Volume 1, 535-539.
- Zhang S.H., Wang G.Y, Ou J.P. (2002). Intelligent Assessment Method for High-rise Building Aseismic Form – Selection. *World Information on Earthquake Engineering*, 22(4): 28-35.
- Zhang S.H., Ou J.P., Wang G.Y. (2005). Integrated Weighted Fuzzy Inference Network Method for High-rise Structure Aseismic Form Selection. *China Civil Engineering Journal*, 38(6): 13-19.
- Zhang S.H., Wang Li, Ou J.P., Wang G.Y. (2006). Present State and Perspectives of Structural Intelligent Form-optimazition Method of High-rise Buildings. *Journal of Harbin Institute of Technology*, 38(2): 194-198, 319.

# A New Methodology for Designing Minimum-Weight Dual-Material Truss Structures with Curved Support Boundaries

Peter Dewhurst<sup>1\*</sup>, Ning Fang<sup>2</sup> and Sriruk Srithongchai<sup>2</sup>

<sup>1</sup>Department of Industrial and Systems Engineering, University of Rhode Island, Kingston, RI 02881, U.S.A.

<sup>2</sup>College of Engineering, Utah State University, Logan, UT 84322, U.S.A.

**Abstract.** The design of light-weight structures is a subject of central importance in the development of numerous civil and mechanical engineering products, such as bridges, roofs, and aerospace constructions. Based on matrix operators, a new methodology is established in the present study to design minimum-weight dual-material truss layout structures with curved support boundaries that represent broader engineering applications. To validate the new methodology, logarithmic spirals on a circular support boundary are investigated to determine the radii of curvature along the boundary points. A torsion structure case study is explored to compare deflections with calculated results obtained from the optimality criteria. The solutions are very close to theoretical values.

**Keywords:** minimum-weight truss structures, dual-material, curved support boundaries, matrix operators

## 1 Introduction

The design of light-weight structures is a subject of central importance in the development of numerous civil and mechanical engineering products, such as bridges, roofs, and aerospace constructions. As early as 1904, Michell (1904) laid down the criteria for absolute minimum-weight structures; namely that all structure members must follow the orthogonal network of lines of maximum and minimum strain in a constant-magnitude strain field. Hemp (1958) then demonstrated the similarity of minimum-weight frameworks and metal deformation in slip-line fields. This equivalence can be exploited in the construction of optimal structure layouts from known slip-line theory solutions. Rozvany (1996) indicated that the

---

\* Corresponding author, email: dewhurst@egr.uri.edu

optimal structure layout for non-statistically determinate cases changes for different ratios of compression and tension strengths and for different ratios of density for statically indeterminate structures; a result previously indicated by Hemp (1958). Several examples of dual-material design are provided by Srithongchai and Dewhurst (2003) and Dewhurst and Srithongchai (2005).

Almost all of the existing optimum solutions obtained from Michell’s original work (Michell, 1904) are only for straight boundary problems. This paper presents a new methodology to design minimum-weight dual-material truss layout structures with curved support boundaries that represent broader engineering applications. The new methodology is based on the method of matrix operators (Dewhurst and Collins, 1973) and Ewing’s approach (Ewing, 1967), which has been applied to slip-line boundary problems along flat tool surfaces with constant and varying surface friction (Dewhurst, 1985; Fang, 2003).

To validate the developed new methodology, logarithmic spirals on a circular support boundary are investigated in this study to determine the radii of curvature along the boundary points. A torsion structure case study is explored to compare deflections with calculated results obtained from the optimality criteria. The solutions are very close to theoretical values.

## 2 Series and Matrix-Operator Methods of Solution

Figure 1 shows  $\alpha$  and  $\beta$  curvilinear co-ordinates starting from origin  $O$  on the desired boundary. Both have linear relationship of the form  $\beta = \lambda\alpha$  where  $\lambda$  is a positive constant factor.

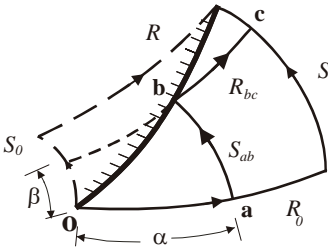


Figure 1. Construction of Michell layout lines

The initial layout curve is represented by a column vector  $\mathbf{R}_0$ ; therefore the associated initial curve  $\mathbf{S}_0$  can be represented by

$$\mathbf{S}_0 = \mathbf{H}_{\lambda,\gamma} \cdot \mathbf{R}_0 \tag{1}$$

$$\mathbf{H}_{\lambda,\gamma} = (\mathbf{I}_\lambda \cos \gamma + \mathbf{J}_\lambda \sin \gamma)^{-1} \cdot \left( -\mathbf{J}_1 \cos \gamma + \frac{1}{\lambda} \mathbf{I}_1 \sin \gamma \right) \tag{2}$$

where  $\mathbf{I}_\lambda$  and  $\mathbf{J}_\lambda$  are defined as

$$\mathbf{I}_\lambda = \begin{bmatrix} \lambda^0 & 0 & 0 & \dots \\ 0 & \lambda^1 & 0 & \dots \\ 0 & 0 & \lambda^2 & \dots \\ \dots & \dots & \dots & \dots \end{bmatrix}, \quad \mathbf{J}_\lambda = \begin{bmatrix} 0 & 0 & 0 & \dots \\ \lambda^0 & 0 & 0 & \dots \\ 0 & \lambda^1 & 0 & \dots \\ \dots & \dots & \dots & \dots \end{bmatrix} \tag{3}$$

Hence the solutions in figure 1 are as follows

$$\mathbf{S}_{ab} = \mathbf{P}_{-\alpha}^* [\mathbf{S}_0 + \mathbf{Q}_\alpha^* (\mathbf{R}_\alpha^* \mathbf{R}_0)] \tag{4}$$

$$\mathbf{R}_{bc} = \mathbf{S}_\alpha^* (\mathbf{P}_{\alpha\beta} (\mathbf{R}_\alpha^* \mathbf{R}_0) - \mathbf{Q}_{\beta\alpha} \mathbf{S}) \tag{5}$$

where basic matrix operators,  $\mathbf{P}^*$  and  $\mathbf{Q}^*$ , a reversion matrix operator,  $\mathbf{R}^*$ , and a shift operator,  $\mathbf{S}^*$ , are defined as

$$\mathbf{P}_\varphi^* = \begin{bmatrix} \varphi^{(0)} & 0 & 0 & \dots \\ \varphi^{(1)} & \varphi^{(0)} & 0 & \dots \\ \varphi^{(2)} & \varphi^{(1)} & \varphi^{(0)} & \dots \\ \dots & \dots & \dots & \dots \end{bmatrix}, \quad \mathbf{Q}_\varphi^* = - \begin{bmatrix} \varphi^{(1)} & \varphi^{(2)} & \varphi^{(3)} & \dots \\ \varphi^{(2)} & \varphi^{(3)} & \varphi^{(4)} & \dots \\ \varphi^{(3)} & \varphi^{(4)} & \varphi^{(5)} & \dots \\ \dots & \dots & \dots & \dots \end{bmatrix} \tag{6}$$

$$\mathbf{R}_\varphi^* = - \begin{bmatrix} \varphi^{(0)} & \varphi^{(1)} & \varphi^{(2)} & \dots \\ 0 & -\varphi^{(0)} & -\varphi^{(1)} & \dots \\ 0 & 0 & \varphi^{(0)} & \dots \\ \dots & \dots & \dots & \dots \end{bmatrix}, \quad \mathbf{S}_\varphi^* = \begin{bmatrix} \varphi^{(0)} & \varphi^{(1)} & \varphi^{(2)} & \dots \\ 0 & \varphi^{(0)} & \varphi^{(1)} & \dots \\ 0 & 0 & \varphi^{(0)} & \dots \\ \dots & \dots & \dots & \dots \end{bmatrix} \tag{7}$$

and  $\varphi^{(m)} = \varphi^m / m!$ . The matrices  $\mathbf{P}$  and  $\mathbf{Q}$  are given by

$$\mathbf{P}_{\theta\eta} = \mathbf{R}_\theta^* \mathbf{P}_\eta^* \tag{8}$$

$$\mathbf{Q}_{\theta\eta} = \mathbf{R}_\eta^* \mathbf{Q}_\theta^* \tag{9}$$

### 3 Validation of the Numerical Methodology

Refer to figure 2, the initial logarithmic spiral line is indicated as the  $\alpha$  line, which intersects the circular boundary  $ab$  and all other concentric arcs at constant angle  $\gamma$ . Polar equation of  $\alpha$  with a boundary radius  $r_b$  is  $r = r_b e^{p\theta}$  where  $p = \cot(\gamma)$ . Since  $\theta = \alpha$ , the radius of curvatures  $R(\alpha)$  and  $S(\beta)$  are

$$R(\alpha) = \frac{(\dot{x}^2 + \dot{y}^2)^{3/2}}{|\dot{x}\ddot{y} - \dot{y}\ddot{x}|} = (1 + p^2)^{1/2} r_b e^{p\alpha} = (1 + p^2)^{1/2} r_b e^{p\alpha} \tag{10}$$

$$S(\beta) = -(1 + 1/p^2)^{1/2} r_b e^{(1/p)\beta} \tag{11}$$

This gives the column vectors

$$\mathbf{R}_0 = (1 + p^2)^{1/2} r_b \left[ 1, p, p^2, \dots \right]' \tag{12}$$

$$\mathbf{S} = -(1 + 1/p^2)^{1/2} r_b \left[ 1, \frac{1}{p}, \frac{1}{p^2}, \dots \right]' \tag{13}$$

The parameter values,  $p = (1/\sqrt{3})^{1/2}, r_b = 1.5, \phi = 2\pi/3$ , give numerically solutions in the following equations; see figure 3. All of the curves in the network agreed with the column vectors given in Eqs. (14) to (15). The calculated radii of curvature values at the boundary nodes were all correct to seven decimal places.

$$\mathbf{R}_0 = [1.8839, 1.4314, 1.0877, 0.8264, 0.6280, 0.4771, 0.3626, 0.2755, 0.2093, 0.1590]' \tag{14}$$

$$\mathbf{S} = [-2.4793, 3.2630, 4.2943, 5.6517, 7.4380, 9.7890, 12.8830, 16.9550, 22.3140, 29.3669]' \tag{15}$$

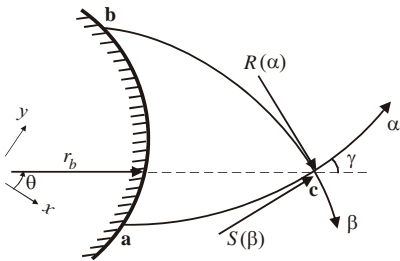


Figure 2. Intersecting pair of log spirals

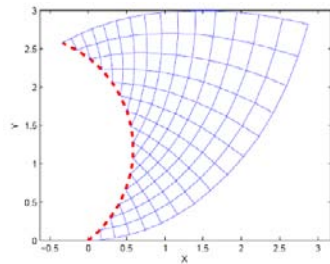


Figure 3. Validation of solutions

## 4 A Case Study of Minimum-Weight Torsion Structure

The case of a minimum-weight torsion structure is considered as illustrated in figure 4 and 5. The force  $F$  forms an applied torque that causes the structure to rotate about the boundary center. A pair of spirals, for which the radii of curvature increase linearly with the angle turned through, and straight line members are radiating outwards from the inner fixed circular boundary. For this particular case, all the members meet the boundary at constant angle,  $\gamma = \pi/4$ .

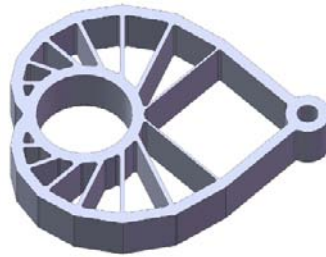
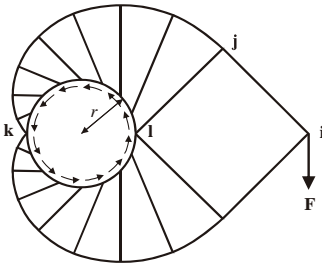


Figure 4. Torsion structure layout

Figure 5. CAD solid model of Figure 4

The volume of this structure can be written as (Dewhurst et al., 2009).

$$V_s = 2(V_c + V_T) = (Fr/\sigma)(2\pi + \pi^2) \quad (16)$$

Applying virtual strain energy,  $F\delta = V\sigma\varepsilon$ , the vertical tip deflection is given by

$$\delta_y = -r\varepsilon(2\pi + \pi^2) \quad (17)$$

Since the line  $il$  is a zero strain direction, the horizontal deflection  $\delta_x = 0$ .

The tip deflection using Mastan truss analysis ( $E = 100 \text{ psi}$ ,  $\sigma_{max} = 1 \text{ psi}$ ,  $1 \text{ lbf}$  tip load) was  $\delta_x = 1.2737\text{E-}16$  and  $\delta_y = -1.6239\text{E-}01$ . This agrees with the theoretical calculation ( $\delta_x = 0$  and  $\delta_y = -1.6153\text{E-}01$ ).

## 5 Conclusions

Almost all of the existing optimum solutions obtained from Michell's original work are only for straight boundary problems. This paper presents a new metho-

dology based on matrix operators to determine the initial curve in one family of structural layout lines from any given curve in the opposite layout lines family for minimum-weight design around a curved boundary, which represents broader engineering applications. A minimum-weight torsion structure subjected to a point load and sitting on a circular boundary is shown to represent the application of the new methodology. The tip deflections of the torsion structure using Mastan truss analysis agree with the analytical predictions from the developed methodology.

## Acknowledgements

This material is based upon work supported by the National Science Foundation under Collaborative Research Grant No. 0620752 (University of Rhode Island) and No. 0620387 (Utah State University).

## References

- Dewhurst P. and Srithongchai S. (2005). An investigation of minimum-weight dual material symmetrically loaded wheels and torsion arms. *J App Mech*, 72: 196-202.
- Dewhurst P. and Collins I.F. (1973). A matrix technique for constructing slip-line field solutions to a class of plane strain plasticity problems. *Int J Numer Meth Engng*, 7:357-378.
- Dewhurst P. (1985). A general matrix operators for linear boundary value problems in slip-line field theory. *Int J Numer Meth Engng*, 21:169-182.
- Dewhurst P., Fang N. and Srithongchai S. (2009). A general boundary approach to the construction of Michell truss structures. *Struct Multidisc Optim*, in press.
- Ewing D.J.F. (1967). A series-method for constructing plastic slipline fields. *J Mech Phys Solids*, 15: 105-114.
- Fang N. (2003). Slip-line modeling of machining with a rounded-edge tool, Part I: new model and theory. *J Mech Phys Solids*, 51: 715-742.
- Hemp W.S. (1958). Theory of the Structural Design. The College of Aeronatics, Cranfield. Report No. 115.
- Michell A.G.M. (1904). The limits of economy of material in frame structures. *Phil Mag*, 8:589-597.
- Rozvany G.I.N. (1996). Some shortcomings in Michell's truss theory. *Struct Optim*, 12:244-250.
- Srithongchai S. and Dewhurst P. (2003). Comparisons of optimality criteria for minimum-weight dual material structures. *Int J Mech Sci*, 45:1781-1797.

# Optimization Design of Deepwater Steel Catenary Risers Using Genetic Algorithm

Hezhen Yang<sup>1\*</sup>, Ruhong Jiang<sup>1</sup> and Huajun Li<sup>2</sup>

<sup>1</sup> State Key Lab of Ocean Engineering, Shanghai Jiao Tong University, Shanghai 200030, China

<sup>2</sup> College of Engineering, Ocean University of China, Qingdao 266100, China

**Abstract.** This work presents the implementation of genetic algorithms in the optimization design of deepwater Steel Catenary Risers (SCRs) with discrete design variables. For deepwater developments, riser system requirements become a significant factor in the cost of the overall oil field investment. Hence, riser design must consider safety before reducing costs. Firstly, three dimensional nonlinear SCRs models were constructed by finite element method; In addition, nonlinear characteristics of soil/structure interaction are also included according to regulations. Secondly, a steel catenary riser is analyzed for several typical ocean environmental conditions to prove the vast potential of the proposed strategy as a design tool; thirdly, SCRs design based on genetic algorithm were applied for given design parameters such as riser thickness, coating properties and constraints. Compared with conventional design method, the optimized configuration not only can cut the cost while satisfied all constraints, but also reduce the maximum von Mises stress. According to the above analysis, the optimization strategy base on genetic algorithm is a useful tool for SCRs design, and that the proposed method for selection of optimum design variables will enable an engineer to identify designs with minimum costs in an efficient way.

**Keywords:** optimization, genetic algorithm, steel catenary riser, deepwater, touch down point, finite element method

## 1 Introduction

Recently, offshore exploitation and exploration have been developed in deeper and deeper water environments. Steel catenary risers (SCRs) are being considered and used in conjunction with a semi-submersible or Tension Leg Platform (TLP) in deepwater harsh environments. However, for ultra-deep waters flexible risers can frequently reach or exceed the technical and economical feasibility limits. This fact can occur due to the limitation of the viable riser diameter, particularly

---

\* Corresponding author, e-mail: yanghz@sjtu.edu.cn

when associated to high external pressures and temperatures, and to significant static offsets and heave motions, associated with reduced capability of sustaining harsh service conditions (Fu and Yang, 2009). Recently, the SCRs concept has been shown to be able to overcome such limitations, and to comprise a feasible alternative.

As the riser system is highly nonlinear, this analysis is computationally very expensive, and time consuming (Karunakaran and Meling, 2006). So it is necessary to apply optimization techniques to construct better structural model, use suitable materials, select better techniques of manufacturing, and speed up the design process (Larsen and Hanson, 1999). Deepwater production and export risers will have to meet many design requirements, and the significance of these requirements will vary along the riser. This means that an optimized riser will not have constant wall thickness and coating properties along its entire length.

In order to satisfy all these conditions, this work analyzes the use of an optimization algorithm to minimize the riser cost while keeping all constraints satisfied. This problem is characterized by a very large space of possible solutions; the use of traditional methods is an exhaustive work, since there are a large number of variables and constraints that defined for SCRs (Engseth et al., 1988; Mathisenand and Bergan, 1986). Genetic algorithms are more robust than the more commonly used optimization techniques (Goldberg, 1989). This work presents the implementation of Island based Genetic Algorithms (IGA) in the optimization design of deepwater Steel Catenary Risers (SCRs) with discrete design variables.

## 2 Genetic Algorithms

Genetic algorithms (GAs) and the closely related evolutionary strategies are a class of non-gradient methods which has grown in popularity. For a more comprehensive study of genetic algorithms, see Goldberg (1989) on the subject. Genetic Algorithm has proven to be able to produce high-quality solution for many optimization problems and competitive with other sophisticated algorithms such as Simulated Annealing, Tabu Search and force-directed algorithms (API, 1998). However, since the runtime of GA is relatively longer than other algorithm. Therefore, researchers are seeking parallel GA implementation for better performance, such as Island based Genetic Algorithm (IGA).

Island based Genetic Algorithm (IGA) is a multi-population GA in which chromosomes can migrate between the islands (sup-population). Each design point is perceived as an individual with a certain value of fitness based on the value of the objective function. Constraint penalties increase the objective function value, i.e. individuals with a better value of objective function and penalty have a higher fitness value. In contrast to traditional genetic algorithms the entire population is divided into several sub-populations called "islands". In order to increase the diversity and avoid stagnation within the evolutionary process, some individuals are selected and migrate to different islands periodically. The best individuals migrate

between islands in each migration step. At the same time, the worst individuals are replaced by the immigrants. A migration step repeats after every predefined number of generations. The flow chart for IGA main algorithm is shown in Figure 1.

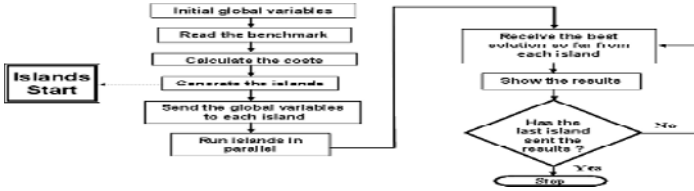


Figure 1. Island based Genetic Algorithm main algorithm

### 3 Mathematical Model

#### 3.1 Soil-Riser Interaction

In most deepwater fields, relatively loose clay is found on the seabed. The common practice is to model the soil-riser interaction by nonlinear soil spring. This is done using the following relationship:

$$F=p(y).L \tag{1}$$

where F: axial force in the spring, (N); p: soil resistance, (N/m); y: deflection, (m); L: length of casing over which force acts.

#### 3.2 Stress Constraints

According to the commonly employed criteria API (API, 1998) and DNV (DNV, 2001, 2005) for the design and analysis of the riser, the developed configuration needs to fulfil the load controlled conditions criteria. Hoop Stress  $\sigma_h$  can be determined using the equation:

$$\sigma_h = (p_i - p_e) \frac{D-t}{2t} < \eta \cdot SMYS \cdot k_T \tag{2}$$

where  $p_i$  : internal pressure;  $p_e$  : external pressure;  $D$  : outside diameter of pipeline;  $t$  : minimum wall thickness of pipeline;  $\eta$  : design factor;  $k_T$  : temperature factor.

The longitudinal stress is the axial stress experienced by the pipe wall, and consists of stresses due to:

$$\sigma_1 = 0.3\sigma_{lh} + \sigma_{lb} + \sigma_{lt} + \sigma_{lc} \tag{3}$$

The combined stress is determined differently depending on the code/standards utilized. However, the equivalent stress can usually be expressed as:

$$\sigma_e = \sqrt{\sigma_h^2 + \sigma_1^2 - \sigma_h\sigma_1 + 3\tau_{lh}^2} < \eta SMYS \tag{4}$$

where  $\sigma_h$  : hoop stress;  $\sigma_1$  : longitudinal stress;  $\tau_{lh}$  : tangential shear stress.

## 4 Numerical Studies

### 4.1 Steel Catenary Riser Model

For the numerical study, a typical marine riser shown in Figure 2 is chosen for the optimization study, suspended from a floating platform and landed onto a horizontal seafloor. It is installed at a sea depth of 1462m, and considering a horizontal projection of 2886m. Its specifications are given in Table 1.

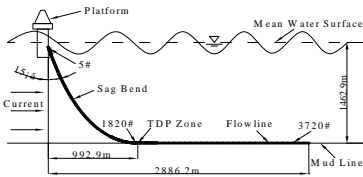


Figure 2. Typical profile of a Steel Catenary Riser

The Steel Catenary Riser (SCR) is designed for the 100yr wave condition in combination with 10yr current profile. The wave data are for a typical Northern North Sea location. The 100yr sea state is: Significant wave height 15.5m; corresponding wave peak period 16s.

Table 1. Steel catenary riser modeling data

Water Depth	1462m
Water density	1024kg/m <sup>3</sup>
Riser inner diameter	0.4064 m
Normal Coating density	800 kg/m <sup>3</sup>
Light Coating density	650 kg/m <sup>3</sup>
Heavy Coating density	2800 kg/m <sup>3</sup>
Coating thickness	0.075m
Modulus of elasticity	2.10E+11 N/m <sup>2</sup>
Internal fluid of density	146 kg/m <sup>3</sup>
Steel density	7850 kg/m <sup>3</sup>
Possion's ratio	0.3

## 4.2 Optimization Methodology

The deep-sea riser optimization problem can be solved in a rather robust way by genetic algorithms like the Island based Genetic Algorithm (IGA). A case study is performed, varying the material of the riser coating, riser thickness, and analyzing the obtained results. The thickness and coating density were treated as discrete variables. Some properties, such as linear weight, cross-section area, flexional and axial stiffness are function of the design variables and thus vary during the optimization process. For preliminary design, riser configurations were developed with varying weight of cross sections along the length.

In engineering design, the objective functions are generally non-linear functions of the design variables and are usually implicit, discontinuous and non-convex. This work intends to find the cheapest possible riser. The objective function to be minimised is the riser material cost. The riser was also required to meet collapse criteria and maximum allowable stress for each of the selected materials. The curvature radius was left unrestricted, because the stress restriction would naturally limit it. The riser configuration should fulfil the commonly employed criteria API (1998) and DNV (2001, 2005). The material of the riser coating and riser thickness are specified as optimisation variables.

## 4.3 Results

This section presents the optimization results, employing for the representation of variables in the implementation of Island based Genetic Algorithms (IGA). A typical optimized SCR configuration is shown in Figure 3. Figure 3 presents a schematic model showing the coating parameters that defined for optimum result. Case

A is original configuration without optimization, and Case B is optimum solution by IGA. The structural behaviour constraints are determined from regulations. The static analysis was performed by nonlinear dynamic FE analyses. According to regulation, Case A is not fulfilling common design requirement.

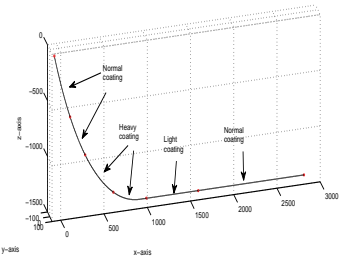


Figure 3. SCR optimal configurations

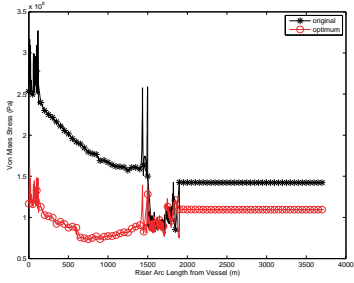


Figure 4. Maximum Von Mises stress for original case and optimum

After applying IGA for optimization design, the SCR cost was reduced obviously while all stresses satisfied with the requirement of rules. Maximum von Mises stresses for original case and optimum case are compared in Figure 4, from which the optimum results is better than original case.

The peak values of maximum von Mises stress envelope were concentrated within a length of about 20m along the riser, as shown in Figure 4. The predicted fatigue life for the optimized configuration and the conventional SCR was compared as shown in Figure 5. It can be seen that with the optimized weight coatings, SCR fatigue life was improved considerably. Fatigue life at Touch Down Zone for SCR is shown in Figure 6.

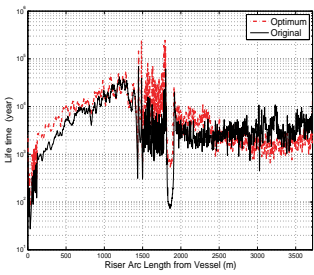


Figure 5. Fatigue life along riser arc length

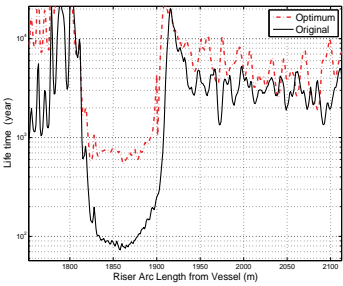


Figure 6. Fatigue life at Touch Down Zone for SCR

## 5 Discussion and Conclusions

The purpose of the work is to develop a strategy for the optimum design of steel catenary risers (SCRs) at deep and ultra-deep waters. Optimization procedure is presented for minimum cost optimization with discrete design variables and constraints. In addition nonlinear characteristics of soil/structure interaction are also included according to regulations. The following conclusions can be drawn from the study:

1. With the implementation of optimized weighted sections, SCR strength is improved significantly.
2. IGA optimized coatings and thickness for SCR can improve the fatigue life at TDA.
3. Normally the end point of sagging section with heavy coating has a specific position is not far from the TDP. Moving this end either closer to or further from the TDP will increase the stress level considerably.
4. By IGA optimization strategy for SCR design, the cost was reduced, and the fatigue life was extended effectively.

The results of this study can lead to the conclusion that the optimization tool described here, the IGA is able to search technically feasible configurations for discrete design variables and multi-constraint problems such as those found in the design of SCRs.

## Acknowledgments

This work was financially supported by the National Key Natural Science Foundation of China (Grant No. 50739004) and the Research Fund for the Doctoral Program of Higher Education (Grant No. 20070248104).

## References

- API (1998) API RP 2RD, Design of Riser for Floating Production Systems (FPSs) and Tension Leg Platforms (TLPs).
- DNV (2001) Offshore standard DNV-OS-F201: dynamic risers. Det Norske Veritas.
- DNV (2005) Recommended practice DNV-RP-F204: riser fatigue. Det Norske Veritas.
- Engseth A., Bech A. et al (1988) Efficient method for analysis of flexible risers, BOSS'88, Trondheim, Norway.
- Fu J.J. and Yang H.Z. (2009) Dynamic response analysis of a deepwater steel catenary riser at the touchdown point. *Ocean Engineering* [in Chinese].
- Goldberg D.E. (1989) *Genetic algorithms in search, optimization and machine learning*. Addison-Wesley, Reading MA.

- Karunakaran D. and Meling T.S. (2006) Robust SCR design against fatigue in deepwater harsh environments. In: Deep Offshore Technology Conference. Houston, USA.
- Knight L. and Wainwright R. (1992) HYPERGEN – A distributed genetic algorithm on a hypercube. In: the Scalable High Performance Computing Conference. Williamsburg, Virginia.
- Larsen C.M. and Hanson T. (1999) Optimization of catenary risers. *Journal of Offshore Mechanics and Arctic Engineering, Transactions of the ASME*, 121(2): 90-94.
- Mathisen K.M. and Bergan P.G. (1986) Nonlinear static analysis of flexible risers, The International Symposium & Exhibition, OMAE 1986, Tokyo.

# Two Methodologies for Stacking Sequence Optimization of Laminated Composite Materials

Dianzi Liu<sup>1</sup>, Vassili Toropov<sup>1</sup>, David Barton<sup>1</sup> and Ozz Querin<sup>1</sup>

<sup>1</sup>School of Mechanical Engineering, University of Leeds, Leeds LS2 9JT, Great Britain

**Abstract.** Two approaches are examined for seeking the best stacking sequence of laminated composite wing structures with manufacturing constraints: smeared stiffness-based method and lamination parameter-based method. In the first method, minimizing the total number of plies is the objective function at the global level and shuffling the stack of all the layers to satisfy manufacturing constraints is optimized at the local level. The second method introduced in this paper is to use lamination parameters related with out-of-plane stiffness matrix and numbers of ply angle (90, 0, 45/-45) as design variables with considerations of buckling and strength constraints in the top level optimization. Given lamination parameters from top level optimization as objective function for the local level, optimal stacking sequence will be determined to satisfy industrial manufacturing requirements. The results of a three-part wing box example using these two approaches are compared to results from published papers to demonstrate their potencies.

**Keywords:** optimization, lamination parameters, stacking sequence, laminates

## 1 Introduction

The superior advantage of composite material is its better ratio of stiffness to weight and strength to weight as compared to metals. Thus, design of composite materials for engineering structures has become popular in recent years. Stacking sequence of these laminas and their thickness are quite vital for composite mechanical characteristics such as in-plane stiffness, flexural or bending behaviour and bucking behaviour. It is import to tailor laminate layups in the stiffness optimization of laminated composites.

Stacking sequence optimization of laminated composite structures to satisfy ply continuity (blending) requirements has recently attracted considerable attentions (Liu, 2000; Soremekun, 2007 and Liu, 2009). Liu and Haftka (2000) developed two level (global and local) optimization strategies for laminated wing box struc-

ture. At the global level, minimum weight of wing box was objective function with considerations of strain and buckling constraints. GAs was applied at the local level to optimize the stacking sequence of layers, which were obtained from the global level. Three different design-space optimizations were discussed. Lamination parameters method is another approach to represent the stiffness optimization of laminated composites. It was first used as geometric factors by Tsai and Pagano (1968). Ply compatibility (or blending) between adjacent panels has been considered by Haftka (2001) and Gurdal (2007). Liu and Haftka (2001) defined continuity index measurement between adjacent panels at the local level only. Gurdal *et al* (2007) developed two blending methods, inward and outward blending, to improve the continuity between adjacent panels with multi-chromosomal GAs.

## 2 Optimization Strategies

In order to minimize the total weights of all the panels, the number of layers of each fibre orientation ( $45^\circ, -45^\circ, 90^\circ, 0^\circ$ ) of panels and stiffeners will be defined as design variables to do optimization under the conditions of buckling constraints and strain limit. At the local level, maximum ply compatibilities will be achieved by optimization of stacking sequence of these layers, which are constant in thickness after the top level optimization.

### 2.1 Smeared Stiffness-Based Method

Smeared stiffness-based method is an approach to neutralize the stacking sequence effects on buckling performance and set up homogeneous sections with quasi-isotropic lay-ups. Unless the stack preference of laminated model is intended to follow, no pre-defined stacking sequence of plies is needed at the top level optimization of the total weight. The  $\mathbf{D}$  stiffness matrix of laminae is formulated as:

$$\mathbf{D} = \mathbf{A} t/12 \tag{1}$$

The application of this method on concept optimization of composite laminates was successfully illustrated by Zhou (2007). In this paper, two level optimizations will be achieved using this technology. At the top level, minimum number of total layers is objective function. Buckling and strength constraints will be considered as well in this level. At the local level, all the layers given by the top level without buckling and strength constraint violation will be shuffled.

### 2.2 Lamination Parameter-Based Method

Lamination parameter-based method is an efficient stiffness optimization approach. Using lamination parameters as design variable in the stiffness optimization is quite efficient. In this paper, lamination parameters related with out-of-plane stiffness matrix and numbers of each ply angle (45°, -45°, 90°, 0°) are design variables. Subjected to the constraints on buckling, strength, ply percentages and the feasible area of lamination parameters, the minimum weight will be the objective function in the global level. Then, stacking sequence optimization for matching the lamination parameters that came from the top level will be performed by permutation GA with the loads constraints and manufacturing conditions in order to maximize the compatibility of adjacent panels. The optimization design for this local level is shown in Figure 1.

The non-dimensional lamination parameters related with out-of-plane stiffness matrix are formulated as:

$$(V_{[1,2,3]}^D)^i = \left(\frac{2}{h_i}\right)^3 \int_{-h_i/2}^{h_i/2} [\cos 2\theta, \sin 2\theta, \cos 4\theta] z^2 dz \tag{2}$$

- Where  $D$  presents the out-of-plane bending stiffness,
- $i$  is the panel number,
- $h_i$  is the total thickness of the panel  $i$ ,
- $\theta$  is ply angle.

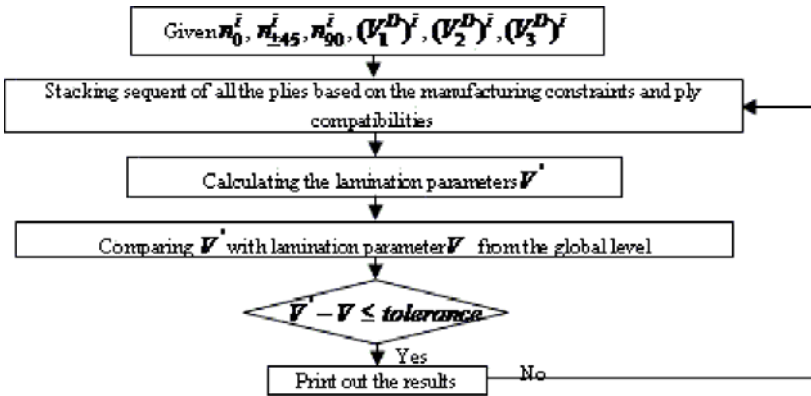


Figure 1. Flow chart of the optimization process for panels

### 3 Layups Design Rules

Local laminate layups design rules applied to each panel are as follows according to aerospace industrial manufacturing requirements (Niu, 1992):

- a. The stack is balanced, for example, the number of 45° and -45° plies is the same in each of the components.
- b. Due to the damage tolerance requirements, the outer plies for the skin should always contain at least one set of ±45° plies
- c. The number of plies ( $N_{max}$ ) in any one direction placed sequentially in the stack is limited.

$$N_{max} = 4, \text{ if } t_{ply} = 0.125 \text{ mm}$$

$$3, \text{ if } t_{ply} = 0.25 \text{ mm}$$

- d. Avoid 90° change of angle between two adjacent plies, if possible.

### 4 Wing Box Example

The wing model and its material property (Liu, 2001) are given to illustrate the methods discussed in previous sections in Figure 2 and 3. Due to the symmetric and balanced laminates, only half number of ply angle (45°, -45°, 90°, 0°) of each panel will be given.

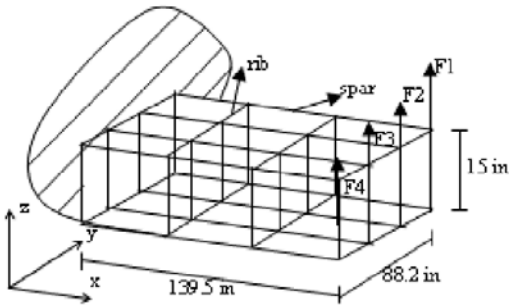


Figure 2. Geometry for wing box

1	6	7
2	5	8
3	4	9

10	15	16
11	14	17
12	13	18

Figure 3. Bottom and top skin configurations

The wing box skin is divided into three parts: root part, intermediate part and tip part. Thus buckling performance on the top skin of wing box can be analyzed with high accuracy. Each part includes three same panels as shown in Figure 3. There are 18 design variables for smeared stiffness-based method and 36 design

variables for lamination parameters-based method. From Table 1 and 2, the total number of stacks for the continuous design was 448.82 and increased to 460 for rounded design in the first method. By comparing with the results (Liu, 2000), we obtained less weight of the wing box subjected to the same optimization constraints. Due to ply continuity consideration among three parts in the lamination parameter-based method, a slight heavier wing structure was obtained than the one by smeared stiffness-based method from Table 3 and 4. Also the first buckling mode happens at bottom skin instead of the top skin. A few numbers of plies with 0 degree can be added to bottom skin to prevent buckling. The buckling mode factor 1.0332 happens at top skin, which was close to buckling mode factor 1.0349 from top level optimization. The reason is that at the local level optimization the minimum difference of objective function is the target to achieve (lamination parameters) in the lamination parameter-based method.

Table 1. Continuous and rounded optimal design with 18 variables for smeared stiffness-based method

	$n_{0^\circ}/n_{45^\circ}/n_{90^\circ}$ (Continuous)	$n_{0^\circ}/n_{45^\circ}/n_{90^\circ}$ (Rounded)	Active constraints
Top skin panels			
Panel no.16	30.20/12.54/24.56	30/13/25	
Panel no.17	18.69/ 20.53/12.10	19/21/12	
Panel no.18	24.43/5.40/8.92	24/6/9	buckling
Bottom skin panels			
Panel no.7	1.50/1.32/1.45	2/1/2	
Panel no.8	2.38/1.01/1.32	3/1/2	
Panel no.9	7.81/3.06/3.35	8/3/4	
Buckling load factor	0.9960	1.0440	
Objective function	448.82	460	
(Total number of stacks)			
Liu and Haftka (2001)	465.63	464	

Table 2. Stacking sequence of top and bottom skin panels for the rounded design

Panel no.	Stacking sequence
16	$[(\pm 45)_2/(0_4/90/45/0/-45)_2/(0_4/90/45/90/-45)_2/90_2/0/(\pm 45)_3/(90/(\pm 45)_4/(90_4/0_3)_3/90/0_2)_s]$
17	$[(\pm 45)_2/(0_4/90/45/0/-45)_2/(0_4/90/45/90/-45)_2/90_2/0/(\pm 45)_3/(90/(\pm 45)_4/(\pm 45)_8)_s]$
18	$[(\pm 45)_2/(0_4/90/45/0/-45)_2/(0_4/90/45/90/-45)_2/90_2/0_4/90/0_2)_s]$
7	$[\pm 45/90_2/0_2)_s]$
8	$[\pm 45/90/0/90/0_2)_s]$
9	$[\pm 45/90/0/90/0_2/(\pm 45)_2/0_4/90_2/0)_s]$
Buckling mode factor	1.019

### 5 Conclusions

A bi-level wing optimization was investigated. Two approaches were examined for seeking the best stacking sequence of laminated composite wing structures with manufacturing constraints. By comparing with the results from published papers, the potencies of these two methods were demonstrated.

Table 3. Continuous and rounded optimal design with 36 variables for lamination parameter-based method

	$n_{0^\circ}/n_{45^\circ}/n_{90^\circ}$ (Continuous)	$n_{0^\circ}/n_{45^\circ}/n_{90^\circ}$ (Rounded)	$V_1/V_2/V_3$
Top skin panels			
Panel no.16	30.20/12.54/24.56	28/16/22	1.1268/1.0102/1.2132
Panel no.17	18.69/ 20.53/12.10	26/13/19	1.1610/1.0086/1.3022
Panel no.18	24.43/5.40/8.92	22/6/14	1.2398/1.0098/1.0982
Bottom skin panels			
Panel no.7	4.39/1.30/1.28	5/1/1	1.3715/1.0579/0.7382
Panel no.8	3.92/1.20/2.06	4/1/2	1.1144/1.0576/0.7906
Panel no.9	7.48/1.72/2.68	8/2/3	0.8432/1.0485/0.9308
Buckling load factor	1.0039	1.0349	
Objective function	456.68	464	
(Total number of stacks)			
Liu and Haftka (2001)	465.63	464	

Table 4. Stacking sequence and lamination parameters of the panel at local level

	Panel no.	$V_1/V_2/V_3$	Buckling load factor
Shared layers based permutation GA:	16	1.1592/1.0070/1.2177	
	17	1.1812/1.0081/1.2030	
	18	1.2398/1.0139/1.0987	1.0332 (2 <sup>nd</sup> buckling factor)
	7	1.2630/1.0547/0.8958	
	8	1.2604/1.0547/0.8958	
	9	1.2084/1.0296/1.1270	0.9615 (1 <sup>st</sup> buckling factor)
Stacking sequence:			
16	[( ± 45) <sub>2</sub> /(0 <sub>2</sub> /45/0 <sub>2</sub> /-45) <sub>2</sub> /0 <sub>2</sub> /45/90/-45/(0/90) <sub>3</sub> /90/0 <sub>2</sub> /90 <sub>2</sub> /0 <sub>3</sub> /90/0/90 <sub>3</sub> /45/90/-45/0 <sub>3</sub> /90 <sub>2</sub> /( ± 45) <sub>2</sub> /90 <sub>2</sub> /(90/0) <sub>3</sub> /45/0/-45/( ± 45) <sub>6</sub> /90 <sub>2</sub> /45/90/-45/(45/0/-45) <sub>2</sub> ] <sub>s</sub>		
17	[( ± 45) <sub>2</sub> /(0 <sub>2</sub> /45/0 <sub>2</sub> /-45) <sub>2</sub> /0 <sub>2</sub> /45/90/-45/(0/90) <sub>3</sub> /90/0 <sub>2</sub> /90 <sub>2</sub> /0 <sub>3</sub> /90/0/90 <sub>3</sub> /45/90/-45/0 <sub>3</sub> /90 <sub>2</sub> /( ± 45) <sub>2</sub> /90 <sub>2</sub> /(90/0) <sub>3</sub> /45/0/-45/( ± 45) <sub>6</sub> ] <sub>s</sub>		
18	[( ± 45) <sub>2</sub> /(0 <sub>2</sub> /45/0 <sub>2</sub> /-45) <sub>2</sub> /0 <sub>2</sub> /45/90/-45/(0/90) <sub>3</sub> /90/0 <sub>2</sub> /90 <sub>2</sub> /0 <sub>3</sub> /90/0/90 <sub>3</sub> /45/90/-45/0 <sub>3</sub> /90 <sub>2</sub> ] <sub>s</sub>		
7	[ ± 45/0 <sub>4</sub> /90/0] <sub>s</sub>		
8	[ ± 45/0 <sub>4</sub> /90 <sub>2</sub> ] <sub>s</sub>		
9	[ ± 45/0 <sub>4</sub> /90 <sub>2</sub> /45/90/-45/0 <sub>4</sub> ] <sub>s</sub>		

## References

- Liu B, Haftka RT, Akgun MA (2000) Two-level composite wing structural optimization using response surface. *Struct Multidisc Optim.* 20: 87-96.
- Liu B, Haftka RT (2001) Composite wing structural design optimization with continuity constraint. *Proc. of the 42<sup>th</sup> AIAA SDM Conf.*, Seattle, USA.
- Liu D, Toropov VV (2008) Weight and stacking sequence optimization of laminated composite panels with blending and manufacturing constraints. *PGR Conference*, University of Leeds, UK, July.
- Liu D, Toropov VV, Querin O, Barton DC (2009) Stacking sequence optimization of laminated composite materials with blending and manufacturing constraints. *50th AIAA/ASME/ASCE/AHS/ASC Structures, Structural Dynamics, and Material Conference and 5th AIAA Multidisciplinary Design Optimization Specialist Conference*, Palm Springs, CA, May 4-7.
- Niu MCY (1992) *Composite Airframe Structures, Practical Design Information and Data*, Conmil Press Ltd., Hong Kong.
- Seresta O, Gurdal Z, Adams DB, Watson LT (2007) Optimal design of composite wing structures with blended laminates. *Composites Part B: Engineering* 38: 469-480.
- Tsai SW, Halpin JC, Pagano NJ (1968) *Composite materials workshop*. Technomic, Westport, Connecticut, 233-253.
- Zhou M, Fleury R (2007) Optimization of composite structures – Understanding and meeting the challenges. Altair Composite Seminar, Lemington spa, UK.

*“This page left intentionally blank.”*

# Minimum Cost Design of a Welded Stiffened Pulsating Vacuum Steam Sterilizer

Yunkang Sui<sup>1\*</sup>, Cairui Yue<sup>1</sup> and Huiping Yu<sup>1</sup>

<sup>1</sup>Numerical Simulation Center for Engineering, Beijing University of Technology, Beijing 100124, China

**Abstract.** Researches on how to save the design cost of pressure vessel are investigated here, in which the thickness of the vessel and the number of stiffeners are considered as the design variables. This paper presents an algorithm based on hierarchical architecture. It is convenient and feasible to apply stratification optimization method to solve the problem with discrete-continuum mixed variables. At the same time, considering the independence of sample point analysis and used parallel computing, the present software in this paper is of more efficiency and utility.

**Keywords:** cost, hierarchical architecture, discrete-continuum mixed variables, parallel computing

## 1 Introduction

Pressure vessel is a kind of holding equipment used widely in chemical industry, petrochemical industry, and machinery industry etc. Because the safe problem of pressure container is significant, traditionally, the pressure vessel design is prone to conservative, which makes the container designing cumbersome, material-wasting and high-costing, all of which have brought about large amount of dissipation. To get an economical structure in the period of assembling costs increasing, one should take into account as many elements of costs as possible.

The main purpose of this paper is to show the application of efficient mathematical methods to study the problem of optimizing costs of pulsating vacuum steam sterilizer. For the objective function, an advanced cost function (Farkas et al., 2005; Jármai et al., 2006) is used including material, assemblies, transports, utilization, maintenance and so on (Jármai et al., 1990), the assemble cost include the cost of welding, cutting, preparation, assembly, tacking, painting, etc. Therefore, how to save most cost of construction is a high degree of nonlinear problem, with the number of stiffeners and thickness of wall as its variables. A new ap-

---

\* Corresponding author, e-mail: ysui@bjut.edu.cn

proach is raised on the optimization problem with discrete-continuum mixed variables (Sui, 1996).

## 2 Welded structure for sterilizer

Pressure steam sterilizer with rectangle cross section is interbedded structure, both ends of which are closed to form a sealing and the inner cavity is the main space where things to be sterilized. The interlayer is filled with steam to heat the inner cavity. In order to reinforce the stiffness of the inside and outside cavity and improve the force situation, stiffeners are used between the inside and outside of the cavity.

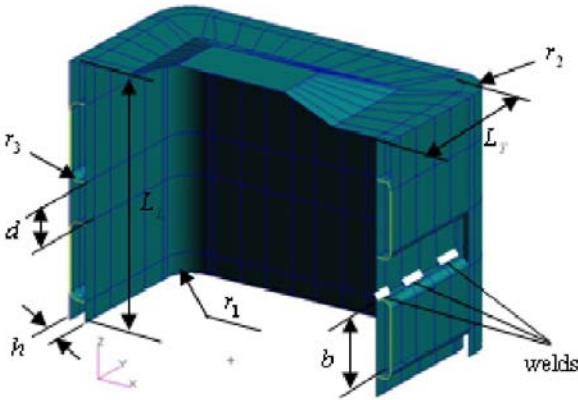


Figure1. Geometrical mode

where  $t_1$  : the thickness of the inner wall (mm),  $t_2$  : the thickness of the outer wall (mm),  $t_3$  :the thickness of stiffeners (mm),  $d$  : the distance between stiffeners (mm).

## 3. Formulation and Solution of Optimization Model

Combined with the previous work (Yu et al., 2008; Yue et al., 2008), this article developed the numerical analysis into the optimization design. Because it is difficult to set the upper limit of the cost, it has little significance to pursue the minimization of the maximum stress, thus, in the presupposition of ensuring the life of the sterilizer, the design variables are included of the inner wall  $t_1$ , the outer wall  $t_2$ , the strengthen wall thickness  $t_3$  and the number  $J$ , the constraint condition is the

maximum stress of the inner wall, and the optimization objective function is the total cost of the sterilizer.

$$\begin{cases}
 \text{Find } J, t_1, t_2, t_3 \\
 \text{Make } C(J, t) \rightarrow \min \\
 \text{s.t. } \sigma_l(J, t) \leq \bar{\sigma} \quad (l=1, \dots, m) \\
 \quad \underline{t}_i \leq t_i \leq \bar{t}_i \quad (i=1, \dots, 3) \\
 \quad J \in \{0, 1, \dots, 13\}
 \end{cases} \tag{1}$$

In the Equation (1),  $t$  is the design wall thickness, cost of construction function  $C(J, t)$  is the function about thickness and the number of stiffener;  $\sigma_l$  is the stress of number  $l$  element,  $m$  is the number of required strain points,  $\bar{\sigma}$  is that strain required according to the model;  $\underline{t}_i$  is lower limit of the number  $i$  thickness,  $\bar{t}_i$  is upper limit of the number  $i$  thickness. The following is a step-by-step procedure for such an analysis:

1. Cost function: According to Farkas and Jármai (1996), the cost function includes material ( $C_M$ ) and total manufacturing (fabrication, welding, cutting and painting) costs ( $C_F$ ),  $C_F$  in the function of different times, the total cost is given by Equation (2):

$$C = C_M + C_F = \sum_{i=1}^n k_{Mi} \rho_i V_i + k_F \sum_{i=1}^n T_i \tag{2}$$

Where,  $K_M$  KM and  $K_F$  KF are the corresponding cost factors,  $\rho$  is the material density,  $V$  is the volume of the structure,  $T_i$  are the production times.

2. To avoid the iterative oscillation phenomenon, K-S function is adopted in transforming multiple constrained optimizations model into a single constrained optimization model. The stress of inner wall can be denoted as

$$\sigma_{K-S} = \ln[e^{p\sigma_{\max 1}} + \dots + e^{p\sigma_{\max m}}] / p \leq \bar{\sigma} \tag{3}$$

where  $\sigma_{K-S}$  is the response value of the constraint function from the K-S function.

### 3. Solution of optimization model

(1) The objective function is extremely nonlinear function, in this paper, according to the high order contraction method, the object function and the constraint function of the structural optimization model with discrete-continuum design variables are expanded in logarithm space, consequently, it gets a more precise approximate description than the model expanded by Taylor expansion, and the procedure of model optimization is a more precise solution.

(2) According to RSM method, the structural optimization model based on the sampling points is mainly studied in this dissertation. The parallel computing approaches is shortening the time consumed for the response surface methodology.

(3) A method, hierarchical architecture, has been used to make the process more convenient and easier as following below. Firstly, Fibonacci is used to deal with discrete variable  $J$  problem, then solves the continuous variables  $t$  problem is solved in term of the number of stiffeners.

Due to the analysis above, then at the point  $t^0$ , the objective function is expanded to the second order of the high order contraction approximation whose constant terms are omitted. While constrain function is expanded to the first order approximation of the high order (Duffin). Then Equation (1) can be transformed as follows:

$$\left\{ \begin{array}{l} \text{Find } t \in E^3 \\ \text{Make } \frac{1}{2} \sum_{i=1}^3 \sum_{j=1}^3 \frac{\partial^2 \ln f(t^0)}{\partial \ln t_i \partial \ln t_j} \ln t_i \ln t_j + \sum_{i=1}^3 \left( \frac{\partial \ln f(t^0)}{\partial \ln t_i} - \sum_{j=1}^3 \frac{\partial^2 \ln f(t^0)}{\partial \ln t_j \partial \ln t_i} \ln t_j^0 \right) \ln t_i \rightarrow \min \\ \text{s.t. } \sum_{i=1}^3 \frac{\partial \ln \sigma_{K-S}(t^0)}{\partial \ln t_i} \ln(t_i) \leq \ln \bar{\sigma} + \sum_{i=1}^3 \frac{\partial \ln \sigma_{K-S}(t^0)}{\partial \ln t_i} \ln(t_i^0) - \ln \sigma_{K-S}(t^0) \\ \underline{t}_i \leq t_i \leq \bar{t}_i \quad (i = 1, \dots, 3) \end{array} \right. \quad (4)$$

Define  $z_i = \ln t_i$  ( $i = 1, \dots, 3$ ) in Equation(4), thus the above optimization model is transformed, then the constant term of the objective function is omitted, and the transformed model can be changed into a formulation of a quadratic programming, the model is expressed as

$$\left\{ \begin{array}{l} \text{Find } z \in E^3 \\ \text{Make } z^T H z / 2 + c^T z \rightarrow \min \\ \text{s.t. } A z \leq b \\ \underline{z}_i \leq z_i \leq \bar{z}_i \quad (i = 1, \dots, 3) \end{array} \right. \quad (5)$$

Here, elements of Hessian matrix is  $H_{ij} = \frac{\partial^2 \ln f(t^0)}{\partial \ln t_i \partial \ln t_j}$ , elements of coefficient

matrix for the objective functions are  $c_{ij} = \frac{\partial \ln f(t^0)}{\partial \ln t_i} - \sum_{j=1}^3 \frac{\partial^2 \ln f(t^0)}{\partial \ln t_j \partial \ln t_i} \ln t_j^0$ , ele-

ments of coefficient matrix for the constraint function are  $A_i = \frac{\partial \ln \sigma_{K-S}(t^0)}{\partial \ln t_i}$ ,

elements of the vector is  $b_i = \ln \bar{\sigma} + \sum_{i=1}^3 \frac{\partial \ln \sigma_{K-S}(t^0)}{\partial \ln t_i} \ln(t_i^0) - \ln \sigma_{K-S}(t^0)$ .

## 4 Mathematical Optimization and Numerical optimization Results

### 4.1. Application of Fibonacci Array

Numbers of stiffeners  $J \in \{0,1,\dots,13\}$ , with the optimization lower limit  $n_0 = 0$ , and upper limit  $n = 13$ , that is, the original interval is  $[0, 13]$ . Therefore, it defines  $l_1 = \frac{F_{n-2}}{F_n} L_1 = \frac{5}{13} \times 13 = 5$ , and takes  $k_1 = n_0 + l_1 = 5$ ,  $k_2 = n - l_1 = 8$ . The optimization model is analyzed when the number of stiffener is equal to 5 and 8 respectively and the results  $C(k_1) = 3.2694 \times 10^3$ ,  $C(k_2) = 2.7038 \times 10^3$ ,  $C(k_2) < C(k_1)$  are acquired, that means the cost is lower when sterilize is 8. So the models with stiffener number which is not more than 5 are abandoned and the optimize interval changes into  $[5, 13]$ .

By the same way, the number of stiffener 8 and 10 are compared in second steps and it obtains  $C(8) < C(10)$ , and the optimization interval turns into  $[5, 8]$ ; similarly,  $C(7) < C(6)$ , the optimization interval is cut into  $[6, 8]$ . In the 4th step,  $C(7) < C(8)$ . The best optimization parameters are found after 4 iterations.

Table 2. Results for discrete number of stiffeners

$J$	$t_1/\text{mm}$	$t_2/\text{mm}$	$t_3/\text{mm}$	$\sigma/\text{MPa}$	$C/\text{¥}$
5	6.133	4.5	3.0	1.1312e+002	3.269411e+003
6	4.953	4.5	3.0	1.2411e+002	2.873633e+003
7	4.383	4.5	3.0	1.2900e+002	2.691162e+003
8	3.964	4.2	3.0	2.305e+002	2.703824e+003
10	3.759	4.0	3.0	9.2323e+001	2.717902e+003

Table 2 shows that the cost decreases by 6.35%. Therefore, cost is cut down sharply. The costs distribution of each segment is introduced in Figure 2. The processing and assembling cost account for half of total cost. For the cost of welding, inner wall, outer wall and the bottom of sterilizer constitute a large percent. So the data of result can be provided to guide production and process as reference.

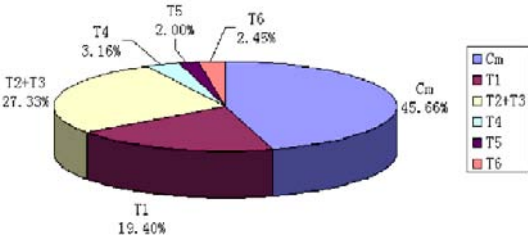


Figure 2. The total cost distribution of sterilizer

### 4.2 Application of Parallel Computing

Based on Windows system, it builds a principal and subordinate parallel environment using C++ and Fortran to set up new procedure and assigns task dynamically, namely, host computer assigns tasks and deals with the data, while subordinate computers use Nastran to analyze FEM model.

The results of serial and parallel program are absolutely the same (exemplify by 3 machines in a parallel relationship). Comparing with serial program, the operating time of parallel program decreases by 49.965%, and the time of analysis by Nastran decreases by 49.837%. As Table 2 shows, parallel method is much more efficient than serial one.

Table 3. Serial and parallel run-time comparison table

Algorithm	Node (p)	Total Time(t)/s	Times for Paralleling/s	Speedup (S)	Paralleling efficiency (E)
Serial	1	5983.062	5623.613	—	—
Parallel	3	2994.156	2820.952	1.9982	0.6660

### 5 Conclusion

Aiming at the minimized cost of welded structure, this paper refers to foreign cost-calculating formula and domestic interrelate material to show the total welding cost explicitly. Besides, the actual requirement is taken into consideration when defining restricted condition. RSM is used to get the stress function. K-S function is used to avoid vibration. When dealing with optimization model with discrete-continuum mixed variables, stratification optimization is applied. And Fibonacci search method is used to solve the discrete variable problem. SQP

method is applied to solve the optimization model. The result of optimizing is proved that the intensity is reinforced and the cost is cut down. In addition, the application of parallel procedure improves solve efficiency and makes it more practical.

## Acknowledgements

Financial supported by National Natural Science Foundation of China (10872012), Opening Foundation of National Key Laboratory for Advanced Design Manufacturing Automobile Body (30715002) and Scientific Research Foundation of Doctoral Subjects in Chinese Universities (20060005010) is gratefully acknowledged.

## References

- Farkas J., Simões L.M.C. and Jármai K. (2005). Jármai. Minimum cost design of a welded stiffened square plate loaded by biaxial compression. *Struct. Multidisc Optim.*, 29: 298-303.
- Jármai K., Snyman J.A. and Farkas J. (2006). Minimum cost design of a welded orthogonally stiffened cylindrical shell. *Computers & Structures*, 84(12): 787-797.
- Jármai K. and Farkas J. (1990). Cost calculation and optimisation of welded steel structures. *Journal of Construction Steel Research*. 50: 115-135.
- Sui Y.K. (1996). *Modelling, transformation and optimization new developments of structural synthesis method [M]*. Da lian: Dalian University of Technology Press [in Chinese].
- Yu H.P., Sui Y.K., Zhang Y.L. et al. (2008). Analysing the mechanical capability of the vacuum sterilizer using experiment and numerical simulation. *Science & Technology Review*, 26(16): 50-54 [in Chinese].
- Yue C.R., Yu H.P., Sui Y.K. et al. (2008). Numerical analysis of several pulsating vacuum steam sterilizers. *Pressure Vessel Technology*, 25(6): 18-24 [in Chinese].

*“This page left intentionally blank.”*

# A Framework of Multiobjective Collaborative Optimization

Haiyan Huang<sup>1\*</sup> and Deyu Wang<sup>2</sup>

<sup>1</sup>School of Naval Architecture and Ocean Engineering, Jiangsu University of Science and Technology, Zhenjiang 212003, P.R. China

<sup>2</sup>State Key Laboratory of Ocean Engineering, Shanghai Jiao Tong University, Shanghai 200030, P.R. China

**Abstract.** A framework for solving the multiobjective optimization problems in multidisciplinary design environment is advised in this paper. Based on the collaborative optimization (CO) algorithm, a new system level objective function is advised to minimize relative value between the collaborative objective function and single disciplinary objective function. It eliminates the effect of dimensions and magnitude orders among different disciplinary objective functions. A new subsystem level objective function is developed that includes the disciplinary objective function and the consistency constraint. A new framework of multiobjective collaborative optimization (MOCO) is developed. In MOCO framework, the system level optimizer does not only independently invoke the subdisciplinary analysis tools, but also invoke its subdisciplinary optimizer. The feasibility and reliability of the MOCO are highlighted by the successful convergence of two examples.

**Keywords:** multiobjective, collaborative optimization, multidisciplinary design optimization

## 1 Introduction

Most real-world design problems are actually complex and multidisciplinary with almost more than one objective function to be analyzed simultaneously. Those objective functions are often conflicting and non-commensurable, such as improving performance and increasing cargo in ship design problem. Multiobjective optimization algorithms are usually used to solve these multiobjective optimization problems. But many multiobjective optimization problems belong to the multidisciplinary optimization problem. So the multiobjective optimization algorithms are poor in solving this kind of problem because different models are usually used in dif-

---

\* Corresponding author, e-mail: [expressemail@126.com](mailto:expressemail@126.com)

ferent disciplinary analysis. The multidisciplinary design optimization (MDO) algorithms are good at solving those problems.

Collaborative optimization (CO), one of MDO, is characterized by a distributed, bi-level structure, wherein a system problem seeks to optimize system performance, whereas disciplinary problems attempt to minimize the interdisciplinary inconsistency in the variables and responses shared by the disciplines. The CO method has been successfully used in many cases (Budianto and Olds, 2004, Ilan and Valerie, 2000, Jun et al., 2004). But the existing CO framework is often poorly suited for multilevel distributed design (Ilan and Valerie, 2000). At the same time, some difficulties will be encountered in the analysis process of solving the multiobjective optimization problems with the existing CO.

The goal of this paper is to develop a new CO framework that is suitable for solving the multiobjective design problems in multidisciplinary design environment. In order to achieve this goal, modification to the existing CO algorithm is done to develop a multiobjective collaborative optimization (MOCO) algorithm. Then two examples are used to demonstrate the MOCO model.

## 2 Framework of Multiobjective Collaborative Optimization

Multiobjective optimization has been defined as finding a vector of design variables satisfying constraints to give acceptable values to all objective functions. In general, it can be mathematically defined as

$$\begin{aligned}
 \text{Min} \quad & F(\mathbf{X}) = [f_1(x), f_2(x), \dots, f_k(x)]^T \\
 \text{s.t.} \quad & g_i(\mathbf{X}) \leq 0 \quad (i = 1, \dots, l) \\
 & h_i(\mathbf{X}) = 0 \quad (i = 1, \dots, m) \\
 & x_{i,\text{low}} \leq x_i \leq x_{i,\text{up}} \quad (i = 1, \dots, n)
 \end{aligned} \tag{1}$$

where  $\mathbf{X}=[x_1, x_2, \dots, x_n]^T$  is the vector of design variables;  $g_i(\mathbf{X})$  ( $i=1, \dots, l$ ) are the inequality constraints;  $h_i(\mathbf{X})$  ( $i=1, \dots, m$ ) are the equality constraints.  $x_{i,\text{low}}$  and  $x_{i,\text{up}}$  define the lower and upper bounds for the  $i^{\text{th}}$  design variable  $x_i$ , respectively;  $F(\mathbf{X})$  is the vector of objective functions, which must be either minimized or maximized. Without loss of generality, it is assumed that all objective functions are to be minimized. A maximization type objective can be converted to a minimization type by multiplying negative one.

## 2.1 System Level Objective Function

At the system level of the CO algorithm, the optimization problem is stated as

$$\begin{aligned}
 &\text{Min } F \\
 &\text{s.t. } J_i(z) = 0 \\
 &\quad z_{i,\min} \leq z_i \leq z_{i,\max}
 \end{aligned} \tag{2}$$

where  $F$  is the system level objective function.  $J_i(z)$  is the consistency constraint for the  $i^{\text{th}}$  subdiscipline optimization problem.  $z_i$  is the system level design variable vector.  $z_{i,\min}$  and  $z_{i,\max}$  define the lower and upper bounds of  $i^{\text{th}}$  design variable  $z_i$ , respectively.

In the CO algorithm, the system level objective function (Eq. (2)) is a single objective function. Some difficulties will be encountered in the actual design (Eq. (1)). For example, the minimum structural mass may be the objective function in the static discipline of truss bridge optimization problem. The minimum acceleration of bridge structure under various dynamic loads may be the objective function in the dynamic discipline. Two different objective functions will simultaneously be selected in this case. This problem belongs to multiobjective optimization problem. Those different objective functions have not only different dimensions (the dimension of mass and acceleration is kg and  $\text{m/s}^2$ , respectively), but also different magnitude order. At the same time, these two kinds of analysis belong to different discipline respectively. For overcoming those difficulties, the relative values are used in the new system level objective function of the MOCO model.

On the other hand, the design variables in different disciplinary model might have different values in the process of optimization. Because all the design variables will change along the way to the optimal design that is controlled by their disciplinary constraints and objective function. Since the shared variables have the same values in the final design, all the subsystems have to come to compromise each other. That means the optimum solution coming from single disciplinary optimization model is prior to the multidisciplinary optimum solution. So it is the goal of the system level optimization model that how to minimize the discrepancy of those solutions.

For avoiding encounter no-solution or convergence difficulties, the consistency equality constraints are replaced by the inequalities using a relax factor (Alexandrov and Lewis, 2002, Xiang Li et al., 2008) which ensures both interdisciplinary and multilevel compatibility. The mathematical formulation can be posed as a constrained minimization problem of the following form which considers a two-discipline multiobjective optimization problem

$$\begin{aligned}
 & \text{Min} \quad \left| \frac{F_1(z)}{F_1^*} \right| + \left| \frac{F_2(z)}{F_2^*} \right| \\
 \text{s.t.} \quad & J_i(z) \leq \varepsilon \\
 & z_{i,\min} \leq z_i \leq z_{i,\max}
 \end{aligned} \tag{3}$$

where  $F_i(z)$  ( $i=1,2$ ) is the  $i^{\text{th}}$  disciplinary optimum solution in the system level model directly coming from disciplinary analysis.  $F_i^*$  ( $i=1,2$ ) is the subsystem level optimum solution in its disciplinary model lonely.  $J_i(z) \leq \varepsilon$  is the inequality consistency constraint.  $\varepsilon$  is the relax factor.

### 2.2 Subsystem Level Objective Function

At the subsystem level of the CO algorithm, the  $i^{\text{th}}$  discipline optimization problem is stated as

$$\begin{aligned}
 \text{Min} \quad & J_i(z) = \sum_{k=1}^n \sum_{j=1}^2 (x_{jk} - z_k)^2 \\
 \text{s.t.} \quad & \text{Disciplinary constraints}
 \end{aligned} \tag{4}$$

where  $J_i(z)$  is the subsystem level objective function. It is the system compatibility constraint too.  $x_i$  is the subsystem level design variable.

But at the subsystem level of the MOCO algorithm, the  $i^{\text{th}}$  discipline optimization problem is modified as

$$\begin{aligned}
 \text{Min} \quad & F_i^* + J_i(z) \\
 \text{s.t.} \quad & \text{Disciplinary constraints}
 \end{aligned} \tag{5}$$

In these discipline optimization models, the objective function includes the  $i^{\text{th}}$  disciplinary objective function  $F_i^*$  and the  $i^{\text{th}}$  system compatibility constraint  $J_i(z)$ .

### 2.3 Framework of Collaborative Optimization

The framework of the CO based on Equation (2) and (4) is shown in Figure 1(a) which considers a two-discipline optimization problem. For solving the same question, a new framework of the MOCO based on Equation (3) and (5) is shown in Figure 1(b). In MOCO algorithm, the system level optimizer does not only in-

independently invoke the disciplinary analysis tools, but also invoke its subsystem level optimizer. The subsystem level optimizer is made up of a series of modules that they are correlative to disciplines. The number of modules and the system level objective function (Eq. (3)) can be adjusted according to the discipline number used in the analysis process. It can not only solve the single objective optimization problem, but also solve the multiobjective optimization problem. The MOCO framework is more suitable for multiobjective multidisciplinary optimization problems.

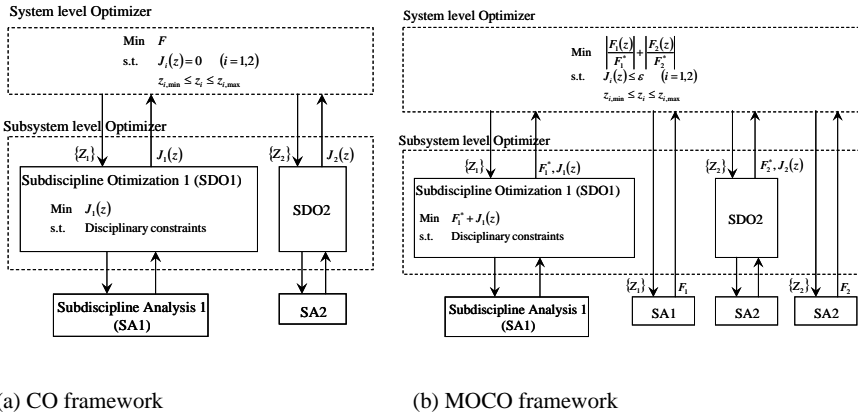


Figure 1 Framework of a two-discipline optimization problem

### 3 Numerical Examples

#### 3.1 Design of a Speed Reducer

The speed reducer optimization problem is one of ten standard examples being used to evaluate the performance of MDO method. Along the lines of CO, the speed reducer optimization problem can be decomposed into three subsystems (Azarm and Li, 1989).

(1) The CO model

The system level model is stated as

$$\begin{aligned}
 \min \quad & F = F_1 + F_2 + F_3 \\
 \text{s.t.} \quad & J_1 = (x_1^* - z_1)^2 + (x_2^* - z_2)^2 + (x_3^* - z_3)^2 = 0 \\
 & J_2 = (x_1^* - z_1)^2 + (x_2^* - z_2)^2 + (x_3^* - z_3)^2 = 0 \\
 & J_3 = (x_1^* - z_1)^2 + (x_2^* - z_2)^2 + (x_3^* - z_3)^2 = 0
 \end{aligned} \tag{6}$$

The 1<sup>st</sup> discipline optimization model (design of the first shaft) is stated as

$$\begin{aligned}
 \min \quad & J_1 = (x_1^* - z_1)^2 + (x_2^* - z_2)^2 + (x_3^* - z_3)^2 \\
 \text{s.t.} \quad & g_j - 1.0 \leq 0.0 \quad (j = 1, 2, 7, 8, 9)
 \end{aligned} \tag{7}$$

The 2<sup>nd</sup> discipline optimization model (design of the second shaft) is stated as

$$\begin{aligned}
 \min \quad & J_2 = (x_1^* - z_1)^2 + (x_2^* - z_2)^2 + (x_3^* - z_3)^2 \\
 \text{s.t.} \quad & g_j - 1.0 \leq 0.0 \quad (j = 1, 2, 3, 5, 7, 8, 9, 10)
 \end{aligned} \tag{8}$$

The 3<sup>rd</sup> discipline optimization model (design of the gear tooth) is stated as

$$\begin{aligned}
 \min \quad & J_3 = (x_1^* - z_1)^2 + (x_2^* - z_2)^2 + (x_3^* - z_3)^2 \\
 \text{s.t.} \quad & g_j - 1.0 \leq 0.0 \quad (j = 1, 2, 4, 6, 7, 8, 9, 11)
 \end{aligned} \tag{9}$$

(2) The MOCO model

The system level model is stated as

$$\begin{aligned}
 \min \quad & \left| \frac{F_1(z)}{F_1^*} \right| + \left| \frac{F_2(z)}{F_2^*} \right| + \left| \frac{F_3(z)}{F_3^*} \right| \\
 \text{s.t.} \quad & J_i \leq 0.001 \quad (i = 1, 2, 3)
 \end{aligned} \tag{10}$$

The 1<sup>st</sup> discipline optimization model (design of the first shaft) is stated as

$$\begin{aligned}
 \min \quad & F_1^* + J_1 = F_1^* + (x_1^* - z_1)^2 + (x_2^* - z_2)^2 + (x_3^* - z_3)^2 \\
 \text{s.t.} \quad & g_j - 1.0 \leq 0.0 \quad (j = 1, 2, 7, 8, 9)
 \end{aligned} \tag{11}$$

The 2<sup>nd</sup> discipline optimization model (design of the second shaft) is stated as

$$\begin{aligned}
 \min \quad & F_2^* + J_2 = F_2^* + (x_1^* - z_1)^2 + (x_2^* - z_2)^2 + (x_3^* - z_3)^2 \\
 \text{s.t.} \quad & g_j - 1.0 \leq 0.0 \quad (j = 1, 2, 3, 5, 7, 8, 9, 10)
 \end{aligned} \tag{12}$$

The 3<sup>rd</sup> discipline optimization model (design of the gear tooth) is stated as

$$\begin{aligned}
 \min \quad & F_3^* + J_3 = F_3^* + (x_1^* - z_1)^2 + (x_2^* - z_2)^2 + (x_3^* - z_3)^2 \\
 \text{s.t.} \quad & g_j - 1.0 \leq 0.0 \quad (j = 1, 2, 4, 6, 7, 8, 9, 11)
 \end{aligned} \tag{13}$$

(3) Optimization Strategy

The bi-level optimization strategy is made up of the Modified Method of Feasible Directions in system level and the Sequential Quadratic Programming in subsystem level model.

(4) Results

The model is analyzed by the CO algorithm and the MOCO algorithm proposed in this paper. The same initial target point and optimal technology are used in two kinds of analysis. The results are shown in Table 1.

Table 1 Comparison between two CO Algorithms

Method	Design Variables							Object
	$x_1$	$x_2$	$x_3$	$x_4$	$x_5$	$x_6$	$x_7$	
CO	3.5000	0.7000	17.0000	7.3000	7.7100	3.3500	5.2900	2994.00
MOCO	3.5000	0.7000	17.0000	7.3000	7.7228	3.3492	5.2865	2988.24

Some conclusions are drawn from the comparative study. (1) The analysis results mean that this gear reducer design problem is solved successfully by the MOCO algorithm proposed in this paper. Successful convergence proved the feasibility and reliability at both system and subsystem levels. (2) The system analysis times of the MOCO (32 times) at system level is less than that of the CO (47 times). In MOCO, the system level objective function has a reference solution  $F_i$ . The modules do not exchange more information each other. So the MOCO algorithm is faster than the CO algorithm.

**3.2 Design of a 10-bar Planar Truss**

The second example is a 10-bar planar truss shown in Figure 2. The design parameters are  $L=1.0\text{m}$ ,  $E=68.95\text{GPa}$ ,  $\mu=0.3$ ,  $\rho =2770\text{kg/m}^3$ . The structure is subjected to two harmonic forces with the magnitude of 10kN at node B and C that the excitation frequency is 0.9HZ. The given discrete set of sectional area for the

design variables is  $S(\text{cm}^2)=\{1.13, 1.43, 1.46, 1.75, 1.86, 2.11, 2.28, 2.36, 2.66, 2.76, 3.09, 3.38, 3.49, 3.79, 4.29, 5.08\}$ . The behaviour constraints are as follows: the upper bound of displacement is 6mm; the upper bound of stress is 100MPa; the upper bound of velocity and acceleration is 10mm/s and  $6\text{m/s}^2$ , respectively.

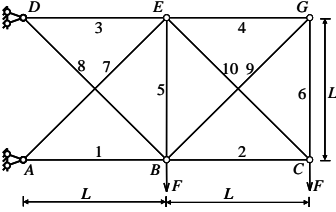


Figure 2 A 10-bar planar truss

(1) The MOCO model

According to Equation (3) and (5), the first objective function  $F_1$  in static discipline is the structural mass, and the second objective function  $F_2$  in dynamic discipline is the maximum acceleration of structure. The relax factor  $\epsilon$  is 0.001. All the sectional areas are the shared design variables, shown in the Table 2. The maximum stress and displacement are the state design variables in the static discipline. The maximum velocity and dynamic stress and dynamic displacement are the state design variables in the dynamic discipline.

(2) Optimization analysis

This model is analyzed with finite element method. The Adaptive Simulated Annealing (ASA) algorithm is used in double level models.

Table 2. Comparison between the initial and final design variables

Design Variables	$A_1$	$A_2$	$A_3$	$A_4$	$A_5$	$A_6$	$A_7$	$A_8$	$A_9$	$A_{10}$
Initial design( $\text{cm}^2$ )	3.09	3.09	3.09	3.09	3.09	3.09	3.09	3.09	3.09	3.09
Final design( $\text{cm}^2$ )	4.29	3.09	1.86	2.66	3.09	1.86	3.09	3.09	3.38	3.49

(3) Results

The final design is reached after 278 collaborative iterations. The optimum solution of various design variables is shown in the Table 2. The values of the initial and final response are shown in Table 3.

Table 3. Comparison between the initial and final design responses

Design response	Static		Dynamic				Mass (kg)
	$d_{\max}$ (mm)	$\sigma_{\max}$ (MPa)	$d_{\max}$ (mm)	$\sigma_{\max}$ (MPa)	$v_{\max}$ (mm/s)	$a_{\max}$ ( $\text{m/s}^2$ )	
Initial	5.136	66.225	5.139	66.257	9.193	5.135	9.977
Final	5.507	94.079	5.508	94.087	0.497	1.407	9.780

The following conclusions can be drawn from the present study. (1) This problem can be solved efficiently and reliably with the MOCO model. (2) After the design variables changed, all the final design response values satisfy the constraints. The maximum velocity of the structure changes from 9.193mm/s to 0.497mm/s, about -94.59%. The maximum acceleration changes from 5.135mm/s<sup>2</sup> to 1.407mm/s<sup>2</sup>, about -72.60%. In a word, the whole mechanical characters are better than before.

## 4 Conclusions

The MOCO framework provides solution capabilities for multiobjective multidisciplinary problems. The feasibility, reliability and computing efficiency of the MOCO model are highlighted by the successful convergence of two examples.

## Acknowledgements

Financial support by Key Laboratory of Jiangsu Advanced Marine Technology Foundation (Sanction No.CJ0805) and 'Knowledge-based Ship-design Hyper-integrated Platform (KSHIP)' of Ministry of Education and Ministry of Finance of P. R. China (Sanction No.200512) is gratefully acknowledged.

## References

- Alexandrov N.M. and Lewis R.M. (2002). Analytical and computational aspects of collaborative optimization for multidisciplinary design. *AIAA Journal*, 40(2):301-309.
- Azarm S. and Li W.C. (1989). Multi-level design optimization using global monotonicity analysis. *Journal of mechanisms, transmissions and automation in design*. 111(2):259-263.
- Budianto I.A. and Olds J.R. (2004). Design and deployment of a satellite constellation using collaborative optimization. *Journal of spacecraft and rockets*. 41(6):956-963.
- Ilan K. and Valerie M. (2000). Collaborative optimization: status and directions. AIAA-2000-4721. 8th AIAA/NASA/ISSMO Symposium on Multidisciplinary Analysis and Optimization, Long Beach CA.
- Jun S., Jeon Y.H., Rho J. and Lee D.H. (2004). Application of collaborative optimization using response surface methodology to an aircraft wing design. AIAA-2004-4442, 10th AIAA/ISSMO Multidisciplinary Analysis and Optimization Conference. Albany, New York.
- Li X., Li W. J. and Liu Chang'an (2008). Geometric analysis of collaborative optimization. *Structural Multidiscipline Optimization*. 35:301-313.

*“This page left intentionally blank.”*

# An Optimal Design of Bi-Directional TMD for Three Dimensional Structure

Jianlin Zhang<sup>1\*</sup>, Ke Zeng<sup>2</sup> and Jiesheng Jiang<sup>1</sup>

<sup>1</sup>Department of Civil Engineering, Northwestern Polytechnical University, Xian 710072, P.R. China

<sup>2</sup>Department of Civil Engineering, Xiamen University, Xiamen 361005, P.R. China

**Abstract.** In this paper, the passive control approach to three dimensional building structures excited by 2-dimensional earthquake ground motions is presented by using Bi-direction tuned masse damper (TMD) system. The mathematic model of a multi-storey building structure including the TMD system is established and its combined equation of motion is given. The optimization of TMD parameters can be obtained by using the Genetic Algorithm Method based on the object function. The numerical example shows that the presented method is effective and flexible. It may obviously control the translational response and rotational response of three dimensional building structures.

**Keywords:** passive control, tuned massed damper, optimization, seismic analysis

## 1 Introduction

Building structures which are resistant to earthquake and wind excitation had been a challenging job for more than a century. In recent years, considerable attention has been paid to research and development of structural control devices, with particular emphasis on alleviation of wind and seismic response of buildings and bridges. Tuned mass damper (TMD) has been applied to the Tall buildings and High rise structures. However, the building model structure was generally limited to a plane frame structure in previous researches, which can not really reflect many properties of structure dynamic response, such as the translational response and rotational response. The effect of TMD can not be obtained well. Some researchers adopted active mass damper (AMD) active control for irregular buildings based on the combined method of the genetic algorithm (GA)-back propagation (BP) neural network. This active control is hard to implement and waste so much energy. In this paper, the passive control approach to three dimensional

---

\* Corresponding author, e-mail: zhangjl@xmu.edu.cn

structures excited by 2-dimensional earthquake ground motions is presented by using Bi-directional tuned mass damper (TMD) system. The optimization of TMD parameters can be obtained by using the GA Method based on the object function. A numerical example shows that the proposed optimal design method is effective and flexible.

## 2 Dynamic Model of Three Dimensional Control System

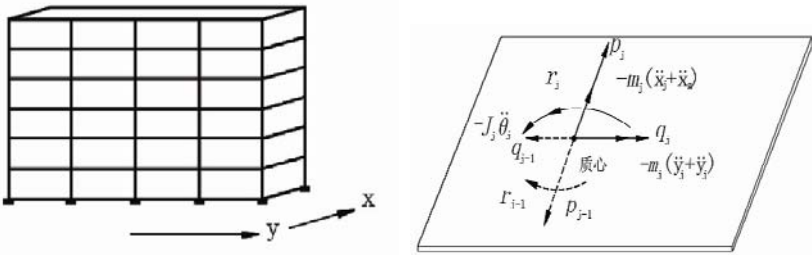


Figure 1. 3-Dimensional building structure. Figure 2. Parameters of each floor

A three dimensional, N-storey, shear model building structure is shown in figure 1. It is assumed that the mass of each floor is centralized at the floor plate. There are two seismic waves along the x-direction and y-direction respectively, whose torsional components are zero.

$$m_j \ddot{x}_j + p_{j-1} - p_j = -m_j \ddot{x}_g(t) \tag{1}$$

$$m_j \ddot{y}_j + q_{j-1} - q_j = -m_j \ddot{y}_g(t) \tag{2}$$

$$J_j \ddot{\theta}_j + r_{j-1} - r_j = 0 \tag{3}$$

where  $x_j$  and  $y_j$  are the  $j$ th floor displacement in x-direction and y-direction respectively relative to the ground,  $\theta_j$  is the  $j$ st floor torsion angle relative to the ground.  $p_{j-1}$  and  $q_{j-1}$  are the  $j$ th floor column shear forces in x-direction and y-direction respectively action on the floor,  $p_j$  and  $q_j$  are the  $j+1$ th floor column shear forces in x-direction and y-direction respectively.  $r_{j-1}$  is the  $j$ th floor torque generated by the shear forces and  $r_j$  is the  $j+1$ th floor torque.  $m_j$  is the mass of the  $j$ th floor and  $J_j$  is the rotational inertia. Bi-directional tuned mass damper

system is fixed on the centroid position of the top floor.  $m_d$  is the mass of Bi-directional tuned massed damper (TMD).  $K_x$  and  $K_y$  are the stiffness coefficient in x-direction and y-direction of the TMD system,  $C_x$  and  $C_y$  are the damping coefficient in x-direction and y-direction. The combined motion equation of a multi-storey building structure including the TMD system is given as follows:

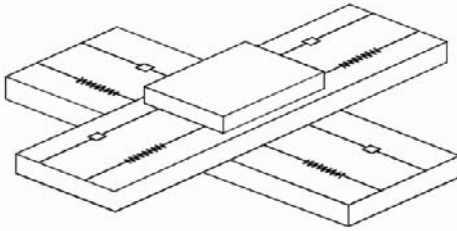


Figure 3. The schematic diagram of Bi-directional tuned massed damper

$$M\ddot{X} + C\dot{X} + KX = -MIa_g(t) \tag{4}$$

where  $M_{3N+2 \times 3N+2}$ ,  $C_{3N+2 \times 3N+2}$ ,  $K_{3N+2 \times 3N+2}$  are total mass matrix, total damping matrix and total stiffness matrix of whole building respectively, including bi-directional TMD system. They are complicated coupled with x-direction vertical frame, y-direction vertical frame, plane torsion and bi-directional TMD system. Other parameters are:

$$X = [x \quad y \quad \theta]_{3N+2 \times 1}^T, \quad x = [x_1 \quad x_2 \quad \cdots \quad x_N \quad x_d]^T, \quad y = [y_1 \quad y_2 \quad \cdots \quad y_N \quad y_d]^T$$

$$\theta = [\theta_1 \quad \theta_2 \quad \cdots \quad \theta_N]^T, \quad I = [I_1 \quad I_2 \quad O]^T, \quad a_g(t) = [\ddot{x}_g(t) \quad \ddot{y}_g(t) \quad O]$$

### 3 Parametric Optimization

Based on the Fourier transform, the displacement and torsion angle response of a three-dimensional building structure can be obtained from equation (4) in frequency domain.

$$X(\omega) = -\left(-\omega^2 M + i\omega C + K\right)^{-1} MI\ddot{x}_g(\omega) = H_x(\omega)\ddot{x}_g(\omega) \tag{5}$$

The velocity response can be obtained as:

$$\dot{X}(\omega) = i\omega H_X(\omega)\ddot{x}_g(\omega) = H_{\dot{X}}(\omega)\ddot{x}_g(\omega) \tag{6}$$

According to the theory of random vibration, the matrices of cross-power spectral density functions of  $X(\omega)$  and  $\dot{X}(\omega)$  can be written as:

$$\Phi_X = H_X(\omega)\bar{H}_X^T(\omega)A_g(\omega) \tag{7}$$

$$\Phi_{\dot{X}} = H_{\dot{X}}(\omega)\bar{H}_{\dot{X}}^T(\omega)A_g(\omega) = \omega^2\Phi_X \tag{8}$$

where  $\bar{H}_X^T(\omega)$  and  $\bar{H}_{\dot{X}}^T(\omega)$  are the conjugated transposes of  $H_X(\omega)$  and  $H_{\dot{X}}(\omega)$  respectively,  $A_g(\omega)$  is the power spectral density function of base acceleration.

$$A_g(\omega) = \frac{1 + 4\xi_g^2\omega^2 / \omega_g^2}{(1 - \omega^2 / \omega_g^2)^2 + 4\xi_g^2\omega^2 / \omega_g^2} \cdot \frac{1}{1 + \omega^2 / \omega_h^2} S_0 \tag{9}$$

where  $\xi_g$  and  $\omega_g$  are the damping ratio and transcendental frequency of the covering soil respectively;  $\omega_h$  is the spectral parameter dependent upon the properties of the bedrock which is proposed to be  $8\pi$ rad / s ;  $S_0$  is the earthquake intensity, which may be considered as the white noise caused by the stochastic motion of the bedrock. Since the diagonal elements of  $\Phi_Y$  and  $\Phi_{\dot{Y}}$  are real functions. They represent the energy distribution density of displacement and velocity responses at corresponding DOFS of the whole system respectively, the energy index of the whole system can be defined as:

$$J = \int_{-\infty}^{+\infty} [\text{trace}(\Phi_X) + \text{trace}(\Phi_{\dot{X}})]d\omega \tag{10}$$

When parameters of TMD system are optimal, the value of index J would be the minimum. The paper adopts Genetic Algorithm Method and Direct Search Method to optimize the parameters of TMD system. Firstly, the stiffness and damping coefficient of the TMD system are selected as the variables. Secondly, choosing the initial points, the energy index J is selected as the fitness function. By searching the new points around the present points, the points whose value of fitness function is less than the present points can be reserved. Through multi-iterations, the optimal result can be obtained.

### 4 Numerical Example

A six storey building structure including the TMD system is given as Figure 4. The parameters of the building structural model are shown in table 1. Let  $\omega_g = 15.0rad/s$ ,  $\xi_g = 0.65$ ,  $S_0 = 4.0 \times 10^{-3} m^2 \cdot rad^{-1} \cdot s^{-3}$ . The mass of bi-directional tuned massed damper is 10% of the top floor mass. Then the optimal damping and stiffness coefficients can be obtained by using genetic algorithm method and direct search method. They are:

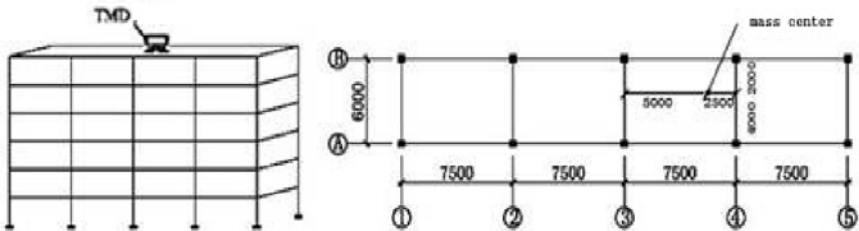


Figure 4. Calculation model of building structure

$$K_x = 2.55 \times 10^4 \text{ (N/m)}, \quad K_y = 3.14 \times 10^4 \text{ (N/m)}$$

$$C_x = 5.86 \times 10^3 \text{ (N} \cdot \text{s/m)}, \quad C_y = 7.48 \times 10^3 \text{ (N} \cdot \text{s/m)}$$

In order to check the control effect of optimal design of the TMD, the seismic responses of three dimensional structural under EL-Centro wave are calculated in control and uncontrolled cases respectively. Figure 5 shows that the TMD system can obviously control the seismic response of three dimensional building. The control effect of maximum displacement of mass centre is shown in Table 2.

Table 1. The parameters of building structure

Floor	Mass (kg)	Rotation-inertia (kN.m)	Stiffness of vertical plane (N/m)	Damping of vertical plane (N.S/m)	Stiffness of transverse plane (N/m)	Damping of transverse plane (N.s/m)
1	3105	173880	$5.217 \times 10^5$	$3.91 \times 10^3$	$17.08 \times 10^5$	$11.64 \times 10^3$
2	3105	173880	$5.217 \times 10^5$	$3.91 \times 10^3$	$17.08 \times 10^5$	$11.64 \times 10^3$
3	3105	173880	$3.866 \times 10^5$	$2.98 \times 10^3$	$11.46 \times 10^5$	$7.92 \times 10^3$
4	3105	173880	$3.866 \times 10^5$	$2.98 \times 10^3$	$11.46 \times 10^5$	$7.92 \times 10^3$
5	3105	173880	$2.645 \times 10^5$	$1.44 \times 10^3$	$6.58 \times 10^5$	$5.76 \times 10^3$
6	3105	173880	$2.645 \times 10^5$	$1.44 \times 10^3$	$6.58 \times 10^5$	$5.76 \times 10^3$

Table 2. The control effect of TMD on EL-centro input

floor	X maximum displacement of mass center (mm)		Control effect (%)	Y maximum displacement of mass center (mm)		Control effect (%)
	Uncontrolled	Controlled		Uncontrolled	Controlled	
1	2.16	1.22	43.5	8.05	5.75	28.6
2	4.15	2.34	43.6	15.4	10.9	29.2
3	6.36	3.38	46.8	24.9	17.4	30.1
4	7.92	4.64	41.4	32.8	22.8	30.5
5	9.92	6.02	39.3	43.6	30.5	30.0
6	11.2	6.83	43.0	49.9	34.8	29.3

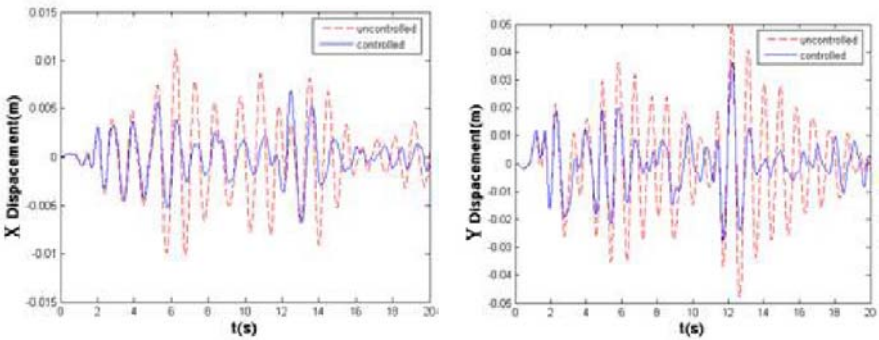


Figure 5. The displacement control effect of top floor.

### 5 Conclusions

The optimal design for three-dimensional building structure including the TMD system is presented in this paper. By comparing the control results of responses of three-dimensional building structure between control and no control cases, we can obtain that the optimal parameters of the damping devices can be obtained by using genetic algorithm method and direct search method. The mass centre displacement in both x-direction and y-direction of each floor are obviously reduced. It means that the bi-directional TMD system can be used to combine with building structures and reduce the seismic responses.

## References

- Clough R.W. and Penzien J. (1981). Structural dynamic, *Computers and Structures*.
- Ou J.P. and Niu H.T. and Du X.L. (1991). Design use of structure model and parameters under random vibration, *Seismic Engineering and Engineering Vibration*, 11(3), 45-53.
- Rana Rahul and Soong T.T. (1998). Parametric study and simplified design of tuned mass damper, *Engineering Structures*, 20(3): 193-204.
- Wu B., Ou J.P. and Soong T.T. (1997). Optimal placement of energy dissipation devices for three-dimensional structures, *Engineering Structure*, 19(2), 113-125.

*“This page left intentionally blank.”*

# **NUMERICAL METHODS AND NUMERICAL SIMULATION**

*“This page left intentionally blank.”*

# A Thermo-Mechanical Model for Fire Exposed RC Structures

Matthias Aschaber<sup>1\*</sup>, Christian Feist<sup>2</sup> and Günter Hofstetter<sup>1</sup>

<sup>1</sup> Institute for Basic Sciences in Civil Engineering, University of Innsbruck, A-6020 Innsbruck, Austria

<sup>2</sup> CENUMERICS – Consultant Engineers for Numerical Simulation, A-6020 Innsbruck, Austria

**Abstract.** A thermo-mechanical model based on a phenomenological approach is presented for the evaluation of the load-carrying behavior of fire exposed reinforced concrete structures. It is validated by the numerical simulation of fire tests on concrete specimens and of a large scale fire test on a reinforced concrete slab and it is applied to the evaluation of the structural response of a fire exposed tunnel structure.

**Keywords:** fire, finite element analysis, high temperatures, reinforced concrete, tunnelling

## 1 Introduction

A variety of methods of different complexity for considering the effects of a fire on the load-carrying capacity of a structure is available, ranging from simple design rules for the dimensions of cross-sections (Eurocode 2, 2004) to sophisticated multi-phase models for fire exposed concrete (Gawin, et al., 1999; Colin, et al., 2006; Pichler, et al., 2006; Li, et al., 2006). A compromise between these two extremes are thermo-mechanical models (cf., e.g., Pearce, et al., 2004; Ožbolt, et al., 2005). They allow a good representation of the time-dependent overall structural behaviour during a fire and, hence, the assessment of structural safety. However, they are not suited to investigate, e.g., the possibility of spalling of concrete.

The proposed thermo-mechanical model for fire exposed concrete structures consists of a material model for concrete, formulated within the framework of plasticity theory and enhanced by considering stiffness degradation due to damage which is extended considering the material properties of concrete at elevated temperatures.

---

\* Corresponding author, e-mail: Guenter.Hofstetter@uibk.ac.at

Special attention is paid to the validation of the proposed numerical model by means of fire tests on plate-type concrete specimens and a large-scale fire test on a RC slab, before the numerical model is applied to the numerical simulation of the load-carrying behavior of a tunnel structure exposed to fire.

## 2 Thermo-Mechanical Model

Within the framework of a phenomenological description of the material behavior of concrete subjected to high temperatures a coupled thermo-mechanical approach yields a consistent numerical model. However, assuming the temperature distribution in the structure as independent of the structural behaviour allows performing the thermal analysis and the mechanical analysis in consecutive steps.

The transient temperature distribution within a fire exposed structure is determined on the basis of a FE-formulation of Fourier's differential equation for heat conduction, taking into account the dependence of the thermal diffusivity of concrete on temperature and moisture content.

The heat flux through the surface of the structure is prescribed by means of Robin's boundary condition, considering both, the heat flux due to convection and due to radiation. For structures with roughly known thermal loads the time-dependent gas temperature within the area on fire can be prescribed in terms of standardized time-temperature profiles, also known as fire curves (cf., e.g., ISO 834, 1999; ÖVBB, 2004).

The plastic damage model for concrete (Lee and Fenves, 1998) serves as the basis for the concrete model for high temperatures. It is formulated within the framework of plasticity theory in combination with damage mechanics. Hence, plastic strains as well as stiffness degradation due to damage are taken into account. Stiffness degradation is described by a simple isotropic damage model in terms of a scalar damage variable. The yield function is formulated in terms of the effective stresses and equivalent tensile and compressive plastic strains. The plastic strain rate is obtained from a non-associated flow rule.

The isotropic hardening and softening laws for concrete in compression and tension are obtained from the respective stress-strain relations for uniaxial compression and tension by subtracting the elastic strain. Hence, the hardening and softening laws can be easily determined from the respective stress-strain relations, obtained by uniaxial compression and tension tests. If respective test data is not available, the stress-strain relations, provided in Eurocode 2 (Eurocode 2, 2004) can be employed.

The ratio  $f_{bc}/f_c$  of the biaxial strength to the uniaxial compressive strength increases with increasing temperature, i.e. with increasing temperature the uniaxial compressive strength decreases faster than the biaxial compressive strength (Ehm, 1986). Starting with  $f_{bc}/f_c \approx 1.16$  at ambient temperatures this ratio increases to  $f_{bc}/f_c \approx 1.30$  at 300°C and up to  $f_{bc}/f_c \approx 1.70$  at 750°C.

In uniaxial tension a linear constitutive relationship is assumed up to the tensile strength. According to (Eurocode 2, 2004) a linear decrease of the tensile strength with increasing temperature from 100°C can be assumed until at 600°C the tensile strength vanishes.

Cracking is modelled by the smeared crack concept, assuming an exponential softening law in the post-peak domain. Objective numerical results of a finite element analysis based on the smeared crack concept are ensured - at least in an approximate manner - by adjusting the softening curve to the respective element size by means of the specific fracture energy of concrete  $G_f$  and the equivalent length  $h_e$  of the respective finite element.

The dependence of the specific fracture energy on temperature is taken into account according to test results (Bićanić and Zhang, 2002; Ožbolt, et al., 2005), i.e., the value for  $G_f$  at 20°C increases up to 1.6  $G_f$  at 280°C and decreases with still increasing temperature until at 600°C a value of 0.8  $G_f$  is attained.

In addition, the thermal strains are taken into account according to the provisions given in (Eurocode2, 2004).

The constitutive relations for reinforcing steel consist of a linear-elastic part up to the proportional limit, a nonlinear  $\sigma\varepsilon$  - relation up to the yield strength followed by ideal plastic material behavior and finally a softening branch. The modulus of elasticity, the proportional limit and the yield strength are assumed to depend on temperature according to (Eurocode2, 2004).

Details of the employed concrete model for high temperatures are provided in (Feist, 2007).

### 3 Validation

Fire tests on plate-type concrete specimens with the dimensions  $200 \times 200 \times 50$  mm were conducted by Ehm (1986) at the Technical University at Brunswick. Here, a comparison between measured and computed results is presented for two of the extensive test series, conducted by Ehm. In the first test series the plate-type specimens were heated at constraint deformations in both directions of the specimens midplane and the resulting stresses were measured (Figure 1). In the second test series the specimens were first loaded by biaxial compressive stresses  $\sigma_1 = \sigma_2 = \alpha f_c$ ,  $0 < \alpha < 1$ , and then the loaded specimens were heated at constant stresses and the resulting strains were measured (Figure 2).

Several large-scale fire tests on RC slabs with dimensions of  $4300 \times 3300$  mm and a thickness of 100 mm were carried out at the University of Canterbury in New Zealand (Lim, 2003). The uniformly loaded slabs were placed above a furnace, which was heated for three hours following the ISO 834 standard fire curve (ISO834, 1999). The experimental program during the fire tests included measurements of the temperature across the thickness of the slab, the deflection at the center of the slab and the vertical displacement of the corners of the slab. Com-

parisons of results of the numerical simulation by means of the proposed thermo-mechanical model with measurement data are reported in (Feist, 2007).

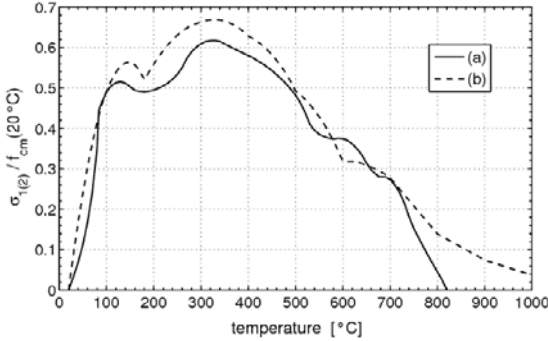


Figure 1. Comparison of measured and computed stresses for bi-axially constrained heated concrete specimens: (a) measurement data, (b) numerical results

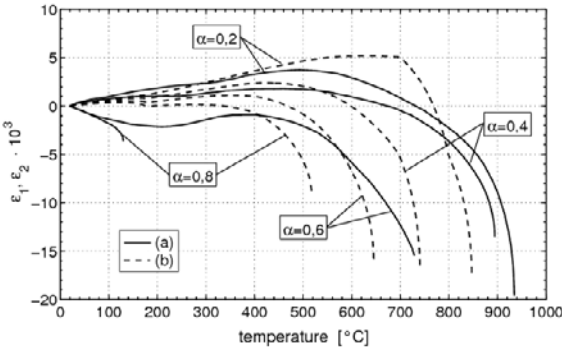


Figure 2. Comparison of measured and computed strains for bi-axially loaded concrete specimens: (a) measurement data, (b) numerical results

### 4 Application

The proposed model is applied to the numerical simulation of the response of a shallow RC tunnel structure, exposed to a fire of 90 minutes duration. The double-track railway tunnel, put up by the cut and cover method, is characterized by a double box section (Figure 3).



fic loads. Subsequently, the time-dependent temperature changes are applied in the transient part of the mechanical analysis. Figure 4 shows the deformations of the tunnel structure (magnified by a factor of 50) and the damage (in terms of the fictitious crack strains, plotted in black colour) after 90 minutes of fire.

The numerical simulation confirms that despite of the considerable damage of the structure by the fire, its load carrying capacity is sufficient to withstand a fire of 90 minutes duration.

## References

- Bićanić N. and Zhang B. (2002). Residual fracture toughness of normal- and high strength gravel concrete after heating to 600°C. *ACI Materials Journal*, 99(3):217-226.
- CEN. Eurocode 2. (2004). Design of concrete structures – Part 1-2: General rules – Structural fire design. prEN 1992-1-2.
- Colin T., Pearce D.C.J. and Bićanić N. (2006). Coupled heat and moisture transport in concrete at elevated temperatures – Effects of capillary pressure and adsorbed water. *Numerical Heat Transfer*, 49(8):733-763.
- Ehm C. (1986). Versuche zur Festigkeit und Verformung von Beton unter zweiaxialer Beanspruchung und hohen Temperaturen. Institut für Baustoffe und Brandschutz der technischen Universität Braunschweig, Heft 71.
- Feist C., Aschaber M. and Hofstetter G. (2007). Numerical Simulation of the structural behavior of RC tunnel structures subjected to fire. *Proceedings of the ECCOMAS Thematic Conference on Computational Methods in Tunnelling (EURO:TUN 2007)*, J. Eberhardsteiner et al. (Eds), CD-ROM, 14p.
- Gawin D., Majorana C.E. and Schrefler B.A. (1999). Numerical analysis of hygro-thermal behaviour and damage of concrete at high temperature. *Mechanics of Cohesive-Frictional Materials*, 4(1):37-74.
- ISO 834: Fire-Resistance Tests – Elements of Building Construction – Part 1: General Requirements. *International Organization for Standardization*, ISO 834-1:1999.
- Lee J., Fenves G.L. (1998). Plastic-damage model for cyclic loading of concrete structures. *Journal of Engineering Mechanics*, 124(8): 892-900.
- Li X., Li R. and Schrefler B.A. (2006). A coupled chemo-thermo-hygro-mechanical model of concrete at high temperature and failure analysis. *International Journal for Numerical and Analytical Methods in Geomechanics*, 30(7): 635-681.
- Lim LCS. (2003). Membrane action in fire exposed concrete floor systems. Ph.D. Thesis, University of Canterbury, New Zealand.
- ÖVBB: (2004) Richtlinie Erhöhter Brandschutz mit Beton für unterirdische Verkehrsbauwerke. Österreichische Vereinigung für Beton- und Bautechnik, Wien.
- Ožbolt J., Kožar I., Eligehausen R. and Periškić G. (2005). Instationäres 3D thermo-mechanisches Modell für Beton. *Beton- und Stahlbetonbau*, 100:39-51.
- Pearce C.J., Nielsen C.V. and Bićanić N. (2004). Gradient enhanced thermo-mechanical damage model for concrete at high temperatures including transient thermal creep. *International Journal for Numerical and Analytical Methods in Geomechanics*, 28(7,8):715-735.
- Pichler C., Lackner R. and Mang H.A. (2006). Safety assessment of concrete tunnel linings under fire load. *Journal of Structural Engineering*, 132(6):961-969.

# Numerical Modeling of Restrained RC Columns in Fire

Yihai Li<sup>1\*</sup>, Bo Wu<sup>1</sup> and Martin Schneider<sup>2</sup>

<sup>1</sup> State Key Laboratory of Subtropical Building Science, South China University of Technology, Guangzhou 510640, China

<sup>2</sup> University of Technology Vienna, Karlsplatz 13/206, 1040 Wien, Austria

**Abstract.** The paper presents a numerical modeling of Reinforced Concrete (RC) columns under fire and loading simultaneously. It proposes a concrete model at high temperature considering both transient strain and load path, which is an improvement of the concrete model in EC2. The parameters of the concrete model are tuned so that they are suitable for the concrete materials that are commonly found in China. The concrete model is implemented in the FE software SAFIR, which is developed in the University of Liege by Prof. J. M. Franssen for calculation of structures in fire. The paper continues to validate the material models by experimental results of restrained concrete columns under fire conditions.

**Keywords:** numerical modeling, concrete model, transient creep

## 1 Introduction

Nowadays, the mechanical behavior of concrete structures in fire can be simulated by many finite element software tools such as ABAQUS and ANSYS considering the effect of temperature. In these methods, the unresolved parameters are commonly the nodal displacements. The corresponding strain is the total strain, which comprises of different parts. For steel, it is usually accepted that there are three components, namely, thermal strain, instantaneous stress-related strain and creep strain. For concrete, apart from the three components, there exists an additional term-*transient strain*, although the creep strain may also be ignored for the relative short period of exposure to fire. The transient strain is said to be implicitly incorporated into the stress-strain relationship in Eurocode 2 (CEN, 2004).

Li and Purkiss (2005) reviewed the currently available models for the mechanical behavior of concrete at elevated temperatures. They compared the difference among the models and concluded that absence of transient strain when high stress

---

\* Corresponding author, email: yihai.li@mail.scut.edu.cn

level may yield unsafe results. Purkiss (1996) also pointed out that the effect of ignoring any transient strain in the concrete can be substantial. The paper proposes a concrete model that considers the effect of load history and transient creep. The concrete model is calibrated against experimental results of axially restrained concrete columns that were recently fire tested.

## 2 Material Properties

The total strain  $\varepsilon_t$  of concrete is the sum of different separating parts and can be given by Equation (1),

$$\varepsilon_t = \varepsilon_\sigma + \varepsilon_{tr} + \varepsilon_{th} \quad (1)$$

where  $\varepsilon_\sigma$ ,  $\varepsilon_{tr}$ , and  $\varepsilon_{th}$  are the stress induced strain, transient creep strain, and free thermal strain, respectively. In EC2,  $\varepsilon_{tr}$  is simplified as incorporated in  $\varepsilon_\sigma$  for all stress level. Furthermore, the stress level, which can have great influence on the material properties, is also ignored in EC2.

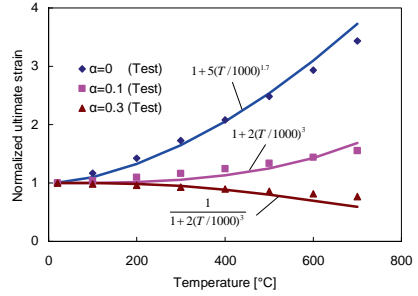
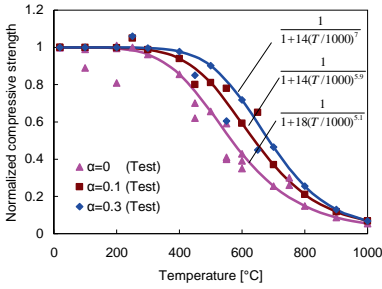
### 2.1 Stress Induced Strain

It is well known that the compressive strength of concrete increases when it is stressed. A parameter load factor  $\alpha$ , defined as the ratio of the current stress to the compressive strength at room temperature, is introduced in the constitutive law of normal concrete in EC2 and the stress-strain relationship is represented by Equation (2),

$$\sigma(t) = f_c(T, \alpha) \times \frac{3 \times [\varepsilon_\sigma(T, \alpha) / \varepsilon_u(T, \alpha)]}{2 + [\varepsilon_\sigma(T, \alpha) / \varepsilon_u(T, \alpha)]^3} \quad (2)$$

where  $f_c(T, \alpha)$  and  $\varepsilon_u(T, \alpha)$  are the compressive strength and ultimate strain corresponding to the temperature  $T$  and load factor  $\alpha$ , respectively. The ultimate strain will increase with the increase of temperature because of increase of ductility, but it will decrease when stressed. Figure 1 (a) and (b) show the compressive strength and ultimate strain as a function of  $T$  and  $\alpha$ , respectively.

It should be noted that the upper limit of the load factor  $\alpha$  is 0.3, as further increase of load stress can not yield considerable difference with  $\alpha=0.3$  (Schneider, 2008).



(a) Compressive strength

(b) Ultimate strain

Figure 1. Compressive strength and ultimate strain as a function with T and  $\alpha$

### 2.2 Transient Creep Strain

Transient creep is the difference between free thermal strain and strain under load. Transient creep depends on stress level and temperature, as can be given by

$$\varepsilon_{tr} = \frac{\varphi \times \sigma(T, \alpha)}{E(T)} - \varepsilon_{pl}(T, \alpha) - [\varepsilon_{el}(T, \alpha) - \varepsilon_{el}(T)] \tag{3}$$

where  $\varphi$  is called “the transient creep” function in the literature. As there are no tests that have been performed to yield such results in China, the  $\varphi$  function used by Schneider (Schneider, 2008) is adopted here. The influence of load history originates from plasticity effects in  $\varepsilon_{pl}$  and to a small extent from the load effect on the modulus of elasticity in  $\varepsilon_{el}$ .

### 2.3 Young’s Modulus

The stiffness of concrete will also increase as a result of crack closure when it is stressed. The variation of Young’s modulus is displayed in Figure2. Both the test results and proposed models are presented in Figure 1 and 2. It can be seen that the proposed model for unstressed concrete, which is derived from the test data in China (Guo and Shi, 2003), also fits well with the test results (Schneider, 2008).

### 2.4 Thermal Strain

When concrete is heated under no stress, it expands freely and the corresponding strain is thermal strain. Thermal strain mainly depends on aggregate type, water-cement ratio and heating rate. The stress level does not have an influence on thermal strain. Equation (4) gives the function of thermal strain for siliceous concrete (Guo and Shi, 2003), which is based on the test data in China.

$$\epsilon_{th} = 28 \times T^2 \times 10^{-9} \leq 12 \times 10^{-3} \tag{4}$$

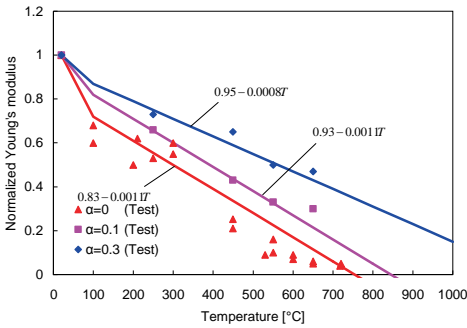


Figure 2. Relation of Young's modulus with T and alpha

### 2.5 Strain Reversal in Cooling

Although most properties of steel are considered reversible during cooling, this is not the case for concrete. Thermal strain is considered irreversible during cooling down, because cracks do not close completely and lead to residual strain. As tests have shown that transient creep is only relevant to the maximum temperature and it does not recover during cooling. Elastic strain is reversible when the concrete is cooling whereas the plastic strain can not recover during cooling.

In the case where the concrete response may dominate, such as reinforced concrete columns, the fire performance mainly depends on concrete properties. For this reason, the material properties for steel are taken as in EC2 and will not be presented here.

### 3 Numerical Comparisons

We can get the mechanical strain from Equation (1) as follows

$$\varepsilon_m = \varepsilon_t - \varepsilon_{th} = \varepsilon_\sigma + \varepsilon_{tr} \quad (5)$$

Following an iteration process, the material law described above for concrete was implemented in the numerical software SAFIR (Franssen, 2005) by the third author of the paper.

Recently, sixteen axially restrained RC columns have been fire tested at South China University of Technology. As the axial forces in the columns varied with time, it is important to take into account the load history of concrete model. The test results have been used here for validation of the proposed concrete model. Figure 3 and 4 show schematic arrangement of the test set-up and the structural model used in the analysis, respectively. Only the structural results will be presented here, other information such as details of the test set-up and the thermal analysis can be found in a previous paper (Wu and Li, 2008).

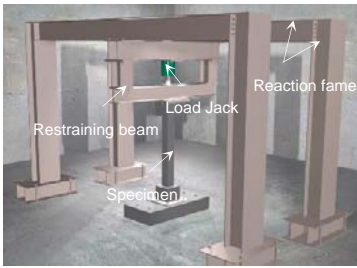


Figure 3. Arrangement of the test set-up

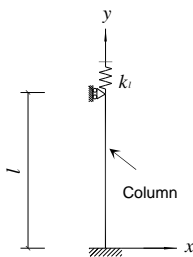
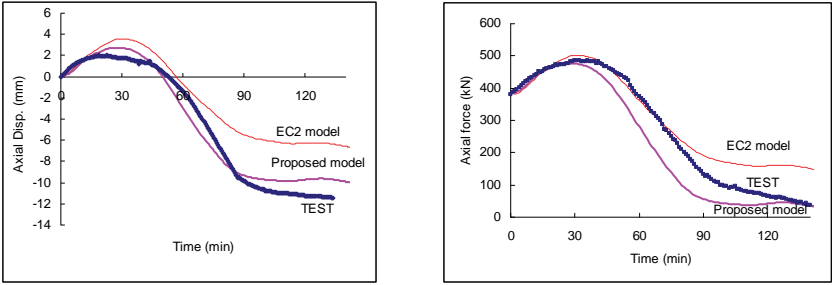


Figure 4. Structural model for SAFIR analysis

Figure 4 shows the structural model for the analysis in SAFIR. The spring stiffness  $K_l$  represents the restraining effect of the structure in the test. Figure 5 shows the comparison of SAFIR prediction with proposed model to EC2 model

for concrete. Only the result of RCL21 is presented here. It has to be noted that the same steel model from EC2 and the same temperature distribution from the thermal analysis were used in both calculations.



(a) Axial displacement

(b) Axial force

Figure 5. Variation of axial deformation and axial force with time

When a column which forms part of a structure is heated in fire, it will be subjected to restraint by adjacent structure. The loads in the column will vary during the fire exposure. Transient strain is present when concrete is stressed and exposed to high temperature simultaneously. It is impossible to simulate the behavior of concrete structure without considering the transient creep. It can be seen that the proposed model predicts much better results than the EC2 model.

### 4 Summary and Conclusions

As for the interactions between adjacent members, the behaviors (such as displacement, internal force and redistribution of load) of concrete structures can only be modeled correctly considering the appropriate material laws. The paper presents and verifies a concrete model that can be used to simulate the behaviors of concrete structures. This numerical model, which is a development of the one in EC2, can predict the response of concrete columns better. It is believed that the concrete model can be utilized for the purpose of research or introduced in the standard for the advanced calculation method. The verification results show that the proposed model can predict the behavior of restrained RC columns under fire very well, both in the heating and cooling phase.

## References

- CEN (2004). Eurocode 2: Design of concrete structures – Part 1-2: General rules – structural fire design, Brussels: European Committee for Standardisation.
- Franssen J. M. (2005). SAFIR-a thermal/structural program modelling structures under fire. *Engineering Journal, AISC*, 42(3): 143-158.
- Guo Z. H. and Shi X. D. (2003). *Behaviour of reinforced concrete at elevated temperature and its calculation*, Tsinghua University Press, Beijing.
- Li L. Y. and Purkiss J. A. (2005). Stress-strain constitutive equations of concrete material at elevated temperatures. *Fire Safety Journal*, 40: 669-686.
- Purkiss J. A. (1996). *Fire safety engineering design of structures*. Butterworth-Heinemann, Oxford.
- Schneider U., Schneider M. and Franssen J. M. (2008). Consideration of nonlinear creep strain of siliceous concrete on calculation of mechanical strain under transient temperatures as a function of load history. In *Proc. of the Fifth International Conference on Structures in Fire*, 463-476.
- Wu B. and Li Y. H. (2008). Experimental research on fire performance of axially restrained RC columns with L-shaped cross section. In *Proc. of the Fifth International Conference on Structures in Fire*: 451-462.

*“This page left intentionally blank.”*

# Temperature Field of Concrete Beam Based on Simulated Temperature-Time Curves

Limin Lu<sup>1\*</sup>, Yong Yuan<sup>1,2</sup>, Chunlong Yu<sup>1</sup> and Xian Liu<sup>1,2</sup>

<sup>1</sup>Department of Geotechnical Engineering, Tongji University, Shanghai 200092, P.R. China

<sup>2</sup>Key Laboratory of Geotechnical and Underground Engineering of Ministry of Education

**Abstract.** This paper based on the basic theory of field simulation, analyzed the characteristics of typical subway station through FDS (Fire dynamic simulator), obtained the temperature curve based on the analysis of fire scene, compared and analyzed with the ISO-834 standard temperature curves. Then, calculated the temperature field of the component-section, compared and analyzed the influence of the simulated temperature curve and the standard temperature curve on the component cross-section temperature field.

**Keywords:** subway station, FDS simulation, temperature curve, concrete beam

## 1 Introduction

Fire is one of the most dangerous disasters that cause severe damage to urban underground building. Data shows that fire accounted for 1/3 of all the disaster happened in underground structures (Zhou, et al., 2006). So fire-resistant design of underground structures received great attention in recent years. However, most of the researches and standards are focus on the tunnels, with long but not wide space, little research on the wide space structures like subway station, garage and underground markets. As the differences of ventilation system, space, structure style, the temperature-time (T-time) curve will be different. Simply use the ISO-834 standard T-time curve or RABT T-time curve (commonly used in tunnels) is not always proper. Therefore, according to performance-based fire resistant design theory, it is necessary to analyze the fire scene of typical subway station and analyze the effect of T-time curves on the inner temperature state of structures.

This paper use FDS (Fire dynamic simulator, released by American National Standards Committee) (Mc Grattan and Forney, 2005) simulated fire happened in a typical subway station, analyzed the fire characters of underground structures, got simulated T-time curve and compared the T-time curve with ISO-834 T-time

---

\* Corresponding author, email: dami21th@hotmail.com

curve and RABT T-time curve. Then calculated the inner temperature field of a rectangular beam under the three T-time curves, comparative analyzed the influence of T-time curve to the inner temperature field of members.

## 2 Fire Simulation of a Typical Subway Station

### 2.1 Model and Control Factors

The simulated station is a typical one in shanghai, which is composed of the hall layer (the first layer underground), the platform layer (the second layer underground). It is a two-layer three-spend two-row-column subway stations. The effective dimensions are 140.0 meters long, 19.2 meters wide (net). The net height of the public areas of the hall layer is 4meters and platform layer is 4.7meters. There are four entrances in the hall layer connect to the outside, each side has two. The thickness of the clapboard between the hall layer and the platform is 0.4m with two staircases connecting (which are located at  $x = 32 \sim 38m$ ,  $x = 70 \sim 76m$ ). Take the longitudinal direction as X-axis, width direction as Y-axis, and height direction as Z-axis. The station model is shown in Figure 1 and Figure 2.

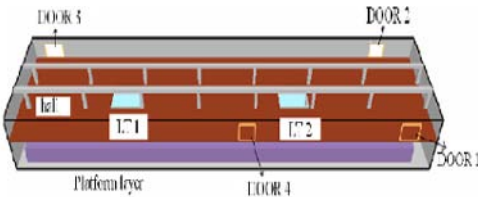


Figure 1. The subway station model



Figure 2. Front view of the subway station model

(1) Fire source. Fire source is located at the central site, the burning material is gasoline, and fire intensity is 5MW.

(2) Ventilation. Under the requirement of ‘Code for Design of Metro (GB 50157-2003)’, the downward airflow from the hall layer to the platform layer should be faster than 1.5 m/s. In the simulation, when there is a fire in platform layer, turn off air supply system of the platform and the hall layer exhaust system, exclude the smoke by smoke fans (each side of the station has one).

(3) Simulation time. The simulation time is 120min without considering the dropping stage of the fire temperature.

## 2.2 Simulated T-time Curve

Figure3 and Figure4 shows the simulated T-time curve of the roof point up the fire, and compared it to ISO-834 standard T-time curve and RABT T-time curve.

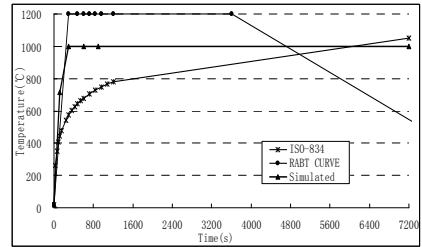
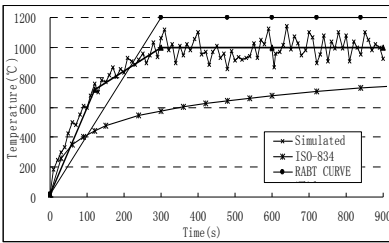


Figure 3. Temperature–time curve (t=15min)

Figure 4. Temperature–time curve (t=120min)

1. The simulated temperature curve grows faster than the RABT T-time curve in the first three minutes, but the top temperature is lower. Fire-resistance design of subway stations with RABT curve may be too conservative.
2. Fire temperature of underground structure grows faster than the ISO-834 standard T-time curve, and will reach to a higher top, which may means that fire in underground structures will cause even severe damage to the structures.
3. Figure 4 is the simplified curves which approach the simulated curve. After 15min calculation time, the temperature reaches to 1000°C, and then stay at 1000°C for a long time without considering the dropping stage.

## 3 Temperature Field Analysis of Rectangular Beam

### 3.1 Basic Assumption

As the fire temperature change over time, the temperature field in member is up to non-linear transient problem, the control equation is a parabolic partial differential equation. The following assumptions (Liu, 2006; Guo and Shi, 2002) are needed.

1. Assumed that the concrete is the isotropic material, the relationship of conductivity and temperature is the same in all directions.
2. Ignore the difference of fire in the longitudinal direction, so the beam can be simplified as a two-dimensional problem.
3. Heat is not generated in the component, effects of water evaporation in the
4. Concrete is negligible.

- 5. Steel occupies a small part of the cross section, and its conductivity is much bigger than concrete, so steel can be ignored in temperature field calculation.
- 6. Ignore the change of local boundary conditions caused by deformation.

### 3.2 Component Temperature Field Calculation

The calculation model is a rectangular beam with cross section 250mm×400mm. Disperse the section into 5mm×5mm unit in the finite element calculation. Take three key point, y=30mm (steel site), y=100mm (1/4 of the section height), y=200mm (core of the section), to show there temperature changing condition.

- 1. The beam is fire-loaded on three sides, the bottom and two sides. The heating curves were ISO-834 standard curve, simulated curve and RABT curve, comparing there effect on the inner temperature field of the beam.
- 2. Take the integrated conductive coefficient 12W/(m2.°C) of the surface face to fire, 6.5 W/(m2.°C) of the surface far from the fire (Harmathy and Alto, 1972).
- 3. Solve. Select Newton equation-Raphson method, and select node-heat-imbalance criteria as non-linear iteration convergence criteria (Shi, Guo, 1996). Set the automatic time-step length 60s. The total computing time is 120min.

### 3.3 Temperature Field Calculation Results

Figure 5, Figure 6 and Figure 7 give the temperature field of the component cross-section under three T-time curves at t=60min and t=120min. Figure 8 give the temperature of three points y=30mm, y=100mm, y=200mm.

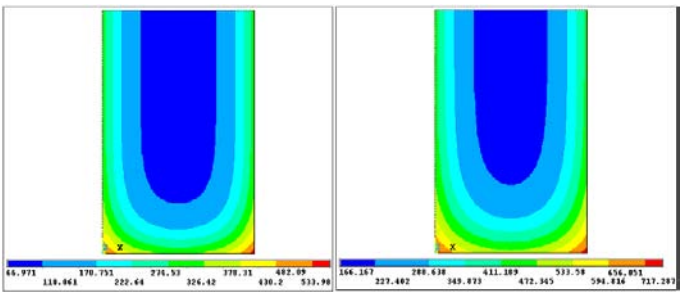


Figure 5. Temperature field of beam under ISO-834 T-time curve (t = 60min and t = 120min)

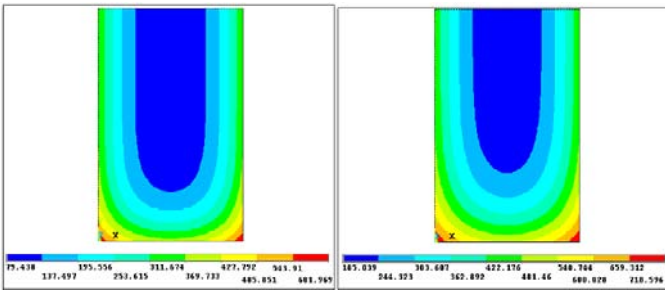


Figure 6. Temperature field of beam under simulated T-time curve ( $t = 60\text{min}$  and  $t = 120\text{min}$ )

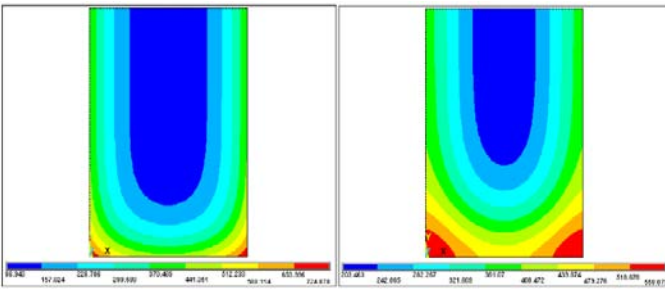


Figure 7. Temperature field of beam under RABT T-time curve ( $t = 60\text{min}$  and  $t = 120\text{min}$ )

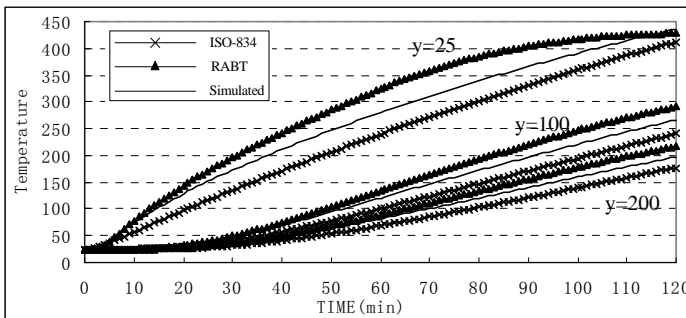


Figure 8. Temperature changing curve of the three key points

1. The inner temperature field of the beam with three sides in fire appears layered parabolic state. The temperature gradient goes smaller while away from the in-fire surfaces, this is mainly because the thermal inertia of concrete. According

to the temperature field, it can be seen that the temperature of the two corners of the section in fire rise the fastest, which are more prone to spalling.

2. The contrast of Figure 4, Figure 5 and Figure 6 shows that different T-time curves have little influence on the overall state of temperature distribution, only has great impact on the maximum temperature of the surface in fire. T-time curve with higher top temperature lead to higher cross-section temperature. The order is RABT T-time curve, simulated curve, ISO-834 standard curve.
3. The T-time curves have great effect on the temperature of the section near the surface in fire. The influence becomes smaller while away from the fire. After 120min, the temperature deference between different T-time curves on the  $y=100\text{mm}$  point is  $50^{\circ}\text{C}$  or less, and on the center point is  $30^{\circ}\text{C}$  or less.

## 4 Conclusions

Through fire simulation of a typical subway station by FDS and temperature field calculation of a beam by finite element method, we get the following conclusions:

1. Fire temperature in subway station grows much faster than ground structure and reach to a higher top. Compared with tunnel fire, the initial temperature is lower, but the fire is hard to control and the high temperature will last longer.
2. The temperature field of the cross-section is layered, and the temperature gradient becomes smaller from against-fire side to another side. The temperature of the two corners against fire rise fast, which may lead to spalling.
3. Heating process has little influence on the temperature field distribution, but the T-time curve with higher top temperature will cause higher inner temperature of beam, and direct to more severe damage to the structure.

## References

- Code for design of metro (2003). (GB 50157-2003), Beijing: China Planning Press.
- Guo Z.H. and Shi X.D. (2002). *High-temperature reinforced concrete's performance and calculation*. Beijing: Tsinghua University Press.
- Harmathy T.Z., Alto L.W. (1972). Thermal properties of concrete subject to elevated temperature. *Concrete for Nuclear Reactors*. Detroit, ACISP34, 376-406.
- Liu Y.J. (2006). *The numerical simulation basis of temperature field in fire building component*. Beijing: Science Press.
- McGrattan K., Forney G. (2005). *Fire Dynamics Simulator (Version 4) User's Guide*. 5-15.
- Shi X.D., Guo Z.H. (1996). Fire-resistant properties of reinforced concrete beams in different concrete cover thickness. *Industrial building*, 26 (9): 12-19.
- Zhou Yun, Tang Tongbi, Liao Hongwei (2006). Review and prospect of disaster prevention of urban underground space. *Chinese Journal of Underground Space and Engineering*, 7(2).

# Numerical Tests of Spalling Delamination of Concrete at Elevated Temperatures

Yufang Fu<sup>1,2\*</sup>, Lianchong Li<sup>3</sup>, Wanheng Li<sup>1,2</sup> and Jinquan Zhang<sup>1,2</sup>

<sup>1</sup>Research Institute of Highway, MOT, Beijing 100088, China

<sup>2</sup>Key Laboratory of Bridge Detection & Reinforcement Technology, MOT, Beijing 100088, China

<sup>3</sup>Dalian University of Technology, School of Civil & Hydraulic Engineering, Dalian 116024, China

**Abstract.** With using a numerical model proposed by the authors, numerical tests were performed to investigate the effects of thermally cracking process with considering the heterogeneity of material properties on the spalling in concrete exposed to a transient thermal load. The numerical results showed that the thermal cracking is the key factor causing the corner and surface spalling.

**Keywords:** numerical tests, concrete, elevated temperatures, spalling

## 1 Introduction

High-strength concrete contains extremely fine pores with water in various forms, such as free or capillary water, adsorbed and chemically bound water. Fire or other severe thermal environmental conditions cause the release and evaporation of significant amounts of water, and induce temperature gradients. Due to this reason, internal stresses are built up in concrete with a superposition of the pore pressures, the thermal stress derived from the thermal gradient and the shrinkage by the water release. When the internal stresses exceed the maximum allowable tensile stresses of the concrete materials, the thermal cracks and spalling of concrete occur. Small scales of spalling fall out from the surface of the concrete structure, and the process is repeated as long as the conditions are met (progressive spalling); the concrete element may also suddenly fail with a very large release of energy (explosive spalling) (Sanjayan and Stocks, 1993; Kalifa *et al.*, 2000).

---

\* Corresponding author, e-mail: yf.fu@rioh.cn

## 2 Numerical Models and Methods

Until now, the prediction of concrete spalling during heating-up has been largely an imprecise empirical exercise. It is still difficult to predict spalling by analytical methods owing to the complex microstructure and multiphase nature of heated concrete. The inability to predict the occurrence of spalling has been a limiting factor in the development of robust models capable of predicting the response of concrete structures to fire.

From the point of view of fracture mechanism, the nature of all kinds of spalling are similar, because at the mesoscopic level, the spalling is a damage evolution process including crack formation, extension, coalescence and final fragmentation of concrete. The heterogeneities of the constitute materials and its influence on the thermally induced cracks maybe play an important role in the occurrence uncertainties of explosive spalling of concrete.

In this paper a coupled thermo-mechanical-damage (TMD) models have been adopted with using MFPA<sup>2D</sup> (Fu *et al.*, 2004). In order to simulate the cracking process of concrete subjected to coupled thermo-mechanical actions, the heterogeneity of mesoscopic structures of concrete has been considered and included in the numerical models (Fu *et al.*, 2004). In order to reflect the heterogeneity of each phase in concrete at mesoscopic level, the concrete is numerically described with many mesoscopic elements with the same size, and the mechanical parameters of these elements in three phases of concrete are assumed to conform to specific Weibull distribution functions (as shown in Equation(1)) (Fu *et al.*, 2004). In this way, an elastic damage constitutive relationship for meso-level elements is incorporated to account for the degradation of the mechanical properties of the composite materials as a function of temperature (as shown in Equation (2) and (3)). The cracking process simulation is attained when using finite element method (FEM) as the basic stress analysis tools, where the four-node isoparametric element is chosen in the finite element mesh. Based on a transient heat transfer equation (as shown in Equation(4)), a series of numerical simulation using MFPA<sup>2D</sup> have been conducted to investigate the effects of heterogeneity and cracks on the stress redistribution and the spalling process of concrete exposed to rapidly rising temperatures. For the detailed introduction to the models and verifications, the readers can refer to literature (Fu *et al.*, 2007).

The heterogeneity of concrete can be described with Weibull function as following:

$$\varphi(\beta) = \frac{h}{\beta_0} \cdot \left(\frac{\beta}{\beta_0}\right)^{h-1} \cdot e^{-\left(\frac{\beta}{\beta_0}\right)^h} \quad \beta, \beta_0 \geq 0, h > 0 \quad (1)$$

where  $h$  is the shape parameter (or slope);  $\beta_0$  is the scale parameter, and  $\varphi(\beta)$  is the density of variable  $\beta$ .

The general expression of the damage variable is  $D=D(\varepsilon_\sigma, T)$ . Let  $D_m$  and  $D_T$  denote the scalar variables of thermo-mechanical damage and thermo-dehydrated damage respectively. If they are independent, the damage variable  $D(\varepsilon_\sigma, T)$  can be expressed as follows:

$$D(\varepsilon_\sigma, T) = 1 - (1 - D_m) \cdot (1 - D_T) \tag{2}$$

$$D(\varepsilon_\sigma, T) = 1 - \frac{E(\varepsilon_\sigma)}{E^0} \cdot \frac{E(T)}{E^0} \tag{3}$$

$E^0$  is the elastic modulus in a reference/undamaged condition (such as at reference temperature), and  $\varepsilon_\sigma$  is the strain.

$$\frac{\partial}{\partial x} k_x \frac{\partial T(x, y, t)}{\partial x} + \frac{\partial}{\partial y} k_y \frac{\partial T(x, y, t)}{\partial x} + Q(x, y, t) = \rho c \frac{\partial T}{\partial t} \tag{4}$$

where  $k_x$  and  $k_y$  are heat conductivity in directions  $x$  and  $y$ , respectively;  $Q(x, y, t)$  is heat generation by material per unit volume and time;  $\rho$  and  $c$  are density and specific heat of material, respectively. The produce  $\rho c$  is called volume specific heat.

Two cases are carried out to investigate the effects of thermal shock on the corner spalling and the surface spalling in concrete subjected to rapidly rising temperatures. The geometries of the specimens are 300mm×300mm for square and  $\Phi$ 300mm for disc. The specimens are subdivided into 360000 and 282743 elements, produced randomly by computer according to the Weibull distribution. The geometry, properties of the materials are listed in Table 1.

Table 1. Material parameters for numerical specimen

Parameters	Matrices	Aggregates
Homogeneity index	3	6
Young's modulus (GPa)	40	70
Compressive strength (MPa)	200	300
Poisson's ratio	0.2	0.18
Conductivity (W/m <sup>2</sup> ·°C)	1.8	3.0
Specific heat (J/m <sup>3</sup> ·°C)	1.93 e+6	1.2 e+6
Expansion coefficient (/°C)	1.0e-5	1.2e-5

A constant temperature ( $T_0$ ) of 25°C is assigned to all elements in models as initial temperature for the two cases. The surfaces exposed to a standard fire (BS 476), which is assumed to behave as a convective boundary.

### 3. Numerical Results and Discussions

The stress field reflects the levels of stresses, but it doesn't predict the cracking occurrence. For a given element in the numerical specimens, the ratio of stress to strength is an effective index to determine whether or not the element breaks out. For the cement-based materials, the ratio values are largely different for all elements even though in the same stress field due to the heterogeneity of material properties. However, if the cement-based materials are assumed as homogeneous, the ratios have the same values for all elements in the same stress field. It means that all the elements fail if the stresses reach their strength. Such methods cannot be used to study the process of thermal damage of concrete subjected to elevated temperatures, so it is also not available to investigate the scaling process by spalling.

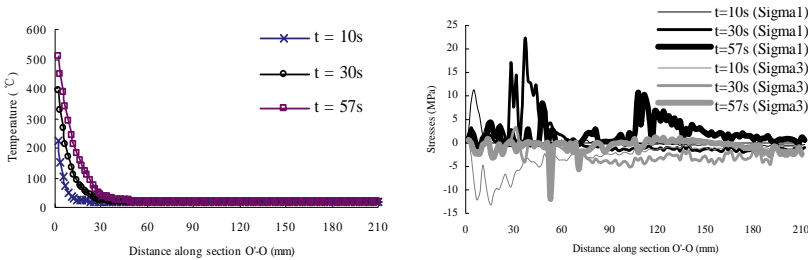


Figure 1. Temperature profile and stress distributions in case 1

**Case 1.** The temperature profile and the principal stress distributions for case 1 are plotted in Figure 1 respectively. A smooth gradient profile shapely decreases and then remained flatten along the diagonal *O-O*, while a fluctuant stress distribution was observed due to the heterogeneity of material properties. It was obvious that stress concentrations were formed on the two top corners, where few small cracks gradually appeared

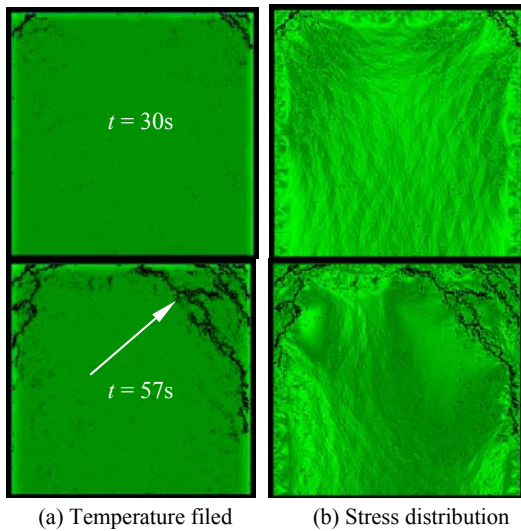


Figure 2. Numerical results of spalling process in case 1



Figure 3. Experimental observation

due to the heterogeneity even though at lower temperatures (as shown in Figure 2). With rising the temperatures, more new cracks initiated and propagated one by one from the corner point  $O'$  ( $O''$ ) to the center point  $O$  of the specimen. Generally, these cracks paralleled each other and are vertical to the diagonal  $O'-O$  (as shown in Figure 2). The aggregates formed obstacles to the cracks' propagation and their distribution pattern induced a network of irregular and rough cracks which were randomly distributed in the specimen. The scaling thickness between the thermal cracks was controlled by the temperature gradient and the aggregate distribution. The spalling process accompanied by delamination is quite similar to the experimental observations (as shown in Figure 3).

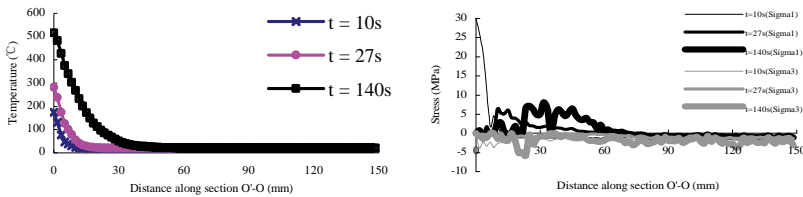


Figure 4. Temperature profile and stress distributions in case 2

**Case 2.** Figure 4 shows the temperature profile and the principal stress distributions in case 2 respectively. It was observed that temperature profile became steeper nearby the specimen surface. The stress gradient developed to reach a much less fluctuant profile above a certain position along the line  $O'-O$ . Generally, the temperature gradient and stress distribution are similar to the case 1. It was found that rapid heating induced substantial fluctuant stresses in the area nearby the specimen surface due to the thermal gradient. Since the all surface of circular specimen exposed to a same heating source, the tangential thermal cracks induced by the high stress concentration were distributed randomly along the surface area. With further increasing the temperatures, the tangential thermal cracks were formed layer by layer due to the gradual increase of thermal stresses. The paths of thermal cracks were also obviously controlled by the aggregate distribution (as shown in Figure 5). The thickness of scaling layer between the paralleling thermal cracks was not only closely related to the thermal gradient, but also to the aggregate distribution.

As above-mentioned, spalling will occur when the surface layer at a delamination falls away and exposes the internal concrete. The severe temperature gradient is the key factor causing the concrete delamination nearby the specimen surface.

After forming the cracks (the concrete scaled off layer by layer), the reinforcement directly exposed to high temperatures. Reinforcement has lower fire resistance than the concrete, the restriction of steel bars to plain concrete greatly reduced with increasing temperatures and the collapse risk of concrete reinforced structures largely increased. Hence, the simulation of spalling process and the calculation of delamination thickness are quite helpful to the design of concrete protection.

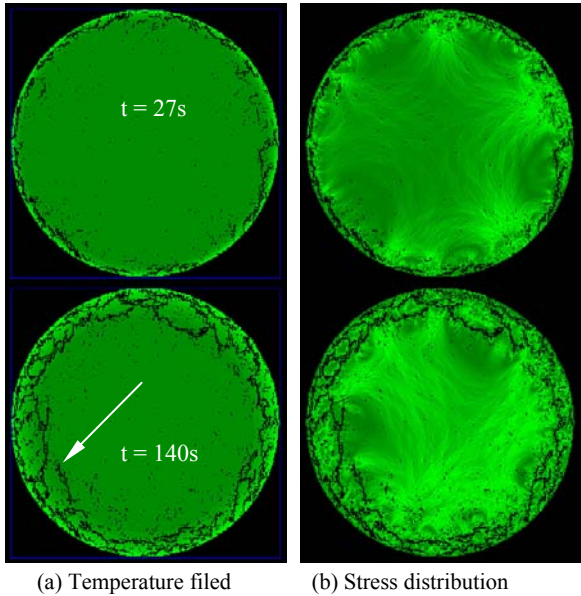


Figure 5. Numerical results of spalling process in case 2

For the corner spalling (case 1), the thermal damage of concrete was essentially caused by the high gradients of thermal stresses at the corner areas, where  $x$ - and  $y$ -thermal gradients overlap (as shown in Figure 5). When  $t=20s$ , the initial thermal crack occurred at  $d=12.4mm$  away from the corner point. The other cracks took place at  $d=33.6mm$  and  $84.8mm$  when  $t=30s$  and  $57s$ .

For surface spalling (case 2), the specimen shape had great influence on the temperature gradient and pattern of thermal cracking. The tangential cracks took place along the circular boundary of disc specimen which was uniformly heated (as shown in Figure 5). Spalling depth reached  $6mm$  and  $59mm$  at  $t=27s$  and  $140s$ . As compared to case 1, the disc specimen had better spalling resistance than the square one.

Experimental evidence indicates that the concrete surface temperatures when spalling occurs at temperatures of about  $250-420^{\circ}C$ , are dependent upon the heating rate and the characteristics of the concrete material (Jumpannen, 1989; Connolly, 1995). Numerical results showed that the spalling critical surface temperatures for case 1 and case 2 were  $315^{\circ}C$  and  $282^{\circ}C$  respectively, which were consistent with the experimental ones.

## 4 Conclusions

Through the numerical tests presented in this paper, the spalling mechanism could be understood as following:

1. The thermally cracking process cannot be simulated numerically without considering the heterogeneity and introducing the damage model at a mesoscopic level.
2. The spalling process cannot be tested numerically without considering the effects of thermal cracks.
3. Thermal cracks mainly are located within the area controlled by the severe temperature gradients.
4. The formations of thermal cracks cause the concrete delamination from the surface to the interior of specimen.
5. Circular specimen has the better fire resistance than the square one when subjected to the same temperature conditions.

## Acknowledgements

The work presented in this paper was financially supported by National Natural Science Funds, P.R. China (Grant No. 50778084 and 50408029).

## References

- British Standards Institution. BS 476. (1987). Fire tests on building materials and structures. London.
- Connolly R.J. (1995). The spalling of concrete in fires. PhD Thesis. Aston University.
- Fu Y.F., Wong Y.L., Tang C.A., Poon C.S. (2004). Thermal induced stress and associated cracking in cement-based composite at elevated temperatures (Part I): Thermal cracking around single inclusion. *Cement & Concrete Composites*, 26(2): 99-111 [in Chinese].
- Fu Y.F., Wong Y.L., Poon C.S. (2007). Numerical tests of thermal cracking induced by temperature gradient in cement-based composites under thermal loads. *Cement & Concrete Composites*, 29: 103-116 [in Chinese].
- Jumpmann U.M. (1989). Effect of strength on fire behaviour of concrete. Nordic Concrete Research Publication No. 8.
- Kalifa P., Menneteau F.D, Quenard D. (2000). Spalling and pore pressure in HPC at high temperatures, *Cement and Concrete Research*, 30: 1-13.
- Sanjayan G., Stocks L.J. (1993). Spalling of high strength silica fume concrete in fire. *ACI Materials Journal*, 90(2): 170-173.

*“This page left intentionally blank.”*

# Highlighting the Effect of Gel-Pore Diffusivity on the Effective Diffusivity of Cement Paste – A Multiscale Investigation

Xian Liu<sup>1\*</sup>, Roman Lackner<sup>2</sup> and Christian Pichler<sup>3</sup>

<sup>1</sup>Department of Geotechnical Engineering, Tongji University, 200092 Shanghai, China

<sup>2</sup>Material-Technology Unit, University of Innsbruck, 6020 Innsbruck, Austria

<sup>3</sup>Institute for Mechanics of Materials and Structures, Vienna University of Technology, 1040 Vienna, Austria

**Abstract.** The determination of the effective diffusivity of cement-based materials is a point of major importance to control service life of concrete structures. In this contribution, a multiscale model for cement-based materials focusing on the prediction of effective diffusivity is developed, treating cement-based materials as hierarchically organized material separated by three length scales. The comparison with experimental data taken from the literature reveals the non-negligible contribution of gel-pore.

**Keywords:** cement paste, diffusion, multiscale modeling, continuum micromechanics

## 1 Introduction

It is well-known that most chemical or physical degrading processes in concrete and concrete structures are dependent on the transport of ions within the saturated material. It is important to understand the rate of ionic migration, i.e., the effective diffusivity, in order to predict and control service life of concrete structures.

As regards the description of effective diffusivity, the bulk of existing materials models are formulated at the so-called macroscale. More recently, homogenization models were developed to estimate the macroscopic diffusion coefficients of cementitious materials, aiming at an estimate of diffusivity based on the material microstructure and diffusive properties of the phases constituting the material. The variation within these models lies in the consideration of the material microstructure, where capillary pore and gel pore are thought to have more or less influence

---

\* Corresponding author, email: xian.liu@tongji.edu.cn

on diffusivity, thus different separation schemes and different analytical homogenization methods have been developed.

Recent advances in micromechanics provide the basis for the development of multiscale models, in which processes within the material are considered at the respective observation scale and their effect on the macroscopic material performance is obtained by means of appropriate upscaling schemes. E.g., early-age elastic properties (Bernard et al., 2003) and autogenous-shrinkage (Pichler et al., 2007) of cement-based materials have been determined in this multiscale framework based on continuum micromechanics (Zaoui, 2002).

The purpose of this study is to propose a multiscale model to estimate the diffusivity of cement-based materials. The article is organized as follows: Section 2 presents multiscale modeling attempts of the microstructure of cement-based materials. Upscaling schemes for each observation scales to arrive at the macroscopical diffusivity are dealt within Section 3. In Section 4, experimental data taken from the open literature are employed to assess the proposed model.

## 2 Multiscale Modeling of Microstructure

When dealing with the diffusive transport in cementitious materials, its relationship with pore properties should be identified firstly. It is now widely accepted that the pore system inside material system is composed of gel pores within the calcium-silicate-hydrates (CSH) with pore width from a few nm to  $\mu\text{m}$  and capillary pores in  $\mu\text{m}$  to mm range (Jennings, 2000). Regarding the role these two types of pores take in diffusion, uncertainty persists. Oh et al. (2004), Care et al. (2004) and Pivonka et al. (2004) predict the diffusivity mainly considering the role of capillary porosity, while Carboczi et al. (1992) and Sotra et al. (2008) have pointed out the non-negligible contribution of gel porosity.

In order to investigate the role of different pores and to offer a sound model, the gel porosity is taken into account in current work, with gel pores and capillary pores separated by different scales depending on their pore sizes during the representation of microstructure.

### 2.1 Representation of Microstructure

For purpose of diffusive analysis, the employed multiscale microstructural model comprises three length scales, which are depict in Figure 1.

1. The lowest level (Scale I) refers to two types of CSH, low-density CSH (LD-CSH) and high-density CSH (HD-CSH), respectively. By morphological observation, the two types of CSH can be separated into the CSH gel porosity and

the impermeable solid phase. Thus, both HD-CSH and LD-CSH are considered as a porous polycrystalline containing different sized gel pores (Jennings, 2000).

2. Scale II (porous CSH) comprises the two types of CSH and capillary pore with a size of the underlying represent volume element (RVE) of  $10^{-8} \sim 10^{-6}$  m. At this scale, both HD-CSH and capillary pore are located in the space confined by LD-CSH.
3. At Scale III (cement-paste), the porous CSH represent the material matrix, while anhydrous cement, large CH crystals, aluminates, and macro-pores in case of water-to-cement ratios ( $w/c > 0.4$ ), form the size of RVE of  $10^{-6} \sim 10^{-4}$  m.

The three length scales obey the separability of scale requirement, i.e., scales are separated one from each other by at least one order of magnitude.

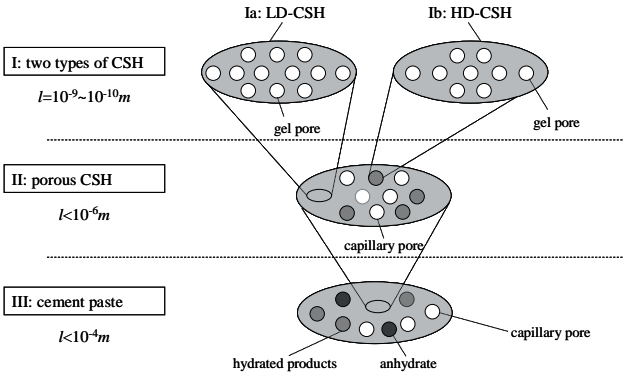


Figure 1. Scale separation for upscaling of properties of materials

## 2.2 Volume Fraction of Phases

Having separated the microstructure into different scales, the volume fractions of the different phases have to be determined. For this purpose, the hydration model outlined by Bernard et al. (2003) and Pichler et al. (2007) is employed. In this model, (i) the hydration degree is obtained by means of reaction kinetic laws and (ii) volume changes associated with chemical reactions can be considered. Based on the model, the volume fraction of HD CSH, LD CSH, capillary pores, and the remaining phases can be predicted as a function of the degree of hydration or the age.

With regards to gel pore volume, the assumption made here is that the gel porosity values are intrinsic to all cement-based materials as they are the consequence of the formation process of CSH during hydration (Ulm et al. 2004). The

gel pore volume is determined once volume of LD CSH and HD CSH is known. Ulm et al. (2004) proposed gel porosity values of 0.24 and 0.37, respectively, employed for HD CSH and LD CSH in this work.

The capillary pore volume belongs to two different scales in the employed scale-separation, for part of capillary pores should exit in the scale III for high water-to-cement ratios (Bernard et al., 2003). However, the hydration model offers the entire capillary porosity. In order to separate the capillary volume to two parts, the parameter  $X$  is introduced, defined as the ratio of capillary pores at scale II to the entire capillary pore volume.  $X$  depends on the water-to-cement ratio and the degree of hydration. A similar strategy has also been employed by Sanahuja et al. (2007) to model elasticity of a hydrating cement paste.

### 3 Diffusivity Modeling

Once microstructure is separated into different length scales and the volume fraction at each scale are obtained, homogenization schemes based on continuum micromechanics can be employed to upscale information from the lower scales to the macroscale. For the sake of simplicity, the diffusivity of the materials phases is assumed to be isotropic hereafter.

#### 3.1 Effective Diffusivity of LD-CSH or HD-CSH

At scale I, the solid matrix, i.e., either high-density CSH or low-density CSH, is assumed as nondiffusive ( $\mathbf{D}_s = 0$ ) compared to the diffusivity of the gel pores  $\mathbf{D}_{gp}$ . A micro-macro transition relating  $\mathbf{D}_{gp}$  to the effective diffusivity of HD-CSH,  $\mathbf{D}_{HD-CSH}$ , or LD-CSH,  $\mathbf{D}_{LD-CSH}$ , has been proposed as (Dormieux et al., 2001):

$$\mathbf{D}_{HD-CSH} = \phi_{gp} \mathbf{D}_{gp} : \mathbf{T}, \text{ and, } \mathbf{D}_{LD-CSH} = \phi_{gp} \mathbf{D}_{gp} : \mathbf{T} \tag{1}$$

where  $\phi_{gp} = V_{gp} / (V_{pore} + V_{pore})$  is the gel porosity of HD-CSH and LD-CSH respectively.  $V_{gp}$  is the gel pore volume in the RVE with volume  $V_{LD-CSH}$  or  $V_{HD-CSH}$  respectively. The so-called ‘tortuosity tensor’  $\mathbf{T}$  considers the morphology of the porous space on the overall diffusive properties and is estimated as  $\mathbf{T} = \phi^{1/2} \mathbf{1}$  in case of the spherical pores when employing differential scheme (Dormieux et al., 2001).

Taking isotropic of HD-CSH and LD-CSH into account, the overall diffusivity can be thus written as:

$$D_{HD-CSH} = \phi_{gp}^{3/2} D_{gp}, \text{ and, } D_{LD-CSH} = \phi_{gp}^{3/2} D_{gp} \tag{2}$$

### 3.2 Effective Diffusivity of Porous CSH and Cement Paste

At the porous CSH and cement paste scale, the diffusion process is described according to Fick’s first law as:

$$J = -D\nabla c \tag{3}$$

where  $J$  denotes the diffusion flux,  $D$  is the diffusion coefficient or diffusivity and  $c$  is the concentration of ions, e.g., chloride ions.

Fick’s first law defines diffusivity in the view of a continuum. In fact, this continuum-diffusivity is higher scale (e.g. cement paste) counterpart of the flow at the sub-level (e.g., porous CSH and capillary pore). In order to take this scale transition into account, Equation (3) can be recast as:

$$\langle J \rangle_v = -D^{hom} \cdot \langle \nabla c \rangle_v \tag{4}$$

where  $\langle \cdot \rangle_v$  denotes the volumetric averages over the respective RVE.

The sub-level is considered to be subjected to an up-level action prescribed at the boundary  $\partial V$  of the RVE as a Hashin-type boundary condition:

$$\forall x \in \partial V : c(x) = H \cdot x \tag{5}$$

where  $H$  denotes the gradient of density at up-level;  $c(x)$  is the density of the component in sub-level;  $x$  is the position vector at sub-level.

The up-level gradient of density  $H$  is related to the sub-level gradient of density by the volume-averaging relation:

$$H = \langle \nabla c \rangle_v = \frac{1}{V} \int_v \nabla c dV \tag{6}$$

To take the assumption of linear continuum micromechanics, the up-level gradient of density  $H$  can be linked to the sub-level gradient of density  $\nabla c$  as:

$$\nabla_x c = A_r \cdot H \tag{7}$$

where  $A_r$  is concentration tensor obeying to the consistency condition:

$$H = \langle \nabla c \rangle_V = \langle A_r \cdot H \rangle_V \Leftrightarrow \langle A_r \rangle_V = 1 \tag{8}$$

Combing the above equations yields:

$$D^{hom} = \langle D_r \cdot A_r \rangle_V = \sum_r f_r D_r \cdot A_r \tag{9}$$

The problem remaining is estimation of the concentration tensor for different phases, which can be derived for some idealized geometrical configurations. The most widely used one is an Eshelbian-type ellipsoidal inclusion embedded in a reference medium, given as (Zaoui, 2002):

$$\langle A \rangle_r = A_r^{est} = [1 + S_r^{est} \cdot (D_0^{-1} \cdot D_r - 1)]^{-1} \cdot \langle [1 + S_r^{est} \cdot (D_0^{-1} \cdot D_r - 1)]^{-1} \rangle_V^{-1} \tag{10}$$

where  $D_0$  denotes the diffusivity of the reference medium;  $D_r$  is the diffusivity of phase  $r = 1, n$ ; and  $S_r^{est}$  is the Eshelby tensor of phase  $r$ , which depends on the aspect ration and orientation of phases reducing in the spherical case to  $S_r^{est} = 1/3$  (Dormieux et al., 2001).

Combing the above equations, the homogenized diffusivity  $D_{hom}^{est}$  is obtained as:

$$D_{hom}^{est} = \langle D_r \cdot [1 + S_r^{Est} \cdot (D_0^{-1} \cdot D_r - 1)]^{-1} \rangle_V \cdot \langle [1 + S_r^{Est} \cdot (D_0^{-1} \cdot D_r - 1)]^{-1} \rangle_V^{-1} \tag{11}$$

To apply this procedure to the porous CSH or cement paste, the appropriate reference medium is chosen and thus the corresponding estimation scheme is selected.

In the case of porous CSH, it is assumed that the HD-CSH is located in the space confined by LD-CSH. Thus the HD-CSH and capillary pore are considered as inclusion in a LD-CSH matrix. The Mori-Tanaka (MT) scheme at this scale gives  $D_0 = D_m$ .

The cement paste scale includes porous CSH, capillary pores, anhydrate and other hydration products characterized by a polycrystalline microstructure. Thus, the self-consistent (SC) scheme may be used in the upscaling procedure with  $D_0 = D_{hom}^{est}$ .

### 4 Model Evaluation

In order to apply the developed multiscale model, the diffusivities of gel pores and capillary pores are required as basic input. Most existing models consider the ion diffusivity in capillary pore to be equal to the diffusion coefficient of ions in bulk water, e.g.  $1.61 \times 10^{-9} \text{ m}^2 / \text{ s}$  for chloride diffusivity in bulk water at  $T = 298\text{ K}$ . As there are no conclusive experimental nor modeling results on gel-pore diffusivity, a back-analysis method is employed to obtain intrinsic parameter and a value of  $D = 3.0 \times 10^{-11} \text{ m}^2 / \text{ s}$  is identified for the chloride diffusivity in gel pore hereafter.

First, the effect of parameter  $X$  on effective diffusivity is investigated by varying  $X$  from 0.5 to 1.0 for a fixed water-cement ratio, as shown in Figure 2. Only cases with water-cement ratio larger than 0.4 are depict as mentioned at Section 2. According to Figure 2, the effective diffusivity is insensitive with regard to the parameter  $X$ . For a water-cement ratio of 0.4, the effective diffusivity varies from  $3.1 \times 10^{-12} \text{ m}^2 / \text{ s}$  to  $3.3 \times 10^{-12} \text{ m}^2 / \text{ s}$  (7.9%). Simultaneously, the corresponding capillary porosity at scale III drops from 0.16 to 0. Thus, it can be concluded that parameter  $X$  doesn't take the decisive role with regard to diffusivity. In order to simplify the formulation, a constant value 1 is employed for parameter  $X$  for different water-cement ratios.

Experimental data sets taken from the literature (Ngala et al., 1995; Macodonald et al., 1995; Castellote et al., 2001) compared to the results of the multiscale mode. For the latter, the phase volume fractions are obtained from the hydration model at a state of complete hydration. From Figure 3, the experimental results differ for the same water-cement ratio, while the model predicted values locate in-between. This shows the suitability of the current model, which could be improved by further experiments.

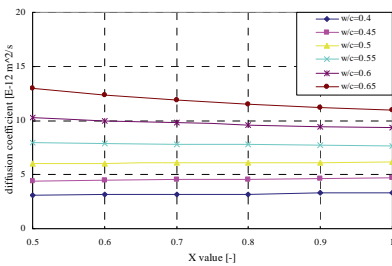


Figure 2. Influence of X value on diffusion coefficient

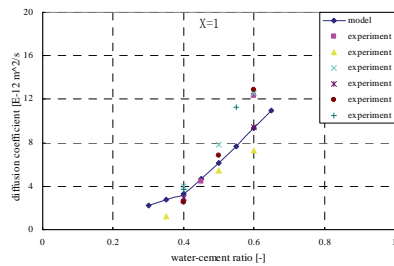


Figure 3. Model and experiment effective chloride diffusion coefficient with various w/c ratios

## 5 Summary

A multiscale micromechanics model for the effective diffusivity properties of cement-based materials has been proposed in this work. Reflecting the importance of different types and sizes of pores on the overall diffusivity, the model separates (i) the gel pores in two types of CSH, and (ii) the capillary pores at the porous CSH and cement paste scale. According to the respective morphology at the different scales of observation, different homogenization schemes based on continuum micromechanics were employed, allowing consideration of the pore properties such as shape and tortuosity. The predictive capability of the proposed model is assessed by comparison with data taken from the literature, highlighting the non-negligible contribution of gel porosity to the overall diffusivity. Future work will focus on the improvement of modelling of gel pore transport properties.

## Acknowledgements

The first author expresses his sincere appreciation to the financial support from Austrian Exchange Service (OEAD), Austria.

## References

- Bernard O., Ulm F.J., Lemarchand E. (2003). A multiscale micromechanics-hydration model for the early-age elastic properties of cement-based materials, *Cement and Concrete Research*, 33, 1293-1309.
- Care S., Herve E. (2004). Application of a n-phase model to the diffusion coefficient of Chloride in mortar, *Transport in Porous Media*, 56, 119-135.
- Castellote M., Alonso C., Andrade C., Chadbourn G.A., Pare C.L. (2001). Oxygen and chloride diffusion in cement pastes as a validation of chloride diffusion coefficients obtained by steady-state migration tests, *Cement and Concrete Research*, 31, 621-625.
- Dormieux L., Lemarchand E. (2001). Homogenization approach of advection and diffusion in cracked porous material, *Journal of Engineering Mechanics*, 127(12), 1267-1274.
- Garboczi E.J., Bentz D.P. (1992). Computer simulation of the diffusivity of cement-based materials, *Journal of Materials Science*, 27, 2083-2092.
- Jennings H.M. (2000). A model for the microstructure of calcium silicate hydrate in cement paste, *Cement and Concrete Research*, 30, 101-116.
- Krabbenhoft K., Hain M., Wriggers P. (2008). Computation of effective cement paste diffusivities from microtomographic images, *Proceedings of the ECCOMAS Thematic Conference Composites with Micro- and Nano-Structure*, V. Kompis, Springer, Heidelberg.
- Macdonald K.A., Northwood D.O. (1995). Experimental measurements of chloride ion diffusion rates using a two-compartment diffusion cell: Effect of material and test variables, *Cement and Concrete Research*, 25, 1407-1416.

- Ngala V.T., Page C.L., Parrott L.J., Yu S.W. (1995). Diffusion in cementitious materials: II, further investigations of chloride and oxygen diffusion in well-cured OPC and OPC/30%PFA pastes, *Cement and Concrete Research*, 25, 819-826.
- Oh B.H., Jang S.Y. (2004). Prediction of diffusivity of concrete based on simple analytic equations, *Cement and Concrete Research*, 34, 463-480.
- Pichler C., Lackner R., Mang H. (2007). A multiscale micromechanics model for the autogenous-shrinkage deformation of early-age cement-based materials, *Engineering Fracture Mechanics*, 74, 34-58.
- Pivonka P., Hellmich C., Smith D. (2004). Microscopic effects on chloride diffusivity of cement pastes – A scale-transition analysis, *Cement and Concrete Research*, 34, 2251-2260.
- Sanahuja J., Dormieux L., Chanvillard G. (2007). Modelling elasticity of a hydrating cement paste, *Cement and Concrete Research*, 37, 1427-1439.
- Sotra E., Bary B., He Q.C. (2008). On estimating the effective diffusive properties of hardened cement pastes, *Transport in Porous Media*, 73, 279-295.
- Ulm F.J., Constantinides G., Heukamp F.H. (2004). Is concrete a poromechanics material? – A multiscale investigation of poroelastic properties, *Materials and Structures*, 37, 43-58.
- Xi Y.P., Willam K., Frangopol D.M. (2000). Multiscale modeling of interactive diffusion process in concrete, *Journal of Engineering Mechanics*, 258-265.
- Zaoui A. (2002). Continuum micromechanics: Survey. *Journal of Engineering Mechanics*, 128(8), 808-816.

*“This page left intentionally blank.”*

# An Efficient Nonlinear Meshfree Analysis of Shear Deformable Beam

Dongdong Wang<sup>1\*</sup> and Yue Sun<sup>1</sup>

<sup>1</sup>Department of Civil Engineering, Xiamen University, Xiamen, Fujian 361005, China

**Abstract.** A geometrically nonlinear total Lagrangian meshfree formulation based on the stabilized conforming nodal integration is presented for efficient analysis of shear deformable beam. The incremental equilibrium equation is obtained by the consistent linearization of variational equation. The meshfree shape function is constructed purely based on the initial configuration. Subsequently to accelerate the computation the method of stabilized conforming nodal integration is systematically implemented through the Lagrangian gradient smoothing operation. Both stability and efficiency are gained in the proposed nonlinear meshfree beam formulation. The effectiveness of the present method is validated by two typical numerical examples.

**Keywords:** meshfree methods, beam, geometric nonlinearity, stabilized conforming nodal integration, efficiency

## 1 Introduction

Meshfree methods have experienced substantial developments and applications in recent years (Li and Liu, 2004). Various meshfree formulations have been proposed to analyze beams, plates, and shells which form an important class of engineering structures. One distinguished advantage for meshfree methods is that they can relieve the mesh tangling burden of FEM and are favorable for large deformation analysis. However, due to the non-polynomial characteristic of the frequently utilized moving least square or reproducing kernel approximation, the time-consuming higher order Gauss quadrature rule is required to evaluate the weak form. Consequently different methods have been developed to improve the computational efficiency. The stabilized conforming nodal integration proposed by Chen et al (2001) doesn't need artificial parameters and offers stability and efficiency simultaneously. Thereafter the stabilized conforming nodal integration-based meshfree methods have been systematically developed for beams, plates,

---

\* Corresponding author, e-mail: ddwang@xmu.edu.cn

and shells by Wang and Chen (2004, 2006, 2008), Wang et al (2006), Chen and Wang (2006), and Wang and Wu(2008). In this work the meshfree formulation with stabilized conforming nodal integration is extended to geometrically nonlinear analysis of shear deformable beam with a total Lagrangian formulation.

## 2 Basic Equations of Beam

Consider a two dimensional beam undergoing finite deformation as shown in Fig.1, the beam occupies a domain  $\Omega(\mathbf{X}) = L \times A$  with  $L$  and  $A$  being the length and cross-section area, respectively. The neutral axis of the beam is set to be coincided with the  $X$ -axis. In the shear deformable beam theory (Li, 2001), the dependent displacement and rotation variables at a generic point  $X$  on the neutral axis are two translational displacements and one rotation denoted by  $\{u, v, \theta\}$ , then the position vector  $\mathbf{x}$  that varies over the thickness can be expressed as:

$$\mathbf{x} = \boldsymbol{\varphi}(\mathbf{X}) = \begin{Bmatrix} x \\ y \end{Bmatrix} = \begin{Bmatrix} X + u(X) - Y \sin \theta(X) \\ Y + v(X) - Y(1 - \cos \theta(X)) \end{Bmatrix} \quad (1)$$

where the rigid fiber hypothesis is adopted, i.e., the fiber that is perpendicular the neutral axis remains no length change before and after the applied deformation, i.e.,  $\|\mathbf{x} - \mathbf{x}_N\| = \|\mathbf{X} - \mathbf{X}_N\|$ . From Equation (1), the deformation gradient  $\mathbf{F}$  and Green-Lagrangian strain  $\mathbf{E}$  can be obtained as:

$$\mathbf{F}(\mathbf{X}) = \begin{bmatrix} 1 + u_{,X} - Y\theta_{,X} \cos \theta & -\sin \theta \\ v_{,X} - Y\theta_{,X} \sin \theta & \cos \theta \end{bmatrix} \quad (2)$$

$$\mathbf{E}(\mathbf{X}) = \begin{bmatrix} \{u_{,X} + (u_{,X}^2 + v_{,X}^2) / 2 + Y^2 \theta_{,X}^2 / 2 & v_{,X} \cos \theta - (1 + u_{,X}) \sin \theta \\ -Y\theta_{,X} [(1 + u_{,X}) \cos \theta + v_{,X} \sin \theta] & \\ v_{,X} \cos \theta - (1 + u_{,X}) \sin \theta & 0 \end{bmatrix} \quad (3)$$

The Saint-Venant Kirchhoff hyperelastic material model is employed here to relate the 2<sup>nd</sup> Piola-Kirchhoff stress  $\mathbf{S}$  and the Green-Lagrangian strain  $\mathbf{E}$ :

$$\Delta S_{IJ} = C_{IJKL} \Delta E_{KL}, \quad C_{IJKL} = \lambda \delta_{IJ} \delta_{KL} + \mu (\delta_{IK} \delta_{JL} + \delta_{IL} \delta_{KJ}), \quad \{I, J\} = \{1, 2\} \quad (4)$$

where  $\lambda$  and  $\mu$  denote the Lamé's constants.

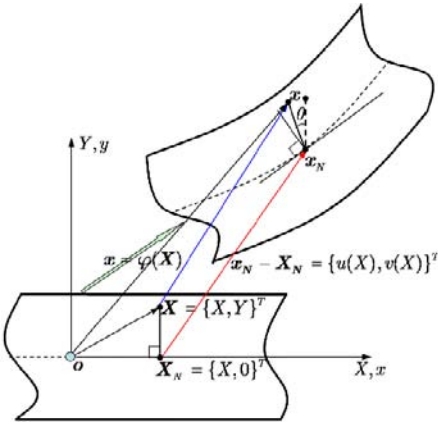


Figure 1. Kinematics of a beam under finite deformation

A weak statement of the beam equilibrium is given by:

$$\begin{cases} \delta\Pi(\mathbf{x}) = \delta W^{int}(\mathbf{x}) - \delta W^{ext}(\mathbf{x}) = 0 \\ \delta W^{int} = \int_{\Omega} \delta E_{IJ} S_{IJ} d\Omega = \int_{\Omega} (\delta E_{XX} S_{XX} + 2\delta E_{XY} S_{XY}) d\Omega \end{cases} \quad (5)$$

where use is made of the fact  $S_{YY} = 0$  based on Eqns. (3) and (4).  $\delta W^{ext}$  is the virtual work done by the external forces. Since Equation (5) is nonlinear, the following Newton-Raphson scheme is utilized to obtain the solution:

$$\delta\Pi(\mathbf{x}_{n+1}^{m+1}) \approx \delta\Pi(\mathbf{x}_{n+1}^m) + \Delta\delta\Pi(\mathbf{x}_{n+1}^m) \approx 0 \quad (6)$$

where  $n$  and  $m$  denote the load step and iteration number, respectively.  $\Delta\delta\Pi(\mathbf{x}) = \Delta\delta W^{int}(\mathbf{x}) - \Delta\delta W^{ext}(\mathbf{x})$  is the incremental virtual work,  $\Delta\delta W^{ext}(\mathbf{x})$  is given and  $\Delta\delta W^{int}(\mathbf{x})$  that can be obtained via the standard linearization process:

$$\Delta\delta W^{int}(\mathbf{x}) = \int_{\Omega} \delta \hat{u}_{i,j} (D_{ijkl} + T_{ijkl}) \Delta \hat{u}_{k,l} d\Omega, \quad D_{ijkl} = F_{iI} F_{jK} C_{IJKL}, \quad T_{ijkl} = \delta_{ik} S_{jL} \quad (7)$$

where  $\hat{u} = \boldsymbol{\varphi}(X) - X$ ,  $D_{ijkl}$  and  $T_{ijkl}$  refer to the material stiffness and geometric stiffness, respectively.

For convenience of development, Equation (7) can be rewritten as:

$$\Delta\delta W^{int}(\mathbf{x}) = \int_{\Omega} \delta \mathbf{e}^T (\mathbf{D} + \mathbf{T}) \Delta \mathbf{e} d\Omega \quad (8)$$

with  $\mathbf{e}^T = \{\widehat{u}_{1,1}, \widehat{u}_{2,2}, \widehat{u}_{1,2}, \widehat{u}_{2,1}\}$ .  $\mathbf{D}$  and  $\mathbf{T}$  are given by

$$\mathbf{D} = \begin{bmatrix} D_{1111} & D_{1122} & D_{1112} & D_{1121} \\ D_{2211} & D_{2222} & D_{2212} & D_{2221} \\ D_{1211} & D_{1222} & D_{1212} & D_{1221} \\ D_{2111} & D_{2122} & D_{2112} & D_{2121} \end{bmatrix}, \quad \mathbf{T} = \begin{bmatrix} S_{11} & 0 & S_{12} & 0 \\ 0 & 0 & 0 & S_{12} \\ S_{12} & 0 & 0 & 0 \\ 0 & S_{12} & 0 & S_{11} \end{bmatrix} \tag{9}$$

From Equation (2) it is straightforward to get:

$$\Delta \mathbf{e} = \begin{Bmatrix} \Delta \widehat{u}_{1,1} \\ \Delta \widehat{u}_{2,2} \\ \Delta \widehat{u}_{1,2} \\ \Delta \widehat{u}_{2,1} \end{Bmatrix} = \begin{Bmatrix} \Delta F_{11} \\ \Delta F_{22} \\ \Delta F_{12} \\ \Delta F_{21} \end{Bmatrix} = \begin{Bmatrix} \Delta u_{,x} - Y(\cos \theta)\Delta \theta_{,x} + Y\theta_{,x}(\sin \theta)\Delta \theta_{,x} \\ -(\sin \theta)\Delta \theta \\ -(\cos \theta)\Delta \theta \\ \Delta v_{,x} - Y(\sin \theta)\Delta \theta_{,x} - Y\theta_{,x}(\cos \theta)\Delta \theta_{,x} \end{Bmatrix} \tag{10}$$

### 3 Meshfree Discretization and Stabilized Nodal Integration

In a Lagrangian version of the moving least square or reproducing kernel meshfree approximation, the material problem domain, i.e., the neutral axis of beam,  $[0, L]$ , is discretized by a set of  $NP$  particles,  $X_I$ 's,  $I = 1, 2, \dots, NP$ , an approximation of a scalar field variable  $g(X)$ , denoted by  $g^h(X)$ , can be expressed by:

$$g^h(X) = \sum_{I=1}^{NP} \Psi_I(X)d_I, \quad \Psi_I(X) = \mathbf{p}^T(X_I - X)\mathbf{b}(X)\phi_a(X_I - X) \tag{11}$$

where  $\Psi_I(X)$  is the Lagrangian meshfree shape function and  $d_I$  is the nodal coefficient.  $\phi_a(X - X_I)$  is a kernel function centered at  $X_I$  with a support size of  $a$ .  $\mathbf{p}(X - X_I)$  is the  $Q$ -th order monomial basis defined as:

$$\mathbf{p}(X_I - X) = \{1, X_I - X, (X_I - X)^2, \dots, (X_I - X)^Q\}^T \tag{12}$$

The unknown coefficient vector  $\mathbf{b}(X)$  can be obtained through the enforcement of the following  $Q$ -th order reproducing conditions:

$$\sum_{I=1}^{NP} \Psi_I(X)X_I^i = X^i \quad 0 \leq i \leq Q \tag{13}$$

Equation (13) can be recast into the following matrix form:

$$\mathbf{M}(X)\mathbf{b}(X) = p(\boldsymbol{\theta}), \quad \mathbf{M}(X) = \sum_{I=1}^{NP} \mathbf{p}^T(X_I - X) \mathbf{p}(X_I - X) \phi_a(X_I - X) \quad (14)$$

Thus one has  $\mathbf{b}(X) = \mathbf{M}^{-1}(X)p(\boldsymbol{\theta})$  and the meshfree shape function becomes:

$$\Psi_I(X) = \mathbf{p}^T(\boldsymbol{\theta})\mathbf{M}^{-1}(X)\mathbf{p}(X_I - X)\phi_a(X_I - X) \quad (15)$$

Introducing the meshfree approximation into the beam displacement field gives:

$$\begin{Bmatrix} \Delta u^h(X) \\ \Delta v^h(X) \\ \Delta \theta^h(X) \end{Bmatrix} = \sum_{I=1}^{NP} \Psi_I(X) \begin{Bmatrix} \Delta u_I \\ \Delta v_I \\ \Delta \theta_I \end{Bmatrix} = \sum_{I=1}^{NP} \Psi_I(X) \Delta \mathbf{d}_I \quad (16)$$

With Equation (16), Equation (10) becomes

$$\Delta \mathbf{e}^h = \sum_{I=1}^{NP} \mathbf{B}_I \mathbf{d}_I, \quad \mathbf{B}_I = \begin{bmatrix} \Psi_{I,X} & 0 & Y(\theta_{,X} \sin \theta - \cos \theta) \Psi_{I,X} \\ 0 & 0 & -(\sin \theta) \Psi_I \\ 0 & 0 & -(\cos \theta) \Psi_I \\ 0 & \Psi_{I,X} & -Y(\sin \theta + \theta_{,X} \cos \theta) \Psi_{I,X} \end{bmatrix} \quad (17)$$

Substituting Eqns. (16) and (17) into Eqns. (6)-(8) yields the following linearized incremental Equation:

$$\mathbf{K}_{n+1}^m \Delta \mathbf{d}_{n+1}^m = \mathbf{f}_{n+1}^{ext} - \mathbf{f}_{n+1}^{int}, \quad \mathbf{K}_{IJ} = \int_{\Omega} \mathbf{B}_I^T (\mathbf{D} + \mathbf{T}) \mathbf{B}_J d\Omega \quad (18)$$

To improve the computational efficiency and maintain the spatial stability, the stiffness is integrated by the stabilized conforming nodal integration method, i.e., the integration is carried out nodally:

$$\mathbf{K}_{IJ} = \sum_{K=1}^{NP} \tilde{\mathbf{B}}_I^T (\mathbf{D} + \mathbf{T}) \tilde{\mathbf{B}}_J \Omega_K \quad (19)$$

where in  $\tilde{\mathbf{B}}_I$  the gradient term  $\Psi_{I,X}(X_K)$  associated with membrane and shear deformation is evaluated directly to relieve the locking, while  $\Psi_{I,X}(X_K)$  related to the bending behavior is replaced by the smoothed gradient  $\tilde{\Psi}_{I,X}(X_K)$ :

$$\tilde{\Psi}_{I,X}(X_K) = L_K^{-1} \int_{L_K} \Psi_{I,X} dX = [\Psi_I(X_K^+) - \Psi_I(X_K^-)] / L_K \tag{20}$$

with  $L_K = \|X_K^+ - X_K^-\|$ .  $(X_K^-, X_K^+)$  is the integration domain for the node  $X_K$ .

### 4 Numerical Examples

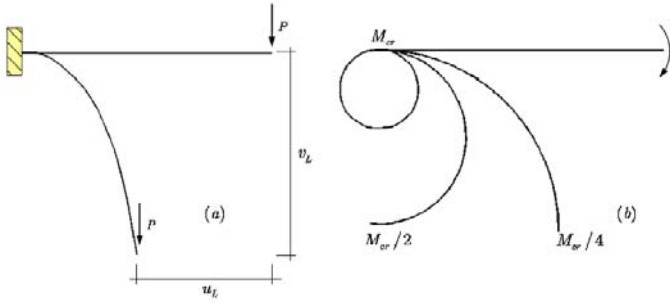


Figure 2. Cantilever beam subject to: (a) end force; (b) end moment

Two benchmark numerical examples as shown Fig. 2 are analyzed here to test the present nonlinear meshfree method. The problems consist of a cantilever beam subjected to a force  $P = 75$  or a moment  $M_{cr} = 2\pi EI / L$  at the free end, where  $EI$  represents the bending rigidity. The beam has a unit square cross-section area and a length of  $L=10$ . The shear correction factor is set to be  $5/6$  in this study. The material parameters are: Young’s modulus  $E = 10000$  and shear modulus  $\mu = 5000$ . Throughout the meshfree computation a normalized support size of 2 is employed. For the end force problem, 11 meshfree particles are utilized and the solution of  $u_L = 0.5346$  and  $v_L = 0.8017$  is obtained at the final stage, which agrees well with the analytical solution of  $u_L^e = 0.5318$  and  $v_L^e = 0.7991$  (Mattiasson, 1981). In case of the end moment problem 21 uniform meshfree particles are used and the resulting deformation exhibits an expected circular curve (Mattiasson, 1981).

### 5 Summary

A geometrically nonlinear meshfree method was presented under the total Lagrangian framework for the solution of shear deformable beam. In the proposed me-

thod, the Lagrangian meshfree shape function was employed and the domain integration was performed via the method of stabilized conforming nodal integration on the material domain. Two benchmark numerical examples demonstrated the efficacy of the present method.

## Acknowledgements

Support of this work by the Program for New Century Excellent Talents in Fujian Province University, the Natural Science Foundation of Fujian Province (D0710023), and NSFC (10602049), is gratefully acknowledged.

## References

- Chen J.S., Wu C.T., Yoon S., You Y. (2001). A stabilized conforming nodal integration for Galerkin meshfree methods. *Int. J. Numer. Methods Eng.*, 50: 435–466.
- Chen J.S., Wang D. (2006). A constrained reproducing kernel particle formulation for shear deformable shell in Cartesian coordinates, *Int. J. Numer. Methods Eng.*, 68:151–172.
- Li M. (1997). The finite deformation theory for beam, plate and shell. Part I: the two dimensional beam theory. *Comput. Methods Appl. Mech. Eng.*, 146:53–63.
- Li S., Liu W.K. (2004). *Meshfree Particle Methods*, Springer-Verlag.
- Mattiasson K. (1981). Numerical results from large deflection beam and frame problems analyzed by means of elliptic integrals. *Int. J. Numer. Methods Eng.*, 17:145–153.
- Wang D., Chen J.S. (2004). Locking free stabilized conforming nodal integration for meshfree Mindlin-Reissner plate formulation, *Comput. Methods Appl. Mech. Eng.*, 193:1065–1083.
- Wang D., Dong S.B., Chen J.S. (2006). Extended meshfree analysis of transverse and inplane loading of a laminated anisotropic plate of general planform geometry, *Int. J. Solids Struct.*, 43:144–171.
- Wang D., Chen J.S. (2006). A locking-free meshfree curved beam formulation with the stabilized conforming nodal integration, *Computational Mechanics*, 39:83–90.
- Wang D., Wu Y. (2008). An efficient Galerkin meshfree analysis of shear deformable cylindrical panels, *Interaction and Multiscale Mechanics*, 1:339–355.
- Wang D., Chen J.S. (2008). A Hermite reproducing kernel approximation for thin plate analysis with sub-domain stabilized conforming integration, *Int. J. Numer. Methods Eng.*, 74:368–390.

*“This page left intentionally blank.”*

# Variance-Based Methods for Sensitivity Analysis in Civil Engineering

Zdeněk Kala<sup>1\*</sup> and Libor Puklický<sup>1</sup>

<sup>1</sup>Department of Structural Mechanics, Brno University of Technology, Faculty of Civil Engineering, Czech Republic

**Abstract.** The objective of the presented paper is the ultimate limit state sensitivity analysis of a steel plane frame to input imperfections. The Sobol's variance based strategy was applied for the sensitivity analysis evaluation. The ultimate limit state was solved by the geometrical nonlinear finite element solution. The load-carrying capacity, solved on behalf of the Monte Carlo numerical simulation method, was the output random quantity. Input imperfections were measured, and their histograms have been applied in the Monte Carlo method. In the paper, there are demonstrated the changes of sensitivity coefficients in dependence on system lengths of columns.

**Keywords:** sensitivity, frame, imperfections, system, variance, reliability, design

## 1 Introduction

Generally, engineering procedures employed in the design of load-bearing structures of building objects are essentially based on computational procedures that verify valid normative criteria emanating from the static, respectively the dynamic solution of a model of the real structural system. Most imperfections with random character are taken into consideration only in a very simplified way by standard regulations, although their effect can take part in substantial lowering of their load-carrying capacity.

In the presented paper, the effect of input imperfections on the steel plate load-carrying capacity is evaluated by sensitivity analysis. In recent years, there was developed a number of various stochastic methods of the sensitivity analysis and a number of possibilities of their practical application was offered (Kala, 2005; Saltelli, 2008; Saltelli et al., 2007; Sobol', 1993). With the development of new conceptions of the reliability analysis the procedures can contribute to a qualitative improvement of the reliability analysis of structures. In building engineering, the

---

\* Corresponding author, e-mail: kala.z@fce.vutbr.cz

results of sensitivity analysis can be applied for optimization of control activities in production process with the aim to lower the variability of quantities studied.

## 2 Stability Problems and Ultimate Limit State of Steel Plane Frame

Two methods are usually applied for solution of the ultimate limit state of steel structures with members under compression. The stability solution with buckling length is a solution frequently used in practice. The geometrically nonlinear solution with initial imperfections is applied for a more accurate analysis. One of the possibilities is to consider the geometrical imperfection of a system to be the first eigen mode buckling shape. In the paper presented here there will be analyzed ultimate limit state of a steel frame, see Figure 1.

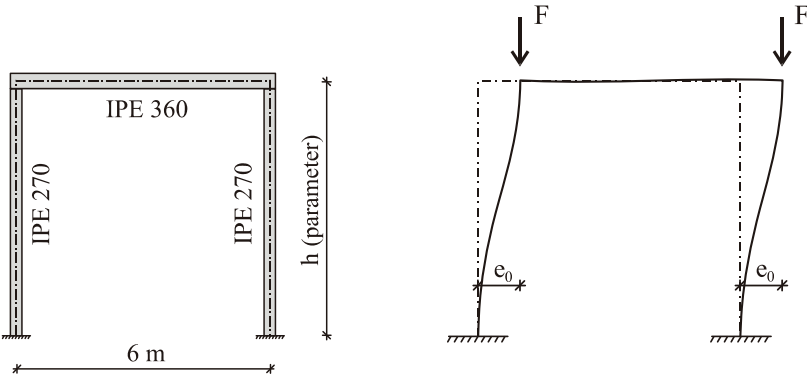


Figure 1. Frame geometry, load actions and frame system imperfections.

The theoretical analysis is based on a nonlinear finite element method (Kala, 2005). In our study, the frame geometry was modelled using beam elements with initial curvature in the form of a parabola of the 3rd degree (Kala, 2005). The geometrical nonlinear Euler incremental method combined with the Newton-Raphson method was considered.

The first criterion (i.e. strength condition) for the load-carrying capacity is given by loading at which plasticization of the flange is initiated. The second criterion (i.e. stability condition) for the load-carrying capacity is represented by loading corresponding to a decrease of the determinant to zero.

The ultimate one-parametric loading is defined as the lowest value from the strength and stability criterion of load-carrying capacity. This phenomenon occurs at high yield point values with small geometrical member imperfections. In each

simulation run, the load-carrying capacity was determined with an accuracy of 0.1 percent (Kala, 2005).

The author of this article is the author of the applied software programme. The software programme was compiled in the programming language Pascal within the framework of scientific researches and is not intended for commercial use.

### 3 Input Random Imperfections

Load-carrying capacity is, in general, a random quantity, statistically dependent on random input imperfections. The most important information on input material and geometrical characteristics of steel products is provided by the experimental research (Strauss et al., 2006, Melcher et al., 2004). For non-measured quantities (e.g., Young's modulus), the study was based on the data obtained from technical literature; for example, statistical characteristics of Young's modulus are given in (Soares et al., 1988).

Table 1. Input random quantities

Symbol	Meaning	Probability distribution	Mean Value	Standard deviation
$h_1$	Cross-sectional height	Histogram	270.27 mm	1.196 mm
$b_1$	Cross-sectional width	Histogram	136.81 mm	1.341 mm
$t_{w1}$	Web thickness	Histogram	6.963 mm	0.277 mm
$t_{f1}$	Flange thickness	Histogram	10.126 mm	0.466 mm
$f_{y1}$	Yield strength	Histogram	297.3 MPa	16.8 MPa
$E_1$	Young's modulus	Gauss	210 GPa	12.6 GPa
$h_0$	Cross-sectional height	Histogram	360.36 mm	1.595 mm
$b_0$	Cross-sectional width	Histogram	172.3 mm	1.689 mm
$t_{w0}$	Web thickness	Histogram	8.44 mm	0.335 mm
$t_{f0}$	Flange thickness	Histogram	12.611 mm	0.582 mm
$f_{y0}$	Yield strength	Histogram	297.3 MPa	16.8 MPa
$E_0$	Young's modulus	Gauss	210 GPa	12.6 GPa
$h_2$	Cross-sectional height	Histogram	270.27 mm	1.196 mm
$b_2$	Cross-sectional width	Histogram	136.81 mm	1.341 mm
$t_{w2}$	Web thickness	Histogram	6.963 mm	0.277 mm
$t_{f2}$	Flange thickness	Histogram	10.126 mm	0.466 mm
$f_{y2}$	Yield strength	Histogram	297.3 MPa	16.8 MPa
$E_2$	Young's modulus	Gauss	210 GPa	12.6 GPa
$e_0$	System imperfection	Gauss	0	$h / 1000$

The information on system imperfection  $e_0$  is described only indefinitely or is totally lacking in the literature. The Gauss density function with mean value zero was considered for system imperfection  $e_0$ . Furthermore, we have assumed that 95% of realizations of  $e_0$  are found within the tolerance interval of  $\pm h/500$ . The statistical characteristics of input quantities are given in Table 1. All the input random quantities are considered statistically independent.

The introduction of the system imperfection according to first eigen mode buckling shape is a frequently applied approach. Another possible approach, which has not been applied here, is the introduction of system imperfection and of imperfection of beams as four random quantities.

## 4 Sobol Sensitivity Analysis

The description of Sobol's decomposition theory is listed e.g. in (Saltelli et al., 2007; Strauss et al., 2006). The Sobol's first order sensitivity indices may be written in the form:

$$S_i = V(E(Y | X_i)) / V(Y) \quad (1)$$

Sobol proposed an alternate definition  $S_i = \text{corr}(Y, E(Y | X_i))$  based on the evaluation of the correlation between output random variable  $Y$  and the conditional random arithmetical mean. Analogically we can write the second order sensitivity indices:

$$S_{ij} = V(E(Y | X_i, X_j)) / V(Y) - S_i - S_j \quad (2)$$

Sensitivity index  $S_{ij}$  expresses the influence of doubles on the monitored output. In our study, the sensitivity analysis of load-carrying capacity (random output  $Y$ ) to input imperfections (input random quantities  $X_i$ ) was evaluated.

The sensitivity indices were evaluated utilizing the Monte Carlo method. The conditional random arithmetical mean  $E(Y | X_i)$  was evaluated for 10000 simulation runs; the variance  $V(E(Y | X_i))$  was calculated for 10000 simulation runs, as well. It was proceeded analogously to evaluate  $V(E(Y | X_i, X_j))$  in (2). The variance  $V(Y)$  of load-carrying capacity is calculated under the assumption that all the input imperfections are considered to be random ones; 10000 simulation runs were applied, as well. Other Sobol' sensitivity indices enabling the quantification of higher order interactions may be expressed similarly.

The number of terms in is  $2^{M-1}$ , i.e., we obtain 7 sensitivity indices  $S_1, S_2, S_3, S_{12}, S_{23}, S_{13}, S_{123}$  for  $M=3$ ; for  $M=10$ , we obtain 1023 sensitivity indices; it is excessively large for practical usage. The main limitation in the determination of all members is the computational demand. The sensitivity analysis results given here represent a synopsis of many studies carried out during last two years. In each par-

tial study, the sensitivity indices were calculated for the constant frame height  $h$ , the parameter  $h$  having been assigned by another value. It was preceded systematically, and calculations were processed on modern computers.

The results obtained by the Sobol's sensitivity analysis would be available by means of other methods only with difficulties. The Sobol's sensitivity analysis counts among the variance based methods which provide more complex information on sensitivity of an output quantity to input quantity than, e.g., the correlation analysis between the input and output does (Saltelli, 2008). When evaluating the sensitivity analysis by means of the Spearman rank-order correlation coefficient, it must be preceded very carefully. It is necessary to note that dependence and correlation are not synonymous. A correlation implies dependence, while the opposite is not true.

## 5 Sensitivity Analysis Results

The sensitivity analysis results are presented in Figure 2. For the clearness' sake, only sensitivity indices are drawn. As the frame, load action and boundary conditions are symmetrical, the values of sensitivity coefficients of both left and right columns are the same, i.e., they are depicted by one curve only. The changes of courses of sensitivity indices in dependence on the frame height  $h$  are evident from Figure 2.

If the frame height  $h < 3.2$  m, then the load-carrying capacity variance is most influenced by the yield stress variance of the left and the right column, see the values of the first order sensitivity indices (1)  $f_{y1}, f_{y12}$  and those of the second order sensitivity indices (2)  $f_{y1} - f_{y12}$ .

If the frame height  $h > 3.2$  m, then the system imperfection  $e_0$  is dominant. The maximum effect  $S_{e_0} = 0.9$  was calculated for the frame with height  $h = 9.3$  m (buckling length  $L_{cr} = 9.66$  m).

If the frame height  $h > 9.3$  m, then the load-carrying capacity is almost not sensitive to the yield stress changes in both columns. With increasing height, the load-carrying capacity is approaching the Euler critical force, and therefore it is more sensitive to changes of Young's module values and of flange thickness in both columns  $E_1, E_2, t_{fy}, t_{f2}$ .

It must be remarked that the effect of residual stress was neglected in calculations. According to the relating studies, this imperfection shows high effect for beams with nondimensional slenderness in interval from 0.5 to 0.9.

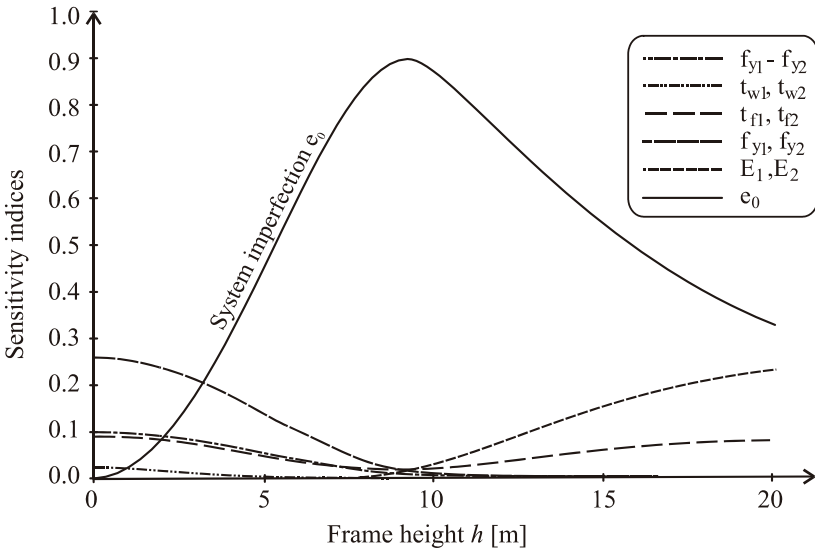


Figure 2. Measured values of yield strength of plates 4 to 100 mm.

### 6 Conclusions

The sensitivity analysis results identify the imperfections the variability of which can influence the structure reliability. Above all, it is necessary to study the imperfections the quality of which can be positively influenced by manufacturing process, e.g., yield strength, and geometrical characteristics.

The results concerning the frame solved here show that the system imperfection  $e_0$  takes the dominant effect on ultimate limit state for  $h > 3.2$  m. It has been confirmed by related studies that a system imperfection shows the maximum effect if and when the nondimensional slenderness (calculated from buckling length) lies in the interval 0.9 to 1.0. This conclusion is in good agreement also with the results of sensitivity analysis of one beam under compression (Saltelli, 2008). Let us remark that different courses of sensitivity coefficients were obtained, when the frame with columns terminated with joints was solved; the sensitivity index is increasing with increasing frame height.

The basic difference between the analysis of ultimate limit state of one beam of the system lies in the fact that also height order interactions effects can be applied to the system in a more important manner among input quantities. Calculations concerning the frame solved here showed, for low values  $h$ , significant values (2) of second order terms between yield strength of the left and the right column.

Identification of critical or otherwise interesting regions in the set of input factors is important because factors which interact may thus generate extreme values.

## Acknowledgements

The article was elaborated within the framework of projects GAČR 103/08/0275, AVČR IAA201720901 and research MSM0021630519.

## References

- Kala Z. (2005). Sensitivity Analysis of the Stability Problems of Thin-walled Structures, *Journal of Constructional Steel Research* 61, 415–422.
- Kala Z. (2008). Sensitivity Assessment of Steel Members under Compression. *Journal Engineering Structures*, doi:10.1016/j.engstruct.2008.04.001.
- Melcher J., Kala Z., Holický M., Fajkus M., Rozlívka L. (2004). Design Characteristics of Structural Steels Based on Statistical Analysis of Metallurgical Products, *Journal of Constructional Steel Research* 60, 795–808.
- Saltelli A., Ratto M., Andress T., Campolongo F., Cariboni J., Gatelli D., Saisana M., Tarantola S. (2007). *Global Sensitivity Analysis Guiding the Worth of Scientific Models*, New York: John Wiley and Sons.
- Soares G.C. (1988). Uncertainty Modelling in Plate Buckling, *Journal Structural Safety*, (5), 17–34.
- Sobol' I. (1993). Sensitivity Estimates for Nonlinear Mathematical Models, *Matematicheskoe Modelirovanie* 2, 112–118, 1990 [from Russian, translated into English in Sobol' 1993].
- Strauss A., Kala Z., Bergmeister K., Hoffmann S., Novák D. (2006). Technologische Eigenschaften von Stählen im europäischen Vergleich. *Stahlbau*, 75, Januar 2006, Heft 1.

*“This page left intentionally blank.”*

# Coupled Multi-Physical Fields Analysis of Early Age Concrete

Yiming Zhang<sup>1\*</sup> and Yong Yuan<sup>2</sup>

<sup>1</sup>Department of Geotechnical Engineering, Tongji University, Shanghai 200092, P.R. China

<sup>2</sup>Key Laboratory of Geotechnical and Underground Engineering of Ministry of Education, Tongji University, Shanghai 200092, P.R. China

**Abstract.** This paper focuses on the multi-physical fields' evolution in early age concrete, which has great importance to the work performance and durability of concrete material. This paper presented some simple and comprehensible formulas to connect different multi-physical field of early age concrete. Then a simplified model is proposed to analyze the early age concrete after which the numerical analysis methods are built. We compared the simulated results with the passively confined concrete experiments data and find they agree well, which proved this method feasible and effective.

**Keywords:** multi-physical fields, capillary pressure field, permeability, numerical simulation

## 1 Introduction

The multi-physical fields of early age concrete change a lot with close connection to the concrete type and the curing environment. Moreover, different physical fields connect to each other, which results in many difficulties in precisely analysis and simulation of early age concrete. This paper makes rational simplification and improvement on the former models and theories then presents an analysis method which is easy to build efficient numerical program. The numerical analysis & simulation results are proved to agree well with the experiments data.

Since Powers and his colleagues set up empirical model for the phase distribution of a hardening cement paste 60 years ago (Powers and Brownyard, 1948), scientists and engineers have built and improved many models and calculation methods to analyze the early age concrete materials. In the 1970s and 1980s, Bazant built the moisture field equation with humidity diffusion theory (Bazant and Najjar, 1972) and the total strain method (Bazant, 1988) which presented a

---

\* Corresponding author, e-mail: midnightduke@gmail.com

good thought to calculate the early age concrete. Then in the 1990s, many researchers including Cervera (Cervera et al., 1999) built the coupled methods which used the hydration degree theory and analyze the chemical change of early age concrete. Nowadays, many researchers have built their models on the base of basic porous material analysis theories among which the models of Gawin and his colleagues (Gawin et al., 2006) is very inspiring and comprehensive.

In this paper, the authors cut some minor effects among multi-physical fields, and then improve the moisture field calculation to the capillary pressure field analysis, which is widely used in porous material simulation. In the whole analysis process, the authors take the hydration degree as the bridge between time forward and fields' evolution. By these methods, the authors largely reduce the computation burden caused by asymmetric matrixes which are very common in traditional porous material numerical simulations. Furthermore, all the parameters need in this method is already acquired or deducible through former experiments' data.

## 2 Multi-Physical Fields Relationship

When the concrete hydration process on, the multi-physical fields changes with each other. But some effects that one physical field have on another can be neglected. In our coupled multi-physical fields analysis methods, we neglect some effects among the fields including: the effects strain field to thermal field & capillary pressure field, the effects capillary pressure field to thermal field & damage field, the effect between damage field and thermal field.

At last, the relationship of multi-physical fields is showed by Figure 1.

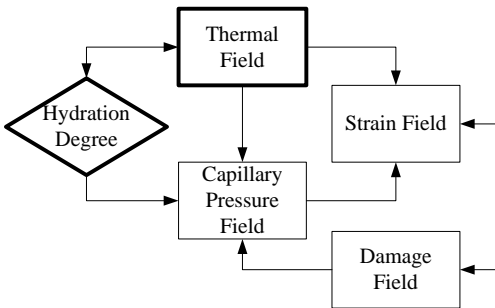


Figure 1. The relationship of multi-physical fields

From Figure 1, we can know the calculation of thermal field is only involved with the hydration degree, which has unilateral effects to the other physical fields. On the other hand, the calculation of capillary pressure field is much more complicated, which is affected by the calculation of almost all the other physical fields.

Consequently, in the whole calculation process, the calculation of thermal field is the sally port when the calculation of capillary pressure field is the keystone.

Firstly, we calculate the thermal field and the hydration degree (the broad-brush frames part in Figure 1) in the early age concrete after which we can use the calculation result in the next field calculation. Secondly, we calculate capillary pressure field, strain field and damage field together step by step. Especially, we take into account the effect damage field to the capillary pressure field by the relationship between damage degree and permeability coefficient.

### 3 Fields Equation

#### 3.1 Hydration Degree & Thermal Field

Because of the strong connection between hydration process and thermal field evolution, the hydration degree and thermal field should be analyzed and calculated together.

Cervera et al. (1999) proposed the formula (1) to calculate the hydration degree of the early age concrete.

$$\frac{d\Gamma_{\text{hydr}}}{dt} = A_1 \left( \frac{A_2}{\kappa_{\infty}} + \kappa_{\infty} \Gamma_{\text{hydr}} \right) (1 - \Gamma_{\text{hydr}}) \exp(-\bar{\eta} \Gamma_{\text{hydr}}) \exp\left(-\frac{E_a}{RT}\right) \quad (1)$$

The coefficients  $A_1, A_2, \bar{\eta}$  can be obtained from experiments data.  $E_a$  is the activation energy of concrete.  $\kappa_{\infty}$  is the ratio between the real final hydration degree value and the theoretical one, which depends on the water/cement ratio of a concrete.

In analysis of early age concrete, the calculation of thermal field is very mature. The heat equation (2) is used to describe thermal field in early age concrete.

$$\frac{\lambda}{c\rho} \left( \frac{\partial^2 T}{\partial x^2} + \frac{\partial^2 T}{\partial y^2} + \frac{\partial^2 T}{\partial z^2} \right) + \frac{\dot{Q}(\Gamma_{\text{hydr}})}{c\rho} = \frac{\partial T}{\partial t} \quad (2)$$

where  $c\rho$  are specific heat capacity and the mass density of the concrete.  $\dot{Q}(\Gamma_{\text{hydr}})$  is the heat release function.

Though the effective thermal conductivity of early age concrete is affected by the saturation degree which depends on the capillary pressure, we can just use the average saturation degree of concrete here which is only the function of hydration degree.

### 3.2 Capillary Pressure Field

In early age concrete, when temperature difference is the driving force of heat flux, capillary pressure difference is the main driving force of moisture flux.

The moisture flux  $J$  can be expressed as Equation (3) (Ishida et al., 2007).

$$J = -(P_P \nabla p_C + P_T \nabla T) \tag{3}$$

where  $P_P$  is the moisture conductivity with respect to the capillary pressure gradient,  $P_T$  is the moisture conductivity with respect to the temperature gradient.

Like the thermal field, the capillary pressure field can be described by another heat equation (4).

$$\frac{P_P}{g(p_C, T)} \left( \frac{\partial^2 p_C}{\partial x^2} + \frac{\partial^2 p_C}{\partial y^2} + \frac{\partial^2 p_C}{\partial z^2} \right) + \frac{\dot{m}_w(\Gamma_{\text{hydr}})}{g(p_C, T)} + k_T \frac{\partial T}{\partial t} = \frac{\partial p_C}{\partial t} \tag{4}$$

where the function  $\dot{m}_w(\Gamma_{\text{hydr}})$  is the hydrated water mass function.  $g(p_C, T)$  is the bridge function that connects the capillary pressure with the water mass balance.

Because of the porosity of concrete material, the evaporation and the hydration of the water inside the concrete cause desorption process of concrete. Hence, the function  $g(p_C, T)$  can be deduced from the concrete sorption isotherms. Though the sorption isotherms experiment aims to the mature concrete, the porosity and volumetric changes with hydration degree are considered to modify the results adapt to early age concrete as well.

Baroghel-Bouny (1999) proposed the following formula (5) from sorption isotherms to describe the relationship between the saturation degree and the capillary pressure.

$$S_w = \left[ 1 + \left( \frac{p_C}{a} \right)^{b/(b-1)} \right]^{-1/b} \tag{5}$$

where  $a, b$  are empirical parameters related to the temperature  $T$ .

When we neglect the water vapour change inside the concrete, the water mass balance equation can be got as Equation (6).

$$\left[ 1 + \left( \frac{p_C}{a} \right)^{\frac{b}{b-1}} \right]^{-\frac{1}{b}} \cdot \rho_w + \frac{\Delta m_w}{n(\Gamma_{\text{hydr}})} = \left[ 1 + \left( \frac{p_C + \Delta p_C}{a} \right)^{\frac{b}{b-1}} \right]^{-\frac{1}{b}} \cdot \rho_w \tag{6}$$

where  $n(\Gamma_{\text{hydr}})$  denotes the porosity of concrete with specific hydration degree.  $\rho_w$  is the density of liquid water. From Equation (6), we can get the function  $g(p_c, T)$ .

If the water vapour changes too fast to neglect, we just need to use the Kelvin equation and the Clausius-Clapeyron equation, then put the additional vapour mass per unit pore volume formula Equation (7) inside (6).

$$m_{\text{vap}}(p_c, T) = \left( 1 - \left[ 1 + \left( \frac{p_c}{a} \right)^{\frac{b}{b-1}} \right]^{\frac{1}{b}} \right) \cdot \exp\left( -\frac{p_c M_w}{\rho_w R T} \right) \cdot \rho_{\text{vsat}}(T) \quad (7)$$

where  $M_w$  is the molar mass of water (vapour).  $R$  is the gas constant.  $\rho_{\text{vsat}}(T)$  is the vapour part density of saturation vapour at temperature  $T$ .

On the other hand, the permeability coefficient  $P_p$  is also involved with hydration degree and temperature. The effect that damage degree  $D$  causes to  $P_p$  will be discussed in the next section.

According to the Kozeny-Carman equation, there is an approximate linear relationship between the porosity and the permeability coefficient. When considering the relationship between the water viscosity and the temperature in (283K~363K), we can build another approximate linear relationship between the temperature and the permeability coefficient as well. Hence, the formula (8) is proposed here.

$$P_p(\Gamma_{\text{hydr}}, T) = \frac{P_{pMa} n(\Gamma_{\text{hydr}})}{n_{\infty}} \left( A \frac{T}{T_c} + B \right) \quad (8)$$

where  $P_{pMa}$  is the permeability coefficient of mature concrete.  $n_{\infty}$  is the porosity of mature concrete.  $T_c$  is the reference temperature.  $A, B$  are empirical parameters.

Then, we have got the field equation of capillary pressure field.

### 3.3 Strain Field & Damage Field

The strain of early age concrete on any calculation step at  $i$ th time intervals is defined as Equation (9) (Bazant, 1988)

$$\Delta \varepsilon_i^{\text{total}} = \Delta \varepsilon_i^{\text{th}} + \Delta \varepsilon_i^{\text{sh}} + \Delta \varepsilon_i^{\text{load}} + \Delta \varepsilon_i^{\text{cr}} \quad (9)$$

where  $\Delta\varepsilon_i^{th}$  is the thermal strain.  $\Delta\varepsilon_i^{sh}$  is the shrinkage strain.  $\Delta\varepsilon_i^{load}$  is the load strain.  $\Delta\varepsilon_i^{CT}$  is the creep strain.

The strains due to thermal variation are assumed to linear Equation (10)

$$\varepsilon_{th} = \alpha \Delta T \quad (10)$$

where  $\alpha$  is the thermal dilation coefficient (TDC) of concrete.

The strains due to capillary pressure can be calculated by Equation (11)

$$d\varepsilon_{sh} = -\frac{nS_w dp_c}{K_0} \quad (11)$$

where  $K_0$  is the drained bulk modulus of concrete.

In our model, we used the scalar damage parameter–damage degree  $D$  to describe the damage situation of concrete.

The permeability coefficient will be affected by damage degree  $D$ . And in the next calculation step, this kind of effect will be taken into account. We take the advice of Gawin (Gawin et al., 2002) and use the Bary's formula (Bary, 1996) Equation (12) to calculate the permeability coefficient's change by damage degree.

$$P_{p-D} = P_p \cdot 10^{A_D \cdot D} \quad (12)$$

where  $A_D$  is material constant that was evaluated as equal to 4.

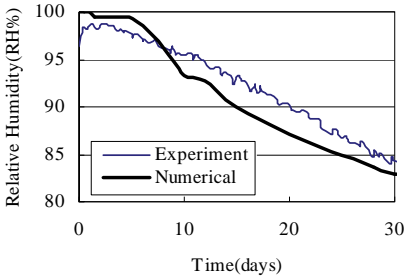
## 4 Numerical Examples

Two numerical examples are discussed in this section. The experiments data were got from passively confined concrete tests. Table 1 showed the experiments conditions.

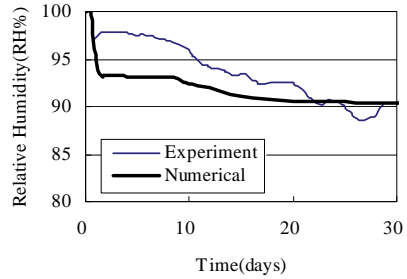
Table 1. Experiments conditions

Sample Size	Concrete Grade	Environment RH, Temperature
100mm×100mm×1000mm	C-30	45%±5%, 20°C
100mm×100mm×1000mm	HPC	45%±5%, 20°C

The ends of the concrete sample of the load test are cuneiform which can be fixed on a firm steel framework. The load recorder works on the framework and records the loads that the framework provides to the concrete sample. On the other hand, a humidity sensor was put inside the core of another sample whose mixture is the same as the load test sample to record the humidity change inside the concrete. Three sides except the bottom of the sample are exposed to the air.

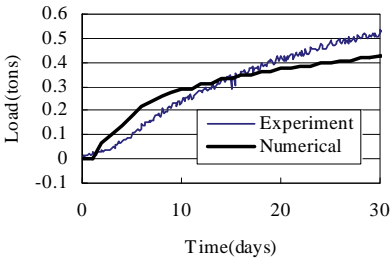


(a)C-30 sample

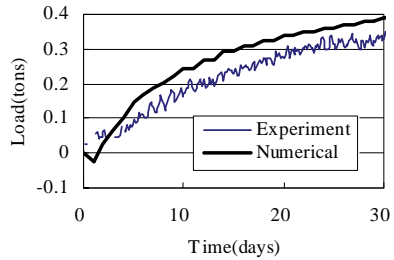


(b)HPC sample

Figure 2. Comparison of the measured and simulated RH changes of C-30 sample(a) and HPC sample(b)



(a)C-30 sample



(b)HPC sample

Figure 3. Comparison of the measured and simulated framework load changes of C-30 sample(a) and HPC sample(b)

We find our method can calculate and simulate the whole trend of the RH changes and the framework load changes of ordinary concrete and HPC. However, some problems still exist. For example, the simulated relative humidity changes in first 0.5~2 days didn't fit well with the experiment. This problem was caused by the  $\dot{m}_w(\Gamma_{hydr})$  in Equation (4), which will be fixed in our future works.

## 5 Conclusions

In this paper, we take the advantage of relative small variation of temperature and small water vapor proportion of whole water in early age concrete then build a feasible and comprehensible numerical model. The calculation results of this numerical model fit well with the experiments data.

## Acknowledgements

Financial support by National Nature Science Foundation of China Program (Sanction No 50678133) and National Nature Science Foundation of China Key Program (Sanction No 50838004) is gratefully acknowledged.

## References

- Baroghel-Bouny V., Mainguy M., Lassabatere T. and Coussy O. (1999). Characterization and identification of equilibrium and transfer moisture properties for ordinary and high-performance cementitious materials. *Cement and Concrete Research*, 29(8): 1225-1238.
- Bary B. (1996). Etude de couplage hydraulique-mécanique dans le béton endommagé, Laboratoire de Mécanique et Technologie, C.N.R.S. de Cachan, Paris.
- Bazant Z.P. (1988). *Mathematical Modeling of Creep and Shrinkage of Concrete*. Wiley: Chichester.
- Bazant Z.P. and Najjar L.J. (1972). Nonlinear water diffusion in nonsaturated concrete. *Materials and Structures* 5(25): 3-20.
- Cervera M., Olivier J. and Prato T. (1999). A thermo-chemo-mechanical model for concrete. I: hydration and aging. *Journal of Engineering Mechanics (ASCE)*, 125(9): 1018-1027.
- Gawin D., Pesavento, F. and Schrefler, B.A. (2002). Simulation of damage-permeability coupling in hygro-thermo-mechanical analysis of concrete at high temperature, pp. 113-119.
- Gawin D., Pesavento F. and Schrefler B.A. (2006). Hygro-thermo-chemo-mechanical modelling of concrete at early ages and beyond. Part I: hydration and hygro-thermal phenomena. *International Journal for Numerical Methods in Engineering*, 67(3): 299-331.
- Ishida T. Maekawa K. and Kishi T. (2007). Enhanced modeling of moisture equilibrium and transport in cementitious materials under arbitrary temperature and relative humidity history. *Cement and Concrete Research*, 37(4): 565-578.
- Powers T.C. and Brownard T.L. (1948). *Studies of the Physical Properties of Hardened Portland Cement Paste*, Research Laboratories of the Portland Cement Association, Chicago.

# Rigid Plasticity Analysis of Defect Beam Suffering Step Loads

Nansheng Li<sup>1\*</sup>, Xingzhou Li<sup>1</sup> and Yu Wang<sup>1</sup>

<sup>1</sup>Department of Hydraulic Engineering, Tongji University, Shanghai 200092, P.R. China

**Abstract.** It's a most common dynamics phenomenon of subject to impact for the structural beam. The conclusions drawn from dead load status cannot be always applied to the circumstance directly when the structure is suffered to impact loads. The deformation models of structure beam caused from impact-load cannot be even explained by the analysis of dead load status. In this paper, by selecting the constitutive model—rigid plasticity, of cantilever beam with a main crack suffering to step load status, analyzes its deformation history. We can find that there is a quite different reactivity between defective beam and non-defective beam and the beam will have a counter movement when effected by strong impact load due to the existence of crack effect. In the end of the analysis, benchmark examples are provided respectively. This paper introduces the usual crack phenomena into impact dynamics, referring to previous research and obtains a primary research which is necessarily be verified by more experiments. However, the conclusion is drawn under the premises, such as the centralization of crack effect, and neglecting the subordinate effect.

**Keywords:** defective beam, step loads, rigid-plasticity, deflection curve, plastic hinge

## 1 Introduction

The deformation analysis of structures suffering the impact load are being paid a widely attention nowadays. As early as 1952, Lee E. H. and Symonds P. S. (Lee E.H. and Symonds, 1952) analyzed the rigid-plastic dynamic response of a two-ends-free beam with the triangular pulse acting on the mid-point. Their analysis shows that when the load is small, the beams are only forced to make a rigid body movement. When  $PL/M_p > 4$  ( $P$  is the outside load,  $L$  is the half length of the beam,  $M_p$  is the plastic limit moment of the beam section), besides the mid-point of the beam forms a plastic hinge, the two wings also form plastic hinges, and

---

\* Corresponding author, e-mail: linansheng@online.sh.cn

along with the growth of  $PL/M_p > 4$ , the plastic hinge in the two wings will move towards the mid-point. Thus a very important concept is imported: the transitional hinge. Parkes (Parkes, 1948) analyzed the dynamic response of a cantilever beam with its end knocked by a mass of  $G$ , the initial speed of the rigid block being  $V_0$ . He assumed that after the impact the rigid block attached to the post-impact beam and worked together with the beam. The model was known as the Parkes model. Stronge and Yu Tongxi (Zhou and Yu, 1987) found that when the rigid linear strengthening cantilever beam with its end collided by the rigid block, there were a gradually shrinking plastic loading zone and a gradually expanding unloading zone occurring in the beam. The interface between them moved from the impacting end to the beam roots. When the material's strengthening was rather weak, the transitional interface would degrade to a transitional hinge of Parkes.

Some deficiency existing in the beam structure which bears the impacting load will reduce the yielding moment of the cross-section. What is more important is that it appears as a singular point of the configuration which causes a mutation of the stress-strain distribution surrounding the defective area and an absolutely different deformation mode than the non-defective beam. In this paper we try to analyze one type of the most common structural defects – cracks in beam components bearing step-load to consider the following information of the beam components: the plastic hinge position and its migration of various stages; the (angular) displacement, (angular) velocity, angular acceleration of different sections within various segments at different moment (including rigid and plastic zones), as well as the moment and shear force distribution of each section of rigid zones at different moment. We give out an analysis of the criterion to judge if the defect effect with the reaction of the beam elements suffering a sudden load can be ignored. We also give out an analysis of the conditions of the plastic hinge to occur in various segments suffering different size of loads and an analysis of the location of the plastic hinge and the basic formulas of the deformation mode of each segment on the premise that the defect effect can not be ignored. For a kind of crack widely existed in the practice, we draw a fairly common conclusion, which reveals the crack's effect with the ability of the beam to resist the impact loads. This part of the research is based on some basic assumptions, ignoring the secondary effects. The results of the analysis can be used for reference for the future research of related areas.

## 2 Deformation Mode of the Defect Beam Suffering Step Load

Model shown in Figure 1, adopts the Parkes modified model: The material of the beam is ideal rigid-plastic. The length of the beam is  $L$ . The mass of unit length of the beam is  $m$ . The plastic yielding moment is  $M_p$ . The cross section is uniform. When  $t=0$ , the step load is acting at the free end of the beam. Its function can be

expressed as  $p = p_0$  ( $t \geq 0$ ). The details of the cracks are shown in figure 2~3. When a sudden load is acted on, because the cracks meet the formula as follow:

$$K > \sigma_s \sqrt{\pi \left(\frac{H}{2} - a\right)} \tag{1}$$

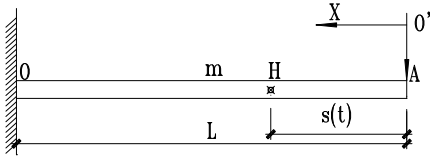


Figure 1. Modified Parkes' model

The surrounding part of B point has entered into the plastic status. As for the cracking section (C-C' section), the stress on the x direction is  $\sigma_s$ . At this time, the size of the moment of B point is different with the different types of crack.

For crack 1,  $M_B = \sigma_s \left(\frac{H}{2} + a\right) \left(\frac{H}{2} - a\right) b$ ; For crack 2,  $M_B = \frac{1}{4} \sigma_s \left(\frac{H}{2} - a\right)^2 b$ .

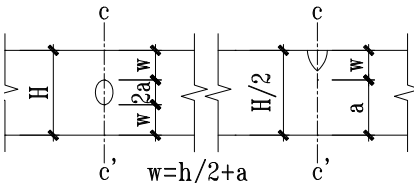


Figure 2. Crack 1      Figure 3. Crack 2

Choose AB segment to analyze: The AB segment rotating round B point at the angular acceleration of  $\omega_1$ , the length of AB is  $x_B$ . Then the equation of motion is as follow:

$$\begin{cases} \frac{1}{2} m x_B^2 \cdot \omega_1 = p_0 \cdot Q_B \\ \frac{1}{3} m x_B^3 \cdot \omega_1 = p_0 \cdot x_B - M_B \end{cases} \tag{2}$$

At this time:

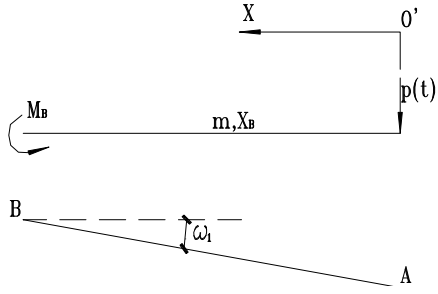
$$\dot{z}(t) = \frac{3t}{mx_B} \left( p_0 - \frac{M_B}{x_B} \right)$$

$$\alpha(t) = \frac{3t}{mx_B^2} \left( p_0 - \frac{M_B}{x_B} \right)$$

$$\omega(t) = \frac{3}{mx_B^2} \left( p_0 - \frac{M_B}{x_B} \right)$$

$$Q(x) = p_0 - \frac{3}{2} \left( p_0 - \frac{M_B}{x_B} \right) \left( \frac{x}{x_B} \right)^2$$

$$M(x) = p_0 x - \left( p_0 x - M_B \frac{x}{x_B} \right) \left( \frac{x}{x_B} \right)^2$$



The deformation mode of  $BH$  is quite different from each other according to the value of  $Q_B$  (negative or positive). Here we have the following discussion depending on the various value of  $Q_B$  :

1. When  $Q_B = \frac{3}{2} \frac{M_B}{x_B} - \frac{1}{2} p_0 > 0$ , that is  $p_0 < 3 \frac{M_B}{x_B}$ , if  $M_B + Q_B L \geq M_S$ , that is:

$L \geq \frac{M_S - M_B}{Q_B}$ , then the plastic hinge H appears in the middle of BO, otherwise

the plastic hinge O appears in the beam root. When the plastic hinge appears in the middle of the beam, select the BH part, then:

$$x_0 = 3 \frac{M_S - M_B}{Q_B}$$

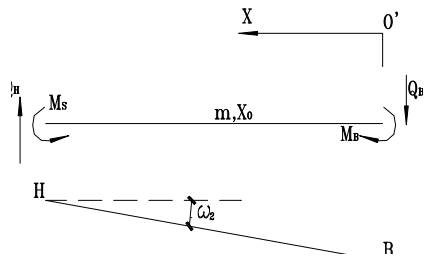
$$\dot{z}(t) = \frac{2Q_B^2 t}{3m(M_S - M_B)}$$

$$\alpha(t) = \frac{2Q_B^3 t}{9m(M_S - M_B)^2}$$

$$\omega(t) = \frac{2Q_B^3}{9m(M_S - M_B)^2}$$

$$Q(x) = Q_B - \frac{Q_B^3 x^2}{9(M_S - M_B)^2}$$

$$M(x) = M_B + Q_B x - \frac{2Q_B^3 x^3}{27(M_S - M_B)^2}$$



As the plastic hinge appears in the middle of the beam, then  $x_0 = 3 \frac{M_S - M_B}{Q_B} < L$ , this makes the condition  $L > \frac{M_S - M_B}{Q_B}$  satisfied natu-

rally. And when  $\frac{M_S - M_B}{Q_B} \leq L \leq 3 \frac{M_S - M_B}{Q_B}$ , the plastic moment hinge appears at

the beam root. At this time, we select the BO part to analyze as follows:

BO Segment rotates round O point at the angular acceleration of  $\omega_3$ , and then according to the balance equation of the beam section, we have:

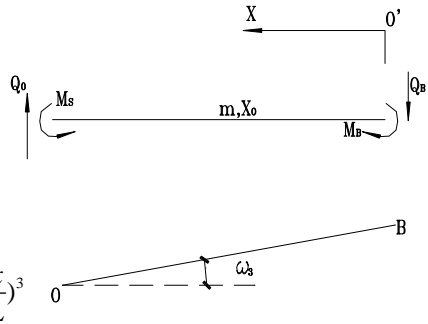
$$\dot{z}(t) = \frac{3[Q_B L - (M_S - M_B)]}{mL^2} t$$

$$\alpha(t) = \frac{3[Q_B L - (M_S - M_B)]}{mL^3} t$$

$$\omega(t) = \frac{3[Q_B L - (M_S - M_B)]}{mL^3}$$

$$Q(x) = Q_B - \frac{3}{2} \left( Q_B - \frac{M_S - M_B}{L} \right) \left( \frac{x}{L} \right)^2$$

$$M(x) = M_B + Q_B x - [Q_B L - (M_S - M_B)] \left( \frac{x}{L} \right)^3$$



Because the analysis is based on:

$$\frac{M_S - M_B}{Q_B} \leq L \leq 3 \frac{M_S - M_B}{Q_B} \tag{3}$$

So  $Q_0 > 0$ .

2. When  $Q_B = \frac{3}{2} \frac{M_B}{x_B} - \frac{1}{2} p_0 = 0$ , that is  $p_0 = 3 \frac{M_B}{x_B}$ , then the shear force of B point is zero, and  $M_B < M_S$ , that is that the BO part is rigid entirely. At this time, the plastic hinge only forms at the point B where the cracks locate. In this critical state, there is only one plastic hinge in the whole beam.

3. When  $Q_B = \frac{3}{2} \frac{M_B}{x_B} - \frac{1}{2} p_0 < 0$  that is  $p_0 > 3 \frac{M_B}{x_B}$ , if  $Q_B L - M_B \geq M_S$ , that is :

$$L \geq \frac{M_S + M_B}{Q_B}, \text{ then the plastic hinge } H \text{ appears in the middle of BO. Or the plastic hinge O appears in the beam root.}$$

When the plastic hinge appears in the middle of the beam, select the BH part, then:

BH Segment rotates round H point at the angular acceleration of  $\omega_2$ , H is the plastic moment hinge. The length of BH is  $x_0$ , then according to the movement balance equation as follows:

$$x_0 = 3 \frac{M_S + M_B}{Q_B}$$

$$\dot{z}(t) = \frac{2Q_B^2 t}{3m(M_S + M_B)}$$

$$\alpha(t) = \frac{2Q_B^3 t}{9m(M_S + M_B)^2}$$

$$\omega(t) = \frac{2Q_B^3}{9m(M_S + M_B)^2}$$

$$Q(x) = Q_B - \frac{Q_B^3 x^2}{9(M_S + M_B)^2}$$

$$M(x) = -M_B + Q_B x - \frac{2Q_B^3 x^3}{27(M_S + M_B)^2}$$

From the above deduction we know:

(1) The conclusion of the defect beam is different from that without defects. The shear force of the crack where the plastic hinge forms is not zero any longer. And the size of the force is depending on the features (including the position) of the cracks, and the size of outside dynamic load.

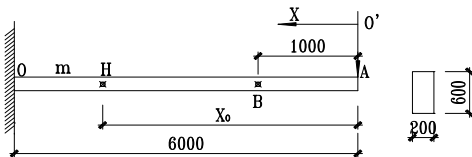
(2) With the sudden increase in the value of the dynamic load, the beam deform

mode is quite different. When the crack meets  $K > \sigma_s \sqrt{\pi(\frac{H}{2} - a)}$  , as long as

there is the dynamic load on the5the plastic hinge will form around the crack surely. And the criterion to judge this second plastic hinge’s emergence and its location is quite different either. For the non-defective beam, it is only depending on the outside load and the limit yielding moment of the beam. But for the beam with defects, there is a counter angular velocity in the beam’s deformation mode according to the value of outside load  $p_0$  , which can never be observed in the model based on the static load.

### 3 The Numerical Example

Take a cantilever beam, the Q235 steel, 6000mm long, cross section:  $200 \times 600mm^2$  ,1000mm from the free end, there is a crack in the form of crack 1, the crack length is  $2a = 200$  .At the end of the free end of the beam, there is a step impact load. And structures have different patterns of response according to the size of the impact load.



So, take three different loads, as follows: The density of the steel is 7800, we have:

$$m = \gamma bh = 7800 \times 0.2 \times 0.6 = 936 \text{ kg/m}$$

$$EI = \frac{E}{6} bh^3 = \frac{2.0 \times 10^8}{6} \times 0.2 \times 0.6^3 = 1.44 \times 10^6 \text{ kN} \cdot \text{m}^2$$

$$M_S = \frac{1}{4} \sigma_s bh^2 = \frac{1}{4} \times 235 \times 200 \times 600^2 = 4230 \text{ KN} \cdot \text{m}$$

$$M_B = \sigma_s \left( \frac{H}{2} + a \right) \left( \frac{H}{2} - a \right) b = 235 \times (300 + 100) \times (300 - 100) \times 200 = 3760 \text{ KN} \cdot \text{m}$$

The static limit load is:  $p_S = \frac{M_S}{L + x_B} = 705 \text{ KN}$ . The two critical loads are:

$$3 \frac{M_B}{x_B} = 3 \frac{3760}{1} = 11280 \text{ kN} \quad 3 \frac{p_S}{x_B} L = 3 \times \frac{705}{1} \times 6 = 12960 \text{ kN} . \text{ Here , we se}$$

lect  $p_0 = 5000 \text{ KN}$  ,  $p_0 = 13000 \text{ KN}$  to compute as follows:

When the impact load is  $13000 \text{ KN}$  , because  $p_0 > 3 \frac{p_S}{x_B} L$  , then because the

crack locates in the plastic zones too, the crack effect can be ignored. Because  $p_0 > 3p_S$  , according to the theoretical analysis, on the loading stage, a stationary plastic hinge will occur in the middle of the beam and When the loading stage ends, the location of the plastic hinge will migrate towards the beam root; When it reaches the beam root, the remained energy in the beam will be consumed around the plastic hinge about the root until the movement stops.

a. When  $0 \leq t \leq \tau$  :

$$x(t) = \frac{3p_S}{p_0} L = \frac{3 \times 4230}{13000} = 0.97 \text{ m}$$

$$\dot{z}(t) = \frac{2p_0^2 t}{3mp_S L} = \frac{2 \times 13000^2 \times t}{3 \times 936 \times 4230} = 28.46t \text{ m/s}$$

$$\alpha(t) = \frac{2p_0^3 t}{9mp_S^2 L^2} = \frac{2 \times 13000^3 \times t}{9 \times 936 \times 4230^2} = 29.15t \text{ 1/s}$$

$$\omega(t) = \frac{2p_0^3}{9mp_S^2 L^2} = \frac{2 \times 13000^3}{9 \times 936 \times 4230^2} = 29.15 \text{ 1/s}^2$$

$$Q(x) = p_0 \left[ 1 - \left( \frac{p_0 x}{3p_S L} \right)^2 \right] = 13000 \times \left[ 1 - \left( \frac{13000 \times x}{3 \times 705 \times 6} \right)^2 \right] = 13000 \times (1 - 1.024x^2) \text{ kN}$$

b. When:  $\tau \leq t \leq t_0 = \frac{p_0}{3p_S} \tau = \frac{13000}{3 \times 705} = 6.15 \text{ s}$

$$x(t) = \frac{3p_S}{p_0} \cdot \frac{t}{\tau} L = \frac{3 \times 705}{13000} \times \frac{t}{1} \times 6 = 0.98t \text{ m}$$

$$\begin{aligned} \dot{z}(t) &= \frac{2p_0^2\tau^2}{3mp_sL \cdot t} = \frac{2 \times 13000^2}{3 \times 936 \times 705 \times 6 \times t} = 28.46 \frac{1}{t} \text{ m/s} \\ \alpha(t) &= \frac{2p_0^3\tau^3}{9mp_s^2L^2 \cdot t^2} = \frac{2 \times 13000^3}{9 \times 936 \times 705^2 \times 6^2 \times t^2} = 19.15 \frac{1}{t^2} \text{ 1/s} \\ \omega(t) &= -\frac{4p_0^3}{9mp_s^2L^2} \left(\frac{\tau}{t}\right)^3 = -\frac{4 \times 13000^3}{9 \times 936 \times 705^2 \times 6^2} \left(\frac{1}{t}\right)^3 = -58.30 \frac{1}{t^3} \text{ 1/s}^2 \\ Q(x) &= \frac{p_0\tau}{t} \left(1 - \frac{p_0x(t)\tau}{3p_sLt}\right)^2 = \frac{13000 \times 1}{t} \left(1 - \frac{13000 \times x}{3 \times 705 \times 6 \times t}\right)^2 = \frac{13000}{t} \left(1 - 1.024 \frac{x}{t}\right)^2 \text{ kN} \\ M(x) &= \left(\frac{p_0x(t)\tau}{3p_sLt}\right)^2 \left(2 - \frac{p_0x(t)\tau}{3p_sLt}\right) p_sL \\ &= \left(\frac{13000 \times x}{3 \times 705 \times 6 \times t}\right)^2 \left(2 - \frac{13000 \times x}{3 \times 705 \times 6 \times t}\right) \times 705 \times 6 = 4439.19 \left(2 - 1.024 \frac{x}{t}\right) \left(\frac{x}{t}\right)^2 \text{ kN} \cdot \text{m} \end{aligned}$$

c. When  $t_0 < t \leq t_1 = \frac{p_0}{p_s} \tau = \frac{13000}{705} = 18.44s$  :

$$\begin{aligned} x(t) &= L = 6 \text{ m} \\ \dot{z}(t) &= \frac{3}{mL} (p_0\tau - p_s t) = \frac{3}{936 \times 6} (13000 \times 1 - 705t) = 6.94 - 0.38t \text{ m/s} \\ \alpha(t) &= \frac{3}{mL^2} (p_0\tau - p_s t) = \frac{3}{936 \times 6^2} (13000 \times 1 - 705t) = 1.16 - 0.06t \text{ 1/s} \\ \omega(t) &= -\frac{3p_s}{mL^2} = -\frac{3 \times 705}{936 \times 6^2} = -0.06 \text{ 1/s}^2 \\ Q(x) &= \frac{3}{2} \left(\frac{x}{L}\right)^2 p_s = \frac{3}{2} \left(\frac{x}{6}\right)^2 \times 705 = 29.38x^2 \text{ kN} \\ M(x) &= x \left(\frac{x}{L}\right)^2 p_s = x \left(\frac{x}{6}\right)^2 \times 705 = 19.58x^3 \text{ kN} \cdot \text{m} \end{aligned}$$

### 4 Conclusions

Now we compare the results of the defective beam and the non-defective beam when the beam suffers the step load  $p_0 = 5000KN$ . The basic parameters are given in Table 1.

Table 1 Displacement (angular displacement and line displacement)

Displacement	$z_{\tau}$	$\theta_{\tau}$	$z_0$	$\theta_0$	$z_1$	$\theta_1$
Defective model	2.10	0.83	5.73	1.79	6.62	2.49
Non-defective model	9.46	18.62	18.75	21.46	22.96	22.16

Here we mainly talk about the differences of the displacements between the two cases simply: On the one hand, the crack effect on the displacement of the beam is mainly embodied on the increase of the displacement. And the increase is more apparent on the angular displacement. On the other hand, it is embodied on the increase of time which the beam structure costs. As for the example in this article, the whole period is more than doubled. Calculate the spring stiffness which simulates the soil medium.

As the various stages are concerned, we can see that the angular displacements of three stages are basically the same for the non-defective beam model. The largest contribution to the linear displacement comes from the stages of the stationary hinge and the traveling hinge. They occupied 86.56% of the total displacement. Each part's contribution is more or less the same. As for the defective beam model, the largest contribution to the angular displacement comes from the stationary hinge, traveling hinge and the beam root stationary plastic hinge, in the loading process. They are about 15.39% of the total. As for the linear displacement, the contribution of the stationary hinge is more or less the same as that of the traveling hinge. The sum of them has accounted for 15.39% of the total.

## References

- De Oliveila J.G. and Jones N. (1978). Some remarks on the influence of transverse shear on the plastic yielding of structures, *Int. J. Mech. Sci.*, 20:759-765.
- Duwez P. E., Clark D.S. and Bohnenblust H.F. (1950). The behaviour of long beams under impact loading, *J. Appl. Mech., Trans. ASME*, 72:27-34.
- Jin Quanlin (1988). Dynamic response of an infinitely large rigid-plastic plate impacted by a rigid cylinder with transverse shear and rotatory inertia, *Int. J. Impact Engng.*, 7:391-400.
- Jones N. and De Oliveila J.G. (1983). Impulsive loading of a cylindrical shell with transverse shear and totatory inertia, *Int. J. Solids Struct.*, 19:263-279.
- Lee E.H. and Symonds P.E. (1952). Large plastic deformation of beams under transverse impact, *J.Appl.mech.*, 74:308-314.
- Liu J.H. and Jones N. (1988). Dynamic response of a rigid plastic clamped beam struck by a mass at any point on the span, *Int. J. Solids Struct.*, 24:251-270.
- Stronge W.J., Shu D. and Shim V.P.W. (1990). Dynamic modes of plastic deformation for suddenly loaded,curved beams, *Int. J. Impact Engng.*, 9:1-18.
- Yu T.X. and Stronge W. J. (1990). Large deflection of a rigid-plastic beam-on-foundation form impact, *Int. J. Impact Engng.*, 9:115-126.

Zhang T.G. and Yu T. X. (1986). The large rigid-plastic deformation of a circular cantilever beam subjected to impulsive loading, *Int. J. Impact Engng.*, 4:229-241

Zhou Qing, Yu Tongxi (1987). The plastic hinge in beams of variable cross-section under intense dynamic loading, *Explosive and Impact*, 7(4):311-318

# A Computational Approach to the Integration of Adaptronical Structures in Machine Tools

Michael F. Zaeh<sup>1\*</sup>, Matthias Waibel<sup>1</sup> and Matthias Baur<sup>1</sup>

<sup>1</sup>Institute for Machine Tools and Industrial Management (*iwb*), Technische Universitaet Muenchen, 85748 Garching, Germany

**Abstract.** The increasing competition on the international market requires intensified efforts of the machine tool manufacturers to further improve production accuracy and machining speed. Piezoelectric actuators can help to reach these goals by counteracting structural vibrations that impair the manufacturing process (e.g. chatter). By equipping production machines with piezo actuators, sensors, and a controller an adaptronical system is created. However, the application of these components requires high capital costs and engineering know-how. Likewise, it is difficult to predict the attainable manufacturing accuracies of adaptronically optimised machine tools. These facts impede the industrial use of this technical innovation. So far, a systematic and efficient integration of adaptronics into the design process of machine tools is missing. This paper deals with the development of a computational approach to the integration of adaptronical structures in machine tools. Hence, the machine tool manufacturer will be enabled to design an adaptronical vibration damping system according to the process requirements of his customer.

**Keywords:** active vibration control, machine tools, actuator placement, simulation based design, adaptive control

## 1 State of Research

There exist several research approaches for reducing vibrations at machine tools. Rashid and Nicolescu (2006) distinguish between the classical adaptive control of the cutting parameters and the specific influence of structural dynamic properties. Using the classical approach Ismail and Ziaei (2002), Al-Regib et al. (2003), and Mei et al. (2006) realised the avoidance of chatter vibrations of machine tools by adjusting specific cutting parameters. A vibration absorber mounted close to the tool by Lee et al. (2001) has reduced the machine compliance significantly during

---

\* Corresponding author, e-mail: Matthias.Baur@iwb.tum.de

turning. An analytical procedure to layout the properties of these passive damping devices were figured out by Sims (2007). Other ideas seek to increase the system damping by additional force transmission. Appropriate control strategies for this active damping approach are presented by Preumont (2002) and Gawronski (2004). Locatelli (2001) and Ehmann (2003) compare selected controllers regarding their suitability and stability. The standard work of Kuo and Morgan (1996) provides a good overview over controllers for vibration extinction deduced from the area of active noise cancellation. Hereby, Sims and Zhang (2003) could counteract process vibrations by attaching piezo films directly on the workpiece. This idea focuses on the fast processing of large, lightweight components occurring in the aviation industry. Rashid and Nicolescu (2006) use piezoelectric actuators to move the workpiece holder in a way that the relative displacement between tool and workpiece becomes minimal. Homann (2007) was able to compensate the first bending eigenmode of an aircraft tail with a piezoelectrically controlled suspension. The multiplicity of research projects shows the relevance of the topic. The developed systems mostly consist of specific solutions achieved by trial and error. A systematic approach for the design of actively damped mechanical systems is missing.

The initiating point of the systematic design method presented in this paper is the derivation of the modal system matrices of the mechanical machine tool structure by calculation or measurement. From these matrices a state-space model can be generated (Gawronski, 2004) for further investigation within Matlab/Simulink. On the basis of this model the structural weaknesses with dominant influence on the relative compliance between tool and workpiece can be identified. Due to the change of the mass distribution through the movement of the axes the mechanical behaviour of the machine tool is a function of its position within the workspace (Altintas, 2004). Therefore, adaptive algorithms for the controller design are used.

## 2 Position Dependence of the Machine Tool Dynamics

A portal milling machine developed by the *iwb* (Virtumat, 2000) served as an object for experimental investigations on the position dependence of the machine tool dynamics. An experimental modal analysis and a multi-body simulation were conducted. The excitation of the machine structure for the modal analysis was realised with an electro-dynamic shaker at the spindle nose. To analyse the machine tool position dependence of the dynamic behaviour, the three positions of the portal milling machine demonstrated in Figure 1 were measured.

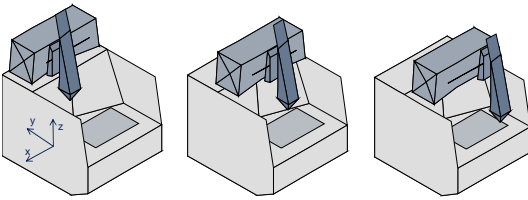


Figure 1. Measured machine tool positions

Figure 2 shows the location of the eigenfrequencies within the workspace. The position of the spindle ( $z$ -direction) has the greatest impact on the 6<sup>th</sup> and 7<sup>th</sup> eigenfrequency. The associated mode shapes are characterised by a pitch motion of the  $x$ -saddle around the  $x$ - and  $y$ -axis.

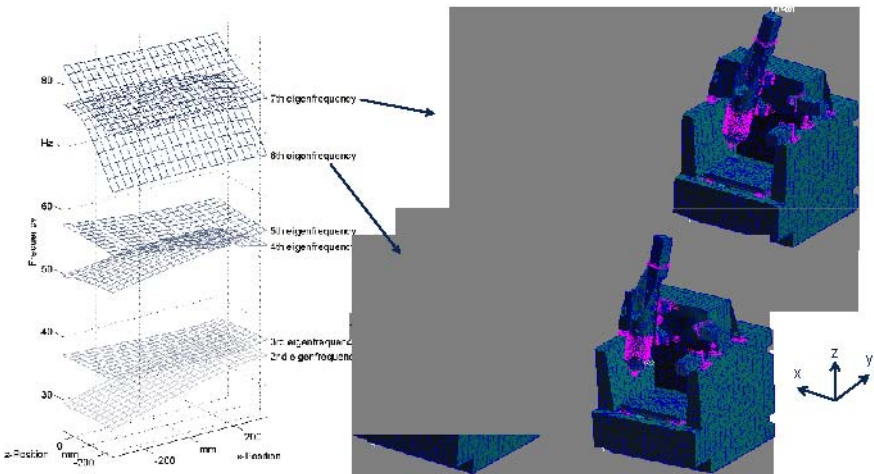


Figure 2. Location of the eigenfrequencies of the simulation model for one machine tool position

### 3 Actuator Placement

In order to counteract the present mode shapes a piezoelectric actuator has to be integrated into the structure. The challenge is the optimal placement of the active component to achieve a large influence on the dynamic properties of the system. Therefore, impulse forces are applied between node pairs of a finite element model representing the coupling points of the actuators. The relative compliances between tool and workpiece in the three coordinate directions describe the rate for

the efficiency of the actuator locations. The  $H_2$ -norm is used for quantification of the spindle nose response strength. The norm allows the comparison between different configurations. All built-in capabilities of piezoelectric actuators can be investigated. Figure 3 shows the best solution for mounting an actuator to reduce the dominant dynamic compliance at the spindle nose. One boundary condition for the algorithm was to integrate the actuator between coupled structural components. The detailed mathematical approach for this method is described in Zaeh and Waibel (2007).

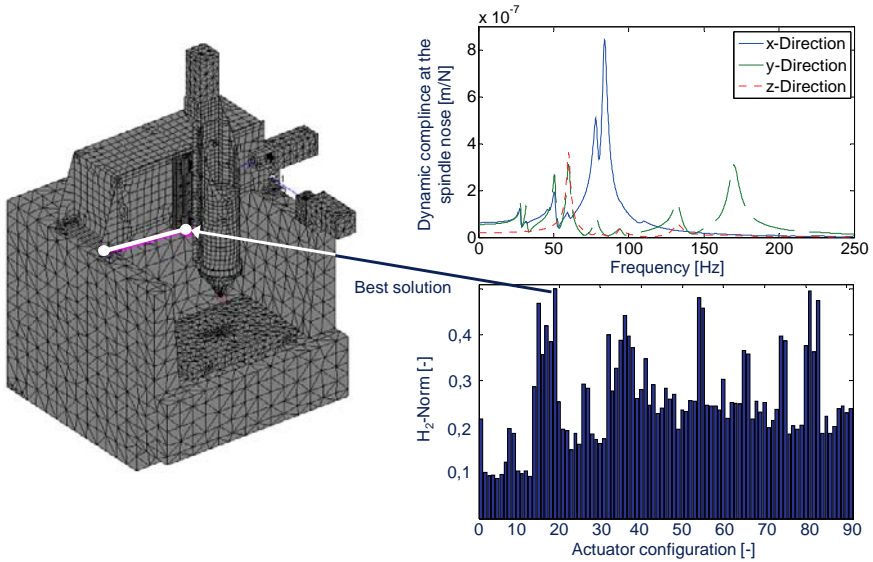


Figure 3. Best actuator solution found by the developed software tool to reduce the dominant dynamic compliance at the spindle

#### 4 Derivation of a Feasible Actuator Coupling Configuration

The actuator placement algorithm presented in chapter 2 does not yet take into consideration constructive restraints of the machine tool to be optimised. Thus, the integration of a damping actuator according to Figure 3 would block the movability of the x-saddle. Deriving a technically feasible actuator coupling configuration from the result of the mathematical optimisation procedure therefore still remains a task for a human being.

Concretely, the mathematical proposition (Figure 3) was transferred to the configuration shown in Figure 4. The main issue here was to ensure the movability of the x-axis. This requirement was met by mounting the upper coupling element on

an additional runner block. By this means, both the theoretical as well as the practically implemented actuator placement generate a torque around P, counteracting the dominant eigenmode.

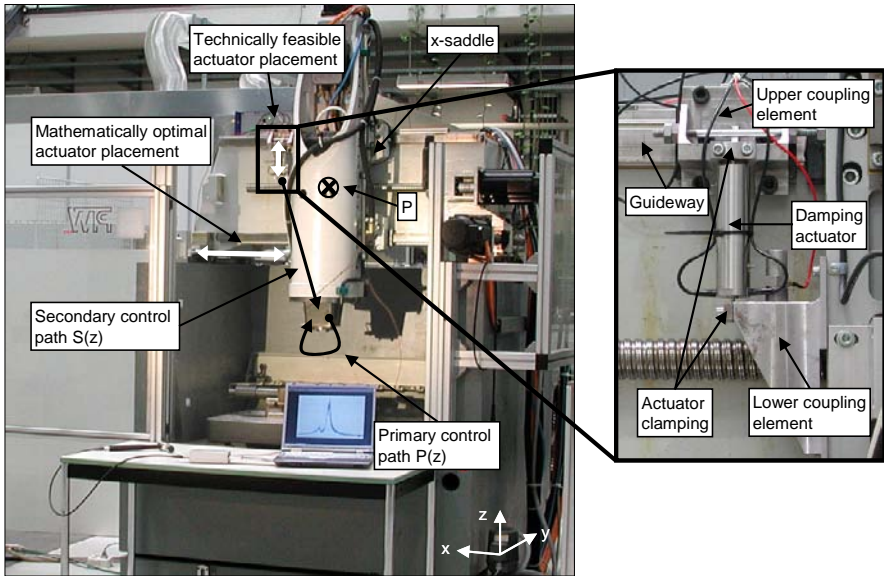


Figure 4. Placement of the damping actuator – Derivation of a technically feasible configuration

However, the subsequent experimental validation of the active damping system has shown a significant lack of mechanical stiffness of the actuator coupling – resulting in an only moderate damping of the vibrations at the spindle nose. To figure out if there is room for improvement each component of the actuator coupling was analysed. In detail, the influence of the actuator clamping and the coupling elements was tested. The results are presented below.

The actuator clamping has turned out to be reliable as no slippage effects could be observed. The measurement of the coupling elements has shown that the upper element yields a displacement of approximately  $80\ \mu\text{m}$  with the actuator being fully extended ( $\Delta l \approx 100\ \mu\text{m}$ ). At the lower coupling element a displacement of only  $5\ \mu\text{m}$  was measured. Furthermore, finite element calculations have revealed that there is no significant structural deformation of the coupling elements themselves.

However, the damping efficiency mainly depends on the displacement – respectively force – exerted on the lower coupling element. The upper coupling element could therefore be identified as the weak point. A further survey of this component has evinced that the runner block is responsible for the high compliance of the system (Figure 5). The reason for this is a lever arm of about  $70\ \text{mm}$  which evolves from the distance between runner block and load application line

(i.e. centreline of the actuator). Thus, the actuator force creates a momentum which leads to the runner block being bent up – instead of the vibration at the spindle nose being counteracted. In other words, the damping power is dissipated at the “wrong” side.

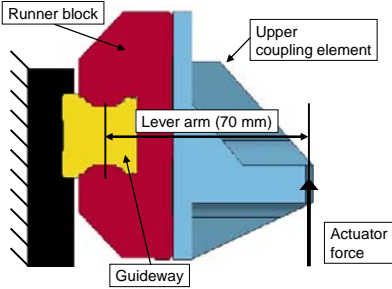


Figure 5. Formation of the bending moment at the upper coupling element

Hence, a concept to overcome this problem was developed. The main focus here was on the reduction of the lever arm which causes the unwanted bending moment. For that purpose, the upper coupling was amended by a second runner block which means a doubling of the stiffness of the system. In this configuration the actuator is clamped in the space between the two runner blocks (Figure 6 right). Thus, the length of the lever arm could be reduced from 70 to 20 mm due to shifting the load application line towards the guideway (Figure 6).

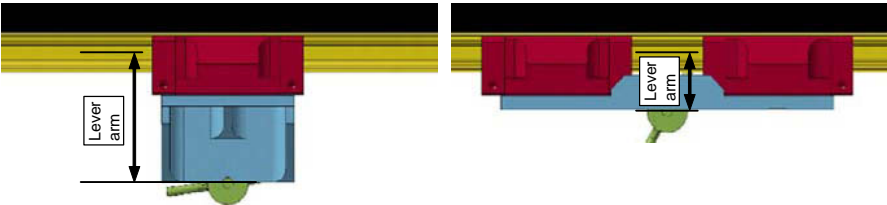


Figure 6. Comparison of lever arms at the original (left) and revised (right) actuator coupling configuration

Figure 8 shows the reduction of the dynamic compliance concerning the dominant eigenmode at the spindle nose that was achieved by optimising the mechanical stiffness of the actuator configuration (Figure 7).



Figure 7. Comparison of the original (left) and the revised (right) actuator coupling configuration

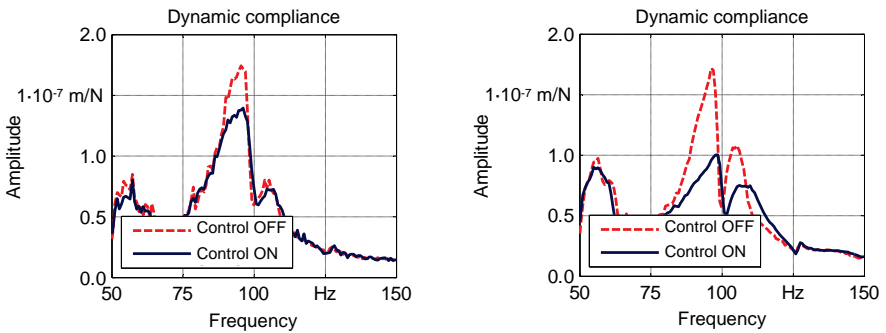


Figure 8. Comparison of the achievable damping efficiency with the original (left) and the revised (right) actuator coupling configuration (cf. Figure 7)

The experience made within this project points out clearly that the consideration of constructive restraints at the computer-assisted actuator placement is a crucial factor for achieving the optimal efficiency of an active vibration control system. In the long run, the aim is to obtain an actuator coupling configuration from the automated placement algorithm that can be implemented without need for further revision.

## 5 Adaptive Control with FxLMS

The FxLMS algorithm was identified as a reasonable adaptive control strategy satisfying the requirements caused by the changing dynamic compliance. A consideration of this control approach in the frequency domain as shown in Figure 9 helps to understand its functionality. The explanations for the algorithm are based on Paschedag (2007). The primary control path  $P(z)$  is excited by a periodical

force at a frequency  $\omega_1$  (cf. Figure 4). Each block element contains the corresponding frequency response function and for some signals the Fourier transformation result is given.

A time-linear system excited with a single frequency causes a response in the steady state just with this frequency. The response signal only changes in amplitude and phase. Thus, for the primary control path  $P(z)$ , excited by a force with the dominant frequency  $\omega_1$  a signal with the same frequency has to be expected as a response. To compensate this parasitic oscillation, an inversely phased vibration has to be applied. This is why the error signal  $e(n)$  contains only this frequency. The consequence for the control is that all emerging signals consist of the excitation frequency.

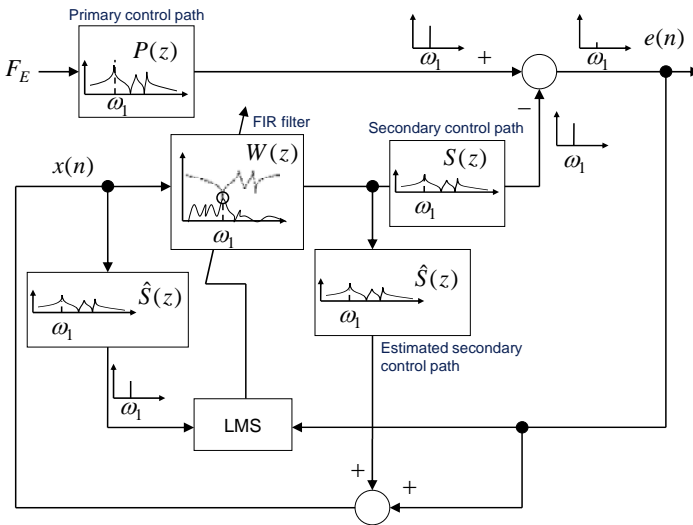


Figure 9. Illustration of an adaptive control strategy in a steady state (according to Kuo and Morgan 1996)

During the adjustment of the FIR filter  $W(z)$ , the LMS algorithm considers only frequencies of the reference signal. As the reference signal  $x(n)$ , filtered by the estimated secondary control path  $\hat{S}(z)$  only consists of the frequency  $\omega_1$ , the algorithm only matches the inverse transfer function at this special frequency. If the reference signal contains multiple frequencies, the corresponding points of the inverse are reproduced simultaneously. The more frequencies occur, the more difficult is the adjustment.

The LMS algorithm is applied on the previously presented machine tool structure. Within the simulation the algorithm achieves an almost complete extinction of the interference after about 0.7 seconds (Figure 10).

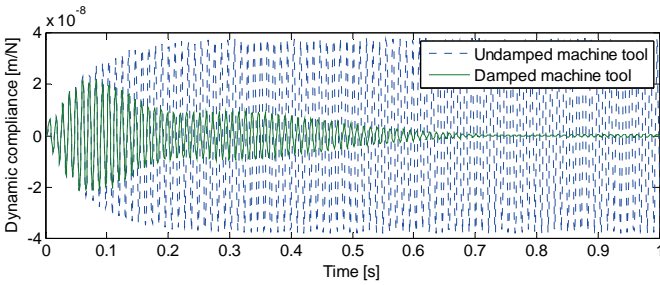


Figure 10. Comparison of the vibration at the spindle nose for the undamped and the damped case

## 6 Integrated Simulation of Machine Tool, Cutting Process, and Active Vibration Control System

The integrated simulation of machine tool structure, cutting process, and adaptional damping system constitutes the conclusion of the computer-assisted design process. Thus, predications concerning the system performance can be made before the fabrication of a prototype. This forms the basis for subsequent optimisation loops of the system.

For this purpose, a state-space model of the machine tool structure is completed by an analytical model of the cutting process (Altintas 2000) as well as of the active damping system. The state-space model is calculated from the modal matrices of a finite-element simulation and subjected to a successive modal order reduction. The piezoelectric damping actuator is modelled by the linear piezoelectric equations (Holterman 2004). In order to map the non-linearities appearing particularly in the large signal area, a test bed for the characterisation of the actuators has been developed.

The relative movement between tool and workpiece ( $x_{\text{relative TCP-WP}}$ ) is chosen as the control variable to be minimised by the damping system because that is decisive for process stability and surface quality. Proportional velocity feedback has been implemented as the control law in the simulation due to its simplicity. Figure 11 shows the simulation model as a block diagram.

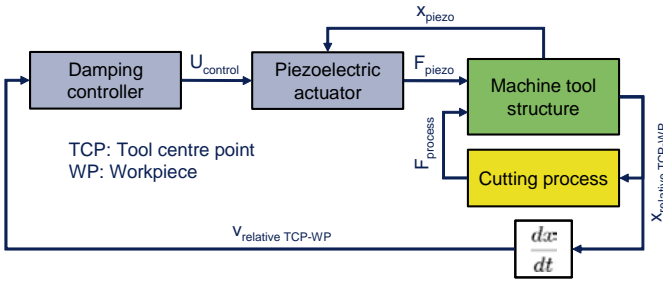


Figure 11. Block diagram of the integrated simulation of machine tool structure, cutting process, and active vibration control system

A time-domain simulation of a (stable) end-milling process for the machine tool described in chapter 2 yields a significant reduction of the relative displacement between tool and workpiece due to the application of an adaptronical vibration damping system (Figure 12). Thus, the surface quality of the workpiece is improved.

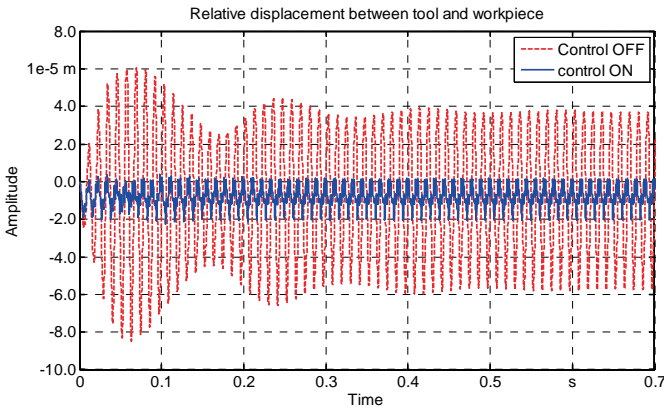


Figure 12. Time-domain simulation of the relative displacement between tool and workpiece

Besides that, active damping systems also effectuate an enhancement of the stability limits. Figure 13 shows the stability lobe diagrams (calculated according to Altintas 2004) for an end-milling process with the control once being engaged and once being disengaged. The area below the curves encloses the stable machining region whereas the area above the curves reflects the unstable region. A significant increase of the level of stability – especially in the stability minima – can be observed. These simulation results indicate the high potential of active vibration control systems for machine tools.

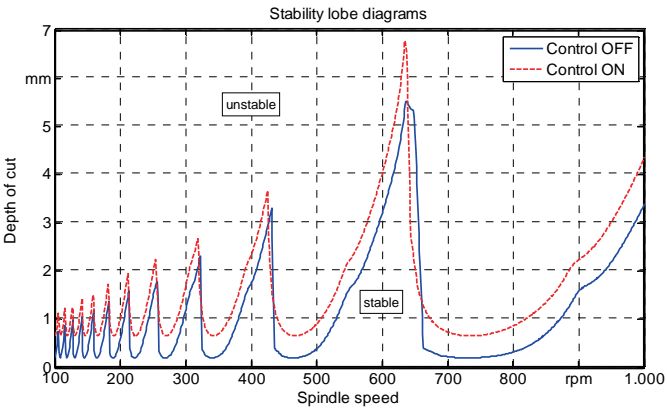


Figure 13. Stability lobe diagrams for an end-milling process with control OFF and control ON

Current research activities at the *iwb* deal with the refinement and experimental validation of the simulation-based design methods presented above. Hence, the machine tool manufacturer will be enabled to design an adaptronic vibration damping system according to the process requirements of his customer.

## References

- Altintas Y. (2000). *Manufacturing Automation: Metal Cutting Mechanics, Machine Tool Vibrations, and CNC Design*. University Press, Cambridge.
- Altintas Y., Weck M. (2004). Chatter stability of metal cutting and grinding. *CIRP Keynote Paper*, 53(2): 619-642.
- Al-Regib E., Ni J. et al. (2003). Programming spindle speed variation for machine tool chatter suppression. *International Journal of Machine Tools and Manufacture*, 43(12): 1229-1240.
- Ehmann C. (2003). Methoden und Komponenten für die Realisierung aktiver Schwingungsdaempfung. Dissertation, Technische Universitaet Darmstadt.
- Gawronski W.K. (2004). *Advanced Structural Dynamics and Active Control of Structures*. Springer, Berlin.
- Holterman J. (2004). Vibration control of high-precision machines with active structural elements. Dissertation, University of Twente.
- Homann S. (2007). Aktive Bedaempfung einer piezo-elektrisch beeinflussten Struktur auf der Basis modaler Ansatzes. *Schwingungsdaempfung – Modellbildung – Numerische Umsetzung – Experimentelle Verfahren – Praxisrelevante passive und adaptive Anwendungen*, VDI-Bericht Nr. 2003: 245-258.
- Ismail F., Ziaei R. (2002). Chatter suppression in five-axis machining of flexible parts. *International Journal of Machine Tools and Manufacture*, 42(1): 115-122.
- Kuo S.M., Morgan D.R. (1996). *Active Noise Control Systems: Algorithms and DSP Implementations*. Wiley, New York.
- Lee E.C., Nian C.Y. et al. (2001). Design of a dynamic vibration absorber against vibrations in turning operations. *Journal of Materials Processing Technology*, 108(3): 278-285.

- Locatelli G. (2001). Piezo-actuated adaptive structures for vibration damping and shape control – Modeling and testing. Dissertation, Technische Universität München.
- Mei C., Chermg J.G. et al. (2006). Active control of regenerative chatter during metal cutting process. *Journal of Manufacturing Science and Engineering*, 128: 346-349.
- Paschedag J. (2007). Dämpfung der Motorvibrationen im Kfz mittels Filtered-x-LMS Algorithmus: Implementierung am Prüfstand und Konvergenzanalyse. Forschungsbericht, Technische Universität München.
- Preumont A. (2002). *Vibration Control of Active Structures – An Introduction*. Kluwer Academic Publishers, Dordrecht.
- Rashid A., Nicolescu C.M. (2006). Active vibration control in palletised workholding system for milling. *International Journal of Machine Tools and Manufacture*, 46(12-13): 1626-1636.
- Sims N., Zhang Y. (2003). Active damping for chatter reduction in high speed machining. *AMAS Workshop on Smart Materials and Structures*, 195-212.
- Sims N.D. (2007). Vibration absorbers for chatter suppression: A new analytical tuning methodology. *Journal of Sound and Vibration*, 301(3-5): 592-607.
- Virtumat (2000). Final report of the research project “Neue Lösungsansätze für kostengünstige Funktionalität von Werkzeugmaschinen”.
- Zaeh M.F., Waibel M. (2007). Rechnergestützte Konfigurationsoptimierung adaptiver Komponenten für Werkzeugmaschinen. *Schwingungsdaempfung – Modellbildung – Numerische Umsetzung – Experimentelle Verfahren – Praxisrelevante passive und adaptive Anwendungen*, VDI-Bericht Nr. 2003: 271-287.

# Adaptive Nearest-Nodes Finite Element Method and Its Applications

Yunhua Luo<sup>1\*</sup>

<sup>1</sup>Department of Mechanical and Manufacturing Engineering, Faculty of Engineering, University of Manitoba, Winnipeg, MB R3T 5V6, Canada

**Abstract.** In this paper, an adaptive finite element method is formulated based on the newly developed nearest-nodes finite element method (NN-FEM). In the adaptive NN-FEM, mesh modification is guided by the gradient of strain energy density, i.e., a larger gradient requires a denser mesh and vice versa. Mesh intensity is introduced to correlate gradient of strain energy density and mesh density. Relative error in the total potential energy is used to indicate when mesh modification should be stopped. Numerical examples are presented to demonstrate the performance of the proposed adaptive NN-FEM.

**Keywords:** strain energy density, mesh density, mesh intensity

## 1 Introduction

With powerful modern computers, the Finite Element Method (FEM) is now able to solve many complicated engineering problems. Nevertheless, it is still incompetent to deal with extremely large scale problems that may require billions or even trillions of degrees of freedom (DOF) to achieve a specified accuracy. Therefore, a lot of research effort has been devoted to developing more efficient adaptive finite element methods, e.g. (Babuška and Miller, 1984; Oñate et al., 2006) among others, so that more complicated engineering problems can be solved with available existing computer capacity. A so-called nearest-nodes finite element method (NN-FEM) was recently developed by (Luo, 2008a; Luo, 2008b; Luo, 2008c), and (Luo, 2009). In NN-FEM, elements are mainly used for numerical integration; shape functions are constructed for each quadrature point by selecting a set of nodes that are the nearest to the quadrature point. In implementing the above strategy, there are several ways available for constructing shape functions. In (Luo, 2008b), shape functions are constructed by local moving polynomials, while in (Luo, 2008a) and (Luo, 2008c) they are built using local multivariate Lagrange in-

---

\* Corresponding author, e-mail: luoy@cc.umanitoba.ca

terpolation method (Luo, 2008d); inter-dependent shape functions are adopted in (Luo, 2009). Among the above options, NN-FEM with inter-dependent shape functions has the optimal convergence rate and it is used here as a base for implementing an adaptive algorithm.

There are basically three types of error estimators or error indicators for guiding mesh modification: smoothing-based (Zienkiewicz and Zhu, 1987), residual-based (Babuška and Rheinbildt, 1978) and gradient-based (Luo et al., 2003). Although in principle any of the above error estimators can be adopted in NN-FEM, the gradient-based error indicator is selected here. Strain energy density contains all relevant information needed for mesh adaptation, e.g. material distribution, deformation, etc. The gradient-based error indicator has been successfully implemented in a meshless method (Luo et al., 2003). One attractive feature of NN-FEM is that higher-order shape functions can be constructed from simplex finite element meshes. High-order shape functions are required for calculating the strain energy density and its gradients; while finite element meshes consisting of only simplexes are easy to operate in mesh adaptation. Therefore, NN-FEM provides a favorable environment for implementing the gradient-based error indicator.

## 2 Nearest-nodes Finite Element Method

In NN-FEM, finite elements are used only for numerical integration, while shape functions are constructed in a similar way as in meshless methods, i.e. by using a set of number of element nodes that are the nearest to a concerned quadrature point. A typical scenario is shown in figure 1, where element stiffness matrix for the

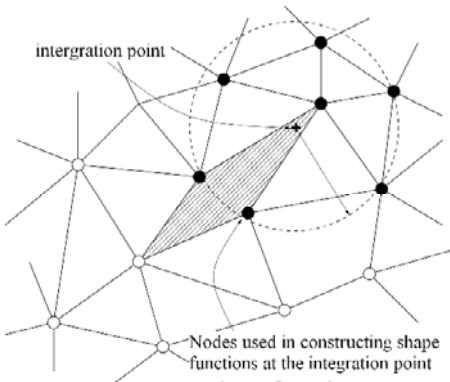


Figure 1. Nearest-nodes finite element method

Shaded element is being calculated. For the quadrature point denoted by '+', a number of nearest nodes, marked as dark circles in figure 1, are selected for constructing shape functions. Not all the selected nodes belong to the shaded element; one node of the shaded element is not included as it is not near enough to the concerned quadrature point. For the next quadrature point, the same procedure is repeated and the selected nodes may or may not be the same as the previous ones. Even before conducting any numerical investigation, it can be expected that the quality of shape functions obtained in the above way is mainly determined by the locations of selected nodes; It has very little to do with the shape of an element.

### 3 Gradient of Strain Energy Density as Error Indicator for Mesh Modification

The main idea of the gradient-based error indicator is that for regions where there is a large variation of strain energy density, a denser mesh is needed and vice versa. Mesh density is introduced in the following to correlate gradient of strain energy density to mesh density. In solid mechanics, the strain energy density is defined as the scalar product of the stress and the strain vectors. Theoretically, the strain energy density is a continuous or piece-wise continuous function of spatial coordinates. In nearest-nodes finite element method, the strain energy density can be approximated by nodal displacements as

$$e \approx \tilde{e}(\mathbf{x}) = \frac{1}{2} \mathbf{u}_q^T \tilde{\mathbf{K}}_q \mathbf{u}_q = \frac{1}{2} \mathbf{u}_q^T \mathbf{B}_q \mathbf{D} \mathbf{B}_q \mathbf{u}_q \quad (1)$$

where  $\mathbf{u}_q$  is a vector consisting of nodal displacements from the involved finite element nodes;  $\mathbf{D}$  is the material property matrix;  $\mathbf{B}_q$  is the B-matrix relating the strains and the displacements.

After solving the finite element equations, values of strain energy density at element nodes are obtained by equation (1). The gradients of the strain energy density at element nodes can be calculated by the moving least square (MLS) method (Lancaster et al., 1981) or the local multivariate Lagrange interpolation (Luo, 2008d),

$$\nabla e = [e_x \quad e_y \quad e_z]^T = \left[ \frac{\partial e}{\partial x} \quad \frac{\partial e}{\partial y} \quad \frac{\partial e}{\partial z} \right]^T \quad (2)$$

where  $x$ ,  $y$  and  $z$  represent, respectively, the three coordinate axes in a rectangular coordinate system.

Mesh intensity is defined as

$$M_I = \frac{\sqrt{e_x^2 + e_y^2 + e_z^2}}{M_D} \tag{3}$$

where  $M_D$  is mesh density that is defined as the number of element nodes per unit volume of the problem domain.

An alternative definition of mesh intensity is based on variation of strain energy density along element edges, i.e.,

$$M_I^{(k)} = \frac{|e_{k_1} - e_{k_2}|}{l_k^2} \tag{4}$$

where sub- or superscript ( $k$ ) represents the  $k$ -th element edge; subscripts  $k_1$  and  $k_2$  indicate the two element nodes connected by the edge.  $l_k$  is the length of the element edge.  $e_{k_1}$  and  $e_{k_2}$  are the strain energy density at the two nodes. Equation (4) is much easier to implement and computationally more efficient.

It is very difficult, if not impossible, to establish an explicit function relation between a specified solution accuracy and the required mesh intensity. An iteration procedure has to be adopted to gradually tune the mesh intensity to achieve a specified accuracy. The tuning job is done by mesh modification using a set of mesh modification operators, i.e., mesh refinement, mesh coarsening and mesh smoothing. The selection of a specific operator is based on the following criterion

$$M_I^{(k)} (k = 1, 2, \dots, N_{edge}) \begin{cases} > c & \text{refine} \\ = c & \text{unchanged} \\ < c & \text{coarsen} \end{cases} \tag{5}$$

where  $c$  is the mesh density corresponding to a prescribed accuracy. If the specified accuracy is not satisfied, the mesh intensity will be reduced and a new iteration loop will be started.

There are different convergence criteria adopted in the literature, for example, the displacement at a control point, the stress at a critical location, etc. Most of them are based on local rather than global information. According to the principle of minimum potential energy, among all the admissible solutions for a structure under static external forces, the real solution would make the system have the minimum potential energy. Accordingly, the convergence criterion should be global and it should be based on the total potential energy. Therefore, the relative error in total potential energy is adopted as a convergence criterion for the adaptive NN-FEM.

## 4 Numerical Examples

The performance of the proposed adaptive NN-FEM was examined by numerical examples. The first example is a cantilever beam as shown in figure 2. The beam has a length  $L=10$  and a width  $2b=2$ . The material is linear elastic with Young's modulus  $E=1000.0$  and Poisson's ratio  $\nu=0.0$ . The convergence criterion, i.e. the relative error in the total potential energy, was specified as  $\eta \leq 1\%$ .

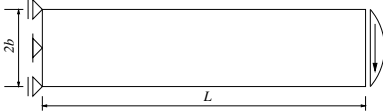
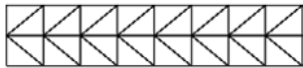
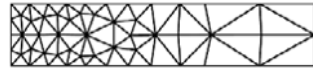


Figure 2. Cantilever beam under shear force

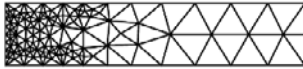
The mesh adaptation was started with a coarse structured mesh, figure 3(a). The adapted meshes are displayed in figure 3(b), (c) and (d). After three loops of iteration, the convergence criterion was reached.



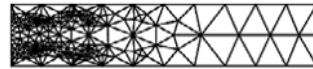
(a) 27 nodes



(b) 55 nodes



(c) 126 nodes



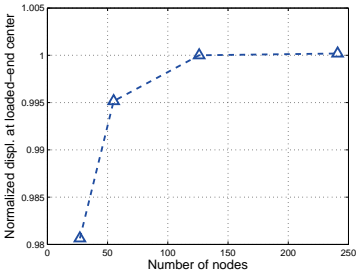
(d) 236 nodes

Figure 3. Initial and adapted finite element meshes

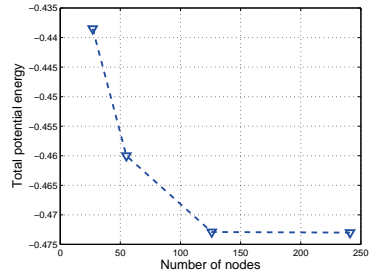
The convergence in the displacement (at the cross-section center of the loaded end) and in the total potential energy are shown in figure 4(a) and (b),

Where the obtained displacements are normalized using the theoretical solution.

It can be observed from figure 4 that the convergence trends in the total potential energy and in the displacement are similar, if the sign of the total potential energy in figure 4(b) is reversed. More examples will be given in the presentation.



(a) Displacement at the loaded tip



(b) Total potential energy

Figure 4. Convergence in solutions

## 5 Concluding Remarks

An adaptive finite element method is formulated in this paper. The adaptive finite element method is based on the newly developed nearest-nodes finite element method (NN-FEM). Mesh modification is guided by the gradient of strain energy density, i.e., a larger gradient requires a denser mesh and vice versa. To relate the gradient of strain energy density to mesh density, mesh intensity is introduced. The selection of a proper operator for a specific mesh region is determined by a set of criteria based on mesh intensity. Numerical results demonstrate that the proposed adaptive NN-FEM is sensitive, robust and effective.

## References

- Babuška I. and Rheinboldt W. C. (1978). Error estimates for adaptive finite element computations. *SIAM J. Numer. Anal.*, 15:736–754.
- Babuška I. and Miller A. (1984). Post-processing approach in the finite element method – Part 3: a posteriori error estimates and adaptive mesh selection. *International Journal for Numerical Methods in Engineering*, 20:2311–2324.
- Lancaster P. and Salkauskas K. (1981). Surfaces generated by moving least squares method. *Math. Comp.*, 37:141–158.
- Luo Y. and Häußler-Combe U. (2003). A gradient-based adaptation procedure and its implementation in element-free Galerkin method. 56:1335–1354.
- Luo Y. (2008a). A nearest-nodes finite element method with local multivariate Lagrange interpolation. *Finite Elements in Analysis and Design*, 44:797–803.
- Luo Y. (2008b). 3D nearest-nodes finite element method for solid continuum analysis. *Advances in Theoretical and Applied Mechanics*, 1:131–139.

- Luo Y. (2008c). Dealing with extremely large deformation by nearest-nodes fem with algorithm for updating element connectivity. *International Journal of Solids and Structures*, 45:5074–5087.
- Luo Y. (2008d). A local multivariate Lagrange interpolation method for constructing shape functions (in press, DOI: 10.1002/cnm.1149).
- Luo Y. (2009). Nearest-nodes finite element method with inter-dependent shape functions. *Computational Mechanics* (accepted).
- Oñate E., Arteaga J., Garcia J., and Flores R. (2006). Error estimation and mesh adaptivity in incompressible viscous flows using a residual power approach. *Computer Methods in Applied Mechanics and Engineering*, 195(4-6):339–362.
- Zienkiewicz O. C. and Zhu J. Z. (1987). Simple error estimator and adaptive procedure for practical engineering analysis. *International Journal for Numerical Methods in Engineering*, 24:337–357.

*“This page left intentionally blank.”*

# An Orthogonalization Approach for Basic Deformation Modes and Performance Analysis of Hybrid Stress Elements

Canhui Zhang<sup>1\*</sup>

<sup>1</sup>Department of Civil Engineering, Xiamen University, Xiamen 361005, China

**Abstract.** A new orthogonalization method is presented for the basic deformation modes. The inner products between basic deformation modes both including and excluding the element stiffness matrix are employed and the orthogonality within the orthogonal basic deformation modes is fully independent of the material properties so that they can serve as a uniformed tool to assess a given element. In the proposed approach, the arbitrary displacement field of deformation for different hybrid element can be easily decoupled into a linear combination of a series of basic modes. Thereafter their relating deformation energy, namely the element performance, can be directly studied. In the numerical examples the performances of several hybrid elements that are constructed by different assumed stress fields are provided using the proposed method. The results show that the method is very effective.

**Keywords:** hybrid stress element, basic deformation mode, orthogonalization method, performance analysis

## 1 Introduction

The hybrid stress finite element method with the independent assumed stress field (Pian, 1964) has experienced significant developments (Sze et al., 2004, Zhang et al., 2007c). The key issue for hybrid element is to correctly construct the assumed stress field. Various methods have been proposed for this purpose (Sze et al., 2004, Huang, 1991, Feng et al., 1997). The modal technique and natural method are employed to compare the performance of different elements with different assumed stress fields (Sze et al., 2004, Huang, 1991). However, the eigenvector and natural deformation modes are very complicated and dependent upon the assumed stress field and materials parameters. The basic deformation modes are a better choice but several modes belonging to the same deformation type are often

---

\* Corresponding author, e-mail: chzhang@xmu.edu.cn

coupled together. This brings difficulty to clearly assess the element performance for specific deformations.

In this paper, a novel orthogonalization procedure for the basic deformation modes is suggested. It turns out the proposed procedure leads to an operation that does not involve any material parameters. So the orthogonal basic deformation modes can serve as standard deformation modes for comparative performance analysis for different hybrid stress element.

## 2 Basic Deformation Modes for Hybrid Stress Element

In a hybrid stress element, the stress and displacement fields are assumed independently as follows:

$$\boldsymbol{\sigma} = \sum_{i=1}^M \boldsymbol{\sigma}_i \beta_i = \mathbf{P}\boldsymbol{\beta}, \quad \mathbf{u} = \mathbf{N}\mathbf{a} \tag{1}$$

where  $\boldsymbol{\sigma}_i$ 's are the assumed stress modes,  $\mathbf{P}$  is the assumed stress matrix and  $\boldsymbol{\beta}$  is the corresponding stress coefficient vector.  $\mathbf{N}$  is the shape function matrix and  $\mathbf{a}$  is the nodal displacement vector of the element. A standard stationary variational argument of the Hellinger-Reissner variational principle results the element stiffness matrix as:

$$\mathbf{K} = \mathbf{G}^T \mathbf{H}^{-1} \mathbf{G}, \quad \mathbf{H} = \int_{\Omega^e} \mathbf{P}^T \mathbf{S} \mathbf{P} d\Omega, \quad \mathbf{G} = \int_{\Omega^e} \mathbf{P}^T (\mathbf{L}\mathbf{N}) d\Omega \tag{2}$$

where  $\Omega^e$  represent the element domain,  $\mathbf{L}$  is the differential operator,  $\mathbf{S}$  is the material compliant matrix respectively. Consider an element that has  $n$  degrees of freedom including  $r$  rigid body degrees of freedom and  $m = n - r$  deformation degrees of freedom, then any displacement of the given element can be expressed as a linear combination of  $n$  linearly independent basic deformation modes:

$$\mathbf{u} = \sum_{i=1}^m \alpha_i \mathbf{u}_i + \sum_{k=1}^r \alpha_{m+k} \mathbf{u}_{m+k} \tag{3}$$

with

$$\mathbf{u}_i = \mathbf{N}\mathbf{a}_i, \quad i = 1, \dots, n \tag{4}$$

For 3D 8-node hexahedral element with  $n = 24$ ,  $r = 6$ ,  $m = 18$ , the following basic deformation modes can be derived (Zhang et al., 2006b):

$$\{\mathbf{u}_1, \dots, \mathbf{u}_{18}\} = \begin{bmatrix} \xi & 0 & 0 & 0 & \zeta & \eta & \xi\eta & 0 & \zeta\xi & 0 & 0 & 0 & -\eta\zeta & \eta\zeta & \eta\zeta & \xi\eta\zeta & 0 & 0 \\ 0 & \eta & 0 & \zeta & 0 & \xi & 0 & 0 & 0 & \eta\zeta & \xi\eta & 0 & \zeta\xi & -\zeta\xi & \zeta\xi & 0 & \xi\eta\zeta & 0 \\ 0 & 0 & \zeta & \eta & \xi & 0 & 0 & \eta\zeta & 0 & 0 & 0 & \zeta\xi & \xi\eta & \xi\eta & -\xi\eta & 0 & 0 & \xi\eta\zeta \end{bmatrix} \quad (5)$$

These deformation modes can be conveniently used to describe arbitrary deformation field. They are independent on the material relationship and practically each mode exhibits a clear physical meaning and thus can be employed to study the element performance. However, several modes belonging to the same deformation type are often coupled together. This brings difficulty to clearly assess the element performance for specific deformations. Thus it is desired to construct a set of orthogonal basic deformation modes which are fully deformation separable and do not involve the material parameters.

### 3 Orthogonalization of Basic Modes and Assessment of Element Performance

For convenience of expression, we define the following energy inner product:

$$(\mathbf{a}, \mathbf{Kb}) = \mathbf{a}^T \mathbf{Kb}, \quad \mathbf{a}, \mathbf{b} \in D \quad (6)$$

where

$$D = \left\{ \sum_{i=1}^m \alpha_i \mathbf{a}_i, \alpha_i \in \mathbb{R} \right\} \subset \mathbb{R}^n \quad (7)$$

is the deformation subspace spanned only by the  $m$  deformation modes. Besides for clarity we refer the standard inner product as:

$$(\mathbf{a}, \mathbf{b}) = \mathbf{a}^T \mathbf{b}, \quad \mathbf{a}, \mathbf{b} \in \mathbb{R}^n \quad (8)$$

For the complete set of deformation modes  $\mathbf{a}_i \in D$ ,  $i=1, \dots, m$ , it is found that for different elements with isotropic material properties, only the tension and bending basic deformation modes are coupled to each other. Their inner product of Equation (6) can be put into a unified form as:

$$\begin{cases} (\mathbf{a}_i, \mathbf{Ka}_i) = a, (\mathbf{a}_i, \mathbf{Ka}_j) = a', & i, j = 1, 2, 3, i \neq j \\ (\mathbf{a}_i, \mathbf{Ka}_i) = b, (\mathbf{a}_i, \mathbf{Ka}_j) = b', & i, j = 7, 8; 9, 10; 11, 12; i \neq j \end{cases} \quad (9)$$

where the parameters  $a$ ,  $a'$ ,  $b$  and  $b'$  are dependent on the material properties. Consider the following mode transformation:

$$d_i = a_i + \sum_{j=1}^{i-1} t_{ji} a_j + \sum_{j=i+1}^n t_{ji} a_j \tag{10}$$

where  $t_{ji}$ 's are the transformation coefficients and  $d_i$ 's are the desired orthogonal deformation modes. In order to obtain the orthogonal basic deformation modes free of the material parameters, here we require the new modes satisfy the following orthogonal conditions both including and excluding the element stiffness matrix:

$$(d_i, Kd_j) = 0, (d_i, d_j) = 0, i, j = 1, \dots, m, i \neq j \tag{11}$$

As mentioned above, only parts of the deformation modes are coupled to each other, thus they can be orthogonalized in different groups based on the various coupling relationship. Using the orthogonal conditions of Equation (11), the new mode vectors of tension and bending deformation modes are given by:

$$\begin{cases} d_1 = a_1 + a_2 - 2a_3 \\ d_2 = a_2 - a_1 \\ d_3 = a_1 + a_2 + a_3 \end{cases} \begin{cases} d_7 = a_7 + a_8 \\ d_8 = a_8 - a_7 \end{cases} \begin{cases} d_9 = a_9 + a_{10} \\ d_{10} = a_{10} - a_9 \end{cases} \begin{cases} d_{11} = a_{11} + a_{12} \\ d_{12} = a_{12} - a_{11} \end{cases} \tag{12}$$

The orthogonal deformation modes by the present method are shown in Figure 1.

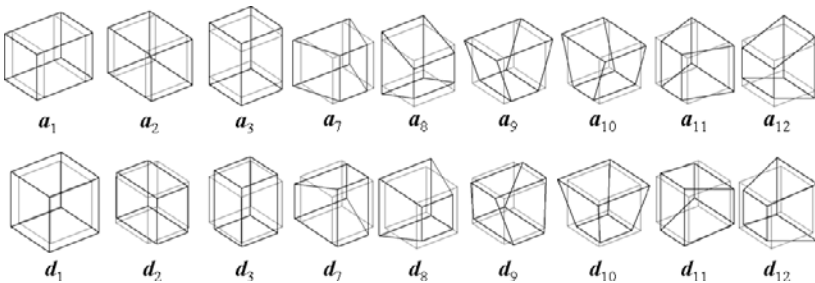


Figure 1. Orthogonal basic deformation modes belonging to tension and bending

Take the orthogonal advantage of the proposed basic deformation modes, the corresponding element energy for an arbitrary deformation mode  $a = \sum_{i=1}^m \alpha_i d_i$  for  $\alpha_i \in \mathbb{R}$  reduces to

$$U(\mathbf{a}) = \frac{1}{2} \mathbf{a}^T \mathbf{K} \mathbf{a} = \sum_{i=1}^m \alpha_i^2 U(\mathbf{d}_i), \quad U(\mathbf{d}_i) = \frac{1}{2} \mathbf{d}_i^T \mathbf{K} \mathbf{d}_i = \frac{1}{2} (\mathbf{d}_i, \mathbf{K} \mathbf{d}_i) \quad (13)$$

Obviously the element energy of Equation (13) can be used to comparably investigate the performance of different elements.

### 4 Numerical Examples

The hybrid elements constructed by the following assumed stress matrices are considered

$$\begin{aligned}
 P_1 &= \{ \bar{\sigma}_1, \bar{\sigma}_3, \bar{\sigma}_4, \bar{\sigma}_6, \bar{\sigma}_8, \bar{\sigma}_{11}, \bar{\sigma}_9, \bar{\sigma}_{14}, \bar{\sigma}_{15}, \bar{\sigma}_{16}, \bar{\sigma}_{17}, \bar{\sigma}_{19}, \bar{\sigma}_{22}, \bar{\sigma}_{23}, \bar{\sigma}_{28}, \bar{\sigma}_{30}, \bar{\sigma}_{34}, \bar{\sigma}_{37} \} \\
 P_2 &= \{ \bar{\sigma}_1, \bar{\sigma}_{45}, \bar{\sigma}_{43}, \bar{\sigma}_6, \bar{\sigma}_8, \bar{\sigma}_{46}, \bar{\sigma}_{44}, \bar{\sigma}_{14}, \bar{\sigma}_{15}, \bar{\sigma}_{47}, \bar{\sigma}_{48}, \bar{\sigma}_{19}, \bar{\sigma}_{22}, \bar{\sigma}_{23}, \bar{\sigma}_{28}, \bar{\sigma}_{30}, \bar{\sigma}_{34}, \bar{\sigma}_{37} \} \\
 P_3 &= \{ \bar{\sigma}_1, \bar{\sigma}_{55}, \bar{\sigma}_{56}, \bar{\sigma}_6, \bar{\sigma}_8, \bar{\sigma}_{59}, \bar{\sigma}_{54}, \bar{\sigma}_{14}, \bar{\sigma}_{15}, \bar{\sigma}_{57}, \bar{\sigma}_{58}, \bar{\sigma}_{19}, \bar{\sigma}_{22}, \bar{\sigma}_{23}, \bar{\sigma}_{28}, \bar{\sigma}_{30}, \bar{\sigma}_{34}, \bar{\sigma}_{37} \} \\
 P_4 &= \{ \bar{\sigma}_1, \bar{\sigma}_3, \bar{\sigma}_4, \bar{\sigma}_6, \bar{\sigma}_8, \bar{\sigma}_{11}, \bar{\sigma}_9, \bar{\sigma}_{14}, \bar{\sigma}_{15}, \bar{\sigma}_{16}, \bar{\sigma}_{17}, \bar{\sigma}_{19}, \bar{\sigma}_{22}, \bar{\sigma}_{49}, \bar{\sigma}_{28}, \bar{\sigma}_{51}, \bar{\sigma}_{34}, \bar{\sigma}_{50} \} \\
 P_5 &= \{ \bar{\sigma}_1, \bar{\sigma}_3, \bar{\sigma}_4, \bar{\sigma}_{60}, \bar{\sigma}_8, \bar{\sigma}_{11}, \bar{\sigma}_9, \bar{\sigma}_{61}, \bar{\sigma}_{15}, \bar{\sigma}_{16}, \bar{\sigma}_{17}, \bar{\sigma}_{62}, \bar{\sigma}_{22}, \bar{\sigma}_{23}, \bar{\sigma}_{28}, \bar{\sigma}_{30}, \bar{\sigma}_{34}, \bar{\sigma}_{37} \}
 \end{aligned} \quad (14)$$

where  $\bar{\sigma}_i$ 's are the assumed stress modes listed in (Zhang et al., 2006b). By using the proposed orthogonal basic deformation modes the energies are clearly depicted in Figure 2. From these results, one can see that: For different elements the energies for tension and shear deformations remain the same since they represents the constant strain fields. While the rigidities associated with other deformations for the hybrid elements are improved to some extent compared with the counterpart displacement-based element.

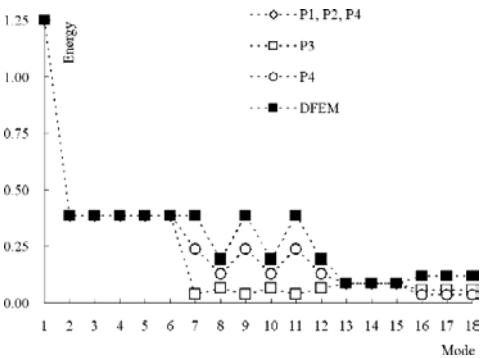


Figure 2. Energy comparison using orthogonal basic deformation modes for 3D 8-node hybrid element

## 5 Conclusions

A novel orthogonalization approach for basic deformation modes method was developed for analysis of the deformation energy of different hybrid stress finite elements. This evaluation procedure here remains invariant for different elements due to the fact that the resulting orthogonal basic deformation modes are free of the material parameters. The detailed information for 3D 8-node hexahedral element revealed that the present method is effective and robust.

## Acknowledgements

The support of this work by the scientific program of Fujian Province of China under grant No. 2007F3096 and the scientific program of Xiamen City of China under grant No. 3502Z20073012 is gratefully acknowledged.

## References

- Feng W., Hoa S.V., Huang Q. (1997). Classification of stress modes in assumed stress fields of hybrid finite elements. *International Journal for Numerical Methods in Engineering*, 40: 4313-4339.
- Huang Q. (1991). Modal analysis of deformable bodies with finite degree of deformation freedom – An approach to determination of natural stress modes in hybrid finite elements. *Advances in Applied Mathematics & Mechanics in China*, 3:283-303, IAP.
- Pian T.H.H. (1964). Derivation of element stiffness matrices. *AIAA Journal*, 2: 576-577.
- Sze K.Y., Liu X.H., Lo S.H. (2004). Hybrid-stress six-node prismatic elements. *International Journal for Numerical Methods in Engineering*, 61: 1451-1470.
- Zhang C., Huang Q., Feng W. (2006a). Deformation rigidity of assumed stress modes in hybrid elements. *Applied Mathematics and Mechanics*, 27(7): 861-869.
- Zhang C., Wang D., Zhang J.L. (2006b). Suppression of zero-energy modes in hybrid finite elements via assumed stress fields. *Proceedings of the Computational Methods in Engineering and Science (EPMESC X)*: 254.
- Zhang C., Wang D., Zhang J., Feng W., Huang Q. (2007). On the equivalence of various hybrid finite elements and a new orthogonalization method for explicit element stiffness formulation. *Finite Elements in Analysis and Design*, 43(4): 321-332.

# Nonlinear Numerical Analysis on a New Type of Composite Shell

Qibin Zhang<sup>1\*</sup>, Zhuobin Wei<sup>1</sup> and Changhong Huang<sup>1</sup>

<sup>1</sup>Department of Logistics Command and Engineering, Naval University of Engineering, Tianjin 300450, China

**Abstract.** In order to meet the special demand of protection work, a new structure type of composite shell was put forward. The composite shell, which composed of spatial latticed shell structure and steel-concrete composite slab and the former is covered by the later, is a half-bred structure. With all merits of latticed shell and composite slab, the composite shell's structural performance is very excellent. To instruct structure design and test, the nonlinear property of new type of composite latticed shell, which based on spatial integral action is analyzed overall by FEM software ANSYS. The result of analyses shows that the new type of composite shell is a very excellent form of protection structure because of its prominent mechanical property.

**Keywords:** protection work, latticed shell, composite slab, composite shell, nonlinear, FEM

## 1 Introduction

To meet the special demand of protection work, a new structure type of composite shell was put forward. The composite shell, which composed of spatial latticed shell structure and steel-concrete composite slab and the former is covered by the later, is a half-bred structure. The spatial latticed shell, composed of two layers semi-circular cylindrical shell which supported by two longitudinal sides, adopts square pyramid grids structure system. The web member and low-boom member are made of steel tube. The top plane adopts square steel plate with stiffening rib which served as top-boom in installation phase of steel work and served as bottom formwork in phase of concreting. When the design strength of concrete reached, the composite slab is formed.

With uniform specification, the member of steel work can be made into square pyramid in factory beforehand. The steel work can be installed by the methods

---

\* Corresponding author, e-mail: zhangqibing11@163.com

such as upper air assembly, upper air slippage and bulk erection. With the adaptation of High-powered and self-compact concrete, concreting is very convenience and rapid without forming, lashing and vibration.

Latticed shells have excellent monolithic stability and spatial stiffness, and the composite slab have outstanding impact property and ductility. With all merits of latticed shell and composite slab, the composite shell's anti-detonating property increase obviously. The structural performance of the composite shell, obtained by the traditional construction method and technology, is very excellent. The composite shell is a new type structure system with far-ranging applied occasion in future.

To instruct structure design and test, the nonlinear property of new type of composite latticed shell, which based on spatial integral action ,is analyzed overall by FEM software ANSYS.

## 2 Model of Composite Shell

### 2.1 Geometry of Computation Model

The geometry of computation model is shown in Table 1. The whole computation model, the square pyramid grids and the inner shell are shown in Figure 1. (J10566-2005).

Table 1. Geometry of computation model

Parameter		Value
	Longitudinal length	15m
	Outer radius	12.4m
Composite shell	Inner radius	10m
	Thickness of shell	2m
	Thick of concrete	0.4m
Thickness of steel plate		10mm
Steel tube	Radius	50mm
	Thickness	6mm

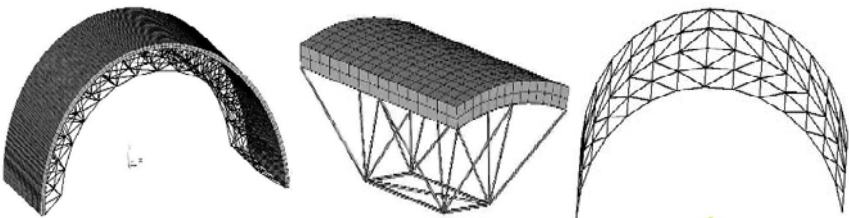


Figure 1. FEM model

## 2.2 Element Types

An eight-node solid element, Solid65, was used to model the concrete. The solid element has eight nodes with three degrees of freedom at each node – translations in the nodal x, y, and z directions. The element is capable of plastic deformation, cracking in three orthogonal directions, and crushing. The element model the nonlinear response of brittle materials based on a constitutive model for the tri-axial behaviour of concrete after Williams and Warnke.

A Link8 element was used to model the steel reinforcement. Two nodes are required for this element. Each node has three degrees of freedom, – translations in the nodal x, y, and z directions. The element is also capable of plastic deformation.

Steel plate was modelled with SHELL63, a 4-node shell element, with both bending and membrane capabilities. Each node has six degrees of freedom: x, y, and z directions and rotations about the nodal x, y, and z-axes. The element is also capable of plastic deformation (ANSYS Inc.).

## 2.3 Material Properties

Concrete is characterized by excellent load carrying behaviour in compression but also by brittle failure in tension. Development of a model for the behaviour of concrete is a challenging task. Concrete is a quasi-brittle material and has different behavior in compression and tension. The tensile strength of concrete is typically 8-15% of the compressive strength. The data of C40, which were reported in *Code for Design of Concrete Structures* (GB50010-2002), were used for defining concrete 'CONCR' in ANSYS. The shear transfer coefficients in opening or closing are assumed to take a value of 0.25 and 0.70 respectively.

Properties of steel Q235, such as elastic modulus and yield stress for steel tube and steel plate used in this FEM study follow the design material properties reported in *Code for Design of Concrete Structures* (GB50010-2002). The steel for the finite element model was assumed to be an elastic-perfectly plastic material and identical in tension (GB50010-2002).

## 2.4 Load and Combination of Work Condition

The structure was assumed to sustain six kind of load. The kind and value of each load are shown in Table 2. Four work conditions are also considered for the composite shell and Table 3 shows each work condition.

Table 2. The value of load

Load	Value	Load	Value
Dead weight	Computed by program	Snow load	0.40kN/m <sup>2</sup>
Live load	2.00kN/m <sup>2</sup>	Wind load	0.55kN/m <sup>2</sup>
Dust load	0.30kN/m <sup>2</sup>	Shock load	100kN*0.5s

Table 3. Combination of load

Work condition	Dead weight	Live load	Dust load	Snow load	Wind load	Shock load
1	Y	N	N	N	N	N
2	Y	Y	Y	Y	Y	N
3	Y	Y(half span)	Y(half span)	Y(half span)	Y	N
4	Y	N	Y	Y	N	Y

### 3 Results and Discussions

Figure 2 and Figure 3 show the stress of concrete layer, steel plate respectively. The axial stress of lower chord and web member are presented in Figure 4 and Figure 5. The deformation of composite shell is also reported in Figure 6 and the maximum displacement of composite shell, which subject to different work conditions, are reported in Table 4. From those figures, we can draw some conclusions as following:

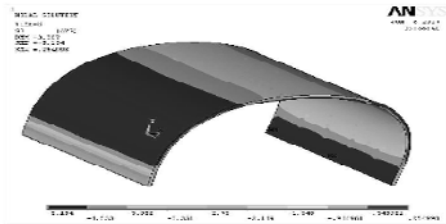


Figure 2. 3rd stress of concrete shell (work condition 2)

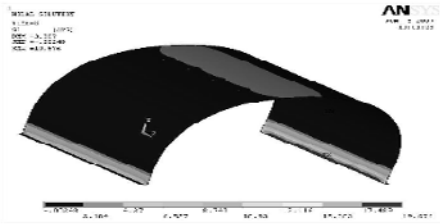


Figure 3. Tensile stress of steel plate (work condition 2)

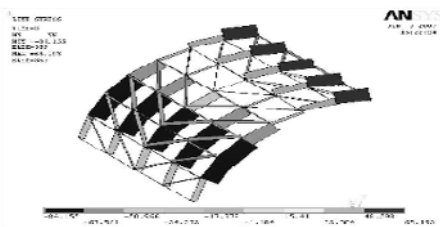


Figure 4. Axial stress of l lower chord (work condition 2)

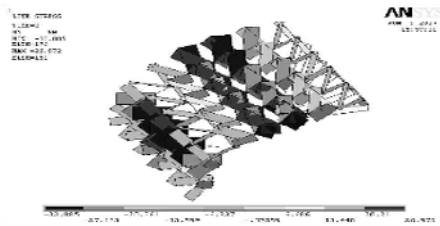


Figure 5. Axial stress of web member (work condition2)

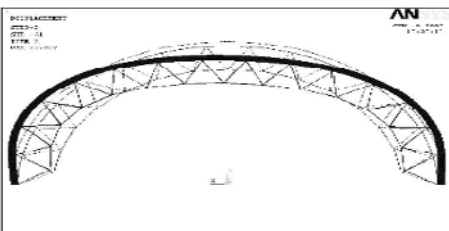


Figure 6. Deform of composite shell (work condition 2)

Table 4. Maximum displacement

Work condition	Maximum displacement
1	3.003mm
2	3.807mm
3	4.144mm
4	5.625mm

1. When subject to ordinary load, s composite shell’s stress level is not very high and the concrete shell subject to most load. Although the stiffness of concrete shell is greater than that of latticed shell, both concrete shell and latticed shell can deformed jointly and subject to load jointly.
2. The axial stress of circumferential lower chord is much greater than that of longitudinal lower chord and diagonal lower chord. The axial stress of web member is also less than that of circumferential lower chord. In actual structure, the section area of circumferential lower chord should be oversized area of section. Otherwise the section area of longitudinal lower chord and web member should be reduced.
3. The displacement of composite shell is far less than the displacement stipulated in relevant criterion. The stiffness and bearing capacity of composite are very huge.

Figure 7 shows the 3rd stress of concrete shell when composite shell subject to shock loads. The displacement-versus-time curves of climax and the 3rd stress-versus-time curves of concrete in support are presented in Figures 8 and 9 respectively.

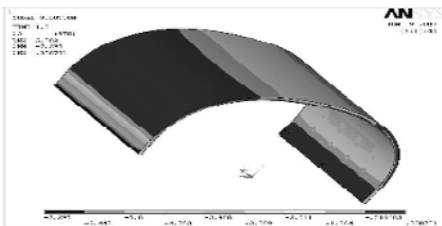


Figure 7. 3rd stress of concrete shell (work condition 4)

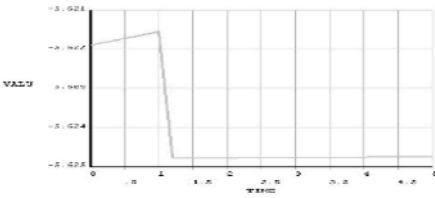


Figure 8. Displacement-versus-time curves of climax (work condition 4)

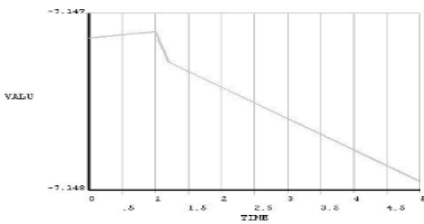


Figure 9. 3rd stress-versus-time curves of concrete in support (work condition 4)

When comparing with the response of composite shell to shock load, the following conclusion can be made: (1) the stress level of concrete shell when subject to shock load is almost similar to the stress when subject to ordinary load. From the Figure 9, a fact can be seen that the 3rd stress change very slightly. (2) The displacement of climax increase very slightly when composite shell subject to shock load. All of those indicate that the composite shell has outstanding capacity of resistance shock load.

## 4. Conclusions

A numerical study is carried out for composite shell using finite elements adopted by ANSYS. The numerical results show that the composite shell, which integrated both composite slab's and latticed shell's merits, has very outstanding structural performance such as huge stiffness, bearing capacity and wonderful shock resistance. Considering its simple and rapid contracture method, the composite shell will have far-ranging applied occasion in future. This numerical modeling is helpful for further research on composite shell.

## References

- ANSYS, Guide to ANSYS user programmable features, ANSYS Inc., Feb. 2000.  
Code for Design of Concrete Structures.GB50010-2002, China.  
Technical Specification for spatial grid structures, J 10566-2005, Tientsin China.

# Rectangular Membrane Element with Rotational Degree of Freedom

Guiyun Xia<sup>1,2\*</sup>, Maohong Yu<sup>1</sup>, Chuanxi Li<sup>2</sup> and Jianren Zhang<sup>2</sup>

<sup>1</sup>School of Aeronautics and Astronautics, Xi'an Jiaotong University, Xi'an 710049, China

<sup>2</sup>School of Civil and Architectural Engineering, Changsha University of Science and Technology, Changsha 410076, China

**Abstract.** Using finite strips of unit length and width, a rectangular membrane element with rotational degree of freedom is presented. This element can be used to solve planar stress/strain questions and combined with rectangular plate bending element to form plate-type shell element with six degrees of freedom at each node. With its linear interpolating function in the axial direction and cubic interpolating function in transverse direction, it can be coupled and superposed by beam element. Numeric analyses and comparison are carried out to verify the properties of this element, which show that this element has excellent precision and convergence.

**Keywords:** finite strip, membrane element, rotational degree of freedom

## 1 Introduction

It is very interesting and significant to construct a planar membrane element with rotational degree of freedom, which can improve its performance and precision, and can contribute to form flat shell element by coupling plate bending element. As for the state of the art, Long (1992, 1997) made a summary, and put forward with a general conforming theory to construct membrane element with rotational degree of freedom. A series of elements, such as GR12, GR12M, GT9, GT9M, GT9M8, have been composed to analyze planar stress /strain questions. Long (2001) put forward with quadrangular area coordinate method, and have constructed many elements by this method. Zeng (1984) put forward with a general method to construct element by using linear function and cubic function as shape functions for beam element and plate element. This method is named as finite belt method. Wang (1999) successfully constructed Timoshenko beam element, thick plate element, shell element by this method.

---

\* Corresponding author, e-mail: xiagy72@163.com

## 2 Shape Function

The delicacies of finite belt method are represented by using linear function as axial displacement mode, cubic function as transverse displacement mode, which are identical with beam element. Insinuating the essence of finite belt method into constructing membrane element, the displacement functions are as follows.

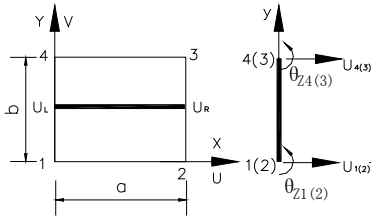


Figure 1 Horizontal finite belt

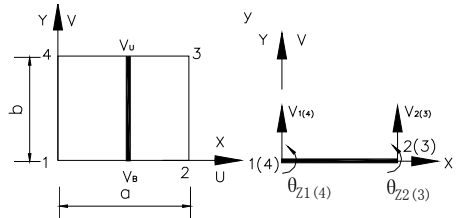


Figure 2 Vertical finite belt

Transversal displacement mode:

$$u = [M_1 \quad M_2] \{u_L \quad u_R\}^T \tag{1}$$

in which

$$M_1 = 1 - x/a, \quad M_2 = x/a$$

$$u_L = [N_1 \quad N_2 \quad N_3 \quad N_4] \{u_1 \quad -\theta_{z1} \quad u_4 \quad -\theta_{z4}\}^T$$

$$u_R = [N_1 \quad N_2 \quad N_3 \quad N_4] \{u_2 \quad -\theta_{z2} \quad u_3 \quad -\theta_{z3}\}^T$$

$$N_1 = 1 - 3\left(\frac{y}{b}\right)^2 + 2\left(\frac{y}{b}\right)^3, N_2 = y - \frac{2y^2}{b} + \frac{y^3}{b^2}$$

$$N_3 = 3\left(\frac{y}{b}\right)^2 - 2\left(\frac{y}{b}\right)^3, N_4 = -\frac{y^2}{b} + \frac{y^3}{b^2}$$

$$\{\delta_e\} = \{u_1 \quad v_1 \quad \theta_{z1} \quad u_2 \quad v_2 \quad \theta_{z2} \quad u_3 \quad v_3 \quad \theta_{z3} \quad u_4 \quad v_4 \quad \theta_{z4}\}^T$$

Longitudinal displacement mode:

$$v = [\bar{M}_1 \quad \bar{M}_2] \{v_B \quad v_U\}^T \tag{2}$$

in which

$$\begin{aligned} \bar{M}_1 &= 1 - y/b, & \bar{M}_2 &= y/b \\ v_B &= [\bar{N}_1 \quad \bar{N}_2 \quad \bar{N}_3 \quad \bar{N}_4] \{v_1 \quad \theta_{z1} \quad v_2 \quad \theta_{z2}\}^T \\ v_U &= [\bar{N}_1 \quad \bar{N}_2 \quad \bar{N}_3 \quad \bar{N}_4] \{v_4 \quad \theta_{z4} \quad v_3 \quad \theta_{z3}\}^T \\ \bar{N}_1 &= 1 - 3\left(\frac{x}{a}\right)^2 + 2\left(\frac{x}{a}\right)^3, \bar{N}_2 = x - \frac{2x^2}{a} + \frac{x^3}{a^2} \\ \bar{N}_3 &= 3\left(\frac{x}{a}\right)^2 - 2\left(\frac{x}{a}\right)^3, \bar{N}_4 = -\frac{x^2}{a} + \frac{x^3}{a^2} \end{aligned}$$

### 3 Element Stiffness

With displacements known at all points within element, the strains at any point can be determined. These will always result in a relationship that can be written in matrix notation as

$$\{\varepsilon\} = [B]\{\delta\}^e \tag{3}$$

For the plane stress case, the relevant strains of interest are those occurring in the plane and are defined in terms of the displacements by well-known relations between displacements and strains, which define the relationships as follows.

$$\varepsilon = \begin{Bmatrix} \varepsilon_x \\ \varepsilon_y \\ \gamma_{xy} \end{Bmatrix} = \begin{bmatrix} -\frac{N_1}{a} & 0 & \frac{N_2}{a} & \frac{N_1}{a} \\ 0 & -\frac{\bar{N}_1}{b} & -\frac{\bar{N}_2}{b} & 0 \\ \left(1-\frac{x}{a}\right)N'_1 & \left(1-\frac{y}{b}\right)\bar{N}'_1 & -\left(1-\frac{x}{a}\right)N'_2 + \left(1-\frac{y}{b}\right)\bar{N}'_2 & \frac{x}{a}N'_1 \\ 0 & -\frac{N_2}{a} & \frac{N_3}{a} & 0 \\ -\frac{\bar{N}_3}{b} & -\frac{\bar{N}_4}{b} & 0 & \frac{\bar{N}_3}{b} \\ \left(1-\frac{y}{b}\right)\bar{N}'_3 & -\frac{x}{a}N'_2 + \left(1-\frac{y}{b}\right)\bar{N}'_4 & \frac{x}{a}N'_3 & \frac{y}{b}\bar{N}'_3 \end{bmatrix}$$

$$\begin{bmatrix} -\frac{N_4}{a} & -\frac{N_3}{a} & 0 & \frac{N_4}{a} \\ \frac{\bar{N}_4}{b} & 0 & \frac{\bar{N}_1}{b} & \frac{\bar{N}_2}{b} \\ -\frac{x}{a}N_4 + \frac{y}{b}\bar{N}_4 & \left(1 - \frac{x}{a}\right)N_3 & \frac{y}{b}\bar{N}_1 & -\left(1 - \frac{x}{a}\right)N_4 + \frac{y}{b}\bar{N}_2 \end{bmatrix} \{\delta_e\}^T = [B]\{\delta_e\} \quad (4)$$

in which

$$N_i = \frac{\partial N_i}{\partial y}, \bar{N}_i = \frac{\partial \bar{N}_i}{\partial x} \quad (i = 1, 4)$$

The virtual work principle is applied, the stiffness matrix and equivalent node force are retained.

$$[K]_e = \iint_A [B]^T [D][B] dA \quad (5)$$

$$R^e = \int_A [N]^T \cdot f \cdot t \cdot dA + \int_s [N]^T \cdot \bar{T} \cdot t \cdot ds \quad (6)$$

in which

$$[D] = \frac{Et}{1 - \mu^2} \begin{bmatrix} 1 & \mu & 0 \\ \mu & 1 & 0 \\ 0 & 0 & \frac{1 - \mu}{2} \end{bmatrix}$$

## 4 Numeric Analyses

### 4.1 Cantilever Beam under Concentrated Load at the Free End

To verify the validity and precision of this element, a cantilever beam under concentrated load at the free end is analyzed. Numeric values are compared with theory and other methods.

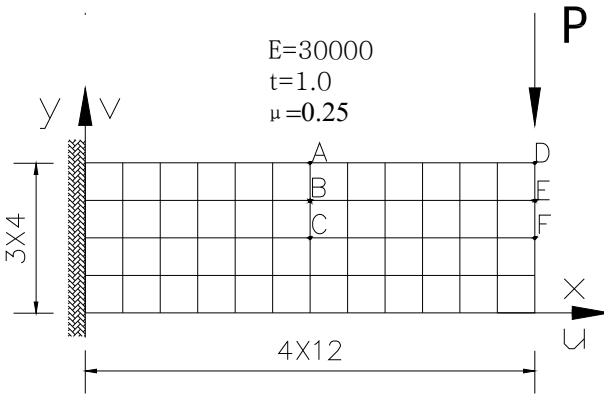


Figure 3 Cantilever beam under concentrated loading at the free end

Table 1 Stress and deflection of cantilever beam under concentrated load at the free end

Node		A	B	C	D	E	F
Predictions of this paper	u	0.11998	0.05943	0.00017	0.16966	0.07858	-0.00041
	v	-0.28260	-0.28073	-0.28010	-0.89714	-0.88358	-0.87981
	$\theta$	-0.02061	-0.02024	-0.02015	-0.03848	-0.02645	-0.02586
	$\sigma_x$	110.01	55.88	1.66	41.82	-7.69	-1.81
Predictions of ANSYS (PLANE42)	u	0.11996	0.05928	-0.67E-6	0.16419	0.07915	-0.00067
	v	-0.28420	-0.28233	-0.28170	-0.89478	-0.88248	-0.88382
	$\sigma_x$	108.35	54.16	-0.01	21.40	-1.04	-0.77
Elastic solutions	u	0.11563	0.05711	0.00000	0.15563	0.07711	0.00000
	v	-0.26917	-0.26729	0.26666	-0.85333	-0.85333	-0.85333
	$\theta$	-0.02094	-0.02063	-0.02052	-0.02760	-0.02729	-0.02718
	$\sigma_x$	100.00	50.00	0.00	0.00	0.00	0.00

Numeric values of elastic solution are computed by using elastic theory as follows:

$$\begin{cases} u = \frac{P}{6EI} [3xy(2L-x) + (2+\mu)y^3] \\ v = -\frac{P}{EI} \left[ \frac{\mu(L-x)}{2}y^2 + \frac{Lx^2}{2} - \frac{x^3}{6} + \frac{(1+\mu)h^2x}{4} \right] \\ \theta = -\frac{P}{2EI} \left[ 2Lx - x^2 + y^2 + \frac{(1+\mu)h^2}{4} \right] \end{cases}$$

From the view of point, apart from some local point stress, results agree with theoretical analyses and other methods well, which prove this method.

### 4.2 Pure Bending of Plate

A square plate is subjected to linear load at the ends (figure 4), which is a case of pure bending. The stress distributions at both ends are  $\sigma_x|_{x=\pm L/2} = 2\sigma_0 Y / L$ . Out of symmetry, a quarter plate is selected to mesh. The results of point C are compared (Table 2).

It is clear that results of this element are very precise.

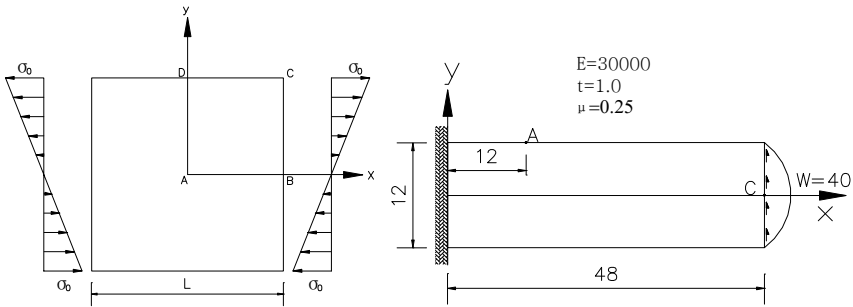


Figure 4. Quadrate plate under pure bending. Figure 5. Cantilever beam under shear load at free end.

Table 2. Deflection and stress of C point in quadrate plate under pure bending

Mesh	1 × 1			2 × 2		
Element	$\frac{Eu_C}{\sigma_0 L}$	$\frac{Ev_C}{\sigma_0 L}$	$\frac{\sigma_{XC}}{\sigma_0}$	$\frac{Eu_C}{\sigma_0 L}$	$\frac{Ev_C}{\sigma_0 L}$	$\frac{\sigma_{XC}}{\sigma_0}$
	R4 <sup>[5]</sup>	0.4461	-0.2900	0.9363	0.4797	-0.3120
Allman <sup>[5]</sup>	0.4738	-0.3070	0.9784	0.4910	-0.3191	0.9912
GR12 <sup>[5]</sup>	0.4823	-0.3108	1.0220	0.4941	-0.3206	1.0129
GR12M <sup>[5]</sup>	0.4961	-0.3218	1.0055	0.4987	-0.3241	1.0029
Results of this paper	0.4880	-0.3033	1.0113	0.4960	-0.3096	1.0065
mesh	4 × 4			8 × 8		
Element	$\frac{Eu_C}{\sigma_0 L}$	$\frac{Ev_C}{\sigma_0 L}$	$\frac{\sigma_{XC}}{\sigma_0}$	$\frac{Eu_C}{\sigma_0 L}$	$\frac{Ev_C}{\sigma_0 L}$	$\frac{\sigma_{XC}}{\sigma_0}$
	R4 <sup>[5]</sup>	0.4931	-0.3206	0.9894	0.4978	-0.3236
Allman <sup>[5]</sup>	0.4971	-0.3231	0.9956	0.4991	-0.3244	0.9978
GR12 <sup>[5]</sup>	0.4982	-0.3237	1.0066	0.4994	-0.3246	1.0033
GR12M <sup>[5]</sup>	0.4996	-0.3247	1.0015	0.4999	-0.3249	1.0007
Results of this paper	0.4988	-0.3116	1.0033	0.4996	-0.3122	1.0016
Precise solutions	0.5000	-0.3250	1.0000			

### 4.3 Cantilever Beam Subjected to Shear Load

Table 3. Deflection and stress of cantilever beam under shear load

mesh	4 × 1		8 × 2		16 × 4	
	$v_c$	$\sigma_{XA}$	$v_c$	$\sigma_{XA}$	$v_c$	$\sigma_{XA}$
R4 <sup>[5]</sup>	0.2424	-43.64	0.3162	-55.70	0.3447	-59.28
Allman <sup>[5]</sup>	0.3026	-52.70	0.3394	-58.40	0.3512	-59.70
GR12 <sup>[5]</sup>	0.3283	-60.00	0.3475	-61.31	0.3535	-60.76
GR12M5 <sup>[5]</sup>	0.3446	-60.00	0.3527	-60.65	0.3550	-60.20
Results of this paper	0.3333	-73.81	0.3520	-65.69	0.3544	-63.24
Theoretical values	$v_c=0.35601, \sigma_{XA}=-60.0$					

As shown in figure 5, a cantilever beam is subjected to quadratic shear load as

$$\tau_{xy}|_{x=L} = \frac{3W}{2Ht} \left[ 1 - 4 \left( \frac{y}{H} \right)^2 \right],$$

whose height, width and thickness taken as 12, 40 and 1.0. Displacement at the end side and stress of quarter point A agree with other results well.

## 5 Summary and Conclusions

A membrane element with rotational degrees of freedom is constructed in this paper, and numeric tests are carried out to verify the precision and validity. Numeric results agree with other methods well. This element can be coupled with plate bending element to form shell element. With the rotational degrees of freedom contained in the plane stress displacement mode, the singularity can be avoided. An outstanding property is that the displacement mode is the same as the beam element, and the element can be overlapped with beam element. So, this element can be used to compute the ribbed plate structure, to analyze box girder of bridge engineering.

## References

- Budynas R.G. (1991). *Advanced Strength and Applied Stress Analysis* (second edition). McGraw-Hill.
- Li J.X. (1995). Biquadratic generalized conforming rectangular element. *Engineering Mechanics*, 12(1):46-52 [in Chinese].
- Long Y.Q. (1992). *Introduction to New Finite Element*. Beijing: Qinghua University Press [in Chinese].
- Long Y.Q. (1997). A generalized conforming quadrilateral membrane element insensitive to geometric distortion. *Acta Mechanica Sinica*, 29(6):692-699 [in Chinese].
- Long Zh.F. (2001). *New Theory Program Development of Finite Element Methods*. Beijing: China Waterpower Press [in Chinese].
- Sheng X.W. (2000). Analysis theory and test study of prestressed concrete skew box beam. Changsha: Central South university doctor thesis [in Chinese].
- Xu Y. (1993). The generalized conforming triangular element with drilling degrees of freedom. *Engineering Mechanics*, 10(2):31-39 [in Chinese].
- Xu Y. (2000). The generalized conforming triangular element with drilling degrees of freedom including bubble displacement. *Engineering Mechanics*, 17(3):1-9 [in Chinese].
- Wang R.H. (1999). *Computing Theory and Application of Bar, Slab, Shell*. Beijing: China Railway Press [in Chinese].
- Wang R.H. (2000). A rectangular plate bending element based upon finite strip in length and breadth. *Engineering Mechanics*, 17(1):114-119 [in Chinese].
- Zeng Q.Y. (1981). Slab-beam frame method for thin box beam, *Journal of the China Railway Society*, 7(3):92-104 [in Chinese].

# Coupling Analysis on Seepage and Stress in Jointed Rock Tunnel with the Distinct Element Method

Yanli Wang<sup>1,2\*</sup>, Yong Wang<sup>3</sup> and Yifei Dai<sup>4</sup>

<sup>1</sup>Department of Geotechnical Engineering, Tongji University, Shanghai 200092, P.R. China

<sup>2</sup>Key Laboratory of Geotechnical and Underground Engineering of Ministry of Education, Tongji University, Shanghai 200092, P.R. China

<sup>3</sup>Institute of Rock and Soil Mechanics, Chinese Academy of Science, State Key Laboratory and Geotechnical Engineering, Wuhan, Hubei 430070, P.R. China

<sup>4</sup>School of Civil Engineering and Architecture, Wuhan University of Technology, Wuhan, Hubei 430070, P.R. China

**Abstract.** Based on the postulate of the characteristics of fluid flow through joint networks of rock mass, the numerical simulation on coupled problem of seepage and stress in jointed rock tunnel was theoretically analyzed with the distinct element method. The theory of tunnel excavation and coupling effects between lining structure and groundwater seepage were studied. The numerical results show that the maximum stress of the wall rock increases but the maximum displacement decreases after the liner is applied. When considering the effects of seepage, the maximum stress and displacement of the tunnel wall rock have increased in varying degrees, the axial force and shear force of the liner decrease slightly, and the bending moment is large. The effects on the bending moment of the liner from the deformation are greater than that from the shear force in this condition.

**Keywords:** seepage field, stress field, coupling, the distinct element method

## 1 Introduction

With the development of construction technology and construction machinery, the tunnel project appears long, large, deep and difficult in recent years (Yang and Wang, 2006). There are mostly a gushing, pouring water and high water pressure problems in railway and highway tunnels through water-rich strata. Groundwater is an important factor in the tunnel construction and operation. Geological disasters from the water in the tunnel project are caused by the interaction between wa-

---

\* Corresponding author, e-mail: wyldhh@126.com

ter and rock mass (Ji and Wang, 2005). The original distribution of stress field and seepage field is changed by the tunnel excavation. The disturbance and changes in groundwater pressure will cause changes in the stress distribution of rock mass, and changes in rock stress also make rock porosity or crack opening degrees changed, which in turn change the groundwater flow and water pressure. This constitutes a coupling relation between stress field and seepage field. Currently, there are more researches on waterproof and drainage technology in the tunnel engineering, the research on coupling mechanism of groundwater seepage field and stress field is less when the leakage in wall rock tunnel takes place (Li et al., 2007), especially coupling analysis on seepage and stress in jointed rock tunnel excavation in supporting conditions.

In order to ensure the stability of wall rock, the seepage law of discontinuous medium is studied and applied in underground engineering such as tunnel and the groundwater movement rules is accurately simulated. In view of this, hydraulic coupling problems in the rock tunnel are simulated with the discrete element method, and the theory of tunnel excavation and coupling effects between lining structure and groundwater seepage are studied.

## 2 Seepage Model of Jointed Rock Mass

The characteristics of fluid flow through joint networks of rock mass are that the fluid flows along the joint network, which manifests the obvious heterogeneity and anisotropy (Wu and Chai, 2000). According to this, the numerical implementation for fluid flow makes use of the domain structure described in UDEC manual (Itasca Consulting Group Inc, 1996). For a closely packed system, there exists a network of domains, each of which is assumed to be filled with fluid at uniform pressure and which communicates with its neighbors through contacts.

## 3 Numerical Example of Fluid-Solid Coupling

A jointed rock mass highway tunnel is constructed through the rock mass which is full of joints, fissures and faults (Figure 1). There are mainly two prominent joint sets projected on tunneling surface which is  $40^\circ$ ,  $80^\circ$  respectively with an average spacing of 8 m. The excavation will have a horse-shaped cross-section of dimensions  $15\text{ m} \times 20\text{ m}$ , the floor of the tunnel is located 105 m below the ground surface. The level of the phreatic surface is 5 m below the ground surface. After the tunnel is excavated, a shotcrete lining with a thickness of 200mm and C20 strength grade as the initial supporting structure is applied instantaneously. Due to the calculation of tunnel excavation focusing on the differences between coupling calculation and the uncoupling calculation, the mechanical effects of the shotcrete

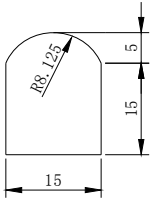


Figure 1. Cross-section of the tunnel (unit: meter)

is only considered in the numerical simulation, without considering the effects of anchor and secondary support.

The distinct element method is an effective method to study the distortion and stability of the jointed rock mass (Wang, 2004). In order to simplify the computation, the plane model is used to simulate the tunnel excavation. A system of coordinate axes is defined with the origin at the level of the phreatic surface; the x-axis points vertically the axis of the tunnel and the y-axis points upward. The top of the model, at  $y = 0$ , is a free surface. The base of the model, at  $y = -150\text{m}$ , is fixed in the y-direction, and roller boundaries are imposed on the sides of the model, at  $|x| = 200\text{ m}$ . The tunnel is constructed in a weak rock that is modeled as a Mohr-Coulomb material and the joints are modeled as Coulomb Slipping material. The Concrete liner is assumed to behave as a linear-elastic material with an elastic modulus of  $21\text{ GPa}$  and the Poisson's ratio is  $0.15$ . The mass density of shotcrete is  $2400\text{ kg/m}^3$ . The material properties associated with the rock and joints are listed in Table 1 and Table 2.

In order to compare the distribution of stress, displacement and pore water pressure in the wall rock, several different calculation conditions are considered: (1) without seepage or lining; (2) without seepage and with lining; (3) with seepage and lining.

Table 1. Mechanical parameters of rock mass

$\rho$ (kg·m <sup>-3</sup> )	K (GPa)	G (GPa)	$\phi_1$ (°)	c (MPa)
2650	6.67	4.0	44	5.04

where  $\rho$  = density of rock, K= bulk modulus of rock, G= shear modulus of rock,  $\phi_1$ =internal friction angle of rock, c =cohesion of rock.

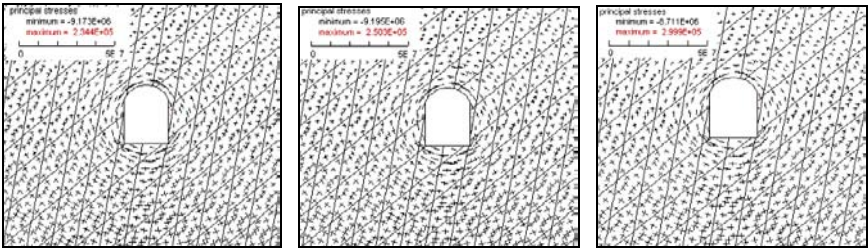
Table 2. Mechanical parameters of joints

$k_n$ (GPa/m)	$k_s$ (GPa/m)	$k_j$ (m·s <sup>-1</sup> )	$a_0$ (mm)	$a_r$ (mm)	$\phi^2$ (°)
10	10	0.25	1.0	0.5	35

where  $k_n$  = joint normal stiffness,  $k_s$  =joint shear stiffness,  $a_0$  =zero stress hydraulic aperture,  $a_r$  =residual hydraulic aperture,  $k_j$  =joint permeability factor,  $\phi^2$  =internal friction angle of joint.

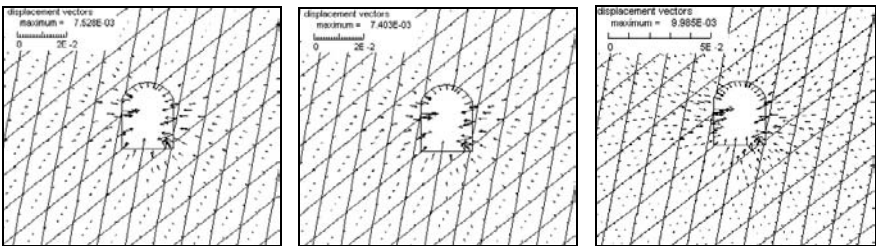
### 4 Results and Discussion

The basic laws of the stress distribution in the three calculation conditions are similar, but different in magnitude (Figure 2). The maximum stress of the wall rock in the three conditions is tensile stress for 0.234Mpa, 0.250Mpa, 0.299Mpa respectively. The minimum stress is compressive stress for 9.173Mpa, 9.195Mpa, 9.711Mpa respectively. The results show that the principal stress of the wall rock increases after the liner is applied without considering fluid seepage. In the lining condition, the maximum and minimum stress increases by 19.6% and 5.6% respectively because of the fluid-solid coupling. This is mainly caused by drag force paralleling the joint surface and osmotic pressure normal to the joint surface.



(a) (b) (c)

Figure 2. Principal stress distribution of the tunnel under different working conditions



(a) (b) (c)

Figure 3. Displacement vector distribution of the tunnel under different calculation conditions

The displacement vector distributions in the three calculation conditions are shown in Figure 3. The maximum displacement appears in the middle of the side wall rock, and the direction is toward the hole. The maximum displacement of the wall rock is 7.528mm, 7.403mm, 9.985mm respectively. The displacement results show that firstly, lining structure that can limit the development of displacement of wall rock and be in favor of the stability of tunnel, secondly, the maximum dis-

placement of the wall rock is greater with considering seepage than without considering seepage by 34.9% in the lining condition, which indicate that the fluid-solid coupling has a great influence on the displacement, it not only can affect the displacement value but also can change the displacement direction. So the fluid-solid coupling is disadvantageous to the stability of the wall rock.

Distribution of axial force, shear force and bending moment on the liner of calculation condition (b) and (c) are shown in Figures 4, 5 separately. In both cases, the maximum of axial force on the liner appears in the middle of tunnel roof, while the largest shear stress occurs in the lower right corner of the tunnel floor. In calculation condition (b), the maximum axial force is tensile with the value 1.459MN and the largest shear force is 39.56kN. The two values in working condition (c) are 1.450MN and 39.46kN respectively. Axial and shear force decrease slightly when considering the seepage, because groundwater flows around tunnel occurs after excavation. And in this case, total stress around the tunnel becomes smaller, thus resulting in the reduction of axial force and shear force. According to the figures, the maximum bending moment with the value 35.59kN · m lies in the lower right corner of the tunnel floor where the largest shear arises in calculation condition (b). However, in calculation condition (c), the maximum bending moment with the value 36.22kN · m lies in the middle of left side wall where the largest displacement occurs and is bigger than that does not consider seepage. This shows that when considering seepage, the influences of deformation to the bending moment are greater than that to the shear force in liner.

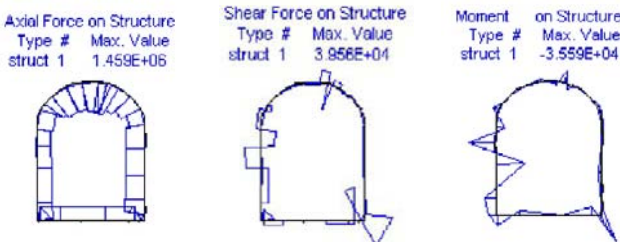


Figure 4. Calculation results on the liner under calculation condition (2)

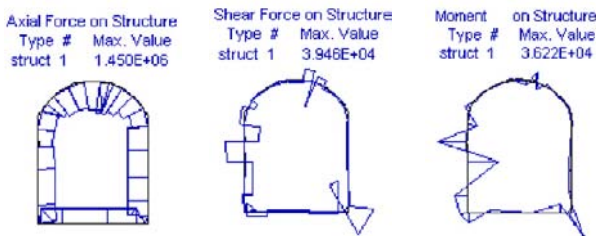


Figure 5. Calculation results on the liner under calculation condition (3)

## 5 Conclusions

The coupling analysis research of seepage and stress in jointed is a very valued but complicated task for discussion. The major results are as follows: The principal stress of the wall rock increases after the liner is applied without considering fluid seepage. The lining structure can limit the development of displacement effectively. The fluid-solid coupling has a great influence on the displacement of wall rock. The seepage influences on the tunnel liner is preliminarily analyzed. The maximum axial force and shear force of the liner is decreased slightly, and the maximum bending moment is larger when considering the effects of seepage, which show that the influences on the bending moment of the liner from the deformation are greater than that from the shear force in this condition.

## References

- Itasca Consulting Group Inc (1996). UDEC (Universal Distinct Element Code) Version 3.0.
- Ji X., and Wang Y. (2005). Hydromechanical coupling analysis of tunnel excavation process. *Chinese Journal of Underground Space and Engineering*, 1(6), 848–852 [in Chinese].
- Li D., Li X., Zhang W. et al(2007). Stability analysis of surrounding rock of multi-arch tunnel based on coupled fluid-solid theorem. *Chinese Journal of Rock Mechanics and Engineering*, 26(5), 1056–1064 [in Chinese].
- Wang G. (2004). DEM analysis on stability of unsupported tunnels in jointed rock masses at different depth. *Chinese Journal of Rock Mechanics and Engineering*, 23(7), 1154–1157 [in Chinese].
- Wu Y. and Chai J. (2000). Analysis of 3-D model of coupled seepage and stress fields in fracture network of rock mass. *Journal of Xi'an University of Technology*, 16(1), 1–6 [in Chinese].
- Yang H. and Wang M. (2006). Numerical simulation of seepage in deep-buried long and big tunnels. *Chinese Journal of Rock Mechanics and Engineering*, 25(3), 511–519 [in Chinese].

# 3D Finite Element Simulation of Complex Static and Dynamic Fracture in Quasi-Brittle Materials

Xiangting Su<sup>1,2</sup>, Zhenjun Yang<sup>2\*</sup> and Guohua Liu<sup>1</sup>

<sup>1</sup>College of Civil Engineering and Architecture, Zhejiang University, Hangzhou 310027, China

<sup>2</sup>Department of Engineering, The University of Liverpool, Liverpool L69 3GQ, UK

**Abstract.** This study proposes a simple but effective finite element method to simulate complex 3D crack propagation in quasi-brittle materials such as concrete. Cohesive interface elements, characterized by softening traction-separation constitutive laws, are embedded into initial meshes to model potential cracks. The method is implemented in connection with Abaqus. Various concrete structures under static and dynamic loadings were modeled with excellent results compared with experiments.

**Keywords:** finite element method, 3D crack propagation, cohesive crack model, quasi-brittle materials, concrete structures, dynamic fracture

## 1 Introduction

Numerical modelling of fracture in quasi-brittle materials such as concrete has been an active research field since 1960s to investigate the cracking behaviour and to predict the residue load-carrying capacity of engineering structures. Among various methods, the finite element method (FEM) is predominant because of its high flexibility in modelling structures with complex geometries, various boundary and loading conditions, and complicated cracking patterns. Another advantage of the FEM is that the cracks can be effectively modelled by cohesive interface elements (CIEs) whose softening traction-separation constitutive laws are regarded as material properties. In general, two types of approaches are used to model cohesive crack propagation. The first ones are based on sophisticated re-meshing procedures that constantly change the meshes as cracks propagate (Wawrzynek and Ingraffea, 1989; Xie and Gerstle, 1995; Yang and Chen, 2004; Yang and Xu, 2008). For problems with crack paths unknown a priori, objective crack propagation criteria are needed to judge when and in which direction a crack

---

\* Corresponding author, e-mail: zjyang@liv.ac.uk

propagates. This usually involves calculation of stress intensity factors and stresses at crack tips, whose accuracy can only be ensured by fine crack-tip meshes or using singular elements, which in turn exacerbate the complexity of the remeshing procedure. It is also very difficult for the remeshing-based approaches to deal with complex crack propagation situations, such as multiple cracking and 3D problems. Indeed, the success of the remeshing-based approaches has been largely limited to 2D static fracture problems with single or a few cracks, although they are computationally efficient because a relatively small number of nonlinear CIEs are inserted into the mesh. Another type of approaches pre-insert or pre-embed CIEs between the finite elements in the initial mesh (Camacho and Ortiz 1996; Yang et al., 2009). Crack propagation is modelled by automatic opening and merging of the CIEs under applied loadings. Neither remeshing procedures nor crack propagation criteria are needed. Complex crack propagation can be modelled. However, these approaches limit the cracks on the finite element edges or surfaces and the predicted crack patterns may thus be mesh-dependent. Another disadvantage is the high computational cost due to the use of large number of nonlinear CIEs. These disadvantages limit their applicability considerably.

This study develops a numerical method to simulate complex 3D crack propagation in quasi-brittle materials under static and dynamic loadings. This method pre-inserts a special type of CIEs called “cohesive elements” in Abaqus (2007) to model potential cracks. An efficient algorithm was devised to insert these CIEs into FE meshes consisting of various types of solid elements. The method is simple to implement and its effectiveness is validated by modelling various fracture problems of concrete structures.

## 2 Modelling Procedure

The proposed method involves the following procedure:

1. Meshing the domain with 3D solid elements using Abaqus/CAE.
2. Inserting CIEs into the initial mesh. This is done by a small computer program. Solid elements including C3D4, C3D6 and C3D8 can be dealt with. Both 6-node and 8-node cohesive elements (COH3D6 and COH3D8) can be inserted. Figure 1(a), 1(b) & 1(c) show a mesh with solid elements only, the mesh after CIEs are inserted and the 3D CIEs respectively.
3. Solving the problem using Abaqus/Explicit solver. The authors' experience shows that the Abaqus/Standard solver often fails in divergence shortly after the peak load is reached for many fracture problems. It is thus suggested that the Abaqus/Explicit solver be used for both static and dynamic problems.

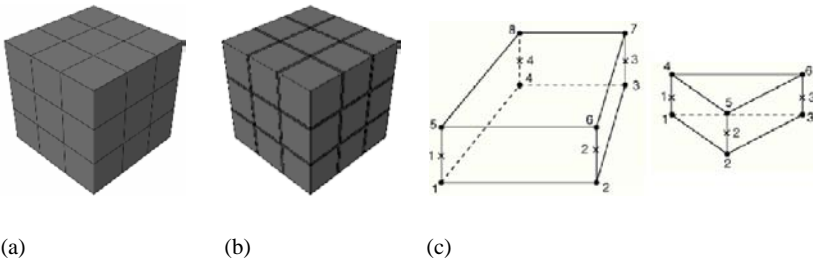


Figure 1: (a) A mesh without CIEs; (b) A mesh with CIEs inserted; (c) CIEs (COH3D8 and COH3D6) in (Abaqus, 2007)

### 3 Numerical Examples

#### 3.1 Wedge Splitting Test

The first example modelled is a concrete wedge splitting test carried out by Trunk (Trunk, 2000). The geometry and the loading condition are shown in Figure 2(a). The concrete has Young’s modulus  $E=28300$  MPa, Poisson’s ratio  $\nu=0.2$  and mass density  $\rho=2.5\times 10^6$  kg/mm<sup>3</sup>. A bilinear softening curve shown in Figure 2(b) is used to model the traction-separation relations of the CIEs. The area under the curve is the fracture energy  $G_f=0.49$ N/mm which is assumed as a material property.

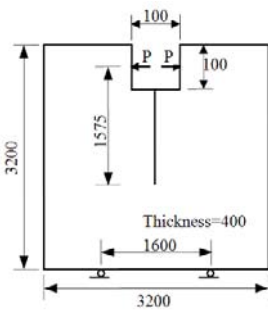


Figure 2(a). Wedge splitting test Specimen (unit: mm)

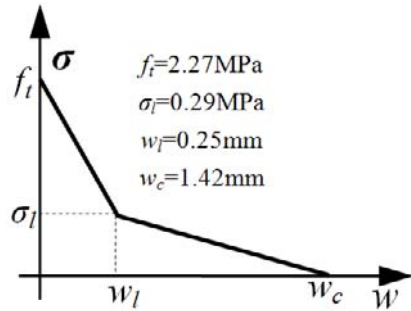


Figure 2(b). Bilinear normal traction-separation law for CIEs

Figure 3 shows a deformed mesh at the post-peak stage when the crack mouth opening displacement CMOD=4mm, where the black area represents the crack. The mesh consists of 774 C3D6, 1392 C3d8 solid elements, 480 COH3D6 and

1374 COH3D8 cohesive elements. The predicted crack is vertical and smooth as expected because the mesh is symmetric with respect to the central line. A random mesh was also modelled leading to a tortuous crack path. Figure 4 compares favourably the predicted CMOD-load curves with the test data.

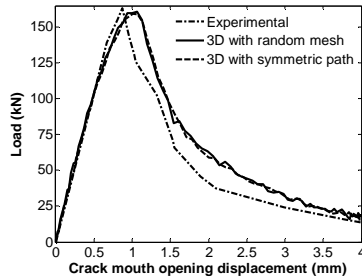
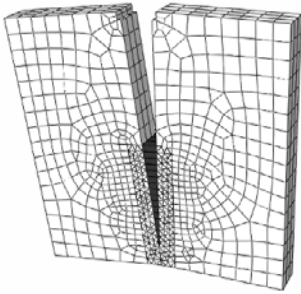


Figure 3. Deformed mesh (CMOD=4mm)

Figure 4. CMOD-load curves

### 3.2 Torsion of a Concrete Bar

The second example is a concrete bar under torsion tested by Brokenshire (Brokenshire, 1996). The geometry and the loading condition are shown in Figure 5(a). The concrete has  $E=35000$  MPa,  $\nu=0.2$  and  $\rho=2.5 \times 10^6$  kg/mm<sup>3</sup>. A linear softening curve (Figure 5(b)) is used to model the traction-separation relations of the CIEs with  $G_f=0.08$ N/mm.

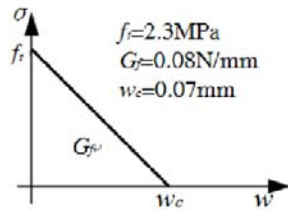
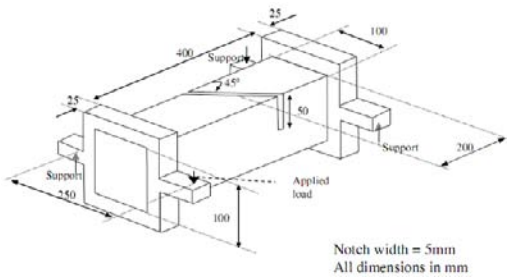


Figure 5(a). A concrete bar under torsion (reprinted from Jefferson et al (2004))

Figure 5(b). Linear traction-separation law for CIEs

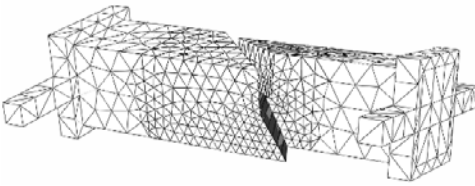


Figure 6. Deformed mesh (displacement at load point=1 mm)

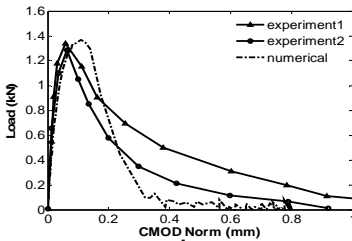


Figure 7. CMOD-load curves

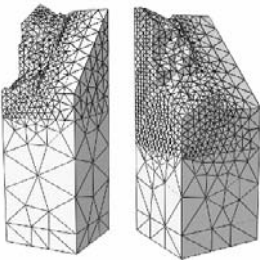


Figure 8. Predicted crack surfaces

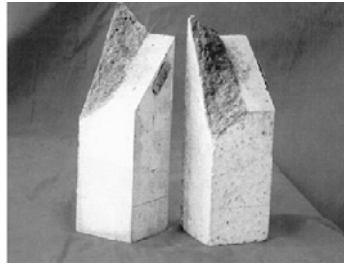


Figure 9. From the test (Brokenshire 1996)

To model the complex crack surface, C3D4 elements were used to model the concrete bulk and COH3D6 to model the crack. A random mesh with 10123 solid elements and 16612 cohesive elements was modelled. A deformed mesh is shown in Figure 6 when the displacement at load point is 1mm at the post-peak stage. The predicted CMOD-load curve is compared with the experimental data in Figure 7. It can be seen that the peak load is accurately predicted. The discrepancy between the post-peak curves is probably due to the use of the simple softening law (Figure 5(b)). The predicted crack surfaces of the two parts after the bar is broken are shown in Figure 8. They are in excellent agreement with the observed as shown in Figure 9.

### 3.3 Impact Test of a Concrete Beam

The third example modelled is a concrete beam under impact tested by Du et al. (Du et al., 1992). The geometry and the loading condition are shown in Figure 10(a). The concrete properties are:  $E=34480$  MPa,  $\nu=0.2$  and  $\rho=2.5 \times 10^6$  kg/mm<sup>3</sup>. An exponential softening curve (Figure 10(b)) used by Du et al. (Du et al., 1992) is used to model the traction-separation relations of the CIEs. The dynamic fracture energy  $G_f=0.152$  N/mm.

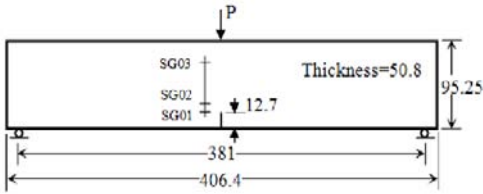


Figure 10(a). A concrete beam under impact

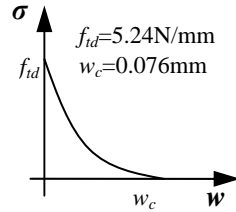


Figure 10(b). Exponential traction-separation law for CIEs

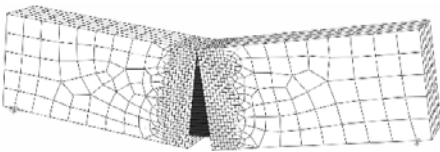


Figure 11 Deformed mesh (t=0.001s)

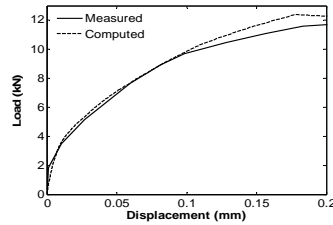


Figure 12 Deflection-load curves

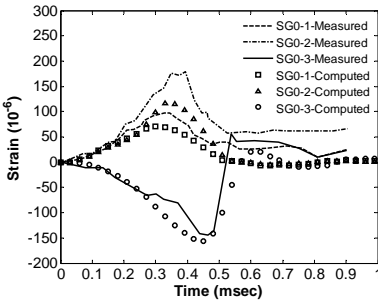


Figure 13. Strain histories

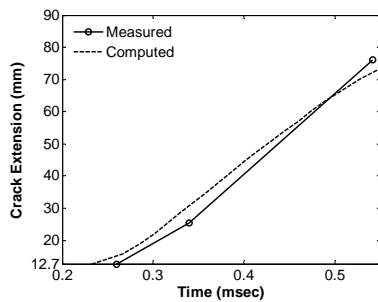


Figure 14. Crack-tip extension history

Figure 11 shows a deformed mesh at the post-peak stage when the time  $t=0.001$ s. The mesh consists of 3645 solid elements and 606 cohesive elements. Figure 12 compares favourably the predicted deflection-load curve with the test data. Figure 13 shows the measured and computed strain histories at three strain gauges (SG01, SG02 and SG03 in Figure 10(a)). The crack-tip extension histories are compared in Figure 14.

## 4 Conclusions

A simple but effective finite element modelling method has been proposed for simulating complex 3D cohesive crack propagation in quasi-brittle materials. An efficient algorithm and a simple computer program have been developed to automatically insert CIEs into FE meshes to model potential cracks. The method, implemented in connection with Abaqus, has proved promising in modelling complex 3D fracture in various concrete structures under static and dynamic loadings.

## Acknowledgement

This study was supported by EPSRC UK (No: EP/F00656X/1). XT Su's one-year visit to the University of Liverpool was supported by the China Scholarship Council and the National Natural Science Foundation of China (No. 50579081).

## References

- Abaqus 6.7, User documentation, Dessault systems, 2007.
- Brokenshire D.R. (1996). A study of torsion fracture tests, PhD Thesis, Cardiff University, U.K.
- Camacho G.T. and Ortiz M. (1996). Computational modelling of impact damage in brittle materials. *International Journal of Solids and Structures* 33(20-22):2899-2938.
- Du J., Yon J.H., Hawkins N.M. et al (1992). Fracture process zone for concrete for dynamic loading. *ACI Materials Journal* 89(3):252-258.
- Jefferson A.D., Barr B.I.G., Bennett T. and Hee S.C. (2004). Three dimensional finite element analysis of fracture tests using the Craft concrete model. *Computers and Concrete* 1(3):261-284.
- Trunk B. (2000). Einfluss der Bauteilgrösse auf die Bruchenergie von Beton, AEDIFICATIO Publishers, Immentalstrasse 34, D-79104, Freiburg, 2000 [in German].
- Wawrzynek P.A. and Ingraffea A.R. (1989). An interactive approach to local remeshing around a propagation crack. *Finite Element in Analysis and Design* 5:87-96.
- Xie M. and Gerstle W.H. (1995). Energy-based cohesive crack propagation modelling. *ASCE Journal of Engineering Mechanics* 121(12):1349-1458.

- Yang Z.J. and Chen J.F. (2004). Fully automatic modelling of cohesive discrete crack propagation in concrete beams using local arc-length methods. *International Journal of Solids and Structures* 41(3-4):801-826.
- Yang Z.J. and Xu X.F. (2008). Heterogeneous cohesive crack model for quasi-brittle materials considering random fracture properties. *Computer Methods in Applied Mechanics and Engineering* 197(45-48):4027-4039.
- Yang Z.J., Su X.T., Chen J.F. and Liu G.H. (2009). Monte Carlo simulation of complex cohesive fracture in random heterogeneous quasi-brittle materials. *International Journal of Solids and Structures*, under review.

# A Practical Method to Determine Critical Moments of Bridge Decks Using the Method of Least Squares and Spreadsheets

Jackson Kong<sup>1\*</sup>

<sup>1</sup>Division of Building Science and Technology, City University of Hong Kong, Hong Kong

**Abstract.** In this paper, a simple yet practical and direct method is presented for the determination of critical bending moments of bridge decks subject to traffic loads by taking the advantages of the concept of influence surfaces and the versatility of commercial FE software. The influence surfaces are obtained by putting unit loads across the region concerned and the corresponding computed results are exported to a spreadsheet. A least square fit to the classical thin-plate solution, based on the computed results can be easily obtained. Based on such a least-square solution, the locations and the corresponding critical moments for different types of designed loads can be calculated exactly by using a simple and readily available optimization tools in Excel. Comparing with conventional approaches in determining critical moments, the method is simple yet versatile and reliable, and it does not require any complicated mathematics or special software for practicing engineers to implement. Such an approach would lead to a more reasonable estimation of stresses in bridge decks or other plate-type structures which are subject to various moving loads with different arrangements.

**Keywords:** influence surfaces, critical moments, bridge decks, Excel, spreadsheets

## 1 Introduction

Structures are subject to dead load and live load; the latter refers to loads which would act on various possible positions. It is very often necessary for practicing structural engineers to determine how stresses/deformation at some critical locations of the structures would vary according to the positions of live loads. For simple structures and simple loadings, engineers could easily assign live loads to positions that would generate the most critical stress components concerned at the critical locations of the structure, based on experience. For complicated structures

---

\* Corresponding author, e-mail: a8990276@graduate.hku.hk

like a bridge deck under traffic loads or similar plate-type structures however such a determination is not always obvious, and two common approaches are usually adopted in practice, namely 1) a manual method by using influence surface charts available in the literature. The method is simple and has the advantage that the chart can be applied for different types of designed loads. However, it suffers from the drawback that such influence surface charts are readily available only at a limited number of locations for uniform plates with simple boundary conditions and geometries. For a box girder bridge as shown in Figure 1 however, simplifications and assumptions are necessary to be made in order to apply these influence surface charts to these structures; 2) alternatively, the designed load is repeatedly placed on various locations of the structure and the corresponding results are computed by commercial finite element software. Critical stresses can be found from the envelope of the computer results. Despite the simplicity and versatility of this approach, a lot of input data processing is necessary should a wide range of designed load positions are used with a fine mesh. The method becomes very tedious in practice, particularly when several designed loads need to be taken into consideration.

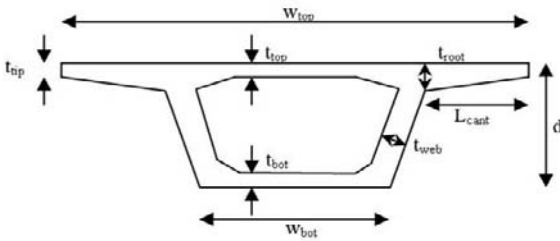


Figure 1. Box girder with non-uniform top flange thickness

In this paper, a simple yet practical and direct method is presented for the determination of critical bending moments of bridge decks subject to traffic loads by using influence surfaces generated from commercial FE software. The influence surfaces are obtained by putting unit loads across the region concerned and the corresponding computed results are exported to a spreadsheet. A least square fit to the classical thin-plate solution, based on the computed results can be easily obtained. Based on such a least-square solution, the locations and the corresponding critical moments for different types of designed loads can be calculated exactly by using a simple and readily available optimization tools in Excel. Comparing with the two aforesaid common approaches, the method is simple, versatile and reliable, and it does not require any complicated mathematics or special software for practicing engineers to implement. Such an approach would lead to a more rea-

sonable estimation of stresses in bridge decks or other plate-type structures which are subject to various moving loads with different arrangements.

## 2 The Problem

Several general approaches have been proposed in the literature to determine influence surfaces. In particular, a simple method of equivalent loads, based on the reciprocal theorem of linear elastic systems (Orakdogan and Girgin, 2005; Shen, 1992) could be used to directly determine influence surfaces. The method is versatile and computationally more effective than the conventional “unit-load” method, but its applications, unfortunately, involves the explicit form of the strain-displacement functions of the finite elements used, which, for many commercial software, are usually not known to practicing engineers, thus hindering its wide applications in practice. In this study, the conventional unit-load method is used.

As a vehicle to illustrate the concept and procedure of the method proposed in this study, only a rectangular plate is considered (see Figure 2a). Influence surfaces are directly generated using commercial FE software; assuming that a unit load is applied successively to each of the  $n$  nodal points of the mesh, the corresponding influence surface of nodal stress,  $M_0$ , at a specified nodal point of the plate can be computed and represented by a column vector  $\{M_0^{fem}\}$  with  $n$  entries. This computed influence surface can be verified against influence surface charts available in the literature (Pucher, 1977).

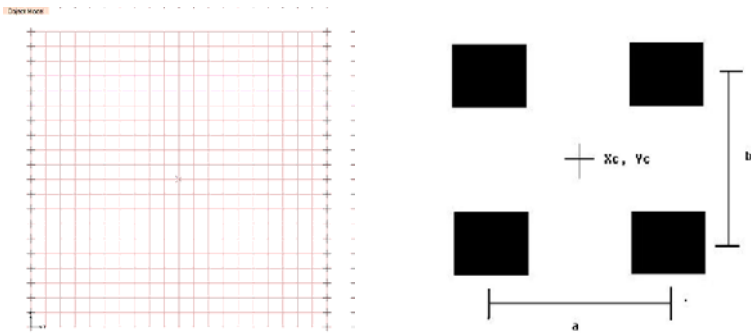


Figure 2(a). SAP model for a square plate

2(b). A designed vehicle with four square wheel loads separated by distances  $a$  and  $b$  apart.

Suppose that the plate is subject to a designed vehicle with four square wheel loads separated apart as shown in Figure 2b. Assuming that the critical bending moment at the center of the plate and the corresponding location of the vehicle is to be determined, this practical problem can be formulated as:

$$\text{Maximize } M_{x0}(x_c, y_c) \tag{1}$$

where  $(x_c, y_c)$  is the center of designed vehicle, and  $M_{x0}$  is the bending moment along x at the center of the plate, subject to the constraints that the vehicle shall travel within the physical boundary of the plate:

$$(x_L, y_L) < (x_c, y_c) < (x_U, y_U) \tag{2}$$

### 3 The Proposed Method

For a thin plate subject to a unit point load at  $(x_i, y_i)$ , the solution of the governing equation of plate bending can be written as the summation of a singular part and a non-singular part, i.e.,

$$w(x, y) = \beta r^2 \ln r / \pi D + \text{non - singular part} \tag{3}$$

where the singularity of the solution is attributed to the logarithmic function.  $\beta$  is a parameter to be determined. The non-singular part of the solution is determined by boundary conditions imposed. D denotes the bending stiffness of the plate and r represents the distance of a generic point  $(x, y)$  from the loaded position:

$$r = \sqrt{(x - x_i)^2 + (y - y_i)^2} \tag{4}$$

Bending moments  $M_x$ ,  $M_y$  and  $M_{xy}$  can be written in terms of the deflection and its derivatives, in particular:

$$M_x = D \left( \frac{\partial^2 w}{\partial x^2} + \nu \frac{\partial^2 w}{\partial y^2} \right) \tag{5}$$

Using equations (3) to (5), the bending moment influence surface for  $M_x$  at a generic point  $(x, y)$  due to a unit load at  $(x_i, y_i)$  can be written as:

$$\begin{aligned} &M_x(x, y; x_i, y_i) \\ &= \beta \left( \frac{\partial^2 (r^2 \ln r)}{\partial x^2} + \nu \frac{\partial^2 (r^2 \ln r)}{\partial y^2} \right) + P(x_i, y_i) \\ &= \beta W_p + P(x_i, y_i) \end{aligned} \tag{6}$$

in which the derivatives of the singular function  $W_p(x, y; x_i, y_i)$  can be easily worked out manually or using Matlab.

In this study, the non-singular part in (6) is approximated as a polynomial function of order n. A complete polynomial of order 7 is adopted, that is,

$$P(x_i, y_i) \approx [1, x_i, y_i, x_i^2, x_i y_i, y_i^2, \dots, y_i^7] \{\mathbf{a}\} \tag{7}$$

where  $\{\mathbf{a}\}$  is a column vector consisting of the corresponding 36 parameters to be determined. Together with  $\beta$ , a total of 37 parameters need to be found. Parameters  $\beta$  and  $\{\mathbf{a}\}$  are then determined by enforcing that the sum of the square of the difference between the moments calculated from (6) and (7) and those obtained from the finite element software is minimum, that is,

$$\text{Minimize } (\{M_{x_0}^{\text{fem}}\} - \{M_{x_0}^s\})^T (\{M_{x_0}^{\text{fem}}\} - \{M_{x_0}^s\}) \tag{8}$$

where  $\{M_{x_0}^{\text{fem}}\}$  is the column vector with n entries of the computed FE bending moment at the center of the plate due to a unit load placed successively at each of the n nodes.  $\{M_{x_0}^s\}$  comprises the center bending moment calculated from (6) and (7) due to a unit load applied at each of the n-1 nodal points, except the center of the plate, which moment cannot be calculated from (6) due to the singularity of  $W_p$  thereat. Denoting each term of the complete polynomial as  $P_i(x, y)$ , the column vector  $\{M_{x_0}^s\}$  can be written as

$$\begin{Bmatrix} M_{x_0}^s(x_1, y_1) \\ \dots \\ M_{x_0}^s(x_0, y_0) \\ \dots \\ M_{x_0}^s(x_n, y_n) \end{Bmatrix} = \begin{bmatrix} W_p(x_0, y_0; x_1, y_1) & P_1(x_1, y_1) & P_2(x_1, y_1) & \dots & P_{36}(x_1, y_1) & 0 \\ & 0 & 0 & 0 & \dots & 0 & 1 \\ & & & & \dots & 0 & \\ & & & & & & \\ W_p(x_0, y_0; x_n, y_n) & P_1(x_n, y_n) & P_2(x_n, y_n) & \dots & P_{36}(x_n, y_n) & 0 \end{bmatrix} \begin{Bmatrix} \beta \\ \alpha_1 \\ \dots \\ \alpha_{36} \\ M_{x_0}^s \end{Bmatrix}$$

$$\{M_{x_0}^s\} = [N] \{\gamma\} \tag{9}$$

where  $(x_0, y_0)$  is the center of the plate. Substituting (9) into (8) and differentiating with respect to  $\{\gamma\}$  gives:

$$([N]^T [N]) \{\gamma\} = [N]^T \{M_{x_0}^{\text{fem}}\} \tag{10}$$

Solving for  $\{\gamma\}$  gives:

$$\{\gamma\} = [K]^{-1} \{f\}$$

where  $[K] = [N]^T [N]$  is a square matrix of size 38 and its inverse can be easily computed using Excel.  $\{f\} = [N]^T \{M_{x_0}^{\text{fem}}\}$  is a column vector of the same length.

The bending moment at the center of the plate due to a an unit load at  $(x_i, y_i)$  is then given by:

$$\beta\left(\frac{\partial^2(r^2 \ln r)}{\partial x^2} + \nu \frac{\partial^2(r^2 \ln r)}{\partial y^2}\right) + [P(x_i, y_i)]\{\alpha\} \tag{11}$$

For a uniformly distributed wheel load  $w$  of area  $h \times h$ , the bending moment at the center of the plate can be found by integrating (11), that is:

$$M_{x_0} = \int_x^{x+h} \int_y^{y+h} \left(\beta\left(\frac{\partial^2(r^2 \ln r)}{\partial x^2} + \nu \frac{\partial^2(r^2 \ln r)}{\partial y^2}\right) + [P(x_i, y_i)]\{\alpha\}\right) dx dy \tag{12}$$

in which the closed form expression for the integral is found using Matlab. The location of each wheel load is defined by the center of the vehicle and the given separation of the wheel loads. The total bending moment due to the designed vehicle is then given by:

$$M_{x_0}(x_c, y_c) = \sum_{\text{numberofwheels}} M_{x_0} \tag{13}$$

Once the closed form expression of (12) is obtained, the optimization problem as defined by equations (1) and (2) method is implemented on Excel using its built-in function “Solver”. With Solver, engineers can find an optimal value of  $M_{x_0}(x_c, y_c)$ , i.e. equation (1), with constraints applied to the “design” variables  $(x_c, y_c)$  i.e. equation (2) to restrict the values.

### 4 Numerical Examples

Bridge decks of box girders were analyzed using the proposed method. SAP model of the whole bridge was used to determine the influence surface of bending moments at the center of the deck. It is found that, depending on the separation of the wheel loads and the size of the wheels, the critical locations of the vehicle that generate the optimal bending moment at various locations can be easily estimated. Due to the limited scope of the paper, details of numerical results, together with other forms of bridge decks like slab-on-girder bridge decks, will be presented in the Conference.

## Acknowledgement

The work described in this paper was partially supported by a grant from City University of Hong Kong (Project No. 7001774).

## References

- Orakdogan E., Girgin K.M. (2005) A Direct determination of influence lines and surfaces by FEM. *Structural Engineering and Mechanics*, 20(3), 279-292.
- Pucher A. (1977). *Influence surfaces of Elastic Plates*. Springer-Verlag, New York.
- Shen W. (1992) The generalized Muller-Breslau principle for higher-order elements. *Computers and Structures*, 44, 207-212.

*“This page left intentionally blank.”*

# Monte Carlo Simulation of Complex 2D Cohesive Fracture in Random Heterogeneous Quasi-Brittle Materials

Xiangting Su<sup>1,2\*</sup>, Zhenjun Yang<sup>2\*</sup> and Guohua Liu<sup>1</sup>

<sup>1</sup>College of Civil Engineering and Architecture, Zhejiang University, Hangzhou 310027, China

<sup>2</sup>Department of Engineering, the University of Liverpool, Liverpool L69 3GQ, UK

**Abstract.** This study develops a numerical method to simulate complex 2D crack propagation in quasi-brittle materials considering random heterogeneous fracture properties. Cohesive interface elements with softening traction-separation laws are inserted into the initial mesh to model potential cracks. The softening laws are modelled by spatially-varying Weibull random fields. Extensive Monte Carlo simulations of a concrete specimen under uni-axial tension were carried out. It was found that increasing the variance of the tensile strength random fields with increased heterogeneity led to reduction in the mean peak load and increase in the standard deviation. The developed method provides a simple but effective tool for assessment of structural reliability.

**Keywords:** random heterogeneity, quasi-brittle materials, cohesive elements, nonlinear fracture modelling, Monte Carlo simulation, finite element method

## 1 Introduction

Random heterogeneity of material properties exists intrinsically in many quasi-brittle materials such as concrete and fibre-reinforced polymer composites, due to random distribution of multiple phases. Experimental characterisation and computational modelling of the random heterogeneity from micro- to macro-scales, so as to determine the performance and reliability of structural systems, has become one of the most critical and challenging engineering problems (Oden et al, 2003). This study focuses on finite element modelling of fracture behaviour of these materials. An extensive literature review recently carried out by the authors (Yang et al, 2009) shows that, although tremendous efforts have been invested on numerical modelling of fracture considering random heterogeneous material properties, success is still largely limited to 2D small-sized problems under static loadings due to high complexities involved. Generating statistical responses using methods such

---

\* Corresponding author, e-mail: zjyang@liv.ac.uk

as Monte Carlo simulations (MCS) to evaluate the structural reliability has hardly been conducted. This study develops a finite element method to simulate complex 2D fracture process in quasi-brittle materials considering random heterogeneous fracture properties, in a view to critically assess the performance and reliability of structures under external loadings. The cracks are modelled by a special type of “cohesive elements” (COH2D4) in Abaqus (2007). The cohesive elements, only available in Abaqus Version 6.5 or higher, are designed to model bonded interfaces. Their effectiveness in modelling cracks has hardly been validated. Another intention of this study is to fully exploit the powerful pre/post-processing modules and standard/explicit solvers of Abaqus in modelling complex fracture problems. The softening laws of the cohesive elements are modelled as spatially-varying Weibull random fields. The statistical information of structural responses is obtained by extensive MCSs for a range of heterogeneity levels. A concrete specimen under uniaxial tension is modelled as a benchmark problem.

## 2 The Methodology

The proposed method involves the following procedure:

- (1) Meshing the domain using Abaqus/CAE and generate an input file;
- (2) Inserting cohesive elements into the initial mesh. This is done using a small in-house computer program. Figure 1a illustrates a mesh around a node in the initial mesh. The mesh after cohesive elements are inserted is shown in Figure 1b. Figure 1c illustrates the 2D four-node cohesive element;
- (3) Generating a Weibull random field of fracture properties;
- (4) Assigning the fracture properties to all the cohesive elements and generate an input file for Abaqus;
- (5) Solving the problem using Abaqus Standard/Explicit solvers; and
- (6) Repeat steps (3) to (5) for a sufficient number of random fields, as required by the MCS method, and conduct statistical analysis.

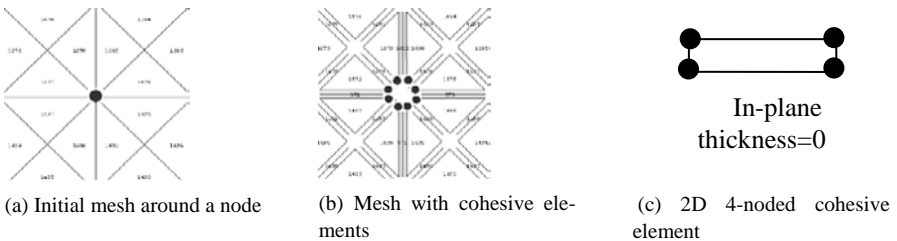


Figure 1. Inserting cohesive elements in the initial mesh

This procedure can be automated by running a batch file.

The constitutive behaviour of the cohesive element COH2D4 in Abaqus can be described by softening traction-separation laws in normal and shear directions.

The resilient feature of COH2D4 is that its formulation is based on the damage mechanics framework, within which the stiffness upon unloading and reloading are degraded as the separations increase, due to irreversibly progressive damage. The damage is characterised by a scalar index  $D$  representing the overall damage of the crack caused by all physical mechanisms.

### 3 Numerical Example

A concrete bar under uniaxial tension was modelled as an example. The geometry, boundary conditions and bulk material properties are illustrated in Figure 2.

The elastic bulk of concrete was modelled using 3/4-noded plane stress elements. The cracks were modelled using the 4-noded cohesive elements. Two meshes were modelled to investigate the mesh dependence of results. The coarse mesh (Figure 3a) has 2104 nodes and 1000 cohesive elements, and the fine mesh (Figure 3b) has 8936 nodes and 4000 cohesive elements.

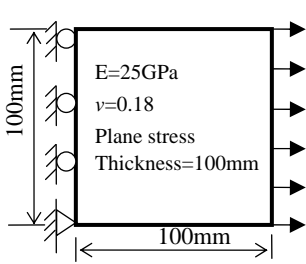


Figure 2. A concrete specimen

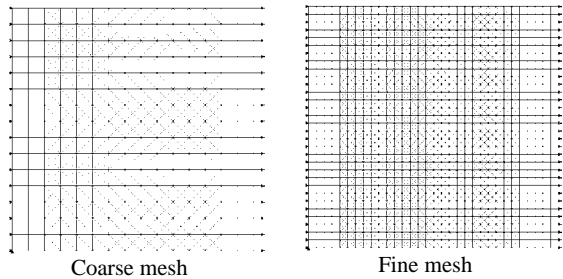


Figure 3. Initial finite element meshes

The concrete tensile strength  $t_{n0}$  was modelled by Weibull random fields with mean 3.5MPa. The fracture energy  $G_f=0.15\text{N/mm}$  was assumed constant. This implied that the failure crack opening displacement was also random fields. Due to the lack of experimental data, the shear fracture properties were assumed to be the same as the normal ones: shear strength  $t_{s0}=t_{n0}$  and shear fracture energy  $G_{fl}=G_f=0.15\text{N/mm}$ , indicating that the normal fracture properties were completely correlated to the shear ones. The fracture energies and more generally, the softening laws could also be modelled as random fields with ease, as in a previous study based on remeshing (Yang and Xu, 2008).

For one Monte Carlo simulation, 500 Weibull random fields of tensile strength were generated and mapped to the coarse mesh. Three correlation lengths  $l_c=6.25\text{mm}$ ,  $12.5\text{mm}$  and  $25\text{mm}$  were modelled. They are within the range of aggregate sizes (10-40mm) normally used in concrete. Three values of variance for  $t_{n0}$  and  $t_{s0}$ ,  $\text{Var}=0.1\text{MPa}^2$ ,  $1.0\text{MPa}^2$  and  $1.5\text{MPa}^2$ , were modelled for each Weibull random field. In total, 9 MCS were carried out with 4500 random fields generated

and the same number of nonlinear analyses conducted for the coarse mesh. A few analyses were also conducted for the fine mesh.

## 4 Results and Discussion

### 4.1 Crack Propagation Process and Crack Patterns

Figure 4 illustrates the fracture process modelled using the fine mesh and a typical Weibull random field (RF1) of tensile strength with  $\text{Var}=1.5\text{MPa}^2$  and  $l_c=12.5\text{mm}$ . The random field (Figure 4a) is described by the filled contours, with deep blue areas indicating low tensile strength (e.g., defects, voids etc.) and dark red areas representing high tensile strength (e.g., strong aggregates). When the displacement  $d$  is small (Figure 4b), a number of small visible cracks, displayed by the opened cohesive elements in red (the red colour represents high damage index  $D$  ( $D=1$  means complete failure)), initiate in the blue areas at the boundary and inside the domain. Closer examination of the deformed mesh shows that more cohesive elements have experienced damage but are invisible because their damage index  $D$  is small. As  $d$  increases, the visible cracks continue to widen. A few vertical cracks are then linked by diagonal cracks and merged into major cracks, while the other cracks are closed due to stress redistribution (Figure 4c). The specimen fails by a major crack passing through the weakest area (Figure 4d). This fracture process looks very realistic. Different crack propagation processes and crack patterns were predicted using different random fields.

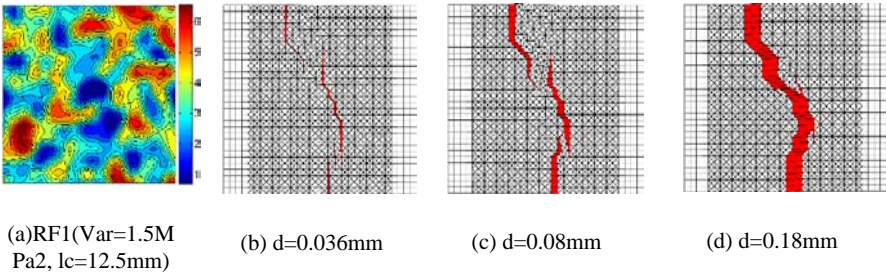


Figure 4. Fracture process predicted using a typical random field RF1: fine mesh

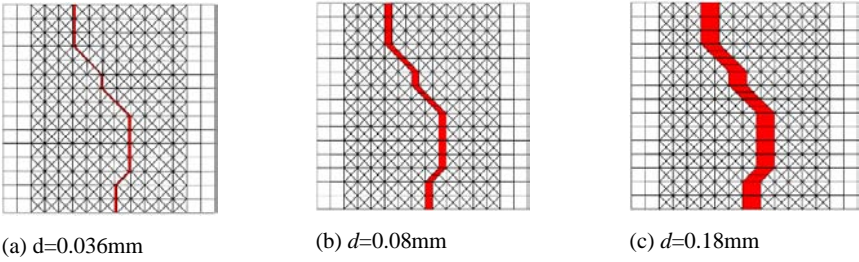


Figure 5. Fracture process predicted using random field RF1: coarse mesh

### 4.2 Mesh Dependence of Results

The random field RF1 in Figure 4a was also mapped to the coarse mesh and the fracture process predicted is shown in Figure 5. An excellent similarity can be seen between Figures 4b-d and Figures 5a-c. The load-displacement curves from the coarse and fine meshes are also very close.

### 4.3 Results of MCS and Implications on Structural Design

Three examples of MCS results are shown in Figures 6a-c, using  $Var=0.1MPa^2$  and 3 correlation lengths respectively. The mean load-displacement curve, the mean value and the standard deviation of the peak load are also calculated.

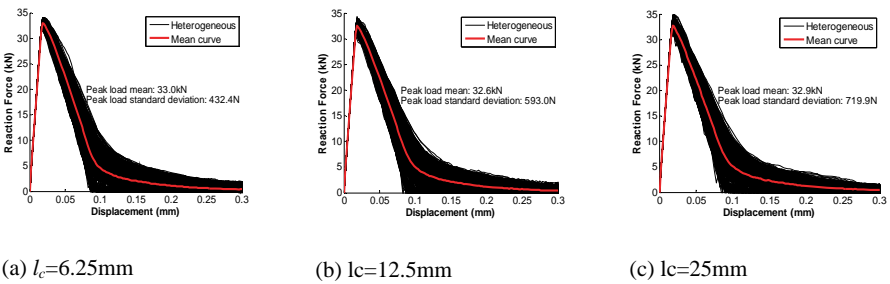


Figure 6. Load-displacement curves from MCS with 500 samples ( $Var=0.1MPa^2$ )

The mean load-displacement curves from all 9 MCS are shown in Figures 7a-c. Clearly the variance has a significant effect on the peak load of the mean load-displacement curves. The average peak load from the three variances is 32.8MPa, 29.8MPa and 26.1MPa respectively. For all the correlation lengths investigated, a higher variance results in a lower peak load. This is because more cohesive ele-

ments in larger areas are mobilised to resist fracture when the variance is small, leading to a higher mean peak load. When the variance is large, the “weakest link” or the crack path can be more easily found because fewer weak cohesive elements contribute to fracture resistance, which results in lower mean peak load. This means a higher heterogeneity in the material properties results in structures with lower strength.

Figures 8a-c show three examples of the probability density functions (PDF) of the peak load from MCS. The mean, standard deviation (SD) and the best-fit Gaussian PDF curve  $p(x)$  are also shown. It can be seen that the peak loads from MCS closely follow the Gaussian distribution. A higher variance leads to lower mean peak load (thus lower strength). It also increases the standard deviation of the peak load, which is an indicator of lower structural reliability.

The probability density curves  $p(x)$  in Figures 8a-c may be used in reliability analysis of existing structures. For example, assuming the external load  $F_d$  is known, the structural reliability can be calculated as

$$P = \int_{F_d}^{\infty} p(x) dx \tag{1}$$

or the failure probability as  $(1-P)$ .

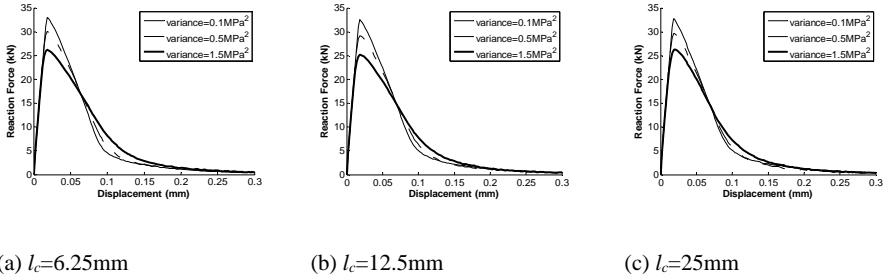


Figure 7. Mean load-displacement curves: effect of variance

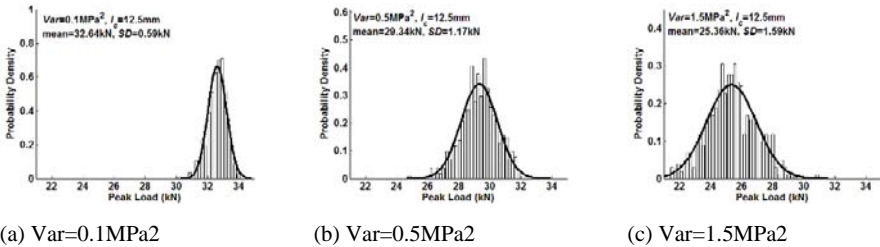


Figure 8. Probability density of the peak load:  $l_c=12.5\text{mm}$

Table 1. Statistics of Monte Carlo simulation results ( $l_c=12.5\text{mm}$ )

Variance of tensile strength (MPa <sup>2</sup> )	Mean of peak load (kN)	SD of peak load (kN)	Failure probability (Fd= 27kN)
0.1	32.64	0.59	0%
0.5	29.34	1.17	2.28%
1.5	25.36	1.59	84.88%

Table 1 summarises the mean and the standard deviation of the peak load and the failure probability against  $F_d=27\text{kN}$  as an example for 3 MCS.

## 5 Conclusions

A modelling methodology has been developed for simulating complex 2D cohesive fracture in quasi-brittle materials, taking into account the random heterogeneity of material properties. Extensive Monte Carlo simulations have demonstrated that an increase of the variance in the Weibull random fields of tensile strength with increased heterogeneity leads to a reduction in the mean peak load and an increase in the standard deviation. The developed method has the potential of becoming a simple but effective numerical tool for assessing structural reliability against external loadings.

## Acknowledgements

This study was supported by EPSRC UK (No: EP/F00656X/1). XT Su's one-year visit to the University of Liverpool was supported by the China Scholarship Council and the National Natural Science Foundation of China (No. 50579081).

## References

- Abaqus 6.7 (2007). User documentation, Dessault systems.
- Oden J.T., Belytschko T., Babuska V., Hughes T.J.R. (2003). Research directions in computational mechanics. *Computer Methods in Applied Mechanics and Engineering* 192:913-922.
- Yang Z.J. and Xu X.F. (2008). Heterogeneous cohesive crack model for quasi-brittle materials considering random fracture properties. *Computer Methods in Applied Mechanics and Engineering* 197(45-48): 4027-4039.
- Yang Z.J., Su X.T., Chen J.F. and Liu G.H. (2009). Monte Carlo simulation of complex cohesive fracture in random heterogeneous quasi-brittle materials. *International Journal of Solids and Structures*, under review.

*“This page left intentionally blank.”*

# Short-Term Axial Behavior of Preloaded Concrete Columns Strengthened with Fiber Reinforced Polymer Laminate

Dechun Shi<sup>1\*</sup> and Zheng He<sup>1</sup>

<sup>1</sup>College of Resource and Civil Engineering, Northeastern University, Shenyang 110004, China

**Abstract.** The behavior of short-term axially preloaded concrete columns with FRP confinement under axial loading is simulated by using finite element software ABAQUS, and the computing results are compared with the test ones. The comparisons show that proper analysis model can accurately simulate the axial compressive property of FRP-confined concrete columns. Then a parameter analysis is carried out to investigate the impact of longitudinal reinforcement ratio, volumetric lateral reinforcement ratio, concrete strength and restrain stiffness of FRP on the bearing capacity of columns and the load-strain curve under different pre-load stress levels. The results have indicated that, the confinement effect decreases as the preloading stress level increases. Under low preloading stress level, the reduction of load bearing capacity is less than 5 percent, and the deformation capacity can be greatly improved by enhancing the restrain stiffness of FRP. Under high preloading stress level, the reduction of load bearing capacity does not have the trend to decrease as the increasing of restrain stiffness of FRP.

**Keywords:** preloading, fiber reinforced polymer, confined concrete, columns, axial compression, ABAQUS

## 1 Introduction

Repairing or strengthening of in-service structures has been popular than ever in engineering practice. As a result of lightweight, high-strength, anti-corrosive quality, convenient for construction etc, fiber reinforced polymer (FRP) materials are more and more widely applied to repair or strengthen concrete structures. As for the subject of FRP-confined concrete short columns, most of the existing research does not take into account the impact of existing preloading stress and consensus in understandings the ultimate load bearing capacity of columns after strengthen-

---

\* Corresponding author, e-mail: hezheng1971@gmail.com

ing with preload has not been achieved. Takeuti et al (2008) think that preload can improve the load bearing capacity while others (Laine, 2008) consider it may reduce the confinement effect. Maalej et al (2008) believe that it does not have significant difference from direct reinforcement. Song (2008) holds the opinion that the load bearing capacity is related to preload stress level, which firstly increases and subsequently reduces. Finite element analysis has become a powerful tool solve a variety of complex structural problems. In this paper, the axial compressive behavior of FRP-confined concrete columns under different preload stress level is simulated and analyzed by using the finite element method through the ABAQUS program and the computing results are compared with the results obtained from tests. The comparisons indicate that finite element method can accurately predict the axial compressive property of FRP-confined concrete columns. In addition, the influence of main parameters is analyzed and the effect of preload stress level on the ultimate load bearing capacity is obtained.

## 2 Finite Element Analysis

### 2.1 Analysis Model

In this paper, the finite element program ABAQUS is used to perform the entire progress analysis of axial compression. The constitutive model used in this paper for concrete is the damaged plasticity model included in ABAQUS. The model include two types of failure mechanisms: cracking in tension and crushing in compression. But this model does not consider the plastic volumetric compression, because it is not a cap model. This deficiency may cause a certain degree of error in predicting the deformation of concrete with FRP confinement. The uniaxial stress-strain relation of concrete adopts Guo's compressive model and Jiang Jianjing's tensile model, as shown in Figures 1 and 2, respectively. Because the finite element model involves in the interaction between FRP and concrete, concrete and reinforcement, so the 3D, eight-node linear element C3D8 in ABAQUS is utilized for modeling the concrete column. For three-dimensional problem, hexahedral element can achieve the best results at the lowest cost.

The two-node linear truss element T3D2 is used for modeling the reinforcement. This element is often used to simulate long, slender structural members that can transmit only axial force, without consideration of moment. The reinforcement is considered to behave in an ideal elastic-plastic manner. In ABAQUS, the reinforcement is embedded into concrete through embedded region method. The software will automatically search for the geometric relationship between the embedded element and the host element. Reinforcement simulated in this way can be shown alone and easy for post-progressing, which is better than rebar layer method.

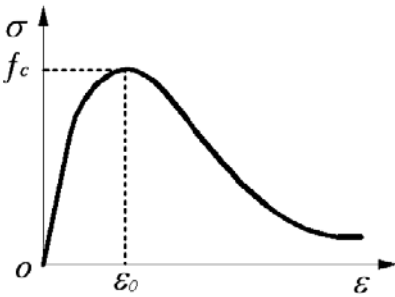


Figure 1. Compressive constitutive model of concrete

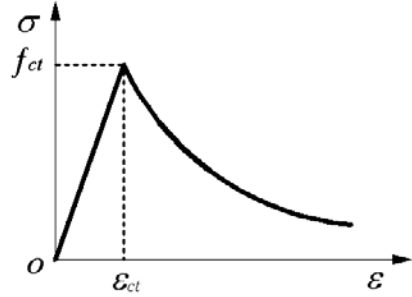


Figure 2. Tensile constitutive model of concrete

The four-node linear membrane element is used to modeling the FRP. This element can offer strength in the plane but have no bending stiffness. The FRP material is linear elastic until failure and we only consider the strength of fiber direction. Thus, the membrane element can only bear the ring-direction tension caused by the expansion of concrete, which accords with the loading condition of FRP in test. The Stress nephogram of FRP is shown as Figure 3. On the basis of test results, when the quality of adhesive is good and construction quality can be guaranteed, bond-slip between FRP and concrete will not happen. So the interaction between FRP and concrete is modeled without considering debonding.

The key point of establishing finite element model of axially preloaded concrete columns is to solve the secondary load effect. In this paper, element birth and death in ABAQUS is adopted to model preloading questions. In the program, we set two analysis steps. In the first step, preload is imposed by force loading method, when the FRP is set to “death”, without taking into account its contribution to the global stiffness and concrete is in uniaxial compression state. In the second step, the displacement loading control method is used, when FRP is set to “birth” and begin to carry load and concrete is in triaxial stress state. So element birth and death can simulate the secondary loading questions. Moreover, after introduction of element birth and death, meshing of reinforcement, concrete and FRP can be completely determined before calculation. We can avoid remeshing operation in calculation and only to remove or add the strengthening element. So the complexity of secondary loading problem is greatly simplified.

## 2.2 Boundary Conditions

The boundary conditions for column are fixed at both ends. In order to extraction the force in the second analysis step more conveniently, the top of the column is coupled with pre-set reference point and the boundary condition of the top can be

applied to the reference point. The calculation model is shown in Figure 4. Specimen is divided into four parts for better mesh quality.

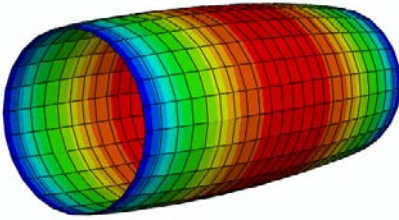


Figure 3. Stress nephogram of FRP

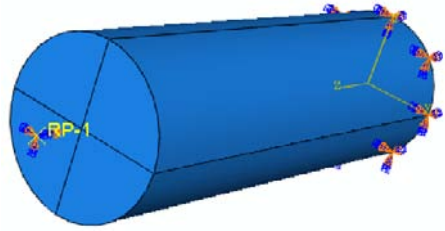


Figure 4. Analysis model

In the calculation, if either of the following two situations appears, we consider the columns achieve the limit state and suspend the calculation. One is that FRP reaches the fracture strain in test. The other is that Iteration does not converge even though the load step is reduced to the lower limit of ABAQUS. At this point, a great deal of plastic deformation has generated to achieve the damage limit state. In this paper's analysis, all examples reach failure as case one.

### 3 Comparisons with Test Results

#### 3.1 Comparisons with FRP-Confined Columns

Through consulted the relative references (Lam et al., 2004; Lam et al., 2006; Teng et al., 2007; Teng et al., 2002; Xiao et al., 2000; Berthet et al., 2005; Zhang et al., 2000; Miyauchi et al., 1997; Theriault et al., 2004; Howie et al., 1994; Tao et al., 2006), 141 test data of FRP-confined concrete columns are collected. Then corresponding finite element analysis models are established to calculate the ultimate compressive strength. It should be point out that if the original text does not give FRP fracture strain in test, reduction factor is used to calculate it from theoretical flatwise tensile strain according to ACI guide for design (ACI 440.2R-XX., 2007). Through statistical analysis, the average value of ratio of ultimate compressive strength calculated to test results is 0.988 and the coefficient of variation was 0.092. Thus, we can see that the finite element model set up in this article can give a good prediction of ultimate strength of FRP-confined concrete columns. The contrast of calculated values and experimental values is show in Figure 5.

### 3.2 Comparisons with Short-Term Preloaded Columns with FRP Confinement

Based on the model of FRP-confined columns, the axial compression performance of preloaded concrete columns strengthened with FRP is investigated through the introduction of element birth and death. Figure 6 shows the comparison of ultimate strength calculated and data from short-term preloading tests done by Pan (2007) and Jin (2008). The discrepancies for nearly all of specimens are less than 10 percent. Through statistical analysis, the average value of ratio of ultimate compressive strength calculated to test results is 0.953 and the coefficient of variation is 0.054. Because the whole process load-strain curves mastered are very few, we only give the comparisons of load-strain curves for specimens BS4-2 and SS4-2 in Jin's (2008) test. As Figure 7 shows, the prediction results and test data agree well with each other. The finite element model in this paper can give a good description of axial compressive behavior for FRP-confined concrete columns no matter with or without preload.

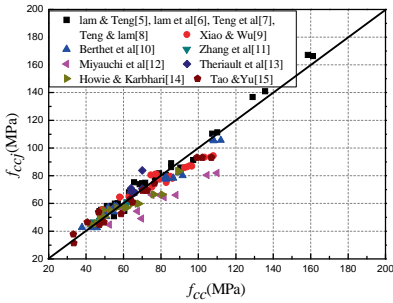


Figure 5. Comparison with columns without preload

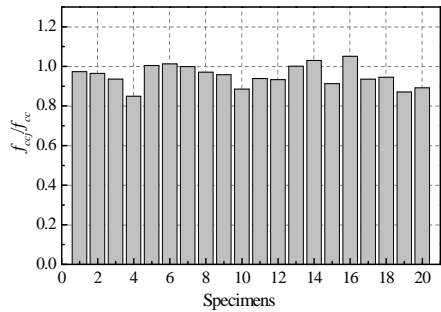


Figure 6. Comparison with columns with preload

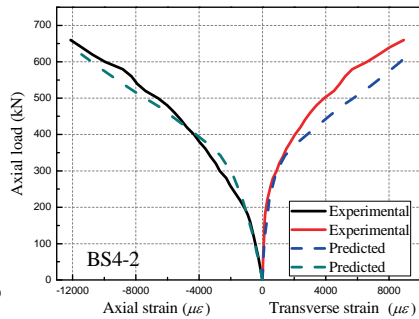
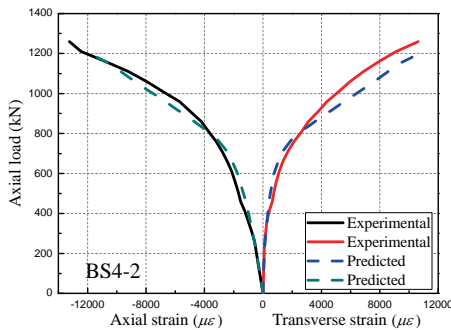


Figure 7. Comparison of load-strain relation

## 4 Parameter Analysis

In order to understand the impact of preload stress level on the FRP-confined concrete columns, the finite element model is applied to perform a parameter analysis in which reinforcement ratio, concrete strength and restrain stiffness of FRP are included. There is one point to be emphasized: when the preload stress level exceeds 0.7, the concrete column has generated a certain amount of crack before strengthen, resulting in local deformation of FRP in crack. This is uncoordinated with the deformation compatibility assumption of concrete and FRP in ABAQUS. So the prediction value in this situation only gives the trend of change and its value should be higher than the actual value. The basic parameters in calculation are  $D=150\text{mm}$ ;  $H=500\text{mm}$ ; the elastic modulus of FRP is  $250\text{GPa}$ ; the fracture strain of FRP is 0.011; the thickness of concrete cover is  $20\text{mm}$ .

### 4.1 Reinforcement Ratio

The elastic modulus of reinforcement is  $2e^5\text{Mpa}$ . The yield strength of stirrup is  $235\text{MPa}$  and the space is  $92\text{mm}$ . The yield strength of longitudinal reinforcement is  $335\text{MPa}$  and the number is six, arranged evenly along the circumference. The concrete strength is  $35\text{MPa}$  and the thickness of FRP is  $0.111\text{mm}$ . When preload stress level is 0.6, we study the effect of longitudinal reinforcement ratio at first. The diameter of stirrup is fixed at  $6\text{mm}$  and the cross-section of longitudinal reinforcement takes 10, 20, 30, 40, 50,  $60\text{mm}^2$ , respectively. Then the load bearing capacity is calculated in turn and the results are shown in Figure 8. Secondly, the effect of volumetric percentage of stirrups is investigated. Fix the diameter of longitudinal reinforcement at 8 and the cross-section of stirrup takes 5, 10, 15, 20, 25,  $30\text{mm}^2$ , respectively. The results calculated are shown in Figure 9. It's easy to find out that the load bearing capacity of preloaded concrete columns is approximate linear relationship with longitudinal reinforcement ratio and volumetric percentage of stirrups.

### 4.2 Concrete Strength

The thickness of FRP is  $0.222\text{mm}$ . The concrete strength takes 25, 35, 45,  $55\text{MPa}$ , separately. Reinforcement is not considered in this part. Then, the axial compressive behavior is simulated in software and the results are shown in Figure 10. Figure 11 is the curve of improvement of strength to strain when the preload stress level is 0.5.

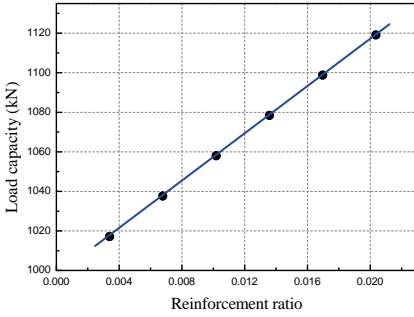


Figure 8. The relation of load bearing capacity and longitudinal reinforcement ratio

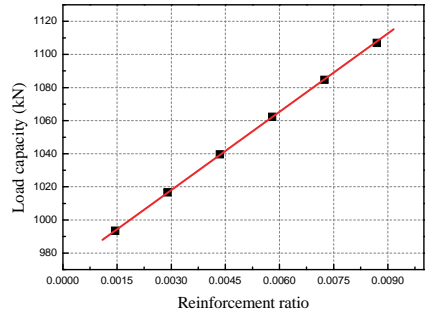


Figure 9. The relation of load bearing capacity and volumetric percentage of stirrups

As shown in Figure 10, with the improvement of concrete strength, regardless of preload stress level, the increase amplitude of ultimate compressive strength gradually reduces. For example, when the preloading stress level is 0.5, for concrete strength of 25MPa and 55MPa, the increase amplitude of ultimate compressive strength decreases from 108% to 47%. But it is not evident that different concrete strength has effect on the improvement under different preload stress level. Besides, as the increase of preload stress level, reduction of improvement has an acceleration trend. So under high stress level, ultimate compressive strength decays faster. From Figure 11, with the improvement of concrete strength, axial deformation capacity decrease gradually. Thus, for high-strength reinforced concrete column, in addition to improving strength, we must also consider the improvement of its deformation capacity. In addition, the slope of deformation curve has a trend to increase in the last, which is caused by the concrete model's defect as described above. So the strain value calculated may be a certain degree of error.

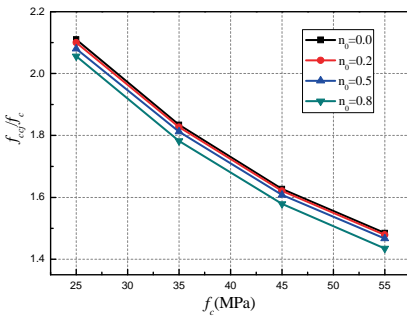


Figure 10. Variation of improvement with concrete strength

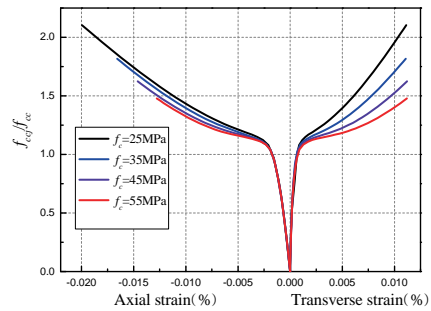


Figure 11. Variation of improvement with strain,  $n_0=0.5$

### 4.3 Restrain Stiffness of FRP and Preload Stress Level

It is known from calculation that when the product of FRP thickness and elastic modulus is the same, the confinement effect for the same column is completely identical. This can be attributed to the effect of FRP restrain stiffness  $E_f$ . Therefore, the thickness of FRP layer takes 0.111, 0.222 and 0.333mm, respectively, which is equivalent to fixing FRP thickness and changing its elastic modulus. The concrete strength is 35MPa. Then, the ultimate compressive strength is calculated under preload stress level 0, 0.15, 0.3, 0.45, 0.6, 0.75 and 0.9 separately. The results are shown in Figure 12. Figure 13 is the curve of improvement of strength to strain when the preload stress level is 0.6.

As shown in Figure 12, with the improvement of FRP thickness, the ultimate compressive strength of columns significantly increases. No matter how much the thickness is, the improvement of ultimate compressive strength decreased monotonously with the increase of preload stress level. However, when the preload stress level reaches to 0.75, extent of reduction is only 5 percent. Besides, with the improvement of FRP thickness, reduction of improvement does not have the trend to decrease, which may suggest that under high preload stress level, the confinement effect will not improve with increasing the amount of FRP. From Figure 13, when the preload stress level is 0.6, the axial strain of concrete column significantly improves. This kind of circumstance is also seen for columns without preload stress. So under low preload stress level, better deformation capacity can be obtained by increasing the restrain stiffness of FRP, too.

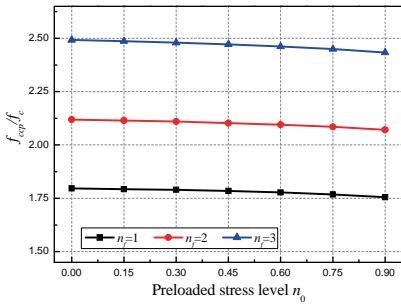


Figure 12. Variation of improvement with preload stress level

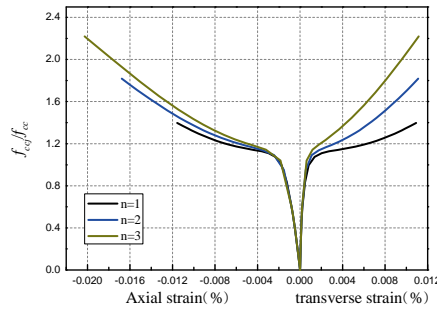


Figure 13. Variation of improvement with strain,  $n=0.6$

## 5 Conclusions

By using finite element method, analysis model for short-term axially preloaded concrete columns with FRP confinement is established. The comparisons of calculation results and test results indicate that the model built in this paper can give a good prediction of axial compressive behavior of FRP-confined columns. The conclusions are as follows: the load capacity of preloaded concrete columns is approximate linear relationship with longitudinal reinforcement ratio and volumetric percentage of stirrups; different concrete strength has no effect on the improvement of ultimate strength under different preload stress level; with the increase of preload stress level, the improvement of ultimate compressive strength decreased monotonously, but under low preload stress level, extent of reduction is only 5 percent or so and the deformation capacity can be greatly improved by increasing the restraint stiffness of FRP. For the accurate simulation of short term preloaded concrete columns confined with FRP under high preload stress level, the constitutive model of concrete in ABAQUS as well as the interface behavior between FRP and concrete require further research and improvement.

## Acknowledgements

This research work is financially supported by the National Natural Science Foundation of China (Grant No. 50778035).

## References

- ACI 440.2R-XX. (2007). Guide for the Design and Construction of Externally Bonded FRP Systems for Strengthening Concrete Structures. *American Concrete Institute*. Detroit, MI, USA.
- Berthet J.F., Ferrier E. and Hamelin P. (2005). Compressive Behavior of Concrete Confined by Composite Jackets. Part A: experimental study. *Construction and Building Materials*, 19(3): 223-232.
- Howie I. and Karbhari V.M. (1994). Effect of Materials Architecture on Strengthening Efficiency of Composite Wraps for Deteriorating Columns in the North-East. In: *Infrastructure: New Materials and Methods of Repair*, Proceedings of the 3rd Materials Engineering Conference, K. D. Basham, ed., Material Engineering Division, ASCE, 199-206.
- Jin J.P. (2008). Experimental Study on the Axial Mechanical Behavior of Preloaded Circular Concrete Columns with CFRP Confinement. Northeastern University, Shenyang, China [in Chinese].
- Laine D. P. (2004). Effect of Axial Preloads on Confined Concrete. Department of Civil Engineering, University of Toronto, Toronto, Ontario, Canada.
- Lam L. and Teng J.G. (2004). Ultimate Condition of Fiber Reinforced Polymer-Confined Concrete. *Journal of Composites for Construction*, ASCE, 8(6): 539-548.
- Lam L., Teng J.G., Cheung C.H. and Xiao Y. (2006). FRP-Confined Concrete under Axial Cyclic Compression. *Cement and Concrete Composites*, 28(10): 949-958.

- Maalej M, Tanwongsva S and Paramasivam P (2003). Modelling of Rectangular RC Columns Strengthened with FRP. *Cement & Concrete Composites*, 25(2): 263-276.
- Miyauchi K., Nishibayashi S. and Inoue S. (1997). Estimation of Strengthening Effects with Carbon Fiber Sheet for Concrete Column. Proceedings of the Third International Symposium on Non-Metallic FRP for Concrete Structures, Sapporo, Japan, 217-224.
- Pan C.J. (2007). Experiment Study on the Compressive Behavior of Circular Concrete Columns Confined with FRP Considering the secondary Load. China Academy of Building Research, Beijing, China [in Chinese].
- Song J.G. (2008). Numerical Simulation of Axially Compressive Mechanical Behavior of Preloaded Circular Concrete Columns with CFRP Confinement. Master thesis, Northeastern University, Shenyang, China [in Chinese].
- Takeuti A.R., Hanai. J.B. and Mirmiran A (2008). Preloaded RC Columns Strengthened with High-Strength Concrete Jackets under Uniaxial Compression. *Materials and Structures*, 41(7), 1251-1262.
- Tao Z. and Y.Q. (2006). New Type of composite structural columns. Beijing: science press. [in Chinese].
- Teng J.G., Yu T., Wong Y.L. and Dong S.L. (2007). Hybrid FRP-Concrete-Steel Tubular Columns: Concept and Behavior. *Construction and Building Materials*, 21(4): 846-854.
- Teng J.G. and Lam L. (2002). Compressive Behavior of Carbon Fiber Reinforced Polymer-Confined Concrete in Elliptical Columns. *Journal of Structural Engineering*, ASCE, 128(12): 1535-1543.
- Theriault M., Neale K.W. and Claude S. (2004). Fiber-reinforced Polymer-confined Circular Concrete Columns: Investigation of Size and Slenderness Effects. *Journal of Composites for Construction*, ASCE, 8(4): 323-331.
- Xiao Y. and Wu H. (2000). Compressive Behavior of Concrete Confined by Carbon Fiber Composite Jackets. *Journal of Materials in Civil Engineering*, ASCE, 12(2): 139-146.
- Zhang S., Ye L. and Mai Y.W. (2000). A Study on Polymer Composites Strengthening Systems for Concrete Columns. *Applied Composite Materials*, 7: 125-138.

# Nonlinear Numerical Simulation on Composite Joint between Concrete-Filled Steel Tubular Column and Steel Beams-Covered Concrete under Low-Cyclic Reversed Loading

Chiyun Zhao<sup>1\*</sup>, Hua Li<sup>2</sup>, Menghong Wang<sup>1</sup> and Liyun Li<sup>2</sup>

<sup>1</sup>Department of Civil Engineering, Beijing University of Civil Engineering and Architecture, Beijing 100044, P.R. China

<sup>2</sup>Department of Civil Engineering, China University of Mining and Technology, Beijing 100083, P.R. China

**Abstract.** The nonlinear response of the joints between concrete-filled steel tubular column and steel beams-covered concrete under low-cyclic reversed loading are simulated by using software ANSYS. Using a separated model, element concrete solid65 is used to model concrete material, element shell181 is used to model steel tubular, H-shaped steel beam and stiffened steel ring plate, element link8 is used to model steel bars. The numerical analysis results are compared with the data of the experimental research. The advantages and shortcoming of the finite element model are given. A better numerical simulation method and a use for reference to the similar case are expected to be afforded.

**Keywords:** composite joint, low-cyclic reversed loading, hysteretic curve, computer simulation

## 1 Introduction

Seismic performance of steel-concrete composite joints has been caused great concerns by more and more application in high rise buildings. Different constructions of composite joints have different effects on mechanical characters of them. Reasonable composite joints constructions must meet the principle of stronger columns, weaker beams, and even much stronger joints and must be consistent with the used calculation model. Beams and columns at joints should be transmit subjected forces of them clear and simple, and further consider simpler construction, more convenient fabrication and save more steels for joints.

---

\* Corresponding author, e-mail: zhaocy@bucea.edu.cn

Scholars in domestic and abroad have made a great deal of experimental research and computer simulation on composite joints, but many studies focus on the concrete-filled steel tubular column-steel beam composite joints. For seismic performance of concrete-filled steel tubular column-steel beams-covered concrete composite joints, with advantages of high bearing capacity, better ductility, less steel consumption, better corrosion-resistant and fire-resistant, studies are far from enough.

In this paper, the test results (Zhang, 2003) of nonlinear response of the joints between concrete-filled steel tubular column and steel beams-covered concrete under low-cyclic reversed loading are simulated by using commercial finite element software ANSYS.

## 2 Experimental Introductions

The experimental composite joint was composed of concrete-filled steel tubular column and steel beams-covered concrete. The two beams connected with the column by welding two stiffened steel ring plates to steel tubular column and the upper and lower flanges of steel beams, by bolting ear plates of steel tubular column to the steel beam webs, by welding longitudinal steel bars in composite beam to steel tubular column.

Details of the experimental composite joint were all real sizes of actual project (Figure 1). Steel grade of steel tubular column and steel beam was Q345. Steel grades of longitudinal steel bars and stirrups in composite beams were HRB335 and HPB235 respectively. Stirrups and its steel grade in the core zone of the composite joint were single-loop  $\Phi 12@200$  and HRB335 respectively. Concrete grades in composite column and composite beam were C60 and C30 respectively. Experimental measure strength values of concrete were shown in Table 1.

Table 1. Measure strength values of concrete (N/mm<sup>2</sup>)

Grade	Elastic modulus	Compression	Tension
C30	$3.73 \times 10^4$	33.84	2.88
C60	$3.40 \times 10^4$	41.79	3.41

The experimental composite joint was loaded before yielding and applied displacement after yielding to facilitate easier convergence. Hysteretic curves obtained in experiment were shown in Figure 2.

### 3 Computational Models

Separated model in software ANSYS are used. Because construction of the experimental composite joint was complicated, numbers of parts and members were large and computational capacity of personal computer was limited, some relative unimportant factors were neglected and the model is simplified as follows:

1. Welding connections of top and bottom ring stiffener plates on tubular column with upper and lower flanges of steel beams are not considered. Bolts connections of ear plates on column with the web of steel beams are not considered.
2. The bond slippages of interfaces between the steel tubular column, the steel beam, the upper and lower ring plates for stiffening composite joint and the steel bars and the surrounding concrete of them are not occurred. Those can be realized by dividing any of the contact surfaces between the two components into consistent and sharing common element nodes in element mesh process.
3. The ring stirrups in the core zone of composite joint, that is area of column between with the two ring stiffened plates, are not fully considered in accordance with the actual distribution of ring stirrups of the experimental specimen. Only the two ring stirrups located ends of the core zone of composite joint are considered in finite element model.

#### 3.1 Elements Selection and Meshing

Concrete was modelled using element Solid65, a dedicated three-dimensional eight noded solid isoparametric element to model the nonlinear response of brittle materials based on a constitutive model for the triaxial behavior of concrete. Steel pipe, steel beams and steel ring plates were modelled using element Shell181. All steel bars were modelled using element Link8, a three dimensional spar element with plasticity.

The finite element mesh for the composite joint is plotted in Figure 3, the mesh for the steel tubular column, steel beams and steel ring plates is shown in Figure 4, the mesh for the steel bars is shown in Figure 5.

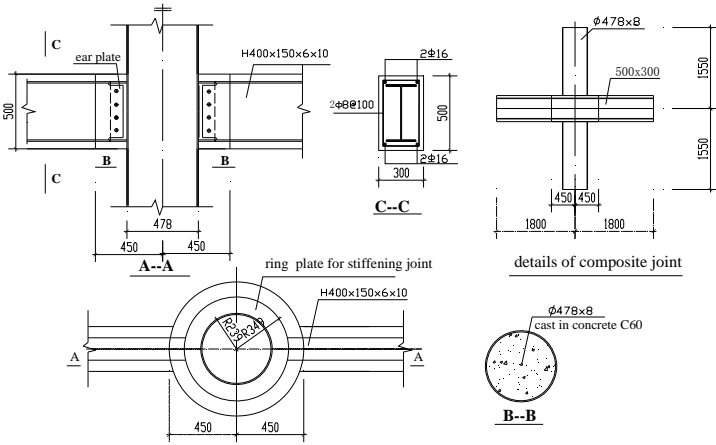


Figure 1. Details of the composite joint.

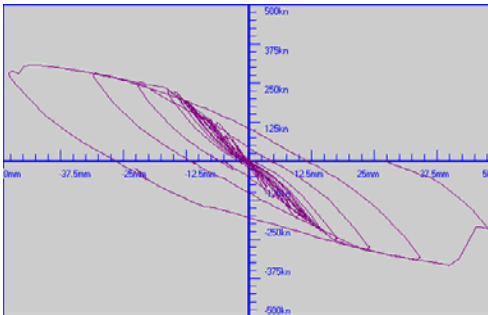


Figure 2. Hysteretic curve obtained in experiment.

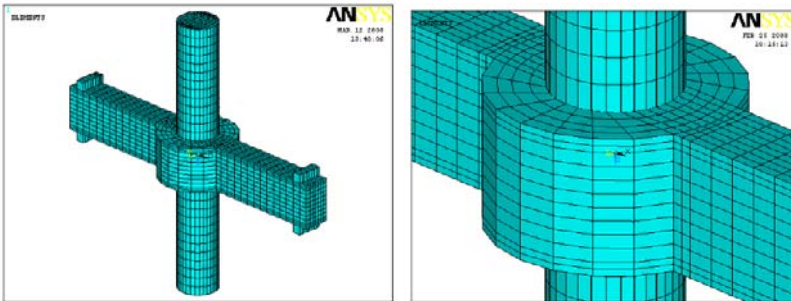


Figure 3. Details of finite element mesh of the overall composite joint.

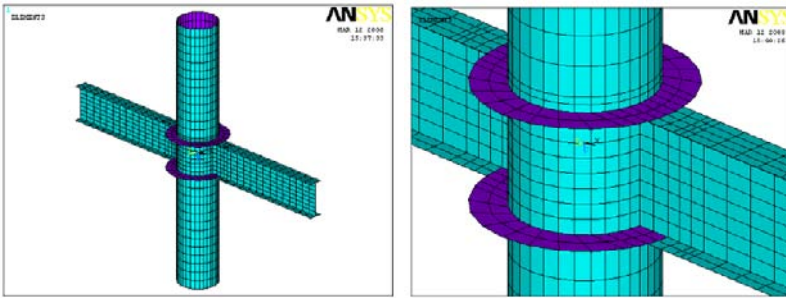


Figure 4. Details of element Shell181 mesh of steel tube and beam and steel ring plates.

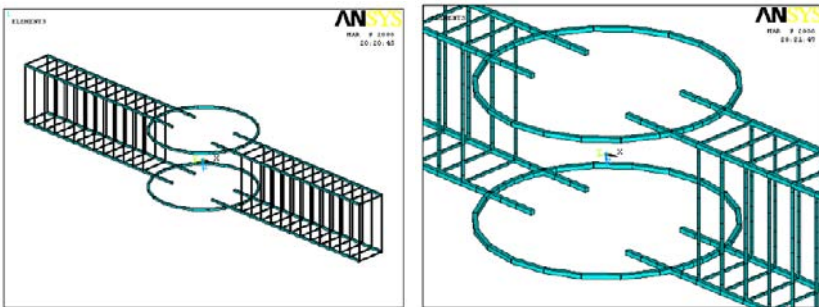


Figure 5. Details of element Link8 mesh of steel bars.

### 3.2 Constitutive Models

Concrete material was modeled by multilinear isotropic hardening constitutive curve and Williams and Warnke failure criteria. Steel material was modelled by bilinear kinematic hardening constitutive curve and Von-Mises failure criteria (Figure 6, concrete left, steel right).

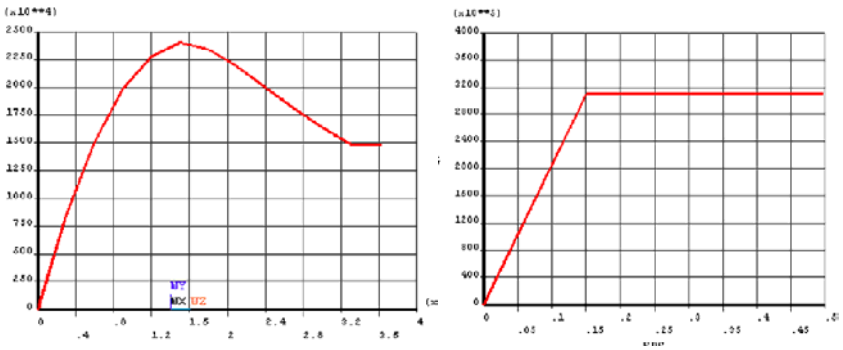


Figure 6. Sketches of constitutive models of concrete material and steel material.

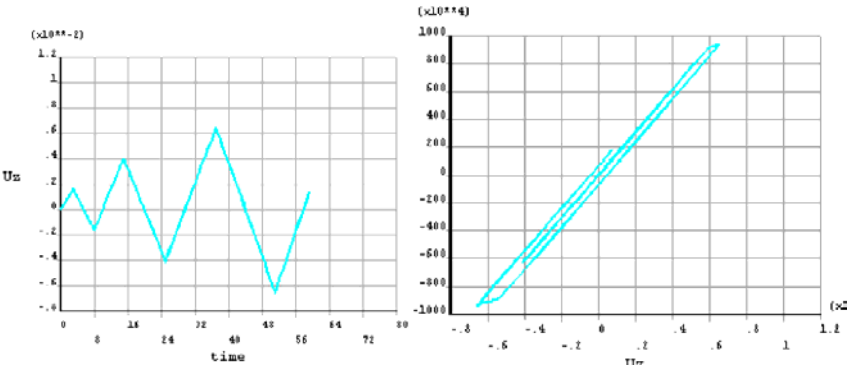


Figure 7. Applied displacement - time curve and hysteretic curve obtained in software ANSYS.

### 3.3 Computational Results

The computational model was applied displacement to facilitate easier convergence. The system of applied displacement and corresponding hysteretic curves obtained by software ANSYS were shown in Figure 7.

## 4 Discussions

By computational analysis used finite element method in software ANSYS, the nonlinear response of the composite joint, which was configured of concrete-filled

steel tubular column, with stiffened steel ring plates, and steel beams covered concrete, under low-cyclic reversed loading, some meaningful point of discussion is as follows:

1. Under smaller magnitude low-cyclic reversed loading, the separated finite element model provided in software ANSYS can be more consistent with the test results for nonlinear response of the composite joint.
2. When the separated model provided in software ANSYS is used to analyse a structure under low-cyclic reversed loading, the response of the structure is easier convergence by applied displacement than by applied loading.
3. The hysteretic curve of the composite joint under low-cyclic reversed loading, obtained by separated finite element model in software ANSYS, is more smooth than the test result. This may be that a concrete material in computational model is a more homogeneous material than actual.
4. The serious slippages can occur between steel and concrete in the composite joint with applied reversed load increasing to failure load, so the finite element model without contact elements in steel and concrete, cannot load to composite joint to failure condition.

## References

- ANSYS (2003). ANSYS manual set. *ANSYS Inc.*, USA.
- Group of codes (2002). Code for design of concrete structures (GB50010-2002). China Architecture & Building Press, Beijing [in Chinese].
- William, K.J., Warnke E.D. (1975). Constitutive model for the triaxial behaviour of concrete. *Proceedings of the International Association for Bridge and Structural Engineering*, Italy, 174–175.
- Zhang L.R., Wang M.G. (2003). Experimental research on load-bearing capacity of joints for a steel-concrete composite structure. *Journal of Architecture Science*, 19(5), 146–19 [in Chinese].

*“This page left intentionally blank.”*

# Performance Evaluation of the High Rise Structural Form Selection Based on Fuzzy Inference Network

Shihai Zhang<sup>1,2</sup>, Shujun Liu<sup>2\*</sup>, Jinping Ou<sup>1</sup> and Guangyuan Wang<sup>1</sup>

<sup>1</sup>School of Civil Engineering, Harbin Institute of Technology, Harbin 150090, China

<sup>2</sup>Department of Civil Engineering, Nanyang Institute of Technology, Nanyang 473004, China

**Abstract.** Firstly, analyzing the characteristic and shortage of the traditional evaluation methods such as fuzzy integrated evaluation, fuzzy inference and fuzzy inference network, combining the fuzzy integrated evaluation and fuzzy inference network, we have set up two improved weighted inference networks and shown the topological structures and algorithms. Secondly, applied the improved methods in high-rise building structural integrated performance evaluation, we presented the membership functions of the evaluation process, performance index system, weight and evaluation grade and structural anti-disaster performance, gave the engineering example. It is shown that: The methods provide a more intelligent and efficient methods for intuitive express and utilize the experts' evaluation knowledge and strategy.

**Keywords:** high-rise structure, form selection, performance evaluation, improved fuzzy inference network

## 1 Introduction

High-rise structural form selection is a kind of integrated intelligent optimization problem with multi-targets, multi-variables, multi-restraints, multi-schemes and multi-solutions. In the same condition, there are many building schemes, and each scheme often uses a variety of structural types; and different properties between the structures are often quite different. Therefore, many scholars have made many researches in different ways (He, 1991; Ming, 1996; Ou, 1997; Zhang, 2002): respectively established structural form selection methods and their supportive programs based on fuzzy integrated evaluation, fuzzy inference, etc. Also the fuzzy integrated evaluation has an intuitive process, but the knowledge it used is diffi-

---

\* Corresponding author, e-mail: lsj.6290@163.com

cult to understand; the fuzzy inference can overcome above weak point, but the efficiency is too lower. Therefore, we improved the traditional fuzzy inference network in this paper and evaluate the performance of the high rise building structure.

## 2 Fuzzy Inference Network Algorithms and Its Improvement

### 2.1 Basic Structure and Algorithm of Weighted Fuzzy Inference Network

Weighted fuzzy inference network is made up of  $s$  ( $s \geq 2$ ) weighted fuzzy inference units with which have  $m$  ( $m \geq 2$ ) inputs. This network, as NN, can realize non-linear mapping between the input and the output of complex questions, and is less strict with the input data than NN. Its solution strategy is mainly to "divide and solve", namely, decompose a complex question into some smaller and easier ones (i.e. the reasoning units), then by combining the output of each reasoning unit to obtain the solution. Figure 1 provides the basic topological structure of the weighted fuzzy inference network, where, the first layer was inputs, the last  $m$  ( $m \geq 2$ ) points of the layer directly pass on the input fuzzy variables to next layer. The second layer is the parameter membership functions carrying on fuzzy processing of every input parameter; Equation (1) is the triangle membership function that  $i^{\text{th}}$  attribute vs  $k^{\text{th}}$  evaluation grade ( $[c_{k1}, c_{k2}]$  is the interval ). The third layer is the fuzzy inference units; the weight value of reasoning unit  $a_k$  may be ascertained with the  $T$  model operator or the  $S$  model operator, Equation (2) provides the expression a  $T$  operator; the output function of  $k$  reasoning unit  $f_k(x)$  may take the form of function based on input variables linear combination in the  $TSK$  fuzzy inference model (Zhang, 2006) (Equation (3)), joint weighted value  $w_{ik}$  between the second and the third layer is the parameter of  $f_k(x)$ . The fourth layer is the weighted output layer of the reasoning network; Equation (4) has given the output function algorithm expression of the network. With Equation (4), we can get the non-linear mapping function between the inputs and outputs of the weighted reasoning network.

Studies have demonstrated that, while racking may be caused by waves propagating horizontally or obliquely, vertically propagating shear waves

$$\mu_{ik}(x_i) = \exp[-0.5(x_i - c_{ik})^2 / \sigma_i^2] \quad (1)$$

$$a_k = \prod_{i=0}^m \mu_{ik}(x_i) \quad (2)$$

$$f_k(x) = \sum_{i=0}^m w_{ik} x_i \quad (3)$$

$$f(x) = \frac{\sum_{k=1}^s a_k f_k(x) \sum_{k=1}^s \sum_{i=0}^m w_{ik} x_i \prod_{i=0}^m \exp[-0.5(x_i - c_{ik})^2 / \sigma_i^2]}{\sum_{k=1}^s a_k \sum_{k=1}^s \prod_{i=0}^m \exp[-0.5(x_i - c_{ik})^2 / \sigma_i^2]} \quad (4)$$

## 2.2 Improvement in Structure and Algorithm of the Fuzzy Inference Network

By choosing and constructing membership function  $\mu_{ik}$ , weighted value  $w_{ik}$  and  $a_k$ , output functions  $f_k(x)$  and  $f(x)$ , the above weighted fuzzy inference network may realize an explicit input-output mapping, but its weighted values did not clearly express the difference in importance of the input variables, cannot satisfy the relative importance degree of various performances in structure scheme evaluation and optimization selection. At the same time, the outputs of each reasoning unit are the linear combination of input vectors, not fuzzy or explicit. So, on the basis of the network structure and its algorithm shown in Figure 1, two kinds of improved weighted fuzzy inference network structures (Figure 2) (multi-input-multi-output and multi-input-single-output) are offered and their corresponding improved algorithm (see Equation (5) and Equation (6), where, the first layer is the input one of the system; the second layer is parameter membership functions; the third is fuzzy inference units, for the output evaluation function of  $k$  reasoning unit please see Equation (5), and the function value of output function  $b_k(x)[0,1]$  expresses the membership degree of the  $k$  reasoning unit to its corresponding performance evaluation rank  $v_k$ , the fourth layer is the output layer. Equation (6) gives us the output evaluation function of the defuzzification of the system. It is a weighted combination of outputs of each reasoning unit;  $w_{ij}$  jointing the second and the third layers is the weight of inputs  $x_i$ ,  $c_k$  jointing the third and fourth layers is the value of the evaluation rank  $v_k$ . This method has overcome the shortcomings of the above-mentioned reasoning network, such as ignorance of input variable weights, ambiguity of reasoning unit significance, inability of conveniently using experts' fuzzy rules, etc. Besides, it can also realize non-linear mapping between inputs and outputs directly.

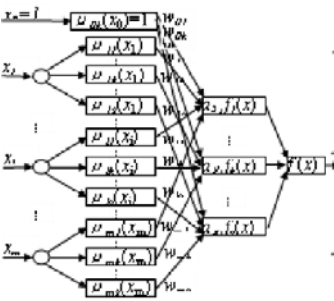


Figure 1. Topology structure of the weighted fuzzy inference network

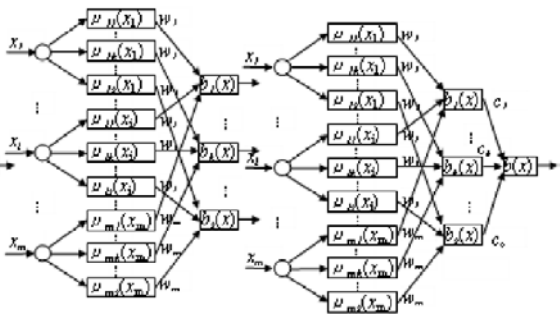


Figure 2. Topology structure of the improved weighted fuzzy inference network

$$b_k(x) = \sum_{i=1}^m \mu_{ik}(x_i) w_i \tag{5}$$

$$b(x) = \frac{\sum_{k=1}^s \sum_{i=1}^m \mu_{ik}(x_i) w_i c_k}{\sum_{k=1}^s \sum_{i=1}^m \mu_{ik}(x_i) w_i} \tag{6}$$

### 3. Performance Evaluation of the High Rise Building Structural Form Selection Based on Improved Fuzzy Inference Network

#### 3.1 The Performance Evaluation Process

The main content of the evaluation include: confirming the evaluation model; confirming the weighted value of each performance; confirming the unifying evaluation grade and setting up the evaluation standard and the quantizing method based on it; setting up the scientific evaluation method and the supportive system etc. according to the content and the inner relation, Figure 3 shows the model of the evaluation process. Limit to the length, we only introduce the evaluation method and process based on improved fuzzy inference network.

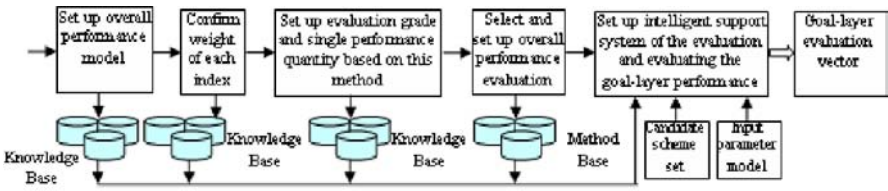


Figure 3. System model of performance evaluation process in structural form selection .

### 3.2 The Performance System Model of the High-rise Structural Form Selection

After referring to the related specialty literature, criteria and experts, we has established three layers of 28 performances system as shown in Figure 4, where, the first three layers are performance indexes respectively of the policy-making layer, goal layer and attribute layer;  $y_r, y_{ri}$  and  $w_r, w_{ri}$  are markers respectively of evaluation index and its corresponding weights. The paper of (Zhang, 2005) offers uniform evaluation grades, evaluation criteria, corresponding weighted vectors and attribute performance evaluation membership function of every performance index.

High-rise anti-seismic performance $y_0$																																																																			
$y_1, W_1$				$y_2, W_2$				$y_3, W_3$				$y_4, W_4$				$y_5, W_5$				$y_6, W_6$																																															
Function adaptability				Advanced structure				Base force rationality				anti-disaster				capable construction				life-span serving ability																																															
$y_{11}$	$y_{12}$	$y_{13}$	$y_{14}$	$y_{21}$	$y_{22}$	$y_{23}$	$y_{24}$	$y_{31}$	$y_{32}$	$y_{33}$	$y_{34}$	$y_{41}$	$y_{42}$	$y_{43}$	$y_{44}$	$y_{51}$	$y_{52}$	$y_{53}$	$y_{54}$	$y_{61}$	$y_{62}$	$y_{63}$	$y_{64}$																																												
$w_{11}$	$w_{12}$	$w_{13}$	$w_{14}$	$w_{21}$	$w_{22}$	$w_{23}$	$w_{24}$	$w_{31}$	$w_{32}$	$w_{33}$	$w_{34}$	$w_{41}$	$w_{42}$	$w_{43}$	$w_{44}$	$w_{51}$	$w_{52}$	$w_{53}$	$w_{54}$	$w_{61}$	$w_{62}$	$w_{63}$	$w_{64}$																																												
standard-layer resistance	resistance	resistance	resistance	component rigidity	component and rigidity	component and rigidity	component and rigidity	structure technology application	structure technology application	structure technology application	structure technology application	space integrate	space integrate	space integrate	space integrate	elastic adaptability	elastic adaptability	elastic adaptability	elastic adaptability	multi-level ductility	multi-level ductility	multi-level ductility	multi-level ductility	structure integrate space and energy saving	structure integrate space and energy saving	structure integrate space and energy saving	structure integrate space and energy saving	anti-seismic integrate space and energy saving	anti-seismic integrate space and energy saving	anti-seismic integrate space and energy saving	anti-seismic integrate space and energy saving	structure integrate space and energy saving	structure integrate space and energy saving	structure integrate space and energy saving	structure integrate space and energy saving	building cost	building cost	building cost	building cost	construction condition applicability	construction condition applicability	construction condition applicability	construction condition applicability	congruence quality controllability	congruence quality controllability	congruence quality controllability	congruence quality controllability	resistance cost																			

Figure 4. Performance Index System of High-rise Building Structure Form Optimum Selection.

### 3.3 The Weighted and Evaluation Grade of the Performance Index

Considering the comparative importance degree of the different influence factor, we primary confirmed the weighted vector of the performance index based on investigating the experts:  $\{w_r\}_6 = \{0.15, 0.12, 0.28, 0.18, 0.15, 0.12\}$ ,  $\{w_{ri}\}_3 = \{0.40,$

$0.35, 0.25\}$ ,  $\{w_{2i}\}_4 = \{0.25, 0.35, 0.20, 0.20\}$ ,  $\{w_{3i}\}_4 = \{0.35, 0.25, 0.25, 0.15\}$ ,  $\{w_{4i}\}_4 = \{0.30, 0.20, 0.25, 0.25\}$ ,  $\{w_{5i}\}_3 = \{0.45, 0.35, 0.20\}$ ,  $\{w_{6i}\}_3 = \{0.45, 0.30, 0.25\}$ . In order to solve the incommensurability and the contradictory, we must set up a unified performance evaluation grade for all performance indexes. The propositional grade in this paper is 7 grade, it is  $V = \{v_k\}_s = \{\text{very poor, quite poor, poor, general, good, quite good, very good}\} (s=7)$ . In order to quantizing the result, we suggest the staff scale vector corresponding to  $V = \{v_k\}_7$  is  $C = \{c_k\}_7 = \{1/12, 1/6, 1/3, 1/2, 2/3, 5/6, 11/12\}$ .

### 3.4 The Membership Function of the Attribute-layer Performance Evaluation

Using the fuzzy distributing method, we can confirm the memberships of the single performance evaluation for 21 attribute-layer performance. The structural disaster-resistant attribute  $y_4$  as an example, we give their four evaluation membership function of the attribute-layer performance ( $y_{41}, y_{42}, y_{43}, y_{44}$ ), the other attribute-layer evaluation function are omitted.

The surrounding ground, that provides the embedment of the structure, is simulated by spring elements. The following is a step-by-step procedure for such an analysis:

1. The fuzzy evaluation function of the structural overall ductility and energy dissipation capacity ( $y_{41}$ ): Equation (7) shows the fuzzy membership function of  $y_{41}$ . where the input parameter  $x_{j41} = \lambda_j ( [\theta_p]_j / [ \theta_e ]_j - 1 )$ ,  $[ \theta_p ]_j$  and  $[ \theta_e ]_j$  is the ductility energy dissipation factor, the elastoplastic and elastic-story drift angle limited value respectively. Where  $[ \theta_p ]_j$  and  $[ \theta_e ]_j$  can confirmed directly according to related criterion (see Table 1).

$$\mu_{j4_{11}}(\lambda_j) = \begin{cases} (2.5 - \lambda_j) / 1.5 & \lambda_j \in [1, 2.5] \\ 0 & \lambda_j > 2.5 \\ 1 & \lambda_j < 1 \end{cases} \tag{7a}$$

$$\mu_{j4_{1k}}(\lambda_j) = \begin{cases} (1 - |1 + (k - 1)1.5 - \lambda_j|) / 1.5 & \lambda_j \in [(k - 2)1.5 + 1, 1.5k + 1] \\ 0 & \text{other (where, } k = 2, 3, 4, 5, 6) \end{cases} \tag{7b}$$

$$\mu_{j4_{17}}(\lambda_j) = \begin{cases} (\lambda_j - 8.5) / 1.5 & \lambda_j \in [8.5, 10] \\ 0 & \lambda_j < 8.5 \\ 1 & \lambda_j > 10 \end{cases} \tag{7c}$$

2. The fuzzy evaluation function of the structural fire resistance ( $y_{42}$ ): Equation (8) shows the fuzzy membership function of  $y_{42}$ . Where the input parameters  $x_{j42} = t_{jp}$ , and  $t_{dp}$  is the actual fire resistance limited value of the  $j^{\text{th}}$  structure of the  $p^{\text{th}}$  main force component and the fire resistance limited value of the  $d^{\text{th}}$  fire resistance grade of the  $p^{\text{th}}$  force component in current criterion (see Table 2).

$$\mu_{j421}(t_{jp}) = \begin{cases} (4t_{dp} - 6t_{jp})/t_{dp} & t_{jp} \in [t_{dp}/2, 2t_{dp}/3] \\ 0 & t_{jp} < t_{dp}/2 \\ 1 & t_{jp} > 2t_{dp}/3 \end{cases} \quad (8a)$$

$$\mu_{j41k}(t_{jp}) = \begin{cases} (1 - |(k+2)t_{ds} - 6t_{jp}|)/t_{ds} & t_{jp} \in [(k+1)t_{ds}/6, (k+3)t_{ds}/6] \\ 0 & \text{other (where, } k=2,3,4,5,6) \end{cases} \quad (8b)$$

$$\mu_{j427}(t_{jp}) = \begin{cases} (6t_{jp} - 8t_{ds})/t_{ds} & t_{jp} \in [4t_{ds}/3, 3t_{ds}/2] \\ 0 & t_{jp} < 4t_{ds}/3 \\ 1 & t_{jp} > 3t_{ds}/2 \end{cases} \quad (8c)$$

Table 1 Displacement angel limit value of high-rise structure’s elasticity and elasticity-plasticity and ductility energy dissipation factor

Structure type	$[\theta_e](h < 150)$	$[\theta_e](h \geq 250)$	$[\theta_p]$	$\lambda_j$	Structure type	$[\theta_e]$	$[\theta_p]$	Interlayer displacement ductility ratio	$\lambda_j$
RC frame	1/550	1/500	1/50	10	Steel frame	1/300(1/250)	1/50(1/70)	(3.5)	(9.5)
RC frame - shearing, frame-tube, Ban post-shearing	1/800	1/500	1/100	7	Partiality support steel frame	1/300(1/250)	1/50(1/70)	(3.0)	(8)
					Center support steel frame	1/300(1/250)	1/50(1/70)	(2.5)	(6)
RC-shearing, tube-tube	1/1000	1/500	1/120	7.3	RC-shearing steel frame	1/800, 1/500	1/100	(2.0)	(5)

Note: the data in this table get from current criterion GB50011-2001 and JGJ3-2002, the data in () get from current criterion JGJ99-98, when the height  $h \in [150, 250]$ ,  $[\theta_e]$  should be get from linear interpolation, for steel structure, energy ductility factor  $\lambda_j = 3u - 1$

Table 2. Limit Values of Structure Side-displacement and Fire-resistant Limitation

Structure type	<i>u/H</i> limited value		Component kind( <i>p</i> =1~4)	Fire resistance grade and limited value <i>t<sub>sp</sub></i> (h)			
	Under the wind	Earthquake		first	second	third	four
RC frame	1/650	1/550	wall(bearing, lift well)	3.0	2.5	2.5	0.5
RC frame -shearing, frame-tube	1/950	1/850	post	3.0	2.5	2.5	0.5
RC tube-tube	1/1050	1/950	girder	2.0	1.5	1.0	0.5
RC-shearing	1/1200	1/1100	Floor ban	1.5	1.0	0.5	0.25
Above data come from JGJ3-91 table 4.94			Above data come from GB5004 and JGJ99-98				

3. Confirming the fuzzy evaluation function of the structural integrated stability (*y<sub>43</sub>*): Equation (9) shows the fuzzy membership function of *y<sub>43</sub>*. Where the input parameters  $x_{j43} = [u/H]_j = u_{hj}$  is the limited value of the *j*<sup>th</sup> structure of the *p*<sup>th</sup> main force component and the fire resistance limited value of the ratio of the peak maximum displacement and the total height when the structural scheme is *u<sub>j</sub>*, and the fortification intensity is *i*. (see Table 2).

$$\mu_{j431}(u_{hj}) = \begin{cases} 3-2000u_{hj} & u_{hj} \in [1/1000, 3/2000] \\ 0 & u_{hj} > 3/2000 \\ 1 & u_{hj} < 1/1000 \end{cases} \tag{9a}$$

$$\mu_{j43k}(u_{hj}) = \begin{cases} 1 - |k+1-2000u_{hj}| & u_{hj} \in [k/2000, (k+2)/2000] \\ 0 & \text{other} \quad (\text{where, } k=2,3,4,5,6) \end{cases} \tag{9b}$$

$$\mu_{j437}(u_{hj}) = \begin{cases} 2000-7u_{hj} & u_{hj} \in [7/2000, 1/250] \\ 0 & u_{hj} < 7/2000 \\ 1 & u_{hj} > 1/250 \end{cases} \tag{9c}$$

4. Confirming the fuzzy evaluation function of the structural aseismic disaster (*y<sub>44</sub>*): Equation (10) shows the fuzzy membership function of *y<sub>44</sub>*. Where the input parameters  $x_{j44} = e_j$  is the limited value of aseismic fortification of structural scheme *u<sub>j</sub>*.

$$\mu_{j441}(e_j) = \begin{cases} 1 & e_j = 1 \\ 0 & \text{other} \end{cases} \tag{10a}$$

$$\mu_{j44k}(e_j) = \begin{cases} 1 & e_j = k \\ 0 & e_j \neq k \quad (\text{where, } k=2,3,4,5,6) \end{cases} \tag{10b}$$

$$\mu_{j47k}(e_j) = \begin{cases} 1 & e_j \geq 7 \\ 0 & e_j < 7 \end{cases} \quad (10c)$$

### 3.5 Target-grade Integrated Performance Evaluation Based on the Improved Fuzzy Inference Network

1. Performance evaluation based on the improved fuzzy inference network with multi-inputs and multi-outputs: According to the performance index system shown in Figure 3 and the improved weighted fuzzy inference network shown in Figure 2 and the Equation (11), we can evaluate the six improved integrated performance index, and confirm the evaluation matrix  $b_j = \{b_{jrk}\}_{6 \times 7}$  of the candidate  $u_j (j=1, 2, \dots, n)$ , and easy to do optimization according to the optimal methods.

$$b_{jrk}(x_{jr}) = \sum_{i=1}^{m_r} \mu_{jr_{ik}}(x_{jri}) w_{ri} \quad (11)$$

2. Performance evaluation based on the improved fuzzy inference network with multi-inputs and single-output: According to the performance index system shown in Figure 3 and the improved weighted fuzzy inference network shown in Figure 2 and the Equation (12), we can evaluate the six improved integrated performance index, and confirm the evaluation matrix  $b_j = \{b_{jr}\}_6$  of the candidate  $u_j (j=1, 2, \dots, n)$ , and easy to do optimization according to the optimal methods.

$$b_{jr}(x_{jr}) = \frac{\sum_{k=1}^7 \sum_{i=1}^{m_r} \mu_{jr_{ik}}(x_{jri}) w_{ri} c_k}{\sum_{k=1}^7 \sum_{i=1}^{m_r} \mu_{jr_{ik}}(x_{jri}) w_{ri}} \quad (12)$$

## 4 The Engineering Example of the High Rise Building Structure

### 1. The engineering example

A high rise building structure, 28 floors, height  $H=100.8\text{m}$ , 7 degree fortification intensity, the first design seismic group, II site classification, site characteristic period  $T_g=0.35\text{s}$ , square shape, length to width  $L/B=1$ , height to width  $H/B=2.76$ . Typical function space of standard floor is big, middle and small respectively, fitment standard is quite well, and the space maybe regulate for the future, the first

grade fireproofing. The structure will be frame-shearing force. We'll evaluate the six target-layer performance of this structure.

2. The evaluation based on improved MIMO weighted fuzzy inference network

Using the network, according to the input parameter  $x = (0.7, 0.6, 0.6, 1, 0.6, 0.8, 0.8, 100.8, 1, 1.68, 2.76, 7, 5, 1/850, 3, 0.8, 0.8, 0.8, 0.8, 0.6, 0.6)$ , we can confirm the evaluation vector of the six target-layer performance of this structure in turn, and the composed evaluation matrix  $b$  of this structure is:

$$b = \{b_{rk}\} = \begin{bmatrix} 0 & 0 & 0 & 0.24 & 0.68 & 0.08 & 0 \\ 0 & 0 & 0 & 0 & 0.11 & 0.56 & 0.33 \\ 0 & 0.17 & 0.13 & 0.10 & 0.07 & 0.28 & 0.25 \\ 0.08 & 0.17 & 0.25 & 0 & 0.30 & 0 & 0.20 \\ 0 & 0 & 0 & 0 & 0.20 & 0.80 & 0 \\ 0 & 0 & 0 & 0.33 & 0.31 & 0.36 & 0 \end{bmatrix}_{6 \times 7} \tag{13}$$

3. The evaluation based on improved MISO weighted fuzzy inference network each row of the evaluation matrix expresses the corresponding membership degree the target-layer performance evaluation to the seven performance grades. In order to expressing the evaluation value of each target-layer performance, we can adopt the evaluation method based on improved MISO weighted fuzzy inference network and confirm the evaluation value in interval  $[0,1]$ . We can confirm the corresponding performance evaluation vector  $b_j = \{b_{jr}\}_6 = \{0.64, 0.84, 0.63, 0.50, 0.80, 0.67\}$  according to Equation (12).

### 5 Conclusions

Performance evaluation is the basic and key step in high-rise building structural form selection. Analyzing the characteristic and shortage of the traditional evaluation methods such as fuzzy integrated evaluation, fuzzy inference and fuzzy inference network, combining the fuzzy integrated evaluation and fuzzy inference network, we have set up two improved weighted inference networks: MIMO and MISO inference network; shown the topological structures and algorithms and applied in high-rise building structural integrated performance evaluation. At the same time, we presented 4 attribute-layer membership functions of the evaluation process, performance index system, weight and evaluation grade and structural anti-disaster performance, gave the engineering example. It is shown that: The performance evaluation method provide a more intelligent and efficient methods for revealing candidate performance, and give full play with the proper application of the structure and special features, avoid the structural performance defects and the

unnecessary waste of resources, improve the overall performance of structural systems etc.

## References

- He G. and Lin S.P.(1991). *Summarizing of the Expert System of High-rising Structure Primary Designing*. Beijing: China Academy of Building Research, 1-19.
- Lai M. and Yang B. (1996). Anti-seismic form selection and fuzzy synthesis evaluation of High-rising RC structure. *Journal of Building Structures*, 17(8): 44-51.
- Ou J.P., Zhang S.H., and Liu H.Y., et al. (1997). Anti-seismic form selection and fuzzy expert system of high-rising RC structure. *Earthquake Engineering and Engineering Vibration*, 17(2): 82-91.
- Wang G.Y., and Ou J.P. (2002). Intelligent assessment method for high-rise building aseismic form-selection. *World Earthquake Engineering*, 18(3): 161-167.
- Zhang S.H., Liu X.Y., Ou J.P., and Wang G.Y. (2006). Method and system of fuzzy inference based high-rise structure intelligent form optimization. *Chinese Journal of Computational Mechanics*, 23(6): 647-650, 658.

*“This page left intentionally blank.”*

# Deflection Analysis of Pretensioned Inverted T-Beam with Circular Web Openings Strengthened with GFRP by Response Surface Method

Hock Tian Cheng<sup>1\*</sup>, Bashar S. Mohammed<sup>2</sup> and Kamal Nasharuddin Mustapha<sup>2</sup>

<sup>1</sup>Faculty of Civil and Environmental Engineering, Universiti Malaysia Pahang, Karung Berkunci 12, 25000 Kuantan, Pahang, Malaysia

<sup>2</sup>Department of Civil Engineering, Universiti Tenaga Nasional, KM7, Jalan Kajang-Puchong, 43009 Kajang, Selangor, Malaysia

**Abstract.** The experimental program reported in this paper tested three inverted-tee girders with circular web openings strengthened with GFRP to failure to evaluate the openings' effect on girder behavior. Parametric study using response surface methodology through finite element analysis may form efficient approximation to deflection.

**Keywords:** GFRP, finite element, prestressed inverted T-beam, response surface, web opening

## 1 Introduction

Utility requirement may make it desirable to use openings in the pretensioned inverted T-beams. However, introducing an opening into the web of a prestressed concrete beam reduces stiffness and leads to more complicated behavior. Therefore, the effect of openings on strength and service ability must be considered in the design process. Numerous investigations such as Mansure (Mansur, 1988) have been carried out on reinforced concrete beams with opening. The first published work on prestressed beam with web openings was conducted by Regan and Warwaruk (Regan and Warwaruk, 1967). Since then, several other researchers (Mohsen, et al. 1999; Savage, et al. 1996; Thompson and Pessiki, 2006) have investigated prestressed beams with web openings. Authors realized that there were scarce published research works on strengthening around web openings with GFRP. As such, this piece of research report focuses on this particular area.

---

\* Corresponding author, e-mail: cheng@ump.edu.my

## 2 Experimental Program

One series of beams, A1, comprising three prestressed beam with web openings with strengthening with GFRP laminates altogether, were tested. Series A1 has three beams. This particular series of beams contained one single bonded GFRP laminate at the tension face, but these beams were provided with external anchorages as detailed in Figure 1. All external anchorages were made of GFRP laminates, bonded to concrete with the same adhesives, after surface preparation similar to that used for GFRP laminates at tension faces.

Tests were carried out on three bonded prestensioned inverted T-beams. Typical reinforcement details for all beams and the as-tested details are shown in Figure 2. All tests were conducted with a closed-loop hydraulic servo-controlled MTS testing system. A four-point loading scheme, with an effective span of 4000 mm and a distance of 1200 mm between the load points was used to limit the presence of shear stress in the mid-span zone. Figure 3 shows the layout of four-points bending test of the three prestensioned inverted T-beam.

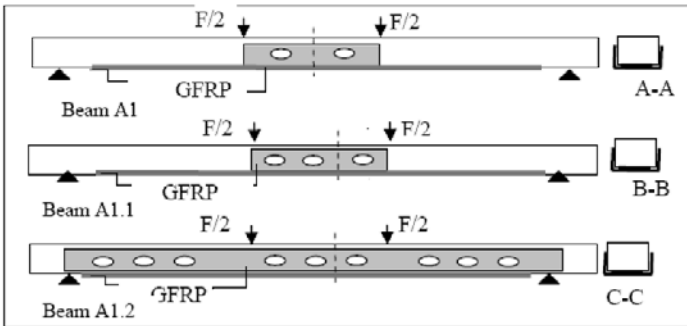


Figure 1. Details of test beams of series A1

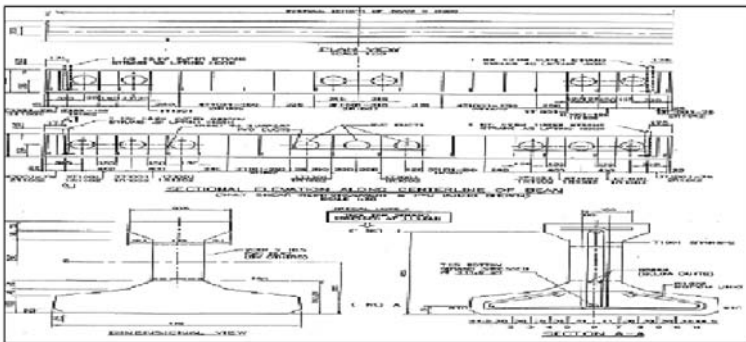


Figure 2. Detailings of prestressing steel and beam overall dimensions

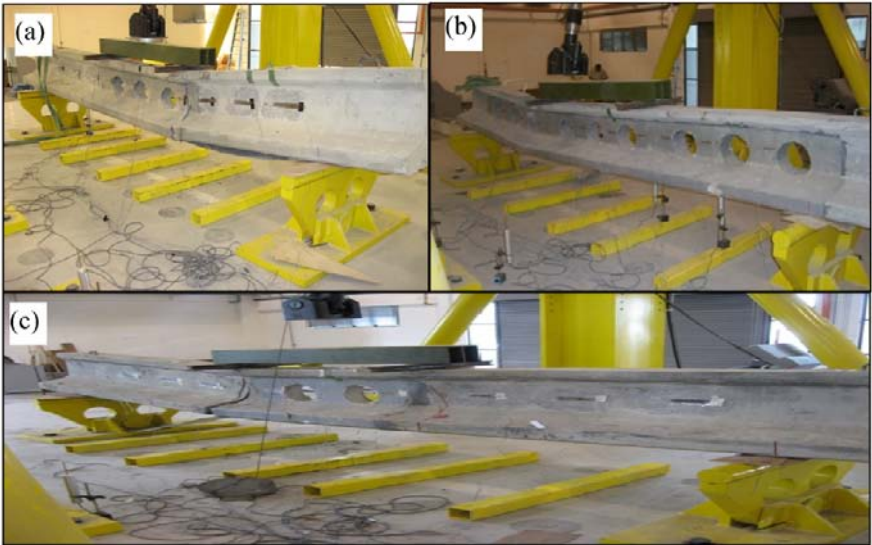


Figure 3. Four-points bending test of pretensioned inverted T-beam: (a) three web openings; (b) nine web openings; (c) two web openings, all strengthened with GFRP

### 3 Response Surface Method in Finite Element Analysis

In this paper, three-dimensional finite element beam models are developed before and after FRP strengthening using the finite element analysis (FEA). Modeling methodology and nonlinear analysis approach in ANSYS are presented. The results obtained from the FE beam model are compared with the test data in terms of load-deflection curve. In addition, the study of effects of FRP strengthening is made. The nonlinear finite element program ANSYS was used for theoretical study. In ANSYS, the load is applied gradually in small increments. The size of each increment depends on the convergence of the iteration process in the previous increments of loading. The concrete under compression is modeled by an elastic-plastic theory, using a simple form for the yield surface expressed in term of the equivalent pressure stress. Response surface methods (RSM) are based on the fundamental assumption that the influence of the random input variables on the random output parameters can be approximated by mathematical function. Hence, response surface methods locate the sample points in the space of random input variables such that an appropriate approximation function can be found most efficiently; typically, this is a quadratic polynomial. The fundamental idea of response surface methods is that once the coefficients of a suitable approximation function are found, then we can directly use the approximation function instead of looping through the finite element model. To perform a finite element analysis

might require minutes to hours of computation time; in contrast, evaluating a quadratic function requires only a fraction of a second. Hence, if using the approximation function, we can afford to evaluate the approximated response parameter thousands of times. Figure 4 to Figure 6 show the response surface plot of beam with different configuration of web openings. A quadratic polynomial is sufficient in many cases of engineering analysis (for example, the evaluation of the deflection mentioned above). For that evaluation, the circular web opening diameter and the applied loads coefficient both have a linear effect on the deflection, which is taken into account in a quadratic approximation by the mixed quadratic terms.

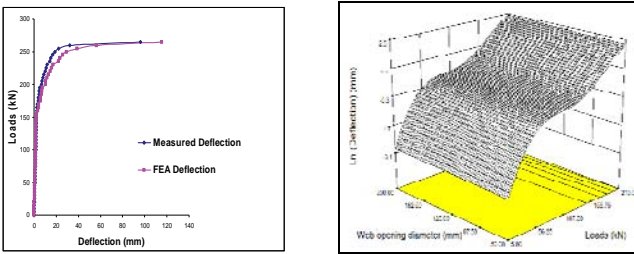


Figure 4. Load-deflection and RSM plot for beam with two web openings with GFRP laminates

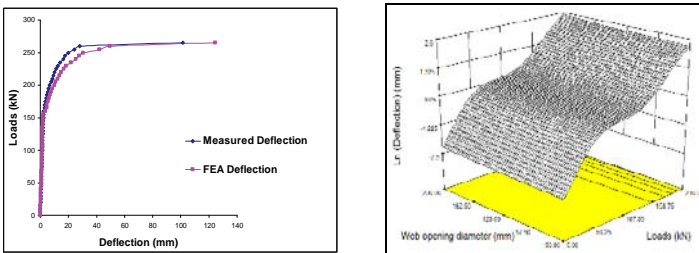


Figure 5. Load-deflection and RSM plot for beam with three web openings with GFRP laminates

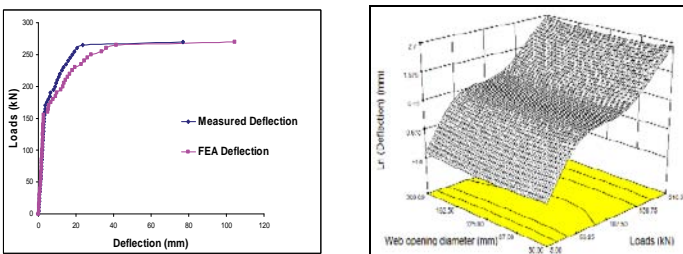


Figure 6. Load-deflection and RSM plot for beam with nine web openings with GFRP laminates

## 4 Results

The random output parameter i.e. deflection was fitted with a quadratic regression model including cross-terms. Natural logarithm transformation was used for the regression analysis. No filtering technique was used to fit the random output deflection. The response surface is the sum of the regression terms, where each regression term includes regression coefficients. The regression coefficients of the response surface are given in Table 1.

Table 1. Final equations in terms of actual factors

Beam Types	Beam with two web openings	Beam with three web openings	Beam with nine web openings
Final equation in terms of actual factors	$\ln(\text{deflection}) =$ $-3.47267$ $+0.076869 \text{ }^* \text{Loads}$ $+1.24754\text{E-}003 \text{ }^* \text{opening diameter}$ $+2.33335\text{E-}017 \text{ }^* \text{Loads} \text{ }^* \text{opening diameter}$ $+1.70457\text{E-}004 \text{ }^* \text{Loads}^2$ $-7.45145\text{E-}007 \text{ }^* \text{opening diameter}^2$ $-1.18038\text{E-}019 \text{ }^* \text{Loads} \text{ }^* \text{opening diameter}$ $+2.96049\text{E-}019 \text{ }^* \text{Loads} \text{ }^* \text{opening diameter}^2$ $-1.79263\text{E-}005 \text{ }^* \text{Loads}^3$ $+4.23021\text{E-}010 \text{ }^* \text{opening diameter}^3$ $+1.81104\text{E-}007 \text{ }^* \text{Loads}^4$ $-7.02905\text{E-}010 \text{ }^* \text{Loads}^5$ $-9.66680\text{E-}013 \text{ }^* \text{Loads}^6$	$\ln(\text{deflection}) =$ $-2.68431$ $+0.023075 \text{ }^* \text{Loads}$ $+3.21090\text{E-}003 \text{ }^* \text{opening diameter}$ $+2.94475\text{E-}017 \text{ }^* \text{Loads} \text{ }^* \text{opening diameter}$ $+1.38070\text{E-}003 \text{ }^* \text{Loads}^2$ $-2.13808\text{E-}005 \text{ }^* \text{opening diameter}^2$ $-7.42307\text{E-}020 \text{ }^* \text{Loads} \text{ }^* \text{opening diameter}$ $+2.32005\text{E-}019 \text{ }^* \text{Loads} \text{ }^* \text{opening diameter}^2$ $-3.14741\text{E-}005 \text{ }^* \text{Loads}^3$ $+8.88911\text{E-}008 \text{ }^* \text{opening diameter}^3$ $-2.60621\text{E-}007 \text{ }^* \text{Loads}^4$ $-9.34968\text{E-}010 \text{ }^* \text{Loads}^5$ $+1.23129\text{E-}012 \text{ }^* \text{Loads}^6$	$\ln(\text{deflection}) =$ $-3.38551$ $+0.028574 \text{ }^* \text{Loads}$ $+0.049255 \text{ }^* \text{opening diameter}$ $+6.46264\text{E-}017 \text{ }^* \text{Loads} \text{ }^* \text{opening diameter}$ $+9.79589\text{E-}004 \text{ }^* \text{Loads}^2$ $-4.64654\text{E-}004 \text{ }^* \text{opening diameter}^2$ $-2.45388\text{E-}019 \text{ }^* \text{Loads} \text{ }^* \text{opening diameter}$ $+2.28362\text{E-}019 \text{ }^* \text{Loads} \text{ }^* \text{opening diameter}^2$ $-2.43907\text{E-}005 \text{ }^* \text{Loads}^3$ $+1.30278\text{E-}006 \text{ }^* \text{opening diameter}^3$ $-2.04138\text{E-}007 \text{ }^* \text{Loads}^4$ $-7.25757\text{E-}010 \text{ }^* \text{Loads}^5$ $+9.38431\text{E-}013 \text{ }^* \text{Loads}^6$

Table 2. Regression analysis summary of three types of beams with different configuration of web openings strengthened with GFRP laminates

Goodness-of-fit measures	Value (beam with 2 openings)	Value (beam with 3 openings)	Value (beam with 9 openings)
Adjusted Error Sum of Squares	0.954E-03	0.435E-04	0.896E-04
Adjusted Coefficient of Determination (Adjusted R2)	0.972	0.948	0.967
Maximum Absolute Residual	0.223E-01	0.445E-02	0.655E-01
Maximum Relative Residual	0.067	0.082	0.056
Maximum t-statistic of constant variance test	1.434E+01	1.165E+01	1.891E+01
Probability of constant variance test	20.287%	28.382%	26.759%

### ***4.1 Regression Analysis Summary: Deflection***

Several goodness-of-fit measures are provided for each random output parameter in each response surface set. Table 2 shows regression analysis summary for deflection of three types of beam with different configuration of web openings strengthened with GFRP.

## **5 Conclusions**

The comparisons between ANSYS predictions and the experimental data show that the proposed FE models are good representations for both the GFRP strengthened beams with web openings in terms of the number of elements, structural details, and, especially, reasonably accurate results in general. The response surface methodology could be implemented in finite element analysis to help designer in decision making. From response surface plot, designer will obtain important interaction information between wide range of input parameter i.e. load (from 0 kN to 200 kN) and web opening diameter (from 20mm to 200mm) and their influence towards respective response, i.e. deflection.

## **References**

- Mansur M.A. (1988). Ultimate Strength Design of Beam with Large Openings, *Int. J. Struct.*, 8(2): 107-125.
- Regan H. S and Warwaruk J. (1967). Tee Members with Large Web Openings. *PCI Journal*, 12(4): 52-65.
- Saleh Mohsen, Tadros M. K., Einea A., Fischer L. G and Foster E. T. (1999). Standardized Design of Double Tees with Large Web Openings. *PCI Journal*, 67(4): 68-78.
- Savage J. M., Tadros M. K., Arumugasaamy P. and Fischer, L. G. (1996). Behaviour and Design of Double Tees with Web Openings. *PCI Journal*, 41(1): 46-62.
- Thompson J. M. and Pessiki S. (2006). Experimental Investigation Precast, Prestressed Inverted Tee Girders with Large Web Openings. *PCI Journal*, 109(2): 2-17.

# 2-D Numerical Simulation of Crack Growth by Three Kinds of Growth Criteria

Weizhou Zhong<sup>1,2\*</sup>, Jingrun Luo<sup>2</sup>, Shuncheng Song<sup>1</sup>, Gang Chen<sup>2</sup> and Xicheng Huang<sup>2</sup>

<sup>1</sup>School of Mechanics and Engineering, Southwest Jiaotong University, Chengdu 610031, P.R. China

<sup>2</sup>Institute of Structural Mechanics, China Academy of Engineering Physics, Mianyang 621900, P.R. China

**Abstract.** The 2-D model of plate with inner crack is simulated by ABAQUS finite element software. Three kinds of crack growth criteria (critical stress, crack opening displacement and crack propagation as a function of time) are applied to simulate crack growth process in this paper. The results indicate that the critical stress criterion, which is based on stress value near the crack tip, is applicable to brittle material crack growth. Crack opening displacement criterion, which is based on node displacement value near crack tip, is applicable to ductile material fracture. Crack length versus time criterion can be applied when the crack growth process is known in advance. As crack growth problem is with stress and strain singularities, the mechanical parameters near crack tip can be taken as crack growth criterion to simulate crack growth in finite element analysis.

**Keywords:** crack growth, fracture mechanics, numerical simulation, fracture criterion

## 1 Introduction

Fracture mechanics is applied in engineering analysis field widely. Crack growth is a high nonlinear problem in fracture mechanics (Zhao, 1996). It mainly includes crack growth criterion and numerical simulation method. The shapes of most fatigue crack growth show regular characters. For example, surface fatigue crack is frequently ellipse and grows along “the prior path” (Wu, 2007). Main research on crack growth is about microcosmic and macroscopic crack structures presently. Microcosmic research is to study fatigue crack growth theory and correlative mechanics model. Macroscopic research is about crack growth mechanics model and crack growth velocity expression (Wang, 2002).

---

\* Corresponding author, e-mail: wz\_zhong@sina.com

Recently many researchers have done much study on crack growth measuring and numerical simulation. For instance, Research concrete I-II composite fracture by stress intensity factor and energy methods (Dong et al., 2006). Analyze measuring technique of fatigue crack growth threshold value (Goecke and Moshier, 2007). A nodal release procedure and a substructure method are used to simulate stable crack growth in power law hardening materials under mode-I plane stress condition (Zhu, 1995). A fracture criterion of variable resistance, which will take actual fracture resistance under different stress state into account, is proposed to simulate the geometric features of surface crack growth under quasi-static loading (Chen et al., 1996). Material Failure Process Analysis code is used to simulate the different types of debonding propagation along FRP-concrete interface and crack distribution in the concrete (Zhang et al., 2006). A new numerical technique, by combining the virtual laminated element method, is given in detail to construct the structure stiffness matrices for the special finite elements intersecting with the existing crack, which can naturally resolve the difficulties due to the constructed functions of interposing displacement field are discontinuous across the crack faces (Li et al., 2006). A stochastic finite element method is proposed to calculate the fracture mechanics parameters of a single edged crack plate. The parameters include the J-integral, the crack opening displacement, the relative displacement and angle of rotation of upper and lower of the plate (Sun et al., 2001). Although many research methods of crack growth are presented presently. Mostly the simulation methods are complicated and low efficient. Users have to compile subroutine to achieve crack growth process in finite element analysis.

Three kinds of crack growth criteria (critical stress, crack opening displacement and crack propagation as a function of time) are applied to simulate crack growth process of plate with inner crack in this paper. Verify the applicability and validity of crack growth criteria by numerical simulation example.

## **2 Crack Growth Criterion**

There are three processes in material fracture problem, which includes crack initiation, crack propagation and rupture. As stress and strain of crack tip are great and singularity. Force field parameters can be taken as crack growth criterion in crack propagation finite element analysis.

### ***2.1 Critical Stress***

It is to specify a critical stress criterion at a critical distance ahead of the crack tip. The crack-tip node debonds when the local stress across the interface at the specified distance ahead of the crack tip reaches a critical value. This criterion is typi-

cally used for crack propagation in brittle materials. The corresponding scheme is shown in Figure 1.

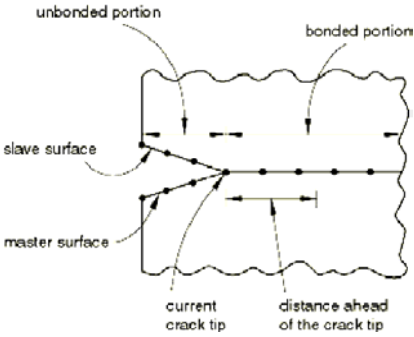


Figure 1. Critical stress criterion scheme

The critical stress criterion is defined as

$$f = \sqrt{\left(\frac{\sigma_n}{\sigma_f}\right)^2 + \left(\frac{\tau}{\tau_f}\right)^2} \quad (1)$$

where  $\sigma_n$  is the normal component of stress carried across the interface at the distance specified.  $\sigma_f$  is the normal failure stresses.  $\tau$  is the shear stress in the interface.  $\tau_f$  is the shear failure stress. The crack-tip node debonds when the fracture criterion,  $f$ , reaches the value 1.0.

## 2.2 Critical Crack Opening Displacement

The crack-tip node debonds when the crack opening displacement (*COD*) at a specified distance behind the crack tip reaches a critical value. This criterion is used for crack propagation in ductile materials. The corresponding scheme is shown in Figure 2.

The crack opening displacement criterion is defined as

$$f = \frac{\delta}{\delta_c} \quad (2)$$

where  $\delta$  is the measured value of crack opening displacement and  $\delta_C$  is the critical value of *COD* which is specified by user. The crack-tip node debonds when the fracture criterion reaches the value 1.0.

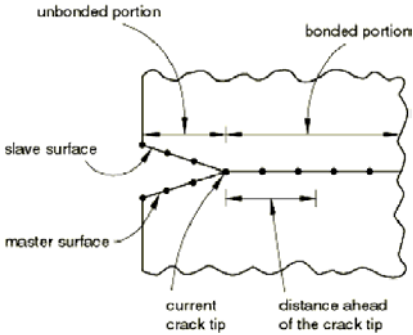


Figure 2. Crack opening displacement criterion scheme

### 2.3 Crack Length versus Time

The user must provide a crack length versus time relationship and a reference point from which the crack length is measured. During crack propagation, the crack length is measured from the user-specified reference point along the slave surface in the deformed configuration. The corresponding scheme is shown in Figure 3.

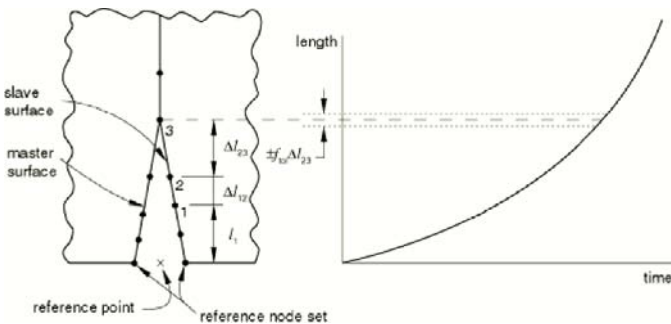


Figure 3. Crack propagation as a function of time criterion scheme

Referring to Figure 3, let node 1 be the initial location of the crack tip and node 3 be the current location of the crack tip. The distance of the current crack tip located at node 3 is given by

$$l_3 = l_1 + \Delta l_{12} + \Delta l_{23} \quad (3)$$

The fracture criterion,  $f$ , is given by

$$f = \frac{l - (l_3 - \Delta l_{23})}{\Delta l_{23}} \quad (4)$$

where  $l$  is the length at the current time obtained from the crack length versus time curve specified by the user. Crack-tip node 3 will debond when the failure function  $f$  reaches the value of 1.0.

### 3 Numerical Simulation

The meshing model of plate with inner crack is depicted in Figure 4. There are 3940 triangular elements and 2103 nodes. Height of specimen  $W$  is 40 millimeter. Length of specimen  $L$  is 160mm. The inner crack length is 10mm. Elastic modulus of material is 210GPa. Poisson ratio is 0.3. Density of specimen is 7800kg/m<sup>3</sup>. The tensile stress  $P$  is 200MPa.

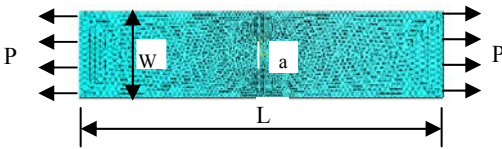


Figure 4. Mesh of plate with inner crack

#### 3.1 Simulation Result by Critical Stress Criterion

According to numerical model (Figure 4), the stress of 1mm ahead of the crack tip is specified as crack growth criterion. The critical stress value of crack propagation is 180MPa. Crack growth processes gained by ABAQUS finite element software are shown in Figure 5.

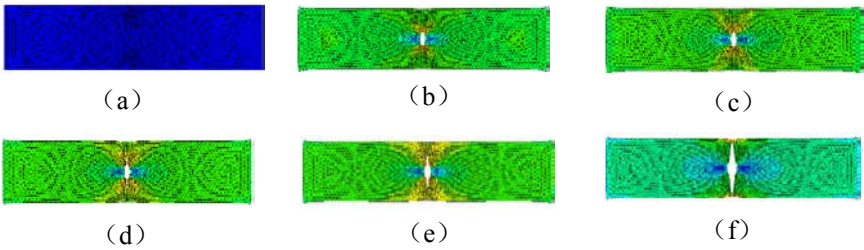


Figure 5. Crack growth process (critical stress criterion)

Stress around crack-tip is very great when crack plate is acted by tensile loading. If the specified position stress is satisfied to critical stress value, The crack-tip node debonds and crack growth process is realized.

**3.2 Simulation Result by COD Criterion**

The crack opening displacement of 4mm behind the crack tip is taken as crack growth criterion. The critical displacement value is 0.02mm. The model (Figure 4) is analyzed by ABAQUS finite element software. Process of crack propagation is depicted in Figure 6. When opening displacement of specified nodes is up to critical displacement value, crack-tip node debonds and crack grows along the preconcerted path.

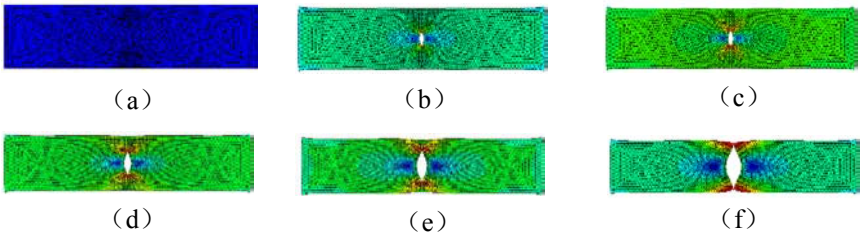


Figure 6. Crack growth process (Critical crack opening displacement criterion)

**3.3 Simulation Result by Crack Length versus Time Criterion**

Assuming crack length versus time is quadric function, The expression is given by

$$y = 0.03125t^2 \quad t \in [0, 0.8] \quad (5)$$

Equation (5), as crack growth criterion, is adopted to simulate crack growth model (Figure 4). Simulation results is shown in Figure 7. The crack length grows according to the function of crack length versus time. Node of crack-tip debonds continuously and crack extends forward.

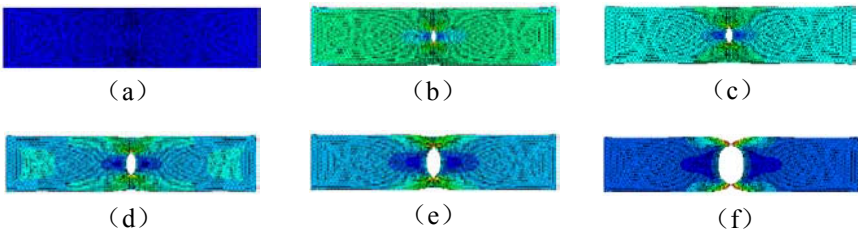


Figure 7. Crack growth process (crack length versus time criterion)

## 4 Discussion

Three crack growth criteria are applied to simulate the crack growth of inner crack plate in the numerical simulation examples. The criteria of critical stress and crack opening displacement are relative to mechanical parameters of crack tip. It is difficult to measure crack opening displacement for brittle material. So critical stress criterion is suited to simulate brittle material crack growth problem. The crack opening displacement is often obvious in ductile materials fracture. Crack opening displacement criterion can be availablely adopted in ductile materials crack growth problem. Owing to crack length versus time criterion is based on corresponding experiment result, it can be applied no matter brittle material or ductile material.

Both critical stress and crack opening displacement criteria can be expressed by stress intensity factor. The equation of dynamic stress intensity factor and stress is given by Fan (2003).

$$\sigma_{ij}(t) = \frac{K_I(t)}{\sqrt{2\pi r}} f_{ij}(\theta) \quad (6)$$

when  $\theta = \pi$  and  $r$  is much less, the relation between dynamic stress intensity and stress can be given by

$$K(t) = \sqrt{2\pi r} \sigma_y \quad (7)$$

Crack opening displacement can be used to compute dynamic stress intensity factor approximately. The equation is given by (Rubio, 2003)

$$K_I(t) = \frac{E w_M(t) k_\beta(\alpha)}{4\sqrt{a\alpha} v_\beta(\alpha)} \quad (8)$$

where  $\beta$  is ratio of crack length to height,  $K_\beta$  and  $v_\beta$  are dimensionless parameter.

According to Equation (7) and (8), it is clear that stress intensity factor can be deduced by crack displacement or stress field parameter. Critical stress and crack opening displacement can be taken for fracture criterion which are dominated by stress intensity factor. So the numerical simulation results are equivalent by different crack growth criteria.

## 5 Conclusions

Crack growth criteria and corresponding numerical simulation methods are depicted in the paper. Crack plate acted by tensile loading is simulated by the three crack growth criteria. The results show that the mechanical parameters near crack tip can be taken as crack growth criterion to simulate crack growth effectively in finite element analysis. The critical stress criterion can be used for crack propagation in brittle materials. Critical crack opening displacement criterion can be used to simulate crack propagation in ductile materials. And crack length versus time criterion can be adopted if the relation of crack length versus time is known in advance.

## References

- Chen J., Lou Y.Q. et al. (1996). The finite element simulating calculation of surface crack growth under quasi-static loading. *Computational Structural Mechanics and Applications*, 13(4), 435–440 [in Chinese].
- Dong W., Wu Z.M. et al. (2006). Advances in fracture criteria of mixed model fracture in concrete. *Mechanics in Engineering*, 28(6), 9–14 [in Chinese].
- Fan T.Y. (2003). *Foundation of Fracture Theory*. Beijing: Publishing House of Science [in Chinese].
- Goecke K.E., Moshier M.A. (2002). Technique to measure fatigue crack growth threshold. *Experimental Mechanics*, 42(2), 182–185.

- Li J.B., Chen J.Y. et al. (2006). Extended finite element without remeshing (2: Method for modeling cracks numerical implementation). *Chinese Journal of Computational Mechanics*, 23(3), 317–323 [in Chinese].
- Rubio L. (2003). Determination of dynamic fracture-initiation toughness using three-point bending tests in a modified Hopkinson pressure bar. *Experimental Mechanics*, 43(4), 379–386.
- Sun S.F., Li J.K. et al. (2001). The stochastic finite element method in engineering fracture analysis. *Acta Mechantica Solida Sinica*, 22(1), 85–88 [in Chinese].
- Wang H. (2002). Quantitative assessment of fatigue and fracture properties of materials. Xian: Northwestern Polytechnical University, [in Chinese].
- Wu Z.X. (2007). Numerical Simulation to Surface Crack Fatigue Growth (II). *Chinese Journal of Applied Mechanics*, 24(1), 42–46 [in Chinese].
- Zhang J.X., Tang C.A. et al. (2006). Numerical simulation of fracturing behaviors of FRP-strengthened concrete members. *Engineering Mechanics*, 23(12), 143–148 [in Chinese].
- Zhao Y.P. (1996). The advances of studies on the dynamic initiation of cracks. *Advances in Mechanics*, 26(3), 362–377 [in Chinese].
- Zhu W.H. (1995). A finite element simulation of stable crack propagation in power law hardening materials under plane stress. *ACTA Aeronautica ET Astronautica Sinica*, 16(2), 247–252 [in Chinese].

*“This page left intentionally blank.”*

# Nonlinear Numerical Simulation on Shearing Performance of RC Beams Strengthened with Steel Wire Mesh-Polymer Mortar

Chiyun Zhao<sup>1\*</sup>, Sihua Deng<sup>1</sup>, Yajing Chen<sup>1</sup>, Shimin Huang<sup>2</sup> and Qiulai Yao<sup>2</sup>

<sup>1</sup>Department of Civil Engineering, Beijing University of Civil Engineering and Architecture, Beijing 100044, P.R. China

<sup>2</sup>Institute of Earthquake Engineering, China Academy of Building Research, Beijing 100013, P.R. China

**Abstract.** The numerical analysis by using software ANSYS for shearing performance of rectangular reinforced concrete beams strengthened with steel wire mesh-polymer mortar formed U-shaped are studied. The numerical results are compared with experimental results. Two models, named separated model and composite model respectively in software ANSYS, are used to analyze the beams. In separated model, strains of longitudinal steel bars and stirrups are in good agreement with the test results. In composite model, strains of longitudinal steel bars are also in good agreement with the test results, while strains of stirrups are not. But both of steel wire deformations obtained by two models of software ANSYS are slightly different with the tests results. Cracks distribution in beams obtained by software ANSYS, comparing with test results, are not very obvious.

**Keywords:** steel wire mesh, polymer mortar, strengthening, reinforced concrete beam, shearing performance, experiment, finite element method

## 1 Preface

The strengthened method of steel wire mesh-polymer mortar usually forms a composite layer with thickness of 25mm to 30mm in use. Steel wires have advantages like high strength, no rust, convenience for transportation and construction. Polymer mortar is inorganic materials and has better properties bonded with concrete. So this technology has the advantages of better resistance of high temperature, corrosion and aging, simple construction.

---

\* Corresponding author, e-mail: zhaocy@bucea.edu.cn

In recent years, scholars in domestic have made a wide range of experimental studies by using imported polymer mortar (Nie et al., 2005, Cao et al., 2006, Bu et al., 2006) and numerical studies (Liu et al., 2006, Zeng et al., 2008) in this field.

In this paper, the finite element software ANSYS is used for nonlinear numerical simulation analysis on shearing performance of RC beams strengthened with steel wire mesh and polymer mortar made in China. The numerical results are compared with the experimental results.

## 2 Experimental Introductions

In tests, the bending capacities of the reinforced concrete beams were far greater than their shearing capacities, so that the beams failed in shear failures. More longitudinal steel bars and lesser stirrups were designed in the specimen beams. In order to consider a actual beam with a slab on the beam, a reinforcement layer of U-shaped was strengthened at bottom and on both sides of the beam.

3 RC beams were designed in the experiments (Figure 1). The steel strength grades of longitudinal steel bars and stirrups were HRB335 and HPB235 respectively. Concrete strength grade was C20. The beam BS-1 is an unstrengthened member, BS-2 and BS-3 were strengthened members with a U-shaped layer of thickness of 25mm. The ultimate tensile strength and modulus of elasticity of a steel wire were 1650MPa and  $1.34 \times 10^5$ MPa respectively. A steel wire was made of 6 × 7 + IWS, the steel wire mesh were made of  $\phi 3.05@30$ . The compressive strength and tensile strength of polymer mortar were 24MPa and 4.8MPa respectively. The shear span ratios of BS-1, BS-2 and BS-3 were 1.87, 1.87 and 2.28 respectively.

Measurements of the tests were values of loading, strains of steel, concrete and mortar, displacements of supported-point, midspan point and loading-point, elongation of steel wires (Figure 2).

## 3 Computational Models

Two types of finite element methods in software ANSYS, separated model and composite model, were used to simulate the experimental beams. This is assumed that the steel wire mesh and the polymer mortar, concrete and the polymer mortar are bonded well, have not slippage relatively.

In separated finite element model, concrete and polymer mortar use element Solid65, steel and steel wire use element Link8 (Figure 3, left). In composite finite element model, only element Solid65 is used. In order to better simulate the arrangement of steel, composite finite element model use three layers to build, in the beam top we input 2 @18 and direction of the beam width stirrups as reinforcement

ratio, the middle layer for the direction of beam high stirrups, to the beam bottom  $3\phi 25$  and the direction of the beam width stirrups as reinforcement ratio (Figure 3, right).

Concrete, polymer mortar and steel bars, steel wires took Poisson's ratio of 0.2 and 0.3 respectively. Stress - strain curves of concrete, mortar and steel bars , steel wires took multilinear isotropic hardening and bilinear kinematic hardening model (Figure 4, right) respectively.

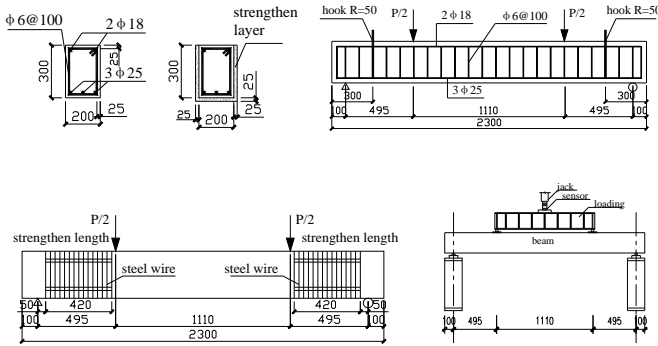


Figure 1. Details of strengthened RC beams and loading equipment.

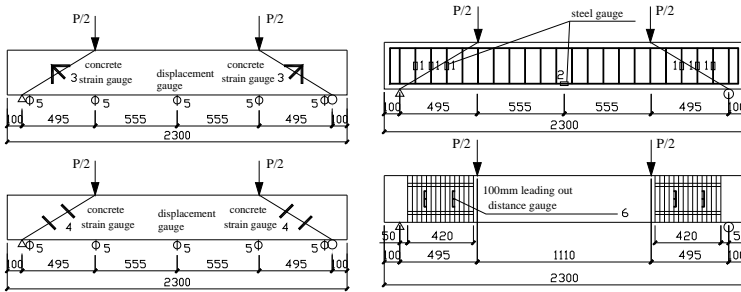


Figure 2. Sketch of measured points of steel, steel wire mesh, mortar and concrete in beams.

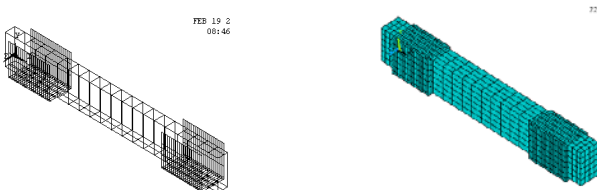


Figure 3. Steel and steel wire mesh in separated model and composite finite element model.

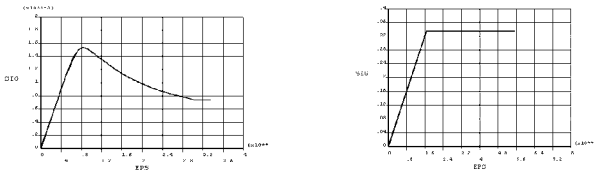


Figure 4. Sketch of concrete and mortar  $\sigma$ - $\epsilon$  curve, steel and steel wire mesh  $\sigma$ - $\epsilon$  curve.

Displacement convergence criteria were used in nonlinear analysis.

### 4 Comparisons of Experimental and Numerical Results

1. Cracks distribution in beams.

Cracks distribution in the unstrengthened beam is more wide and regular, while cracks distribution in the strengthened beams is more close and irregular (Figure 5 to Figure 7). Failure modes of beam BS-1 and BS-2 are shear failures, while failure mode of BS-1 with larger shear span ratio, is shear-bending failure (but not typical).

2. Strains of longitudinal steel bars at beam bottom.

Strains of longitudinal steel bars in separated and composite model agree well with the test results (Figure 8, BS-2 left, BS-3 right).

3. Strains of stirrups.

Strains of stirrups in separated model are closer to the test results than them in composite model, because a real distribution of stirrups is simulated in separated model (Figure 9, BS-2 left, BS-3 right).

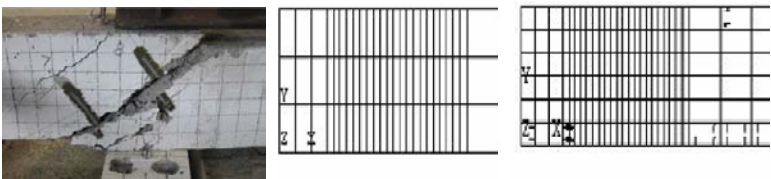


Figure 5. Cracks distribution of test, separated model and composite model in beam BS-1.

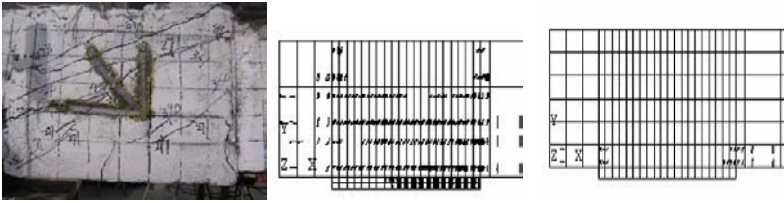


Figure 6. Cracks distribution of test, separated model and composite model in beam BS-2.

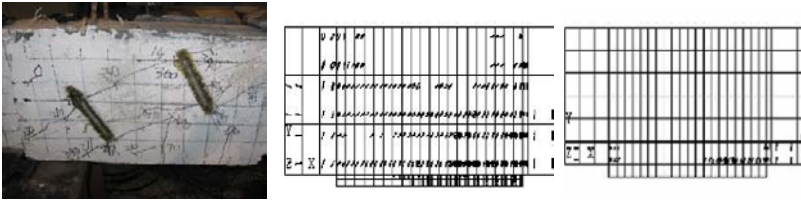


Figure 7. Cracks distribution of test, separated model and composite model in beam BS-3.

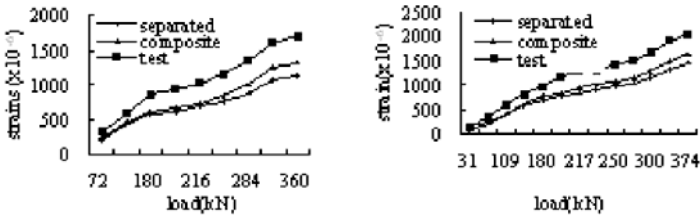


Figure 8. Strains of steel bars of BS-2 and BS-3 in test, separated and composite model.

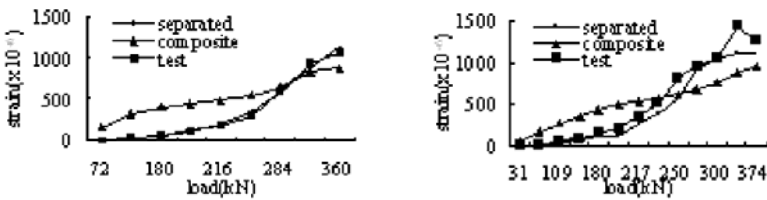


Figure 9. Strains of stirrups of BS-2 and BS-3 in test, separated and composite model.

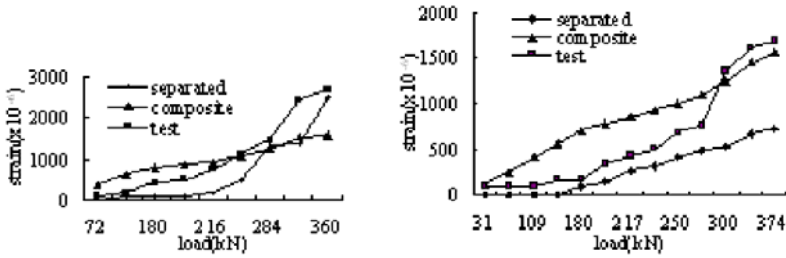


Figure 10. Strains of steel wires of BS-2 and BS-3 in test, separated and composite model.



Figure 11. Indirect measure of elongations of steel wires in experiment.

4. Strains of steel wires.

When a load is small, there has a larger gap between values of strains of steel wires by software ANSYS and by tests, the gap becomes smaller and stable under increasing load (Figure 10, BS-2 left, BS-3 right). This may be that elongations of steel wires in tests can not be directly measured. In tests, elongations of parallel bars with sufficient rigidity, to steel wires are measured. When in an ideal situation, those values equal to elongations of steel wires in theory (Figure 11).

5 Conclusions

1. Experiments and numerical calculations show that RC beams strengthened by steel wire mesh-polymer mortar improve obviously shear capacities of beams.
2. RC beams strengthened with steel wire mesh-polymer mortar delay cracks occur and development. Cracks distribution of strengthened beams is more close, dense and irregular than that of unstrengthened beams. Cracks in beams obtained by software ANSYS, comparing with test results, are not obvious.

3. In separated model, strains of longitudinal steel bars and stirrups are in good agreement with the test results. In composite model, strains of longitudinal steel bars are also in good agreement with the test results, while strains of stirrups are not.
4. Both deformations of steel wires obtained by two models of software ANSYS are slightly different with the tests results.

## References

- Bu Liangtao, Wang Yuehong (2006). Experimental study on shear behaviors of RC beams strengthened with ferrocement Mortar. *Journal of HUST*, 23(4), 35–38 [in Chinese].
- Cao Zhongmin, Li Aiqun et al. (2006). Experimental study on beam-column connections strengthened with high-strength steel wire mesh and polymer mortar. *Journal of Building Structures*, 27(4), 10–15 [in Chinese].
- Code for design of concrete structures (GB50017-2002). China Architecture & Building Press, Beijing [in Chinese].
- Liu Boquan, Xing Guohua et al. (2006). Experimental investigation and finite element simulation about RC T-beams strengthened with wire cable mesh and polymer mortar. *Journal of Xi'an Univ. of Arch. & Tech*, 38(5), 603–608 [in Chinese].
- Nie Jianguo, Wang Hanbing et al. (2005). Experimental study on shear behavior of RC beams strengthened with stainless steel wire mesh and permeability polymer mortar. *Journal of Building Structures*, 26(2), 10–14 [in Chinese].
- Zeng Linghong, Shang Shouping et al. (2008). Reinforced concrete beams shear strengthened with high-performance ferrocement. *Journal of Guilin University of Technology*, 28(28), 34–38 [in Chinese].

*“This page left intentionally blank.”*

# **APPLICATION AND OTHERS**

*“This page left intentionally blank.”*

# Flexural Behavior of HS Composite Beams via FEM

Huiling Zhao<sup>1,2\*</sup>, Shashi Kunnath<sup>1</sup> and Yong Yuan<sup>3</sup>

<sup>1</sup>University of California at Davis, California, USA

<sup>2</sup>Tongji University, Shanghai, China

<sup>3</sup>Key Laboratory of Geotechnical and Underground Engineering of Ministry of Education, Shanghai, China

**Abstract.** The present investigation focuses on the flexural behavior of HS steel-concrete composite beams using the commercial finite element (FE) software LS-DYNA. Herein, HS steel-concrete composite beams were constructed with a welded high strength steel I section beam and high strength concrete slab. The proposed three-dimensional FE model is able to simulate the overall flexural behavior, including load deflection behavior and failure modes, of simply supported composite beams subjected to two-point concentrated loads. The reliability of the model is demonstrated by comparisons with experiments results. The load-slip effects on the accuracy of the FE model analysis is also discussed in detail. The accuracy and simplicity of the proposed model make it suitable to predict and/or complement experimental investigations.

**Keywords:** HS composite beam, finite element method, nonlinear analysis, LS-DYNA

## 1 Introduction

Two series of tests on half-scale models of composite beams with high-strength or normal-strength steel and concrete were carried out by Yuan and Zhao (2008). Six composite beams having the span to height ratios of 16.0 and 13.3 were tested to failure in this experimental study. Obviously, the high-strength composite beams applied in long-span structures was the focus of this study. The report herein is concerned with the finite element modeling of such tested composite beams. Numerical modeling is developed and the results were calibrated against the experimental elastic and ultimate load behavior and the load carrying capacity.

It has been recognized that an accurate assessment of deflections and stresses are difficult even for ordinary reinforced concrete members. In the case of compo-

---

\* Corresponding author, e-mail: zhaohuiling1668@gmail.com

site beams, the problem becomes complicated because of the difficulty in accounting for the effect of changes in the degree of composite action. In addition, the material property of the composite beam is nonhomogeneous. Because of these factors, it is difficult to develop an accurate theoretical model to capture the complete behavior of composite plate girders accurately. FE analysis using the general-purpose FE software LS-DYNA has been chosen in this study to carry out the analysis of steel-concrete composite plate girders.

More research has been reported on nonlinear FE analysis of steel-concrete composite members. Ayoub and Filippou (2000) presented an inelastic beam element for the analysis of steel-concrete composite girders with partial composite action under monotonic and cyclic loads. This element is derived from a two-field mixed formulation. Fiber discretization of section and hysteric material models for the constituent materials are used to achieve the nonlinear response.

Sebastian and McConnel (2000) developed another beam element with layered steel beam and layered concrete slab for the analysis of steel-concrete composite girders. In this element, they also included the modeling of profiled steel sheeting. A specialized stub element with an empirical nonlinear shear force-slip relationship is used at the concrete slab-steel beam interface to permit the modeling of either full or partial shear connector action.

A specific kinematic model of the cross section is proposed by Fabbrocino et al. (2000) for the analysis of continuous composite beams including partial interaction and bond. Rex and Easterling (2000) studied the axial force deformation behavior of a reinforced composite slab under tension. Furthermore, there are more numerical modeling works reported on steel-concrete composite beams by various researchers like Arda et al. (1995), Decker et al. (1995), Dorey et al. (1997), Ramm and Elz (1997), Tehami (1997), Manfredi et al. (1999), and Thevendran et al. (1999).

From the available literature, it is noticed that the research on the numerical modeling of a steel-concrete composite beam has been carried out extensively and, researchers proposed different methods of modeling approaches, new elements for the composite member, and closed-form solutions. It is also noticed that there is no reported work on the numerical modeling of long-span steel-concrete composite beams where the steel portion and the concrete slab is made up of high-strength materials. In such beams, high loading capacity occurred with the large deformation. Especially, the specific properties present at the nonlinear stage. Therefore, it is decided to propose a new FE model to carry out the nonlinear analysis of a steel-concrete composite plate girder under monotonic loading.

## 2 Specimens Considered in Analysis

A total of four simply-supported composite beams were constructed and tested. All the specimens are designed in accordance with the simple plastic method. The

concrete slab and the steel beam are directly connected by means of studs. Shear connections for all the specimens are 1, namely full connection, as defined by the Eurocode 4.

Table 1 Main experimental parameters

Specimens		SCB1	SCB2	SCB3	SCB6
$f_{ys}$ (MPa)		340.7	450.0	450.0	450.0
$f_{us}$ (MPa)		390.0	481.0	481.0	481.0
$f_{cu}$ (MPa)		34.4	35.2	74.9	76.8
$f_{yr}$ (MPa)		338.0	338.0	338.0	338.0
Steel beam /H×W×t1×t2 (mm)		150×130×10×10			200×130×10×10
Studs spacing (mm)	Transversal	70			
	Longitudinal	190 pure bend, 230 shear span	125 in pure bend span, 200 in shear span		100 pure bend, 150 shear span
Longitudinal reinforcements ratio		1.04%	1.04%	1.04%	1.04%
Transversal reinforcements ratio		1.73%	2.45%	2.45%	2.85%

The main experimental parameters are the strength of steel, concrete and steel beam depth, shown in Table 1. Specimens SCB-1 to SCB-3 and SCB6 were simply-supported and under positive bending. SCB-1, SCB-2, and SCB3 with the same geometry size are constructed by Q345 steel and C30 normal concrete, Q450 high strength steel and C30 normal concrete, and Q450 high strength steel and C80 high strength concrete, respectively. Specimens SCB-3 and SCB-6, both are constructed with Q450 high strength steel and C80 high strength concrete, whereas with different steel beam depths, 150 mm and 200 mm, were adopted to investigate its influence on the behavior of composite beams.

The detailed geometry of the test beams can be seen in Figure. 1. The concrete slab and the steel beam are directly connected by means of studs. Each of the beams under positive bending was 4300 mm long, simply supported on a span of 4000 mm. By using the depth/span length ratio of about 1/13.3–1/16, the span length of the specimen beams was large enough to minimize the effect of vertical shear and thus to assure a flexural failure.

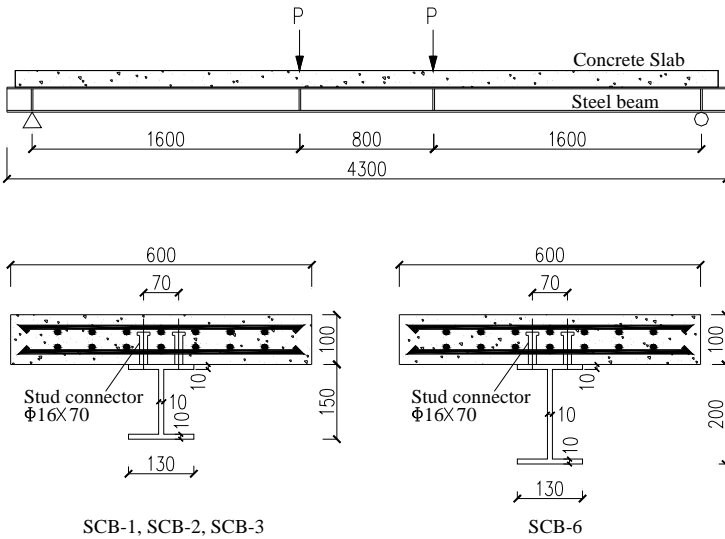


Figure 1. Dimensions of composite beams (Units: mm)

### 3 Finite Element Modeling

In the present study, various combinations of material models and element models have been investigated to identify a suitable model to predict the ultimate load behavior of steel-concrete composite beams. These models are described in detail in the following sections.

#### 3.1 Element Types

The finite element types considered in the model are as follows: elastic-plastic shell and solid elements for the steel section and the concrete slab, respectively, and nonlinear discrete beam element to represent the shear connectors. Both longitudinal and transverse reinforcing bars are modeled by truss elements.

Symmetry of the composite beams is taken into account by modeling one quarter of the beam span. A typical FE model for composite beam is shown in Figure 2.

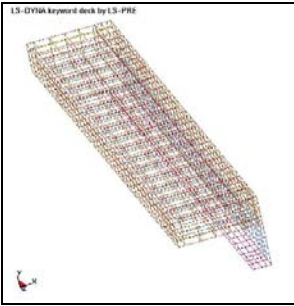


Figure 2. Finite element model of a typical composite beam

### 3.2 Nonlinear Material Models

The description of concrete behavior is adopted the Karagozian & Case (K&C) Concrete Model which is a three-invariant model, uses three shear failure surfaces, includes damage and strain-rate effects. A smeared fix or rotating crack approach is used in the model to represent the concrete cracking and post-peak behavior, confinement effect and tension stiffening can be simulated. This concrete model in LS-DYNA was developed and verified by Javier Malvar (1997) and it showed this implementation provide the most stable and accurate model of concrete behaviors among all available models. Steel behavior is modeled using bilinear stress-strain relationship where first segment of the relationship represents elastic behavior and residual plastic modulus is taken as one percent of the elastic modulus. Monotonic curves and related model parameters are shown in Figure 3 both for steel and concrete. The necessary material parameters such as strength, elastic modulus are taken as the actual measured values shown as Table 1.

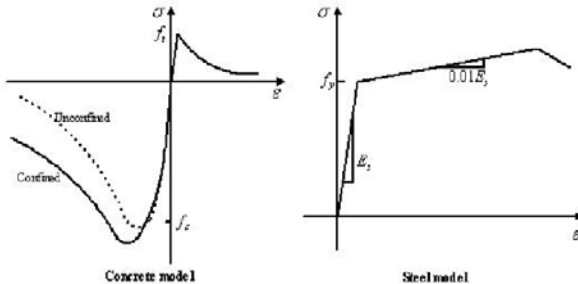


Figure 3. Material properties for finite-element model

### 3.3 Modeling with Shear Studs

The model allows for any pattern of stud distribution to be considered, for instance: the conventional uniform arrangement and a triangular spacing scheme where the stud distribution follows the nominal elastic shear diagram. In this study, four discrete beam elements are utilized to model the behaviour of studs. As far as the shear connector behaviour is concerned, the measured load-slip curves for 1/8, 1/4, 3/8 and beam end are used for the nonlinear discrete beam elements. These springs are modelled at the steel-concrete interface, as shown in Figure 4.

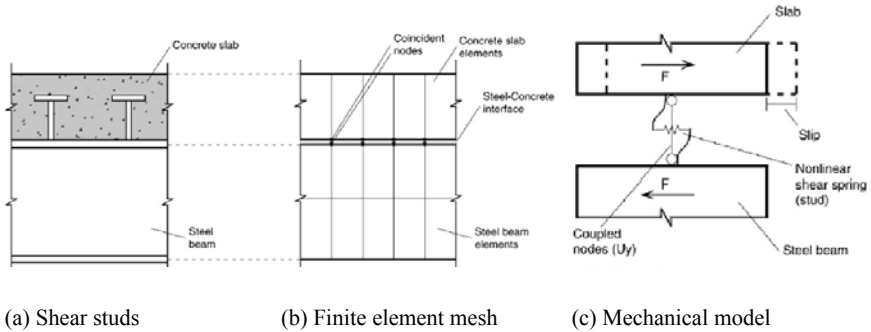


Figure 4. Shear stud model

### 3.4 Application of Load and Numerical Control

Regarding application of load, concentrated loads are incrementally applied to the model by means of an equivalent displacement to overcome convergence problems (displacement control). Uniformly distributed loads are represented by means of point loads applied at concrete nodes. The displacement-control loading strategy is necessary for the significant nonlinear effects including descending stage.

## 4 Results Comparison

For all composite beams shown in Table 1, load-midspan deflection curves are compared to the test results. Figures 5–8 (beams SCB-1 to SCB-3, and SCB-6) depict comparisons between the FE model results and the experimental data for the composite beams under positive bending and negative bending, respectively. In the following figures, no-slip curves represent the modeling results with the finite element model without considering the interface slip.

It can be seen that from Figures 5, 6, 7 and 8, the curves for all the specimens exhibited three stages, the initial elastic behavior, and then transiting into elasto-plastic nonlinear until reaching the utmost moment capacity, followed by load descending.

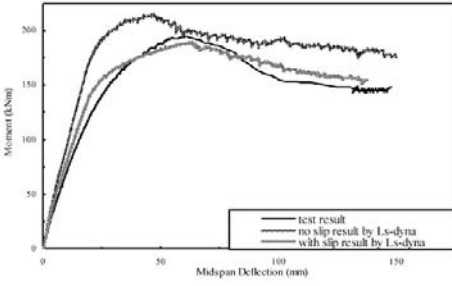


Figure 5. Moment-deflection curves for SCB-1

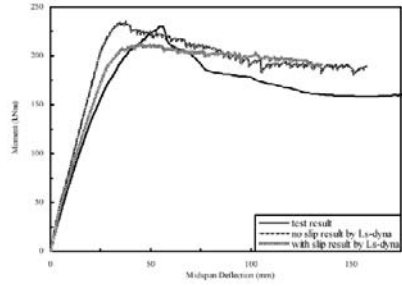


Figure 6. Moment-deflection curves for SCB-2

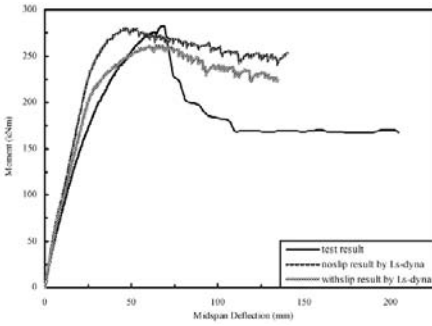


Figure 7. Moment-deflection curves for SCB-3

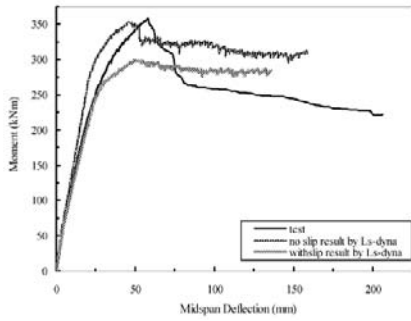


Figure 8. Moment-deflection curves for SCB-6

For the SCB-1, SCB-2, and SCB3 composite beams with the same geometry but different material strengths, the moment-deflection curves show almost the same elastic-linear response at the early age of elastic stage. However, significant differences are followed. Behaviour of SCB-1 beam transited into nonlinear, at the load of about 80% of its utmost capacity, accompanied the yield developed in steel beam. The load-descend stage is very gradual after load-peak. The slop for the entire curve of SCB-1 is gentle and smooth, so the mechanical behaviour of SCB-1 beam was relatively ductile. Compared with SCB-1, the age of SCB-2 beam transiting into nonlinear is late due to its higher steel strength than that of SCB-1 beam.

Meanwhile, SCB-2 can also reach a larger load capacity despite prior to a sudden load drop. SCB-3 beam showed the longest duration of elastic-linear stage in the three beams. Compared with SCB-2, the moment capacity of SCB-3 beam had

been improved dramatically. It was induced by that the neutral axis of the section for SCB-3 was close to the interface between concrete slab and steel beam, so the large strength potential of both Q450-steel for tension and C80-concrete for compression were exhibited fully. On the other hand, the more drastic load descending occurred in post-peak stage for SCB-3 composite beam. It should be noted that despite a more brittle failure mode, the ultimate deflections at failure of the SCB-3 composite beams were larger than SCB-2 Specimen. Due to the high-strength concrete for SCB-3, the rigidity degradation was postponed and resistance to compression of concrete slab had been enhanced effectively.

In the case of SCB-6 beam, the rigidity and moment capacity reached more than 350.0 kN\*m, increased 26.5% and 55.4% respectively compared to SCB-2 and SCB-3 beam. The curve shape of SCB-6 beam was similar to that of SCB-2. Their deformation abilities were relatively weak. It can be explained by that for both of their section composition the compressive capacity of concrete slabs was relatively weak compared to the strong steel beam with either high strength or large height.

From these figures, more disparities with experiment results in no-slip LS-DYNA 3D FE model than the model considering slip at interface. The former would provide unconservative prediction. It can be noticed that the analysis result by LS-DYNA 3D FE model considering slip at interface can reach favourable agreement with the experiment result. Especially, it can predict most of the load-deflection behaviour during the post-peak descending stage. Stiffness properties adopted for the discrete beam elements modelling the studs may result in differences between the simulation and experiment data. Therefore, more study should focus on the reasonable adoption of load-slip properties for studs.

## 5 Conclusion

A three-dimensional finite element model of composite beams is proposed based on the use of the commercial software LS-DYNA. It has proved to be effective in terms of predicting the load-deflection response for beams subjected to concentrated loads. This paper has briefly presented the analysis of composite beams constructed with different strength steel beam and different strength concrete slab. The effects of high-strength steel and concrete on the mechanical behavior of composite beams have been explored. The failure of composite beams with high-strength steel or/and concrete is brittle, compared to beams with normal-strength steel and concrete. However, the former has quite improved moment capacity and the deformability is favorable when the strength match of steel and concrete is proper. The high-strength concrete slab has stronger resist to the longitudinal split than normal-strength concrete slab.

Comparisons against experimental results indicate that the FE model considering slip at interface can reach favorable agreement with the experiment result. The

analysis of no-slip LS-DYNA 3D FE model may be quite unconservative for predicating the moment capacity of composite beams with high-strength steel or concrete. Further research is suggested to enable shear-deformation relationship adopted for the discrete beam elements modeling the studs.

## Acknowledgements

The authors would like to appreciate the financial support of Chinese Scholarship Council and University of California at Davis for the visiting research of Ms Zhao. The appreciation may extend to the grant of MOST on the project 'Hazard Prevention for Urban Underground' (No. 2006BAJ27B04) which is led by Professor Yuan Yong.

## References

- Ayoub, A. and Filippou, F. C. (2000). Mixed formulation of nonlinear steel-concrete composite beam element. *J. Struct. Eng.*, 126(3): 371–381.
- Fabroccino, G., Manfredi, G., and Cosenza, E. (2000). Analysis of continuous composite beams including partial interaction and bond. *J. Struct. Eng.*, 126(11): 1288–1294.
- Arda, T. S. and Mengene, N. (1995). Strength of composite beams with web concrete under negative bending. *J. Struct. Eng.* 121(8): 1170–1174.
- Dekker, N. W., Kemp, A. R., and Trincherro, P. (1995). Factors influencing the strength of continuous composite beams in negative bending. *J. Constr. Steel Res.*, 34(2–3): 161–185.
- Dorey, A., Cheng, B., and Roger, J. J. (1997). Behavior of composite beams with no flexural steel under negative moment. *Proc., Structures-Design, Concrete and Reinforced Concrete Structures, Bridges Annual Conference*, Canadian Society for Civil Engineering, Montreal, 7, 281–290.
- Manfredi, G., Fabbroccino, G., and Cosenza, E. (1999). Modeling of steel-concrete composite beams under negative bending. *J. Eng. Mech. Div., Am. Soc. Civ. Eng.*, 125(6): 654–662.
- Ramm, W., and Elz, S. (1997). Behavior and cracking of slabs as part of composite beams in regions with negative bending moments. *Proc., Engineering Foundation Conf.*, ASCE, New York, 871–886.
- Rex, O. C. and Easterling, W. S. (2000). Behavior and modeling of reinforced composite slab in tension. *J. Struct. Eng.*, 126(7): 764–771.
- Sebastian, W. M., and McConnel, R. E. (2000). Nonlinear FE analysis of steel-concrete composite structures. *J. Struct. Eng.*, 126(6): 662–674.
- Tehami, M. (1997). Local buckling in class 2 continuous composite beams. *J. Constr. Steel Res.*, 43(1–3): 141–159.
- Thevendran, V., Chen, S., Shanmugam, N. E., and Liew, J. Y. R. (1999). Nonlinear analysis of steel-concrete composite beams curved in plan. *Finite Elem. Anal. Design*, 32(3): 125–139.

*“This page left intentionally blank.”*

# Study on Design and Mechanics of Bucket Foundation Offshore Platform with Two Pillars

Meng Jiang<sup>1\*</sup>, Lihua Han<sup>1</sup> and Rixiang Zhang<sup>1</sup>

<sup>1</sup>School of Civil & Hydraulic Engineering, Dalian University of Technology, Dalian 116024, P.R. China

**Abstract.** The bucket foundation offshore platform with two pillars is introduced in this paper. The structural outline, main dimensions and construction technology of the platform are discussed. The platform has many advantages, such as not needing piles, easy to be constructed, low cost and can be moved and used again. Static and dynamic analyses are carried out by means of space finite element model. The shell elements are used to establish the steel offshore platform and the spring element are used to imitate the interaction between the bucket and the soft soil in the model. Multiple disadvantageous loading conditions of wave and ice are considered in the static structural analysis, and dynamic modes and seismic responses of the platform are also researched in this paper. The results of the analysis show that this kind of platform has enough strength and stability when subjected to the loads of wave, ice and seismic. On the basis of the numerical results, some useful advices are presented to optimize the design of the platform.

**Keywords:** bucket foundation, structural strength, two pillars

## 1 Introduction

As a new type of foundation in beach-shallow sea, bucket foundation platform makes up defects of traditional pile platform and gravity platform. The new kind of steel piles with a large-diameter is just like a steel bucket placed upside down. It is especially suitable for complex condition such as marine soft soil ground and worse sea environments. During installation of bucket foundation platform on sea, negative pressure system must be utilized and controlled effectively (Wang et al., 2000).

Bucket foundation is circular plate with skirts and has some advantages, for example, saving investment and iterative. The application and promotion of this platform are of great significance to offshore oil development. In 1994 and 1995, Sta-

---

\* Corresponding author, e-mail: jiangm2006@sohu.com

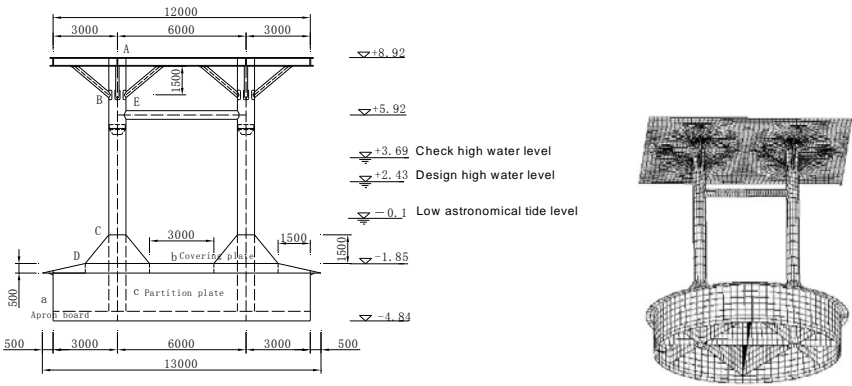
toil (Norway) constructed two platforms with bucket foundation in the North Sea, Eurpipe 16/11 platform and Sleipner Vest SLT platform. They marked the birth of platforms with bucket foundation. In China, research and design of offshore bucket foundation commenced in the past few years (Li and Liu, 2007). The first offshore platform CB20B composed of bucket foundation was constructed successfully in beach-shallow sea in Shengli oil field (Wang and Xu, 2003). This platform works excellently by now and is acclaimed as a good novel type of platform. The success in design and construction of this platform offers practical experiences to other offshore applications of bucket foundation in China.

In this article, a platform structure with a large diameter and short height bucket foundation is proposed for an offshore well of Liaohe oil field in recognition of a thick underlying soft soil layer and a 0~5m water depth. The structure is studied in detail. This study may serve as engineering reference to static and dynamic analysis and computation of similar platforms.

## 2 Structural Design and Analysis Model

Bucket foundation falls into single bucket foundation, three bucket foundation, and four foundation bucket types, etc., with their own advantages and disadvantages. Single round bucket foundation type is chosen based on the marine environment of the well location (large tidal range and small current), as single bucket platform is easy to be constructed and can be controlled with comfort during lowering down. After design optimization, the dual-column bucket foundation platform consists of three parts, namely deck, columns, and bucket foundation, as shown in Figure 1(a). The platform deck is of beam-slab structure made of longitudinal and transversal beams. Crude oil production facilities are arranged on the deck. Two columns of 800mm in diameter are provided under the deck. These columns, along with round steel beam, support the deck system. The bottom of the column is joined to the large-sized bucket foundation with cone steel structures.

According to computation, analysis and structural optimization, the bucket foundation is divided by baffles into four independent enclosed compartments. During platform towing, every other of the four compartments is filled with air so as to reduce draft of the platform. The bucket foundation is 12m in diameter and 2.5m in height and consists of three sections: bucket top, bucket superstructure, and bucket substructure. The bucket top is 0.5m high, while the bucket superstructure has a height of 2m. The bucket substructure is provided with 0.5m high apron board. The enforced plates in the bucket superstructure are jointed to the bucket panel, so that the axial force and bending moment of the columns can be transmitted to the bucket panel.



(a) Elevation of bucket foundation platform (in mm)

(b) Finite element model

Figure 1. The bucket foundation platform and analysis model

In this paper, the two-column bucket foundation platform is simulated by spatial finite element model shown in Figure 1(b). The platform, columns, and bucket foundation are represented by board shell elements. On the other hand, the supporting that the soil exerts upon the foundation is simulated by spring elements total (Zhang et al., 2005). Meanwhile, this model also incorporates the bracing plates on the bucket panel, on the bucket top, and inside the bucket. Computation is done with the aid of ANSYS finite element software.

### 3 Static Analysis of the Structure

Dual-column bucket foundation platform works under the following loads: environmental loads like wind load, ice load, wave load, marine current load, and seismic load, and equipment on the deck and all weights of the deck. For static calculation of structural strength, 8 load cases and 3 load stages (positioning during construction, normal operation, and extreme environment situation) are considered.

1. Construction stage: the greatest stress condition is considered for the check calculation during construction period. To be specific, two load cases, namely when bogging down depth is 0.5m and approaches 2.5m, are studied together with a negative pressure of 15kPa in this article.
2. Normal operation stage: the most unfavorable load combination with the highest design water level is considered. Three load cases, as shown in Table 1, are studied for this stage.

3. Extreme environment stage: the load combination when the ice load has a recurrence period of 50 years is considered. Three load cases, as shown in Table 1, are studied for this stage.

Table 1. Load case during normal working stage and under extreme environmental conditions

	Water level	Load action direction	Load case	Load combination
Normal working stage	Design high water level	0°	Load case 1	Structure self-weight+ equipment self-weight+ live load+ extreme wind, wave + current
		45°	Load case 2	
		90°	Load case 3	
Extreme ice conditions	Low astronomical tide level	0°	Load case 4	Structure self-weight+ equipment self-weight+ live load+ wind load + ice load
		45°	Load case 5	
		90°	Load case 6	

According to computation results, the maximum horizontal displacement at the top of the column is 18.90mm when marine ice load acts in a 45° direction (load case 4). This is found in agreement with the condition of the maximum horizontal force. In contrast, its maximum vertical displacement is 2.87mm. The center point of the bottom cover plate produces small displacements: 1.60mm in horizontal direction and 1.55mm in vertical direction.

The platform members shall demonstrate enough strength and stability under various load combinations. In this article, structure static analysis is performed to estimate the internal forces of each member. Structure strength and stability is checked using the computation methods recommended in Code for Construction and Check of Fixed Platforms in Shallow Sea.

When a member subjects to axial forces and is under bending moment in two planes, its strength can be checked using the following formula:

$$\sigma = \frac{N}{A} \pm 0.9 \frac{\sqrt{M_x^2 + M_y^2}}{W} \leq [\sigma] \tag{1}$$

where  $\sigma$  is axial stress,  $N$  is axial force,  $M_x, M_y$  are bending moments relative to  $x, y$  axis,  $A$  is cross section area of the member,  $W$  is section modulus of the member,  $[\sigma]$  is allowable stress of the material.

When non-reinforced circular pipe structure is under the combined action of axial force and bending moment, the member stability can be checked using the following formula:

$$\sigma = \frac{N}{A} + 1.5\phi \frac{\sqrt{M_x^2 + M_y^2}}{W} \leq [\sigma_c] \tag{2}$$

where  $[\sigma_c]$  is allowable critical yielding stress,  $[\sigma_c] = \phi \sigma_s$  and  $\sigma_s$  is yielding strength of steel,  $\phi$  is overall stability coefficient; the other symbols have the same meanings as above.  $\phi$  is estimated from the following formula:

$$\phi = \frac{1 - 0.25\lambda_0^2}{1.67 + 0.265\lambda_0^2 - 0.044\lambda_0^3} \quad \text{when } \lambda_0 \leq \sqrt{2} \quad (3)$$

$$\phi = \frac{1}{1.92\lambda_0^2} \quad \text{when } \lambda_0 > \sqrt{2} \quad (4)$$

where  $\lambda_0 = \lambda / \lambda_s$ ,  $\lambda$  is slenderness ratio of the member,  $\lambda_s$  is the slenderness ratio when the critical stress corresponding to overall yielding of the structure is equal to the yielding stress of the steel.

Under extreme load conditions, the allowable stress is permitted to increase by 1/3.

From the above strength and stability check, the maximum resultant stresses corresponding to different load cases during these three stages are given in table 2 and table 3. The maximum resultant stresses during the three stages are located in the bracing rods under the platform, as shown in Figure 2. The maximum stress is 280.11MPa. The allowable critical yielding stress of the material takes a value of 344.8MPa in the design. The maximum stress ratio is 0.812, less than 1, indicating all the members satisfy stability requirement.

It can be inferred from the computation results that the check stress of each plate of the platform is less than the allowable stress.

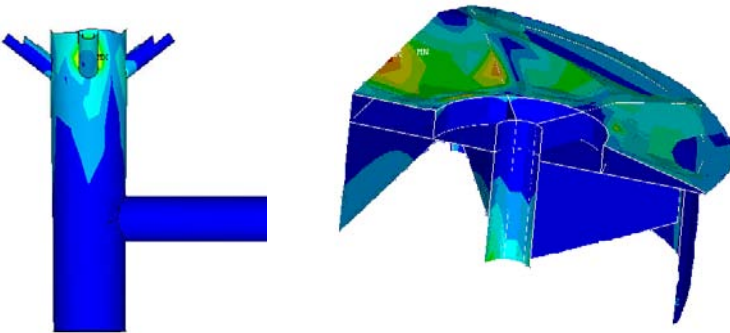


Figure 2. Local distribution of stresses of bucket foundation platform

Table 2. Stresses during normal working stage and under extreme environmental conditions

Load case	A		B		C		D		E	
	$\sigma$ (MPa)	$\sigma/[\sigma_c]$								
1	186.6	0.54	280.0	0.81	19.8	0.08	118.4	0.51	42.1	0.12
2	186.4	0.54	279.8	0.81	17.0	0.07	106.6	0.46	37.2	0.11
3	176.0	0.51	279.6	0.81	12.7	0.05	85.71	0.37	28.9	0.08
4	186.6	0.54	280.1	0.81	20.1	0.09	145.5	0.62	48.8	0.14
5	186.5	0.54	276.4	0.80	38.5	0.17	187.3	0.80	47.5	0.14
6	186.4	0.54	276.1	0.80	28.4	0.12	68.4	0.29	28.7	0.08

Table 3. Stresses during construction period

Load case	A		B		C	
	$\sigma$ (MPa)	$\sigma/[\sigma_c]$	$\sigma$ (MPa)	$\sigma/[\sigma_c]$	$\sigma$ (MPa)	$\sigma/[\sigma_c]$
1	9.32	0.040	62.89	0.268	41.38	0.176
2	30.40	0.129	150.20	0.639	76.95	0.327

### 4 Dynamic Response Analysis

The design basic seismic intensity of this platform structure is degree 8. Response spectrum analysis techniques are employed in order to make dynamic response analysis under earthquake. The computation model adopted is the same as that used for static analysis.

Seismic loads mainly include seismic inertia forces and dynamic water forces. A platform is a multiple mass points system. Horizontal seismic force  $F_{ij}$  for mass point  $i$  of  $j$  vibration mode is expressed as:

$$F_{ij} = CK_H \gamma_j \psi_{ij} \beta_j m_i g \tag{5}$$

Where  $\gamma_j$  is vibration mode participation coefficient of the structure,  $\psi_{ij}$  is horizontal displacement of platform mass point  $i$  in the vibration mode of the  $j$ th order,  $\beta_j$  is dynamic amplification coefficient corresponding to the vibration mode of the  $j$ th order;  $m_i$  is mass of mass point  $i$ ,  $g$  is acceleration of gravity,  $K_H$  is horizontal seismic coefficient, takes a value of 0.2 when the design intensity is of degree 8,  $C$  is comprehensive influence coefficient, takes a value of 0.5.

Dynamic water force  $F$  sustained by a slender member during earthquake is estimated by the following formula:

$$F = CK_H \beta (C_M - 1) V \gamma \sin^2 \phi(i, j) \tag{6}$$

where  $C_M$  is attached water mass coefficient, which shall be determined by test whenever possible, assumed to be 2.0 in this article,  $V$  is volume of the underwater portion of the member ( $m^3$ ),  $\gamma$  volumetric weight of sea water ( $kN/m^3$ ),  $\phi(i,j)$  angle formed by the member with the earthquake vibration direction(in rad); the rest symbols have the same meanings as above.

According to calculation, dynamic water force during earthquake is small and can be neglected in earthquake analysis.

Under seismic loads, the seismic force in the horizontal direction (the main axis, also the most unfavorable direction for structure stress) assumes a value of 100% of the force; the horizontal seismic force perpendicular the main axis assumes 100% of the force along the main axis; the vertical seismic force assumes 50% of the force along the main axis. The mass on the deck is distributed to the corresponding nodes of deck grids. The attached water mass under the design water level is distributed to the corresponding nodes. The deck structure mass is generated by a program automatically.

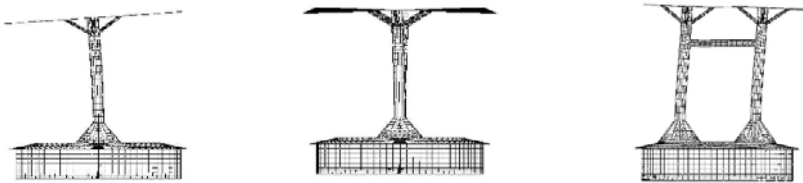
Class III site soil is assumed for seismic response study. The spectrum curve has three segments, expressed by:

$$\beta = 2.25 \quad 0.0 \leq T < 0.7$$

$$\beta = 1.575/T \quad 0.7 \leq T < 3.5$$

$$\beta = 0.05 \quad T \geq 3.5$$

Natural frequency and vibration mode of the platform have been calculated in order to understand the dynamic properties of this platform structure. Figure 3 presents its first three natural frequencies and vibration modes. They first vibration mode is a 2-dimensional vibration perpendicular to the dual-column, with a natural frequency of 0.585Hz; the second variation mode a torsion vibration centering around the bucket axis, with a natural frequency of 0.839Hz; the third one a vibration in the plane in which the two columns locate, with a natural frequency of 0.1138Hz.



(a) First order vibration mode (b) Second order vibration mode (c) Third order vibration mode

Figure 3. Vibration modes of platform structure

The seismic response of this platform has been calculated with seismic response spectrum analysis. According to the analysis results, seismic action does

not have significant influence upon displacement, with a horizontal displacement of 20.22mm at the top of the column. As indicated by stability check of this structure, the maximum resultant stress is 116.3MPa and occurs at an elevation of -2.34m, less than the maximum stress calculated in static analysis. Therefore, this platform satisfies the design requirements under seismic action as far as strength and stability are concerned.

## 5 Conclusion

In this article, static and dynamic studies are conducted in detail on a real platform with dual-column bucket foundation. According to the study results, the structure satisfies the design safety requirements in terms of rigidity, strength, and stability. Marine ice load case is found to be the predominant factor determining the design strength of the structure. During normal working stage, the joint between the column and the bracing rod under the platform has the maximum stress when the wave and current action is in the 45° direction. Local reinforcement measures are suggested for these places. Monolithic board shell element model is able to simulate satisfactorily the stress conditions of a dual-column bucket platform. The boundary conditions of the model shall be treated as a shallow foundation and the lateral elastic restraint action of the soil shall be accounted for.

## References

- Jiang S. Z., Chen G. X., Yang X. L. and Zhu Q. M. (1999). Finite element method application in static analysis of survey platform structure with bucket foundation, *China Offshore Platform* 16(1), 11-14 [in Chinese].
- Li C. and Liu Z. W. (2007). Analysis of seismic response for bucket foundation platform on Dagan soft clay. *China Offshore Platform* 22(1), 38-42 [in Chinese].
- Wang Q., Ren G. Y. and Yang S. G. (2000). Structural analysis of offshore production platform with bucket foundation. *China Offshore Platform* 15(6), 85-90 [in Chinese].
- Wang J. and Xu T. (2003). Comprehensive analysis of offshore production platform with bucket foundation, *Marine Information* 16(1), 27-28 [in Chinese].
- Zhang Y., Wang M. and Lou Z. G. (2005). A study on the mechanism of interaction between bucket foundation and soil under vertical loadings. *China Civil Engineering Journal* 38(2): 97-101 [in Chinese].

# Study on Hysteretic Behavior of Double Angle Connections

Aiguo Chen<sup>1\*</sup>, Ruizeng Shan<sup>1</sup> and Qiang Gu<sup>2</sup>

<sup>1</sup>School of Civil Engineering and & Architecture, Beijing Jiaotong University, Beijing 100044, P.R. China

<sup>2</sup>Department of Civil Engineering, University of Science & Technology of Suzhou, Suzhou 215011, P.R. China

**Abstract.** In order to study hysteretic behavior of double angle framing connections, based on considering material, geometric and contact state nonlinearity, finite element analysis for steel double web angles framing connections under cyclic load is carried out. Three dimensional solid element is adopted in the connection models. Hysteretic behavior and failure mechanism of this type of connection are analyzed. Experiment study is conducted in order to investigate the seismic behavior of connection further and verify the reliability of the finite element model. The test consisted of subjecting four connection assemblages to increasing level of large cyclic displacements until failure occurred. The results of finite element and experiment indicate that specimens exhibit good ductile behavior; connection rotation exceeded 0.04 radians; the length of angles and the diameter and gage of bolts significantly affect the strength and ductility of connections. As the results of this investigation indicate, considerable moments can be developed in these connections. Therefore, to ensure safety and a realistic dynamic response analysis of steel frames with double angle connections, inclusion of realistic hysteretic characteristics of connection similar to those provided in this paper is essential.

**Keywords:** double angle connections, hysteretic behavior, finite element, experiment study, failure mechanism, ductile

## 1 Introduction

Beams and columns are often connected by double angles in low-rise steel frames. The double angle connection is commonly considered as a simple shear connection. But it has been found in Astaneh-Asl (1989), Guravich (1998), Stefano (1994), and Chen (2003) that significant moments can be transferred to the sup-

---

\* Corresponding author, e-mail: agchen@bjtu.edu.cn

porting members by various double angle connection configurations. It has significant effect on whole joints, and even on whole structures: on one hand, can increase lateral stiffness of structures, on the other hand, the connections can transfer a part of moment to columns, which may fail due to the extra moment not being considered in design. Especially under earthquake, this type of connections is subjected to large cyclic rotation, and has significant influence on whole behavior and dynamic response of structures. Therefore, it is essential to study hysteretic behavior of the connections under cyclic loading. The connections may be welded or bolted to the beam web and to the column flange. The column bolted, beam web welded connection is investigated in this paper.

## 2 Finite Element Model

ANSYS is used to carry out a 3D finite element analysis. Symmetry is utilized and only one of the angles is analyzed. The angle, bolts and welds are discretized using SOLID95 20-node linear-strain elements and SOILD92 10-node tetrahedron elements. The beam and column away joint zones are discretized using SOLID45 eight-node constant-strain brick elements and near joint zone using SOLID95 elements. Pretension forces are applied to the bolts using PRETS179 element in ANSYS to simulate the minimum bolt tension required when fully-tightened bolts are used. The contact between the bolt heads or nuts and the outstanding leg of the angle or column flange, the contact and bearing interactions between the bolt shanks and bolt holes and the contact between the angle and column flange is simulated in the ANSYS program. The boundary condition of the column top is laterally restrained in X, Y direction, and the column bottom is fixed fully. External force P is exerted the beam end by displacement loading. Loading history adopted SAC Phase 2 loading protocol. Deformation parameter controlling loading history is interstory drift angle  $\theta$ , it is defined as  $\Delta/L$ , in which,  $\Delta$  is beam tip loading displacement and L is the distance between the beam tip and the centerline of the column. Kinematic hardening material behavior is assumed for the angle, bolt, column and beam elements, and the Von Mises yield criterion is adopted. The angles, beam and column are assumed to be made of Q235 steel, with modulus of elasticity  $E=206\text{GPa}$ , tangent modulus  $E_t=0.02E$ , yield strength  $\sigma_y=235\text{MPa}$ , ultimate strength  $\sigma_u=375\text{MPa}$  and Poisson's ratio of 0.3. For 10.9 Grade bolts,  $\sigma_y=940\text{MPa}$ ,  $\sigma_u=1140\text{MPa}$ ,  $E=206000\text{ MPa}$ ,  $E_t=0.02E$ . For welds,  $\sigma_y=330\text{MPa}$ ,  $\sigma_u=470\text{MPa}$ ,  $E=206000\text{MPa}$ ,  $E_t=0.05E$ .

The connection finite element model configuration investigated is shown in Figure 1 and the angle detailing is shown in Figure 2. The emphasis in this paper is to investigate hysteretic behavior and failure mechanism of connections. BASE specimen is designed firstly, and other series of specimens are derived from BASE specimen by varying the above mentioned connection parameters. A  $H450\times450\times12\times24$  column, with height of 3.6m and a  $H350\times250\times8\times13$  beam, with

length of 2.775m used in finite element model are considered. The angle is  $L100 \times 80 \times 8$ , and the height of angle weld is 8mm. The bolts adopt 10.9 Grade M20, with the bolt hole diameter of 21.5mm. The distance between the centerline of bolts and the corner of the angle is 55mm, and the friction coefficient is 0.30.

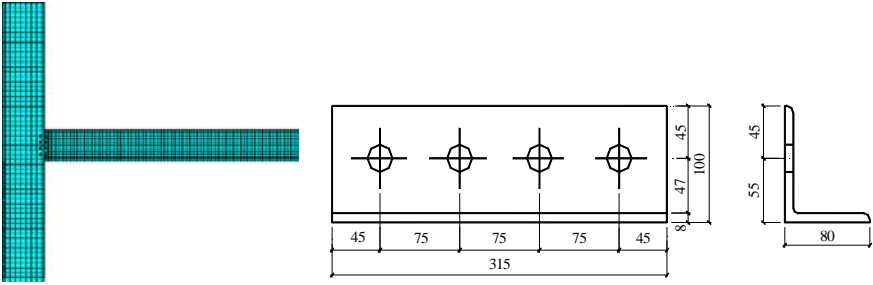


Figure 1. Finite element model configuration    Figure 2. Detailing of angle assemblage

### 3 Finite Element Results

#### 3.1 Hysteretic Behavior of Connections

M/M<sub>p</sub>-θ hysteretic curve of connection is given in Figure 3, where, M is connection moment, defined as  $M=P \times L$ , M<sub>p</sub> is the beam full plastic moment resistance. It is shown that connection fails when connection cycles one loop at  $\Delta=120\text{mm}$  displacement level. At every cycling displacement level, stiffness of the first loop is larger than second loop, and with beam tip displacement increasing, the overall stiffness of curve is gradually reducing. The maximum moment capacity and the maximum interstory angle that connection attained are 0.22MP and 0.04rad before failure, respectively. Connection exhibits good ductility and has good seismic behavior. In addition, it is shown from Figure 3 that hysteretic curve exhibited pinching at higher load levels. Pinching is characterized by an increase in rotation without a significant increase in moment, thus resulting in a loss on stiffness of the connection. In the double angle connection, pinching was observed to occur due to excessive separation of the angle from the column flange. When the angle leg separated from the column flange, the moment-rotation hysteretic plot was observed to become very flat (i.e. rotation increased without any significant increase in moment), until contact between the angle leg and column flange again occurred during the load reversal. Then, the moment-rotation plot shown that the connection started to once again resist moment, and the connection rotation increase was accompanied by a significant increase in moment.

### 3.2 Failure Mechanism Analysis

Figure 4 is Mises stress SEQV distribution at adjacent region of angle fillet. Horizontal axis in Figure 4 is angle length directional coordinate. Coordinate value  $x=0\text{mm}$  and  $315\text{mm}$  is the edge of angle, and  $x=45\text{mm}$ ,  $120\text{mm}$ ,  $195\text{mm}$ ,  $270\text{mm}$  is position of the first, second, third and fourth bolt. Vertical axis denotes Mises stress SEQV of nodes. At  $\Delta= -30\text{mm}$  displacement level, except that the section between third and fourth bolt, other regions near fillet enter basically plasticity states. The maximum stress is at tension region near the external bolt, and the value with  $318\text{MPa}$  is almost twice higher than the lowest stress. The maximum stress at compression region is at the compression edge, and arrived  $280\text{MPa}$ . With load and displacement increasing, the stresses at  $y=0-157.5\text{mm}$  of tension region (about half of angle length) develop rapidly, and at  $\Delta= -120\text{mm}$ , stresses at these regions approximately distribute uniformly. The maximum stress at last attains  $370\text{MPa}$  due to hardening effect. Distribution region of the minimum stress is between the third and fourth bolt, this is duo to that the neutral axis of connection shifts down, and is not at centroid of high strength bolts group traditionally assumed.

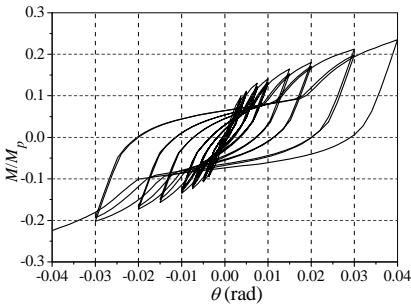


Figure 3.  $M/M_p-\theta$  hysteretic curve of connection

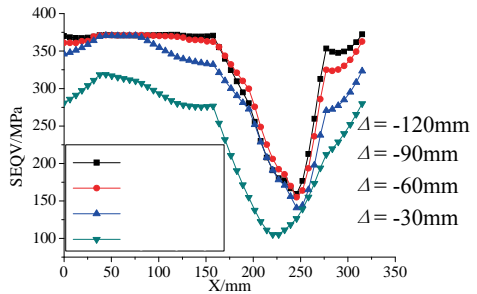


Figure 4. Mises stress distribution at angle fillet

Figure 5 is Mises stress of angle nodes at  $\Delta= -120\text{mm}$ . It is shown that deformation of angle is obvious under moment, and stress hardening at angle fillet and tension bolt region is appeared. Otherwise, region of bolt-line and angle leg toe is basically in elastic state, especially stress at  $x=315\text{mm}$  is far lower than yield stress. This is contribution to constraint of welds to angle leg connected to beam and make the most regions enter elastic stress state.

Figure 6 is Mises stress distribution of angle leg connected to column flange. It is seen that plasticity of regions located above the third bolt (see from down to up) develops fully, and that the section of the third and fourth bolt is basically in elastic state. Local stress at left-down corner of angle is very large due to very large compression force.

It is known from above analysis that failure of connection is due to cyclic plasticity at angle fillet. The failure mode of the connection was the plastic hinge line at the angle fillet. The angle fillet enter plasticity firstly due to stress concentration, then stress concentration developed further under cyclic loading, and at last failed with forming plastic hinge line. This failure mode was ductile.

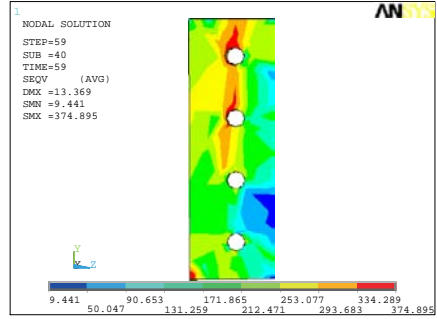
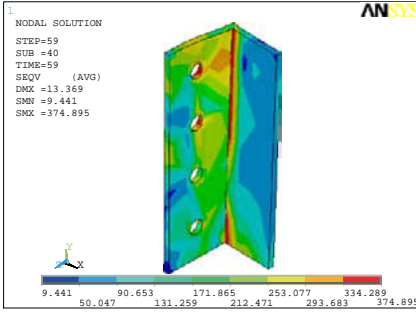


Figure 5. Mises stress distribution of angle fillet      Figure 6. Mises stress distribution of bolt-line

## 4. Experiment Study on Double Angle Connections

### 4.1 Experimental Program

Four test specimens are designed together. The contour of specimens is shown in Figure 7. A  $H200 \times 200 \times 10 \times 16$  column, with height of 0.8m and a  $H350 \times 150 \times 8 \times 10$  beam with length of 1.4m in test specimens are considered. The distance from the loading point to column flange surface is 1.26m. The specimen design parameters included angle length, bolt diameter and gage distance. The angles used in specimens 1 to 4 were  $L70 \times 8$ . Q235-B steel was used for the members and connection elements. The fasteners were 16mm or 20mm diameter 10.9 grade heavy-hex, high-strength bolts and nuts. The interface slippage coefficient is 0.3. One angle leg is welded with the beam web and the other leg is bolted with the column flange. The height of the weld is 8mm in order to avoid weld failure. The detailing and strain gauge arrangement of specimens are shown in Figure 8.

### 4.2 Experimental Process

To measure the hysteretic loop stability of angle connections, the every displacement level is cycled twice. The four specimens were tested at displacement of  $\pm 10\text{mm}$ ,  $\pm 20\text{mm}$ ,  $\pm 30\text{mm}$ ,  $\pm 40\text{mm}$ ..., until the test was terminated when fracture along the toe of the fillet, bolt shear, or the bearing failure of angle edge occurred. The beam tip displacement and connection rotation is measured during test process, and simultaneous strain of the angle bolted the column flange is recorded. The measuring point position is seen in Figure 8, and there are three strain gauges at every measuring point.

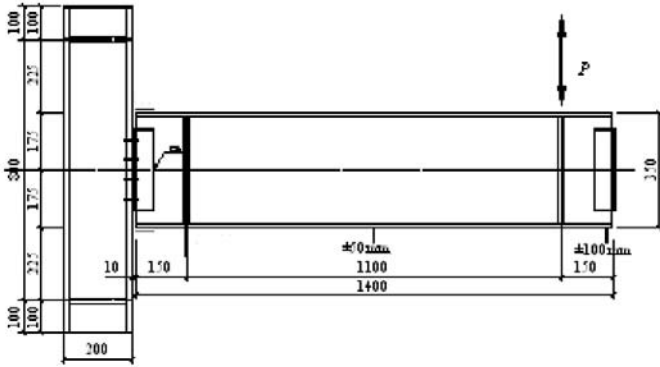
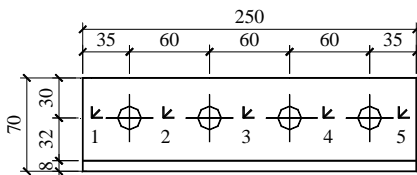
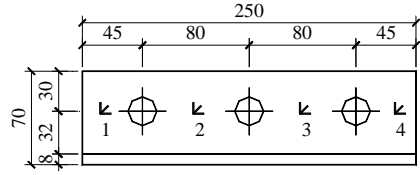


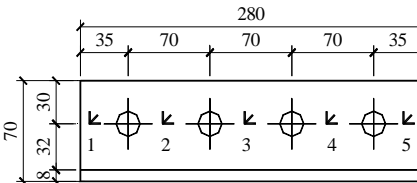
Figure 7. Contour of specimens



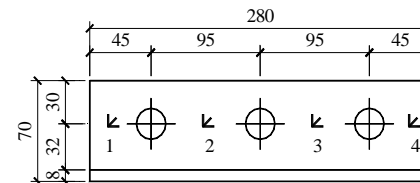
(a) Specimen PIN-1 with 16mm diameter bolt



(b) Specimen PIN-2 with 20mm diameter bolt



(c) Specimen PIN-3 with 16mm diameter bolt



(d) Specimen PIN-4 with 20mm diameter bolt

Figure 8. Detailing requirement and arrangement of strain measuring points

### 4.3 Experimental Results

Specimen PIN-1 and PIN-2 began to crack in the vicinity of the angle fillet when the beam tip displacement reached 50mm, while specimen PIN-2 and PIN-4 began to crack in the vicinity of the angle fillet when the beam tip displacement reached 60mm. Crack further developed with displacement increase, and at last plastic fractures occurred. This failure mode is ductile. The ultimate moment of connections is among 0.2~0.34Mp (the full plastic moment of beam) as shown in Table 1. Rotation of four specimens all exceeded 0.04rad, and they exhibit good ductile behavior. The hysteretic curve of PIN-4 (limited to paper space, only given curve of PIN-4) under cyclic loading are shown in Figure 9, where, P is the beam tip load and  $\Delta$  is the beam tip vertical displacement. The maximum beam tip displacement of specimen PIN-4 reached 70mm. The variation regularity of PIN-4 is similar to computational curve in Figure 10.

Table 1 Summary of experimental results

Specimen Label	$P_u$ (kN)	$M/M_p$	$\Delta_u$ (mm)	$\theta$ (rad)	Failure modes
PIN-1	27.0	0.272	70	0.047	Plastic fracture failure at one side angle fillet
PIN-2	20.8	0.203	70	0.047	Plastic fracture failure at one side angle fillet, crack occurred at the other side angle
PIN-3	35.2	0.343	60	0.040	Plastic fracture failure at one side angle fillet
PIN-4	34.0	0.332	70	0.047	Plastic fracture failure at one side angle fillet, crack occurred at the other side angle

Note:  $P_u$  is connection ultimate load,  $M$  is connection ultimate moment,  $M_p$  is the full plastic moment of beam,  $\Delta_u$  is beam tip displacement corresponding to  $P_u$ ,  $\theta$  is connection ultimate rotation.

### 4.4 Effects of Major Parameters on Connection Behavior

#### 1. Angle length

As the angle length become small, on one hand, the bending stiffness of the angle decreases and the demand for elongate deformation of bolts also reduces, on the other hand, the number of bolts arranged is reduced, and restriction for the angle is weakened. So the strength of connections decreases and deformation capacity of connections improves.

## 2. Arrangements of bolts

Comparing PIN-1 with PIN-2, PIN-3 with PIN-4, when bolt spacing is larger, the plastic deformation of angle is more easily developed, and angle crack relative later, so connection exhibits better ductility.

## 3. Bolt diameter

Comparing PIN-1 with PIN-2, bolt diameter of the former is smaller, and can provide larger elongate deformation. While bolt spacing of the latter is larger, the plastic deformation of angle is more easily developed, so both of maximum beam tip displacement is basically same.

### 4.5 Verification of Finite Element Model

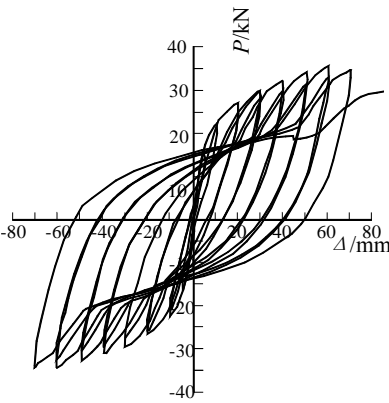


Figure 9. Experimental curve of PIN-4

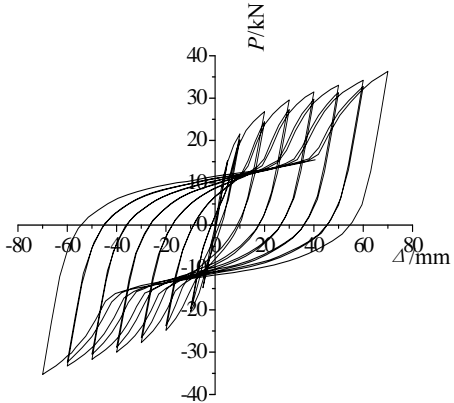


Figure 10. Computational curve of PIN-4

Comparison between experimental curve and computational curve can be observed from Figure 9 and Figure 10. It is verified that finite element results are in accordance with testing results so well that they even approximate on values. As a result, advanced numerical simulation should be performed to further studies on seismic behavior and it can be instead of part of tests.

## 5. Conclusions

According to the finite element and experiment results, the following conclusions are drawn from this study:

1. In order to ensure safety of steel frames, connections shall be designed to be able to transfer shears and accommodate the corresponding end rotation of beams. Connections should not transfer excessive moment, which has disadvantage to the structural members.
2. Stress analysis of connections is very complicated and finite element model established can precisely simulate seismic behavior of connections.
3. Most of connection exhibit good ductility. Failure of connections is due to cyclic plasticity at angle fillet.
4. The strength of connections is mainly related to the angle length. Larger length can increase bending rigidity of connection, and simultaneously require larger deformation for the angle and bolt.
5. When bolt spacing is larger, the plastic deformation of angle is more easily developed, and connections exhibit good ductility. When bolt diameter is smaller, connection ductility can be improved.
6. Finite element results agree with experimental results very well, so finite element analysis can replace part of experiment.

## References

- Astaneh-Asl A., Nader M.N. and Lincoln M. (1989). Cyclic behavior of double angle connections. *Journal of Structural Engineering*, 115(5): 1101–1118.
- Chen A.G., Gu Q., Su M.Zh. and Li Q.C. (2003). Cyclic behavior of double angle beam-to-column connections, *Journal of Building Structures*, 24(6): 67–71 [in Chinese].
- Guravich S. and Dawe J.L. (1998). Simple beam connections in combined shear and tension. *Journal of Constructional Steel Research*, 46: 241–242.
- Stefano M.D., Luca A.D. and Astaneh-Asl A. (1994). Modeling of cyclic moment-rotation response of double-angle connections. *Journal of Structural Engineering*, 120(1): 212–229.

*“This page left intentionally blank.”*

# Research on Limit Span of Self-Anchored Suspension Bridge

Wenliang Qiu<sup>1\*</sup>, Meng Jiang<sup>1</sup> and Zhe Zhang<sup>1</sup>

<sup>1</sup>School of Civil & Hydraulic Engineering, Dalian University of Technology, Dalian 116024, P.R. China

**Abstract.** Self-anchored suspension bridges are increasingly appreciated by engineers for their aesthetic look, low cost and more adaptive for geological environment than earth-anchored suspension bridges. Many self-anchored suspension bridges have been completed or are in construction in the world. For huge horizontal component of main cable in the stiffening girder and the different construction method, self-anchored suspension bridge has much less limit span than earth-anchored suspension bridges. In this paper, the limit span of three-span self-anchored suspension bridge with two towers is deduced. Some factors, such as ratio of rise to span of main cable, ratio of side-span to mid-span, second dead load and live load, are analyzed in this paper. Based on the common used material and considering the main factors, the limit spans of self-anchored suspension bridges with concrete stiffening girder and with steel stiffening girder, are discussed in detail, and the corresponding limit spans are given.

**Keywords:** suspension bridge, self-anchored, limit span

## 1 Introduction

The horizontal component of the main cable force is carried by stiffening girder in a self-anchored suspension bridge (John and David, 1999). The value of the horizontal component force vary with the deadweight of the girder, main cables, deck system and the live load, and increase with increase of the length of span. Assuming the strength of the main cable is certain, the main cable will reach its ultimate strength when the span increases to a certain limit. Under such circumstances, it is apparent that the deadweight can't not be afforded needless to say load by the stiffening girder and the bridge beck system and so on. Besides, the axial compression force can be carried by the girder is limited when its own material strength and cross section are given. The limit span of self-anchored suspension bridges

---

\* Corresponding author, e-mail: qwl2002@263.net

differs from that of the earth-anchored suspension bridges as both the main cable strength and the girder strength are in charge.

The limit span of bridge is influenced by factors such as material strength, construction technique and economic rationality (Li et al., 1999; Wu, 1996a; Wu, 1996b). To make it simple, the limit spans of self-anchored suspension bridges are studied only considering the material strength in this paper.

## 2 Deduction of Limit Span of Self-Anchored Suspension Bridge

Figure 1 shows a symmetric three-span suspension bridge with two towers. The mid-span length of the main cable is  $L$  with the rise of  $f$ , and the side-span length of main cable is  $L_1$ . To simplify the problem, we assume: the configuration of the main cable is second order parabola (Cobo and Aparicio, 2001), stiffening girder is horizontal and deadweight of the deck system is distributed uniformly along the whole bridge, live load is also distributed uniformly along the whole girder and the structural deformation caused by live load is neglected. So the sum of deadweight and live load distributed horizontally is  $q$ .

$$q = \gamma_c A_c + \gamma_b A_b + q_m + q_l \tag{1}$$

where  $A_c$  is cross section of the main cable ( $m^2$ ),  $A_b$  is cross section of the stiffening girder ( $m^2$ ),  $\gamma_c$  is density of main cable ( $kN/m^3$ ),  $\gamma_b$  is density of the girder ( $kN/m^3$ ),  $q_m$  is load of bridge deck system ( $kN/m$ ) including deck pavement, bump wall, handrail ect.  $q_l$  is live load ( $kN/m$ ) including motor vehicles, human crowds or non-motor vehicles ect.

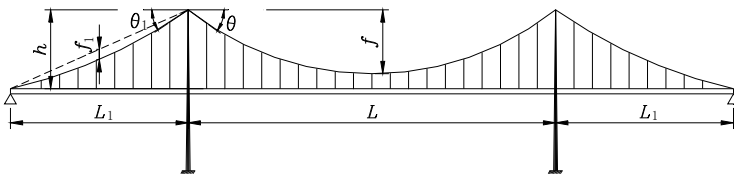


Figure 1. Three-span self-anchored suspension bridge with two towers

As the configuration of main cable is second order parabola, and the horizontal component of the mid-span main cable force is  $H$ .

$$H = \frac{qL^2}{8f} = \frac{L}{8\lambda}(\gamma_c A_c + \gamma_b A_b + q_m + q) \quad (2)$$

where  $\lambda$  is ratio of rise to span and  $\lambda = f / L$ . The horizontal component of the side-span main cable force is  $H_1$ .

$$H_1 = \frac{qL_1^2}{8f_1} = \frac{qL_1}{8\lambda_1} \quad (3)$$

where  $\lambda_1$  is ratio of rise to side span and  $\lambda_1 = f_1 / L_1$ .

Since the unbalanced horizontal component born by cable tower is negligible, the following expression can be obtained when the horizontal components of both sides of cable tower are equal.

$$f_1 = \frac{L_1^2}{L^2} f = \beta^2 f \quad (4)$$

where  $\beta = L_1 / L$  is ratio of side-span to mid-span.

So the stress in girder is  $\sigma_b = H / A_b$  and the maximum tensile stress of the main cable is  $\sigma_c = \frac{H}{A_c \cos(\theta_{\max})}$ , where  $\theta_{\max}$  is the bigger one of the two angles

$\theta$  and  $\theta_1$ .  $\theta$  and  $\theta_1$  are the inclination angles of mid-span cable and side-span cable at the upper supporting point respectively, and they can be deduced from the equation of main cable configuration. For the mid-span, we have

$$\cos(\theta) = \frac{1}{\sqrt{1 + (\text{tg}(\theta))^2}} = \frac{1}{\sqrt{1 + (4\lambda)^2}} \quad (5)$$

and for the side-span,

$$\text{tg}(\theta_1) = \frac{1}{\beta}(\lambda + 4\beta^2\lambda + \frac{d}{L}) \quad (6)$$

where  $d$  is the vertical distance between the lowest point of the mid-span main cable and the anchored end of the side-span main cable. From the above expression, we know that if  $d$  is increased, the tension force in the main cable will increase correspondingly due to the accretion of  $\text{tg}(\theta_1)$ . In order to lessen the tension force  $T$  in the main cable at a given horizontal component force  $H$ ,  $d$  should be de-

creased. In this paper, the minimum value  $d=0$  is discussed to obtain the limit span, which yields,

$$\cos(\theta_1) = \frac{1}{\sqrt{1+(\text{tg}(\theta_1))^2}} = \frac{1}{\sqrt{1+(\frac{1}{\beta}(\lambda + 4\beta^2\lambda))^2}} \tag{7}$$

hence, comparing  $\cos(\theta)$  with  $\cos(\theta_1)$ ,  $\cos(\theta_{\max})$  can be achieved from the following expression:

$$\cos(\theta_{\max}) = \min\{\cos(\theta), \cos(\theta_1)\} \tag{8}$$

The stresses in the stiffening girder and the main cable depend directly on the horizontal component  $H$ , which is directly affected by  $A_c$  and  $A_b$ . Therefore, when the shape of the main cable and cross-sections of the main cable and the stiffening girder are given, that is  $A_c$ ,  $A_b$ ,  $\lambda$ ,  $\beta$  are determined, span  $L$  will reach its maximum value  $L_j$  under the condition that the compressive stress in the stiffening girder and the tensile stress in the main cable reach their allowable stress  $[\sigma_c]$  and  $[\sigma_b]$  respectively, that is,

$$\frac{H}{A_b} = [\sigma_b], \quad \frac{H}{A_c \cos(\theta_{\max})} = [\sigma_c] \tag{9}$$

Substitute the above expressions into equation (2), we can get the following expression,

$$L_j = \frac{8\lambda[\sigma_b]}{\frac{[\sigma_b]}{[\sigma_c]\cos(\theta_{\max})}\gamma_c + \gamma_b + \frac{q_m + q_l}{A_b}} \tag{10}$$

The above expression gives the limit span of three-span self-anchored suspension bridge with two towers.

### 3 Upper Limit of the Limit Span

If the suspension bridge only carry its self-weight and doesn't carry load  $q_m + q_l$ , the limit span  $L_j$  will get to its upper limit  $L_{j,\max}$  when the materials of the structure reach their allowable stress, that is,

$$L_{j,\max} = \frac{8\lambda}{\frac{\gamma_c}{[\sigma_c]\cos(\theta_{\max})} + \frac{\gamma_b}{[\sigma_b]}} \quad (11)$$

It can be seen that the upper limit span  $L_{j,\max}$  depends on the parameters of the suspension bridge, such as ratio of rise to span of main cable  $\lambda$ , ratio of side-span to mid-span  $\beta$ , the weight density of stiffening girder and main cable materials ( $\gamma_b, \gamma_c$ ) and their allowable stress ( $[\sigma_b], [\sigma_c]$ ) as well. Hence, to gain higher upper limit of limit span, the following measures can be taken:

1. To enhance ratio of rise to span of main cable of mid-span  $\lambda$ .
2. To build the main cable using high strength and lightweight material.
3. To build the stiffening girder using high strength and lightweight material.

Further analysis of commonly used materials in current suspension bridges can be seen as follow.

For self-anchored suspension bridge with reinforced concrete stiffening girder, C50 concrete is commonly used whose allowable stress is  $[\sigma_b] = 17.5 \times 10^3$  kPa. Since the girder is subjected to axial compression force, only very few reinforcements are required and the density of girder is  $25 \text{ kN/m}^3$ . Considering that the anchor blocks of the hanger and the transverse structures don't carry axial compression force, the effective area  $A_b$  of the stiffening girder doesn't include these parts of concrete. Correspondingly, a factor should be added to the original weight density of concrete ( $25 \text{ kN/m}^3$ ), and  $\gamma_b = 25 \times 1.25 = 31.25 \text{ kN/m}^3$ .

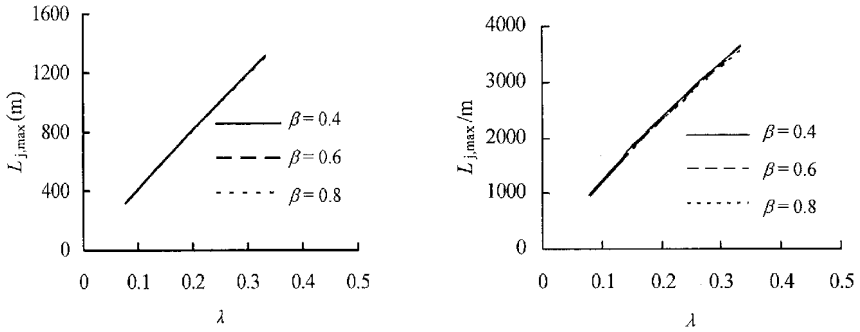
For self-anchored suspension bridge with steel stiffening girder, Steel Q345 is commonly used in china currently, whose allowable axial compressive stress is  $[\sigma_b] = 200 \times 10^3$  kPa. Same as the concrete suspension bridge, the density of steel girder is  $\gamma_b = 78.5 \times 1.25 = 98.125 \text{ kN/m}^3$ .

Parallel steel wires of ultimate strength of 1670Mpa are used to constitute a main cable. With a safety factor of 3.0, the allowable stress  $[\sigma_c] = 556.7 \times 10^3$  kPa. The weight density of main cable is  $\gamma_c = 78.5 \text{ kN/m}^3$ .

Figure 2 shows the relationships of the upper limit span  $L_{j,\max}$  and the ratio of rise to span of main cable  $\lambda$  when ratio of side-span to mid-span  $\beta$  equals 0.4, 0.6, and 0.8 respectively.

For concrete self-anchored suspension bridge, the  $L_{j,\max} \sim \lambda$  curves shown in Figure 2(a) denote that the relationships between  $L_{j,\max}$  and  $\lambda$  are nearly linear. The curves of different  $\beta$  maintain nearly the same line. Thus, ratio of side-span to mid-span  $\beta$  has little influence on the limit span. Therefore, regardless of the influence of  $\beta$ , limit spans corresponding to different ratios of rise to span of main cable can be obtained by taking the average result of the 6 curves, which are given in table 1.

For steel self-anchored suspension bridge, To some extent, the  $L_{j,max} \sim \lambda$  curves shown in Figure 2(a) denote that the relationships between  $L_{j,max}$  and  $\lambda$  are non-linear, and the ratio of side-span to mid-span  $\beta$  has little influence on the limit span. Therefore, regardless of the influence of  $\beta$ , limit spans corresponding to different ratios of rise to span of main cable can be obtained by taking the average result of the 6 curves, which are given in table 2.



(a) Concrete suspension bridge

(b) Steel suspension bridge

Figure 2.  $L_{j,max} \sim \lambda$  curve of self-anchored suspension bridge

Table 1. Value of  $L_{j,max}$  corresponding with different for concrete suspension bridge

$\lambda$	1/4	1/5	1/6	1/7	1/8	1/9	1/10	1/11	1/12
$L_{j,max}(m)$	1006.2	813.0	681.5	586.3	514.4	458.0	412.8	375.6	344.6

Table 2. Value of  $L_{j,max}$  corresponding with different for steel suspension bridge

$\lambda$	1/4	1/5	1/6	1/7	1/8	1/9	1/10	1/11	1/12
$L_{j,max}(m)$	2887.3	2377.4	2015.9	1747.4	1540.6	1376.9	1244.1	1134.4	1042.2

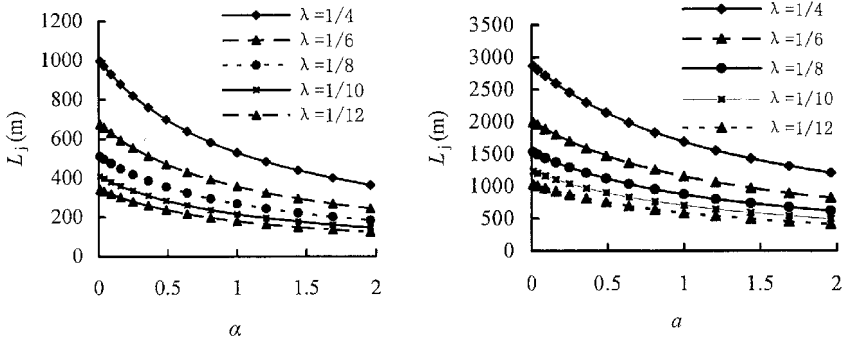
### 4 Study of the Influence of $q_l + q_m$ on Limit Span

Limit span, regardless of second dead load and live load, has been studied previously under deadweight of the bridge. Such a result is the upper limit span with the consideration of  $q_l + q_m$ . However, the result can not be applied practically. The following study on limit span is related to the influence of  $q_l + q_m$ . It has been studied that the influence of ratio of side-span to mid-span  $\beta$  can be neglected, so  $\beta=0.4$  will be applied in the following calculation.

First of all,  $\alpha = \frac{q_m + q_l}{\gamma_b A_b}$ ,  $\alpha$  denotes the ratio of sum of second dead load and live load to deadweight of stiffening girder. Then

$$L_j = \frac{8\lambda[\sigma_b]}{\frac{[\sigma_b]}{[\sigma_c]\cos(\theta_{\max})}\gamma_c + \gamma_b + \alpha\gamma_b} \tag{12}$$

Main cable is constituted by parallel steel wires. Stiffening girder is constituted by concrete and steel respectively. Allowable stress and specific weight are taken as before. By the above expression, the relationship curves of the limit span  $L_j$  and ratio of load  $\alpha$ , corresponding to different ratios of rise to span of main cable  $\lambda$ , are shown in Figure 3.



(a) Concrete suspension bridge

(b) Steel suspension bridge

Figure 3.  $L_j \sim \alpha$  curve of self-anchored suspension bridge

As shown in the figures, limit span decreases rapidly with the increase of ratio of load  $\alpha$ . In practical design, live load  $q_l$  is given by the design requirements of bridge. Therefore, in order to get larger span, second dead load  $q_m$  should be reduced probably by taking some measures, that is, the stiffening girder surface is paved by materials with light weight and small thickness, and the steel guardrails with light weight are applied to avoid the use of concrete bumper with heavy weight.

## 5 Conclusions

In this paper, the limit span of three-span self-anchored suspension bridge with two towers is deduced. Some factors, such as ratio of rise to span of main cable, ratio of side-span to mid-span, second dead load and live load, are analyzed in this paper. Based on the common used material and considering the main factors, the limit spans of self-anchored suspension bridges with concrete stiffening girder and with steel stiffening girder, are discussed in detail, and the corresponding limit spans are given. The study shows that, we can meet the aim of enlarging the limit spans of self-anchored suspension bridges though the following methods:

- (1) To enhance ratio of rise to span of mid-span main cable.
- (2) To build the main cable and stiffening girder with high strength and lightweight materials.
- (3) To reduce second dead load as much as possible by paving the bridge surface light weight materials and small thickness, and by using steel guardrails with light weight.

## References

- Cobo D.A. and Aparicio A.C. (2001). Preliminary static analysis of suspension bridges. *Engineering Structure*, 1096-1103.
- John A.O. and David P.B. (1999), Self-anchored suspension bridges. *Journal of Bridge Engineering*, 4, 151-156.
- Li J.SH., He D.R. and Liu Y. (1999). Analysis of the limit span of cable-stayed bridge. *East China Highway*, 1, 7-8 [in Chinese].
- Wu X.G. (1996a). Study on limit span of cable-stayed bridge. *Journal of Chongqing Jiaotong University*, 3, 36-38 [in Chinese].
- Wu X.G. (1996b). Study on limit span of arch bridge. *North and East Highway*, 3, 54-56 [in Chinese].

# Study on Percolation Mechanism and Water Curtain Control of Underground Water Seal Oil Cavern

Cheng Liu<sup>1\*</sup>

<sup>1</sup>Department of Geotechnical Engineering, Tongji University, Shanghai 200092, China

**Abstract.** The large span underground water seal oil cavern not only need to rely on the natural conditions of the buried groundwater, but must also rely on the water curtain hole installed around the cavern in a certain pressure to provide a stable water injection pressure to prevent oil leakage. Taking a large domestic underground oil cavern as an example, seepage of fractured rock is analyzed under the three-dimensional stress field. Combining the relationship between the effective stress of infiltration formation and water pressure around the caverns, the analysis of different water curtain systems is done to get the proper ways to solve the seepage problems. The theory of flow closed loop is proposed and critical storage pressure according to the theory is given. Some suggestions are raised according to specific issues to meet the water closure effect and prevent oil leakage while reducing cavern inflow.

**Keywords:** water curtain system, inflow, water seal, seepage field

## 1 Introduction

With the rapid development of industry, growth of population and improvement of people's living standards, energy shortage has become a global issue and energy security grabs the attention of more and more countries. Petroleum occupies an extremely important position in the international people's livelihood and it is indispensable resource to the development of society and the survival of human. China is a huge importer of petroleum in recent years. It holds the rapid growth of consumption and continuously high record. So it is necessary to set up a strategic reserve base of oil in the country. The underground petroleum-storage caverns is safer, more environmentally than it is on the ground, occupies less land, and can save investment and operating costs. China has set up a number of underground

---

\* Corresponding author, e-mail: liucheng83@yahoo.com.cn

petroleum-storage caverns and obtains a wealth of experience. So that it can provide the technical support for setting up more and more energy storage facilities.

## 2 Fundamental of Oil or Gas Sealing under Underground Storage

To store petroleum or Liquefied Petroleum Gas (LPG) using artificial unlined oil storage caverns is required to ensure sealing effect in which to prevent leakage. The general approach is storing oil products in caverns with better lithology, sealing the leakage channels with water and preventing oil product from flowing away.

Fracture aperture size and open fissures affect oil-flow mode and flow pressure. Oil product may mixture with water or convection happens between them if fracture aperture size is large enough. And because oil product is lighter than water, aperture size is large, oil product will flow into cavern rocks along the aperture channels. Specific to engineering practice, fracture aperture does not necessarily lead to oil product leakage. For example, external water pressure will push water into caverns, if there is abundant water supply, oil product cannot come into aperture and leakage will not happen.

The method the author recommend is analyse water inflow of different stress-seepage coupled fields, examining the design of water curtain systems whether providing sufficient pressure control and what width of fracture aperture in the caverns rock need common sealing measures or other special treatment programs. The common treatment to fracture aperture is sealing grouting on fault or fissure zone and also the bottom and top of chamber to reduce water flow channels. Before the oil product is pushed back into the caverns, the walls of them need to be watering, in order to avoid oil product wet dry aperture. Once the oil product goes into the aperture, it will stay in some cracks even though water level resume and some oil product is push back to cavern.

Considering capillary pressure in narrow aperture is important though it is often ignored in early studies. Both petroleum and LPG have capillary phenomenon with water, however, their contact angles are different. Adams, Aberg, Goodall et al (Adams (1941), Goodall (1988)), for example, believe that grasp has an important aspect that a pressure difference can exist across any flow-flow or two-phase interface irrespective of orientation and may be calculated using the Laplace equation, which is as follows:

$$p_c = T(1/r_1 + 1/r_2) \quad (1)$$

where  $r_1, r_2$  are curvatures of two-phase mediums perpendicular to the interface plane.  $T$  is the surface tension between the two-phase mediums.

In the region where apertures are narrow enough, capillary phenomenon is taken into account. Domestic and foreign scholars brought up some criteria for judgement whether oil product can leakage through theoretical and experimental means, and some combination of engineering practice. One of the more popular criteria is proposed by Aberg (1977), Goodall et al (1988). Aberg classified the relationship of aperture and caverns as one dimensional infinite model and cylinder model (no involving more complex geometric model), characterize the region with vertical hydraulic gradient, and believe that it can be guaranteed that the caverns are tight on condition that vertical hydraulic gradient is greater than one. This criteria ignores the gravity and capillary's effects. Goodall inherited and developed Aberg's theory. His design criteria of prevention of gas migration is that, gas escape from a rock cavern can be prevented by ensuring that for all possible leakage paths away from a cavern, the water pressure increases for some interval along these paths. It can be thought as a generalization of Aberg's theory (1977). Although Goodall's (1988) design criteria can guarantee prevention of gas migration, but there is still room for improve to be more economical by giving full play to the water curtain system. A reasonable layout of horizontal and vertical water injection holes can seal oil product in a larger region than caverns outline. Oil may come into the region, and circulate in it but cannot migrate away from the region. Because this region is closed and water pressure is sure to be low than the pressure according to Goodall's criteria, reducing the water inflow, reducing the volume of sewage treatment, and reducing heat loss of water away, so that more economical and reasonable. The actual region for oil product circulating is called flow closed loop. This can be evidently shown in Figure 1, where the fluid flow around the single cavern under the special water curtain system.

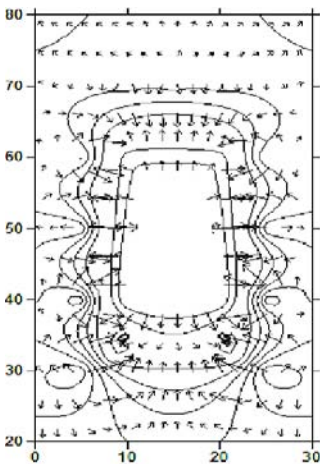


Figure 1. Flow closed loop in single cavern under the special water curtain system

### 3 Critical Storage Pressure

In order to store the largest volume of oil under the conditions of the same volume of chamber, it needs to consider the temperature of oil products and the conditions of reservoir pressure. Under the conditions of low-temperature and atmospheric pressure or at room temperature and high-pressure or at high-pressure and low-temperature, it can change into liquid, the volume is about 1/250 of gas state. To the oil, it can reduce the waste of oil products caused by evaporation.

Water storage at room temperature and high pressure is discussed here. Foreign scholars Liang (1994) and Goodall (1988) and so on defined the critical size of reservoir pressure from different angles. However, they are based on the design criteria of the hydraulic gradient. Liang, etc. considered that the critical pressure is the storage pressure which is able to ensure that it does not produce any oil leaking. He made a number of semi-empirical formulas.

Critical storage pressure proposed by Liang, Goodall et al is determined based on the criteria of the vertical hydraulic gradient. In accordance with the principle of flow closed loop put forward by the author, the water curtain pressure which seals oil product in caverns is different from the criteria proposed by Liang. It should be in a range of values ( $p_{\min}$ ,  $p_{\max}$ ).  $p_{\min}$  is the minimum value of the water curtain pressure, which should be able to guarantee oil product is stored in liquid phase, and ensure the oil product will not change quickly from one phase into another phase which may influence the rock stability and disturb the seepage field in equilibrium.  $p_{\max}$  is the maximum values of the pressure of water curtain. The higher the oil pressure in caverns is, the higher standards of water curtain system it demands in order to provide adequate water pressure and sealing effect. Simultaneously in order to meet the stability requirements of cavern, pore pressure can't exceed the maximum principal stress of surrounding rock which is the critical pressure of hydraulic fracturing of rock, the formula is as follows:

$$p_{\text{liquid}} + \Delta p + p_{\text{extra}} \leq p_{\min} < p_{\max} \leq \min(p_{\text{economic}}, p_{\text{break}}) \quad (2)$$

where  $p_{\text{liquid}}$  is the critical pressure under which oil product is kept in the liquid state;  $p_{\text{extra}}$  is pressure on the surplus;  $\Delta p = \rho g h_{\text{liquid}}$  is oil self-generated pressure as gradient gravity changes;  $p_{\text{economic}}$  is economic and reasonable storage pressure;  $p_{\text{break}}$  is the critical pressure leading to hydraulic fracturing of rock.

### 3 Water Curtain System Evaluation

The unlined underground petroleum-storage caverns, whose design capacity is more than  $50 \times 10^4 \text{ m}^3$ , is to be built in a coastal city. Its main design procedure is: site investigation, information collection, the research of water seal principle, rock caverns layout design, caverns inflow analysis and water curtain system evaluation. Here the main topic is water curtain system evaluation. It is carried out with several water curtain systems using the FLAC3D codes. The layout of caverns and water curtain system is shown in Figure 2.

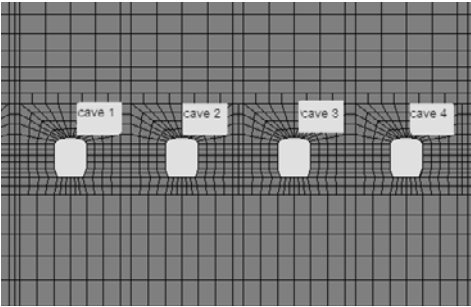


Figure 2. Water curtain system layouts model.

Mechanical properties determined from laboratory test are:

- Deformation Modulus:
  - 69.71 GPa (gabbros)
  - 78.21 GPa (granite)
- Uniaxial Compressive Strength:
  - 78.1~247.3 MPa (gabbros)
  - 93.8~147.4 MPa (granite)

The initial stresses measured at the site show that the max major principal stress (SH) in the horizontal plane is in the range of 6 to 12 MPa with the direction of  $12^\circ$  and the minor principal stress (Sh) in the range of 2~9 MPa. The vertical stress is small than two horizontal stress, and it is in the range of 1 and 3 MPa. The ratio of horizontal stress to vertical stress is between 1 and 4.

The coefficient of permeability of the unweathered rock at this site is between  $1 \times 10^{-9} \text{ m/s}$  and  $1 \times 10^{-6} \text{ m/s}$ , this rock is almost impermeable. However, the rock's permeability is between  $1 \times 10^{-8} \text{ m/s}$  and  $5 \times 10^{-6} \text{ m/s}$  whose elevation is between -30m and -80m.

Several water curtain systems are examined with different injection pressure of water holes. Keeping injection pressure in 1, 1/2, 1/4, 1/8 times the pore pressure of natural static seepage field without any cavern excavation, compared to no water curtain system condition, different inflow is get and listed in table 1.

The results show that caverns inflow comes down gradually along with decreasing of curtain holes pressure. When the holes pressure is 1/8 times the pressure of natural static seepage field, the caverns inflow is nearly equal to that under no water curtain system condition, at this times, water curtain system effect can be neglected. When the holes pressure is 1 or 1/2 times, pore pressure contour in the region surrounded by water curtain system looks like a dumbbell, and sealing effect is good with balanced seepage field.

Table 1. Water inflow for different water curtain systems (units: m<sup>3</sup>/d)

Injection pressure in holes	Cave 1	Cave 2	Cave 3	Cave 4
No water curtain system	5.23E+02	5.36E+02	5.95E+02	1.09E+03
1 times pressure	2.74E+03	2.61E+03	2.63E+03	2.75E+03
1/2 times pressure	1.54E+03	1.50E+03	1.52E+03	1.62E+03
1/4 times pressure	9.44E+02	9.43E+02	9.73E+02	1.06E+03
1/8 times pressure	6.45E+02	6.65E+02	6.97E+02	7.81E+02

## 4 Conclusions

After the analysis of the domestic and foreign scholars' theories and practice in the oil storage, the theory of flow closed loop is proposed. The flow closed loop theory reduce the pressure radius of water curtain hole compared to Goodall's theory, and it reduces water pressure of water curtain system, water inflow of caverns and energy loss under the promise of ensuring no leakage of oil product. It is a generation of Goodall's theory that the condition of no oil leakage is that water pressure is increasing in a certain distance from the path for gas migration. Flow closed loop theory determined the oil product critical storage pressure for economical and safety.

A variety of solutions of water curtain systems are designed according to the measured data and evaluation is given according to cavern stability and economic rationality. To keep low water inflow and their difference among different caverns, it should set up reasonable layout of water curtain system and adjust hole pressure not only according to caverns respiration schedule, but also taking account of season change.

## References

- Aberg, B. (1977). Prevention of gas leakage from unlined reservoirs in rock. *Proc. Int. Symp. on Storage in Excavated Rock Caverns*, 399-413.

- Adam, N.K. (1941). *The Physics and Chemistry of Surfaces*. 3rd edition. Oxford University Press.
- Benardos, A.G., Kaliampakos D.C. (2005). Hydrocarbon storage in unlined rock caverns in Greek limestone. *Tunnelling and Underground Space Technology*, 20(2):175-182.
- Goodall, D. C., Aberg, B., Brekke, T.L. (1988). Fundamental of gas containment in unlined rock caverns. *Rock Mechanics and Rock Engineering*, 21(4):235-258.
- Liang J., Lindblom U. (1994). Analyses of gas storage capacity in unlined rock caverns. *Rock Mech. Rock Engng.*, 27(3):115-134.
- Lindblom, U. (1990). City energy management through underground storage. *Tunnelling and Underground Space Technology*, 5(3):225-232.
- Lee, C.I., Song, J.J. (2003). Rock engineering in underground energy storage in Korea. *Tunnelling and Underground Space Technology*, 18:467-483.
- Pruess, K. (1997). On water seepage and fast preferential flow in heterogeneous, unsaturated rock fractures. *Journal of Contaminant Hydrology*, 30:333-362.

*“This page left intentionally blank.”*

# Finite Element Analysis on the Static Intensity and Dynamic Characteristics of Drilling Rig Derricks

Lijun Liu<sup>1\*</sup>, Fuquan Chen<sup>2</sup> and Yan Yu<sup>2</sup>

<sup>1</sup> R.D. Center of Hudong Heavy Machinery Co. Ltd., 2851 Pudong Avenue, Shanghai 200129, P.R. China

<sup>2</sup> National Oilwell Varco Petroleum Equipment (Shanghai) Co. Ltd., 1263 Zhenbei Road, Shanghai 200333, P.R. China

**Abstract.** Drilling rig derrick is one of the most important equipment in hoist system of oilfield, which can be used to install crown block and hang tackle, hoisting hook and special tools, and also complete manipulations such as making a trip, casing running and so on. The static intensity and dynamic properties of derricks are the main parameters determining the safety of drilling rig derricks. A finite element model based on the non-linear beam element was built in this paper. The static stress and dynamic characteristics of the derricks was calculating by using FEM software ANSYS. Furthermore, optimization method and stability calculating method are using to improve the structural load-carrying capability of derricks. Results indicated that the load-carrying capability and stability of optimal structures have been improved greatly. It can give constructive guidance to structure design of derrick and safety production in oilfield.

**Keywords:** Derricks, finite element analysis, static intensity, stability factor

## 1 Introduction

Drilling rig derricks is one of the most important equipment in hoist system of oilfield. Crown block, hang tackle, hoisting hook and special tools can be installed on it, and almost all kinds of manipulations, both making trip and casing running, can be carried out. Derricks always work at worse circumstances than other common steal structure, which can undergo hook load in tripping, wind load outdoors and vibration load when drilling machine is running (Zou, 2006) At present, it can only satisfy the base requirement in stage of design to research derrick structure by static equivalent method, nothing done further when derricks undergo the dy-

---

\* Corresponding author, e-mail: llj609@163.com

dynamic load (Guan et al. 2005) It is feasible and necessary to carry out dynamic mechanics performance analysis of derrick with dynamic method instead of static method (Zhou and Guo, 1999). So it is important, and can give constructive guide to structure design of derrick and safety production in oilfield.

In this paper, a finite element model based on the different type element was built by the theory of elastic body and principle of model equivalent. The static stress and dynamic characteristics of the derricks was calculated by FEM software ANSYS. The first 5 natural frequencies and modes of derrick are calculated. Furthermore, optimization method and stability calculating method are using to improve the structural load-carrying capability of derricks. It draws some conclusions including the changes of deformation and stress of derrick structure under dynamic loads, and the vibration rules and characteristic of time responses in different orientation in the main parts such as top, racking platform and propeller strut of drilling rig derrick. Results of static and dynamic analysis indicate that the load-carrying capability and stability of optimal structures have been improved greatly.

## 2 Theoretical Method

### 2.1 Static Assumption

The members are designed according to the Von-Mises equivalent stress criterion, where the equivalent stress,  $\sigma_{eqv}$ , defined as follows, is not to exceed  $F_y/F.S.$  The Factor of Safety (F.S.) will be specially considered when the stress components account for surface stress due to lateral pressures.

The von-Mises Equivalent Stress Criteria for plated structures can be written as

$$F = \sqrt{\sigma_x^2 - \sigma_x\sigma_y + \sigma_y^2 + 3\tau_{xy}^2} \leq F_y / F.S. \quad (1)$$

where  $\sigma_x$ ,  $\sigma_y$  are in-plane stress in the x and y direction, respectively.  $\tau_{xy}$  is in-plane shear stress.  $F_y$  is manufacturer's guaranteed minimum yield point. F.S. is 1.11 for combined loading. The material of the structural model and described as column and plate, is Q345 Steel (Yield Strength 345 MPa). Based on ASD method, the allowable design stress will be 310.81 MPa (\*1/1.11) complying with the factor of F.S. noted above.

## 2.2 Modal Theory

The purpose of modal analysis is to characterize the vibration behavior of the structure. According to operational properties of drilling rig derricks, the differential Equation of N-degree of freedom system, that is,

$$Mu'' + Ku = f(t) \quad (2)$$

where M, K are the mass and stiffness matrices, respectively. f is forcing vector. Free vibration of elastic structures can be decomposed by a series of simple harmonic oscillation. Assuming harmonic oscillation can be expressed as

$$u = \delta \sin(\omega t) \quad (3)$$

where  $\delta$  and  $\omega$  are the amplitude vector and the natural frequency vector, respectively.

Substituting Equation (3) into Equation (2), we obtain

$$(-\omega^2 M + K) \delta = 0 \quad (4)$$

In order to get system natural frequencies and mode shapes, it is necessary to solve the generalized eigenvalue problem. The eigenvalues can be obtained from the determinant of characteristic polynomial

$$|K - \omega^2 M| = 0 \quad (5)$$

Each corresponding eigenvector, or mode shape  $\delta$ , can be obtained by substituting  $\omega$  into Equation (4).

By normalizing about mass matrix M, each mode shape can be described as

$$\delta_i^T M \delta_i = 1, \delta_i^T M \delta_j = 0 \quad (i \neq j) \quad (6)$$

## 2.3 Stability Theory

Buckling is the result of unbalance between loading and resistance of structure, which can result in increasing structure deformation sharply. Then structure under yield strength limits will be destroyed.

The eigenvalue equation of structural linear buckling can be described as

$$(K - \lambda KG) u = p \quad (7)$$

where  $K_G$  is geometry rigid matrix,  $p$  is load vector and  $\lambda$  is the eigenvalue.

Supposing structure still in the state of balance, relatively little displacement is produced. Adding disturbing term  $u'$  to Equation (2), then

$$(K - \lambda KG)(u + u') = p \quad (8)$$

From Equation (7) and (8)

$$(K - \lambda KG)u' = 0 \quad (9)$$

Obviously  $u' \neq 0$ , that is, equation coefficient determinant equal to 0. Then

$$|K - \lambda KG| = 0 \quad (10)$$

By solving above equation, structural eigenvalue  $\lambda$  (also called scale factor and load factor) can be obtained.

Derricks framework mostly occur transverse buckling of superstructure. Vibration modes from modal analysis can reflect derrick buckling shape. When structures in top domain reach critical loads, structural deformation will increase sharply, and derrick can not keep in balance as original state, which will result in overturn and destroyed of superstructure.

### 3 Finite Element Model

Finite element model of land drilling derricks can be seen as Figure 1. Joints of all members are supposed to be reliable and rigidly. There are not relatively displacement and rotation between derrick foundation and ground base. Boundary conditions can be found in Figure 2. Beam element, bar element, shell element and mass element types are used to build up finite element model including 3517 nodes and 3269 elements. The beam sections include I, box and channel types, and so on. Material properties are defined as following: Elastic module  $E=2.1 \times 10^5 \text{MPa}$ , Poisson ratio  $\mu=0.3$  and density  $\rho=1.1 \times 7850 \text{ kg/m}^3=8635 \text{ kg/m}^3$  because of weld influence.

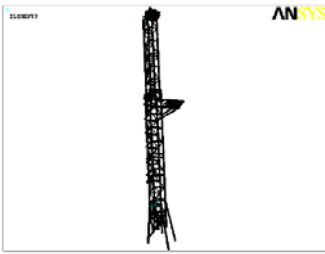


Figure 1. Finite element model of derrick

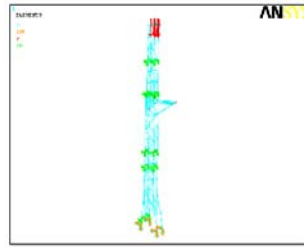


Figure 2. Boundary condition of FE model

## 4 Results Discussion

### 4.1 Static Results

Finite element software ANSYS is used to calculating structure stress. As shown in Figure 3 and Figure 4. The Maximum Von-Mises of derrick's upper and lower part are 176 and 209 MPa, respectively. Simulating results indicate that the withstanding stress of operational derrick is lower than the allowable stress. So the derrick is in the scope of the safety according to static intensity theory.

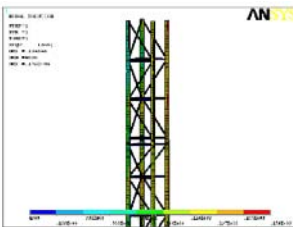


Figure 3. Stress contour of upper part

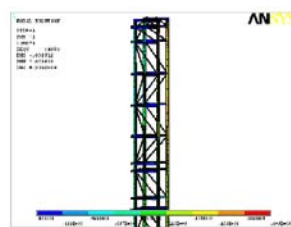
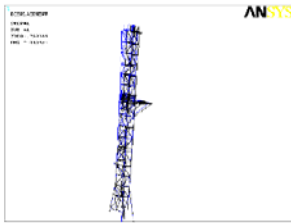


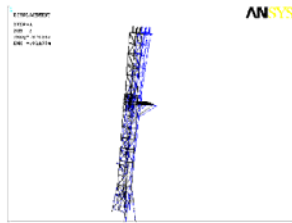
Figure 4. Stress contour of lower part

### 4.2 Modal Results

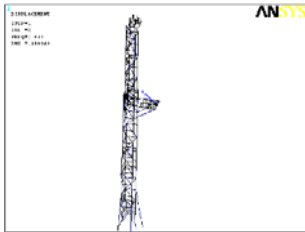
Finite element software ANSYS is also adopted to obtain the first 5 modes of land drilling derricks, and responding mode shapes can be seen in Figure 5.



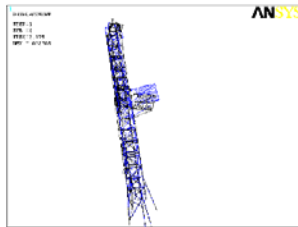
a) 1st transversal bending 0.79 Hz



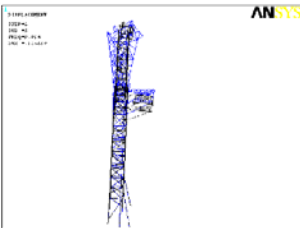
b) 1st longitudinal bending 0.87 Hz



c) Local bending modal 1.61 Hz



d) 1st torsion 2.08 Hz



e) 2nd torsion 2.92 Hz

Figure 5. The first 5 mode shapes of derrick

### 4.3 Buckling Results

From linear buckling analysis, original stability factors can be obtained. From Table 1, we can find that the first 4 stability factors are below 2.0. In order to improve the stable capacity of drilling rig derrick, the structure is updated by increasing stability of beam section. From the optimized results, the stability factors increase obviously.

Table 1. Comparison original with optimized stability factor

Order	1	2	3	4	5
Original	1.61	1.73	1.83	1.92	2.40
Optimized	2.66	3.00	3.85	4.67	4.75

## 5 Conclusions

In this paper, the static and dynamic characteristics analysis is made for the structures of the drilling rig derricks. Static intensity, dynamics analysis and stability are mainly analyzed by finite element method. The result shows that the legs of open orientation at the connection of two parts are the weak parts of the whole derrick. The first several vibration modes reveal the oscillation shape of the derrick. And the stability of optimized structure is improved greatly. Following conclusion can be drawn:

1. Drilling rig derrick is working in the worse circumstances, whose components are undergoing complicated extra loads and displacement. Besides satisfying static stress requirements, derrick members must satisfy dynamics properties conditions.
2. Structural natural frequencies and mode shapes of derrick can be obtained by dynamic analysis, from which we can prejudge the vibration shape of the derricks.
3. From buckling analysis, the stability and weak link of the derricks can be determined. And the stability capacity of derricks is improved greatly by structure optimization.

## References

- Guan X.J., Zhou G.Q. et al. (2005). Dynamic characteristics analysis of derrick structure for off shore drilling rig, *Journal of Daqing Petroleum Institute*, 29(3): 53-54 [in Chinese].  
 Reference on Guide for the Certification of Drilling Systems, 2004.1, Section 3, Chapter 7.1.  
 Zhou G. Q., Guo Y.S. (1999). Probing into derrick structure test with dynamic method instead of static method, *Oil Field Equipment*, 28(1): 22-24 [in Chinese].  
 Zou L.Q. (2006). Analysis for the dynamic response of drilling rig derricks. Harbin Engineering University [in Chinese].

*“This page left intentionally blank.”*

# Design Standards Comparison of Reinforced Concrete Strengthening Using FRP Composite in Chinese and ACI Codes

Asal Salih Oday<sup>1\*</sup>, Yingmin Li<sup>2</sup>, Mohammad Agha Houssam<sup>1</sup>,  
Al-Jbori A'ssim<sup>1</sup>, Thabit Saeed Ayad<sup>1</sup> and Lu Wang<sup>1</sup>

<sup>1</sup>College of Civil Engineering, Chongqing University, Chongqing, P.R. China

<sup>2</sup>Department of Disaster Prevention Engineering, College of Civil Engineering, Chongqing University, Chongqing, P.R. China

**Abstract.** The application of Fiber Reinforced Polymer (FRP) in civil engineering is a growing field worldwide. Many countries have different ideas and opinions on the applications of FRP. It includes general researches, standards design and specifications. Based on these key parameters, an exhaustive comparison between design standards of FRP-Strengthened reinforced concrete in the Chinese code and that of American Concrete Institute (ACI) is carried out in this paper. From a general viewpoint, the strategies of both codes for strengthening reinforced concrete structures are uniform. Nevertheless, the calculation methods of the bonded length, flexural capacity, and shear capacity are different from one another. The differences and sameness would deepen designers' understanding of FRP and illuminate them to pay more attention on these issues during calculation. This will contribute in making FRP an important material that could be effectively used and widely applied in the civil structures throughout the world.

**Keywords:** FRP-strengthening, reinforced concrete, Chinese and ACI codes

## 1 Introduction

The application of Fiber Reinforced Polymer (FRP) in civil engineering is a growing field worldwide. Many countries have different ideas and opinions on the applications of FRP. It includes general researches, standards design and specifications. The American Concrete Institute (ACI) has published several important documents through its Emerging Technology Series to provide engineers and designers with information and direction regarding new technologies not covered in ACI 318. Established in 1990, Committee 440 is recognized as a leader in devel-

---

\* Corresponding author, e-mail: odaycivileng@yahoo.com

oping FRP composite specifications for concrete structures. With a growing membership of 190+ worldwide experts in the field of concrete and FRP composites technology, Committee 440 carries out its mission to develop and report information on fiber-reinforced polymer for internal and external reinforcement of concrete. In 1996, Committee 440 prepared the first of several industry documents with ACI 440.4R-96, State-of-the-Art Report on Fiber Reinforced Plastic (FRP) Reinforcement for Concrete Structures. Since 1996, Committee 440 has focused on development of guideline documents. These guidelines are based on the knowledge gained from worldwide experimental research, analytical work, and field applications of FRP reinforcement. Four guide documents are available including concrete members reinforced internally with FRP rebars, externally bonded FRP systems for strengthening concrete structures, test methods for FRP bars and laminates, and prestressing with FRP tendons. In 2002, the second of the guides was published: ACI 440.2R-02 - Guide for the Design and Construction of Externally Bonded FRP Systems for Strengthening Concrete Structures. The guide covers FRP systems for strengthening concrete structures as an alternative to traditional strengthening techniques, such as steel plate bonding, section enlargement, and external post-tensioning. FRP systems offer advantages over traditional strengthening techniques such as lightweight, relatively easy to install, and non-corrosive. The guide provides general information on the history and use of FRP strengthening systems, a description of the unique material properties of FRP, and committee recommendations on the engineering, construction, and inspection of FRP systems used to strengthen concrete structures.

The Southeast Asian Region, namely China and India, has witnessed a rapid growth in the use of external FRP systems in strengthening works in recent years. In China, for example, it is estimated that about 600,000 m<sup>2</sup> of FRP sheets had been used in structural strengthening works in the year 2003. The application of FRP systems in these regions has largely been confined to typical strengthening works to include flexural and shear strengthening as well as seismic strengthening. The China Association for Engineering Construction Standardization has issued a document entitled “Technical Specification for Strengthening Concrete Structures with CFRP Laminates (CECS146:2003)”. This document gives the method to calculate the flexural and shear capacities of RC beams, and the axial load and seismic capacities of RC columns strengthened with FRP laminates. In addition, construction measures for structural RC members strengthened with FRP laminates are given in details. In Shanghai, a local standard, “Technical Code for Strengthening Concrete Structures with FRP (DG/TJ08-012-2002)” was developed in 2002.

## 2 Reinforced Concrete Strengthening Using FRP in Chinese Code

### 2.1 The Bonded Length in Chinese Code

The bonded length (is shown by Figure 1) should not be less than 200mm and more than the bonding and extending length. Namely:

$$\text{The bond length} \geq \max \left( \frac{E_{cf} \varepsilon_{cf} A_{cf}}{\tau_{cf} b_{cf}}, 200 \right) \quad (1)$$

where  $E_{cf}$  is elastic modulus of FRP;  $\varepsilon_{cf}$  is tensile strain in full utilization section of FRP, according to the 4.3.2 clause of Technical specification for strengthening concrete structures with carbon fiber reinforced polymer laminate;  $A_{cf}$  is the FRP tension face sectional area;  $\tau_{cf}$  is the design value for bonding strength between FRP and concrete, the value is 0.5MPa and  $b_{cf}$  is the width of FRP.

### 2.2 The Flexural Strengthening in Chinese Code

#### 1) Fundamental hypotheses

- When members reach the bending ultimate limit state, tensile strain of FRP is determined based on the plane section assumption and is no more than ultimate strain of FRP in tension ( $\varepsilon_{cf}$ ).
- When considering the effect of secondary load, initial strain  $\varepsilon_i$ , on the extreme tension fiber of concrete is calculated according to the plane section assumption before strengthening.
- Tensile stress  $\sigma_{cf}$ , of FRP is equal to products of elastic modulus  $E_{cf}$ , and tensile strain  $\varepsilon_{cf}$ , of FRP.
- Perfect bond exists between FRP and concrete in one part, and steel and concrete in the other part.

#### 2) Calculation

In Chinese codes, flexural strengthening calculation of rectangular section is classified into three types:

- When concrete compression height  $x$ , is between  $\xi_{cfb} h$  and  $\xi_b h_0$  (Figure 2(a)), calculation formula is as follows.

$$M \leq f_c b x \left( h_0 - \frac{x}{2} \right) + f_y' A_s' (h_0 - a') + E_{cf} \varepsilon_{cf} A_{cf} (h - h_0) \tag{2}$$

Concrete compression height  $x$  and tensile strain  $\varepsilon_{cf}$  of FRP are determined using formula (6).

$$\left\{ f_c b x = f_y A_s - f_y' A_s' + E_{cf} \varepsilon_{cf} A_{cf} , \text{ and } x = \frac{0.8 \varepsilon_{cu}}{\varepsilon_{cu} + \varepsilon_{cf} + \varepsilon_i} \cdot h \right. \tag{3}$$

- When concrete compression height  $x$  is less than  $\xi_{cfb} h$  (Figure 2(b)), calculation formula is as follows.

$$M \leq f_y A_s (h_0 - 0.5 \xi_{cfb} h) + E_{cf} (\varepsilon_{cf}) A_{cf} h (1 - 0.5 \xi_{cfb}) \tag{4}$$

- When concrete compression height  $x$  is less than  $2a'$ , calculation formula is as follows.

$$M \leq f_y A_s (h_0 - a') + E_{cf} (\varepsilon_{cf}) A_{cf} (h - a') \tag{5}$$

where  $M$  is the design moment including initial moment;  $A_s$  and  $A_s'$  are the area of steel reinforcement subjected to tension and the area of steel reinforcement subjected to compression respectively;  $A_{cf}$  is area of FRP reinforcement;  $f_y$  and  $f_y'$  are the design yield strength of tensile reinforcement and design compressive strength of compressive reinforcement respectively;  $f_c$  is the design concrete compressive strength;  $E_{cf}$  is the elastic modulus of FRP;  $x$  is the concrete compression height;  $\xi_{cfb}$  is the relative limit height of compression region when the ultimate strain of FRP in tension and the concrete compression failure simultaneously reach the value  $\frac{0.8 \varepsilon_{cu}}{\varepsilon_{cu} + (\varepsilon_{cf}) + \varepsilon_i}$ ;  $\varepsilon_i$  is the bending moment acting before FRP strengthening;  $(\varepsilon_{cf})$  is the ultimate strain of FRP in tension; and  $\varepsilon_{cf}$  is the strain of FRP.

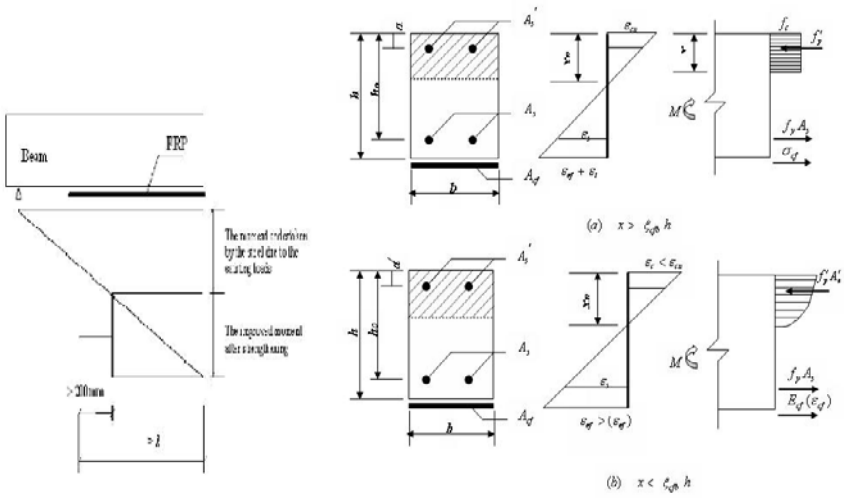


Figure 1. The bonded length (Chinese code) Figure 2. Flexural strengthening calculations Chinese code

### 2.3 The Shear Strengthening in Chinese Code

In Chinese code, shear strengthening of concrete beam should be calculated according to the following formula:

$$V_b \leq V_{brc} + V_{bcf}, \text{ where } V_{bcf} = \varphi \left( \frac{2n_{cf} \omega_{cf} t_{cf}}{s_{cf} + \omega_{cf}} \right) \epsilon_{cfv} E_{cf} h_{cf}, \quad \epsilon_{cfv} = \frac{2}{3} (0.2 + 0.12\lambda_b) \epsilon_{cfu} \quad (6)$$

where  $V_b$  represents shearing force design value;  $V_{brc}$  is the shear capacity of concrete before FRP strengthening;  $V_{bcf}$  is the shear undertaken by FRP;  $\epsilon_{cfv}$  is the strain of FRP when members reach ultimate limit states of shear capacity;  $\epsilon_{cfu}$  is the ultimate strain of FRP;  $\varphi$  is the FRP strengthening formal coefficient (completely wrapped:  $\varphi = 1.0$ , U-wrapped:  $\varphi = 0.85$ , side bonding:  $\varphi = 0.7$ ),  $\lambda_b$  is the shear span ratio (when load is uniform load  $\lambda_b = 3.0$ ; when load is concentrated load,  $\lambda_b = a/h$ , if  $\lambda_b > 3.0$  then  $\lambda_b = 3.0$ , if  $\lambda_b < 1.5$ , then  $\lambda_b = 1.5$ ),  $n_{cf}$  is the number of bonded layers in the FRP;  $h_{cf}$  is the side bonding height of FRP;  $s_{cf}$  is the spacing of FRP;  $t_{cf}$  is the thickness of FRP; and  $\omega_{cf}$  is the width of FRP.

### 3 Reinforced Concrete Strengthening Using FRP in ACI Code

#### 3.1 The Flexural Strengthening in ACI Code

The nominal flexural capacity of an FRP-strengthened concrete member can be determined based on strain compatibility, internal force equilibrium, and the controlling mode of failure. The internal strain and stress distribution for a rectangular section under flexure at ultimate stage is illustrated in Figure 3.

$$M_n = A_s f_s \left( d - \frac{\beta_1 c}{2} \right) + \psi_f A_f f_{fe} \left( h - \frac{\beta_1 c}{2} \right), \text{ where } c = \frac{A_s f_s + A_f f_{fe}}{\gamma f'_c \beta_1 b} \quad (7)$$

where  $c$  the depth of neutral axis. An additional reduction factor  $\psi_f = 0.85$ , is applied to the contribution of the FRP system. The terms  $\gamma$  and  $\beta_1$  are parameters defining a rectangular stress block in the concrete equivalent to the actual nonlinear distribution of stress. Because the stress level in FRP at failure is not known (no yielding), an iterative design approach is usually required. It is important to determine the strain level in the FRP reinforcement at the ultimate-limit state. Because FRP materials are linearly elastic until failure, the level of strain in the FRP will dictate the level of stress developed in the FRP. The flexural strength of a section depends on the controlling failure mode. Concrete crushing is assumed to occur if the concrete compressive strain  $\epsilon_{cu}$ , reaches 0.003. Rupture of the FRP laminate is assumed to occur if the strain in the FRP  $\epsilon_f$ , reaches its design rupture strain  $\epsilon_{fu}$ , before the concrete reaches strain of 0.003. In order to prevent debonding of the FRP laminate, the FRP design strain is reduced using a bond-dependent coefficient  $k_m$  which is a function of the number of FRP plies  $n$ , ply thickness  $t_f$ , and FRP stiffness  $E_f$ .

$$k_m = \begin{cases} \frac{1}{60\epsilon_{fu}} \left( 1 - \frac{nE_f t_f}{2000000} \right) \leq 0.90 & \text{for } nE_f t_f \leq 1000000 \\ \frac{1}{60\epsilon_{fu}} \left( \frac{500000}{nE_f t_f} \right) \leq 0.90 & \text{for } nE_f t_f > 1000000 \end{cases} \quad (8)$$

The use of externally bonded FRP reinforcement for flexural strengthening will reduce the ductility of the original member. The  $\phi$ -factor approach is that a section with low ductility should compensate with a higher reserve of strength. The higher reserve of strength is achieved by applying a strength-reduction factor of 0.70 to brittle sections, as opposed to 0.90 for ductile sections with a linear transi-

tion between these two extremes. Strength-reduction factor based on the strain in the steel at ultimate-limit state  $\varepsilon_s$ , can be found from.

$$\phi = \begin{cases} 0.90 & \text{for } \varepsilon_s \geq 0.005, \text{ and } 0.70 \text{ for } \varepsilon_s \leq \varepsilon_{sy} \\ 0.70 + \frac{0.20(\varepsilon_s - \varepsilon_{sy})}{0.005 - \varepsilon_{sy}} & \text{for } \varepsilon_{sy} < \varepsilon_s < 0.005 \end{cases} \quad (9)$$

### 3.2 The Shear Strengthening in ACI Code

In beam applications, where an integral slab makes it impractical to completely wrap the member, the shear strength can be improved by wrapping the FRP system around three sides of the member (U-wrap) or bonding to the two sides of the member. The FRP system can be installed continuously along the span length of a member or placed as discrete strips. The nominal shear capacity of an FRP-strengthened concrete member can be determined by adding the contribution of the FRP reinforcing to the contributions from the reinforcing steel (stirrups, ties, or spirals) and the concrete (see Figure 4). An additional reduction factor  $\psi_f$ , is applied to the contribution of the FRP system:

Shear resistance:

$$\phi V_n = \phi (V_c + V_s + \psi_f V_f) \quad (10)$$

FRP shear contribution:

$$V_f = \frac{A_{fv} f_{fe} (\sin \alpha + \cos \alpha) d_f}{s_f}, \quad \text{where } A_{fv} = 2n t_f w_f \quad (11)$$

To preclude loss of aggregate interlock of the concrete, the maximum fiber strain used for design should be limited to 0.4%. Additionally, bond-reduction coefficient  $K_v$ , is used to calculate the effective FRP strain for shear.

$$\varepsilon_{fe} = K_v \varepsilon_{fu} \leq 0.004 \quad (12)$$

The bond-reduction coefficient is a function of the concrete strength, the type of wrapping scheme used, and the stiffness of the laminate.

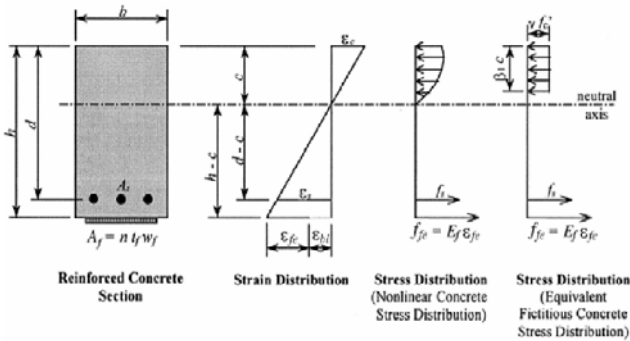


Figure 3 Strain and Stress distribution for a rectangular section at Ultimate (ACI code).

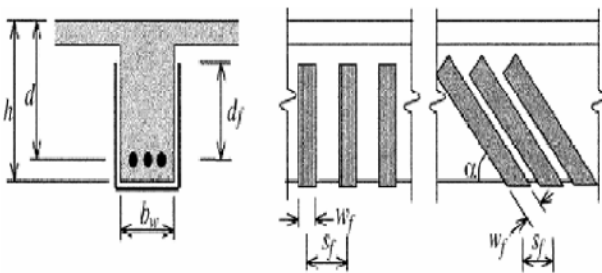


Figure 4 Illustration of the variables used in shear-strengthening calculations (ACI code).

## 4 Conclusion

This paper compares the design standards of Chinese and ACI codes about FRP-strengthening for R/C structures in detail. The FRP-strengthening related specifications of both codes are essentially consistent in principle point of view. Nevertheless, the calculation methods of the bonded length, flexural strengthening, and shear strengthening are different from one code to another. The difference mainly comes from two aspects: different partial coefficient and different calculation methods. The flexural and shear capacity in both codes comes from three parts: concrete, steel bar, and FRP. However, details on calculation are different if to consider the two codes. In both codes, FRP strengthening configuration is classified

into three types: side bonding, U-wrapped, and completely wrapped beams. In Chinese code, three FRP strengthening configurations are realized based on three coefficients ( $\varphi = 0.7$ ,  $\varphi = 0.85$ ,  $\varphi = 1.0$ ).

## References

- American Concrete Institute – Committee 318 (1999). Building Code Requirements for Structural Concrete and Commentary, ACI 318-99/R-99, ACI, Farmington Hills, MI, USA.
- American Concrete Institute – Committee 318 (2002). Building Code Requirements for Structural Concrete and Commentary, ACI 318-02/R-02, ACI, Farmington Hills, MI, USA.
- American Concrete Institute – Committee 440 (2002). Guide for the Design and Construction of Externally Bonded FRP Systems for Strengthening Concrete Structures, ACI 440.2R-02, ACI, Farmington Hills, MI, USA.
- Code for design of concrete structures. (2002). China building industry press.
- Ng. C.K., Private communication, University Sarawak Malaysia, East Malaysia.
- Quek M.L., Private communication, Fyfe Co. Pte. Ltd., Singapore.
- Technical specification for strengthening concrete structures with carbon fiber reinforces polymer laminate (2002).
- Ye L.P., Private communication, Tsinghua University, China.

*“This page left intentionally blank.”*

# Think about Structural Fail State to Solve Geometric Reliability

Junbo Tao<sup>1\*</sup> and Zhangdun Wu<sup>1</sup>

<sup>1</sup>Civil and Architecture Engineering Department of Guangxi University, Nanning Guangxi 530004, P.R. China

**Abstract.** The geometric reliability is usually applied in the structural analysis of the large projects. The structure-function is usually discrete or implicit. It is necessary to use penalty function to convert the constrained optimization problem into non-constrained optimization problem. We also analyze possible cheats of penalty in un-ultimate state (mostly happen in penalty safe state). So it is proposed that only use structural fail regional variables by random sampling to solve the geometric reliability, obtain an non-constrained optimization problem and un-introduction penalty function. It proposed use discrete optimization (such as the GA, ACO, PSO and so on) to solve geometric reliability, the penalty is carried out on the variables in the safe state not in the structural fail and ultimate state. Through comparison of benchmarks from Monte-Carlo method, random sampling and GA in SFSCGR (Structural Fail State Calculation Geometric Reliability) and PSUUSCGR (Penalty Structural Un-Ultimate State Calculation Geometric Reliability), it is illustrated that SFSCGR is feasible, and it is very stable and accurate in geometric reliability solving.

**Keywords:** penalty, geometric reliability, structural fail state

## 1 Introduction

Geometric reliability convert the reliability problem into mathematical constrained optimization problem (Ditlevsen and Madsen, 2005; Jie et al., 2004). Geometric reliability is rough, and it cannot distinguish the different tangent ultimate state curved surfaces at the check point in the standard state-space. However, compared with the general reliability calculation, the geometric reliability can obtain higher precision results (Zhao, 1996). The undesirable large errors caused by first-order second moment method in the high-order nonlinear structure function would not

---

\* Corresponding author, e-mail: ulanala@hotmail.com

take place in geometric reliability calculation. In addition, geometric reliability retain the important practicability.

In the large projects of structural analysis, such as the application of artificial neural network, the response surface method and the vector supporting machine, the structure-functions are solved by the geometric reliability. In these problems, the structure functions are always very complex implicit-functions. To simplify these problems, penalty functions are introduced, so that the constrained optimization problems are converted into un-constrained optimization problems. In this paper, we would analyze two different penalty functions for solving reliability index: formula (2) and formula (4), and show that the method of considering the fail state in the solving of geometric reliability index is superior to the other.

## 2 Penalty Method of Solving Geometric Reliability

According to the definition from Hasofer-Lind, reliability index is the distance from the coordinate origin to the ultimate state surface in standard normal state space (Ditlevsen and Madsen, 2005). The ultimate state function is defined as  $Z=G(\mathbf{X})$ , where  $\mathbf{X}$  is an n dimension vector. The elements of  $x_i$  are independent random variables. Normality of random variables. We could obtain the mean  $\mu_{\mathbf{X}}$ , the standard deviation of  $\sigma_{\mathbf{X}}$ , and reliability index  $\beta$  of the equivalent normal distribution of  $\mathbf{X}$ . We also define the floor and ceiling of  $\mathbf{X}$  as  $\mathbf{X}^d$  and  $\mathbf{X}^u$ , respectively.

$$\begin{cases} \mu_{x_i'} = x_i^* - \varphi^{-1}[F_{x_i}(x_i^*)]\sigma_{x_i'} \\ \sigma_{x_i'} = \phi\left\{\varphi^{-1}F_{x_i}(x_i^*)\right\}/f_{x_i}(x_i^*) \\ \min \beta^2 = \sum \left[ \left( x_i - \mu_{x_i'} \right) / \sigma_{x_i'} \right]^2 \\ s.t. \mathbf{X}^d \leq \mathbf{X} \leq \mathbf{X}^u \end{cases} \tag{1}$$

Compared with other methods (check-point method, mapping transformation method and practical analysis method, etc.), optimization model for calculation of structural reliability indexes has the following features (Ou and Hou, 2001):

1. Computing model reflects the geometric meaning of structural reliability index.
2. This model could take full advantage of a variety of optimization algorithms (such as linear programming, quadratic programming, neural network, etc.) to calculate the structural reliability index. So that the powerful optimization algorithm library could be used.
3. This method combines structural analysis and calculation of reliability index together. At the same time, it avoids the requirement that ultimate state func-

tion must be explicit-function. Thus the reliability analysis and application are simplified.

Because different algorithms have their own suitable area and special conditions, the selection of the optimization algorithm should be based on the specific problem.

Penalty function is an important approach to solve the problem of constrained optimization. There are many effective algorithms to solve the unconstrained optimization problem. Therefore, converting constrained optimization problem into unconstrained optimization problem is a natural idea. The main idea is to design a penalty function, and add it to the objective function. In the process of solving the unconstrained optimization problem, the iteration points which violate the constraint would be given a large objective function value. So that a series of minimum points of the unconstrained problem are forced to be near the feasible region or maintain in the feasible region until iteration converge to extreme value of the original constrained problem(Jie et al., 2004).

In the engineering application, exterior penalty function methods are usually used for solving the geometric reliability. Penalty Un-Ultimate state for solving geometric reliability (Penalty Structural Un-Ultimate State Calculation Geometric Reliability, PSUUSCGR).  $\sigma_k|G(\mathbf{X})|^\alpha$ ,  $\sigma_k \max(0, \mathbf{X}^d - \mathbf{X})$  and  $\sigma_k \max(0, \mathbf{X} - \mathbf{X}^u)$  are introduced, and formula (2) is obtained. Considering the general range of the reliability index is in [0,10], the  $\alpha$  takes value of 2, the penalty factor  $\sigma_k$  takes value of 100. When  $G(\mathbf{X}) < 0.00005$ , reliability index is required to maintain 6 decimal digits.  $\sigma_k$  takes smaller numeric, The ill-condition in Augmented Matrix should be avoided at some extent. It is not necessary to use complex Multiplier Method.

$$\begin{aligned} \min \beta = & \sqrt{\left\{ \left[ \frac{x_i - \mu_{x_i}}{\sigma_{x_i}} \right]^2 \right\} + \sigma_k \left[ |G(\mathbf{X})|^\alpha \right.} \\ & \left. + \max(0, \mathbf{X}^d - \mathbf{X})^\alpha + \max(0, \mathbf{X} - \mathbf{X}^u)^\alpha \right] \end{aligned} \tag{2}$$

$$s.t. \sigma_k \geq 1, \alpha \geq 1$$

### 3 Think about Structural Fail State to Solve Geometric Reliability

When the constraint  $G(\mathbf{X}) > 0$ , the structure is in safe state, and optimal value of the objective function is 0. When the structural is in fail state, the optimal value of the objective function is approximated to the structural reliability index. Application of structural fail state regional variables to solve geometric reliability (Structural

Fail State Calculation Geometric Reliability, SFSCGR). To determine whether  $G(\mathbf{X})$  is at the fail state. (3) applicable to random sample solutions which meet the condition  $G(\mathbf{X}) < 0$  for calculating reliability index, obtain the formula (3) (Zhao, 1996). The geometric reliability problem is converted into an unconstrained optimization problem.

$$\begin{aligned} \min \quad & \min \beta^2 = \sum \left[ \left( \frac{x_i - \mu_{x_i'}}{\sigma_{x_i'}} \right)^2 \right] \\ \text{s.t.} \quad & \mathbf{X}^d \leq \mathbf{X} \leq \mathbf{X}^u \quad G(\mathbf{X}) < 0 \end{aligned} \tag{3}$$

Formula (2) is modified to the formula (4). The penalty is carried out on the variables in the safe state not in the structural failure and ultimate state. Formula (4) is suitable for iterative algorithm in solving the reliability index.

$$\begin{aligned} \min \beta = & \text{sqr}t \left\{ \sum \left[ \left( \frac{x_i - \mu_{x_i'}}{\sigma_{x_i'}} \right)^2 \right] + \sigma_k \left[ \max \left( 0, |G(\mathbf{X})| \right) \right]^\alpha \right. \\ & \left. + \max \left( 0, \mathbf{X}^d - \mathbf{X} \right)^\alpha + \max \left( 0, \mathbf{X} - \mathbf{X}^u \right)^\alpha \right\} \end{aligned} \tag{4}$$

$$\text{s.t.} \sigma_k \geq 1, \alpha \geq 1$$

#### 4 Penalty Method of Geometric Reliability CHEATS and Analysis

$$\begin{cases} G(\mathbf{X}, t) < 0 & \text{fail} \\ G(\mathbf{X}, t) = 0 & \text{ultimate} \\ G(\mathbf{X}, t) > 0 & \text{safe} \end{cases} \quad t \in (0, T) \tag{5}$$

Some are revealed from Figures 1-4 of structural working condition and formula (5) of the structure-function (Qin and Lin, 2006; Wu, 2001). In Figure 1-4 the distance between point X and the origin O (XO) is the reliability index. The distance between point X and ultimate state surface (XY) is the absolute value of  $G(\mathbf{X})$ . T is the designed structural life. When the global search of optimal solution is carried out, PSUUSCGR would lead to errors in calculating the objective function value. Moreover, 4 CHEATs may be caused.

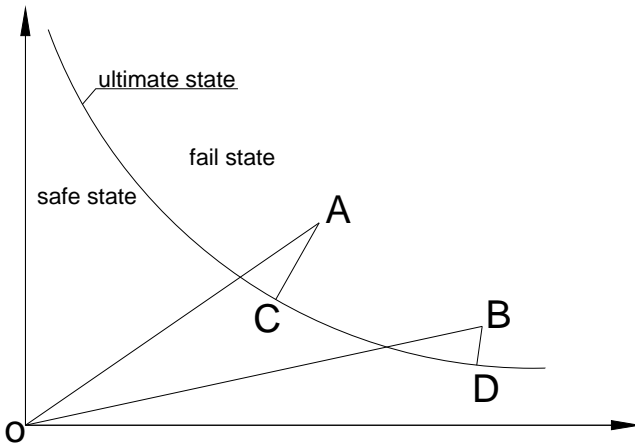


Figure 1. Possible cheat 1 of penalty un-ultimate state

CHEAT 1: both Point A and Point B are in the fail state region, and the current reliability index  $OA < OB$ . Using penalty function method, the false result of  $OA > OB$  may be generated by penalty function method due to the  $|G(\mathbf{X})| AC > BD$ . However, SFSCGR would not cause CHEAT 1.

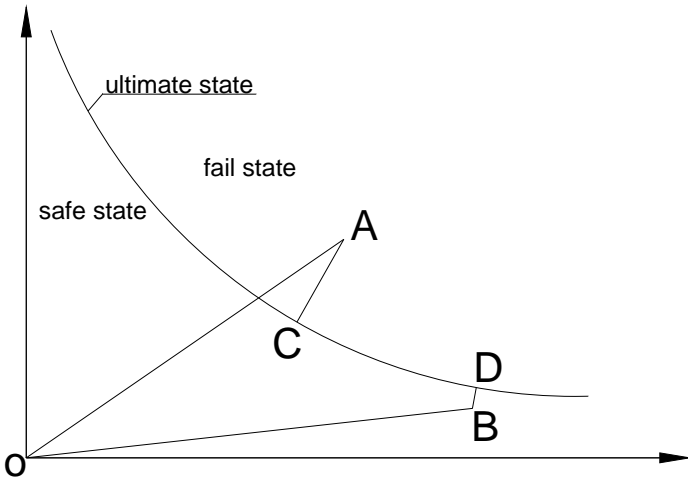


Figure 2. Possible cheat 2 of penalty un-ultimate state

CHEAT 2: Point A is in the fail state region, point B is in the safe state region,  $OA < OB$ . But the false result of  $OA > OB$  may be generated due to  $AC > BD$  (Figure 2) but SFSCGR would not cause CHEAT 2.

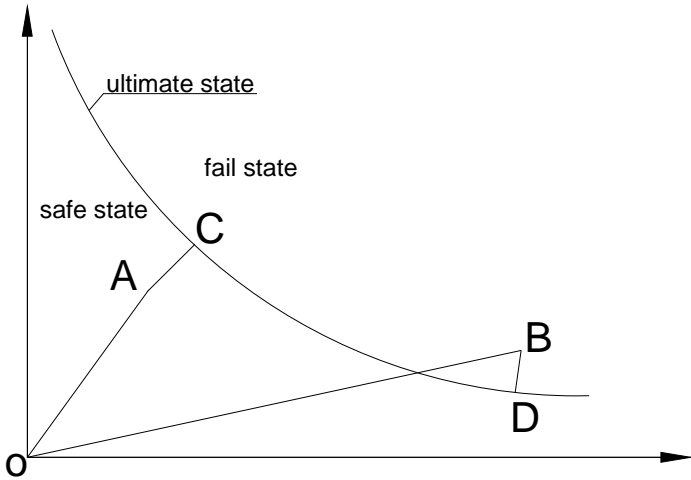


Figure 3. Possible cheat 3 of penalty un-ultimate state

CHEAT 3: Point A is in the safe state region, point B is in the fail state region,  $OA < OB$ . But the false result of  $OA > OB$  may be generated due to  $AC > BD$  (Figure 3). Because  $BD=0$  in SFSCGR, SFSCGR would lead to more CHEAT 3 than PSUUSCGR.

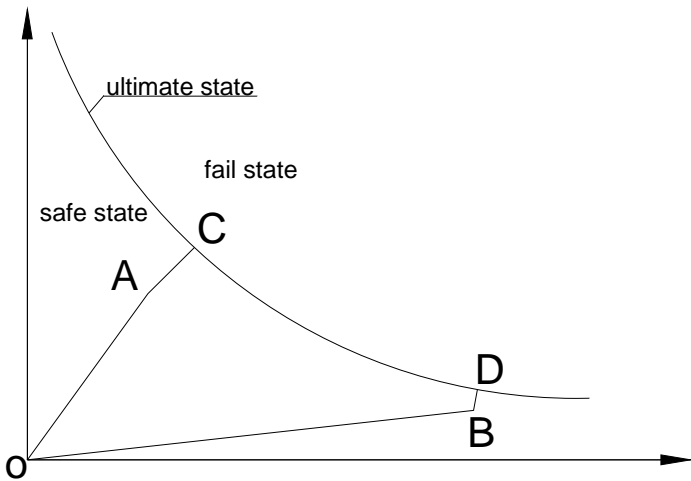


Figure 4. Possible cheat 4 of penalty un-ultimate state

CHEAT 4: Point A and Point B are in safe state region,  $OA < OB$ . Since the  $AC > BD$ , that may arise the fault result of  $OA > OB$  (Figure 4). The number of CHEAT 4 in PSUUSCGR is equal to that in SFSCGR.

The possible cheats in PSUUSCGR will deviate the searching of optimal solution from the check point. The optimal solution may even not be a feasible solution.

Formula (4) SFSCGR will generate CHEAT 3 and 4. Because there is no punish in the fail state region, the accuracy of calculation of reliability indexes would get better optimization results.

We also use genetic algorithm, the population size is 200. The graphs in the first row of Figure 5 reveal the relationship between iteration number and the number of solutions in fail state of example 1-5 in SFSCGR. The graphs in the second row of Figure 5 show the same relationship of example 1-5 in PSUUSCGR.

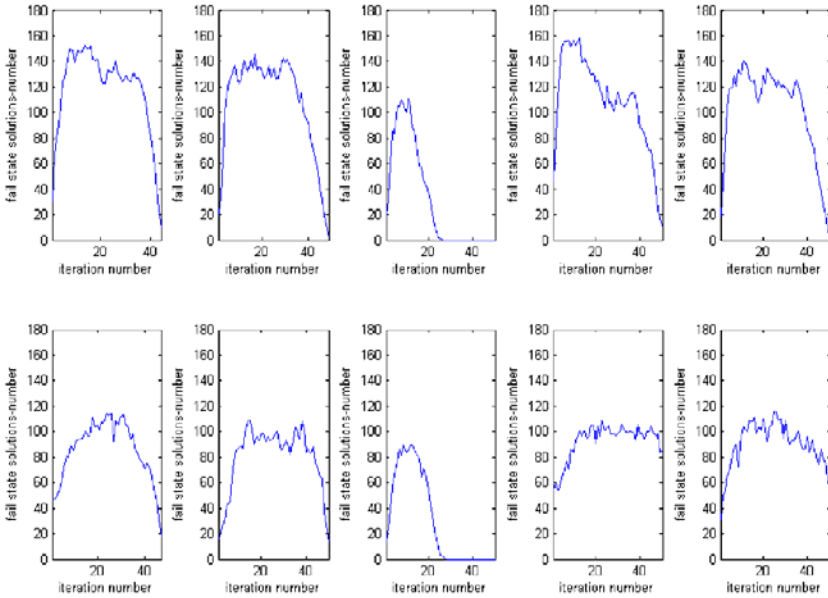


Figure 5. PSUUSCGR and SFSCGR’s relationship of fail state solutions-number and iteration number

In both PSUUSCGR and SFSCGR, number of solutions in fail state firstly increase and then decrease. Because of the influence of Penalty item  $\sigma_k|G(\mathbf{X})|^a$ , the fail state region of PSUUSCGR is much smaller than the safe state region. The  $\mathbf{X}$  in fail state regional are closed to  $\mathbf{X}^*$ , so that it is inevitable that the average of the fail state regional  $|G(\mathbf{X})|$  is less than the average of the safe state regional  $|G(\mathbf{X})|$ . This makes the penalty of the reliability indexes in the fail state region smaller than that in the safe state regional, and the reliability indexes in fail state region is also smaller than safe state region. It leads to that all individuals tend toward the fail state region, so that the number of solutions in the fail state increase firstly. For SFSCGR, punishment does not take place in fail state region (it is equivalent

to  $|G(\mathbf{X})|=0$ ), thus reliability indexes in fail state region are even smaller than PSUUSCGR at same situation. It is bound to force all individuals tend toward the fail state region faster than PSUUSCGR. Therefore, for the same generation, the number of solutions in the fail state for SFSCGR is larger than that for PSUUSCGR.

In the latter part of the iteration, the search of solution is focus on the region near the check points,  $|G(\mathbf{X})|$  tends to 0, and the impact of the punishment item of  $\sigma_k|G(\mathbf{X})|^a$  is weakening. The possibility of individual falls in safe state region is larger than it falls in the fail state region. Thus, the most of individuals are bound to close to the safe state region at last. So that, the number of solutions in the fail state region increases at first, but decreases in the latter part of the iteration.

The individuals falling in the fail state region occupies large proportion. SFSCGR does not generate CHEAT 1, so that the efficiency would be greatly increased.

## 5 Benchmarks

Example 1: given that the ultimate state function  $Z=G(f,w)=fw-fw-960=0$ , random variables  $f$  and  $w$  are subject to normal distribution and independent from each other, their mean and standard deviation are :  $\mu_f=36$ ,  $\mu_w=44$ ,  $\sigma_f=4.8$ ,  $\sigma_w=3.7$ . Solve the reliability index (Li et al., 1999).

Example 2: given that the ultimate state function  $Z=G(R,G,Q)=R-G-Q=0$ ,  $R$ ,  $G$  and  $Q$  are independent of each other, and their means and standard deviations are:  $\mu_R=309.2$ ,  $\sigma_R=52.6$ ;  $\mu_G=53$ ,  $\sigma_G=3.7$ ;  $\mu_Q=70$ ,  $\sigma_Q=20.3$ .  $R$  are subject to lognormal distribution,  $G$  are subject to normal distribution,  $Q$  are subject to extremum I distribution. Solve the reliability index (Li et al., 1999).

Example 3: given that the ultimate state function  $Z=G(R, S)=R-S=0$ . Resistance  $R$  is subject to lognormal distribution, and the mean  $\mu_R=100$ , variance equals to 12.  $S$  are subject to extremum I distribution, and the mean  $\mu_S=50$ , variance is 7.5.  $R$  and  $S$  are independent of each other, Solve the reliability index (Zhao, 1996).

Example 4: given that the ultimate state function  $Z=G(f,r,H)=567fr-0.5H^2=0$ ,  $f$  are subject to normal distribution,  $\mu_f=0.6$ ,  $\sigma_f=0.0786$ ;  $r$  are subject to normal distribution,  $\mu_r=2.18$ ,  $\sigma_r=0.0654$ ;  $H$  are subject to lognormal distribution,  $\mu_H=32.8$ ,  $\sigma_H=0.984$ .  $f$ ,  $r$  and  $h$  are independent of each other, Solve the reliability index (Zhao, 1996).

Example 5: given that the ultimate state function  $Z=G(f_y,d,P)=0.25\pi d^2f_y-P=0$ . Random variables of yield strength  $f_y$ , bar diameter  $d$  and stretching force  $P$  are subject to normal distribution and independent of each other. Their means and standard deviations are:  $\mu_{f_y}=335\text{MPa}$ ,  $\mu_d=14\text{mm}$ ,  $\mu_P=25\text{kN}$ ,  $\sigma_{f_y}=26.8\text{MPa}$ ,  $\sigma_d=0.7\text{mm}$ ,  $\sigma_P=6.25\text{kN}$ . Solve the reliability index (Li et al., 1999).

We compare the results of reliability index from random sampling, Monte Carlo method (MCM) and genetic algorithm (GA).

Table 1 compares the results from formula (3) in SFSCGR and MCM. For small reliability indexes, due to the large fail region, it is necessary to collect a large number of random samples at fail region. But for large reliability index, it only needs a few random samples in fail region. The second sampling of SFSCGR is introduced. The first sampling size is  $N_1=200$ , and the second sampling size is based on the reliability index  $\beta$  from first sampling.

$$N_2 = \text{round} (10^{(10-\beta)/1.75}) \tag{6}$$

The estimation of  $N_2$  can also based on the population size and iterations of GA. MCM simulation is carried out for  $10^6$  times to calculate reliability index, the result is less than actual reliability index. In Table 1 SFSCGR the sampling time is  $N_1+N_2$ .

Table 1. Comparison of Random sampling and MC method results

Calculation Method		1	2	3	4	5
SFSCGR	Reliability index	2.4144	3.5890	3.2487	1.9769	3.0646
	Sampling number	14928	3241	5192	18817	6001
MCM	Reliability index	2.3762	3.5905	3.2379	1.9522	3.0456

The results of formulae (2) and (4) in GA are shown in Table 2. Real-coded genetic algorithm and single-point cross is used in the calculation with maximum iteration of 50 and population size of 200. When  $|G(X^*)| < 0.00005$ , iteration of GA finishes. The penalty factor in PSUUSCGR Example 1 to 4 is  $\sigma_k=100$ . Because of the larger value of structural constraints function, the penalty factor in Example 5 takes  $\sigma_k=0.01$ , and the penalty item  $\alpha=2$  (Chen and Ma, 2006).

Table 2. Comparison of GA results

Calculation Method		1	2	3	4	5
PSUUSCGR	Average $\beta$	2.4142	3.5855	3.2464	1.9658	3.0582
	Best $\beta$	2.4136	3.5824	3.2460	1.9643	3.0567
	Worst $\beta$	2.4199	3.6047	3.2520	1.9736	3.0709
SFSCGR	Average $\beta$	2.4803	3.6449	3.2506	2.0952	3.1083
	Best $\beta$	2.4136	3.5825	3.2460	1.9647	3.0568
	Worst $\beta$	2.9703	3.8183	3.2878	2.6412	3.3222

## 6 Conclusions

This paper analyzes geometric meaning of the reliability and the role of penalty function method, and compares the benchmarks of the applications of the different algorithm. Compare to punish non-structural limit state (PSUUSCGR) and MCM, structural fail state calculation geometric reliability (SFSCGR) has better calculation results.

## References

- Ditlevsen O., Madsen H.O. (2005). *Structural Reliability Methods*. Shanghai: Tongji University Press, 9.
- Jie K.X., Han J., L Y.I. (2004). *Optimization Method*, revised edition. Tianjin: Tianjin University Press [in Chinese].
- Zhao G.F. (1996). *Engineering Structure Reliability Theory and Its Applications*. Dalian: Dalian University of Technology Press [in Chinese].
- Hou G.L., Ou J.P. (2001). Optimization model for calculation of structural reliability indexes and its implementation in MatLab environment. *Haerbin: Journal of Harbin University of C.E. & Architecture* [in Chinese].
- Qin Q., Lin D.J. (2006). *Theory and Application Reliability SFEM*. Beijing: Tsinghua University Press [in Chinese].
- Chen G., Ma G.W. (2006). Application of the ant colony optimization algorithm for reliability of arch dam. *Hydroelectric Power*, 32(7): 34-36 [in Chinese].
- Wu Z.D. (2001). *Structural Reliability Analysis*. Nanning: College of Civil Engineering, GuangXi University Structural Reliability Analysis Handouts [in Chinese].
- Li G.F., Gao J.L., Le J.C. (1999). *Engineering structure reliability principles*. Zhengzhou: Yellow River Water Conservancy Press [in Chinese].
- Tao J.B. (2008). *The Research of System Analysis and Application of the Water Conservancy Projects*. Nanning: Guangxi University [in Chinese].

# Research on the Optimum Stiffness of Top Outriggers in Frame-Core Structure with Strengthened Story

Yuan Su<sup>1,2\*</sup>, Chuanyao Chen<sup>1,2</sup> and Li Li<sup>1,2</sup>

<sup>1</sup>School of Civil Engineering and Mechanics, Huazhong University of Science & Technology, Wuhan 430074, China

<sup>2</sup>Hubei Key Laboratory of Control Structure, Huazhong University of Science & Technology, Wuhan 430074, China

**Abstract.** Using lateral deflection calculation formula for frame-core structure with top horizontal outriggers, analysis of the optimum stiffness of outriggers in frame-core structure with strengthened story is carried out. The method that confirms the optimum stiffness of horizontal outriggers which base on reduced structure lateral deflection magnitude and precise parameters are presented. The result of case study shows that this method is creditable. The conclusion can be referenced for designing and especially for confirming structure scheme.

**Keywords:** horizontal outriggers, frame-core structure, optimum stiffness

## 1 Introduction

In frame-core structure, the horizontal outriggers with larger bending rigidity can take full advantage of the axial force of perimeter frame columns, which forms inversely directed moment to reduce the overturning moment, thus reduce the lateral deflection of the whole structure under the horizontal loads and the moment at the bottom of the core. Obviously, lateral deflection of the structure will be reduced correspondingly, the bigger of the stiffness of horizontal outriggers the greater the reverse moment which provided to the structure. But, previous studies show that, when the stiffness of horizontal outriggers increased to some extent, the reduction of the structure lateral deflection by continuing to intensify the stiffness of horizontal outriggers is very limited, and the vertical stiffness mutation will increase when the stiffness of horizontal outriggers increase, which is unfavorable for seismic resistance of the structure, so “limited stiffness” (Xu, 2005; Fang et al.) design concept was proposed. But the problems such as how to value the “limited

---

\* Corresponding author, e-mail: syuan-027@163.com

stiffness”, correlate what are the factors effect the value, are lack of quantitative analysis, so it is inconvenient for the engineering application of “limited stiffness” of horizontal outriggers. This paper quantitatively analyzes the “limited stiffness” of horizontal outriggers in frame-core structure base on previous studies.

## 2 Lateral Deflection Analysis of Frame-Core Structure with Top Outriggers

In literature (Zhang and Zhao, 2007), through the use of the principle of minimum potential energy, the functional variation method and continuous analysis methods for tall structures (computing model is shown in Figure 1), the expressions of lateral deflection curve for frame-core structure with top horizontal outriggers under horizontal distributed load, top concentrated load and top moment are obtained. The analysis of this calculation method is much comprehensive by considering the effect of the perimeter frame beams and columns, floor beams, horizontal outriggers and the stiffness of the core on the lateral deflection of the structure.

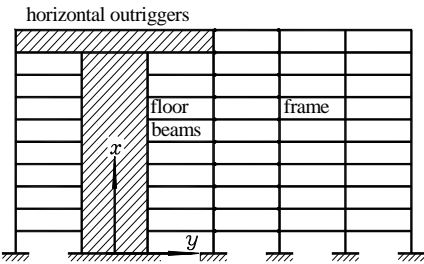


Figure 1. Computing model of structure

The lateral deflection of the structure under inverted triangle distributed load  $q$  is expressed as

$$y = \frac{qH^2}{2\tau} \left[ \frac{1 + \frac{\gamma}{2} + \left(\frac{1}{2} - \frac{1}{\lambda^2}\right)(\gamma \cosh \lambda + \lambda \sinh \lambda - \gamma)}{\lambda (\gamma \sinh \lambda + \lambda \cosh \lambda)} (\cosh \lambda \xi - 1) + \left(\frac{1}{2} - \frac{1}{\lambda^2}\right) \left( \xi - \frac{\sinh \lambda \xi}{\lambda} \right) - \frac{\xi^3}{6} \right] \quad (1)$$

The lateral deflection of the structure under uniformly distributed load  $q$  is expressed as

$$y = \frac{qH^2}{2\lambda\tau} \left[ \frac{\gamma \cosh \lambda + \lambda \sinh \lambda + 1}{\gamma \sinh \lambda + \lambda \cosh \lambda} (\cosh \lambda\xi - 1) - \sinh \lambda\xi + \lambda\xi \left( 1 - \frac{\xi}{2} \right) \right] \quad (2)$$

The lateral deflection of the structure under top concentrated load  $P$  is expressed as

$$y = \frac{PH^3}{2\lambda^3\omega} \left[ \frac{\gamma \cosh \lambda + \lambda \sinh \lambda - \gamma}{\gamma \sinh \lambda + \lambda \cosh \lambda} (\cosh \lambda\xi - 1) - \sinh \lambda\xi + \lambda\xi \right] \quad (3)$$

where  $\lambda$  is defined as frame stiffness characteristic parameter  $\lambda = H\sqrt{\frac{\tau}{\omega}}$  (4)

$\gamma$  is defined as stiffness characteristic parameter of outriggers;  $\gamma = H\frac{\rho}{\omega}$  (5)

$\xi$  is relative coordinate.  $H$  is the total height of the structure.  $\xi = \frac{x}{H}$  (6)

In the expressions of characteristic parameters:

$$\omega = \frac{EI_t}{2} \quad (7)$$

$$\rho = \frac{3EI_L}{(1 + \chi_o)2L} (1 + c)^2 + \frac{9(EI_L)^2(1 + c)^2 H}{2\beta EA_c L^4}, \quad \chi_o = 1 + \frac{3\mu EI_L}{GA_L L^2} \quad (8)$$

$$\beta = \frac{e^{\eta H} + e^{-\eta H}}{e^{\eta H} - e^{-\eta H}} \eta H, \quad \eta^2 = \frac{12EI_f}{EA_c hl_f^3} \quad (9)$$

$$\tau = \frac{6EI_f}{(1 + \chi_f)hl_f} (1 + a + b)^2 + \frac{24EI_b}{(1 + \chi_b)(2 + K)^2 hl} + \frac{6EI_c K^2}{(1 + \chi_c)(2 + K)^2 h^2} \quad (10)$$

$$\chi_f = 1 + \frac{12\mu EI_f}{GA_f l_f^2}, \quad \chi_b = 1 + \frac{12\mu EI_b}{GA_b l^2}, \quad \chi_c = 1 + \frac{12\mu EI_c}{GA_c h^2} \quad (10a)$$

where  $E$  is the modulus of elasticity;  $G$  is the shear modulus;  $I_t$  is the section moment of inertia of the core.  $A_L$  and  $I_L$  are the section area and section moment of inertia of horizontal outriggers respectively;  $c$  is the rigid region parameter;  $\mu$  is the nonuniformity parameter of shear stress (for rectangular section,  $\mu=1.2$ );  $\beta$  is

calculative value;  $A_b$  and  $A_c$  are the section areas of perimeter frame beams and columns;  $I_b$  and  $I_c$  are the section moment of inertia of perimeter frame beams and columns;  $h$  is floor height;  $l$  is calculation span of perimeter frame beams;  $K$  is line stiffness ratio of frame beams and columns.  $I_f$  and  $A_f$  are respectively the section moment of inertia and section area of floor beam;  $l_f$  is calculation span of floor beam;  $a$  and  $b$  are the rigid region parameter of floor beams respectively.

The lateral deflection and internal forces for the frame-core structure with strengthened story can be calculated by using formulas (1) to (3). For the structure under inverted triangle distributed load, which are very common in practice, substituting (5) and (8) into formula (1), it can be obtained:

$$y = \frac{qH^4}{\lambda^2 EI_t} \left[ \frac{1 + \frac{\gamma}{2} + \left(\frac{1}{2} - \frac{1}{\lambda^2}\right)(\gamma \cosh \lambda + \lambda \sinh \lambda - \gamma)}{\lambda (\gamma \sinh \lambda + \lambda \cosh \lambda)} (\cosh \lambda \xi - 1) + \left(\frac{1}{2} - \frac{1}{\lambda^2}\right) \left( \xi - \frac{\sinh \lambda \xi}{\lambda} \right) - \frac{\xi^3}{6} \right] \tag{11}$$

For the convenience of analysis, the structural drift parameter can be defined as  $y(\xi) / f_H$  ( $f_H = \frac{11qH^4}{120EI_t}$ )

where  $f_H$  is the displacement at the top of the cantilever bar under inverted triangle distributed load).

Under the above definitions, formula can be obtained as follows:

From Equation (11), the drift parameter of the structure is given by

$$\frac{y(\xi)}{f_H} = \frac{120}{11\lambda^2} \left[ \frac{1 + \frac{\gamma}{2} + \left(\frac{1}{2} - \frac{1}{\lambda^2}\right)(\gamma \cosh \lambda + \lambda \sinh \lambda - \gamma)}{\lambda (\gamma \sinh \lambda + \lambda \cosh \lambda)} (\cosh \lambda \xi - 1) + \left(\frac{1}{2} - \frac{1}{\lambda^2}\right) \left( \xi - \frac{\sinh \lambda \xi}{\lambda} \right) - \frac{\xi^3}{6} \right] \tag{12}$$

In the equation (11), the parameters of the drift is only related to parameters  $\lambda$ ,  $\gamma$  and relative coordinate  $\xi$ , and has no matter with specific structures. Therefore the result obtained from the analysis is of generality.

### 3 Analysis of the Optimum Stiffness of Horizontal Outriggers for Frame-Core Structure with Top Horizontal Outriggers

As mentioned above, the purpose for setting horizontal outriggers in frame-core structure is to reduce the lateral deflection of the structure. The formula (11) (suppose  $\xi=1$ ) can be used to analyze the relationship between parameters  $\lambda$ ,  $\gamma$  and the lateral deflection of structure (the results are shown in Figure 2 and Table 1). From the results of analysis, the efficiency of reducing the lateral deflection by changing the stiffness characteristic parameter of horizontal outriggers can be obtained and the optimum “limited stiffness” of the horizontal outriggers can be obtained.

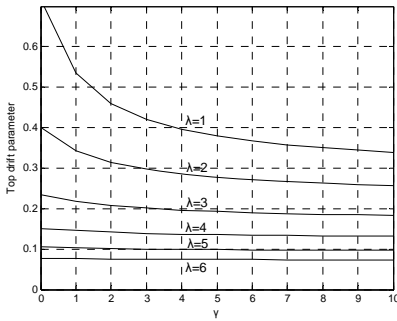


Figure 2. Top drift parameter

Table 1. Value of the top drift parameter

Value of $\gamma$	0	1	2	3	4	5	6
$\lambda=1$ Top drift parameter	0.7208	0.5342	0.4603	0.4206	0.3959	0.3790	0.3667
$\lambda=1$ Reduction of the top drift		25.9%	36.1%	41.6%	45.1%	47.4%	49.1%
$\lambda=2$ Top drift parameter	0.3992	0.3433	0.3148	0.2976	0.2860	0.2777	0.2715
$\lambda=2$ Reduction of the top drift		14.0%	21.1%	25.4%	28.3%	30.4%	32.0%
$\lambda=3$ Top drift parameter	0.2343	0.2177	0.2078	0.2011	0.1964	0.1928	0.1900
$\lambda=3$ Reduction of the top drift		7.1%	11.3%	14.2%	16.2%	17.7%	18.9%

The equations (4)-(10) show that, stiffness characteristic parameter  $\lambda$  is the product of the stiffness of floor beams, beams and columns of the perimeter frame, and the height of the structure. And  $\gamma$  is the product of the ratio the stiffness of outriggers to the stiffness of the core, and the height of the structure. It is also con-

sidered that,  $\lambda$  is the stiffness of floor beams and beams and columns of the perimeter frame, and  $\gamma$  is the stiffness of horizontal outriggers. When  $\gamma = 0$ , the structure is a common frame-core structure without outriggers. It can be known from Figure 2 that the curve of the top drift is nearly horizontal as the value  $\gamma$  is large, in other words, with the increases of  $\gamma$ , the lateral deflection at the top of the structure hardly decrease. From the curve in the figures above, it can be known that the value of  $\gamma$  is related to  $\lambda$ . When  $\lambda$  is small, the value of  $\gamma$  can be set larger; when the value of  $\lambda$  is great, it is unnecessary for large value of  $\gamma$ , because the increasing  $\gamma$  has little effect on the reduction of the lateral deflection of the structure, and at the same time it may induce the increment of vertical stiffness and the internal forces mutation of the structure. The definite conclusions can be obtained from the concrete data of the curve in Figure 2 (the data are shown in Table 1).

According to the "limited stiffness" design concept of horizontal outriggers, the principle to determine the value of the stiffness of horizontal outriggers is: under the condition of the code in the lateral deflection of the structure, the stiffness should be minimum. It is suggested in this paper that, when setting top outriggers, meeting the requirement base on the need top drift reduction and stiffness characteristic parameter of frame, the minimal  $\gamma$  is taken from the data in Table 1.

In the preliminary design phase, to simplify the calculation, the effects of the shear deformation of floor beams, perimeter frame and the rigid region of floor beams can not be considered, then Equation(8) can be rewritten as:

$$\tau = \frac{6 EI_f}{hl_f} + \frac{24 EI_b}{(2 + K)^2 hl} + \frac{6 EI_c K^2}{(2 + K)^2 h^2} \quad (13)$$

After the value of  $\tau$  is estimated using above formula, then  $\lambda$  can be calculated easily. Similarly, the effects of the shear deformation and the stiffness of floor beams, perimeter frame column can not be considered in the preliminary identification the stiffness of the outriggers. Then Equation (6) can be rewritten as:

$$\rho = \frac{3 EI_L (1 + c)^2}{2L} \quad (14)$$

After the value of  $\gamma$  is estimated using the method that shows in Section 2, the flexural rigidity of the outriggers can be calculated using Equations (5) and (16).

## 4 Case Study

In the paper, a typical frame-core reinforced concrete structure is considered. The structure floor plan is shown in Figure 3. The structure has 30 stories with floor height of 3m and  $H=90m$ . The sectional areas of the perimeter frame beams and

columns are 300mm×600mm and 800mm×800mm respectively. The thickness of the concrete core wall is 300mm. The concrete strength of the structure, the reference wind pressure and roughness of the terrain are assumed as C40, 0.7kN/m<sup>2</sup> and grade B respectively. Using Equation (13) and (4), we can obtain  $\tau=2.53\times 10^5$  and  $\omega=1.54\times 10^9$ .

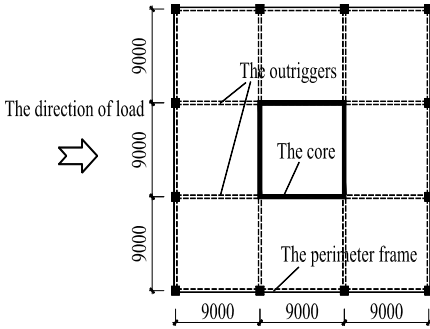


Figure 3. Structure plane

Using finite element software SATWE, according to typical frame - core structure without outriggers calculation, the top drift of the structure is 52.3mm. If we need to reduce top drift about 30% by setting top outriggers, according to Table 1 parameters, preliminary estimate of the value of  $\gamma$  is 1.5. From Equation (5), we can get  $\rho=2.567\times 10^7$ . From Equation (14), the total flexural rigidity of the outriggers can be obtained, i.e.  $EI_L=8.7\times 10^7$ . Because 4 outriggers are set up in x direction, the flexural rigidity of each outrigger is  $2.175\times 10^7$  and corresponding  $I_L=0.669\text{m}^4$ . The cross-section size of the outrigger is set to 0.3m×3m, and  $I_L=0.675\text{m}^4$ , the values are input SETWE program (outriggers are inputted by the body wall), the result of the top drift is 35.9mm. The reduction of the top drift is 31.3% and the result is similar with pre-requirement.

## 5 Conclusions

Strengthened story of the structure contains outriggers and belt component, and generally they are set in the same floor. Settings of belt component increase the stiffness of strengthened story and it can also be considered to increase the stiffness of outriggers (The increase of stiffness by belt component is still relatively smaller compared to the stiffness of outriggers). So the value of  $\gamma$  in formulas mentioned above is greater in fact. So when the outriggers and belt component are both set in the same strengthened story, the values of stiffness of horizontal outriggers need to decrease appropriately according to the stiffness of belt component.

By using lateral deflection calculation formula for frame-core structure with top outriggers, analyses of the optimum stiffness of outriggers for frame-core structure with strengthened story are carried out. The method for determining the optimum stiffness of outriggers, according to the need of reduction of the top drift of the structure, is presented. The result of case study shows this method is creditable. The conclusions in this paper can be used for the engineering design especially for determining the scheme of structure.

## References

- Fang E.H., Qian J.R. and Yie L.P. *Tall Building Structure Design*. Beijing: China Architecture and Building Press, 379-386 [in Chinese].
- Wu J.R. and Li Q.S. (2003). Structural performance of multi-outrigger-brace buildings. *The Structure Design of Tall and Special Buildings*, 12(2):155-176.
- Xu P.F. (2005). *Design of Complex Tall Building Structure*. Beijing: China Architecture & Building Press, 379-386 [in Chinese].
- Zhang S.Y. and Li ZH.X. (2008). Continuum analysis method for frame-core structure with top horizontal outriggers. *Journal of Huazhong University of Science & Technology (Natural Science Edition)*, 36 (9):109-112 [in Chinese].
- Zhang ZH.X., Zhao N. (2007).The impact of mechanical properties of belt component to tall building structure with top horizontal outriggers members. *Journal of Huazhong University of Science & Technology (Urban Science Edition)*, 24(3):5-6 [in Chinese].

# Numerical Analysis of Mechanical Multi-Contacts on the Interfaces in a PEM Fuel Cell Stack

Zhiming Zhang<sup>1</sup>, Christine Renaud<sup>1</sup> and Zhiqiang Feng<sup>1\*</sup>

<sup>1</sup>Laboratoire de Mécanique et d'Énergétique d'Evry, Université d'Evry-Val d'Essonne  
40 rue du Pelvoux, 91020 Evry, France

**Abstract.** The PEM (Proton Exchange Membrane) fuel cell is a multi-layers structure which is constructed by different components in contact. In this work, we propose a 3D parametric numerical modeling which permits to investigate the mechanical effect of contact behavior concerned with the performance of a PEM fuel cell. Numerical results can help to increase the knowledge of fuel cell's performance and to determine the parameters for the structural design of a PEM fuel cell.

**Keywords:** PEM fuel cell, contact, finite element

## 1 Introduction

Faced to the decrease of fossil fuel resources with increasing environmental problem, fuel cell technology is an area of rising interest in the world. In all kinds of fuel cells, PEM fuel cells would be a desirable energy for transportation devices resulted in the interests (Hoogers, 2003). The PEM fuel cell is typically a multi-layers structure (Figure 1). The MEA (Membrane Exchange Assemblage) is inserted into two GDL (Gas Diffusion Layers) coated with catalyst, and which is further sandwiched between two BPP (BiPolar Plate) to form one cell. Multiple cells are stacked together by two clamping end plates (EP) to provide sufficiently high power density and a desirable voltage supply. The clamping bolts provide uniform pressure to avoid the gas and fluid leakage and to ensure normal operation of a PEM fuel cell. This assembly stack leads to two typical mechanical behaviors: multi-contacts (between GDL and MEA, GDL and BPP, BPP and EP) and the distribution of contact pressure between compressed components. Under the clamping loads, the assembly structure leads to power loss because of the contact resistance between components (Mann et al., 2002). The other important pa-

---

\* Corresponding author, e-mail: feng@iup.univ-evry.fr

parameter is the distribution of contact pressure in the fuel cell stack (Kolde and Bahar, 1995). High pressure can increase the conductivity and the power density of a fuel cell. However, as components such as MEA or GDL are relatively brittle and thin, high pressure may leads to damage as observed by Su *et al* (Su et al., 2008) and Vesna *et al* (Stanic and Hoberecht, 2005) (Figure 2).



Figure 1. A PEM fuel cell stack

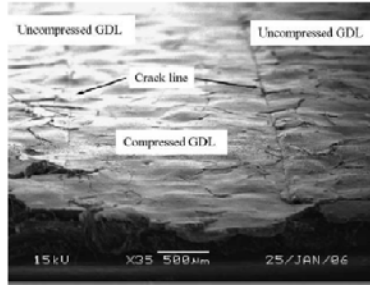


Figure 2. Crack line on GDL (Su et al., 2008)

Several researchers have studied the contact resistance between fuel cell’s components. Mathias *et al.* (Mishra et al., 2005) showed that the contact resistance between GDL and BPP is greater than their bulk resistance. Zhou *et al.* (Zhou et al., 2006) developed a 2D model between GDL and BPP by the finite element method. They studied the contact behavior with a part of GDL and the rib of BPP. Zhang *et al.* (Zhang et al., 2006) developed a more practical 3D numerical model with three types of clamping loads. Lee *et al.* (Lee et al., 2005) created a 3D model with contact elements, but only one cell is considered.

In the present work, we propose a three dimensional numerical modeling of a PEM fuel cell stack with several cells. The analyses are performed by using the finite element method taking into account the multi-contacts on the interfaces between different components of the cells.

## 2 Contact Mechanics

Classically, a contact law is characterized by a geometric condition of non penetration, a static condition of no-adhesion and a mechanical complementary condition. These three conditions are so-called Signorini’s conditions written in terms of the signed contact distance  $x_n$ , and the normal contact pressure  $r_n$ :

$$Signorini(x_n, r_n) \hat{U} \quad x_n \geq 0, r_n \leq 0, x_n r_n = 0 \tag{1}$$

where  $x_n$  denotes the magnitude of the distance between the contact surface and the target surface. A rate independent dry friction law is characterized by a kinematic slip rule. The Coulomb's cone is defined by:

$$K_m = \{r \hat{\mathbf{I}} R^3, \|r\| \mathbf{e} m r_n\} \tag{2}$$

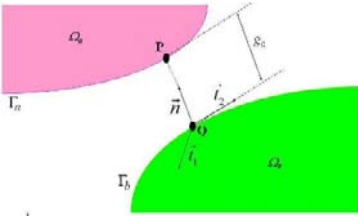


Figure 3. Local contact

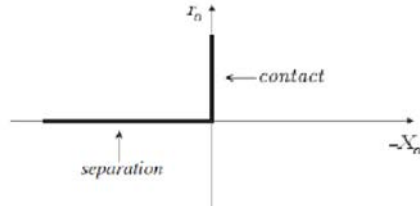


Figure 4. Signorini's conditions

The complete contact law is a complex non smooth dissipative law including three statures: no contact, contact with sticking and contact with sliding as shown in Figure 5.

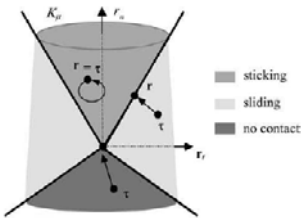


Figure 5. Coulomb's friction law (Renaud and Feng, 2002)

The contact problem can be solved by the penalty method, the boundary element method (Renaud and Feng, 2002), the augmented Lagrangian method (Feng, 1995), etc.

### 3 Computational Model

In this study, a 3D finite element model with three cells has been developed. Due to geometrical repetitive structure of MEA, GDL and BPP in the modeling, we have adopted a parametric modeling. Mechanical properties of components are chosen from (Lee et al., 2005). In this modeling, chemical reaction and fluid behavior are not considered. A mapping mesh is adopted in order to ensure the prop-

er connectivity of elements between contact components. Because of symmetry, only the half model is meshed with 135,438 elements and 138,802 nodes. Boundary conditions must be carefully chosen to prevent free movement and to reflect the real condition case. Because all the plates are fixed by clamping bolts (Figure 1), then the surface of bolt holes are fixed and the clamping forces are directly applied on the end plate as presented in Figure 6 and Figure 7.

Contact elements are inserted between components of fuel cell modeling: MEA and GDL, GDL and BPP, BPP and EP as shown in Figure 7.

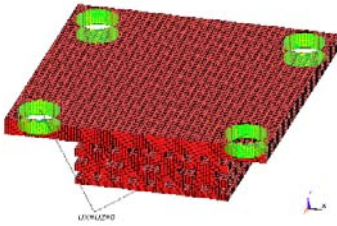


Figure 6. Meshing

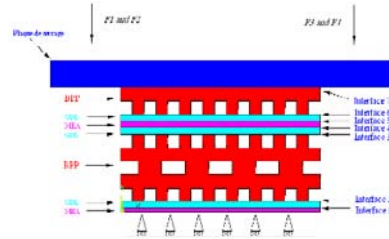


Figure 7. Boundary conditions

## 4 Numerical Results

As we can see from Figure 8, the deformation of MEA and GDL is more important than that of BPP and the contact separation is observed at the extremities between MEA and GDL. But no separation happens between BPP and GDL. Figure 9 shows the contact pressure distribution on the interfaces of MEA and GDL. The zone of zero contact pressure corresponds to the contact separation as shown in Figure 8. Contact pressure distributes on parallel bands because of the interaction of GDL and the ribs of BPP on the interfaces, the numerical results correspond to the experimental results of Lee *et al.* (2005).

The power density of fuel cell will be decreased as the contact separation at the extremities between MEA and GDL.

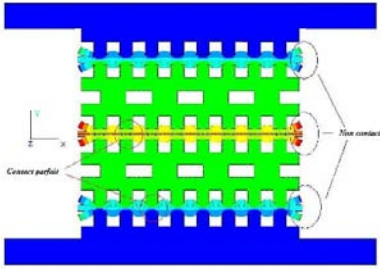


Figure 8. Contact behavior

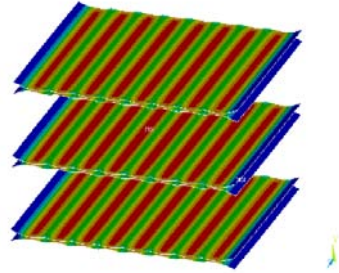


Figure 9. Contact pressure between MEA and GDL

Because the maximum contact pressure is an important parameter to the durability of fuel cell, so its distribution on the interfaces in the stack is shown in Figure 10. We can find that maximum contact pressures on the interfaces are different. The maximum contact pressure on the interfaces of BPP and EP is superior to the corresponding value on the interfaces of BPP and GDL, which is superior to the maximum contact pressure on the interfaces of MEA and GDL. For the maximum contact pressure on the interfaces of BPP and GDL, the first few interfaces at the top and bottom of the fuel cell stack experience the higher pressure level than the other interfaces of BPP and GDL near the center. As shown in Figure 10, the maximum contact pressure on the interface 6 is superior to corresponding value on the interface 3, which is superior to the maximum contact pressure on the interface 2. The maximum contact pressures on the interfaces of MEA and GDL (interface 5, 4, 1) have the same values. The difference of the maximum contact pressure is resulted in the different deformation of the fuel cell's components, further in the heterogeneity of materials.

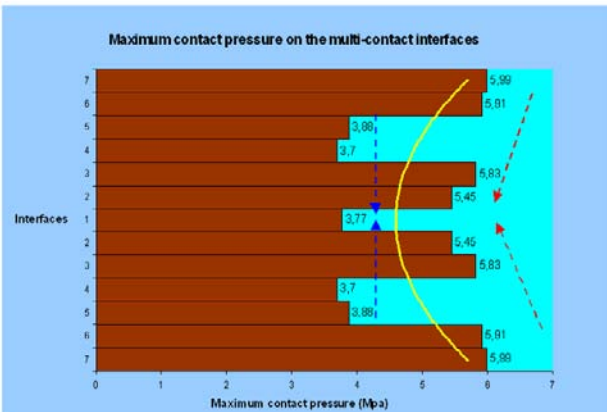


Figure 10. Distribution of maximum contact pressure on the interfaces in the fuel cell stack

## 5 Conclusions

In this paper, we have proposed a numerical modeling of a PEM fuel cell. From numerical simulation, we have found that:

- The contact pressure is zero at the extremities on the interface of MEA and GDL where contact separation occurs. The contact is however perfect between BPP and GDL, BPP and EP in the modeling, no contact separation occurs.
- For all the maximum contact pressures on the interfaces, maximum contact pressure on the interface of BPP and EP is superior to the corresponding value on the interfaces of GDL and BPP, which is superior to the maximum contact pressure on the interfaces of GDL and MEA.
- For the maximum contact pressure on the interfaces of BPP and GDL, the first few interfaces at the top and bottom of the fuel cell stack experience the higher pressure level than the other interfaces of BPP and GDL near to the center. The maximum contact pressures on the interfaces of MEA and GDL have the same values.

Moreover, numerical results will increase knowledge of performance and to the design of PEM fuel cell. We will deepen our work on refining the finite element model in some areas where local contact behavior is important. It would also be interesting to add more cells in the current model to be close to the real case.

## References

- Feng Z.-Q. (1995). 2D or 3D frictional contact algorithms and applications in a large deformation context, *Communications in Numerical Methods in Engineering*, 11: 409-416.
- Hoogers G. (2003). *Fuel cell Technology Handbook*. CRC Press.
- Kolde J. A., Bahar B. (1995). Advanced composite polymer electrolyte fuel cell membranes. *Electrochemical Society Proceedings*, 193:95-23.
- Lee S.-J., Hsu C.-D., Huang C.-H. (2005). Analyses of the fuel cell stack assembly pressure. *Journal of Power Sources*, 145:353-361.
- Mann R. F., Amphlett J. C., Hooper M. A. I. et al (2002). Development and application of a generalized steady-state electrochemical model for a PEM fuel cell. *Journal of Power Sources*, 86:173-180.
- Mishra V., Yang F., Pitchumani R. (2005). Analysis and design of PEM fuel cells. *Journal of Power Sources*, 141:47-64.
- Renaud C., Feng Z.-Q. (2002). BEM and FEM analysis of Signorini contact problems with friction, *Computational Mechanics*, 31: 390-399.
- Stanic V., Hoberecht M. (2005). Mechanism of pinhole formation in membrane electrode assemblies for PEM fuel cells. <http://ntrs.nasa.gov/archive/nasa/casi.ntrs.nasa.gov>
- Su Z. Y., Liu C. T., Chang H. P. et al. (2008). A numerical investigation of the effects of compression force on PEM fuel cell performance. *Journal of Power Sources*, 183:182-192.
- Zhang L. H., Liu Y., Song H. et al. (2006). Estimation of contact resistance in proton exchange membrane fuel cells. *Journal of Power Sources*, 162:1165-1171.
- Zhou P., Wu C. W., Ma G. J. (2006). Contact resistance prediction and structure optimisation of bipolar plates, *Journal of Power Sources*, 159: 1115-1122

# Analysis Model for Concrete Infill Slit-Wall

Xufeng Mi<sup>1\*</sup>, Lin Wang<sup>1</sup> and Guobao Zhou<sup>1</sup>

<sup>1</sup>School of Civil and Architecture Engineering, Jiangsu University of Science and Technology Zhenjiang 212003, P.R. China

**Abstract.** This paper discussed analytic models of frame-slit-wall system suggested by JGJ99-98 and pointed out the necessity of considering shear deformation of web of steel beams when determining the section of equivalent cross bracing or shear plate. The models suggested by JGJ99-98 cannot predict the actual shear forces in steel girders, its bending deformation have not be included either. This paper suggested a wall-column model, the rigidities of various parts in this model are proposed. A very low axial rigidity is assigned to the wall-columns modeling the slit-walls to implement the design philosophy of carrying no vertical loads by slit-wall. Comparison between three models is carried out and it is found that three models predict nearly the same lateral stiffness. But the wall-column model can correctly predict the internal forces and deformations of each member in the model, thus implies an improvement over the cross bracing or shear plate models.

**Keywords:** slit-wall, wall-column frame system model, cross brace model, shear plate model

## 1 Overview

Steel frame-reinforced concrete infill slit-walled system (SF-CSW) is a kind of structural system. Because the silts were set, the lateral stiffness is weakened greatly so as to overcome higher lateral stiffness and bigger earthquake force in cast-in-place shear wall. Walls between silts, whose high-span ratio is 2, are under co-action of press, bending and shear. A lot of cracks appear in the slit-wall under earthquake action (Lian and Zou, 1996a; Lian and Zou, 1996b; Muto, 1986). When the cracks appear in wall, the pressure limited the development of cracks, which was produced by concrete expansion. The disadvantages of integral cast in-situ shear wall were overcome by slit-wall. In the integral cast in-situ shear wall, the cracks fast development, the big cracks width, the cracks concentration, the

---

\* Corresponding author, e-mail: mixf@163.com

low energy dissipation and ductility were the main disadvantages. In China, the design methods were present in JGJ99-98. The slit-walls were converted to equivalent cross bracing or shear plate for analysis.

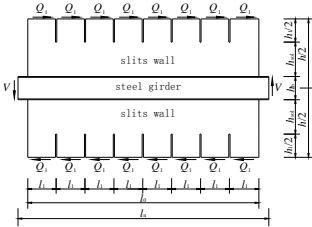


Figure 1. Shear force equilibrium of slit-wall and girder

The links between beam and column were rigid joints in the outer steel frame, and there were the interspaces between the slit-walls and columns. The isolated body was selected in Figure 1. Every wall limb of slit-wall bear shear force  $Q_1$ . Under the action of horizontal forces, the points of contra flexure are in the middle of slit-wall, and moment is zero. When the vertical load is same in the wall limb, the bottom of steel girders will bear shear force  $V$  so as to keep balance in the isolated body. Through the FEA analysis, it can be known that the moments of the steel girders' bottom is so little that it can be ignored. Therefore, we can gotten  $\sum Q_1 h = Qh = V l_n$ , in which  $l_n$  is the clear span of steel girders and  $Q$  is shear force in slit-wall. However, the brace model and the shear plate model were suggested to calculate in JGJ99-98 (Ministry of Construction P. R. China, 1998). From the reaches, it can be known that neither the brace model nor the shear plane one may study the behavior of SF-CSW.

In the paper, the analysis model is proposed from the design philosophy of the slit-wall.

## 2 Analysis of Model

In the sits wall, it can only bear shear force. When the lateral stiffness of steel girders and wall is studied, model should be same as Figure 2. In the models, the up half one of slit-wall, the down half one and the gird are selected to analysis. And the bottom of model is completely constrained.

From Figure 1, it can be known that the link of steel girders and slits wall locates at the steel girders which are on the silts. Therefore, the constrains are shown in Figure 2. From Figure 2, the constrains between the girder and the slit-wall is coupling the lateral freedoms so that the shear forces can transfer from the girder to walls, but vertical forces can not do; meanwhile, the links between the bottoms

of steel girders and the shear wall is coupled and vertical constrains are applied in the bottoms of steel girders. Through analyzing, it can be found that the stress of ends of the steel girders is lager, but the one of other regions of steel girder is very little.

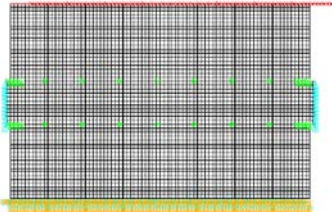


Figure 2. Model of structure

### 3 Analysis Models of Slit-wall

#### 3.1 Lateral Displacements of Slit-wall

For the silts, when the slit-wall bears the shear force  $Q$ , the deformations include the three parts: the bending one  $\Delta_{cs1}$  of the wall between the silts, the shear one  $\Delta_{cs2}$  of the wall between the silts, and the shear one  $\Delta_c$  of the up and down solid wall.

$$\Delta_c = \frac{1.2Q(h_0 - h_1)}{G_c l_0 t} \quad \Delta_{cs1} = \frac{Q(1.25h_1)^3}{12 \sum_{i=1}^n E_c I_{csi}} \quad \Delta_{cs2} = \frac{1.2Qh_1}{\sum_{i=1}^n G_c l'_{it}} \quad (1)$$

When analyzing SF-CSW, the concentrated shear force may appear in the ends of steel girders. However, if the equivalent cross braces model or shear plane one are used, the concentrated shear force can not be gotten. So the webs' shear deformations of steel girders are underestimated, the shear deformation  $\Delta_b$  of steel girders should be considered. From the stress of ends of the steel girders, it can be gotten that the shear force influence depth is  $0.1h_w$ . And the shear stress in the ends of steel girders quickly decreases. When the inerstorey force is  $Q$ , the shear

force in the ends of steel girders is  $Qh/l_n$  , and shear strain in web is  $Qh/l_n G_s t_w h_w$  . Base on the principle of virtual work, it can be gotten:

$$\Delta_b = 2 \int_0^{h_w} \int_0^{0.1h_w} \tau \cdot \bar{\gamma} t_w dx dy = 2 \int_0^{h_w} \int_0^{0.1h_w} \frac{Qh}{l_n h_w t_w} \cdot \frac{h}{G_s l_n h_w t_w} t_w dx dy = \frac{Qh_w}{G_s l_n t_w} \cdot \frac{hh}{5l_n h_w}$$

$$\Delta_b = \frac{Qh^2}{5G_s l_n^2 t_w} \tag{2}$$

The total shear deformation is:

$$\Delta = \Delta_c + \Delta_{cs1} + \Delta_{cs2} + \Delta_b \tag{3}$$

For the models of code ignore the shear deformation of the ends of the steel girders, the models should be modified. The principle is to adopt the cross braces or shear plane to substitute the slit-wall, whose lateral stiffness are same.

### 3.2 Wall Frame Model

The limb of wall can be the column of wall frame. In models, the columns, which are from the slit-wall, include three part of columns and two part of beams.

1. The first part of column *B* is from the wall between the silts. This part of column can bear only the moment and shear force, but not vertical loads. The axial stiffness of this part of column's section should be multiplied by 0.01 in order to implement the design philosophy of carrying no vertical loads by slit-wall. This part is the column *B* which is shown in Figure 3.
2. The solid wall is simplified as the column *C* which is shown in Figure 3. The column section area  $A_g$  and moment of inertia  $I_g$  are:

$$\sum_{i=1}^{n_1} I_{gi} = I_{sol}, I_{gi} = I_{sol} / n_1 \qquad \sum_{i=1}^{n_1} G_c A_{gi} = G_c A_{sol}, A_{gi} = A_{sol} / n_1 \tag{4}$$

3. Steel girder web is simplified as the column *D* which is shown in Figure 3.
4. In Figure 3, *E* represents steel girders.
5. In Figure 3, beam *F* represents the steel girders and solid walls which can bear moment and shear forces together. In the wall-frame model, the flexural rigidi-

ty, axial stiffness and shear stiffness of the beam  $F$  are  $E_c t[(2h_{sol} + h_b)^3 - h_b^3]/12 + E_s I_b$ ,  $E_s A_b + 2E_c t h_{sol}$  and  $E_s A_{bw} + 2E_c t h_{sol}/1.2$ .

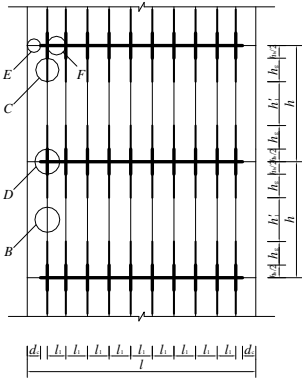


Figure 3. Wall-column frame system model of frame-reinforced concrete infill slit-walled system

### 4 Results of the Wall-Frame Model, Cross Braces Model and Shear Plate model

The 1~20 storied SF-CSW and two loading modes are selected. The loading modes include: 1. the lateral loads are applied on the top of SF-CSW (L1); 2. The lateral loads are applied on the every story (L2). The structure size and material of SF-CSW use the structural standard story of Mitsui & Co. Building (Muto, 1986).

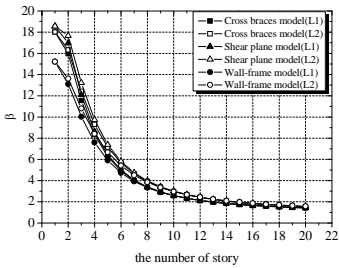


Figure 4. Comparison of three kinds of models' lateral stiffness

The ANSYS finite element analysis program is used to calculate the lateral displacement. In the FEA model, Beam189 is used to simulate the steel frame; Link8 simulates the steel cross brace; Shell28 simulates the shear plane. The results are

shown in Figure 5, where  $\beta$  is the steel frame displacements divided by the SF-CSW model ones.

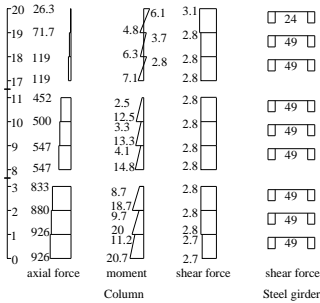


Figure 5. Frame internal forces of wall-column frame system model

From Figure 4, it can be known that the height of the structures increasing, three models predict nearly the same lateral stiffness. When the number of SF-CSW story is less, the results of wall-frame model is smaller than other models. The main reason is that the length of column *B* is  $h'_1 = h_1 + 2 \times 0.25l'_1$  in the wall-frame model. Through the calculation, the length is overestimated so that the lateral stiffness decreases. In the model, the length of column *B* is still  $h'_1 = h_1 + 2 \times 0.25l'_1$ .

Using the wall-frame model, the 20-storied SF-CSW is selected to calculate the internal force. On the top of structure, the lateral force  $Q = 100\text{kN}$  is applied. The results are shown in Figure 5. From Figure 5, wall-frame model can get the shear force in steel girder. And the shear force is only bear by the steel girder.

### 5 Conclusions

This paper discussed analytic models of frame-slit-wall system suggested by JGJ99-98 (Ministry of Construction P. R. China, 1998) and pointed out the necessity of considering shear deformation of web of steel beams when determining the section of equivalent cross bracing or shear plate. The models suggested by JGJ99-98 cannot predict the actual shear forces in steel beams, its bending deformation has not be included either.

A wall-column model is suggested, and the rigidities of various parts in this model are proposed. A very low axial rigidity is assigned to the wall-columns modeling the slit-walls to implement the design philosophy of carrying no vertical loads by slit-wall. Comparison between three models is carried out and it is found that, three models predict nearly the same lateral stiffness. But the wall-column

model can correctly predict the internal forces and deformations of each member in the model, thus implies an improvement over the cross bracing or shear plate models.

## References

- Lian X.F., Zou C.Y. (1996a). A suggestion for the design method of RC shear panels with vertical seams in high-rise steel structure, *Journal of Harbin University of Civil Engineering and Architecture*, 29(2): 13-19 [in Chinese].
- Lian X.F., Zou C.Y. (1996b). Test research on the working behavior of RC shear panels with vertical seams under low-cyclic loading, *Journal of Harbin University of Civil Engineering and Architecture*, 29(1): 31-36 [in Chinese].
- Muto K. (1986). A seismic design analysis of buildings, China Architecture & Building Press, Beijing [in Chinese].
- Ministry of Construction P. R. China, (1998). Technical Specification for Steel Structure of Tall Buildings, China Architecture & Building Press, Beijing [in Chinese].
- Tong X, Schultz A.E., Hajar J.F., Shield C.K. (2001). Seismic behavior of composite steel frame-reinforced concrete infill wall structural system, Report No. ST-01-2, Minneapolis (MN), Department of Civil Engineering, University of Minnesota.

*“This page left intentionally blank.”*

# Test Data Processing Method of Fracture Experiments of Dam Concrete for Inverse Analysis

Zhifang Zhao<sup>1\*</sup>, Lijian Yang<sup>1</sup>, Zhigang Zhao<sup>2</sup> and Minmin Zhu<sup>1</sup>

<sup>1</sup>College of Civil Engineering and Architecture, Zhejiang University of Technology, Hangzhou, Zhejiang 310014, P.R. China

<sup>2</sup>School of Electron and Information, Zhejiang University of Media and Communications, Hangzhou, Zhejiang 310018, P.R. China

**Abstract.** In recent years, researchers identify the complete softening curve of concrete materials by employing inverse analysis method. The inverse analysis method based on fracture experiments of concrete is numerical simulations by using discrete approach of non-linear fracture mechanics. First, a softening curve is assumed and the load–displacement curve obtained by the numerical simulation is compared to the one determined experimentally by fracture experiment of concrete. By updating the assumed softening curve, the numerical results optimally fit the measured ones. When the best fit of the numerical and the experimental results is obtained, the assumed softening curve is viewed as the one for characterization of the material behavior. Load-crack mouth opening displacement curve (P-CMOD curve) is an important measured curve which characterizes fracture property of concrete in fracture experiment. For each group of fracture experiment specimens, there are three companion specimens tested in the group. The emphasis of this paper is as follows: Developed a processing program for the original test data which length is up to 30000~300000 lines for each specimen. The program can filter test data scattered far from the P-CMOD curve and remove the effect of fluctuation in the measurement of fracture experiment. A new test data processing method for fracture experiment of concrete was proposed based on crack propagation process of concrete materials. Thus a representative P-CMOD curve which characterizes the fracture property of the companion specimens for each concrete specimen group is achieved by averaging the above-mentioned test results of three companion specimens. Since the number of data points used in optimal fitting of inverse analysis have an effect on the computer running time observably, the minimum number of data points adequately representing P-CMOD curve is desirable. The minimum of data points were extracted from the averaged data for the companion specimens by an optimization procedure. This paper employed the proposed method to analyze the original test data of different sizes of wedge-splitting

---

\* Corresponding author, e-mail: zhaozhifang7@126.com

specimens made of dam concrete. The representative P-CMOD curves were obtained for companion specimens of different fracture specimen groups. The obtained representative P-CMOD curves were prepared for an inverse analysis to find the softening curves of dam concrete and were employed to investigate the fracture property of dam concrete.

**Keywords:** inverse analysis, dam concrete, fracture experiment, fracture property, test data processing method, optimization

## 1 Introduction

The fictitious crack model (Hillerborg et al., 1976) and crack band model (Bazant and Oh, 1983) are typical approaches to simulate fracture processes of cement-based materials in structures. If fracture processes of civil and hydraulic engineering structures are simulated by employing these models, the experimentally determined fracture parameters, such as tensile strength, fracture energy and softening curve are needed.

In recent years, researchers began to identify the complete softening curve of concrete materials by employing the inverse analysis method. This method is based on fracture experiments and numerical simulations of these experiments by using the discrete approach of non-linear fracture mechanics. First, a softening curve is assumed and the load–displacement curve (such as load-crack mouth opening displacement P-CMOD curve) obtained by the numerical simulation is compared to the one determined experimentally by the fracture experiment. By updating the assumed softening curve, the numerical results are fitted to the measured ones. When the best fit of the numerical and the experimental results is obtained, the assumed softening curve is viewed as the one for characterization of the material behavior (Roelfstra and Wittmann, 1986; Kim et al., 2004).

The dam concrete which is a kind of mass concrete and contain large size aggregate are now widely used for the construction in hydraulic engineering. The difficulties in the determination of fracture properties increased with the use of this material because of the limitations of specimen size, testing machine and testing method. Thus, the available test data of dam concrete is very little (Li et al., 2002). And the corresponding test data processing method is absent. This paper proposed a test data processing method to deal with the test data by wedge-splitting tests conducted on dam concrete specimens. The representative P-CMOD curve is obtained for each group and is prepared for an inverse analysis to identify the softening curve of dam concrete.

## 2 Test Data Preliminary Processing of Wedge-Splitting Specimens of Dam Concrete

The test data of this paper come from the literature (Zhou et al., 2004), including test data of five different specimen sizes wedge-splitting dam concrete specimens. The geometry of specimen is shown in Figure 1 and sizes are shown in Table 1.

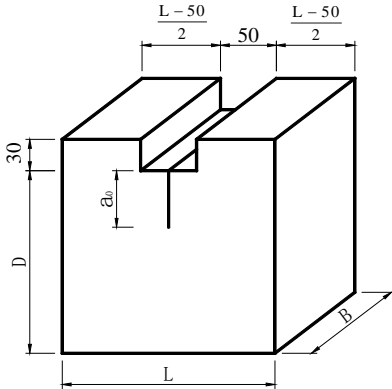


Figure 1. Geometry of wedge-splitting specimen (unit:mm).

Table 1. Sizes of wedge-splitting specimens.

Specimen	Grade of concrete strength	Maximum aggregate size $d_{\max}$ (mm)	Sizes of specimens (mm)			$a_0$	Number of companion specimens	Number of Effective companion specimens
			B	D	L			
WS22	C20	80	250	450	450	225	4	3
WS23	C20	80	250	600	600	300	4	2
WS24	C20	80	250	800	800	400	4	3
WS25	C20	80	250	1000	1000	500	4	3
WS26	C20	80	250	1200	1200	600	4	2

There are 4 companion specimens in each group of wedge-splitting specimens of dam concrete. By wedge-splitting test, the load-crack mouth opening displacement curve (P-CMOD curve) of dam concrete can be measured (Zhou et al., 2004; Zhao, 2004). Because the acquired test data reached up to 30000~300000 lines, selection and simplification of the test data are required.

The preliminary processing of test data consists of the following 3 steps: (1) The P-CMOD curve of one specimen may have large deviation from the other P-CMOD curves of the same group specimens because the scattering of concrete specimens preparation and abnormal phenomena occurring in the test. Such specimens should not be selected. The remaining specimens are called effective companion specimens and listed in Table 1. (2) The acquired test data of which the load P is negative should be eliminated. (3) The test data scattered far from the original P-CMOD curve should be filtered.

The results of a group specimens are shown in Figure 2 by the preliminary processing method of original test data.

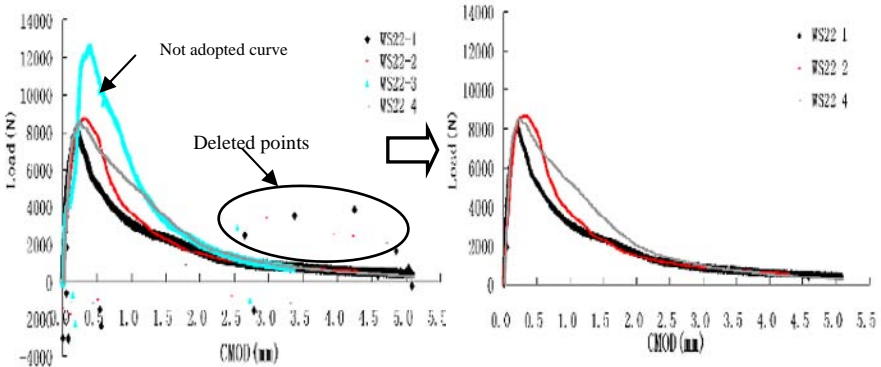
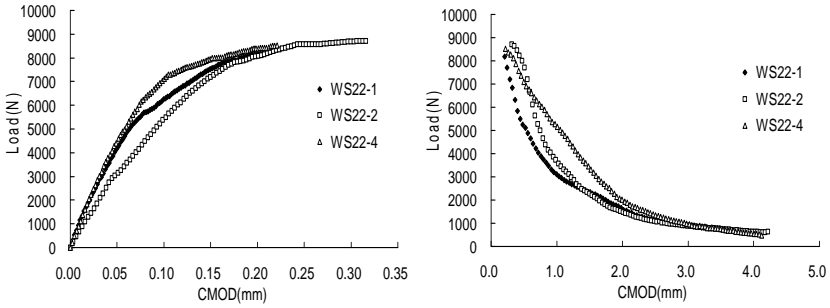


Figure 2. Preliminary processing of original test data.

### 3 Data Processing of Companion Specimens

After the preliminary processing on the two or three companion specimens in each group, further data processing should be conducted. Namely, one point is selected from every twenty points in the P-CMOD curve. Then, an average was taken of five points around a given point, two points above the given point and two points below the given point. By averaging the five adjacent points, the effect of fluctuation in testing the P-CMOD curve can be greatly weakened.

It is necessary to process the P-CMOD curves of two or three companion specimens in each group into a representative P-CMOD curve because there exists dispersion of concrete material and possibility of fluctuation in the measurement. The data processing of companion specimens is illustrated by specimen group WS22 in Figure 3.



(a) Ascending part

(b) Descending part

Figure 3. Data processing of companion specimens in a specimen group

For the processed P-CMOD curves of companion specimens, the peak load point of each specimen was achieved. From the original point to the CMOD at the peak point and from the peak point to the CMOD at the end point, CMOD values were divided into one hundred equally, respectively.

The end point of CMOD for each companion specimen is chosen according to the way that the distance from the peak point to the end point is identical for each companion specimens (in order to obtain the data points under the same status that the fracture process zone is equally far from the peak), for example, 3.9 mm from the CMOD at the peak point for the specimen group WS22. The load values corresponding to the one hundred equal CMOD values each for ascending part and descending part of P-CMOD curve are calculated by interpolation between the data points of each companion specimen. Two hundreds data points were obtained, one hundred for ascending part and the other points for descending part. The processing results of three ascending part and descending part of P-CMOD curves for each of the three companion specimens in group WS22 are shown in Figure 3.

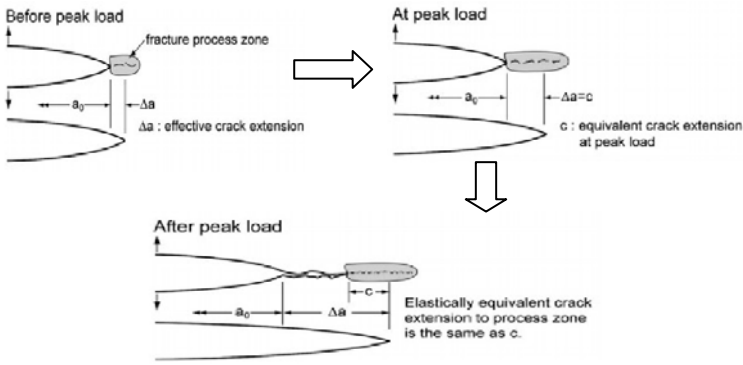


Figure 4. Equivalent crack extension in different crack extension stages.

According to the equivalent elastic crack method (Jenq and Shah 1985; Bazant and Kazemi, 1990), illustrated in Figure 4, the fracture process zone (FPZ) progressively grows with increasing applied load. When the load reaches the peak value, FPZ grow completely and its equivalent extension reaches up to the maximum value  $c$ . After the peak load, FPZ which equivalent extension maintain  $c$  always moves forward along the crack path. The data points of the same crack extension status can be averaged between the three companion specimens in each group. For each companion specimen, the 100th data point which is in the peak load status is under the same status of crack extension. The  $i$ th step of increasing the FPZ corresponds to each of the equally spaced 100 CMODs and their corresponding loads for the ascending part of P-CMOD curve, thus the  $i$ th data point for each specimen can be assumed to be in the same crack extension status. For the descending part it is in a similar way. So two hundred equally spaced CMOD values and the corresponding load values for each companion specimen can be averaged. The processing of ascending part is shown in Figure 5. The whole averaged P-CMOD curve of specimen group WS22 is shown in Figure 6.

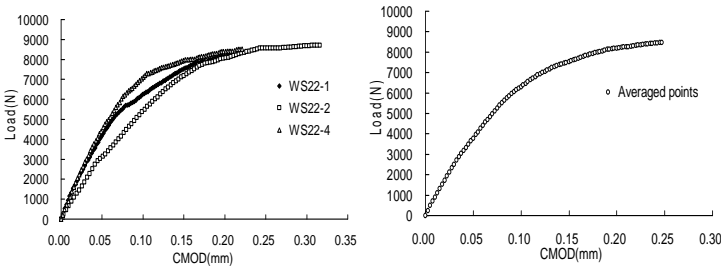


Figure 5. Averaged ascending part of P-CMOD curve.

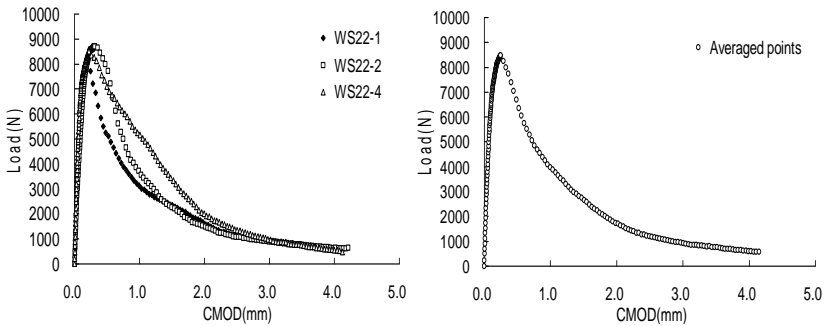


Figure 6. Averaged P-CMOD curve of companion specimens WS22.

### 4 Determination of Measured P-CMOD Curve for Inverse Analysis

The averaged P-CMOD curves intend to be used as input data for inverse analysis to obtain the softening curves of dam concrete. However, the number of data points of the averaged P-CMOD curve has great influence on the computer running time on the optimization issue concerned with the inverse analysis. It is very necessary to find the minimum number of data points sufficiently representing the P-CMOD curve of each specimen group. Taking specimen WS22 as an example, a processing method for extracting representative data points is proposed here.

The minimum data points were extracted from the averaged P-CMOD curve of companion specimens by employing an optimization method. A multi-linear function was adopted to fit the ascending part and descending part of the averaged P-CMOD curve, respectively. For the ascending part, trail calculation results show that multi-linear function consisting of 7 lines can accurately fit the ascending part. By employing more than 7 lines, it hardly improves the accuracy. In fact the fitting is an optimization and used the Marquardt-Levenberg method (Brown, 1970). For the descending part, the processing is in a similar way. The 14 data points were extracted from the peak load point to the end point from the descending part. The extracted P-CMOD curve from the averaged P-CMOD curve for specimen WS22 is shown in Figure 7.

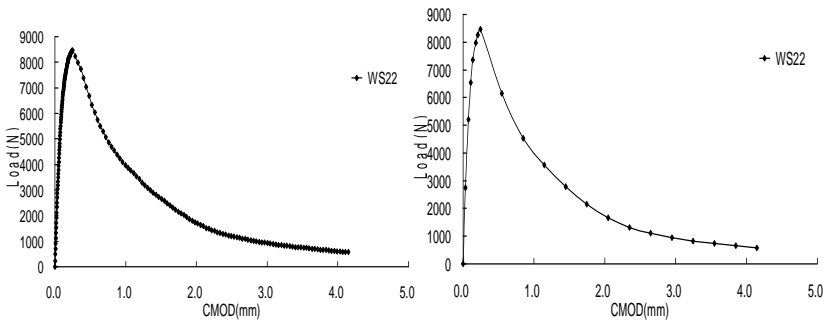


Figure 7. Extracted P-CMOD curve of specimen WS22 for inverse analysis.

The representative P-CMOD curves of five different specimen sizes of wedge-splitting specimens of dam concrete were obtained by the proposed test data processing method can be employed in the inverse analysis for identifying the softening curves of dam concrete and are shown in Figure 8.

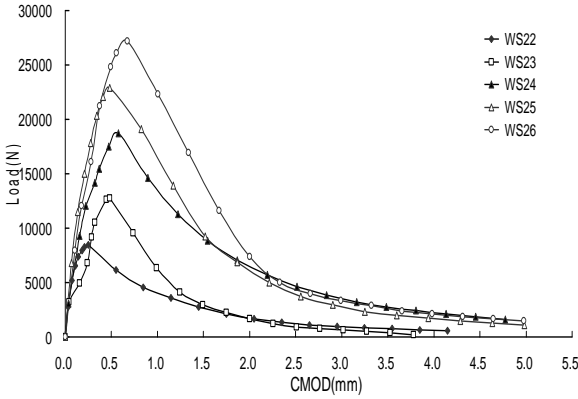


Figure 8. Representative P-CMOD curves of five different specimen sizes of wedge-splitting specimens of dam concrete.

### 5 Conclusions

The original test data of P-CMOD curves of fracture specimens of dam concrete are very large quantity. The original test data for each specimen reaches up to 30000~300000 lines and there are two or three effective companion specimens in each specimen group. The representative P-CMOD curve which can characterize the fracture property of each specimen group was achieved by filtering, averaging and extraction with the optimization method. The original P-CMOD curve of five different specimen sizes wedge-splitting specimens of dam concrete were processed by the proposed test data processing method. The obtained representative P-CMOD curves can be employed in the inverse analysis for identifying the softening curves of dam concrete and to investigate the fracture property of dam concrete.

### Acknowledgments

This work was supported by a grant from Zhejiang Provincial Natural Science Foundation of China (Grant No. Y106486) and National Natural Science Foundation of China (Grant No. 50409005). They are gratefully appreciated.

## References

- Bazant Z.P. and Kazemi M.T. (1990). Determination of fracture energy, process zone length and brittleness number from size effect with application to rock and concrete, *International Journal of Fracture*, 4, 111–131.
- Bazant Z.P. and Oh B.H. (1983). Crack band theory for fracture of concrete. *Materials and Structures*, 16, 155–177.
- Brown K.M. (1970). Derivative-free analogues of the Levenberg, Marquardt and Gauss algorithms for non-linear least square approximations, IBM, Philadelphia Scientific Center Technical Report, No. 320-2994.
- Hillerborg A., Modeer M. and Petersson P.E. (1976). Analysis of crack formation and crack growth in concrete by means of fracture mechanics and finite elements. *Cement and Concrete Research*, 6(6), 773–782.
- Jenq Y.S. and Shah S.P. (1985). A two parameter fracture model for concrete. *Journal of Engineering Mechanics*, 111(4), 1227–1241.
- Kim J.K., Lee Y. and Yi S.T. (2004). Fracture characteristics of concrete at early ages. *Cement and Concrete Research*, 34, 507–519.
- Li Q.B., Duan Y.I. and Wang G.I. (2002). Behavior of large concrete specimen in uniaxial tension. *Magazine of Concrete Research*, 54(5), 385–391.
- Roelfstra P.E. and Wittmann F.H. (1986). Numerical method to link strain softening with failure of concrete. In: F.H. Wittmann (Ed.), *Fracture Toughness and Fracture Energy of Concrete*, Elsevier, Amsterdam, pp. 163–175.
- Zhao Z.F. (2004). Research on fracture behaviors of dam concrete based on cohesive force of cracks. Postdoctoral Research Report of Tsinghua University and China Gezhouba Group Co. [in Chinese].
- Zhou H.G., Li Q.B. and Zhao Z.F. (2004). Research on fracture simulation of mass concrete cracks. Cooperative Research Report of China Gezhouba (Group) Corporation, Tsinghua University and Yantai University [in Chinese].

*“This page left intentionally blank.”*

# Surface Reconstruction of the “False” Tools to Compensate for the Springback in Sheet Forming Process

Yuming Li<sup>1\*</sup>, Fabien Bogard<sup>1</sup>, Boussad Abbes<sup>1</sup> and Yingqiao Guo<sup>1</sup>

<sup>1</sup>Groupe de Recherche en Sciences pour l'Ingénieur (EA4301), Laboratoire de Modélisation Numérique, Université de Reims Champagne Ardenne, Moulin de la House, BP1039, 51687 Reims Cedex 2, France

**Abstract.** In sheet forming process the springback after the tool withdraw often causes a deformed geometry. In order to obtain the desired geometry, the springback effect should be compensated by the modified tools, called “false” tools in this study. In the numerical simulation, the forming process simulation gives a FE part mesh which fits well the tools and then the springback simulation gives a “deformed mesh” which has the same nodes and element connectivity as the part mesh. A displacement adjustment of the nodes on the part mesh in the opposite direction of the springback deformation leads to a “false mesh”. This mesh defines the geometry of the “false” tools which will be used in the next forming and springback simulations until a part with desired dimensions is obtained. In this paper, we propose a technique of surface reconstruction in order to facilitate the parametric shape optimization and tool manufacturing. In our technique of surface reconstruction, we discretize the tools' surfaces one by one by a triangle mesh and move these nodes (sample points) onto the “false mesh” in keeping their local surface coordinates, then we project them on to a local quadratic surface, finally we reconstruct Nurbs surfaces using the moved nodes on the “false mesh”. The main idea is to take a surface of the initial design tools or a newly created Nurbs as the reference surface and move its control points in order to obtain a new surface (surface of “false” tool) that is very close to the “false mesh”. The surfaces of the “false” tools are created one by one by minimizing the gaps between the new surfaces and the moved sample points on the “false” mesh in keeping the sample points' normal on the border of two surfaces. The Nurbs surface creation is fulfilled on the “Open CASCADE” platform and the numerical simulations are carried out in ABAQUS.

**Keywords:** sheet forming, springback, “false” tools, surface reconstruction, Nurbs

---

\* Corresponding author, e-mail: yuming.li@univ-reims.fr

## 1 Introduction

The springback often leads to a deformed geometry of the part and so assembly difficulties. Therefore, it is necessary to create the modified tools (called “false” tools in this paper) that are different from the desired shape to compensate for the springback effect.

Some researchers have studied the tool compensation for springback. Stander et al. (2002) proposed to use the parameterized geometry and optimise the parameters to get the modified tools for the springback compensation. Moshefegh (2002) and Jansson (2002) used the parameterization of the Iges tool surfaces for the tools surfaces’ modification. Meanwhile, the parameterization seemed very difficult to realize for the complex parts. Jernberg (2003) proposed a heuristic iterative method to modify the tool geometry based on the difference between the sheet after the springback and the desired shape. The tool geometry described with discrete finite elements is modified by moving its nodes in the opposite direction of the springback. This method completely abandoned the parameterization. Similarly, Gan et al. (Gan and Wagoner, 2004a; Gan et al., 2004b) presented the displacement adjustment (DA) method in which the nodes defining the tools’ surfaces (2D) were moved in the opposite direction of the springback with the same distance. Weiher et al. (2004) made some promotions to the DA method. They proposed the smooth displacement adjustment (SDA) method in 3D applications. The main idea is to approximate the discrete tool by an analytical function. In the same literature, still based on the DA method, they presented the surface controlled overbending (SCO) method with which the shape modifications of the tools were defined in such a way that they can be applied to CAD geometries as well, and the Bézier and B-spline surfaces were chosen as approximation surfaces. An inconvenience of this method is that the gap between two adjacent surfaces may take place and the C1 continuity could not be guaranteed. Also based on the DA method, Păunoiu et al. (2007) proposed a compensation method with the reconfigurable multipoint forming (RMF) tools. In this method the contact points between the pins and the part are found to configure the tool. Cimolin et al. (2008) introduced a linear combination of the shape functions on the die weighted by some coefficients to obtain the deformed die. An optimization procedure was used to realize the die compensation. Dan et al. (2006) proposed a reconstruction of the “false” tool by using B-spline interpolation with a serial of regular measured fitting points and Cai et al. (2006) proposed the utilization of Nurbs surfaces in their digitized tools. The B-spline or Nurbs attempts are suitable for industrial applications because nowadays the tool’s CAD geometry is almost created by B-spline or Nurbs surfaces.

In this study, our aim is to build an industrial tool that can automatically reconstruct the surfaces of the “false” tools to compensate for the springback effect. A global iterative procedure is adopted. The forming-springback simulations and the tool geometry modifications are iterated until the desired part shape is obtained.

Both the sheet forming and the springback simulations are realized by using ABAQUS. The free open libraries of “Open CASCADE” are used to read the Nurbs in Iges files, to convert the non-Nurbs in Nurbs, and to carry out calculations on Nurbs. In the tool geometry modification step, the tools’ original surfaces (Nurbs) are taken as the reference surfaces, and each tool surface is discretized into a triangle mesh by using an in-house mesher. The nodes of the tool mesh are taken as the sample points which follow the displacement adjustment for the springback correction. Then we use an optimization procedure to move the control points of the reference surface in order to minimize the gaps between the moved surface and sample points. Furthermore, we use the topology of the original surfaces and build surfaces one by one in keeping the normal at the common nodes shared by two adjacent surfaces. The built surfaces of “false” tools can be regarded as the surfaces of “deformed” tools but still keeping the data structure of the original tools’ surfaces.

## 2 Methodology and Key Techniques

### 2.1 Methodology

The global iterative procedure consists of the forming simulation, springback calculation by Abaqus and the tool geometry modification. Here we will present the reconstruction of the surfaces for the tool geometry modification.

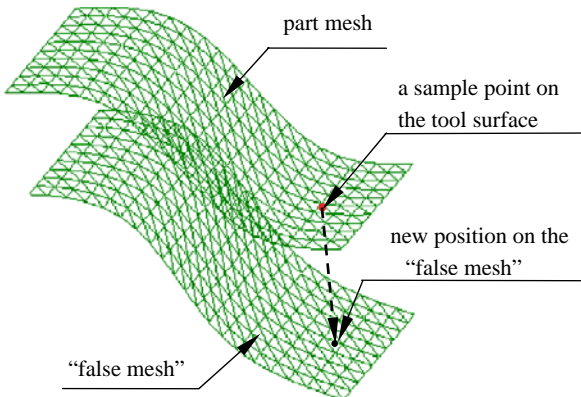


Figure 1. Determination of new position of a node on the “false mesh”

The forming simulation gives the part mesh that fits well the tools surfaces, then the springback simulation gives the deformed part, the “false mesh” is ob-

tained by moving the part’s nodes in the opposite directions of springback (Figure 1). Thus the “false mesh” and the part mesh have the same node number and the same connectivity. To well separate the original tool surfaces and reconstruct the “false tool” surfaces one by one, we discretize each tool surface with a triangle mesh and take the mesh nodes as sample points. As the sample points on each surface of the tools move with the part mesh to reach onto the “false mesh”, we can build the corresponding Nurbs surface of the “false” tools by minimizing the gaps between the surface and these moved points.

The basic idea of the geometry modification is to take a tool surface as the reference surface and then move its control points in order that this surface approaches well the nodes of the “false mesh” by an optimization method. This optimization procedure allows to deform and move each reference surface in order to well fit the false mesh. In practice, if the displacements of the reference surface’s control points are very long compared to the surface’s dimension, the optimisation procedure may fail. In this case, a B-spline surface that is close to the “false mesh” has to be built to guarantee the optimization convergence.

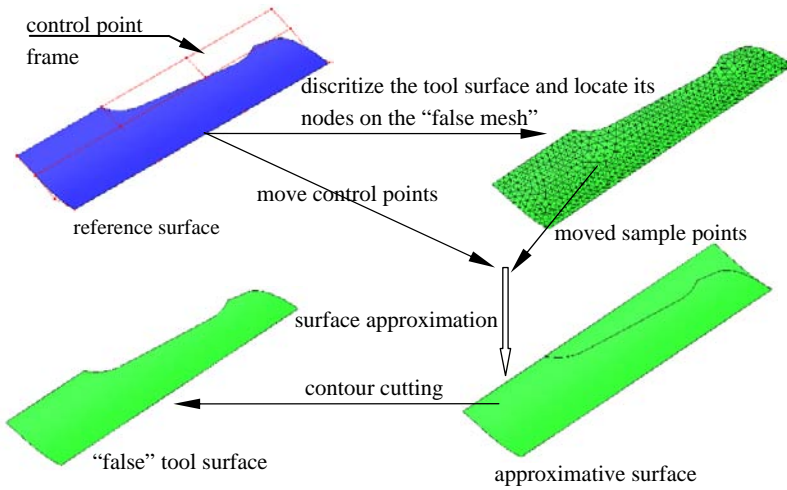


Figure 2. Schema of the reconstruction of a “false” tool surface

We propose to build the surfaces of “false” tools in 5 steps (Figure 2):

1. To mesh the tools’ surfaces one by one to obtain a tool mesh scrupulously respecting the surface borders. Two adjacent surfaces should share the same nodes on their common border. This tool mesh and the part mesh after forming fit surface’s tools perfectly. The nodes of the tool mesh are taken as the sample points which represent the tool surface.

2. To locate each sample point in the part mesh: that implies to know the element containing this point and the local surface coordinates of the point in this element.
3. To determine the new position of the sample point in the “false mesh”: in the element having the same number as the element located in the part mesh, one calculates the Cartesian coordinates by using the same local surface coordinates obtained in step 2). And then a local approximate quadratic surface near by the new position of the sample points is built and each newly obtained point is projected onto this surface to determine the coordinates of the sample point on the surface of the “false tool”.
4. Surface approximation: to move the control points of each reference surface in order that the surface well approaches the moved sample points by optimization (section 2.4). We minimize the sum of distance squares between these moved points and the corresponding points having the same parametric coordinates  $u$  and  $v$  ( $x$  and  $y$  for example) on the new approximate surface.
5. Contour cutting. This step becomes possible when the reference surface is a cut surface. This function allows keeping the surface topology and changing the contour.

## ***2.2 Description and Construction of a Nurbs Surface in “Open CASCADE”***

The free libraries of “Open CASCADE” that is a powerful platform of developments for the applications of 3D modeling are used in our development. A Nurbs surface is defined by the following parameters:

a control points matrix of  $m \times n$  dimension; a weights matrix of  $m \times n$  dimension; knots according to the directions  $u$  and  $v$ ; knots multiplicities according to  $u$  and  $v$  directions; interpolations degrees for  $u$  and  $v$ ; periodicities according to  $u$  and  $v$  directions.

With the above description, “Open CASCADE” disposes of the function to create directly a Nurbs surface, and to convert a non Nurbs surface in Nurbs surface. The B-spline surface is considered as a Nurbs surface with identical weights.

## ***2.3 Point Location and New Coordinates Determination of the Sample points***

In the tool geometry modification procedure, one important problem is the point location technique. That is, in which element of the part mesh is located the sample points of the tool’s surface. We propose to locate these points in two steps:

1. Find the node of the part mesh that is the nearest one to the query sample point.
2. In the elements connecting to the nearest node, locate the point and calculate the surface coordinates if the query point is in one of these elements; otherwise the sample point is out of the range of the part mesh and is abandoned.

The nearest point query method (Franklin, 2006) is used to find the nearest node of the part mesh in our study. When the sample point is located, the coordinates on the “false mesh” are interpolated using the element’s nodes’ coordinates and the local surface coordinates. The coordinates on the surface of the “false” tools will be determined. A local quadratic surface is used to obtain the coordinates. The node that has the same number of the tool mesh’s node which is the nearest one to the sample point is taken as the origin of local coordinates system, and the Max normal (Max, 1999) direction determined by the neighbor nodes is the  $z$  direction. The local plan  $xoy$  is perpendicular to the normal.

The local quadratic surface is supposed to be:

$$z = ax^2 + bxy + cy^2 \quad (1)$$

In our study the local coordinates  $(x,y)$  are interpolated in the element where the sample point is located and then  $z$  is calculated by using equation (1).

## 2.4 Surface Approximation by the Least Square Method

In the literature (Fisher et al., 2004), a surface approximation method is proposed: a matrix of points  $m \times n$ , is written  $D_{kl} (1 \leq k \leq m, 1 \leq l \leq n)$ . With the right degrees according to  $u$  and  $v$  direction, one tries to find a Nurbs surface  $S(u, v)$  that is able to approximate the points  $D_{kl}$  by the least squares. More precisely, one must find the control points of the Nurbs surface  $P_{ij}$  chosen by the user to minimize the function:

$$f(P_{ij}) = \sum_{k=1}^m \sum_{l=1}^n |S(u_k, v_l) - D_{kl}|^2 \quad (2)$$

The control points’ coordinates are the conception variables.

In fact, in our study, the points by which the approximate surface must pass are given by the point location procedure. In order to keep the tangency on the samples points between two adjacent surfaces, the normal of these sample points can be taken into consideration. The objective function is modified as following:

$$f(P_1, P_2, \dots, P_n) = \sum_{i=1}^{nbPm} |S_i(u, v) - D_i(u, v)|^2 + \sum_{j=1}^{nB} |C_j(u, v) - N_j(u, v)|^2 \quad (3)$$

where  $p_1, p_2, \dots, p_n$  are the controls points, their initial values are the control points of the reference surface;  $nbPnt$  is the number of points by which the approximate surface must pass.  $S(u, v)$  is the Nurbs surface that is initially the reference Nurbs surface taken from the Iges file or B-spline surface created by the user.  $D_i(u, v)$  are the located points on the surface of the “false” tools. These points and the corresponding points on the approximate surface have the same parametric coordinates  $u$  and  $v$ , for example,  $x$  and  $y$  can be taken as  $u$  and  $v$ .  $nB$  is the sample points number on shared by two adjacent surfaces,  $C(u, v)$  is the normal that is given by  $S(u, v)$ ,  $N_j(u, v)$  is the Max normal of the sample points shared by two adjacent surfaces predetermined.

## 2.5 Contour Cutting

For an industrial part, there are often some Nurbs surfaces that are cut in the CAD design. Therefore, the control points may not be on the border of the surface. When the control points are moved in the surface approximation mentioned above, the movement of the points on the contour has to be determined. Usually, a contour is composed of several B-spline curves. Based on the located sample points on these curves, we can build the corresponding B-spline curves on the “false” tool and then we use the function of contour replacement offered by Open CASCAD to get a cut Nurbs surface.

## 3 Numerical Validation

Springback is the main concern in U-shaped part forming, which would adversely affect desired part geometries. The presented method is applied to the computational model shown in Figure 3. The geometry and material parameters of the model are: sheet thickness  $h_0 = 1mm$ , punch's and die's width  $B = 30mm$ , drawing depth  $H = 45mm$ , Young's modulus  $E = 206 GPa$ , Poisson coefficient  $\nu = 0.3$ , uniaxial tensile curve  $\bar{\sigma} = 565.2 (\bar{\epsilon}_p + 0.007117)^{0.2589} MPa$ , the interval friction coefficient  $\mu = 0.144$  and the blank holder force  $F = 17 kN$ . Three dimensional triangular shell elements and elasto-plastic material model are used. The whole FEM simulation process is divided into two steps: forming and springback. The initial sheet is meshed using 3000 shell elements. A half FEM model is built because of the symmetry. The computation is accomplished by Abaqus/Explicit 6.7 for the forming step and Abaqus/Standard 6.7 for the springback step.

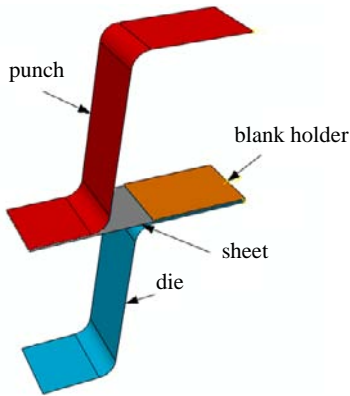


Figure 3. Geometry definition of U-shaped forming problem

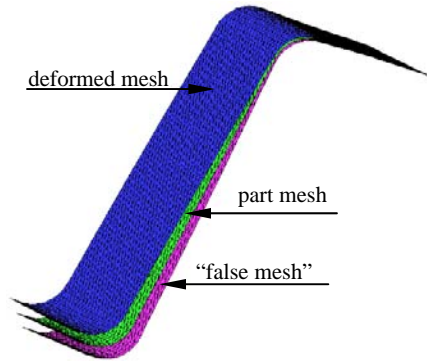


Figure 4. Deformed shapes after forming, springback steps and the displacement adjustment

In figure 4, we have presented the part mesh at the end of the forming step without the springback effect, the deformed mesh at the end of the springback step, and the “false mesh”.

After the global optimisation using the algorithm presented in this paper, we obtain the “false” punch presented in Figure 5 which allows obtaining the desired U-shape.



Figure 5. Optimal “false” punch.

## 4 Conclusions and Discussions

In the stamping of thin sheets, the “false” tools are created to compensate the springback effect in order to obtain a part with good dimensions. A method to reconstruct the surfaces of the “false” tools one by one from the moved sample

points in minimising the distances between the moved points and the approximate surface in keeping the normal of the border points has been proposed on the “Open CASCADE” platform. An application showed the simplicity and the feasibility of the methodology.

This method can be directly used in the bending process but limited in deep-drawing. In fact, in the deep-drawing process, the wall of the tools must not have the vertical waves that will block the deep drawing. Even if during the global iteration process, special techniques can be applied to avoid this case, a “false” tool that can compensate 100% for the springback effect doesn’t exist. Future work will be oriented to predict the feasibility of the springback compensation.

## References

- Cai Z.Y., Li M.Z. and Chen X.D. (2006). Digitized die forming system for sheet metal and springback minimizing technique. *Int. J. Adv. Manuf. Technol.* 28(11–12):1089–1096.
- Cimolin F., Vadori R. and Canuto C. (2008). Springback compensation in deep drawing applications – A new methodology for automatic die compensation through a suitable optimization *Meccanica* 43:101–113.
- Dan J. and Lancheng W. (2006). Direct generation of die surfaces from measured data points based on springback compensation. *Int. J. Adv. Manuf. Technol.* 31(5–6):574–579.
- Fisher J., Lowther J., et al. (2004). Curve and Surface Interpolation and Approximation: Knowledge Unit and Software Tool. ITiCSE’04 June 28–30, 2004, Leeds, UK.
- Franklin W.R. (2006). Nearest point query on 184,088,599 points in E3 with a uniform grid, <http://www.ecse.rpi.edu/Homepages/wrf/Research/nearpt3/nearpt3.pdf>
- Gan W. and Wagoner R.H. (2004). Die design method for sheet springback, *Int. J. Mech. Sci.* 46: 1097–1113.
- Gan W. et al. (2004). Practical design methods using FE modeling applied to sheet parts and dies, *J. Mater. Process Technol.* 126:360–367.
- Jansson T. (2002). Optimization of Sheet Metal Forming Processes, LIU-TEK-LIC-2002:59, Linköping University, Linköping 2002.
- Jernberg A. (2003). A method for modifying the forming tool geometry in order to compensate for springback effects. 4th European LS-DYNA Users Conference. 22nd–23rd of May 2003 in Ulm, Germany Metal Forming III.
- Max N. (1999). Weights for computing vertex normals from facet normals. *J. Graph. Tools* 4(2):1–6.
- Moshefegh R. (2002). Hybrid prototyping in sheet metal forming application, Nordic LS-DYNA Users Conference, Gothenburg 2002.
- Pănuoiu V., Maier C. et al. (2007). Virtual compensation of springback in sheet metal deformation using reconfigurable multipoint die. The Annals “Dunarea de Jos” University of Galati Fascicle V, *Technologies in Machine Building*, 1221–4566 2007.
- Stander N., Burger M. et al. (2002). An optimization procedure for springback compensation using LS-OPT, 7th International LS-DYNA User Conference, Detroit 2002.
- Weither J. et al. (2004). Controlling springback with compensation strategies, in: *NUMIFORM 2004 Proceedings*, Columbus, 2004, pp. 1011–1015.

*“This page left intentionally blank.”*

# Grey-Correlation Analysis of Factors Influencing Xiamen Xiang'an Subsea Tunnel Surrounding Rock Displacement

Haiming Chen<sup>1,2\*</sup>, Xiong Chen<sup>3</sup> and Jun Yu<sup>1,2</sup>

<sup>1</sup>Department of Geotechnical Engineering, Tongji University, Shanghai 200092, P.R. China

<sup>2</sup>Key Laboratory of Geotechnical and Underground Engineering of Ministry of Education, Tongji University, Shanghai 200092, P.R. China

<sup>3</sup>Shanghai Investigation, Design & Research Institute, Shanghai 200434, P.R. China

**Abstract.** Xiamen Xiang'an Subsea Tunnel is the first subsea tunnel in Chinese mainland which is independently designed by the domestic experts. The design service life is 100 years. Drilling and blasting method is employed for excavation. One of the most difficulties during the process of construction is how to cross the deep weathering slots successfully and safely. In this paper BEM software BMP 2000 was used to simulate the surrounding rock displacement of F1 deep weathering slot, and uniform design and grey-correlation analysis method was applied to analyze the correlation between surrounding rock displacement and the influencing factors. The results show that lateral pressure coefficient is the most sensitive factor to horizontal convergence of surrounding rock, followed by the tensile strength of surrounding rock; but to the vault crown settlement of surrounding rock, Poisson's ratio is the most sensitive factor, followed by the internal friction angle. The research achievement has been using in the design and construction of Xiang'an Subsea Tunnel, and good results have been achieved.

**Keywords:** subsea tunnel, grey-correlation analysis, uniform design, sensitivity analysis, surrounding rock displacement, deep weathering slot

## 1 Introduction

Xiamen Xiang'an subsea tunnel is situated in the east sea area of Xiamen, is 8.695 km long, of which the sea area section is 4.2 km long. The tunnel is 13.5 m high and 5.0 m wide. The maximum burial depth of the tunnel is about 70m under sea level. The design speed is 80 km/h. Xiang'an tunnel is the first subsea tunnel in

---

\* Corresponding author, e-mail: chm818@163.com

Chinese mainland which is independently designed by the domestic experts (Jun Sun, 2006). The design service life is 100 years.

Drilling and blasting method is employed for excavation. One of the most difficulties during the process of construction is how to cross the deep weathering slots successfully and safely. In order to analyze the correlation between surrounding rock displacement and the influencing factors, the authors have carried on numerical simulation to the surrounding rock displacement of F1 deep weathering slot by BEM software (BMP 2000). Uniform design and grey-correlation analysis method were applied to carry on sensitivity analysis of the factors.

## **2 Introduction of Grey-correlation Analysis and Uniform Design**

### ***2.1 The Basic Principle of Grey-Correlation***

Gray-correlation analysis method is a factor analysis method to study the correlation between things and factors, proposed by Julong Deng in 1985 (Julong Deng, 1985). The factors are expressed as data (reference sequence  $x_0$  and comparison sequence  $x_i, i=1,2,\dots,n$ ); the correlation is analyzed by comparing the geometric curves of the data. The closer the curves and their development trend are, the bigger the corresponding sequences' correlation degrees are, otherwise the smaller. If there are many sequences and each corresponds to several times, there will be many correlation coefficients, thus the information will be too scattered and not easy to compare. So the correlation coefficient of different times should be concentrated into a value, averaging is one of the information concentration processing methods. The average value is correlation degree. The correlation degree is big which shows that the correlation between the comparison sequence and the reference sequence is big.

### ***2.2 Computation Method of Grey-correlation***

To carry on correlation analysis, we must first specify the reference sequence and comparison sequences, then compute the correlation degree of them (Dong, 2005). There are the following three steps mainly:

1. Sequences being dimensionless

If the sequences' dimension is different, they will be made being dimensionless by initialization method or method of mean value. Initialization method is that all data are divided by the first one to get new sequences; mean value method is that all

sequences are divided by the mean value to obtain new sequences. Here initialization method was used.

## 2. Determining correlation coefficients

Reference sequence is expressed as  $x_0$ , which consist of values of different times. The value of No.1 time is expressed as  $x_0(1)$ , one of No.2 time is  $x_0(2)$ , and so on. So reference sequence  $x_0$  can be expressed as  $x_0=(x_0(1), x_0(2)\dots x_0(n))$ . Correspondingly, the comparative numbers can be expressed as:  $x_i=(x_i(1), x_i(2)\dots x_i(n))$ .

Correlation coefficients  $\xi_i(k)$  are used to express the differences between reference sequence  $x_0$  and comparison sequences ( $x_1, x_2\dots x_n$ ) at all times. The expression is as follows:

$$\xi_i(k) = \frac{\min_i \min_k |x_0(k) - x_i(k)| + \zeta \max_i \max_k |x_0(k) - x_i(k)|}{|x_0(k) - x_i(k)| + \zeta \max_i \max_k |x_0(k) - x_i(k)|} \quad (1)$$

In the above equation,  $\zeta$  is resolution coefficient,  $\zeta \in (0,1)$ , usually taken as 0.5.

## 3. Determining correlation degree

Correlation degrees  $r_i$  between comparison sequences  $x_i$  and reference sequence  $x_0$  can be obtained by the following equation:

$$r_i = \frac{1}{N} \sum_{k=1}^N \xi_i(k) \quad (2)$$

## 2.3 Brief Introduction of Uniform Design

Uniform Design method is a new concept proposed by Kaitai Fang and Yuan Wang in the late-1970s (Fang and Ma, 2001), which can make the experiment have homodisperse with only a few experiment numbers and is a useful complement to experimental design. After nearly three decades of development, the theoretical system of uniform design has become increasingly sophisticated, which provides a set of design and analysis methods suitable for multi-level and multi-factor experiments (Chen et al., 2008).

The authors chose uniform design method to arrange the computation combinations to research on the displacement states of the surround rock in different conditions, which can guarantee that the computation combinations have homodisperse and lower deviations and that the research has scientific nature and high accuracy.

### 3 Grey-correlation Analysis of the Influencing Factors

Uniform design table  $U_{12}^*(12^{10})$  and its use-table were used to arrange the computation combinations. BEM software (BMP 2000) was used to carry on computation analysis of Xiamen Xiang'an Subsea Tunnel surrounding rock displacement. Then the results of computation were analyzed with above grey-correlation method.

#### 3.1 Numerical Analysis

BMP2000 is a kind of boundary element software compiled by Shihui Li, whose name is cave surrounding rock deformation and failure analysis program. Here the surrounding rock was regarded as elastic medium, and uniform continuous linear elastic model was used. The yield criterion is Mohr-Coulomb criterion. The computation model and results are shown as Figure 1.

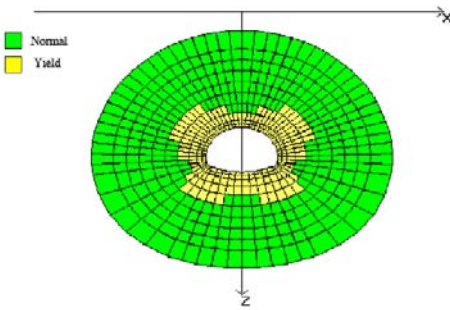


Figure 1. The surrounding rock displacement and failure figure

The computation parameters are shown in Table 1. Here the main influencing factors of surrounding rock displacement are considered as the seven factors:  $\lambda$ ,  $c$ ,  $\varphi$ ,  $\mu$ ,  $E$ ,  $\sigma_c$ , and  $\sigma_t$ .  $\lambda$  is lateral pressure coefficient;  $c$  is cohesion;  $\varphi$  is internal friction angle;  $\mu$  is Poisson ratio;  $E$  is elastic modulus;  $\sigma_c$  is compressive strength and  $\sigma_t$  is tensile strength. The surrounding rock of F1 deep weathering slot is designated as category V. The value ranges of the parameters are determined by experiments and design code JTG D70-2004.

Table 1. Value ranges of the influencing factors

$\lambda$	$c$ (MPa)	$\varphi$ (°)	$\mu$	$E$ (MPa)	$\sigma_c$ (MPa)	$\sigma_t$ (MPa)
0.4-0.7	0.035-0.2	16-27	0.35-0.4	100-300	1-10	0.2-0.5

The computation combinations and results are shown in Table 2.  $\sigma_h$  is horizontal crustal stress which equal to vertical crustal stress  $\sigma_v$  multiplied by  $\lambda$ ;  $u_x$  is horizontal convergence maximum and  $u_y$  is vault crown settlement maximum. The vertical crustal stress  $\sigma_v=1.5\text{Mpa}$  in F1 deep weathering slot of Xiamen Xiang'an Subsea Tunnel.

Table 2. The computation combinations and results

No.	$c$ (MPa)	$\varphi$ ( $^\circ$ )	$\mu$	$E$ (MPa)	$\sigma_c$ (MPa)	$\sigma_t$ (MPa)	$\sigma_h$ (MPa)	$u_x$ (mm)	$u_y$ (mm)
1	0.035	17	0.375	230	9.0	-0.425	1.05	7.246	5.825
2	0.04	19	0.4	230	9.0	-0.35	0.975	12.372	10.40
3	0.05	21	0.37	130	5.0	-0.275	0.938	4.990	4.863
4	0.06	23	0.397	280	1.0	-0.2	0.9	7.538	7.178
5	0.08	25	0.365	190	10.0	-0.45	0.862	12.084	13.77
6	0.095	27	0.395	100	6.0	-0.375	0.825	5.142	5.618
7	0.105	16	0.36	245	2.0	-0.3	0.788	6.790	9.293
8	0.13	18	0.39	150	11.0	-0.225	0.75	3.576	4.636
9	0.145	20	0.355	300	7.0	-0.5	0.712	3.934	6.723
10	0.16	22	0.385	210	3.0	-0.4	0.675	7.688	12.23
11	0.175	24	0.35	115	12.0	-0.325	0.637	2.444	5.502
12	0.2	26	0.38	260	8.0	-0.25	0.6	4.084	8.367

### 3.2 Grey-correlation Analysis

Here horizontal convergence maximum and vault crown settlement maximum were selected as reference sequences separately; the influencing factors were comparison sequences. The authors have carried on sensitivity analysis by the above grey-correlation method using the data of Table 2. The analysis results are shown in Table 3 and Table 4.

Table 3. The results of correlation degree of the influencing factors to horizontal convergence maximum

Item	$c$	$\varphi$	$\mu$	$E$	$\sigma_c$	$\sigma_t$	$\lambda$
$r_i$	0.607	0.848	0.891	0.838	0.870	0.900	0.910

Table 4. The results of correlation degree of the influencing factors to vault crown settlement maximum

Item	$c$	$\varphi$	$\mu$	$E$	$\sigma_c$	$\sigma_t$	$\lambda$
$r_i$	0.622	0.848	0.854	0.788	0.799	0.817	0.809

## 4 Conclusions

In the paper, the authors have carried on influencing factors sensitivity analysis of F1 deep weathering slot surrounding rock displacement of Xiamen Xiang'an Subsea Tunnel by grey-correlation, uniform design and BEM. The results of analysis are as follows:

1. The correlation degrees of the seven influencing factors of horizontal convergence of surrounding rock all are bigger than 0.6, which shows that they all have a significant impact on horizontal convergence. Lateral pressure coefficient is the most sensitive factor to horizontal convergence of surrounding rock, followed by the tensile strength of surrounding rock. The seven influencing factors' sensitivity sorting is:  $c < E < \varphi < \sigma_c < \mu < \sigma_t < \lambda$ .
2. The correlation degrees of the seven influencing factors of the vault crown settlement of surrounding rock all are bigger than 0.6, which shows that they all have a significant impact on the vault crown settlement. To the vault crown settlement of surrounding rock, Poison's ratio is the most sensitive factor, followed by the internal friction angle. The seven influencing factors' sensitivity sorting is:  $c < E < \sigma_c < \lambda < \sigma_t < \varphi < \mu$ .
3. After knowing the influencing factors' sensitivity sorting, the designers can modify the design parameters to control the surrounding rock displacement and assure the stability (Haug, 1986). The research achievement has been using in the design and construction of Xiang'an Subsea Tunnel, and good results have been achieved.

## Acknowledgments

This research is supported by China Postdoctoral Science Foundation (Grant No. 20080440652).

## References

- Chen G.F., Lu Y.F., et al (2008). Grey correlation analysis of slope stability sensitivity base on uniform design. *Disaster and Control Engineering*, 54(1), 1-6 [in Chinese].
- Deng J.L. (1985). *Basic method of grey system*. Huazhong Institute of Technology Press, Wuhan [in Chinese].
- Dong X.Z., Zhang C.M., Dong Y.C. (2005). Grey-correlation analysis of factors influencing deflection of the round foundation pit of the south anchorage of Wuhan Yangluo Yangtze river highway bridge. *Chinese Journal of Rock Mechanics and Engineering*, 24(14), 2576-2580 [in Chinese].
- Fang K.T., Ma C.X. (2001). *Orthogonal and uniform experiment design*. Science Press, Beijing [in Chinese].

- Haug E.J., Choi K.K., Komkov V. (1986). *Design sensitivity analysis of structural systems*. Academic Press, New York.
- Sun J. (2006). Discussion on some key technical issues for design and construction of undersea tunnels. *Chinese Journal of Rock Mechanics and Engineering*, 25(8), 1513-1521 [in Chinese].

*“This page left intentionally blank.”*

# Secondary Development of FLAC<sup>3D</sup> and Application of Naylor K-G Constitutive Model

Juan Kong<sup>1,2\*</sup>, Juyun Yuan<sup>1,2</sup> and Xiaoming Pan<sup>1,2</sup>

<sup>1</sup>Department of Geotechnical Engineering, Tongji University, Shanghai 200092, P.R. China

<sup>2</sup>Key Laboratory of Geotechnical and Underground Engineering of Ministry of Education, Tongji University, Shanghai 200092, P.R. China

**Abstract.** Because of the complexity and variety of geotechnical material, the constitutive models put forward by existing FLAC<sup>3D</sup> software can't satisfy all the requirements of actual numerical analysis. In accordance with fundamental code-run-principle of FLAC<sup>3D</sup> software, the basic principle of the secondary development program is made, the modified Naylor constitutive model is developed in FLAC<sup>3D</sup> with VC++(7.0) environment. A series of simulations of triaxial tests are performed to verify the correctness of the compiled model. The Secondary development environment is more friendly and effective in support of object-oriented approach. Therefore, the design mode proposed in this paper can be served as references for secondary development of other constitutive models.

**Keywords:** Naylor K-G model, FLAC3D, secondary development, object-oriented approach

## 1 Introduction

FLAC<sup>3D</sup> is three-dimensional explicit finite difference methods for analyzing and computing mechanics problem which can effectively simulate the structure of rock and other material behaviour of engineering mechanics. FLAC<sup>3D</sup> has essential constitutive models, which can meet the needs of geotechnical engineers. It contains three elastic constitutive models and eight elastic-plastic models and five kinds of creep constitutive models. For static, dynamic, creep, flow, temperature and their mutual coupling effect of engineering problems, we can select the appropriate models to achieve different types of problems. But only those of the constitutive models can not satisfy all of the engineers, FLAC<sup>3D</sup> V3.0 provides a relatively convenient development environment in order to facilitate the user-defined constitutive model. For example, Wei-Jiang Chu et al. have made secondary de-

---

\* Corresponding author, e-mail: pxm155138@163.com

velopment of a viscoelasto-plastic rheological constitutive model (Chu, 2006); Yu-Min Chen et al. have carried on Duncan-Zhang constitutive model implementation (Chen, 2007); Chuan-Qing Zhang et al. have established elasto plastic constitutive model based on the unified strength theory (Zhang, 2007); Ping Xu et al. have made research on generalized Kelvin model implementation (Xu, 2004). In this paper, Object-oriented language VC++7.0 is used as tools to develop modified Naylor constitutive model, which expands the applicability of FLAC<sup>3D</sup> procedures. Finally through the triaxial test, it shows that the developed interface program of development is correct and the program can be used to analyze the engineering problems.

## 2 Secondary Development Environment of FLAC<sup>3D</sup>

FISH is an embedded programming language in FLAC<sup>3D</sup>, which can extract and modify cell material parameters for constitutive model changes (Itasca Software Company, 2003).

By using Fish language, Simple modifications of the constitutive models can be done, but for the realization of complex secondary development constitutive models, we must use Visual C++ object-oriented language to develop a dynamic-link library (.dll) to call the main program through FLAC<sup>3D</sup>. The user-defined models depend on the following files which incorporate in four header files (stensor.h, axes.h, contable.h, conmodel.h) and the import library vcmodels.lib, as well as user defines derived class userkg.h file and userkg.cpp file. Contents and main functions of these files are described separately as follow.

Stensor.h header file defines the structure Stensor, whose data can define a symmetric second-order tensor and so on.

Axes.h header file defines the structure Axes, which is used to define coordinate system.

Contable.h header file defines and deals with the tables.

Conmodel.h file contains two structures, and a constitutive model of pure virtual class: struct State, struct Model Save Object, class Constitutive Model.

User-defined header file, it defines a new category of Constitutive Model of inheritance of the abstract base class, which mainly asks the user to define member function, and the derived class's private members, including the model of the basic parameters and intermediate procedures variables for implementation of the main procedures.

Userkg.cpp file, User redefines member functions, implements the overloaded member functions.

### 3 Mathematical Expression of Modified Naylor K-G Constitutive Model

In practical work, it is difficult to select the appropriate value of modulus of deformation  $E$  and Poisson's ratio  $\nu$ , because they are affected by lots of factors such as test methods, test conditions, etc. So, many scholars believe that any changes of the stress-strain matrix is similar to the changes of volumetric deformation modulus  $K$  and shear modulus  $G$ ; the relationship of elasticity stress-strain can be expressed by  $E$  and  $\nu$ , a little change of  $\nu$  will cause a small change of shearing strain and a large change of matrix normal strain. This shows that the usage of modulus  $K$  and  $G$  is superior to the deformation parameters  $E$  and  $\nu$ . There are some detail introductions in some literatures (Duncan, 1970; Qu, 1987; Li, 2004). In nonlinear elastic analysis, the stress can be expressed by spherical tensor of stress  $p$  and deviatoric tensor  $q$ , the strain can be expressed by spherical tensor of strain (bulk strain)  $\varepsilon_v$  and deviatoric strain (shearing strain)  $\varepsilon_s$ . The modified Naylor nonlinear elastic K-G constitutive model has a certain representation. In this article, secondary development program is made about the modified Naylor nonlinear elastic K-G constitutive model.

The generalized stress-strain space of modified Naylor K-G constitutive model can be expressed as:

$$\{\sigma\} = [p \quad q]^T, \{\varepsilon\} = [\varepsilon_v \quad \varepsilon_s]^T \tag{1}$$

where

$$p = \frac{1}{3}(\sigma_1 + \sigma_2 + \sigma_3), \varepsilon_v = \varepsilon_1 + \varepsilon_2 + \varepsilon_3 \tag{2}$$

$$q = \frac{1}{\sqrt{2}}\sqrt{(\sigma_1 - \sigma_2)^2 + (\sigma_1 - \sigma_3)^2 + (\sigma_2 - \sigma_3)^2}, \varepsilon_s = \frac{\sqrt{2}}{3}\sqrt{(\varepsilon_1 - \varepsilon_2)^2 + (\varepsilon_1 - \varepsilon_3)^2 + (\varepsilon_2 - \varepsilon_3)^2} \tag{3}$$

From the tests,  $p$  and  $\varepsilon_v$  as well as  $q$  and  $\varepsilon_s$  can be expressed by differentiation:

$$d\varepsilon_v = \frac{dp}{K_t}, d\varepsilon_s = \frac{dq}{3G_t} \tag{4}$$

The modified Naylor assumed the nonlinear tangent volumetric modulus  $K_t$  and the nonlinear tangent shear modulus  $G_t$  as:

$$K_t = K_i + \alpha_k p, G_t = G_i + \alpha_g p + \beta_g q \tag{5}$$

$K_i$ ,  $\alpha_k$ ,  $G_i$ ,  $\alpha_g$ ,  $\beta_g$  are the five parameters of nonlinear K-G model, where  $\alpha_k$  and  $\alpha_g$  are positive values,  $\beta_g$  is a negative value. The shear modulus will increase with the mean normal stress, and increase with the decline of the shearing force.

From Eq. (5), we can get next expression:

$$\varepsilon_v = \frac{1}{\alpha_k} \ln\left(\frac{K_i + \alpha_k p}{K_i}\right), \varepsilon_s = \frac{1}{3\beta_g} \ln\left(\frac{n + mp - q}{n + mp}\right) \quad (6)$$

where

$$n = -\frac{G_i}{\beta_g}, m = -\frac{\alpha_g}{\beta_g} \quad (7)$$

So, the incremental constitutive equation of K-G model can be calculated as:

$$\Delta\sigma_{ij} = 2G_i\Delta\varepsilon_{ij} + \alpha\Delta\varepsilon_{kk}\delta_{ij}, \alpha = K_i - \frac{2}{3}G_i \quad (8)$$

## 4 Development Process of FLAC<sup>3D</sup> Constitutive Model

The secondary development environment of FLAC<sup>3D</sup> has provided an open user interface, the software has provided the source code of self-constitutive model, the code can be modified and developed according to the required constitutive model. Program flowchart of K-G model is shown in Figure 1.

## 5 Example Verification

In order to verify the calculation format of K-G model, this paper adopts numerical simulation of triaxial tests to verify the correctness of the development model. The parameters of K-G model are shown in Table 1.

Table 1. Parameters of K-G model

Nonlinear elastic model	$K_i$ ( $10^2$ kPa)	$\alpha_k$	$G_i$ ( $10^2$ kPa)	$\alpha_g$	$\beta_g$
K-G model	51.7	54.9	22.1	103.0	-63.4

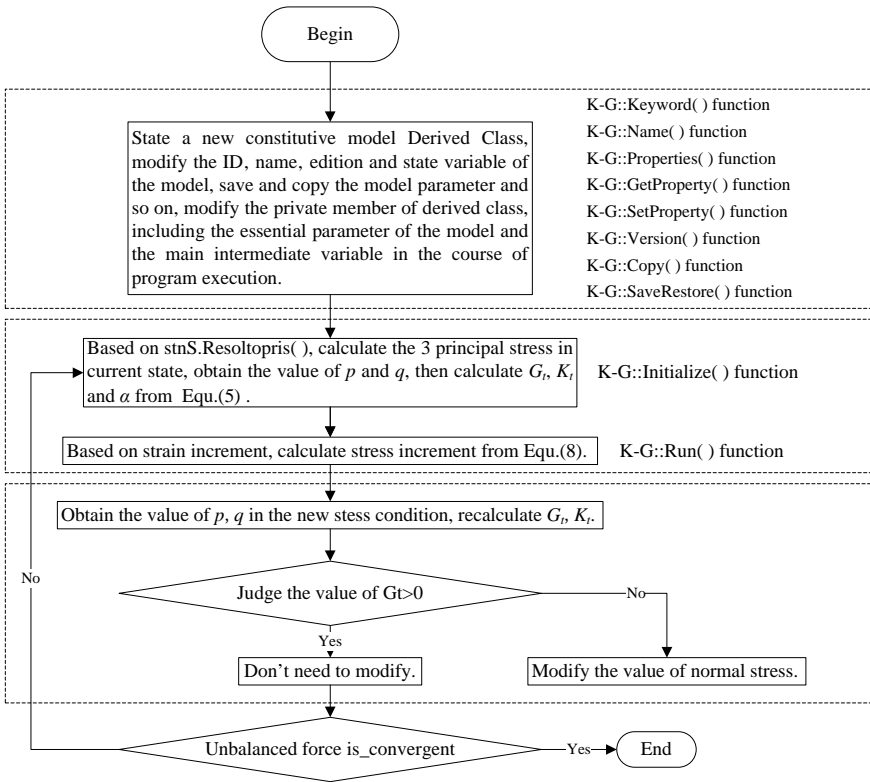


Figure 1. Program flowchart of K-G model

Computing model’s dimension employs the size of large-scale triaxial test specimen. Simultaneously in order to simplify the boundary conditions, an edge length of 600mm cube brick element is used, which has the vertical displacement constraints on the base and four stress boundary conditions around the cubic.

Here two loading schemes are adopted.

1. Gradual load pressure to the consolidation deduces  $p-\varepsilon_v$  relation and compare the relationship with the results of the theoretical formula (6).
2.  $p$  is a constant of the triaxial shear test, the relations of  $q-\varepsilon_s$  can be gotten under different values and compare it with the results of the analytical formula (6).

During first step 1, each level load increase 10kPa in the x, y, z three direction of model by the use of FISH function;

In the second step 2, under the different  $p$  values such as 100kPa, 150kPa, 200kPa, 250kPa, each level load imposed by FISH classification function increases 10kPa at the top of in z direction, reduces 5kPa in the x, y direction respectively. Mechanical model uses Naylor K-G model developed by this article. For me-

chanical static calculations, the steady-state solution is detected, by default, when the unbalanced force ratio reaches  $1 \times 10^{-5}$ .

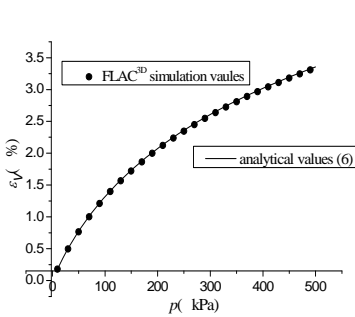


Figure 2. Curves of  $p$  and  $\varepsilon_v$

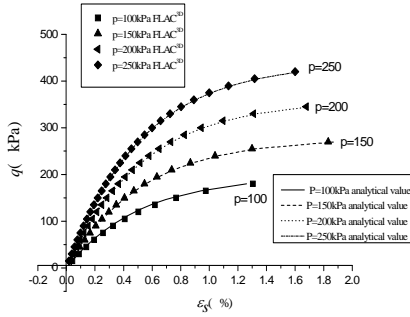


Figure 3. Curves of  $q$  and  $\varepsilon_s$

Compare the results of Figure 2 and Figure 3, calculated results of FLAC<sup>3D</sup> tally with the K-G theoretical values, which means that Naylor K-G model results developed in the implementation of FLAC<sup>3D</sup> are correct.

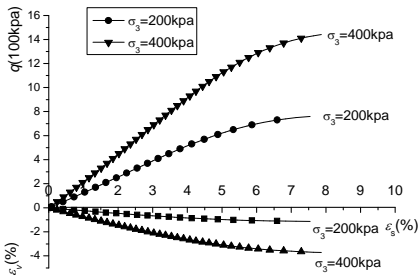


Figure 4.  $q - \varepsilon_s$  and  $\varepsilon_v - \varepsilon_s$  at different confining pressure

Figure 4 shows the relationship curves of  $q - \varepsilon_s$  and  $\varepsilon_v - \varepsilon_s$  under different confining pressure. From the graphic, the developed K-G model in FLAC<sup>3D</sup> can reflect nonlinear elastic-hardening and shear dilatation of soil.

## 6 Conclusions

Geotechnical material is a complex engineering medium, the existed constitutive model provided by FLAC<sup>3D</sup> often can not meet the actual needs of numerical analysis. Therefore, in this paper, based on FLAC<sup>3D</sup> provided by the secondary

development of programming interfaces, combining with the Naylor K-G nonlinear elastic constitutive model and its incremental iterative format in FLAC<sup>3D</sup>, the corresponding UDM interface program is gotten, which generates the dynamic link library of this constitutive model called by FLAC<sup>3D</sup> software. In order to verify the correctness of this model, this article designs the numerical simulation of triaxial tests at different pressure  $p$  and generalized shear stress  $q$ . The results show that the model calculation results are very similar to the analytical values. When values of  $\alpha_g$  and  $\beta_g$  are zero, the model degenerates to the linear elastic model. The ideas of secondary development research are universal. Therefore, proposed design mode can provide references for the secondary development of other constitutive models.

## References

- Chen Y.M. and Liu H.N. (2007). Development and implementation of Duncan Chang constitutive model in FLAC3D. *Rock and Soil Mechanics*, 28(10):2123-2126 [in Chinese].
- Chu W.J. et al. (2006). Secondary development of a viscoelasto-plastic rheological constitutive model of rock based on FLAC3D. *Rock and Soil Mechanics*, 27(11):2005-2010 [in Chinese].
- Duncan J.M., Chang C.Y. (1970). Nonlinear analysis of stress and strain in soils. *Journal of the Soil Mechanics and Foundations Division, ASCE*, 96(5):1629-1653.
- Itasca Software Company (2003). Theory and back ground, constitutive model: theory and implementation . Minneapolis Minnesota USA.
- Li G.X. (2004). *Advanced soil mechanics*. Tsinghua University Press, Beijing [in Chinese].
- Qu Z.J. (1987). *Soil plasticity*. Chengdu Science and Technology University Press, Chengdu [in Chinese].
- Xu P., Li Y.P. and Ding X.L. (2004). Secondary development and application of visco-elasto constitutive model in FLAC3Dsoftware. *Journal of Yangtze River Scientific Research Institute*, 21(2):10-14 [in Chinese].
- Zhang C.Q., Zhou H. and Feng X.T. (2007). Numerical format of elastoplastic constitutive model based on the unified strength theory in FLAC3D. *Rock and Soil Mechanics*, 29(3):596-602 [in Chinese].

*“This page left intentionally blank.”*

# Experimental Validation on the Simulation of Steel Frame Joint with Several Frictional Contacts

Hongfei Chang<sup>1,2\*</sup> and Junwu Xia<sup>1,2</sup>

<sup>1</sup>Key Laboratory of Deep Geotechnical and Underground Engineering, China University of Mining & Technology, Xuzhou 221116, P.R. China

<sup>2</sup>School of Architecture & Civil Engineering, China University of Mining & Technology, Xuzhou 221116, P.R. China

**Abstract.** In this paper we handled the problems with several coexistent frictional contacts by finite element method, and checked the results of the numerical simulation by laboratory test. We simulated a spliced friction component and a steel frame joint with high strength bolts splicing, in which a number of frictional contacts such as the flange splicing to the beam flange; the web splicing to the beam web; the bolt head to the splicing and the bolt shank to the bolt hole were considered. By comparing and analyzing, we find that the predictions from the finite element simulation are proved to be in good agreement with experimental results. The applicability of finite element method on the solution of complex coexistent contact is affirmed.

**Keywords:** experimental validation, frictional contact, finite element simulation, steel frame joint, high strength bolt splicing

## 1 Introduction

The nonlinearity of contact problems is challenging, and it is difficult to determine the shape of the contact area and the pressure distribution on it. Hertz had studied the contact problems of elastic bodies systematically early in the 1880s, and established the classical Hertz contact theory. With the development of the finite element method, the study of contact problems has made great progress in recent years (Johnson, 1985; Kikuchi and Oden, 1988; Wang et al., 2001; Feng and Owen, 2002; Wriggers, 2003). There are two aspects are mainly concerned in contact problems, the contact search and the contact pressure calculation. Plenty of search strategies (Wang et al., 2001; Feng and Owen, 2002) and contact pressure

---

\* Corresponding author, e-mail: honfee@126.com

algorithms (Hughes et al., 1976; Simo et al., 1985; Carpenter et al., 1991; Hallquist et al., 1985) are reported in the last several decades. Briefly, the aim of contact search is to determine the contact shape, and the substance of contact pressure calculation is to subject the system to the constraint condition. The solution of contact with clearance and friction (Cui, 1980) is also widely concerned. Description of the friction phenomenon as a constitutive Equation has been attained first as a rigid-plasticity (Fredriksson, 1976; Seguchi et al., 1974). Further, it has been extended to an elastoplasticity (Gearing et al., 2001; Kikuchi and Oden, 1988; Cheng and Kikuchi, 1985; Wriggers et al., 1990; Anand, 1993; Peric and Owen, 1992; Wriggers, 2003) in which the penalty concept is introduced, and the reliability of the finite element solution is improved.

The finite element method is proved to be credible for the solution of simple contact problems (Hughes et al., 1976; Simo et al., 1985; Oden and Pires, 1983; Gearing et al., 2001). While the study on complicated contact problems, especially in the case of considering many coexistent contacts in one model, are seldom reported at present. To check the applicability of the finite element method on the solution of model with several contacts, we simulate a friction component and a steel frame joint with high strength bolt splicing using finite element method, in which the friction and the sliding of the contacts are considered.

## 2 Finite Element Model

The general finite element procedure ANSYS is adopted for the simulation. The procedure is intelligent and efficient in handling the contact problems (ANSYS User Manual, 2001).

### 2.1 Dimensions of the Model

The dimensions in millimeter of the friction component are shown in Figure 1(a). To increase computational efficiency, we construct a symmetrical half-model of the component as shown in Figure 1(b). All possible contacts are contained in the model, and the interface friction coefficient is 0.3. The high strength bolts is M20 with a pretension of 155 kN.

Figure 2(a) indicates the dimensions of a T-shaped joint, which represents an exterior beam-to-column connection, isolated from a moment frame at the inflection points of the column and the beam. The subassemblage consists of an H-shaped  $H300 \times 160 \times 8 \times 10$  (dimensions in mm for depth, width, web thickness, and flange thickness, respectively) beam, 1500mm long and a H-shaped column of  $H300 \times 200 \times 10 \times 10$  with 3000mm span length. The beam-column connection is strengthened to avoid destroy of beam end welding Figure 2(b) shows the finite

element meshing of the model. More details related to the finite element modeling can be found in the literature (Chang, 2006).

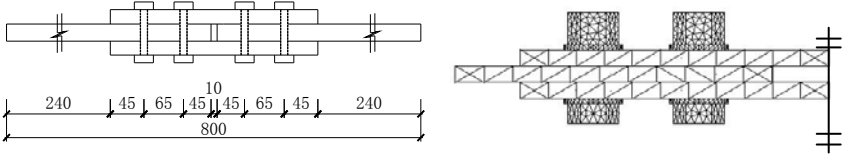


Figure 1. Dimensions and meshing of the friction component

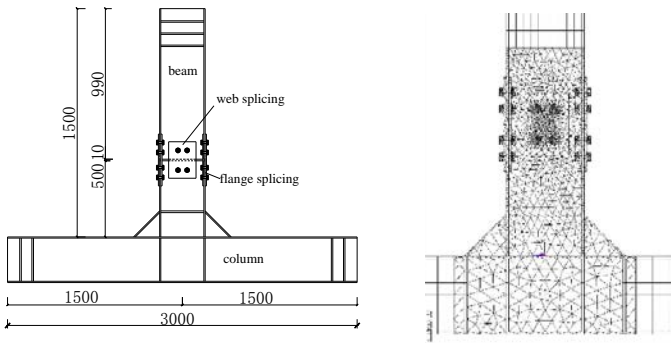


Figure 2. Dimensions and local meshing of the T-shape joint

## 2.2 Material Model

Multi-linear behavior is assumed for the steel used for the column-beam and the high strength bolts. The yielding strength of the column-beam and the bolts is  $255 \text{ N/mm}^2$  and  $980 \text{ N/mm}^2$  respectively, and the ultimate strength is  $375 \text{ N/mm}^2$  and  $1100 \text{ N/mm}^2$  respectively. The tangent module of the material is  $E=2.06 \times 10^5 \text{ N/mm}^2$ , and the Poisson ratio is  $\mu=0.3$ . Von-Mises yielding criterion and bilinear kinematic strengthen model is used.

## 2.3 Element Type

There are totally six types of element in the T-shaped joint model. Table 1 lists the name and the description of each element as well as the total element quantity. Element types used in the friction component are similar.

## 2.4 Contact Solution

We consider four kinds of contacts in the model, that is: the flange splicing to the beam flange; the web splicing to the web; the high strength bolts head to the splicing; the bolts shank to the bolt hole. In the finite element procedure, a number of settings should be executed beforehand. We treat the surface-to-surface contact as flexible-flexible problem, and select augmented Lagrangian multiplier algorithm to solve it. Using the Coulomb friction model, in which an equivalent shear stress is predefined, and frictional slippage will occur when the interface shear stress exceed the defined stress.

Table 1. Element description

Location	Name	Description	Quantity
Beam-column core zone	Solid92	10 node quadrangle 3D solid	9926
Beam-column non-core zone; bolts	Solid45	8 node hexagon 3D solid	5127
Strengthen ribs	Shell63	Elastic shell	318
Pretension	Prets179	Bolt pretension	492
Contact	Contact174	8 node 3D surface contact	1652
	Target170	3D target segment	2858
Total			27613

## 3 Experimental Validation

To evaluate the reliability of the finite element simulation, we carry out a full scale test on the pre-mentioned model in the structure laboratory of China University of Mining and Technology. The material; dimensions and configurations of the test specimens are same to the finite element model. The electric-fluid drive servo (PWS-500) is adopted for loading, and TDH7130 data collection system is used for data gathering. The load and displacement as well as the strain of beam are isochronously measured. Some pictures of the test setup are shown in Figure 3.



(a) Friction component test                      (b) T-shaped joint test

Figure 3. Test setup of the component and the joint

### 3.1 Validation of Friction Component

When subjected to an axial force, the spliced friction component will slid and a load-displacement curve can be pictured. Figure 4 shows the simulated curve as well as the tested. The tested curve demonstrates an interrupt wave at the load level of 154kN, which indicates the slippage of the splicing. The load goes up again after the slip and the deformation of the joint is considerably. We draw the simulation curve accompany with the test result, and the two match well with each other. The slip load of simulation is slightly higher than the test, which probably because the actual friction coefficient of steel is less than 0.3.

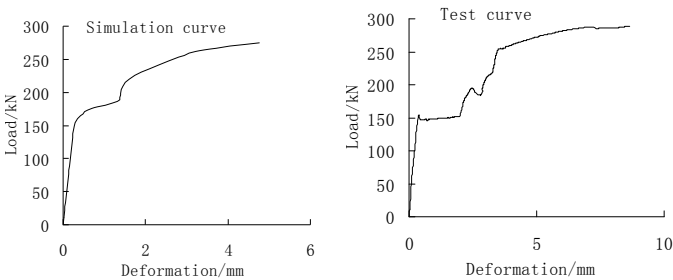


Figure 4. Load-displacement curves of friction component

The failure of the friction component is shown in Figure 5, in which the left is laboratory tested and the right is simulated. It can be indicated that the failure of

the component appears at the first hole of the plate, and the circular hole is compressed to oval. The finite element simulation reconstructs the test well.

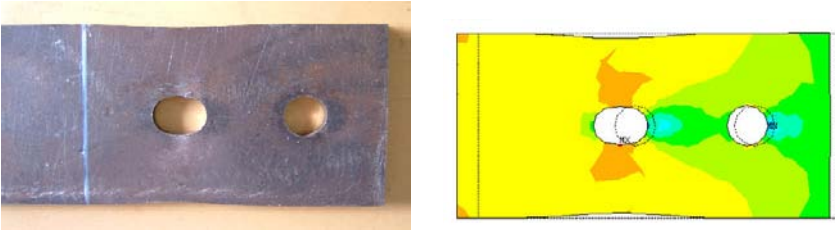


Figure 5. Failure of friction component

### 3.2 Validation of T-Shaped Joint

1. *Force-displacement relation.* The force-displacement relation of the joint is shown in Figure 6, in which the solid curve is simulated result and the dashed curve is laboratory tested. Both curves indicate the slippage of the contact, that is, the load keep flat while the displacement increase abruptly. The tested slippage load  $F_{slip}$  is 93kN and the simulated  $F_{slip}$  is 100.5kN, which is 8.06 percent more than the test. The difference probably aroused by the lower friction coefficient of the experiment.
2. *Beam deformation.* Figure 7 indicates the contrast of displacement along the beam length between simulation and test. The spliced beam keeps uniform and the displacement curve is flat in the low load level, and the beam rotates around the splicing center when contact slippage appears. The simulated deformation is in very good agreement with the experimental results.
3. *Beam flange strain.* We dispose a set of strain gauges along the beam flange, and collect the data during loading in the test. By joining the data of each stain gauge we get a series of transition lines (Figure 8), in which F represent the strain of the beam flange and FS represent the data of flange splicing. It can be indicated that the simulation results are quite close to the test results when the load is less than 100kN.

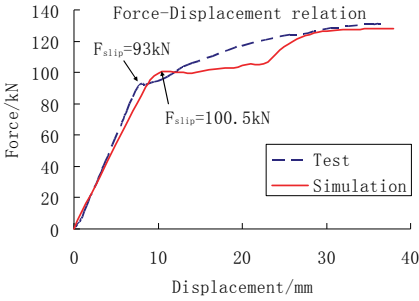


Figure 6. Force-displacement relation

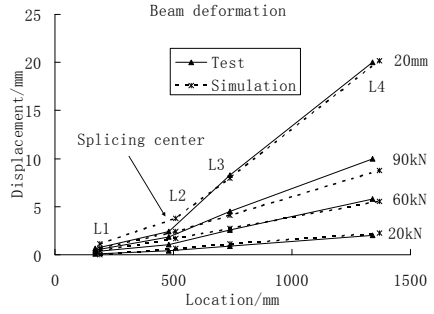


Figure 7. Beam deformation

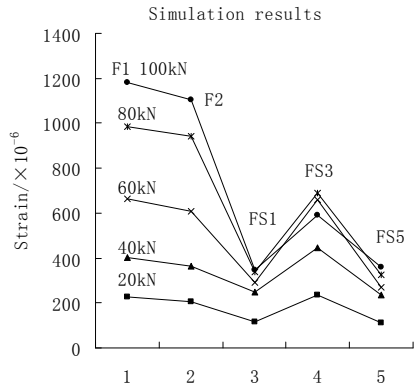
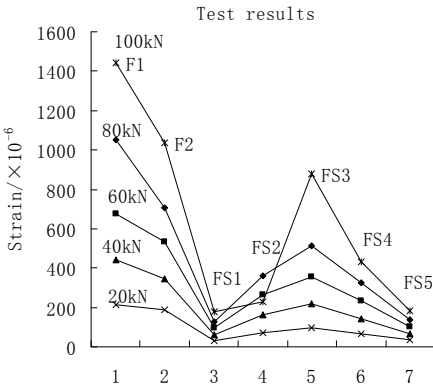


Figure 8. Contrast of beam flange strain

## 4 Conclusion

We check the simulated load-displacement curve of the friction component with the laboratory test, and find that they fit well with each other. The finite element method reconstructs the tested failure of the component perfectly. The simulated strain and deformation results of steel frame joint with several contacts agree with the test as well. The finite element method, for its reliability and efficient as well as economization, is recommended for the solution of problems with complicated frictional contacts.

## Acknowledgements

This paper is financially supported by the Key Laboratory of Deep Geotechnical and Underground Engineering of CUMT, the Chinese National Natural Science foundation (50774081), the “eleventh five-year plan” national science support major program (2006BAJ14B07; 2006BAJ05A08) and the youth fund of China University of Mining and Technology.

## References:

- ANSYS User Manual (2001) ANSYS, Inc.
- Anand L. (1993) A constitutive model for interface friction. *Comput. Mech.*, 12:197-213.
- Carpenter N.J., Taylor R.L. and Katona M.G. (1991) Lagrange constraints for transient finite-element surface contact. *International Journal for Numerical Methods in Engineering*, 32:103-128.
- Chang H. (2006) Study on Energy Dissipation and Design Method of Steel Frame Joint with Cantilever Beam Splicing. Graduated degree paper of China University of Mining & Technology, Xuzhou.
- Cheng J.H. and Kikuchi N. (1985) An incremental constitutive relation of uniaxial contact friction for large deformation analysis. *Appl. Mech. (ASME)*, 52: 639-648.
- Cui J. (1980) On problems of elastic contact with initial gaps. *Chinese Journal of Theoretical and Applied Mechanics*. (3): 261-268.
- Feng Y.T. and Owen D.R.J. (2002) An augmented spatial digital tree algorithm for contact detection in computational mechanics. *International Journal for Numerical Methods in Engineering*, 55:159-175.
- Fredriksson B. (1976) Finite element solution of surface nonlinearities in structural mechanics with special emphasis to contact and fracture mechanics problems. *Comput. Struct.* 6: 281-290.
- Gearing B.P., Moon H.S. and Anand L. (2001) Plasticity model for interface friction: Application to sheet metal forming. *Int. J. Plasticity*, 17: 237-271.
- Hallquist J.O., Goudreau G.L. and Benson D.J. (1985) Sliding interfaces with contact-impact in large-scale Lagrangian computations. *International Journal for Numerical Methods in Engineering*, 51:107-137.

# Numerical Investigation on Tubular Joints Strengthened by Collar Plate

Yongbo Shao<sup>1\*</sup>, Yongsheng Yue<sup>1</sup>, Yanfei Jin<sup>1</sup>, Tao Li<sup>1</sup> and Jichao Zhang<sup>2</sup>

<sup>1</sup>School of Civil Engineering, Yantai University, Yantai 264005, P.R. China

<sup>2</sup>School of Civil Engineering, Guangzhou University, Guangzhou 510006, P.R. China

**Abstract.** As the stiffness of a circular hollow section tube in radius direction is generally much smaller than its stiffness in axial direction, failure occurs easily at the position close to the weld toe on the chord surface of a tubular joint. To improve the bearing capacity of a tubular joint, collar plate can be used. Using finite element (FE) modelling, the static strength of collar plate strengthened tubular joints is analyzed and the accuracy of the numerical results are evaluated. Furthermore, the influence of the joint & the collar geometries and the material property on the static strength of the tubular joints is investigated. And finally, some advice is proposed for design purposes.

**Keywords:** tubular joint, collar plate, static strength, bearing capacity

## 1 Introduction

Tubular structures are used widely in onshore and offshore structures such as stadium, bridge, railway, airport and oil drilling platform etc. In these tubular structures, one or several small tube members, which are called brace, are welded onto a big tube, which is called chord. The connection between the braces and the chord is called tubular joint, which is critical in tubular structures because failure frequently occurs at this position. In tubular joints, high stress concentration exists at the weld toe. Furthermore, the chord member is generally subjected to loading in radius direction which is transferred from the brace members since all the tubes in tubular structures are mainly subjected to axial loading. As for circular hollow section, the stiffness in radius direction of a tube is much smaller than that in axial direction. Therefore, failure occurs easily on the chord surface near the weld toe, and the bearing capacity of a tubular joint is often determined by the local stiffness of the chord near the weld.

---

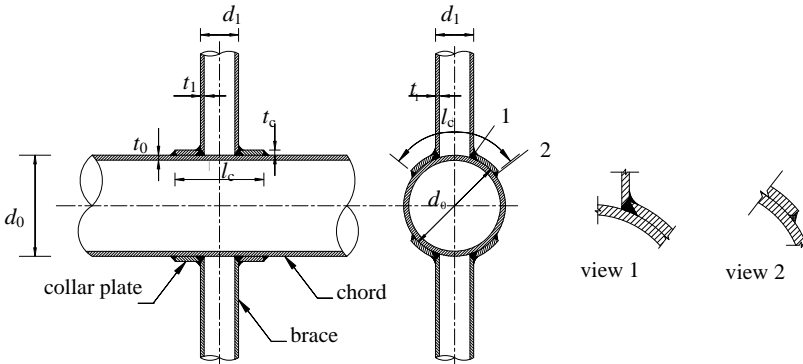
\* Corresponding author, e-mail: cybshao2009@hotmail.com

To improve the bearing capacity of a tubular joint, strengthening method is necessary. There are several reported strengthening methods for tubular joints in the literature. These methods can be generalized as two classifications: outer reinforcement and inner reinforcement. The classification is up to the placement of the reinforcement. In the inner reinforcement, i.e., stiffened internal ring and inner plate are typically used in tubular structures. The study on the reinforcement of tubular joints using internally stiffened ring is carried out by some researchers (Lee and Llewelyn, 2004, 2005; Thandavamoorthy, 1999). Wang (2007) investigated the reinforcing efficiency of inner plate on the improvement of static strength of tubular joints. From the reported research, it is found that a tubular joint strengthened by internally stiffened ring or inner plate can improve its bearing capacity remarkably. However, the disadvantage of the two inner reinforcing methods is that it is difficult to place the reinforcement inside the tube during fabrication. These two methods are also impossible to be used for strengthening a servicing tubular joint. Doubler plate reinforcement is an outer reinforcement as the plate is welded onto the outer surface of the chord. It is also proved by some researchers (Choo, 2005a, 2004) that this method is effective to increase the static strength of a tubular joint. However, doubler plate reinforcement can still not be used in the servicing period of a tubular joint. To overcome this problem, collar plate reinforcement is presented by (Choo et al., 2005b). This method is proved to be effective in increasing the static strength of a tubular joint, and it is also convenient for strengthening a tubular joint in its servicing time. However, detailed study is still necessary at present because the design criterion of this strengthening method is still not mature.

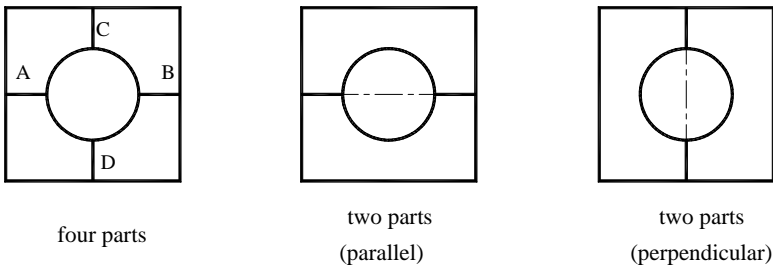
Using finite element (FE) method, the static strength of collar plate reinforced tubular joints is analyzed. The influence of some parameters on the strengthening efficiency is also investigated.

## **2 FE Analysis of Collar Plate Reinforced Tubular Joints**

For a collar plate reinforced tubular joint, the collar plate is firstly drilled a hole. Then it is curved to the same curvature as that of the chord. Finally, the collar plate is welded onto the chord by using fillet weld, and it is welded to the intersection by using penetrated weld. A typical collar plate is illustrated in Figure 1(a). The collar plate can be divided into four parts or two parts in practical fabrication, which is shown in Figure 1(b).



(a) A tubular joint reinforced with collar plate



(b) View of collar plate

Figure 1. Details of collar plate reinforcement on a tubular joint.

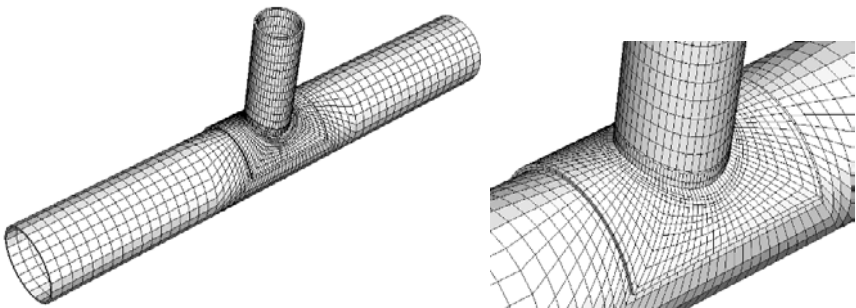
In the FE analysis, the accuracy of the numerical results depends much on the proposed modelling method. The modelling method includes the FE mesh generation, the material properties, loading applying method and boundary conditions used. Generally, the FE results must be verified with experimental measurements to ensure the reliability.

### 2.1 FE Mesh of a Collar Plate Reinforced Tubular Joint

In the literature, shell elements and brick elements have both been used to produce the FE mesh of a tubular joint. It has also been proved that both shell elements and brick elements are suitable in the FE analysis for un-stiffened tubular joints. However, shell elements are not flexible in modelling a collar plate tubular joint due to

several reasons. Firstly, it is not easy to model the weld accurately by using shell elements because the weld size around the brace/chord intersection is varying. Furthermore, contact surfaces between the collar plate and the chord surface are not simulated conveniently by using shell elements. In the literature, the modelling of weld in the FE analysis is generally ignored due to the above difficulty. It is found by some researchers that underestimation of the static strength of a tubular joint may reach 20% if the weld is not considered in the FE analysis. To overcome such deficiency, brick elements are used in this study.

In the mesh generation of a collar plate reinforced tubular joint, sub-zone mesh generation method is used. The entire structure is divided into different sub-zones according to the computational requirements. In the high stress gradient region, refined mesh is produced. Accordingly, coarse mesh is used in the low stress gradient for saving computing time. For a tubular joint, the mesh near the weld is refined because high stress concentration is located at this position. The weld around the intersection is simulated using brick element. The collar plate is welded onto the chord surface and the brace/chord intersection. Except such welding connection, the collar plate does not contact the chord, and there is a small gap between the collar plate and the chord surface. The value of the gap in the FE analysis is 0.1 in this study. The FE mesh of a collar plate reinforced T-joint using the above proposed mesh generation method is shown in Figure 2.



(a) Global view of FE mesh

(b) Close view of collar plate reinforced region

Figure 2. FE mesh of a collar plate reinforced tubular T-joint.

In Figure 2, 96 elements around the brace/chord intersection are used, and there are three layers in the tube thickness direction near the weld. In the region far away from the weld of the chord, one layer in tube thickness direction is used. For the collar plate, there are two layers of elements in plate thickness direction.

## 2.2 FE Analysis of Static Strength for Collar Plate Reinforced Tubular Joint

To evaluate the reliability and accuracy of the presented FE model, a typical tubular T-joint reinforced with collar plate is analyzed. The geometry of the reinforced T-joint model is tabulated in Table 1. The yield stress of the tubular joint is  $285 \text{ N/mm}^2$ , and the yield stress of the collar plate is  $461 \text{ N/mm}^2$ . Elastic-perfect plastic relationship is used for the stress-strain curve. During the FE analysis, both ends of the chord are fixed, and it is assumed that a compressive displacement increment is applied at the brace end. The load-displacement curve is then obtained.

Table 1. Geometry of the collar plate reinforced T-joint

T-joint	$d_o$ (mm)	$\beta$	$\gamma$	$\tau$	$\tau_d = t_1/t_0$	$l_c/d_1$
un-stiffened	409.5	0.54	25.3	0.84	-	-
stiffened	409.5	0.54	25.3	0.84	0.79	1.37

The FE results of the load-displacement curves of the un-stiffened and stiffened T-joints are plotted together in Figure 3. Apparently, the collar plate reinforced T-joint has a much bigger static strength compared with the un-stiffened T-joint model. For the T-joint without collar plate reinforcement, the numerical result of the bearing capacity is 287 kN. However, the numerical value of the collar plate reinforced model is 460 kN. There is an increment of about 60%. The experimental results for the un-stiffened and stiffened T-joint models, which can be found in (Choo et al., 2005b), are 305 kN and 426 kN respectively. The FE results agree reasonably well with the experimental measured values. Thus, the accuracy and the reliability of the FE results can be guaranteed.

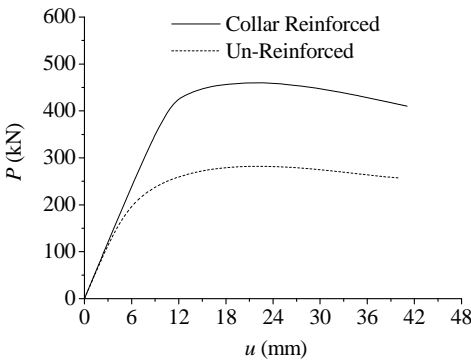


Figure 3. Load-displacement curves of T-joint models.

Although it is effective to increase the bearing capacity of a tubular joint by using collar plate reinforcement, the reinforcing efficiency must be analyzed from a parametric study, which considers the effect of the collar plate dimension and the material property.

### 3 Investigation of Reinforcing Efficiency of Collar Plate on Tubular Joints

To assess the strengthening efficiency of collar plate on tubular joints, a parametric study on 9 reinforced T-joint models is analyzed. The geometries of the T-joint and the collar plate of the 9 models are tabulated in Table 2. Additionally, the corresponding 3 un-stiffened T-joint models are also analyzed. For the analyzed 9 strengthened and the 3 un-stiffened T-joint models, the chord diameters are all 400 mm, and the yield stress of the T-joint are  $235 \text{ N/mm}^2$ .  $\sigma_{cy}$  and  $\sigma_y$  are the yield stresses of the collar plate and the tubular joint respectively. Square collar plate is used as the reinforcement. For the 3 un-stiffened T-joint models, they have the same geometry as the reinforced ones.

Table 2. Geometry of the collar plate reinforced T-joint

Model	$\gamma$	$\beta$	$\tau$	$\tau_c = t_c/t_0$	$l_c/d$	$\sigma_{cy}/\sigma_y$
1				1.0		
2	12	0.3	0.6	1.2	2.0	1.0
3				1.5		
4					2.0	
5	18	0.6	1.0	1.0	2.5	1.0
6					3.0	
7						1.0
8	24	0.8	1.0	1.0	2.0	1.5
9						2.0

The FE results of the bearing capacity for the 3 un-stiffened T-joints,  $P_0$ , and for the 9 collar plate reinforced T-joints,  $P_0$ , are all tabulated in Table 3. From Table 3, it can be found that the reinforcement of collar plate sometimes is not very efficient. It can be seen from the FE results of models 7-9 that the reinforced T-joint models have no remarkable improvement in bearing capacity when the material of the collar plate is same as that of the tubular joint. This is because the chord thickness ratio,  $\gamma$ , is too big, and thus the thickness of the chord is very small. Local buckling occurs very easily. In this case, it is important to use collar plate with high strength steel.

Table 3. Geometry of the collar plate reinforced T-joint

Model	P0 (kN)	P1 (kN)	P1 / P0
1		700	1.21
2	577	736	1.28
3		768	1.33
4		710	1.12
5	636	795	1.25
6		876	1.38
7		685	1.06
8	644	730	1.13
9		760	1.18

It is also interesting that the reinforcing efficiency is high for thick tube, and not very remarkable for thin tube. Therefore, it is better to use high strength steel material for the collar plate when the chord thickness ratio is big. Additionally, it is not effective to increase the static strength of a tubular T-joint when the brace/chord diameter ratio,  $\tau$ , is too small. In this case, it is easy for the brace to yield before the failure occurs on the chord. As shown in Figure 4, the brace yields at the position close to the weld. As the yield of the brace occurs before the failure of the chord, it is not efficient to continue strengthening the chord.

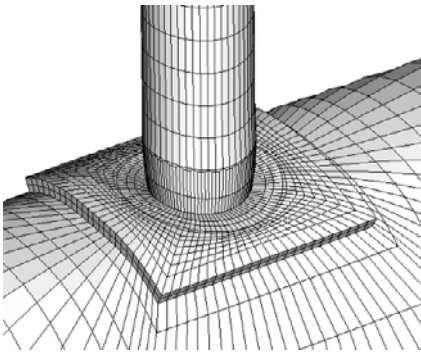


Figure 4. Yielding of brace near the weld.

## 4 Conclusions

The static strength of collar plate reinforced tubular joints is analyzed using FE method. The influence of the joint geometry and steel material property on the im-

provement of the bearing capacity of tubular joints is carried out, and some useful conclusions are given.

## Acknowledgements

This research work is supported by National Natural Science Foundation (No. 50808153). Such support is greatly appreciated by the authors.

## References

- Choo Y.S. (2005a). Recent development and innovation in tubular structures. *Advances in Structural Engineering*, 8(3): 217-230.
- Choo Y.S., Liang J.X. et al. (2004). Static strength of doubler plate reinforced CHS X-joints loaded by in-plane bending. *Journal of Constructional Steel Research*, 60: 1725-1744.
- Choo Y.S., van der Vegte G.J. et al. (2005b). Static strength of T-joints reinforced with doubler or collar plates-part I: experimental investigations. *Journal of Structural Engineering, ASCE*, 131(1):119-128.
- Lee M.M.K., Llewelyn-Parry A. (2004). Offshore tubular T-joints reinforced with internal plain annular ring stiffeners. *Journal of Structural Engineering, ASCE*, 130(6): 942-951.
- Lee M.M.K., Llewelyn-Parry A. (2005). Strength prediction for ring-stiffened DT-joints in offshore jacket structures. *Engineering Structures*, 27(3): 421-430.
- Thandavamoorthy T.S., Madhava Rao A.G., Santhakumar A.R. (1999). Behavior of internally ring stiffened joints of offshore platforms. *Journal of Structural Engineering, ASCE*, 125(11): 1348-1352.
- Van der Vegte G.J., Choo Y.S. et al. (2005). Static strength of T-joints reinforced with doubler or collar plates – Part II: Numerical simulations. *Journal of Structural Engineering, ASCE*, 131(1): 129-139.
- Wang Ge, Zhang Ji-Chao et al. (2007). Study on application of IGP-Stiffen CHS joints in Guangdong Science Center. *Industrial Construction*, 37(10): 93-97.

# Research on Structural Health Monitoring of Seaport Wharf

Changhong Huang<sup>1\*</sup> and Zhuobin Wei<sup>1</sup>

<sup>1</sup>Tianjin School District, Naval Engineering University, Tanggu Tianjin 300450, China

**Abstract.** With rigorous working condition, the seaport wharf is dilapidated more quickly than other structures, which havoc its security and applicability. For the lower durability, the health monitoring for the seaport wharf is necessary and urgent. In this paper, base on detection data and considering the different working ways of seaport wharfs, the effect factors for the security and durability of wharfs are researched. And indicators of the structural health monitoring for wharfs are proposed. Sensors, such as fiber optic sensors, which suit the health monitoring of seaport wharf, are introduced. Damage identification methods for gravity quay, quay wall of sheet pile and open wharf on piles are discussed. Finally, the current status of application of structural health monitoring for seaport wharf is presented and some suggestions are proposed.

**Keywords:** seaport wharf, health monitoring, durability

## 1 Introduction

Wharfs are very important marine structure in seaport. Gravity quay, quay wall of sheet pile and open type wharf on piles are the three common types of seaport wharfs (Ju, 2002). Usually, the life of a wharf is divided into construction period, effective serving period and ageing period. In the three life stages of a wharf, the failure probability of the structure is higher in the first and last ones. In the building period, there more attention and many monitoring and control techniques have been applied to insure the security of the wharfs, so unnecessary details about it are not given in this paper. In the serving period, with rigorous working condition, the seaport wharf is dilapidated more quickly than other structures, which havoc its security and applicability. For the lower durability, the health monitoring for seaport wharfs is necessary and urgent.

---

\* Corresponding author, e-mail: hch991@sina.com

## 2 Failure Mode and Structure Health Monitoring Indicators of Seaport Wharfs

As working in different ways, each kind of seaport wharfs has different failure mode. In this paper, the influencing factors on safety and durability of the three type wharfs are analyzed. Based on the analysis and inspection data, health monitoring indicators for each type wharfs are proposed.

### 2.1 Gravity Quay

Similar to gravity retaining wall, the weight of gravity quay is essential to maintain the wharf's stability. It resists slip force and overturning moment which are mainly caused by earth pressure. To have enough weight, most of the gravity quays are solid structures, and main bodies of them are made of concrete blocks or caissons. Being as solid structures, gravity quays can endure impact load and overload better than open type wharfs, and their durability are better too. According to our inspection data, in recent 10 years, there are only three gravity wharfs damaged badly, and both of them had worked long enough and all beyond their design terms. According to statistic, quay wall incline, component damage and dumped filling lack are considered as the main failure or damage modes of gravity quays.

The important reasons for the structural damage of gravity quays are shown as follows.

1. Unequal settlement of rubble-mound foundation or unequal settlement of foundation soil;
2. Settlement of filling;
3. Ageing and dilapidation of the reinforced concrete thin walls;
4. Overload;
5. Erosion at rubble-bedding by wave or ocean current.

Among the damage reasons, unequal settlement of rubble-mound foundation or unequal settlement of foundation soil is the common one. The unequal settlement along long direction of a gravity quay may cause additional stress in components of the structures and lead to grievous cracks. More dangerously, the unequal settlement along cross direction of a gravity quay may bring about the structure's overturn. As the essential element, which affect the applicability of a gravity quay mostly, the cracks or collapse of concrete wearing course are caused by settlement of filling mainly. Ageing and dilapidation of the reinforced concrete thin walls will reduce the structure's bearing capacity and lead the filling loss. The overall instability of a gravity quay is seldom happened but more danger. As the warning signs, the post-inclination of quay wall and quick settlement behind the structure have been noticed.

It is suggested in view of the foregoing that the displacements (especially the vertical ones) are the main representation for the health of a gravity quay. So the displacements in the key points of a gravity quay should be the main structure health monitoring indicator.

## ***2.2 Quay Wall of Sheet Pile***

Sheet piles are the main component of quay wall of sheet pile, which are driven into the sea earth one by one to form the wall of quay, and fillings is filled behind them. The earth pressure of the backfill is the main load in the quay. To resist the earth pressure, draw bars are fixed to the sheet piles and anchored by anchor wall far from the sheet piles. At statistics, mainly failure or damage modes of quay wall of sheet pile are sheet piles slide, deterioration of sheet piles, quay wall incline, dumped filling lack and draw bar rupture.

Reasons for the failure of quay wall of sheet pile are multiplex and complex and the main influencing factors are listed as follows.

1. Too deep dredging in front of quay walls;
2. Overload;
3. Ageing, corrosion and dilapidation of steel components or reinforced concrete components of the structure;
4. Instability of the anchor wall;

Too deep dredging in front of quay walls often may cause sheet pile wall revolve on its waling. In this moment, a back lateral displacement in the cap beam and a lateral displacement to sea under the guide beam will happen. Overload of heaped loads can bring excess moment in middle of sheet piles where a lateral displacement would be occurred towards sea before the moment exceeds the piles' flexural capacity. Besides, overload of heaped loads may bring about the rupture of draw bars and the guide beams will have a lateral displacement towards sea before this too. Degradation of steel or concrete components is often accelerated by marine environment which will reduce their bearing capacity. Instability of the anchor wall may cause the overturning of the sheet pile wall with steel draw bars, and the warning sign is the lateral displacement of guide beams towards sea.

It is suggested that the effect structure health monitoring indicators for the safety of the quay wall of sheet pile are the magnitude of strains of draw bars and displacement of key position of the structure, especially the horizontal displacement of the waling and coping beams.

### ***2.3 Open Type Wharf on Piles***

Usually, Open type wharf on piles is made up of piles, cross beams, longerons and slabs. Cross beams, longerons and slabs form the upper structure, and piles which send the load from upper structure into bearing stratum are not only substructure but also the foundation of the wharf. According to statistic, main failure or damage modes of open type wharf on piles are concrete cracking and spalling, steel bars being rust, unequal settlement and horizontal displacement of the whole structure, the torsion of upper structures (Wei et al., 2008).

The important reasons for the structural damage of open type wharf on piles are listed as follows.

1. Corrosion of reinforcing steel bars;
2. Overload;
3. Unequal settlement of stake-slope system.

To the safety of an open type wharf on piles, there two effects of the corrosion of reinforcing bars. One is that the corrosion would reduce the cross-section area of steel bars to reduce the bearing capacity of the components. The other is that the expansion of rust on steel bars can bring cracks along the bars and even make concrete protective layer peel off, and both of them will reduce the bond force. According to statistics, corrosion of reinforcing steel bars has been considered as the main factor for the bad durability of open type wharfs on piles. Not to be compared with gravity quay or quay wall of sheet pile, the open type wharf on piles is sensitive to overload. Overload could reduce the safety and durability of the wharf. On the one hand, components can be destroyed by overload directly. Usually, the components of beams and slabs can be damaged by the overload of heaped load or traffic load, and the stakes may be broken by the overload of ship impact load. On the other hand, excessive creaks may occur with the steel bars' plastic deformation caused by the overload, then the excessive creaks would accelerate the corrosion of the steel bars. Unequal settlement of stake-slope system of an open type wharf on piles may generate a whole slip or downward fraction force on piles, which may result in tensile failure in the piles.

According to the analyses above, the main monitoring index for an open wharf on piles should be the corrosion degree of its reinforcing steel bars. Structural damages caused by overload must be monitored too. As open structure, open wharf on piles has the similar structure health monitoring indicators with bridge. Unequal settlement of stake-slope system of an open type wharf on piles can be monitored through the displacement variation of the pile platform.

## **3 Application of the Health Monitoring for Wharfs**

### ***3.1 Health Monitoring System of Wharfs***

With the passage of time, material performance of wharfs will decrease; meanwhile, damage will accumulate in the structures gradually. The health monitoring for wharfs mean to obtain all kinds of structure characteristic information by non-destructive testing to realize the change caused by structure damages or depre-dates. One of the key goals of the health monitoring is to find out the critical point of security, and before this critical point the warning signal should be send out. The health monitor of wharf is a real-time course.

The structural health monitoring system for wharfs should includes three parts as follows: the sensor system which include the choice of sensors and the layout scheme of sensing network in wharf structure; the data gathering and analysis system which is made up of computers where all kinds of information sources and physical signals will be collected and pretreated, furthermore, the system can perform date decomposition and transformation according to requirement to obtain proper parameters which will be stored in certain form then; the control center which can forecast the unusual behaviors of wharf structure and diagnose whether, where and what the damage be.

### ***3.2 Displacement Monitoring***

The displacement monitoring is an important content in the structural health monitoring for seaport wharfs. There are many techniques can be used to monitor the displacement, for example, a total station can also do it in a certain way. But considering that the visible condition will be interfered by the routine operation in the wharf, the optical measurements do not suit longtime displacement monitoring, and the photoelectric hydrostatic leveling technique is proposed for it.

Usually, the displacement of seaport wharfs developed slowly, and it is expensive and unnecessary to apply the health monitoring always. Therefore, the integration of traditional routine detection techniques and real-time structural health monitoring is suggested for the displacement monitoring in wharfs. For example, to monitor the displacements of a quay wall of sheet pile, the periodic examination is enough, and if there are any abnormal displacements of key points or some big construction operation, which like dredging, the real-time displacement monitoring should be applied long as soon as possible.

As the effect of pile foundation, the unequal settlement of the pile-soil system is difficult to be measured by the vertical displacement of the pile platform in an open type wharf on piles; therefore, indirect monitoring method is applied. Be-

cause the unequal settlement of open type wharf on piles often brings negative friction to the piles near the shore, the monitoring can fulfilled indirectly by the monitoring of the long-term change of axial force of the piles. Furthermore, if there are any sign of the whole slide failure of the structure, the shear deformation of the slop must be monitored.

### ***3.3 Stress Monitoring and Vibration Monitoring***

There many techniques can be used to monitor strain and vibration of a structure, and their suitable sensors are various in kind, such as piezoelectric force transducer, acceleration transducer, impedance force sensor and strain-gauge transducer. In recent years, fiber optic sensors (FOSs) have been developed rapidly. FOSs has exhibited a lot of virtues such as flexibility, corrosion resistance, durability, multiplexing and electrical or magnetic interference immunity. In view of this, they are recommended for the embedded health monitoring sensors. Those sensors are used widely in engineering practice and will not be discussed in detail in this paper.

### ***3.4 Corrosion Monitoring***

Usually, the corrosion degree of steel bars in RC is detected by half-cell potential testing. The corrosion of steel bar in concrete is an electro-chemical process which creates anode area and cathode area its surface. According this method, the rust degree of one piece of steel bar's surface can be evaluated by the potential comparison with the referenced bluestone electrode. To seaport wharfs, the half-cell potential testing is unsuitable for the corrosion monitoring. On one hand, as the corrosion monitoring is a long period process, the durability of the half-cell potential testing system is usually not enough. On the other hand, by the influence of salty air in marine environment, the error-detecting of this method is too big to perform the monitoring. In view of this, effective method must be researched to perform the corrosion monitoring of the wharfs, and a new corrosion monitoring method is proposed in this paper. The theory of this method is introduced as follows.

The time during the corrosion development period and before the rust expansion crack appears is taken for the best early alarm time for corrosion monitoring. Before the time, the corrosion of steel bar develops slowly, and the reliability of the structure drops little. But after the time, the rust of steel bar develops quickly, the cross-sectional areas of steel bars and the adhesion between the steel bars and concrete decrease rapidly which make the reliability of the structure drops quickly. During the early alarm period, rust stain increases with time, and the stress of the

RC component will be changed by the expansion of the rust. After the relation between the stress and its distribution of the RC component and the corrosion degree of its steel bars is confirmed, corrosion monitoring can be performed through stress monitoring in the component by stress sensors.

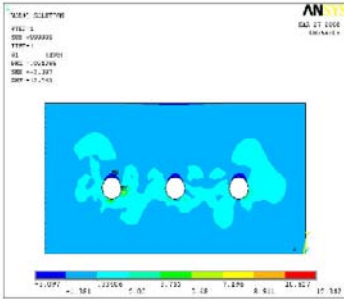


Figure 1. The stress distribution of the RC slab

To illustrate this theory, in this paper, a part of cross section of a slab in an open type wharf on piles was taken into analysis. With top constraint, the stress and stress distribution of the slab were analyzed by FEM software ANSYS. When the volume expansion coefficient of the steel bars was 1.1%, the stress distribution in the cross section was shown as Figure 1. Here, cracks appeared beside the side and underside of the bars, and the cracks didn't expand to the surface of the slab. The result showed that the stress in the cross section of the component was sensitive to the rust expansion of the steel bars. The stress distribution had some regular pattern and the stress was big enough to be measured by most stress sensors. Therefore, corrosion monitoring can be fulfilled by stress monitoring in the cross sections of the components.

### 3.5 Health Diagnoses System

The purpose of the health diagnoses system for wharf is to evaluate the structure's operation state, safety and durability. The health of wharfs are diagnosed not only by the wharf structure monitoring data, but also by other information, such as design files, relevant norms, relevant standards, the longtime operation information and the longtime management information.

1. For gravity wharf, the damage form and location of wharf can be diagnosed through soil mechanics principle based on the displacement monitoring in key points, then the health status can be evaluated.
2. For quay wall of sheet pile, according to the monitoring data of displacement of key points, strain and stress of the sheet piles and the draw bars, the damage

form and its location can be diagnosed through vertical elastic foundation beam model, and the health status can be evaluated.

3. For open wharf on piles, the health diagnoses system is similar to that of the big bridge. There are several methods can be applied on it, such as dynamic signature analysis method, model updating and system identification method, neural networks method and genetic algorithm method (Yang, 2006). In this paper, dynamic signature analysis method with stress monitoring in emphatic components is proposed as the health diagnose method. The dynamic signatures are the frequency, mode of vibration and strain of the wharf. The emphatic components of the wharf include the brace piles, front vertical piles and front cross beams. To calculate the reliability of the open wharf on piles, the data of the working load must be collected during the structure health monitoring.

## 4 Conclusions and Suggestions

In this paper, the structural health monitoring for the seaport wharf is studied and discussed, and some conclusions and suggestions are proposed as follow.

1. Based on the survey data and detection data, the failure mechanisms of three type seaport wharfs are discussed. Displacement of structural key points, corrosion of steel bars and structural dynamic response are proposed to be monitored for the health of these structures.
2. Because most of the on-service seaport wharfs haven't been designed and fabricated with structure health monitoring systems, then to monitor the health of them, the sensors are often stuck on the surface of the wharfs' components. In the coastal marine environment, the sensors and lines connected with them aging quick and easy to be damaged, and it is expensive to keep the whole monitoring system working well at all time. Hence, traditional detection techniques should be integrated into the structure health monitoring for wharfs. Some failure mode and failure moment of the structure can be forecasted by traditional detection techniques, and then the structure health monitoring will be applied on them efficiently.
3. A new method for corrosion monitoring in RC structures is proposed. In the method, corrosion monitoring in RC structures can be implemented through the stress monitoring which caused by the rust expansion before the throughout expansion cracks come into being. Stress distribution of a RC slab with rusty steel bars is analyzed, and some advices for the stress monitoring are proposed.
4. When dynamic signature analysis method is applied to the damage diagnosis of open wharfs on piles, the stakes are assumed as elastic stakes with the moment transmitting joints in earth foundation. The damp of water for stakes of the open wharfs must be taken into account in the diagnosis model, and to realize the real-time health diagnosis, tide must be taken into account too.

## References

- Ju Q. (2002). Port Engineering structure, Tianjin University Publication, China.
- Kersey A.D., Davis M.A., Patrick H.J. et al. (1997). Fiber-grating sensors. *Journal of Lightwave Technology*, 15(8).
- Li H.N., Li D.S. (2002, 2003). Safety assessment, health monitoring and damage diagnosis for structures in civil engineering. *Earthquake Engineering and Engineering Vibration*.
- Ma Y., Zhao L. P., Xu H. (2007). The actuality inspectability and test evaluation for wharf limiting state. *China Water Transport*.
- Wei B.L., Su X.H. (2008). Analysis of current situations of research on bridge structure health monitoring, *Northern Communications*, 01(045).
- Yang X.M. (2006). Research on performance monitoring system and damage identification method for civil engineering structures. Tianjin University, China.

*“This page left intentionally blank.”*

# Quantity of Flow through a Typical Dam of Anisotropic Permeability

R. R. Shakir<sup>1\*</sup>

<sup>1</sup>Thi-Qar University, Iraq

**Abstract.** In this research a computer program based on finite element method is used as a tool to study the effect of anisotropic permeability on the flow of water through an earth dam. The program has been checked with the typical solution of constant permeability of Dupuit solution, which is giving a good agreement with it. The program is used to compute the quantity of flow through a soil with anisotropic permeability for different cases of upstream and downstream and length of flow. Relationships between normalized quantity of seepage through dam and downstream-upstream head ratio are presented for an-isotropic ratio  $K_x/K_y$  (20,10,5, 4,2,10,5,0.1,0.05). According to the obtained results, anisotropic permeability plays an important role in calculating an accurate value of the quantity of seepage, and should be considered in design.

**Keywords:** finite element, earth dam, anisotropic, quantity of seepage, permeability, layers

## 1 Introduction

Practically, the permeability values are taken constant in designing of dams, but really it is non-homogeneous and an isotropic. To study the effect of anisotropic permeability on the quantity of seepage through dam, program of finite element is used to calculate the quantity of seepage. Finite element formulation of free surface flow includes two main approaches: 1) fixed mesh algorithms in which the element properties are iteratively adjusted within a fixed mesh to reflect the location of the free surface, and 2) adaptive mesh algorithms in which the element properties are held constant and the mesh is iteratively deformed to match the free surface profile. This boundary can be found by iteration in several ways for example a fixed mesh can be used and nodes can be separated into active and inactive ones depending upon whether fluid exists at that point.

---

\* Corresponding author, e-mail: rsshakir@yahoo.com

The numerical methods for solving free-surface seepage problems are not commonly used in engineering practice, mainly because they require rather complicated derivations and implementations. Nonlinear numerical techniques include adaptive mesh using finite difference method (Cryer, 1970), finite element method (Finn, 1967; Neuman and Witherspoon, 1970) and fixed mesh with finite element method (Bathe and Khoshgoftaar, 1979; Kikuchi, 1977; Oden and Kikuchi, 1980) are used to solve the free surface that delimits the flow boundaries. Another method called "Extended Pressure" (EP) is developed by (Bardet and Tobita, 2002) and is used by finite difference method to solve different problems. The EP method was applied to various types of free-surface seepage problems and numerical solution schemes (Lacy and Prevost, 1987; Borja and Kishnani, 1991). Other investigators such as (Cividini and Gioda, 1990; Billstein et al., 1999) applied other numerical techniques to determine the quantity of seepage and locus of the phreatic line.

## 2 Hydraulic Conductivity

It is well known that soil exhibit high variability in hydraulic properties. It is paramount to take this variability into account, when solving the problem of seepage quantity through dam. Several method could be depended on to include the effect of variability such as randomly model, layers model, anisotropic model.

Griffiths and Fenton (1993) and Fenton and Griffiths (1995) proposed a random model of an earth dam and investigated the effects of spatially random hydraulic properties on two quantities of classical interest: i) the total flow rate through the dam, and ii) the amount of drawdown of the free surface at the downstream face of the dam. According to Fenton and Griffiths (1995) the computation of flow through an earth dam is complicated by the fact that the location and profile of the free surface is not known *a-priori* and must be determined iteratively. Nevertheless, the finite element code requires to perform such analysis is really quite straightforward, involving a simple Darcy flow model and iteratively adjusting the nodal elevations along the free surface to match their predicted potential heads (Smith and Griffiths, 1998). An alternative approach was suggested employing a fixed mesh (Lacy and Prevost, 1987).

In this paper we deal with permeability as a ratio between vertical to horizontal permeability and investigate the effect of permeability on the quantity of seepage. The fixed mesh method developed by Smith and Griffiths (1998) is used since its simplicity.

### 3 Simplified Fluid Flow Steady State

According to Smith and Griffiths (1998) Steady flow through the dam or beneath the water retaining structure is expressed as:

$$K_x \frac{\partial^2 \phi}{\partial x^2} + K_y \frac{\partial^2 \phi}{\partial y^2} = 0 \tag{1}$$

where  $\phi$  is fluid potential and  $K_x, K_y$  are permeability in x, y direction.

$$Kp\phi = q \tag{2}$$

The continuous variable  $\phi$  is approximated in terms of nodal values,  $\phi_1, \phi_2, \phi_3, \phi_4$  through simple functions of the space variable called “shape functions”. That is

$$\phi \approx N_1\phi_1 + N_2\phi_2 + N_3\phi_3 + N_4\phi_4 \tag{3}$$

In matrix form it can be written as:

$$\phi \approx \begin{bmatrix} N_1 & N_2 & N_3 & N_4 \end{bmatrix} \begin{Bmatrix} \phi_1 \\ \phi_2 \\ \phi_3 \\ \phi_4 \end{Bmatrix} \tag{4}$$

For the case of four node rectangular element the shape function can be derived as:

$$N_1 = \left(1 - \frac{x}{a}\right)\left(1 - \frac{y}{b}\right), N_2 = \left(1 - \frac{x}{a}\right)\frac{y}{b}, N_3 = \frac{x}{a}\frac{y}{b}, N_4 = \frac{x}{a}\left(1 - \frac{y}{b}\right) \tag{5}$$

From the semi discretisation of partial differential equation, (Equation 1) and application of Galerkin’s method, Equation 1 could be written as follows:

$$\iint \begin{Bmatrix} N_1 \\ N_2 \\ N_3 \\ N_4 \end{Bmatrix} \frac{\partial^2}{\partial x^2} \{N_1 \ N_2 \ N_3 \ N_4\} \begin{Bmatrix} \phi_1 \\ \phi_2 \\ \phi_3 \\ \phi_4 \end{Bmatrix} dx dy + \iint \begin{Bmatrix} N_1 \\ N_2 \\ N_3 \\ N_4 \end{Bmatrix} \frac{\partial^2}{\partial y^2} \{N_1 \ N_2 \ N_3 \ N_4\} \begin{Bmatrix} \phi_1 \\ \phi_2 \\ \phi_3 \\ \phi_4 \end{Bmatrix} dx dy \tag{6}$$

Integration by parts of the weighted form of the (Equation 6) leads to integral:

$$\iint N_i \frac{\partial^2 N_j}{\partial x^2} dx dy = - \iint \frac{\partial N_i}{\partial x} \frac{\partial N_j}{\partial x} dx dy + \int_S N_i \frac{\partial N_j}{\partial x} l_n dS \tag{7}$$

where  $l_n$  is the direction cosine of the normal to boundary S and we assume that the contour integral is zero between elements.

$$Kp = \iint T^T K T dx dy \tag{8}$$

where K is matrix of permeability

$$k = \begin{bmatrix} K_x & 0 \\ 0 & K_y \end{bmatrix}, T = \begin{bmatrix} \frac{\partial N_1}{\partial x} & \frac{\partial N_2}{\partial x} & \frac{\partial N_3}{\partial x} & \frac{\partial N_4}{\partial x} \\ \frac{\partial N_1}{\partial y} & \frac{\partial N_2}{\partial y} & \frac{\partial N_3}{\partial y} & \frac{\partial N_4}{\partial y} \end{bmatrix}, T^T = \begin{bmatrix} \frac{\partial N_1}{\partial x} & \frac{\partial N_1}{\partial y} \\ \frac{\partial N_2}{\partial x} & \frac{\partial N_2}{\partial y} \\ \frac{\partial N_3}{\partial x} & \frac{\partial N_3}{\partial y} \\ \frac{\partial N_4}{\partial x} & \frac{\partial N_4}{\partial y} \end{bmatrix} \tag{9}$$

For a given permeability values, the free surface location and flow through the earth dam are computed using a two-dimensional iterative finite element model derived by (Smith and Griffiths, 1997), Program 7.3. The elements are 4-nodes quadrilaterals and the mesh is deformed on each iteration until the total head along the free surface approaches its elevation head above a pre-defined horizontal datum. Convergence is obtained when the maximum relative change in the free surface elevation at the surface nodes becomes less than 0.005.

### 4 Classical Solution

The Dupuit theory of unconfined flow stems from two assumptions first made by Dupuit in 1863. Dupuit assumed that: 1) for small inclinations of the line of seepage the streamlines can be taken as horizontal (hence the equipotential lines approach the vertical lines; and 2) the hydraulic gradient was equal to the slope of the free surface and was variable with depth.

A variety of equations have been developed to calculate the amount of seepage of earth dams placed on an impervious base. To find the amount of seepage from any vertical profile of the dam the following Dupuit equation is used

$$q = k \frac{h_1^2 - h_2^2}{2L} \tag{10}$$

where  $q$  is the Darcy flux or flow rate,  $k$  is the hydraulic conductivity or permeability,  $h$  is the upstream head,  $h_1$  is the downstream head,  $L$  is the length of the flow path. This equation shows that the shape of free surface is parabolic. The resulting free water surface is generally called as Dupuit parabola (Harr, 1962).

### 5 Verification

In order to use finite element program as a tool for case studying, a simple problem or even complicated problem should be solved firstly and should be compared with the solution available in literatures. The exact solution for the discharge quantity for a section with vertical slopes including the effects of tail water, was represented by chart. Figure 1 shows the schematic diagram for the problem of rectangle with upstream  $h$ , and downstream head  $h_1$ .

Figure 2 shows the finite element mesh consist of 48 elements where  $L$  represent length of the flow. The problem was solved for different ratio of upstream and downstream and also different length ( $L/h$ ) 1, 1.5, 2.5, 3 and 3.5. The solution for this problem is available in literatures (Harr, 1962). The finite element program gives excellent agreement with the analytical solution. Figure 3 shows the relations between quantity seepage with head ratio for different length of flow. The result shows an excellent agreement.

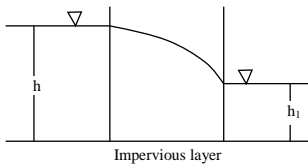


Figure. 1. Schematic diagram for the steady state problem

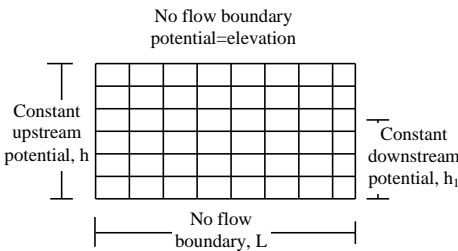


Figure. 2. The finite element mesh

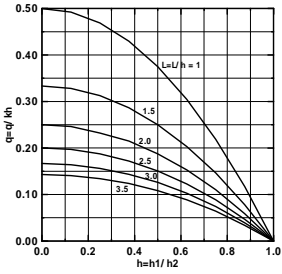
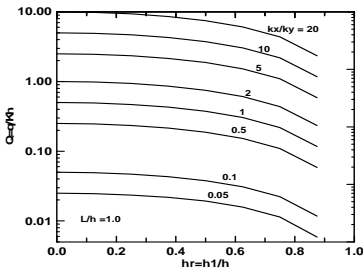


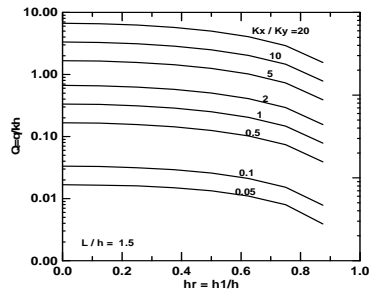
Figure. 3 The relation between quantity of seepage and pressure head ratio

### 6 Soil of Anisotropic Permeability

If the coefficient of permeability doesn't change with directions and if it has constant value along each direction, the soil said to be homogeneous and anisotropic with respect to permeability property. Most soils are anisotropic to some degree. Sedimentary soils often exhibit thin alternating layers. Stratification may result from particle orientation. Generally, in homogeneous natural deposits, the coefficient of permeability in the horizontal direction is greater than that in the vertical. In the earth dam the fill constructed in layers which make the permeability in x direction greater than the permeability in y direction. The example of typical dam type was used to investigate the effect of permeability anisotropic. This problem was solved for different types of flow length and anisotropic permeability. Anisotropic permeability ratios ( $K_x/K_y$ ) were 20, 10, 5, 2, 1, 0.5, 0.1, 0.05 and the flow length ratios were 1, 1.6, 2, 2.5, 3, 3.5. Figure 4a shows that normalized quantity of seepage approximately equal to ten ( $Q=10$ ) for ( $K_x/K_y = 20$ ) and ( $Q=0.3$ ) for ( $K_x/K_y = 1$ ). The quantity of seepage shows high different values as anisotropic permeability ratio increases.



(a)



(b)

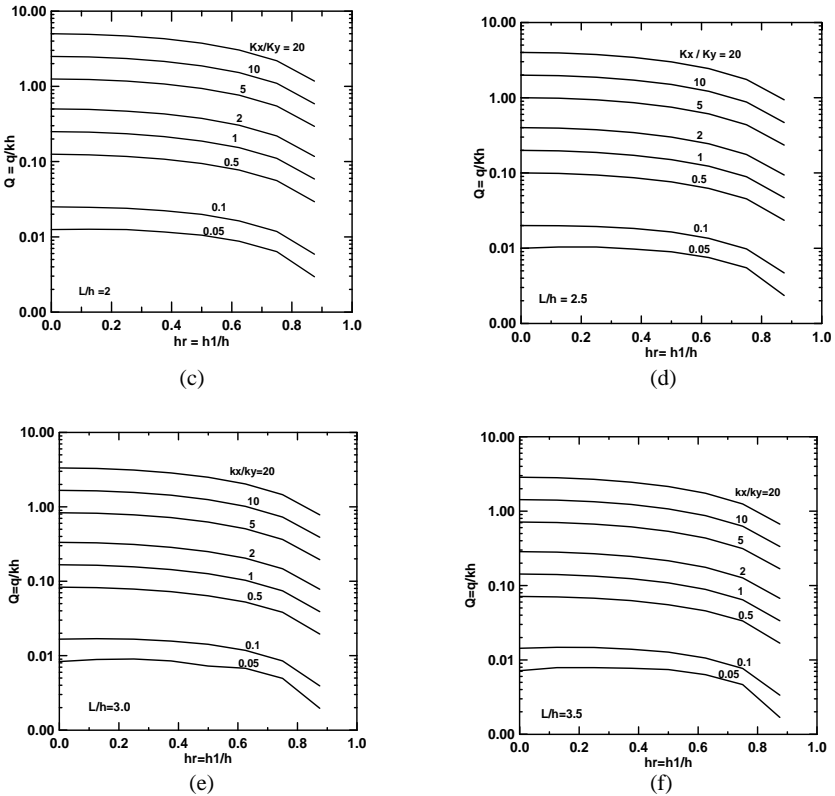


Figure 4. Quantity of seepage for different ratio of anisotropic permeability flow length; a: (L/h=1.0); b:(L/h=1.5) ; c:(L/h=2.0);d: (L/h=2.5); e: (L/h=3.0); f:(L/h=3.5)

## 6 Conclusions

Finite element computer program with fixed mesh method was used successfully to study the effect of anisotropic permeability on the quantity of seepage and free surface line locus in the earth dam. It was concluded that the anisotropic permeability has a great effect on both the quantity of seepage and surface line. For typical case of rectangular dam when the ratio  $h_1/h$  is approximately 0.7 the program results show obvious reduction in quantity of seepage. The computer program results were verified with the case of constant permeability that can be solved by classical solution such as Dupuit theory. Different cases of dam are used, and the results show obvious effect of anisotropic. It is strongly recommended to consider the anisotropic permeability in the design purposes.

## Acknowledgments

This research was achieved under support of Thi-Qar University.

## References

- Bathe K. J., and Khoshgoftaar M. R. (1979). Finite element free surface seepage analysis without mesh iteration. *International Journal for Numerical and Analytical Methods in Geomechanics*, 3:13–22.
- Bardet, J. P., and Tobita, T. (2002). A practical method for solving free surface seepage problems. *Comp. Geotechn.*, 29, 451–475.
- Billstein, M., Svensson, U., and Johansson, N. (1999). Application and validation of a numerical model of flow through embankment dams with fractures: Comparison with experimental data. *Can. Geotech. J.*, 36, 651–659.
- Borja R. I., Kishnani S. S. (1991). On the Solution of elliptic free-boundary problems via Newton's method. *Computer Methods in Applied Mechanics and Engineering*, 88:341–61.
- Cividini, A., and Gioda, G. (1990). On the variable mesh finite element analysis of unconfined seepage problems. *Geotechnique*, 40(3), 523–526.
- Cryer C. W. (1970). On the approximate solution of free boundary problems using finite differences. *Journal of the Association for Computing Machinery*, 17(3):397–411.
- Finn W. D. L. (1967). Finite-element analysis of seepage through dams. *Journal of the Soil Mechanics and Foundations Division*, ASCE, 93(SM6):41–8.
- Fenton, G. A., and Griffiths, D. V. (1995). Flow through earthdams with spatially random permeability, *Proceedings of the 10th ASCE Engineering Mechanics Conference*, Boulder, Colorado, 341–344.
- Griffiths, D. V., and Fenton, G. A. (1993). Seepage beneath water retaining structures founded on spatially random soil, *Géotechnique*, 43(6), 577–587, 1.
- Harr M. E. (1962). *Ground water and seepage*, McGraw-Hill, New York, 315.
- Kikuchi N. (1977). An analysis of the variational inequalities of seepage flow by finite-element methods. *Quarterly of Applied Mathematics*, 35:149–63.
- Lacy S. J., and Prevost J. H. (1987). Flow through porous media: a procedure for locating the free surface. *International Journal for Numerical and Analytical Methods in Geomechanics*, 11:585–601.
- Neuman S. P., and Witherspoon P. A. (1970). Finite element method of analyzing steady seepage with a free surface. *Water Resources Research*, 6(3):889–97.
- Oden J. T., and Kikuchi N. (1980). Recent advances: Theory of variational inequalities with applications to problems of flow through porous media. *International Journal of Engineering Science*, 18:1173–284.
- Smith and Griffiths (1998). *Programming the finite element method*, John Wiley & Sons Canada; 3rd Edition (January 1998).